

HEAT POWERED CYCLES 2021
Conference Proceedings
Final Version



Heat Powered Cycles Conference
University of the Basque Country, Bilbao, Spain
10th - 13th April 2022

Published by Heat Powered Cycles

These Conference Proceedings have been prepared with the manuscripts that were accepted by the Organizing Committee of the Ninth Heat Powered Cycles Conference. This material aims to assist authors and presenters to easily access the presentations and have a brief explanation regarding the subject of each accepted work, including Keynote Lectures and regular Oral Presentations.

Art Work and information related to the Conference, Organizing Committee, Executive Committee, and Advisory Board were taken from the conference's website.

Edited by:

Prof. Dr. Roger R. Riehl - GamaTech Thermal Solutions - Brazil

Reviewed by:

Prof. Dr. Jesús María Blanco Ilzarbe - Universidad del País Vasco / E.H.U., Bilbao, Spain

Dr. Jesús Esarte San Martín - NAITEC. Centro Tecnológico en Automoción y Mecatrónica, Navarra, Spain

Prof. (FH) Dr.-Ing. Markus Preißinger - Energy Research Center, University of Applied Sciences Vorarlberg, Austria

HEAT POWERED CYCLES 2021
Conference Proceedings - *Final version*

Copyright©2021 is claimed by Heat Powered Cycles for the printed cover, layout, and foreword of the publication, which must not be copied or distributed in any way without the permission of Heat Powered Cycles. Notwithstanding these claims and conditions, individual articles contained herein remain entirely the copyright© property of the authors and permission must be sought from them to reproduce or distribute any part in any way.

Welcome to the 9th Heat Powered Cycles Conference

This is the 9th Heat Powered Cycles Conference. The first edition of the conference was held at Nottingham in 1997. This time the event was co-organized by the *University of the Basque Country*, (Bilbao, Spain), *The University of Applied Sciences, Vorarlberg*, (Austria), and *GamaTech Thermal Solutions*, (Brazil). The conference took place at the University of the Basque Country and hosted by the Department of Energy Engineering at the University of the Basque Country by *Prof. Jesús María Blanco Ilzarbe*. In addition to formal presentations of technical papers, including invited Keynote papers, the event includes poster sessions and two Special Sessions, being one related to *Intelligent Thermal Energy Systems* and *The Energy in the Post-Covid Scenario*, along with a full social program. The conference is concerned with scientific and technological innovations relating to the efficient and economic use of heat, derived from all its sources, for the production of cooling, heating, and mechanical power either independently or co-generatively.



Faculty of Engineering, University of the Basque Country

Subject areas of particular interest include; hybrid cycles, ORCs, Stirling cycle machines, thermo-acoustic engines and coolers, sorption cycle refrigerators and heat pumps, jet-pump (ejector) machines, temperature amplifiers (heat transformers), chemical heat pumps, new working fluids, mass and heat transfer phenomena, desalination of brackish water and seawater, compact heat exchanger research (including foams and other micro-channel research), thermo-economics, process optimisation and modelling, process, and cycle thermodynamics.

History



2018: Bayreuth

The eighth Heat Powered Cycles conference was hosted by the Bayreuth University, Germany.



2016: Nottingham

The seventh Heat Powered Cycles conference was co-organised by the Universities of Nottingham and Bristol. The conference was held at the University of Nottingham and was hosted by the HVASCR & Heat Transfer Group.



2012: Alkmaar

The sixth Heat Powered Cycles conference was hosted by Energy research Center of the Netherlands (ECN) in the Golden Tulip Hotel in Alkmaar.



2009: Berlin

The fifth Heat Powered Cycles conference was hosted by the Technical University of Berlin.



2006: Newcastle

The fourth Heat Powered Cycles conference was hosted by University upon Tyne Newcastle.

Three Special Issues after HPC 2021

The Organizing Committee of the Heat Powered Cycles Conference selected some of the presented manuscripts after the conference was finished. They were invited for publication in a special issue of *Thermal Sciences and Engineering Processes* (TSEP - Elsevier), and *Cleaner Energy Systems* (CLES - Elsevier). The selection of the manuscripts was based on their quality and presentation. The selected manuscripts underwent a normal review process for those journals.

Organizing Committee

Local Conference Chair

Prof. Dr. Jesús María Blanco Ilzarbe - Universidad del País Vasco / E.H.U., Bilbao, Spain

Conference Co-Chair

Prof. (FH) Dr.-Ing. Markus Preißinger

illwerke vkw Endowed Professor for Energy Efficiency, Energy Research Center, University of Applied Sciences Vorarlberg, Austria

Program and Review Chair

Prof. Dr. Roger R. Riehl

Faculty of Thermal/Fluid Sciences and Thermal Control Specialist, National Institute for Space Research - INPE/DMC - Brazil

Executive Committee

Prof. Dr. Roger R. Riehl, National Institute for Space Research - INPE/DMC - Brazil

Prof. (FH) Dr.-Ing. Markus Preißinger, Energy Research Center, University of Applied Sciences Vorarlberg, Austria

Prof. Dr. Ian W. Eames, University of Nottingham, UK

Dr. Mike Tierney, University of Bristol, UK

Scientific Advisory Panel

Adriano Milazzo, University of Florence, Italy

Angelo Freni, CNR-ITAE, Italy

Bob Critoph, University of Warwick, UK

Brian Agnew, University of Newcastle, UK

Christian Schweiger, Munich University of Applied Sciences, Germany

Christos Markides, Imperial College, London UK

David A. Reay, David Reay & Associates, UK

David Hann, Nottingham University, UK

Francis Meunier, CANAM, Paris, France

Giovanni Restuccia, CNR-ITAE, Italy

Giulio Santori, University of Edinburgh, UK

Guangming Chen, Zhejiang University, China

Hisham Sabir, QNRF, Qatar

Ian Eames, University of Nottingham, UK

Joan Carlos Bruno, Universitat Rovira i Virgili, Spain

Larisa Gordeeva, Boreskov Institute of Catalysis

Markus Preißinger, Vorarlberg University of Applied Sciences, Austria
Michel van der Pal, ECN, Alkmar, Netherlands
Mike Tierney, University of Bristol, UK
Philip Davies, Aston University, UK
Phillipe Blanc-Benon, École Centrale de Lyon , France
Pierre Neveu, University of Perpignan, France
Rayah Al-Dadah, University of Birmingham, UK
Robert Keolian, Penn State University, USA
Roger R. Riehl , National Institute for Space Research – INPE/DMC, Brazil
Ruzhu Wang, SJTU, Shanghai, China
Steven Garrett, Penn State University, USA
Yann Bartosiewicz , University Catholique de Louvain UCL, Belgium
Yukitaka Kato, Tokyo Institute of Technology, Japan
Yuri Aristov, Boreskov Institute of Catalysis, Russia
Zacharie Tamainot-Telto , University of Warwick, UK

The 9th Heat Powered Cycles (HPC) Conference was sponsored by the following partners.



EUSKO JAURLARITZA
GOBIERNO VASCO

EKONOMIAREN GARAPEN,
JASANGARRITASUN
ETA INGURUMEN SAILA

DEPARTAMENTO DE DESARROLLO
ECONÓMICO, SOSTENIBILIDAD
Y MEDIO AMBIENTE

eman ta zabal zazu



Universidad
del País Vasco

Euskal Herriko
Unibertsitatea

ikerlan

MEMBER OF BASQUE RESEARCH
& TECHNOLOGY ALLIANCE



IDOM



Bilbao



entropy

an Open Access Journal by MDPI

FH Vorarlberg
University of Applied Sciences



Table of Contents

KEYNOTES	1
Steamy Issues – why the steam engine was the first implemented heat engine and its impact on future energy systems - A. P. Weiß, Ph. Streit, T. Popp	2
Multi-scale modelling of ejector refrigeration systems - Giorgio Besagni	3
My thermodynamic journey from Carnot to Gibbs – A physical interpretation of maximum work - Dr. Robert T. Hanlon	27
Adsorption Heat Pumps: Challenges and Future Perspectives - Dr Z. Tamainot-Telto	29
Adsorption for Heat Conversion and Storage: What Have We Learned over the Past Decade of this Century? - Yu.I. Aristov	30
 MANUSCRIPTS	 36
An experimental investigation of oily wastewater treatment in a bubble column humidifier using an improved method for measuring humidity - E. Eder, F. Stemer, D. Brüggemann, M. Preißinger	37
Projects for the desalination of brackish water and seawater at the Faculty of Engineering in Bilbao - Natalia Alegría and Igor Peñalva	46
The Potential of Heat and Mass Recovery for Adsorption Heat Transformers - M. Engelpracht, D. Rezo, P. Postweiler, A. Gibelhaus and A. Bardow	57
On heat regeneration limitations in heat engines with dense working fluids - N. Mügge, A. Kronberg, M. Glushenkov and E. Y. Kenig	72
An experimental study on the effect of the heat and mass transfer characteristic lengths on the adsorption dynamics in two different open-structured plate heat exchangers - Makram Mikhaeil, Matthias Gaderer and Belal Dawoud	88
Waste heat recovery systems with isobaric expansion technology using pure and mixed working fluids - S. Roosjen, M. Glushenkov, A. Kronberg and S.R.A. Kersten	102
Experimental study of an isobaric expansion engine-pump - M. Glushenkov, A. Kronberg	117
Numerical study on the influence of different H ₂ /CH ₄ mixtures and air-fuel equivalence ratios in micromix-type burners for industrial boilers - G. Lopez-Ruiz, I. Álava, J. M. Blanco	131
Effect of residual air on dynamics of temperature- and pressureinitiated adsorption cycles for heat transformation - I. Girnik and Y. Aristov	144

Development of a latent heat storage for industrial application based on adipic acid – graphite composite - M. van der Pal, K. Ingenwepelt and R. de Boer	151
The cost of manufacturing adsorption chillers - AL-Hasni. Shihab, Grant. Rachael and Santori. Giulio	160
Environmental Process Optimisation of Adsorption-based Direct Air Capture of CO ₂ - P. Postweiler, M. Engelpracht, A. Gibelhaus and N. von der Assen	171
Evaluation of ad/desorption dynamics of S-PEEK/Zeolite composite coatings by T-LTJ method - D. Palamara, V. Palomba, L. Calabrese, A. Frazzica	186
Experimental characterization of a full-scale geothermal adsorption heat pump - A. Bonanno, V. Palomba, S. Löwe, U. Wittstadt, A. Frazzica, Davide La Rosa	194
Modelling and design of an ammonia/salt resorption domestic heat pump - R.W. Moss and R.E. Critoph	207
NMR study of water exchange in MOFs for adsorption heat transformation Processes - S. Pizzanelli, A. Freni, F. Martini, L. G. Gordeeva, M. V. Solovyeva and C. Forte	221
Early Stage Adsorber Material Selection for Adsorption Heat Transformers - E. Piccoli, V. Brancato, A. Frazzica, F. Maréchal, S. Galmarini	226
An analytical design tool for pin fin sorber bed heat and mass exchanger - MJ. Darvish, H. Bahreghand and M. Bahrami	242
Experimental Investigation of a Gas Driven Absorption Heat Pump and In-Situ Monitoring - Camila Dávila1, Nicolas Paulus and Vincent Lemort	257
3D printed adsorption heat transformer - AL-HASNI. Shihab, MANGANO. Enzo and Santori. Giulio	271
Testing of a falling-film evaporator for adsorption chillers - T. Toppi, M. Aprile, M. Motta, S. Vasta, W. Mittelbach and A. Freni	282
Experience from the operation of an absorption power cycle with LiBr working fluid and its prospects for future - Vaclav Novotny, Jan Spale, Jan Pavlicko, Jan Novotny, Michal Kolovratnik	290
Testing of a Carbon-Ammonia Gas-Fired Heat Pump - S.J. Metcalf, A.M. Rivero-Pacho and R.E. Critoph	305
Ammonia-Salt Reactions for Heat Pumping and Thermal Transforming Applications - S. Hinners, G. H. Atkinson, R. E. Critoph and M. Van der Pal	310
Extended Frequency Response Analysis for Loading and Temperature Dependent Heat and Mass Transfer Evaluation in Adsorbent Coatings - E. Laurenz, G. Földner, A. Velte and L. Schnabel	321

Control of solution flow rate in single stage absorption chillers - Stefan Petersen, Walther Hüls Guido	324
Composite “LiCl/Vermiculite” for Adsorption Thermal Batteries: Giant acceleration of methanol sorption due to the adsorbent modification - S. Strelova, L. Gordeeva, A. Grekova and Yu. Aristov	335
Composite sorbents Salt/MIL-101(Cr) for atmospheric water harvesting - I.O. Krivosheeva, M.V. Solovyeva, Yu. Aristov and L.G. Gordeeva	350
Assessment of an adsorption based solar heating system for domestic heating applications in Ladakh - Sai Yagnamurthy	362
Stacked adsorption module with aluminium composite foil: Simulation and experimental evaluation of a novel concept - E. Laurenz, M. Linke, A. Velte, R. Volmer, J. Weise and G. Földner	373
Thermal operation map for the mechanical discharging process of the Lamm-Honigmann Energy Storage - E. Thiele1, F. Ziegler	375
Thermodynamic Evaluation of an Experimental WHR ORC Test Rig with Quasi-Impulse Cantilever Turbine - T. Popp, A. P. Weiß, F. Heberle, P. Streit and D. Brüggemann	395
Parametric simulation of a solar coupled heat pump system - G.E. Dino, A. Frazzica, D. Chèze, A. Gabaldón, D. Ntimos, G. Tardioli, F. Fuligni	407
CO ₂ Power Cycle Assessment for Low Grade Waste Heat Recovery - V. Wolf, E. J. Rabadàn Santana and S. Leyer	423
Design, Build and Initial Testing of a Novel Energy Management System - T. Weller, M. Johnson, F. Trebilcock, S. Lecompte and D. Bauer	436
An Improved Thermodynamic Model for Supersonic Ejectors - A. Metsue, R. Debroeyer, S. Poncet, Y. Bartosiewicz	449
Propane-isobutane mixtures in heat pumps with higher temperature lift: an experimental investigation - J. Quenel, M. Anders and B. Atakan	463
Failure detection in a water treatment system of a biomass CHP - G.Prokhorskii, C.Stegh, V.Seiler, M.Netzer and M.Preißinger	474
Theoretical investigation of the potential of capillary heat exchangers in heat pumps - M. Aps, F. Durmus and B. Atakan	485
Predictive maintenance in thermal power plants: a systematic literature survey - M. Preißinger	496
A Steam Rankine Cycle Pilot Plant for Distributed High Temperature Waste Heat Recovery - F. Raab, H. Klein, F. Opferkuch	516

Experimental Development of Additively Manufactured Turboexpanders towards an Application in the ORC - Jan Spale, Vaclav Novotny, Jan Novotny, Andreas P. Weiß, Michal Kolovratnik	524
Artificial Neural Network based marine diesel engine modelling - Joseba Castresanaa, Gorka Gabiñaa, Leopoldo Martinb, Zigor Uriandob	539
Algorithm-Based Optimization for Energy-Efficient Operation of Refrigeration Systems - J. Bentz, T. Hamacher, C. Schweigler	554
Optimal volume fraction of support material in a heat transferenhanced composite for thermochemical energy storage - S. Funayama, T. Harada, H. Takasu and Y. Kato	566
Piston compressors driven by isobaric expansion heat engines - A. Kronberg, M. Glushenkov	572
Annual energy analysis of a trigeneration solar system using radiative cooling in Mediterranean climate - M. Noro, S. Mancin and R. Riehl	587
Algorithmic optimisation of the electrical power output of a low-cost, multicore thermoacoustic engine with varying resonator pressure - F. Huntingford, W. Kisha	600
Electro Deionization for treatment of Condensate of Steam Bottoming Cycles - M. Mazzetti and G. Skaugen	615
Solar tower plant extra electricity production potential by means of harnessing excess solar energy - U. Oyarzabal, A. Erkoreka, I. Gomez-Arriaran, D. Novales, B. Herrazti ..	622
Modelling of a Food Processing Plant for Industrial Demand Side Management - P. Wohlgenannt, G. Huber, K. Rheinberger, M. Preißinger, P. Kepplinger	638
A Cloud-Based Flexibility Estimation Method for Domestic Heat Pumps - C. Baumann, G. Huber, M. Preißinger, and P. Kepplinger	650
Numerical Investigation of Desiccant Cooling Using Aluminium Fumarate Metal Organic Framework Material - Andrew N. Aziz, Saad Mahmoud, Raya Al-Dadah, Ibrahim Albaik	662
Solar cooling system for a buildings using parallel ejectors - M. Falsafioon, M. Poirier and P. Simard	673
Vortex Tube Thermodynamic Model Operating with Two-Phase Fluids - A. Mansour, J. Lagrandeur, S. Poncet	679
Design and experimental validation of a R290 dual-source reversible heat pump prototype - X. Peña, L. Alonso, J. Iturralde and A. Agirre	690
Stability of Nanofluids Towards Their Use in Thermal Management Systems - Roger R. Riehl and S M Sohel Murshed	705

Influence of nanofluid on a connected thermosyphons - M.Aresti, J.Estella, A. Azcárate, L.Hurtado, J.Esarte	715
POSTERS	720
Numerical model of a latent heat storage unit for industrial application - K. Ingenwepelt, M. van der Pal	721
Design and characterisation of low NOx hydrogen diffusion burners for domestic and industrial heating applications - G.López-Ruiz, I. Álava and J.M. Blanco	722
Economic analysis of Absorption Heat Transformers and Compression Heat Pumps for industrial heat upgrade - José Luis Corrales Ciganda and Asier Martínez-Urrutia	724
LHP model with structured primary wick - J. Esarte, J.M ^a . Blanco, U. Izquierdo	725
Structural properties of a transformer oil-based nanofluid under an external electric field - neutron reflectometry study - M. Karpets, M. Rajnak, V. Petrenko, I. Gapon, M. Avdeev, Z. Mitroova, L. Bulavin, M. Timko and P. Kopcansky	726
Optimization of the energy balance at desalination plants - M. Urrestizala, J. Azkurreta	729
Transformation and installation of CNG refuelling for a Bilbao River´s tourist boat - Alex Segura Coronado, Jesús M ^a Blanco Ilzarbe and Roberto González Andrés	734
Optimizing Carnot battery configuration for waste heat recovery integrated system with ORC - Miroslav Rathan, Jan Spale, Vaclav Novotny	735
Assessment and comparison of a power-to-heat-to-power (P2H2P) storage systems based on resistance heating and Brayton heat pump using liquid salts for energy storage - Václav NOVOTNÝ, František HRDLIČKA	736
Absorption power cycle with aqueous salt solution for low temperature heat utilization - Vaclav NOVOTNY, Michal KOLOVRATNIK, Hung-Yin TSAI	737
Sensitivity analysis of supercritical CO2 cycles for future high-temperature concentrating solar power plants - D. Novales, A. Erkoreka, I. Flores, U. Oyarzabal and I. Gomez-Arriaran	738
Desalination in the management of the hydraulic resources - I. Arrieta, L. Davila, J. del Olmo, A. García, U. Ozaita, E. Parrón, A.E. Quiñones, I. Sever	739
CFD Study on the Impact of Combustion and Radiation Models in Aluminium Scrap Furnaces - G. Lopez-Ruiz, I. Garcia-Beristain, J.M. Blanco Ilzarbe	740
Desalination Of Brackish Water And Seawater In Spain By The Faculty Of Engineering In Bilbao - M. Díez, D. Herrero, X. Landa, A. Martínez, O. Peña, J. San Juan, P. San Pelayo, I. Serna	741
Solar Thermal Façades and Heat Pumps; A case study - P. Elguezabal, J.M. Blanco and J.C. Chica	743

Analysis of the heat transfer during the filling and cooling of die cast pieces with large surface through CFD - Primitivo Carranza Torme and Jesús M ^a Blanco Ilzarbe	744
Evaluation of burning alternative fuels in thermal power plants as a previous step towards a full scale implementation - Francisco Peña Fernandez and Jesús M ^a Blanco Ilzarbe	745
Experimental Study of a Two-Stage Compression R744 refrigeration System with Vapour Injection and Inter-Cooling - J. Vega, S. Gendebien and V. Lemort	746

Keynote Lectures

Steamy Issues – why the steam engine was the first implemented heat engine and its impact on future energy systems

A. P. Weiß*¹, Ph. Streit¹, T. Popp²

¹ Centre of Excellence for Cogeneration Technologies, Technical University of Applied Sciences Amberg-Weiden, Kaiser-Wilhelm-Ring 23, 92224 Amberg, Germany

² Center of Energy Technology, University of Bayreuth, Universitätsstraße 30, 95447 Bayreuth, Germany

*Corresponding author: a.weiss@oth-aw.de

Abstract

Thomas Newcomen invented the very first steam engine in 1712 - over three hundred years ago. Fifty years later it was significantly improved by James Watt enabling the First Industrial Revolution. Today, steam power plants cover about 50% of world's annual electricity demand. Modern nuclear or fossil fired steam power plants are steam engines as well – although equipped with large turbo generators instead of a reciprocating piston engines. The authors discuss the reasons why the steam engine was invented and introduced significantly before e.g. the internal combustions engines or the gas turbine appeared. Some answers are given.

In the 21st century, some countries have already decided or at least consider abandoning nuclear power plants as a reaction to the Fukushima Daiichi nuclear disaster. The same applies for fossil power plants, in order to slow down the global climate change. Therefore, the question arises whether the steam engine or Rankine cycle still has a future? The authors are convinced that the characteristics, which were responsible that the steam engine was the first heat engine, will also ensure that Rankine cycles will still be implemented in future sustainable energy systems. Current and future examples are briefly introduced.

Keywords: Steam Rankine Cycle (SRC), Organic Rankine Cycle (ORC), steam engine

Introduction/Background

In the 17th century, boiling water and wet steam were very familiar to people from daily life e.g. when cooking meals. Furthermore, it was obvious that steam can move things e.g. the lid of the tea pod. This might partly explain that early scientists and craftsmen, already hundreds of years ago, experimented with steam in order to build a heat engine. Thomas Savery was successful in 1698 and built his steam pump called “Miner’s friend” [1,2]. However, this was not really an engine but just a pump. Thomas Newcomen introduced the world’s first heat engine in 1712: An atmospheric steam engine, which was limited to move the piston of a water pump in a mine up and down. It was James Watt who improved the steam engine significantly 50 years later, by applying a separate condenser, a double acting piston and a planetary gear so that it could work in continuous rotary movement and was able to drive any machine in various factories. The industrial revolution started with on-site power generation and changed the world. Nowadays, decentralized energy supply is again one of our goals in order to put the energy transition into practice.

The gas turbine (Joule-Brayton Cycle), for example, needed nearly 200 years more (1939) [3] for implementation, although its functional principle was patented in 1791 by Barber and was even tested by Stolze at the end of the 19th century. However, Stolze’s gas turbine did not work at all due to its inefficient compressor and expander.

A major advantage of the steam engine, no matter with volumetric or dynamic expander, is its work ratio r_w . The work ratio r_w of a heat engine is the network output of the engine divided by the work performed while expanding the fluid from maximum to minimum pressure. In a Rankine cycle r_w is close to unity (Figure 1 right) because the working fluid is pumped from lowest to highest cycle pressure in liquid state, what needs pretty little work. Hence, the expansion work is almost completely available as network output of the Rankine cycle. In a gas turbine i.e., a Joule-Brayton cycle, a gaseous fluid must be compressed from low to high cycle pressure. This change of state requires far more work due to the significant change of specific volume. Thus, r_w of the Brayton cycle, as shown in Figure 1, is only about 0.35 for the given pressures - assuming an ideal compressor and an ideal expander. The network output is the small difference of the huge expansion and the huge compression work. At practical applications, where the compressor and expander do not work with 100% efficiency, this difference tends to become significantly smaller or can even become negative – the gas turbine does not work at all, like Stolze’s engine in 1900. In contrast, a steam engine might be inefficient like Newcomen’s engine with about 0.5% thermal efficiency [4], but it will at least work by itself. In the authors’ point of view, this is the main reason why the steam engine was the first successfully implemented heat engine in the world.

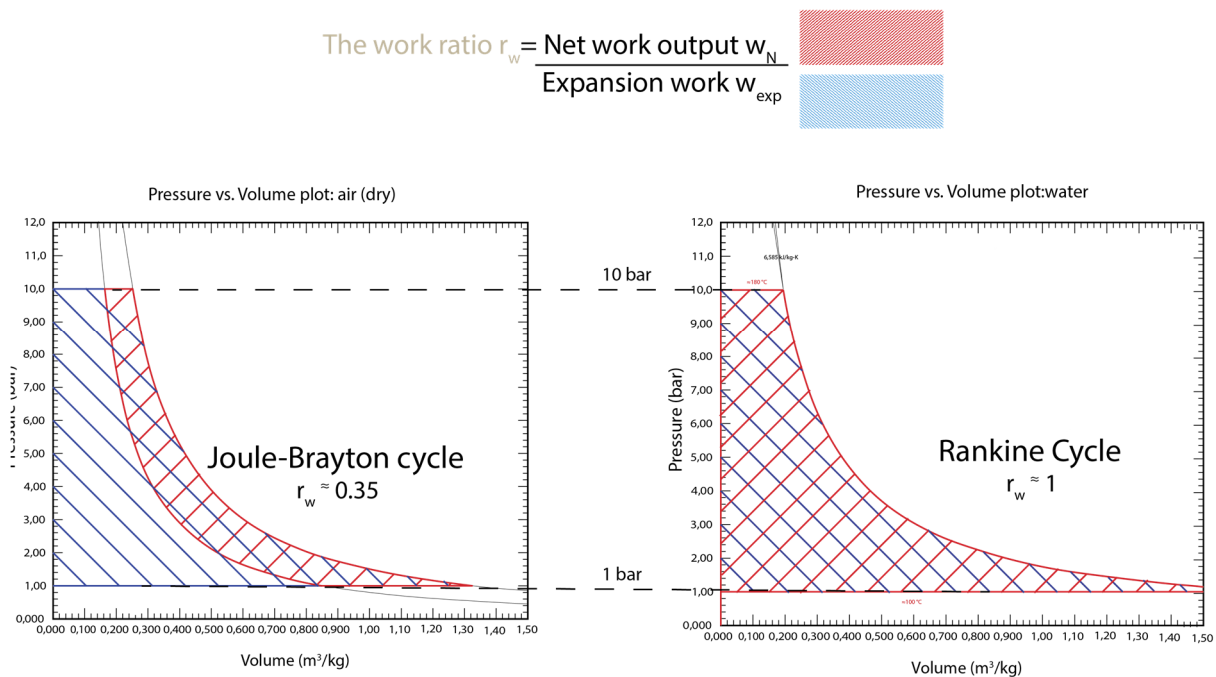


Fig. 1: The p, V-diagram of a Joule-Brayton Cycle (left) and a Rankine cycle (right) between 1 bar and 10 bar and the definition of the work ratio r_w .

Newcomen's as well as Watt's engines were known as atmospheric steam engines. The pressure of the live steam which they applied was only slightly above atmospheric pressure. Newcomen used saturated steam of about 1.01 bar ($t = 101.5\text{ }^{\circ}\text{C}$), Watt used saturated steam of about 1.1 bar ($t = 103.3\text{ }^{\circ}\text{C}$). They achieved condensing pressure of about 0.03 bar, thanks to their fresh water cooled ($20 - 30\text{ }^{\circ}\text{C}$) condensers. As a result, most of the work performed on the piston was done by the ambient air pressure against vacuum (Newcomen about 100%, Watt about 60%) and not by the live steam itself. By exploiting this deep vacuum, both inventors were able to implement effective engines which avoided high, unmanageable pressures and temperatures.

Another important advantage is the external, atmospheric combustion or heating, respectively. This is simpler to implement than an internal, pressurized combustion in a combustion chamber or cylinder. Thus, a steam engine or Rankine cycle can be fired by any fuel, even sewage sludge. At the same time any heat source can be used such as solar, geothermal or nuclear.

All these advantages also apply to the descendant of the old piston steam engine: the modern steam power plant with closed water-steam circuit and multi-stage steam turbine as the expander. Both, the piston steam engine and the steam power plant, consist of a feed pump, a boiler, an expander and a condenser by which they implement the Rankine cycle (see Figure 2).

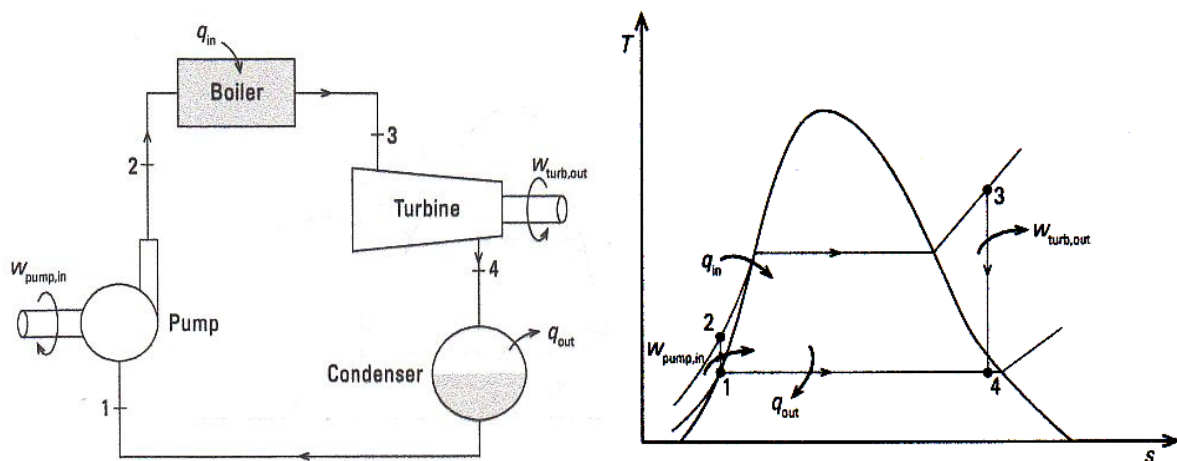


Fig. 2: Scheme of a steam engine/power plant (left) and the corresponding Rankine cycle in the T, s diagram (right) [5]

Results and Discussion

Thanks to the benefits described above, the steam engine enabled the First Industrial Revolution in the 18th century. Furthermore, it revolutionized the transportation system. The railway, driven by steam locomotives, connected countries, big steam ocean liners connected continents [4]. With the transition from the 19th to the 20th century, central power stations appeared [6]. Their rating rose quickly and achieved about 1000 MW at the end of the 20th century as a standard for nuclear heated as well as coal fired thermal plants. In 2017, about 50% of the world's electricity demand was generated by steam turbines [7]. However, in the 21st century, some countries already have decided or at least consider abandoning nuclear power plants as a reaction to Fukushima. The same applies for fossil power plants to slow down climate change. Therefore, the question arises whether the key technology of steam

engines or Rankine cycles, respectively, still does have a future? In the authors' opinion, it does – thanks to its advantageous characteristics.

Waste incineration might be an inconvenient but necessary task. In Europe in 2018, 166 million tons of non-recyclable municipal waste was collected and about 29% of it was burned in waste-to-energy plants. About 40 billion kWh electricity, sufficient for the demand of 18 million citizens for one year, was produced by waste-to-energy steam power plants [8,9]. No other heat engine is able to convert municipal waste to electricity.

Almost the same holds true for biomass power plants burning (CO₂ neutral) e.g. sawmill residuals, coconut shells, empty fruit bunches, palm kernel shells, cotton gin waste, paper etc. Many of these plants deploy an Organic Rankine Cycle (ORC) which is similar to a steam Rankine cycle but uses an alcohol, a hydrocarbon or silicon oil as working fluid. Figure 3 depicts the plant scheme of the biomass power plant at Lienz [10]:

Obernberger [10] in his 2002 paper summarized the advantages of this type of process:

“Due to the fact that the biomass furnace is coupled with a thermal oil boiler operated at atmospheric conditions, no steam boiler operator is needed and the steam boiler operation law does not apply. Thus, the personnel cost are reduced in comparison to steam boilers.”

This is one of several advantages of an ORC plant for biomass conversion. For more details see [10,11].

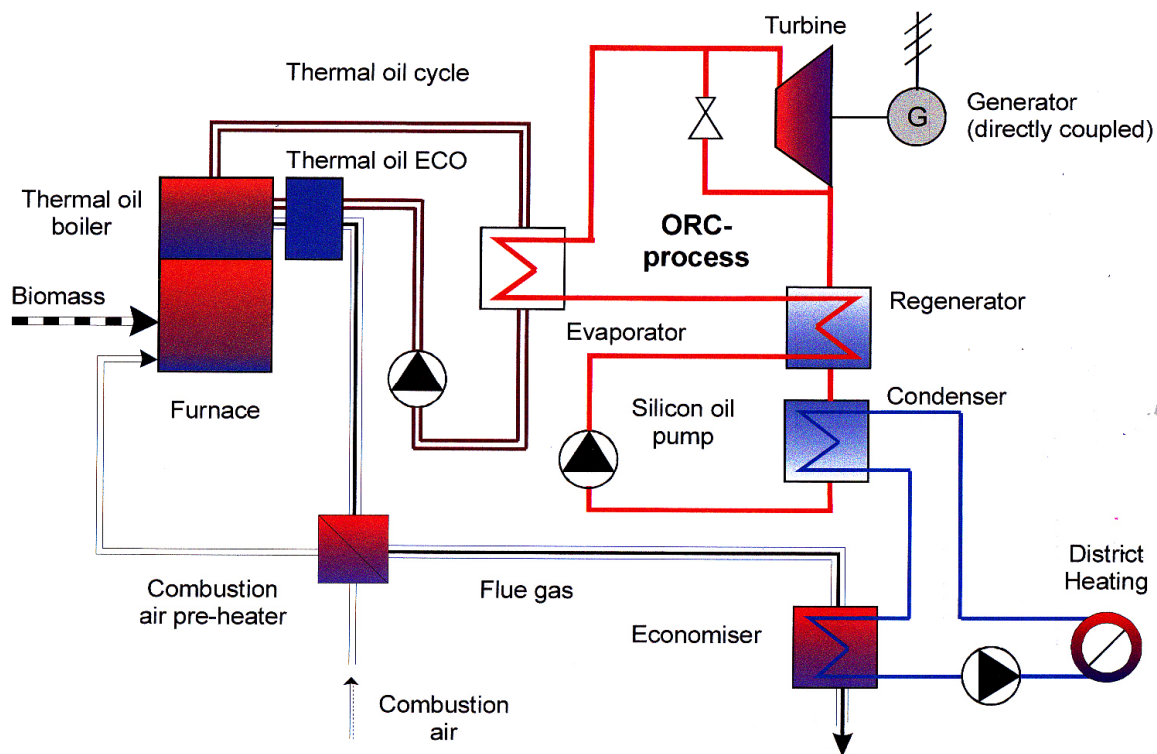


Fig. 3: Scheme of the wood-fired ORC Combined Heat and Power Plant at Lienz/Austria [10]

Already more than 100 years ago, the first geothermal power plant at Larderello was commissioned in Italy [11]. Larderello has been lucky and still uses direct steam blowing out of the hot ground in a steam Rankine cycle. However, most of the geothermal power plants worldwide have to work with lower hot well temperatures in the range 100 °C – 150 °C. Therefore, the ORC technology was originally developed to exploit those low temperature

hot wells by applying an organic fluid like e.g. a hydrocarbon which provides by far lower critical temperatures and pressures than water. Thus, a higher portion of the low temperature heat can be converted into electricity. Of course, there are only few countries all over the world where geothermal plants are technically and even economically reasonable such as Italy, Turkey, the US, Indonesia. However, the worldwide installed geothermal power has been continuously rising for the last decades [12].

In the seventies of the 20th century, the first concentrated solar power plants (CSP) were built in California [13]. Many other plants have been built since then like the Noor Power Station in Morocco providing currently 500 MW_{el}. Most of these CSP plants rely on a classical steam Rankine cycle. The steam is evaporated by a thermal oil circuit which is heated by parabolic-trough collectors as displayed in Figure 4. An advantage of CSP compared to photovoltaics (PV) is the option of a thermal energy storage (e.g., salt tank). Thanks to these storages, the CSP plant can be operated even during night, if the storage was charged by the solar field over day. Again, CSP is not a general solution for satisfying world's electricity demand. A yearly solar radiation of about 2000 kWh/m²/a is required [13] for economical operation which occur e.g. in Spain, Morocco, California, Brazil. Israel etc.

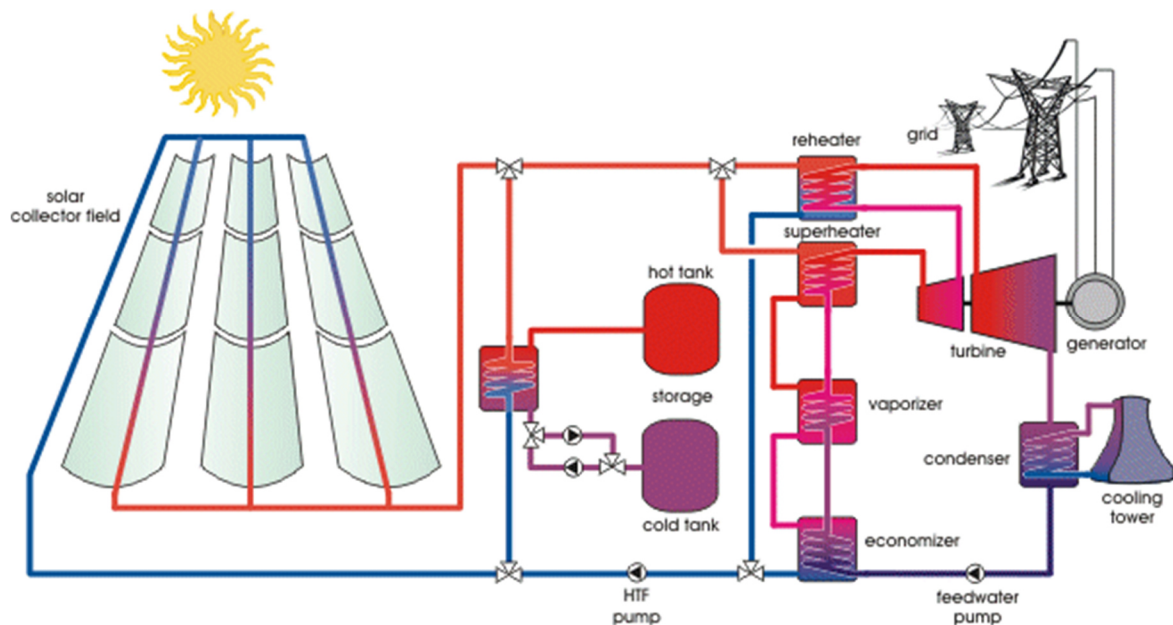


Fig. 4: Scheme of parabolic trough CSP plant with heat storages [14]

Waste heat in contrast to geothermal heat or solar radiation is an energy resource which can and should be exploited all over the world. Pehnt et al. 2010 [15] reported that about 80 GWh of waste heat $>140\text{ }^{\circ}\text{C}$ are rejected yearly only in German industry. Assuming a conversion efficiency of about 10%, which is realistic for small ORC units, 8 GWh per year could be extracted. This is the yearly electricity production of a 1000 MW steam power plant. In cases where the waste heat temperature is below $300 - 350\text{ }^{\circ}\text{C}$, an ORC system is the preferred solution for waste heat recovery [11]. In Combined Cycle Power Plants (CCPP), a steam turbine reuses the waste heat of the upstream gas turbine ($500 - 600\text{ }^{\circ}\text{C}$), which leads to an overall electric efficiency of more than 60% [16]. In future, CCPPs might be fired by green hydrogen (CO_2 -free) or synthetic (green) natural gas and will be thereby converted to sustainable energy systems.

So far, well established applications of the Rankine cycle have been discussed. Beside these, many innovative, interesting new ideas are appearing, in order to implement the energy transition. One approach is a Power-to Heat-to-Power (P2H2P) plant like ETES (Electrical

Thermal Energy Storage) erected by SIEMENS Gamesa [17] 2019 close to Hamburg/Germany. In this plant, surplus electricity from wind or PV, which is becoming more and more frequent due to the growing share of renewable energies, is converted into heat by a resistive heating. The heat is stored at 600 °C in 1000 t of volcanic stone (Figure 5). If the electricity is needed again, e.g. during the night, the heat is retransformed to electricity by a steam power plant. The power-to-power efficiency is about 25% - not very high due to the simple but reliable technology.

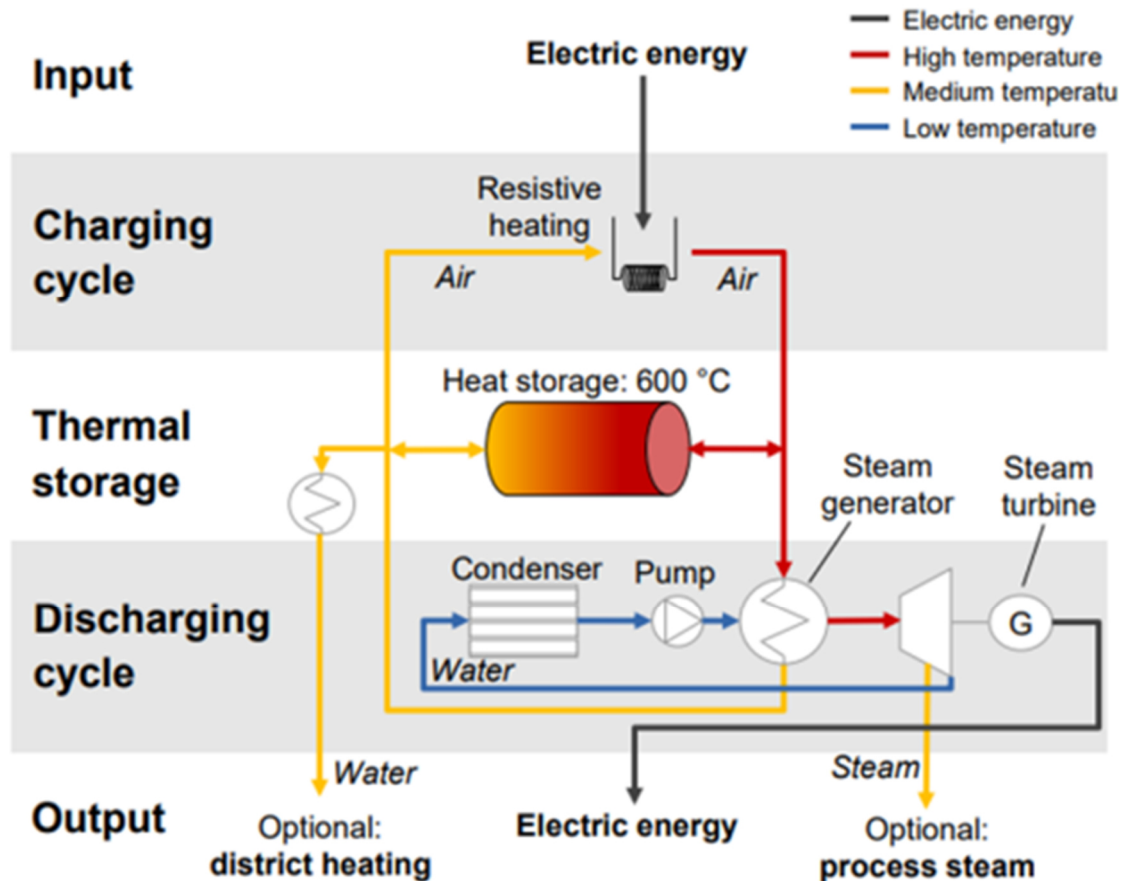


Fig. 5: Scheme of the P2H2P plant ETES by SIEMENS Gamesa [17]

In order to make this approach more cost effective, already available coal fired power plants can be equipped with the described electrical thermal energy storages, heated up by surplus electricity from wind or PV. In Germany [18] and Chile [19] projects have been recently started which put this idea into practice. An option is to use salt storages which are already well proven from CSP plant applications (see Fig. 4). The final goal is to remove once the coal fired boilers and to operate the plants in a pure storage mode. According to [18], about 50% of the overall costs of a P2H2P plant can be saved by repurposing an existing coal fired plant instead of building a new one.

As a more promising alternative, the surplus electricity can be used in an electrically driven compression heat pump which raises ambient or waste heat to a higher temperature (100 – 200 °C, Figure 6) and stores it. When the electricity is demanded, it will be converted by an ORC engine which could ideally serve as the compression heat pump as well in reverse mode. Power-to-power efficiency could be significantly improved [20] up to 70% which is almost competitive to hydro pump storage plants. This approach is sometimes called a CARNOT battery.

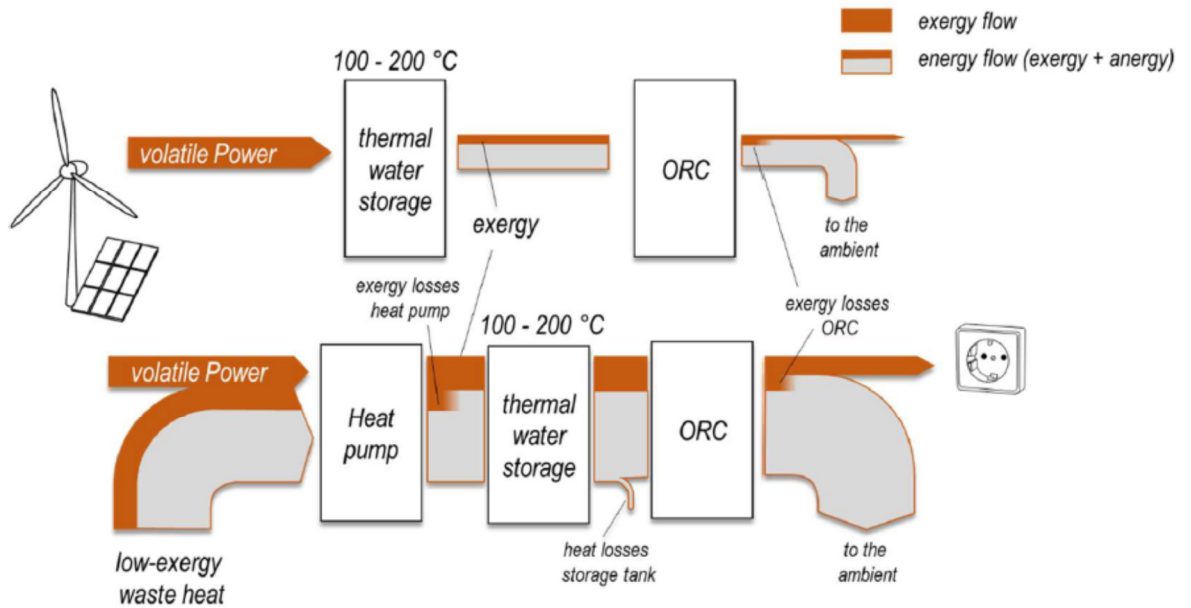


Fig. 6: Comparison of the energy and exergy fluxes of a simple resistant heated ETES (top) and an advanced one applying a heat pump (bottom) [20]

By far more futuristic but nevertheless already in operation is Liquid Air Energy Storage (LAES) [21,22]. Here, surplus electricity is used to liquefy ambient air and store it in insulated tanks at atmospheric pressure. This already has become a well proven technology. When electricity is required again, the liquid air is pumped to high pressure, evaporated and superheated by ambient or waste heat. The air vapor drives a turbo generator, then evaporates the liquid air regeneratively in a recuperator and is finally released into the environment (simplified explanation). Therefore, a Rankine cycle is implemented using air as the working fluid and the environment as a heat source.

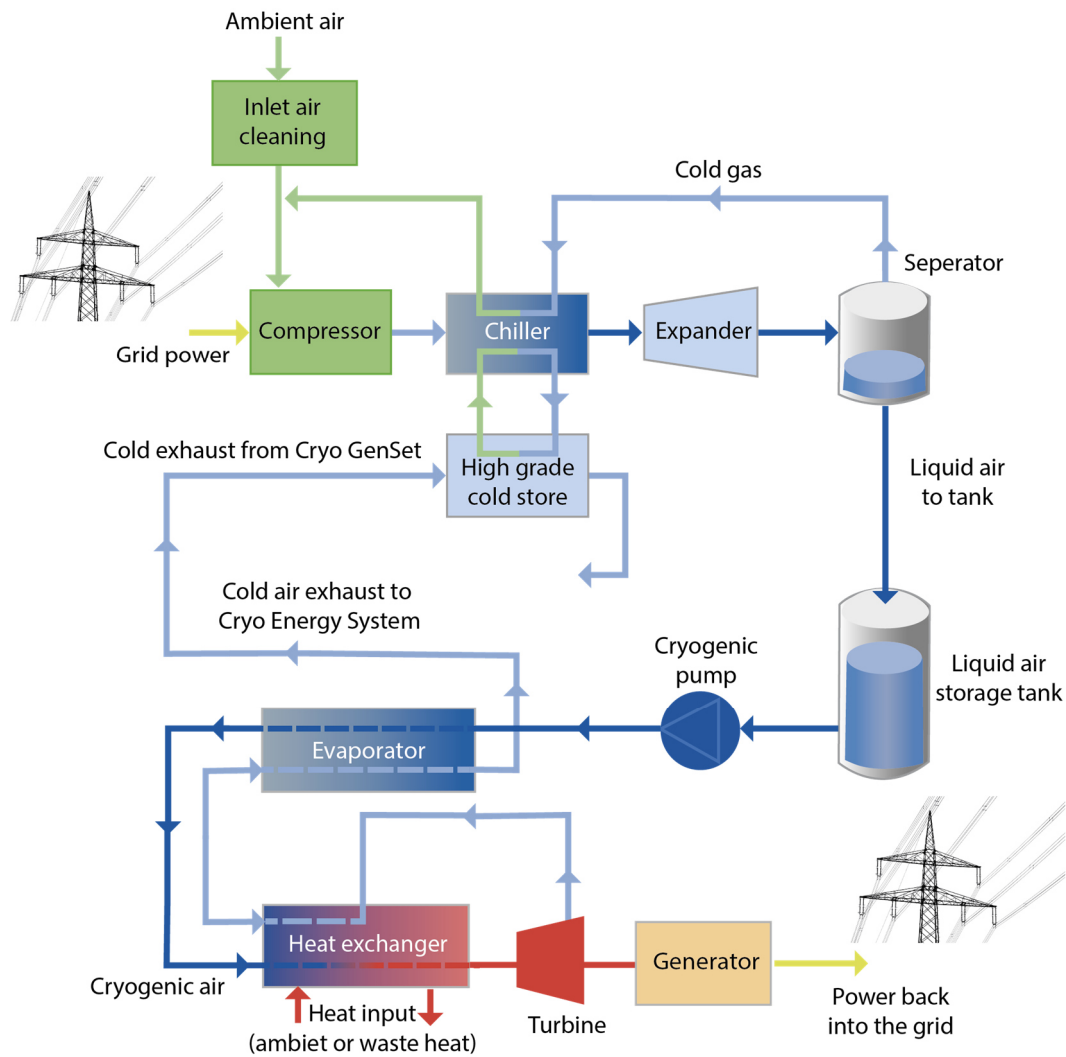


Fig. 7: Scheme of an Liquid Air Energy Storage (LAES) plant [22]

Summary/Conclusions

The reason why the steam engine was the first implemented heat engine have been discussed briefly: Steam was familiar in daily life already 300 years ago. Atmospheric combustion was and is easy to put into practice with any fuel. Furthermore, exploiting vacuum facilitated low pressure/low temperature engines and finally a work factor of almost unity guaranteed an effective engine. These characteristics lead to the success of the steam engine as worldwide prime mover in various forms and applications which have been discussed without claim to completeness. Moreover, these characteristics ensure that the steam engine or Rankine cycle will serve mankind even in future in quite new and advanced energy systems like e.g. LAES. Upcoming supercritical CO₂-cycles, which have not been discussed in this paper, could be regarded as direct descendants of the good old steam engine – at least in their transcritical form [23].

References

- [1] *Propyläen Technikgeschichte*. Berlin: Propyläen; 1997.
- [2] Wisniak J., *James Watt The Steam Engine*. Para quitare el polvo 2007:323–36.
- [3] Meher-Homji CB. ,*The Historical Evolution Of Turbomachinery* 2000:281–322. <https://doi.org/10.21423/R1X948>.
- [4] Rosen W., *The most powerful idea in the world: A story of steam, industry and invention* / William Rosen. London: Pimlico; 2011.
- [5] Pauken M., *Thermodynamics for dummies*. 1st ed. Hoboken, N.J: Wiley; 2011.
- [6] Harris FR., *The Parsons Centenary—a Hundred Years of Steam Turbines. Proceedings of the Institution of Mechanical Engineers, Part A: Power and Process Engineering* 1984;198(3):183–224. https://doi.org/10.1243/PIME_PROC_1984_198_024_02.
- [7] International Energy Agency., *Electricity Information: Overview* 2019; 2019.
- [8] ESWET-European Suppliers of Waste-to-Energy Technology. *Energy, Heat, Steam and Materials from Waste: Waste-to-energy is definitely more than just burning waste*.
- [9] ESWET-European Suppliers of Waste-to-Energy Technology., *The treatment of non-recyclable waste*.
- [10] Obernberger I, Thomhofer P, Reishofer E., *Description and evaluation of the Organic-Rankine-Cycle process*,. Euroheat & Power;2002(10/2002).
- [11] Macchi E., *Organic Rankine Cycle (ORC) Power Systems [electronic resource]*. Kent: Elsevier Science; 2016.
- [12] DiPippo R., *Geothermal power plants: Principles, applications, case studies and environmental impact*. Amsterdam [u.a.]: Butterworth-Heinemann, imprint of Elsevier; 2016.
- [13] Mohr M, Svoboda P, Unger H., *Praxis solarthermischer Kraftwerke*. Berlin, Heidelberg: Springer Berlin Heidelberg; Imprint; Springer; 1999.
- [14] Quaschnig V. , *Technology Fundamentals: Solar thermal power plants*. [January 01, 2021]; Available from: <https://www.volker-quaschnig.de/articles/fundamentals2/index.php>.
- [15] Pehnt DM, Bödeker J, Arens M, Jochem DE, Idrissova F., *Die Nutzung industrieller Abwärme – technisch-wirtschaftliche Potenziale und energiepolitische Umsetzung: Bericht im Rahmen des Vorhabens „Wissenschaftliche Begleitforschung zu übergreifenden technischen, ökologischen, ökonomischen und strategischen Aspekten des nationalen Teils der Klimaschutzinitiative“*. Heidelberg, Karlsruhe; 2010.
- [16] Tanuma T., *Advances in steam turbines for modern power plants*. Oxford: Woodhead Publishing; 2016.
- [17] Barthelemy DT., *Electric Thermal Energy Storage (ETES)*; November 8th 2017.
- [18] Herrmann U, Schwarzenbart M, Dittmann-Gabriel S., *Integration thermischer Stromspeicher in vorhanden Kraftwerksstandorte: Speicher statt Kohle*. Energie Forum 2019;71(4):42–5.
- [19] Geyer M, Trieb F, Giuliano S, Schröder R., *Repurposing of existing coal-fired power plants into Thermal Storage Plants for renewable power in Chile: 2nd International Workshop on Carnot Batteries*. Stuttgart; 2020.

- [20] Staub S, Bazan P, Braimakis K, Müller D, Regensburger C, Scharrer D et al., *Reversible Heat Pump–Organic Rankine Cycle Systems for the Storage of Renewable Electricity*. *Energies* 2018;11(6):1352. <https://doi.org/10.3390/en11061352>.
- [21] Brett G, Barnett M., *The application of liquid air energy storage for large scale long duration solutions to grid balancing*. EPJ Web of Conferences 2014;79:3002. <https://doi.org/10.1051/epjconf/20137903002>.
- [22] Strahan D., *Liquid air in the energy and transport systems: Opportunities for industry and innovation in the UK ; full report*. York: Centre for Low Carbon Futures; 2013.
- [23] White MT, Bianchi G, Chai L, Tassou SA, Sayma AI., *Review of supercritical CO 2 technologies and systems for power generation*. *Applied Thermal Engineering* 2021;185:116447. <https://doi.org/10.1016/j.applthermaleng.2020.116447>.

Multi-scale modelling of ejector refrigeration systems

Giorgio Besagni¹

¹Politecnico di Milano, Department of Energy, Via Lambruschini 4a, 20156 Milano, Italy

*Corresponding author: giorgio.besagni@polimi.it

Abstract

It is known that the efficiency of ejector-systems (the "*system-scale*") relies on the behaviour of the ejector itself (the "*component-scale*"), which is influenced by to the local flow phenomena (the "*local-scale*"). Because of these multi-scale relationships, the precise prediction of the "*local-scale*" is needed to support the deployment and implementation of commercially viable ejector refrigeration systems (*ERSs*). This paper summarizes the research activities and achievements regarding the multi-scale modelling of *ERSs* carried out by the author. First, a comprehensive validation of a *CFD* approach for single-phase ejectors is reported, encompassing a broad range of refrigerants, boundary conditions as well as ejector designs. In this activity, a comprehensive set of sensitivity studies have been completed, encompassing geometrical modelling (3-Dimensional vs 2-Dimensional approaches), solver settings (pressure-based vs density-based), mesh criteria and turbulence models (*k-ε RNG* vs *k-ω SST*). Second, the validated *CFD* approach has been coupled with a lumped-parameter model (*LPM*) of the *ERS* to clarify the multi-scale influences of the refrigerants and ejector designs, encompassing the *local*-, *component*- and *system*-scales. To this end, natural refrigerants and fourth generation refrigerants have been compared with third-generation refrigerants on different ejector geometries (obtained changing the mixing chamber dimension and nozzle exit position). One of the tested geometries has been then selected along with R290 as a refrigerant and has been equipped with a spindle: it has been tested for different spindle positions and under a broad range of boundary conditions, obtaining a complete performance map. The reported results and methods are of practical interest, to be implemented in predictive and multi-scale ejector control systems.

Keywords: Ejector; Multi-scale; Computational fluid dynamics.

1. Introduction

Ejector is a device constituted by a primary nozzle, a suction chamber, a mixing chamber, and a diffuser, whose main geometrical parameters are pictured in Figure 1. The "*high energy*" primary flow accelerates and expands through the primary nozzle creating a low-pressure region nearby the nozzle exit; subsequently, the secondary flow is entrained into the mixing chamber because of the vacuum-effect and the shear action between the primary and secondary flows. The primary and the secondary flows mix within the mixing chamber and the resulting stream moves into a diffuser where the high velocity fluid is gradually decelerated and increased in pressure due to subsonic conditions. The entrainment, the pressure recovery, and the mixing effects provided by the ejector, makes it suitable to be employed in ejector refrigeration systems (*ERSs*; Figure 2a presents the layout of a standard ejector refrigeration system, *SERS*) [1]. In general, *ERSs* are promising alternative compared with compressor-based technologies owing to their reliability, limited maintenance, low initial and operational costs, and no working fluid limitations [2]; also, the generator of an *ERS* might exploit low-grade heat energy, making *ERSs* valuable in contributing towards reducing electricity consumption in the residential sector [3].

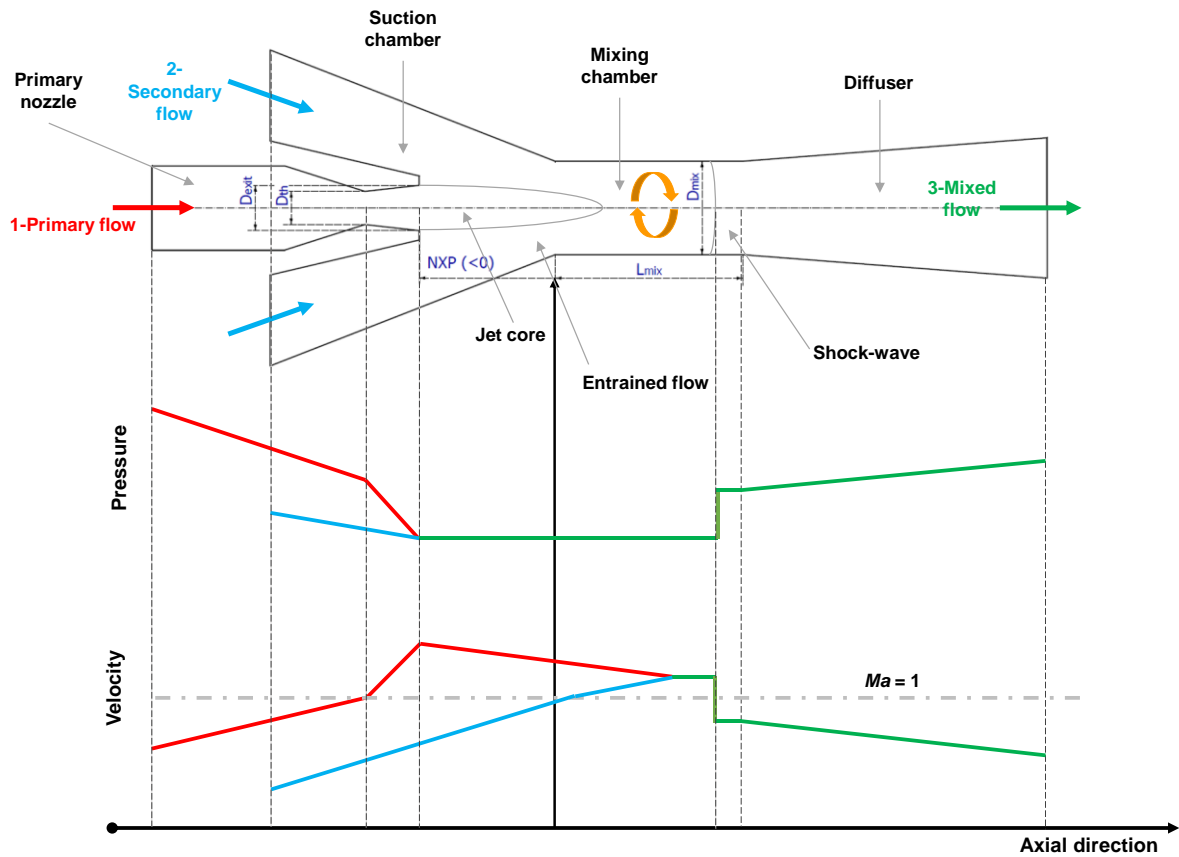
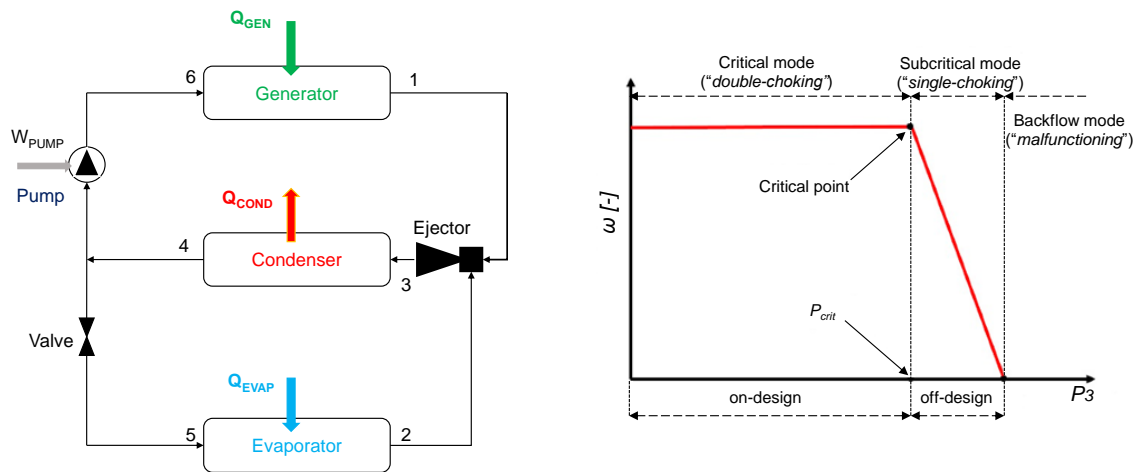


Figure 1. Ejector design and qualitative axial pressure and velocity trends.



(a) Layout of a standard ejector refrigeration system

(b) Ejector operating curve

Figure 2. Ejector component (a) and ejector refrigeration system (b).

Unfortunately, the large-scale deployment of ERSs is hindered owing to two main drawbacks: (a) the low coefficient of performance (in the range of 0.1–0.7) and (b) the relevant influence of ejector operation on the performance of the whole system. The latter can be easily explained by the fact that the ejector is a fluid-dynamics controlled device, where the fluid-dynamic interactions at the “local-scale” impact on the performances at the “component-scale”, namely the entrainment ratio ω (viz- the ratio between secondary and primary mass flow rates, Figure 2b – it should be noted that the ejector operating curve reported in Figure

2b can be represented either using the outlet pressure or the outlet saturated temperature). These multi-scale relationships can be easily explained considering that the ejector operation relies on two concurrent physical phenomena: (a) the low-pressure fluid entrainment process caused by the primary flow expansion and (b) the compression effect, provided by the diffuser, which raises the secondary flow pressure from the evaporator to the condenser pressure. These two effects are contrasting, and an improvement of the former would deteriorate the latter: hence, for a given nozzle area ratio, the ejector operating curve is imposed by the primary and secondary flow boundary conditions. On the other hand, Variable Geometry Ejectors (*VGE*) represent a promising solution to increase the flexibility and operation range of this component. In a *VGE*, the spindle acts on the nozzle area, and primary flow rate, and changes the ejector's response by adjusting its entrainment ratio accordingly with the requirements of the system. (i.e., temperature set point, thermal load, ...). In addition, the present-day discussion regarding ejector technology is even more challenging owing to the current transition in refrigerants; given the European regulation aimed to limit the emission of fluorinated greenhouse gases, the existing market is expected to change sharply in the next years, and 3rd generation refrigerants (i.e., R134a) will be most likely replaced by natural (i.e., hydrocarbons) and 4th generation fluids (i.e., hydrofluoroolefins) [4]. Given the above-reported state-of-the-art, this paper summarizes the research activities and achievements regarding the multi-scale modelling of *ERSs* carried out by the author. First, a comprehensive validation of a *CFD* approach for single-phase ejectors is reported, encompassing a broad range of refrigerants, boundary conditions as well as ejector designs. Second, the validated *CFD* approach has been coupled with a lumped-parameter model (*LPM*) of the *ERS* to clarify the multi-scale influences of the refrigerants and ejector designs, encompassing the *local*-, *component*- and *system-scales*. One of the tested geometries has been then selected along with R290 as a refrigerant and has been equipped with a spindle: it has been tested for different spindle positions and under a broad range of boundary conditions, obtaining a complete performance map.

2. CFD model set-up and validation [5]

A comprehensive set of experimental benchmarks have been collected in ref. [5] and have been used for the *CFD* model validation procedure. In the following of this paragraph, the main numerical settings are presented and, subsequently, the sensitivity analysis regarding geometrical modelling (3-Dimensional vs 2-Dimensional approaches), solver settings (pressure-based vs density-based), mesh criteria and turbulence models (*k-ε RNG* vs *k-ω SST*) are described and commented. The finite volume code ANSYS Fluent (*Release 2020 – R1*) has been used to solve the steady-state Reynolds Averaged Navier-Stokes (*RANS*) equations for the turbulent compressible Newtonian flow. To limit the numerical diffusion, second-order upwind numerical schemes have been used for the spatial discretization, except for the pressure equation. In this case, PRESTO! scheme has been chosen since it is designed for flows involving steep pressure gradients. Second-order upwind schemes also for the turbulence model variables have been used. Gradients are evaluated by a least-squares approach. The initialization has been performed by a two-step approach: a hybrid initialization followed by a full multi-grid (*FMG*) scheme. Pseudo-transient option was enabled, which was found to speed up the steady-state solution. Real gas properties, when needed, have been evaluated with the real-gas NIST database. Ejector inlets boundary conditions are prescribed in terms of total pressure and temperature, while the turbulence boundary conditions have been implemented as hydraulic diameter and the turbulent intensity (5% for the primary flows and 2% for the secondary one). Outlet condition has been modelled as a pressure boundary condition. Regarding sensitivity studies, first, a detailed mesh screening study has been performed, and guidelines for the definition of a grid-

independent mesh are achieved, based on a reference cell size, a maximum aspect ratio, wall requirements and mesh refinement, as summarized in ref. [5]. Also, a comparison between 2-Dimensional and 3-Dimensional approaches is conducted, showing no significant differences between the two approaches. Second, a comparison between *Pressure-Based* and *Density-Based* solvers has been conducted, showing no significant differences and a faster convergence and stability of the *Pressure-Based* solver. Thus, *Pressure-Based* solver with Coupled-based algorithm has been adopted. Finally, a broad validation against the experimental benchmark gathered in ref. [5] has been conducted, and two turbulence models ($k-\varepsilon$ RNG and $k-\omega$ SST) have been extensively compared: $k-\omega$ SST has shown better agreement with the experimental measurements concerning both global and local flow quantities. The outcome of this comparison is proposed in Table 1.

Table 1. Model validation outcomes: relative errors.

Ref.	ω prediction error				Local pressure prediction error		T_{crit} prediction error	
	On-design		Off-design		mean [%]	max [%]	mean [%]	max [%]
	mean [%]	max [%]	mean [%]	max [%]				
[6]	11.8	11.8	59.4	173.6	8.2	13.1	0.7	0.7
[7]	11	18.6	229.9	635	14	19.5	4.7	7.9
[8]	11.6	15.6	12.1	32.7	11.4	26.3	1.8	4.4
[9]	24.6	36.3	48.8	90.2	/	/	0.8	1.7
[10]	42.7	42.7	57.5	68.7	/	/	0.3	0.3
[11]	16.1	17.4	/	/	7.3	9.1	/	/
[12]	8.8	16.7	42.8	112.1	/	/	2.1	3
[13]	11.7	21.7	55.4	247.6	/	/	1.4	1.7
[14]	1.2	1.2	29.1	33.3	14.7	19.1	6.2	6.2
[15]	7.3	12.1	30.2	63.3	10.9	14.3	2.5	4.4
[16]	9.9	26.2	/	/	/	/	/	/

For all tested benchmarks data regarding entrainment ratio, for both *on-* and *off-design* operation mode, local prediction capability and the critical point prediction capability have been presented in ref. [5]. The entrainment ratio has been well predicted with an average *on-design* relative error of 14% and a maximum of 20%. The *off-design* operation mode is instead affected by a higher average relative error of 63% which is however aligned with other studies deviations registered in the single-choking mode because of the inherent complex fluid-dynamics which characterize the subcritical operation. On the other hand, good performances on the critical pressure prediction are obtained with an average relative error equal to about 3%. Regarding the influence of the turbulence model, $k-\omega$ SST showed better agreement compared with $k-\varepsilon$ RNG in terms of entrainment ratio prediction in both *on-design* and *off-design* mode. The great difference between the *on-design* and the *off-design* performance can be attributed to two main reasons: (i) while in the double-choking mode the secondary flow entrainment is not affected by the outlet pressure because of the second shock train occurring at the end of the mixing chamber which prevent the downstream information to travel upwards, in the subcritical operation instead, due to higher outlet pressure, the second shock is no longer occurring. In such a condition, while the primary flow is not affected, the entrainment process and mixing are highly influenced by the outlet flow reversing in the mixing chamber, with the result that the secondary mass flow rate (which affect the entrainment ratio) is predicted with average less accuracy. (ii) in the *off-design* operating mode the value of the entrainment ratio decreases (compared with the *on-design* value) which leads to a greater relative error (even when the absolute difference between the predicted value and the experimental one is the same). In conclusion, the proposed CFD

approach with turbulence model which is simulated by $k-\omega$ SST model can predict a wide range of boundary conditions on different supersonic ejector design operating with different working fluids. The stability of the simulation and the rapidity reaching a converged solution (granted by the *Pressure-Based* approach and a systematic mesh generation criteria) is furthermore a very significant result which could be useful for future numerical study on supersonic ejector component.

3. Multi-scale modelling approach [17]

The above-described and validated *CFD* model is used to solve the “*component-scale*” (viz., the entrainment ratio ω) and the fluid-dynamics (“*local-scale*”). Once such information is derived, the ejector component is then included within a refrigeration cycle, which is modelled by a *LPM* approach, to estimate the “*system-scale*” performances [17]. The considered cycle has been the *SERS* architecture (Figure 2a) since it is the elementary scheme and, thus, its results could be extended to any other derived system. The advantage of such approach is to consider the fluid dynamics phenomena within the cycle performances. *SERS* input data concern (i) P_1, T_1, P_2, T_2 and P_3 , which act as boundary conditions for the *CFD* simulations, and (ii) the mass flow rates \dot{m}_1 and \dot{m}_2 and T_3 , which are the *CFD* model output. To model the *SERS*, the prevailing assumption concerns the absence of pressure losses within the heat exchangers, so to relate ejector boundary conditions to the cycle pressure and pressure levels (Figure 2a). Given the ejector boundary conditions, the thermodynamic points of the *SERS* cycle have been obtained; in particular, in this process, the pump has been modelled considering an isentropic efficiency equal to 0.9. After all thermodynamic points of the *SERS* cycle have been obtained, the cooling power, input thermal power and electrical power required by the pump are computed using the mass flow rates \dot{m}_1 and \dot{m}_2 , which are *CFD* model output. Such multi-scale modelling approach has been used to perform the screening of the refrigerants and ejector design criteria described in the forthcoming sections.

4. Influence of the refrigerants and ejector design [18]

Fourth generation and natural refrigerants (R1233zd(E), R1234yf, R1234ze(E), R290, R1270, R600a) have been compared to commonly used refrigerants (R134a, R245fa, R152a) on five ejector geometries, obtained by changing the nozzle exit position and the mixing chamber throat dimension from a reference case (Table 2). The reference geometry (*Geom#1*) is the geometry provided by Del Valle et al. [11], which was given the code *Geom#F* provided in ref. [5]. The design sensitivity analysis has been performed from *Geom#1*, varying the nozzle exit position (*NXP*) and increasing and decreasing the mixing chamber diameter.

Table 2. Geometries definition and relative code name.

Geometry code	<i>NXP</i> [mm]	<i>NXP/D_{exit}</i> [-]	<i>D_{mix}</i> [mm]	Area ratio [-]
Geom#1-Reference case	-4.37	-1.46	4.8	5.76
Geom#2	-1.7	-0.57	4.8	5.76
Geom#3	-7.05	-2.35	4.8	5.76
Geom#4	-4.37	-1.46	5.28	6.97
Geom#5	-4.37	-1.46	4.32	4.67

The screening of refrigerants has been performed for fixed operating conditions: $T_1 = 84.2^\circ\text{C}$ (10 K superheating) and $T_2 = 14^\circ\text{C}$ (4 K superheating), which corresponds to *Case Fla*, defined in ref. [5] (except for secondary flow superheating which was 10 K). Superheating requirements have been set to avoid condensation inside the ejector. For the different geometries, different outlet conditions have been tested for the given inlet conditions to obtain the ejector operating curves and compare the critical conditions (Table 3 - It should be

noted that the primary flow is labelled as one, the secondary flow two and the outlet stream three, according to the *SERS* scheme of Figure 2a). This screening allows comparing the refrigerant performances for given generator and evaporator temperature conditions, changing for pressure levels to match these specifications (*SERS* performances have been computed based on the modelling approach described in Section 3). A summary of all tested cases, for the different ejector designs and refrigerants, is proposed in ref. [17].

Table 3. List and boundary conditions of the refrigerant screening and design sensitivity analysis simulated cases.

Refrigerant	T_1 [°C]	$T_{1,R}$ [-]	P_1 [kPa]	T_2 [°C]	$T_{2,R}$ [-]	P_2 [kPa]	T_3^{sat} [°C]	P_3 [kPa]
R134a	84.2	0.95	2,330.3	14	0.77	414.6	21 – 29.3	589.6 – 753.7
R245fa	84.2	0.84	683.0	14	0.67	82.4	23 – 32.5	137.9 – 194.4
R152a	84.2	0.92	2,075.2	14	0.74	372.8	21 – 29	528.8 – 670.0
R1233zd	84.2	0.81	571.4	14	0.65	73.4	23 – 32	120.8 – 165.7
R1234yf	84.2	0.97	2,241.1	14	0.78	437.5	21 – 29	609.1 – 762.5
R1234ze	84.2	0.93	1,774.8	14	0.75	308.3	21 – 29.5	440.9 – 569.9
Propane-R290	84.2	0.97	2,813.5	14	0.78	636.6	18 – 27	965.6 – 1,001.5
Isobutane-R600a	84.2	0.88	1,193.9	14	0.7	220.6	21 – 29	311.5 – 393.4
Propylene-R1270	84.2	0.98	3,346.5	14	0.79	778.6	18 – 27	965.6 – 1,213.0

The results are presented in Figure 4 and Figure 5 (ejector performance curves in terms of the entrainment ratio) and in Figure 6 and Figure 7 (ejector performance curves in terms of the coefficient of performance). In particular, Figure 4 and Figure 6 present the ejector operating curve as a function of the outlet pressure; conversely, Figure 6 and Figure 7 present the ejector operating curve as a function of the outlet saturating temperature, which might be more useful when looking at the practical use of such systems, which real plants. These outcomes showed how tested refrigerants could be divided into three groups:

- R1270 and R290, having higher COP (0.5 – 1.03) but lower T_{crit} (20.7 – 25.0 °C);
- R134a, R152a, R1234yf, R1234ze R600a, with an intermediate value of COP (0.27 – 0.83) and T_{crit} (22.8 – 28.0 °C);
- R245fa and R1233zd, with lower COP (0.25 – 0.58) but higher T_{crit} (26.0 – 31.0 °C).

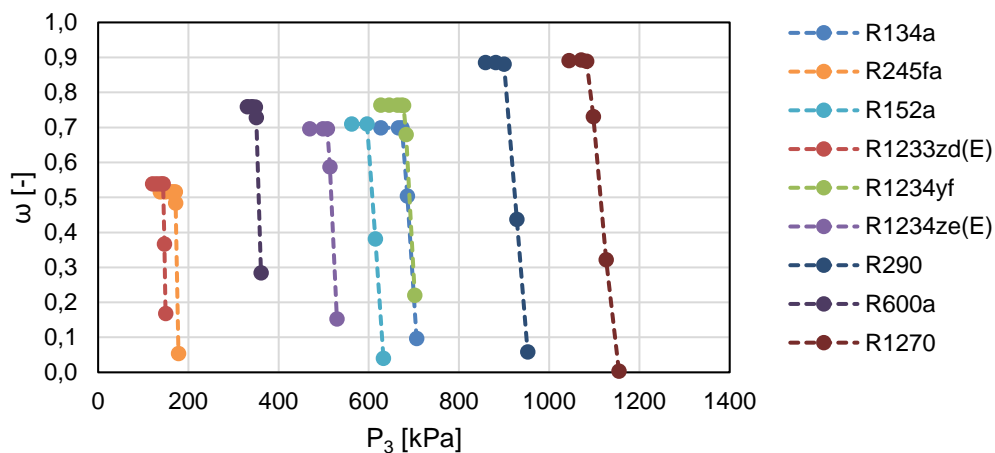


Figure 4. The ejector "component-scale" (*Geom#1* in Table 3): ejector operating curves (ω) as a function of the outlet pressure.

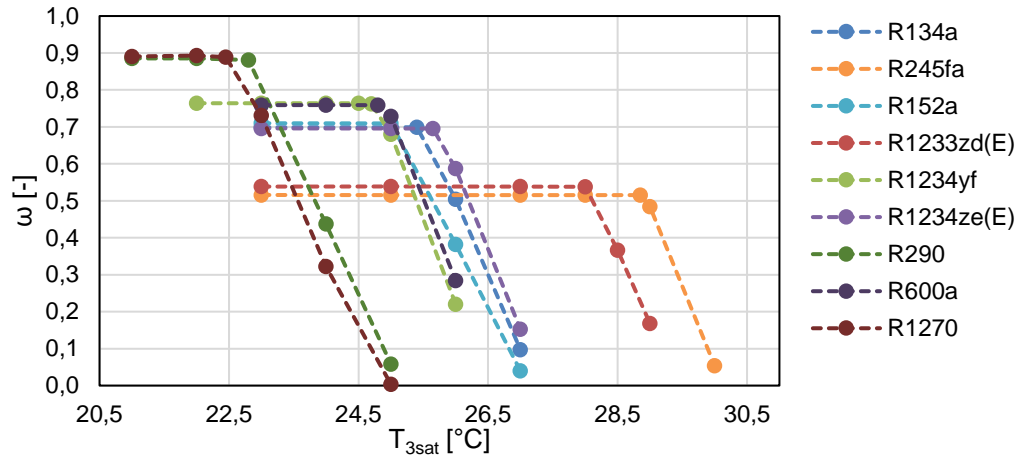


Figure 5. The ejector "component-scale" (*Geom#1* in Table 3): ejector operating curves (ω) as a function of the outlet pressure.

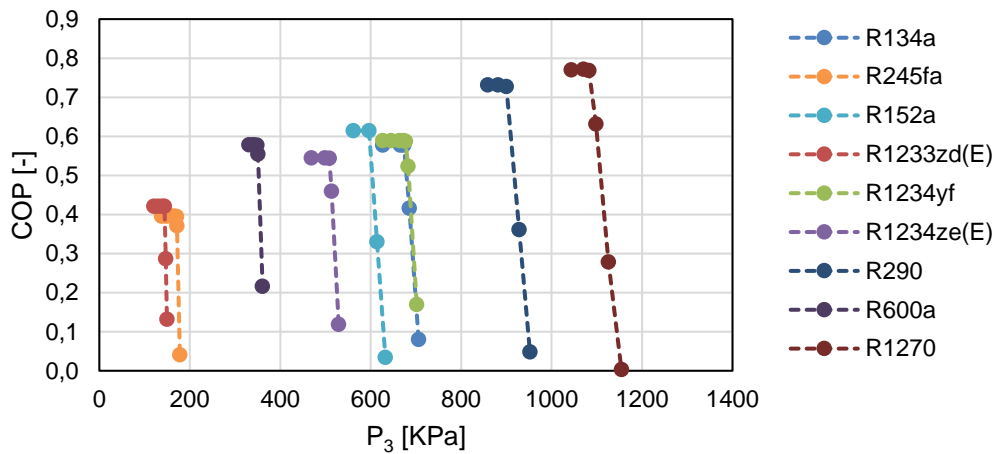


Figure 6. The ejector "component-scale" (*Geom#1* in Table 3): ejector operating curves (COP) as a function of the outlet saturating temperature.

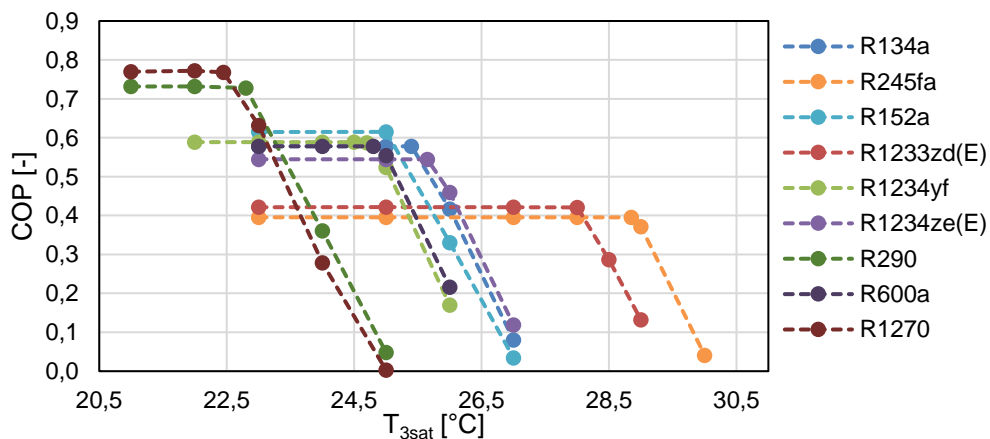


Figure 7. The ejector "component-scale" (*Geom#1* in Table 3): ejector operating curves (COP) as a function of the outlet pressure.

The reason behind the different behaviour can be found in ref. [17]: such different behaviours rely on the different primary jet expansions in the mixing chamber and, hence, the allowable

entrainment duct for secondary suction. An increase in the primary expansion angle reduces the annular cross-section area for the secondary flow to be draught in, with a consequent decrease in entrainment ratio (and performances). On the other hand, due to a less low-pressure secondary flow entrainment, the momentum transfer from the highly energetic primary flow is reduced, which results in a more comprehensive on-design operating mode due to higher critical temperature. As regards the design sensitivity analysis, it has been noted that increasing NXP (getting the nozzle exit closer to the mixing chamber inlet) improves both COP and T_{crit} , which suggests they have the same positive trend. Concerning the mixing chamber diameter sensitivity, increasing the mixing chamber (+10%) ejector achieved higher performances but lower T_{crit} , which could be quantified with an average variation on all the tested refrigerants of +35.65% on COP , and -7.8% considering T_{crit} . Conversely, the reduction of the mixing channel (-10%) enhanced the critical point temperature (+9.2%) but lowered the performances (-33.5%). Figure 9 compares the different ejector operating curves obtained in the different cases.

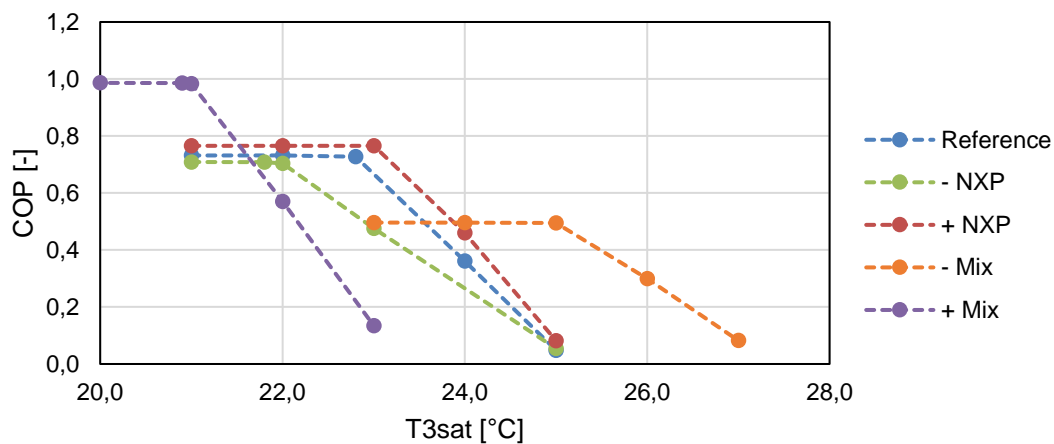


Figure 8. The ejector "component-scale" (*Geom#1*): influence of the ejector design criteria

5. Influence of the variable geometry ejector [19]

Given the outcomes presented in Section 4, an enhanced geometry has been selected with R290 as operative fluid to perform a boundary conditions sensitivity analysis, which has showed how generator, condenser, and evaporator temperature of *SERS* systems have a strong influence on ejector performances. It should be noted how, compared with the previous case, the mixing chamber diameter has been reduced to 4 mm to extend the on-design operating mode. The present ejector has been provided of a spindle (Figure 9) which can move axially within the primary nozzle.

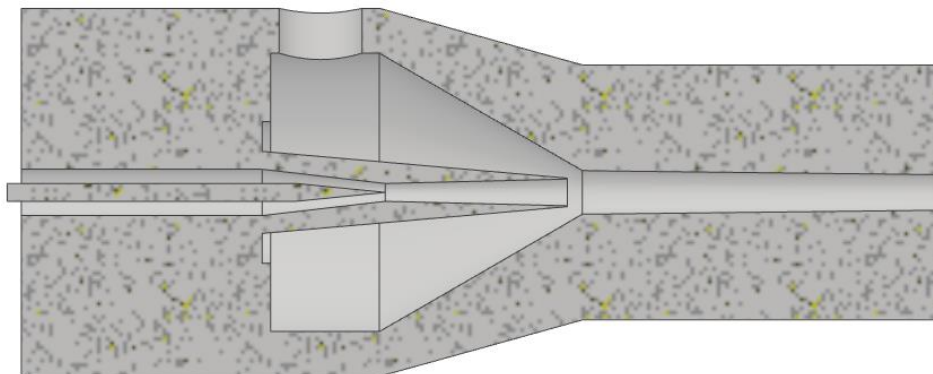


Figure 9. Ejector primary nozzle equipped with the spindle.

The neutral spindle position (SP) in which the tip of the spindle is placed right in the nozzle throat has been named as $SP\#0$. Moving the spindle towards the nozzle exit, the nozzle throat area is reduced, and the area ratio is increased. The effects of the SP have been analyzed in the range 0-7 mm, with a discretization of 1 mm each position, whose code name will be referred as $SP\#0..7$, depending on the spindle position. A 2D axysymmetric geometrical model has been designed and discretized according to the mesh criteria defined in Ref. [5], with an average cell number of 228,000 after the double cycle mesh adaption. Propane ($R290$) has been selected as refrigerant and the ejector has been tested with fixed thermodynamic conditions (temperature and pressure) at primary and secondary inlet. The whole operating curve for 3 primary flow and 3 secondary flow temperature (hence a total of 9 cases, Table 4) have been derived for each of the eight positions of the spindle. Primary inlet superheating has been set equal to 10°C , while secondary superheating equal to 4°C , according, to avoid condensation inside the ejector, since propane is a wet refrigerant. The complete set of the tested boundary conditions and relative code-names have been provided in Table 4 (each of the cases reported in Table 4 have been simulated for the different spindle positions). It should be noted that the primary flow is labelled as one, the secondary flow two and the outlet stream three, according to the $SERS$ scheme of Figure 2a. To ensure a full overview of the ejector operating conditions, the corresponding saturation temperatures of P_1 , P_2 and P_3 have also been provided.

Table 4. Ejector component (a) and ejector refrigeration system (b)

Case	$T_1^{\text{sat}} [^{\circ}\text{C}]$	$T_2^{\text{sat}} [^{\circ}\text{C}]$	$T_3^{\text{sat}} [^{\circ}\text{C}]$
A	74.3	10	13-29
B	84.3	10	17-34
C	94.3	10	21-40
D	74.3	5	11-27
E	84.3	5	14-32
F	94.3	5	19-38
G	74.3	15	17-31
H	84.3	15	20-36
I	94.3	15	23-41

$SERS$ performances have been computed based on the modelling approach described in Section 3, whereas the outcomes (for case A in Table 4) are presented in Figures 10-14. Figure 10 displays the ejector operating curves for the different spindle positions and the critical point operation is highlighted in red. Figure 11 displays the relationship between the spindle position and the primary and secondary mass flow rates as well as the generator and evaporator thermal powers, for the ejector operated in the critical conditions. Figure 12 displays the relationship between the spindle position and ejector ω and T_{crit} , and system COP are presented. for the ejector operated in the critical conditions. Figure 13 displays the $SERS$ $P-h$ representations and Figure 14 display and the Mach contours of the flow fields within the ejector at the critical conditions. Looking at Figure 10, it is noted that when moving the spindle towards the mixing chamber, ω is increased, but T_{crit} is decreased, limiting the maximum allowable condenser temperature. This effect can be explaining by considering that the spindle position affects the primary and secondary mass flow rates: the former decreases as the spindle moves towards the nozzle exit, whereas the latter is slightly increased (Figure 11). Indeed, shifting the spindle inside the nozzle, the nozzle throat area is reduced and so does the primary mass flow rate (related to the generator thermal power); the trend is not linear with the spindle position, as the nozzle throat area is ring-shaped, hence the first positions of the spindle have a smaller impact on ejector performances than the

following ones. Although less pronounced than the primary mass flow rate change, the increase in secondary mass flow rates is caused by the different expansion of the primary jet (Figure 14): increasing the nozzle area ratio leads the primary flow to a more pronounced contraction of the jet core, which frees more cross-section area to secondary flow entrainment.

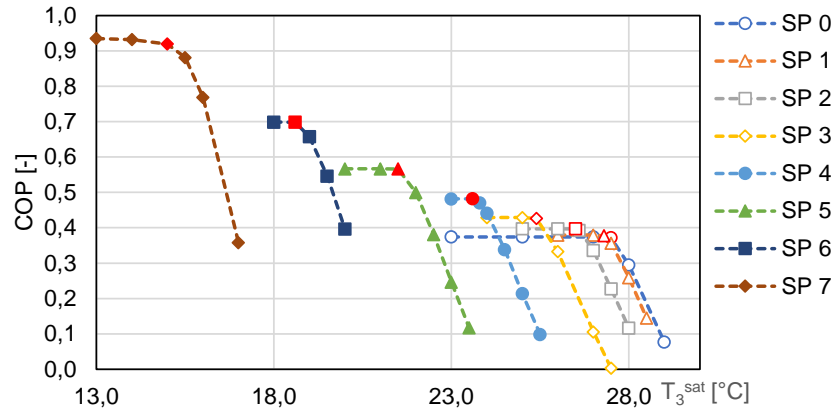


Figure 10. Ejector operating curves for the different spindle positions; case A in Table 4.

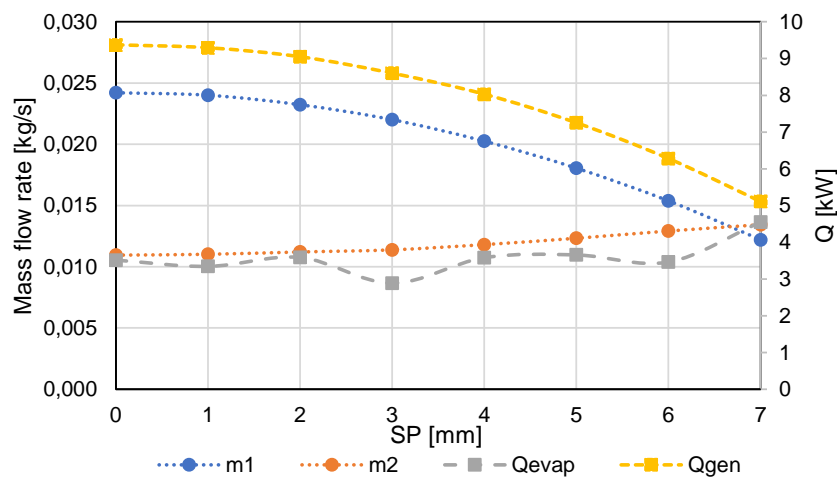


Figure 11. The effect of the Spindle position on mass flow rates and thermal power (critical condition); case A in Table 4.

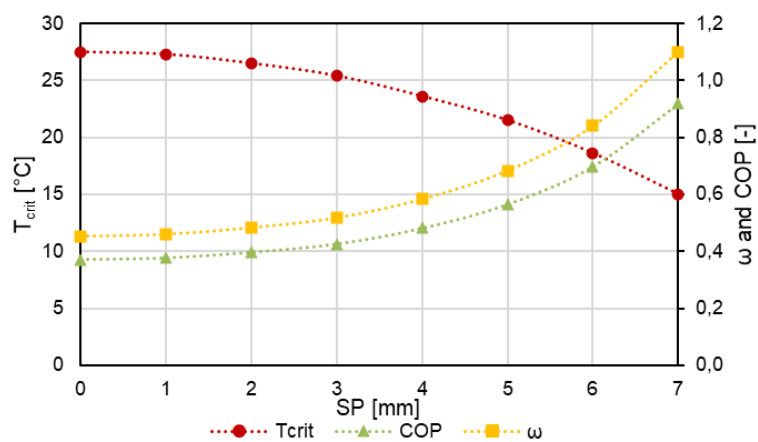


Figure 12. The effect of the Spindle position on T_{crit} , ω and COP (critical condition); case A in Table 4.

The concurrent increase of secondary flow rate and decrease of the motive one results in a noticeable improvement of the ejector entrainment ratio (Figure 12). It should be noted that the higher entrainment performance is countered by a lower T_{crit} , (Figure 10 and Figure 12) which is found to be reduced when the spindle is moved towards the nozzle exit position: moving the spindle from 0 to 7 mm ω is increased by 85.8% while the T_{crit} is reduced by 32.4%. The above-reported improvement of the ejector entrainment ratio, moving the spindle toward the nozzle exit position, can also be observed by considering the changes in the thermodynamic representation of the cycle (Figure 13, comparing *SERS P-h* at critical conditions for *SP#0* and *SP#7*).

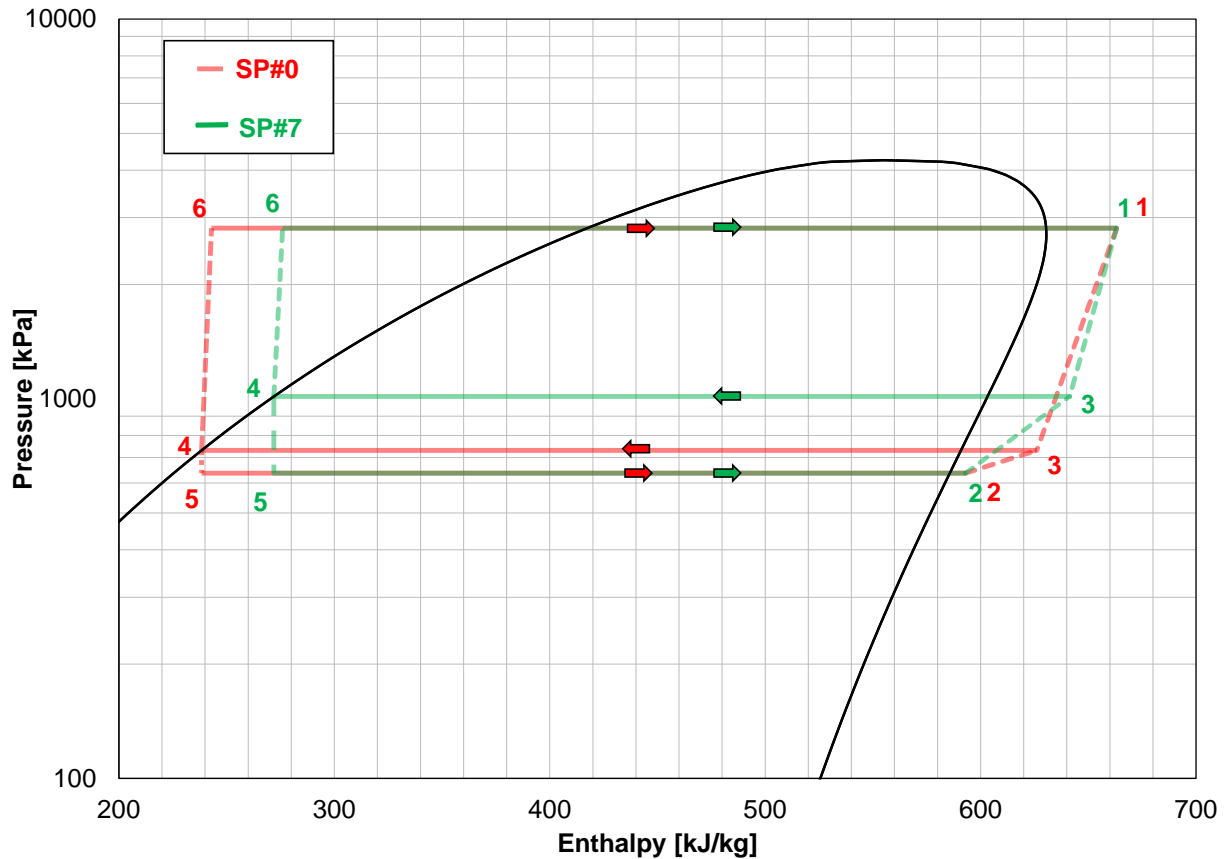


Figure 13. *SERS P-h* representations of *SP#0* and *SP#7* at the ejector critical conditions; case A in Table 4.

The different spindle positions affect the two main performance parameters of ejectors, namely ω and T_{crit} , which influence the system performance, in turn. ω directly influences the *COP* of the cycle, as it can be concluded by observing the *COP* definition as a function of the cycle properties. T_{crit} , instead, not only affects the maximum allowable condenser temperature of the system for which the ejector works at its best efficiency in the double-chocking operating mode but has a lower impact on the cooling capacity, too (Figure 14), the lower condenser temperature for the ejector used with *SP#7* mm (owing to the lower P_{crit}), results in a different positioning of point# 4,5,6 which are shifted toward the left part of the *P-h* diagram. This causes the specific generator input and the specific cooling capacity to increase with the result that their ratio; It should also be noted that the cooling power, is also increased because of the higher secondary mass flow rate \dot{m}_2 .

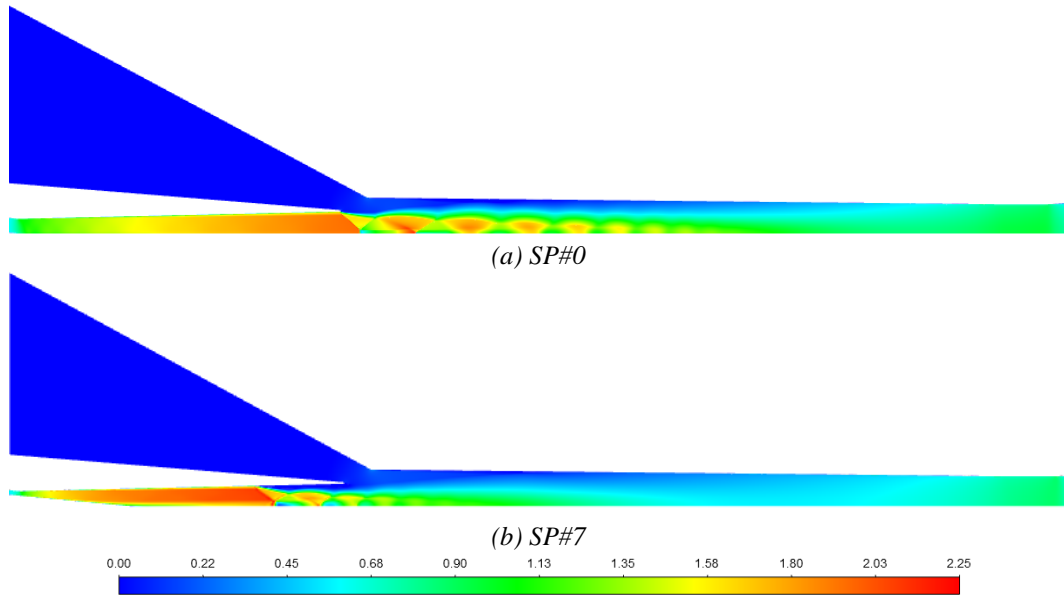


Figure 14. Ejector flow fields (Mach number contours) of *SP#0* and *SP#7* at the ejector critical conditions; case A in Table 4.

Once clarified the physics behind the ejector operation and the influence of the spindle position, primary flow saturation temperature and secondary flow saturation temperature on the performance of the component and the system, in this paragraph a more applicative discussion regarding the variable geometry ejector will be given. Recalling the system cycle in which the simulated ejector is assumed to operate, the generator supplies the primary flow, the secondary flow carries out the cooling effect, while in the condenser heat is discharged to the ambient, closing the cycle. In the present analysis, the primary flow temperatures have been varied between 84.2 and 104.2 °C, which is suitable for a small solar collector system coupled with small capacity storage. Three saturation evaporator temperatures have been selected to evaluate the performance in three different uses (Table 4): case D, E, F have been tested with $T_{2sat} = 5^{\circ}\text{C}$ which could be used to produce cold water (7-12°C) for conditioning dehumidification purposes; case A, B, C have been tested with $T_{2sat} = 10^{\circ}\text{C}$ which could provide water (12-17°C) for radiant cooling applications; case G, H, I with $T_{2sat} = 15^{\circ}\text{C}$ could instead provide general cooling equipment. The condenser temperature is in the range 20-40°C, which would allow the correct operation for warm climate conditions. The performance curves of COP versus T_{crit} of any simulated case and operated at the critical point has been presented in Figure 15. As it may be cleared noted, for fixed primary and secondary conditions, the critical point operating point moves along a curve when changing the spindle position. In agreement with the previous discussion, increasing the SP leads the ejector to operate with higher entrainment effect which improves the COP , but also decreases the maximum allowable discharge pressure (or saturation temperature) with the consequent reduction of T_{crit} . The described capability to dynamically change its performance ensures a more efficient operation of a variable ejector system in comparison to a fixed geometry one. To clarify this concept, the operating curves for case C with two SP (0 and 5 mm) and the performance curve at the critical point for the different critical positions (as in Figure 16). In the warmest moment of the day, the system would likely operate at high condenser temperatures, and hence the primary nozzle would be fully opened to maximize the pump effect of the ejector at the expense of a low system COP (in the figure, it is equal to 0.215).

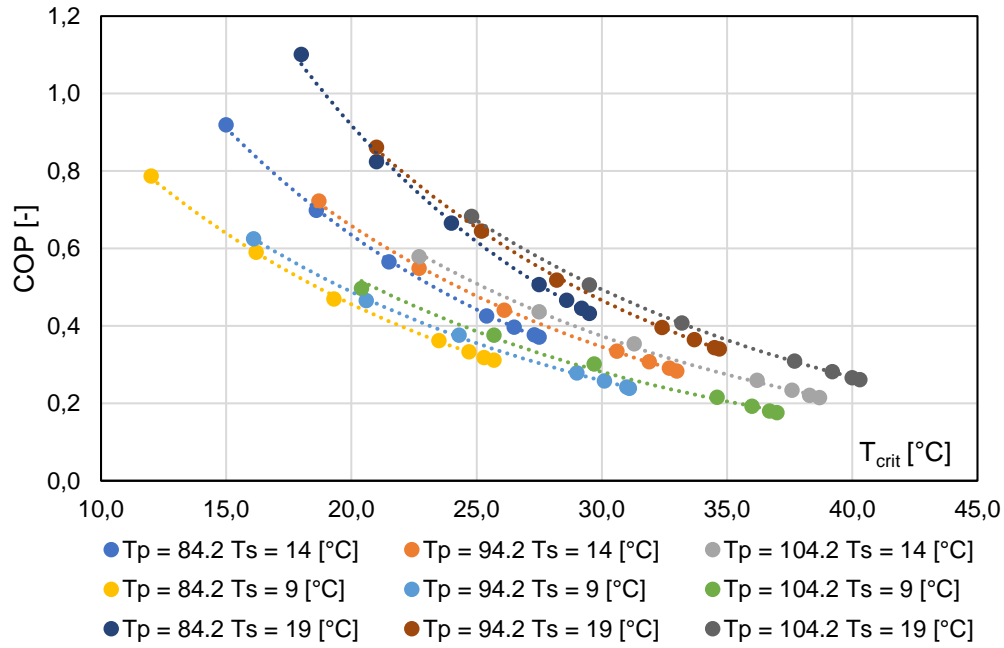


Figure 15. The effect of the Spindle position on T_{crit} , ω and COP (critical condition).

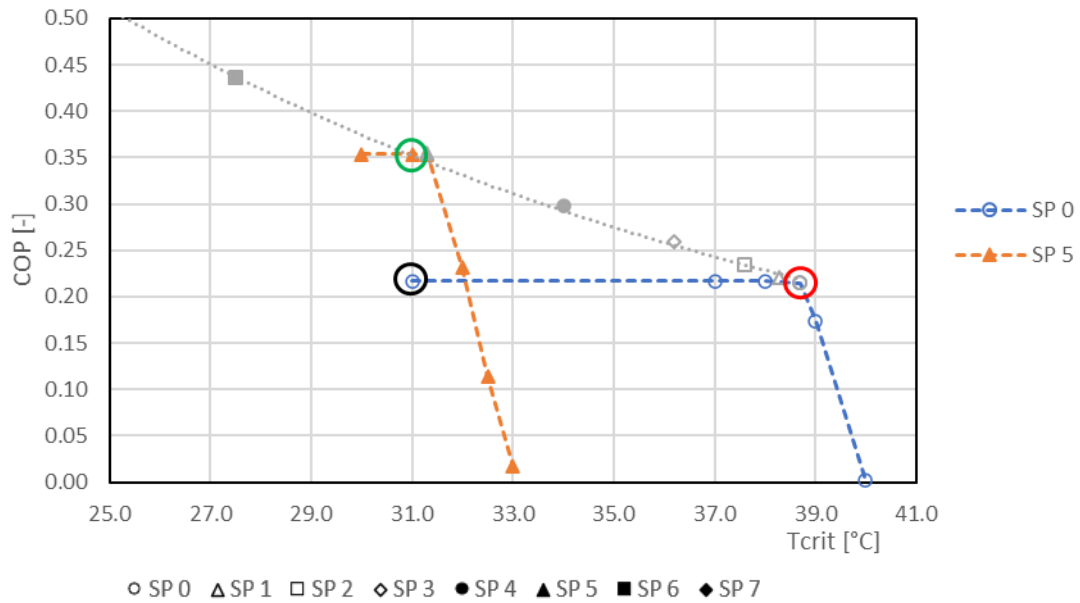


Figure 16. Performance curve of case C (Table 4) and operating curve for case $SP\#0$ and $SP\#5$.

A fixed geometry ejector operated at the same conditions would be designed to meet the worst possible requirements, and hence its fixed area ratio would equal the variable ejector's one. Both ejectors, therefore, would operate at the point shown in Figure 16 with the red circle with the same system performance. However, when the ambient conditions vary and the outside temperature decreases, the condenser temperature could be reduced. The *VGE* can effectively adjust its spindle to achieve the desired condenser temperature, for example, $T_{3sat} = 31^\circ\text{C}$ improving the system performance as shown by the green circle ($COP = 0.353$). In contrast, the fixed geometry would only shift the operating point along the same operative curve (black circle) without any improvement on the system performance. The fixed geometry ejector would work with the same motive flow rate, obtaining a mixed flow with

higher momentum than necessary, which would be dissipated by a stronger shockwave at the diffuser entrance. The *VGE* solution could also be useful when dealing with variable primary temperature. Small domestic and commercial ejector system is powered by the solar source, which leads to variable generator temperature conditions. A storage tank and a *VGE* system would stabilize the performance of the system allowing the ejector to operate at the maximum desired efficiency even when driven by different temperatures heat-source.

6. Conclusions

This paper summarizes the research activities and achievements regarding the multi-scale modelling of *ERSs* carried out by the author. First, a comprehensive validation has been described, encompassing a wide range of ejector designs, boundary conditions, and working fluids. In this procedure, a broad screening of modelling approaches is conducted. Then, a multi-scale integrated Computational Fluid Dynamics (*CFD*) - Lumped Parameter Model (*LPM*) of the *SERS* has been presented. The integrated model relies on a *CFD* approach to solve the ejector fluid-dynamics (viz., the “*local-scale*”) and the ejector performance (viz., the “*component-scale*”). Conversely, the *SERS* system is instead modelled by an *LPM* that evaluates the cycle performances (viz., the “*system-scale*”) based on *CFD* outcomes. The proposed multi-scale model has been applied to investigate the ejector design influence on the cycle performances and to perform a refrigerant screening, being able to relate the internal fluid- dynamics (“*local-scale*”) to the “*system-scale*” performances. Results showed how, based on the performance curves, tested refrigerants could be divided into three groups: (i) high *COP* and low T_{crit} , (ii) intermediate *COP* and T_{crit} , (iii) low *COP* and high T_{crit} . As regards the design sensitivity analysis, it has been noted that increasing *NXP* (getting the nozzle exit closer to the mixing chamber inlet) improves both *COP* and T_{crit} . Concerning the mixing chamber diameter sensitivity analysis, increasing the mixing chamber diameter leads to higher ejector performances but lower T_{crit} . One of the tested geometries has been then selected along with R290 as a refrigerant and has been equipped with a spindle: it has been tested for different spindle positions and under a broad range of boundary conditions, obtaining a complete performance map. It has been found that using a moving spindle control system might ensure an improvement of the ejector performance; this is of practical use, for example, when the condenser saturation pressure decreases (i.e., owing to a lower solar heat source). Future works will be devoted to developing dynamic look-up tables to be implemented in a variable ejector control system.

Acknowledgements

Author is grateful to Nicolò Cristiani, for the meaningful discussions and for his valuable support.

References

- [1] Aidoun, Z., Ameer, K., Falsafioon, M., & Badache, M. (2019). Current advances in ejector modeling, experimentation and applications for refrigeration and heat pumps. part 1: single-phase ejectors. *Inventions*, 4(1), 15.
- [2] Besagni, G., Mereu, R., & Inzoli, F. (2016). Ejector refrigeration: a comprehensive review. *Renewable and Sustainable Energy Reviews*, 53, 373-407.
- [3] Knobloch, F., Pollitt, H., Chewprecha, U., Daioglou, V., & Mercure, J. F. (2019). Simulating the deep decarbonisation of residential heating for limiting global warming to 1.5 C. *Energy Efficiency*, 12(2), 521-550.
- [4] Cavallini, A. (2020, August). The state-of-the-art on Refrigerants. In *Journal of Physics: Conference Series* (Vol. 1599, No. 1, p. 012001). IOP Publishing.

- [5] Besagni, G., Cristiani, N., Croci, L., Guédon, G. R., & Inzoli, F. (2021). Computational fluid-dynamics modelling of supersonic ejectors: Screening of modelling approaches, comprehensive validation and assessment of ejector component efficiencies. *Applied Thermal Engineering*, 186, 116431.
- [6] Han, Y., Wang, X., Sun, H., Zhang, G., Guo, L., & Tu, J. (2019). CFD simulation on the boundary layer separation in the steam ejector and its influence on the pumping performance. *Energy*, 167, 469-483.
- [7] Gagan, J., Śmierciew, K., & Butrymowicz, D. (2018). Performance of ejection refrigeration system operating with R-1234ze (E) driven by ultra-low grade heat source. *International Journal of Refrigeration*, 88, 458-471.
- [8] Poirier, M., Giguère, D., & Sapoundjiev, H. (2018). Experimental parametric investigation of vapor ejector for refrigeration applications. *Energy*, 162, 1287-1300.
- [9] Thongtip, T., & Aphornratana, S. (2017). An experimental analysis of the impact of primary nozzle geometries on the ejector performance used in R141b ejector refrigerator. *Applied Thermal Engineering*, 110, 89-101.
- [10] Yan, J., Lin, C., Cai, W., Chen, H., & Wang, H. (2016). Experimental study on key geometric parameters of an R134A ejector cooling system. *International journal of refrigeration*, 67, 102-108.
- [11] Del Valle, J. G., Sierra-Pallares, J., Carrascal, P. G., & Ruiz, F. C. (2015). An experimental and computational study of the flow pattern in a refrigerant ejector. Validation of turbulence models and real-gas effects. *Applied Thermal Engineering*, 89, 795-811.
- [12] Shestopalov, K. O., Huang, B. J., Petrenko, V. O., & Volovyk, O. S. (2015). Investigation of an experimental ejector refrigeration machine operating with refrigerant R245fa at design and off-design working conditions. Part 2. Theoretical and experimental results. *international journal of refrigeration*, 55, 212-223.
- [13] Del Valle, J. G., Jabardo, J. S., Ruiz, F. C., & Alonso, J. S. J. (2014). An experimental investigation of a R-134a ejector refrigeration system. *International journal of refrigeration*, 46, 105-113.
- [14] Chong, D., Hu, M., Chen, W., Wang, J., Liu, J., & Yan, J. (2014). Experimental and numerical analysis of supersonic air ejector. *Applied Energy*, 130, 679-684.
- [15] Sriveerakul, T., Aphornratana, S., & Chunnanond, K. (2007). Performance prediction of steam ejector using computational fluid dynamics: Part 1. Validation of the CFD results. *International Journal of Thermal Sciences*, 46(8), 812-822.
- [16] Huang, B. J., Chang, J. M., Wang, C. P., & Petrenko, V. A. (1999). A 1-D analysis of ejector performance. *International journal of refrigeration*, 22(5), 354-364.
- [17] Besagni, G., Croci, L., Cristiani, N., Inzoli, F., & Guédon, G. R. (2021, April). Multi-scale performance evaluation of ejector refrigeration systems. In *Journal of Physics: Conference Series* (Vol. 1868, No. 1, p. 012013). IOP Publishing.
- [18] Besagni, G., Cristiani, N., Croci, L., Guédon, G. R., & Inzoli, F. (2021). Multi-scale evaluation of ejector performances: The influence of refrigerants and ejector design. *Applied Thermal Engineering*, 186, 116502.
- [19] Besagni, G., & Cristiani, N. (2021). Multi-scale evaluation of an R290 variable geometry ejector. *Applied Thermal Engineering*, 188, 116612.

My thermodynamic journey from Carnot to Gibbs – A physical interpretation of maximum work

Dr. Robert T. Hanlon¹

¹ Senior Lecturer, Department of Chemical Engineering, Massachusetts Institute of Technology

*Corresponding author: rthanlon@mit.edu

Abstract

Gibbs' concept of maximum work continues to both fascinate and confuse, largely due to the fact that it arrived without an underlying physical explanation. In this talk, I share the history, the science, and my interpretation of Gibbs' maximum work and explain why ΔG_{rxn} quantifies the energy available to do useful work while $T\Delta S_{\text{rxn}}$ quantifies the change in "structural energy" between reactants and products and thus represents the energy component of ΔH_{rxn} unavailable for useful work.

Keywords: J. Willard Gibbs, entropy, maximum work, electrochemical cell

Background

The concept of maximum work continues to both fascinate and confuse. Many thermodynamics students and graduates, including myself, have struggled with this concept, largely on account of the need to include entropy in the calculations. We are given the equations to do the calculations but not the physical reasoning behind them. My frustration with this and with other similar aspects of thermodynamics motivated my twenty-year effort to research these topics and publish my findings in the form of my recently released book, *Block by Block – The Historical and Theoretical Foundations of Thermodynamics*.

My journey took me from Sadi Carnot's invention of an ideal process by which to convert heat into useful work to the capstone effort of J. Willard Gibbs to complete the new science of thermodynamics based on the concepts of energy and entropy. While many scientists embraced the rise of energy as a unifying concept in physics, such was not the case for entropy. Viewed as a "ghostly" entity by some, entropy created confusion as there was no visceral feel for the physical phenomenon it represented. Jacobus Henricus Van't Hoff even found a way to write a massive and influential textbook on physical chemistry in 1898-1900 without once mentioning the word entropy.

So how did entropy finally win over the chemist community? By explaining the thermodynamics of an electrochemical cell. In the early days of this technology, many chemists believed the cell's voltage to be proportional to the energy change of the reaction ($-\Delta H_{\text{rxn}}$). This belief rose from the proposal of Danish chemist Julius Thomsen and later French chemist Marcellin Berthelot that the maximum work for a process corresponds to its heat release. Despite its lack of a theoretical underpinning, the Thomsen-Berthelot *thermal theory of affinity*, as it became known, worked reasonably well, and since scientists linked the voltage to maximum work, they naturally, in turn, linked voltage to heat release. It was Gibbs and his use of entropy who corrected this error.

Gibbs created a new property of matter, $G = U - TS$, from which he derived the following: maximum work = $-\Delta G_{\text{rxn}} = -(\Delta H_{\text{rxn}} - T\Delta S_{\text{rxn}})$ (constant temperature and pressure). He then used this theory to bring clarity to the electrochemical cell process by showing that voltage corresponds to ΔG_{rxn} and that the observed heating / cooling requirements of the cell's constant temperature bath correspond to $T\Delta S_{\text{rxn}}$.

Unfortunately, Gibbs' equation for maximum work, as powerful as it proved to be, arrived absent a physical explanation based on the behavior of atoms and molecules. The fact that I couldn't find an answer to this and many other questions motivated me to write my book and to develop my own explanations for the physical meaning behind thermodynamic phenomena, including the following.

Discussion

ΔH_{rxn} is measured by the amount of heat removed by the reaction calorimeter's constant temperature bath. While one might think that it quantifies a single type of transformation, it actually quantifies two types, the re-arrangement of orbital electrons and the change in intermolecular forces. This is shown by re-arranging Gibbs' equation to the following: $\Delta H_{\text{rxn}} = \Delta G_{\text{rxn}} + T\Delta S_{\text{rxn}}$. While this equation doesn't reveal itself in the calorimeter, it does in the electrochemical cell since ΔG_{rxn} is directly measured by the cell's voltage and thus directly quantifies maximum work, for it's the electron re-arrangement that leads to the voltage that generates the work. But given this, what does the term $T\Delta S_{\text{rxn}}$ represent?

While Gibbs didn't speculate, intentionally so, about the underlying physics behind his equation, especially since the atomic theory of matter had not yet arrived, he did suggest a path to these physics by stating that $T\Delta S_{\text{rxn}}$ corresponds to the heating and cooling requirements of the constant temperature bath. Based on this, I propose that this term reflects the difference in intermolecular forces between reactants to products.

The entropy of a system is quantified by integrating $(\delta Q/T)$ from absolute zero to a given temperature, for which δQ encompasses the total thermal energy required to reach the temperature. This energy is distributed between both kinetic and potential forms in the system. It's the energy that puts molecules in kinetic motion and the energy that overcomes intermolecular attractions to push the molecules apart and so establish the structure of the system. At constant temperature, I propose that the difference in entropy between reactants and products (ΔS_{rxn}) times temperature (T) quantifies the latter, the difference in the "structural energy," as I call it, between each.

Summary/Conclusions

For a constant temperature and pressure reaction, ΔG_{rxn} quantifies the energy available to do useful work while $T\Delta S_{\text{rxn}}$ quantifies the change in "structural energy" between reactants and products and thus represents the energy component of ΔH_{rxn} unavailable for useful work. In my talk, I will share the history, the science, and my interpretation of Gibbs' maximum work equation.

Adsorption Heat Pumps: Challenges and Future Perspectives

Dr Z. Tamainot-Telto
Sustainable Thermal Energy Technologies (STET)
School of Engineering - University of Warwick
Coventry CV4 7AL - UK

In the past two decades, there has been a considerable interest in adsorption heat driven refrigeration and heat pump systems to reduce greenhouse gas (GHG) emissions associated to conventional heating and cooling systems. In fact, in the UK, the annual emission of CO₂ due to heating is about 180Mt CO₂ equivalent corresponding to 38% of all greenhouse GHG emissions. The domestic heating alone (hot water and space heating) counts for about 87Mt CO₂ equivalent (48%). Although substantial progress has been made to overcome scientific and technical challenges of adsorption technology, the commercial adsorption heat pumps and refrigeration machines are still marginal on the market worldwide. The current presentation main objectives are, not only to spell out the key factors that are holding back this technology and to list few commercially available machines, but more importantly to outline future perspectives in both short and long terms. Illustration examples will include a domestic gas fired Adsorption Heat Pump developed by University of Warwick as shown in **Figure 1**.

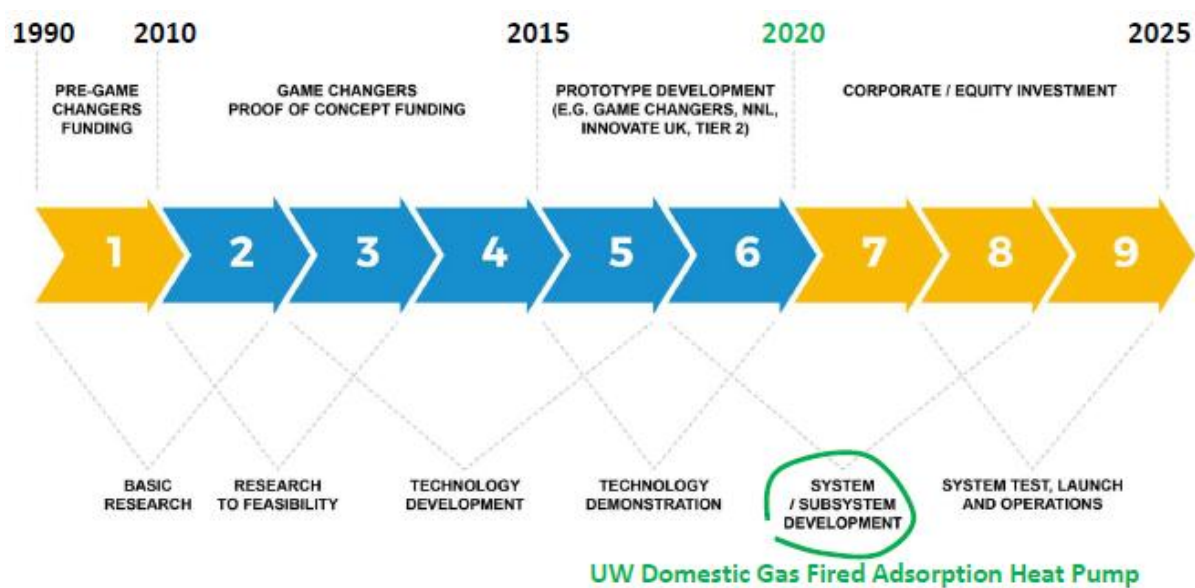


Figure 1: Technology Readiness Level (TRL) roadmap for an Adsorption Heat Pump.

Adsorption for Heat Conversion and Storage: What Have We Learned over the Past Decade of this Century?

Yu.I. Aristov

¹Boreskov Institute of Catalysis, Lavrentieva Av. 5, Novosibirsk, 63090 Russia

Abstract

This lecture addresses current trends in the conversion and storage of low-temperature heat in closed adsorption systems, including the development of new adsorbents, improvement of adsorption dynamics and the study of new cycles. This review is based on the analysis of literature results reported mostly in the second decade of this century.

Keywords: Adsorption, Heat conversion/storage, Thermodynamics, Adsorption dynamics

Introduction/Background

An adsorption heat conversion/storage (AHCS) attracts increasing attention as it contributes to smoothing global climate changes, reduced fossil fuel consumption, and rational use of renewable and waste energy [1, 2]. A short and fascinating history of solid sorption heat pumps/chillers is described in [3, 4]. By now, more than a dozen companies have offered adsorption chillers to the market; however, their share is almost negligible as compared with the traditional compression chillers [5]. Therefore, still, there is big room for improving ACHS units and making them more competitive. Furthermore, this complex, multi-level scientific and technical task (Fig 1) needs an intelligent trade-off between thermodynamic, kinetic, structural and other issues. This paper aims to reveal and highlight new trends in heat conversion/storage in *closed* adsorption systems, which appeared/developed mainly in the past decade of this century. The subject includes designing new adsorbents, developing new cycles, applying advanced experimental techniques, enhancing AHCS dynamics and other related issues.

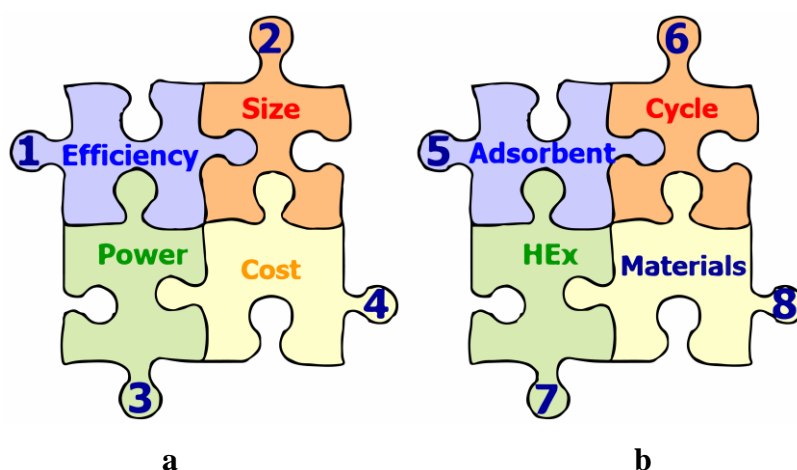


Fig 1. General (a) and technical (b) issues to be a subject of a trade-off for the adsorptive/chemical heat conversion/storage applications.

Discussion and Results

Adsorbents. In the second decade of the 21st century, only one class of new adsorbents has been successfully adapted for AHCS, that is metal-organic frameworks (MOFs). MOFs were first proposed for AHCS in [6] and widely tested in Janiak's lab [7, 8] and then in many other groups [9]. MOFs are interesting for AHCS because of their tunable adsorption properties,

large surface area and pore volume; however, their main drawbacks are high cost, small production scale and complex synthesis [10]. Adsorbents rapidly adapted/developed for AHCS in the first decade of the 21st century (aluminophosphates [11, 12], coals [13, 14, 15], composites "salt in a porous matrix" (CSPM) [Erro! Indicador não definido.16, 17], were lately gradually improved to fit particular AHCS cycles. For instance, CSPMs were ameliorated mainly by searching for new salts [16, 18] and matrices [16, 19, 20]. As the main sorbing substance of CSPMs is a salt inserted in the matrix pores, the most attractive matrices should be cheap and have a large specific pore volume to take in plenty of salt (e.g., vermiculite [21]). The ever-increasing attempts to use expensive matrices, like MOFs (see [19] as just one of many examples), seem to be contrived and unproductive. For aluminophosphates, the main direction of improvement is increasing hydrothermal stability and reduce cost, whereas for coals is making micropore volume larger.

Another idea regarding adsorbents was proposed a long time ago, but became very popular in the past decade, namely, the use of adsorbent in the form of a compact layer [22]. This was done to overcome the main disadvantage of the granulated adsorption bed - its low thermal conductivity due to the high bed porosity [23]. Even a simple filling of the space between large granules with smaller ones allows increasing both the COP and the AHCS specific power [24]. A much greater effects are obtained by gluing the granules to each other and ensuring good thermal contact between the bed and the heat exchanger plate. Larger binder content leads to a decrease in porosity, an increase in heat transfer to and in the adsorbent bed, and an improvement in the adsorption dynamics. On the other hand, a decrease in porosity results in worse mass transfer in the bed, which can compensate for the overall accelerating effect. In denser adsorbent beds described (see, e.g., [25]), a reasonable mass transfer rate is observed only at small bed thickness of 100-200 μm . The disadvantage of such thin beds is that the mass of the adsorbent in them turns out to be much less than other inert masses of the AHCS unit. As a result, COP significantly decreases [26, 27].

Thus, when organizing the layer, a clever trade-off is needed between improving heat transfer and impairing mass transfer. To achieve it, a combination of the consolidated layer with loose [28] or bridged [29] grains was proposed. In my opinion, this approach has great potential and can lead to significant improvement of AHCS dynamics.

Heat exchangers. For common air-to-liquid HEXs, the basic perfection indexes are the *compactness* and the *material utilization* that are the ratios S/V_{HEX} and S/V_{m} , where S is the air-side surface area, V_{HEX} is the total HEX volume, V_{m} is the HEX material (metal) volume. The higher both values are, the better HEX is. For AHCS units, one more parameter, the ratio $M_{\text{HEX}}/m_{\text{ad}} = (\text{HEX mass})/(\text{adsorbent mass})$, is widely used to account for the effect of inert thermal masses (see, e.g., [26, 27]). The definition of thermal mass M_{HEX} depends on the control volume chosen, which is affected by the HEX type and AHCS cycle [27, 30].

Various types of commercial HEX designs (finned flat-tube, spiral plates, shell and tube, hairpin, annulus tube, etc.) were surveyed in [31, 32, 33] in terms of SCP, COP, and ($M_{\text{HEX}}/m_{\text{ad}}$). The finned flat-tube and "shell and tube" HEXs were recommended for AHCS. However, the correct comparison is difficult since many parameters change at once for the HEXs analyzed. Therefore, the quest for the universal parameters that characterize AdHEX in ever more general terms could greatly promote the analysis.

On this path, the ratio (S/m_{ad}) was suggested [34] as a measure of HEX dynamic perfection, where S is the area of heat transfer surface between the HEX and adsorbent. It was revealed that for flat beds of loose adsorbent grains, adsorption dynamics of water and methanol is invariant with respect to this ratio [34]: (i) at equal (S/m_{ad})-values, the uptake/release curves are close, and (ii) the maximal SCP is proportional to (S/m_{ad}). It hints that the rate-limiting process is heat transfer in the AdHEX. A significant SCP-reduction at the same (S/m_{ad}) was

found for more complex AdHEX configuration - a commercial finned flat-tube HEX [34]. It follows that the enhancement of AHCS dynamics can rather be achieved not by improving the adsorbent itself but by eliminating system imperfections, such as non-optimal cycle time [35], lower efficiency of secondary HEX fins, and/or the presence of non-adsorbable gas [36]. In the latter case, it looks like that the S -value in the ratio (S/m_{ad}) should be the area of mass transfer surface between the HEX and vapour [36].

For seasonal heat storage, especially in cold countries, a new figure of HEX merit can be introduced, namely, M_{HTF}/M_{HEX} , where M_{HTF} is the HTF mass inside the HEX channels. This “dead” mass should be minimized to reduce sensible heat spent on its useless heating from the ambient to minimal heating temperature [37].

All these examples clearly demonstrate that HEXs optimal for AHCS can differ significantly from conventional HEXs, developed for other applications [31, 32, 33]. This implies the need to develop HEX production industry for AHCS, including new materials (e.g., wider use of plastics [38, 39]), advanced structures (fibres, foam, etc.) and innovative production methods, such as 3D printing [39, 40].

Cycles. Development of new cycles is another important direction of the AHCS development [33, 41]. In particular, new, more complex and realistic cycles were considered for seasonal storage [37, 42], amplification [43], and transportation [44] of low-temperature heat. A smart combination of two common approaches – cycle time reallocation [35] and mass recovery [45] – was proposed for optimizing a three-bed AHCS unit [46].

Another tendency is the use of water vapour as a refrigerant for AHCS cycles occurring at a temperature below 0°C. The authors of [47] and [27] proposed to add ethylene glycol or, respectively, use an aqueous salt solution instead of pure water for preventing ice formation in the evaporator/condenser. The proposed substitutions could expand the temperature range for water application below 0 °C. It is very profitable from the thermodynamic point of view and acceptable from the dynamic one, although further study of prototypes is necessary.

One more new trend, the benefits of which the future will show, is the application of novel energy sources, such as ultrasound and microwaves, for intensification of heat and mass transfer in AHCS units [48, 49].

New experimental methods. A Large Temperature Jump (LTJ) method has become the most informative and fruitful approach for analysing the AHC dynamics. Four LTJ-versions - volumetric, gravimetric, calorimetric, and thermal - have been installed in plenty of research labs worldwide. Many important features of the AHC dynamics were revealed by means of this method for single adsorbent grain, flat bed and entire AdHEX module.

A new Transport Impedance Analysis method [50, 51] has been developed to discriminate between heat and mass transport. It gives useful information about these processes at the adsorbent bed level. Extending this approach to the AdHEX level would make it a handy quantitative tool for practical optimising heat and mass transfers in real AHC units.

Summary/Conclusions

By now, the adsorption technologies of heat conversion and storage have made significant progress, and several adsorptive chillers have already appeared in the market. However, there is still a big room for improving these units and making them competitive with common compression chillers/(heat pumps). It can be reached by developing new adsorbents and cycles, and enhancing AHCS dynamics, as shown in this review, which mainly includes findings and tendencies emerging in the AHCS field in the past decade of this century.

Acknowledgements

This work is supported by the Ministry of Science and Higher Education of the Russian Federation within the governmental order for Boreskov Institute of Catalysis (project AAAA-A21-121011390006-0) and the Russian Foundation for Basic Research (grant 18-58-80047).

References:

- [1] Wang, R., Wang, L., Wu, J., *Adsorption Refrigeration Technology: Theory and Application*, John Wiley & Sons, 2014.
- [2] *Advances in Adsorption Technologies*, Eds. Saha, B., Ng, K., Nova Science Publishers, 2010.
- [3] Critoph, R. E., "Solid sorption cycles: A short history", *International Journal of Refrigeration*, 2012.
- [4] Meunier, F., "Adsorption heat powered heat pumps", *Applied Thermal Engineering*, 2013.
- [5] Jacob, U., "Is thermal cooling a sleeping giant or just wishful thinking?" Presentation at "Friends of Sorption" Workshop, 2018, Pisa, Italy. <https://www.sorptionfriends.org/presentations-keynotes/keynote-is-thermal-cooling-a-sleeping-giant-or-just-wishful-thinking-uli-jakob-green-chiller-association-for-sorption-cooling-e.v>.
- [6] Aristov, Yu. I., "Novel materials for adsorptive heat pumping and storage: screening and nanotailoring of sorption properties (review)", *Journal of Chemical Engineering of Japan*, 2007.
- [7] Henninger, S. K., Habib, H. A., Janiak, C., *Journal of American Chemical Society*, 2009.
- [8] Steinert, M., Ernst, S.-J., Henninger, S. K., Janiak, C., "Metal-Organic Frameworks as Sorption Materials for Heat Transformation Processes", *European Journal of Inorganic Chemistry*, 2020.
- [9] Liu, X., Wang, X., Kapteijn, F., "Water and Metal-Organic Frameworks: From Interaction toward Utilization", *Chemical Reviews*, 2020.
- [10] Gordeeva, L. G., Tu, Y., Pan, W., Palash, M. L., Saha, B., Aristov, Yu. I., Wang, R., "MOFs for adsorption heat conversion and water harvesting: a bridge between thermal engineering and materials science", *Nano Energy*, 2021.
- [11] Kakiuchi, H. M. Iwade, S., Shimooka, K., Ooshima, K., Yamazaki, M., Takewaki, T., "Water vapour adsorbent FAM-Z02 and its applicability to adsorption heat pump, Kagaku Kogaku Ronbunshu, 2005.
- [12] Jänchen, J., Ackermann, D., Weiler, E., Stach, H., Brösicke, W., "Calorimetric investigation on zeolites, AlPO₄'s and CaCl₂ impregnated attapulgite for thermochemical storage of heat", *Thermochimica Acta*, 2005.
- [13] Tamainot-Telto, Z., Metcalf, S., Critoph, R., Zhong, Y., Thorpe, R., "Carbon–ammonia pairs for adsorption refrigeration applications: ice making, air conditioning and heat pumping", *International Journal of Refrigeration*, 2009.
- [14] El-Sharkawy, I. I., Hassan, M., Saha, B. B., Koyama, S., Nasr, M. M., "Study on adsorption of methanol onto carbon based adsorbents", *International Journal of Refrigeration*, 2009.
- [15] Henninger, S. K., Schick Tanz, M., Hugenell, P. P. C., Sievers, H., Henning, H.-M., "Novel Sorption Materials for Solar Heating and Cooling", *International Journal of Refrigeration*, 2012.
- [16] Gordeeva, L. G., Aristov, Yu. I., "Composites "salt inside porous matrix" for adsorption heat transformation: a current state of the art and new trends", *International Journal of Low Carbon Technologies*, 2012.
- [17] Aristov, Yu. I., *Nanocomposite Sorbents for Multiple Applications*, Jenny Stanford Publishing, 2020.

-
- [18] Gordeeva, L. G., Grekova, A.D., Krieger, T.A., Aristov, Yu. I., "Adsorption properties of composite materials (LiCl+LiBr)/silica", *Microporous Mesoporous Materials*, 2009.
- [19] Sun, Y., Spieß, A., Jansen, C., Nuhnen, A., Gökpinar, S., Wiedey, R., Ernst, S.-J., Janiak, C., 'Tunable LiCl@UiO-66 composites for water sorption-based heat transformation applications', *Journal of Materials Chemistry A*, 2020.
- [20] Shkatulov, A. I., Joosten, R., Fischer, H., Huinink, H., "Core-shell encapsulation of salt hydrates in mesoporous silica shells for thermochemical energy storage", *ACS Applied Energy Materials*, 2020.
- [21] Grekova, A. D., Gordeeva, L. G., Aristov, Yu. I., "Composite "LiCl/vermiculite" as advanced water sorbent for thermal energy storage", *Applied Thermal Engineering*, 2017.
- [22] Capri, A., Frazzica, A., Calabrese, L., "Recent developments in coating technologies for adsorption heat pumps: A review", *Coatings*, 2020.
- [23] Tsotsas, E., Schluender, E.-U., "Numerical calculation of the thermal conductivity of two regular bi-dispersed beds of spherical particles", *Computational Chemical Engineering*, 1990.
- [24] Girnik, I. S., Aristov, Yu. I., "Making adsorptive chillers more fast and efficient: the effect of bi-dispersed adsorbent bed", *Applied Thermal Engineering*, 2016.
- [25] van Heyden, H., Munz, G., Schnabel, L., Schmidt, F., Mintova, S., Bein, T., "Kinetics of water adsorption in microporous aluminophosphate layers for regenerative heat exchangers", *Applied Thermal Engineering*, 2009.
- [26] Freni, A., Maggio, G., Sapienza, A., Frazzica, A., Restuccia, G, Vasta, S., "Comparative analysis of promising adsorbent/adsorbate pairs for adsorptive heat pumping, air conditioning and refrigeration", *Applied Thermal Engineering*, 2016.
- [27] Girnik, I. S., Aristov, Yu. I., "Water as a working fluid for adsorptive cycles operating at temperature below 0°C", *Energy*, 2020.
- [28] Li, G., Qian, S., Lee, H., Hwang, Y., Radermacher, R., "Experimental investigation of energy and exergy performance of short term adsorption heat storage for residential application", *Energy*, 2014.
- [29] Ammann, J., Ruch, P., Michel, B., Studart, A. R., "High-power adsorption heat pumps using magnetically aligned zeolite structures", *ACS Applied Materials and Interfaces*, 2019.
- [30] Gluesenkamp, K. R., Frazzica, A., Velte, A., Metcalf, S., Yang, Z., Rouhani, M., Blackman C., Qu, M., Laurenz, E., Rivero-Pacho, A., Hinners, S., Critoph, R., Bahrami, M., Földner, G., Hallin, I., "Experimentally measured thermal masses of adsorption heat exchangers", *Energies*, 2020.
- [31] Sharafian, A., Bahrami, M., "Assessment of adsorber bed designs in waste-heat driven adsorption cooling systems for vehicle air conditioning and refrigeration" *Renewable and Sustainable Energy Reviews*, 2014.
- [32] Zhang, Y., Wang, R., "Sorption thermal energy storage: Concept, process, applications and perspectives", *Energy Storage Materials*, 2020.
- [33] Li, X., Hou, X., Zhang, X., Yuan, Z., "A review on development of adsorption cooling - Novel beds and advanced cycles", *Energy Conversion and Management*, 2015.
- [34] Aristov, Yu. I., Girnik, I. S., Glaznev, I. S., "Optimization of adsorption dynamics in adsorptive chillers: Loose grains configuration", *Energy*, 2012.
- [35] Aristov, Yu. I., Sapienza, A., Ovoshchnikov, D., Freni, A., Restuccia, G., "Reallocation of adsorption and desorption times for optimisation of cooling cycles", *International Journal of Refrigeration*, 2012.

-
- [36] Sapienza, A., Frazica, A., Freni, A., Aristov, Yu. I., "Dramatic effect of residual gas on dynamics of isobaric adsorption stage of an adsorptive chiller", *Applied Thermal Engineering*, 2016.
- [37] Palomba, V., Sapienza, A., Aristov, Yu.I., "Dynamics and useful heat of discharge stage of adsorptive cycles for long term thermal storage", *Applied Energy*, 2019.
- [38] Chen, X., Su, Y., Reay, D., Riffat S., "Recent research developments in polymer heat exchangers - A review", *Renewable and Sustainable Energy Reviews*, 2016.
- [39] Sapienza, A., Brancato, V., Aristov, Yu.I., Vasta, S., Plastic heat exchangers for adsorption cooling: Thermodynamic and dynamic performance, *Applied Thermal Engineering*, 2021.
- [40] AL-Hasni, S., Santori, G., "3D printing of vacuum and pressure tight polymer vessels for thermally driven chillers and heat pumps", *Vacuum*, 2020.
- [41] Gordeeva, L. G., Aristov, Yu. I., "Adsorptive heat storage/amplification: new cycles and adsorbents", *Energy*, 2019.
- [42] Mehari, A., Xu, Z. Y., Wang, R. Z., "Thermally-pressurized sorption heat storage cycle with low charging temperature", *Energy*, 2019.
- [43] Aristov, Yu. I., "Adsorptive transformation of ambient heat: a new cycle", *Applied Thermal Engineering*, 2017.
- [44] Gao, J. T., Xu, Z., Wang, R. Z., "Enhanced sorption heat transportation cycles with large concentration glide", *Energy Conversion and Management*, 2019.
- [45] Wang, R., "Performance improvement of adsorption cooling by heat and mass recovery operation", *International Journal of Refrigeration*, 2001.
- [46] Zajackowski, B., "Optimizing performance of a three-bed adsorption chiller using new cycle time allocation and mass recovery", *Applied Thermal Engineering*, 2016.
- [47] Seiler, J., Hackmann, J., Lanzerath, F., Bardow, A., "Refrigeration below zero °C: Adsorption chillers using water with ethylene glycol as antifreeze", *International Journal of Refrigeration*, 2001.
- [48] Zhang, W., Yao, Y., Wang, R., "Influence of ultrasonic frequency on the regeneration of silica gel by applying high-intensity ultrasound," *Applied Thermal Engineering*, 2010.
- [49] Demir, H., "Experimental study on a novel microwave-assisted adsorption heat pump," *International Journal of Refrigeration*, 2014.
- [50] Ammann, J., Ruch, P., Michel, B., Studart, A., 'Quantification of heat and mass transport limitations in adsorption heat exchangers: Application to the silica gel/water working pair", *International Journal of Heat and Mass Transfer*, 2018.
- [51] Ammann, J., Michel, B., Ruch, P., "Characterization of transport limitations in SAPO-adsorbent coatings for adsorption heat pumps", *International Journal of Heat and Mass Transfer*, 2019.

Manuscripts

An experimental investigation of oily wastewater treatment in a bubble column humidifier using an improved method for measuring humidity

E. Eder^{1*}, F. Stemer¹, D. Brüggemann², M. Preißinger¹

¹illwerke vkw Endowed Professorship for Energy Efficiency, Research Center Energy, Vorarlberg University of Applied Sciences, Dornbirn 6850, Austria

²Department of Engineering Thermodynamics and Transport Processes (LTTT), Faculty of Engineering Science, University of Bayreuth, Bayreuth 95440, Germany

*Corresponding author: elias.eder@fhv.at

Abstract

Bubble column humidifiers (BCHs) are frequently used for the humidification of air in various water treatment applications. A potential but not yet profoundly investigated application of such devices is the treatment of oily wastewater. To evaluate this application, the accumulation of an oil-water emulsion using a BCH is experimentally analyzed. The amount of evaporating water vapor can be evaluated by measuring the humidity ratio of the outlet air. However, humidity measurements are difficult in close to saturated conditions, as the formation of liquid droplets on the sensor impacts the measurement accuracy. We use a heating section after the humidifier, such that no liquid droplets are formed on the sensor. This enables us a more accurate humidity measurement. Two batch measurement runs are conducted with (1) tap water and (2) an oil-water emulsion as the respective liquid phase. The humidity measurement in high humidity conditions is highly accurate with an error margin of below 3 % and can be used to predict the oil concentration of the remaining liquid during operation. The measured humidity ratio corresponds with the removed amount of water vapor for both tap water and the accumulation of an oil-water emulsion. Our measurements show that the residual water content in the oil-water emulsion is below 4 %.

Keywords: Bubble column humidifier, Air humidification, Water treatment, Humidification-dehumidification, Oily wastewater

Nomenclature

Acronyms

BCH Bubble column humidifier
HDH Humidification-dehumidification

Physical Properties

\dot{m} Mass flow (kg/s)
 \dot{Q} Heat flow (W)
 ω Humidity ratio (–)
 ε Effectiveness (–)
 φ Relative humidity (%)
 C Oil mass fraction (%)
 h Liquid height (m)
 m Mass (kg)
 p Pressure (Pa)
 T Temperature (°C)

v Velocity (m/s)

Subscripts

0 Initial
a Air
b Bulk liquid
c Condensate
cw Cooling water
dh Dehumidifier
h Humidifier
hum Humidity sensor
i Inlet
max Maximum
o Outlet
surf Liquid surface
v Water vapor

Introduction

Humidification-dehumidification (HDH) is a desalination technology to address water scarcity in arid and remote regions [1]. Its importance is ever-growing due to its benefits such as (1) a low maintenance requirement, (2) the ability to use low-grade thermal energy and therefore renewable heat sources and (3) an insensitivity to various feed liquids [2, 3, 4]. This insensitivity indicates the potential of HDH to also treat oily wastewater.

Different industrial processes generate oily wastewater as a byproduct. Vast amounts of oily wastewater are generated in the petrochemical industry [5] and in the hull of ocean-going vessels as bilge water [6]. Centrifugal or gravitational separation, membrane processes [7, 8], ultrafiltration [7, 9] or electrocoagulation [10, 11] are selected processes that are applied to treat oily wastewater. Due to its unique advantages, HDH can also be a promising candidate for this application [3]. This process imitates the natural water cycle and consists of the humidification and subsequent dehumidification of a carrier gas, mostly air. For the humidification, different humidifier designs have been tested and recommended, including spray towers, wetted-wall towers and packed bed towers [12]. Additionally, bubble column humidifiers (BCHs) have often been proposed for HDH cycles. In comparison with conventional humidifiers, they provide advantages, such as (1) high heat and mass transfer, (2) direct contact humidification and (3) a low technological demand [12, 13].

Several studies have measured air conditions directly at the BCH outlet using different kinds of hygrometers [14, 15, 16], measuring full or close to saturation of the air stream at the humidifier outlet. However, measurements show that humidity sensors are consistently covered with liquid droplets if installed directly at the humidifier outlet due to the high temperature and relative humidities. Consequently, the sensor indicates full saturation of the air stream. We also encountered this issue in a previous study [17], as did Katz et al. [18]. So far, it is inconclusive whether the air at the outlet of a BCH is really in a saturated state.

We intend to overcome the described measurement issue with a novel configuration for measuring humidity at the outlet of a BCH. The accumulation of an oil-water emulsion representing oily wastewater will be investigated using this approach. We use our improved measurement method to calculate the current oil concentration of the investigated oil-water emulsion during accumulation. With this study, we intend to lay the foundation for treating oily wastewater with the HDH process.

Methods and Materials

Experimental test setup

The HDH test setup used for our experiments is depicted in Fig. 1. We are using a complete HDH cycle consisting of a humidifier, a dehumidifier and a heat source. This allows us to compare the measured outlet humidity ratio ω_{hum} to the corresponding liquid weight decrease Δm in the humidifier and the measured condensate production m_c at the dehumidifier.

The BCH (1) consists of acrylic glass cylinders with an inner diameter of $d = 0.14$ m and stainless steel parts. A plate fin heat exchanger (2) is used to dehumidify the air stream. A floater-based sensor is used to continuously measure the change in liquid height and a magnetic stirrer is installed in the humidifier for continuous mixing of the emulsion. Measurements on our setup show that phase separation of the emulsion occurs without using a magnetic stirrer. The liquid temperature T_b is measured by a resistance thermometer (3) and controlled by heating cartridges. Inlet air is controlled by a mass flow controller and then dispersed into fine bubbles in the sparger module. A sparger plate with an orifice diameter of $d_0 = 0.001$ m is installed in the sparger module. Air temperature is measured at the humidifier inlet $T_{h,i}$ (4), at the humidifier outlet $T_{h,o}$ (5) and at the dehumidifier outlet $T_{dh,o}$ (6) using resistance thermome-

ters. Furthermore, a heating line is installed after the humidifier outlet to prevent condensation of the humid air stream. Thermal insulation is also applied to the BCH and all pipes before the heating line to minimize heat loss to the environment. After this heating line, temperature and relative humidity of the air are measured by a capacitive hygrometer ($T_{\text{hum}}, \varphi_{\text{hum}}$) (7). In a preliminary measurement run, this hygrometer is installed at the humidifier inlet to measure the inlet conditions of the air stream. A separate cooling water cycle ensures the cooling of the air stream in the dehumidifier, which leads to condensation of water vapor. The produced condensate is continuously collected and weighed by a digital scale. All relevant data are logged in intervals of 30 seconds throughout the measurement periods.

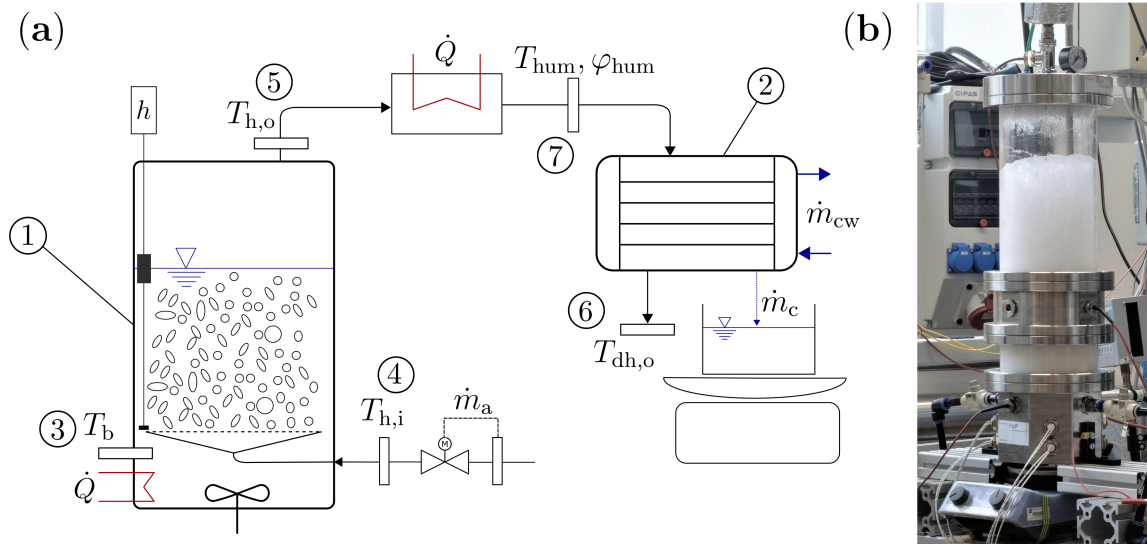


Figure 1. a) HDH process scheme and b) photograph of the BCH without thermal insulation

The amount of water vapor carried out of the humidifier \dot{m}_v is calculated using Equ. 1, where \dot{m}_a is the air mass flow and $\omega_{h,o}$ and $\omega_{h,i}$ are the air humidity ratio values at the humidifier outlet and inlet, respectively.

$$\dot{m}_v = \dot{m}_a \cdot (\omega_{h,o} - \omega_{h,i}) \quad (1)$$

The humidity ratio of the air stream at the humidifier inlet is measured and is equal to $\omega_{h,i} = 0.2 \text{ g}_v/\text{kg}_a$. As changes to this value are negligible during operation, it is assumed to be constant for all measurements.

To estimate the air state after humidification in the BCH, relative humidities of the air at liquid temperature T_b and humidifier outlet temperature $T_{h,o}$ are calculated for the reference measurement run with tap water. For this, Equ. 2 is used, where ω_{hum} is the measured air humidity ratio at the sensor position, p_{atm} is the atmospheric pressure and p_s is the saturation vapor pressure, which is calculated for the respective temperatures using the Antoine equation. These calculations give insight into the air state at the liquid surface.

$$\varphi = \frac{\omega_{\text{hum}} \cdot p_{\text{atm}}}{(0.622 + \omega_{\text{hum}}) \cdot p_s(T)} \quad (2)$$

with

$$\omega_{\text{hum}} = 0.622 \cdot \frac{\varphi_{\text{hum}} \cdot p_s(T_{\text{hum}})}{p_{\text{atm}} - \varphi_{\text{hum}} \cdot p_s(T_{\text{hum}})} \quad (3)$$

Fig. 2 indicates the respective sensor positions and the relative humidities to be calculated.

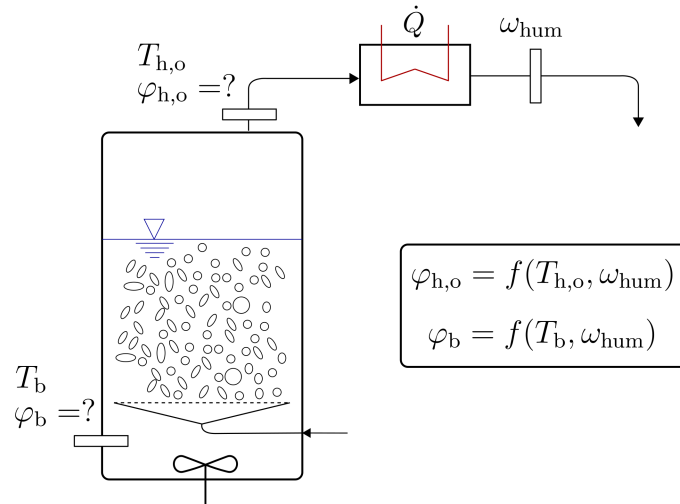


Figure 2. Bubble column humidifier with sensor positions for calculations of the outlet air state

Parametric settings and preparation of emulsion

Tab. 1 lists the parametric settings for the two individual measurement runs, namely the liquid temperature T_b , the superficial air velocity v_a and the initial liquid mass m_0 .

Table 1. Parametric settings

Liquid phase	T_b °C	v_a m/s	m_0 g
Tap water	60	0.03	5217
Oil-water emulsion	70	0.02	4994.2

The oil-water emulsion is prepared in accordance with Tab. 2. Sodium Dodecylbenzenesulfonate (SDBS) is used as an emulsifier. Additionally, Rimagents-L is used as an anti-foaming agent to prevent foam formation on top of the liquid surface. The batch run is conducted at an initial oil mass concentration of about $C = 55\%$. It is attempted to reach an oil mass concentration of 100 % by removing the entire water phase from the liquid mixture. For calculations of the oil mass concentration, the emulsifier and anti-foaming agent amounts are neglected, as they only make up around 0.5 % of the entire emulsion.

Table 2. Emulsion makeup

Constituent	Name	Amount g
Industrial white oil	Petro Canada Purity FG WO 35	2750
Tap water	-	2206
Emulsifier	SDBS	11
Anti-foaming agent	Rimagents-L	27

Error Analysis

The installed sensors and instruments are listed in Tab. 3 with their range and accuracy. As the respective instrumentation errors are relatively small, they are not visualized by error bars in the respective figures. Error propagation is calculated for derived values where it is applicable.

Table 3. Sensors, measurement ranges and uncertainties

Sensor type	Measurement Range	Uncertainty
PT1000 thermometer class B (3,4,5,6)	0 – 100 °C	$\pm[0.3 + 0.005 \cdot T]$ °C
PT1000 thermometer class AA (7)	-40 – 180 °C	$\pm[0.1 + 0.0017 \cdot T]$ °C
Capacitive humidity sensor (7)	0 – 100 %RH	$\pm[1 + 0.007 \cdot \varphi]$ %RH
Floater based liquid height sensor	0 – 500 mm	± 0.5 mm
Mass flow meter	0 – 10 m _{stp} ³ /h	± 0.01 m _{stp} ³ /h
Digital scale	0 – 3100 g	± 0.01 g

Results and Discussion

In Fig. 3 our results with tap water as the liquid phase are visualized. These include (a) system temperatures, (b) calculated relative humidities, (c) liquid height and (d) amount of carried out water vapor in dependence of time.

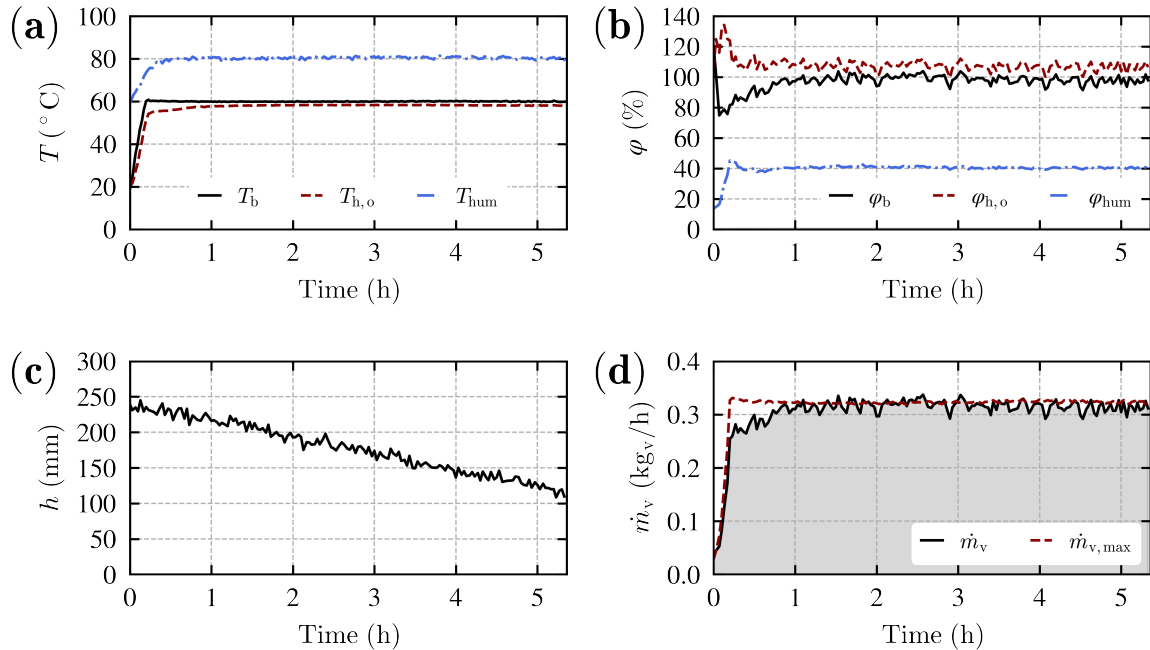


Figure 3. Tap water batch run; a) system temperatures, b) relative humidities, c) liquid height and d) amount of carried out water vapor in dependence of time

The humidifier outlet temperature $T_{h,o}$ reaches a steady-state at a value slightly below the liquid temperature T_b (see Fig. 3 (a)). This indicates a high heat transfer from the liquid column to the air stream.

To reach the measured humidity ratio ω_{hum} , the relative humidity of the air would need to be slightly below 100 % and therefore almost completely saturated, if the air was at bulk

liquid temperature T_b and clearly above 100 %, therefore supersaturated and containing liquid droplets, if the air was at humidifier outlet temperature $T_{h,o}$ (see Fig. 3 (b)). As the air temperature at the liquid surface has to be between these two temperatures, it is concluded and empirically shown that the air at the liquid surface is at 100 % relative humidity and therefore saturated.

It is also evident that the decrease in liquid height is linear, once a steady-state value of carried out water vapor \dot{m}_v is reached (see Fig. 3 (c)).

By integrating \dot{m}_v , the amount of water vapor carried out of the humidifier overall m_v , can be computed. This integration is visualized by the filled area (see Fig. 3 (d)). The amount of water vapor carried out of the humidifier \dot{m}_v strongly increases at the beginning of the measurement, as the HDH system is heating up. Once system temperatures reach a steady-state, the amount of water vapor carried out of the humidifier stays constant as well. In steady-state, it is very close to the maximum value $\dot{m}_{v,max}$, which corresponds to the air stream reaching liquid temperature and saturation.

In Fig. 4 the results of the accumulation of an oil-water emulsion are visualized including (a) system temperatures, (b) oil mass concentration, (c) liquid height and (d) amount of carried out water vapor. The oil mass concentration C is derived from the integrated amount of carried out water vapor.

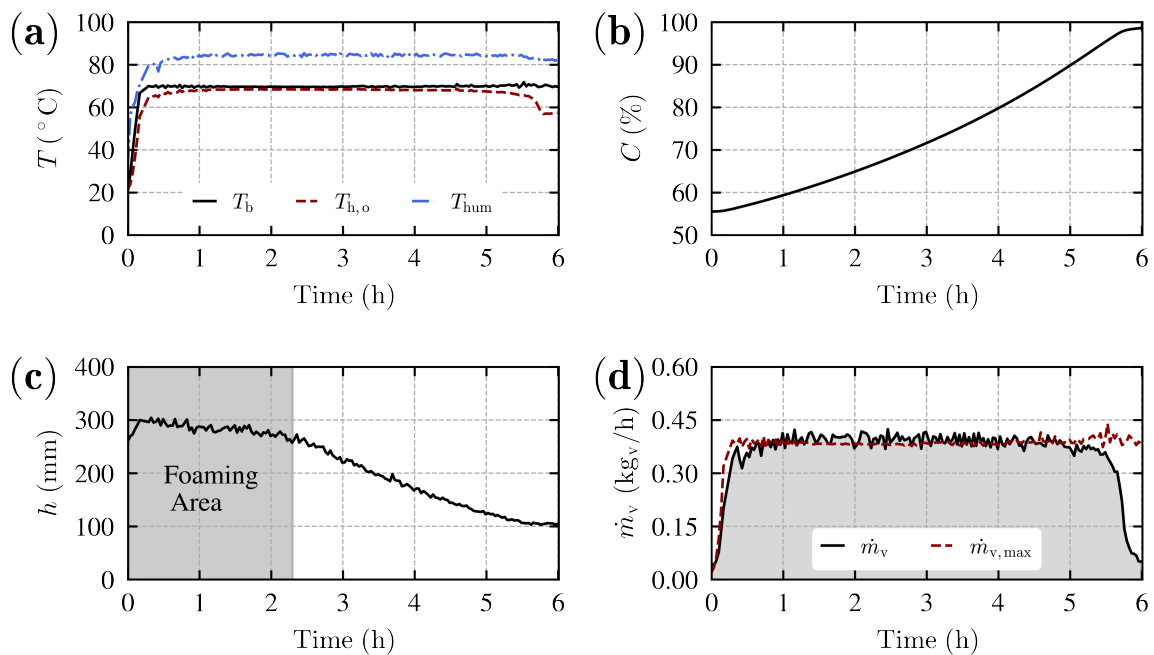


Figure 4. Oil-water emulsion batch run; a) system temperatures, b) oil mass concentration, c) liquid height and d) amount of carried out water vapor in dependence of time

According to Fig. 4 the humidifier outlet temperature $T_{h,o}$ is gradually reaching a steady state and remains constant for the majority of the measurement duration. At approximately 5.5 hours, however, there is a drop in humidifier outlet temperature. This drop happens in accordance with a drop in measured air humidity ratio ω_{hum} at an oil mass concentration of approximately 97 % (see Fig. 4 (d)). The investigated temperature drop is an indicator for the drop in humidity ratio as the humid air stream has a higher thermal mass and is therefore cooled to a lower extent in comparison with a low humidity air stream.

Even though an anti-foaming agent is used to prevent the formation of too much foam, such formation occurred for low oil mass concentrations. This formation affects the decrease in liquid height. In the foaming area (see Fig. 4 (c)), the reduction in liquid height is partially compensated by a reduction in foam volume. The reduction in liquid height reaches its maximum once there is no more occurring foam.

Finally, it can be seen that at some point, the liquid height is not reduced anymore and the measured humidity ratio at the humidifier outlet drops to the initial value. This can be explained by Tab. 4, which lists the calculated amounts of water vapor carried out m_v as well as the measured reduction in liquid phase Δm in the humidifier. The feed liquid is measured with a digital scale at the beginning and the end of the measurement run to measure the liquid weight reduction for tap water. For the oil-water emulsion, the initial amount of water is already known from preparing the emulsion.

Table 4. Measurement results

Liquid phase	Δm	m_v	m_c
	g	g	g
Tap water	1704	1633 ± 68	1411
Oil-water emulsion	2206	2167 ± 89	1944

The findings, according to Tab. 4 are summarized as follows:

- **The humidity measurement has a very good accuracy:** This is evident as the integrated amount of water vapor carried out of the humidifier predicts the liquid weight reduction with an accuracy of 4.1 % and 1.8 %, for tap water and the oil-water emulsion, respectively.
- **The produced condensate is lower than the amount of water vapor carried out of the humidifier:** A dehumidifier effectiveness lower than $\varepsilon_{dh} = 1$ leads to this behavior. This indicates that HDH productivity is not suitable to characterize the humidification unless dehumidifier losses are accounted for.
- **Our calculations indicate that the residual water content in the oil-water emulsion is below 4 %:** This is derived by the difference of the initial water content in the emulsion and the integrated amount of extracted water vapor.

Selected probes are depicted for optical inspection in Fig. 5.

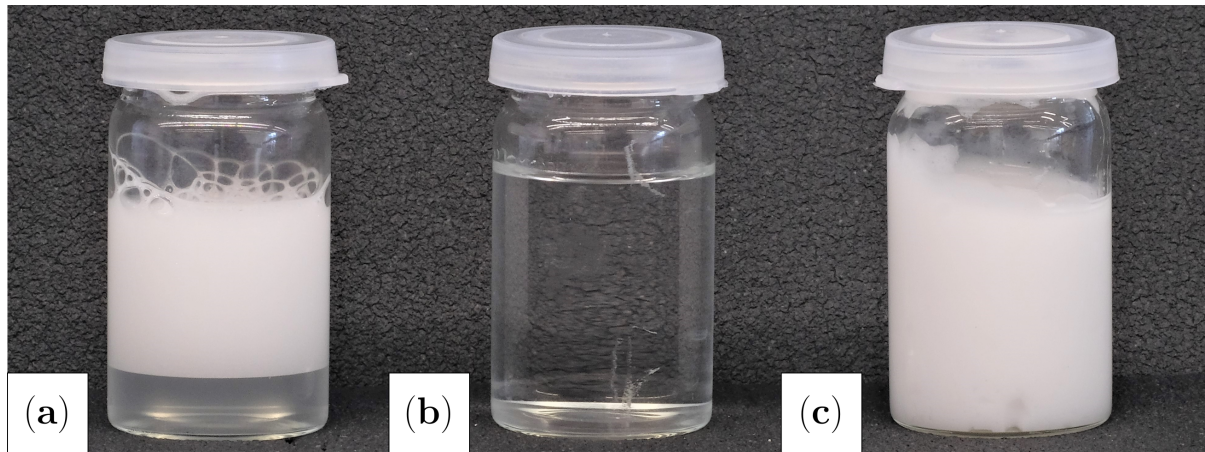


Figure 5. Liquid probes of a) the initial emulsion with visible phase separation, b) the produced condensate and c) the accumulated and emulsified oil phase

The initial oil-water emulsion (a) shows a phase separation that is not occurring during operation due to the magnetic stirrer. The prepared emulsion is an oil-in-water emulsion, thus water is the continuous phase. The produced condensate (b) is highly pure, still there are minimal traces of oil visible on the surface. The final emulsion (c) is highly viscous after the removal of almost the entire water phase.

Conclusion

Our new approach of measuring air humidity at the outlet of a BCH allows for measurements of the humidity ratio at the humidifier outlet with an error margin of less than 5 %. The liquid weight reduction in the humidifier is predicted for (1) a reference measurement run with tap water and (2) the accumulation of an oil-water emulsion with equally good accuracy. System calculations indicate that almost the entire water phase is removed from the oil-water emulsion. Our results improve current methods for experimentally investigating humidification in bubble columns and underline the potential of bubble columns for the treatment of oily wastewater.

Acknowledgement

This work is financed by the Austrian Science Fund (FWF) via project grant number P31103.

References

- [1] A.S.A. Mohamed, M.S. Ahmed, H.M. Maghrabie, and A.G. Shahdy. Desalination process using humidification–dehumidification technique: A detailed review. *International Journal of Energy Research*, October 2020.
- [2] Y. Ghalavand, M.S. Hatamipour, and A. Rahimi. A review on energy consumption of desalination processes. *Desalination and Water Treatment*, pages 1–16, March 2014.
- [3] M. Preißinger. Bilge water treatment and desalination based on HDH-technology: an experimental investigation of a demonstration plant. *Desalination and Water Treatment*, 127:50–56, 2018.
- [4] P. Gao, M. Zhang, Y. Du, B. Cheng, and D. Zhang. Study on bubble column humidification and dehumidification system for coal mine wastewater treatment. *Water Science and Technology*, 77(7):1909–1919, April 2018.
- [5] L. Yu, M. Han, and F. He. A review of treating oily wastewater. *Arabian Journal of Chemistry*, 10:S1913–S1922, May 2017.
- [6] P. Tiselius and K. Magnusson. Toxicity of treated bilge water: The need for revised regulatory control. *Marine Pollution Bulletin*, 114(2):860–866, January 2017.
- [7] M. Tomaszewska, A. Orecki, and K. Karakulski. Treatment of bilge water using a combination of ultrafiltration and reverse osmosis. *Desalination*, 185(1-3):203–212, November 2005.
- [8] M. Gryta. Bilge water separation by membrane distillation. *Separation and Purification Technology*, 237:116332, April 2020.
- [9] K. Karakulski, W.A. Morawski, and J. Grzechulska. Purification of bilge water by hybrid ultrafiltration and photocatalytic processes. *Separation and Purification Technology*, 14(1):163–173, August 1998.
- [10] M. Asselin, P. Drogui, S.K. Brar, H. Benmoussa, and J. Blais. Organics removal in oily bilgewater by electrocoagulation process. *Journal of Hazardous Materials*, 151(2):446–455, March 2008.
- [11] Y. Bian, Z. Ge, C. Albano, F.L. Lobo, and Z.J. Ren. Oily bilge water treatment using DC/AC powered electrocoagulation. *Environmental Science: Water Research & Technology*, 5(10):1654–1660, 2019. Publisher: The Royal Society of Chemistry.

- [12] G.P. Narayan, M.H. Sharqawy, E.K. Summers, J.H. Lienhard, S.M. Zubair, and M.A. Antar. The potential of solar-driven humidification–dehumidification desalination for small-scale decentralized water production. *Renewable and Sustainable Energy Reviews*, 14(4):1187–1201, May 2010.
- [13] M. Faegh, P. Behnam, and M. B. Shafii. A review on recent advances in humidification-dehumidification (HDH) desalination systems integrated with refrigeration, power and desalination technologies. *Energy Conversion and Management*, 196:1002–1036, September 2019.
- [14] A. Khalil, S.A. El-Agouz, Y.A.F. El-Samadony, and Ahmed Abdo. Solar water desalination using an air bubble column humidifier. *Desalination*, 372(Journal Article):7–16, 2015.
- [15] M.T. Ghazal, U. Atikol, and F. Egelioglu. An experimental study of a solar humidifier for HDD systems. *Energy Conversion and Management*, 82:250–258, June 2014.
- [16] K. Srithar and T. Rajaseenivasan. Performance analysis on a solar bubble column humidification dehumidification desalination system. *Process Safety and Environmental Protection*, 105:41–50, January 2017.
- [17] E. Eder and M. Preißinger. Experimental analysis of the humidification of air in bubble columns for thermal water treatment systems. *Experimental Thermal and Fluid Science*, 115:110063, July 2020.
- [18] Y. Katz, V. Dubovsky, G. Ziskind, and R. Letan. Air-Water Transient Heat Transfer in a Bubble Column. In *HT2003*, pages 341–346, Heat Transfer: Volume 2, July 2003.

Projects for the desalination of brackish water and seawater at the Faculty of Engineering in Bilbao

Natalia Alegría^{1*} and Igor Peñalva¹

¹Energy Engineering Department, Faculty of Engineering in Bilbao, University of the Basque Country (UPV/EHU), Plaza Ingeniero Torres Quevedo nº 1, 48013 Bilbao, Spain

*Corresponding author: natalia.alegria@ehu.eus

Abstract

Desalination of brackish water and seawater is a process in constant development and improvement that needs to be taken into account nowadays in order to provide fresh water for different uses. Students that have studied the specialty of Hydraulic Engineering at the Faculty of Engineering in Bilbao in University Master in Industrial Engineering are qualified to design and/or improve these kinds of facilities. These students have developed several projects in collaboration with top companies of the sector in the recent years. This work summarizes the main contributions of these projects focusing on the advances and improvements obtained for the desalination process.

Keywords: desalination, degree, master, energy efficiency

Introduction/Background

The educational offer at the Faculty of Engineering in Bilbao includes the University Master in Industrial Engineering where the Specialty of Hydraulic Engineering with 30 ECTS credits can be studied [1]. The world of fluids implies many disciplines that are difficult to bring together. Figure 1 shows a brief summary of the possible applications of the Hydraulic Engineering.



Figure 1: Hydraulic Engineering Applications

That specialty was developed for the Industrial Engineering degree in order to work on the most relevant issues of the water sector (Management, Operation, Pipeline Networks and Hydroelectric Power Plants [2, 3]), together with some other disciplines related to the operation such as Computational Fluid Dynamics (CFD), Hydraulic Power or Pneumatics. This specialty is a unique case in Spain among all the Master's degrees offered in Industrial Engineering.

More than 90 % of the world water is brackish water and seawater. Therefore, it is necessary to take into account this kind of water as a resource. In this sense, among the specialty subjects, one of them called Management of Hydraulic Resources and Hydroelectric Power Plants [4] with 6 ECTS credits is studied during the 1st academic year of the master. When developing this subject, desalination techniques for brackish water and seawater are explained to the students in order to be able to adapt them to the different uses of fresh water (domestic, for agricultural-livestock use or for industrial use).

In relation to hydraulic machinery, which is a fundamental part of these kind of facilities (pumps, for example, are the most used type of machine after engines), there is a compulsory subject that analyzes Fluid Facilities and Machinery, with 4,5 ECTS credits also during the 1st academic year of the master.

The knowledge gained by the students in this subject in relation to the desalination processes is then applied when carrying out their Master's Thesis.

Students need to get the competences by carrying out alternative activities, based on the innovation. After passing the subjects, they are ready to incorporate to the job market. An Educational Cooperation Program sets the students in the path of the job market for the first time, where they can develop their Master's Thesis in situ. Often, after finishing their studies at the university, they end up working in the same companies. The university teaching encompasses a curriculum of a degree that enables the practice of the Industrial Engineering profession with regulated professional assignments [5]. Among the competences, the following are included: design, test and analysis of fluid machinery and design and development of projects for fluid facilities.

The Basque Country is not an area that has a specific need of brackish water or seawater desalination, which can be a critical issue in the Canary Islands, Balearic Islands or in the southeast of the Iberian Peninsula. However, the top companies of the sector Acciona [6], Suez [7], Ferrovial-Cadagua [8], and so on, are located in the Basque Country and the students develop these topics in a satisfying way in collaboration with these companies.

The final objective is to get the students into the job market within the hydraulic area such as desalination. The covered academic path will be described in the following sections.

Discussion and Results

In order to study in the specialty of Hydraulic Engineering, students have previously had to complete the Bachelor's Degree in Engineering in Industrial Technology or have had to take additional training in order to access the Master's Degree in Industrial Engineering at the Faculty of Engineering in Bilbao.

In the Degree in Engineering in Industrial Technology, and in practically all degrees in Engineering, Fluid Mechanics needs to be studied. The basic principles are focused in that subject in order to be able to develop advanced skills for the specialty. This means that any student from an engineering degree would not have to take additional training in this area to access the Master in Industrial Engineering and therefore the specialty in Hydraulic Engineering.

All students taking the master's degree in Industrial Engineering at the Faculty of Engineering in Bilbao will have to study the Fluid Facilities and Machinery subject. This subject is designed so

that students who do not choose the specialty of Hydraulic Engineering develop at least some basic notions of these machines, while those of the specialty can increase their knowledge about them in the subjects of the specialty through practical applications.

In addition to the skills of the degree [5], by taking this specialty, students will acquire the following skills:

- IH1. Design, operate and maintain hydraulic systems.
- IH2. Project, calculate, design and manage hydraulic resources and hydroelectric plants.
- IH3. Project, calculate and design fluid networks and oleopneumatic components.
- IH4. Have knowledge and advanced capabilities of calculation methods in fluid mechanics.
- IPCC4. Knowledge and skills to project and design electrical and fluid facilities, lighting, air conditioning and ventilation, energy saving and efficiency, acoustics, communications, home automation and smart buildings and security facilities.
- IPCC6. Knowledge and skills to perform verification and control of facilities, processes and products.
- IT5. Knowledge and skills for the design and analysis of heat engines and machines, hydraulic machines and industrial heat and cold installations.
- TI8. Ability to design and project automated production systems and advanced process control.

Concretely, with the subject of Management of Hydraulic Resources and Hydro-Electric Plants, the student will be provided with an elementary theoretical base to solve specific problems, typical within engineering, in the management of hydraulic resources and hydroelectric facilities.

Among the theoretical or practical contents of that subject, the following contents need to be highlighted:

- Water and hydrology.
- History of hydraulic planning. Scope.
- Water management in the world. Applications.
- The balance between uses and resources.
- Necessary endowments of use.
- The management of the demand.
- Water cycle. Precipitation.
- Surface water. Watersheds.
- Stochastic analysis of hydrological information.

So, seawater desalination and the reuse of water are explained in this topic.

Before finishing the studies, students can do External Practices subject that correspond to 9 ECTS credits during the 2nd academic year of the master. An Educational Cooperation Program allows getting the first job, passing the subject and developing their Master's Thesis in situ.

Master's Thesis must be carried out during at least 600 hours of personal work, which corresponds to 24 ECTS credits during the 2nd academic year of the master.

As long as some of the most important companies of the water sector operate in the surroundings of the Faculty, the desalination of brackish water and seawater is a topic for their Master's Thesis.

Different type of Master's Thesis in relation with brackish water and seawater have been presented:

- Design a new desalination plant in the island or Mediterranean coast
- Improvement of an existing facility
- Use of renewable energy in a desalination plant (solar thermal or wind energy)

The typical structure of these type of Master's Thesis is the following:

- Brief abstract in Spanish, Basque and English
- Introduction considering water resources (characteristics of the water quality, percentage of water used for activities, and salinity)
- Objectives and scope
- Description of a typical desalination facility and its fundamental parts
- Analysis of studied facility checking the hydraulic machinery (for example, the point of operation of the pump)
- Description of the different methods of energy recovery from reject
- Design and description of the improvement proposal
- Economic calculation of the proposed solution implementation
- Planning of Master's Thesis and economic cost
- Conclusions
- Bibliography

In order to pass satisfactorily the Master's Thesis, students have to write a memory and present it in an oral communication during 15 minutes. The cover page of one Master's Thesis is shown in Figure 2.



Figure 2: Cover page of one Master's Thesis

During the development of their Master’s Thesis, students are encouraged to analyse the water needs of the area. Then, they also check the available water resource of the region (saline and/or brackish) before studying the types of desalination plants that can be implemented. They usually focus on plants based on reverse osmosis as long as they are more widespread and all the stages of the process are analysed. In general, the critical step in terms of energy consumption, that consequently makes the process more expensive, is the high pressure pumping. This phase is usually studied in detail, trying to find cheaper but equally effective alternatives with the aim of improving the energy recovery system according to the latest existing developments in the market. In the past, the solution for that problem was choosing one of the several types of turbines (Pelton, Francis, and so on), but at this moment the new designs of energy recuperators are being implemented, such as ERI [9-15].

Also new membranes for reverse osmosis are being considered [16-19].

Table 1 shows some information about the Master’s Thesis related to desalination facilities of the recent years. Three types of Master’s Thesis have been identified: Design (D) / Implement (I) / Renewable energies (RE).

Table 1: Important information about the Master’s Thesis

Academic Year	Type	Title
2010/2011	RE	Reverse Osmosis Desalination with Thermal Solar Energy
2012/2013	D	Reverse Osmosis Desalination Plant
2013/2014	RE	Applying Wind Power to a Desalination Plant
2014/2015	I	Improving the Energy Efficiency of Adeje-Arona's EDAM
2017/2018	I	Taking advantage of the Rejection of the Son Tugores Salty Water Plant
2017/2018	D	Analysis of the different Methods of Energy Recovery from the Rejection of a Desalination Plant
2019/2020	I	Energy Revaluation of the El Atabal Salty Water Plant

A brief summary of these Master’s Thesis will be provided in the next paragraphs:

Master’s Thesis 1: Reverse Osmosis Desalination with Thermal Solar Energy

The objective of this final master's project is to carry out an analysis and a design of a desalination system using reverse osmosis of seawater in which the main energy consumption of the reverse osmosis process is provided by a solar thermal system. It is intended to be able to desalinate 15000 m³ of seawater to supply a population of 50000 inhabitants. The study of 3 possible sites on the southern desert coast of Peru (Arequipa, Moquegua and Tacna) has been carried out in order to obtain 300 l/d.

Unlike what happens with photovoltaic solar energy and wind energy, practical experiences regarding the coupling between reverse osmosis desalination systems and solar thermal technologies are very scarce. And there are no examples of commercial direct steam generation (DSG) generation plants.

In the case of solar technologies for DSG, by means of parabolic collectors, it is remarkable to note that, despite being an advanced technology, up to now it does not meet expectations due to its high costs and low yields. However, with the development of new materials this situation could change.

Master's Thesis 2: Reverse Osmosis desalination plant

The objective is to carry out a reverse osmosis desalination plant on the island of Ibiza so that the amount of drinking water produced can be increased and, thus, supply the demand, especially in populations where there is still no total coverage.

The desalination plant will provide 5500 m³/d so that the amount of drinking water obtained by this system will increase from the current 44500 m³/d, to 50000 m³/d.

The phases of the plant are:

- Catchment: necessary to capture and displace the feed water at the foot of the plant.
- Physical and chemical pre-treatment: in order to leave the water in appropriate conditions before coming into contact with the membranes in the core of the process.
- Reverse osmosis core: where the physical phenomenon of reverse osmosis takes place and where most of the energy consumption of the global process is concentrated.
- Brine flow rate or rejection: it will be sent to an energy recovery system in which it gives much of its energy back to the feed flow.
- Post treatment: to adapt the water product in relation to some of its physical-chemical characteristics and make it suitable for consumption.
- Pumping system: to move desalinated water from the point of production to the storage or consumption point.

As a novel feature, a power recovery system based on PX (Pressure Exchanger) devices will be applied. These devices consist of a rotating positive displacement pump that recovers energy from the reject jet, with 98 % efficiency and almost no maintenance.

The site of the plant will be in the vicinity of the town of Vista Alegre (south of Ibiza), which is located in the municipality of San José, the only one that does not have its own source of drinking water.

The operation of the plant will be carried out by a company that provides the drinking water supply service.

Master's Thesis 3: Applying Wind Power to a Desalination Plant

Motivated by the field of sustainability in the energy and water sector, the objective of the project aims to introduce the concept of water sustainability and desalination in particular.

The site chosen to develop the application, consisting of a self-tested desalination by a wind farm is the Canary Islands. Firstly, because the Islands are a paradigm in everything that refers to the water-energy binomial. Having been able to adapt to the times, and innovate to take advantage, in the most efficient and exquisite possible way, of natural water resources. The second reason is that the demand for primary energy in them is currently almost entirely covered by petroleum-derived fuels, resulting in an energy-dependent, non-competitive model with large negative environmental impact.

In addition, it is necessary to take into account the uniqueness of the Canary electric system. This system consists of six electrically insulated and small subsystems. This makes quality of service and service stability more complicated than large interconnected systems. Therefore, it is important to be self-sufficient as much as possible in each of the islands. That is why renewable energy is one of the keys to regional energy policy, aimed at reducing energy dependence and reducing emissions.

Master's Thesis 4: Improving the Energy Efficiency of Adeje-Arona's EDAM

The main objective of this project was to improve the energy efficiency of the processes that are carried out in the desalination plant, either in the osmosis area, or in the product water pumping area. This will reduce energy consumption per cubic meter of desalinated water. It will also reduce the maintenance costs of equipment today, when installing new ones, and improve safety.

The energy saving target set is 0,3 kWh/m³, as from that figure, the improvement becomes profitable.

Within the plant, improvement efforts are to focus on the membrane area, and on the product pumping area. The actions to be carried out in the elements are then being described in general.

In terms of electronic regulation and control in electric motors, speed drives will be incorporated, and motors will be replaced with more energy-efficient ones.

In relation to the pumps of the osmosis part, the impellers that are already installed will be replaced with others rectified by the same manufacturer, improving efficiency. In the product water pumping area, the old pumps will be replaced with new ones.

Energy recovery systems: Pelton turbines operating at the moment will be replaced by energy exchange systems, specifically ERI px models.

For the system to function properly, the pipe network will be redesigned, with its corresponding valves, transmitters, gaskets, and filters. The plant control system will also have to be adapted.

Master's Thesis 5: Taking advantage of the Rejection of the Son Tugores Salty Water Plant

The water treatment plant of Son Tugores, in Palma de Mallorca, supplies around 30 % of the daily water needs of the Balearic capital, since it is the convergence point of all water resources capable of being suitable for human consumption which EMAYA has, "Municipal Water and Sewer Company" of Palma.

In 1995, the desalination plant was built, which purifies 30000 m³/d, to solve the problem of salinization of the Na Burguesa and Pont d'Inca aquifers and to provide the city with water of high quality.

The plant was designed to treat water with a salt concentration between 2 and 10 g/L, but the values collected are between 5 g/L and 8 g/L. Thanks to the construction of desalination plants like this one, and thanks also to a good rainfall in the area, it has been possible to recover the aquifers in 15 years and reduce the salinity of the confined waters.

The work comprises the study carried out in this plant about the recovery of the water rejecting, which, at the moment, is drained to the sea without obtaining any benefit. Rejecting water will be used to produce more quantity of desalinated water without increasing the inflow to the plant and, through an energy recovery system, the specific consumption will be reduced. As a result, the cost per cubic meter of water produced will be lower.

The study is composed of divided into several parts. In the first sections the current situation of desalination worldwide, at the level of Spain and the Balearic Islands, is described. Afterwards, the different types of desalination are explained, especially the process based on reverse osmosis as long as it is the most used and the one operating in this plant. Finally, the existing plant and the new reject recovery plant are described and the calculations made to design this new plant are detailed.

The study also consists of a planning of the proposed project and a budge, as well as a summary of the future operating costs of the plant. At the end of the document, several annexes are included in which the calculations carried out are developed and the plans of the new plant are presented, as well as an environmental impact study and specifications of the selected turbo-pump and the membranes.

Master's Thesis 6: Analysis of the different Methods of Energy Recovery from the Rejection of a Desalination Plant

The aim of this Master's Thesis is to analyse the different energy recovery methods of the brine flow in a Sea Water Reverse Osmosis plant (SWRO) located in Adeje (Canary Islands). Following the analysis, the plant's economic and technical viability is studied in order to determine whether the method currently used could be substituted with a more efficient one.

The desalination plant, with a 30 000 m³/d capacity, covers the water supply of the Adeje-Arona region. Given that the plant started operating in 1998, its facilities and equipment are now less efficient than those currently available in the market. Therefore, the substitution or the replacement of the equipment currently installed in order to optimise the desalination process is a subject of great interest.

First, this work introduces desalination in a global context and explains the specificities of water needs in the Canary Islands, as well as the objectives, the scope and advantages of the project. Next, the desalination process and specifically the characteristics of the SWRO plant of Adeje-Arona are described. The different energy recovery alternatives are analysed, and an assessment is given as to the most adequate option. One of the systems, DWEER (Dual Work Exchanger Energy Recovery), that has been studied is shown in Figure 3.

The planning of the project and final quotation are also included. Finally, the conclusions extracted from the completion of this project are outlined.

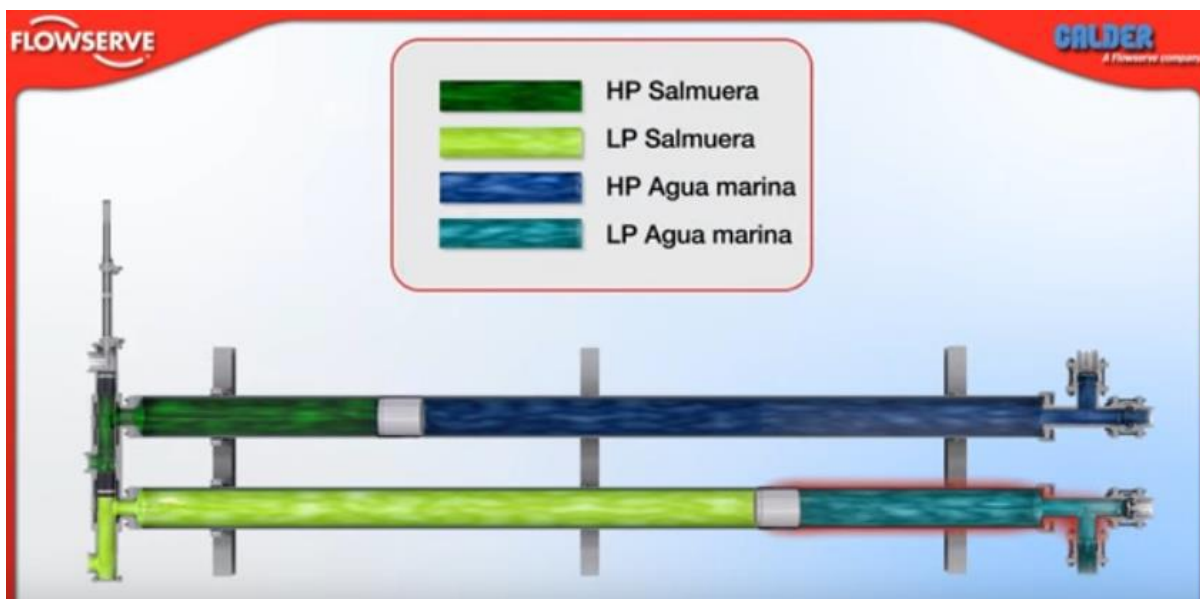


Figure 3: DWEER devices [11]

Master's Thesis 7: Energy Revaluation of the El Atabal Salobre Water Plant

The El Atabal desalination plant in Malaga, with a nominal production of 165000 m³/d, supplies most of the region's needs. In 2002, the old ETAP (Drinking Water Treatment Station) was modified to add a desalination process to the old water treatment plant and, therefore, solve the problem of water scarcity that plagued the area.

The plant was analyzed to treat water with a concentration of up to 8 g/L. the values collected so far ranged between 0,8 g/L and 6,5 g/L, far from the recommendation of values less than 0,5 g/L for human consumption.

Thanks to the construction of desalination plants like this one and to the technological advances in desalination, it has been possible to recover the country's aquifers in 15 years and reduce the salinity of confined waters.

This work deals with the study carried out in the aforementioned plant on the energy recovery of rejection waters, which, today, pose as an obsolete energy recovery system based on a turbopump that does not take advantage of energy capacity that this flow has. It is intended, on the one hand, to propose an improvement that allows increasing the production of the plant, and, on the other hand, to develop an alternative to the current energy recuperator that allows obtaining specific lower energy consumption, that is, reducing the cost per cubic meter of produced water.

Summary/Conclusions

Students who take the subject of Management of Hydraulic Resources and Hydroelectric Power Plants (specialty of Hydraulic Engineering, University Master in Industrial Engineering at the Faculty of Engineering in Bilbao) acquire the concepts and skills to be able to develop their Master's Thesis on the subject of desalination in an efficient way. This way, these students will be prepared to join the labour market by designing or improving facilities of this kind.

Acknowledgements

We would like to thank the Faculty of Engineering in Bilbao for supporting the Hydraulic Engineering specialty and the sector companies for the confidence in the knowledge acquired by our students.

References:

- [1] Webpage of Master of Industrial Engineering, (1st of March 2021) <https://www.ehu.es/es/web/master/master-ingenieria-industrial>
- [2] G. Ibarra, R. García. (1997), An educational example using free software in an industrial engineering master/Un ejemplo educativo del uso de software libre en un master de ingeniería industrial, DYNA 1997, 8-9, <http://dx.doi.org/10.6036/8555>
- [3] G. Ibarra, R. García. (2017), Using Open Source Software in Engineering Studies to Teach Water Operation & Management EDUCON 2017. IEEE Global Education Engineering Conference. ISBN: 978-1-5090-5466-4, Athens
- [4] Webpage of Management of Hydraulic Resources and Hydroelectric Power Plants subject in the Master of Industrial Engineering (1st of March 2021) https://www.ehu.es/es/web/master/master-ingenieria-industrial/materia?p_anyo_ofd=20180&p_anyo_pop=20160&p_cod_centro=345&p_cod_materia=8902&p_cod_asignatura=503959&p_tipo_asignatura=1
- [5] Web page of the accreditation of Master of Industrial Engineering, (1st of March 2021) <https://www.ehu.es/es/web/master/master-ingenieria-industrial/acreditacion>
- [6] ACCIONA. (1st of March 2021). <https://www.accion-a-agua.com/es/>
- [7] DEGREMONT. (1st of March 2021). <http://www.degremont.es/es/index.php>
- [8] CADAGUA. (1st of March 2021). <https://www.ferrovi-al.com/es-es/cadagua/>
- [9] Estudio de los Sistemas de Recuperación de Energía en Plantas Desaladoras por Ósmosis Inversa (1st of March 2021) bibing.us.es/proyectos/abreproy/5645/fichero/Proyecto+Sistemas+recuperaci%C3%B3n+energ%C3%ADa+desalaci%C3%B3n.pdf
- [10] Análisis de la operación y fiabilidad de los recuperadores de energía comerciales basados en cámaras isobáricas instalados en Canarias y estudio de la adaptación de dichos equipos al régimen de operación variable a diferentes escalas. (1st of March 2021) acceda.ulpgc.es:8443/bitstream/10553/16075/4/0720056_00000_0000.pdf
- [11] Flowserve webpage (1st of March 2021) www.flowserve.com
- [12] ERI (1st of March 2021) www.energyrecovery.com
- [13] Mataix, C. (1986). “Mecánica de fluidos y Máquinas hidráulicas”: Turbinas hidráulicas. Editorial: Del Castillo.
- [14] Mataix, C. (2006). “Máquinas hidráulicas”. Editorial: Comillas.
- [15] Agüera, J. (2003). “Mecánica de fluidos incomprensibles y turbomáquinas hidráulicas”. Editorial: S.A. Distribucion.
- [16] Diseño de una desaladora de agua de mar de 60.000 m³/día con pretratamiento de ultrafiltración (1st of March 2021) www.eoi.es/es/file/17186/download?token=mJOGDq9I

- [17] Lenntech. Procesos: desalación del agua de mar. (1st of March 2021)
<https://www.lenntech.es/procesos/mar/general/desalacion-puntos-clave.htm>
- [18] Viciano Fuerte, Claudia (2015). Estudio de los Sistemas de Recuperación de Energía en Plantas Desaladoras por Ósmosis Inversa.
- [19] Tesis “Proceso de desalación de agua de mar mediante un sistema de ósmosis inversa de muy alta conversión en tres etapas de recirculación de permeado y doble sistema de recuperación de energía” 2016 (1st of March 2021) <https://addi.ehu.es/handle/10810/18530>
- [20] *revista*
- [21] Webpage of Master of Industrial Engineering, (1st of March 2021):
https://www.ehu.eus/documents/6810447/13459782/2019-12-05_TFM_R%C3%BAbrica+Evaluaci%C3%B3n_castellano.pdf/02d8cdb2-0f68-9ecb-cb94-3437399cc332?t=1593606092000

The Potential of Heat and Mass Recovery for Adsorption Heat Transformers

M. Engelpracht¹, D. Rezo¹, P. Postweiler¹, A. Gibelhaus¹ and A. Bardow^{2,3*}

¹Institute of Technical Thermodynamics, RWTH Aachen University, Aachen, Germany

²Institute of Energy and Climate Research (IEK-10), Forschungszentrum Jülich, Germany

³Energy & Process Systems Engineering, ETH Zurich, Switzerland

*Corresponding author: abardow@ethz.ch

Abstract

Adsorption Heat Transformers (AdHTs) can upgrade low-temperature waste heat from below to above 100 °C, where heat is often required in industry. Recent theoretical and experimental studies proved that closed AdHTs could upgrade heat to above 100 °C; steady-state analyzes showed that the AdHT efficiency could significantly increase when applying heat recovery. However, the impact of neither heat recovery nor other recovery strategies on power density is known yet. To close this gap, we study the potential to improve the exergy efficiency and the power density of AdHTs by applying heat and mass recovery in two-bed setups. For this purpose, we employed a dynamic model of a two-bed AdHT, and we optimized its components and cycle control for three recovery strategies. As a use case, we studied the working pair silica gel 123 & water and transforming heat from 90 to 110 °C, with condensation heat released at 25 °C. All recovery strategies improve the AdHT performance. The exergy efficiency increases most (7%) to 0.69 J/J when applying mass recovery, and the power density increases most (13%) to 171 W/kg when applying simultaneous heat and mass recovery.

Keywords: heat amplification, thermal heat upgrade, adsorber design, dynamic optimization.

1. Introduction

The recovery of low-temperature waste heat has the potential to increase industrial energy efficiency [1]. At the same time, industrial processes often require heat above 100 °C [2]. For upgrading low-temperature waste heat above 100 °C, thermally driven heat transformers are discussed recently. In particular, Adsorption Heat Transformers (AdHTs) based on weak physical interactions are promising because they allow exploiting very low-temperature waste heat [3]. AdHTs investigated in the literature use both open and closed concepts.

For open AdHTs, Xue et al. demonstrated the experimental feasibility of cyclic steam generation with temperatures above 100 °C by exploiting direct contact of liquid refrigerant and sorbent [4, 5]. Afterward, Ye et al. investigated the potential of heat and mass recovery, and they showed that the recovery strategies improve efficiency and power density by about 10% [6]. However, open AdHTs may be challenging to integrate into industrial processes as the refrigerant is also the working fluid. The refrigerant and working fluid can be decoupled in closed AdHTs.

For closed AdHTs, the research group of Aristov proved the experimental feasibility focussing on heat upgrade at arctic temperatures around 0 °C [7]. For example, the dynamics were studied for the pressure-initiated AdHT cycle: The isotherms of the optimal working pair were found to have a concave shape for the desorption phase and a convex shape for the adsorption phase [8]. The pressure-initiated desorption phase was experimentally demonstrated, finding that the desorption time increases with the sorbent layer thickness [9]. Gordeeva et al. built the first one-bed AdHT prototype: They demonstrated an averaged useful heat flow of 350 W for transforming heat from 20 to 29 °C with the working pair ACM-35.4 & methanol [10]. However,

the maximum temperature lift was lower than expected due to the heat required to heat the thermal masses, showing the need for design optimization [10]. The first two-bed AdHT prototype has been assessed experimentally for transforming heat from 20 to 30 °C and releasing condensation heat at -30 °C: The efficiency and power density reached 44% and 350 W/kg, respectively, using the working pair LiCl/SiO₂ & methanol [11].

Focussing on heat transformation around 100 °C, Chandra and Patwardhan [12] and Frazzica et al. [13] determined the maximal theoretical performance of one-bed and two-bed AdHTs using idealized steady-state models. The performance strongly depended on the selected working pair: Working pairs with S-shaped isotherms were found particularly advantageous for high efficiencies [12, 13]. Furthermore, sensible heat losses should be avoided to significantly improve efficiency, e.g., by applying heat recovery in a two-bed configuration [12, 13]. For future analyzes, Chandra and Patwardhan suggested considering optimal AdHT designs to improve heat transfers by minimizing the required temperature driving forces [12]. Frazzica et al. recommended including process kinetics for evaluating achievable power densities [13].

Our recent study evaluated power densities and exergy efficiencies for closed AdHTs in a one-bed configuration [14]. For this purpose, we included adsorption kinetics and thermal masses of heat exchangers in a dynamic AdHT model with ideal evaporator and condenser models, and we numerically optimized AdHT design and cycle control. For the working pair AQSOA Z02 & water, we showed promising exergy efficiencies of more than 60% with competitive power densities higher than 600 W/kg when transforming heat from 90 to 100 °C and releasing condensation heat at 35 °C [14]. In addition, we recently demonstrated the experimental feasibility of upgrading heat from 90 to 110 °C, using a closed, one-bed AdHT [15].

Summarizing the literature review, closed AdHTs seem promising for upgrading heat from below to above 100 °C, and steady-state models demonstrated that the AdHT performance could be significantly enhanced by applying heat recovery. However, heat recovery also depends on process kinetics and thermal masses of heat exchangers. Moreover, the potential of other recovery strategies like mass recovery or simultaneous heat and mass recovery has not been evaluated yet. This work, therefore, analyzes a two-bed AdHT with different recovery strategies using dynamic simulation and numerical optimization. For this purpose, we introduce the AdHT cycles with heat and mass recovery in Section 2. In Section 3, we set up a dynamic model of a two-bed AdHT, allowing for design and control optimization. Afterward, we formulate and solve the multi-objective optimal control problem to maximize efficiency and power density by the recovery strategies. We show and discuss the optimization results in Section 4, and we conclude the main findings in Section 5.

2. Adsorption heat transformer cycles

An Adsorption Heat Transformer (AdHT) uses heat at a medium temperature T_{med} as driving energy to provide useful heat at a high temperature T_{high} while releasing heat at a low temperature T_{low} [12]. The simplest AdHT consists of the three main components evaporator, condenser, and adsorber, which are realized as heat exchangers [12]. A second adsorber is needed to achieve a quasi-continuous heat supply in a two-bed AdHT (**Figure 1**). A two-bed AdHT also enables applying recovery strategies like active heat or mass recovery to increase efficiency [12, 13]. Active heat recovery requires a hydraulic connection of the adsorber heat exchangers (red circuit, Figure 1). In contrast, mass recovery requires a hydraulic connection of the adsorber chambers (blue connection, Figure 1).

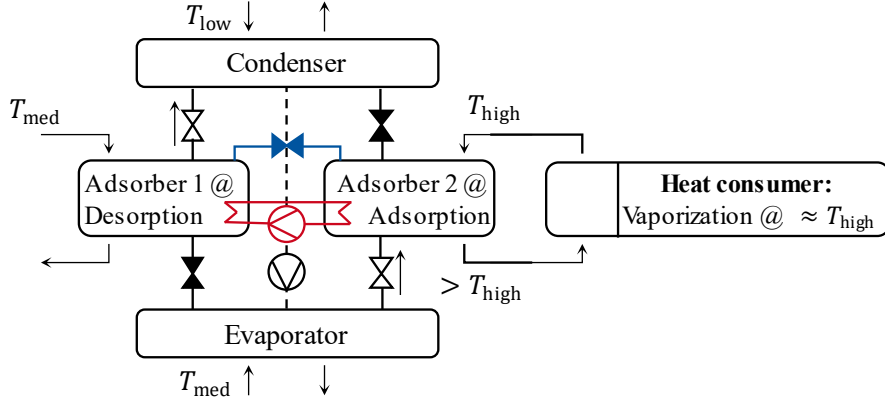


Figure 1. Scheme of a two-bed AdHT showing its main components and temperature levels. The connection and valve highlighted in blue are required for mass recovery; the connection and pump highlighted in red are required for heat recovery.

The ideal AdHT cycle with an arbitrary recovery strategy has 6 phases: 1) Adsorption-based heating phase, 2) adsorption phase (i.e., use phase), 3) recovery phase, 4) pre-desorption phase, 5) desorption phase, and 6) recovery phase. Without recovery phases, the basic AdHT cycle consists of 4 phases [12, 14]. Here, we assume that the second adsorber always operates in the opposite phase of the first adsorber (**Figure 2a**). This assumption is typical for commercial adsorption chillers to keep the system and control complexity low and is therefore adopted in this study for AdHTs.

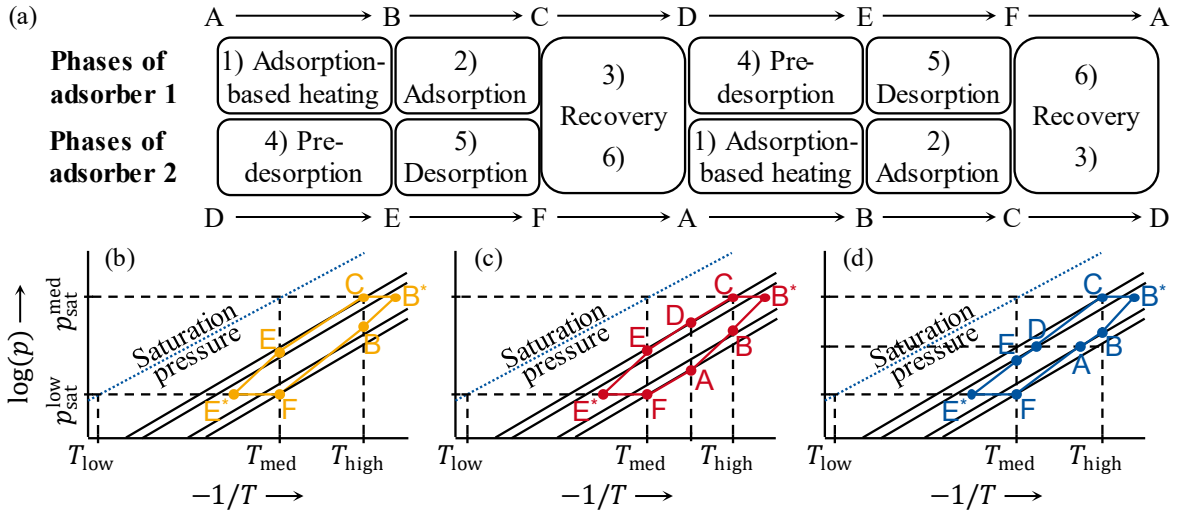


Figure 2. Top: (a) Phases of the AdHT cycle. Bottom: Ideal AdHT cycles, which operate at the temperature triple $T_{low} / T_{med} / T_{high}$ and the saturated vapor pressures $p_{sat}^{low} = p_{sat}(T_{low}) / p_{sat}^{med} = p_{sat}(T_{med})$ (b) without a recovery strategy, (c) with active heat recovery, and (d) with mass recovery.

In the following, we briefly describe the 6 phases of the ideal AdHT cycle with an arbitrary recovery strategy [12, 14]:

- 1) During the adsorption-based heating phase (cf. $A \rightarrow B$, Figure 2c-d), the evaporator is kept at the medium temperature T_{med} and its corresponding vapor pressure $p_{sat}(T_{med})$ by supplying the heat flow \dot{Q}_{evap} at the medium temperature T_{med} . The evaporator is connected to the adsorber, which starts at the medium temperature T_{med} and the vapor pressure $p_{sat}(T_{low})$. The pressure difference between both components induces a vapor flow into the adsorber. The vapor is then adsorbed by the sorbent, releasing the heat of adsorption. The heat of adsorption

heats the adsorber from the medium to the high temperature, as the heat transfer fluid does not flow through the adsorber. The phase ends when the adsorber temperature is equal to the high temperature T_{high} .

- 2) During the use phase (cf. $B \rightarrow B^* \rightarrow C$, Figure 2b-d), the heat transfer fluid flows through the adsorber and absorbs the useful heat flow \dot{Q}_{use} . The heat transfer fluid enters the adsorber at the high temperature T_{high} and leaves the adsorber at a temperature greater than the high temperature T_{high} (cf. Figure 1). Thus, useful heat is provided at a constant high temperature T_{high} , e.g., to vaporize a fluid (e.g., water). The phase ends when the adsorber pressure and temperature reach the evaporator pressure $p_{\text{sat}}(T_{\text{med}})$ and high temperature T_{high} , respectively.
- 3) After the use phase, an optional heat or mass recovery phase can be applied (cf. $C \rightarrow D$, Figure 2c-d). During the heat recovery phase, the heat transfer fluid circuits of both adsorbers are connected hydraulically. Thereby, sensible heat is actively recovered and transferred from the hot adsorber (i.e., after the use phase) to the cold adsorber (i.e., after the desorption phase). Thus, the heat recovery phase reduces heat demand for the adsorption-based heating phase. The heat recovery phase ends when both adsorbers have the same equilibrium temperature (c.f. points A and D, Figure 2c). During the mass recovery phase, both adsorber chambers are connected hydraulically via a valve. Thereby, the loaded adsorber (i.e., after the use phase) desorbs vapor, which is adsorbed by the dry adsorber (i.e., after the desorption phase). Thus, the mass recovery phase reduces heat demands for both the adsorption-based heating phase and desorption phase. The mass recovery phase ends when both adsorbers have the same equilibrium pressure (c.f. points A and D, Figure 2d). Simultaneous heat and mass recovery are also possible.
- 4) During the pre-desorption phase (cf. $D \rightarrow E$, Figure 2c-d), the adsorber is connected to the condenser. The pressure difference between both components induces a vapor flow into the condenser, where the vapor condenses. The condenser is kept constant at the low temperature T_{low} and its corresponding vapor pressure $p_{\text{sat}}(T_{\text{low}})$ by releasing the heat flow \dot{Q}_{cond} to the environment. The heat required for desorption is provided by the sensible heat of the adsorber itself. Thus, the adsorber cools from the high to the medium temperature, as the heat transfer fluid does not flow through the adsorber. The phase ends when the adsorber temperature is equal to the medium temperature T_{med} .
- 5) During the desorption phase (cf. $E \rightarrow E^* \rightarrow F$, Figure 2b-d), the heat transfer fluid flows through the adsorber, and the adsorber receives the desorption heat flow \dot{Q}_{des} . The heat transfer fluid enters the adsorber at the medium temperature T_{med} and leaves the adsorber at a lower temperature than the medium temperature T_{med} . The phase ends when the adsorber pressure and temperature reach the condenser pressure $p_{\text{sat}}(T_{\text{low}})$ and the medium temperature T_{med} , respectively.
- 6) After the desorption phase, the optional heat or mass recovery phase is applied again to close the AdHT cycle (cf. $F \rightarrow A$, Figure 2c-d). Furthermore, the condensed refrigerant is continuously returned to the evaporator using a small pump during the AdHT cycle.

In summary, recovery strategies like heat or mass recovery can decrease the heat demands during the desorption phase and adsorption-based heating phase. Reducing heat demand can increase the AdHT performance, which we systematically evaluate by developing a dynamic AdHT model and applying numerical optimization.

3. Dynamic modeling and optimization of the adsorption heat transformer

To develop a dynamic model of an Adsorption Heat Transformer (AdHT) suitable to investigate heat and mass recovery strategies, we used our open-source Modelica library SorpLib [16],

which is available on GitLab [17]. The AdHT model (**Figure 3**) consists of the following three sub-models: 1) Working pair model including models for the adsorption equilibrium, heat transfer, and mass transfer; 2) phase separator model including a heat transfer model; and 3) heat exchanger model including models for the wall, heat transfer fluid, and heat transfer. Aggregating the model of the heat exchanger and phase separator results in the condenser or evaporator model (cf. dashed-dotted green boxes, Figure 3), and aggregating the model of the heat exchanger and working pair results in the adsorber bed model (cf. dashed orange box, Figure 3).

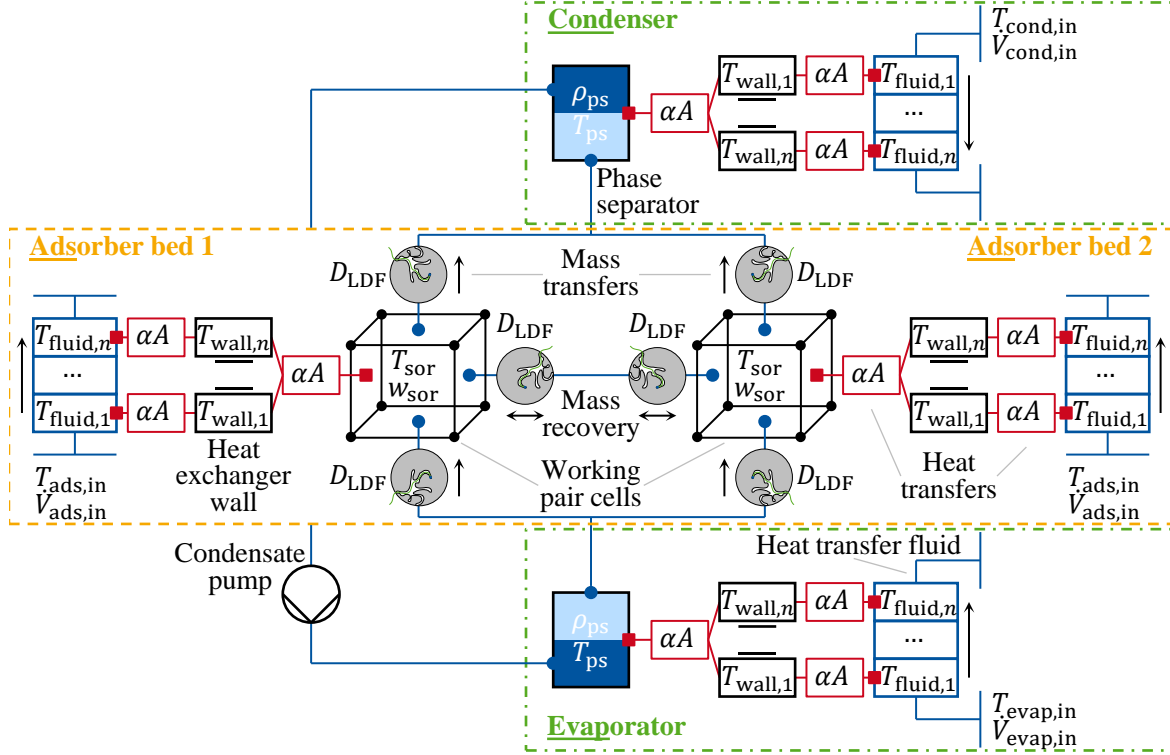


Figure 3. Scheme of the dynamic AdHT model. Differential states are: Temperatures T_{SOR} and loadings w_{SOR} of sorbents in both adsorbers, temperatures of all heat exchanger walls T_{wall} and all heat transfer fluids T_{fluid} , and densities ρ_{ps} and temperatures T_{ps} of the fluid in the phase separators of evaporator and condenser. Details are given in the text.

Details of all sub-models can be found in the literature, but essential modeling approaches are summarized in the following. Our recent study [14] describes the working pair model and adsorber heat exchanger model in full detail (cf. dashed orange box, Figure 3). We modeled the adsorption equilibrium using the Dubinin theory [18] and the mass transfer using a Linear Driving Force (LDF) approach [19]. The adsorber heat exchange was modeled using a finned-tube heat exchanger made from aluminum, which design can be freely parameterized [14]. The sorbent-side heat transfer was modeled considering the fin efficiency of the finned-tube heat exchanger, which was calculated according to the method presented in the VDI heat atlas [20]. The tube-side heat transfer of the adsorber heat exchanger was modeled using the correlation of Gnielinski, Dittus, and Boelter [24] to account for both laminar and turbulent flow regimes. Thereby, we can optimize the volume flow of the heat transfer fluid in the adsorber during the use phase, also allowing for a laminar flow regime. The phase separator model and the heat exchanger models of the evaporator and condenser are described in Ref. [21] in full detail (cf. dashed-dotted green boxes, Figure 3). The Sieder-Tate [22] and Schmidt [23] correlations were used to model the tube-side heat transfer of the evaporator and condenser, respectively.

In this study, we used silica gel 123 & water as working pair, with equilibrium data measured and fitted by Schawe [25]. We parametrized the AdHT model according to components of an adsorption chiller experimentally characterized by Lanzerath et al. (cf. **Table 1**) [26]. The evaporator heat exchanger is a low-finned tube with an inner turbulence structure made from copper, and the condenser heat exchanger is a spiral coil made from copper [26]. All fluid properties of water were calculated using the Modelica library TILMedia [27] based on RefProp [28] with the equation of state from Wagner and Pruß [29] and auxiliary models for the thermal conductivity and viscosity from Huber et al. [30, 31].

The resulting AdHT model is fully described by a set of partial differential equations, which were transformed into ordinary differential equations using an upwind finite-difference discretization scheme. Finally, the resulting differential-algebraic equation system was solved using the solver DASSL.

Table 1. Kinetic parameters to describe the AdHT model. All parameters are based on Lanzerath et al. [26].

Parameter	Symbol	Value	Unit
Heat transfer coefficient between sorbent and adsorber heat exchanger	α_{sor}	160	W/m ² /K
Diffusion coefficient	D_{LDF}	1.8e-10	m ² /s
Product of heat transfer coefficient and heat transfer area in the evaporator	$(\alpha A)_{\text{evap}}$	176	W/K
Product of heat transfer coefficient and heat transfer area in the condenser	$(\alpha A)_{\text{cond}}$	3174	W/K

To evaluate the AdHT performance, we used the two key performance indicators 1) exergetic Coefficient Of Performance (COP_{ex}) and 2) Specific Heating Power (SHP), defined by

$$\text{COP}_{\text{ex}} = \int_0^{\tau_{\text{cycle}}} \frac{\dot{E}_{\text{use}}}{\dot{E}_{\text{evap}} + \dot{E}_{\text{des}}} d\tau \text{ and} \quad (1)$$

$$\text{SHP} = \frac{\int_0^{\tau_{\text{cycle}}} \dot{Q}_{\text{use}} d\tau}{\tau_{\text{cycle}} (m_{\text{sor}} + m_{\text{hx,ads}} + m_{\text{hx,evap}} + m_{\text{hx,cond}})}. \quad (2)$$

The COP_{ex} describes the exergy efficiency of the AdHT and integrates the ratio of the useful exergy flow during the use phase (\dot{E}_{use}) and the exergy flows required for vaporization and desorption ($\dot{E}_{\text{evap}} + \dot{E}_{\text{des}}$) over one complete cycle with the cycle time τ_{cycle} . The SHP describes the power density of the AdHT and relates the average useful heat flow ($\bar{Q}_{\text{use}} = \int_0^{\tau_{\text{cycle}}} \dot{Q}_{\text{use}} d\tau / \tau_{\text{cycle}}$) to the system mass, including the sorbent mass (m_{sor}) and masses of the adsorber ($m_{\text{hx,ads}}$), evaporator ($m_{\text{hx,ads}}$), and condenser ($m_{\text{hx,cond}}$) heat exchangers.

COP_{ex} and SHP show a trade-off when maximizing them [14]. The exergy efficiency increases either by increasing cycle time or increasing sorbent mass relative to adsorber heat exchanger mass. Thus, the useful exergy flow increases because 1) adsorption equilibrium is reached with long cycle times and 2) less heat of adsorption is needed to heat the thermal mass of the adsorber heat exchanger from the medium to high temperature. In contrast, the specific heating power increases with decreasing cycle time and decreasing system mass. However, the system mass cannot be reduced arbitrarily. For example, the adsorber heat exchanger mass depends on the adsorber design. The adsorber design also affects the heat transfer, which in turn influences the cycle time. Thus, a design trade-off exists for the specific heating power.

The trade-off between exergy efficiency and power density leads to a multi-objective optimal control problem. The problem was solved by applying numerical optimization and simultaneous optimization of control and design parameters. To characterize the control of the AdHT cycle, we selected four control parameters, which are summarized in the control vector Φ_{control} : 1) Phase time for adsorption-based heating and pre-desorption $\tau_{\text{heating/pre-des}}$; 2) phase time for use phase and desorption $\tau_{\text{use/des}}$; 3) recovery time τ_{recovery} ; and 4) volume flow during the use phase \dot{V}_{use} . The corresponding cycle time τ_{cycle} results as

$$\tau_{\text{cycle}} = 2(\tau_{\text{heating/pre-des}} + \tau_{\text{use/des}} + \tau_{\text{recovery}}). \quad (3)$$

To characterize the AdHT design, we selected five design parameters, which are summarized in the design vector Φ_{design} : 1) Number of fins n_{fins} , 2) height of fins h_{fins} , and 3) thickness of fins t_{fins} of the adsorber heat exchanger; 4) linear scaling factor of the evaporator SF_{evap} ; and 5) linear scaling factor of condenser SF_{cond} . The scaling factors allow to scale sizes and volume flows of the evaporator and condenser linearly, which corresponds to adding or removing an identical evaporator or condenser to the AdHT. Thereby, evaporator and condenser sizes can be optimized to maximize the performance indicators. For data reduction, we introduced the time constant of the adsorber heat exchanger τ_{hx} as [14]

$$\tau_{\text{hx}} = \frac{C_{\text{sor}}(n_{\text{fins}}, h_{\text{fins}}, t_{\text{fins}}) + C_{\text{hx,ads}}(n_{\text{fins}}, h_{\text{fins}}, t_{\text{fins}})}{(\alpha A)_{\text{sor-hx,ads}}(n_{\text{fins}}, h_{\text{fins}}, t_{\text{fins}})}, \quad (4)$$

where C_{sor} and $C_{\text{hx,ads}}$ are the heat capacities of the sorbent and the adsorber heat exchanger, respectively. The product of heat transfer coefficient and area $(\alpha A)_{\text{sor-hx,ads}}$ describes the heat transfer between the sorbent and adsorber heat exchanger (i.e., sorbent-side heat transfer). Thus, the time constant τ_{hx} summarizes the design parameters of the adsorber and indicates how fast heat can be transferred between the sorbent and adsorber heat exchanger. Details are given in Ref. [14].

The resulting multi-objective optimal control problem reads

$$\begin{aligned} \min_{\substack{x(\cdot), z(\cdot), \\ \Phi_{\text{control}}, \\ \Phi_{\text{design}}}} & \begin{aligned} & -\text{COP}_{\text{ex}}(x(\tau_{\text{cycle}}), z(\tau_{\text{cycle}}), \Phi_{\text{control}}, \Phi_{\text{design}}) \\ & -\text{SHP}(x(\tau_{\text{cycle}}), z(\tau_{\text{cycle}}), \Phi_{\text{control}}, \Phi_{\text{design}}) \end{aligned} & \text{(objective function)} \\ \text{s.t.} & \begin{aligned} \dot{x} &= f(x(\tau), z(\tau), \Phi_{\text{control}}, \Phi_{\text{design}}) & \text{(dynamic model)} \\ 0 &= g(x(\tau), z(\tau), \Phi_{\text{control}}, \Phi_{\text{design}}) & \text{(equality constraints)} \\ x(\tau = 0) &= x(\tau = \tau_{\text{cycle}}) & \text{(cyclic steady-state)} \\ 0 &\geq M(x(\tau), z(\tau), \Phi_{\text{control}}, \Phi_{\text{design}}) & \text{(inequality constraints)} \end{aligned} \end{aligned}$$

where x are the differential states and z are the algebraic states. The multi-objective optimal control problem is solved subjected to (s.t.) the dynamic AdHT model, described by a differential-algebraic equation system. Furthermore, it is ensured that initial state values do not influence the AdHT performance by applying the cyclic steady-state condition. Equality constraints ensure, e.g., fixed operating conditions like the temperature levels. Inequality constraints guarantee, e.g., that the adsorber is heated from the medium to the high temperature by only using the heat of adsorption released during the adsorption-based heating phase or the enthalpy recovered during a recovery phase. **Table 2** summarizes the lower and upper bounds of all control and design parameters used to solve the multi-objective optimal control problem.

To solve the multi-objective optimal control problem, we transformed the multi-objective problem to multiple single-objective problems using the ε -constraint method [32]. We then applied the efficient multiple-shooting algorithm MUSCOD-II [33, 34]. The optimization problems were set up in MUSCOD-II using the Python module MoBa MUSCOD [35]. The optimization problems were coupled with the dynamic AdHT model using the functional mock-up interface. Solving all single-objective optimization problems results in a Pareto Frontier of Pareto-optimal solutions regarding exergy efficiency and power density of the AdHT. Details of the optimization framework were published previously in Ref. [36].

Table 2. Lower and upper bounds of control and design parameters.

Parameter	Symbol	Unit	Lower bound	Upper bound
Time of heating and pre-desorption phase	$\tau_{\text{heating/pre-des}}$	s	25	3000
Time of use and desorption phase	$\tau_{\text{use/des}}$	s	0	250
Time of recovery phase	τ_{recovery}	s	0	250
Volume flow during the use phase	\dot{V}_{use}	l/min	0.1	15
Number of fins	n_{fins}	-	100	500
Height of fins	h_{fins}	mm	1	30
Thickness of fins	t_{fins}	mm	0.12	1
Linear scaling factor of the evaporator	SF_{evap}	-	0.1	15
Linear scaling factor of the condenser	SF_{cond}	-	0.1	15

4. Discussion and results

The impact of different recovery strategies on the performance of a two-bed Adsorption Heat Transformer (AdHT) is exemplarily studied for the operating temperature triple $T_{\text{low}} = 25 \text{ }^\circ\text{C} / T_{\text{med}} = 90 \text{ }^\circ\text{C} / T_{\text{high}} = 110 \text{ }^\circ\text{C}$. Studied recovery strategies are 1) heat recovery, 2) mass recovery, and 3) simultaneous heat and mass recovery. Note that simultaneous heat and mass recovery cannot set heat or mass recovery to zero, but both are performed simultaneously.

4.1 Trade-off between exergy efficiency and power density

Pareto frontiers express the AdHT performance by showing the trade-offs between exergy efficiencies COP_{ex} and power densities SHP at optimal design and cycle control (**Figure 4**). Thus, each point on each Pareto Frontier corresponds to different AdHT designs and cycle controls.

As shown in Figure 4, the AdHT shows promising performances for upgrading heat from below to above $100 \text{ }^\circ\text{C}$, with maximum exergy efficiencies greater than 64% and maximum power densities greater than 150 W/kg . All three recovery strategies improve the AdHT performance compared to the simple AdHT operation. The simultaneous heat and mass recovery increases the maximum power density SHP by 13% to 171 W/kg , reaching the highest power density. The mass recovery increases the maximum exergy efficiency COP_{ex} by 7% to 0.69 J/J, reaching the highest exergy efficiency. Besides, the AdHT with simultaneous heat and mass recovery consistently dominates the AdHT with heat recovery and lies between the AdHT performance with heat or mass recovery. The overall Pareto frontier combines two recovery strategies: Simultaneous heat and mass recovery and mass recovery. Reasons for improvements in exergy efficiency and power density compared to the simple AdHT operation are discussed in detail in the following sections.

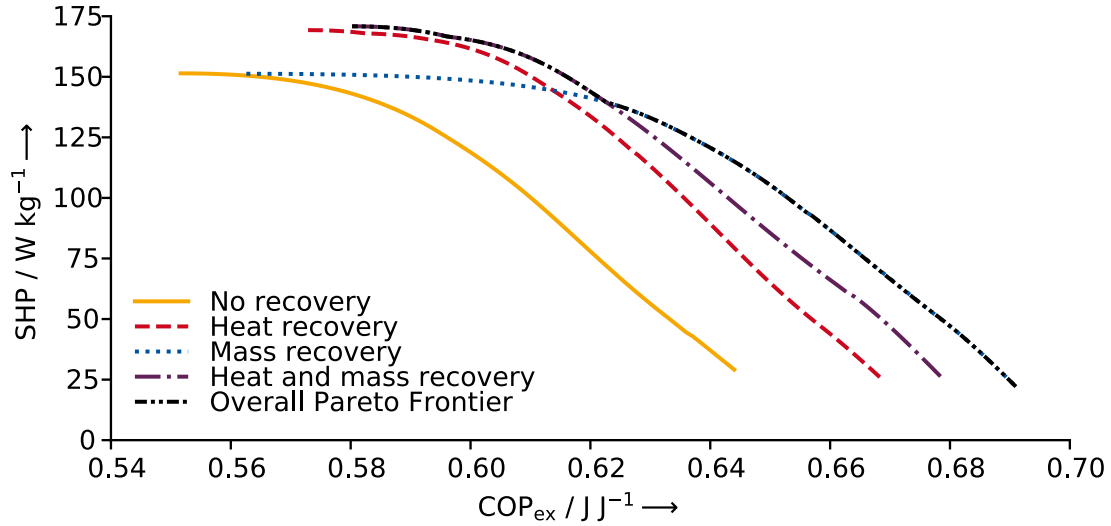


Figure 4. Trade-offs between exergetic coefficient of performance COP_{ex} and specific heating power SHP for various recovery strategies at optimal AdHT designs and cycle controls.

4.2 Heat and mass recovery mechanisms to increase exergy efficiency

The exergy efficiency COP_{ex} increases with increasing useful exergy during the use phase or decreasing exergy demand for vaporization and desorption (cf. Equation 1). Three effects influence the exergy efficiency of the AdHT with heat recovery:

- 1) At the start of the adsorption-based heating phase, the adsorber starts at a temperature higher than the medium temperature T_{med} due to the recovered enthalpy (cf. **Table 3**). Thus, less heat of adsorption is required to heat the adsorber to the high temperature T_{high} , indirectly provided by the evaporator (cf. Section 2). Consequently, the exergy demand for vaporization decreases.
- 2) However, at the start of the pre-desorption phase, the adsorber starts at a temperature lower than the high temperature T_{high} because enthalpy is recovered from the hot to the cold adsorber (cf. Table 3). Thus, less heat required for desorption can be provided by the sensible heat of the adsorber (cf. Section 2), and the exergy demand for desorption increases.
- 3) As less heat of adsorption is required to heat the adsorbers in the adsorption-based heating phases, more heat of adsorption can be used to generate useful exergy.

In summary, the decreased exergy demand for vaporization and the increased useful exergy outweigh the increased exergy demand for desorption. Thereby, the AdHT with heat recovery improves the exergy efficiency compared to the AdHT without recovery strategy. In contrast, the AdHT with mass recovery improves the exergy efficiency most due to four impacts:

- 1) As for the AdHT with heat recovery, the adsorber starts at a temperature higher than the medium temperature T_{med} at the beginning of the adsorption-based heating phase (cf. Table 3). However, the start temperature can become higher than the high temperature T_{high} because the AdHT with mass recovery recovers both the sensible heat of the adsorber and latent heat of the desorbed vapor (cf. Section 2). The latent heat of the vapor is not used but condensed when using the AdHT with heat recovery. Hence, the exergy demand for vaporization decreases significantly for the AdHT with mass recovery.
- 2) The mass recovery also decreases the start temperature of the adsorber during the pre-desorption phase. The start temperature decreases below the high temperature T_{high} because the adsorber provides the heat required for desorption during the mass recovery by its sensible heat

(cf. Table 3). However, the exergy demand for desorption does not increase as the sensible heat is already used for desorption. In other words, the pre-desorption phase is partly shifted in the mass recovery phase.

- 3) Less refrigerant needs to be desorbed during the desorption phase because the mass recovery itself partly desorbs the adsorber (cf. Section 2). As a result, the exergy demand for desorption decreases.
- 4) Although less heat of adsorption is required during the adsorption-based heating phase, the heat of adsorption applicable to generate useful exergy does not increase because the mass recovery reduces the working capacity exploitable during the use phase. Instead, the exploitable working capacity can even decrease with long recovery phases, reducing the useful exergy.

In summary, the reduced useful exergy is outperformed by decreased exergy demands for vaporization and desorption. Thus, the AdHT with mass recovery improves the exergy efficiency compared to the AdHT without recovery strategy.

Table 3. Impacts of recovery strategies on the recovered enthalpies and temperatures reached after the first recovery phase (cf. Figure 2a) for the AdHT designs and cycle controls that maximize the specific heating power (SHP^{\max}) or exergetic coefficient of performance ($\text{COP}_{\text{ex}}^{\max}$) (cf. Figure 4).

Parameter	Unit	Heat recovery		Mass recovery		Combined recovery	
		SHP^{\max}	$\text{COP}_{\text{ex}}^{\max}$	SHP^{\max}	$\text{COP}_{\text{ex}}^{\max}$	SHP^{\max}	$\text{COP}_{\text{ex}}^{\max}$
Recovery time	s	3.1	188.2	3.0	173.8	3.1	26.8
Recovered enthalpy	kJ	28.9	360.7	13.1	829.7	36.2	637.5
Recovered enthalpy due to heat recovery	kJ	28.9	360.7	0	0	27.6	-12.8
Recovered enthalpy due to mass recovery	kJ	0	0	13.1	829.7	8.6	650.3
Recovery rate	K/s	5.28	0.09	1.88	0.21	6.37	1.07
Sorbent temperature of first adsorber	°C	108.4	104.1	108.2	93.5	104.8	96.8
Temperature of first adsorber heat exchanger	°C	99.2	104.1	109.9	93.6	98.7	102.6
Temperature of heat transfer fluid of first adsorber	°C	98.3	104.1	110.5	94.2	98.3	105.0
Sorbent temperature of second adsorber	°C	93.4	104.0	95.2	121.5	98.4	116.7
Temperature of second adsorber heat exchanger	°C	101.5	104.0	92.4	121.5	102.3	110.2
Temperature of heat transfer fluid of second adsorber	°C	102.3	104.0	89.7	120.7	102.6	107.7

For the AdHT with simultaneous heat and mass recovery, all reasons discussed apply simultaneously. Therefore, it could be expected that the exergy efficiency improves further compared to applying single heat or mass recovery. Indeed, the AdHT with simultaneous heat and mass recovery dominates the AdHT with heat recovery and achieves higher exergy efficiencies (cf. Figure 4) because more enthalpy can be recovered due to the additional mass recovery (cf. Table 3). Thus, the overall exergy input decreases. However, the AdHT with simultaneous heat and mass recovery does not reach the highest exergy efficiency of the AdHT with mass recovery (cf. Figure 4). The highest exergy efficiency is not reached because high exergy efficiencies require increasing recovery times, for which mass recovery and heat recovery start to work against each other. For the AdHT designs and cycle controls that lead to the highest exergy efficiencies, the AdHT with mass recovery achieves temperatures up to 121 °C for the adsorber receiving the recovered enthalpy and temperatures as low as 94 °C for the adsorber providing the enthalpy (cf. Table 3). In comparison, the AdHT with heat recovery achieves an equilibrium temperature of 104 °C in both adsorbers (cf. Table 3). When applying simultaneous heat and mass recovery, the desirable temperature difference created by mass transfer is destroyed by heat transfer. Thus, the heated adsorber is cooled, and the cooled adsorber is heated, which contradicts the actual purpose of the recovery phases. As a result, the length of the recovery phase is limited (cf. Table 3), and the AdHT cannot achieve the maximum exergy efficiency with simultaneous heat and mass recovery.

4.3 Heat and mass recovery mechanisms to increase power density

The power density can increase by either increasing the average useful heat flow per cycle or decreasing the overall system mass (cf. Equation 2). The AdHT with heat recovery improves the power density for five reasons:

- 1) A larger part of the heat of adsorption can generate useful heat instead of heating the adsorber during the adsorption-based heating phase (cf. Section 4.2). Thus, the average useful heat flow per cycle increases.
- 2) The cycle time decreases by 37-71% (cf. **Figure 5a**) at the same exergy efficiencies mainly because the overall heating time can be decreased by about 20-54%. The overall heating time τ_{heating} is the adsorption-based heating time $\tau_{\text{heating/pre-des}}$ plus the recovery time τ_{recovery} (cf. Section 3). The overall heating time decreases because the heat recovered is transferred to the adsorber at a higher temperature than the saturated vapor, entering the adsorber during the adsorption-based heating phase (cf. Section 2). Thus, the adsorber can be heated faster from the medium temperature T_{med} to the high temperature T_{high} .
- 3) The time constant of the adsorber heat exchanger decreases by 16-54% (cf. Figure 5c) at the same exergy efficiencies, leading to an adsorber design characterized by faster heat transfer and lower thermal masses. The time constant decreases because less heat of adsorption, which correlates with the sorbent mass, is required for heating the adsorber due to the mass recovery: Thus, a smaller adsorber with less sorbent relative to the adsorber heat exchanger mass is sufficient to operate the AdHT.
- 4) As the recovered enthalpy heats the adsorber to temperatures already higher than the medium temperature T_{med} (cf. Table 3), less heat of adsorption is required to heat the adsorber, indirectly provided by the evaporator during the adsorption-based heating phase. Thus, a smaller evaporator is sufficient to operate the AdHT (cf. Figure 5d), reducing the evaporator heat exchanger mass by 34-76% at the same exergy efficiencies.
- 5) The condenser heat exchanger mass reduces by 22-80% (cf. Figure 5e) at the same exergy efficiencies because the temperature of the vapor, which enters the condenser during the desorption phase, is reduced due to the heat recovery. Thus, a smaller condenser is sufficient to operate the AdHT.

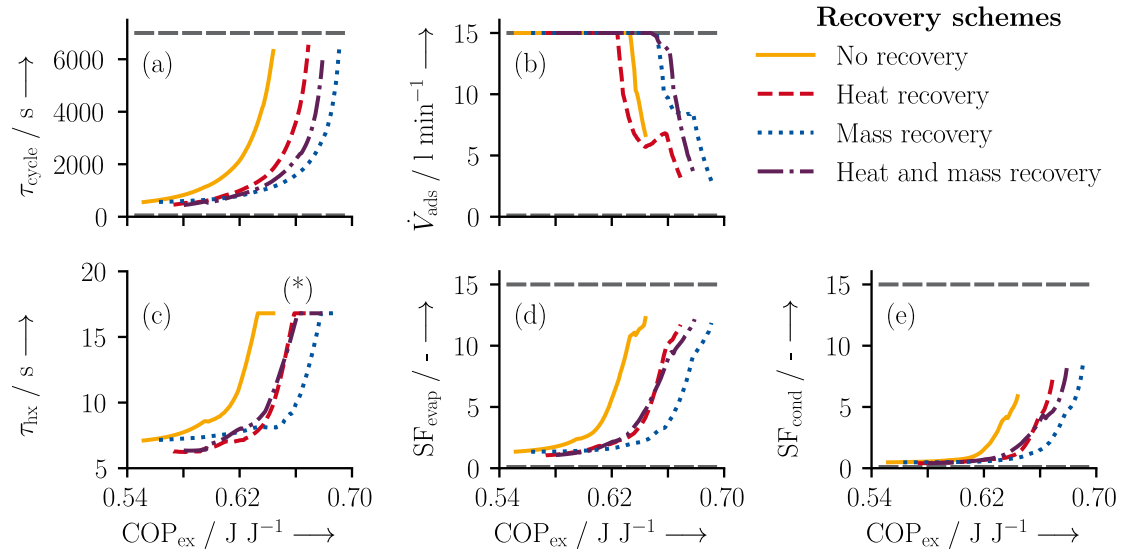


Figure 5. Optimal design and control parameters for various recovery strategies applied to an AdHT. All solutions are plotted over the exergetic coefficient of performance COP_{ex} (cf. Figure 4): (a) Overall cycle time τ_{cycle} , (b) volume flow during the use phase \dot{V}_{ads} , (c) time constant of the adsorber heat exchanger τ_{hx} , (d) linear scaling factor of the evaporator SF_{evap} , and (e) linear scaling factor of the condenser SF_{cond} . Gray dashed horizontal lines mark lower and upper bounds of design and control parameters. The star (*) marks the time constant of the adsorber heat exchanger at which a sorbent monolayer is achieved at the maximum height of fins (i.e., 30 mm) and the minimum thickness of fins (i.e., 0.12 mm).

Focussing on the AdHT designs and cycle controls that maximize the specific heating power, the mass recovery does not reach power densities higher than 150 W/kg as achieved by the heat recovery. Heat recovery achieves higher power densities because the recovery rate is faster due to lower transport resistances (cf. Table 3). Still, the AdHT with mass recovery improves the power density at the same exergy efficiencies compared to the AdHT without recovery for similar reasons as the AdHT with heat recovery:

- 1) The cycle time decreases by up to 82% because the overall heating time decreases up to 51% (cf. Figure 5a). The overall heating time decreases since the vapor, entering the adsorber during the recovery phase, has a higher temperature than the saturated vapor, entering the adsorber during the adsorption-based heating phase (cf. Section 2).
- 2) The cycle time is also reduced since less heat of adsorption is required during the adsorption-based heating phase. Thus, an adsorber design with less sorbent mass is selected, allowing to increase the adsorber heat exchanger mass to improve the heat transfer: The time constant of the adsorber heat exchanger decreases up to 52% (cf. Figure 5c). As a result, heat is transferred faster in all AdHT phases, and the cycle time decreases.
- 3) The mass of the evaporator decreases by 7-82% (cf. Figure 5d) because the recovered enthalpy can heat the adsorber strongly (cf. Table 3) and less vapor needs to be generated during the adsorption-based heating phase. Thus, a smaller evaporator is sufficient to serve the reduced evaporator load.
- 4) The mass recovery decreases the amount and temperature of the vapor, which enters the condenser during the desorption phase. As a result, a smaller condenser optimally operates the AdHT, and the condenser mass decreases by 11-82% (cf. Figure 5e).

As discussed in Section 4.2, all effects discussed above apply simultaneously to the AdHT with simultaneous heat and mass recovery. Below exergy efficiencies of 62.2% (cf. Figure 4), simultaneous heat and mass recovery dominates both heat or mass recovery because the recovery rate increases up to 6.4 K/s (cf. Table 3) due to the enthalpy recovered additionally. Thus, the cycle time reduces (cf. Figure 5a), and the power density increases. For higher exergy efficiencies, the power densities lie between the power densities of the AdHT with heat or mass recovery as heat and mass recovery start to work against each other (cf. Section 4.2). The faster heat recovery limits the recovery time below 27 s (cf. Table 3), leading to overall heating times and cycle times longer than for the AdHT with mass recovery (cf. Figure 5a). Thus, the power densities are lower than the power densities achieved by mass recovery. Consequently, the adsorber design and scalings of the evaporator and condenser are very similar to the AdHT with heat recovery (cf. Figure 5c-e) because heat recovery is the dominant recovery mechanism.

Besides, the volume flow shows the same trend for all recovery strategies during the use phase: The volume flow is at its maximum value for high specific heating powers and decreases above a specific exergy efficiency with increasing exergy efficiency (cf. Figure 5b). The volume flow starts at its maximum value to increase the tube-side heat transfer, leading to decreased cycle time and higher power density. The volume flow decreases to ensure an optimal ratio between useful exergy and exergy input. If the volume flow stayed constant, the tube-side heat transfer in the adsorber would stay high, and thus the average adsorber temperatures would decrease and almost reach the high temperature T_{high} at the end of the use phase. At the same time, the adsorber pressure would still reach the evaporator pressure given by the medium temperature T_{med} . In turn, the working capacity exploitable in the AdHT cycle would increase. As a result, both the useful exergy and exergy input would increase, but the ratio of useful exergy and exergy input would not be optimal. Indeed, the result on the volume flow may not be universally valid, and we expect a dependency on the selected working pair, the operating temperatures, and the process kinetics. Hence, further analyzes are required in the future.

5. Conclusions

The analysis highlights that all heat and mass recovery strategies improve AdHT performance. The AdHT with simultaneous heat and mass recovery leads to the highest power density (171 W/kg), while the AdHT with mass recovery leads to the highest exergy efficiency (0.691 J/J). The AdHT with simultaneous heat and mass recovery dominates the AdHT with heat recovery with respect to efficiency and power density.

Compared to the literature, heat and mass recovery improve the AdHT performance by about 10%, similar to results reported for AdHTs using open concepts [6]. As reported by the idealized analyzes performed for AdHTs using closed concepts [12, 13], heat recovery can improve the maximum efficiency by 4% but not by 10-15%. However, mass recovery improves maximum efficiency by 13%.

Consequently, the AdHT with simultaneous heat and mass recovery seems most promising as it combines high power densities with high exergy efficiencies. However, when considering the system complexity, the AdHT with mass recovery seems most promising as it only requires one additional valve between the two adsorbers. Thereby, the AdHT with mass recovery avoids the complex hydraulic connections of the adsorber heat exchangers needed for heat recovery. Therefore, the AdHT with mass recovery should be easier to implement in practice.

Overall, AdHTs have the potential to recover low-temperature waste heat efficiently, and their performance can be improved by 7-13% when applying heat, mass, or simultaneous heat and mass recovery.

Acknowledgments

This study was funded by Excellence Initiative of the German federal and state governments. Simulations were performed with computing resources granted by RWTH Aachen University under project rwth0746.

References:

- [1] Xu, Z. Y., Wang, R. Z., Yang, C., “Perspectives for low-temperature waste heat recovery”, *Energy*, 176:1037–1043, 2019.
- [2] Arpagaus, C., Bless, F., Uhlmann, M., Schiffmann, J., Bertsch, S. S., “High temperature heat pumps. Market overview, state of the art, research status, refrigerants, and application potentials”, *Energy*, 152:985–1010, 2018.
- [3] Frazzica, A., Palomba, V., Dawoud, B., "Thermodynamic Performance of Adsorption Working Pairs for Low-Temperature Waste Heat Upgrading in Industrial Applications", *Applied Sciences*, 11, 8:3389, 2021.
- [4] Xue, B., Iwama, Y., Tanaka, Y., Nakashima, K., Wijayanta, A. T., Nakaso, K., Fukai, J., “Cyclic steam generation from a novel zeolite–water adsorption heat pump using low-grade waste heat”, *Experimental Thermal and Fluid Science*, 46:54–63, 2013.
- [5] Xue, B., Ye, S., Zhang, L., Wei, X., Nakaso, K., Fukai, J., “High-temperature steam generation from low-grade waste heat from an adsorptive heat transformer with composite zeolite-13X/CaCl₂”, *Energy Conversion and Management*, 186:93–102, 2019.
- [6] Ye, S., Xue, B., Meng, X., Wei, X., Nakaso, K., Fukai, J., “Experimental study of heat and mass recovery on steam generation in an adsorption heat pump with composite zeolite-CaCl₂”, *Sustainable Cities and Society*, 52:101808, 2020.
- [7] Aristov, Y.I., “A new adsorptive cycle “HeCol” for upgrading the ambient heat. The current state of the art”, *International Journal of Refrigeration*, 105, 4:19–32, 2019.
- [8] Aristov, Y. I., ““Heat from Cold” – A new cycle for upgrading the ambient heat. Adsorbent optimal from the dynamic point of view”, *Applied Thermal Engineering*, 124:1189–1193, 2017.
- [9] Girnuk, I. S., Aristov, Y.I., “A HeCol cycle for upgrading the ambient heat. The dynamic verification of desorption stage”, *Applied Thermal Engineering*, 146:608–612, 2019.
- [10] Gordeeva, L. G., Tokarev, M. M., Aristov, Y. I., “New Adsorption Cycle for Upgrading the Ambient Heat”, *Theoretical Foundations of Chemical Engineering*, 52, 2:195–205, 2018.
- [11] Tokarev., “A Double-Bed Adsorptive Heat Transformer for Upgrading Ambient Heat. Design and First Tests”, *Energies*, 12, 21:4037, 2019.
- [12] Chandra, I., Patwardhan, V. S., “Theoretical studies on adsorption heat transformer using zeolite-water vapour pair”, *Heat Recovery Systems and CHP*, 10, 5-6:527–537, 1990.
- [13] Frazzica, A., Dawoud, B., Critoph, R. E., “Theoretical analysis of several working pairs for adsorption heat transformer application”, In *Heat Powered Cycles*, 2016.
- [14] Engelpracht, M., Gibelhaus, A., Seiler, J., Graf, S., Nasruddin, N., Bardow, A., “Upgrading Waste Heat from 90 to 110 °C. The Potential of Adsorption Heat Transformation”, *Energy Technology*, 9, 1:2000643, 2021.
- [15] Engelpracht, M., Driesel, J., Jürgens, B., Seiler, J., Bardow, A., “Transforming Heat From 90 °C to 110 °C: Demonstration of a Lab-Scale Adsorption Heat Transformer(AdHT)”, In *ISHPC 2021 proceedings – online pre-conference 2020*, 2020.
- [16] Bau, U., Lanzerath, F., Gräber, M., Graf, S., Schreiber, H., Thielen, N., Bardow, A., “Adsorption energy systems library - Modeling adsorption based chillers, heat pumps, thermal storages and desiccant systems”, In *The 10th International Modelica Conference*, 2014.

- [17] RWTH Aachen University, *SorpLib: Dynamic simulation of adsorption energy systems*, https://git.rwth-aachen.de/ltt_public/SorpLib, 2018.
- [18] Dubinin, M.M., “Adsorption in micropores”, *Journal of Colloid and Interface Science*, 23, 4:487–499, 1967.
- [19] D. Bathen, M. Breitbach, *Adsorptionstechnik*. Springer Berlin Heidelberg, 2001.
- [20] Schmidt, K. G., *VDI Heat Atlas: M1 – Heat Transfer to Finned Tubes*, 2nd Ed., Springer-Verlag Berlin Heidelberg, 2010.
- [21] Bau, U., Braatz, A.-L., Lanzerath, F., Herty, M., Bardow, A., “Control of adsorption chillers by a gradient descent method for optimal cycle time allocation”, *International Journal of Refrigeration*, 56:52–64, 2015.
- [22] Sieder, E. N., Tate, G. E., “Heat Transfer and Pressure Drop of Liquids in Tubes”, *Industrial & Engineering Chemistry*, 28, 12:1429–1435, 1936.
- [23] Schmidt, E. F., „Wärmeübergang und Druckverlust in Rohrschlangen“, *Chemie Ingenieur Technik - CIT*, 39, 13:781–789, 1967.
- [24] H. D. Baehr, K. Stephan, *Wärme- und Stoffübertragung*. Springer Berlin Heidelberg, 2013.
- [25] Schawe, D., *Theoretical and Experimental Investigations of an Adsorption Heat Pump with Heat Transfer between two Adsorbers*, PhD thesis, Universität Stuttgart, 2000.
- [26] Lanzerath, F., Bau, U., Seiler, J., Bardow, A., “Optimal design of adsorption chillers based on a validated dynamic object-oriented model”, *Science and Technology for the Built Environment*, 21, 3:248–257, 2015.
- [27] Schulze, C. W., *A Contribution to Numerically Efficient Modelling of Thermodynamic Systems*, PhD thesis, Technische Universität Carolo-Wilhelmina zu Braunschweig, 2013.
- [28] E. W. Lemmon, I. H. Bell, M. L. Huber, M. O. McLinden, *NIST Standard Reference Database 23. Reference Fluid Thermodynamic and Transport Properties-REFPROP*, Version 10.0, National Institute of Standards and Technology, 2018.
- [29] Wagner, W., Pruß, A., “The IAPWS Formulation 1995 for the Thermodynamic Properties of Ordinary Water Substance for General and Scientific Use”, *Journal of Physical and Chemical Reference Data*, 31, 2:387–535, 2002.
- [30] Huber, M. L., Perkins, R. A., Friend, D. G., Sengers, J. V., Assael, M. J., Metaxa, I. N., Miyagawa, K., Hellmann, R., Vogel, E., “New International Formulation for the Thermal Conductivity of H₂O”, *Journal of Physical and Chemical Reference Data*, 41, 3:33102, 2012.
- [31] Huber, M. L., Perkins, R. A., Laesecke, A., Friend, D. G., Sengers, J. V., Assael, M. J., Metaxa, I. N., Vogel, E., Mareš, R., Miyagawa, K., “New International Formulation for the Viscosity of H₂O”, *Journal of Physical and Chemical Reference Data*, 38, 2:101–125, 2009.
- [32] Haimes, Y. Y., Lasdon, L. S., Wismer, D. A., “On a Bicriterion Formulation of the Problems of Integrated System Identification and System Optimization”, *IEEE Transactions on Systems, Man, and Cybernetics*, SMC-1, 3:296–297, 1971.
- [33] Leineweber, D. B., Bauer, I., Bock, H. G., Schlöder, J. P., “An efficient multiple shooting based reduced SQP strategy for large-scale dynamic process optimization. Part 1. Theoretical aspects”, *Computers & Chemical Engineering*, 27, 2:157–166, 2003.
- [34] Leineweber, D. B., Schäfer, A., Bock, H. G., Schlöder, J. P., “An efficient multiple shooting based reduced SQP strategy for large-scale dynamic process optimization”, *Computers & Chemical Engineering*, 27, 2:167–174, 2003.
- [35] TLK Energy GmbH, *MoBa MUSCOD*, <https://tlk-energy.de/moba-muscod.html>, 2021.
- [36] Bau, U., Hoseinpoori, P., Graf, S., Schreiber, H., Lanzerath, F., Kirches, C., Bardow, A., “Dynamic optimisation of adsorber-bed designs ensuring optimal control”, *Applied Thermal Engineering*, 125, 1565–1576, 2017.

On heat regeneration limitations in heat engines with dense working fluids

N. Mügge¹, A. Kronberg², M. Glushenkov² and E. Y. Kenig^{1*}

¹Paderborn University, Chair of Fluid Process Engineering, Paderborn, Germany

²Encontech B.V., Enschede, Netherlands

*Corresponding author: Eugeny.kenig@upb.de

Abstract

Industrial processes represent a significant source of waste heat with a low temperature level below 100°C. Very often, there are no reliable ways to use this low-grade heat directly, e.g., for district heating or to convert it to electricity which is the most universal energy carrier. Organic Rankine Cycle (ORC) is the only commercially available technology for low temperature application. However, this technology is rather complex and not economically sound for practically interesting low temperature ranges, especially for small-scale (< 500 kW) applications. The concept of the isobaric expansion (IE) engine is a promising alternative to ORC as well as to other known energy conversion technologies for the conversion of low-grade and medium-grade heat (>30°C) into mechanical energy or electricity. In this work, a thermal model describing heat transfer in regenerator of IE engine is developed and a study on the heat regeneration potential is carried out.

Keywords: dense working fluids, isobaric expansion, low-grade heat, heat driven pump, heat transfer limitation, regenerative heat engine, phase transition

1. Introduction

Regeneration plays an important role in numerous heat engines, such as Organic Rankine Cycle (ORC) plants or Stirling-type engines. Generally, a higher degree of regeneration in regenerative heat engines helps to reach better thermal efficiencies [1]. Until now, the actual degree of regeneration that can be achieved in heat engines with working fluids undergoing phase change has hardly been investigated. Even for ideal gas working fluids, the regeneration process is very difficult to model accurately. Therefore, only models with significant simplifications are used [2, 3]. Often actual regeneration is even not considered. Instead, ideal regeneration [4, 5] or a certain regeneration degree is assumed [5-8]. As recently shown by Kronberg *et al.* [9], this procedure can easily violate the second law. An improved estimation of the regeneration potential can be obtained by so-called *cumulative enthalpy curves* [10]. The degree of regeneration in counter-current heat exchangers in a steady-state operation is evaluated using a pinch-point analysis of the heat delivering and heat receiving curves, with due consideration of the minimum temperature difference necessary to realise the heat transfer [11, 12]. The pinch-point analysis represents a good tool for process design and energy-potential analysis. However, for the description of heat exchangers it is not suitable. A more general thermodynamic analysis of the heat regeneration problem applicable to transient processes is presented in [9] where a method to calculate the maximum degree of energy transferrable between two arbitrary fluid streams is presented that takes the second law into account.

A promising heat engine type is the so-called *isobaric expansion (IE) engine* described by Glushenkov *et al.* [11] and studied experimentally in [13]. The IE engine operates with dense working fluids, i.e. fluids which are fully liquid in cold state and gaseous or supercritical in hot state [14, 15]. In [11], IE engines were subdivided into two classes, namely Bush-type and Worthington-type engines. In this paper, only Bush-type engine (or displacer-type

engine) is considered. Such engines operate in an unsteady-state mode and are difficult to model because of cyclic flow reversal and high pressure changes.

A schematic of the Bush-type IE engine is shown in Fig. 1. A cylinder filled with a working fluid is divided into a cold space (Cs) and a hot space (Hs) by a displacer. The displacer movement pumps the working fluid through a heat exchanger sequence comprising a heater (H), a regenerator (R) and a cooler (C). When the working fluid is cyclically displaced between the cold and the hot space, its temperature changes in cycles, so that the working fluid expands and compresses thus causing the power piston to move. If the expansion and compression of the working fluid take place at different pressures, a certain net work, positive or negative, is generated per cycle.

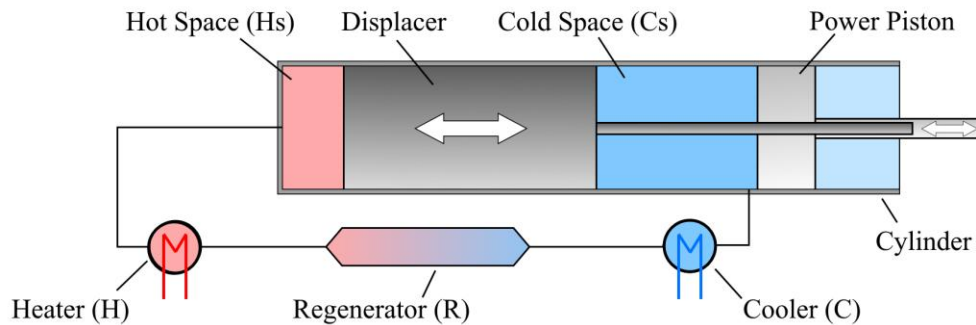


Fig. 1: Schematic view of the regenerative isobaric expansion engine.

The IE engine performance can compete with that of conventionally used ORC plants; furthermore, for low temperature heat sources (below 100°C), IE engines achieve relatively high efficiencies, up to 15% [6, 11]. The thermal efficiency can reach even higher values for higher heat source temperatures (>200°C) [11, 16]. Thermodynamic analysis shows a huge potential for regenerative IE engine application, with efficiencies up to 80% of Carnot efficiency [11]. However, the evaluation given in [11] is based on idealised model assumptions, such as ideal heat transfer conditions in the heater and cooler. Later the model was extended in [16] by considering dead volumes (internal volumes of the heat exchanger equipment) and frictional pressure losses of the heat exchanger equipment. It was found that, due to the combined influence of these two factors, heat exchangers with compact design, characterised by a large surface density, would be beneficial. In addition, a simplified steady-state design method for compact heat exchangers was presented in [16]. Since the regeneration strongly affects the thermal efficiency of the IE engine, further efforts must be undertaken that are capable of predicting realistic degrees of regeneration.

In this work, a thermal model describing the regeneration process in IE engine application is presented. The model takes into account the transient heat transfer process between the fluid and the solid. A model-based analysis is carried out showing the difference in the regeneration of the phase-changing working fluid R134a and supercritical carbon dioxide. Furthermore, the model is extended to govern a recuperative process with the working fluid R134a. The results are compared with the heat exchanger efficiency values obtained by the theoretical approach of Kronberg *et al.* [9]. The presented method can easily be applied to regenerative processes in other heat engine applications.

2. Physical model and numerical method

2.1 The isobaric expansion engine

The thermodynamic description of the IE engine was detailed in [6, 11, 16]. Here, we only address the inherent features of the thermal model. The IE engine work can be followed with the help of Fig. 1. At the beginning, the displacer is at the extreme left position and the working fluid is mostly in the cold space at cold state and at the initial pressure p_{low} . The displacer starts moving and displaces the fluid from the cold space through the cooler,

regenerator and heater to the hot space. While passing the solid regenerator, the fluid receives heat stored during the previous cooling phase. Thus, both the average fluid temperature and the pressure inside the engine rise. When a certain pressure level p_{high} is reached, the power piston starts moving. The pressure p_{high} is determined by the engine load. Reaching the extreme right position, the heating phase ends and the cooling phase begins. As the fluid is displaced from the hot to the cold space passing the heat exchanger sequence, the fluid is cooled and a certain amount of heat is stored in the regenerator. Due to the temperature decrease, the pressure drops down and reaches the initial pressure p_{low} . As soon as the pressure level p_{low} is reached, the power piston starts moving to its initial position due to the fluid volume reduction.

The thermodynamic behaviour of the IE engine can be represented by an ideal rectangular cycle, Fig. 2 [6]. During the stages 1→2 (pressurisation) and 2→3 (isobaric expansion), heating takes place, whereas during the stages 3→4 (depressurisation) and 4→1 (isobaric contraction), the working fluid is cooled.

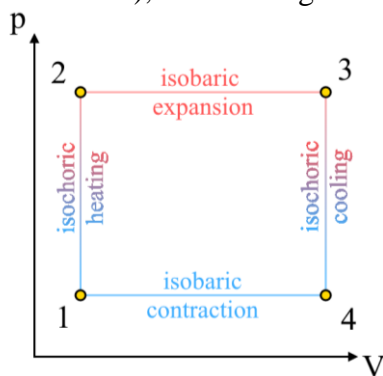


Fig. 2: Idealised rectangular cycle consisting of two isobaric and two isochoric stages (according to [6]).

Both dead internal volumes of the heat exchanger equipment (compressible volumes not swept by the displacer) as well as frictional pressure losses negatively affect the thermal efficiency of the IE engine [6, 16]. Thus, in [16] it is recommended to use the so-called *printed circuit heat exchangers* (PCHE) with a high specific surface, as shown in Fig. 3a [17]. Besides, a very high pressure resistance is required, because a working IE engine can reach very high pressures (up to several hundred bars), and PCHE are highly pressure-resistant [18]. A PCHE consists of several plates in which small-diameter channels are chemically etched. The plates are joined together by diffusion bonding. Both the individual plate design and the variation in the arrangement of single plates (e.g. alternating order for hot and cold fluid streams) provide a high degree of freedom [19].

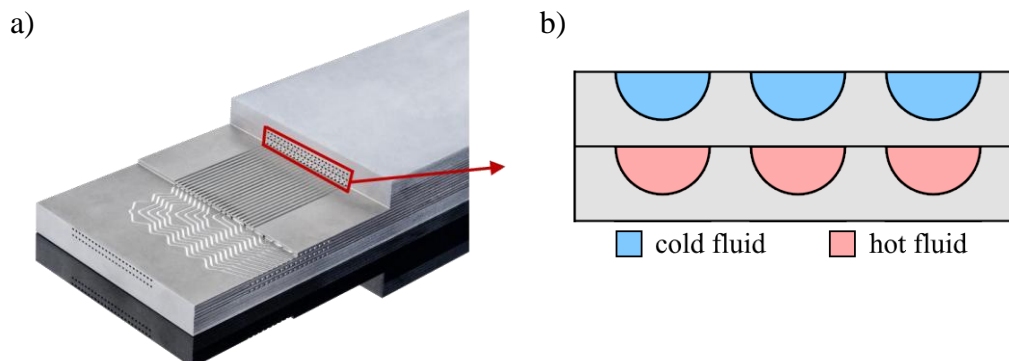


Fig. 3: Printed circuit heat exchanger: a view on the single layers [17] (a); a schematic cross-section (b).

2.2 Regenerator modelling and mathematical description

A physical model describing the regeneration is presented in Fig. 4. Fig. 4a illustrates the arrangement of the regenerator domain with the length L_R within the IE engine. Depending

on the displacer movement, the working fluid is pumped from the cooler to the heater or vice versa, which is indicated by the red and blue arrows showing the flow directions. A schematic of the cross-section of the regenerator is shown in Fig. 4b, with the channel diameter d_R , plate thickness δ_R and the wall thickness s_R .

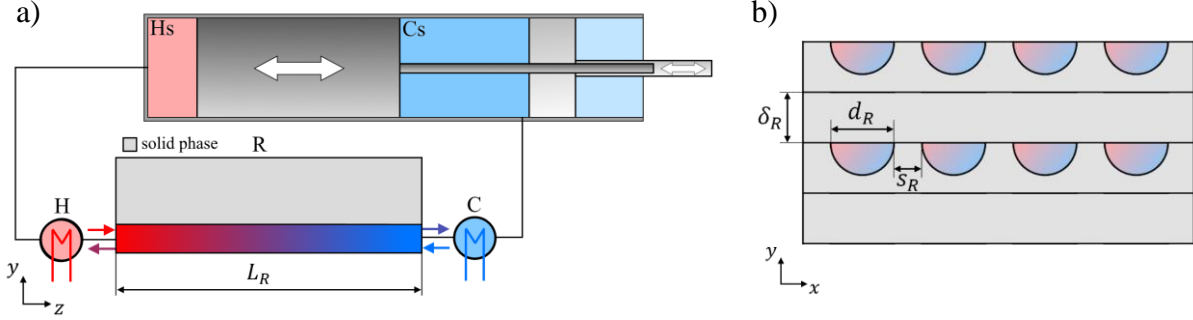


Fig. 4: Schematics of the IE engine regenerator model (a) and of a cross-section of the regenerator (b).

Based on Fig. 4, relevant geometric characteristics for the heat transfer process can be derived. The cross-sectional area of the flow in a semi-circular channel A_{cr} , the circumference of this channel P , the fluid volume within the regenerator V_R and the hydraulic diameter d_h are given by the following relationships:

$$A_{cr} = \frac{\pi d_R^2}{8} \quad (1)$$

$$P = d_R(1 + 0.5\pi) \quad (2)$$

$$V_R = N_{Ch} A_{cr} L_R \quad (3)$$

$$d_h = 4 \frac{A_{cr}}{P} = \frac{\pi d_R}{2 + \pi} \quad (4)$$

with N_{Ch} being the total number of channels in the regenerator. The swept volume V_{sw} of the displacer can be related to the fluid volume within the regenerator as follows:

$$V_{sw} = V_R \cdot \theta \quad (5)$$

where θ is the corresponding volumetric ratio. Its value is determined by the construction of the engine. The displacer movement is approximated by a sinusoidal function. The volumetric flow rate of the streams entering the hot space or leaving it is:

$$\dot{V}_{Hs}(t) = \pi f V_{sw} \sin(2\pi f t) \quad (6)$$

where f is the operating frequency of the IE engine.

Assuming that thermal conduction in flow direction is negligible compared to the convective energy transport, the energy equation for the fluid phase is given by

$$\frac{\partial(\rho u)}{\partial t} + \frac{\partial}{\partial z}(\rho h w_z) = s_u \quad (7)$$

where u is the specific internal energy, ρ is density, h is the specific enthalpy, w_z is the velocity component in z direction and s_u is a volume specific source term. The continuity equation in a one-dimensional form reads as:

$$\frac{\partial \rho}{\partial t} + \frac{\partial}{\partial z}(\rho w_z) = s_m \quad (8)$$

where s_m is a volumetric mass source term due to phase change. Heat transport in the solid phase is described by

$$\frac{\partial T_s}{\partial t} = \frac{\lambda_s}{\rho_s c_{p,s}} \left(\frac{\partial^2}{\partial x^2} + \frac{\partial^2}{\partial y^2} \right) T_s \quad (9)$$

where T_s denotes the solid phase temperature and λ_s , ρ_s , $c_{p,s}$ are the thermal conductivity, density and the heat capacity of the solid phase, respectively.

The computational domain is divided into a fluid part containing n_f segments (white) and a solid part containing $n_s = n_f \cdot n_{n,y}$ segments, as shown in Fig. 5. The indices i and j identify the solid phase segments.

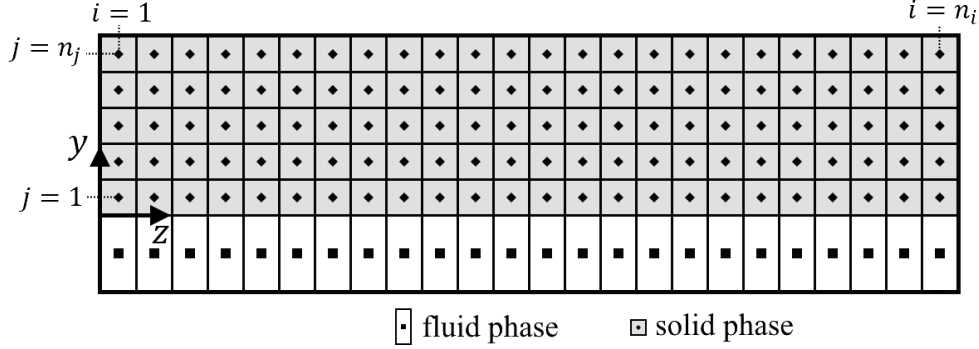


Fig. 5: Computational domain of the regenerator with solid phase segments (grey, diamonds) and fluid segments (white, squares).

On the regenerator side adjacent to the heater ($z = z_H$), a mass flow boundary condition is set for the fluid phase to ensure the same amount of mass passing the regenerator during the heating and cooling phase. The boundary condition is defined, depending on the volumetric flow rate determined by the displacer movement in Eq. (6):

$$\dot{m}(z_H, t) = \dot{V}_{Hs}(t) \cdot \rho(T_H, p_{low}). \quad (10)$$

where \dot{m} is the mass flow rate and T_H is the heat source temperature. The fluid enters the fluid channel either from the heater ($z = z_H$) or from the cooler ($z = z_C$) at hot or cold state, respectively. The specific enthalpy of the fluid entering or leaving the computational domain is

$$h(z_H) = \begin{cases} h(T_H, p) & \dot{m}(z_H) > 0 \\ h(u(z_{RH}), p) & \dot{m}(z_H) \leq 0 \end{cases} \quad (11)$$

at the hot end and

$$h(z_C) = \begin{cases} h(T_C, p) & \dot{m}(z_C) < 0 \\ h(u(z_{RC}), p) & \dot{m}(z_C) \geq 0 \end{cases} \quad (12)$$

at the cold end, where T_C is the temperature of the heat source and p is pressure. The pressure in Eq. (11) and (12) is set to p_{low} during the cooling phase and to p_{high} during the heating phase. At the interface boundary at $y_0 = 0$, the following condition is imposed:

$$\dot{Q} = \alpha(z) \cdot A_w \cdot [T_s(z, y_0) - T_f(z)] \quad (13)$$

with \dot{Q} being the heat flow rate, α denotes the heat transfer coefficient and A_w is the area of the fluid channel wall. The heat transfer coefficient in Eq. (13) is determined based on Nusselt number correlations. The correlations used in the presented work were primarily chosen based on the recommendations for micro-channels and mini-channels given in [20, 21]. They are summarised in Table 1.

Table 1: Nusselt number correlations used in this work

Single-phase flow	Condensing flow	Flow-boiling	Supercritical flow
Gnielinski [22]	Akers and Rosson [23]	Bertsch <i>et al.</i> [24]	Mokry <i>et al.</i> [25]

In accordance with the requested good insulation of heat exchanger equipment, adiabatic boundary conditions are assumed at the front and back faces of the regenerator:

$$\frac{\partial T_s}{\partial z} \Big|_{z=z_H} = 0 \quad (14)$$

$$\frac{\partial T_s}{\partial z} \Big|_{z=z_c} = 0$$

At $y = y_n$, a symmetry boundary condition given by

$$\frac{\partial T_s}{\partial y} \Big|_{y=y_n} = 0 \quad (15)$$

is used. Fig. 6 gives an overview of the boundary conditions for the regenerator thermal model.

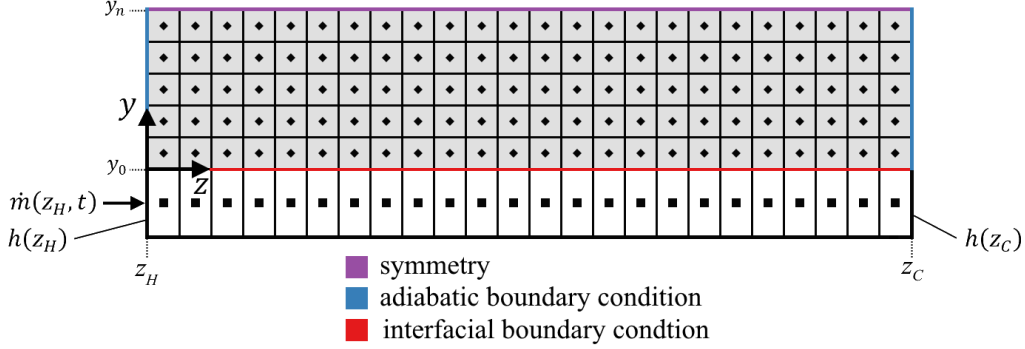


Fig. 6: Boundary conditions of the computational domain: Symmetry (purple), adiabatic condition (blue) and interfacial boundary condition (red). The specific enthalpies on each end of the regenerator and the mass flow rate at the very left end are set for the fluid phase.

The flow direction within the fluid domain changes periodically according to the movement of the displacer, as described by Eq. (6). Consequently, the alternating heating and cooling of the fluid takes place; they can be described by the following two half cycles:

$$\text{heating phase: } (n_{\text{cycle}} - 1)\tau \leq t < (n_{\text{cycle}} - 0.5)\tau \quad (16)$$

$$\text{cooling phase: } (n_{\text{cycle}} - 0.5)\tau \leq t < n_{\text{cycle}}\tau \quad (17)$$

where n_{cycle} is the current cycle, starting with $n_{\text{cycle}} = 1$ and τ is the cycle period. The thermodynamic cycle consists of two isobaric and two isochoric stages (cf. Fig. 2). We assume that the duration of the isobaric stages is much longer than that of the isochoric stages, i.e. the heat transfer mostly takes place during the isobaric stages. Thus, the pressure during the heating and cooling phase is equal to p_{high} and p_{low} respectively. This simplification was also used in [16]. After each half cycle, a reinitialisation is performed using the following relationships:

$$t = (n_{\text{cycle}} - 1)\tau : p = p_{\text{low}}; u(z) = u(T_H, p_{\text{low}}) \quad (18)$$

$$t = (n_{\text{cycle}} - 0.5)\tau : p = p_{\text{high}}; u(z) = u(T_C, p_{\text{high}}) \quad (19)$$

The model equations are now discretised, according to Fig. 5. The mass, the specific internal energy and the temperature of the fluid and the vapour volume fraction ϕ are determined in the centre of a segment. The mass flow rates and enthalpy flow rates entering the segment are determined on the adjacent surfaces, as visualised in Fig. 6. Integration of Eq. (7) over the volume of a fluid segment gives

$$\int \frac{\partial(\rho u)}{\partial t} dV + \int \frac{\partial}{\partial z} (\rho h w_z) dV = \int \dot{Q}_V dV \quad (20)$$

Applying the Gaussian divergence theorem to the convective term results in

$$\frac{du}{dt} m + u \frac{dm}{dt} = \dot{H}^{sf-} - \dot{H}^{sf+} + \dot{Q} \quad (21)$$

where \dot{H}^{sf-} and \dot{H}^{sf+} are the enthalpy flow rates on the adjacent left (-) and right (+) faces of a segment (see Fig. 6).

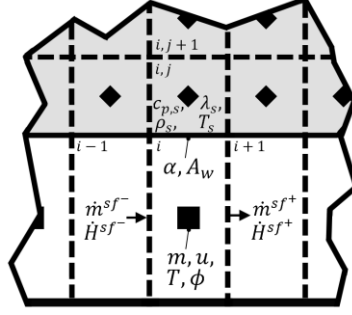


Fig. 7: A section of the computational domain with energy and mass flows entering and leaving a segment.

The mass balance equation for a segment covers the mass change of the vapour phase (subscript v) and the liquid phase (subscript l):

$$\frac{dm}{dt} = \frac{dm_v}{dt} + \frac{dm_l}{dt} \quad (22)$$

The time derivatives for each phase are obtained from Eq. (8), by integrating over a segments volume and applying the Gaussian divergence theorem

$$\frac{dm_v}{dt} = \dot{m}_v^{sf-} - \dot{m}_v^{sf+} + \dot{m}_{pc} \quad (23)$$

$$\frac{dm_l}{dt} = \dot{m}_l^{sf-} - \dot{m}_l^{sf+} - \dot{m}_{pc} \quad (24)$$

with \dot{m}_{pc} being the mass undergoing phase change per unit time. Based on the heat transferred between the solid and fluid phases according to Eq. (13), the evaporating or condensing mass per unit time is determined by:

$$\dot{m}_{pc} = \frac{\dot{Q}}{\Delta h_v(p)}. \quad (25)$$

Here Δh_v is the heat of evaporation which depends on the pressure. Consequently, the heat of evaporation differs in cooling and heating phase. The mass flow rates of the vapour and the liquid phase in Eq. (23) and (24) are

$$\dot{m}_v^{sf} = \dot{V}^{sf} \cdot \phi^{sf} \rho_v^{sf} \quad (26)$$

$$\dot{m}_l^{sf} = \dot{V}^{sf} \cdot (1 - \phi^{sf}) \rho_l^{sf} \quad (27)$$

where ϕ is the vapour volume fraction and ρ_v^{sf} and ρ_l^{sf} are the vapour and the liquid densities on the surface. The density of the vapour and liquid phase on the adjacent surface is

$$\rho_{v/l}^{sf+} = \begin{cases} \rho_{v/l}^i & \dot{V}^{sf} \geq 0 \\ \rho_{v/l}^{i+1} & \dot{V}^{sf} < 0 \end{cases} \quad (28)$$

while the vapour volume fraction is obtained by

$$\phi = \frac{q}{q + \frac{\rho_v}{\rho_l} - q \frac{\rho_v}{\rho_l}} \quad (29)$$

with q as the vapour mass fraction. The volumetric flow rate is determined by the volume entering a segment and the change of the overall fluid volume within a segment

$$\dot{V}_i^{sf} = \dot{V}_{i-1}^{sf} + \frac{dV_{v,i}}{dt} + \frac{dV_{l,i}}{dt}. \quad (30)$$

where the time derivatives of the vapour and liquid volumes represents the volume change of each phase due to thermal effects, e.g., evaporation/condensation or thermal expansion/contraction:

$$\frac{dV_v}{dt} = \frac{-1}{\rho_v} \left(V \phi \frac{d\rho_v}{dt} + \dot{m}_{pc} \right) \quad (31)$$

$$\frac{dV_l}{dt} = \frac{-1}{\rho_l} \left[V(1 - \phi) \frac{d\rho_l}{dt} - \dot{m}_{pc} \right]. \quad (32)$$

Initially, the process starts with a cooling phase, in which heat is transferred from the fluid to the solid at low pressure, Eq. (33). The internal energy of the fluid is initialised with the heater temperature T_H and low pressure p_{low} , since the fluid enters the domain from the hot side (Hs) after having passed the heater (H), Eq. (34). As at the beginning the displacer starts at the extreme right position, the mass flow rate everywhere is equal to zero, Eq. (35). The solid-phase temperature is initially set to the mean temperature of the heater and cooler, Eq. (36).

$$p = p_{low} \quad (33)$$

$$u_f(z) = u(T_H, p_{low}) \quad (34)$$

$$\dot{m}(z) = 0 \quad (35)$$

$$T_s(y, z) = \frac{T_H + T_C}{2} \quad (36)$$

The fluid properties are obtained by the REFPROP 9.1 database [26]. The thermal model is integrated in time with an implicit time stepping scheme which provides reasonable accuracy and stability for larger time-steps. The heat transfer equation for the solid phase is discretised with finite-difference method and the model is implemented in MATLAB.

3. Results

3.1 Regenerative process with subcritical working fluid R134a

In a first study, the commonly used R134a is applied as a working fluid in the thermal model. The pressure values of $p_{low} = 4.2 \text{ bar}$ and $p_{high} = 36.9 \text{ bar}$ are chosen that are close to the saturation conditions at the heat source temperature $T_H = 370 \text{ K}$ ($p_{sat}(T_H) = 37.3 \text{ bar}$) and heat sink temperature $T_C = 283 \text{ K}$ ($p_{sat}(T_C) = 4.1 \text{ bar}$). The operating frequency is 1 Hz . A grid independence study was carried out, by varying the number of segments in flow direction and normal to it. Satisfactory results were obtained for 1 segment/cm in flow direction and 1 segment/mm in normal direction. The design parameters of the regenerator are given in Table 2; they are kept for all other cases. The solid phase regenerator material was selected to be steel ($\lambda_s = 47 \frac{\text{W}}{\text{m}^2\text{K}}$, $c_{p,s} = \frac{470\text{J}}{\text{kgK}}$, $\rho_s = 7900 \frac{\text{kg}}{\text{m}^3}$).

Table 2: Design parameters of the regenerator

d_R	L_R	δ_R	θ	N_{Ch}
3 mm	0.5 m	10 mm	10	300

During the post-processing the frictional pressure drop is calculated from pressure drop correlations. They are summarised in Table 3.

Table 3: Pressure drop correlations used in this work

Single-phase flow	Condensing flow	Flow-boiling	Supercritical flow
Fang <i>et al.</i> [27]	Zhang and Webb [28]	Kim and Mudawar [21]	Fang <i>et al.</i> [29]

Fig. 8 shows the temperature of the fluid over time for the hot (red line) and cold (blue line) side of the regenerator. The temperature of the hot side shown in Fig. 8a is evaluated at the end of the heating phase and the temperature of the cold side at the end of the cooling phase. From Fig. 8a it can be seen that a quasi-steady-state is reached after 350 cycles.

A more detailed view on the regeneration process is depicted in Fig. 8b. It shows the temperature at the hot end (red) and cold end (blue) over time for the last cycle of the

simulation. The dash lines represent the heat source (red) and the heat sink (blue) temperature, respectively. During the cooling phase (first half cycle), the fluid enters the regenerator from the hot side under the heater conditions ($u = u(T_H, p_{low})$) and leaves the regenerator at approximately 313 K, i.e. the fluid is cooled by $\Delta T_{cp} = 57$ K. During the heating phase (second half cycle), the fluid enters the regenerator in cold state ($u = u(T_C, p_{high})$) from the cooler. The temperature difference between the fluid leaving and entering the regenerator here is rather small with approximately $\Delta T_{hp} = 7$ K. This can be attributed to the difference between the values of the fluid heat capacity at $p = p_{low}$ (cooling phase) and at $p = p_{high}$ (heating phase). The larger value results in a smaller temperature difference ΔT_{hp} , since in both cooling and heating phase the change of internal energy is equal.

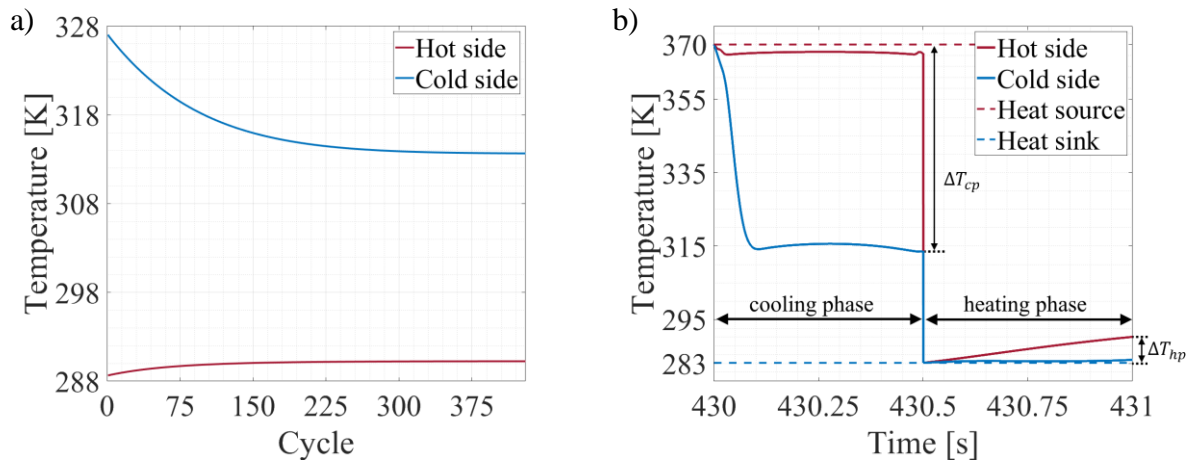


Fig. 8: Temperature of the fluid at the regenerator hot side (heating phase) and at the cold side (cooling phase) (a); temperature profile for the last simulated cycle (b)

The temperature of the solid phase is depicted in Fig. 9, while the solid segments correspond to those adjacent to the fluid. In Fig. 9a, the temperature at each end of the regenerator is shown for the first 50 cycles of the simulation, starting with the initial temperature $T_{R0} = 326.5$ K. A growing temperature difference between the hot and cold side is visible. In Fig. 9b, the temperatures at each end are plotted for the last 5 cycles. The temperature at each side of the regenerator shows a quasi-steady behaviour, as the temperature profiles have a repeated form in each of the cycles.

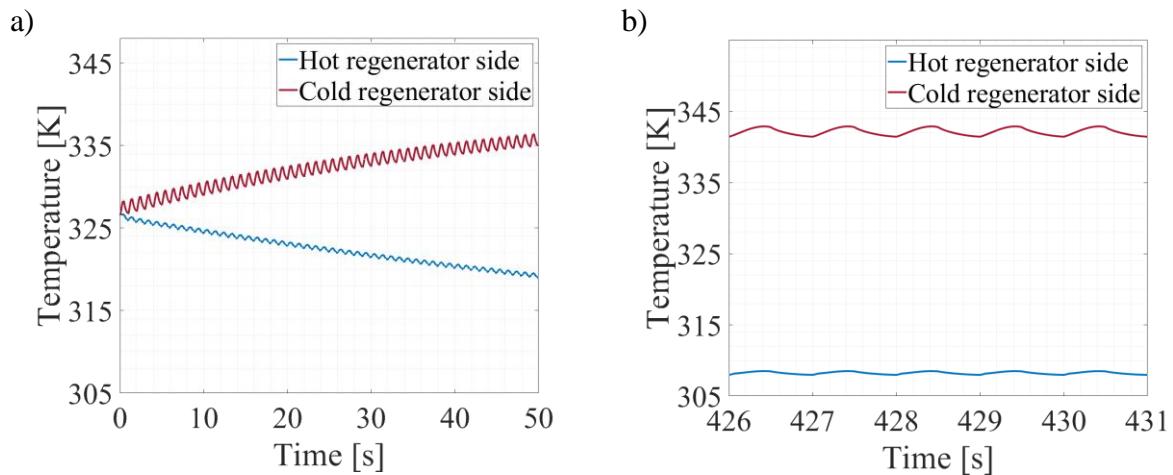


Fig. 9: Solid-phase temperature at the hot (red) and cold (blue) end for the first 50 cycles of the simulation (a) and for the last 5 cycles (b).

In Fig. 10, the temperature along the length of the regenerator is illustrated for the solid segments adjacent to the fluid. The blue line shows the temperature profile at the end of the cooling phase and the red line at the end of the heating phase. The difference between the temperature profiles is rather low (maximum 2 K) compared to the temperature difference between the hot and cold end of the regenerator (nearly 34 K).

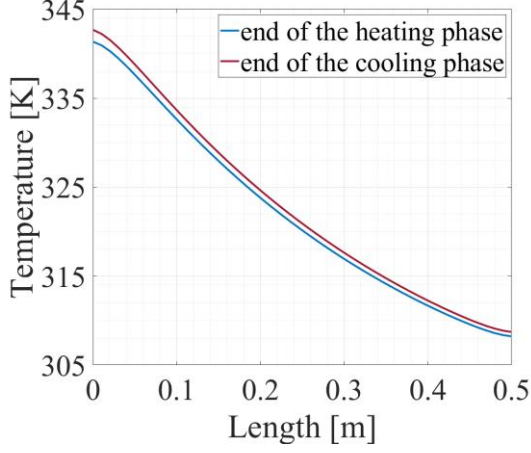


Fig. 10: Temperature of the solid phase along the regenerator length for segments adjacent to the fluid.

We compared the results of the transient simulations with those by Kronberg *et al.* [9]. In [9], the thermodynamically maximum amount of heat $\Delta H_{R,max}$ transferrable between two fluids was derived based on the enthalpy curves of the fluids delivering and receiving heat. We applied the approach suggested in [9] to the working fluid R134a at $p_{low} = 4.2 \text{ bar}$ and $p_{high} = 36.9 \text{ bar}$ in the temperature range between $T_C = 283 \text{ K}$ and $T_H = 370 \text{ K}$. Fig. 11 illustrates the results. The enthalpy of the heating phase H_{hp} (fluid receiving heat) is given by the red line, while the cooling phase enthalpy H_{cp} (fluid delivering heat) is depicted by the solid blue line for an ideal case of zero temperature difference at the pinch point ($\Delta T_{pp} = 0 \text{ K}$). Since some temperature difference is always required to realise heat transfer between the fluids, a small pinch point temperature difference ΔT_{pp} is assumed, resulting in a shift of the heat delivering curve, which is illustrated by the dash blue line in Fig. 11 for $\Delta T_{pp} = 5 \text{ K}$.

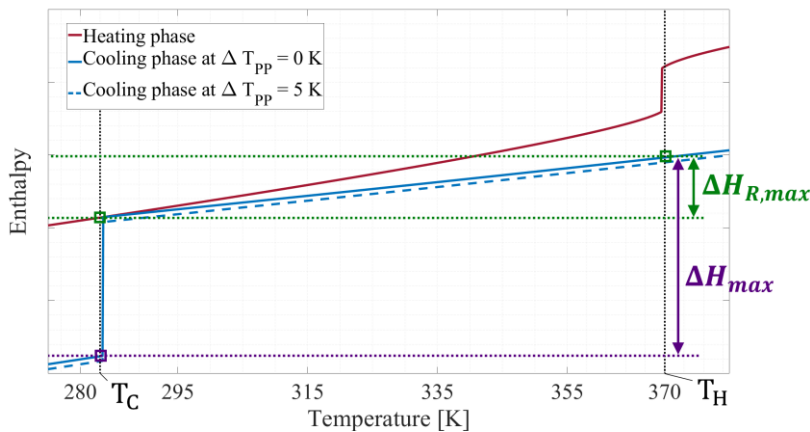


Fig. 11: Cumulative enthalpy curves for R134a obtained based on the approach suggested in [9]. Heating phase curve (red) at p_{high} and cooling phase curves (blue) at p_{low} , both for 0 K and 5 K pinch point temperature difference.

The maximum amount of heat $\Delta H_{R,max}$ that can be transferred from the cooling to the heating phase is defined by

$$\Delta H_{R,max} = H_{cp}(T_H) - H_{hp}(T_C) \quad (37)$$

The results obtained from the transient solution are now evaluated by means of the heat exchanger efficiency [30]

$$\epsilon = \frac{\Delta H}{\Delta H_{max}} \quad (38)$$

where ΔH is the simulated enthalpy difference and ΔH_{max} is the working fluid enthalpy difference determined at heat source and heat sink temperatures. The heat exchanger efficiency evaluates the transferred heat in relation to the maximum enthalpy difference of the process. For the ideal case with the zero pinch point temperature difference ($\Delta T_{pp} = 0 \text{ K}$), the efficiency value of $\epsilon_0 = 0.40$ is obtained. With a finite pinch point temperature difference of $\Delta T_{pp} = 5 \text{ K}$, the efficiency value decreases to $\epsilon_{pp5} = 0.37$. The heat exchanger efficiency for the last cycle of the transient simulation is shown in Fig. 12 where the first half cycle shows the heat exchanger efficiency defined for the cooling phase

$$\epsilon_{cp} = \frac{\Delta H_{cp}}{\Delta H_{cp,max}} \quad (39)$$

and the second half cycle depicts the efficiency of the heating phase:

$$\epsilon_{hp} = \frac{\Delta H_{hp}}{\Delta H_{hp,max}} \quad (40)$$

The cooling efficiency (blue line) increases rapidly at the beginning and reaches a plateau at a value of $\epsilon_{cp} = 0.19$ whereas the heating efficiency (red line) rises slowly from the beginning of the half cycle until a value of $\epsilon_{hp} = 0.04$ is achieved at the end of the cycle. It can be seen that the heating phase efficiency is still rising towards the end of the process. A higher heat exchanger efficiency could be reached by increasing the length of the regenerator or reducing the operating frequency. However, an increased regenerator length is equivalent to a larger dead volume and also to an increased frictional pressure drop. Both have a negative impact on the thermal efficiency of the IE engine. In the current simulation, the frictional pressure drop $\Delta p_{fr} = 0.12 \text{ bar}$, which is just 0.4 % of the pressure difference $\Delta p = p_{high} - p_{low}$.

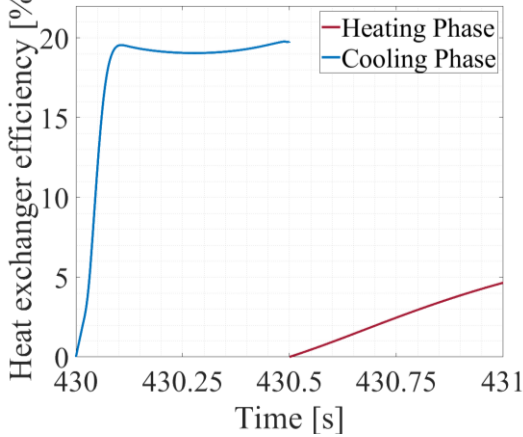


Fig. 12: Heat exchanger efficiency during the cooling phase (blue) and heating phase (red) obtained for the simulated last cycle.

When evaluating a regeneration process, it is reasonable to consider the results based on the maximum possible regeneration $\Delta H_{R,max}$ (as depicted in Fig. 11). Therefore, in [9], the overall heat transfer efficiency was defined as

$$\eta = \frac{\Delta H}{\Delta H_{R,max}} \quad (41)$$

For R134a, an overall heat transfer efficiency of $\eta_{cp} = 0.43$ for the cooling phase and $\eta_{hp} = 0.1$ for the heating phase are obtained.

3.2 Regenerative process with supercritical working fluid carbon dioxide

In [6], working fluids operating in supercritical state at high pressure level were found to be promising enhancing the thermal efficiency of IE engines. Such fluids have a high regeneration potential [11]. For this reason, in the present work, the thermal model is applied to supercritical carbon dioxide. The temperatures of the heat source and heat sink are kept at $T_C = 283\text{ K}$ and $T_H = 370\text{ K}$, while the pressure values are set to $p_{low} = 45\text{ bar}$ and $p_{high} = 95\text{ bar}$. To facilitate the solution, the solid temperature profile from the previous simulation with R134a is now used as the initial condition for the solid phase. A quasi-steady-state was reached after 50 cycles. For the given operating conditions, an ideal heat exchanger efficiency $\epsilon_0 = 0.378$ is estimated. The heat exchanger efficiency for the last cycle of the supercritical regeneration process is depicted in Fig. 13. The supercritical regeneration process reaches heat exchanger efficiencies up to 25 % in the cooling phase and 23 % in the heating phase. Thus, the heat exchanger efficiency of the heating phase is eight times higher than in the process with R134a. Using Eq. (41), an overall heat transfer efficiency value of $\eta_{hp,CO_2} = 0.61$ is reached, which is a significant improvement to the R134a values $\eta_{hp,R134a} = 0.1$.

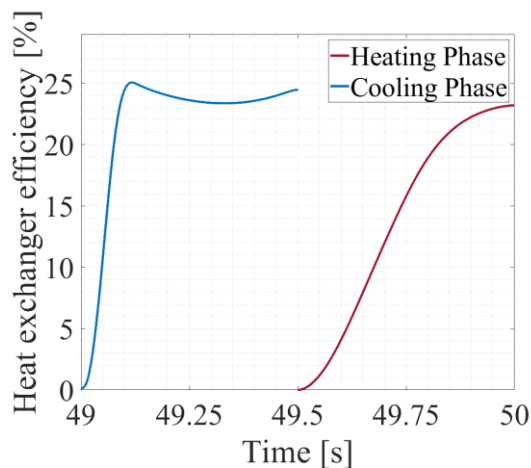


Fig. 13: Heat exchanger efficiency of the supercritical process operating with carbon dioxide.

3.3 Recuperative process with subcritical working fluid R134a

Another promising application of the IE engine is the duplex arrangement of two IE engines operating in a counter-phase mode, first proposed in [11] and depicted in Fig. 14. Operating in the counter-phase mode means that the cooling phase is in progress in engine A at the same time as the heating phase in engine B. In this way, the regenerator becomes a recuperative (counter-current) heat exchanger and the working fluid from engine A directly supplies heat for the heating phase of engine B.

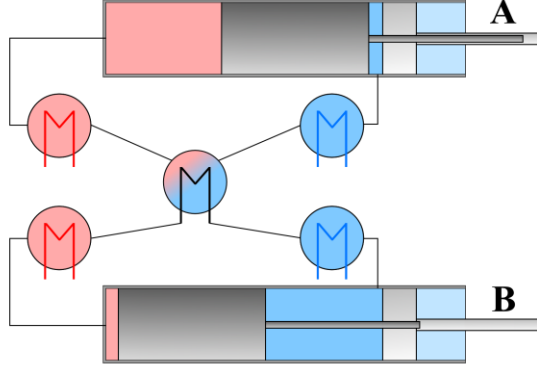


Fig. 14: Duplex arrangement of two IE engines (engine A and engine B operating in a counter-phase mode) coupled through a recuperator.

The duplex arrangement in the thermal model is considered using the overall heat transfer coefficient for the exchange between engine A and engine B as follows:

$$kA = \left(\frac{1}{A_A \alpha_A} + \frac{\delta_R - \frac{1}{2} d_{ch}}{\lambda_R A_R} + \frac{1}{A_B \alpha_B} \right)^{-1} \quad (42)$$

The overall heat transfer coefficient is derived based on Fig. 3b, assuming an alternating pattern of plates with fluids related to engine A and engine B. The recuperative process is now considered under the same conditions as previously used in the case with R134a ($T_C = 283 \text{ K}$, $T_H = 370 \text{ K}$, $p_{low} = 4.2 \text{ bar}$, $p_{high} = 36.9 \text{ bar}$) and for the heat exchanger design parameters from Table 2.

Fig. 15a shows the temperature at the hot (red) and the cold (blue) side of the recuperator over time. The recuperative cycle can be divided into five sections. First section ends at approximately 0.07 s , while the heat transfer between the heat delivering stream (in the cooling phase) and heat receiving stream (in the heating phase) dominates the recuperation. Thus, the fluid at the cold side cools down to 310 K . Between 0.07 s and 0.13 s , the temperature increases, both for the hot and cold side, since more hot fluid enters the recuperator from the heater. In the third period, between 0.13 s and 0.25 s , the temperature decreases due to higher heat transfer coefficient values reached at higher velocities. Afterwise, the conditions reverse and the temperature increases, because the fluid entering from the heater overwhelms the energy transport between the two fluid streams. When the motion of the displacer slows down during the time period between 0.4 s and 0.5 s , the convective transport significantly slows down and, consequently, the temperature falls. At the end of the cooling phase, a temperature difference $\Delta T_{cp} = 60 \text{ K}$ and at the end of the heating phase $\Delta T_{hp} = 12 \text{ K}$ is reached between the hot and col end of the recuperator. In Fig. 15b, the heat exchanger efficiency of the recuperative process is depicted. The heat exchanger efficiency achieved with the recuperative process exceeds the value of the regenerative process. At the end of the heating phase, the efficiency rises towards the value of $\epsilon_{hp} = 0.08$, which is two times higher than the value of the regenerative process.

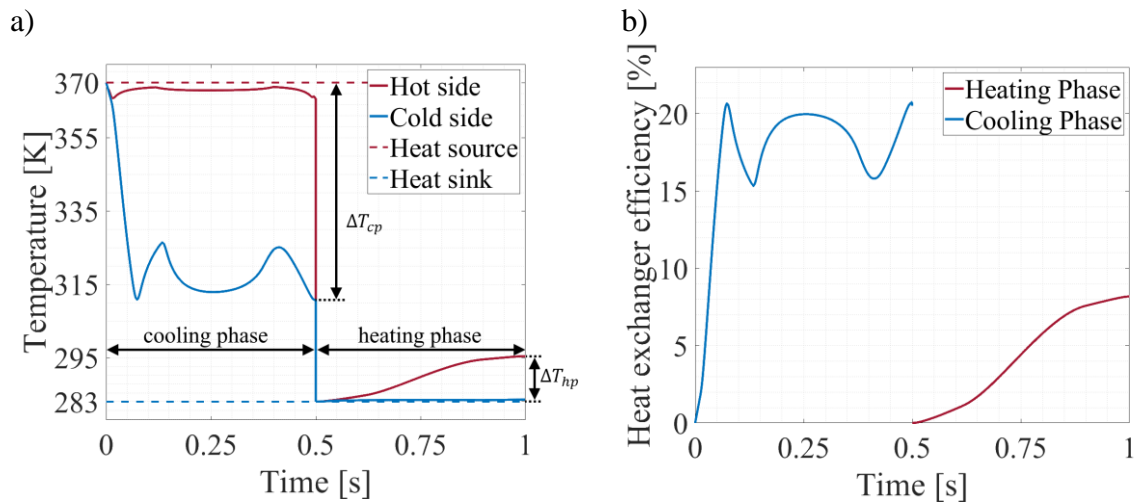


Fig. 15: Recuperative cycle with R134a, a heat source temperature of 283 K and a heat sink temperature of 370 K. The engines operate at 1 Hz: temperature over time (a) and the heat exchanger efficiency (b).

4. Conclusions

A thermal model for the regeneration / recuperation process in IE engines was developed, both for subcritical and supercritical fluids, to capture the strongly unsteady heat transfer processes during the heating and cooling phases. The efficiency of the heat transfer process for one subcritical and one supercritical working fluid as well as for one subcritical recuperation process was studied numerically. The results confirm the expectations of improved regeneration with supercritical fluids (61 % of maximum possible regeneration) as well as the beneficial impact of using a duplex arrangement with a recuperator which increases the heat exchanger efficiency of the heating phase by a factor of two.

Further investigations will focus on the impact of the transient behaviour on the heat transfer to derive a quasi-steady model that can be combined with a thermodynamic model from Glushenkov *et al.* [11]. The heater and cooler will be included in the modelling in order to perform an overall analysis of the heat transfer processes in IE engines. Furthermore, experimental investigations are planned to generate the validation basis for the presented model.

Acknowledgements of A. Kronberg and M. Glushenkov

This publication was made possible by NPRP grant # NPRP11S-1231-170155 from the Qatar National Research Fund (a member of Qatar Foundation). The findings achieved herein are solely the responsibility of the authors.

This project has received funding from the European Union's Horizon 2020 research and innovation programme under grant agreement No 764042. This presentation reflects only the authors' views and neither Agency nor the Commission are responsible for any use that may be made of the information contained therein.

References:

- [1] Javanshir, A., Saunac, N. Razzaghpanah, Z., "Thermodynamic analysis of a regenerative organic Rankine cycle using dry fluids", *Applied Thermal Engineering*, 123, pp. 852-864, 2017.
- [2] Walker, G., *Stirling Engines*, New York: Oxford University, 1980.
- [3] Hargreaves, C. M., *The Philips Stirling Engine*, Amsterdam, Elsevier, 1991.
- [4] Walker, G., "Stirling Cycle cooling engine with two-phase, two-component working fluid", *Cryogenics*, 14, pp. 459-462, 1974.
- [5] Invernizzi, C. M., "Stirling engines using working fluids with strong real gas effects",

- Applied Thermal Engineering, 30, pp. 1703-1710, 2010.
- [6] Knoke, T., Kenig, E. Y., Kronberg, A., Glushenkov, M., “Model-based Analysis of Novel Heat Engines for Low-Temperature Heat Conversion“, Chemical Engineering Transactions, 57, pp. 499-504, 2017.
- [7] Yaqi, L., Yaling, H., Weiwei, W., “Optimization of solar-powered Stirling heat engine with finite-time thermodynamics“, Renewable Energy, 36, pp. 421-427, 2011.
- [8] Ahmadi, M. H., Ahmadi, M. A., Pourfayaz, F., Bidi, M., Hosseinzade, H., Feidt, M., “Optimization of powered Stirling heat engine with finite speed thermodynamics“, Energy Conversion and Management, 108, pp. 94-105, 2016.
- [9] Kronberg, A., Glushenkov, M., Knoke, T., Kenig, E. Y., “Theoretical limits on heat regeneration degree“, International Journal of Heat and Mass Transfer, 161, p. 120282, 2020.
- [10] Olsen, D., Abdelouadoud, Y., Liem, P., Wellig B., “The Role of Pinch Analysis for Industrial ORC Integration“, Energy Procedia, 129, pp. 74-81, 2017.
- [11] Glushenkov, M., Kronberg, A., Knoke, T., Kenig, E. Y., “Isobaric Expansion Engines: new opportunities in energy conversion for heat engines, pumps and compressors“, Energies, 11, pp. 154-175, 2018.
- [12] Kemp, I. C., *Pinch Analysis and Process Integration: A User Guide on Process Integration for the Efficient Use of Energy*, Oxford, UK, Elsevier, 2007.
- [13] Glushenkov, M., Kronberg, A., “Experimental study of an isobaric expansion engine-pump“, private communication, 2021.
- [14] Feher, E. G., “The supercritical thermodynamic power cycle“, Energy Conversion, 8, pp. 85-90, 1968.
- [15] Allen, P., Knight, W. R., Paulson, D. N., Wheatley, J. C., “Principles of liquids working in heat engines“, Proc. Natl. Acad. Sci., 77, pp. 39-43, 1980.
- [16] Knoke, T., Kronberg, A., Glushenkov, M., Kenig, E. Y., “On the design of heat exchanger equipment for novel-type isobaric expansion engines“, Applied Thermal Engineering, 167, p. 114382, 2020.
- [17] V. P. Engineering, “www.vpei.com“ [Online], Available: <https://www.vpei.com/wp-content/uploads/Hex-Core-Layered.jpg>, [accessed 23rd April 2021].
- [18] Li, X.-H., Deng, T.-R., Ma, T., Ke, H.-B., Wang, Q.-W., “A new evaluation method for overall heat transfer performance of supercritical carbon dioxide in a printed circuit heat exchanger“, Energy Conversion and Management, 193, pp. 99-105, 2019.
- [19] Kim, I. H., Zhang, X., Christensen, R., Sun, X., “Design study and cost assessment of straight, zigzag, S-shape, and OSF PCHEs for a FLiNaK-SCO₂ Secondary Heat Exchanger in FHRs“, Annals of Nuclear Energy, 94, pp. 129-137, 2016.
- [20] Kim, S.-M., Mudawar, I., “Review of databases and predictive methods for heat transfer in condensing and boiling mini/micro-channel flows“, International Journal of Heat and Mass Transfer, 77, pp. 627-652, 2014.
- [21] Kim, S.-M., Mudawar, I., “Review of databases and predictive methods for pressure drop in adiabatic, condensing and boiling mini/micro-channel flows“, International Journal of Heat and Mass Transfer, 77, pp. 74-97, 2014.
- [22] Gnielinski, V., “Ein neues Berechnungsverfahren für die Wärmeübertragung imim Übergangsbereich zwischen laminarer und turbulenter Rohrströmung“, Forschung im Ingenieurwesen, 61, pp. 240-248, 1995.
- [23] Akers, W. W., Rosson, H. F., “Condensation inside a horizontal tube“, Chemical

- Engineering Progress Symposium, 56, pp. 145-149, 1960.
- [24] Bertsch, S. S., Groll, E. A., Garimella, S. V., “Effects of heat flux, mass flux, vapor quality and saturation temperature on flow boiling heat transfer in microchannels“, *International Journal of Multiphase Flow*, 35, pp. 142-154, 2009.
 - [25] Mokry, S., Pioro, I., Farah, A., King, K., Gupta, K., Peiman, W., Kirillov, P., “Development of supercritical water heat-transfer correlation for vertical bare tubes“, *Nuclear Engineering and Design*, 241, pp. 1126-1136, 2011.
 - [26] NIST, *Reference Fluid Thermodynamic and Transport Properties Database (REFPROP): Version 9.1*, <https://www.nist.gov/srd/refprop>, 2019.
 - [27] Fang, X., Xu, Y., Zhou, Z., “New correlations of single-phase friction factor for turbulent pipe flow and evaluation of existing single-phase friction factor correlations“, *Nuclear Engineering and Design*, 241, pp. 897-902, 2011.
 - [28] Zhang, M., Webb, R. L., “Correlation of two-phase friction for refrigerants in small-diameter tubes“, *Experimental Thermal and Fluid Science*, 25, pp. 131-139, 2001.
 - [29] Fang, X., Xu, Y., Su, X., Shi, R., “Pressure drop and friction factor correlations of supercritical flow“, *Nuclear Engineering and Design*, 242, pp. 323-330, 2012.
 - [30] Shah, R. K., Sekulić, D. P., *Fundamentals of Heat Exchanger Design*, Hoboken, New Jersey, USA, John Wiley & Sons, 2003.

An experimental study on the effect of the heat and mass transfer characteristic lengths on the adsorption dynamics in two different open-structured plate heat exchangers

Makram Mikhaeil¹, Matthias Gaderer² and Belal Dawoud^{1*}

¹ Laboratory of Sorption Processes, OTH Regensburg, Galgenbergstraße 30, 93053 Regensburg, Germany, +49 941/943-7124

¹ Laboratory of Sorption Processes, OTH Regensburg, Galgenbergstraße 30, 93053 Regensburg, Germany, +49 941/943-9298

² TUM Campus Straubing for Biotechnology and Sustainability, Chair Regenerative Energy Systems, Technical University of Munich, Schulgasse 16, 94315 Straubing, Germany, +49 9421/187-100

*Corresponding author: belal.dawoud@oth-regensburg.de

Abstract

This study aims at investigating the effect of the adsorbent domain dimensions or the heat and mass transfer characteristic lengths on the adsorption dynamics in two different open-structured adsorber plate heat exchangers (APHE). To this aim, three test frames have been prepared to allow performing the adsorption kinetic tests according to the large-temperature-jump methodology in a constant volume kinetic setup on loose grains of Siogel (0.71-1.0 mm) under different operating conditions. The first test frame (TF1) corresponds to the newly introduced APHE [1, 2], while the third (TF3) follows the design of a commercially available PHE (GLXN30 [3]). TF2 has been prepared with the same heat transfer characteristic length (HTCL) of TF1 and the mass transfer characteristic length (MTCL) of TF3 as a variety of each PHE. All obtained adsorption kinetic curves could be described very well with one time constant for each tested boundary condition and frame. Increasing the HTCL from 1.5 to 3mm at a MTCL of 58.5 mm (TF2 to TF3) resulted in a slight increase in the characteristic time to reach 80% of the equilibrium water uptake ($\tau_{80\%}$) of 3.8 to 26% at the tested boundary conditions. This small effect implies that such a MTCL is quite high, so that the mass transfer resistance becomes more dominant than the heat transfer resistance. At the same HTCL of 1.5 mm, increasing the MTCL from 27 mm (TF1) to 58.5 mm (TF2) results in much slower adsorption kinetics (increase in $\tau_{80\%}$ with a factor of 1.75 and 2.56 at the operating conditions 5/35/90 and 15/30/90 °C, respectively). The obtained results indicate the importance of considering the MTCL beside the HTCL upon designing an adsorber heat exchanger. A new methodology to compare the adsorption kinetic data for different operating conditions and, correspondingly, different equilibrium differential water uptakes is introduced based on the obtainable, time-averaged instantaneous evaporator power. The newly introduced APHE [1, 2] offers up to 2.8 times higher evaporator power if compared to the GLXN30 [3].

Keywords: Siogel, Adsorber, Plate heat exchanger, Adsorption kinetics, heat transfer characteristic length, mass transfer characteristic length

1. Introduction

According to the international energy agency, the global air conditioning demand (space cooling and heating) is expected to grow very fast over the next 30 years and contribute by 49.4% in the global electricity demand [4]. This can be avoided if the market of chillers and heat pumps is released from the domination of the electric driven machines, i.e. the traditional vapour compression systems. Therefore, non-electric, environment friendly, efficient, non-expensive and durable cooling and heating machines are crucially required in the next decades. The application of the adsorption chillers and heat pumps seem highly promising to enable sustainable cooling and heating, as the driving energy is low-grade heat [5, 6], which is abundantly available from solar and waste heat sources. In addition, the adsorption systems enable the use of water as refrigerant, which is natural, safe and has neither a global warming potential (GWP) nor an ozone depletion potential (ODP). However, thermally driven adsorption chillers (TDAd-C) and heat pumps (TDAd-HP) are still, by far, less efficient and more expensive than traditional vapour compression systems. Nevertheless, there is a wide margin for improving their performance and reliability.

In the literature, there are many attempts to raise the performance of thermally driven adsorption (TDAd) systems to make them competitive to the vapour compression systems. The research in the field of the TDAd systems can be categorized into three main areas. The first is the area of developing novel adsorbents, such as the new family of adsorbents called selective water sorbents (SWS) [7,8] and the metal organic frameworks (MOFs) [9,10,11,12]. Different adsorbent families suitable for the application in the adsorption heat pumps, chillers and thermal storage systems are listed and compared in [13,14,15]. The second research area is the design improvement of the system components, such as developing heat exchangers to act as adsorber/desorber [16,17] or as evaporator/condenser [18] for the application in the adsorption heat transformation systems. The last research area concerns the system management, such as the adsorption cycle time and the time allocation of the adsorption and desorption phases [19]. The heat and mass recovery [20], which aims at enhancing the system coefficient of performance (COP), belongs to this area of research. Aside from the applied working pair and the system management, the efficiency of each system component affects the whole adsorption system performance. However, the adsorber heat exchanger (Ad-HEX) is the most decisive component and its development and investigation dominates the research activities. In the literature, the application of finned-circular and finned-flat tube heat exchangers attracts the highest interest. Comparisons between several Ad-HEXs with different designs have been reported in [21, 22]. The authors concluded that the finned-circular and finned-flat tube Ad-HEX provide the best performance in comparison with other adsorber designs. Indeed, at the first thought, the application of finned-circular and -flat tube HEXs seems to be the best choice, thanks to their wide availability and large heat transfer surface area. However, when the sustainability is taken into consideration, they could suffer from high heat transfer resistance at the interface between the root of the extended surfaces (fins) and the main tube surface [23]. As the fins are normally made of aluminium or copper and the tubes of copper or stainless steel, corrosion does take place with all known refrigerants for TDAd systems; namely water, ammonia, methanol or ethanol [24]. In case of applying a composite sorbent including a corrosive salt like CaCl_2 , LiBr or LiCl , the corrosion becomes even more pronounced [25, 26]. Also if the finned circular-tube or flat-tube heat exchangers are made of a highly resistive material such as stainless steel, the poor thermal contact at the interface between the fins root and the main tube surface can only be avoided if the fins are perfectly brazed to the tubes, which implies an additional corrosion potential. Bahrehmand [17] proposed an optimized adsorber HEX prototype, which has been fabricated by completely machining a finned plate adsorber HEX with a fin thickness of 1 mm out of an aluminium block. As this production

methodology is too expensive for a market product, more developments are needed to approach the performance of the optimized HEX by an affordable and sustainable design. In [16,17] an analysis of variance (ANOVA) has been conducted for evaluating the weightiness of each design and operating parameter, upon applying finned circular-tube heat exchanger to act as an adsorber in sorption cooling system (SCS). It was illustrated that, the contribution of the fin thickness to the COP of the SCS amounts to 48.67 % in case of constructing the Ad-HEX from copper and applying silica gel-water as a working pair [16], which is reduced to 29% as reported in [17], upon constructing the Ad-HEX from aluminium and applying the composite adsorbent (CaCl₂ in silica gel). In addition, the contribution of the fin thickness to the COP of the SCS, upon applying aluminium finned-plate Ad-HEX, has been reported in [17] to be 33%. Abd-Elhady et al, [27] investigated numerically the effect of the fin design parameters on the performance of a two-bed SCS and reported a reduction in the COP by 9.4% upon increasing the fin thickness of a finned-circular tube Ad-HEX from 0.2 mm to 0.4 mm.

The application of an embossed plate heat exchanger, made of copper to act as adsorber heat exchanger has been suggested for the first time by Hong et al [28]. They conducted a numerical parametric study with the application of the SWS-1L and water as adsorbent-adsorbate pair. The optimal value of the COP and the specific cooling power (SCP) reported in [28] at operating conditions of 15 °C evaporator temperature, 30°C condenser temperature and 80°C desorption temperature are 0.5118 and 662.8 W kg⁻¹, respectively. However, the authors in [28] did not discuss the manufacturability of their suggested embossed plate heat exchanger and did not care about the high corrosion potential, which their PHE could face if it is actually made of copper and some salt may leak out of the SWS-1L [29].

Indeed, an adsorption process is a combined heat and mass transfer process, which takes place inside the adsorbent bed of an adsorber heat exchanger. Accordingly, the length of the heat transfer path (termed afterwards as the heat transfer characteristic length HTCL) together with length of the refrigerant vapour diffusion path (termed afterwards as the mass transfer characteristic length MTCL) inside the adsorbent bed are the most decisive parameters influencing the dynamic performance of an adsorber heat exchanger. In the literature, there exist many attempts to theoretically optimize the design of circular finned-tube adsorber heat exchangers in terms of fin pitch and fin height [30,31], which are indicators for both HTCL and MTCL, respectively. However, few studies addressed the optimization experimentally. Kubota et al, [32] presented the improvement in the SCP and the COP values of a finned-tube adsorber heat exchanger, introduced in [33], after utilizing a numerical simulation model for optimizing the HEX design [34]. They reported in [32] that the optimized HEX (having a fin-pitch of 2.32 mm) can achieve more than twice higher cooling output per unit adsorber volume than the un-optimized one (having a fin-pitch of 5 mm) [33]. In [35, 36], the effect of varying the thickness of adsorbent sample of AQSOA-Z02 grains in different size ranges on the adsorption dynamics has been investigated. The ratio of the heat transfer surface area to the adsorbent dry mass (S/m) is introduced as a design parameter. The influence of S/m ratio on the specific cooling power SCP for different adsorbent grain sizes has been carefully studied. For one adsorbent, the S/m ratio is, indeed, inversely proportional to adsorbent thickness or the HTCL of the adsorbent bed. It was concluded in [35] that, for the grain size range of 0.2-0.9 mm, the average SCP of the adsorption chiller is linearly proportional to the ratio S/m of the Ad-HEX.

Aristov et al. [37] investigated the influence of the ratio (S/m) on the adsorption dynamics of small-scale adsorbent samples of loose grains. They compared the adsorption dynamics of the small-scale adsorbent samples with representative pieces of different Ad-HEXs, which have the same ratio (S/m). It has been concluded that the measured adsorption dynamics of the representative pieces of Ad-HEXs were 2-6 times lower than the adsorption dynamics of the

small-scale samples. Dawoud [38] investigated the adsorption kinetics of water vapour on small-scale AQSOA-Z02 coated samples and compared them to the adsorption kinetics of two different full-scale coated adsorber heat exchangers with the same adsorbent material at similar operating conditions. The thickness of the tested consolidated adsorbent layers was in the range of 150 to 500 μm . The experimental results discussed in [38] indicated that in general, increasing the adsorbent layer thickness leads to lower adsorption kinetics, however the small-scale samples demonstrated at least twice higher adsorption kinetics than those of the full-scale coated adsorber heat exchangers.

Dawoud [1] introduced a nickel brazed plate heat exchanger composed of stainless steel thin sheets (0.3 mm in thickness), to be highly resistive against any potential corrosion, and designed dedicatedly to act as an adsorber heat exchanger. Mikhaeil et al. [2] have carried out experimental and numerical investigations on the introduced PHE [1] and reported that, the introduced PHE outperformed a coated aluminium finned flat-tube adsorber HEX as well as an extruded aluminium adsorber heat exchanger [38]. Strictly speaking, an enhancement of 310% in the differential water uptake obtained after 300 s of adsorption start has been measured and simulated compared to [38]. The extremely reduced volume of the HTF domain compared to the adsorbent domain, while keeping the uniformity of the temperature distribution over the heat exchanger's plates are the key design advantages of the introduced APHE [1, 2], which explain its superior performance.

Although several studies addressed the influence of adsorbent bed thickness on the adsorption and desorption dynamics using small-scale adsorbent samples of loose grains or consolidated layers, no study so far has treated the influence of the length of the refrigerant vapour diffusion path (MTCL) on the adsorption dynamics. This is definitely the case if plate heat exchangers shall be designed and optimized for adsorption heat transformation processes. Recalling that the adsorption process is a combined heat and mass transfer process, the necessity for a comparative study on the influence of both HTCL and MTCL on the adsorption dynamics becomes obvious.

This work introduces, therefore, an experimental study on the effect of the adsorbent domain dimensions on the adsorption dynamics of representative samples of the adsorbent domains of two different, open-structured and asymmetric adsorber plate heat exchangers (APHE). To this aim, dedicated small-scale test frames have been constructed and tested with loose grains of the silica gel Siogel® of Oker Chemie, Germany in the range of 0.71 to 1.0 mm in a volumetric large temperature jump kinetic setup under different operating conditions of adsorption heat transformation processes.

2. The investigated PHEs and their representative test frames

The GLXN30 PHE is the only, nickel-brazed, stainless steel, open-structured PHE available in the market from Alfa Laval©, Sweden [3]. This very special PHE has been constructed as a cross-flow, gas-liquid plate heat exchanger with embossed plates. The open gas domain can be filled in with loose grains of the adsorbent. Using a suitable stainless steel sieve on each side, the GLXN30 PHE can act as an adsorber heat exchanger. The investigation results of this specific heat exchanger as an adsorber-desorber for different intermittent heat transformation processes is under preparation for publication by the authors of this work. In this work, the GLXN30 PHE shall be investigated concerning the influence of its heat and mass transfer characteristic lengths of the adsorbent domain (gas domain) compared to the newly introduced adsorber PHE in [1,2] on the adsorption dynamics of water vapour in loose grains of Siogel® of Oker Chemie, Germany. Figure 1 presents photos of the newly developed adsorber Plate heat exchanger [1, 2] and the GLXN30 PHE of Alfa Laval© [3].

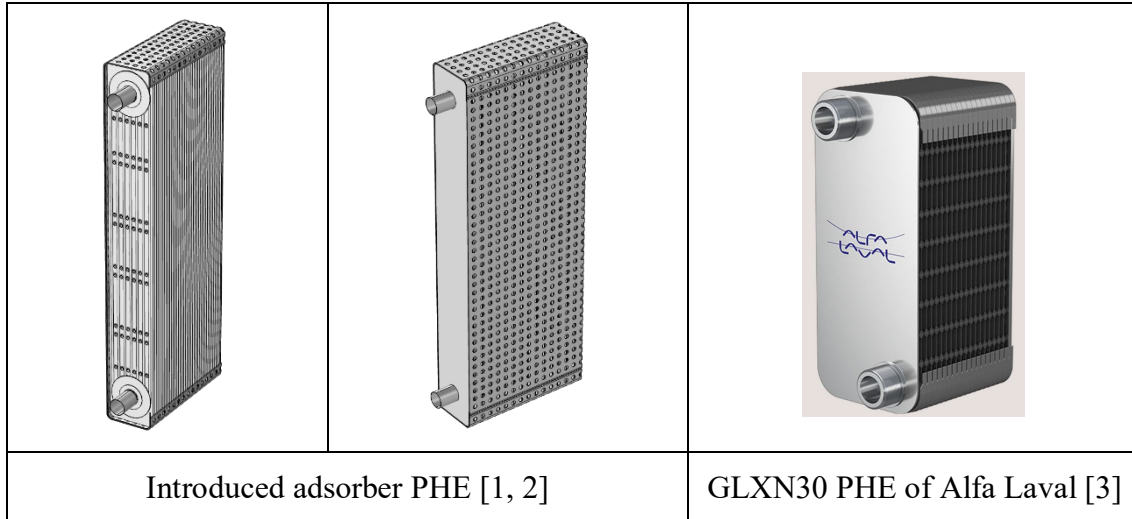


Figure 1: Newly introduced adsorber plate heat exchanger [1, 2] and the GLXN30 PHE [3]

Each PHE comprises a stack of multi, nickel-brazed parallel plate-pairs made of stainless steel 316L, which results in two asymmetric domains, one for the heat transfer fluid (HTF) and the other for the adsorbent loose grains. The thickness of the adsorbent domain equals the space (gap), which exists between each two successive plate-pairs forming the surrounding HTF domains. The thickness of the adsorbent domain of the adsorber PHE [1, 2] amount to 3 mm, while that of the GLXN30 to 6 mm. Table 1 illustrates more specifications for both PHEs.

Table 1: specifications of the two investigated open-structured PHEs

Specification	Introduced APHE in [1, 2]	GLXN30 PHE of Alfa Laval [3]
HTF's inlet and outlet ports diameter (mm)	16	30
Thickness of one plate (mm)	0.3	0.35
gap between each two successive plate pairs (mm)	3	6
Width of the PHE (mm)	54	117
Volume of the adsorbent domain (L)	1.1	1.09
Volume of the HTF domain (L)	0.346	0.57

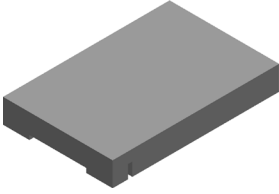
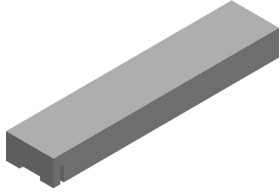
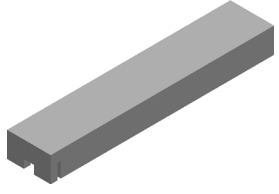
As each adsorbent domain is surrounded by two HTF domains, a symmetrical plane for the heat transfer shall exist in the middle of the thickness of the adsorbent domain, so that the HTCL must equal to half of the gap between each two successive plate pairs. This means that the HTCLs of the newly introduced adsorber PHE [1, 2] and the GLXN30 shall amount to 1.5 and 3.0 mm, respectively.

Recalling that each of the investigated PHEs is open-structured for a gas or vapour flow, the adsorbent domain shall be accessed from both sides by the refrigerant vapour. This implies that the mass transfer shall have a symmetrical plane in the middle width of each PHE. Accordingly, the MTCL of the newly introduced adsorber PHE and the GLXN30 amount to 27 and 58.5 mm, respectively.

In order to guarantee quasi-isobaric adsorption processes in the volumetric LTJ setup [38, 39], the dry sample mass of Siogel shall be limited to 320 mg. Accounting for the density of the investigated Siogel grains, the volume of each test frame shall equal to 526.5 mm³. The width of each adsorbent domain inside the test frames (TF1 and TF3) is estimated to be 13 and 3 mm, respectively as given in Table 2. TF2 has been prepared with the same HTCL of TF1 but with an identical MTCL of TF3 to offer the possibility of comparing the effect of two different

MTCLs at one HTCL and vice-versa on the adsorption kinetics. All test frames have been made of PEEK. The adsorbent sample is closed by a stainless steel sieve to keep the tested adsorbent grains inside each test frame and to allow for the vapour exchange with the adsorbent sample to take place in an identical way to the vapour exchange with each complete PHE. More details on the test frames and the kinetic measurements can be read in [2].

Table 2: Fabricated test frames to investigate the adsorption kinetics of both open-structured PHE in a constant volume, large-temperature-jump kinetic setup (bold: MTCL, underlined: HTCL)

		
27 mm x <u>1.5 mm</u> x 13 mm	58.5 mm x <u>1.5 mm</u> x 6 mm	58.5 mm x <u>3 mm</u> x 3 mm
TF1 [1, 2]	TF2	TF3 [3]

3. Results

The adsorption kinetic tests for identical adsorbent samples (320 mg of loose grains of silica gel Siogel of Oker Chemie, Germany, in the size range between 0.71 and 1.0 mm) have been carried out inside the three representative test frames TF1-TF3. The tested boundary conditions are: evaporator temperatures 5, 10 & 15 °C, adsorber-end and condenser temperatures of 30 and 35 °C, while the desorption-end temperature has been fixed to 90 °C. The measured data has been utilized to investigate the effects of the HTCL and the MTCL on the adsorption kinetics. In addition, the average evaporator power obtained during the adsorption stage upon applying both APHEs illustrated in Figure 1 to act as an adsorber for an adsorption chiller has been estimated and presented for all investigated operating conditions.

3.1. Criteria for evaluating the adsorption kinetic performance

Figure 2 depicts the measured adsorption kinetic data and the exponential fitting curves of the adsorption kinetics of the adsorbent Siogel inside the three test frames TF1-TF3 illustrated in Table 2 at all applied operating conditions. The exponential behaviour of every adsorption kinetic curve is described by

$$w(t) = w_o + \Delta w_f (1 - \exp(-t/\tau)) \quad (1)$$

where $w(t)$ is the instantaneous water uptake in the sample, w_o refers to the initial water uptake in the sample, Δw_f to the final or equilibrium differential water uptake, and τ is the characteristic time constant. The detail results of the measuring campaign and the values of the time constants (τ) and the coefficient of determination (R^2) are presented in Table 3. The lowest R^2 value amounts to 0.9890 and is obtained for TF3 at operating conditions of 15/30/90°C. It can be concluded that, all adsorption kinetic curves for the Siogel sample inside all three test frames do follow the exponential relationship described in equation (1). Because of the excessive slowing down of the kinetic curves upon approaching the final uptake [39], it has been recommended to consider the duration of the isobaric adsorption stage to reach 80% of the final differential water uptake ($\tau_{80\%}$) as the upper limit for the adsorption phase time [38]. This makes a good compromise between the COP, which tends to increase by increasing the cycle time and the specific power SP, which increases by decreasing the cycle time of an

adsorption heat transformation unit. The time ($\tau_{80\%}$) for each boundary condition and TF is, therefore, evaluated and given in Table 3.

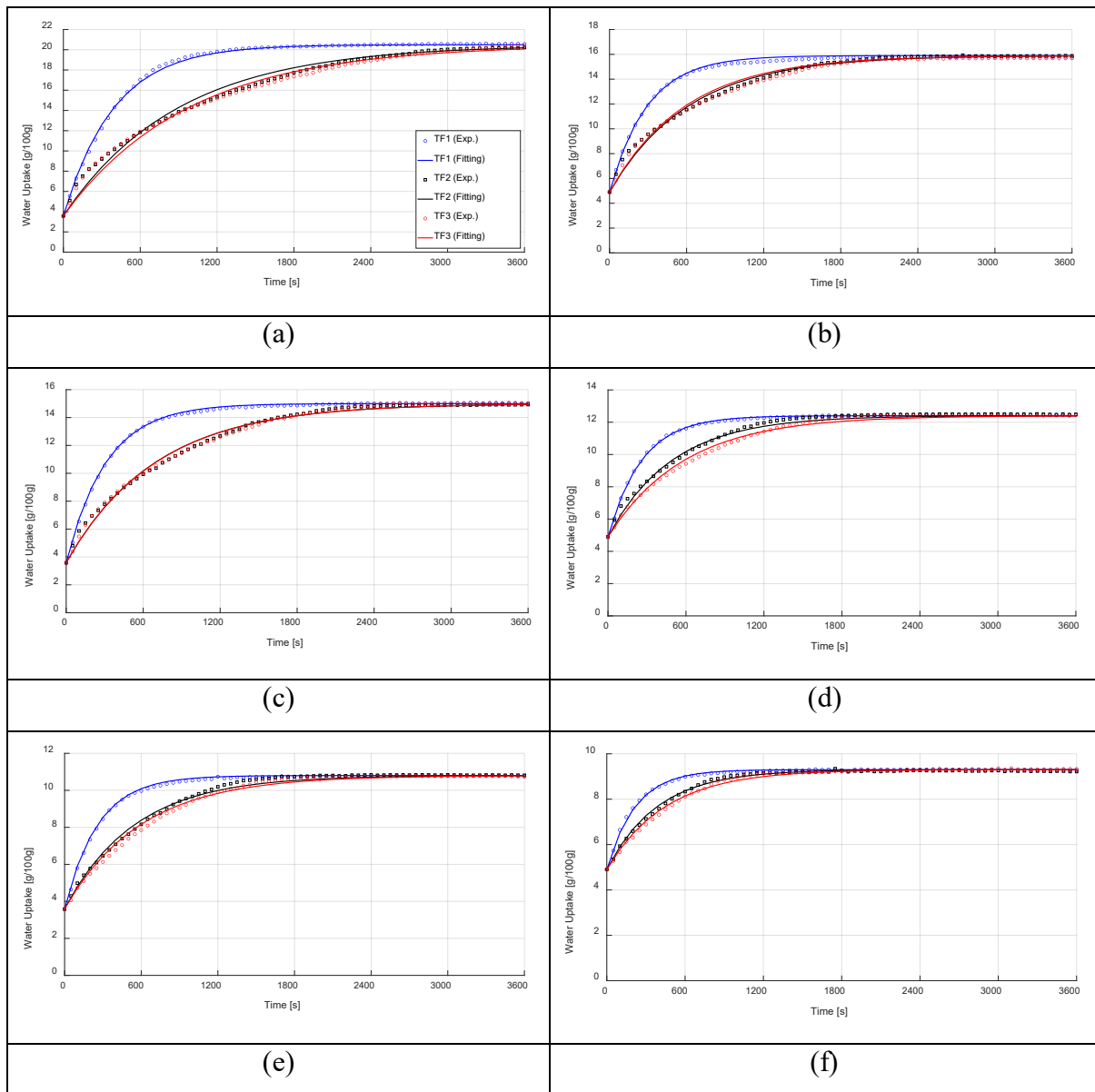


Figure 2: Adsorption kinetic curves for loose grains of Siogel inside the three test frames depicted in Table 2 at evaporator, condenser/adsorption-end and desorption temperatures of a) 15/30/90 °C , b) 15/35/90, c) 10/30/90, d)10/35/90, e) 5/30/90 and f) 5/35/90

3.2. Effect of the HTCL between TF2 and TF3

Enhancing the thickness of the adsorbent domain (HTCL) from 1.5 to 3.0 mm (TF2 and TF3) while keeping the MTCL equal to 58.5 mm corresponding to the GLXN30 PHE, results in enhancing the value of $\tau_{80\%}$ by 3.8% at the operating condition of 15/35/90 °C to a maximum percentage of 26% at operating conditions of 5/35/90°C. This implies that the effect of doubling the HTCL of the adsorbent domain on the adsorption dynamics is quite low as long as the MTCL is in the order of 58.5 mm. In other words, at such high MTCL, the influence of the HTCL is less pronounced on the upper limit of the adsorption phase time $\tau_{80\%}$. The same is valid if the adsorption characteristic time (τ) is considered.

It can be further observed that, the effect of doubling the HTCL between TF2 and TF3 on enhancing the adsorption characteristic times becomes more pronounced at severer operating conditions, at which the differential water uptake becomes smaller (low evaporator temperatures and/or higher condenser and adsorber-end temperatures).

Table 3: Adsorption start temperature ($T_{ads-start}$), initial water uptake (w_o), final differential water uptake (Δw_{final}), time to reach 80 % of Δw_{final} ($\tau_{80\%}$), the ratios of $\tau_{80\%}$ (r_{2-1} , r_{3-2} and r_{3-1}), the time constant of the exponential fitting (τ) and its (R^2) at each operating condition for the three tested frames

Operating Condition $T_{ev}/T_{cond}/T_{des}$ [°C]	$T_{ads-start}$ [°C]	w_o [g/100g]	Δw_{final} [g/100g]	TF	$\tau_{80\%}$ [s]	r_{2-1}	r_{3-2}	r_{3-1}	τ [s]	R^2
						$= \frac{\tau_{80\%TF2}}{\tau_{80\%TF1}}$	$= \frac{\tau_{80\%TF3}}{\tau_{80\%TF2}}$	$= \frac{\tau_{80\%TF3}}{\tau_{80\%TF1}}$		
15/30/90	70.5	3.6	16.9	1	612	2.56	1.10	2.81	394.6	0.9984
				2	1567				898.3	0.9894
				3	1725				975.6	0.9890
15/35/90	62.4	4.9	11.0	1	457	2.27	1.038	2.36	292	0.9982
				2	1040				614.7	0.9905
				3	1080				591.3	0.9894
10/30/90	66.1	3.6	11.4	1	486	2.44	1.023	2.49	310.5	0.9968
				2	1187				698.5	0.9936
				3	1214				700	0.9923
10/35/90	58.7	4.9	7.5	1	402	2.05	1.21	2.48	257.2	0.9957
				2	824				492.1	0.9945
				3	1000				586.1	0.9913
5/30/90	58.5	3.6	7.2	1	410	2.10	1.112	2.34	258.7	0.9927
				2	863				548.8	0.9931
				3	960				595.7	0.9906
5/35/90	53.2	4.9	4.4	1	326	1.75	1.26	2.21	218	0.9960
				2	572				387.3	0.9944
				3	721				449.3	0.9937

3.3. Effect of the MTCL between TF1 and TF2

Indeed, both TF1 and TF2 have the same HTCL (1.5 mm) and, accordingly, the same S/m ratio. According to the existing experiences in the literature [35, 36,37], they should have the same kinetic performance. The obtained results in Figure 2 puts in evidence that the MTCL does have a major role on the adsorption kinetics for the same HTCL or S/m ratio. Strictly speaking, the adsorption kinetics of the adsorbent samples inside TF2 are much slower than those inside TF1 (175 to 256 % more time is needed to reach 80% of the equilibrium differential water uptake inside TF2 if compared to time needed for TF1). In addition, the ratio of $\tau_{80\%}$ (r_{2-1} in Table 3) decreases if the overall mass transfer (the differential water uptake) is reduced. Reducing the evaporator temperature from 15 down to 10 and 5 °C at 30 °C adsorption-end and condenser temperature results in reducing the differential water uptake from 16.5 down to 11.4 and 7.2 g/100g, which is associated with decreasing r_{2-1} from 2.56 down to 2.44 and 2.10, respectively. The same is valid and more pronounced at the more severe operating condition of 35°C for the adsorption-end and condenser temperatures.

The comparison between the adsorption kinetics of the same adsorbent inside TF1 and TF3 (the ratio r_{3-1} of their $\tau_{80\%}$ in Table 3), reveals that the performance of commercially available heat exchangers (GLXN30) is quite poor if compared with dedicatedly designed heat exchangers [1, 2]. It can be concluded, therefore, that the MTCL and the mass transfer resistance inside the adsorption domain much be taken into account together with the HTCL or the S/m ratio, for designing effective adsorber heat exchangers.

3.3. Estimation of the average evaporator cooling power

So far, the comparison of different adsorption kinetic measurements at different operating conditions have been assessed by comparing the time needed for reaching 80% of the final differential water uptake (Δw_{final} in Table 3). As depicted in Figure 2, both starting and final uptakes do change and, consequently, does the differential water uptake from one operating condition to the other, as illustrated in Table 3. Accordingly, the time to reach 80% of such a variable differential water uptake may not be the most suitable performance indicator. In order to account for the different differential water uptakes and the different time requirements at the investigated operating conditions, we introduce a new performance indicator according to equation (2); namely the moving-averaged or the time-averaged instantaneous specific evaporator power $\bar{q}_{ev}(t)$.

$$\bar{q}_{ev}(t) = \frac{w(t) - w_o}{t} \cdot h_{fg}(T_{ev}) \quad (2)$$

Here $h_{fg}(T_{ev})$ is the latent heat of the water evaporation at the investigated evaporator temperature (T_{ev}).

Figure 3 illustrates exemplarily the $\bar{q}_{ev}(t)$ estimated from the adsorption kinetic results, which discussed previously, at the operating conditions of 15/30/90°C. Because of the high kinetics of adsorption at the beginning of the processes, the $\bar{q}_{ev}(t)$ increases sharply and reaches to maximum value in just some seconds and afterwards starts to drop with a slowing rate.

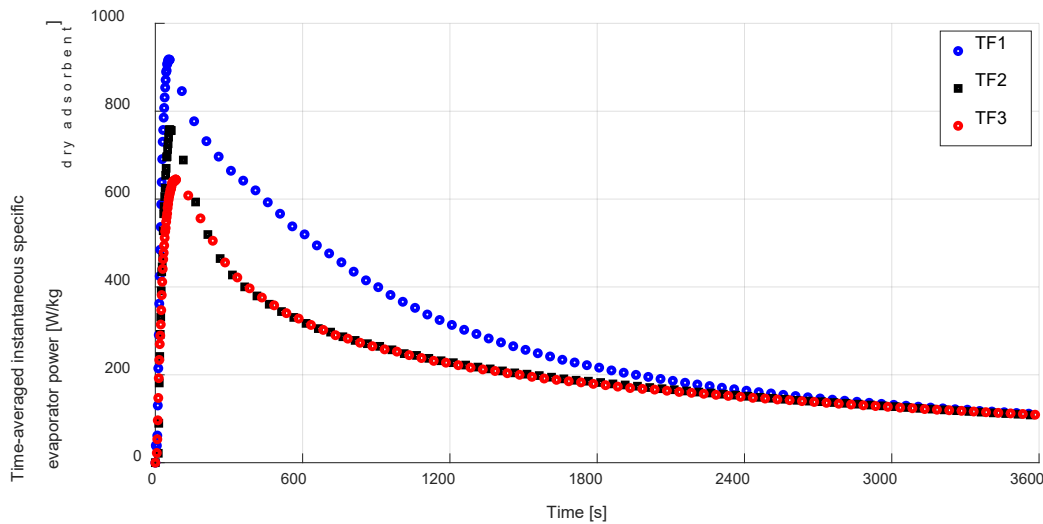


Figure 3: Time-averaged instantaneous specific evaporator power estimated from the kinetic results of the three test frames depicted in Table 2 at the operating conditions of 15/30/90 °C

For instance, at 15/30/90°C, the $\bar{q}_{ev}(t)$ expected from an adsorber heat exchanger according to TF1 reaches 917.4 W/kg_{dry adsorbent} in the first 59 s, then decreases reaches to 517.7 W/kg_{dry}

adsorbent at the characteristic time $\tau_{80\%}$ (612 s). At the same operating condition, i.e. 15/30/90°C, the $\bar{q}_{ev}(t)$ of TF2 reaches to 761.6 W/kg_{dry adsorbent} (16.9% less than that of TF1) in the first 65 s. $\bar{q}_{ev}(t)$ of TF3 reaches 646.1 W/kg_{dry adsorbent} (29.5% less than that of TF1) in the first 85 s. Equation 2 and Figure 3 are quite helpful to obtain a more valuable evaluation of the measured kinetic data concerning the achievable evaporator power at different possible adsorption phase durations.

Figure 4 shows a comparison between time-averaged evaporator powers obtainable from the three investigated test frames in case the time $\tau_{80\%}$ of each boundary condition (as listed in Table 3) is considered for the duration of the adsorption phase. For instance, at 15/30/90°C, Δw_f amounts to 16.9 [g/100g], which is 53.6% higher than Δw_f obtained at 15/35/90°C (11.0 g/100g), however TF2 demonstrates a very close $\bar{q}_{ev}(t = \tau_{80\%})$ at both operating conditions, as $\tau_{80\%}$ at 15/30/90°C (1567 s) is 50.6% higher than that at 15/35/90°C (1044 s). The highest values of $\bar{q}_{ev}(t = \tau_{80\%})$ are obtained for TF1 at all applied operating conditions, which puts in evidence the importance of considering the MTCL together with the HTCL or the S/m ratio upon designing an effective adsorber heat exchanger.

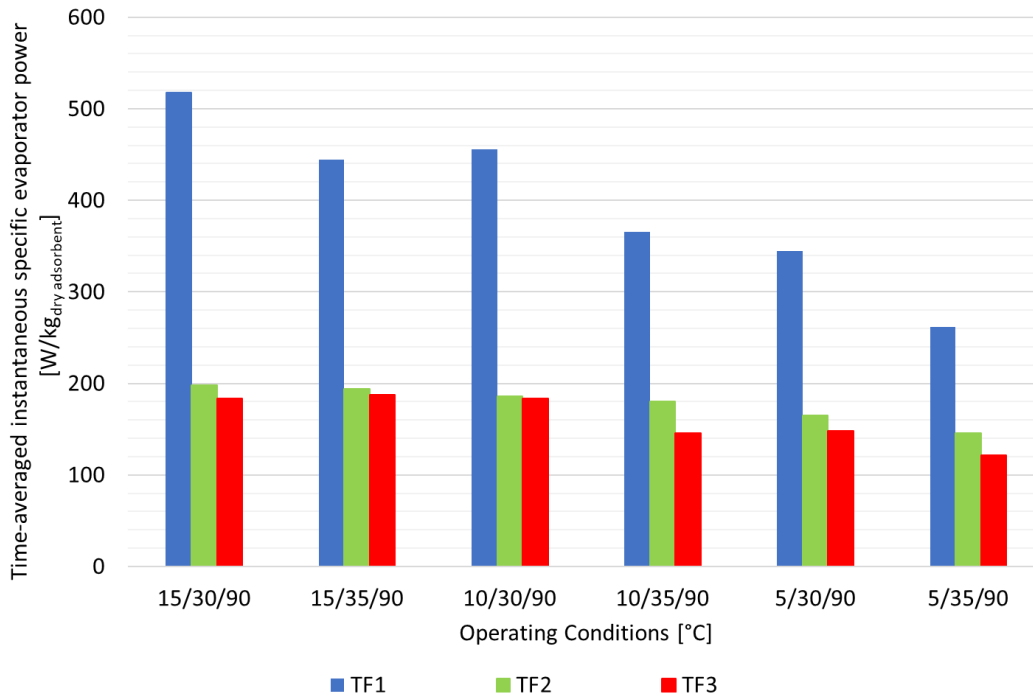


Figure 4: Time-averaged instantaneous specific evaporator powers obtainable from the three investigated test frames at an adsorption phase time equal to the corresponding time to reach 80 % of the related final differential water uptake at each operating condition

4. Conclusion

In the present paper, an experimental study has been carried out to explore the effect of the heat and mass transfer characteristic lengths on the adsorption dynamics of water vapour onto loose grains of Siogel (0.71-1.0 mm) under different operating conditions of adsorption heat transformation processes. The adsorption dynamic tests have been performed on 320 mg samples of the same adsorbent inside three different test frames (TF1-TF3) representing two open-structured plate heat exchangers (PHEs) and one common variety of each. The heat transfer characteristic length (HTCL) is defined as half the thickness of the adsorbent domain between each two successive plate pairs for the heat transfer fluid, which is inversely

proportional to the well-examined S/m ratio in former investigations. The mass transfer characteristic length (MTCL) is defined as half the width of each PHE, which corresponds to the length of the diffusion path inside the PHE until the mass transfer symmetrical plane. The adsorption kinetic measurements have been carried out at evaporation temperatures of 5, 10 and 15°C, condensation and adsorption-end temperatures of 30 and 35 °C, while the desorption end temperature has been set at 90 °C. In addition, a new methodology has been introduced to assess the obtained kinetic data in terms of the obtainable evaporator power at different durations for the adsorption-evaporation phase in a real adsorption heat transformation unit applying the investigated adsorber heat exchangers. To this aim, a new performance indicator, namely the time-averaged instantaneous specific evaporator power is introduced and the obtained results for the investigated APHEs have been compared under the tested boundary conditions. The main outcomes of the study are summarized below:

- All obtained adsorption kinetic curves could be described with one time constant for each tested boundary condition and frame with a better coefficient of determination (R^2) than 0.989.
- Doubling the half thickness of the adsorbent domain from 1.5 to 3mm at a MTCL of 58.5 mm (TF2 to TF3) resulted in a slight increase in the characteristic time ($\tau_{80\%}$) of only 3.8 to 26% at the tested boundary conditions. This small effect implies that such a MTCL is quite high, so that the mass transfer resistance becomes more dominant than the heat transfer resistance.
- At the same HTCL of 1.5 mm (means the same S/m ratio), increasing the MTCL from 27 mm (TF1) to 58.5 mm (TF2) results in much slower adsorption kinetics. The characteristic time $\tau_{80\%}$ increases by a factor of 1.75 and 2.56 at the operating conditions 5/35/90 and 15/30/90 °C, respectively. These results contradict the known results so far; namely to expect the same adsorption dynamics for samples having the same S/m ratio.
- The obtained results puts in evidence the importance of considering the MTCL beside the HTCL upon designing the adsorber heat exchangers.
- The newly introduced adsorber PHE [1, 2] offers up to 2.8 times higher evaporator power if compared with the GLXN30 [3], which is available in the market as a unique cross-flow, gas-liquid plate heat exchanger.

If remarkable achievements concerning more market penetration of sustainable adsorption heat transformation appliances are targeted, dedicatedly designed plate heat exchangers are needed. The target should be to (a) increase the degree of asymmetry between the adsorbent and the HTF domains and (b) to shorten the mass diffusion path length (MTCL) within the adsorbent domain, while keeping the HTCL under 3 mm.

Acknowledgements

This project has received funding from the European Union's Horizon 2020 research and innovation programme under grant agreement No 764025.

References

- [1] B. Dawoud, "European Patent Application, EP 3 382 313 A1," 03.10.2018.
- [2] M. Mikhaeil, M. Gaderer, B. Dawoud, "On the development of an innovative adsorber plate heat exchanger for adsorption heat transformation processes; an experimental and numerical study." *Energy* 207 (2020): 118272.

- [3] „https://www.alfalaval.com/globalassets/documents/products/heat-transfer/plate-heat-exchangers/gas-to-liquid-plate-heat-exchangers/glx/glxn30_product-leaflet_en.pdf“.
- [4] M. Armstrong, “Air Conditioning Biggest Factor in Growing Electricity Demand [Digital image],” pp. <https://www.statista.com/chart/14401/growing-demand-for-air-conditioning-and-energy/>, (August 27, 2020).
- [5] L. W. Wang, R. Z. Wang, J. Y. Wu, X.Y. Xu, S. G. Wang, "Design, simulation and performance of a waste heat driven adsorption ice maker for fishing boat." *Energy* 31.2-3 (2006): 244-259.
- [6] T. Miyazaki, A. Akisawa, "The influence of heat exchanger parameters on the optimum cycle time of adsorption chillers." *Applied thermal engineering* 29.13 (2009): 2708-2717.
- [7] Y. I. Aristov, M. M. Tokarev, G. Cacciola, G. Restuccia, "Selective water sorbents for multiple applications, 1. CaCl₂ confined in mesopores of silica gel: sorption properties." *Reaction Kinetics and Catalysis Letters* 59.2 (1996): 325-333.
- [8] Y. I. Aristov, G. Restuccia, G. Cacciola, V. N. Parmon, "A family of new working materials for solid sorption air conditioning systems." *Applied thermal engineering* 22.2 (2002): 191-204.
- [9] F. Jeremias, A. Khutia, S. K. Henninger, C. Janiak, "MIL-100 (Al, Fe) as water adsorbents for heat transformation purposes—a promising application." *Journal of Materials Chemistry* 22.20 (2012): 10148-10151.
- [10] H. C. Zhou, J. R. Long, O. M. Yaghi, "Introduction to metal–organic frameworks." *Chemical reviews* 112.2 (2012): 673-674.
- [11] B. B. Saha, I. I. El-Sharkawy, T. Miyazaki, S. Koyama, S. K. Henninger, A. Herbst, C. Janiak, "Ethanol adsorption onto metal organic framework: theory and experiments." *Energy* 79 (2015): 363-370.
- [12] M. F. De Lange, B. L. Van Velzen, C. P. Ottevanger, K. J. Verouden, L. C. Lin, T. J. Vlugt, J. Gascon, F. Kapteijn, "Metal–organic frameworks in adsorption-driven heat pumps: the potential of alcohols as working fluids." *Langmuir* 31.46 (2015): 12783-12796.
- [13] Y. I. Aristov, "Challenging offers of material science for adsorption heat transformation: a review." *Applied Thermal Engineering* 50.2 (2013): 1610-1618.
- [14] L.F. Cabeza, A. Solé, C. Barreneche, "Review on sorption materials and technologies for heat pumps and thermal energy storage." *Renewable Energy* 110 (2017): 3-39
- [15] L. G. Gordeeva, Y. I. Aristov, "Adsorptive heat storage and amplification: New cycles and adsorbents." *Energy* 167 (2019): 440-453.
- [16] S. W. Hong, S. H. Ahn, O. K. Kwon, J. D. Chung, "Optimization of a fin-tube type adsorption chiller by design of experiment." *International Journal of Refrigeration* 49 (2015): 49-56.
- [17] H. Bahrehmand, M. Bahrami, "Optimized sorber bed heat and mass exchangers for sorption cooling systems." *Applied Thermal Engineering* 185 (2021): 116348.
- [18] G. B. Abadi, M. Bahrami, "Combined evaporator and condenser for sorption cooling systems: a steady-state performance analysis." *Energy* 209 (2020): 118504.
- [19] A. Sapienza, S. Santamaria, A. Frazzica, A. Freni, "Influence of the management strategy and operating conditions on the performance of an adsorption chiller." *Energy* 36.9 (2011): 5532-5538.

- [20] T. X. Li, R. Z. Wang, L. W. Wang, Z. S. Lu, C. J. Chen, "Performance study of a high efficient multifunction heat pipe type adsorption ice making system with novel mass and heat recovery processes." *International Journal of Thermal Sciences* 46.12 (2007): 1267-1274.
- [21] A. Sharafian, M. Bahrami, "Assessment of adsorber bed designs in waste-heat driven adsorption cooling systems for vehicle air conditioning and refrigeration." *Renewable and Sustainable Energy Reviews* 30 (2014): 440-451.
- [22] Z. Rogala, "Adsorption chiller using flat-tube adsorbers—Performance assessment and optimization." *Applied Thermal Engineering* 121 (2017): 431-442
- [23] S. D. Waszkiewicz, M. J. Tierney, H. S. Scott. "Development of coated, annular fins for adsorption chillers." *Applied Thermal Engineering* 29.11-12 (2009): 2222-2227.
- [24] L. Gordeeva, A. Frazzica, A. Sapienza, Y. Aristov, A. Freni, "Adsorption cooling utilizing the "LiBr/silica–ethanol" working pair: Dynamic optimization of the adsorber/heat exchanger unit." *Energy* 75 (2014): 390-399.
- [25] Y. I. Aristov, M. M. Tokarev, G. Cacciola, G. Restuccia, "Selective water sorbents for multiple applications, 1. CaCl₂ confined in mesopores of silica gel: sorption properties." *Reaction Kinetics and Catalysis Letters* 59.2 (1996): 325-333.
- [26] G. Restuccia, A. Freni, S. Vasta, Y. Aristov, "Selective water sorbent for solid sorption chiller: experimental results and modelling." *International Journal of Refrigeration* 27.3 (2004): 284-293.
- [27] M. M. Abd-Elhady, A. M. Hamed, "Effect of fin design parameters on the performance of a two-bed adsorption chiller." *International Journal of Refrigeration* 113 (2020): 164-173.
- [28] S. W. Hong, O. K. Kwon, J. D. Chung. "Application of an embossed plate heat exchanger to adsorption chiller." *International Journal of refrigeration* 65 (2016): 142-153.
- [29] A. Sharafian, S. M. N. Mehr, P. C. Thimmaiah, W. Huttema, M. Bahrami, "Effects of adsorbent mass and number of adsorber beds on the performance of a waste heat-driven adsorption cooling system for vehicle air conditioning applications." *Energy* 112 (2016): 481-493.
- [30] H. Niazmand, I. Dabzadeh. "Numerical simulation of heat and mass transfer in adsorbent beds with annular fins." *International Journal of Refrigeration* 35.3 (2012): 581-593.
- [31] A. Çağlar, "The effect of fin design parameters on the heat transfer enhancement in the adsorbent bed of a thermal wave cycle." *Applied thermal engineering* 104 (2016): 386-393
- [32] M. Kubota, T. Ueda, R. Fujisawa, J. Kobayashi, F. Watanabe, N. Kobayashi, M. Hasatani, "Cooling output performance of a prototype adsorption heat pump with fin-type silica gel tube module." *Applied Thermal Engineering* 28.2-3 (2008): 87-93.
- [33] R. Fujisawa, K. Tauchi, F. Watanabe, N. Kobayashi, M. Hasatani, "Operating properties of an adsorption heat pump driven by a fuel cell." *Kagaku Kogaku Ronbunshu* 28.3 (2002): 247-254.
- [34] J. Li, M. Kubota, F. Watanabe, N. Kobayashi, M. Hasatani, "Optimal design of a fin-type silica gel tube module in the silica gel/water adsorption heat pump." *Journal of Chemical Engineering of Japan* 37.4 (2004): 551-557.
- [35] I. S. Girmik, Y. I. Aristov. "Dynamic optimization of adsorptive chillers: The "AQSOA™-FAM-Z02–Water" working pair." *Energy* 106 (2016): 13-22.

- [36] A. Sapienza, S. Santamaria, A. Frazzica, A. Freni, Y. I. Aristov, "Dynamic study of adsorbers by a new gravimetric version of the large temperature jump method." *Applied energy* 113 (2014): 1244-1251.
- [37] Y. I. Aristov, I. S. Glaznev, I. S. Girnik, "Optimization of adsorption dynamics in adsorptive chillers: loose grains configuration." *Energy* 46.1 (2012): 484-492.
- [38] B. Dawoud, "Water vapor adsorption kinetics on small and full scale zeolite coated adsorbers; A comparison." *Applied thermal engineering* 50.2 (2013): 1645-1651
- [39] Y. I. Aristov, B. Dawoud, I. S. Glaznev, A. Elyas, "A new methodology of studying the dynamics of water sorption/desorption under real operating conditions of adsorption heat pumps: experiment." *International Journal of Heat and Mass Transfer* 51.19-20 (2008): 4966-4972.

Waste heat recovery systems with isobaric expansion technology using pure and mixed working fluids.

S. Roosjen^{1*}, M. Glushenkov², A. Kronberg² and S.R.A. Kersten¹

¹ SPT/TNW, University of Twente, PO Box 217, 7500 AE Enschede, The Netherlands

² Encontech B.V. TNW/SPT, PO box 217, 7500 AE Enschede, The Netherlands

*Corresponding author e-mail: s.roosjen@utwente.nl

Abstract

Economic expedience of waste heat recovery systems (WHRS), especially for low temperature difference applications, is often questionable due to high capital investments and long pay-back periods. By its simple design isobaric expansion (IE) engines could provide a viable pathway to utilize otherwise unprofitable waste heat streams for power generation and particularly for pumping liquids and compression of gases. Different engine configurations are presented and discussed. A new method of modelling and calculation of the IE process and efficiency is used on IE cycles with various pure and mixtures as a working fluid. Some interesting cases are presented. It is shown in this paper, that the simplest non-regenerative IE engines are efficient at low temperature differences between a heat source and heat sink. Efficiency of non-regenerative IE process with pure working fluid can be very high approaching Carnot efficiency at low pressure and heat source/heat sink temperature differences. Regeneration permits to increase efficiency of the IE-cycle to some extent. Application of mixed working fluids in combination with regeneration permits to significantly increase the range of high efficiencies to much larger temperature and pressure differences.

Keywords: isobaric expansion engines; heat driven pump; compressors; low-grade heat; mixed working fluids;

Introduction

Today the lion's share of electricity generated globally is consumed by pumps and compressors. For instance pumping systems consume around 20% of world's electricity demand [1]. Compressed air systems alone account for 10% of electricity consumed in the U.S. and European Union industry, 9.4% in China [2].

Most of the electricity production is based on big power stations using heat from the combustion of fossil fuels (such as coal and natural gas) accompanied with CO₂, NO_x and particulate emissions. Other methods (solar photovoltaics, wind, tidal, geothermal etc.) constitute a lesser part of electricity market. According to a recent evaluation, 72% of primary high-grade energy is lost after conversion. 63% of this lost energy is waste heat with temperature below 100°C [3]. In fact, the only way to convert low-grade heat to power is based on the Organic Rankine Cycle (ORC). However, the real contribution of ORC produced power to the world's electricity generating capacity is insignificant. For instance, global installed power capacity in 2016 reached 6473 GW of which 61.1% (3954GW) was based on thermal energy sources [4], whereas ORC represented only around 2.7 GW [5].

In other words, the contribution of ORC accounts for 0.04% of the global electricity generating capacity and 0.07% of the generating capacity based on thermal (heat) energy sources. Therefore, it can be said with confidence that low grade and waste heat resources in power generation remain almost untapped. Such an inconsequential contribution of ORC is caused

mostly by economic reasons. ORC-based power generation is too expensive in case of ultra-low-grade heat sources (below 100°C) and low power ranges [6],[7]. For instance, the share of units with power below 500kW does not exceed 2% of total installed ORC capacity [5] i.e. millions of small low-grade and waste heat sources remain unused.

Utilization of waste heat thus provides a possibility to increase efficiency of industrial processes and monetize an otherwise lost energy stream. Waste heat sources are plenty with EU potential estimated at 300TWh/yr. of which one third part in the low temperature range of 100-200°C [8].

Isobaric expansion engines defined in [9] are the oldest type of heat-to-mechanical power converters known. James Watt, Thomas Savery, Denis Papin and Thomas Newcomen, standing at the cradle of this invention [10],[11], set forth the fundamental principles of conversion of heat into work bringing about the industrial revolution. Later on, these machines were displaced by more efficient well-known water steam expansion machines such as piston steam engines as well as steam turbines. Due to simple design by utilization of readily available components, IE machines provide a viable pathway to utilize waste heat steams in the low temperature (difference) range.

However, as it was shown in [9], IE engines can be efficient using some working fluids in a combination with heat regeneration. It will be demonstrated that for the various types of IE-engines configurations attractive results can be obtained for low and ultra-low temperatures waste heat recovery. With a thermodynamic model and the use of the REFPROP 10 database [12], results on some single component and binary mixtures are presented, proving the benefits of mixed working fluids in IE machines on a theoretical basis. We will show that a wide temperature operating range can be achieved with binary mixed working fluids.

As a result, IE technology can be ideally fit for pumping liquids and compression of gases because they permit to use heat for the compression and pumping directly, i.e., without the intermediate step of electricity generation, transmission and further conversion back to mechanical energy typical of today's industry. IE machines can also be attractive for electricity generation in low and medium power ranges.

Worthington type isobaric expansion engines

Worthington type heat engines relate to one out of two classes of IE-machines known. Bush-type engines [13], forming the second class, perform a different working cycle. Theoretically, Bush-type engines are more efficient than Worthington ones; however, the high efficiency can only be realized if dead volume of the heat exchangers does not severely influence the engine power and efficiency [14]. On the contrary, Worthington-type engines are less sensitive in this respect and can use any off-the-shelf heat exchanger. In this publication only Worthington-type engines will be considered as they are more market ready.

The Worthington-type IE machines can literally use all types of heat exchangers, including the most economical ones (gasketed and brazed plate, pillow plate etc.). Moreover, the large internal volume can even be useful for dampening pressure pulsations. In addition, this permits Worthington engines to use multiple heat sources and heat sinks with different temperatures.

To demonstrate the wide variety of possible Worthington-type engine configurations some of them are outlined below.

System configurations

Basic principle of one out of many possible modifications of Worthington-type engines is shown in Figure 1 (left).

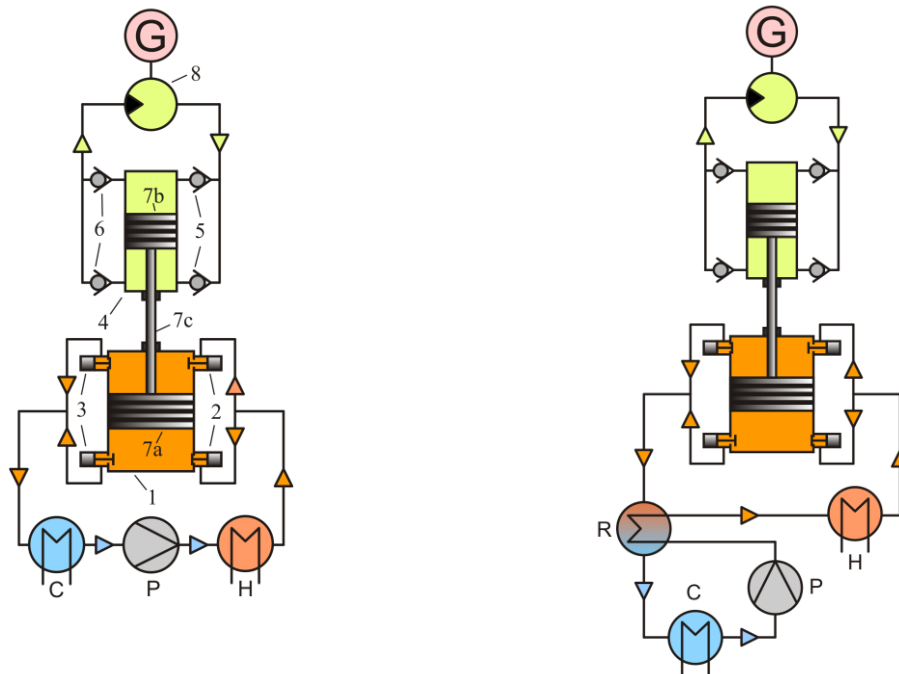


Figure 1. Simplest non-regenerative Worthington-type engine (*left*), and regenerative Worthington-type engine. (*right*)

The engine consists of a power or driving cylinder (1) with a pair of admission valves (2) and a pair of exhaust valves (3), as well as pumping cylinder (4) with a pair of suction valves (5) and a pair of discharge valves (6). The driving and pumping cylinders are equipped with driving and pumping pistons 7a and 7b respectively, rigidly connected by a rod 7c. As a result, both pistons and the rod form a so-called differential piston moving together as one unit. The engine scheme also includes a feed pump (P), heater/evaporator (H) and cooler/condenser (C). If the engine is used as a shaft power or electric generator it can be equipped with a hydraulic motor (8) and electric generator (G). In operation the feed pump (P) delivers a liquid working fluid to the heater (H) where it is heated and turned into vapor. The hot pressurized vapor of the working fluid is supplied to the upper and lower parts of the driving cylinder alternately, providing a reciprocating motion of the differential piston (7a-7b-7c). The spent working fluid exhausts through the exhaust valves (3). The working fluid does not expand in the cylinder providing a constant force for the pumping in the pumping cylinder; therefore, each admission and each exhaust valve in the opposite chamber of the driving cylinder are open during every half of the cycle. The spent working fluid exhausted from the driving cylinder goes to the cooler/condenser (C) and then returns to the feed pump (P).

The pumping cylinder operates as a typical double-acting pump with self-acting valves. At certain conditions the efficiency of the engine can be increased several times by means of heat

regeneration. The regenerative Worthington-type engine is shown in Figure 1 (right). In this case the heat of the hot fluid exhausted from the driving cylinder is used for preheating of the cold working fluid in the regenerator (R) installed upstream the heater (H). This increases efficiency by decreasing the consumption of the heat used for the working fluid heating in the heater (H). The regenerator also decreases the heat load on the cooler/condenser resulting in a smaller heat exchange area and size of the condenser.

In case of high temperature operation, excluding conventional positive seals, a seal-less design can be used. Such a single-acting machine, Figure 2, consists of a cylinder (1) with admission and exhaust valves (2) and (3), a free piston (4) and a diaphragm unit. The diaphragm unit includes two semispherical covers (5) and (6) with a diaphragm (7) clamped in between. The upper cover (6) is equipped with suction and discharge valves (8) and (9). The piston (4) here plays only a role of a heat barrier dividing the hot vapors of working fluid (shown in orange) in the lower part of the cylinder (1) and cold liquid working fluid (shown in blue) in the upper part. In fact, in this design the cold liquid working fluid acts as a driving piston. It transmits the pressure of hot working fluid through the diaphragm (7) to the liquid to be pumped (shown in yellow-green).

Apparently, if the liquid to be pumped can be used also as the driving working fluid, the diaphragm unit can be eliminated. In this case the suction and discharge valves (8) and (9) can be installed directly in the upper part of the cylinder (1). Such a pump can be used, for instance, for pumping of liquefied gases, light hydrocarbons on refineries, in chemical industry etc.

In case of pumping warm or hot liquid the cylinder with the thermal barrier piston can be eliminated at all and the diaphragm unit plays the role of the driving and pumping cylinders at the same time. Here the admission and exhaust valves related to the driving part are also installed directly in the lower cover (5) the diaphragm unit. The diaphragm IE-pump is similar to that of the piston IE-pump; however, the initial and final pressures both in the driving and pumping cylinders are equal. The main advantage of the diaphragm-based design is an almost frictionless and leak-free operation.

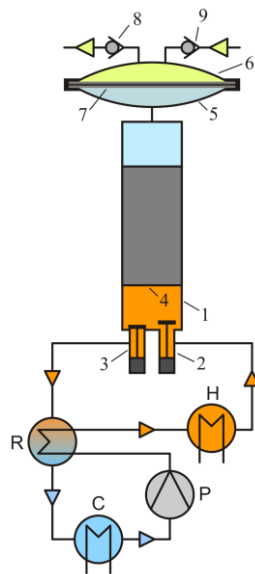


Figure 2. Regenerative Worthington-type engine with thermal barrier piston and diaphragm.

If the IE-machine is used only as a shaft power/electricity generator, the useful work can also be extracted directly from the driving piston by means of some kinematic (crank, swash plate, etc.) mechanism rather than by the hydraulic output. The example with a crank gear is shown in Figure 3 (left). Such a design reminds an old fashion steam engine with a very late cut-off. The admission valve remains open during the whole working stroke and closes at top dead center of the piston. Then the discharge valve opens and remains open during the whole back stroke of the piston. When the piston reaches the bottom dead center, the discharge valve closes and the admission valve opens starting a new working cycle. The reciprocating piston with the crank gear mechanism can be replaced with different rotary piston machines, more convenient in some cases.

A straight forward example of such a machine is a so-called rotary lobe or Roots compressor/blower operating in a reverse mode, i.e., as pressure-to-shaft-power converter shown in Figure 3 (right). The set-up also has a pump (P), heater (H), regenerator (R) and cooler (C). To convert pressure of the hot working fluid to shaft power a special positive displacement rotary lobe machine (RLM) is applied. Such an arrangement is similar to a conventional ORC installation. Roots machines were investigated as ORC expanders [15],[16]. However they do not perform expansion because a so-called built-in volume ratio is close to one i.e. in the Roots converter vapour does not expand during the pressure-to-work conversion. In fact, Roots machines operate as typical hydraulic motor rather than a gas expansion machine. As a result, the functionality of the Roots machine does not differ from that of reciprocating Worthington-type ones outlined above. Moreover, the rotary lobes play the roles of pistons and valves at the same time. Such a simplicity in a combination with high volumetric and mechanical efficiencies as well as low costs makes the Root's-based set-ups appealing. The installation does not produce inertial forces. In addition, power capacity of the biggest Roots machines can reach megawatt power range.

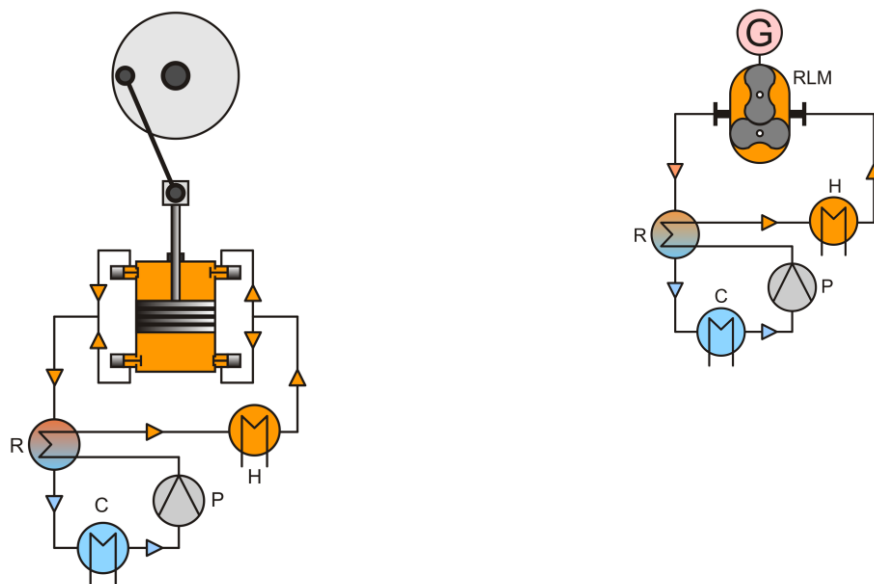


Figure 3. Worthington-type engine with crank gear (*left*) and Worthington-type engine with rotary lobe machine (*right*).

However, the Roots machines cannot work at high temperatures and high pressure drops. For higher pressures and temperatures other types of volumetric machines are necessary.

Cycle Calculations

Heat regeneration processes are rather difficult for modelling, above all in case of cyclic processes. In IE engines using dense working fluids the problem is complicated due to phase changes or operation near the critical point. At such conditions heat capacity is not constant but a strong function of both temperature and pressure. As a result, the second law of thermodynamics poses limitation on the possible heat regeneration degree. This implies that changes of the enthalpies of the fluids/streams participating in the heat exchange process at each temperature level (within the temperature engine cycle temperature interval) matter.

The expansion-compression work performed by the engine per cycle is:

$$W_E = (P_H - P_L)\Delta V_E \quad (1)$$

where P_H and P_L are the high and low cycle pressures (pressures during the expansion and compression processes), and ΔV_E is the change of vapor volume in the cylinder.

If the cylinder volume at the beginning of the admission process (clearance volume) is negligible:

$$\Delta V_E = \frac{m}{\rho(T_H, P_H)} = mv(T_H, P_H) \quad (2)$$

where m is the total mass of the working fluid involved in the cycle and ρ and v are density and specific volume of the working fluid.

The pumping work, assuming an adiabatic process with negligible changes in kinetic and potential energies, can be determined as:

$$W_P = m \left(h(T_{P,out}, P_H) - h(T_L, P_L) \right) \quad (3)$$

where $h(T, P)$ is the enthalpy of the working fluid per unit mass (specific enthalpy), and $T_{P,out}$ is the discharge temperature of the pump.

Assuming an isentropic pump operation the discharge temperature can be found from the constant entropy equation:

$$S(T_L, P_L) = S(T_{P,out}, P_H) \quad (4)$$

The net value of the work produced during the cycle is found as:

$$W = W_E - W_P \quad (5)$$

The working fluid is heated up in a heater from the pump discharge temperature (usually slightly above the temperature of the cooler or the low cycle temperature) to the desired inlet temperature of the power cylinder (high cycle temperature T_H).

Without heat regeneration the amount of heat supplied to the working fluid in the heater is

$$Q_H = m \left(h(T_H, P_H) - h(T_{P,out}, P_H) \right) \quad (6)$$

The thermal efficiency, defined as the useful work produced during a full cycle in relation to the supplied heat, is

$$\eta_{IE} = \frac{W}{Q_H} = \frac{(P_H - P_L)v - (h(T_{P,out}, P_H) - h(T_L, P_L))}{h(T_H, P_H) - h(T_{P,out}, P_H)} \quad (7)$$

The supplied heat can be reduced by recovering a part of the heat of the working fluid exhausted from the power cylinder in a recuperative heat exchanger, Figure 4. In this case working fluid after the feed pump is heated in the regenerator from $T_{P,out}$ to some higher temperature $T_{R,out}$ at the outlet of the regenerator. Thus the duty of the heater becomes

$$Q_H = m (h(T_H, P_H) - h(T_{R,out}, P_H)) \quad (8)$$

$T_{R,out}$ value is determined by the regenerator process. Its scheme is shown in Figure x.

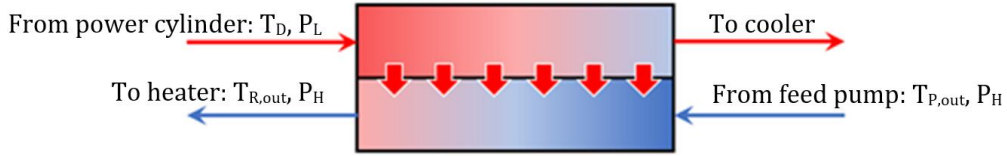


Figure 4. Scheme of the regenerator.

In the regenerator cold stream from the feed pump at pressure P_H is heated by the hot stream discharged from the power cylinder. The temperature and pressure of the fluid discharging from the power cylinder (fluid delivering heat) depend on the way how the discharge is arranged.

We assume that the pressure of the fluid exhausted from the power cylinder decreases from the high cycle pressure P_H to the low cycle pressure P_L in a throttle located before the regenerator. The exhaust valve of the power cylinder may play the role of the throttle. This pressure reduction process is considered as a Joule-Thompson expansion.

Neglecting the changes in kinetic and potential energy, the temperatures in the power cylinder and at the inlet of the regenerator, T_E and T_D , are related by an equation ensuring no enthalpy change in this process:

$$h(P_E, T_E) = h(P_L, T_D) \quad (9)$$

in which P_E is the pressure of the working fluid in the power cylinder (before the exhaust valve) which change during the discharge process consisting of the pressure reduction stage and displacement of the working fluid from the power cylinder at the low cycle pressure.

Change of P_E and T_E during the discharge process can be obtained from the energy balance assuming the adiabatic process in the power cylinder:

$$\rho(T, P)dh = dP \quad (10)$$

Although the amount of working fluid in the cylinder reduces, the balance equation, Eq. (10) is the same as that for adiabatic expansion of a fluid of constant mass.

From Eqs 9 and 10 the variable inlet temperature of the fluid delivering heat T_D can be calculated. Then, applying a method presented in [17] enthalpy of the working fluid entering the heater can be obtained.

To simplify the calculations of the regenerator process we assumed that the working fluid coming from the power cylinder to regenerator is well mixed. In other words, instead of variable inlet temperature T_D its average value found from the enthalpy balance is used. This assumption is justified if amount of the working fluid in the regenerator is much larger than m . Otherwise the assumption results in a conservative value of heat exchanged in the regenerator.

The specific enthalpy of the fluid after discharging and mixing is $h(T_D, P_H) - (P_H - P_L)v$. Therefore T_D can be obtained from equation

$$h(T_D, P_L) = h(T_H, P_H) - (P_H - P_L)v \quad (11)$$

If temperatures of the streams entering the regenerator are known the maximum thermodynamically allowed heat transfer between two fluids, or the maximum amount of regenerated heat Q_R is [17]

$$Q_R = h(T_D, P_L) - h(T_{P,out}, P_H) - Dh \quad (12)$$

where Dh is the maximum enthalpy difference within the temperature interval $T_{P,out} \leq T \leq T_D$:

$$Dh = \max(h(T, P_L) - h(T, P_H)), \quad T_{P,out} \leq T \leq T_D \quad (13)$$

Accordingly, the maximum enthalpy of the working fluid entering the heater is:

$$h(T_{R,out}, P_H) = h(T_{P,out}, P_H) + \Delta h_{max} = h(T_D, P_L) - Dh \quad (14)$$

The efficiency of a regenerative IE-cycle can now be written as:

$$\eta_{IE+R} = \frac{W}{Q_{H+R}} = \frac{(P_H - P_L)v - (h(T_{P,out}, P_H) - h(T_L, P_L))}{(P_H - P_L)v + Dh} \quad (15)$$

To evaluate how an IE machine performs compared to other machines, the calculated efficiency is compared with the Carnot efficiency η_C showing the theoretical maximum, the Novikov η_N [18] efficiency which is a realistic measure for practically achievable efficiencies. This is shown in literature [19] for a variety of power plants i.e. nuclear, geothermal, steam, etc. The relation is also known as the Curzon-Ahlborn efficiency and is a result of the assumption that all engine parts are ideal, yet the heat transfer from the reservoirs is irreversible. The Novikov efficiency relates only to the theoretical maximum power point of the (heat)engine or cycle, but is widely used for comparing power generating processes. Also a newly established empirical correlation based on a survey of 34 commercial ORC installations η_{ORC} [20] is used for comparison. This relation is derived from operational ORC systems and the efficiencies that were reported. Definitions are as follows:

Carnot

$$\eta_C = 1 - \frac{T_L}{T_H} \quad (16)$$

Novikov

$$\eta_N = 1 - \sqrt{\frac{T_L}{T_H}} \quad (17)$$

Gangar et. al. [20]

$$\eta_{ORC} = -0.93\eta_N^2 + 0.87\eta_N \quad (18)$$

Results

All presented results are from running the calculation model against the physical properties of the working fluids referenced from REFPROP version 10 [12]. For single component working fluids we show that with low temperature and pressure difference the efficiency of the IE-cycle will approach the Carnot efficiency. With mixtures the calculation becomes more involved, while multiple mixtures are supported by REFPROP we chose to present the mixtures that have a firm backdrop in practice and literature: ammonia/water ($\text{NH}_3 / \text{H}_2\text{O}$) [21],[22] and carbon dioxide / acetone ($\text{CO}_2/\text{C}_3\text{H}_6\text{O}$) [23],[24] mixtures. These mixtures show a tremendous increase in efficiency when regeneration is applied to the IE-cycle.

By following the calculation method as described in Eqs. 1-15 and in [17], the cumulative enthalpy curves are determined for pure ammonia as a working fluid compared with ammonia

water 65/35 %wt. at equal conditions. By employing a mixture, the theoretical maximum heat transfer with regeneration between the heat delivering and heat receiving fluid is increased drastically. This is graphically shown in Figure 5.

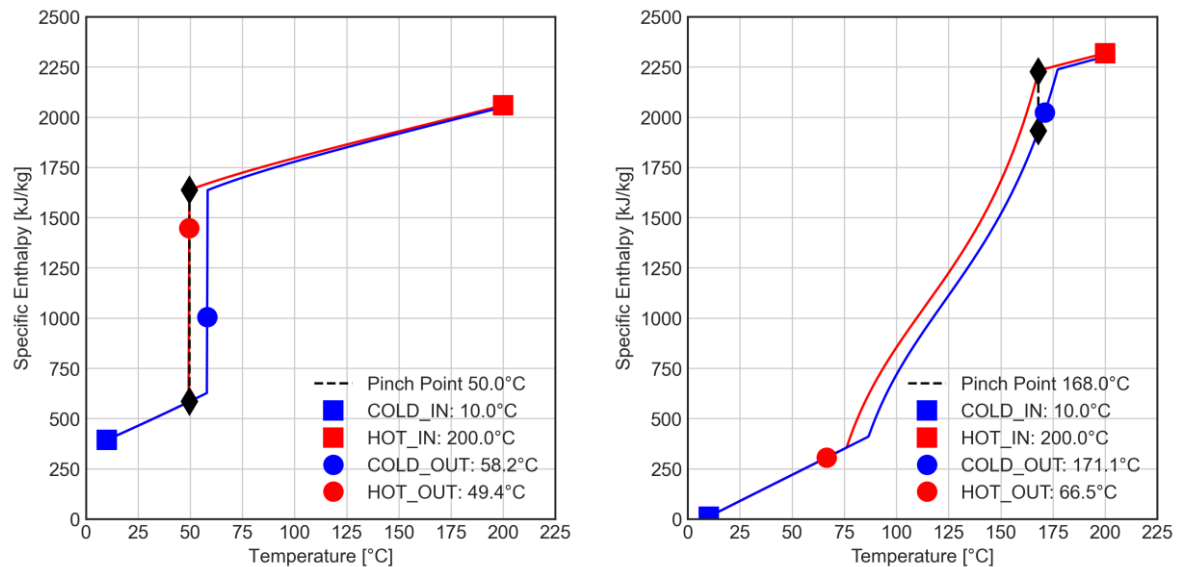


Figure 5. Calculation of the maximum possible heat transfer with regeneration for pure ammonia (*left*) and an ammonia/water mixture 65/35 wt.% (*right*) at $P_L = 20$ bar $\Delta P = 5$ bar

Efficiency of single component working fluids

Efficiencies of several single component working fluids in Worthington cycle with and without regeneration were investigated before [9]. However, in order to understand some critical features of the Worthington cycle we investigated several tens of such fluids calculating a relative (to Carnot) efficiencies at different temperature and pressure differences. As it turned out, all these working fluids demonstrated a similar behaviour shown in Figure 6 for ammonia, water, CO₂ and acetone as typical examples. It can be seen that the highest relative efficiency is reached at the point of phase transition at high cycle pressure P_H . At low temperature and pressure differences (below 5-10°C and 0.5-2 bar) these efficiencies approach to the Carnot efficiency. Any further increase of temperature and pressure difference leads to a decrease of the efficiency. This decline is notably pronounced for the highest efficiencies: the higher the efficiency the sharper the drop. High efficiencies (above 0,7 of the Carnot efficiency) are possible within the temperature range about 20°C. The efficiencies which are of practical, industrial interest (mostly above 0,5 of the Carnot efficiency) can be reached at the temperature difference below 50°C.

It can be also seen that regeneration can slightly extend the temperature and pressure differences. However, the benefit of a regenerative cycle is small and increases towards higher temperature differences. When a pure working fluid becomes supercritical a gradual increase in efficiency is seen, so regeneration becomes more important under supercritical conditions.

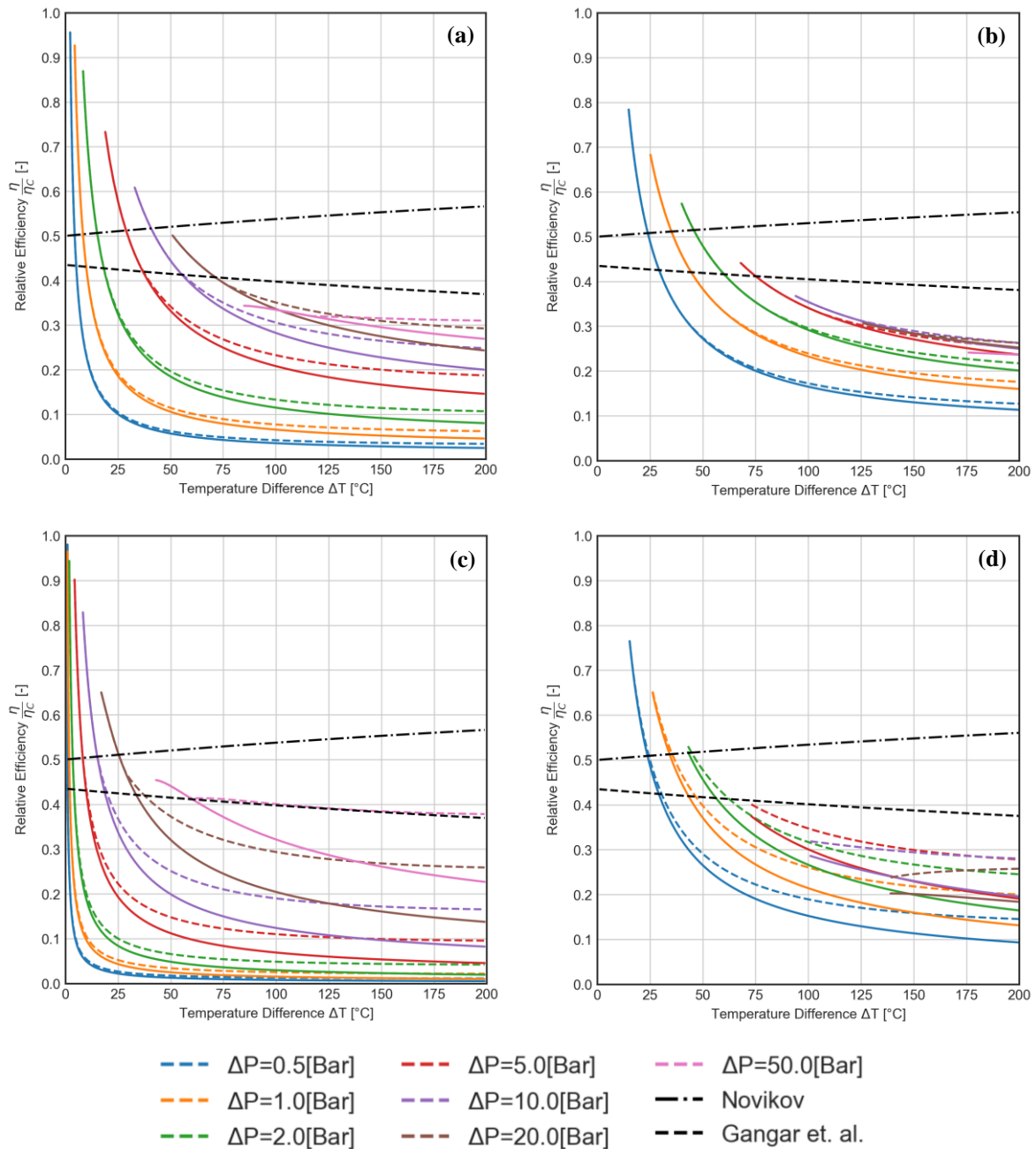


Figure 6. Specific efficiency of pure working fluids: ammonia ($T_L = 10^\circ\text{C}$, $P_L = 6.15$ bar) (a), water ($T_L = 90^\circ\text{C}$, $P_L = 0.70$ bar) (b), CO_2 ($T_L = 10^\circ\text{C}$, $P_L = 11.07$ bar) (c), acetone ($T_L = 46^\circ\text{C}$, $P_L = 0.71$ bar) (d). Solid line = without heat regeneration, dashed line = with heat regeneration.

Efficiency of binary mixture working fluids

It was suggested in [9] that application of mixed working fluids could lead to some efficiency improvements due to better regeneration. In [25] some hydrocarbon mixtures were investigated for Bush-type engines and a slight rise in efficiency was found.

In contrast to pure working fluids, mixtures of working fluids can also provide significant benefits, because the temperature of the reservoirs i.e. heat source and sink temperatures often are not constant [26]. In this case a mixture with a suitable temperature glide can be used to match evaporator and condenser profiles more precisely.

We investigated numerically several tens of binary mixtures with different composition in the temperature range up to 200°C. Among them are binary mixtures of different hydrocarbons, oxygenates (alcohols, ethers etc.), fluorinated refrigerants, hydrofluoroethers (Novec™), inorganic substances etc. The main goal of this investigation was to evaluate whether mixed working fluids are able to considerably improve efficiency of Worthington-type IE-engines due to improved heat regeneration. As it turned out, many mixtures demonstrated a serious rise in efficiency as compared to single component working fluids.

Compared to pure working fluids: at high temperature differences binary mixtures in combination with regeneration can increase efficiency several times. In Figure 7 results are presented for a range of pressures of a 65/35 wt.% mixture of ammonia/water and a 60/40 wt.% CO₂/acetone system. For lower pressure differences the relative efficiencies are the highest >50%. Benefits of regeneration are even more pronounced with the CO₂/acetone mixture, showing efficiencies above the Novikov efficiency for large heat source temperature difference: up to 100°C ΔT for ammonia/water and up to 200°C ΔT for CO₂/acetone.

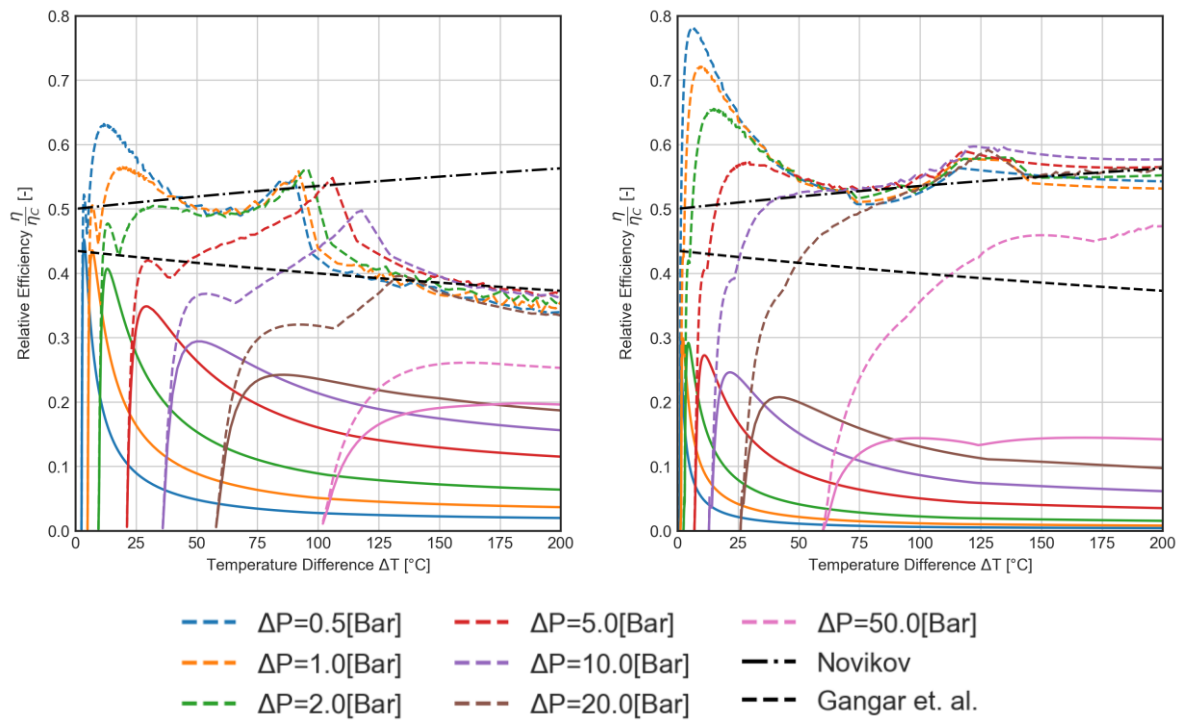


Figure 7. Efficiency calculation for 65/35 % wt. ammonia/water ($T_L=30^\circ\text{C}$, $P_L= 6.0$ bar) (*left*) and 60/40 % wt. CO₂/acetone system ($T_L=30^\circ\text{C}$, $P_L= 35.62$ bar) (*right*).

While pure working fluids show high efficiency peaks at low temperature and pressure difference it is possible to extend this range of high efficiency substantially for both temperature and pressure difference.

Discussion

It can be seen that the simple non-regenerative cycle can provide a high thermal efficiency (close to the maximum possible Carnot efficiency), using a low temperature and pressure difference. However, the Worthington-type machines can provide such high efficiencies only within a narrow temperature-pressure range. At the higher temperature and pressure differences, the relative efficiency inevitably drops down. Regeneration is able to extend this

high-efficiency temperature difference to some extent. Nevertheless, such a simple cycle can be of interest for a number of applications. For instance, in utilisation of low-temperature geothermal energy which can be economical if heat, rejected by IE-engine is used for district heating or in industry (drying etc.). Other examples are heat utilization of low temperature proton exchange membrane fuel cells (LTPEMFC), generally operating between 55°C and 80°C, waste heat recovery of marine diesel engines circulating water etc. The impressive efficiency at low temperature/pressure difference permits to use relatively inexpensive off-the-shelf Roots machines in an IE-cycle.

Another way to extend the temperature difference covered by the simple non-regenerative cycles is a cascade. Such a two-stage cascade is shown in Figure 8 as an example. The cascade is a combination of two IE-installations shown previously in Figure 1; each IE engine utilizes a certain temperature difference. The condenser / cooler (CH) of the first stage in this case plays the role of heater/evaporator for the second stage of the cascade.

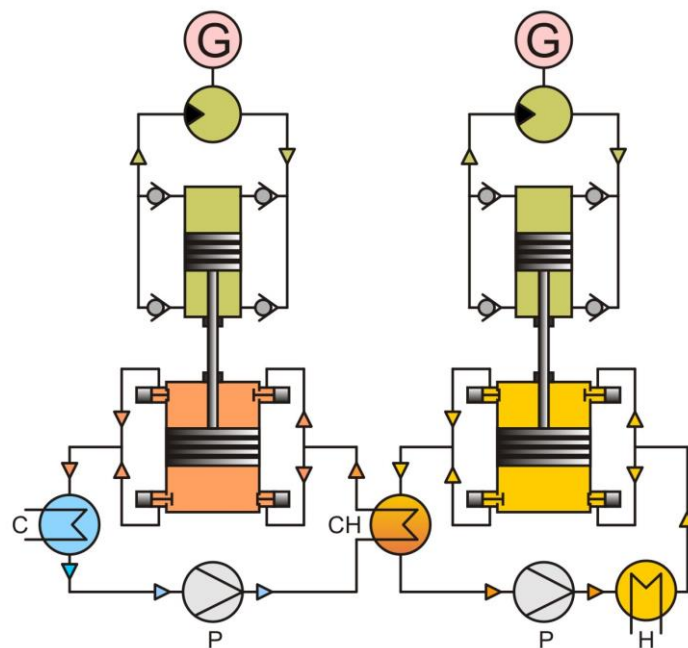


Figure 8. Heat-to-electricity converter based on Worthington-type engine working in cascade configuration.

Therefore, every engine can convert heat with a small temperature difference with a relatively high efficiency. Every engine in the cascade, shown in Figure 8, serves its own pump/motor. However, the cascade set-ups can be designed differently, when all engines drive only one pump and/or hydraulic motor etc. Generally, the cascade can utilise more broad temperature differences as compared single stage IE-engines. Cascade setups are thus suitable to use heat from different temperature waste streams. In this case every stage can use not only the heat from the upstream stage but heat from any other suitable source. This is of interest for the recovery of heat from for example diesel engines by coupling exhaust- and cooling water waste heat i.e., multiple heat streams with two different temperatures. Refineries, chemical and food industry are other typical examples of multiple temperature level heat sources for IE cascade application.

Mixed working fluids make it possible to operate in much broader temperature and pressure difference ranges typical of medium and high-pressure reciprocating piston IE engines. IE-engines with mixed working fluid can be used for power generation and as heat-driven pumps and compressors. The examples are pumps for irrigation, for transfer liquefied gases and refrigerants, for district heating and water supply, air compressors, refrigeration and air conditioning compressors, compressors of heat pumps etc. Air compressors are of interest also in view of the last efforts on development of compressed air energy storage systems. The second particular case today is a high-pressure compression of hydrogen for storage and hydrogen refuelling stations etc.

Conclusion

A high quantity of recoverable energy is still lost in most industrial processes. Possible ways of (ultra) low-grade heat utilization by different types of isobaric expansion (IE) machines are presented and discussed. It is shown that efficiency of non-regenerative machines with single-component working fluids can be high, approaching the Carnot efficiency at a low heat source/heat sink temperature difference. Regeneration permits to increase this efficiency only to some extent. For an efficient utilization of higher temperature differences there are two ways. The first one is a so-called cascade i.e., a combination two or more IE machines; each of them utilizes only some part of the available temperature difference. The second is an application of binary mixtures as working fluid in a combination with regeneration. At high temperature differences such a combination can increase efficiency several times when compared to single component working fluids.

The IE engine can become a suitable means for recovery of heat energy by its simple design, and economical application. Ongoing research and experiments will further develop IE technology and improve system configurations for the plethora of applications.

Acknowledgements

We would like to kindly acknowledge Mr. A. Koedood – CEO of the Koedood Marine Group for in part funding this research.

This project has received funding from the Dutch programme R&D Mobility Sectors, which is executed by Rijksdienst voor Ondernemend Nederland (RVO) under grand number MOB21013, SH2IPDRIVE. This publication only reflects the authors' views and RVO is not responsible for any use that may be made of the information it contains.

This project has received funding from the European Union's Horizon 2020 research and innovation programme under grant agreement No 764042. This publication reflects only the authors' views and neither Agency nor the Commission are responsible for any use that may be made of the information contained therein. 

References

- [1] B. Nesbitt, Ed., *Handbook of pumps and pumping*, 1st ed. Oxford ; Burlington, MA: Elsevier in association with Roles & Associates Ltd, 2006.
- [2] R. Saidur, N. A. Rahim, and M. Hasanuzzaman, 'A review on compressed-air energy use and energy savings', *Renew. Sustain. Energy Rev.*, vol. 14, no. 4, pp. 1135–1153, May 2010, doi: 10.1016/j.rser.2009.11.013.

- [3] M. Langan and K. O'Toole, 'A new technology for cost effective low grade waste heat recovery', *Energy Procedia*, vol. 123, pp. 188–195, Sep. 2017, doi: 10.1016/j.egypro.2017.07.261.
- [4] C. Forman, I. K. Muritala, R. Pardemann, and B. Meyer, 'Estimating the global waste heat potential', *Renew. Sustain. Energy Rev.*, vol. 57, pp. 1568–1579, May 2016, doi: 10.1016/j.rser.2015.12.192.
- [5] T. Tartière and M. Astolfi, 'A World Overview of the Organic Rankine Cycle Market', *Energy Procedia*, vol. 129, pp. 2–9, Sep. 2017, doi: 10.1016/j.egypro.2017.09.159.
- [6] S. Quoilin, M. V. D. Broek, S. Declaye, P. Dewallef, and V. Lemort, 'Techno-economic survey of Organic Rankine Cycle (ORC) systems', *Renew. Sustain. Energy Rev.*, vol. 22, pp. 168–186, Jun. 2013, doi: 10.1016/j.rser.2013.01.028.
- [7] L. Tocci, T. Pal, I. Pesmazoglou, and B. Franchetti, 'Small Scale Organic Rankine Cycle (ORC): A Techno-Economic Review', *Energies*, vol. 10, no. 4, p. 413, Mar. 2017, doi: 10.3390/en10040413.
- [8] M. Papapetrou, G. Kosmadakis, A. Cipollina, U. La Commare, and G. Micale, 'Industrial waste heat: Estimation of the technically available resource in the EU per industrial sector, temperature level and country', *Appl. Therm. Eng.*, vol. 138, pp. 207–216, Jun. 2018, doi: 10.1016/j.applthermaleng.2018.04.043.
- [9] M. Glushenkov, A. Kronberg, T. Knoke, and E. Kenig, 'Isobaric Expansion Engines: New Opportunities in Energy Conversion for Heat Engines, Pumps and Compressors', *Energies*, vol. 11, no. 1, p. 154, Jan. 2018, doi: 10.3390/en11010154.
- [10] B. J. G. van der Kooij, *The invention of the steam engine*. 2015.
- [11] M. Whitmore, 'Development of Coal-Fired Steam Technology in Britain', in *Encyclopedia of the Anthropocene*, Elsevier, 2018, pp. 285–305. doi: 10.1016/B978-0-12-809665-9.10266-6.
- [12] E.W. Lemmon, I.H. Bell, M.L. Huber, M.O. McLinden, *REFPROP*. Gaithersburg: National Institute of Standards and Technology, 2018. [Online]. Available: <https://www.nist.gov/srd/refprop>
- [13] V. Bush, 'Apparatus for compressing gases', US2157229A [Online]. Available: <https://patents.google.com/patent/US2157229A/en>
- [14] T. Knoke, A. Kronberg, M. Glushenkov, and E. Y. Kenig, 'On the design of heat exchanger equipment for novel-type isobaric expansion engines', *Appl. Therm. Eng.*, vol. 167, p. 114382, Feb. 2020, doi: 10.1016/j.applthermaleng.2019.114382.
- [15] O. Dumont, L. Talluri, D. Fiaschi, G. Manfrida, and V. Lemort, 'Comparison of a scroll, a screw, a roots, a piston expander and a Tesla turbine for small-scale organic Rankine cycle', p. 9, 2019.
- [16] A. Parthoens, O. Dumont, L. Guillaume, and L. Vincent, 'Experimental and Numerical Investigation of a Roots Expander Integrated into an ORC Power System', p. 11, 2018.
- [17] A. Kronberg, M. Glushenkov, T. Knoke, and E. Y. Kenig, 'Theoretical limits on the heat regeneration degree', p. 16.
- [18] I. I. Novikov, 'The efficiency of atomic power stations (a review)', *J. Nucl. Energy* 1954, vol. 7, no. 1–2, pp. 125–128, Aug. 1958, doi: 10.1016/0891-3919(58)90244-4.
- [19] M. Esposito, R. Kawai, K. Lindenberg, and C. Van den Broeck, 'Efficiency at Maximum Power of Low-Dissipation Carnot Engines', *Phys. Rev. Lett.*, vol. 105, no. 15, p. 150603, Oct. 2010, doi: 10.1103/PhysRevLett.105.150603.
- [20] N. Gangar, S. Macchietto, and C. N. Markides, 'Recovery and Utilization of Low-Grade Waste Heat in the Oil-Refining Industry Using Heat Engines and Heat Pumps: An International Technoeconomic Comparison', *Energies*, vol. 13, no. 10, p. 2560, May 2020, doi: 10.3390/en13102560.

- [21] R. Tillner-Roth and D. G. Friend, 'A Helmholtz Free Energy Formulation of the Thermodynamic Properties of the Mixture 'Water % Ammonia'', *J Phys Chem Ref Data*, vol. 27, no. 1, p. 34, 1998.
- [22] S. S. H. Rizvi and R. A. Heldemann, 'Vapor-Liquid Equilibria in the Ammonia-Water System', p. 9.
- [23] R. J. B. Moreira-da-Silva, D. Salavera, and A. Coronas, 'Modelling of CO₂/acetone fluid mixture thermodynamic properties for compression/resorption refrigeration systems', *Mater. Sci. Eng.*, p. 14, 2019.
- [24] C.-M. Hsieh and J. Vrabec, 'Vapor-liquid equilibrium measurements of the binary mixtures CO₂+acetone and CO₂+pentanones', *J. Supercrit. Fluids*, vol. 100, pp. 160–166, May 2015, doi: 10.1016/j.supflu.2015.02.003.
- [25] T. Knoke, E. Y. Kenig, A. Kronberg, and M. Glushenkov, 'Model-based Analysis of Novel Heat Engines for Low- Temperature Heat Conversion', *Chem. Eng. Trans.*, vol. 57, p. 6.
- [26] R. Radermacher, 'Thermodynamic and heat transfer implications of working fluid mixtures in Rankine cycles', *Int. J. Heat Fluid Flow*, vol. 10, no. 2, pp. 90–102, Jun. 1989, doi: 10.1016/0142-727X(89)90001-5.

Experimental study of an isobaric expansion engine-pump

M. Glushenkov, A. Kronberg*

Encontech B.V. TNW/SPT, PO box 217, 7500 AE Enschede, The Netherlands

*Corresponding author e-mail: info@encontech.nl

Abstract

We have developed a novel heat engine of the isobaric expansion type. This paper reports preliminary measurements made with the engine operating as a pump, and a comparison of the experimental results to a thermodynamic model. Experiments were carried out at heat source temperature in the range 30 – 90 °C and heat sink temperature around 11 °C; refrigerant R134a was used as the engine working fluid. The pressure difference generated by the engine-pump varied from 2.5 bar at the heat source temperature 30 °C to 23 bar at the heat source temperature 86 °C. At frequency of about 0.25 Hz the engine operates with useful powers up to 500 W, and water pumping flowrate 15 L/min. Depending on the temperature of the heat source the obtained efficiency was 3.5 – 6 %. This efficiency looks very high, considering such a low temperature difference (20 – 75 °C) and low power (< 1 kW). The engine's observed performance is in good agreement with the predictions of the model. The results are very promising showing that the engine is a valuable alternative to the current technologies, especially at low temperatures (< 100 °C) and low power range (< 500 kW) where the current technologies are not economic.

Keywords: Heat engine, heat-driven pump, isobaric expansion, low-grade heat, renewable energy, energy efficiency.

Introduction

Today, a large proportion of the world's electricity is consumed by pumps and compressors. Pumping systems account for nearly 20% of the world's electrical energy demand and can range from 25% to 50% of the energy usage in certain industrial plant operations [1]. Compressed air systems alone account for 10% of industrial electricity consumption in the USA and the EU [2, 3].

Most of the electricity (64.5 %) is generated by large power plants using high temperature heat from burning fossil carbon-based fuels (coal, natural gas and oil). Other methods of electricity generation (hydroelectric power, nuclear power, wind, solar and biomass) accounts for a much smaller portion of the electricity market [4].

According to a recent evaluation, 72% of the global primary energy consumption is lost after conversion; 63% of the waste heat streams arise at temperatures below 100 °C [5].

Today, the only way to convert low-grade heat to power is organic Rankine cycle (ORC). However, the real contribution of ORC in the world's electricity generating capacity is very small. A total installed capacity of ORC plants is about 2.7 GW [6], i.e. 0.042 % of the global electricity generating capacity and 0.068 % of the generating capacity based on thermal (heat) energy sources [7]. Such an insignificant contribution of ORC is caused mostly by economic reasons. ORC systems are too expensive, especially in the case of low grade heat sources (< 100 °C) and low power range [8, 9, 10]. Small ORC units less than 500 kW power do not represent more than 2% of the total installed capacity [6], i.e. countless, readily available small low-grade heat sources are not unused.

Isobaric expansion (IE) technology [11] can be an ideal solution for the mini- and medium-scale low-grade heat utilization. IE engines are the oldest type of heat engines. It will suffice to mention that Savery and Newcomen pumps as well as the first pumps of James Watt (without steam expansion) fit into this group [12]. Since then many IE engines were studied under different names as pumps, compressors etc. [13, 14, 15, 16, 17].

IE process is an alternative to conventional gas/vapour expansion accompanied by a pressure decrease typical of all state-of-the-art heat engines. The elimination of the expansion stage associated with useful work means that the most critical and expensive parts of ORC systems (turbine, screw expander, etc.) are also eliminated. Some versions of the proposed system avoid typical technical problems associated with well-known thermal energy driven systems, mainly failure of sealing components, lubrication, and wear. These systems are very quiet, can be fully balanced and have a very simple, reliable, and inexpensive design [11]. Thus, the technology can be a simple and low-cost alternative to the ORC plants as well as other state-of-the-art energy conversion systems.

IE engines provide usable energy in a very convenient hydraulic or pneumatic form that can be converted to any other form of energy, and therefore they can also perform all known operations of existing heat engines. The energy from the pumped liquid flows can be converted to shaft power (rotary motion) or electricity by means of off-the-shelf hydraulic motors. Another option is the so-called pump as turbine (PAT) technology, which uses mass market centrifugal pumps working in reverse regime i.e. as turbines. In this case the installation is turned into a heat-to-power converter.

IE engines are particularly promising for pumping liquids and compression of gases since the engines themselves operate as positive displacement pumps or compressors. In such applications, heat can be efficiently used to provide direct pumping and compression, that is, without intermediate generation of electricity, its transmission and further conversion back to mechanical energy typical of today's industry

In [11] IE-engines were divided into two classes – Bush- and Worthington-type engines. Each class includes many different design modifications for pumping, compression and power generation.

Thermally driven pumps have been developed over many years [13, 18, 19, 20, 21, 22, 23, 24, 25]. However, the practical application of such pumps was always very limited because of too low efficiency or power. As an alternative Bush-type engine pump (also known as Up-Therm, Encontech, ECT engine) was proposed in [11, 17]. A detailed explanation of this engine-pump concept, its advantages as well as experimental and theoretical data are presented in [26].

In this paper a novel Worthington-type IE engine-pump will be considered. It was developed within CHESTER project [27, 28] as a high pressure feed pump of the ORC unit of 10 kWe.

Description of the IE engine-pump

The engine-pump presented in this paper, Figure 1, is one out of many possible modifications of Worthington type IE engines outlined in [11]. It consists of two power or driving cylinders (1), pumping cylinder (2), three pistons (3), two connecting rods (4), two driving valve covers (5), two pumping valve covers (6) and two pneumatic valve actuators (7) which are used to actuate the valves in the covers (5). Each valve cover (6) is equipped with a non-return (check) suction (8) and discharge (9) valves.

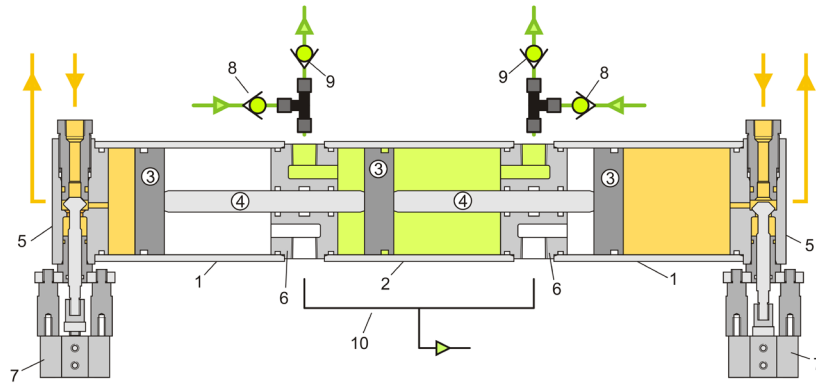


Figure 1. Scheme of the IE engine-pump.

The pistons divide the internal volumes of the cylinders into six chambers: two driving chambers, shown in light brown, two pumping chambers (green) and two auxiliary chambers (colourless). The auxiliary chambers can be used for lubricating the pistons (3) and for collecting leaks from the pumping and driving chambers in case of failure of the piston seals. They are connected by a manifold (10) through which the leaks are displaced to a ventilation. Volumes of each driving and pumping chambers of the engine-pump are 0.482 L and 0.463 L respectively.

The valves in the driving covers (5) operate in counterphase: when, for instance, the right valve delivers hot vapor of the working fluid from a heater to the right driving chamber, the left one provides exhaust of the spent working fluid from the left chamber. Thereby, three pistons and two connecting rods move together as a unit to the left. Both the inlet and outlet valves are open until the pistons complete their stroke from right to left. This piston movement results in the displacement of pumped liquid from the left pumping chamber and suction the liquid into the right pumping chamber. After that, the left valve starts the admission, the right valve synchronously provides the exhaust, and the second half of the cycle begins.

Experimental setup for engine testing

A schematic of the experimental setup for testing the engine is shown in Figure 2.

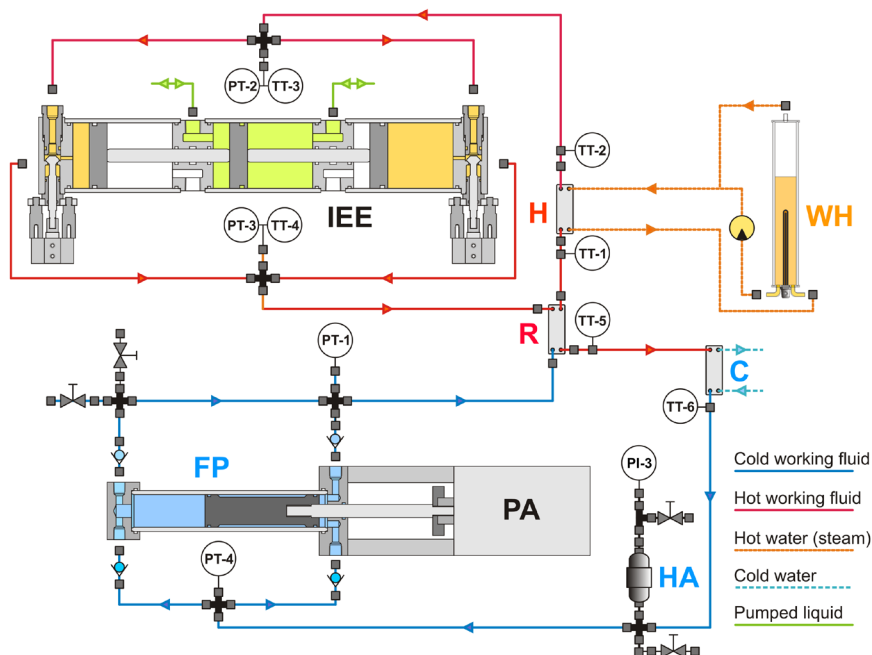


Figure 2. Scheme of the experimental setup.

A photograph of the built setup is presented in Figure 3.

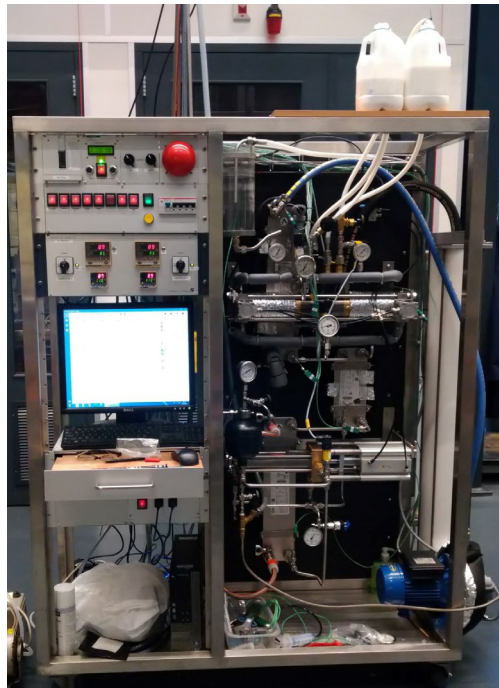


Figure 3. Engine-pump setup.

The setup includes a double acting IE engine-pump **IEE**, working fluid feed pump **FP** actuated by a pneumatic actuator **PA**, hydraulic accumulator **HA**, heater (evaporator) **H**, recuperator **R**, cooler (condenser) **C**, water heater **WH**, pressure indicators **PI**, and pressure and temperature transmitters **PT** and **TT**.

The pneumatic actuator **PA** of the feed pump and pneumatic actuators of the engine valves use compressed air at 7 - 9 bar pressure from the laboratory net.

Pumping in each of the two chambers of the pumping cylinder was studied separately using two pumping circuits. The hydraulic scheme is shown in Figure 4.

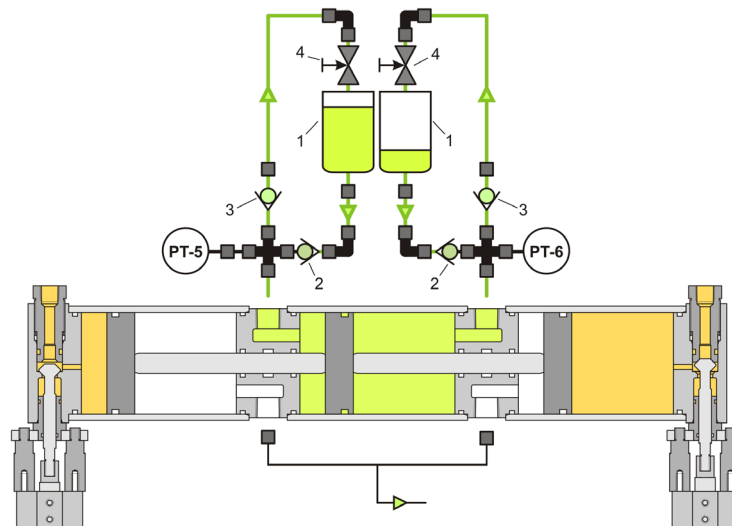


Figure 4. Scheme of the pumping load: 1 – water tank, 2 – suction valves, 3 – discharge valves, 4 – throttle valves.

Each pumping circuit is formed by suction (2) and discharge (3) non-return valves provide one-way flow of water and two throttle valves (4). Water taken from each tank (1) is pumped by the engine pump into the same tank through throttle valve (4). The throttle valves (needle valves or check valves with adjustable cracking pressure used as pressure release valves) imitated the resistance to the water flow in potential applications of the engine-pump.

Components of the experimental setup

The variable flow feed pump, **FP** (Figure 2), is used to supply a low-pressure cold working fluid after the cooler to the recuperator at high cycle pressure. It is driven by a pneumatic actuator (double-acting pneumatic cylinder) with a maximum stroke of 100 mm. The maximum displacement volume of the feed pump per cycle is 0.232 L. In operation the displacement volume is regulated by adjusting stroke of the pneumatic cylinder based on the required amount of working fluid involved in the engine-pump cycle.

From multiple heat exchangers available on the market, three brazed plate heat exchangers (heater **H**, recuperator **R**, and cooler **C**) (Figure 2) produced by company SWEF [29] were selected. All these units are certified to meet 45 bar maximum pressure at 135 °C temperature.

The engine-pump is cooled by tap water flowing through the cooler **C** and heated by hot water circulated by a centrifugal pump through the heater **H** and a specially designed water heater **WH** (Figure 2). The water heater **WH** is a plastic cylindrical vessel with two submerged electric heaters of 12 kW each.

The hydraulic accumulator **HA** (Figure 2) contains a flexible rubber diaphragm, which physically separates the engine working fluid from an inert gas (nitrogen, carbon dioxide) at the set high engine pressure <30 bar. It is used to prevent accidental pressure surges above the set pressure and to suppress possible cavitation in the feed pump suction line.

The pressures at the inlet and outlet of the engine and at the inlet and outlet of the feed pump were measured by pressure transmitters PT (Sendo SS302 model, 40 barg, with 0.5% accuracy and 4 ms response time). Independently, the pressures were controlled by 1 - 40 bar Empeo manometers with 1.6% accuracy installed in parallel with the pressure transmitters. The same manometer type was used to indicate the gas pressure in the hydraulic accumulator.

The working fluid temperature was measured using 1 mm shielded K-types thermocouples TT, pre-calibrated in the range of 0 - 100 °C and installed at the inlet and outlet ports of the heat exchangers and at the inlet and outlet of the engine. The inlet and outlet temperature of heating and cooling water was measured with the same thermocouple type.

All pressure transmitters have 4 - 20 mA output to avoid any influence of cable lengths. The signal from the transmitters was processed and displayed using a 12 bits PicoLog 1012 data acquisition system with a 10 ms sampling interval. The temperatures were measured using a TC-08 DataLogger with a 100 ms sampling interval.

Sealing of the power and pumping cylinders and pistons were provided by seals based on materials with high resistance to all refrigerant classes as well as potentially possible ammonia-water, oxygenates, carbon dioxide, and hydrocarbon-based working fluids. The mating cylinder surfaces were treated by plasma nitriding up to 1100HV on the nitride layer.

Engine-pump testing and results

For testing and adjustment of the test setup components some preliminary, non-thermal measurements were made at room temperature. At first mechanical functionality of the engine-pump and feed pump was tested using compressed air in the range of 5-8 bar pressure as the driving agent for the pistons. Both units were operated without any mechanical issues. The

quantity of water pumped per stroke corresponded well to the displacement volume of the pumping chambers, i.e. 0.463 L.

To prevent corrosion between the stainless-steel and bronze parts the water was replaced with a metal working lubricant/cutting emulsion for chainsaws. The emulsion was prepared using ordinary tap water by adding about 5% of lubricating oil-emulsifying agent mixture. The resulting milky liquid completely suppressed corrosion and exhibited some lubrication ability.

To extend the lifetime of the dynamic seals Fomblin Compressor Oil YL VAC 16/6 was selected as a lubricant in further tests.

The test system setup was filled with refrigerant R134a ($T_{\text{crit}} = 101.08 \text{ }^\circ\text{C}$, $P_{\text{crit}} = 40.6 \text{ bar}$). It was selected from several other potentially applicable working fluids for safety reasons (low flammability).

The engine-pump was heated by hot water in the temperature range 30 - 90 $^\circ\text{C}$ and cooled by tap water at around 12 $^\circ\text{C}$. The flow rate of the hot water pumped through the heater was 30 L/min and the flow rate of the cold water flowing through the cooler was 10 L/min.

The main variables in the experiments were temperature of the heater, an operating frequency (0.1 – 0.5 Hz) and pumped water pressure drop, which determines the high cycle pressure. Hot water temperatures above 90 $^\circ\text{C}$ were not possible due to cavitation in the centrifugal circulation pump. The displacement of the feed pump was set depending on the pressure drop or high pressure of the cycle and the heater temperature (12-60% of the maximum possible displacement).

The low cycle pressure determined by the low cycle temperature and by amount of the working fluid in the system was about 5 bar. This pressure was higher than the equilibrium pressure 4.43 bar at the low cycle temperature of 12 $^\circ\text{C}$ in order to prevent cavitation in the feed pump.

Check valves with adjustable cracking pressure and needle valves were used as resistances to the pumped water flow. With the check valves it was possible to provide approximately constant water pressure drop but not convenient to regulate them during experiments. The needle valves being convenient for the operation could not provide the desired constant pressure drop.

In the experiments, the high cycle pressure (pressure of the driving working fluid) was established by maximizing the loads (pressure drops in the resistances to the water flows) for each chamber until the displaced volumes of pumped water began to fall below the maximum. In other words, the amounts of the displaced water from each chamber were always close to the maximum.

Figure 5 shows examples of the measure temperatures and pressures in the engine-pump setup at the heat source temperature of about 40, 60 and 86 $^\circ\text{C}$ and the cycle frequencies around 0.20 – 0.25 Hz.

The presented in Figure 5 pressures were measured by pressure transmitters PT-2 (heater), PT-3 (cooler) shown in Figure 2, and PT-5 (water 1) and PT-6 (water 2) shown in Figure 4. The temperatures at the inlet and outlet of the heater and cooler were measured by thermocouples TT-1, TT-2, TT-5 and TT-6 respectively, Figure 2

The measured temperatures at the inlet of the engine (driving chambers) and feed pump are not shown in Figure 5; they are very close to the outlet temperature of the heater and cooler. The pressure at the exhaust from the driving chambers is also not shown in the figure; it rapidly drops from the high to low pressure.

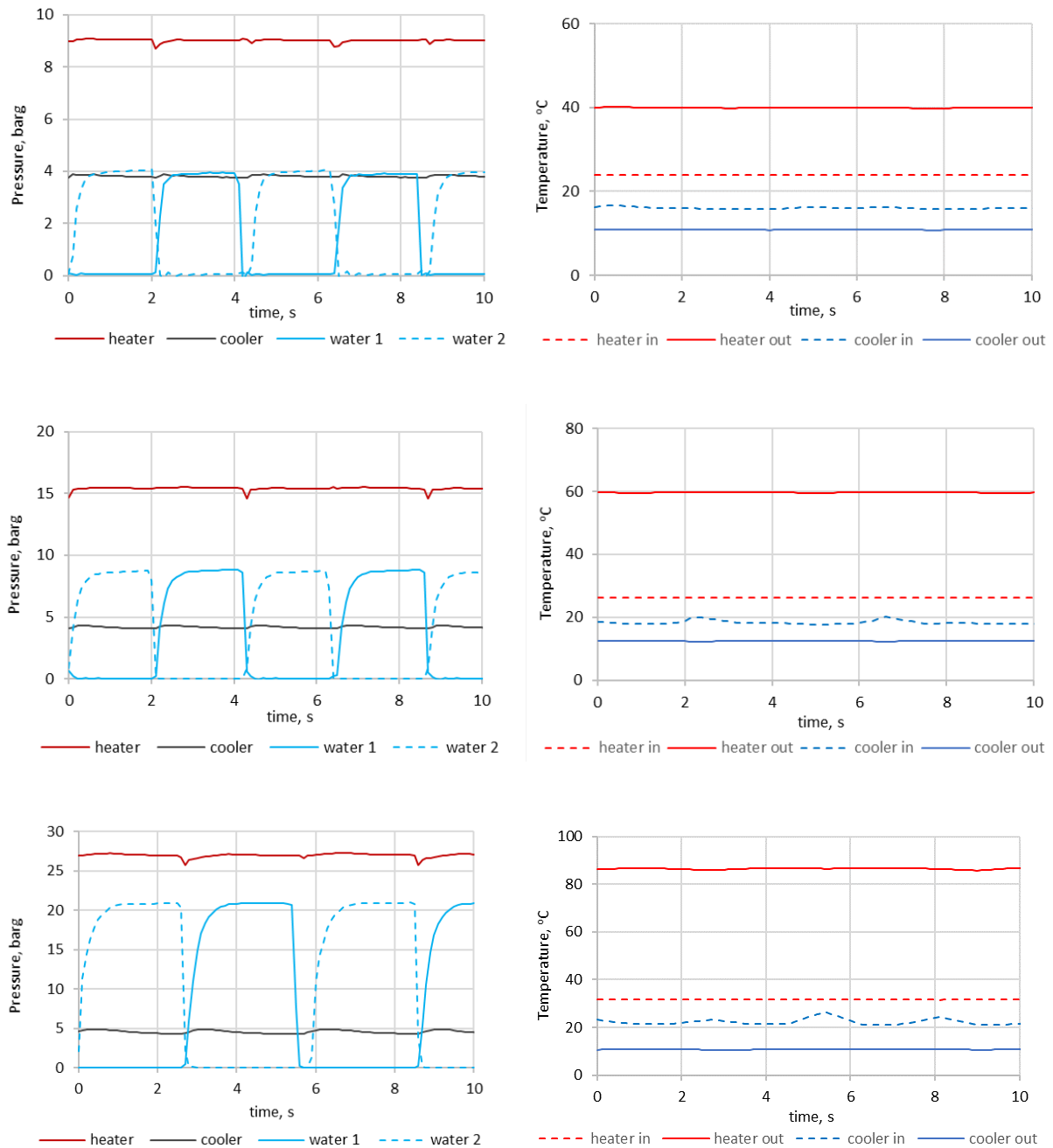


Figure 5. Pressure (left) and temperature (right) changes in the engine-pump parts.

Figure 5 highlights the role of the regenerator. Temperature of the working fluid flowing to the heater increased in the regenerator from 11 - 12 °C (solid blue line) to 25 - 35 °C (red dashed line) providing an increase in thermal efficiency. Some additional information and a video on the engine-pump operation can be found in [30].

Analysis of the experimental data and discussion

The pressure difference generated by the engine-pump varied from 2.5 bar at the heat source temperature 30 °C to 23 bar at the heat source temperature 86 °C. In the used operating mode, the upper cycle pressure was in good agreement with the saturation pressure at the outlet heater temperature. For example, at 86 °C the equilibrium pressure of R134a is 28.26 barg, thus very

close to the measured pressure, Figure 5. This operating mode is thermodynamically advantageous, since heat addition and heat removal occur practically isothermally.

The experimental data permit to evaluate the engine work per cycle, its power and thermal efficiency.

The net value of the work produced in the cycle is:

$$W = W_{pc1} + W_{pc2} - W_{fp} - W_h - W_c \quad (1)$$

where W_{pc1} and W_{pc2} works on pumping water in two pumping chambers, and W_{fp} , W_h , W_c are work of the feed pump, and works for transmission of the heating and cooling water through the heat exchangers respectively.

Pressure drops for pumping of heating and cooling water in the heater and cooler and through the connecting hoses were below 0.1 bar. At flow rates between 10 - 30 L/min the pumping power was very low, 2 - 5 W. Therefore W_h and W_c were neglected in Eq. 1.

The feed pump work was not measured. It was approximately calculated assuming certain value of its isentropic efficiency, η_{fp} , as:

$$W_{fp} = m \left(h(P_H, T_{pump,out}) - h(P_L, T_C) \right) \eta_{fp} \quad (2)$$

where m is the total mass of the working fluid involved in the cycle process), $h(P, T)$ is the enthalpy of the working fluid per unit mass, P_H and P_L are the average outlet and inlet pressure of the feed pump which are equal to the pressures in the heater and cooler (cherry and grey lines in Figure 5), T_C is the temperature at the inlet of the pump (outlet of the cooler) and $T_{pump,out}$ is the discharge temperature of the pump. These temperatures were very close to each other; the difference was within 1 °C and corresponded to the calculated difference assuming an isentropic feed pump operation.

Mass of the working fluid involved in the cycle process m was determined through the displaced volume of the feed pump V_{fp} and density of the working fluid in the feed pump, i.e. at P_L and T_C .

The feed pump work determined from Eq. 2 was in the most cases almost the same as obtained assuming incompressible working fluid, i.e. $(P_H - P_L)V_{fp}$.

The work performed on the pumped water per cycle in each of two pumping chambers can be calculated as

$$W_{pc} = \int_{t_1}^{t_1+t_c} P_{abs}(t)q(t)dt \quad (3)$$

in which W_{pc} is either W_{pc1} or W_{pc2} , $P_{abs}(t)$ is the absolute pressure of the pumped water in the pumping chamber, $q(t)$ is the instantaneous volume flow rate of the water out of the chamber, t_c is the cycle period and t_1 is an arbitrary moment of time; for convenience we choose it as the beginning of the pumping stroke.

Work W_{pc} consists of positive work during the pumping stroke when $q(t) > 0$ and negative work during the suction stroke when $q(t) < 0$.

Amounts of the water coming and leaving the pumping chambers per cycle are equal. Therefore $\int_{t_1}^{t_1+t_c} q(t)dt = 0$ and W_{pc} can be expressed through the measured gauge pressure $P(t) = P_{abs}(t) - P_{atm}$ (blue solid and dashed lines in Figure 5).

$$W_{pc} = \int_{t_1}^{t_1+t_c} P(t)q(t)dt \quad (4)$$

In the experiments presented in this paper the measured gauge pressure during the suction stroke was much less than the pressure during the pumping stroke, Figure 5. Therefore the work performed on the pumping water was calculated as

$$W_{pc} = \int_{t_1}^{t_1+t_c/2} P(t)q(t)dt \quad (5)$$

The instantaneous water volume flow rates $q(t)$ was not measured because it was not possible to find an appropriate flowmeter. A rough value of W_{pc} can be obtained through the measured volume of the pumped water per cycle V_p and average pressure during the pumping stroke \bar{P} :

$$W_{pc} \approx \bar{P}V_p, \quad \bar{P} = \int_{t_1}^{t_1+t_c/2} P(t)dt \quad (6)$$

This value of W_{pc} is less than the actual work. More precise value of the work, although still less than the actual work, can be obtained using the dependence between the pumped water flow rate and pressure drop across the needle valve. According to the valve producer, Swagelok, [31]:

$$q = a\sqrt{P} \quad (7)$$

where the proportionality coefficient a depends on the valve flow coefficient ($C_v = 0.37$) and density of the liquid. Value of a can also be obtained from the experiments using equation for volume of the pumped per cycle water

$$V_p = \int_{t_1}^{t_1+t_c/2} q(t)dt = a \int_{t_1}^{t_1+t_c/2} \sqrt{P}dt \quad (8)$$

Combining Eqs. 5, 7 and 8 we get an equation for work performed on the pumping water

$$W_{pc} = V_p \frac{\int_{t_1}^{t_1+t_c/2} P^{1.5}(t)dt}{\int_{t_1}^{t_1+t_c/2} \sqrt{P}dt} \quad (9)$$

The overall power of the engine-pump was calculated as:

$$Power = fW = f(W_{pc1} + W_{pc2} - W_{fp}) \quad (10)$$

in which f is the cycle frequency and W_{pc1} , W_{pc2} and W_{fp} are determined by Eqs. 2 and 9.

The thermal efficiency is defined as the useful work produced during a full cycle in relation to the supplied heat:

$$\eta = \frac{W}{Q} \quad (11)$$

The heat supplied Q was calculated based on the measured temperatures at the inlet and outlet of the heater, T_H and $T_{h,in}$ respectively (solid and dashed red lines in Figure 5), assuming no heat losses in the heater and taking into account negligible pressure drop in the heater (< 0.25 bar).

$$Q = \left(h(T_H, P_H) - h(T_{h,in}, P_H) \right) m \quad (12)$$

The experimental power and efficiency were compared to a thermodynamic model presented in [11]. The regenerated amount of heat in this model was calculated using a method for determining the thermodynamic limits of heat recovery developed in [32]. Accurate modelling of the regeneration efficiency is a rather complicated task because both the pressure and temperature of the working fluid exiting the driving chambers and entering the recuperator change significantly. To simplify the calculations it was assumed that the working fluid from the driving chambers enters the recuperator at the low cycle pressure being well mixed, i.e. at the average temperature determined from the enthalpy balance. This simplified method provides a conservative value of the regeneration efficiency.

Table 1 below presents some experimental data and the theoretical efficiency, η_{th} , for the experiments presented in Figure 5. The feed pump work was calculated assuming isentropic efficiency, η_{fp} , of 90 %.

Table 1. Experimental data and theoretical efficiency

$T_H, ^\circ\text{C}$	$T_L, ^\circ\text{C}$	P_H, bar	P_L, bar	m, kg	W_{pc}, kJ	W_{fp}, kJ	W, kJ	Q, kJ	$\eta, \%$	$\eta_{th}, \%$
86.5	11.0	28.0	5.5	0.152	1.882	0.301	1.581	29.13	5.43	6.30
59.7	12.5	15.4	5.2	0.073	0.778	0.066	0.711	14.23	5.00	6.32
40.0	10.8	10.0	4.9	0.047	0.355	0.021	0.334	8.78	3.80	5.08

Discussion and conclusions

The experimental results are very promising; they confirm the expected advantages of the IE engine-pumps.

The pumped water flow rate which is determined by the cycle frequency was in the range 6 - 15 L/min. Hence generated power was up to 0.5 kW at frequency of 0.25 Hz corresponding to specific power 0.5 kW/L. This specific power, especially expected at higher frequencies of about 1 Hz, is comparable with that of big diesel engines (2.5 - 3 kW/L), which is achieved at combustion temperatures up to 2500 K and is much higher than the power density of known thermally driven pumps [22, 23, 24].

The engine presented in this paper was supposed to work at frequencies up to several Hz. However most of the experiments were performed at a relatively low frequency in the range 0.1 – 0.25 Hz because at frequencies above 0.25 Hz, the flow rate of the pumped water decreased rapidly. This was due to unsuitable check valves in the suction lines (number 2, Figure 4). Although cracking pressure of the valves was rather low (0.069 bar) their resistance was too high, above 0.5 bar, at operation frequency above 0.25 Hz. Due to this restriction atmospheric pressure which caused water flow from the tanks to the pumping chambers was not sufficient for suction. Also, significant heating of the pumped water during the experiments contributed to the cavitation in the suction strokes. We expect to increase the frequency up to several Hz after replacement of the check valves in the subsequent experiments, and accordingly to increase power up to several kW.

The feed pump is estimated to consume between 3% and 17% of net power generated, which is in the same range as pumping work in the ORC systems with R134a working fluid [33].

The obtained thermal efficiency in the range of 3.5 - 6 % looks very high, considering such a low temperature difference between the heat source and heat sink (20 – 70 °C), low power (< 1 kW) and the fact that the operation was not optimised. This high efficiency can be

explained by: 1) simplicity of the machine; 2) almost isothermal heat addition and heat rejection; 3) relatively high work ratio (i.e. ratio of the net work output and positive work input in cycle) of 0.5 – 0.7.

For the used operating conditions, thermodynamics places severe limitation on the amount of heat exchanged in the recuperator. This amount in the experiments was only 8 – 10 % of the required enthalpy changes of the working fluid stream in the recuperator. However, in spite of the rather low regeneration efficiency, the recuperator was useful for improving overall efficiency.

The experimental values of the thermal efficiency were 10 - 25% lower than those predicted by the thermodynamic model at a heat source temperature of 30-85 °C, respectively. The difference is due to frictional losses in the seals and the used needle valves which imitated engine load. Due to the frictional losses pressure of the pumped water was on average 1.5 - 2 bar lower than the difference between the high and low cycle pressures (pressures in the heater and cooler). The needle valves could not provide constant pressure drop: during the first quarter of the pumping stroke pressure of the pumped water gradually increased from zero to the maximum value, Figure 5. As a result, the average pumping pressure turned out to be 6-9% lower than its maximum value.

Heat losses in the heat exchangers and pipelines were not evaluated in these experiments. However, they should not be significant as the highest temperature was below 90 °C and all hot parts of the experimental setup were insulated; if necessary heat losses could be minimized using improved thermal insulation.

The engine has not been optimised yet. This can be seen from Table 1: the theoretical efficiency at the heat source temperature T_H of 59.7 °C is higher than that at $T_H = 86.5$ °C. Further efficiency gains can be achieved by selecting the optimal combination of high cycle pressure and temperature, improving sealing, admission and suction valves, and overall engine design.

Obviously, higher efficiency can be achieved with increasing size and power of the engine and in real pumping processes with a constant delivery pressure of the pumped liquid.

The engine design presented in this paper, Figure 1, is one of many others. It can be different depending on the application. The diaphragm-type IE engine-pump is an example of an alternative design. In such a single-acting machine, Figure 6, there are no seals and a diaphragm unit plays a role of IE engine-pump. The diaphragm unit includes two semispherical covers (1) and (2) with a metal or polymer diaphragm (3) clamped in between. The top cover (2) is equipped with suction and discharge valves (6) and (7); the bottom cover is equipped with inlet and outlet valves (4) and (5). The diaphragm transmits pressure between working fluid (shown in brown) and the pumped liquid (shown in yellow-green). As the piston engine-pump, Figure 2, it includes, working fluid feed pump P, heater H, recuperator R, and cooler C.

One of the differences between the diaphragm and piston pump presented in this paper is that the suction and discharge pressures in the diaphragm engine-pump are equal to the low and high cycle pressures of the working fluid. The main advantage of the diaphragm-based design is almost friction-free and leak-free operation. Therefore, the frictional losses detrimental for the efficiency of the piston engine-pumps are eliminated.

It is interesting to note that this type of pumps was used as early as 1885 in France for pumping water using ammonia as a working fluid and solar energy as a heat source [33].

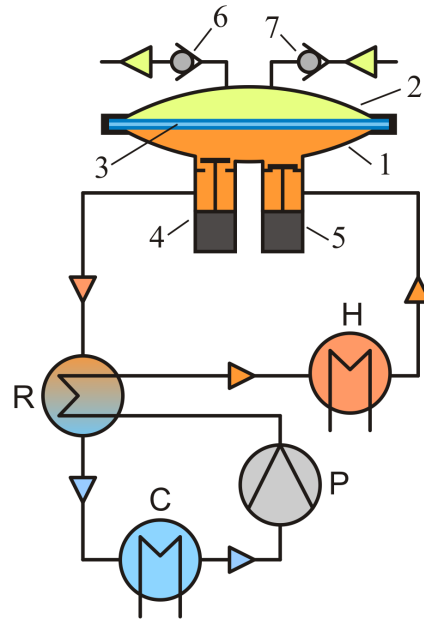


Figure 6. Diaphragm engine-pump

It is worth noting that current research into IE technology shows significant potential for improving engine performance. This can be achieved, for example, by using mixtures of different substances as a working fluid, which can provide a substantial improvement in regeneration [34].

The developed IE engine-pump could be integrated into the ORC unit of the CHEST system [27], for which it was developed as a high-pressure feed pump. Using a differential piston arrangement (a combination of two pistons with different diameters), the IE engine-pump can deliver literally any pressure of the pumped liquid. This allows the engine-pump to be used for high-pressure applications such as heat driven water desalination, oil hydraulic power unit etc. In particular, it can serve as a low-grade heat driven pump for pumping any liquid in the CHEST system.

Since the new engine design is easily scalable up to several MW it can be a very convenient and efficient platform for many industrial applications, especially for low temperature heat (< 100 °C) revalorization at low power range (< 500 kW) where other known technologies are not economic. Thus low-grade solar, geothermal energy and waste heat with temperature above 30 °C can be involved into various energy conversion processes.

Acknowledgements

This project has received funding from the European Union's Horizon 2020 research and innovation programme under grant agreement No 764042. This presentation reflects only the authors' views and neither Agency nor the Commission are responsible for any use that may be made of the information contained therein. 

We thank Benno Knaken, Johan Agterhorst and Ronald Borst (from the High Pressure Laboratory of the University of Twente) for their skilled support during the commissioning of the experimental setup.

References

- [1] B. Nesbitt, *Handbook of Pumps and Pumping*, 1st Edition, Elsevier Science, 2006.
- [2] "Assessment of the Market for Compressed Air Efficiency Services," US department of Energy, Report prepared for Oak Ridge National laboratory and Lawrence Berkeley National laboratory by Xenergy Inc, [Online]. Available: <https://www.energy.gov/sites/prod/files/2014/05/f16/newma>.
- [3] R. Saidur, N. Rahim and M. Hasanuzzaman, "A review on compressed-air energy use and energy savings," *Renewable and Sustainable Energy Reviews*, vol. 14, p. 1135–1153, 2010.
- [4] "Where does our electricity come from?," World Nuclear Association, [Online]. Available: <https://www.world-nuclear.org/nuclear-essentials/where-does-our-electricity-come-from.aspx>.
- [5] C. Forman, I. Muritala, R. Pardemann and B. Meyer, "Estimating the global waste heat potential," *Renew. Sustain. Energy Rev.*, vol. 57, no. May, p. 1568–1579, May 2016.
- [6] T. Tartière and M. Astolfi, "A World Overview of the Organic Rankine Cycle Market," *Energy Procedia*, vol. 129, no. September, pp. 2-9, 2017.
- [7] "Q3 2017: global power markets at a glance," [Online]. Available: <https://www.power-technology.com/comment/q3-2017-global-power-markets-glance/>.
- [8] S. Quoilin, M. Van Den Broek, S. Declaye, P. Dewallef and V. Lemort, "Techno-economic survey of Organic Rankine Cycle (ORC) systems," *Renewable and Sustainable Energy Reviews*, vol. 22, no. June, pp. 168-186, 2013.
- [9] L. Tocchi, T. Pal, I. Pesmazoglou and B. Franchetti, " Small Scale Organic Rankine Cycle (ORC): A Techno-Economic Review. *Energies* . <https://doi.org/10.3390/en10040413>," *Energies*, vol. 10, p. 413, 2017.
- [10] S. Lemmens, *A perspective on cost and cost estimation techniques for organic Rankine cycle systems; 3rd International Seminar on ORC Power Systems, October 12-14, Brussels, Belgium, 2015*.
- [11] M. Glushenkov, A. Kronberg, T. Knoke and E. Kenig, " Isobaric Expansion Engines: New opportunities in energy conversion for heat engines, pumps and compressors," *Energies* , vol. 1, no. 11, pp. 154-175, 2018.
- [12] B. Van der Kooij, *The Invention of the Steam Engine*, Delft: University of Technology. Delft., 2015.
- [13] A. Delgado-Torres, "Solar thermal heat engines for water pumping: An update," *Renewable and Sustainable Energy Reviews*, vol. 13, no. 2, pp. 462-472, 2009.
- [14] A. Date and A. Akbarzadeh, "Theoretical study of a new thermodynamic power cycle for thermal water pumping application and its prospects when coupled to a solar pond," *Applied Thermal Engineering*, vol. 58, no. 1–2, pp. 511-521, 2013.
- [15] O. A. Oyewunmi, C. J. W. Kirmse, A. J. Haslam, E. A. Müller and C. N. Markides, "Working-fluid selection and performance investigation of a two-phase single-reciprocating-piston heat-conversion engine," *Applied Energy*, vol. 186, p. 376–395, 2017.
- [16] C. J. W. Kirmse, O. A. Oyewunmi, A. I. Taleb, A. J. Haslam and C. N. Markides, "A two-phase single-reciprocating-piston heat conversion engine: Non-linear dynamic modelling," *Applied Energy*, vol. 186, p. 359–375, 2017.

- [17] M. Glushenkov, R. Bhosale, A. Kumar, F. AlMomani and A. Kronberg, "Heat powered water pump for reverse osmosis desalination.," in *Materials for Energy, Efficiency and Sustainability: TechConnect Briefs*, TechConnect.org, ISBN 978-0-9975-1171-0, 2016, pp. 201-204.
- [18] R. Mankbadi and S. Ayad, "Small-scale solar pumping: the technology," *Energy conversion and management*, vol. 28, no. 2, pp. 171-184, 1988.
- [19] Y. W. Wong and K. Sumathy, "Solar water pumping systems: a review," *Renewable and Sustainable Energy Reviews*, vol. 3, p. 185–217, 1999.
- [20] A. Date, S. Ghaisas, A. Date and A. Akbarzadeh, "Investigating the prospects of using novel thermal power pump cycle coupled with reverse osmosis system for water desalination," in *Proceedings of the 3rd International Conference on Environment Energy and Biotechnology, 18–19 December 2014*, Bangkok, Thailand, 2014.
- [21] J. Nihill, M. Leary and A. A. Date, "A novel approach to low temperature thermal reverse osmosis desalination," *Procedia Technology*, vol. 20, pp. 144-148, 2015.
- [22] O. Igobo and D. P.A., "Low-temperature organic Rankine cycle engine with isothermal expansion for use in desalination," *Desalin. Water Treat.*, vol. 55, pp. 3694-3703, 2015.
- [23] O. Igobo and P. Davies, "Isothermal Organic Rankine Cycle (ORC) driving Reverse Osmosis (RO) desalination: Experimental investigation and case study using R245fa working fluid," *Applied Thermal Engineering*, vol. 136, no. 25 May, pp. 740-746, 2018.
- [24] J. Nihill, A. Date, V. J and S. Jadkar, "Experimental investigation of the thermal power pump cycle – Proof of concept," *Applied Thermal Engineering*, vol. 134, pp. 182-193, 2018.
- [25] P. Godart, "Design and simulation of a heat-driven direct reverse osmosis device for seawater desalination powered by solar thermal energy," *Applied Energy*, vol. 284, no. 15, p. 116039, 2021.
- [26] M. Glushenkov, A. Kronberg, T. Knoke and E. Y. Kenig, "Heat Driven Pump for Reverse Osmosis Desalination," *Applied Energy*, no. Will be published, 2021.
- [27] "COMPRESSED HEAT ENERGY STORAGE FOR ENERGY FROM RENEWABLE SOURCES," [Online]. Available: <https://www.chester-project.eu/>.
- [28] T. Weller, M. Johnson, F. Trebilcock, S. Lecompte and D. Bauer, "Design, build and initial testing of a novel energy management system," in *Heat Powered Cycles Conference 2021*, Bilbao, 19 - 22 September 2021.
- [29] SWEP, "Braze plate heat exchangers," [Online]. Available: www.swept.net. [Accessed 23 02 2021].
- [30] "IE engine-pump in ECTs laboratory," [Online]. Available: <https://www.chester-project.eu/news/ie-engine-pump-in-ects-laboratory-video>.
- [31] "Swagelok," [Online]. Available: <https://www.swagelok.com/en/product/valves>.
- [32] A. Kronberg, M. Glushenkov, T. Knoke and E. Y. Kenig, "Theoretical limits on the heat regeneration degree," *International Journal of Heat and Mass Transfer*, vol. 161, no. 11, pp. 1-10, 2020.
- [33] "The utilization of solar heat for elevation of water, Scientific American," vol. 53, no. 14, p. 214, 3 October 1885.
- [34] S. Roosjen, M. Glushenkov, A. Kronberg and S. Kersten, "Binary mixtures as working fluids for low temperature waste heat recovery systems with isobaric expansion technology," in *Heat Powered Cycles Conference 2021*, Bilbao, 19 - 22 September 2021.

Numerical study on the influence of different H₂/CH₄ mixtures and air-fuel equivalence ratios in micromix-type burners for industrial boilers

G. Lopez-Ruiz^{1,2}, I. Álava¹, J. M. Blanco²

¹ Ikerlan Technology Research Centre, Basque Research and Technology Alliance (BRTA)
P.º J.M. Arizmendiarieta, 2. 20500 Arrasate/Mondragón, Spain.

²School of Engineering Bilbao, Dept. of Energy Engineering, University of the Basque Country (UPV/EHU)
Plaza Ingeniero Torres Quevedo. Edif.I, Bilbao, 48013, Spain.

*Corresponding author: gontzal.lopez@ikerlan.es

Abstract

The present paper investigates the feasibility of using H₂/CH₄ fuel mixtures in micromix-type burners applied to industrial boilers. The micromix burner concept, characterised by the formation of miniaturised and compact turbulent diffusion flames, was developed for gas turbine hydrogen burners showing low NO_x emissions (below 10 ppm) without flashback risk, which represent the main issues when using pure hydrogen or hydrogen enriched natural gas mixtures as fuel, making it a promising concept to be applied in industrial burners. Since industrial burner operating conditions differ from gas turbine burners, previously studied and well-characterised micromix geometry scaling methodologies were used to scale the burner geometry, taking as basis the fuel mixture properties and re-defined industrial burner operating conditions (different energy densities and air-fuel equivalence ratios). The study was carried out through numerical CFD simulations accounting for detailed chemistry calculations of turbulent micromix flames. The resulting flow, temperature and exhaust emission characteristics for three H₂/CH₄ fuel blends with H₂ content of 90, 75 and 60% respectively were analysed and discussed for air-fuel equivalence ratios at $\lambda = 1.8$ and 1.6 (lower than the well-characterised air-fuel equivalence ratios in micromix gas turbine burners at $\lambda = 2.5$ and closer to current industrial boilers), considering an energy density of 14 MW/m² bar. Results demonstrated that NO_x emissions were maintained below 10 ppm for fuels containing %60 and %75 H₂ at the considered air-fuel equivalence ratio. CO emissions decreased for lower air-fuel equivalence ratios at $\lambda = 1.6$ due to the larger combustion zones and higher oxidation rates of CO across the flame. Finally, a qualitative study was performed for practical design considerations in hydrogen burners, restating the well-established design point of using air-fuel equivalence ratios at $\lambda = 1.3$ in current natural gas burners. The latter comprised a thermodynamic analysis for an ideal reactor control volume, where exergetic efficiencies were evaluated for hydrogen and methane combustion processes respectively. The outcomes demonstrated that due to the lower entropy production (less exergy destruction), H₂/Air ideal reactors at $\lambda \simeq 1.8$ would have the same exergetic efficiency as an ideal reactor of CH₄/Air at $\lambda \simeq 1.3$, reinforcing the idea of using micromix-type burners with higher λ values without loss of exergetic efficiency in industrial boiler burners.

Keywords: Hydrogen combustion, CFD modelling, Exergy analysis, Burner optimisation

Introduction/Background

The quest for energy system decarbonization is becoming a priority, where hydrogen appears as an energy vector to deal with the intermittent and distributed nature of the increasing renewable and non-renewable power plants [1, 2]. Once generated and stored, gaseous hydrogen could be used in several applications. In this context, greenhouse and pollutant emissions from industrial boilers and furnaces could be reduced by using hydrogen as fuel in such combustion devices.

Among others, hydrogen has become a promising alternative to conventional fossil fuels to reduce the overall emissions in different sectors [3, 4]. It can be generated through water electrolysis and other renewable methods using the energy excess in low demand periods and storing it to be afterwards used in different applications, acting as an energy vector. In that sense, several large-scale projects are being carried out across the EU, with several power-to-gas (P2G) pilots [5]. In 2022 a P2G of 100 MW will be connected to the grid in Germany, while 10,000 wind turbines from the North Sea wind farms are also planned to be connected to an artificial island for power-to-hydrogen production after 2030 [6]. Since high-volume hydrogen storage for long time periods still presents technical difficulties [7], distributed hydrogen production and storage arises as an alternative option in contrast to large-scale centralized systems, facilitating the integration of hydrogen technology in smart grids [8, 9, 10].

In this context, the present paper focuses on the use of hydrogen-enriched natural gas mixtures in micromix-type industrial burners. Nonetheless, the combustion characteristics of hydrogen presents several particularities. Among others, hydrogen presents a wide flammability limit in air (4-75 vol%), low ignition energy in air (0.019 mJ), low density (0.0899 kg/m³) and high adiabatic flame temperature (2380 K) [11, 12]. In that sense, non-premixed burners, which are commonly used in industrial boilers and gas turbine combustors, are preferable since they ensure safer operating conditions avoiding flashback and explosion risk when fuelled completely by hydrogen. However, this type of flames react at near stoichiometric conditions, resulting in near-adiabatic flame temperatures and consequent increase in thermal NO_x formation [13, 14, 15]. Therefore, the main technological challenge concerning the design of hydrogen burners is to maintain both a high hydrogen fuel content under safe operating conditions and acceptable levels of thermal NO_x emissions.

In the non-premixed or diffusion combustion technology field related to the industrial sector and considering hydrogen as fuel, the micromix combustion principle (MCP) appears as a novel technology able to minimise the negative impacts derived from the hydrogen combustion. The MCP is based on the jet crossflow principle of miniaturised multiple injectors, where fuel is injected perpendicularly into an air crossflow as shown in Figure 1 (a). Thus, the fast mixing between reactants reduces the residence time of NO_x precursors [16, 17] generating miniaturised turbulent diffusion flames separated each other and stabilised between inner and outer vortices. The main design elements characterising the architecture of a micromix burner prototype with two hydrogen segments are depicted on Figure 1 (b). It must be noted that the number of segments and the final arrangement (linear or concentric rings) depend on the burner integration space and the desired energy density.

The low NO_x MCP was invented in the European Research projects EQHHPP [18] and CRY-OPLANE [19] focused on the greenhouse and pollutant emission reduction in aviation and stationary gas turbines. In recent years, a huge amount of literature has been published on MCP, carried out by Aachen University for Applied Sciences, B&B-AGEMA GmbH and Kawasaki Heavy Industries [20]. More recently, studies carried out by Cranfield University have focused their attention towards hydrogen fuelled MCP aero-engines in the core of ENABLE H2 project [21].

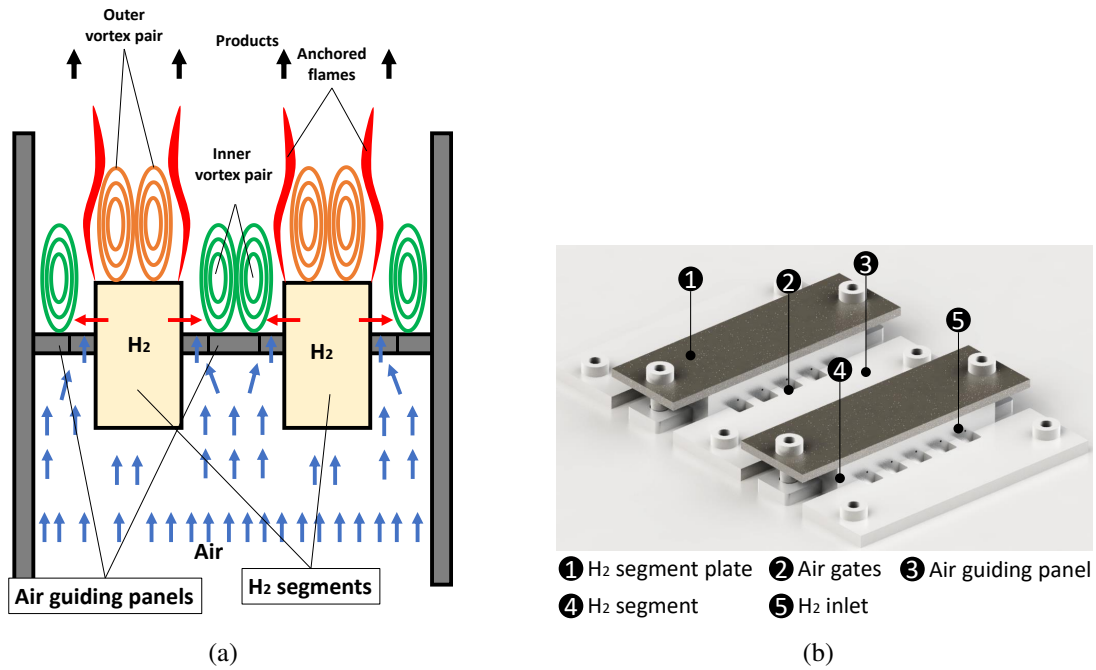


Figure 1. Micromix burner prototype designed in Ikerlan Research Centre

Fuel-flexibility of the micromix gas turbine burners at high air-fuel equivalence ratios (AFR) with $\lambda > 2$ was studied in Ref.[22] focusing on the burner geometry optimisation to keep the main micromix combustion characteristics and low emission levels along with high combustion efficiency for the widest possible range of H_2/CH_4 mixtures.

Thus, the main purpose of the present paper is to analyse the feasibility of extrapolating the MCP for gas turbine burners to industrial boiler burners, using hydrogen enriched natural gas as fuel. For that purpose, a set of numerical simulations were carried out to assess the impact of different operating conditions at lower air-fuel equivalence ratios and higher energy densities.

Objectives and methodology

In contrast to the mentioned well established micromix burner design points, using hydrogen, hydrogen-syngas and hydrogen-methane mixtures [22, 23], the present paper investigates the feasibility of the micromix combustion principle (MCP) for industrial scale boiler burners, which operate with lower air-fuel equivalence ratio (AFR) levels and different power densities [24].

H_2/CH_4 blends with H_2 content of 90, 75, and 60% have been considered respectively based in the Wobbe Index to ensure good interchangeability [22]. Reduced AFR levels have been considered at $\lambda=1.8$ and 1.6, which are closer from current natural gas boiler design points at $\lambda =1.3$ [25]. Furthermore, energy density (ED) was adapted to 14 MW/m² considering atmospheric pressure in contrast to the energy densities studied in previous literature at 40-65 MW/m² considering pressurised combustors with $P_{ref} \sim 6.5$ bar [17, 22].

Thus, in order to achieve the desired energy density value at 14 MW/m² operating with 60% H_2 on CH_4 and lower air-fuel ratios (AFR), the considered burner geometry was previously scaled based on micromix burner scaling methodologies [26, 27]. On the basis of the resulting geometry, the impact of higher hydrogen concentrations on the main micromix combustion characteristics and emission levels will be numerically investigated.

In contrast to conventional natural gas burners, micromix burners would offer not only safe operating conditions without flashback risk and low NO_x emissions when using H_2/CH_4 blends as fuel, but also much shorter flame lengths, leading to smaller combustion chambers and more compact boiler designs. In that sense the main purpose of the present work is to demonstrate that low NO_x values are maintained below 10 ppm for the re-defined operating conditions. Similarly, CO emissions trends will be also analysed.

Finally, the design point of $\lambda = 1.3$ in current natural gas burners was qualitatively addressed from a practical point of view, studying the impact of using higher AFR levels in hydrogen burners. For that purpose exergetic efficiencies were calculated based in system level analysis of ideal reactor control volumes, where hydrogen and methane combustion processes were considered.

Numerical domain

The main characteristics of the computational domain and the selected grid are briefly described in the present section. As shown in Figure 2 (a), a 3D burner slice was used to define the computational domain. Based in previous numerical studies, the domain was simplified considering symmetry flow conditions in both transversal and longitudinal directions, instead of simulating the whole array of micromix flames. Hence, the fluid domain was limited between the plane of symmetry of the half of the hydrogen inlet and the plane of symmetry of the free space between two consecutive flames.

Previous grid independence studies [29] with tetrahedral elements determined that the grid independence for similar geometries can be achieved with 1,300,000 cells. Furthermore, polyhedral grids were used for the numerical studies carried out in Aachen university. Thus, these type of elements present several advantages reducing the number of elements with optimum grid resolutions and lower the overall computational costs [30]. Taking as a reference the results obtained and validated in the mentioned meshes and the benefits of using polyhedral-type elements, they were used for the present domain discretisation as shown in the in Figure 2 (b). The mesh quality was further improved through a gradual mesh refinement during the calculations. The final mesh comprised 1,200,000 cells.

CFD Modelling

The steady three dimensional flow field was obtained by solving the Reynolds-averaged Navier-Stokes equations. Since MCP accounts for several turbulence scales depending on the flow region, the present RANS calculations were performed using the $k - \omega$ SST turbulence model of Menter [31] following the same approach as in the studies carried out in Cranfield University for micromix combustion modelling [32, 33]. This model includes the advantages of the $k - \omega$ model in the inner boundary layer and the benefits of the $k - \epsilon$ model in the outer region. Thus, it is able to capture the scale variability effects along with providing a better representation of the near wall flow physics. In order to capture the flow characteristics in the near wall regions, the grid size for such zones was refined calculating the height and number of thin layers needed to solve the viscous sub-layer and ensure $y^+ \simeq 1$.

The steady transport equations for turbulent kinetic energy k and the specific dissipation rate ω are given in Eq. (1) and (2) respectively.

$$\frac{\partial(\rho u_j k)}{\partial x_j} = P - \beta^* \rho \omega k + \frac{\partial}{\partial x_j} \left[(\mu + \sigma_k \mu_t) \frac{\partial k}{\partial x_j} \right] \quad (1)$$

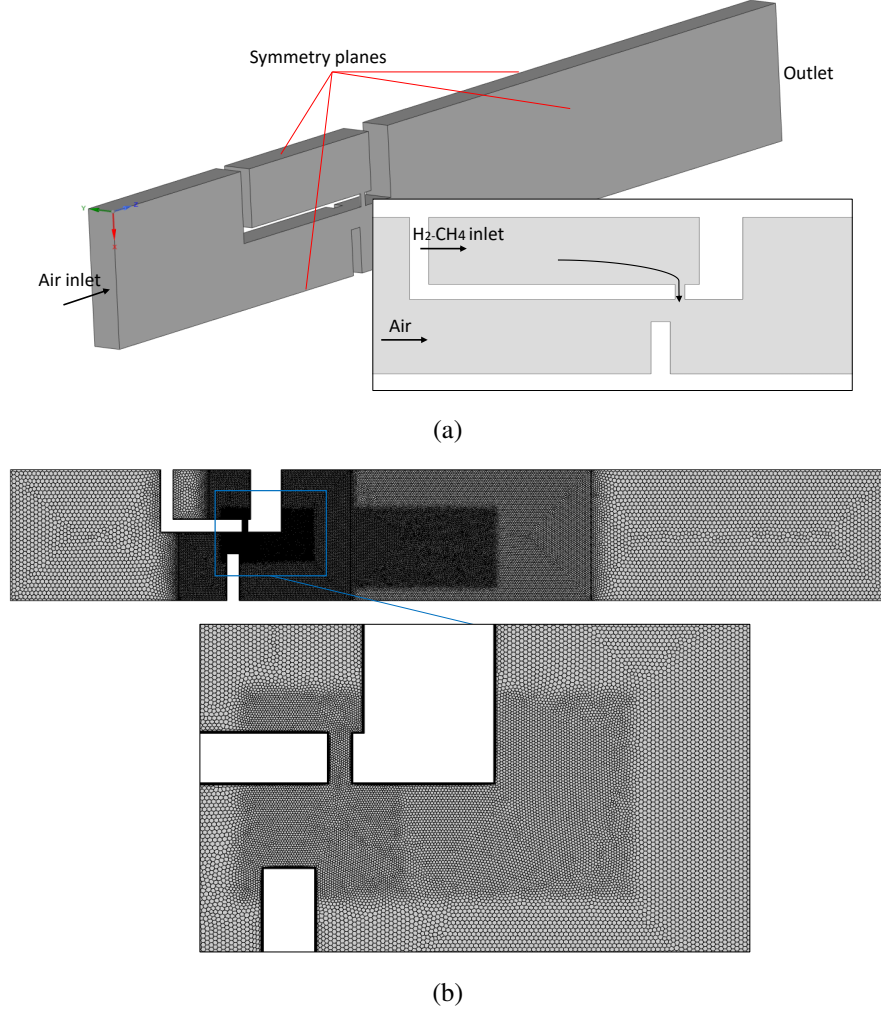


Figure 2. Numerical domain to [28]

$$\frac{\partial(\rho u_j \omega)}{\partial x_j} = \frac{\gamma}{\nu_t} P - \beta \rho \omega^2 + \frac{\partial}{\partial x_j} \left[(\mu + \sigma_\omega \mu_t) \frac{\partial \omega}{\partial x_j} \right] + 2(1 - F_1) \frac{\rho \sigma_{\omega 2}}{\omega} \frac{\partial k}{\partial x_j} \frac{\partial \omega}{\partial x_j} \quad (2)$$

Furthermore, species transport equations including the chemical reaction term and energy conservation equation were also solved considering an incompressible ideal-gas mixture. The reaction source term was calculated through the so-called Eddy Dissipation Concept (EDC) model, which incorporates the influence of finite rate kinetics and the influence of turbulent fluctuations on mean chemical reaction rate. This model is based on the turbulent energy cascade, assuming that the larger eddies lose their energy breaking into smaller eddies. The key assumption in the EDC model is that chemical reactions involved in a turbulence flow take place in those fine scales, which are locally treated as adiabatic, isobaric, Plug Flow Reactor (PFR). Based in the development of Magnussen [34], the mean reaction source term is defined as:

$$\tilde{\omega}_i = \frac{\bar{\rho}(\xi^*)^2}{\tau^*[1 - (\xi^*)^3]} (Y_i^* - \tilde{Y}_i) \quad (3)$$

Where ξ^* and τ^* represent the size of the fine structure and the mean residence time, defined by

means of local viscosity, turbulent kinetic energy and its dissipation rate. Here, Y_i^* represents the species mass fraction calculated from the current value \widetilde{Y}_i by means of the considered reaction mechanism over the time scale τ [35]. The integration of the Arrhenius reaction rates in the fine structures was carried out considering the reaction data from the widely used and validated DRM-22 [36] mechanism, consisting of 24 species and 104 reversible reactions. It must be also noted that ideal-gas-mixing law was used to compute the thermal conductivity and viscosity of the gas mixture. Assuming that the relative mass flux due to molecular diffusion is governed by a Fick's law, mass diffusivity was calculated through the mixture-averaged approach.

Discussion and Results

CFD Results

Temperature contours and velocity streamlines at each AFR level are presented in Figure 3. In order to improve the understanding of the numerical outcomes, results at air-fuel ratios (AFR) $\lambda = 1.6$ and 1.8 were named with "A" and "B" respectively while hydrogen concentrations in the fuel were represented with numbers. Hence, six results will be analysed: A60, A75, A90 and B60, B75 and B90 as indicated in Figure 3. As mentioned, for a given AFR level, higher hydrogen concentrations in the incoming fuel led to a higher fuel jet penetration into the air crossflow. This phenomena is characterised by the momentum flux ratio, which defines the relation between the fuel jet and the air cross-flow momentum, determining the injection depth of the former into the air cross-flow as [17]:

$$r_m = \frac{\rho_{fuel} V_{fuel}^2}{\rho_{Air} V_{Air}^2} = \frac{\dot{m}_{fuel}^2}{\rho_{fuel} A_{jet}} \frac{1}{\rho_{Air} V_{Air}^2} \quad (4)$$

Here the velocity of fuel has been expressed in terms of the inlet mass flow \dot{m}_{fuel} , jet area A_{jet} and fuel density ρ_{fuel} . Accordingly, higher hydrogen concentrations in the fuel reduced its density, increasing the momentum flux ratios and therefore promoting the jet penetration into the cross flow.

As indicated, the fuel jet penetration phenomena was observed in both AFR levels, showing higher vortex temperatures caused by the burning process of the air-fuel mixture in such recirculating zone. This also led to a higher temperatures in the air guiding panel surface that could cause irreversible damages due to the high thermal impact on the burner material [22].

Concerning the nitrogen oxide emissions, numerical results showed that most of the NO_x was produced by the thermal NO_x formation mechanism (more than 95% percent) against the NO_x production by the prompt- NO_x mechanism. It can be see that low NO_x values were maintained below 10 ppm for A60, B60 and B75. In contrast, the higher NO_x concentrations above 10 ppm at A75, A90 may be explained by combination of the post shear layer formation phenomena and the worse mixing in the jet cross-flow zone due to the jet penetration. On the other hand, no shear layer was observed at B90, concluding that the higher NO_x concentrations were caused by the worse mixing. Figure 4 (a) shows that NO_x formation was concentrated in the post shear layer flame zone for A75 and A90, caused by the worse mixing in the jet cross-flow. This led to the combustion of the remaining fuel fraction in such zones, increasing the overall height of the flame and promoting the formation of the post shear layer flame fraction. In contrast to A90, the NO_x fractions for B90 were located in the near flame due to the lack of post shear-layer

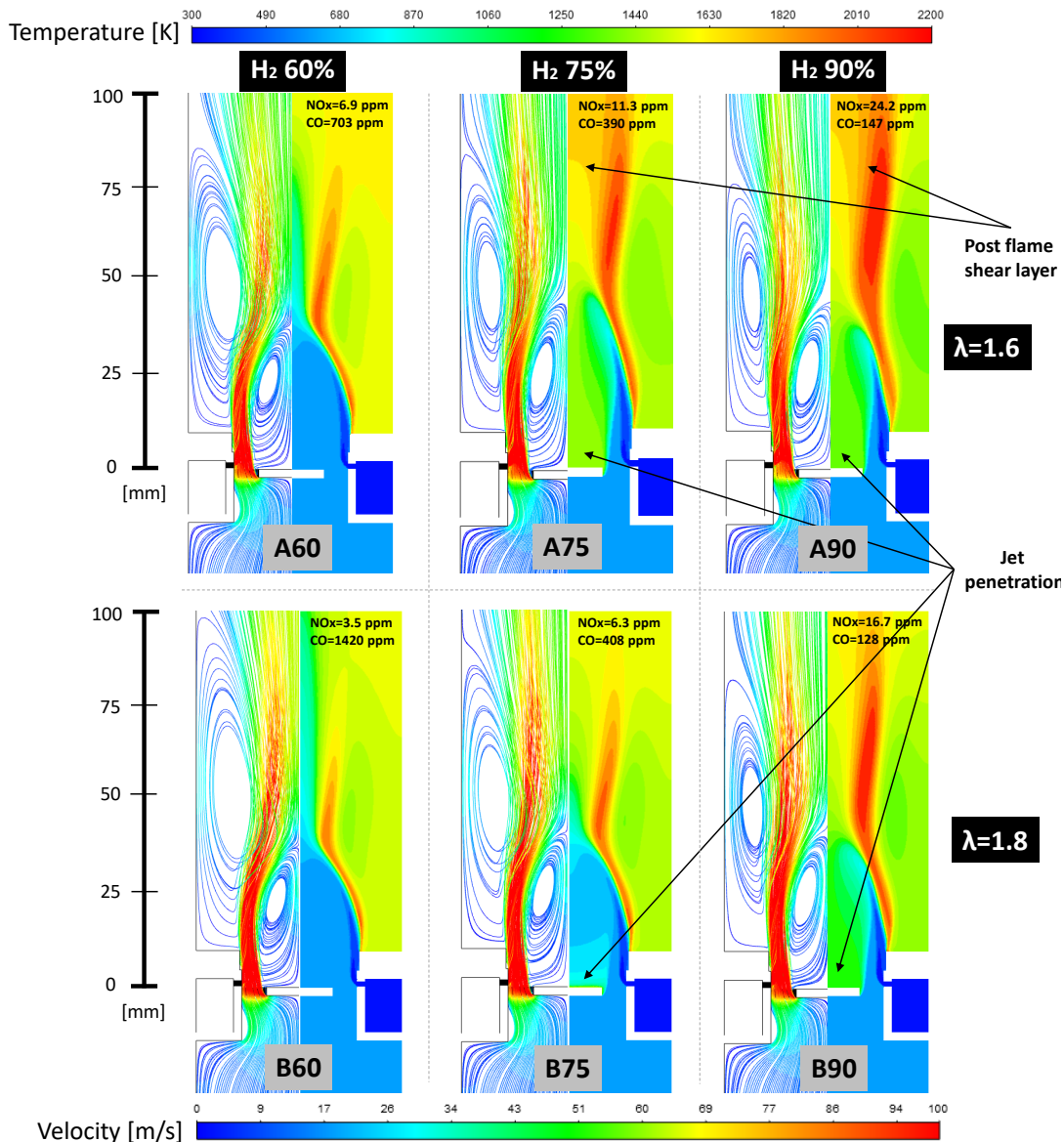


Figure 3. CFD results showing temperature contours and velocity streamlines in each case. NO_x and CO concentrations measured in the domain outlet and measured to 15% O₂ are also included

formation, which may be attributed to the higher air dilution and lower combustion product temperatures at $\lambda = 1.8$.

The CO concentrations presented relatively high values and increased significantly for A60 and B60 due to the higher methane concentration in the fuel. The increment at 60% H₂ was specially higher at $\lambda = 1.8$ (B60). Carbon monoxide is commonly produced when combustion reactions are not fully completed, mostly due to lack of air or low mixing [37]. This may lead to think that higher AFR levels might induce lower CO formation due to an increasing oxygen presence that could oxidise the intermediate CO. However, lower AFR led to a larger combustion zones (in case of higher hydrogen concentrations a post flame shear layer appeared). This can be observed through the temperature contours at A60 and B60. As concluded by [22], the enlarged combustion zone favour the CO oxidation to CO₂, reducing the overall CO emissions. This effect can be appreciated in Figure 4 (b), where CO and CO₂ concentrations for A60 and B60 are compared, showing higher CO conversion across the reacting zone at A60. However,

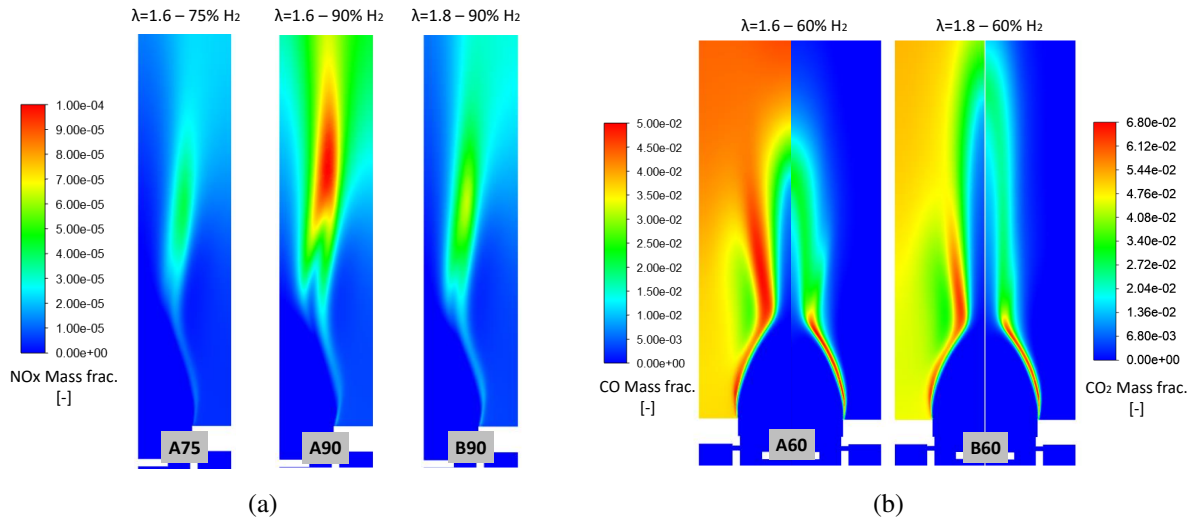


Figure 4. CFD results for: (a) NO_x formation rates and (b) CO₂ and CO mass fractions

this effect had a negative impact on NO_x formation, prompted by the higher temperatures and residence times of the NO_x precursors. Thus, further optimisations should be considered to deal with the combination of this phenomena in order to reach a compromise.

Hence, the numerical results showed that the present burner geometry would be able to work without fuel jet penetration at each AFR level and hydrogen concentrations of 60%, demonstrating that the initial burner geometry dimensions would determine the fuel flexibility of the micromix burner. In the light of the present results, the employed burner geometry showed a low fuel flexibility due to its high impact on the momentum flux ratios. Likewise, NO_x emissions were doubled at $\lambda = 1.6$ for the considered fuel mixtures. Contrarily, CO emissions were halved at $\lambda = 1.6$ for hydrogen content of 60. As observed, the higher the hydrogen content the lower the impact on CO reduction when decreasing AFR (CO emissions increased from B90 to A90). Thus, reducing the AFR could be a good strategy to further reduce the CO emissions at H₂-60% or lower concentrations, as long as the limit of the low NO_x is not exceeded. However, this would reduce the fuel flexibility.

It can be concluded that the discussed numerical outcomes served as an initial baseline study, showing a potential for further burner optimisations for higher fuel flexibility together with low NO_x and CO concentrations. This was already demonstrated in Ref.[22], where geometry optimisations were carried out in order to increase the fuel-flexibility of a micromix burner.

Exergetic analysis for practical design considerations

In contrast to current natural gas burners, which operate at low AFR ($\lambda \approx 1.3$) being a well-established design point, micromix burners are characterised by higher AFR levels to provide a certain air excess able to cool down and dilute the combustion products in the recirculating vortices, avoiding a flame merging. Accordingly, it can be said that this is one of the main differences between conventional natural gas boiler burners and micromix hydrogen burners, which may lead to the loss of the overall system efficiency with respect to current natural gas burners.

Concerning this fact, the present section aims to qualitatively analyse the effect of AFR from a practical standpoint, analysing its influence on the exergetic efficiency of hydrogen and

methane combustion processes respectively, which quantifies the impact of the highly irreversible combustion reactions when using both fuels. The chemical exergy is defined as the maximum theoretical work that could be developed by the combined system (formed by an environment and an amount of fuel). Therefore, the exergetic efficiency represents a measure for the system irreversibilities (entropy production in the considered control volume) with respect to the maximum theoretical work capacity available on the fuel (chemical exergy of the fuel) as defined in Equation 7. It is worth to mention that for the present comparative analysis additional irreversibility sources present in real combustion processes such as heat conduction, mass diffusion, viscous dissipation or entropy diffusion were not considered due to their lower relevance compared to the irreversibilities caused by the chemical reaction [38].

The calculation approach considered the combustion thermodynamics of methane/Air and hydrogen/Air reactions for ideal reactor systems [39]. For that purpose, enthalpy and entropy balances from Equations (5) and (6) were solved in an insulated reactor control volume, which was defined as a black-box system represented in Figure 5 (a).

$$\frac{\dot{Q}_{cv}}{\dot{n}_F} - \frac{\dot{W}_{cv}}{\dot{n}_F} = \sum_P n_e (h_f + \Delta h)_e - \sum_R n_i (h_f + \Delta h)_i \quad (5)$$

$$\sum_j \frac{\dot{Q}_{cv}}{T_j} = \sum_e \dot{m}_e s_e - \sum_i \dot{m}_i s_i - \dot{\sigma}_{cv} \quad (6)$$

Where i and e denote the incoming fuel and air streams and the exiting combustion products respectively. h_f and Δh represent the formation enthalpy and the change in enthalpy from the temperature $T_{ref}=298$ K to the gas temperature T . The respective coefficients of the reaction equations shown in Figure 5 (a) are represented by n , giving the moles of reactants and products per mole of fuel. Similarly, s_i and s_e represent the incoming and exiting specific entropies, while $\dot{\sigma}_{cv}$ is the rate of entropy production in the control volume. Assuming that the considered control volume was perfectly insulated, the first term in both equations is equal to zero since no heat losses were considered from the system.

Thus, the calculation process started by solving the Equation (5) for different AFR levels, solving the temperature of the combustion products. Afterwards, Equation (5) was evaluated at different AFR levels using the previously obtained product temperatures, obtaining the entropy formation rate $\dot{\sigma}_{cv}$. Finally, considering the standard chemical exergy values (e_{ch}) of hydrogen and methane fuels (236,100 and 831,650 kJ/kmol respectively) [40], the exergetic efficiency was evaluated as:

$$\eta_{exg} = 1 - \frac{\dot{E}_d}{\dot{E}_f} = 1 - \frac{T_0 \cdot \dot{\sigma}_{cv}}{\dot{m}_f \cdot e_{ch}} \quad (7)$$

Where \dot{E}_d and \dot{E}_f represent the exergy destruction flux and the exergetic flux of the incoming fuel respectively. The former is defined as the product of the environment temperature T_0 and the previously calculated rate of entropy production in the control volume $\dot{\sigma}_{cv}$. The latter is defined as the product between the incoming mass flow rate and the standard chemical exergy (in kJ/kg). The described calculation process was repeated considering hydrogen and methane as inlet fuels. The equations were solved by means of the commercial Engineering Equation Solver (EES) software package [41].

The resulting outcomes are shown in Figure 5 (b). The calculated exergetic efficiencies demonstrated that for a given thermal power output, hydrogen combustion process at $\lambda \simeq 1.8$, would have the same exergetic efficiency as in the methane combustion process at $\lambda = 1.3$, reinforcing the idea of working at higher AFR levels in micromix burners. From Figure 5 (b) it can be concluded that the lower entropy destruction (less irreversibilities) in the hydrogen/air combustion process led to a higher exergetic efficiencies (about 9% higher) in the whole AFR range.

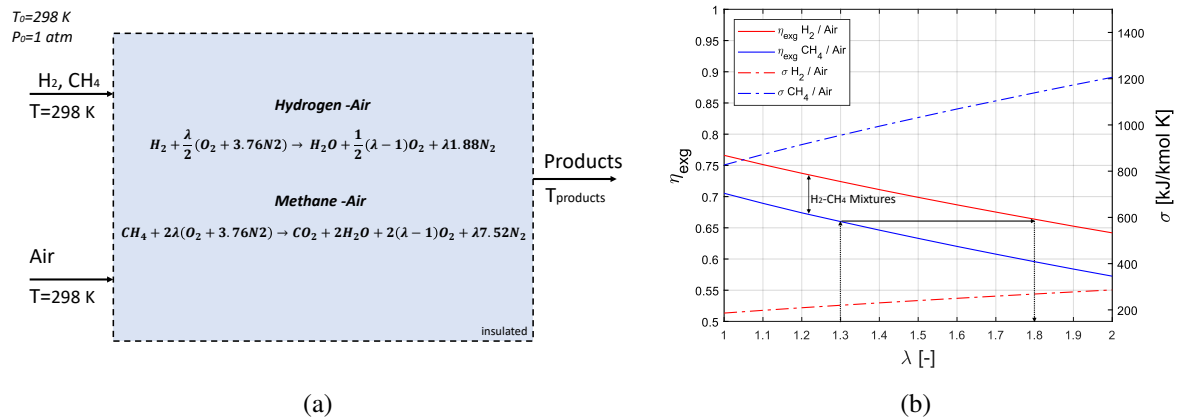


Figure 5. Left: Exergetic efficiencies of micromix burner simulations. Right: Exergetic efficiencies and entropy generation rates for insulated ideal reactors considering H₂ and CH₄ combustion thermodynamics.

As indicated, the exergetic efficiencies for fuel mixtures with 90%, 75% and 60% H₂ concentrations in CH₄, would be located between both results curves. It can be concluded that higher hydrogen concentrations in the incoming fuel are beneficial for micromix burners, allowing higher AFR levels with the consecutive emission reduction as demonstrated in Figure 3.

Summary/Conclusions

The present study lays the groundwork for future research into the usage of H₂/CH₄ mixtures in micromix burners for industrial boilers. CFD simulations for varying hydrogen concentrations (90, 75 and 60 %) and air-fuel ratios ($\lambda = 1.8$ and 1.6) showed that jet penetration occurs for hydrogen concentrations above 60 % in the fuel. Furthermore NO_x formation increased significantly for $\lambda = 1.6$ due to the post-shear layer NO_x formation phenomena. Concerning the CO emissions, results at $\lambda = 1.6$ showed lower concentrations than for $\lambda = 1.8$ at 60%/H₂, concluding that the larger combustion zones at $\lambda = 1.6$ favoured the CO oxidation process across the flame. This CO reduction effect was reduced at 75%/H₂ and dumped at 90%/H₂. Hence, reducing the AFR could be a good strategy to further reduce the CO emissions at H₂-60% or lower concentrations, as long as the limit of the low NO_x is not exceeded. Nevertheless, this would also reduce the fuel flexibility to work with higher hydrogen content in the fuel. Accordingly, it was concluded that further burner optimisation is needed to reduce the CO emissions keeping low NO_x concentrations in a wider range of H₂ concentrations.

Concerning the qualitative analysis for H₂/Air and CH₄/Air combustion processes in ideal reactor control volumes, results showed higher efficiencies and lower entropy generation in H₂/Air combustion for different AFR levels. The results revealed that H₂/Air ideal reactors at $\lambda \simeq 1.8$ would have the same exergetic efficiency as an ideal reactor of CH₄/Air $\lambda \simeq 1.3$. Thus, the use of higher AFR in micromix burners with respect to the well-characterised design points at $\lambda = 1.3$ in current natural gas burners, would not be a penalty from exergetic efficiency point of view if fuels with high hydrogen content are employed.

The paper qualitatively shows that exergy analysis could be a useful tool for future comparative studies between natural gas and hydrogen burners. For that purpose, further numerical and experimental studies are also needed to determine the exergetic efficiency of the whole system, taking into account the air fan, air pre-heater, burner, combustion chamber and heat exchanger. Similarly, further entropy production mechanisms such as the heat conduction, mass diffusion, viscous dissipation or entropy diffusion, involved in the combustion physics of real flames should be also considered.

References

- [1] Zainul Abidin, Ali Zafaranloo, Ahmad Rafiee, Walter Mérida, Wojciech Lipiński, and Kaveh R. Khalilpour. Hydrogen as an energy vector. *Renewable and Sustainable Energy Reviews*, 120(November 2019), 2020.
- [2] Christopher J. Quarton and Sheila Samsatli. Power-to-gas for injection into the gas grid: What can we learn from real-life projects, economic assessments and systems modelling? *Renewable and Sustainable Energy Reviews*, 98(August):302–316, 2018.
- [3] Mark Z. Jacobson. Clean grids with current technology. *Nature Climate Change*, 6:441–442, 2016.
- [4] P.E. Miranda. *Science and Engineering of Hydrogen-Based Energy Technologies: Hydrogen Production and Practical Applications in Energy Generation*. Elsevier Science, 2018.
- [5] A review of technical advances, barriers, and solutions in the power to hydrogen (p2h) roadmap. *Engineering*, 6(12):1364–1380, 2020.
- [6] Hydrogen Roadmap Europe. Technical report, Fuel Cells and Hydrogen 2 Joint Undertaking, 2019.
- [7] Large-scale compressed hydrogen storage as part of renewable electricity storage systems. *International Journal of Hydrogen Energy*, 2021.
- [8] Jinhui Liu, Zhanbo Xu, Jiang Wu, Kun Liu, and Xiaohong Guan. Optimal planning of distributed hydrogen-based multi-energy systems. *Applied Energy*, 281:116107, 2021.
- [9] J M Andújar, F Segura, and M Á Martínez. A renewable sources-based smart grid using hydrogen as backup. Optimization criteria for the energy management. In *2017 Saudi Arabia Smart Grid (SASG)*, pages 1–8, 2017.
- [10] Rong-Heng Lin, Ying-Ying Zhao, and Bu-Dan Wu. Toward a hydrogen society: Hydrogen and smart grid integration. *International Journal of Hydrogen Energy*, 45(39):20164–20175, 2020.
- [11] Boris E. Gelfand, Mikhail V. Silnikov, Sergey P. Medvedev, and Sergey V. Khomik. *Thermo-Gas Dynamics of Hydrogen Combustion and Explosion*. Springer, 2012.
- [12] J Warnatz, U Maas, R W Dibble, and R W Dibble. *Combustion: Physical and Chemical Fundamentals, Modelling and Simulation, Experiments, Pollutant Formation*. Springer, 2001.
- [13] G. Lopez-Ruiz, A. R. Fernandez-Akarregi, L. Diaz, I. Urresti, I. Alava, and J. M. Blanco. Numerical study of a laminar hydrogen diffusion flame based on the non-premixed finite-rate chemistry model; thermal NO_x assessment. *International Journal of Hydrogen Energy*, 44(36), 2019.
- [14] S McAllister, J Y Chen, and A C Fernandez-Pello. *Fundamentals of Combustion Processes*. Mechanical Engineering Series. Springer New York, 2011.
- [15] G Lopez-Ruiz, I Alava, I Urresti, J M Blanco, and B Naud. Experimental and numerical study of NO_x formation in a domestic H₂/air coaxial burner at low Reynolds number. *Energy*, 221:119768, 2021.

- [16] A. Haj Ayed, K. Kusterer, H. H.W. Funke, J. Keinz, and D. Bohn. CFD based exploration of the dry-low-NO_x hydrogen micromix combustion technology at increased energy densities. *Propulsion and Power Research*, 6(1):15–24, 2017.
- [17] H. H.W. Funke, N. Beckmann, and S. Abanteriba. An overview on dry low NO_x micromix combustor development for hydrogen-rich gas turbine applications. *International Journal of Hydrogen Energy*, 44(13):6978–6990, 2019.
- [18] J. Shum, F. and Ziemann. Potential use of hydrogen in air propulsion, Euro-Québec Hydro-Hydrogen Pilot Project (EQHHPP), European Union, Contract No. 4541-91-11 EL ISP PC, Final Report, 1996.
- [19] A. Westenberger. Liquid Hydrogen Fuelled Aircraft – System Analysis, CRYOPLANE, Final Technical Report No. GRD1-1999-10014, to the European Commission, 2003.
- [20] Nurettin Tekin, Mitsugu Ashikaga, Atsushi Horikawa, and Dr.-Ing. Harald Funke. Enhancement of fuel flexibility of industrial gas turbines by development of innovative hydrogen combustion systems. 2019.
- [21] CORDIS — European commission. (2018). Enabling cryogenic Hydrogen based CO₂ free air transport (ENABLE H₂) — Projects — H2020 — CORDIS — European commission.
- [22] N. Beckmann. *Characterization of the Hydrogen-Dry-Low-NO_x-Micromix- Combustion Principle for Hydrogen-Methane Fuel Mixtures*. PhD thesis, 2019.
- [23] H H Funke, N Beckmann, J Keinz, and S Abanteriba. Comparison of Numerical Combustion Models for Hydrogen and Hydrogen-Rich Syngas Applied for Dry-Low-NO_x-Micromix-Combustion. *Proceedings of ASME Turbo Expo*, 2016.
- [24] J. Chacón, J. M. Sala, and J. M. Blanco. Investigation on the design and optimization of a low NO_x - CO emission burner both experimentally and through computational fluid dynamics (CFD) simulations. *Energy and Fuels*, 21(1):42–58, 2007.
- [25] C E B Jr. *Industrial Burners Handbook*. Industrial Combustion. CRC Press, 2003.
- [26] H. H.W. Funke, K. Kusterer, A. Haj Ayed, M. Kazari, J. Kitajima, A. Horikawa, and K. Okada. Experimental and numerical study on optimizing the DLN micromix hydrogen combustor principle for industrial gas turbine applications. *Proceedings of the ASME Turbo Expo*, 2015.
- [27] A. Haj Ayed, K. Kusterer, H. H.W. Funke, J. Keinz, M. Kazari, J. Kitajima, A. Horikawa, K. Okada, and D. Bohn. Numerical Study on Increased Energy Density for the Dln Micromix Hydrogen Combustion Principle. *Proceedings of the ASME Turbo Expo*, 2014.
- [28] X. Sun and V. Sethi. Enabling Cryogenic Hydrogen-Based CO₂-free Air Transport (ENABLEH₂) – Micromix Combustion Research, 2019.
- [29] R. B. Abdallah. NO_x Micromix Hydrogen Combustion System: -Preliminary Design and Performance Assesment of Novel Injectors Using RANS and LES CFD. Technical report, Cranfield University, 2017.
- [30] Marcin Sosnowski, Jaroslaw Krzywanski, and Renata Gnatowska. Polyhedral meshing as an innovative approach to computational domain discretization of a cyclone in a fluidized bed CLC unit. *E3S Web of Conferences*, 14, 2017.
- [31] F. R. Menter. Two-equation eddy-viscosity turbulence models for engineering applications. *AIAA Journal*, 32(8):1598–1605, 1994.
- [32] G. Babazzi, Pierre Q. Gauthier, P. Agarwal, J. McClure, and V. Sethi. NO_x emissions predictions for a hydrogen micromix combustion system. *Proceedings of the ASME Turbo Expo*, 3, 2019.
- [33] Parash Agarwal, Xiaoxiao Sun, Pierre Q. Gauthier, and Vishal Sethi. Injector design space exploration for an ultra-low NO_x hydrogen micromix combustion system. *Proceedings of the ASME Turbo Expo*, 3, 2019.

- [34] BF Bjørn F. Magnussen. The Eddy Dissipation Concept: A Bridge Between Science and Technology. *ECCOMAS Thematic Conference on Computational Combustion*, pages 1–25, 2005.
- [35] Ashoke De, Ernst Oldenhof, Pratap Sathiah, and D. Roekaerts. Numerical simulation of delft-jet-in-hot-coflow (djhc) flames using the eddy dissipation concept model for turbulence–chemistry interaction. *Flow, Turbulence and Combustion*, 87:537–567, 12 2011.
- [36] A. Kazakov and M. Frenklach. Technical report, <http://combustion.berkeley.edu/drm/>.
- [37] Esa Kari Vakkilainen. 2 - solid biofuels and combustion. In Esa Kari Vakkilainen, editor, *Steam Generation from Biomass*, pages 18–56. Butterworth-Heinemann, 2017.
- [38] K. Nishida, T. Takagi, and S. Kinoshita. Analysis of entropy generation and exergy loss during combustion. *Proceedings of the Combustion Institute*, 29(1):869–874, 2002.
- [39] Michael J. Moran, Howard N. Shapiro, Daisie D. Boettner, and B. Margaret. *Fundamentals of Engineering Thermodynamics*. John Wiley & Sons, New York, 2014.
- [40] J Szargut, D R Morris, and F R Steward. Exergy analysis of thermal, chemical, and metallurgical processes.
- [41] Klein, S.A., EES – Engineering Equation Solver, 2020 F-Chart Software, <http://fchart.com>.

Effect of residual air on dynamics of temperature- and pressure-initiated adsorption cycles for heat transformation

I. Girnik^{1*} and Y. Aristov¹

¹Boreskov Institute of Catalysis, Lavrentiev ave., 5, Novosibirsk, 630090, Russia

*Corresponding author: girnik@catalysis.ru

Abstract

It is well known that the presence of residual gas can significantly slow down the adsorption stage of heat transformation cycles. This work addresses the dynamic effect of residual air for two ways of adsorption initiation: by a change of either pressure (PI) or temperature (TI). The effect was studied for the working pairs "AQSOA FAM-ZO2 – water" and "LiCl/(silica gel) – methanol" proposed for adsorption heat transformation (AHT). The residual air pressure ΔP_{air} was varied from 0 to 5 mbar.

The main finding of this study is that the PI adsorption is less sensitive to the presence of residual air than the TI adsorption. This is especially true at a low partial air pressure ΔP_{air} . For instance, at $\Delta P_{\text{air}} \leq 0.5$ mbar, residual air has little or no effect on the PI adsorption dynamics as compared to the TI one. A qualitative explanation of this finding is proposed. Thereby, closed AHT cycles based on the PI process are more robust and resistant against the presence of residual air that is a significant practical advantage.

Keywords: Adsorption dynamics, Residual air, Pressure initiation, Temperature initiation

Introduction/Background

Adsorption heat transformation (AHT) is an environmentally friendly way of converting and storing low-temperature heat from various sources, which attracts increasing attention [1, 2, 3]. Indeed, AHT is based on reversible transitions between two adsorbent states with small and large adsorbate concentrations (weak w_1 and rich w_2 isosteres in Fig 1). The transition can be either isobaric, initiated by temperature change, TI (1-2 in Fig 1a), or isothermal, caused by drop/jump of pressure over adsorbent, PI (1-3 in Fig 1a; 1-4, 2-3 in Fig 1b). TI cycles are implemented in common AHT units driven by a temperature difference between the ambient and an external heat source [4]. PI cycles have mainly been proposed for adsorptive heat amplification, e.g., in a novel cycle "Heat from Cold" (HeCol) [5].

The useful power of *closed* AHT systems mainly depends on the adsorption dynamics, which is determined by many factors [6]. One of the inhibiting factors is the presence of non-adsorbable gases inside the AHT unit. The water adsorption from such binary mixtures can produce extra heat and mass transfer resistances, which can be quite large [7]. Commonly, the non-adsorbable gas is the air that can present inside the AHT unit due to leakage, desorption, or insufficient evacuation. Previous studies showed that even traces of residual air (ca. $\Delta P_{\text{air}} = 0.02$ mbar) could slow down the TI adsorption of water on flat adsorbent beds (monolayer configuration of silica Fuji RD, AQSOA FAM-ZO2 [8] and composite SWS-1L [9]) and representative pieces of real "adsorber – heat exchanger" [10]. Slowing down of the adsorption was attributed to the gradual accumulation of air near the external adsorbent surface caused by a Stephan flux [11]. Because of this, "air pillow" adsorption became controlled by the diffusion of water molecules through this air layer. This effect was studied by mathematical modelling of water adsorption on the composite "CaCl₂/silica gel" [12].

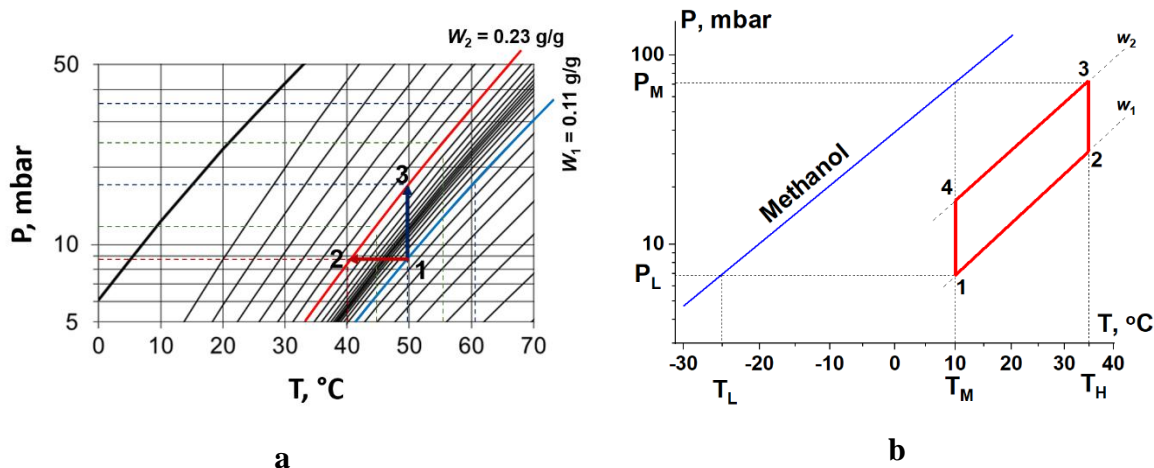


Fig 1. a - P-T diagram of TI and PI adsorption runs for the "FAM-ZO2 – water" pair; b – P-T diagram of HeCol cycle for the " LiCl/silica – methanol" pair.

The main novelty of this work is that the effect of residual air on the adsorption dynamics is studied for pressure initiation. Besides, both water and methanol are used as an adsorptive.

Experimental

Adsorption dynamics was investigated by LPJ and LTJ methods comprehensively described in [13]. The experimental set-up contained three main parts: a measuring cell (volume $V_{MC} = 0.14 \cdot 10^{-3} \text{ m}^3$), vapour vessel (volume $V_{VV} = 30.5 \cdot 10^{-3} \text{ m}^3$) and evaporator filled with liquid water (Fig 2a). Loose grains of FAM-ZO2 ($m_{ad} = 0.31 \text{ g}$) or LiCl(26.5%)/silica ($m_{ad} = 0.33 \text{ g}$) were placed on an isothermal surface of the metal plate as two flat layers (Fig 2b). The plate temperature was adjusted with the accuracy $\pm 0.1^\circ\text{C}$ using a heat carrier circuit coupled by three-way valves 3WV to either thermal bath 1 or 2 (Fig 2a).

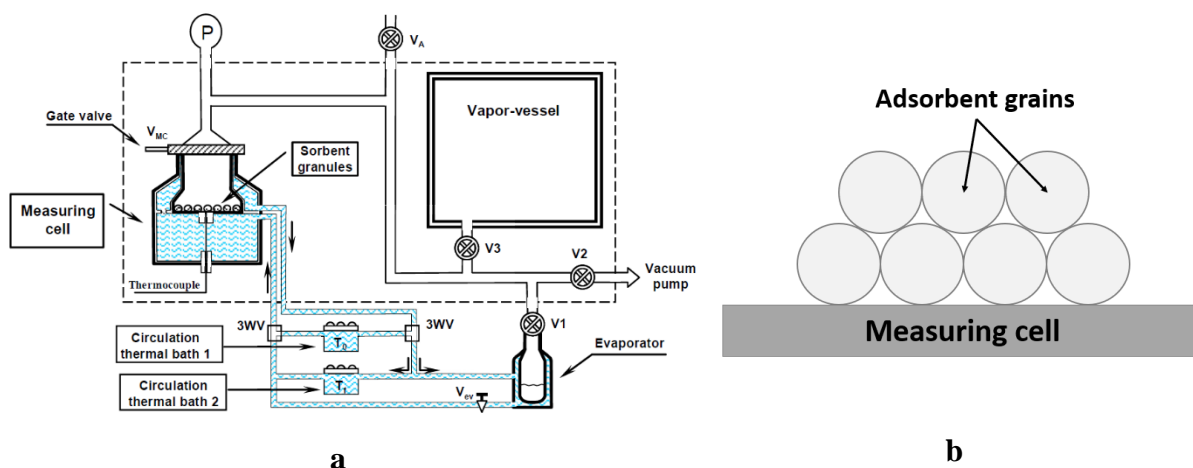


Fig 2. Schematics of the V-LTJ/LPJ experimental setup (a) [13] and adsorbent bed located on metal support (b).

The temperature of the vapour vessel and all connecting pipelines was maintained at $50 \pm 0.5^\circ\text{C}$ by using the air bath oven. The vapour pressure was measured by an absolute pressure transducer MKS Baratron® type 626A (accuracy $\pm 0.01 \text{ mbar}$).

The adsorption dynamics was investigated for a flat adsorbent bed consisting of two layers of loose grains of 0.3-0.35 mm for FAM-ZO2 and 0.4-0.5 mm for LiCl/silica. FAM-ZO2 was studied for two sets of boundary conditions (TI run 1→2 and PI run 1→3, Fig 1a). The composite LiCl/silica was studied under typical conditions of the adsorption stage of the new HeCol cycle (2→3 in Fig 1b).

Before experiments, the entire system was evacuated, and the adsorbent was regenerated at 90 °C under continuous pumping. Then the temperature of the adsorbent was changed to the initial value, and the system was filled with vapour from the evaporator until the adsorbent reached a desired equilibrium state. The adsorption was initiated by fast temperature (TI) or pressure change (PI). The TI process was performed by rotating 3WV valves (Fig 2a). During this experiment, FAM-ZO2 grains were subjected to the temperature change from $T_1 = 50$ °C to $T_2 = 40$ °C at the water vapour pressure $P_1 = 8.8$ mbar (1-2 in Fig 1a). PI tests were as follows: the measuring cell was disconnected from the system by the gate valve (VMC, Fig 2a). The buffering vessel was degassed and then filled with water vapour from the evaporator until desirable pressure was reached. Before starting adsorption runs, the measuring cell was connected to the buffering vessel, which led to a rapid change of the water pressure over the adsorbent. During PI runs, FAM-ZO2 was located on the metal plate maintained at $T_1 = 50$ °C, and the pressure was jumped from $P_1 = 8.8$ mbar up to $P_3 = 16.0$ mbar (1-3 in Fig 1a). Methanol adsorption on LiCl/silica was initiated by the methanol pressure jump from 30.8 to 72.8 mbar at a constant plate temperature of 35 °C (2-3 in Fig 1b). For studying the effect of residual air, a certain amount of air was added inside the measuring cell so that its partial pressure ΔP_{air} varied from 0.1 to 5.0 mbar.

Water adsorption causes small reduction of the water vapour pressure $\Delta P(t) = P(t=0) - P(t)$ that can be recalculated into the dimensionless water uptake:

$$\chi = w(t)/\Delta w = (P(t=0) - P(t))/(P(t=0) - P(t \rightarrow \infty)). \quad (1)$$

The accumulated error in the absolute water loading was lower than $\pm 10^{-3}$ kg/kg, which leads to the accuracy of the differential water loading $w(t)$ equal to $\pm 3\%$.

Discussion and Results

Adsorption of water on FAM-ZO2

TI initiation. Even a small pressure of residual air dramatically decelerates water adsorption (Fig 3a). At $\Delta P_{\text{air}} = 0.1$ mbar, the characteristic time $\tau_{0.8}$ corresponding to 80% conversion becomes 1.5 times longer. At $\Delta P_{\text{air}} \geq 0.5$ mbar, this time increases as $\tau_{0.8} [\text{s}] = A + B \cdot \Delta P_{\text{air}} [\text{mbar}] = 301 + (548 \pm 19) \cdot \Delta P_{\text{air}} [\text{mbar}]$ (Fig 4). The slope B is close to that found in [8] for a monolayer of FAM-ZO2 grains and in [10] for FAM-ZO2 loose grains embedded in a real heat exchanger (Fig 4). This may indicate the same mechanism of the adsorption deceleration by residual air: due to the Stephan flux, the air is effectively swept to the external surface of an adsorbent grain, where it accumulates as an air-rich layer. The adsorption may then be controlled by the vapour diffusion through this layer. This process is slower compared with the adsorption controlled by inter- or intra-particle heat and mass transfer resistances typical for adsorption of pure vapour. The air layer thickness seems to be not dependent whether on the bed configuration nor the fact that the grains are inside the heat exchanger. A dramatic drop in the initial adsorption rate by a factor of ten at $\Delta P_{\text{air}} \geq 2$ mbar can indicate that the amount of residual air is sufficient to block access of water vapour to the internal adsorbent surface.

The characteristic time $\tau_{0.8}$ allows estimating the specific power generated at 80% conversion as $W_{0.8} = 0.8 \cdot \Delta H \cdot \Delta w / \tau_{0.8}$, where $\Delta H = 3240$ J/g is the heat of water adsorption on FAM-ZO2 [14], $\Delta w = w_2 - w_1 = 0.12$ g/g is the mass of water adsorbed. The value of $W_{0.8}$ significantly drops down from 1.2 kW/kg at $\Delta P_{\text{air}} = 0$ mbar to 0.1 kW/kg at $\Delta P_{\text{air}} = 5$ mbar (Fig 4).

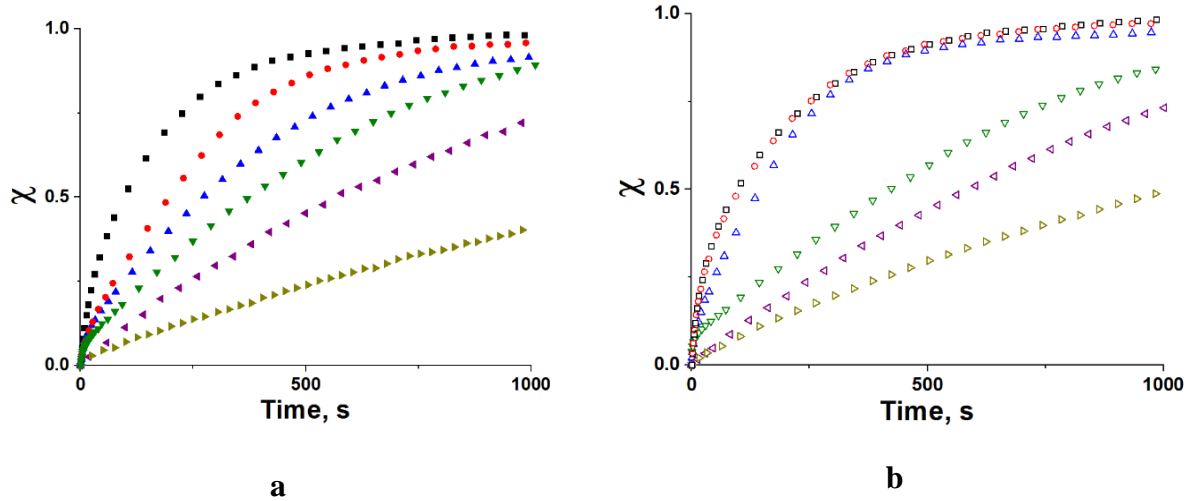


Fig 3. Kinetic curves of the TI (a) and PI (b) adsorption of water on FAM-Z02 depending on the residual air pressure ΔP_{air} : 0 (■), 0.1 (●), 0.5 (▲), 1 (▼), 2 (◄) and 5 (►) mbar.

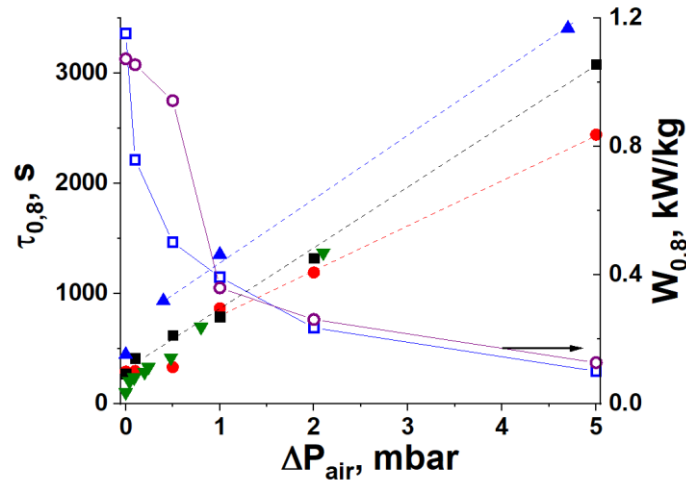


Fig 4. Characteristic time $\tau_{0,8}$ and specific power $W_{0,8}$ vs. air pressure ΔP_{air} for TI (■) and PI (●) water adsorption on FAM-Z02. The dashed lines present the linear approximation. Literature data for TI adsorption on FAM-Z02: ▲ - monolayer of 0.8-0.9 mm grains [8], ▼ - loose grains inside the real heat exchanger [10].

PI initiation. At the air pressure lower than 0.5 mbar, almost no deceleration of the water adsorption is observed (Fig 3b). The characteristic time is almost constant and equal to that in pure vapour (310 ± 20 s). At $\Delta P_{\text{air}} \geq 1.0$ mbar, the linear dependence $\tau_{0,8} [\text{s}] = 434 + (399 \pm 18) \cdot \Delta P_{\text{air}} [\text{mbar}]$ is observed (Fig 4). The specific power $W_{0,8}$ decreases only slightly by some 15% - from 1.1 kW/kg to 0.95 kW/kg when ΔP_{air} rises to 0.5 mbar.

Thus, the residual air has a much smaller deceleration effect on the PI adsorption than on the TI one occurring between the same isosteric lines, as shown in Fig 1a. At low air pressure, there is little to no effect on the adsorption dynamics. At a higher air partial pressure, the characteristic time $\tau_{0,8}$ linearly increases, but the slope B is smaller than for the TI adsorption (Fig 4). Thereby, the main finding of this study is that the PI adsorption is much less sensitive to the presence of residual air than the TI adsorption. Hence, closed AHT cycles based on PI processes are more robust and resistant against air traces that is a very important advantage from the practical point of view.

The lesser sensitivity of the PI adsorption to the air presence can be attributed to

- higher water vapour pressure (16.0 mbar during the PI process vs. 8.8 mbar during the TI one). For this reason, more molecules of water have time to adsorb before the air-rich layer is formed around grains due to the Stephan flux;
- during the PI process, all the grains start adsorbing water immediately after the pressure jump, and a thin “air pillow” is formed around *every* adsorbent grain (Fig 5a). On the contrary, right after the drop of the metal plate temperature (TI process), only grains near the cold plate start adsorbing water (Fig 5b). Thus, residual air is concentrated mainly near these grains. As a result, the air-rich layer is thicker than for the PI process, which slows down the TI adsorption more strongly (Fig 5).

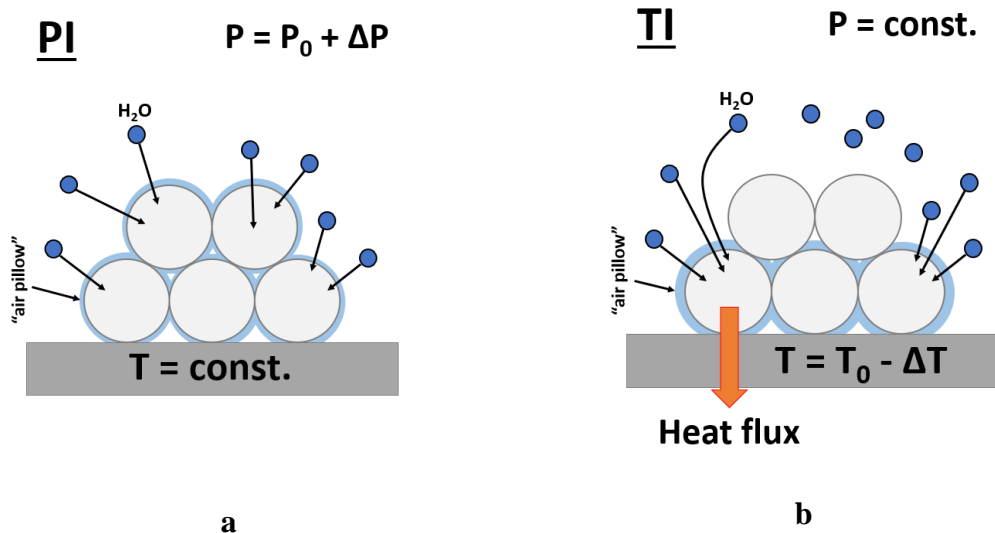


Fig 5. Schematics of the formation of the air-rich layer around adsorbent grains during the PI (a) and TI (b) adsorption.

PI adsorption of methanol on the composite LiCl/silica

The PI adsorption of methanol is studied under conditions of the adsorption stage of the novel HeCol cycle (Fig. 1b) with the temperatures of condensation $T_L = -25$ °C, evaporation/desorption $T_M = 10$ °C, and adsorption $T_H = 35$ °C. In this cycle, the adsorbent exchanges as much as 0.64 [g methanol/g adsorbent].

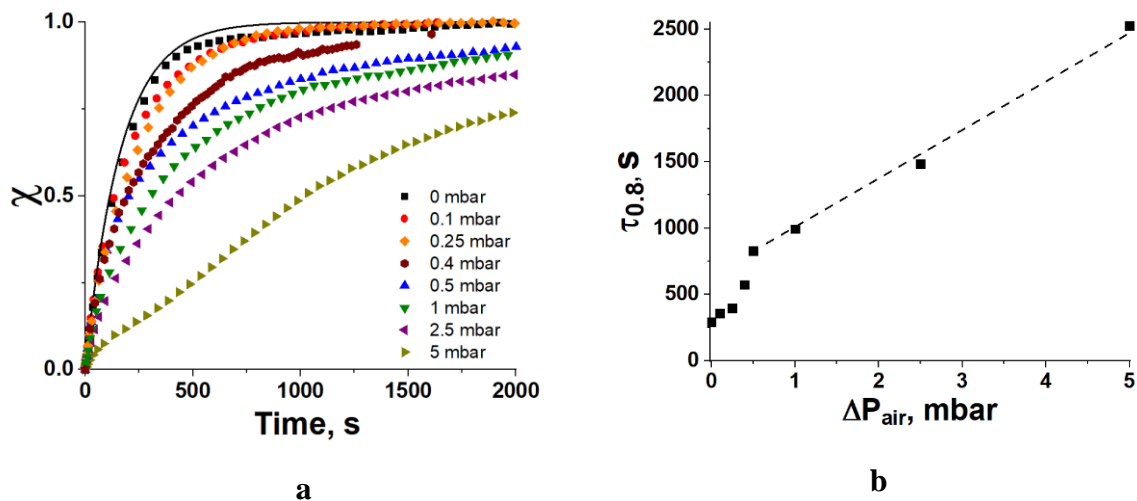


Fig 6. **a** – Kinetic curves of the PI methanol adsorption on LiCl/silica at various air pressure ΔP_{air} . Solid line – exponential approximation $\chi = 1 - \exp(-t/\tau)$; **b** – characteristic time $\tau_{0.8}$ vs. residual air pressure ΔP_{air} . The dashed line is the linear approximation.

An initial part of the uptake curves can be approximated by an exponential function $\chi = 1 - \exp(-t/\tau)$ (Fig 6a). The residual air slightly slows down the methanol adsorption even at $\Delta P_{\text{air}} = 0.1$ mbar (Fig 6a), and this effect becomes stronger at larger air pressure. At $\Delta P_{\text{air}} < 0.4$ mbar, the adsorption rate reduction is relatively small and significantly increases at larger pressure. At $\Delta P_{\text{air}} \geq 0.5$, the time $\tau_{0.8}$ rises linearly as $\tau_{0.8} [\text{s}] = 608 + (378 \pm 16) \cdot \Delta P_{\text{air}} [\text{mbar}]$ (Fig 6b). Such behaviour is similar to the PI adsorption of water on FAM-Z02 (Fig 4) and can be attributed to the formation of an air-rich layer near the external grain surface. This layer hinders both heat and mass transfer and decelerates the methanol adsorption in the same way as water adsorption.

Summary/Conclusions

In many industrial systems such as steam power plants, seawater desalination units, ab- and adsorption chillers, even small traces of air in mixture with steam may lead to a significant reduction in the adsorption or condensation rate. The majority of adsorptive cycles for heat conversion are initiated by a drop in heat transfer fluid temperature (so-called temperature-initiation, TI). This paper addresses the effect of residual air on dynamics of adsorption initiated by a jump of adsorptive pressure over the adsorbent (so-called pressure-initiation, PI). The latter is mainly used in adsorptive cycles for heat amplification. This effect is studied for water adsorption on aluminophosphate AQSOA-FAM-Z02 and methanol sorption on the composite LiCl/silica.

It is found that at $\Delta P_{\text{air}} \leq 0.5$ mbar, the PI adsorption of water is only slightly affected by the presence of residual air. Much stronger deceleration is found for the TI adsorption even at ΔP_{air} as low as 0.1 mbar. The slowing down of the adsorption process is due to effective air sweeping to the external surface of the adsorbent grains, where it accumulates as an air-rich layer. The vapour adsorption may then become controlled by the vapour diffusion through this layer. This process is relatively slow compared with the adsorption process controlled by inter- or/and intraparticle heat and mass transfer resistances typical for adsorption of pure vapour. At $\Delta P_{\text{air}} \geq 0.5$ mbar, characteristic time $\tau_{0.8}$ increases as $\tau_{0.8} [\text{s}] = A + B \cdot \Delta P_{\text{air}} [\text{mbar}]$, where $B = (548 \pm 19)$ and (399 ± 18) [s/mbar] for TI and PI processes, respectively. A similar deceleration was found for PI adsorption of methanol on LiCl/silica under typical conditions of the novel HeCol cycle: at $\Delta P_{\text{air}} \geq 0.5$ mbar, the time $\tau_{0.8}$ rises as $\tau_{0.8} [\text{s}] = 608 + (378 \pm 16) \cdot \Delta P_{\text{air}} [\text{mbar}]$.

The main finding of this study is that the PI adsorption is much less sensitive to the presence of residual air than the TI one. This is especially true at a low air partial pressure ΔP_{air} . The weaker sensitivity of the PI adsorption to the air presence can be attributed to (i) higher water vapour pressure for the PI process and (ii) the fact that all the grains start adsorbing water right after the pressure jump, and a thin air-rich layer is formed around *every* adsorbent grain. For TI adsorption, only grains near the cold plate start adsorbing water right after the drop of the metal plate temperature. Thus, residual air is concentrated mainly near these grains, and the formed air layer is thicker, which slows down the TI adsorption more strongly (Fig 5).

To sum, closed AHT cycles based on the PI process are more robust and resistant against the presence of traces of residual air that can be a significant practical advantage.

Acknowledgements

This work is supported by the Russian Foundation for Basic Research (grant 18-58-7809) and the Russian Science Foundation (grant 16-19-10259). The authors thank W. Lombardo for his experimental contribution.

References:

- [1] Wang, R., Wang, L., Wu, J., *Adsorption Refrigeration Technology: Theory and Application*, John Wiley & Sons, Singapore Pte. Ltd, 2014.
- [2] Choudhury, B., Saha, B.B., Chatterjee, P.K., Sarkar, J.P., “An overview of developments in adsorption refrigeration systems towards a sustainable way of cooling”, *Applied Energy*, 2013.
- [3] Ji, X., Song, X., Li, M., Liu, J., Wang, Y., “Performance investigation of a solar hot water driven adsorption ice-making system”, *Energy Conversion and Management*, 2015.
- [4] Li, T.X., Wang, R.Z., Li, H., “Progress in the development of solid-gas sorption refrigeration thermodynamic cycle driven by low-grade thermal energy”, *Progress in Energy and Combustion Science*, 2013.
- [5] Aristov, Yu.I., “A new adsorptive cycle “HeCol” for upgrading the ambient heat: The current state of the art”, *International Journal of Refrigeration*, 2019.
- [6] Sapienza, A., Frazzica, A., Freni, A., Aristov, Yu., *Dynamics of Adsorptive Systems for Heat Transformation. Optimization of Adsorber, Adsorbent and Cycle*, Springer, 2018.
- [7] Ruthven, D.M., *Principles of adsorption and adsorption process*, John Wiley & Sons, New York, 1984.
- [8] Glaznev, I., Ovoshchnikov, D., Aristov Yu., “Effect of Residual Gas on Water Adsorption Dynamics Under Typical Conditions of an Adsorption Chiller”, *Heat Transfer Engineering*, 2010.
- [9] Glaznev, I.S., Aristov, Yu.I., “Kinetics of water adsorption on loose grains of SWS-1L under isobaric stages of adsorption heat pumps: the effect of residual air”, *International Journal of Heat and Mass Transfer*, 2008.
- [10] Sapienza, A., Frazzica, A., Freni, A., Aristov, Yu.I., “Dramatic effect of residual gas on dynamics of isobaric adsorption stage of an adsorptive chiller”, *Applied Thermal Engineering*, 2016.
- [11] Nusselt, W. Z., “Surface Condensation of Water Vapor”, *Z. Ver. Deut. Ing.*, 1916.
- [12] Okunev, B.N., Gromov, A.P., Zelenko, V.L., Glaznev, I.S., Ovoshchnikov, D.S., Heifets, L.I., Aristov, Yu.I., “Effect of residual gas on the dynamics of water adsorption under isobaric stages of adsorption heat pumps: Mathematical modelling”, *International Journal of Heat and Mass Transfer*, 2010.
- [13] Girnuk, I.S., Okunev, B.N., Aristov, Yu.I., “Dynamics of pressure- and temperature-initiated adsorption cycles for transformation of low temperature heat: Flat bed of loose grains”, *Applied Thermal Engineering*, 2020.
- [14] Kakiuchi, H., Iwad, M., Shimooka, S., Ooshima, K., Yamazaki, M., Takewaki, T., “Water vapour adsorbent FAM-Z02 and its applicability to adsorption heat pump”, *Kagaku Kogaku Ronbunshu*, 2005.

Development of a latent heat storage for industrial application based on adipic acid – graphite composite

M. van der Pal^{1*}, K. Ingenwepelt² and R. de Boer¹

¹TNO Energy Transition, Westerduinweg 3, 1755 LE, Petten, The Netherlands

² Hochschule Düsseldorf, University of Applied Sciences, Münsterstraße 156, 40476 Düsseldorf, Germany

*Corresponding author: michel.vanderpal@tno.nl

Abstract

This study shows the development of a latent heat storage for industrial application based on adipic acid – graphite composite. The system aims at providing low pressure steam (up to 140°C) whilst the system is charged with medium pressure steam (160°C and higher). Small scale testing has been done together with model calculations and subsequent measurements of thermal parameters, in order to predict the prototype performance. A good correlation between model calculations and small-scale measurements was found, yielding an estimated charging/discharging time of one hour for 10K driving force.

Keywords: Latent heat, PCM, storage, industrial application.

Introduction/Background

80% of the energy use in the industry sector is as heat. Currently, this heat is mostly provided for by using natural gas. Electrification is considered as one of the main paths towards a CO₂-neutral industry. However, as electricity production from renewable such as wind and solar will have a transient character, a need for heat storage for industrial processes can be expected in the future. Such a heat storage can provide both the heat for the industrial process as well as generate electricity, e.g. using steam cycles or ORC, in times of scarcity. For this purpose, high temperature latent heat storage is being developed at TNO, and a prototype has been designed and build. This prototype aims at storing 15MJ of heat using adipic acid as phase change material. The adipic acid has a melting temperature of 151°C and can be charged using steam. During discharge, water is circulated to produce steam. Aim is to have a charge and discharge times of less than 1 hour for temperatures of 170°C (charge) and 130°C (discharge). Model calculations together with small-tube testing and material testing have been used to estimate the performance of the prototype. This paper describes the prototype design, the measurements, and the model calculations.

Prototype description

The prototype heat storage system, shown in *Figure 1*, consists of a pressure vessel containing 19 tubes of 2m length and 51mm outer diameter, each filled with 3.5kg of adipic acid – graphite composite. The tubes are wetted via a custom-made header when using the pump during the discharge phase. During the charge phase, steam will condense on the tubes so there is no need for active water circulation whereas upon discharge, the wetting is necessary to extract the heat from the tubes efficiently. At the top of the system, a steam line is connected to a steam boiler and condenser. A flowmeter is placed in the steam line to measure the amount of steam flowing into/out of the prototype system during respectively the charge and discharge phase. Temperature sensors have been placed in the pressure vessel and centred, 15cm from the top and bottom, in two of the 19 tubes to follow the progress of the charging and discharging phase.

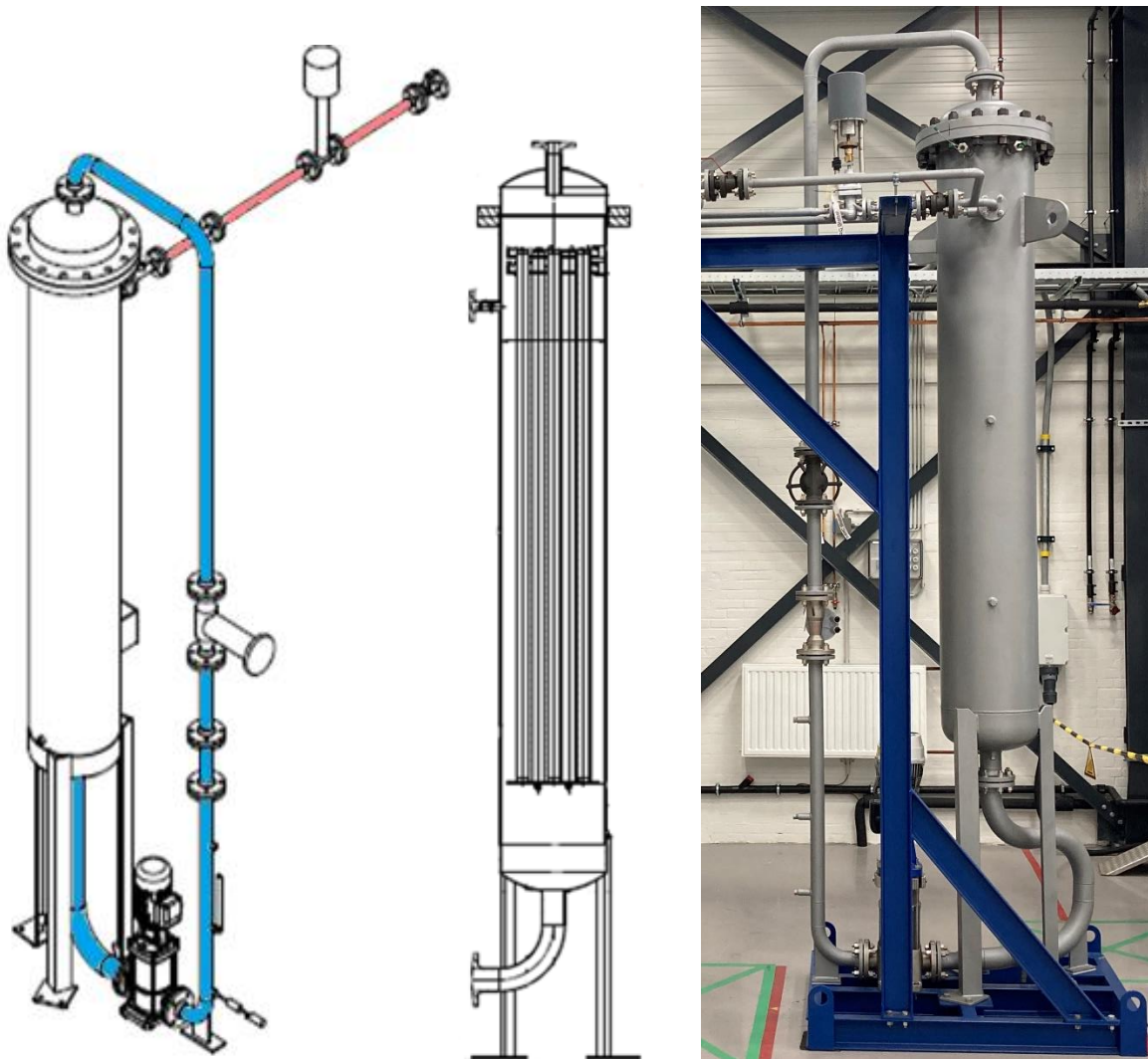


Figure 1. On the left and middle, a drawing of the prototype PCM storage system, on the right a picture of the prototype unit at TNO's Carnot Lab facility.

Material characterisation and small-tube test installation

DSC measurement

A NETZSCH DSC 204F1 has been used for repeatedly measuring the (latent) heat changes of a sample of 25.3mg of adipic acid-graphite composite. A scan-speed of 1.0Kmin^{-1} in the temperature range of 135°C to 160°C was applied for 46 cycles, each consisting of melting and solidification of the composite material. The purpose of this measurement was to establish the cyclic stability of the composite and to confirm the absence over superheating and/or supercooling effects.

Thermal conductivity measurement

The thermal conductivity of the adipic acid-graphite composite has been determined using a light flash analyser. A Netzsch LFA 467 was used to determine the thermal conductivity. Based on the measured thermal diffusivity and heat capacity together with the sample density, the thermal conductivity was determined. Four samples with an average thickness of 3mm were measured in 10K temperature steps over a temperature interval 30°C to 140°C. Reference samples of graphite and Pyroceram were used to verify the accuracy of the measured thermal diffusivity and heat capacity values.

Small-tube test method

Two tubes with 51mm diameter and 150mm height have been filled with 113.9g and 128.9g of the adipic acid – graphite composite. A thermocouple is placed in the centre of the tube to monitor the inner temperature. The tubes are placed in a Julabo type F25 thermally controlled bath filled with Silicon oil (type SIL 300) as shown in *Figure 2*.

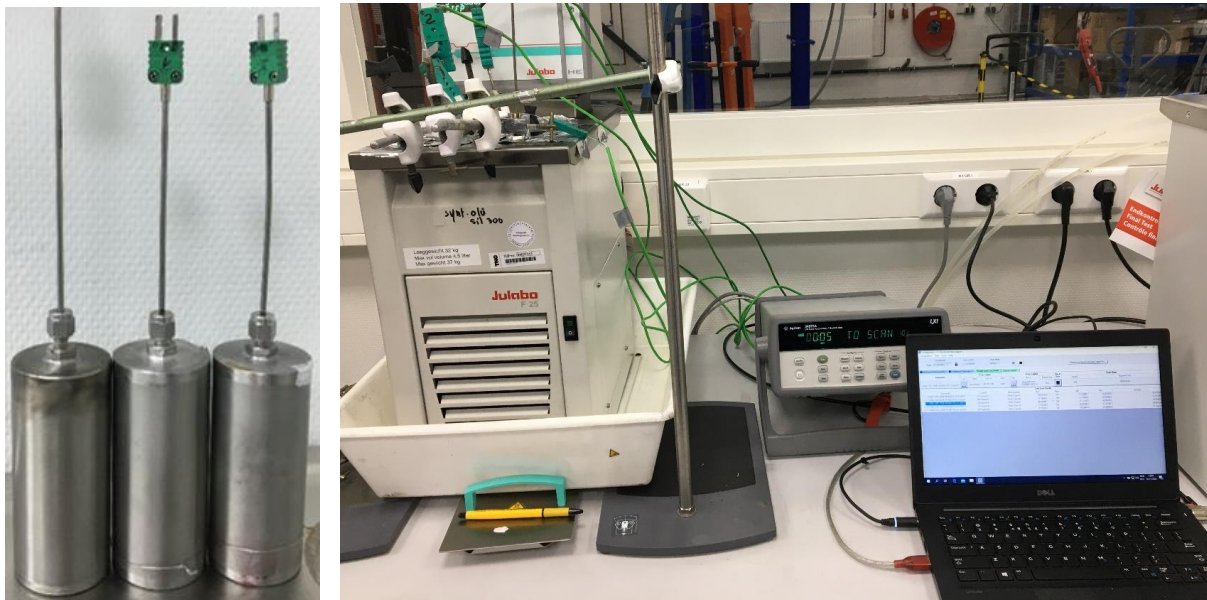
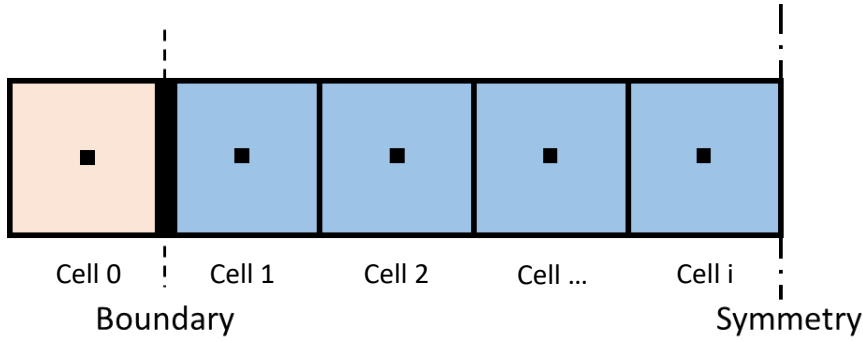


Figure 2. Picture of the small-tube test setup: left three tubes ready for placement in the Julabo thermostatic bath, right: all tubes placed and connected to data-logger.

Model description

Model comprises of a 1D-structure of multiple cells as shown in *Figure 3*. The model uses a temperature on the outside of the tube as input parameter. The heat transfer is calculated from the temperature differences between the cells and the boundary using the cells dimensions (i.e. length, volume, surface area, mass, heat capacity) and its heat transfer properties. The latter consists of the thermal conductivity for the internal transfer and a combined heat transfer coefficient and thermal conductivity of the outer cell containing the PCM-graphite composite.



■ Charging Temperature

■ PCM

Figure 3. Schematic representation of the model. Cell 0 represents the heat transfer medium and uses a given (input) temperature whereas cells 1 to i represent the composite material and their temperatures result from the cell properties and the temperature set in Cell 0. The heat transfer from Cell 0 to Cell 1 includes the heat transfer coefficient required to transfer heat from the heat transfer medium to the tube to the composite material.

The model calculation starts by determining the temperature differences between the cells. The heat transfer resulting from this temperature difference is calculated using the thermal conductivity of the composite material and the spatial parameters of the cells:

$$Q_{i,i+1} = \frac{\lambda \cdot (T_i - T_{i+1}) \cdot A_{i,i+1} \cdot dt}{dx_{i,i+1}}$$

Where:

- $Q_{i,i+1}$ heat transferred from cell i to cell i+1 (J);
- λ thermal conductivity of composite material ($\text{Wm}^{-1}\text{K}^{-1}$);
- T_i temperature in cell i (K);
- T_{i+1} temperature in cell i+1 (K);
- $A_{i,i+1}$ surface area between cell i and cell i+1 (m^2);
- dt timestep set in the model (s);
- $dx_{i,i+1}$ distance between centres of cell i and cell i+1 (m).

For the heat transfer from the outer cell to/from the heat transfer medium, the heat transfer combines the heat transfer coefficient and the thermal conductivity as follows:

$$Q_{0,1} = \frac{(T_0 - T_1) \cdot A_{0,1} \cdot dt}{\frac{1}{\alpha} + \frac{dx_{0,1}}{\lambda}}$$

Where:

- $Q_{1,2}$ heat transfer from heat transfer medium (cell 0) to the outer cell (cell 1) of the composite material (J);
- T_0 temperature of the heat transfer medium (K);
- T_1 temperature of the outer cell of the composite material (K);
- $A_{0,1}$ surface area of outer tube (m^2);
- α heat transfer coefficient ($\text{Wm}^{-2}\text{K}^{-1}$);
- $dx_{0,1}$ distance from centre of outer cell to outer tube (=half the length of cell 1).

The final calculation step is to determine the new temperature for each cell based on the original temperature and the heat flowing in and out of the cell:

$$T_i(t + dt) = T_i(t) + \frac{Q_{i-1,i} - Q_{i,i+1}}{m_i \cdot Cp_i}$$

Where:

$T_i(t+dt)$	temperature of cell i at time t + dt (K);
$T_i(t)$	temperature of cell i at time t (K);
$Q_{i-1,i}$	heat transfer into cell i (J);
$Q_{i,i+1}$	heat transfer out of cell i (J);
m_i	mass of cell i (g);
Cp_i	heat capacity of material in cell i ($J g^{-1}K^{-1}$)

Please note a temperature-dependent heat capacity is used. To implement the phase change, a temperature interval has been assumed over which the phase change takes place, resulting in an apparent heat capacity for this temperature interval, Cp_{int} :

$$Cp_{int} = \frac{\Delta H_{melt}}{T_{int}} + 0.5 \cdot (Cp_{liq} + Cp_{sol})$$

Where:

Cp_{int}	apparent heat capacity over the phase change temperature interval ($J g^{-1}K^{-1}$);
ΔH_{melt}	melting enthalpy of composite material ($J g^{-1}$);
T_{int}	temperature interval for phase change (K);
Cp_{liq}	heat capacity of composite material in liquid phase ($J g^{-1}K^{-1}$);
Cp_{sol}	heat capacity of composite material in solid phase ($J g^{-1}K^{-1}$);

The model assumes an initial temperature for heat transfer medium and the composite material to be equal at t=0. The next temperature of the heat transfer medium is either set or read from a file. The latter allows to do vary the temperature of the heat transfer medium whereas otherwise the heat transfer medium temperature remains constant at set value. For the analysis of the small-test tube setup, the measured oil temperature has been used as input for the model calculation.

Results and discussion

PCM stability testing

Figure 4 shows the DSC diagram of the composite material over 46 cycles. The red line shows the first cycle and the green line the last cycle. It can be seen there is a shift in melting temperature off-set towards a lower temperature, but this effect seems minor, and no change is observed in solidification off-set temperature. Overall, the composite material is considered to be stable over the 46 cycles.

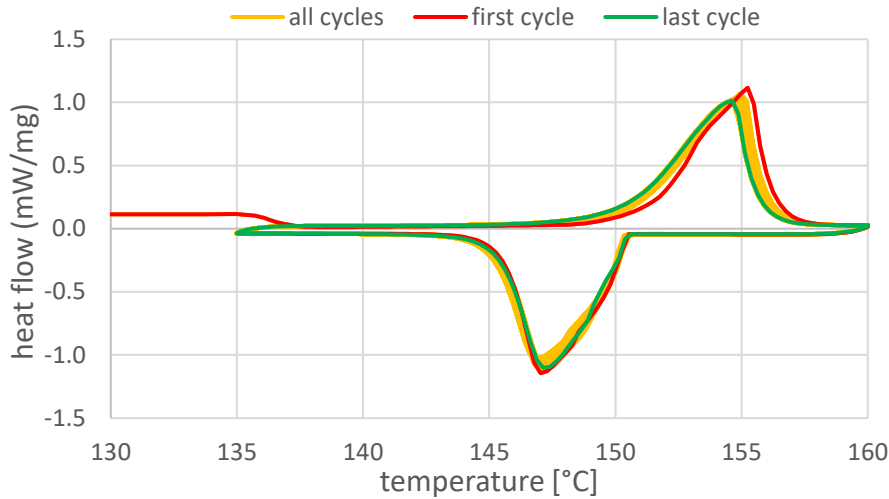


Figure 4. DSC diagram of 46 cycles on adipic acid – graphite composite

Thermal conductivity

Figure 5 shows the thermal conductivity of four samples taken from a test tube. Two of the samples were taken from the top of this tube and two were taken from the bottom to verify the homogeneity of the sample. The results show a thermal conductivity value that reduces from about $4.8 \text{ W m}^{-1} \text{ K}^{-1}$ at 40°C to $4.3 \text{ W m}^{-1} \text{ K}^{-1}$ at 130°C , considerably higher than the $0.8 \text{ W m}^{-1} \text{ K}^{-1}$ reported for adipic acid without graphite present [1]. After this, the value rises sharply again. This might be due to the closeness to the melting point of the material.

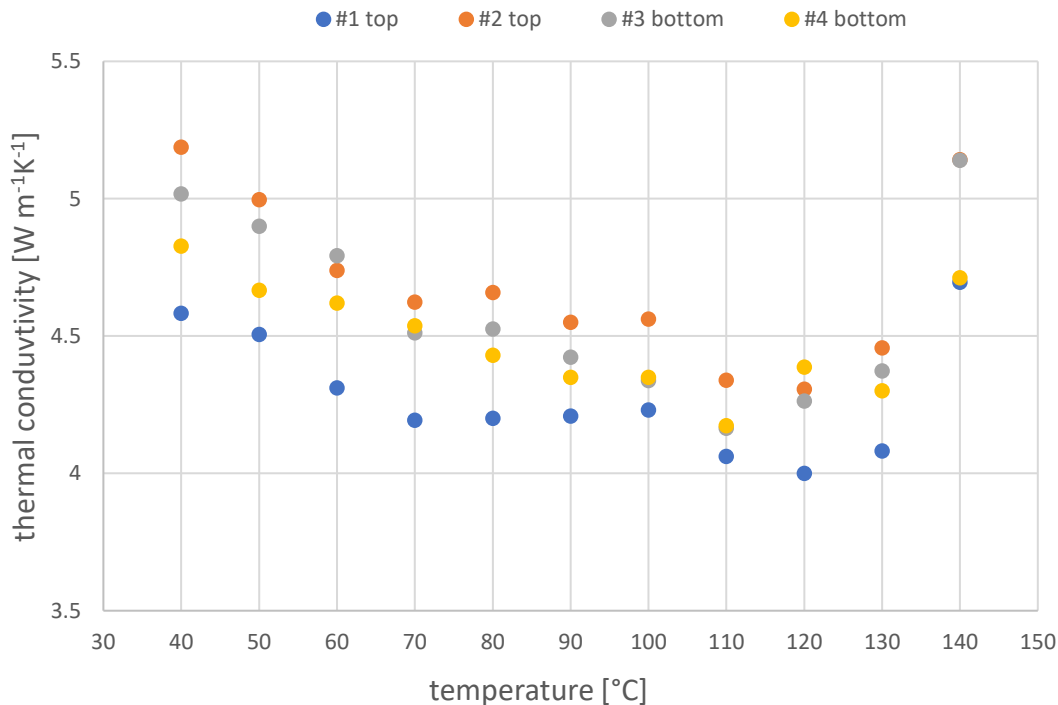


Figure 5. Thermal conductivity of 4 samples of adipic acid – graphite composite as a function of temperature

Small tube testing

Figure 6 shows the measured (set) oil temperatures and the (responding) adipic acid – graphite composite temperatures in centre of tube as a function of cycling time for temperature intervals at 170°C, 130°C, 160°C and 140°C respectively followed by a temperature rise with a constant heating rate of $+0.5\text{Kmin}^{-1}$ to an oil temperature 170°C, and a temperature drop at a constant cooling rate of -0.5Kmin^{-1} to an oil temperature of 130°C.

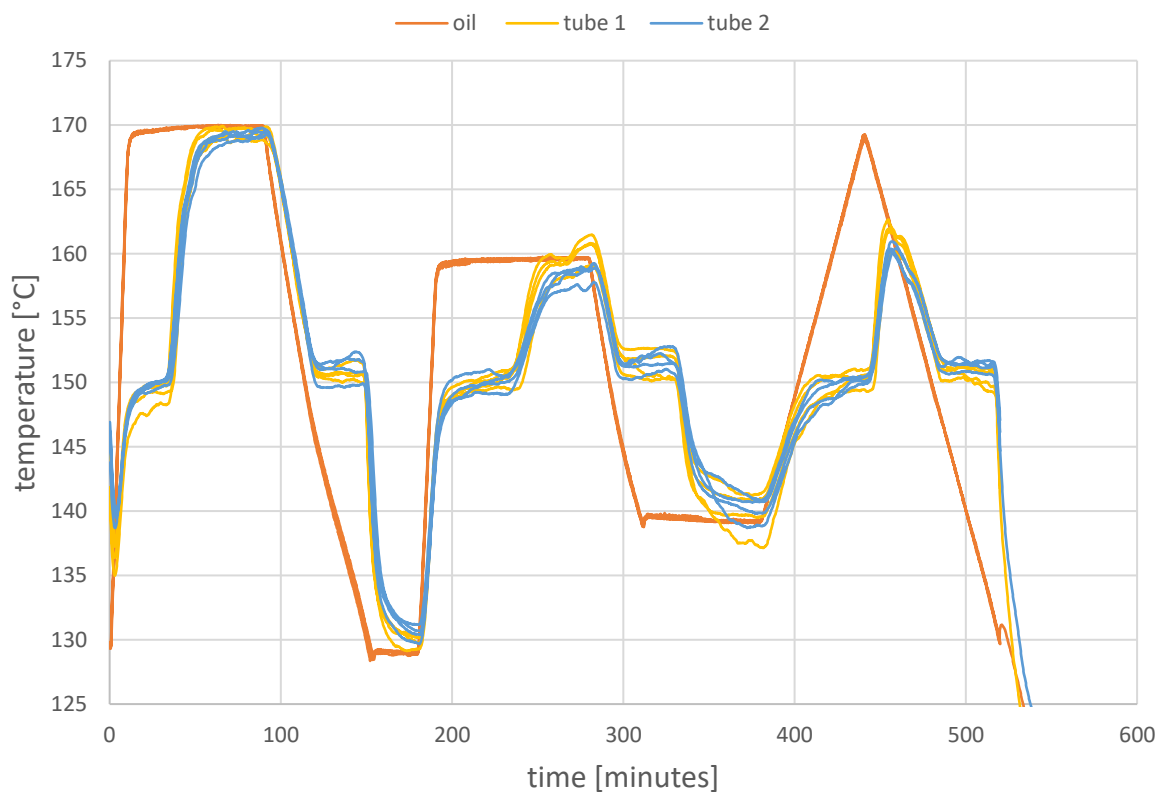


Figure 6. 5 cycles of small tube testing with centre tube and oil temperatures as a function of time with each cycle starting at $t=0$.

Model calculations

Table 1 shows the main input parameters for the model calculations. Figure 7 shows the measured sample temperatures together with the model values as a function of time. These model calculations were done with optimized values for the heat transfer coefficients. The heat transfer coefficients have been optimized by minimizing the difference between measured tube temperature and the modelled value. Surprisingly, the optimal heat transfer coefficient for the liquid phase is considerably lower ($270\text{Wm}^{-2}\text{K}^{-1}$) than for the solid phase ($530\text{Wm}^{-2}\text{K}^{-1}$). This is quite opposite expectations as the liquid was expected to make better contact with the wall rather than worse. A possible explanation, albeit not most likely, is that the melting material fills up cavities left upon solidification of the composite material given that the density of the solid is higher than of the liquid. Destructive analysis of the tubes could provide some insights into this phenomenon. This and other explanations are currently investigated.

Table 1. Input parameters model calculations

dimensions		heat transfer properties		model parameters	
diameter	48mm	λ	$4.33\text{Wm}^{-1}\text{K}^{-1}$	dt	1s
A	1507mm^2	α_{liq}	$270\text{Wm}^{-2}\text{K}^{-1}$	number of cells	10
ρ_{liq}	$1.2 \cdot 10^6\text{gm}^{-3}$	α_{sol}	$530\text{Wm}^{-2}\text{K}^{-1}$	dx	2.4mm
ρ_{sol}	$1.5 \cdot 10^6\text{gm}^{-3}$	Cp_{liq}	$2.1\text{Jg}^{-1}\text{K}^{-1}$	T_{int}	1K
		Cp_{sol}	$2.1\text{Jg}^{-1}\text{K}^{-1}$		
		ΔH_{melt}	210Jg^{-1}		

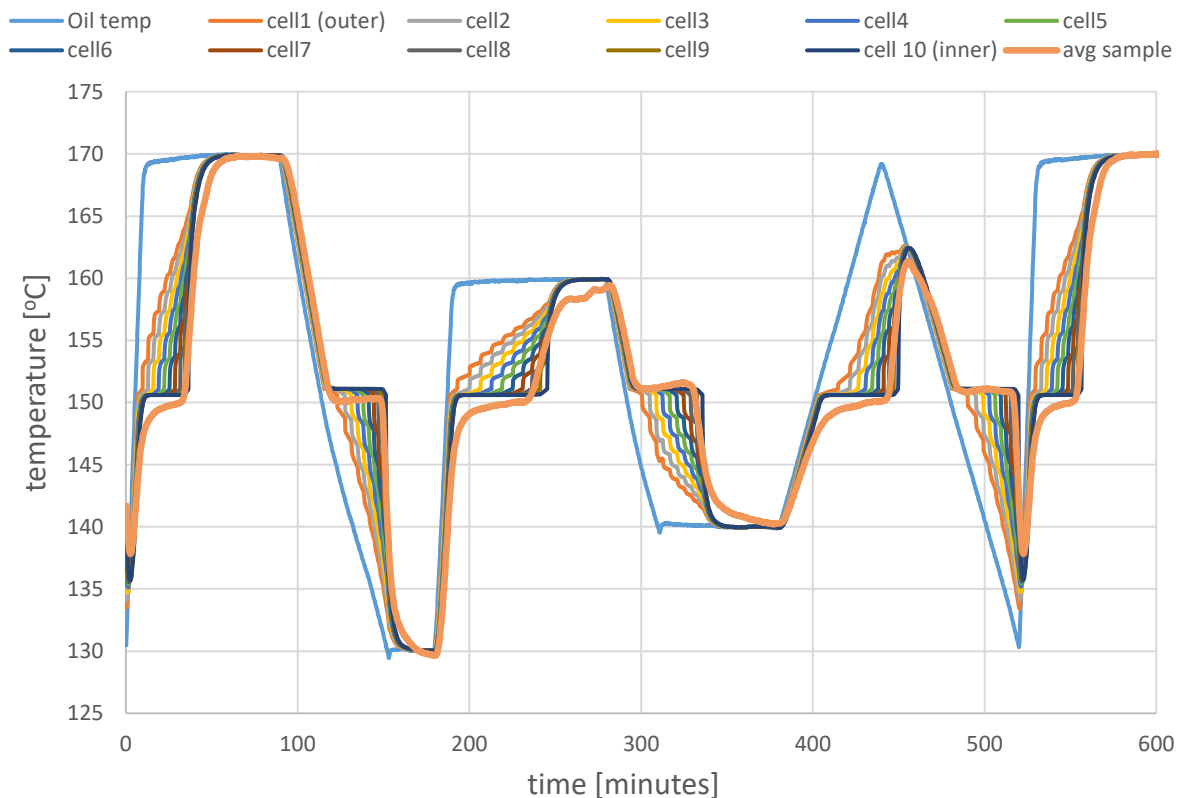


Figure 7. Modelled and measured temperatures as a function of time with the oil temperature as input parameter for the model with cell1 to cell10 (= inner cell) represent the composite material from the wall to the centre. The thick orange line is the average of the two sample tubes measured centre temperature.

Conclusions

Cyclic stability of the adipic acid – graphite composite is shown in repeated DSC measurements and this has been confirmed in small-tube tests where five repeated temperature cycles, each with 6 phase changes. The thermal conductivity measurements showed significantly increased thermal conductivity of the composite compared to pure adipic acid. Using this and other input parameters, a good correlation is found between the model calculations and the temperature measurements in the centre of the tubes containing the composite material. Remarkably, the heat transfer coefficients for solid and liquid phase differ considerably, nearly a factor 2. Further investigation into this phenomenon is needed to understand the mechanisms causing this effect. Possible causes include cavity formation affecting thermal transfer behaviour, some sort of impact on temperature

measurement/contact with composite material and/or the influence of the bottom of tube on the heat flow, which is currently not included in the model calculations.

Overall, the charge and discharge times (time for respectively melting and solidification) measured in the tube tests are within one hour for temperature difference of 10K or more. This is within the set target for the industrial application. It is expected that these times will be reduced when steam is used as heat transfer medium instead of thermal oil as the heat transfer coefficients for steam are significantly higher than those of oil [2]. Given the prototype has arrived in the lab, results from the prototype system using steam are expected soon.

Acknowledgements

This work is part of the Flexsteam project, which is financially supported by the ‘Topsector Energiesubsidie’ of the Dutch ministry of economic affairs.

References

- [1] Zhou W., *Preparation and thermal cycling of expanded graphite/adipic acid composite phase change materials*, Akadémiai Kiadó, 2017.
- [2] Stephan P. et al., *VDI heat atlas*, Springer, 2010.

The cost of manufacturing adsorption chillers

AL-Hasni. Shihab¹, Grant. Rachael¹ and Santori. Giulio^{1*}

¹The University of Edinburgh, School of Engineering, Institute for Materials and Processes, Sanderson Building, The King's Buildings, Mayfield Road, EH9 3BF, Edinburgh, Scotland, UK

*Corresponding author: email address (g.santori@ed.ac.uk)

Abstract

Although attractive for their environment-friendly characteristics, adsorption chillers struggle to penetrate the market because of the unattractive trade-off between cost and performance. While the increase of performance has been the primary objective of a large body of research, its link to the cost of manufacturing remains unclarified. The scope of this study is to assess a benchmark cost of manufacturing along with an end-user price for commercial silica gel adsorption chillers. The analysis takes into account indirect, direct and production costs. The selling price of the technology results in €1030.25 per kW of cooling capacity. Additionally, a sensitivity analysis of the most important parameters affecting the price highlights that the profit can be boosted by 75% compared to the base profit, when the minimum annual selling volume is 384 units. From the profitability viewpoint, this study finds that the economic sustainability of silica gel adsorption chillers depends on the market volume and on the achievement of a minimum set of performance.

Keywords: Adsorption chiller, cost, price, Cost-Volume-Profit analysis, Profitability analysis.

Introduction

Climate change is projected to cost humanity €1.61 trillion annually by the end of the 21st century [1]. According to the International Energy Agency, as the planet warms, the global air conditioner stock will rise to 275 million units in the European Union alone by 2050. These forecasts should favour the widespread use of heat driven cooling solutions such as adsorption chillers. In fact, when comparing adsorption chillers of 8 kW cooling capacity to conventional compression chillers, 8.7 tons of CO₂ emissions can be avoided annually and a household consumer can save nearly €36.5k in electricity bills over a 10 year period [2]. As an additional benefit, being a heat driven technology, adsorption chillers enable the utilization of waste energy [3]. However, the technology is still, in practice, confined to a market niche and has not met the expectations yet. A key reason for scepticism of the technology is the profitability of the business, given the current low performance of the technology. A limited number of approximate values of cost have been disclosed and refer mostly to adsorption desalination rather than cooling. According to [4], €88.5k is the cost of ownership for a 24t silica-gel adsorption desalination unit. This is equivalent to an adsorption chiller with 402kW of cooling power resulting in a capital cost of ~€220 per kW of cooling. In [5], the same authors report a value of ~€330 per kW of cooling, aligned with the capital cost of €314 per kW of cooling [6] for a single stage absorption chillers. Finally, [7] assumes €13k for an adsorption unit with 8kW of cooling power, resulting in ~€1625 per kW of cooling. The large discrepancy between values is due to the capital cost not being the only contributor to the selling price (or cost of ownership). Previous work has exclusively focused on enhancing the performance of the adsorption chiller[8–12], neglecting to examine whether the utilization of advanced technical solutions would be beneficial or detrimental for enabling adsorption chillers to establish a competitive presence in the market, which ultimately depends on the selling price. Commercialization of adsorption chiller using silica gel and water was first attempted in the 1980s [13]. Today, commercial units are available from companies such as FAHRENHEIT (Germany) [2]; SOLABCOOL (Netherlands) [14]; AYEKAWA (Australia) [15] and Bry-Air

(India) [16]. However, the adsorption chiller market remains a niche. Many factors prevent their wide-scale application, including inferior performance and high initial investment. There is a lack of awareness on how technical and economic factors link together and can lead to a profitable business. In all previous insights, the manufacturing cost is given as a lump value, without detailing its composing factors. This investigation is the first of its kind and breaks down all the costs of manufacturing a commercial adsorption chiller. Additionally, the analysis takes into account the profit, in order to reach an end-user price and isolate the main contributors to the final price. A sensitivity analysis is carried out to identify cost drivers of the business and optimise its profitability.

Description of the system

There are two types of design followed by commercial adsorption chiller units. The main feature of the first type (Fig. 1a) consist in two separate vessels that use the same heat exchanger for evaporation and condensation. This design option is chosen to have a low overall manufacturing cost [17] and is currently used in units such as those commercialised by FAHRENHEIT [2]. Other design details can be found elsewhere [18]. The main feature of the second design option is the presence of 4 vessels with individual heat exchangers in each vessel [19]. Along with the 4 vessels, this second design (Fig.1b) requires four expensive vacuum valves which can drive up the overall cost of the unit and ultimately its final price [19]. Consequently, this study focuses on the first design type.

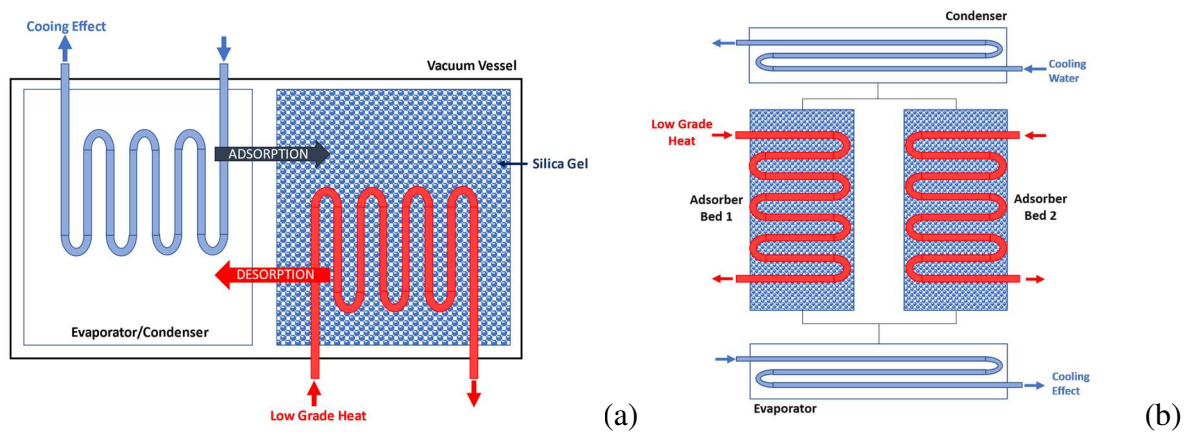


Figure 1: Block flow diagrams of the adsorption chiller design options. (a): Two-vessels adsorption chiller (analysed in this study); (b) Four-vessels adsorption Chiller.

Tools and data on materials and manufacturing

When reliable data on the equipment design and technical specifications are available, a class 3 estimate [20] can be achieved. Table 1 reports the source of the data. Whenever there was a need to fill information gaps, data were complemented by quotations received by the Emerging Sustainable Technologies Lab (ESTech Lab) at The University of Edinburgh [21]. However, the utilization of laboratory quotations was kept at the minimum, aware that quotations on large volumes benefit from scale economy. Adsorption chillers must follow strict manufacturing standards due to the need to preserve vacuum pressures over extended periods of time. Typically, the vacuum level should not cross a limiting pressure that is too detrimental to the efficiency of the device. For this reason, vacuum is usually restored after one year of operation. Adsorption chillers are currently manufactured using metal materials that require laborious operation and skilled labour [22], especially for gas tungsten arc welding [23,24]. However, recent studies have demonstrated that 3D printing can produce a vacuum tight parts [22]. This would enable lower raw material cost, more affordable labour, and freedom to investigate geometries that cannot be realized with traditional manufacturing.

Table1: References used for costing

Contributor	Ref	Contributor	Ref
Adsorption material	[25]	Materials overhead	[26]
Sheet metal	[27]	Indirect Labour	
Control unit	[21,28,29]	Full time engineer	
Hydraulic unit	[21,30–33]	TIG welding	[23,24,34,35]

The manufacturing cost analysis uses CALC4XL (Hamburg, Germany) [26], a tool based on a transparent and accurate bottom-up costing approach that specifies and quantifies all components of a specific product. The estimate ends after identification of all direct or indirect contributors to the cost of each component that has an effect on the final selling price. CALC4XL has an extensive and reliable database specifically designed for industry that includes costs such as cost of labour for a number of manufacturing processes, the cost of raw material, overheads depending on the specific industry etc.

The effect of the system performance on the manufacturing cost

Specific cooling power (SCP) and Coefficient of Performance (COP) are two chief performance indicators in adsorption cooling. A significant body of research aims at improving both SCP and COP. However, higher SCPs and COPs are in most of the cases enabled by more expensive advanced technical solutions. An exemplar case concerns novel adsorption materials, for which a marginal increase of performance can cause a significant increase of material price. The adoption of more efficient novel solutions should be assessed within a framework that considers the whole problem from material to market. The determination of the technology manufacturing cost is the fundamental cornerstone enabling a material to market assessment. Due to its wide use, the present analysis focuses solely on silica-gel adsorption chillers. Nevertheless, this choice does not reduce the complexity of the analysis since several different silica-gel chillers have been tested in the past showing large discrepancies in SCP and COP due to different internal heat and mass transfer patterns. Table 2 compares the maximum SCP and maximum COP achieved in a number of lab- or pilot-scale adsorption chillers.

Table2: Maximum SCP and COP achieved in different silica-gel adsorption chillers and consequent total cost of the heat exchangers.

SCP _{max} [W kg ⁻¹]	COP _{max}	Silica-gel for 8 kW cooling power [kg _{silica-gel}]	Silica-gel total cost ¹ [€]	Adsorber Heat transfer surface area ² [m ²]	Total cost of Adsorber Heat Exchangers [€]	Ref
146	0.51	55	440	102	2541	[36]
168	0.60	48	384	89	2214	[12]
111	0.50	72	576	134	3348	[11]
250	0.64	32	256	60	1488	[10]
113	0.45	71	568	132	3292	[9]
181	N/A	44	352	82	2050	[8]
70	0.23	114	912	210	5250	[37]
106	0.30	75	600	140	3497	[38]
300	0.72	27	216	50	1240	[39]

Note:

¹ the silica gel price is €8 per kg [40]

² 1.84 m² per each kilogram of silica-gel grains is assumed [41,42]

³ €25 per m² of adsorber heat transfer surface area as suggested in [43]

SCP and COP affect heat power of each heat exchanger in the unit according to the following relations:

$$S_{CondP} = \left(1 + \frac{1}{COP}\right) SCP \quad (1)$$

$$SAHP = \frac{SCP}{COP} \quad (2)$$

Where S_{CondP} is the condensing power per kg of silica-gel [$W\ kg^{-1}$] and $SAHP$ is the adsorber heating power per kg of silica-gel [$W\ kg^{-1}$]. Each power correlates proportionally with the heat transfer surface area that in turn decides on the dimension of the vessels. Sapienza *et al.* recommended a minimum of $1.84\ m^2$ for each kilogram of silica-gel grains under the condition of mass of heat exchanger/mass of adsorbent ratio of 1 [41,42] and other experimentations reported in Table 2 have shown values ranging between $1.85\ m^2$ to $1.88\ m^2$ per kilogram of silica-gel grains. In previous studies with a research focus on economics of adsorption chillers and heat pumps, have estimated a cost of €25 per m^2 of adsorber heat transfer surface area [43]. The analysis presented here is performed by assuming the best SCP in Table 2 that is $300\ W\ kg^{-1}$. SCP and COP allow the definition of the specific powers of each heat exchanger according to the following:

$$S_{CondP} = (1 + COP) SAHP \quad (3)$$

$$SCP = COP \times SAHP \quad (4)$$

$$S_{CondP} + SCP = (1 + 2\ COP) SAHP \quad (5)$$

From Eq. (5), the heat transfer surface area of condenser and evaporator is proportional to the heat transfer surface area of the adsorber by a factor of $(1 + 2\ COP)$. At $COP = 1$ (maximum theoretical COP), the heat transfer surface area of the evaporator is equivalent to the adsorber, while the condenser features a heat transfer surface area twice the adsorber. This is the condition requiring the largest set of heat transfer surface areas in both condenser and evaporator. In the design focused by this study, evaporator and condenser are integrated. Therefore, the maximum between the two (twice the surface area of the adsorber) is taken as heat transfer surface area of the integrated evaporator/condenser heat exchanger.

Example: cost of manufacturing of an 8kW adsorption chiller

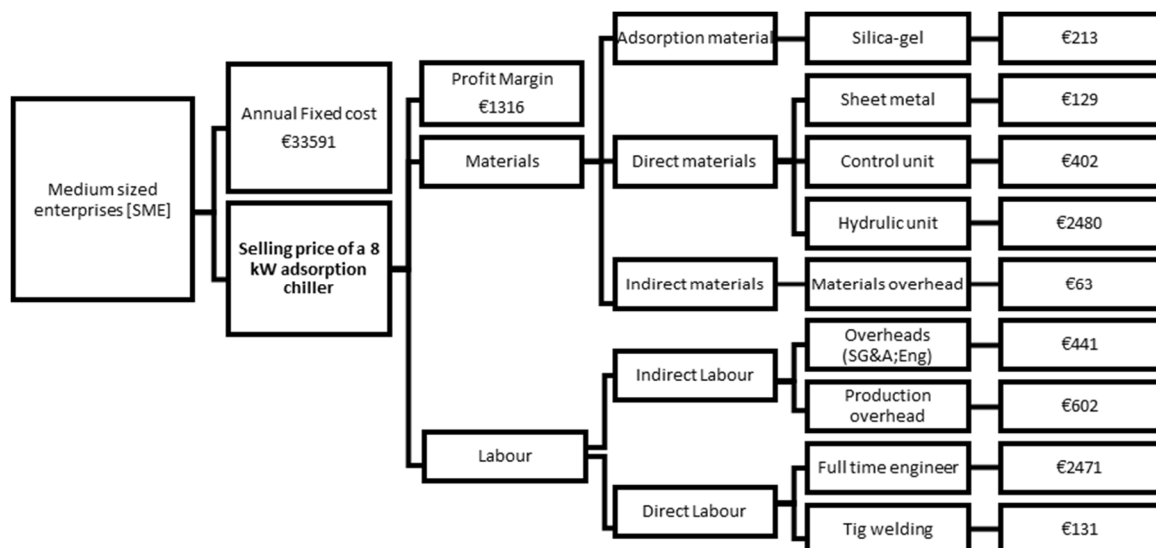
The analysis of the cost of manufacturing and consequently selling price is first applied to the case of an adsorption chiller able to supply a maximum of 8kW cooling power. However, by the end of the analysis, the results can be generalised by referring to a specific cost defined as the cost per kilowatt of cooling effect. This facilitates the application of the analysis outcomes to different cooling powers. The approach can be particularly useful when the chiller results from the assembly of modular sub-units.

Firstly, the costing process requires the identification of the type of industry, and of the scale of the business. Because the scale or size of a particular business is sensitive to overheads and rate per hour, it is therefore critical to choose based on a realistic scale that reflects the business throughput. A medium size business in metalwork industry with a moderate number of employees was assumed to reflect the current dimension of a typical adsorption chiller business. Secondly, the direct materials and indirect materials must be listed. Direct materials include components such as the cost of adsorption material, as well as the hydraulics and the controls. These costs were adapted from quotations received due to the construction of an adsorption chiller in the ESTech Lab [44]. The indirect material cost is estimated by CALC4XL for the type and size of business, resulting in overheads equivalent to 1.94% of the total cost of raw materials and purchased components [26]. Furthermore, the labour is subdivided into direct and indirect labour. The production of one adsorption chiller requires Tungsten Inert Gas (TIG) welding. TIG welding is a process often used to weld stainless steel semifinished products, which are crucial to produce vacuum tight vessels and feedthroughs meeting the standard vacuum leak rate of $10^{-6}\ Pa\ m^3\ s^{-1}$. The TIG welding cost calculation is in Table 3.

Table3: Process costing of TIG welding

Calculation steps	Description	Ref
1. Selection of welding approach	TIG welding is suitable for vacuum tight welds.	
2. Assume whether labour is full-time or on-demand.	We have assumed this job is on demand and based on hourly rate of a skilled welder. This because hiring full time skilled welder can increase the selling price.	[23,24]
3. TIG welding database	This database assigns the necessary values to calculate a cycle time for TIG welding.	[45]
4. Welding cycle time	Estimation of the time needed to weld parts of one adsorption chiller (assumed at 1 hour in this study).	[35]
5. Obtained Machine cost, operator rate.	Machine cost is approximately €11 per hours and the Operator rate per hour is €100.	[26]

A second labour cost arises from the costs of building the adsorption chiller. This includes the design and commissioning of the machine, post-processing such as cleaning the vessels, assembling and packing. We assume these tasks are accomplished by a full-time skilled engineer in a time frame of 30 days. There might be more people taking part to some of the operations, in reality. The assumption of a lumped skilled workforce takes into account the overall cost of all people involved. This part of the analysis relies on the extensive and precise database of labour wages based on skill level for specific manufacturing process and industry sector in CALC4XL. According to CALC4XL database, a skilled worker in metal industry should earn around €15.5 per hour, corresponding to €2471 every month of productive work. In addition, 7.6% of the total cost of the production were costed as standard production overhead (indirect labour costs), following the recommendation of CALC4XL database. Fig. 2 summarizes the hierarchy of costs and their values, showing a manufacturing cost of €6932. The identified cost of manufacturing is not yet the selling price which depends on profit (as percentage of the final price). For a moderate profit gains, CALC4XL database suggests a contribution margin of 30% of the selling price that corresponds to a profit margin of €1316 (19% of the sale price). Using these assumptions, CALC4XL determined the contribution margin ratio C_m to be 0.3. The selling price is the sum of the manufacturing cost and the profit margin which totals €8242.

**Figure 2:** The hierarchy of the contributors to the manufacturing cost and selling price of an adsorption chiller with maximum cooling power of 8 kW.

Cost-Volume-Profit analysis

A Cost-Volume-Profit (CVP) analysis can reveal the profitability of a business over period of time [46]. In general, the CVP analysis is conducted by all businesses to forecast the profit and to calculate the minimum units to be sold to start earning a positive income. In addition, it is a crucial step to evaluate at early stage of process costing the hidden costs that might become irrelevant after a certain production volume. The CVP analysis starts from the calculation of the variable cost V from the selling price $S = €8248$:

$$V = C_m S = €5774 \quad (6)$$

Where $C_m = 0.3$ is the dimensionless contribution margin (C_m) discussed in previous section. This value is linked to the number of tasks performed during the manufacturing process and the type of industry. From the variable cost, the dimensionless break-even point (BEP) is identified by using Eq. (7). The BEP is the minimum number of units to sell to earn a profit.

$$BEP = F / (S - V) \quad (7)$$

with $(S - V) = €2474$ and where $F = €2799$ is the monthly fixed cost that does not change with the throughput of a business. This comes from €33591, the annual fixed cost for a medium-sized corporation producing adsorption chillers that represents the amount paid to cover the business expenses such as rental lease, insurance, property taxes and a potential utility bills. When a target profit T_P in [€] is added to the fixed cost, a target profit-based factor on break-even point ($BEPTP$) is obtained. Therefore, the $BEPTP$ is:

$$BEPTP = (F + T_P) / (S - V) \quad (8)$$

The total cost T in [€] is the sum of the annual fixed cost F and the variable cost V of the manufacturing process:

$$T = F + V \quad (9)$$

The base profit P in [€] from selling a certain number of units (Q) is obtained from:

$$P = (S Q) - (V - Q) - F \quad (10)$$

The CVP analysis was extended with the inclusion of considerations on the payback to provide a prospect customer an insight on expected annual savings and payback period. The dimensionless PayBack Period (PBP) is:

$$PBP = S / NC \quad (11)$$

Where NC is the net cash per period in [€] obtained from the product of Capital Recovery Factor (CRF), where, $i = 5\%$ is the interest rate and $n = 10$ is the lifetime of the chiller:

$$CRF(i, n) = \frac{i(i+1)^n}{(i+1)^n - 1} \quad (12)$$

All the contributors to the CVP analysis are summarised in Table 4. The CVP analysis was then undertaken using the methodology detailed in Eq. (6) to (10). Using the analysis, the break-even point was determined to be 14 units a year. This number of units represents the minimum volume of units that should be sold to render the business sustainable. Furthermore, as shown in Fig. 3 from the positive revenues, at a capacity of 40 units a year this business looks profitable to a perspective investor.

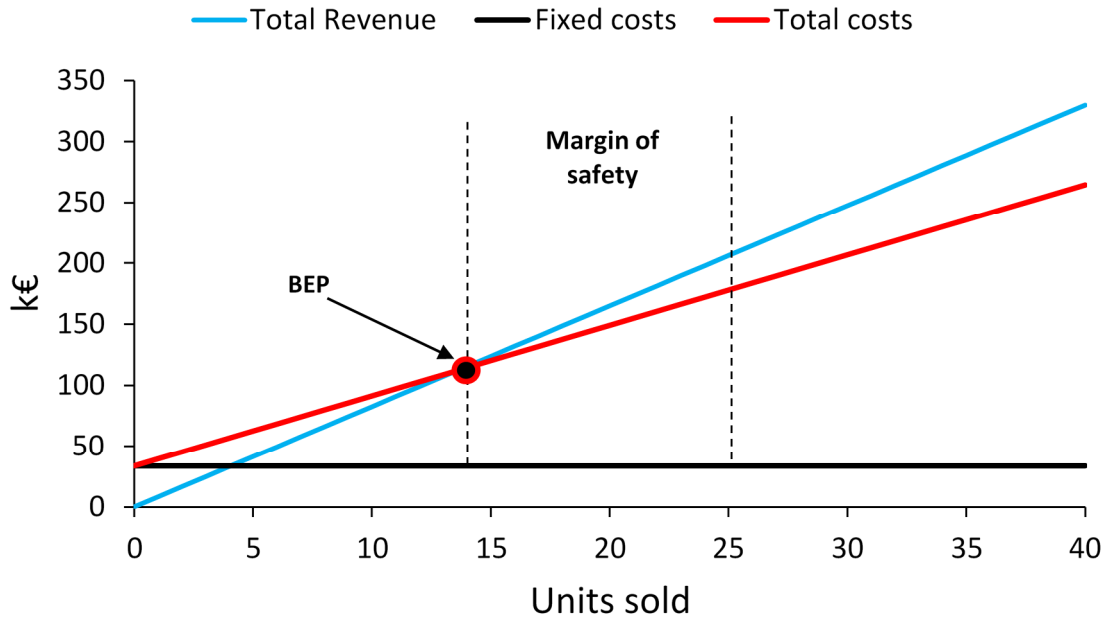


Figure 3: Contributors to the CVP analysis of an adsorption chiller with 8kW maximum cooling power.

Payback period and annual unit cost for a customer

To determine if an adsorption chiller is economical for a customer, a payback analysis can be carried out by following the definition of payback period in Eq. (11). The payback period is the time required to generate an amount of income that is equal to the initial investment. The Net cash flow is essential for the analysis, and is determined by comparing the adsorption chiller with a conventional vapour compression chiller. An 8kW vapour compression chiller was selected for comparison with an initial investment of €3600, and a total operational cost of €5663 per year [2]. In this study, an adsorption chiller with 8 kW cooling power was priced with initial investment value of €8242. In addition, an annual operational cost of €1029 is added as a policy cover for services such as maintenance, that are essential given the technology readiness level lower than the vapour compression counterpart [2]. The Cumulative Cash Flow is shown in Fig 4. This gives a payback period for the adsorption chiller of 2 years. It is interesting to note that when 3D printing is used as manufacturing method [30, [47], the payback period reduces to 1.3 years, thanks to automated manufacturing process and reduced labour cost. Both manufacturing methods result in quicker return on investment compared to similar studies [7,48,49], although other studies feature more complex systems whose adsorption chiller is only one part.

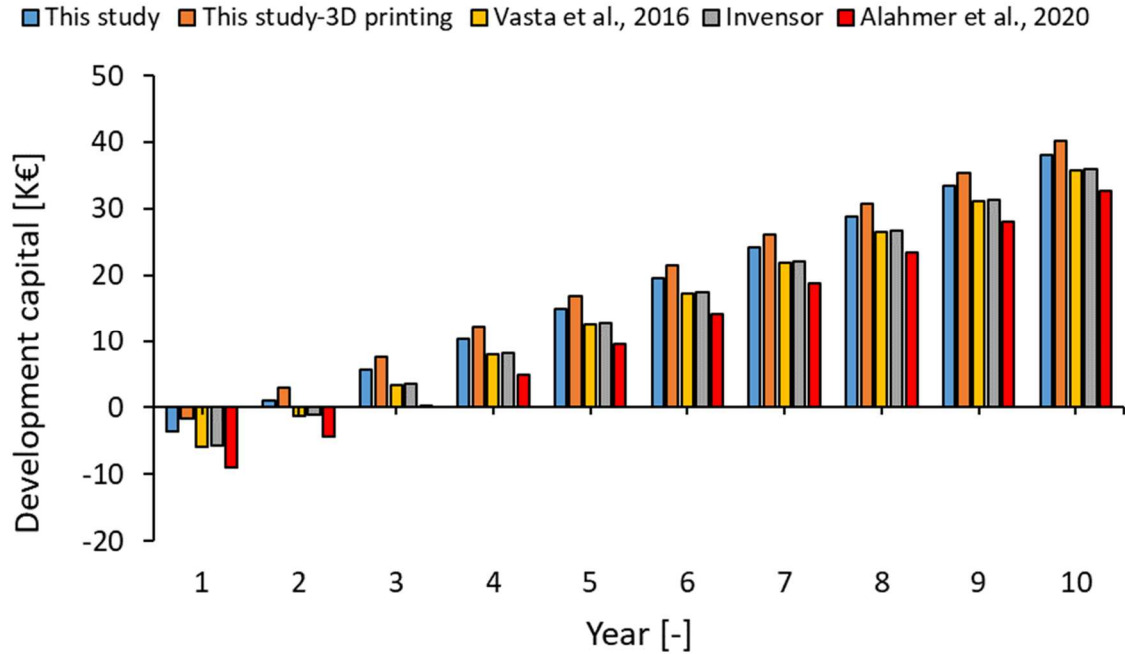


Figure 4: Cash flow development on investing in 8kW adsorption chiller over 10 years life span.

Profit maximisation

Sensitivity analysis allows the identification of the factors that most influence the profitability. Table 4 reports the results of the application of a two-levels full factorial design (FFD) [50–52] to the profitability analysis. The selling price and number of units sold are the most influential variables on positive profit growth. To maximise the profit with an increase of 75% compared to base profit, at least 384 units should be sold, along with a 10% increase of the unit price and a decrease of 10% in the variable costs and fixed costs. A further increase beyond 384 units does not significantly influence the profit.

Table 4: FFD matrix to maximise the profit

Run	<i>S</i> [€]	<i>V</i> [€]	Number of units sold	<i>F</i> [€]	Profit [€]
1	8248	5774	14	33591	1045
2	13000	5774	14	33591	67573
3	8248	9100	14	33591	-45519
4	13000	9100	14	33591	21009
5	8248	5774	384	33591	916425
6	13000	5774	384	33591	2741193
7	8248	9100	384	33591	-360759
8	13000	9100	384	33591	1464009
9	8248	5774	14	100773	-66137
10	13000	5774	14	100773	391
11	8248	9100	14	100773	-112701
12	13000	9100	14	100773	-46173
13	8248	5774	384	100773	849243
14	13000	5774	384	100773	2674011
15	8248	9100	384	100773	-427941
16	13000	9100	384	100773	1396827

Conclusions

Adsorption chillers struggle to penetrate the market since their introduction in 1930. New and efficient adsorbent materials are often too costly for an already expensive and often inefficient technology. There is consensus that the performance can be significantly increased from those

currently achieved [53] and this will lead to a stronger commercialization of the technology. However, nowadays the market still features silica-gel adsorption chiller that achieve in the best case specific cooling powers limited to 250-300 W kg⁻¹. This study highlights that by doubling the specific cooling powers, the overall technology price can be decreased considerably although there are also other factors as influential as the performance that contribute to the technology cost. An alternative is for example the change to less costly manufacturing processes such as 3D printing [22,47]. Using a techno-economic analysis, this study indicates that the current investment value for adsorption chillers is €1030.25 per kW of cooling power. Despite the high value, profit optimisation shows it is a profitable business. Additionally, the return of investment has been proven economical for potential customers too.

NOMENCLATURE

<i>BEP</i>	Break-even point [-]
<i>BEPTP</i>	Break-even point-targeted profit [-]
<i>C_m</i>	Contribution margin ratio, [%]
<i>COP</i>	Coefficient of performance [-]
<i>CRF</i>	Capital Recovery Factor
<i>P</i>	Profit, [€]
<i>PBP</i>	Payback period, [Years]
<i>S</i>	Selling price per unit, [€]
<i>SAHP</i>	The adsorber heating power per kg of silica-gel [<i>W kg⁻¹</i>]
<i>S_{CondP}</i>	The condensing power per kg of silica-gel [<i>W kg⁻¹</i>]
<i>SCP</i>	Specific cooling power per kg of dry silica-gel [<i>W kg⁻¹</i>]
<i>T</i>	Total costs, [€]
<i>V</i>	Variable costs per unit, [€]

References

- [1] F. Ackerman, E.A. Stanton, *The Cost of Climate Change: What We'll Pay if Global Warming Continues Unchecked*, New York. (2008) 42.
- [2] eCoo S - FAHRENHEIT, (2020). <https://fahrenheit.cool/en/product/ecoo-s/> (accessed November 5, 2020).
- [3] Tri-generation - Enersion, (n.d.). <https://enersion.com/trigeneration/> (accessed March 1, 2021).
- [4] K.C. Ng, K. Thu, Y. Kim, A. Chakraborty, G. Amy, Adsorption desalination: An emerging low-cost thermal desalination method, *Desalination*. 308 (2013) 161–179. <https://doi.org/10.1016/j.desal.2012.07.030>.
- [5] K. Thu, A. Chakraborty, B.B. Saha, W.G. Chun, K.C. Ng, Life-cycle cost analysis of adsorption cycles for desalination, *Desalin. Water Treat.* 20 (2010) 1–10. <https://doi.org/10.5004/dwt.2010.1187>.
- [6] U.S. Department of Energy, *Combined Heat and Power Technology Fact Sheet Series: Absorption Chillers for CHP Systems*, (2016) 1–4.
- [7] S. Vasta, V. Palomba, A. Frazzica, G. Di Bella, A. Freni, Techno-Economic Analysis of Solar Cooling Systems for Residential Buildings in Italy, *J. Sol. Energy Eng.* 138 (2016) 031005. <https://doi.org/10.1115/1.4032772>.
- [8] K.C. Ng, K. Thu, B.B. Saha, A. Chakraborty, Study on a waste heat-driven adsorption cooling cum desalination cycle, *Int. J. Refrig.* 35 (2012) 685–693. <https://doi.org/10.1016/j.ijrefrig.2011.01.008>.
- [9] A.S. Alsaman, A.A. Askalany, K. Harby, M.S. Ahmed, Performance evaluation of a solar-driven adsorption desalination-cooling system, *Energy*. 128 (2017) 196–207. <https://doi.org/10.1016/j.energy.2017.04.010>.
- [10] R.J.H. Grisel, S.F. Smeding, R. de Boer, Waste heat driven silica gel/water adsorption cooling in trigeneration, *Appl. Therm. Eng.* 30 (2010) 1039–1046. <https://doi.org/10.1016/j.applthermaleng.2010.01.020>.
- [11] T. Núñez, W. Mittelbach, H.M. Henning, Development of an adsorption chiller and heat pump for domestic heating and air-conditioning applications, *Appl. Therm. Eng.* 27 (2007) 2205–2212. <https://doi.org/10.1016/j.applthermaleng.2005.07.024>.
- [12] K.C. Ng, K. Thu, A. Chakraborty, B.B. Saha, W.G. Chun, Solar-assisted dual-effect adsorption cycle for the production of cooling effect and potable water, *Int. J. Low-Carbon Technol.* 4 (2009) 61–67. <https://doi.org/10.1093/ijlct/ctp008>.
- [13] Q. Pan, J. Peng, R. Wang, Application analysis of adsorption refrigeration system for solar and data center waste heat utilization, *Energy Convers. Manag.* 228 (2021) 113564. <https://doi.org/10.1016/j.enconman.2020.113564>.
- [14] SolabChiller - Solabcool.com, (n.d.). <http://www.solabcool.com/solabcoolcom/en/website/productdetails/product/3->

- solabchiller/ (accessed May 13, 2021).
- [15] mayekawa, Adsorption chiller, (2021) 1–4. <https://www.mayekawa.com.au/494/wp-content/uploads/2011/02/AdRef-Noa-Adsorption-Chiller1.pdf> (accessed May 13, 2021).
- [16] Adsorption Chillers | Bryair, (n.d.). <https://www.bryair.com/en/uae-en/products-solutions/adsorption-chillers/> (accessed May 13, 2021).
- [17] W.S. Chang, C.C. Wang, C.C. Shieh, Experimental study of a solid adsorption cooling system using flat-tube heat exchangers as adsorption bed, *Appl. Therm. Eng.* 27 (2007) 2195–2199. <https://doi.org/10.1016/j.applthermaleng.2005.07.022>.
- [18] T. Núñez, W. Mittelbach, H.-M. Henning, Development of a Small-Capacity Adsorption System for Heating and Cooling Applications, *HVAC&R Res.* 12 (2006) 749. <https://doi.org/10.1080/10789669.2006.10391205>.
- [19] L. Brochard, V. Kamath, J. Corbalán, S. Holland, W. Mittelbach, M. Ott, Cooling the Data Center, in: *Energy-Efficient Comput. Data Centers*, Wiley, 2019: pp. 37–63. <https://doi.org/10.1002/9781119422037.ch3>.
- [20] R.K. Sinnott, G. Towler, *Chemical Engineering Design*, Elsevier Ltd, 2013. <https://doi.org/10.1016/C2009-0-61216-2>.
- [21] C. Olkis, S. Brandani, G. Santori, A small-scale adsorption desalinator, *Energy Procedia.* 158 (2019) 1425–1430. <https://doi.org/10.1016/j.egypro.2019.01.345>.
- [22] S. AL-Hasni, G. Santori, 3D printing of vacuum and pressure tight polymer vessels for thermally driven chillers and heat pumps, *Vacuum.* 171 (2020) 109017. <https://doi.org/10.1016/j.vacuum.2019.109017>.
- [23] C. Hauviller, Design rules for vacuum chambers, n.d. [http://edge.rit.edu/edge/P14651/public/Miscellaneous/Design rules for vacuum chambers.pdf](http://edge.rit.edu/edge/P14651/public/Miscellaneous/Design%20rules%20for%20vacuum%20chambers.pdf) (accessed June 17, 2020).
- [24] Guidelines for the fabrication of vacuum systems and components, *Methods Exp. Phys.* 14 (1980) 425–448. [https://doi.org/10.1016/S0076-695X\(08\)60378-6](https://doi.org/10.1016/S0076-695X(08)60378-6).
- [25] OKER CHEMIE SIOGEL - Small porous siogel granules, Catalyst carrier, Pharma desiccant closure, Adsorption capacity, hydrocarbons drying, gas drying, (n.d.). <https://www.oker-chemie.de/en/products/adsorbents/siogel.html> (accessed March 12, 2021).
- [26] Home | Product-Cost-Calculation for EXCEL, (2020). <https://www.calc4xl.com/en/home/> (accessed November 4, 2020).
- [27] Metal Cut to Size UK | Stainless Steel & Aluminium | Order Now, (2020). <https://www.metalswarehouse.co.uk/custom-cut-metal/> (accessed November 9, 2020).
- [28] Semaphore Systems : Major UK Advantech Distributor, (2020). <https://www.semaphore-systems.co.uk/> (accessed November 9, 2020).
- [29] Thermocouple Probes and Assemblies, (2020). <https://www.omega.co.uk/section/thermocouples.html> (accessed November 9, 2020).
- [30] Finned Coil Water to Air Heat Exchangers, (2020). <https://www.brazetek.com/finned-coil-water-air-heat-exchangers> (accessed November 9, 2020).
- [31] Solenoid Valves World- Solenoid valve world provides the widest possible range of solenoid and process valves for your processing and industrial needs in one place, (2020). <https://www.solenoid-valve.world/> (accessed November 9, 2020).
- [32] Buy Swagelok | Swagelok, (2020). https://www.swagelok.com/en/catalog?gclid=Cj0KCQiA7qP9BRCLARIsABDaZzjip361CfBfWvmZrLTzbYmiw9oZ4fGnrr2sxIlobjoFS1YcrleS_qUaAuyhEALw_wcB&gclid=aw.ds (accessed November 9, 2020).
- [33] Klein Flanges, KF Fittings, Vacuum Traps & Valves, (2020). <https://www.scanwel.co.uk/shop/> (accessed November 9, 2020).
- [34] The Arc Welding Process and a New Type of Welding, (n.d.). <https://tiptig.com/arc-welding-process/> (accessed March 12, 2021).
- [35] Weld Cost Calculator, (2020). <https://www.esab.co.uk/gb/en/support/value-added-engineering/quick-weld-productivity-analyzer.cfm> (accessed November 9, 2020).
- [36] Q.W. Pan, R.Z. Wang, L.W. Wang, D. Liu, Design and experimental study of a silica gel-water adsorption chiller with modular adsorbents, *Int. J. Refrig.* 67 (2016) 336–344. <https://doi.org/10.1016/j.ijrefrig.2016.03.001>.
- [37] A.S. Uyun, T. Miyazaki, Y. Ueda, A. Akisawa, Experimental Investigation of a Three-Bed Adsorption Refrigeration Chiller Employing an Advanced Mass Recovery Cycle, *Energies.* 2 (2009) 531–544. <https://doi.org/10.3390/en20300531>.
- [38] K.C.A. Alam, B.B. Saha, A. Akisawa, Adsorption cooling driven by solar collector: A case study for Tokyo solar data, in: *Appl. Therm. Eng.*, Pergamon, 2013: pp. 1603–1609. <https://doi.org/10.1016/j.applthermaleng.2011.09.028>.
- [39] R. De Boer, S. Smeding, R. Grisel, Development and testing of a sorbent filled heat exchanger for use in compact solid sorption cooling systems, (2005).
- [40] OKER CHEMIE SIOGEL - Narrow-pore Siogel granulate, catalyst carrier, pharmaceutical stopper, adsorption capacity, hydrocarbons, dynamic adsorption, drying of gases, (n.d.). <https://www.oker-chemie.de/produkte/adsorbentien/siogel.html> (accessed February 25, 2021).
- [41] A. Sapienza, S. Santamaria, A. Frazzica, A. Freni, Influence of the management strategy and operating conditions on the performance of an adsorption chiller, *Energy.* 36 (2011) 5532–5538. <https://doi.org/10.1016/j.energy.2011.07.020>.
- [42] A. Sapienza, G. Gullì, L. Calabrese, V. Palomba, A. Frazzica, V. Brancato, D. La Rosa, S. Vasta, A. Freni, L. Bonaccorsi, G. Cacciola, An innovative adsorptive chiller prototype based on 3 hybrid coated/granular adsorbents, *Appl. Energy.* 179 (2016) 929–938. <https://doi.org/10.1016/j.apenergy.2016.07.056>.
- [43] M.A. Lambert, A. Beyene, Thermo-economic analysis of solar powered adsorption heat pump, *Appl. Therm. Eng.*

- 27 (2007) 1593–1611. <https://doi.org/10.1016/j.applthermaleng.2006.09.005>.
- [44] C. Olkis, S. AL-Hasni, S. Brandani, S. Vasta, G. Santori, Solar powered adsorption desalination for Northern and Southern Europe, *Energy*. (2021) 120942. <https://doi.org/10.1016/j.energy.2021.120942>.
- [45] COST COMPARISON | TIP TIG Welding, (2020). <https://tiptig.com/arc-welding-process/> (accessed June 17, 2020).
- [46] M. Cafferky, J. Wentworth, *Breakeven Analysis: The Definitive Guide to Cost-Volume-Profit Analysis*, Second Edition, Business Expert Press, 2014. <https://books.google.co.uk/books?id=9o7DoAEACAAJ>.
- [47] S. AL-Hasni, C. Olkis, A. Freni, G. Santori, A miniature 3D printed sorption heat transformer, *ISHPC 2021 Proc.* (2020) 170.
- [48] InvenSor LTC 10 e plus – InvenSor, (n.d.). <https://invenSor.com/en/products/invenSor-ltc-10-e-plus/> (accessed November 5, 2020).
- [49] A. Alahmer, X. Wang, K.C.A. Alam, Dynamic and Economic Investigation of a Solar Thermal-Driven Two-Bed Adsorption Chiller under Perth Climatic Conditions, *Energies*. 13 (2020) 1005. <https://doi.org/10.3390/en13041005>.
- [50] A. Askalany, C. Olkis, E. Bramanti, D. Lapshin, L. Calabrese, E. Proverbio, A. Freni, G. Santori, Silica-Supported Ionic Liquids for Heat-Powered Sorption Desalination, *ACS Appl. Mater. Interfaces*. 11 (2019) 36497–36505. <https://doi.org/10.1021/acsami.9b07602>.
- [51] A. Freni, G. Maggio, S. Vasta, G. Santori, F. Polonara, G. Restuccia, Optimization of a solar-powered adsorptive ice-maker by a mathematical method, *Sol. Energy*. 82 (2008) 965–976. <https://doi.org/10.1016/j.solener.2008.05.002>.
- [52] G. Santori, A. Frazzica, A. Freni, M. Galieni, L. Bonaccorsi, F. Polonara, G. Restuccia, Optimization and testing on an adsorption dishwasher, *Energy*. 50 (2013) 170–176. <https://doi.org/10.1016/j.energy.2012.11.031>.
- [53] H. Bahrehmand, M. Bahrami, Optimized sorber bed heat and mass exchangers for sorption cooling systems, *Appl. Therm. Eng.* 185 (2005) 116348. <https://doi.org/10.1016/j.applthermaleng.2020.116348>.

Environmental Process Optimisation of Adsorption-based Direct Air Capture of CO₂

P. Postweiler¹, M. Engelpracht¹, A. Gibelhaus¹ and N. von der Assen^{1*}

¹Institute of Technical Thermodynamics, RWTH Aachen University, Aachen, Germany

*Corresponding author: niklas.vonderassen@ltt.rwth-aachen.de

Abstract

Adsorption-based Direct Air Capture (DAC) of CO₂ can limit anthropogenic climate change by actively removing CO₂ from the atmosphere. For this purpose, DAC systems require thermal and mechanical energy as driving energies. The amount and fraction of the driving energies are adjustable by changing the process conditions as degrees of freedom in process control. State of the art is to use an energetic or exergetic evaluation of the DAC process even if this cannot consider whether low-carbon energy sources such as waste heat are used. Instead, we investigate the net carbon capture efficiency as a new key performance indicator for process control optimization. We show that depending on the case, an energetic-optimal DAC process achieves a carbon capture efficiency of 76 % by a given CO₂ purity of 90 %, whereas a carbon capture efficient optimal process achieves a carbon capture efficiency of 88 % for the same purity. Thus, the carbon capture efficiency increases by 14 % by choosing the carbon capture efficiency as objective for the process control optimization.

Keywords: direct air capture, negative emission technologies, life-cycle CO₂ emission

1 Introduction/Background

To limit the global temperature increase below 2 °C, CO₂ must be actively removed from the atmosphere [1]. The required CO₂ removal ranges from 1.8 to 40 Gt per year, depending on the scenario [1]. For technically removing CO₂ from the atmosphere, the following approaches were recently discussed in the literature: 1) Bio-energy with carbon capture, 2) enhanced weathering, 3) ocean fertilization, and 4) direct air capture [2]. The sorption-based Direct Air Capture (DAC) is one of the most promising options among these approaches because DAC systems are scalable, mobile, and can use low-temperature heat as driving energy [2,3]. In an adsorption-based DAC system, CO₂ is adsorbed from the ambient air and desorbed at lower pressure or higher temperature [3]. Thus, the driving energy of the DAC process can be provided either by mechanical or thermal energy. Although a DAC process with one energy type is possible, both types are usually combined, e.g., in the temperature vacuum swing adsorption, to achieve higher CO₂ purities or higher exergy efficiencies [3].

For the temperature vacuum swing adsorption, the achievable CO₂ purity and the ratio between thermal and mechanical energy changes when varying the process conditions, i.e., the desorption temperature and pressure. For this reason, the process control of the DAC system can be optimized, which requires reliable Key Performance Indicators (KPIs) as the objective function. A typical KPI is the Specific Energy Demand (SED), which relates the overall mechanical and thermal energy demand to the captured mass of CO₂ [4]. In contrast, the Specific Exergy Demand (SED_{ex}) considers the amount and quality of the energy used through exergy [5]. However, both the energetic and exergetic performance indicators are not enough to holistically evaluate DAC systems employed for CO₂ removal. As shown by Deutz et al., the CO₂ footprints of the energy sources have a significant impact on the net CO₂ removal of DAC systems [6]. For example, a DAC process with a high energy demand can still be beneficial when using low-carbon energy sources such as waste heat. Thus, we propose the

Carbon Capture Efficiency (CCE) as a new performance indicator for DAC control optimization. The CCE indicates the percentage of captured CO₂ after deducing net CO₂ emissions of the DAC process [6]. The net CO₂ emissions of the DAC process include upstream CO₂ emission from the supply of materials and energy [6].

Although DAC systems have already been assessed for their environmental impact [6,7], the process control has not been optimized regarding the net carbon capture efficiency to the best of the authors' knowledge. Therefore, we investigate the impact of the three different KPIs on the optimal process control and show how the KPIs used for optimization influence the climate benefit of a DAC system. For this purpose, we introduce the examined adsorption cycle in **Section 2**. **Section 3** briefly introduces the dynamic DAC system model. The KPIs and the optimization problem are formulated in **Section 4**. **Section 5** defines our case study, and we show the corresponding results of the process control optimization in **Section 6**. Last, we conclude the main findings in **Section 7**.

2 Adsorption Cycle for CO₂ Removal

Adsorption cycles for CO₂ removal are mainly characterized by the regeneration method. Possible regeneration methods are the following [8]:

1. Temperature Swing: A higher temperature leads to lower equilibrium loading and thus to desorption.
2. Pressure Swing: A lower (partial) pressure leads to lower equilibrium loading and thus to desorption. If the total pressure is below the ambient pressure, it is called a vacuum swing.
3. Inert Purge: The mechanism is identical to the pressure swing (i.e., low partial pressure) but achieved by injecting inert gases.
4. Desorption Displacement: The adsorbate is displaced with another adsorptive with higher or similar affinity.

The regeneration methods are often combined, e.g., a temperature vacuum swing cycle combines the temperature swing and vacuum swing as regeneration methods. The temperature vacuum swing cycle is the most popular cycle for DAC systems [9] and is already commercially used [6]. Besides, the temperature vacuum swing is recommended for high CO₂ purities and high equilibrium working capacities [10]. Therefore, we investigate the temperature vacuum swing in this work. The temperature vacuum swing cycle consists of four phases (**Figure 1**), explained in detail below:

- I. Adsorption phase (ads):** During the adsorption phase with phase duration τ_{ads} , a fan blows an airflow \dot{m}_{ads} with ambient conditions (i.e., temperature T_{amb} , pressure p_{amb} , and relative humidity φ_{amb}) through the adsorber column. Thereby, the fan overcomes the pressure drop of the column by using the mechanical work \dot{W}_{fan} . The selected adsorbent adsorbs CO₂ and H₂O from the airstream at a total pressure near ambient pressure. The heat of adsorption is released to the ambient as heat flow \dot{Q}_{ads} at ambient temperature via the heating and cooling jacket. Thus, an airflow with less CO₂ and H₂O leaves the adsorber column.
- II. Blowdown phase (blow):** The blowdown phase has the phase duration τ_{blow} and starts with closing the column inlet. Then, a vacuum pump decreases the column pressure to the desorption pressure p_{des} and, thus, extracts most of the air from the column. For this purpose, the vacuum pump needs the mechanical work $\dot{W}_{\text{vac,blow}}$. The extracted air is released into the environment.
- III. Heating phase (heat):** During the heating phase with phase duration τ_{heat} , the adsorber column is heated to the desorption temperature T_{des} by absorbing the heat flow \dot{Q}_{heat} from the heating and cooling jacket. The heat flow is mainly used for sensitive heating but also

for providing the heat of adsorption. Due to limited heat transport, the adsorbent is slowly heated to the desorption temperature. Thereby, mainly H₂O is desorbed due to faster kinetics and beneficial equilibrium loading compared to CO₂. The column pressure is kept constant at desorption pressure p_{des} by extracting all desorbed mass via the vacuum pump. For this purpose, the vacuum pump needs the mechanical work $\dot{W}_{vac,heat}$. The extracted mass flow is still released into the environment.

IV. Desorption phase (des): During the desorption phase with phase duration τ_{des} , the adsorber column is further heated and maintained at constant temperature T_{des} . The required heat flow \dot{Q}_{des} is mainly used for providing the heat of adsorption. In this phase, mainly CO₂ is desorbed since most H₂O was already desorbed during the heating phase. Thus, a CO₂-rich product stream leaves the column.

Overall, the ambient conditions (i.e., temperature T_{amb} , pressure p_{amb} , and relative humidity φ_{amb}) define the use case and are fixed. For maximizing the KPIs of the DAC system, the process conditions (i.e., mass flow \dot{m}_{ads} ; phase times τ_{ads} , τ_{blow} , τ_{heat} , and τ_{des} ; and desorption conditions p_{des} and T_{des}) are degrees of freedom of the process optimization.

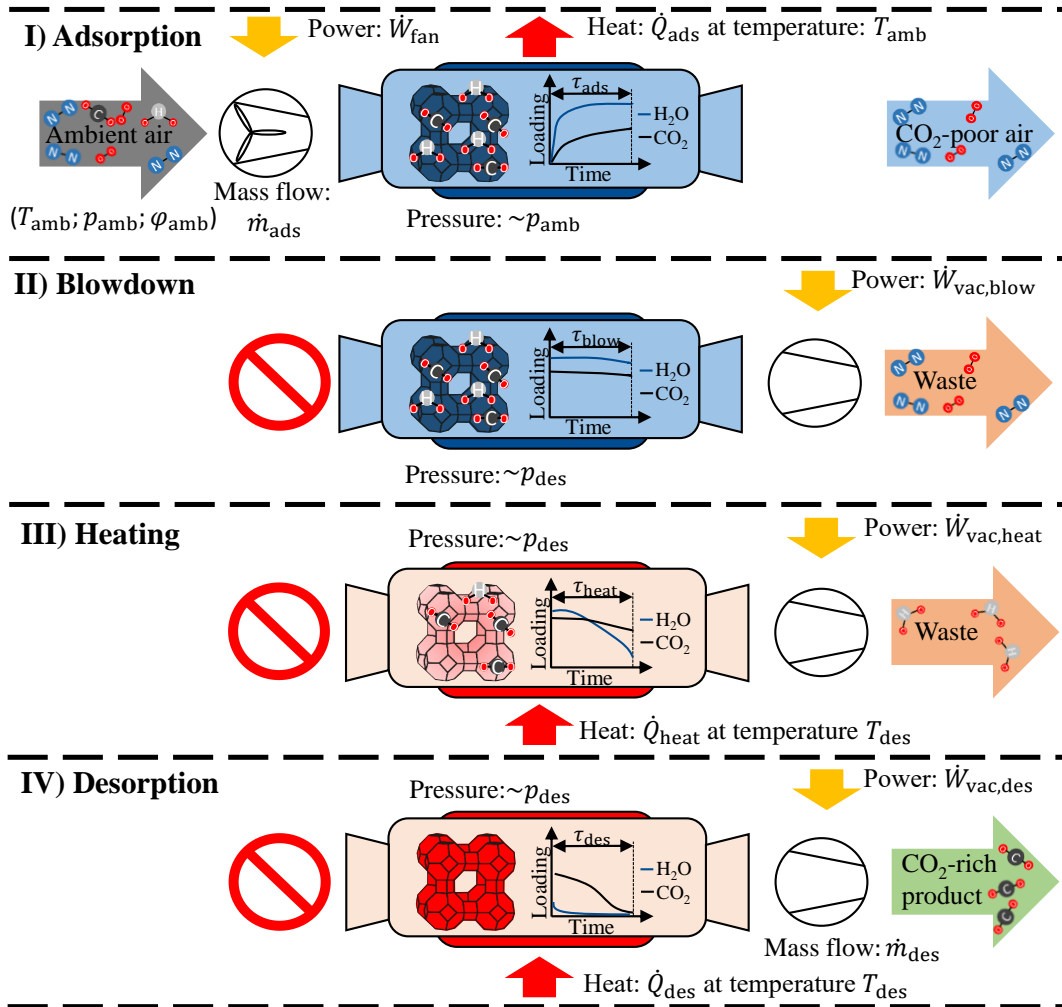


Figure 1: The four phases of the temperature vacuum swing cycle for the DAC application adapted from Stampi-Bombelli et al. [4]. I) Adsorption: Fan blows ambient air through the adsorber; CO₂ and H₂O are adsorbed. II) Blowdown: Vacuum pump decreases the column pressure to desorption pressure as the column inlet is closed. III) Heating: Jacket heats the column to the desorption temperature. IV) Desorption: Extraction of CO₂.

3 Dynamic Model of the Direct Air Capture System

The dynamic Direct Air Capture (DAC) system was modeled with the object-oriented language Modelica using the open-source library SorpLib [11] (available on Gitlab [12]). We calculated all fluid properties with the Modelica library TILMedia [13] based on RefProp [14]. **Figure 2** shows a scheme of the adsorber column model that was discretized in flow direction (here from top to bottom) using an upwind finite volume discretization scheme.

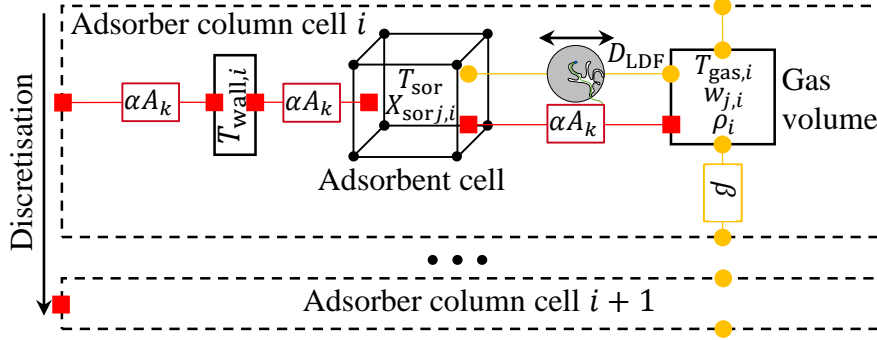


Figure 2: Scheme of the i^{th} cell of the one-dimensionally discretized model of the adsorber column. The main sub-models are the adsorbent (sor), the gas volume (gas), the wall cell (wall), and the heat and mass transfer in red and orange, respectively.

The adsorber column model builds up from four sub-models: 1) The gas volume, 2) the adsorbent cell, 3) the wall cell, and 4) the heat and mass transport between the sub-models 1)-3). The most important details of the sub-models are summarized below.

Gas volume (gas): The main equations of the gas volume model are three transient balance equations: 1) Overall mass balance, 2) component balance, and 3) energy balance. Thus, the selected differential states of the i^{th} -cell are the gas density ρ_i , the mass fraction for each component j of the gas phase $w_{j,i}$, and the temperature $T_{gas,i}$. A detailed description as well as the balance equations of the gas volume model, for one adsorptive, can be found in [11].

Adsorbent (sor): The adsorbent cell is based on the sorbent cell developed by Bau et al. and is adapted for more than one adsorptive in this work. A detailed description of the original adsorbent cell is provided by Bau et al. [11]. The adsorbent cell has a transient component/mass balance and a transient energy balance as main equations. The selected differential states are the adsorbent temperature $T_{sor,i}$ and the loading of each component $X_{sor,j,i}$. As sorbent, we used amine-functionalized cellulose with the name APDES-NFC [15]. The equilibrium loading of CO₂ is described by a modified Toth-isotherm [4]. Thus, the isotherm also captures the change in the equilibrium loading of CO₂ as a function of the water loading [4]. The equilibrium loading of water is modeled by a Guggenheim–Anderson de Boer isotherm [4]. Both isotherms, for CO₂ and H₂O, were refitted to the experimental data from Gebald et al. [15].

Wall cell (wall): The wall cell is modeled by a transient energy balance with the temperature $T_{wall,i}$ as a differential state.

Heat and mass transport: The heat flows between the gas volume and the adsorbent cell; the adsorbent cell and the wall cell; and the wall cell and the environment are modeled by a temperature difference between the components and the corresponding heat transfer coefficients and areas αA_j [11]. The convective mass transport from gas volume i to $i + 1$ is calculated by the total pressure gradient and the mass transfer coefficient β [11]. The mass transport from the gas volume to the adsorbent cell is calculated by the linear driving force approach [16] with the mass transfer coefficient D_{LDF} .

Besides the adsorber column model, the DAC system model has auxiliaries such as the fan and the vacuum pump. We model the fan's power consumption as an isothermal steady flow process and air as an incompressible fluid (due to the minor pressure increase) in the same way as reported by Stambi-Bombelli et al. [4]:

$$\dot{W}_{\text{fan}} = \frac{1}{\eta_{\text{fan}}} \cdot \frac{\dot{m}_{\text{ads}}}{\rho_{\text{air,in}}} (p_{\text{in}} - p_{\text{out}}). \quad (1)$$

Thus, the fan's power consumption was calculated in terms of the inlet pressure p_{in} and outlet pressure p_{out} of the adsorber column, the density of the air at the inlet of the column $\rho_{\text{air,in}}$, the mass flow through the column \dot{m}_{ads} , and the fan efficiency η_{fan} .

The power consumption of the vacuum pump \dot{W}_{vac} ,

$$\dot{W}_{\text{vac}} = \frac{1}{\eta_{\text{vac}}} \cdot \dot{n}RT \ln\left(\frac{p_{\text{amb}}}{p_{\text{des}}}\right), \quad (2)$$

was modeled as an isothermal steady flow process with air as ideal gas [4] and calculated with the molar flow rate \dot{n} , the temperature of the gas stream T , the ideal gas constant R , the vacuum pump efficiency η_{vac} and the quotient of the ambient pressure p_{amb} and desorption pressure p_{des} . Thus, our DAC system model only consists of the three necessary components to run a temperature vacuum swing cycle for a DAC purpose: 1) fan, 2) adsorber column, and 3) vacuum pump. However, additional auxiliaries for purification or compression may be needed to store or utilize the CO₂ [3]. These additional process steps could be cost- and energy-intensive [3]. Since they depend on the specific application of the CO₂ utilization or storage, we do not consider these components in this work.

All model parameters (e.g., geometrical data, heat and mass transfer coefficients, and thermodynamic properties of the adsorbent) are taken from Stampi-Bombelli et al. [4]. However, the heat transfer coefficient between the adsorbent and gas volume is not present in the model from Stampi-Bombelli et al. [4] as there is just one overall energy balance for the adsorbent cell and the gas volume. Therefore, we selected the heat transfer coefficients between the adsorbent cell and gas volume so small that the gas volume and the adsorbent cell have nearly the same temperature (c.f. **Figure 3** (c), gas and sorbent temperature). For numerical reasons, the heat transfer coefficient must remain in our model and cannot be zero.

To verify our model, we compare our simulation results to the reference model from the literature [4] in **Figure 3**. Due to the lack of trajectories for a temperature vacuum swing cycle, we verify our model for the trajectories of a steam-assisted temperature vacuum swing cycle. The only difference between the temperature vacuum swing cycle and the steam-assisted temperature vacuum swing cycle is that a small volume flow of superheated steam \dot{V}_{steam} flows (with desorption temperature T_{des} and desorption pressure p_{des}) through the adsorption column during desorption. **Table 1** summarizes the ambient and process conditions used for the model verification.

Table 1: Ambient conditions and process conditions for the model comparison in **Figure 3** [4]

Ambient conditions			Process conditions			
T_{amb}	p_{amb}	$x_{\text{amb},i}$	T_{des}	p_{des}	phase times	\dot{V}_{steam}
20 °C	1 bar	$x_{\text{amb},\text{N}_2} = 0.7806$	95 °C	0.05 bar	$\tau_{\text{ads}} = 13772 \text{ sec}$	$25 \cdot 10^{-6} \frac{\text{m}^3}{\text{s}}$
		$x_{\text{amb},\text{O}_2} = 0.2075$			$\tau_{\text{blow}} = 30 \text{ sec}$	
		$x_{\text{amb},\text{H}_2\text{O}} = 0.0115$			$\tau_{\text{heat}} = 704 \text{ sec}$	
		$x_{\text{amb},\text{CO}_2} = 0.0004$			$\tau_{\text{des}} = 30000 \text{ sec}$	

Figure 3 shows excellent qualitative agreement with the model from Stampi-Bombelli et al. [4] for the steam-assisted temperature vacuum swing cycle. Only the maximal CO₂ loading differs: there is a minor offset of the CO₂ loading during desorption phase. We expect that this discrepancy is due to minor differences in the fitted equilibrium data. However, due to the excellent agreement for the steam-assisted temperature vacuum swing cycle, we assume that the model trajectories for the vacuum swing cycle will also fit well. Furthermore, a minor deviation would not influence the qualitative conclusions of our study.

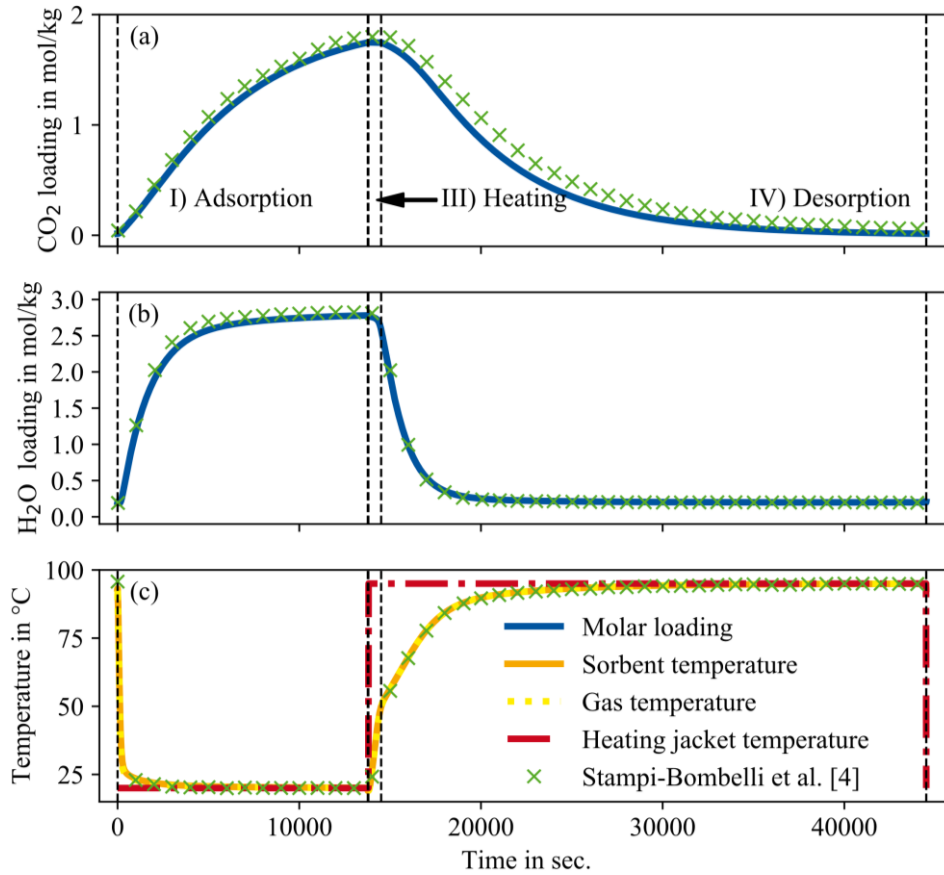


Figure 3: Trajectories of selected differential states of the last cell of the adsorber column of the DAC system model at cyclic steady-state conditions. The vertical dashed lines mark the beginning and end of the four phases of the cycle. Phase II) (Blowdown) is so short that it is not visible in the plot.

4 Key Performance Indicator Used for Optimization

We examine three different Key Performance Indicators (KPIs) for the performance evaluation of a DAC system. The first KPI considered is the Specific Energy Demand (SED):

$$\text{SED} = \frac{W_{\text{total}} + Q_{\text{total}}}{\int_{\tau_3}^{\tau_4} \dot{m}_{\text{des}} \cdot w_{\text{CO}_2} dt} \quad (3)$$

The SED is calculated as the sum of the total mechanical energy W_{total} and the total thermal energy Q_{total} normalized by the mass of CO_2 captured during the desorption phase $\int_{\tau_3}^{\tau_4} \dot{m}_{\text{des}} \cdot w_{\text{CO}_2} dt$ (with: $\tau_3 = \tau_{\text{ads}} + \tau_{\text{blow}} + \tau_{\text{heat}}$ and $\tau_4 = \tau_{\text{ads}} + \tau_{\text{blow}} + \tau_{\text{heat}} + \tau_{\text{des}}$). The total thermal energy,

$$Q_{\text{total}} = \int_{\tau_2}^{\tau_3} \dot{Q}_{\text{heat}} dt + \int_{\tau_3}^{\tau_4} \dot{Q}_{\text{des}} dt, \quad (4)$$

is defined as the sum of the integrated heat flows of the heating phase \dot{Q}_{heat} and of the desorption phase \dot{Q}_{des} (with: $\tau_2 = \tau_{\text{ads}} + \tau_{\text{blow}}$). The total mechanical energy,

$$W_{\text{total}} = \int_0^{\tau_1} \dot{W}_{\text{fan}} dt + \int_{\tau_1}^{\tau_2} \dot{W}_{\text{vac,blow}} dt + \int_{\tau_2}^{\tau_3} \dot{W}_{\text{vac,heat}} dt + \int_{\tau_3}^{\tau_4} \dot{W}_{\text{vac,des}} dt, \quad (4)$$

is calculated as the sum of the integrated power of the fan \dot{W}_{fan} and the vacuum pump \dot{W}_{vac} (with: $\tau_1 = \tau_{\text{ads}}$). The vacuum pump is activated in three phases: blowdown (blow), heating (heat), and desorption (des).

In contrast to the specific energy demand, the Specific Exergy Demand (SED_{ex}),

$$\text{SED}_{\text{ex}} = \frac{W_{\text{total}} + Q_{\text{total}} \cdot \left(1 - \frac{T_{\text{amb}}}{T_{\text{des}}}\right)}{\int_{\tau_3}^{\tau_4} \dot{m}_{\text{des}} \cdot w_{\text{CO}_2} dt}, \quad (6)$$

does not consider the total thermal energy but only the exergy. The exergy of a heat flow is calculated in terms of the Carnot efficiency using the ambient temperature T_{amb} and the heat source temperature (here: desorption temperature T_{des}).

The Carbon Capture Efficiency (CCE) is defined as

$$\text{CCE} = \frac{m_{\text{CO}_2, \text{captured}} - \text{CC}_{\text{cap, process}}}{m_{\text{CO}_2, \text{captured}}}, \quad (7)$$

where $m_{\text{CO}_2, \text{captured}}$ describes the total CO_2 amount captured over the lifetime of a DAC system [7] and $\text{CC}_{\text{cap, process}}$ the Climate Change impact (CC) due to the capturing process. According to Deutz et al., the climate change impact due to the capturing process sums up the climate change impacts of the production of the adsorbent $\text{CC}_{\text{sor, production}}$, of the construction of the DAC system $\text{CC}_{\text{construction}}$, the end of life of the DAC system $\text{CC}_{\text{end of life}}$ and the climate change impact due to the operation of the DAC system $\text{CC}_{\text{operation}}$ [6]:

$$\text{CC}_{\text{cap, process}} = \text{CC}_{\text{sor, production}} + \text{CC}_{\text{construction}} + \text{CC}_{\text{end of life}} + \text{CC}_{\text{operation}}. \quad (8)$$

However, the main contribution to the climate change impact is caused by the operation of a DAC system and within operation, the climate change impact is mostly determined by the carbon footprint of the energy sources [6]. Therefore, we neglected all other parts except the climate change impact due to the energy supply. For the climate change impact due to the energy supply, we distinguish between two cases: 1) The used thermal energy is burden-free as waste heat is used ($\text{CC}_{\text{operation, wh}}$) and 2) the used thermal energy is provided by a heat pump which uses electricity to provide the heat ($\text{CC}_{\text{operation, hp}}$). Thus, for the case of burden-free waste heat, the climate change reads

$$\text{CC}_{\text{operation, wh}} = \text{CFP} \cdot W_{\text{total}}. \quad (9)$$

For this case, we multiply total mechanical energy by the Carbon Footprint (CFP) of the energy source. In contrast, the second case uses heat provided by a heat pump, and thus the climate change impact reads

$$CC_{\text{operation, hp}} = \text{CFP} \cdot \left(W_{\text{total}} + Q_{\text{total}} \cdot \left(1 - \frac{T_{\text{amb}}}{T_{\text{des}}} \right) \cdot \frac{1}{\eta_{\text{ex, hp}}} \right). \quad (10)$$

The mechanical energy needed for the heat pump is calculated by multiplying the heat demand with the reciprocal of the theoretically maximum heat pump efficiency $\left(\frac{T_{\text{des}}}{T_{\text{des}} - T_{\text{amb}}} \right)$ and the reciprocal of the exergy efficiency of a heat pump $\eta_{\text{ex, hp}}$.

To compare the optimized processes fairly, the product of the DAC system has to be identical, i.e., amount and purity must be the same. Therefore, we use the purity of the product stream Φ as a further criterion:

$$\Phi = \frac{\int_{t_3}^{t_4} \dot{n}_{\text{des}} \cdot x_{\text{CO}_2} dt}{\int_{t_3}^{t_4} \dot{n}_{\text{des}} dt}. \quad (12)$$

The purity is the mole fraction of CO₂ in the product stream and is calculated by the integral of the molar flow rate of CO₂ ($\dot{n}_{\text{des}} \cdot x_{\text{CO}_2}$) and the total molar flow rate \dot{n}_{des} during the desorption phase. For each CO₂ purity, there is a control vector p_c that optimizes the KPI. To account for this trade-off, the optimization problem becomes a multi-objective optimization problem and reads:

$$\begin{aligned} \min_{x^{(\cdot)}, z^{(\cdot)}, p_c} \quad & \mp KPI(x(\tau_{\text{cycle}}), z(\tau_{\text{cycle}}), p_c) \quad (\text{objective functions}) \\ & -\Phi(x(\tau_{\text{cycle}}), z(\tau_{\text{cycle}}), p_c) \\ \text{s.t.} \quad & \dot{x} = f(x(\tau), z(\tau), p_c) \quad (\text{dynamic model}) \\ & 0 = g(x(\tau), z(\tau), p_c) \\ & x(t=0) = x(t=\tau_{\text{cycle}}) \quad (\text{cyclic steady-state}). \end{aligned} \quad (13)$$

The differential states are summarized in x , the algebraic states in z , and the control parameters in p_c . As objective functions, we used the KPIs SED (**Eq. 3**), SED_{ex} (**Eq. 6**), and CCE (**Eq. 7**). The purity was always maximized. We exported the dynamic DAC system model as a functional mock-up unit using the functional mock-up interface [17] to solve the optimization problem. Then, the exported model was executed and optimized in Python with the genetic optimization algorithm NASGAI [18] included in the open-source toolbox Distributed Evolutionary Algorithms in Python (DEAP) [19].

5 Case Study

To remain comparable with the literature model shown in **Figure 3**, we used the same ambient conditions for all following optimizations (cf. **Table 1**). For the Carbon Capture Efficiency (CCE) optimization, we considered two cases: 1) Best-case and 2) worst-case. For the best-case, we assumed the thermal energy as waste heat that is burden-free and unlimitedly available up to 100 °C. The electricity has a Carbon Footprint (CFP) of wind power with 10 gCO_{2e} per kWh [20]. The worst-case uses a heat pump as a thermal energy source. The exergetic efficiency of the heat pump is $\eta_{\text{ex, hp}} = 60\%$, as this corresponds to an average exergy efficiency of heat pumps [6]. For the electricity of the worst-case, a CFP of the current European grid mix with 400 gCO_{2e} per kWh is assumed [20]. Thus, we cover a wide range of possible energy sources, and a real case will be somewhere between both cases. To keep the wording clear, we refer the burden-free waste heat case as CCE_{waste heat} and the heat pump case

as $CCE_{\text{heat pump}}$ even if it is the same KPI but with different CFP for the electricity and different heat sources.

Table 2: Control variables with lower and upper boundaries used for DAC process optimization

Control variables	Lower boundaries	Upper boundaries
\dot{m}_{ads}	Fixed (5.972e-5 kg/s)	Fixed (5.972e-5 kg/s)
τ_{ads}	5000 s	40000°s
τ_{blow}	Fixed (30 s)	Fixed (30 s)
τ_{heat}	500 s	10000 s
τ_{des}	5000 s	40000°s
p_{des}	0.01 bar	0.3 bar
T_{des}	50 °C	100 °C

Table 2 shows the control variables and their lower and upper boundaries for control optimization.

The mass flow during the adsorption phase \dot{m}_{ads} is fixed to the mass flow of the base case (c.f. **Figure 3**), as there is no trade-off in our model for this control variable. For the phase time of the adsorption phase, we select the boundaries to ensure that the CO₂ loading ranges between 50 % and 99.9 % of the CO₂ equilibrium loading of the base case (c.f. **Figure 3**).

The phase time of the blowdown phase is fixed as well. The phase time of the blowdown is rather determined by technical factors (e.g., power of the vacuum pump) than by the energy demand. As we did not include such technical constraints yet, the optimization of this control variable is not reasonable. The heating phase is mainly responsible for the purity of the product stream. Therefore, we selected broad boundaries to allow for large ranges of purity.

With the current implementation of the vacuum pump without a baseload, no trade-off exists in the length of the desorption phase. A trade-off would exist by implementing a baseload for the vacuum pump as well, which we plan for our future research. To still get reasonable results, we limited the maximal desorption time to the maximal adsorption time. The boundaries for desorption pressure were chosen to cover a broad operating range. The upper boundary for the desorption temperature was determined by the maximum waste heat temperature of 100 °C. Based on preliminary investigations we chose the lower boundaries sufficiently low so that the lower desorption temperature constraint was never active in any optimization run.

6 Results

This section discusses the optimization results of the introduced DAC system model for 1) the KPIs SED, SED_{ex} , $CCE_{heat\ pump}$, and $CCE_{waste\ heat}$ and 2) the related optimal control variables. All optimizations were performed with at least 600 individuals and 100 generations. However, some noise still exists in some optimal process variables due to genetic optimization. Nevertheless, significant trends can be identified, which are sufficient for the following discussion.

In **Figure 4 a)**, the SED is plotted over purity. The SED_{ex} -optimal and $CCE_{heat\ pump}$ -optimal processes differ marginally in terms of the SED from the SED-optimal process. The offsets in terms of SED are nearly constant over the whole purity range. The similarities of the SED_{ex} and $CCE_{heat\ pump}$ -optimal processes are attributed to similarities of these two KPIs. The SED_{ex} and $CCE_{heat\ pump}$ only differ with the exergy efficiency of a heat pump: For an exergy efficiency of $\eta_{ex, hp} = 1$, they would get the same optimal results (cf. **Eq. 6** and **Eq. 10**). The SED offsets are caused by the reduced weighting of heat in the KPIs SED_{ex} and $CCE_{heat\ pump}$. Thus, the heat used for driving increases and, consequently, the SED increases. In contrast, the $CCE_{waste\ heat}$ -optimal process has a SED, which increases up to 150 % of the minimum SED over purity. The KPI $CCE_{waste\ heat}$ does not consider heat at all. Hence, much heat is used for small advantages in $CCE_{waste\ heat}$, and the SED of the $CCE_{waste\ heat}$ -optimal process increases up to 150 % of the minimum SED.

We show the SED_{ex} over purity in **Figure 4 b)**. As already for **Figure 4 a)**, the SED_{ex} differs only marginal for the SED_{ex} -optimal and $CCE_{heat\ pump}$ -optimal processes. The reason for these minor differences is the similarity of the two KPIs as mentioned above. In contrast, the SED-optimal and the $CCE_{waste\ heat}$ -optimal processes have both a higher SED_{ex} . The SED-optimal process tends to use more mechanical energy than heat for operation, and thus the SED_{ex} increases. We observe the reverse for the $CCE_{waste\ heat}$ -optimal process. Despite these two contrary effects, the SED- and the $CCE_{waste\ heat}$ optimal processes have almost the same SED_{ex} at medium purities.

Figure 4 c) shows the CCE with the heat pump as heat source and electricity with the carbon footprint of the EU grid mix ($CCE_{heat\ pump}$) over purity. The $CCE_{waste\ heat}$ -optimal process has by far the worst performance in terms of the KPI $CCE_{heat\ pump}$ and is about 30 % worse at a purity of 50 %. The $CCE_{heat\ pump}$ -optimal and $CCE_{waste\ heat}$ -optimal processes were optimized with the same KPI but for different scenarios.

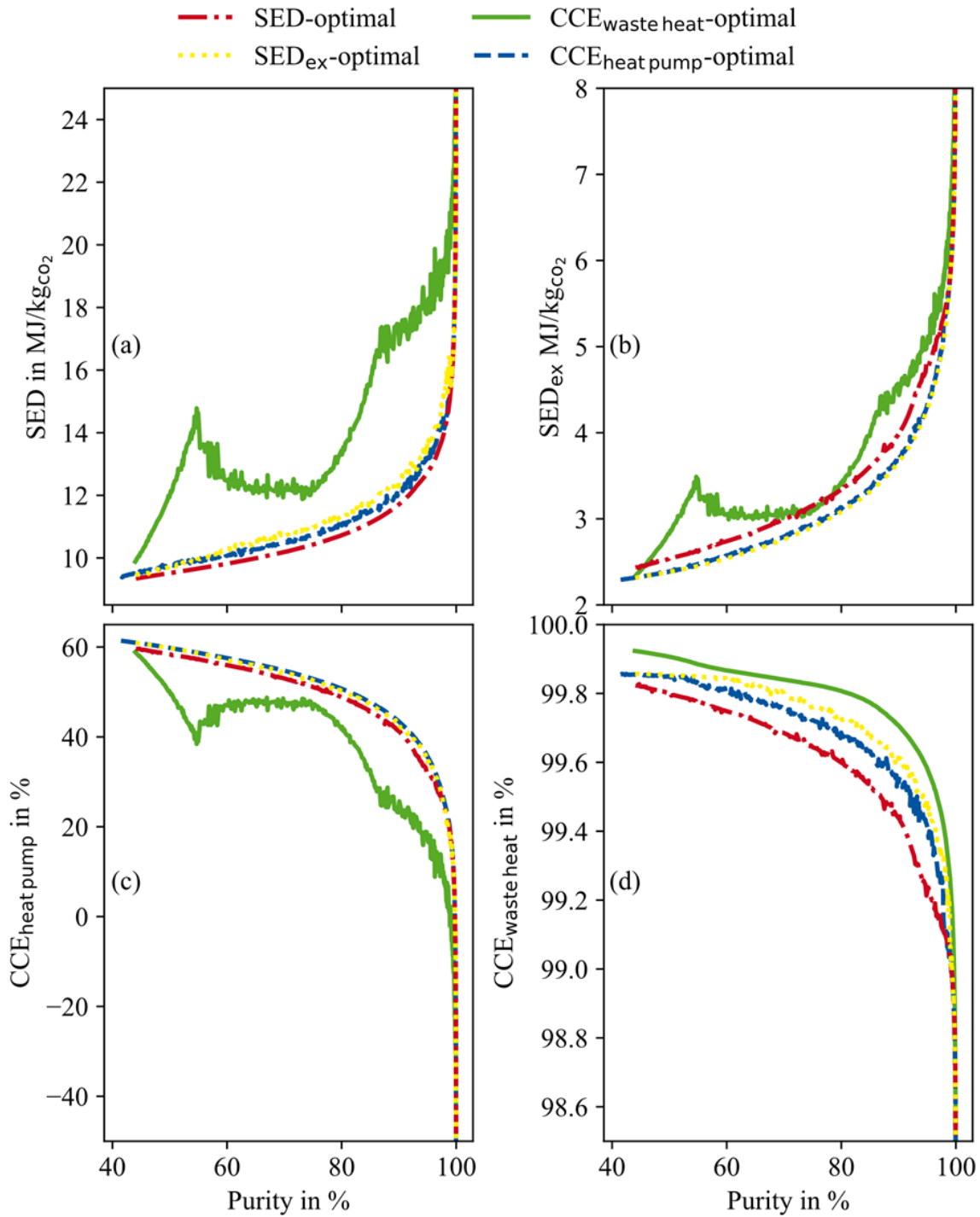


Figure 4: Trade-offs for the optimal processes between the purity and the key performance indicators (a) Specific Energy Demand (SED), (b) Specific Exergy Demand (SED_{ex}), (c) Carbon Capture Efficiency with heat pump (CCE_{heat pump}), and (d) Carbon Capture Efficiency with burden-free waste heat (CCE_{waste heat}).

Figure 4 d) shows the CCE_{waste heat} with waste heat as heat source and electricity with the carbon footprint of wind power. The SED_{ex}-optimal process has the second-best performance compared to the CCE_{waste heat}-optimal process. This is because the SED_{ex} weights heat second-least of all KPIs (only CCE_{waste heat} weights heat less with the factor 0), and thus the mechanical energy demand is minimized second-most. Further, the SED-optimal process has the worst performance in terms of CCE_{waste heat}. For the SED-optimal process, the exact opposite argumentation applies as for the SED_{ex}-optimal process. The KPI SED weighs heat and

mechanical energy equally so that more mechanical energy is used, leading to a weak performance in the KPI $CCE_{\text{waste heat}}$ (Figure 4 d). However, the SED-optimal process is only marginally worse than the $CCE_{\text{waste heat}}$ -optimal process. For example, at the purity of 90 %, the SED-optimal process has a $CCE_{\text{waste heat}}$ of 99.4 %, and the $CCE_{\text{waste heat}}$ -optimal process 99.7 %, showing an improvement of around 0.3 %. The improvement is small because we consider “very clean” power in this scenario, i.e., wind energy. If we consider the CFP of the EU grid mix, the $CCE_{\text{waste heat}}$ -optimal and SED-optimal processes would have a $CCE_{\text{waste heat}}$ of about 88 % and 76 %, respectively. Thus, the improvement of the $CCE_{\text{waste heat}}$ would be about 14 %. In summary, these results show the importance of using a sound KPI and scenario for DAC process optimization.

In addition to the KPIs of the optimized processes (cf. **Figure 4**), the corresponding optimal control variables are shown in **Figure 5** as a function of the purity. **Figure 5 a)** shows the optimal desorption temperature T_{des} . For the $CCE_{\text{waste heat}}$ -optimal process, the desorption temperature is always at the upper boundary because heat consumption has no negative impact on the KPI $CCE_{\text{waste heat}}$. Thus, no trade-off exists, and the maximum heat with the highest available temperature is used. The SED-optimal process has the second-highest temperature over a large purity range: Even the SED-optimal process minimizes the heat amount, a minor penalty of the temperature exists due to the sensitive heating of the adsorber column. The $CCE_{\text{heat pump}}$ -optimal process has the lowest desorption temperature since the temperature is penalized in the objective function (cf. **Eq. 10**). In the $CCE_{\text{heat pump}}$ -optimal process, the desorption temperature is further penalized with the reciprocal exergy efficiency of the heat pump in contrast to the KPI SED_{ex} . Overall, the desorption temperature is almost independent from the purity in all cases and decreases only slightly with increasing purity.

Figure 5 b) shows the desorption pressure p_{des} over the purity. As expected, the $CCE_{\text{waste heat}}$ -optimal process always has the highest desorption pressure. The order of the desorption pressure curves follows exactly the weighting of heat in the KPIs. The KPI SED weights equally between heat and mechanical energy and thus has the lowest desorption pressure. In contrast, the KPI $CCE_{\text{waste heat}}$ neglects the heat and therefore has the highest desorption pressure. However, all desorption pressure curves show a plateau at about 0.1 bar, caused by the efficiency of the vacuum pump. The efficiency of the vacuum pump is not described as constant but has different values in different pressure ranges (see [4]). At 0.1 bar, the efficiency changes why a plateau is formed here.

In **Figure 5 c)**, we show the adsorption time τ_{ads} as a function of purity. Higher adsorption times lead to higher loadings and higher mechanical energy consumption due to the fan. Thus, a trade-off exists for the adsorption time. The adsorption time is mainly determined by the weighting of the mechanical work in the KPIs. In a first approximation, the denominator of all KPIs increases with increasing phase time, i.e., the mass of captured CO_2 per cycle (cf. **Eq. 3**, **Eq. 6**, and **Eq. 7**). However, only the part that depends on the mechanical work increases in the numerator of the KPIs. Consequently, the larger the portion of mechanical work in the numerator, the larger is the trade-off, and thus the shorter is the optimal phase time.

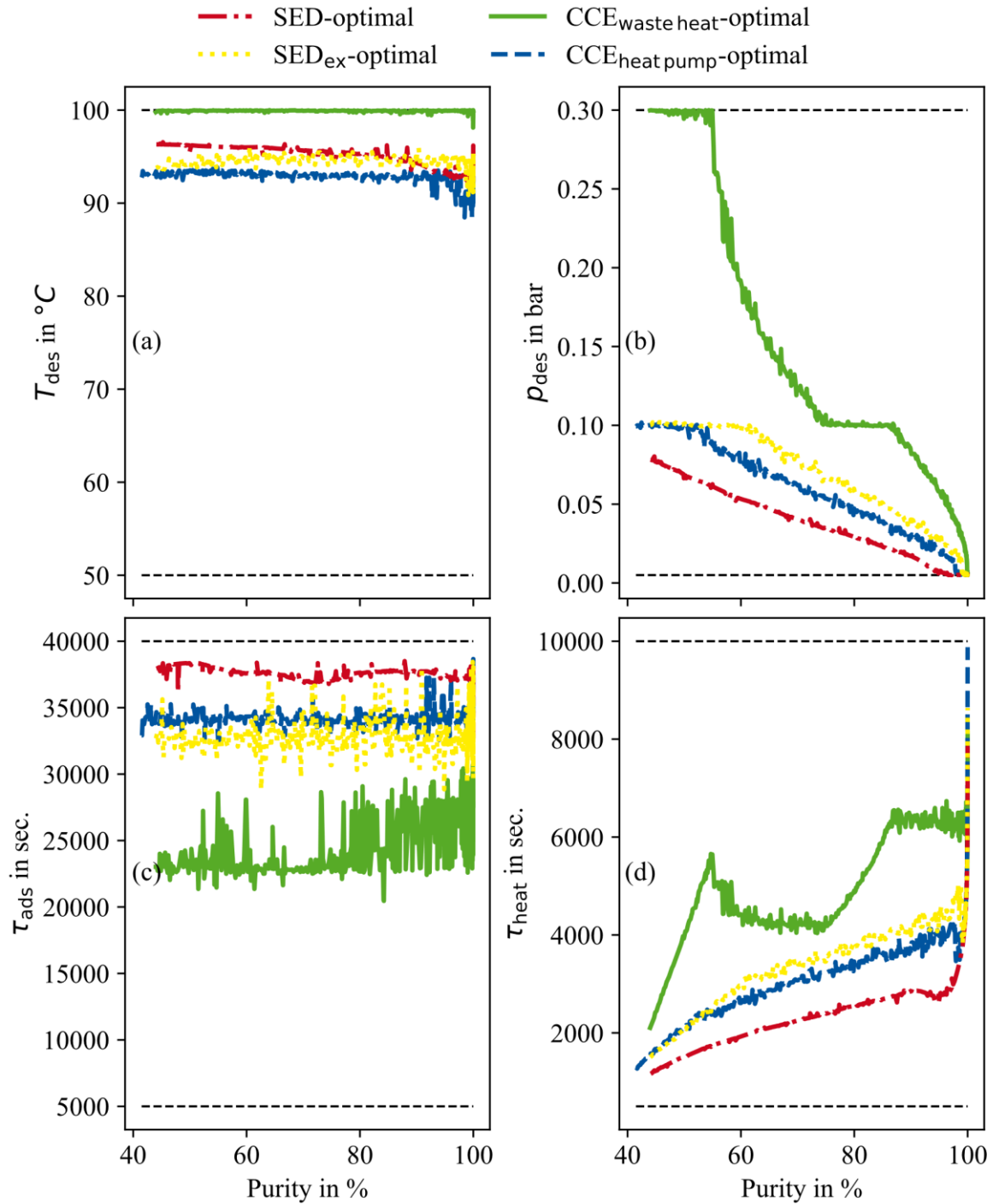


Figure 5: Optimal control variables for a SED-, SED_{ex}-, CCE_{heat pump}-, and CCE_{waste heat}- optimal process. The optimal control variables shown are the (a) desorption temperature T_{des} , (b) desorption pressure p_{des} , (c) adsorption phase duration τ_{ads} , and (d) heating phase duration τ_{heat} . The upper and lower boundaries for each control variable are marked as horizontal dashed black lines each.

Figure 5 d) shows the heating time τ_{heat} over purity. In general, a longer heating time leads to a higher purity. However, the purity is also determined by the desorption pressure, and lower desorption pressure leads to shorter heating times. Lower desorption pressures increase the driving force of desorption and thus the same amount is desorbed in a shorter time. This correlation can

be seen in **Figure 5 d**). The heating times look identical for the SED-, CCE_{heat pump}-, and SED_{ex}-optimal processes (cf. **Figure 5 d**) and for the same purity they are shifted to higher phase times for higher desorption pressures (cf. **Figure 5 b**). The qualitative trend looks different for the CCE_{waste heat}-optimal process and rises strongly, especially at low purities.

7 Conclusions

Using sound key performance indicators (KPIs) is crucial for the optimization of DAC systems. However, how the choice of the KPI as objective affects the carbon capture efficiency (CCE) and thus the climate benefit of a DAC system depends strongly on the case under investigation. For example, if heat is supplied by a heat pump and the used electricity has the carbon footprint of the European grid mix, the CCE of an energetic-optimal process can still be improved by up to 5 % by optimizing the system towards CCE. For the same case (heat pump and European grid mix), the exergetic-optimal process almost corresponds to the CCE-optimal process since the KPIs exergy and CCE are structurally similar in the chosen case. However, if the heat is assumed to be burden-free and the electricity has the impact of the European grid mix, the CCE is improved by up to 14 % compared to an energetic-optimal process and still up to 5 % compared to an exergetic-optimal process. Even though no significant improvements in the CCE are achievable compared to the energetic- or exergetic-optimal process for some cases, we show that CCE is useful as KPI for the process control optimization of DAC systems. Moreover, we show the ability of CCE to cover a wide range of energy scenarios and that it always leads to the DAC system being operated in the most climate beneficial way.

Acknowledgments

We gratefully acknowledge the financial support from the German Federal Ministry for Education and Research (BMBF) in the founding initiative "KMU-innovativ" via the project MoGaTeX (01LY2001B). Simulations were performed with computing resources granted by RWTH Aachen University under project rwth0769.

References:

- [1] Fawzy, S., Osman, I. A., Doran, J., Rooney, D. W., "Strategies for mitigation of climate change: a review", *Environmental Chemistry Letters*, 2020.
- [2] Minx, J. C., et al., "Negative emissions-Part 1: Research landscape and synthesis" *Environmental Research Letters*, 2018.
- [3] Fasihi, M., Efimova, O., Breyer, C., "Techno-economic assessment of CO₂ direct air capture plants". *Journal of Cleaner Production*, 2019.
- [4] Stampi-Bombelli, V., van der Spek, M., Mazzotti, M., "Analysis of direct capture of CO₂ from ambient air via steam-assisted temperature Vacuum swing adsorption" *Adsorption*, 2020.
- [5] Bahamon, D., Díaz-Marquez, A., Gamallo, P., Vega, L. F., "Energetic evaluation of swing adsorption processes for CO₂ capture in selected MOFs and zeolites: Effect of impurities" *Chem. Eng. J.*, 2018.
- [6] Deutz, S. and Bardow, A., "Life-cycle assessment of an industrial direct air capture process based on temperature–vacuum swing adsorption". *Nature Energy*, 2021.
- [7] De Jonge, M. M. J. Daemen, J., Loriaux, J. M., Steinmann, Z. J. N, Huijbregts, M. A. J., "Life cycle carbon efficiency of direct air capture systems with strong hydroxide sorbents" *Int. J. Greenh. Gas. Con.* 2019.
- [8] Cavalcante Jr., C.L., "Industrial Adsorption Separation Processes: Fundamentals, modeling and applications" *Latin American Applied Research*, 2000.

- [9] McQueen, N., Vaz Gomes, K., McCormick, C., Blumanthal, K., Pisciotta, M., Wilcox, J., “A review of direct air capture (DAC): scaling up commercial technologies and innovating for the future” *Progress in Energy*, 2021.
- [10] Elfving, J., Bajamundi, C., Kauppinen, J., Sainio, T., “Modelling of equilibrium working capacity of PSA, TSA and TVSA processes for CO₂ adsorption under direct air capture conditions”, *Journal of CO₂ Utilization*, 2017.
- [11] Bau, U., Lanzerath, F., Gräber, M., Graf, S., Schreiber, H., Thielen, N., Bardow, A., “Adsorption energy systems library - Modeling adsorption based chillers, heat pumps, thermal storages and desiccant systems”, *The 10th International Modelica Conference*, 2014.
- [12] Institute of Technical Thermodynamics, RWTH Aachen University, SorpLib: Dynamic simulation of adsorption energy systems, <https://git.rwth-aachen.de/ltt/SorpLib> (accessed: May 2021).
- [13] Schulze, C. W., *A Contribution to Numerically Efficient Modelling of Thermodynamic Systems*, TU Braunschweig, 2013.
- [14] Lemmon, E. W., Bell, I. H., Huber, M. L., McLinden, M. O., *Reference Fluid Thermodynamic and Transport Properties-REFPROP*, Version 10.0, NIST Standard Reference Database 23, National Institute of Standards and Technology, Gaithersburg, 2018.
- [15] Gebald, C., Wurzbacher, J. A., Borgschulte, A., Zimmermann, T., Steinfeld, A., “Single-component and binary CO₂ and H₂O adsorption of amine-functionalized cellulose” *Environ. Sci. Technol*, 2014.
- [16] Bathen, D. and Breitbach, M., *Adsorptionstechnik*, Berlin: Springer, 2001.
- [17] Functional Mock-up Interface, <https://fmi-standard.org/> (accessed: May 2021).
- [18] Deb, K., Agrawal, S., Pratap, A., Meyarivan, T., “A fast elitist non-dominated sorting genetic algorithm for multi-objective optimization: NSGA-II”, *Parallel Problem Solving from Nature*, 2002.
- [19] Fortin, F.A., De Rainville, F.-M., Gardner, M.-A., Parizeau, M., Gagné, C., “Deap: Evolutionary algorithms made easy”, *Journal of Machine Learning Research*, 2012.
- [20] GaBi. GaBi 9.2.0.58. Software-System and Database for Life Cycle Engineering, DB 8.7 - SP 39 (thinkstep AG, Leinfelden-Echterdingen, Germany, 2019).

Evaluation of ad/desorption dynamics of S-PEEK/Zeolite composite coatings by T-LTJ method

D. Palamara^{1*}, V. Palomba², L. Calabrese¹, A. Frazzica²

¹Department of Engineering, University of Messina, Contrada di Dio Sant'Agata, 98166 Messina, Italy

²CNR - Istituto di Tecnologie Avanzate per l'Energia "Nicola Giordano", Via Salita S. Lucia sopra Contesse 5, 98126 Messina, Italy

*Corresponding Author: dpalamara@unime.it

Abstract

In this work, the adsorption/desorption kinetics of a consolidated bed, for adsorption heat pumps (AHP) application, coated with a new composite adsorbent material based on SAPO-34 zeolite in a matrix of sulfonated polyether ether ketone was investigated. The heat exchanger was coated by drop casting with a composite zeolite/polymer mixture containing 90 wt% of SAPO-34 powder. The adsorption/desorption kinetics was investigated using the Thermal Large Temperature Jump (T-LTJ) method and compared with results reported in literature.

Keywords: coatings, zeolite, adsorption heat pumps, water vapour.

1. Introduction

In the adsorption heat pump (AHP) sector, the suitable design of the adsorbent bed is a key feature in order to improve the system performances. Unconsolidated beds, which are a very simple and economical design option, have a low heat transfer capacity due to the few contact points between the adsorbent material grains and the heat exchanger. Consolidated beds, consisting of a heat exchanger coated with the adsorbing material, allow to overcome these issues. However, a limiting factor on the use of this technology is a low mass transfer due to low porosity and the presence of the binder that reduce the AHP performances and could hinder the sorption capabilities of the adsorbent material. For this reason, several efforts are oriented to find a material able to act as binder in the coating in order i) to preserve good thermal properties, ii) to allow an adequate thickness of adsorbent material and iii) not to act as a barrier to the water vapor permeation of the adsorbate. In such a context, in the present paper, a composite material constituted by high zeolite content (up to 90 wt.% of SAPO-34) and sulfonated poly(ether-ether-ketone) (S-PEEK) binder was proposed. The S-PEEK matrix was chosen thanks to its high water vapor permeability, which makes its use potentially effective in this application context. Based on mechanical and thermo-physical tests, this composite coating has shown promising results in terms of mechanical and thermal stability as well as in terms of ad/desorption performances, indicating it as a potential alternative to conventional coatings. In order to evaluate its applicability in real conditions, it is crucial to evaluate the adsorption/desorption performance of the composite coating under lab-scale AHP system. The lab-scale AHP dynamic performances of a composite coated adsorber were assessed by using a new version of the Large Temperature Jump (LTJ) method, proposed by Aristov et al. [1], and called Thermal Large Temperature Jump (T-LTJ). This method is based on the ΔT measurement at the inlet and outlet of the adsorber due to an abrupt inlet temperature jump. The measured ΔT was used to study the ad/desorption dynamics with a significantly lower complexity than the other LTJ methods, while still keeping a high reliability.

2. Experimental Part

2.1 Description of the system

Figure 1 describes the equipment set-up used for the adsorber characterization. The experimental apparatus is composed of a heating/cooling system and two vacuum chambers separated by a gate valve; one, filled with degassed water, works as an evaporator/condenser and the other one functions as a measuring chamber. Both chambers are evacuated by a vacuum pump connected to the latter chamber. In order to avoid heat dissipation, the whole system has been thermally insulated. In the measuring chamber was placed the heat exchanger to be tested, hydraulically connected to the above mentioned hydraulic system. The thermo-cryostats TCR1 (high temperature T_1) and TCR2 (low temperature T_3), connected to the heating/cooling system, impose the temperature drop/jump in the heat exchanger in order to generate the isobaric adsorption/desorption. The thermo-cryostat TCR3 (set to temperature T_e or T_c) is connected to the chamber that acts as evaporator/condenser in order to generate the pressure and temperature conditions suitable to make the chamber work as an evaporator or as a condenser and maintain a constant vapor pressure inside the measuring chamber during the test. The system is also equipped with pressure transducers (P) and K-type thermocouples (T) to monitor the pressure and temperature inside the two chambers and the temperature at the inlet (T_{in}) and outlet (T_{out}) of the heat exchanger. A flow meter (f) is implemented in the hydraulic system to monitor the carrier flow rate. The data obtained from the sensors are recorded using a LabView data acquisition system (National Instruments Co). The temperature drop/jump is achieved by switching the valves (v_1 , v_2 , v_3 and v_4). The heat exchanger is characterized by analyzing the ΔT values (difference between T_{out} and T_{in}) obtained in response to the temperature drop/jump.

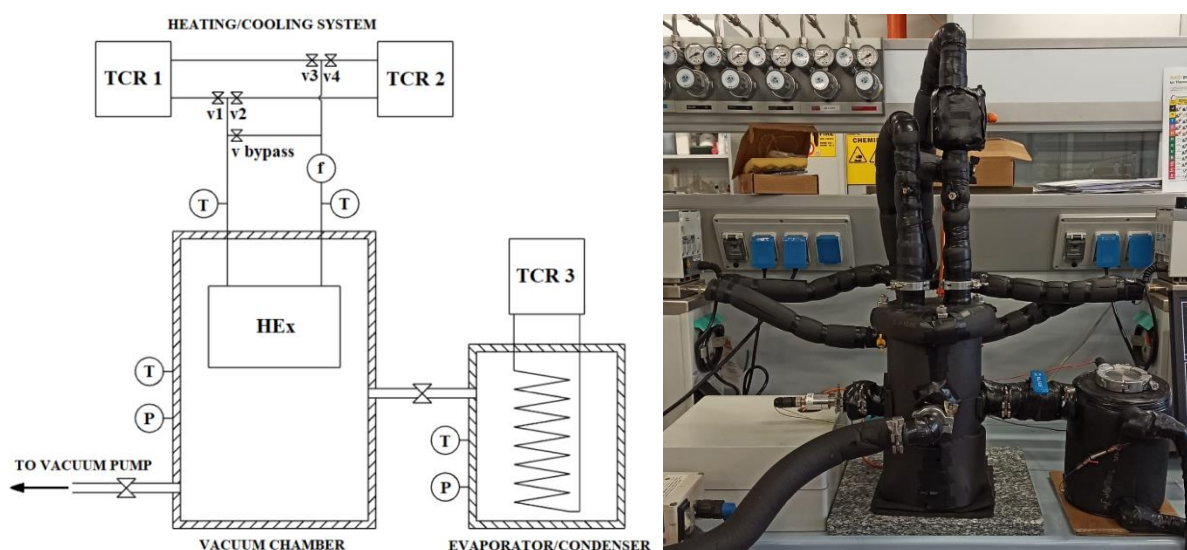


Figure 1. Schematic layout of the T-LTJ system

The performance of a consolidated adsorbent bed coated with a zeolite/S-PEEK mixture with 90 wt% of adsorbent material was investigated. The zeolite was a commercial SAPO-34 powder (Mitsubishi Plastics Inc. - AQSOA Z02). The sulfonation of PEEK (Heroflon S.p.A. - Collebeato (BS), Italy) and the preparation of the coating were carried out following the procedure reported in [2]. The amount of dry zeolite powder into the coating was equal to 40 g. This configuration has been realized using an aluminum heat exchanger with a distance between tanks equal to 120 mm, height and thickness of the radiator unit equal to 80 mm and 22 mm, respectively.

2.2 Description of the procedure

The heat exchangers was analyzed under the boundary conditions typical of the Water-AQSOA FAM-Z02 working pair [3,4]. The condenser was kept at a constant temperature of 30°C whereas the different boundary conditions were obtained by performing three different temperature drops in adsorption (60 → 30, 66 → 30, 72 → 30), corresponding to three different evaporator temperatures (5, 10 and 15 °C), and a single jump in desorption (46 → 90), corresponding to 10 °C at the evaporator. The resulting thermodynamic cycles are shown in Figure 2. Before running the adsorption tests, by opening valves v_2 and v_4 and closing valves v_1 and v_3 , the heat exchanger was kept at 90 °C (TCR1) for 3 hours under continuous pumping. In the meantime, the evaporator was set to the temperature T_e (5, 10, or 15 °C) which corresponds to the pressure P_e (8.7, 12.3 or 17,1 mbar). After 3 hours the heat exchanger was cooled down to the initial temperature (60, 66 or 72 °C) by decreasing the temperature of TCR1. The gate valve was opened to connect the evaporator to the measurement chamber. Once equilibrium was reached, the test could begin: by closing valves v_2 and v_4 and opening valves v_1 and v_3 , the system receives the fluid coming from TCR 2 (30 °C) and the drop from high to low temperature (60, 66 or 72 °C → 30 °C) is realized, triggering the adsorption of water vapor. The test was considered ended when the temperature difference ΔT remained constant at 0 °C for at least 30 min.

Desorption tests were performed in a similar method: TCR1 and TCR2 temperatures was set to 90 °C and 46 °C, respectively (valves are opened and closed in reverse), and the condenser temperature T_c was set to 30 °C which corresponds to the pressure P_c (42,5 mbar). In this case the heat exchanger must be kept for at least 3 hours at the initial temperature of 46 °C to allow the whole chamber to reach the temperature and avoid condensation phenomena.

In order to eliminate from the ΔT measurement the contributions of losses and sensible heats and to isolate the contribution of water ad/desorption ($\Delta T_{ad/des}$), for each condition, a blank test (ΔT_{bl}) is realized to be subtracted from the real test (ΔT_{ov}) as in the following equation:

$$\Delta T_{ad/des} = \Delta T_{ov} - \Delta T_{bl}$$

This test is performed with the same procedures as above but leaving the gate valve closed in order to avoid water vapor contact with the adsorbent.

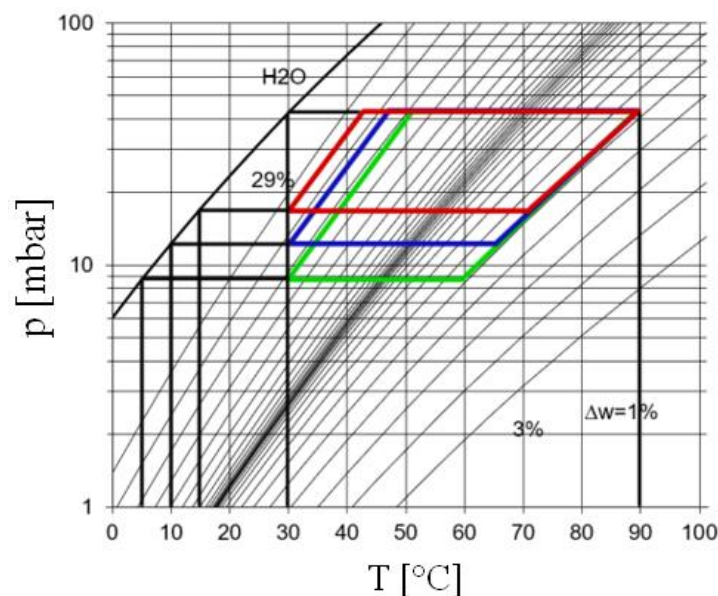


Figure 2. Tested boundary conditions on the isosteric chart ($T_r = 90$ °C, $T_c = 30$ °C $T_e = 5, 10$ and 15 °C).

3. Result and discussion

From the analysis of the data obtained from the tests, it is possible to deduce some important parameters for evaluating the performance of a heat exchanger, such as the heat flow \dot{Q} from the exchanger to the HCF and heat of water adsorption Q_{ad} . The former can be obtained from the following equation:

$$\dot{Q}[W] = C_p(HCF)f\rho(HCF)\Delta T$$

where $C_p(HCF)$ is HCF heat capacity, $\rho(HCF)$ is HCF density, f is the flow rate and ΔT is the temperature difference between output and input.

The latter can be obtained from the difference between the heats Q_{ov} and Q_{bl} :

$$Q_{ad/des}[kJ] = Q_{ov} - Q_{bl}$$

which were derived from the time integration of the heat fluxes \dot{Q}_{ov} and \dot{Q}_{bl} .

Another useful parameter to compare the results of different tests is the characteristic time $\tau_{ad/des}$. For adsorption and desorption processes, the trend of $\Delta T_{ad/des}$ (or \dot{Q}) can be satisfactorily described by an exponential function of the type:

$$\Delta T_{ad/des}(t) = \Delta T_{\infty} + \Delta T_0 e^{(-t/\tau_{ad/des})}$$

where $\tau_{ad/des}$ is the characteristic adsorption/desorption time. This parameter can provide an idea of the speed with which the adsorption/desorption process occurs.

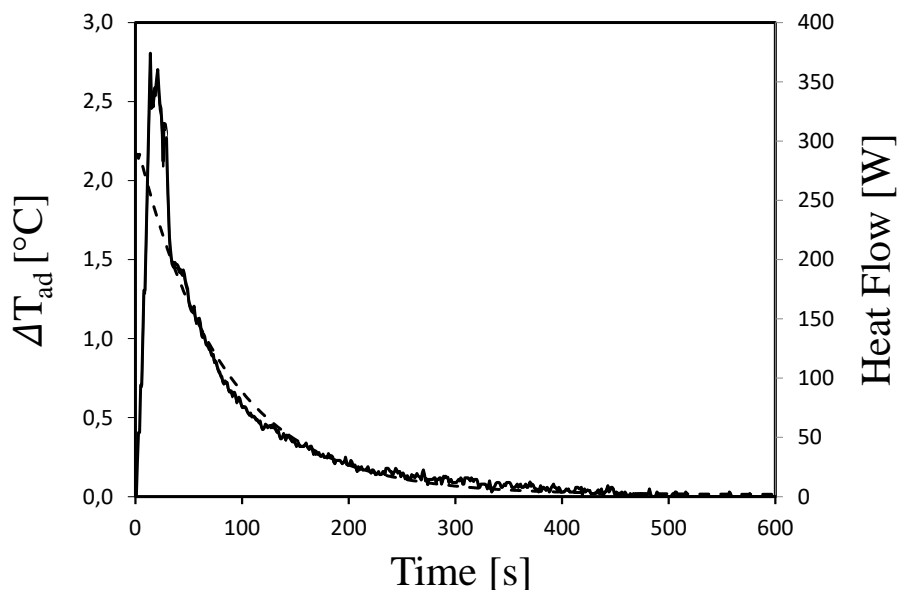


Figure 3. Difference between the ΔT -responses (and related heat flux) in the blank and adsorption runs in the range (90-30-10 °C)

As an example, Figure 3 shows the time evolution of ΔT_{ad} values (and \dot{Q}) for a reference adsorption test with a drop in temperature equal to $66 \rightarrow 30$ °C. Evaluating the ΔT_{ad} trend three regions can be identified: i) At first, the water adsorption process does not affect the ΔT_{ad} response at short time ($t < 20$ s). This stage is not stable and it can be probably due to the adsorbent has not been sufficiently cooled down to trigger the adsorption; ii) Afterward, the

ΔT_{ad} increase reaching a maximum value of about 2,5 °C (with a maximum heat flux slightly above 350 W) in the time range 10-35 s; iii) finally at $t > 35$ s a progressive exponential decay of ΔT_{ad} response is observed, with a characteristic time τ_{ad} of 83.3 s. A stabilization value of ΔT_{ad} was reached at about 600 s. For the chosen test a $Q_{ad} = 25.4$ kJ ($Q_{ad} = 635$ J/g) was obtained.

3.1 Water adsorption dynamics

For the adsorption process, three temperature drops (60, 66, and 72 → 30) corresponding to three different evaporation temperatures (5, 10, and 15 °C) were investigated keeping the condenser temperature constant at 30 °C.

The specific heat of adsorption (ΔH_{ad}) values obtained from the T-LTJ curves can be used as a verification of the calculation accuracy. The values of ΔH_{ad} obtained, shown in Table 1, are comparable to those reported in the literature [1].

Further information can be acquired evaluating Figure 4 that shows the trends of ΔT at three different temperature drops during the adsorption process. In all investigated boundary conditions, the trend described in [1] was observed. After an oscillation around an approximately constant value, the ΔT_{ad} decreases exponentially with a characteristic time decay depending on the analyzed conditions.

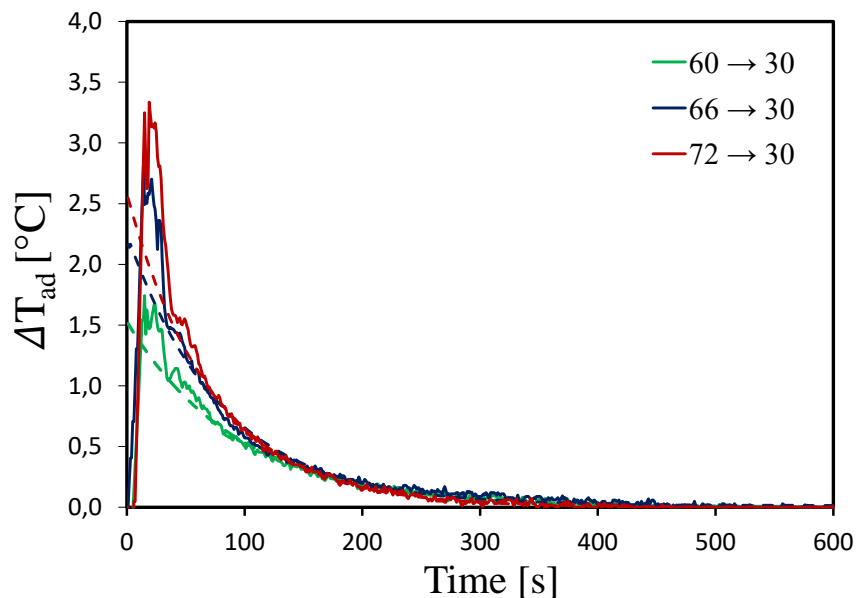


Figure 4. Evolution of ΔT_{ad} as time changes for each temperature drop.

The characteristic times, obtained by fitting the ΔT_{ad} curve in the region of exponential decay, which give an idea about the rate at which the adsorption and desorption phenomena occur, are given in Table 1. They are comparable with those found in literature by using LTJ system. In detail the characteristic time of the coated exchanger for the 66 → 30 drop (83.3 ± 7 s) is lower than values reported in literature for uncoated exchanger filled with grains of zeolite by using T-LTJ (116 ± 10 s) [1] and V-LTJ (114 s $< \tau < 150$ s) [5] method, and for monolayer configuration with grains of zeolite larger than 0,7 mm in size by using G-LTJ method ($\tau > 102$ s) [3,4]

T jump/drop	τ [s]	$Q_{ad/des}$ [kJ]	$Q_{ad/des}$ [J/g]	W_{max} [W/g]	$\Delta H_{ad/des}$ [J]
60 → 30	101.1 ± 13,8	18.7 ± 0.8	467.5 ± 20.3	5.3 ± 0.6	2337 ± 102
66 → 30	83.3 ± 7	25.4 ± 2.1	635.2 ± 52.7	9.7 ± 0.7	3024 ± 251
72 → 30	68.7 ± 6.9	24 ± 1.5	599.3 ± 37.7	11 ± 1.3	2724 ± 171
46 → 90	25.3 ± 4.3	29.7 ± 1.3	742.3 ± 33	22.2 ± 0.9	3535 ± 157

Table 1. Characteristic times, heats of ad/desorption, maximal specific powers and specific heats of ad/desorption for coated HEx.

Furthermore, it is observed that the τ values, in the consolidated configuration, decrease as the temperature drop increases, reaching an average value of 68.7 ± 6.9 s. Moreover, using the consolidated bed, even by reducing the temperature jump to 60 → 30, the characteristic time (101.1 ± 13.8 s) remains lower than or equal to those found in the literature and mentioned above. This means that by increasing driving temperature difference the adsorption process becomes faster from a kinetic point of view.

The heat of adsorption obtained from the integral of the released heat flux can be useful to compare the performance of two different configurations. The heat of adsorption obtained in the consolidated bed (25.4 ± 2.1 kJ) is significantly lower than that obtained by the same method in [1] for the unconsolidated bed (53 ± 7 kJ) and for temperature drop 66 → 30. However, if related to the mass of adsorbent material (40 g for consolidated and 84 g for unconsolidated) the values become comparable (635 kJ/kg vs 631 kJ/kg). Thus indicates the good adsorption capabilities of the SAPO-34 composite coating suggesting furthermore that the S-PEEK not hinder the water vapor diffusion toward the zeolite filler embedded in the polymer matrix.

The heat of adsorption increases from 60 → 30 to 66 → 30 drop, while it remains approximately constant by further increasing the jump to 72 → 30. This is due to the fact that the process becomes faster but at the same time the maximum power value does not increase significantly, causing a loss of adsorption heat.

Another important parameter useful to compare different configurations is the maximum specific power generated at the beginning of the adsorption process. The obtained W_{max} value in relation to the 66 → 30 temperature drop (9.7 ± 0.7 kW/kg) is higher than values reported in literature for uncoated exchanger filled with grains of zeolite by using T-LTJ (3.5 W/g) [1] and V-LTJ (2.6 - 4.7 W/g) [5] method, and for monolayer configuration with grains of zeolite between 0,35 and 2 mm (1.8 - 2 W/g) [3] and between 0.8 and 1.18 mm (3.2 – 4.5 W/g) [4] both using G-TLJ method. This is due to two main reasons: i) the maximal power increases as the zeolite grain size decreases, as reported in [3]; ii) the coating provides better heat transfer between the adsorbent material and the heat exchanger fins.

As shown in Table 1 the maximum power increases by 82% from 60 → 30 to 66 → 30 drop, however by further increasing the driving temperature difference the increase is only 13%.

The values of characteristic time and heat of adsorption obtained confirm that the presence of the S-PEEK/Zeolite coating does not hinder the passage of water vapor and at the same time improves the heat transfer with the surface of the exchanger guaranteeing also higher values of maximum specific power.

3.2 Water desorption dynamics

Only one temperature jump (46 → 90) corresponding to an evaporator temperature of 10 °C and a condenser temperature of 30 °C was investigated for the desorption process. The value of ΔH_{des} obtained, shown in Table 1, is comparable to those reported in the literature [1].

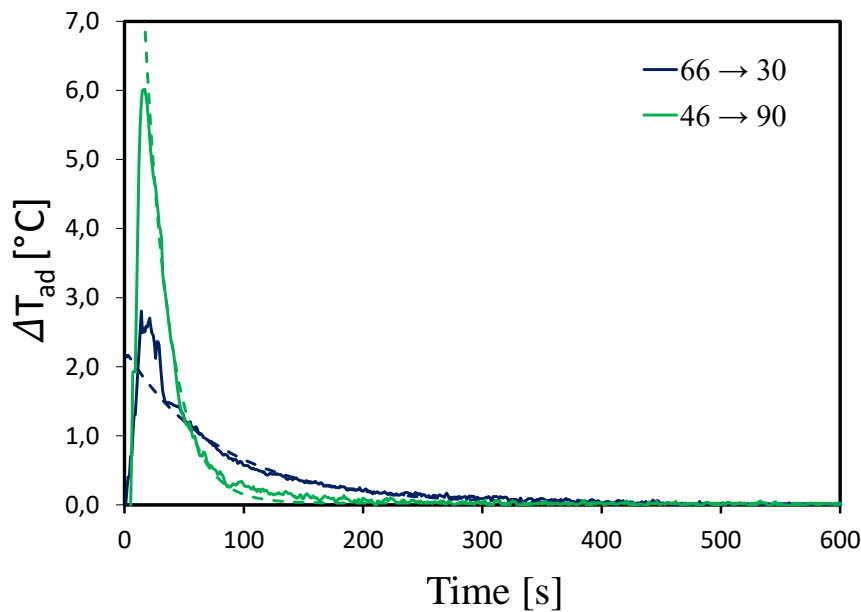


Figure 5. Evolution of $\Delta T_{ad/des}$ as time changes for adsorption and desorption processes with boundary conditions $T_e=10$ °C, $T_c=30$ °C and $T_r=90$ °C.

Figure 5 shows the trends of ΔT for adsorption and desorption processes. Both processes are characterized by a preliminary abrupt increase of ΔT followed by a gradual exponential decrease at increasing time. The desorption process is characterized by a ΔT peak that is higher and narrower than the adsorption one. Hence, the maximal specific power is significantly higher for the desorption process. Indeed, the maximal power is 2.3 times higher than that obtained for the temperature drop 66 → 30 (888.6 ± 34.8 W vs 389.1 ± 27.9 W for desorption and adsorption step, respectively). Higher values of maximum power in the desorption process than the adsorption one was observed for zeolite (V-LTJ) [5] and silica grains (V-LTJ) [6].

Furthermore, considering the narrow peak in ΔT trend, the desorption process is characterized by a characteristic time significantly lower than adsorption one. In particular, the average τ value for the desorption process is 3.3 times lower than that obtained from the adsorption process, 25.3 ± 4.3 s and 83.3 ± 7 s, respectively.

Anyway, the heat of desorption (proportional to the area under the curve) is slightly higher than that of adsorption step (29.7 ± 1.3 kJ vs 25.4 ± 2.1 kJ). This is justified considering that the desorption process is characterized by an higher peak and a faster kinetic that allows to complete the process in a shorter time.

4. Conclusion

In this work, the adsorption/desorption kinetics of a consolidated bed, for adsorption heat pumps (AHP) application. A new composite coating based on SPAO-34 filler and a water vapor permeable polymer matrix (S-PEEK) was assessed for AHP applications. The heat exchanger

was coated by drop casting with a composite zeolite/polymer mixture containing 90 wt% of SAPO-34 powder. In particular, a Thermal Large Temperature Jump (T-LTJ) method was applied in order to investigate the adsorption/desorption kinetics of the consolidate bed HEX compared to literature unconsolidated one. The results highlights that coated HEX exhibit very high specific heating/cooling capacity with a very fast adsorption/desorption kinetic (characteristic times approximately 32% lower compared to zeolite grains filled HEX). Analogously, as reference, the obtained W_{\max} value (in 66 \rightarrow 30 temperature drop) was 9.7 ± 0.7 kW/kg, higher than values reported in literature for uncoated exchanger filled with grains of zeolite by using T-LTJ method (3.5 kW/kg). These results indicate that the polymer matrix not hinder the water vapor diffusion allowing a kinetically suitable sorption desorption process and an effective improvement of the heat transfer at the metal-adsorbent interphase.

References:

- [1] M. M. Tokarev and Y. I. Aristov, "A new version of the Large Temperature Jump method: The thermal response (T-LTJ)," *Energy*, vol. 140, pp. 481–487, 2017, doi: 10.1016/j.energy.2017.08.093.
- [2] L. Calabrese, P. Bruzzaniti, D. Palamara, A. Freni, and E. Proverbio, "New SAPO-34-SPEEK composite coatings for adsorption heat pumps: Adsorption performance and thermodynamic analysis," *Energy*, vol. 203, p. 117814, 2020, doi: 10.1016/j.energy.2020.117814.
- [3] A. Sapienza, S. Santamaria, A. Frazzica, A. Freni, and Y. I. Aristov, "Dynamic study of adsorbers by a new gravimetric version of the Large Temperature Jump method," vol. i, pp. 1244–1251, 2014, doi: 10.1016/j.apenergy.2013.09.005.
- [4] S. Santamaria, A. Sapienza, A. Frazzica, A. Freni, I. S. Girnik, and Y. I. Aristov, "Water adsorption dynamics on representative pieces of real adsorbers for adsorptive chillers," vol. 134, pp. 11–19, 2014, doi: 10.1016/j.apenergy.2014.07.053.
- [5] I. S. Girnik and Y. I. Aristov, "Dynamics of water vapour adsorption by a monolayer of loose AQSOA™-FAM-Z02 grains : Indication of inseparably coupled heat and mass transfer," *Energy*, vol. 114, pp. 767–773, 2016, doi: 10.1016/j.energy.2016.08.056.
- [6] I. S. Glaznev and Y. I. Aristov, "The effect of cycle boundary conditions and adsorbent grain size on the water sorption dynamics in adsorption chillers," *Int. J. Heat Mass Transf.*, vol. 53, pp. 1893–1898, 2010, doi: 10.1016/j.ijheatmasstransfer.2009.12.069.

Experimental characterization of a full-scale geothermal adsorption heat pump

A. Bonanno^{1*}, V. Palomba¹, S. Löwe², U. Wittstadt², A. Frazzica¹, Davide La Rosa¹

¹ CNR ITAE, Salita S. Lucia sopra Contesse 5, 98126, Messina, Italy

² Fahrenheit GmbH, Siegfriedstr. 19, 80803 Munich, Germany

*Corresponding author: antonino.bonanno@itae.cnr.it

Abstract

The reduction of the use of fossil fuels is a key point in the EU strategy to reduce the heating demand in residential applications. This target goes in contrast, often, to the age of the already existing building, therefore the retrofitting of residential buildings, with energy-efficient solutions becomes very interesting. In the present paper, a concept based on a gas-driven sorption heat pump using a geothermal source for evaporation is presented. The idea aims at the deployment of innovative geothermal heat pump solutions for retrofitting applications. In this paper, the experimental results under controlled operating conditions are presented.

Keywords: Heat pump, geothermal, retrofitting

Introduction

According to the “Common Vision for the Renewable Heating & Cooling sector in Europe” [1] in 2007, 48 % of the final energy consumption in EU 27 took the form of heat. Heat accounted for 86 % of the final energy consumption in households, 76 % in commerce, services and agriculture, and 55 % in industry. The thermal energy consumption, in 2007, was estimated in 6800 TWh, quite totally produced from fossil fuels. This value, considering a strong evolution both from the legislative (e.g. obligation to use renewable energies for all new and existing residential, service and commercial buildings as well as for low-temperature industrial applications) and research (e.g. development of cost competitive solutions for high energy density heat storage) point of view, is expected to be reduced to 4000 TWh, in 2050. The use of adsorption heat pump has received an increased attention in the recent years, thanks to its eco-friendly characteristics [2] [3], [4], [5]. The coupling of a vapour compression heat pump and adsorption chiller has been widely studied, especially for cooling applications [6], [7], [8]. Only few studies have been performed focusing on solutions for heating applications. In [7] the performances of a small size solar heating system working in cooperation with an adsorption machine has been studied considering heating and cooling demand and performing a Life Cycle Assessment in different installations across the Europe. Six different heating systems configurations have been studied in [9], comparing the energetic performances as well the economic feasibility. The exploitation of geothermal energy as ambient heat source/sink is considered of great interest [10]. For example, in [11] the heat transfer model of a ground heat exchanger (GHE) and the coupling of this model with the energy conversion model of a heat pump is presented, while in [12] an investigations on a combined solar and ground source heat pump (SGHP) system for a single-family house is discussed. However, the exploitability of this resource in the built environment, for retrofitting applications, becomes quite challenging due to both, technical and regulatory constraints that limit the drilling procedures for the ground source heat exchangers (GSHEX) installation [13]. For these reasons, the EU funded GEOFIT [14] project aims at the deployment of innovative geothermal heat pump solutions for retrofitting applications.

Particularly, an innovative hybrid geothermal heat pump has been developed and tested to be installed in two demo sites. In this paper, the experimental test results of the innovative hybrid heating system developed, incorporating a gas condensing boiler, a zeolite-water adsorption heat pump, and a geothermal field, is presented. The condensing boiler is used to drive the zeolite-water heat pump, while the geothermal system is used to provide heat to the evaporator. The full system has been already modelled [15] using the Dymola software in order to optimize the heat pump control and to evaluate the preliminary design performance. The proposed solution is able to reach the target performances, showing that such a system could be used as retrofit solution. In the GEOFIT project, for example, it has been installed in a historical building placed in Perugia (Italy).

System configuration and layout

The core of the hybrid sorption heat pump developed within GEOFIT consists of a sorption heat pump that makes use of a gas boiler as heat source. The layout of the GEOFIT thermally-driven solution is shown in Figure 1: the sorption heat pump is made up of two modules, each one consisting of an adsorber/desorber and an evaporator/condenser. The desorber is connected through the Heat Transfer Fluid (HTF) circuit to the heat source, i.e. a specifically modified gas boiler allowing regeneration of the sorption material. At the same time, through the vacuum circuit, the refrigerant flows from the desorber to the condenser, that supplies heat at the temperature level requested for space heating. The adsorber is connected in parallel to the condenser through the HTF circuit. The vacuum circuit allows the flow of the refrigerant from the evaporator to the adsorber. The ground heat exchanger allows the use of the soil as heat source for evaporation. The useful effect delivered to the user is represented by the adsorption heat and condensation heat.

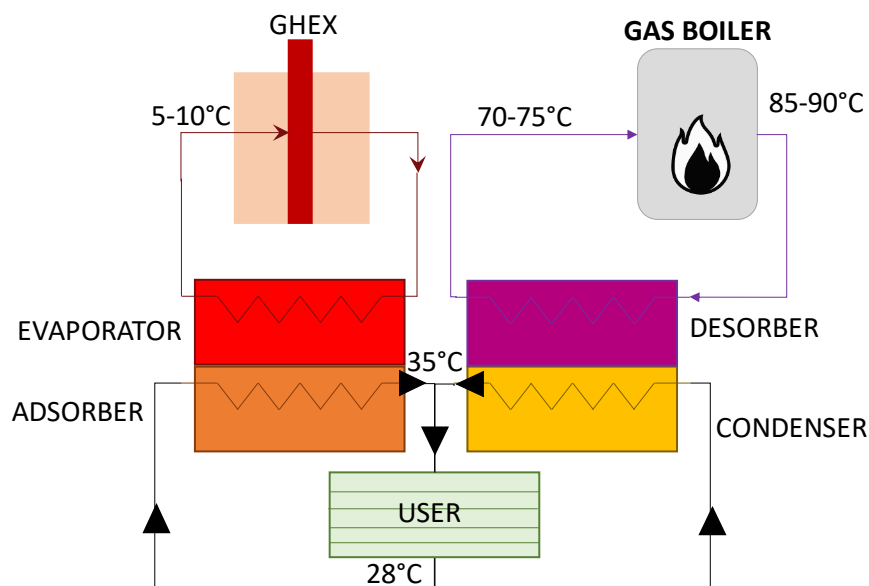


Figure 1: main layout and thermal levels for GEOFIT hybrid gas-driven heat pump.

Contrarily to the electric-driven systems, the thermally-driven heat pump requires a lower amount of heat at the evaporator, due to the lower thermal COP achievable from thermodynamic point of view, thus allowing the installation of a smaller geothermal field, which is a beneficial feature when evaluating retrofitting solutions. The flexibility of the solution for installation in existing building is further marked by the possibility of using a standard gas boiler as driving heat source.

The final layout of the Perugia pilot plant is showed in Figure 2 are:

- A Buderus GB 192 iT boiler (25 kW), used to drive the adsorption heat pump;
- A two beds adsorption heat pump made by Fahrenheit GmbH (nominal power 10 kW);
- An electrically driven vapour compression chiller (nominal power 6 kW)
- A geothermal field, used to drive the evaporator of adsorption heat pump
- Heat exchangers, used to connect the systems (chiller + heat pump) to the ground HEX circuit and to the user.

The layout shows a hybrid solution (electrically driven chiller and gas driven heat pump) in order to exploit all the possible advantages related to the use, in a retrofit application, a of different energy sources (gas or electricity) that could have been available at the installation site. The electrically driven chiller is not presented in this paper.

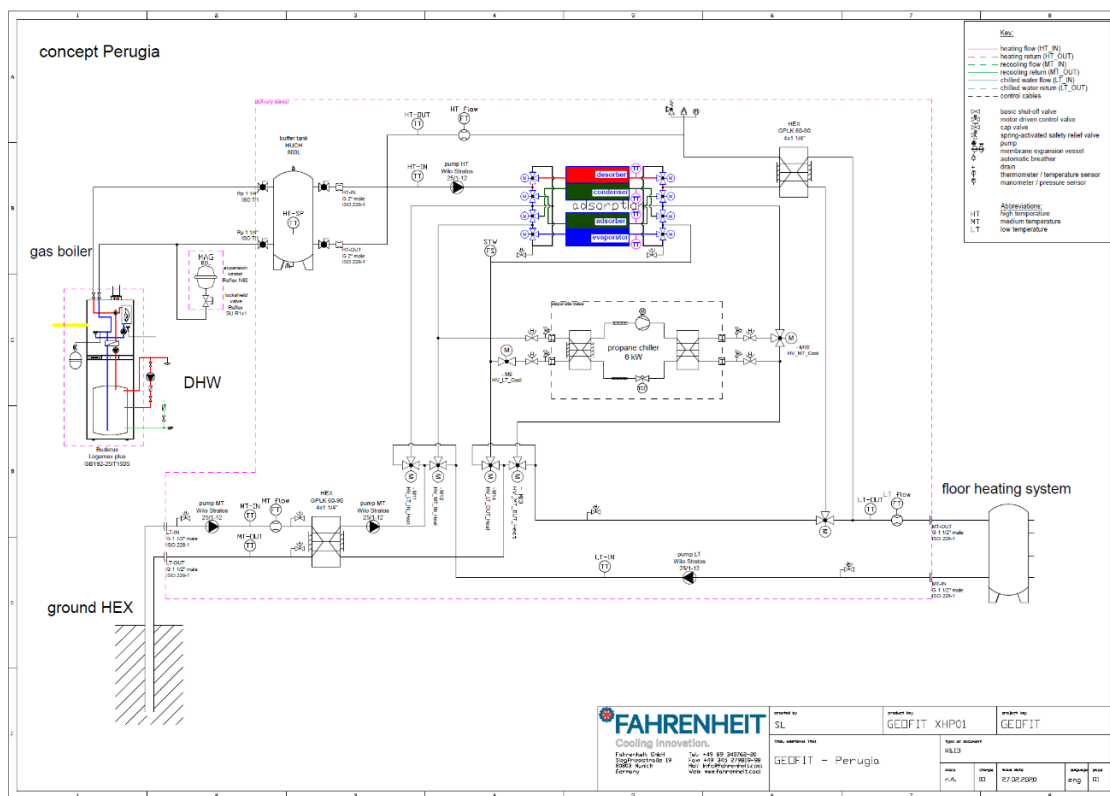


Figure 2: final layout of Perugia pilot plant

Experimental facilities

The testing rig used for the evaluation of the performance of the heat pump is specifically designed to set the different thermal levels required for the operation of thermal components and was presented in [16] and [17]. It, see Figure 4, mainly consists of heat sources and sinks connected to storages: a 0.6 m³ water storage, continuously heated up by a 36 kW electrical heater (HT storage); a 0.3 m³ water storage, filled with a 44.5 % wt. water/glycol mixture, connected to an air-cooled chiller with nominal power of 13 kW (LT storage) and having 4 immersed electrical resistances (3 kW each) to control the storage temperature; a 0.3 m³ storage (MT storage), where the temperature control is obtained by means of 1 immersed

resistance (4.5 kW) and a connection to a 63 kW chiller, which provides cooling power also to another lab test rig. The hot water storage tank is usually used to provide heat to the HT circuit of sorption unit, but not for testing the GEOFIT machine. This because a dedicated gas boiler (25 kW) and an 800L storage was already considered for the final installation in the Perugia demo site. The user heating demand is simulated sending to the MT circuit of the sorption unit a defined temperature level, obtained controlling the water temperature in the MT storage at a desired level.

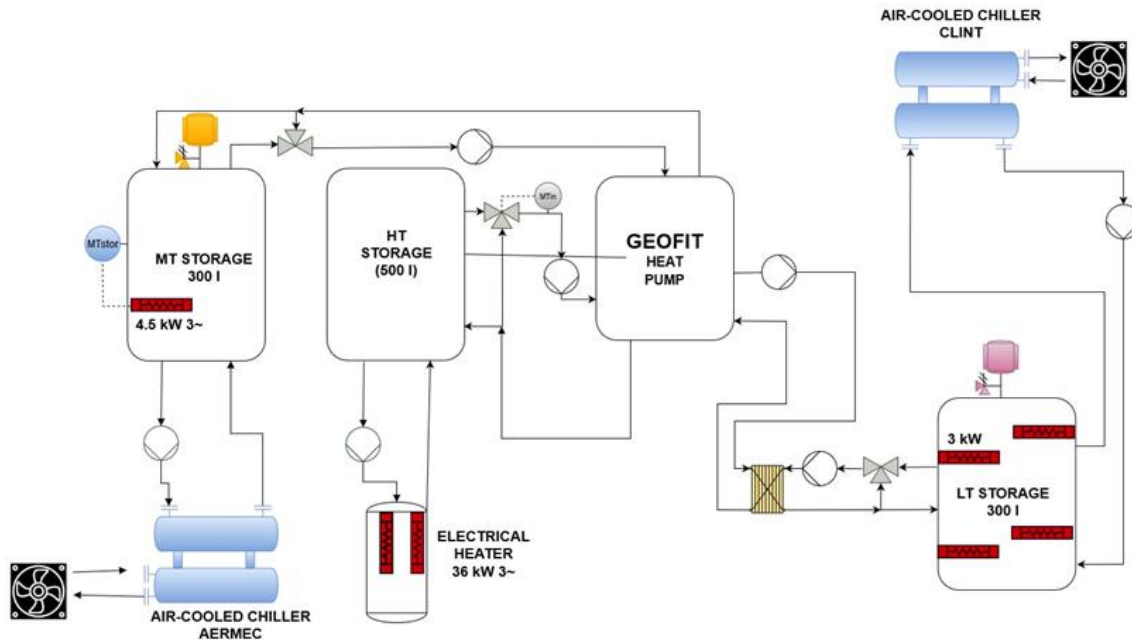


Figure 3: test rig layout and connections to the GEOFIT adsorption heat pump

The geothermal field is simulated using the LT circuit, controlling the water temperature by means of chiller and electrically driven resistance. In this way, three independent water temperature sources (LT-MT-HT) have been obtained. This real-time regulation allows keeping the target set temperature in the inlet circuit of both LT and MT circuits. All the piping is thermally insulated; variable speed pumps are installed in order to manage the operating flow rates in all the circuits. Due to the necessity to use a dedicated mix of water and anti-corrosion fluid in the sorption machine circuits, these have not been directly connected to the LT and MT circuit of the lab test rig, but via plate heat exchangers.

The monitoring and controlling system are operated through a control panel realised in LabVIEW® environment. The testing rig is equipped with the following sensors:

- Type “T” thermocouples with Class 1 tolerances for the measure of all the temperatures in the inlet/outlet pipes of every circuits and in the storages;
- Magnetic flow meters MVM250-PA with 1% of reading accuracy for the measure of all the flow rates;
- Piezoresistive differential pressure meter, to calculate pressure drops inside the circuits of the heat pumps/chillers under testing;
- Electric energy meter SINEAX DM5S with Class 1 tolerances for the measure of electric input delivered to the chillers.
- Pressure difference gas flow meter Bronkhorst F-103E/F-103El (1% tolerance on full scale) for the methane consumption measure.

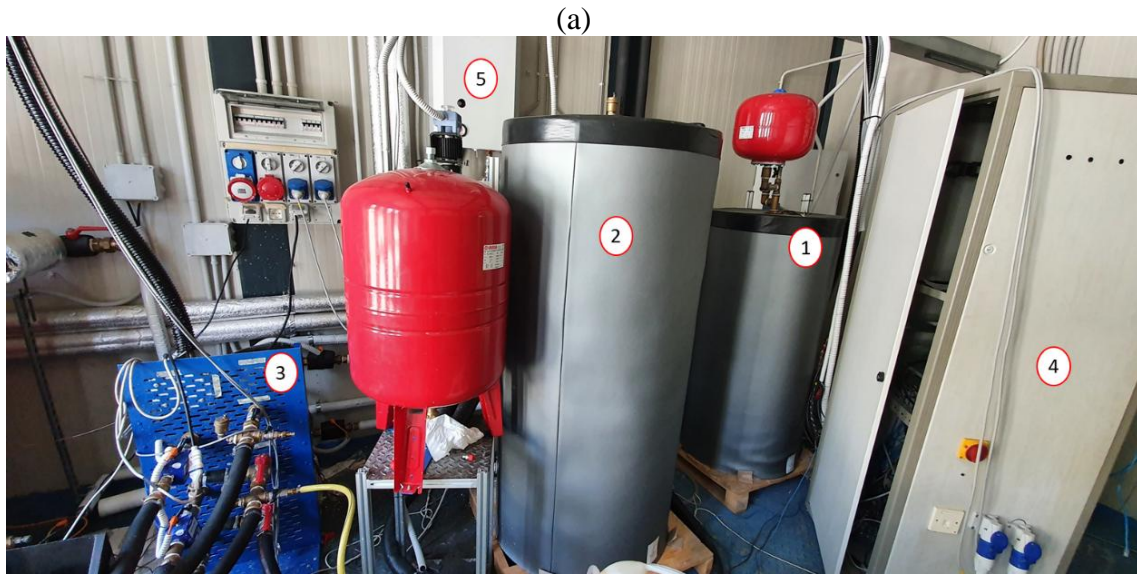


Figure 4: the testing rig at CNR-ITAE. (a) 1: LT storage; 2: HT storage; 3: piping connection manifold; 4: rack for acquisition hardware; 5: electric heating boiler; (b) 6: MT storage

Furthermore, the on-board Fahrenheit monitoring system was connected as well to the LabVIEW monitoring panel, to acquire also the data and compare them to the data acquired by the testing rig.

As explained in the previous section, although a high temperature circuit is already available at the CNR-ITAE lab, in the GEOFIT project a dedicated 25 kW gas boiler was used for providing the heat necessary to drive the heat pump. With the aim of providing enough thermal inertia to the sorption machine, particularly useful during the phase switching of the sorption heat pump, between the gas boiler and the sorption machine an 800 L tank was connected. Thanks to the testing rig described in the previous section the inlet medium temperature (MT_{in}), simulating the return from the external load was maintained at different set-up value, considering the machinery coupled to a floor heating distribution system. The low temperature source was considered at three different levels, in order to evaluate the heat pump behaviour when coupled with the geothermal field. The temperature used in the tests performed on the hybrid sorption pump are resumed in Table 1.

Testing conditions

Two different test cases have been considered:

- **Case 1:** the influence of the MT flow rate has been investigated at the different working conditions. The heat pump is connected to the boiler and to the 800 L tank. The HT temperature is fixed at 80 °C, the MT temperature has been considered in the range 28-32 °C, while the LT temperature (geothermal field) has been considered in the range 6-10 °C. The adsorption machine half cycle time is controlled by the machine control.
- **Case 2:** All the experimental set points are similar to that of Case 1, but the Adsorption machine half cycle time was limited to 250 seconds, while the flow rate was fixed at 50 l/min. Two LT temperatures have been tested 6 °C and 10 °C.

Table 1: setup points used in the different tests performed at the CNR-ITAE lab

Test	HT temp. (C)	MT temp (°C)	LT temp. (°C)	MT flow rate (l/min)	Ads machine time cycle
Case 1	80	28-30-32	6 – 8 - 10	50 – 40 - 30	Auto
Case 2	80	28-30-32	6 – 10	50	Max 250 s

Results and characterization of the unit

Typical test results

In Figure 5 an example of measured parameter during a typical test case is showed. The picture shows the MT_{in} and MT_{out} temperature measured using the sensors installed on the sorption machine ($MT_{in-fahr}$; $MT_{out-fahr}$) or using the sensors installed in the CNR-ITAE lab. The differences between the measures is due essentially to the different sensors position. Anyway, the picture shows how both are able to illustrate a typical sorption machine behaviour.

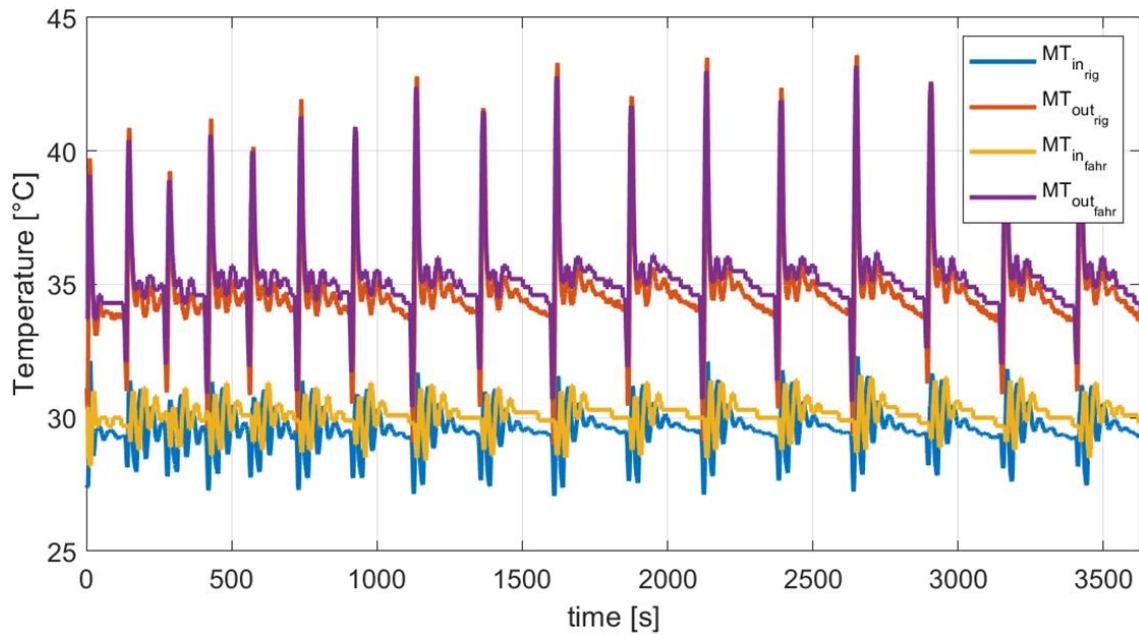


Figure 5: inlet/outlet temperatures measured on the medium temperature (MT) circuit of the adsorption heat pump.

Sorption machines are, contrarily to vapour compression machines, discontinuous, therefore it was expected to see the temperatures peaks in correspondence to the switch between the two sorption chambers.

In Figure 6 the input powers ($Q_{dot_{HT}}$ and $Q_{dot_{LT}}$) as well as the output power ($Q_{dot_{MT}}$) are presented. Following the typical sorption heat pump behaviour, the powers also are not constant. The $Q_{dot_{HT}}$ is the power extracted from the HT heating source, namely the 800 l tank connected to the gas boiler, the $Q_{dot_{LT}}$ is the power that the geothermal circuit provides to the evaporator of the sorption machine, finally, $Q_{dot_{MT}}$ is the power provided by the sorption machine to the user.

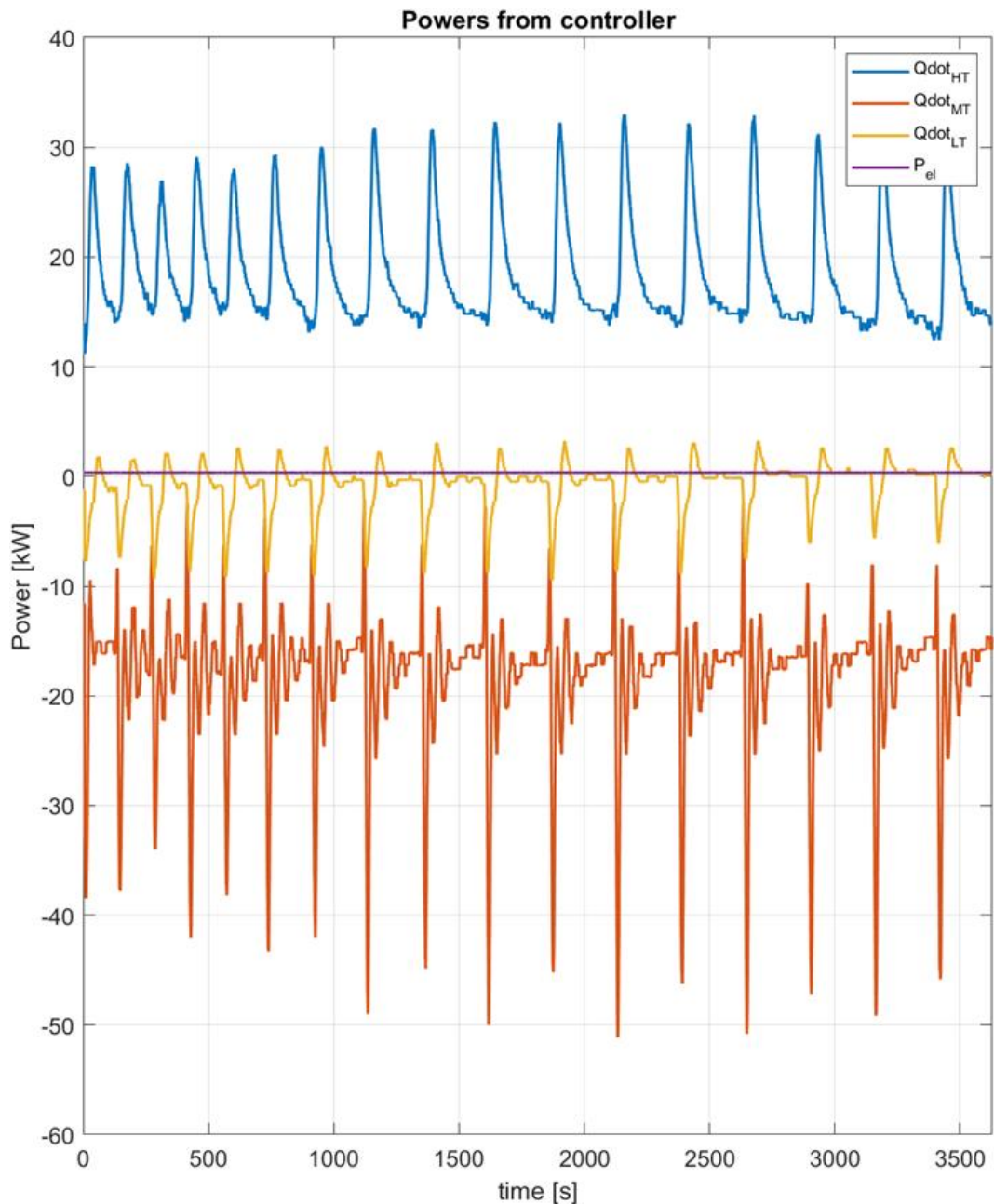


Figure 6: powers exchanged by the sorption machine in a typical test

Influence of different MT flow rate

The influence of the MT circuit water flow rate on the sorption machine performances have been tested at 50 l/min, 40 l/min and 30 l/min. The main goal of this investigation is to find the optimal flow rate which maximizes the output power for a given ΔT . The temperature difference considered (ΔT) is the difference between the MT_{in} (the temperature of the water entering into the sorption machine and coming back from the user) and the LT_{in} (the temperature of the water coming from the geothermal circuit). A low ΔT value means that the temperature difference between the water coming back from the user and the water coming from the geotherm field is low, which means, for example, that we have a very high temperature in the water coming from the geothermal field (e.g. 15 °C or more); while a high ΔT value means that we have a high temperature in the water coming back from the user and a very low temperature provided by the geothermal field. At low ΔT the sorption machine is

working in thermodynamic favourable conditions (low heating demand – high thermal energy availability from the geothermal field). The contrary applies at high ΔT , where the working condition could become critical.

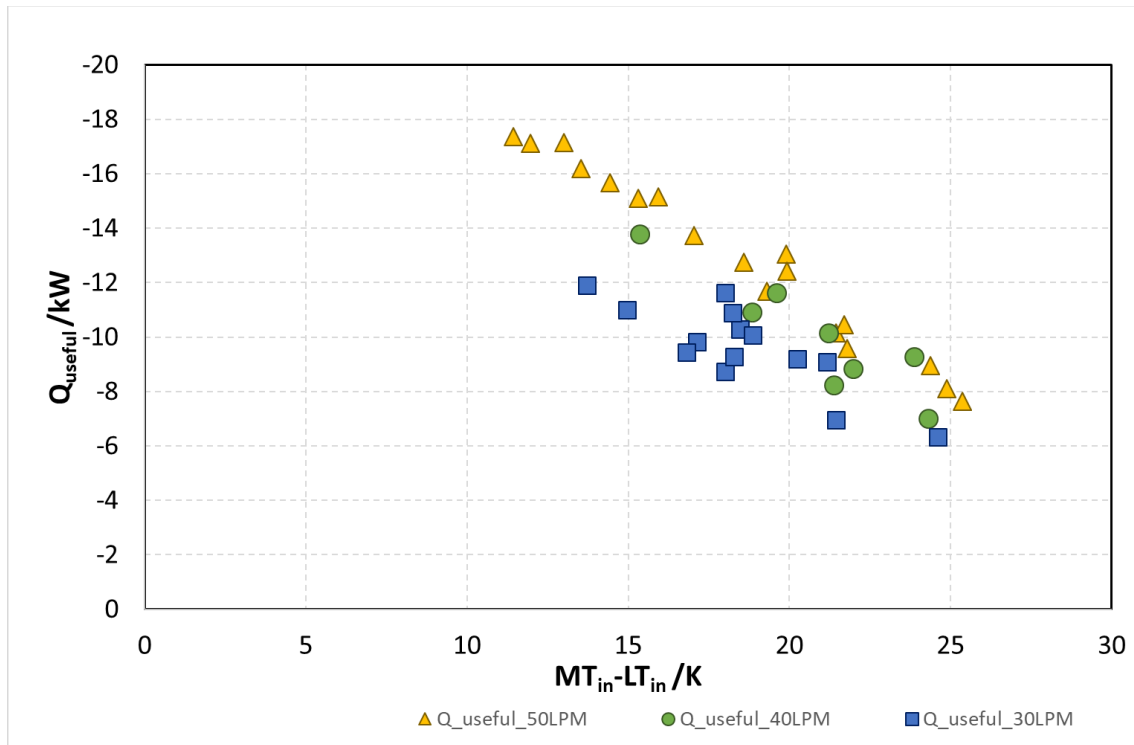


Figure 7: adsorption machine useful power vs ΔT at different MT flow rates

Figure 7 shows the useful power provided by the sorption machine at different ΔT for the tested MT flow rate. As expected, the useful power decrease, almost linearly, with the increase of ΔT . Considering the 50 l/min flow rate, the sorption machine provides $\approx 17 \text{ kW}$ working with a $\Delta T \approx 11 \text{ K}$, while increasing the ΔT to a value higher than 25 K the sorption heat pump is able to provide $\approx 8 \text{ kW}$. Reducing the flow rate the heat pump provides lower useful power, therefore the optimum flow rate for the MT circuit (the circuit connected to the user) should be maintained at 50 l/min.

Figure 8 shows the COP (*Coefficient Of Performance*) measured in the same working conditions. In each sorption heat pump circuit (HT-LT-MT) the instantaneous power was calculated as:

$$\dot{Q} = \rho \dot{V} c_p (T_{in} - T_{out}) \quad (1)$$

Where \dot{Q} [kW] is the instant power, ρ [kg/m³] is the heat transfer fluid density, \dot{V} [m³/s] is the volumetric flow rate of the heat transfer fluid, c_p [kJ/(kg K)] is the specific capacity of the heat transfer fluid and T_{in} and T_{out} [°C] are the inlet and outlet temperatures of the considered circuit. The Coefficient of Performance was calculated using the following equation

$$COP = \frac{\int_{t_0}^{t_f} \dot{Q}_{MT}}{\int_{t_0}^{t_f} \dot{Q}_{HT}} \quad (2)$$

Therefore, the COP was calculated considering the ratio between the heat provided by the adsorption heat pump to the user \dot{Q}_{MT} and the heat provided by the gas boiler to the adsorption heat pump \dot{Q}_{HT} .

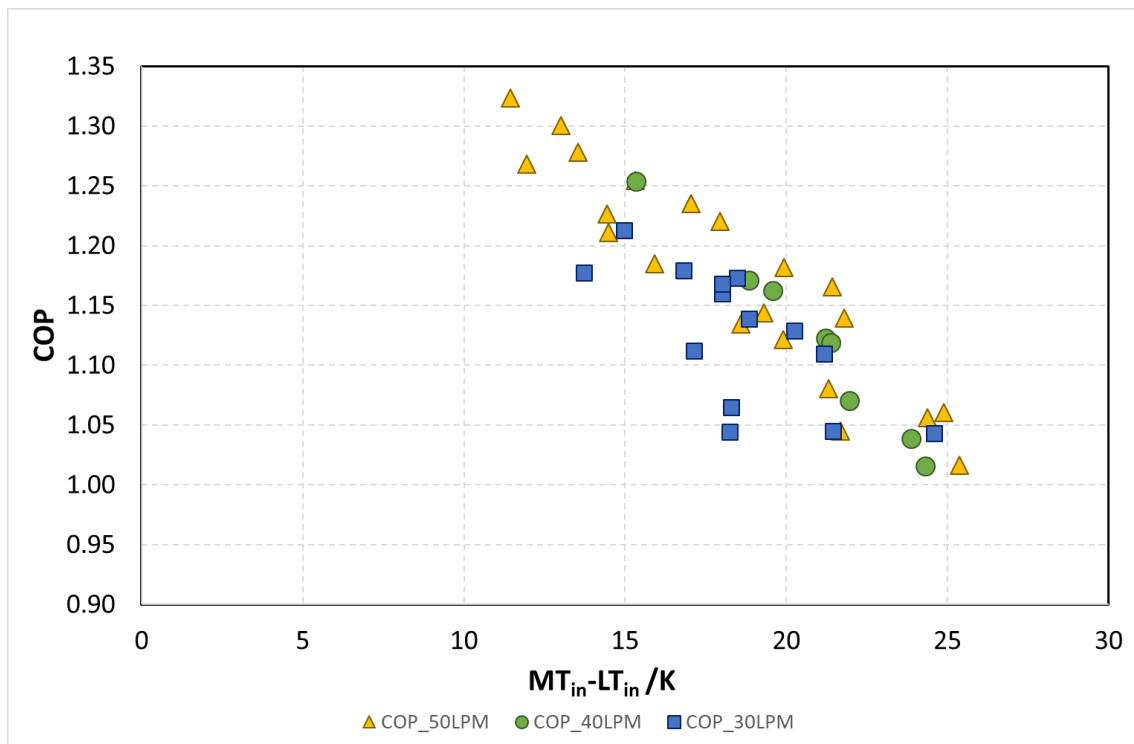


Figure 8: adsorption machine COP vs ΔT at different MT flow rates

Figure 8 shows that COP decreases with the increase of ΔT , starting from a value higher than 1.30 when the sorption machine is working with a $\Delta T \approx 11$ K and reaching a value near to 1 when the heat pump is working with a $\Delta T \approx 25$ K.

The obtained results showed that the best performance can be obtained when the heat pump is working at the higher MT flow rate (50 l/min) and with a ΔT not greater than 20 K, in order to obtain a COP higher than 1.

Influence of phase time

The phase time is the period in which a complete adsorption cycle (see Figure 9) is performed.

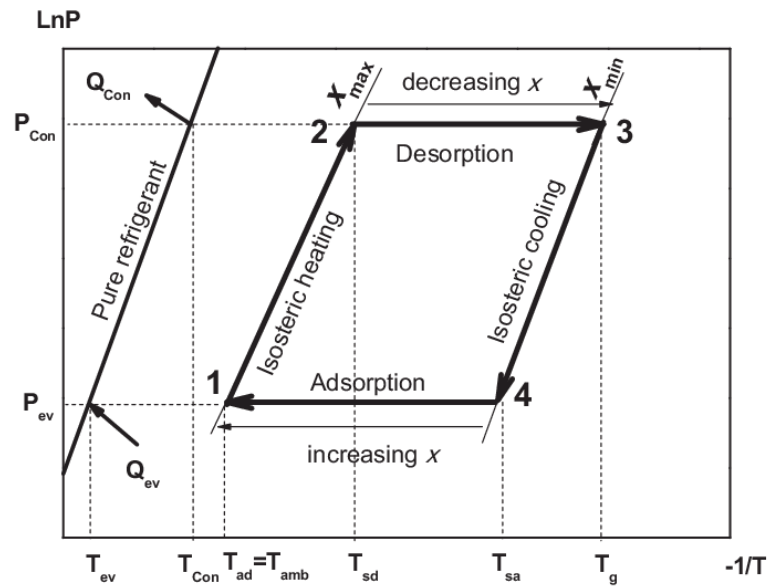


Figure 9: a typical adsorption heat pump cycle.

The tested adsorption machine allows to control the “half cycle time”, which is the time needed to move from point 1 to point 3 (desorption) or from point 3 to point 1 (adsorption) in Figure 9, therefore the time necessary to perform half a cycle. The cycle time is symmetrical, therefore changing the half cycle time it is possible to control the complete adsorption cycle. In order to investigate the optimal cycle time, we have tested the adsorption machine at different “half” phase time, starting from 150 s up to 350 s at two different LT temperatures, as showed in Figure 10.

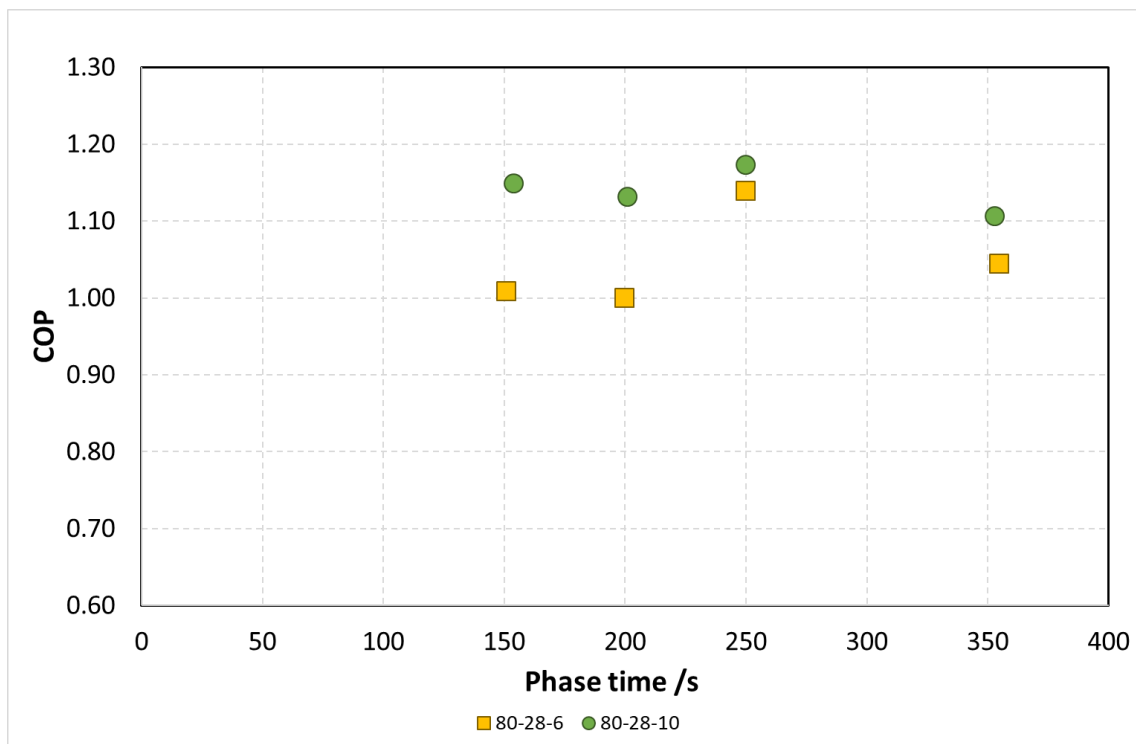


Figure 10: COP calculated at two different LT temperatures (6 °C and 10 °C) and at different phase time

The results clearly show that, independently from the LT temperature considered, the optimal phase time is 250 s. Reducing the cycle time the COP also decreases, especially at much lower LT temperatures. Increasing the cycle time, a similar result is obtained, although a less difference is visible between the two LT temperatures tested.

Conclusion

The complete GEOFIT system, which will be demonstrated in pilot located in a historical building in Perugia (Italy), consists of an adsorption heat pump, driven by a gas boiler, and an electrically driven vapour compression chiller. The adsorption heat pump was completely tested and characterized at the ITAE-CNR test lab, under different working conditions. The main conclusion of the performed work can be summarized as follow:

- The optimal flow rate for the MT circuit is 50 l/min. Reducing the MT flow rate also the useful power decreases.
- The GEOFIT system is able to satisfy the load demand (~ 10 kW) hypothesized during the design stages
- The ΔT between LT_{in} temperature (water coming from geothermal circuit) and the MT_{out} temperature (water provided to the load) strongly influences the adsorption machine useful power and COP: ΔT values greater than 25 °C could become critical for the machinery performances ($COP \approx 1$)
- The best half cycle phase time is 250 s.

Acknowledgements

This work was funded by the project Geofit: Deployment of novel GEOthermal systems, technologies and tools for energy efficient building retrofitting, which has received funding from the European Commission H2020 Programme under Grant Agreement No. 792210

References

- [1] European Commission. Joint Research Centre., *2020-2030-2050-Common Vision for the Renewable Heating & Cooling sector in Europe*, no. January. 2011.
- [2] V. Palomba, E. Varvagiannis, S. Karellas, and A. Frazzica, "Hybrid adsorption-compression systems for air conditioning in efficient buildings: Design through validated dynamic models," *Energies*, vol. 12, no. 6, 2019, doi: 10.3390/en12061161.
- [3] S. Vasta *et al.*, "Adsorption heat storage: State-of-the-art and future perspectives," *Nanomaterials*, vol. 8, no. 7, 2018, doi: 10.3390/nano8070522.
- [4] A. Sapienza *et al.*, "An innovative adsorptive chiller prototype based on 3 hybrid coated/granular adsorbers," *Appl. Energy*, vol. 179, pp. 929–938, 2016, doi: 10.1016/j.apenergy.2016.07.056.
- [5] V. Palomba, U. Wittstadt, A. Bonanno, M. Tanne, N. Harborth, and S. Vasta, "Components and design guidelines for solar cooling systems: The experience of ZEOSOL," *Renew. Energy*, vol. 141, 2019, doi: 10.1016/j.renene.2019.04.018.
- [6] T. C. Roumpedakis, S. Karellas, S. Vasta, U. Wittstadt, and N. Harborth, "Performance results of a solar adsorption cooling and heating unit," *Proc. ISES Sol. World Congr. 2019 IEA SHC Int. Conf. Sol. Heat. Cool. Build. Ind. 2019*, pp. 664–672, 2020, doi: 10.18086/swc.2019.13.03.
- [7] S. Longo, V. Palomba, M. Beccali, M. Cellura, and S. Vasta, "Energy balance and life cycle assessment of small size residential solar heating and cooling systems equipped

- with adsorption chillers,” *Sol. Energy*, vol. 158, no. October, pp. 543–558, 2017, doi: 10.1016/j.solener.2017.10.009.
- [8] A. Buonomano, F. Calise, and A. Palombo, “Solar heating and cooling systems by absorption and adsorption chillers driven by stationary and concentrating photovoltaic/thermal solar collectors: Modelling and simulation,” *Renew. Sustain. Energy Rev.*, vol. 82, no. November 2017, pp. 1874–1908, 2018, doi: 10.1016/j.rser.2017.10.059.
- [9] R. Scoccia, T. Toppi, M. Aprile, and M. Motta, “Absorption and compression heat pump systems for space heating and DHW in European buildings: Energy, environmental and economic analysis,” *J. Build. Eng.*, vol. 16, no. December 2017, pp. 94–105, 2018, doi: 10.1016/j.jobee.2017.12.006.
- [10] S. J. Self, B. V. Reddy, and M. A. Rosen, “Geothermal heat pump systems: Status review and comparison with other heating options,” *Appl. Energy*, vol. 101, pp. 341–348, 2013, doi: 10.1016/j.apenergy.2012.01.048.
- [11] X. Zhang, “Numerical study of geothermal district heating from a ground heat exchanger coupled with a heat pump system,” *Appl. Therm. Eng.*, vol. 185, no. June 2020, p. 116335, 2021, doi: 10.1016/j.applthermaleng.2020.116335.
- [12] C. Zhang, E. Nielsen, J. Fan, S. Furbo, and Q. Li, “Experimental investigation on a combined solar and ground source heat pump system for a single-family house: Energy flow analysis and performance assessment,” *Energy Build.*, vol. 241, p. 110958, 2021, doi: 10.1016/j.enbuild.2021.110958.
- [13] A. Nguyen, “Determination of the ground source heat pump system capacity that ensures the longevity of a specified ground heat exchanger field,” *Renew. Energy*, vol. 169, pp. 799–808, 2021, doi: 10.1016/j.renene.2021.01.035.
- [14] “<http://geofit-project.eu/>,” *Geofit project*. .
- [15] V. Palomba, A. Bonanno, D. La, and S. Löwe, “Design of a gas-driven hybrid adsorption heat pump coupled to geothermal heat exchangers for retrofitting applications,” in *13th IEA Heat Pump Conference*, 2020.
- [16] V. Palomba, G. E. Dino, and A. Frazzica, “Coupling sorption and compression chillers in hybrid cascade layout for efficient exploitation of renewables: Sizing, design and optimization,” *Renew. Energy*, vol. 154, pp. 11–28, 2020, doi: 10.1016/j.renene.2020.02.113.
- [17] A. Sapienza, V. Palomba, G. Gullì, A. Frazzica, and S. Vasta, “A new management strategy based on the reallocation of ads-/desorption times: Experimental operation of a full-scale 3 beds adsorption chiller,” *Appl. Energy*, vol. 205, no. July, pp. 1081–1090, 2017, doi: 10.1016/j.apenergy.2017.08.036.

Modelling and design of an ammonia/salt resorption domestic heat pump.

R.W. Moss^{1*} and R.E. Critoph¹

¹STET research group, School of Engineering, University of Warwick, UK

*Corresponding author: r.moss@warwick.ac.uk

Abstract

Heat pumps will play a key role in the future provision of low carbon domestic heating and the re-use of industrial waste heat. Adsorption cycle heat pumps are advantageous in that they can use the existing natural gas network to avoid electricity supply limitations.

A 2 kW domestic-scale resorption heat pump is being designed as a replacement for a conventional condensing gas boiler. It will be tested in the ThermExS laboratory, University of Warwick.

The heat pump uses a pair of salts infused into an expanded natural graphite matrix, each in its own reactor. The reactor vessels will be insulated internally to minimise their heat capacity.

The initial design was based on a zero-dimensional model to estimate the mass of each salt, taking void space into account. A Matlab-based 2D transient simulation package was then developed to study heat transfer and reaction rate within a pair of linked reactors.

This paper describes the initial reactor design and the unsteady simulation results showing the effect of heat transfer on required cycle time, coefficient of performance and power output.

Keywords: resorption, ammonia, salt, heat pump.

Introduction

Buildings account for 40% of the energy consumption in the UK and USA and the majority of this is for heating. The UK government's forthcoming Future Homes Standard is expected to prohibit the installation of conventional gas boilers in new houses from 2025; heating will instead be provided by heat pump, district heating or low-carbon electricity. It seems probable that gas-fired heat pumps will play an important part in delivering this heat because the UK electricity generation and distribution grid is not expected to grow fast enough to meet projected demands from electric cars and electrical heat pumps.

The marginal CO₂ emission rate due to the additional gas-fired generation of electricity for heat pumps is similar in level to the emissions from conventional gas boilers (Isaacs, 2021). Electric heat pumps therefore only offer a genuine reduction in emissions if they can operate, in conjunction with diurnal or seasonal heat storage, at times when there is an excess of renewable energy. Most houses do not have enough space to install large thermal stores and the expectation of increased electric car use makes it unlikely that there will be an excess of low-carbon electricity before 2045 (Isaacs).

Gas-fired heat pumps therefore have the potential to reduce carbon emissions in the UK until such time as there is sufficient renewable energy and distribution capacity for large-scale adoption of electrically driven heat pumps.

Previous heat pump research at Warwick (Rivero-Pacho, 2017) has concentrated on ammonia adsorption into activated carbon. Ammonia is the preferred refrigerant for domestic heating applications. It has a high heat of

vapourisation and allows heat extraction from a cold environment without risk of freezing or without inconveniently low vapour pressures.

Salts such as NaBr greatly increase the mass of ammonia that can be adsorbed. The salt is typically impregnated into expanded natural graphite (ENG): this supports the small salt crystals in a porous matrix and increases the thermal conductivity.

A simple chemisorption cycle (Wang, 2014) uses an adsorber/desorber (typically filled with ENG and/or a salt) in conjunction with a liquid ammonia evaporator/condenser. At a given temperature, the ammonia-salt equilibrium vapour pressure will be less than the pure ammonia vapour pressure. The two vessels operate at the same pressure, so the liquid ammonia is always at a lower temperature than the salt as it adsorbs and desorbs: this allows the system to function as a thermally-driven heat pump without the expansion valve and mechanically-driven pump required by vapour compression cycles.

A resorption cycle uses a second salt reactor to replace the evaporator/condenser in a chemisorption cycle (Castaing-Lasvignottes & Neveu, 1997). Ammonia is simultaneously desorbed from one salt and adsorbed into the other salt. The salts operate at different temperatures but with a common gas pressure so they can share a common reactor vessel or be located in separate vessels. Compared to a simple chemisorption cycle, the absence of liquid ammonia means that a resorption cycle operates at a lower pressure, thereby allowing a lighter pressure vessel. At 70°C for instance the vapour pressure of ammonia in a chemisorption cycle would be 33 bar.

Vassiliev (2004) built and tested two resorption heat pumps using ammonia with BaCl₂/NiCl₂ and BaCl₂/MnCl₂ respectively as the absorbent pairs. Vassiliev's design was electrically heated and produced both steam (120-130°C) and cool water (3-5°C). The present work is intended for domestic heating and the salts have been chosen to give output temperatures in the range 45-60°C whilst extracting heat from air as cold as -10°C.

The theoretical maximum coefficient of performance for a resorption heat pump, neglecting system heat capacity, is $COP_{hp} = 1 + \frac{\Delta H_L}{\Delta H_H}$ (Vassiliev) where ΔH is the enthalpy change per kg ammonia adsorbed. In

practice the heat capacity of the reactors and adsorbents increases the heat taken from the hot source and reduces the heat extracted from the cold source, giving a practical COP (Vassiliev):

$$COP_{hp} = 1 + \frac{\Delta H_L - C_L \Delta T_L}{\Delta H_H + C_H \Delta T_H} \quad [1]$$

The enthalpy of desorption from a salt is higher than the heat of vapourisation of pure ammonia. This increase to the ΔH_L value in the above equation gives resorption cycles a higher coefficient of performance than a simple chemisorption cycle.

The challenges in designing a resorption heat pump include:

- Identifying a suitable salt pair for the cycle temperature range and appropriate filling factor in the ENG to allow sustainable long-term adsorption/desorption performance
- Identifying the appropriate ratio of salt masses, such that both salts approach the fully adsorbed and desorbed state.
- Defining a cycle period and salt masses for the required output power
- Specifying a control cycle for the valves on each reactor such that they receive and discharge heat as required
- Minimising thermal resistances, to allow rapid cycling with small temperature differences

- Choosing heat transfer fluids

Yang et al (2020) present a thorough review of ammonia-based chemisorption and resorption heat pumps. Castets and Mazet (2001) modelled reaction rates for an adsorption thermal transformer to demonstrate the importance of minimising reactor mass.

Bao et al (2011) tested two possible salt pairs, NaBr/MnCl₂ and NH₄Cl/MnCl₂, in a benchtop demonstration refrigerator. Using a 30-minute cycle they found the ammonium chloride reacted with 17% more ammonia than the equivalent sodium bromide reactor. The sodium bromide cycle achieved a refrigeration COP of 0.31 compared to the theoretical maximum of 0.61.

Materials testing at Warwick in a “Large Temperature Jump” (LTJ) facility has verified the validity of the heat transfer and reaction rate equations used and determined the appropriate modelling parameters for NH₄Cl₂, NaBr, BaCl₂, MnCl₂ and CaCl₂ (Atkinson, 2021). The heat pump described here will be tested using the heating and cooling baths and process instrumentation in the ThermExS facility at Warwick.

Nomenclature

A, y	Reaction rate parameters
C_L, C_H	Sensible heat capacity of the low and high temperature reactors (J/K)
COP_{hp}	Coefficient of performance = $\frac{\text{heat delivered at } T_O}{\text{heat input at } T_H}$
E	Cycle period (seconds).
ΔH	Enthalpy change per mole NH ₃ desorbed (J/mol)
$\Delta H_L, \Delta H_H$	Enthalpy change per cycle for low and high temperature salts (J)
Δn_A	Moles of ammonia desorbed per cycle, reactor A.
$\Delta T_L, \Delta T_H$	Temperature range for each salt, $T_3 - T_1$ and $T_4 - T_2$
ΔH^0	Salt enthalpy change per mol desorbed (J/mol) at standard conditions
\tilde{R}	Universal gas constant 8.314 J/molK
ΔS^0	Salt entropy change per mole NH ₃ desorbed (J/molK) at standard conditions
T	Temperature (K).
α	Thermal diffusivity, $\alpha = \frac{k}{\rho c}$ (m ² /s)
f_A	Fraction of the salt in a given adsorption state A.
v_A	Void space volume in reactor A (m ³)

Reactor design.

The two reactors in a resorption heat pump are essentially shell and tube heat exchangers. The reactor vessels are connected so ammonia can flow between them. Heat transfer fluid is pumped through the tubes to convey heat to and from the salts, Figure 1, with valves to switch the reactors between the three heat sources and sinks. Heat fluxes will be measured using a Coriolis mass flow rate meter on each heat transfer fluid circuit together with thermocouples to read the fluid temperature difference between reactor inlet and outlet.

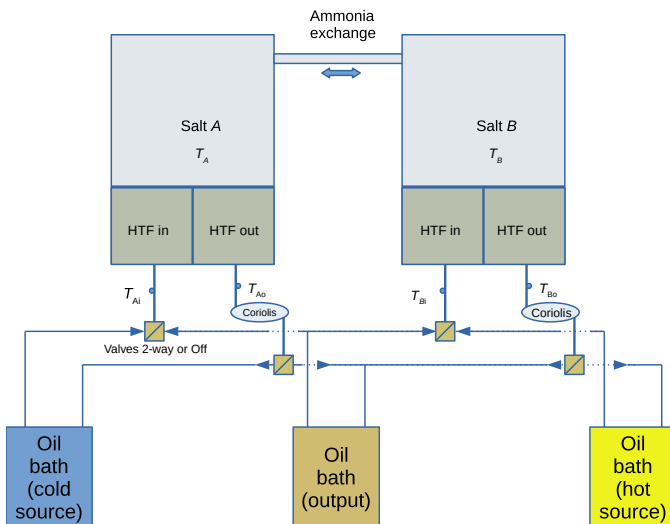


Figure 1. General arrangement of a resorption heat pump in a test facility.

The heat pump cycle is controlled by the timing of valves that route the heat transfer fluid to either the cold source or output (low temperature salt A) or the hot source or output (high temperature salt B). There are four stages to the cycle, starting with salt A fully desorbed at the cold source temperature and B fully adsorbed at the output temperature:

1. Isolate reactor A and route the fluid connection for reactor B to the heat source. Salt B will start to desorb as its temperature rises. As the pressure rises due to this desorption, salt A adsorbs and its temperature rises.
2. When salt A reaches the output temperature, open the reactor A fluid connection to the output sink so A delivers heat. Wait until salt A is fully adsorbed.
3. Isolate reactor A and connect reactor B to the output sink so the temperature of salt B falls and it starts adsorbing & rejects heat to delivery. As the pressure falls, A desorbs and cools.
4. When A reaches the cold source temperature, open the fluid connection to the cold source. Salt A will extract heat from the cold source until fully desorbed, at which point all the ammonia is once again adsorbed in salt B.

When used for domestic heating a thermal store would be required to provide a high flow rate on demand and to buffer the heat-output stages in the heat pump cycle. Two heat pumps operating out of phase might also be used to provide a more continuous heat output. The baths shown in Figure 1 would be replaced by an air-to-water heat exchanger (cold bath), hot water heat exchanger (output) and combustion gas heat exchanger (hot bath).

The heat pump cycle

The pressure/temperature history of the salt in each reactor is determined by the Clapeyron equilibrium line equation:

$$\ln \frac{P}{P_0} = \frac{-\Delta H^0 + T\Delta S^0}{RT} \text{ where } P_0 \text{ is the reference pressure (1 N/m}^2\text{) (Yang, 2020) and } \Delta H^0, \Delta S^0 \text{ are}$$

positive. The equation assumes that ammonia vapour behaves as a perfect gas. Adsorption happens if the partial pressure lies above the line and desorption for pressures below the line.

The salt pair must be chosen to give usefully large temperature differences between the two salts at a given pressure. The minimum pressure should not be so low as to require inconveniently large components for adequate mass transfer. A large number of salts have been considered for adsorption cycles (Bao, 2011; Yang, 2020). Of these, manganese chloride appears the most suitable for a high temperature salt operating between a heat rejection temperature in the range 45-60°C and a heat input temperature of 160-175°C. The heat pump described here is designed to ultimately be driven by a gas burner (the “hot source”) and to extract heat from a “cold source” which might be a borehole or air heat exchanger while delivering heat to the “output” heat sink. For experimental purposes these will be simulated by heating and cooling baths.

The most suitable low temperature salts in terms of thermodynamic properties for pairing with MnCl₂ appear to be either ammonium chloride or sodium bromide. These have almost identical equilibrium lines. Sodium bromide has been chosen because experience within the STET group (Atkinson, 2021) suggests that sodium bromide is more soluble, hence easier to impregnate into the ENG biscuits, and gives more repeatable adsorption and desorption performance than ammonium chloride.

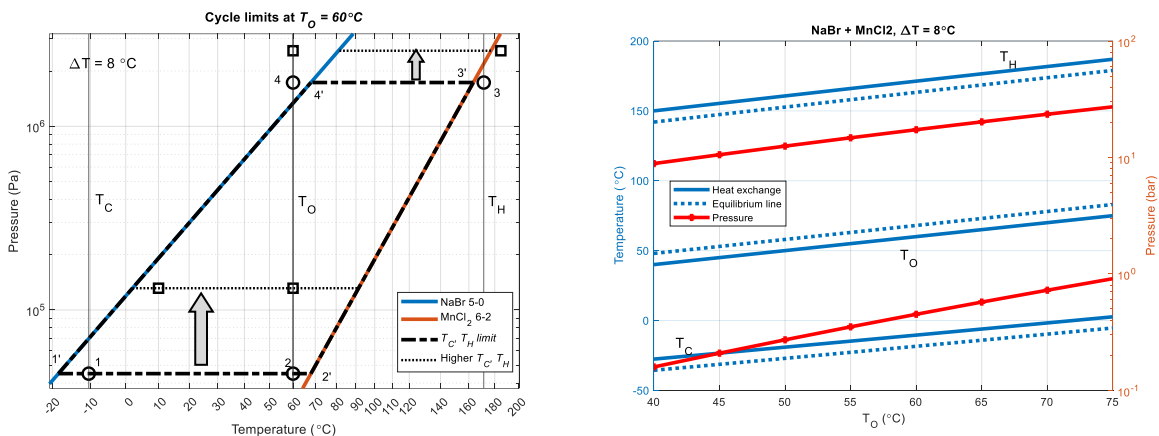


Figure 2. (a) Heat pump cycle pressure and temperature range on a Clapeyron diagram, (b) Minimum T_C, T_H as a function of output temperature T_O for $\Delta T = 8^\circ\text{C}$.

Figure 2(a) shows the equilibrium lines for sodium bromide and manganese chloride with a temperature difference $\Delta T = 8^\circ\text{C}$ between each heat source/sink and its salt to enable heat transfer despite the thermal resistance between each salt and the heat sources and sink. The dots represent the source and sink temperatures. Thermal resistance is inevitable due to the convective heat transfer coefficients at air/metal and metal/fluid interfaces as well as the low thermal conductivity of the ENG/salt composite and any contact resistance between the ENG and heater tubes. The requirement for $T_4 = T_2$ is dictated by the fact that both salts reject heat to a common heat sink at T_O : in a domestic installation this would be the radiators and thermal store.

The lowest possible T_C, T_H are determined by the equilibrium temperatures for salt 1 and salt 2 respectively at the two pressure limits set by T_O . The ----- lines in Figure 2(a) show this limiting case. The lines

demonstrate possible operation with the same output temperature but higher T_C, T_H leading to an increase (vertical arrows) in P_1 and P_2 .

The vertical lines in Figure 2a show source and sink temperatures that lie *between* (cold state) or *outside* (hot state) the equilibrium lines. The cycle will cease to operate if this condition is not met.

The heat pump could deliver heat to radiators and hot water store at two different temperatures by switching between them, e.g. on a daily timer. Simultaneous operation with a DHW temperature higher than the heating requirement would be possible but the COP would be lower than in heating-only mode and a flow control system would be required to enable the hot water to reach a suitable temperature (e.g. 60°C to avoid *legionella* risks).

Figure 2(b) shows the dependence of minimum T_C, T_H on output temperature T_O for this salt pair or, conversely, the maximum output temperature for any given T_C, T_H .

The maximum pressure is typically set by salt 1 at the output temperature T_O , Figure 2(b). This pressure determines the pressure vessel thickness and, more importantly, the thickness and heat capacity of the tube-plates.

T_H must remain within the capabilities of the heat transfer fluid. Water/ethylene glycol based heat transfer fluids are able to operate up to 175°C (Dow, 2008); silicone oils e.g. Huber SilOil can withstand 235°C under an inert atmosphere but have lower conductivity and heat capacity than water-based fluids. 175°C would be sufficient for output temperatures up to 63.5°C (Figure 2b) with $\Delta T = 8^\circ\text{C}$. The two reactors may in principle use different heat transfer fluids, Bao (2011).

The salts will asymptote towards the source and sink temperatures as the adsorption and desorption reactions approach completion. As they do so, the temperature difference and heat flux fall so the reaction rate will also slow. This can also be seen from the rate equation for change in species A in a reaction from A to B:

$$\frac{1}{f_A + f_B} \frac{df_A}{dt} = A_{AB} \left(\frac{f_A}{f_A + f_B} \right)^{y_{AB}} \left(1 - \frac{p_{Clap}}{p} \right) \quad [2]$$

where f_A, f_B are the mole fractions of the salt in states A and B and p_{Clap} is the equilibrium ammonia pressure at the salt temperature. The reaction rate is heat transfer limited: increasing the heat transfer rate alters the salt temperature and increases $|p - p_{Clap}|$.

In the low pressure state, salt A is desorbing and B adsorbing. When they reach the Cold Source and Output temperatures (T_C, T_O), the equilibrium pressure for salt A is higher than for B. Given sufficient time, the reaction will proceed until either:

- (i) A is fully desorbed, with the pressure set by salt B at T_O
- (ii) B is fully adsorbed, with the pressure set by salt A at T_C
- (iii) both (i) and (ii)

Case (iii) will only occur if the A:B ratio is close to the exact required proportion. The pressure is then between the case (i) and (ii) limits and is set by the excess ammonia mass i.e. the void space and initial filling condition.

A similar situation occurs at the end of the high pressure stage in the cycle.

Conceptual design

The two reactors are connected and work at the same pressure: the salts could therefore be placed together in a single vessel. It is however easier to avoid heat leakage between the salts if they are placed in separate reactors.

Two alternative designs are being considered: a fully-welded assembly in which the tubes act as stays to carry the pressure loads and a bolted assembly with single-ended tubes. The latter allows the salt/ENG disks to be examined after testing or replaced to try different compositions.

The choice of pipe length is an optimisation problem which has not yet been considered in detail. The length is limited by heat transfer considerations. This especially true if using thermal oil rather than water: oil avoids boiling and freezing problems but has a relatively low conductivity and specific heat combined with high viscosity. Too high an L/D ratio would require a long cycle time for reduced heat flux: this in turn reduces the specific power output and raises the volume needed for a given power.

Equation [1] shows the effect of component heat capacities on the COP. This effect has been observed experimentally (van der Pal, 2017). The heat capacity of the shell may be significant unless it is insulated internally.

The unavoidable heat capacities are due to the tube-plates, tubes and the fluid within them, ENG and the salt itself. These place an upper limit on the coefficient of performance. Typical values can be obtained by considering a repeating array of tubes with the intervening space filled with ENG (leaving just a minimal path for ammonia transport), Figure 3(a).

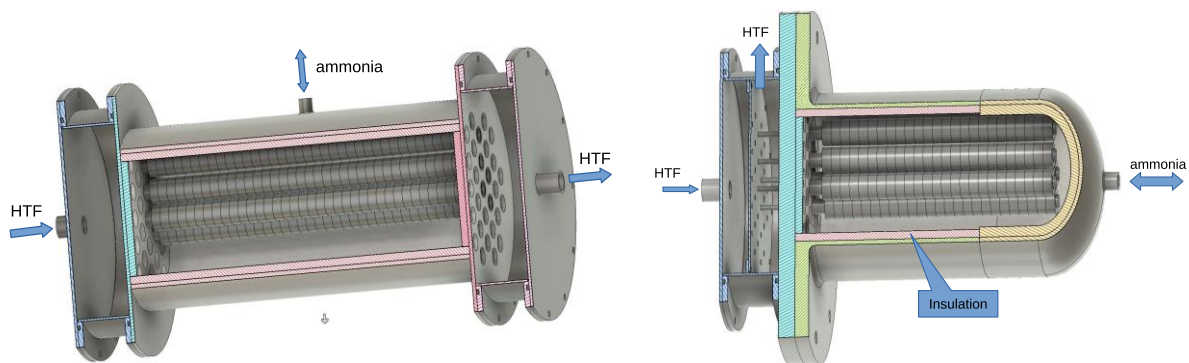


Figure 3. (a) Double-ended reactor design with load-bearing tubes, (b) Single-ended reactor design.

A second concept under consideration is a reactor using single-ended tubes that do not support the end plate structurally, Figure 3(b). This would enable the reactor to be disassembled to replace or examine the salt/ENG composite after testing.

A single-ended reactor would require a single end plate, significantly thicker than in the double-ended design. Whilst in theory this reduces the maximum possible COP, in practice the heat capacity of the end plates is small compared to that of the fluid in the tubes and manifolds. The necessary shell thickness is determined by the hoop stress, not the axial stress, and would therefore be the same as in the double-ended reactor. The tubes would be capped at the inner end: this places them in compression due to the external pressure. Each tube would require a co-axial inner tube to carry fluid to the far end before it returned via the annular outer passage.

Void space effect on ratio of salt masses

The cycle shown in Figure 2(a) assumes that the pressure is set by the mass of ammonia in the system and the salt temperature. There will however inevitably be some gas volume v_A, v_B in each reactor due to the porosity of the ENG as well as any unfilled space between the ENG biscuits and the shell. The mass of ammonia in these spaces will vary with temperature and pressure.

Continuity between the low pressure state 1 and high pressure state 2 requires

$$m_{B1} - m_{B2} = m_{A2} - m_{A1} + \sum m_{v2} - \sum m_{v1}$$

where m_{B1} is the quantity of ammonia (either mass or moles) adsorbed into salt B in state 1 and $\sum m_{v1}$ is the quantity of ammonia in all the gas volumes at state 1.

The volume per mole desorbed in each reactor k_A, k_B is defined as $k_A = \frac{v_A}{\Delta n_A}$ and the ratio of adsorption

capacities is $K_{AB} = \frac{\Delta n_A}{\Delta n_B}$. Assuming the ammonia behaves as a perfect gas, it can be shown that:

$$\left(\frac{k_A P_2}{\tilde{R} T_O} - \frac{k_A P_1}{\tilde{R} T_C} + 1 \right) K_{AB} = 1 + \frac{k_B P_1}{\tilde{R} T_O} - \frac{k_B P_2}{\tilde{R} T_H} \quad [3]$$

Figure 4 shows the required adsorption capacity ratio as a function of a single parameter k for the $k_A = k_B$ case using cycle temperatures from Figure 2.

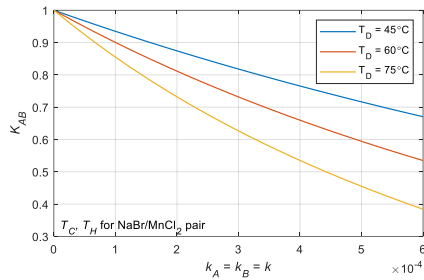


Figure 4. Effect of void space on the ideal salt ratio. The insulated reactors simulated here have

$$k \approx 3.3 \times 10^{-4} \text{ m}^3/\text{mol}.$$

If K_{AB} is higher than the ideal value, the temperature swing for salt A will be limited: this will reduce the maximum delivery temperature for a given cold temperature. Conversely if K_{AB} is too low the hot source temperature will rise relative to the design intent based on delivery point temperature.

Heat capacity of thermal insulation

SuperWool® 607 is a low-density insulation material suitable for temperatures up to 1150°C. During a heat pump cycle a thermal wave would propagate into the insulation. The depth of propagation and hence the

effective heat capacity are a function of cycle length E (seconds) and gas to wall heat transfer coefficient h ($\text{W}/\text{m}^2\text{K}$). The effective heat capacity has been calculated using a 1D transient simulation with a square wave gas temperature cycle, Figure 5. Provided the thermal wave does not reach the far side of the insulation the heat capacity is independent of the insulation thickness.

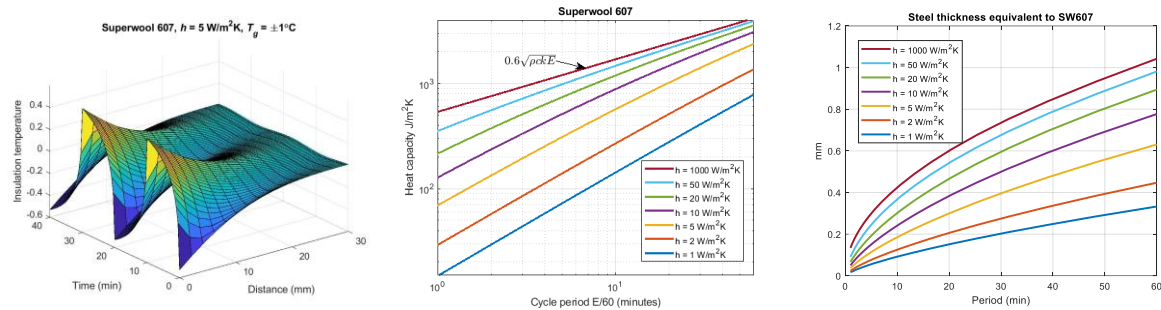


Figure 5. (a) Wave propagation into insulation, (b) insulation effective heat capacity per half-cycle, (c) equivalent stainless steel thickness. [$\rho = 350 \text{ kg}/\text{m}^3$, $c = 754 \text{ J}/\text{kgK}$, $k = 0.05 \text{ W}/\text{mk}$].

Figure 5(b) shows that the heat capacity asymptotes towards $C \propto \sqrt{\rho ckE}$ for very large heat transfer coefficients i.e. when the surface temperature closely follows the gas temperature cycle. This is to be expected because the wave profile for a thermal step propagating into a semi-infinite solid is a function of $\frac{x}{\sqrt{\alpha t}}$. Actual gas to wall coefficients would however be much less than this, possibly $5 \text{ W}/\text{m}^2\text{K}$.

Figure 5(c) shows that for all conceivable cycle period and gas heat transfer coefficients the insulation has a heat capacity equivalent to a steel sheet 1 mm or less in thickness. As this is less than the typical shell thickness it is always beneficial to include insulation. The insulation's porosity will however increase the reactor void space.

A similar analysis for the reactor end plates shows that over a typical cycle period the radial wave penetration depth due to heat transfer in the pipes is larger than the expected pipe spacing when using a water-based fluid ($h \approx 1500 \text{ W}/\text{m}^2\text{K}$) so insulation against the tube-plate faces would provide no benefit. The heat capacity of the metal must therefore be used in the COP calculation and minimising the thickness, e.g. by using load-bearing tubes, would be beneficial.

Thermal oil by comparison provides a much lower heat transfer coefficient ($h \leq 600 \text{ W}/\text{m}^2\text{K}$) which would necessitate a larger reactor and longer cycle time. With low heat transfer coefficients insulation on the end-plates might be advantageous. With radial heat transfer from each hole area, the change in metal temperature over the cycle period may be small compared to the fluid range and the effective heat capacity can then be estimated from the fluid heat transfer coefficient and period.

Multi-reactor transient modelling.

A Matlab-based 2D unsteady simulation package has been written for ammonia-salt reactors. The aim was to allow simple setup and rapid analysis for all the ENG/salt configurations of interest to the STET group.

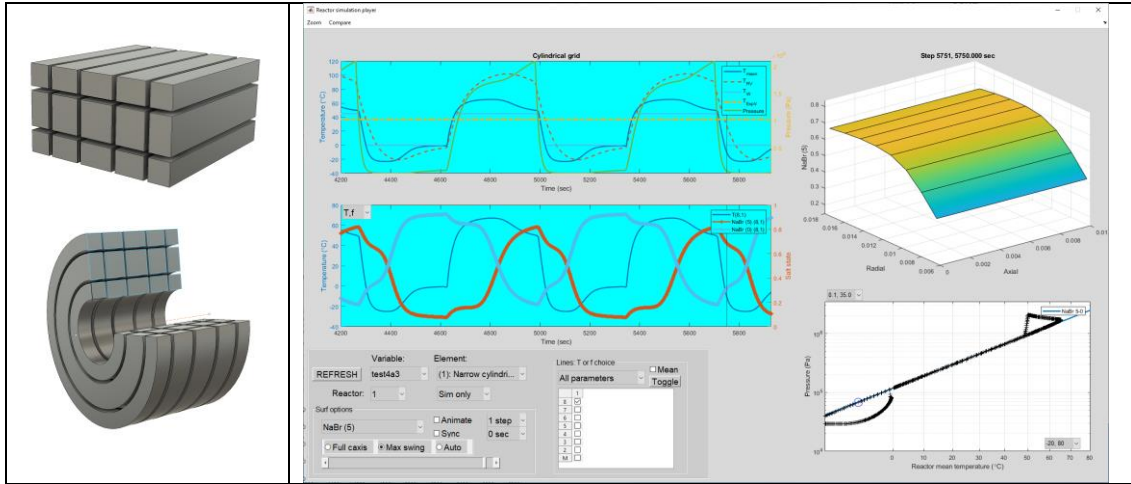


Figure 6. (a) Possible grid configurations, (b) Viewer for simulation output.

The original concept was to use Matlab's Partial Differential Equation toolbox to solve the conduction and reaction rate equations. This proved impractical because there was no facility for a whole-system calculation of the pressure as a function of the ammonia adsorption state across the grid. The present code therefore uses Matlab's linked-ODE solver ODE15s for a "Method of Lines" approach which calculates temperature and ammoniation state for each cell. The system pressure at each time step is calculated from the total mass of ammonia and the salt adsorption states.

The code iterates through multiple reactors and/or salts in each reactor using structured 2D finite volume grids (cuboid or cylindrical, Figure 6a, including metal pipework and fins) and has been validated against analytical conduction models and experimental reaction rate data. The reaction rates for each reaction are evaluated from equation [2] using experimentally-derived thermodynamic properties and rate parameters. The reactions progress in response to a defined temperature-time history for the heat transfer fluid, using a constant heat transfer coefficient at the pipe wall. Thermally isolated periods of zero heat flux are applied during cycle stages 1 and 3.

A plotting tool has also been written to show and compare the output parameters, Figure 6b.

The unsteady energy equation $\frac{dU}{dt} = \dot{Q}_m + \dot{W}_m + \sum \dot{m}_{in,j} h_j$ is used both within the grid and to model the reactor shell temperature change due to ammonia transfer between the vessels. For simplicity the instantaneous flow rate between vessels is estimated such that, for all the vessels, $\left[\frac{1}{M} \frac{dM}{dt} \right]_{i=1,2,3} = \text{constant}$.

(This would be strictly true if gas desorption caused adiabatic compression at constant vessel volume such that $\left[\frac{1}{\rho} \frac{d\rho}{dt} \right]_{i=1,2,3} = \text{constant}$). This value is then updated in the next iteration to match the actual mass in each reactor.

The simulation allows the effect of different fluid heat transfer coefficients to be assessed when designing the reactors such that a suitable cycle time can be identified. Future versions of the code will incorporate a porosity model to account for pressure variation through the ENG.

Heat pump simulation.

A heat pump has been modelled by defining two reactors, each with its own fluid temperature history. Simulations have modelled water/glycol (90% Dowtherm 4000) and silicone oil (Huber SiOil 195/235) as the heat transfer fluids.

The poor conductivity and heat capacity of thermal oil limit the attainable heat transfer coefficient. The water-based simulations used a nominal coefficient of $1500 \text{ W/m}^2\text{K}$ for turbulent flow inside a 10.7 mm bore tube (a conservative value: in practice it will vary depending on the fluid temperature and velocity). The higher viscosity of SiOil reduces the Reynolds number to below 1000 (e.g. $\text{Re} = 430$ for 0.5 m/s at 60°C): for fully developed laminar flow a Nusselt number $\text{Nu} = 4.36$ would be expected. Sarada et al (2011) simulated an oil cooler with a louvered tube insert, resulting in Nusselt numbers of order $\text{Nu} = 50$. Similar Nusselt numbers have been reported by Sheikholeslami (2015) for a wire coil insert. If $\text{Nu} = 50$ were possible in the present design, the heat transfer coefficient would be $h \approx 600 \text{ W/m}^2\text{K}$. This has therefore been taken as a nominal value to explore the impact of low heat transfer conditions.

The ratio of salts obeys equation [3] and a volumetric salt fraction of 0.05 has been adopted based on LTJ experience.

The modelled geometry is a cylindrical tube of salt-impregnated ENG (in practice a large number of rings) that slides onto a central tube carrying the heat transfer fluid. For simplicity the graphs presented here use a 1-D radial grid and rely on the thermal conductivity of the ENG to carry heat radially from the central tube. The code is however capable of modelling a finned-tube system with both axial and radial conduction if such a design were required. For this preliminary design optimisation it has been assumed that the fluid flow rate is high enough that the fluid temperature rise along the tube can be ignored.

The design uses a $\frac{1}{2}$ " OD tube and ENG disk external diameter of 35mm. A typical control cycle in terms of fluid temperatures is shown in Figure 7(a). Reactor A is thermally isolated at two stages in the cycle to allow its temperature to change freely as adsorption and desorption commence without putting heat into the cold source or taking it from the output.

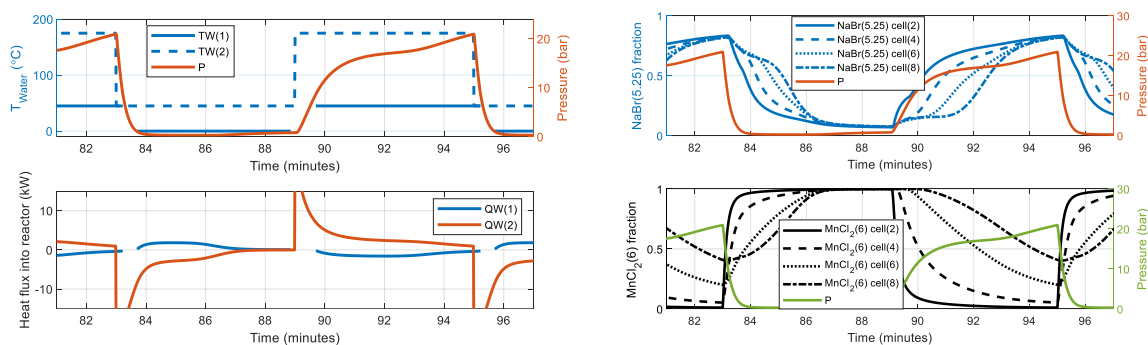


Figure 7. (a) Fluid temperature (control parameter), system pressure and heat flux into each reactor, (b) Salt ammoniation state at 4 radial stations.

Figure 7(b) shows a typical variation in salt states over a 12-minute cycle for 4 radial locations (cell 1 is the metal tube, cells 2-8 are ENG) when using a water/glycol mix ($h = 1500 \text{ W/m}^2\text{K}$). This simulation had approximately 17% excess NaBr so the MnCl_2 swings between fully adsorbed and desorbed whilst the NaBr stays between 0.06 and 0.89 adsorbed.

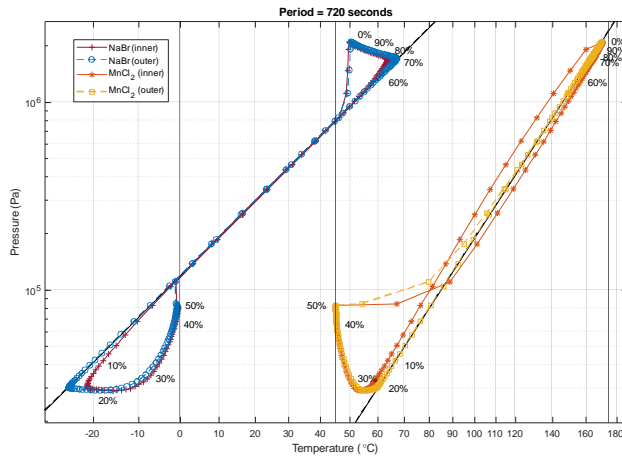


Figure 8. Heat pump cycle on a Clapeyron diagram. Labels show cycle fraction starting from when reactor 2 is cooled to delivery temperature. Vertical lines show the water temperatures.

Figure 8 shows the temperature-pressure history for both salts on a Clapeyron diagram for a given filling mass of ammonia (initially 3.5 bar, reactor 1 at 25°C, reactor 2 at 110°C).

The grid uses 8 radial cells of which the inner is the water pipe: temperatures for cells 2 and 8 are plotted here. The $MnCl_2$ in reactor 2 adsorbs and desorbs in response to changes in water temperature and the resulting heat transfer leads to a temperature difference relative to the Clapeyron line. Conversely the $NaBr$ in reactor 1 adsorbs and desorbs in response to the change in pressure and follows the equilibrium line closely until the valves open and allow heat transfer to the Cold or the Output bath.

COP and power density

The COP has been calculated by post-processing the results to split the heat flux into positive (from sources) and negative (to output) periods. Simulations were performed for delivery temperatures of 45 and 60°C, for a range of cycle periods, using both water/glycol and thermal oil as the heat transfer fluids.

The reactor dimensions are given in Table 1.

	Reactor 1 (NaBr)		Reactor 2 ($MnCl_2$)	
	45°C	60°C	45°C	60°C
Salt mass (dry), kg	0.227	0.221	0.519	0.533
ENG disks (total)	200	194	492	505
Tubes	7		19	
Reactor length (mm)	290		270	
Reactor ID (mm)	158		230	
Reactor volume (litres)	5.7		11.2	
Gas volume (litres)	2.32		3.45	

Table 1. Reactor sizes for a nominal 2 kW output.

Figure 9 compares heat pump COP values and cycle-mean output power from the transient model using either water/glycol or silicone oil. Tube-plate and fluid capacity has been modelled as a lumped heat capacity that transfers heat between source and sink twice per cycle, using a nominal thickness of 4 mm (metal), 10 mm (fluid) at each end of the reactor.

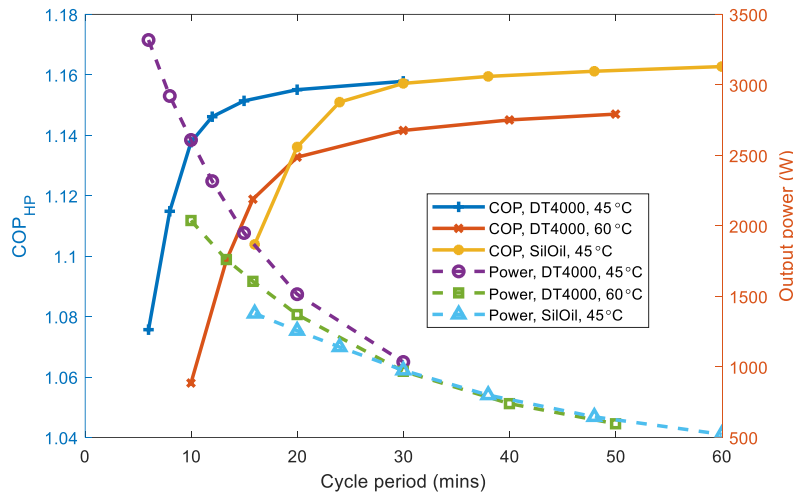


Figure 9. Comparison of two heat transfer fluids: 90% DowTherm 4000 (glycol mix, $h = 1500 \text{ W/m}^2\text{K}$) and Huber SiOil 195/235 ($h = 600 \text{ W/m}^2\text{K}$) in terms of COP and power output. $T_c = 0^\circ\text{C}$, $T_H = 175^\circ\text{C}$

If using thermal oil the cycle period has to be extended to achieve sufficient heat transfer for adsorption and desorption to take place. The longer cycle period reduces the mean power output, unless larger reactors with more salt are used to compensate. Comparing the cycle times required to achieve COP = 1.15 with 45°C output, the cycle period increases from 15 to 24 minutes and the output power is reduced by 42%.

The above simulations assume perfect thermal contact between tubes and ENG. Any slight gap here will increase the thermal resistance and reduce the effective heat transfer coefficient. The effect would be to reduce either the COP or (if the cycle period were extended to maintain the COP) the power output.

COP values of order 1.15 are clearly incapable of providing the necessary drastic cuts in CO₂ emissions. Reducing the heating demand through better domestic insulation and heat recovery systems could have a more immediate impact and, long term, renewable energy together with electric heat pumps and/or seasonal storage has the potential for carbon-free operation. Conversely, such COP levels would be similar in effect to the switch from conventional to condensing boilers (5-14% reduction, EConsult 2018).

Summary/Conclusions

Simulations suggest that a resorption heat pump using NaBr/MnCl₂ can provide a COP of approximately 1.15 and a specific power of order 140 W/litre of gross reactor volume. Use of an ethylene glycol mix as the heat transfer fluid limits the upper temperature to 175°C: this should be sufficient for output temperatures up to 63°C. Thermal oil would allow higher temperatures but, with lower heat transfer coefficients, the cycle period would be longer and the specific power would be reduced.

The reactors would use expanded natural graphite rings in contact with tubes carrying the heat transfer fluid in a shell and tube configuration. The reactor shell should be insulated internally to minimise the effective heat capacity over the cycle period. The tube assembly could be either double-ended, with tubes acting as stays, or single-ended; the latter would allow dismantling to experiment with different salt parameters but would require stronger end plates.

The 2D simulation code provides a user-friendly platform for the optimisation of salt/ammonia multi-reactor systems. Good thermal contact between ENG and tubes will be critical in achieving the desired performance.

Simulations have demonstrated the critical importance of fluid to salt heat transfer: this affects the possible ENG ring diameter, choice of fluid, cycle time and reactor size.

A COP of 1.15 from a gas-fired appliance could make a valuable contribution to reducing domestic heating emissions until there is sufficient renewable electricity to drive electric heat pumps in addition to meeting other demands such as electric car use.

References:

Atkinson, G.H., Critoph, R.E. and Hinmiers, S. *Modelling and Optimisation of Ammonia-Salt Resorption Cycle Heat Pumps and Heat Transformers based on LTJ Testing*. Heat Powered Cycles, Bilbao, 2021

Bao, H.S., Oliviera, R.G., Wang, R.Z., Wang, L.W. and Ma, Z.W., *Working pairs for resorption refrigerator*. Applied Thermal Engineering 31 (2011) <https://doi:10.1016/j.applthermaleng.2011.05.035>

Castaing-Lasvignottes, J. and Neveu, P. *Equivalent Carnot cycle concept applied to a thermochemical solid/gas resorption system* Applied Thermal Engineering 18 (1998) 745-754

Castets, K. and Mazet, N. *Optimization of the reactor configuration on the performance of the cyclic working mode of thermochemical transformers. Reactor miniaturization*. Energy 26 (2001) 271–286

EConsult assessment for the German Renewable Energy Federation. *Final energy and CO2 savings made by replacing aging boilers with condensing boilers*, 2018.

https://www.ehpa.org/fileadmin/red/03_Media/03.02_Studies_and_reports/BW-Kesseltausch_Kurzgutachten_BEE_20180301_CS_EN_1.pdf

Isaacs, T. Heat pumps, boilers and decarbonisation. The Chemical Engineer, July 2021
<https://www.thechemicalengineer.com/features/heat-pumps-boilers-and-decarbonisation/>

Rivero-Pacho, A.M., Critoph, R.E. and Metcalf, S.J. Modelling and development of a generator for a domestic gas-fired carbon-ammonia adsorption heat pump. Renewable Energy 110 (2017) 180-185,
<http://dx.doi.org/10.1016/j.renene.2017.03.089>

Sarada, S.N., Raju, A.V.S.R, Murty, K.N., Murty, M.D. and Radha, K.K., *Simulation of laminar flow heat transfer in oil coolers*. Elixir Mech. Engg. 37 (2011) 3721-3725

Sheikholeslami, M., Gorji-Bandpy, M. and Ganji, D.D., Review of heat transfer enhancement methods: Focus on passive methods using swirl flow devices. Renewable and Sustainable Energy Reviews 49 (2015) 444–469.
<http://dx.doi.org/10.1016/j.rser.2015.04.113>

van der Pal, M. and Critoph, R.E., *Performance of CaCl₂-reactor for application in ammonia-salt based thermal transformers*. Applied Thermal Engineering 126 (2017)
<http://dx.doi.org/10.1016/j.applthermaleng.2017.07.086>

Vasiliev, L.L., Mishkinis, D.A., Antukh, A.A., Kulatov, A.G. and Vasiliev, L.L., Resorption heat pump. Applied Thermal Engineering 24 (2004) 1893–1903. <http://dx.doi:10.1016/j.applthermaleng.2003.12.018>

Wang, R.ZZ., Wang, L. and Wu, J. *Adsorption Refrigeration Technology: Theory and Application*. Wiley, 2014

Yang, Z., Qu, M. and Gluesenkamp, K.R. *Ammonia-based chemisorption heat pumps for cold-climate heating applications: A comprehensive review*. Applied Thermal Engineering 179 (2020)
<https://doi.org/10.1016/j.applthermaleng.2020.115674>

NMR study of water exchange in MOFs for adsorption heat transformation processes

S. Pizzanelli^{1,*}, A. Freni¹, F. Martini², L. G. Gordeeva^{3,4}, M. V. Solovyeva^{3,4} and C. Forte¹

¹ CNR-ICCOM, Institute of Chemistry of OrganoMetallic Compounds, via G. Moruzzi 1, 56124 Pisa, Italy

² University of Pisa, Chemistry Department, via G. Moruzzi 13, 56124 Pisa, Italy

³ Boreskov Institute of Catalysis, Ac. Lavrentiev av. 5, Novosibirsk 630090, Russia

⁴ Novosibirsk State University, Pirogova str. 1, Novosibirsk 630090, Russia

*Corresponding author: silvia.pizzanelli@pi.iccom.cnr.it

Abstract

Solid state nuclear magnetic resonance (NMR) spectroscopy was applied to two metal-organic frameworks (MOFs), MIL-101 (Cr) and NH₂-MIL-101 (Cr), with the aim of investigating their interaction with water. The two MOFs contain coordinatively unsaturated Cr sites showing a strong affinity to water. Analysis of the NMR data allowed us to distinguish water bound to Cr³⁺ from unbound water residing in the porous space and to set a lower boundary to the residence time of water on the Cr site when the porous space is filled with water. This has implications on the adsorption behaviour of the porous matrix and influences the MOF performance in adsorption heat transformation.

Keywords: metal-organic frameworks, adsorption heat transformation, solid state NMR, water residence time.

Introduction

The development of adsorbents is a crucial issue in Adsorption Heat Transformation (AHT) technology. The efficiency of the process is governed by the microporosity, hydrophilicity, and hydrothermal stability of the sorption material. Metal-organic frameworks (MOFs) are emerging as the most capable class of microporous materials in terms of internal surface area and micropore volume, as well as structural and chemical variability, and therefore are receiving considerable attention. [1]

We focused on MIL-101 (Cr), which showed encouraging properties for AHT applications when methanol is the working fluid. [2] In the present work, we studied water as adsorbate, because it is the most used refrigerant in air conditioning and heat pumping applications, due to the high latent heat and environmental benefits. In this MOF, the inorganic building unit consists of a Cr₃O cluster, where two out of three Cr³⁺ ions exhibit an accessible coordinatively unsaturated site (CUS). [3]

We investigated the exchange of Cr³⁺ CUS bound water with unbound water in hydrated samples. Previous studies suggest that the formation of coordinative bonds between the CUS and water is responsible for the observed strong adsorption affinity. [4] However, the residence time of water on the metal ion has never been investigated. We used solid state Nuclear Magnetic Resonance (NMR), and in particular ¹H Magic Angle Spinning (MAS), to directly detect water in different environments, i.e., bound and unbound water, in samples hydrated at different levels and to estimate the residence time of water on CUS Cr³⁺. In order to understand whether an amino group on the organic linker affects water behaviour, NH₂-MIL-101 (Cr) was also investigated.

Experimental

Samples. MIL-101(Cr) and NH₂-MIL-101(Cr) were synthesized according to the procedure described in ref. [2]. Specific surface area, total pore volume, and micropore volume of different batches of the examined samples are displayed in Table 1. These properties were derived from nitrogen adsorption data.

Table 1. Specific surface area, S_{sp} , total pore volume, V_p , and micropore volume, V_μ , of different batches of the examined MOFs as derived from nitrogen adsorption data.

MIL-101 (Cr)			NH ₂ -MIL-101 (Cr)		
S_{sp} [m ² /g]	V_p [cm ³ /g]	V_μ [cm ³ /g]	S_{sp} [m ² /g]	V_p [cm ³ /g]	V_μ [cm ³ /g]
2500-2950	1.95-2.20	1.05-1.20	2300-2450	1.70-1.90	0.70-0.80

For the NMR measurements, the samples were dried at 393 K for 4 h in order to remove all CUS unbound water. Then the powders were exposed to a humid atmosphere to progressively hydrate them. The hydration levels of the samples investigated, measured gravimetrically, are displayed in Table 2.

Table 2. Hydration level of the samples investigated.

	hydration level (g _{H2O} /g _{dry powder}) ^a		
MIL-101	0.05 ^b	0.52	0.82
NH ₂ -MIL-101	0.05 ^b	0.42	0.72

(a) with ‘dry powder’ we indicate the MOFs containing only CUS bound water.

(b) only CUS bound water is present.

Solid state NMR. ¹H MAS NMR experiments were carried out on a Bruker Avance Neo-500 NB spectrometer operating at 500.13 MHz and equipped with a Bruker 1.3 mm double resonance probe. Spectra were recorded using the single pulse excitation sequence at different spinning speeds, namely 0, 10, 20, 40 and 67 kHz at 296 K. The 90° pulse length and the recycle delay were 1.47 μs and 3 s, respectively, and the number of scans accumulated was 64.

Discussion and Results

¹H MAS spectra were acquired on MIL-101 and NH₂-MIL-101 at different hydration levels with the aim of gaining insight into the exchange between bound and unbound water. In the dry sample, water molecules are bound to the strongly interacting CUSs and no additional unbound water molecules are present inside the pores, whereas in the hydrated samples both types of water molecules occur.

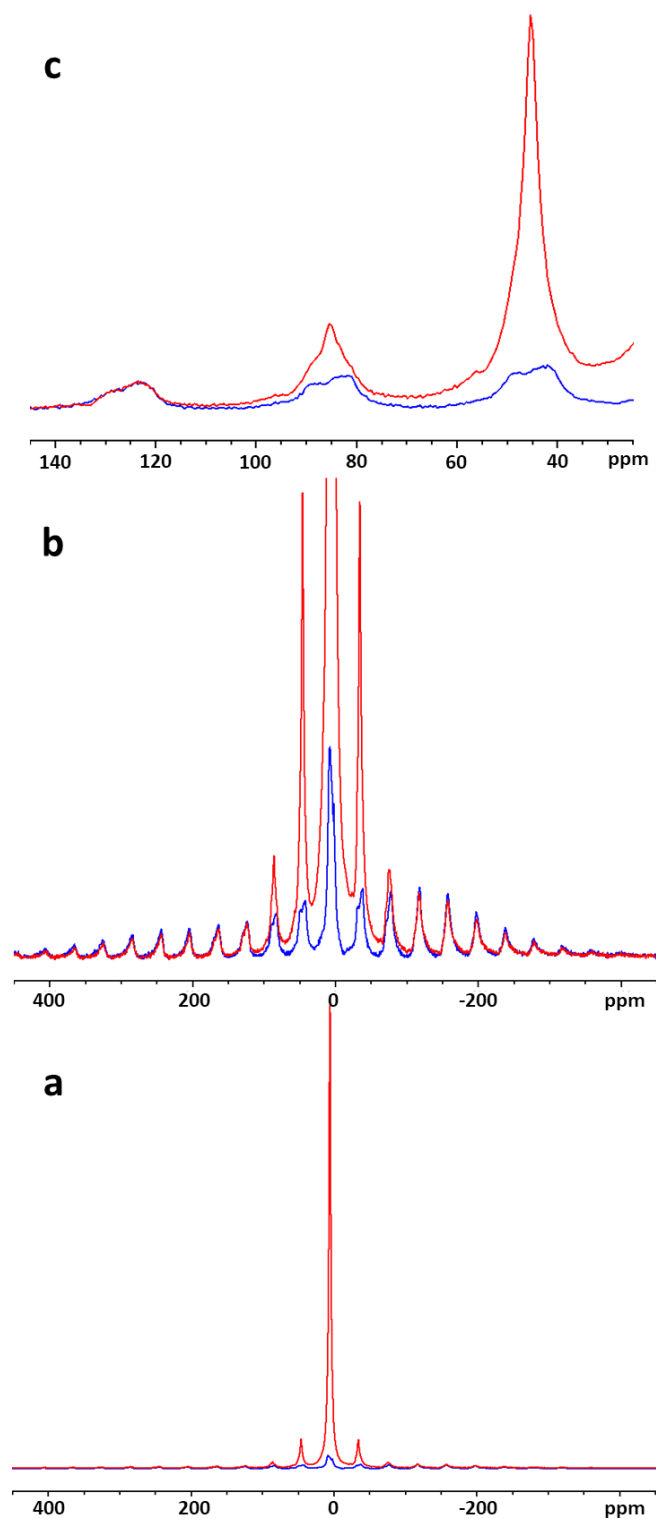


Figure 1. (a) ^1H MAS NMR spectra of MIL-101 at different levels of hydration: 0.05 (blue) and 0.82 g_{H2O}/g_{dry powder} (red). The spectra were recorded at a spinning speed of 20 kHz and the signals were scaled by matching the intensity of the third order side bands. (b) Figure 1 (a) with an expanded vertical scale to highlight the side band patterns. (c) Expansion on the first three side bands on the left of the central peak.

Figure 1a exemplifies ^1H MAS spectra of MIL-101 at two different hydration levels, that is 0.05 and 0.82 $\text{g}_{\text{H}_2\text{O}}/\text{g}_{\text{dry powder}}$, at a spinning speed of 20 kHz. Due to the presence of the paramagnetic cations Cr^{3+} , ^1H side band patterns are dominated by anisotropic hyperfine shift of protons belonging to water and to the MOF organic linker (Figure 1b). In particular, in the sample characterized by 0.05 $\text{g}_{\text{H}_2\text{O}}/\text{g}_{\text{dry powder}}$ (Figure 1b, blue trace), the signal is due to protons belonging to bound water and to the MOF organic linker. A close inspection of the side bands reveals that each band results from the combination of two signals belonging to different patterns, as displayed in Figure 1c (blue trace) for the first three side bands on the left of the central peak. The two patterns are characterized by different isotropic chemical shifts, 8.1 and 2.8 ppm and different anisotropic hyperfine shift interactions. For the former pattern, the anisotropic hyperfine shift interaction is on the order of 30 ppm, as indicated by the occurrence of a maximum of only three side bands on each side of the central peak. Its intensity is $\sim 20\%$ of the total signal. On the contrary, for the latter pattern, ten side bands on each side are observed and the anisotropic hyperfine shift interaction is estimated to be around 300 ppm. On the basis of the relative intensity of the patterns and of the fraction of water (29%) and organic linker (71%) protons as calculated from the chemical formula of MIL-101, we ascribed the pattern centred at 8.1 ppm to bound water, and the other, centred at 2.8 ppm, to the MOF aromatic protons. The latter value with that of 3.0 ppm reported in ref. 4 for the aromatic protons of the same MOF. Generally, one should notice that these protons experience hyperfine shifts leading to differences of the observed isotropic chemical shift values compared to the values exhibited by the same protons in molecules not coordinated to Cr^{3+} .

The addition of water mainly induces an increase in the intensity of the central band and of the first and second order side bands, whereas no effects are observed at higher orders (Figure 1b, red trace). The additional intensity gives rise to a new pattern centred at 5.3 ppm, which is characterized by a smaller anisotropic hyperfine shift compared to that due to bound water. This new pattern is ascribed to unbound water.

The persistence of the bound water pattern at the high hydration level (see Figure 1c) indicates that the residence time of bound water is much longer than the inverse of the bound water anisotropic hyperfine shift, that is $\sim 67 \mu\text{s}$. It is worth to point out that water residence time on Cr^{3+} aqua ion is known to be as long as 10^6 s. [5]

A similar behaviour is exhibited by NH_2 -MIL-101.

Conclusions

The analysis of ^1H MAS spectra of MIL-101 and NH_2 -MIL-101 at different levels of hydration allowed information on their interaction with water to be obtained. Water bound to CUS Cr^{3+} was distinguished from unbound water residing in the porous space. A lower boundary for the residence time of bound water was set to $\sim 67 \mu\text{s}$.

Acknowledgements

Center for Instrument Sharing of the University of Pisa (CISUP) is acknowledged for the use of the Bruker Avance Neo-500 NB spectrometer.

References:

[1] Henninger, S. K., Jeremias, F., Kummer, H., Janiak, C. "MOFs for use in adsorption heat pump processes" *European Journal of Inorganic Chemistry*, 2625-2634, 2012.

-
- [2] Solovyeva, M. V., Gordeeva, L. G., Aristov, Y. I. “MIL-101(Cr)–Methanol as Working Pair for Adsorption Heat Transformation Cycles: Adsorbent Shaping, Adsorption Equilibrium and Dynamics”, *Energy Conversion and Management*, 2020, 182, 299–306.
- [3] Hwang, Y. K., Hong, D.-Y., Chang, J.-S., Jhung, S. H., Seo, Y.-K., Kim, J., Vimont, A., Daturi, M., Serre, C., Férey, G. “Amine Grafting on Coordinatively Unsaturated Metal Centers of MOFs: Consequences for Catalysis and Metal Encapsulation” *Angewandte Chemie International Edition*, 2008, 47, 4144–4148.
- [4] Wittmann, T., Mondal, A., Tschense, C. B. L., Wittmann, J. J., Klimm, O., Siegel, R., Corzilius, B., Weber, B., Kaupp, M., Senker, J. “Probing Interactions of N-Donor Molecules with Open Metal Sites within Paramagnetic Cr-MIL-101: A Solid-State NMR Spectroscopic and Density Functional Theory Study” *Journal of the American Chemical Society*, 2018, 140: 2135–2144.
- [5] Helm, L., Merbach, A. E. “Inorganic and Bioinorganic Solvent Exchange Mechanisms”, *Chemical Reviews*, 2005, 105, 1923-1959.

Early Stage Adsorber Material Selection for Adsorption Heat Transformers

E. Piccoli^{1,2*}, V. Brancato³, A. Frazzica³, F. Maréchal², S. Galmarini¹

¹Empa, Überlandstrasse 129, 8600 Dübendorf, Switzerland

²EPFL Valais, Rue de l'Industrie 17, 1950 Sion, Switzerland

³CNR-ITAE, Salita Santa Lucia Sopra Contesse 5, 98126 Messina, Italy

*Corresponding author: emanuele.piccoli@empa.ch

Abstract

The deployment of adsorption cycles for heating and cooling purposes is often limited by poor efficiency and high reactor volumes determined by the adsorber material used. The appropriate selection of the solid sorbent in early stages of design can allow to identify quickly the most promising solutions. In this work, a reliable and robust methodology for adsorber material screening and selection is proposed and applied to a test set of state-of-the-art candidates. The improvement achieved in the adsorption equilibrium prediction respect to the most frequently used model is above 60%. In the cases analyzed, SAPO-34 from Fahrenheit and Al-fumarate from MOF Tech. emerge as widely usable material. The analysis of exergy and volume performances allowed to emphasize different design strategies according to the system objective.

Keywords: Material Characterization, Adsorption Equilibrium, Performance Estimation, Optimization.

Acronyms

AC Activated Carbon
ATL Averaged Temperature Lift
COP Coefficient Of Performance
DA Dubinin-Astakhov
EN Energy use
EX Exergy use
EV Energy-specific Volume
FHSP Fahrenheit SAPO-34
FJSG Fuji Davison RD silica gel beads
MILP Mixed Integer Linear Programming
MOF Metal-Organic Framework
MOFA MOF Tech. Al Fumarate pellets
MOFC MOF Tech. Al Isophtalate pellets
MSE Mean Square Error
MTSPG Mitsubishi Pl. AQSOA Z02 beads
NU Normalized Use (of energy/exergy)
OBJ Objective function
OKSG Oker Chemie Siogel beads
RMFAC Empa RMF Activated Carbon
RSE Residual Standard Error
SEM Scanning Electron Microscopy

Symbols

C Characteristic energy of adsorption [J/g_w]
 c_p Specific heat capacity [$J/g/K$]
 F Specific work of adsorption [J/g_w]
 f degrees of freedom of the model
 H Specific heat of adsorption [J/g_w]
 k Total number of points predicted
 M Molar weight of water [g/mol]
 n Adsorption exponential coefficient $[-]$
 L Latent heat of evap./cond. [J/g_w]
 p Pressure [$mbar$]
 R Ideal gas constant [$J/mol/K$]
 s Size of the unit $[-]$
 T Temperature [K]
 t Time [s]
 Q Energy stream [J]
 w Specific adsorbed water loading [g_w/g_s]
 W_0 Specific adsorbed water at satur. [g_w/g_s]
 ϵ^2 Squared error
 ρ Density [g/cm^3]
 τ Characteristic time [s]

Sub- and super-scripts

<i>ad</i> Adsorption	<i>i</i> Element in the sum
<i>c</i> Critical point of water	<i>in</i> Initial
<i>con</i> Condenser	<i>max</i> Maximum
<i>de</i> Desorption	<i>need</i> Energy need/requirement of the system
<i>env</i> Environment	<i>s</i> Solid sorbent
<i>eva</i> Evaporator	<i>sat</i> Saturation
<i>fi</i> Final	<i>T</i> Temperature level
<i>hot</i> Hot source of the cycle	<i>w</i> Water

Introduction

Adsorption energy technologies can play an important role in making energy systems more sustainable [1, 2]. Cooling, heating, and energy storage systems can be more efficient using the full potential of adsorbent materials, which allow providing those services requiring little or no electricity. Nonetheless, there are several factors limiting their widespread application, including low thermal efficiencies and large volumes when compared to competing solutions [3].

The performance of adsorption equipment strongly depends on the adsorbent-adsorbate working pair, and because of that it is highly sensitive to the operational conditions (i.e. temperature, pressure) [4]. The selection of the appropriate working pair in the early stage of the design - before prototyping, testing and optimizing the equipment - can therefore enable competitive applications [5] at minimum time and costs for R&D. This can be achieved by characterizing the equilibrium thermophysical properties of the materials. These measurements demand only small amounts of material and allow the estimation of the maximum achievable thermal energy performance, identifying the most suitable adsorbents [6].

In this work, a methodology for screening adsorbents for water as refrigerant fluid is reported, taking into account both the characterisation and selection criteria. The methodology was developed and tested in order to be accurate, easy to implement and applicable to a wide range of materials. The aims include:

- a more accurate estimation of the maximum thermal performance ;
- a robust method to identify the best adsorbent material depending on the temperature boundaries;
- a methodology that is applicable to a wide range of materials with very different characteristics.

This has been achieved by:

- introducing a novel model to describe the equilibrium adsorption characteristics;
- applying Mixed Integer Linear Programming (MILP) techniques as a tool for material selection;
- testing the methodology by estimating the maximum energy performance of state-of-the-art silica gels, zeo-types, Metal Organic Frameworks (MOFs) and activated carbons (ACs) for different heating and cooling scenarios.

Methods

Material Characterization

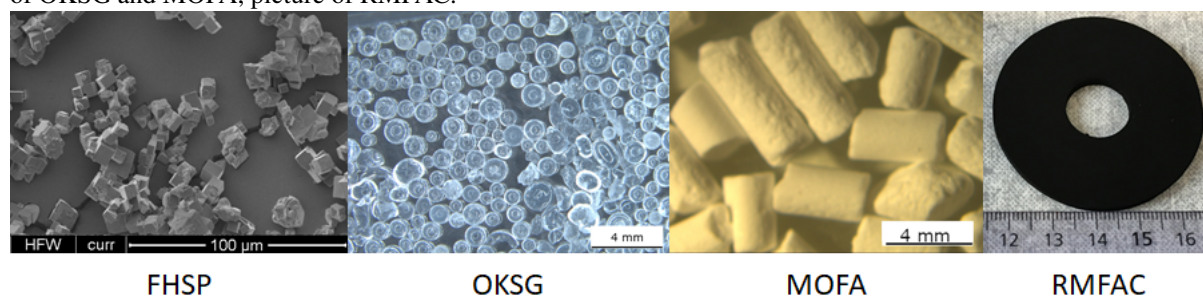
Six adsorbent materials have been selected by virtue of their adsorption characteristics: two amorphous silica gels (Fuji Davison RD and Oker Chemie SIOGEL), adsorbing water over a

wide range of relative pressures; two zeo-types (SAPO-34 powder from Fahrenheit and AQ-SOA Z02 beads from Mitsubishi), adsorbing at low relative pressures; two MOFs (MOF Technologies Al-OH Fumarate and CAU-10-H) and one AC (developed in-house at Empa) adsorbing at intermediate relative pressures.

Specific heat capacity has been measured on dry samples by differential scanning calorimetry using a Mettler Toledo DSC 1 instrument, available at CNR-ITAE. Water adsorption isotherms at temperatures between 10°C and 80°C were measured with a SMS DVS Endeavour and a TA Instruments VTI-SA+, available at Empa. More details about the characterization protocol used can be found elsewhere [7].

Due to different formats of the studied adsorbent candidates (powders, beads, monoliths; see Figure 1) the achieved thermal contact during thermal characterization is not uniform, and when comparing the obtained values for specific heat capacity this should be kept in mind. For the same reason, for the specific heat of sorption the simplified theoretical value [6] $H = L(T) + F(T, p)$ was preferred to experimental values $H = H(w)$. A more detailed discussion of this will follow below.

Figure 1. Images of some of the characterized materials. From left to right, SEM of FHSP, optical microscopy of OKSG and MOFA, picture of RMFAC.



Water Adsorption Equilibrium Modelling

The characterization of equilibrium adsorption and desorption of the selected materials at different temperatures highlighted how the widely diffused Dubinin-Astakhov (DA) modelling approach [8, 9] can fail in terms of accuracy [10]. In fact, the DA model has been developed for non-polar systems with a uniform pore size distribution. When water is used as sorbate, the adsorption equilibrium should in general be expected to be temperature dependent [11]. Additionally many of the studied adsorbent materials are characterized by multiple pore types, ranging from micropores to macropores. Thus, an empirical modification of the DA model, accounting for two different pore types and for additional linear dependence of the DA parameters on temperature, is proposed to increase the accuracy of adsorption equilibria prediction under different conditions, keeping at the same time the original generality.

As with the original DA approach, we assume the density of the water to be constant. However we allowed for two different adsorption sites for every material (see equations 1-2, where w_{ad} is the equilibrium adsorption water loading, W_0 is the maximum loading capacities, C is the characteristic energy of adsorption, and n is characteristic of the width of the adsorption peak and F is the Polanyi adsorption potential, T the temperature, R the ideal gas constant and p_{sat} the saturation pressure and M the molar weight of the sorbate. The subscript 1 and 2 indicates the two adsorption sites.)

$$w_{ad} = W_{0,1} \cdot \exp(-(F/C_1)^{n_1}) + W_{0,2} \cdot \exp(-(F/C_2)^{n_2}) \quad (1)$$

$$F = \frac{R \cdot T}{M} \ln(p/p_{sat}) \quad (2)$$

All parameters $P \in (W_0, C, n)$ are considered to be linearly dependent on temperature (equation 3).

$$P = a_P \cdot T + b_P \quad (3)$$

To calculate the saturation pressure of water, we used the approximation reported by Wagner and Pruss [12] (eq. 4-5, where T_c and p_c are the temperature and pressure of the critical point of water respectively).

$$p_{sat} = p_c \cdot \exp\left(\frac{T_c}{T} \cdot \left(-7.860 \cdot \nu + 1.844 \cdot \nu^{1.5} - 11.79 \cdot \nu^3 + 22.68 \cdot \nu^{3.5} - 15.96 \cdot \nu^4 + 1.801 \cdot \nu^{7.5}\right)\right) \quad (4)$$

$$\nu = 1 - T/T_c \quad (5)$$

Adsorption and desorption isotherms are in general different, and the difference between them is known as the hysteresis. The hysteresis will significantly affect the amount of cyclable water under any conditions that do not encompass both the full adsorption as well as the full desorption peak. Geometrical and chemical features of the pores may determine the need for an additional energy to desorb from certain sites (overcoming a bottleneck for example) [11]. As a consequence of such a "delayed" desorption, the latter can be concentrated in a smaller range than during adsorption, leading to a higher desorption characteristic energy C and a modified shape n . This can be expressed according to equation 6, where ΔC and Δn take into account the difference between ad- and desorption described above. The two terms describing the hysteresis are also considered to be linearly dependent on temperature (eq. 3).

$$w_{de} = W_{0,1} \cdot \exp\left(-\left(\frac{F}{C_1 + \Delta C_1}\right)^{n_1 + \Delta n_1}\right) + W_{0,2} \cdot \exp\left(-\left(\frac{F}{C_2 + \Delta C_2}\right)^{n_2 + \Delta n_2}\right) \quad (6)$$

Water Adsorption Equilibrium Fitting

To ensure a good quality of the parameters describing the adsorption equilibria, and at the same time avoid over-fitting, a rigorous curve fitting procedure has been followed.

Firstly, the water isotherms were analysed according to the protocol produced in the framework of the Hycool project [7]. Each ad/de-sorption step is fitted to an exponential function ($w = w_{in} + \Delta w_{max} * (1 - \exp(\frac{t-t_{in}}{\tau}))$), where w and w_{in} are the current and initial loading, Δw_{max} is the equilibrium uptake for the step, t_{in} and t are the initial and the current time, and τ is the characteristic response time of the system) using the Nelder-Mead method [13] as implemented in R. If most of the steps were interrupted after reaching 95% of the equilibrium loading

change ($t - t_{in} > 3\tau$), the experiment was considered successful and the data accepted. This systematic control lead to a significant improvement of the reproducibility of the adsorption curves, reducing scatter and allowing a more reliable interpretation of the results.

The thus obtained data was split using a stratification based on the total loading into a training set (80%) and a test set (20%), in order to have a more robust fitting in both areas of high loading and low loading. The random split was performed with the Python library *scikit-learn* [14].

The adsorption branch data was then fitted with both the original DA and the adapted model (eq. 1 and 3). The optimal fit was obtained with the R library *nprob* [15]. Subsequently the parameters ΔC and Δn (eq. 6) were fitted on the desorption branches.

Maximum Theoretical Performance Estimation

While a precise analysis of the performance and of the cost of adsorption heat exchangers can only be obtained through a dynamic analysis [16, 17, 18, 19], for a first screening in the early stage of the design, the effort of constructing the lab-scale prototype necessary for such an analysis is excessive. From the measured equilibrium data, it is possible to calculate the maximum achievable energy performance of cooling cycles under well defined working conditions [6]. The maximum theoretical thermal coefficient of performance (COP), evaluating the ratio between delivered energy and thermal energy needed to drive the thermodynamic cycle, for cooling applications can be calculated as a function of the evaporator temperature T_{eva} , the adsorption temperature T_{con} , and the hot source temperature T_{hot} . For an ideal cooling cycle, the transformations are either isosteric or isobar [4]:

$$COP = L(T_{eva}) \cdot \Delta w \cdot \left(\int_{T_{con}}^{T_2} [cp_s(T) + cp_w(T) * w(p_{eva}, T_{con})] dT + \int_{T_2}^{T_{hot}} \left[cp_s(T) + cp_w(T) * w(p_{con}, T) - H_{de}(T) * \frac{dw(p_{con}, T)}{dT} \right] dT \right)^{-1} \quad (7)$$

The temperature T_2 , at which the ideal desorption process switches from isosteric to isobar is [5]:

$$T_2 = \frac{T_{con}^2}{T_{eva}} \quad (8)$$

The energy and exergy use of the cycles can be respectively approximated as:

$$EN = \frac{1}{COP} \quad (9)$$

$$EX = \frac{1}{COP} \cdot \left(1 - \frac{T_{env}}{T_{hot}} \right) \quad (10)$$

As a first indicator of reactor volume, at least in relative terms, the energy-specific adsorbent volume (cm^3/J) could be used:

$$EV = \frac{1}{L(T_{eva}) * \Delta w * \rho_{tap}} \quad (11)$$

COPs were pre-calculated as a function of the temperature boundaries only (evaporator, condenser and energy source temperatures), for all the materials within the following boundaries: evaporator between 5°C and 25°C; condenser between 15 and 55°C; hot source between 25°C and 95°C; environment at 30°C.

Formulation of the Optimization Problem

Finding the most convenient solution to satisfy heating and cooling loads of a specific energy system can be formulated as an optimization problem [20]. To this end, an objective function is defined (e.g. energy or exergy consumption) and optimization is used to find the best values of the decision variables (i.e. the existence and the size of the adsorption heat transformers and the adsorbent used within each of them), within the limits of some constraints (e.g. satisfying all the energy needs and complying with the energy balance of the system).

To explore the possibilities of this approach, almost 700 scenarios have been simulated, with combined heating and cooling demands at different temperature levels ($Q_{need_heating}^T$ and $Q_{need_cooling}^T$). Each of these demands can have a size of 0, 1 or 2 J: their combinations create the collection of scenarios analysed. The adsorption cycles used to satisfy the energy needs are represented by three temperature levels (T_i^{eva} , T_i^{hot} , T_i^{con}), a size (s_i) and three energy streams associated to the three temperature levels (Q_i^T). The energy streams are normalized such that for each adsorption heat transformer the evaporator stream is a unitary stream $Q^{T_{eva}} = 1 J$, the hot source stream is $Q^{T_{hot}} = 1/COP J$, and the condenser streams is $Q^{T_{con}} = 1 + 1/COP J$. The sign convention used is positive streams for energy entering the system (evaporators and hot sources), negative streams for energy streams leaving the system (condensers). For each adsorption heat transformer a different adsorbent material can be chosen.

As an example, a system can consist of 2 units of cooling at 5°C, while another system can consist of 1 unit of cooling at 5°C, 2 units at 15°C, and 2 units of heating at 55°C and so on. This means for each temperature level, an energy balance has to be satisfied (eq. 12-13).

$$\sum_i s_i * Q_i^T = Q_{need-cooling}^T \quad (12)$$

$$\sum_i s_i * Q_i^T \leq Q_{need-heating}^T \quad (13)$$

Furthermore, the overall system energy balance (eq. 14) should be satisfied for every adsorption heat transformer.

$$\sum_{i,T} s_i * Q_i^T = 0 \quad (14)$$

The objective function to minimize can be formulated in a similar way for both energy and exergy consumption, summing over exergy / energy of heating/cooling cycle (according to eqs 9 and 10 respectively) with a hot temperature above the environment temperature T_{env} (chosen to be 30 °C).

$$OBJ_{EN} = \sum_{i \in \{i | T_{hot}^i > T_{env}\}} s_i * EN_i \quad (15)$$

$$OBJ_{EX} = \sum_{i \in \{i | T_{hot}^i > T_{env}\}} s_i * EX_i \quad (16)$$

In the case of minimum required volume, the objective function is summed over the volume of all adsorption heating/cooling cycles (eq. 17).

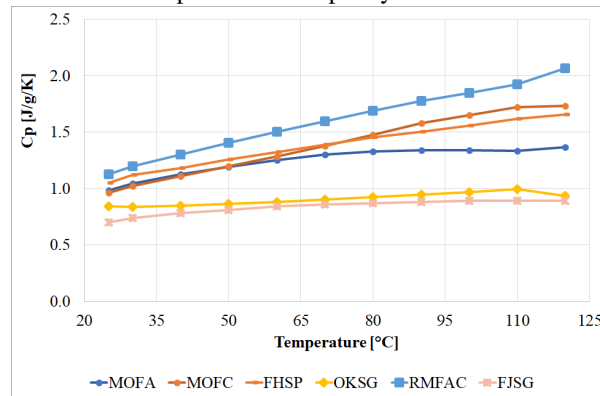
$$OBJ_{EV} = \sum_i s_i * EV_i \quad (17)$$

The Python library *mip* [21] was used to optimize the choice and the connection of materials and boundary temperatures to deliver cooling at temperatures between 5°C and 25°C and heating between 35°C and 55°C, according to energy and exergy use minimization. The evaporators were restricted to sub-environmental temperatures ($T < T_{env} = 30^\circ\text{C}$), pure heat pumping systems were not included in the analysis.

Results and Discussion

The experimental specific heat capacity and tap densities are shown in Figure 2 and summarized in Table 1, showing a good agreement with the data available in the literature [16, 22, 23, 24, 25], with the exception of Empa RMF activated carbon that shows a higher specific heat capacity than typical commercial activated carbons. The specific heat capacity of water has been assumed to be $cp_w = 1.271e - 5 * T^2 - 8.170e - 3 * T + 5.493$ [26].

Figure 2. Measured specific heat capacity of the adsorbent candidates.



More than 25 adsorption isotherms were measured at at least 3 temperatures in the range of 10-80°C, including duplicata to ensure good reproducibility. Even if the results are in general not easy to reproduce in different laboratories and with different sample batches, qualitatively they were found to be in agreement with other data published in literature [6, 22, 27, 28, 29]. The quality of the model has been evaluated according to the residual standard error RSE, which is the square root of the ratio between the sum of the squared errors ϵ_i^2 , and the degrees of freedom f (eq. 18).

Material	Code	Specific Heat Capacity [J/g/K]	Tap density [g/cm ³]
Fuji Davison RD	FJSG	$0.7 + 0.0019 * (T - 273.15)$	0.87
Oker Chemie Siogel	OKSG	$0.79 + 0.0016 * (T - 273.15)$	0.77
Fahrenheit SAPO-34	FHSP	$0.93 + 0.0063 * (T - 273.15)$	0.85
Mitshubishi AQSOA-Z02	MTSPG	$0.84 + 0.0071 * (T - 273.15)$	0.60
MOF Tech. Al Fumarate	MOFA	$0.97 + 0.0034 * (T - 273.15)$	0.51
MOF Tech. Al Isophthalate	MOFC	$0.77 + 0.0086 * (T - 273.15)$	0.33
Empa RMF Carbon	RMFAC	$0.93 + 0.0063 * (T - 273.15)$	0.43

Table 1. Material properties. Specific heat capacity is valid between 298 and 393 K.

Code	W_01 [g _w /g]	$C1$ [J/g]	$n1$ [-]	W_02 [g _w /g]	$C2$ [J/g]	$n2$ [-]
FJSG	$0.2 - 0.00032 * T$	$260 - 0.32 * T$	$0.01 * T$	0.16	$710 - 0.92 * T$	1.7
OKSG	$0.62 - 0.00086 * T$	200	0.94	0.077	150	3.8
FHSP	0.15	500	1.4	$0.39 - 0.00067 * T$	$910 - 1.8 * T$	20
MTSPG	$0.088 + 0.00014 * T$	$720 - 1.1 * T$	$40 - 0.247 * T$	0.26	620	0.4
MOFA	$0.54 - 0.00073 * T$	$490 - 0.96 * T$	14	$0.001 * T$	23	0.36
MOFC	0.087	110	$3.6 - 0.0085 * T$	$0.3 - 0.00015 * T$	$630 - 1.3 * T$	$0.28 * T$
RMFAC	0.25	150	6.2	0.12	210	1.5

Table 2. Proposed water adsorption model fitted parameters

$$RSE = \sqrt{\frac{\sum \epsilon_i^2}{f - 2}} \quad (18)$$

The quality of the fitted curves was checked on the test set according to the mean square errors, obtained dividing the sum of the squared errors by the total number of points k (eq. 19).

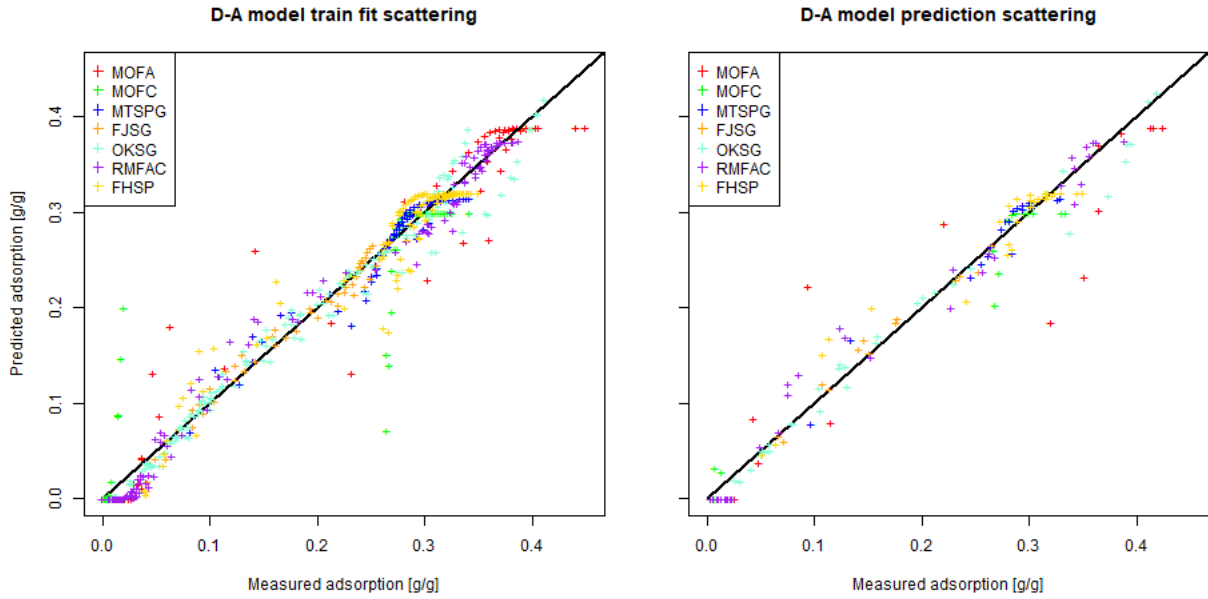
$$MSE = \frac{\sum \epsilon_i^2}{k} \quad (19)$$

The results of train set fitting and of test set predictions of adsorption equilibria for the Dubinin-Astakhov (DA) model are shown in Figure 3, while the same results for the proposed model are shown in Figure 4. The fitted parameters of the proposed model for the adsorption branch are gathered in Table 2. The results of the proposed model for the desorption branches are shown in Figure 5. The fitted parameters for the desorption branch are gathered in Table 3. The result metrics for both models and for both adsorption and desorption are summarized in Table 4.

When comparing the standard DA model with the proposed empirical modification, the latter seems to provide a better representation (i.e. accurate and significant) of the equilibrium adsorption loadings. The relative improvement achieved in model quality (residual standard error eq. 18) is normally between 60% and 87%. The only exception is OKER silica gel (OKSG), which goes from the lowest residual standard error (1.2 %) for the DA model to the highest (1.2 %) for the new approach, thus showing no model quality improvement.

This general model improvement is reflected in better predictions, with an enhancement of the mean square error of 60% to more than 99%, the latter in the case of Al Isophthalate (MOFC), that presents an almost perfect step-like isotherm. Interestingly, also for OKER silica gel

Figure 3. Adsorption modelling results of the Dubinin-Astakhov model.



Code	$\Delta C1$ [J/g]	$\Delta n1$ [-]	$\Delta C2$ [J/g]	$\Delta n2$ [-]
FJSG	13	$0.0092 * T$	—	—
OKSG	$0.04 * T$	0.11	$0.016 * T$	32
FHSP	45	$0.0011 * T$	$280 - 0.63 * T$	$-0.017 * T$
MTSPG	$169 - 0.32 * T$	$92 - 0.25 * T$	170	$0.29 - 0.00087 * T$
MOFA	$0.027 * T$	$0.014 * T$	$75 - 0.2 * T$	0.044
MOFC	$0.028 * T$	—	$170 - 0.5 * T$	—
RMFAC	—	1.4	21	$6.6 - 0.02 * T$

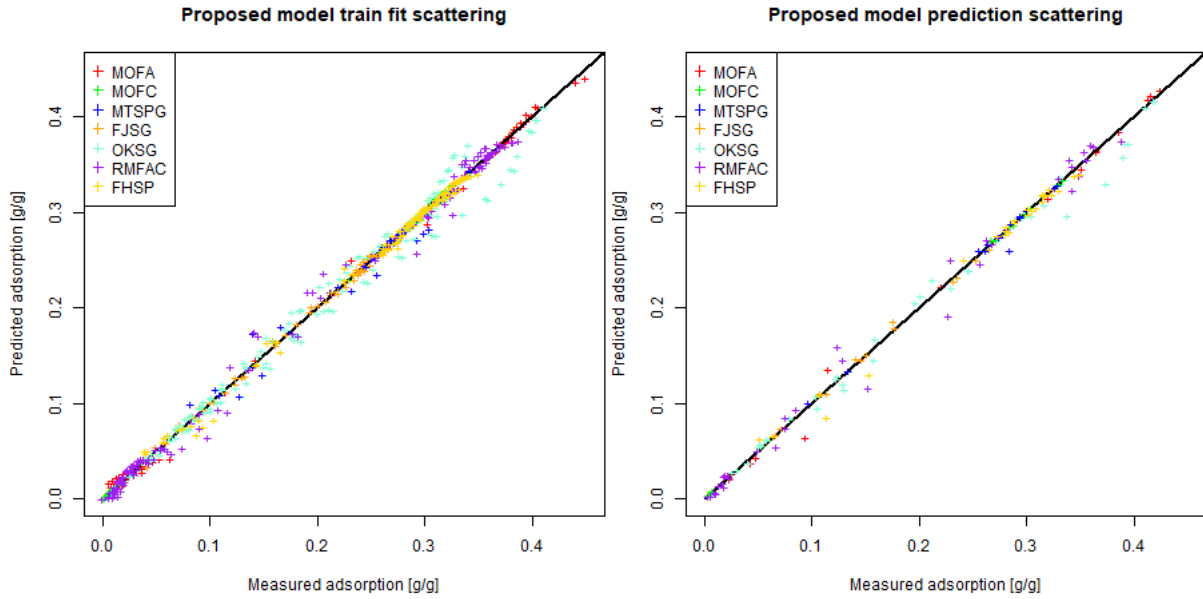
Table 3. Proposed water desorption model fitted parameters

(OKSG) the predictions are greatly improved, highlighting an improved predictive capability of the new approach compared to the DA model. Constraining the desorption branch equation to have the same maximum loading capacities as the adsorption branch is, from the model fitting point of view, an additional constraint, resulting in a slightly higher mean squared error (average mean squared error of $2.16e-4$ compared to $1.28e-4$ for the adsorption branch). Nonetheless, the results of both the model fit and the predictions are good enough to ensure that the physical significance of the model is good for the purpose of this work.

Taking a closer look at the fitting results, one can notice how not all the material have the same dependence on temperature. The Empa RMF activated carbon (RMFAC) has an almost temperature-independent adsorption behavior, which makes it a very reliable candidate. Other materials, such as Fuji silica gel (FJSG) and Al Isophtalate (MOFC), have a stronger dependence on temperature.

The maximum calculated COP of 212 single, ideal cycles with temperature boundaries as described in the methods section ranged between 0.05 and 0.95, with most of the cycles between 0.75 and 0.85, as shown in Figure 6, in agreement with values found in literature [6, 30].

Figure 4. Adsorption modelling results of the proposed model



Code	DA Ads. RSE	DA Ads. MSE	Own Ads. RSE	Own Ads. MSE	Own Des. RSE	Own Des. MSE
FJSG	1.1%	1.1e-4	0.4%	1.6e-5	0.6%	1.4e-4
OKSG	1.2%	3.3e-4	1.2%	2.1e-4	0.8%	4.4e-4
FHSP	2.1%	5.0e-4	0.3%	7.6e-5	0.9%	1.6e-4
MTSPG	1.4%	2.2e-4	0.2%	3.9e-5	0.2%	1.8e-5
MOFA	2.7%	5.2e-3	0.4%	3.6e-4	0.7%	2.2e-4
MOFC	1.5%	5.7e-3	0.2%	1.9e-6	0.2%	4.4e-4
RMFAC	2.2%	4.9e-4	0.7%	1.9e-4	0.9%	9.7e-5

Table 4. Water adsorption modelling results. RSE are calculated over the train sets, while MSE are calculated over the test sets.

In order to show the applicability of the methodology to complex energy needs and to screen among materials to see which ones are more recurrently selected, the energy use, the exergy use, and the reactor volume objective functions were minimized for more than 695 scenarios, as described in the Methods section. As shown in Figure 8 and 9, it was possible to achieve good system efficiencies for most of the scenarios. For analysing the results, the optimal solutions have been plotted against the averaged temperature lift (ATL) respect to the environmental temperature $T_{env}=30$ °C (eq 20).

$$ATL = \frac{\sum_{T_{need}} Q_{need}^{T_{need}} * T_{need}}{\sum_{T_{need}} Q_{need}^{T_{need}}} - T_{env} \quad (20)$$

To compare scenarios with different amount of energy needs, the normalized energy and exergy use (NU, eq. 21) are plotted.

$$NU = \frac{OBJ}{\sum_{T_{need}} Q_{need}^{T_{need}}} \quad (21)$$

Figure 5. Desorption results of the proposed model.

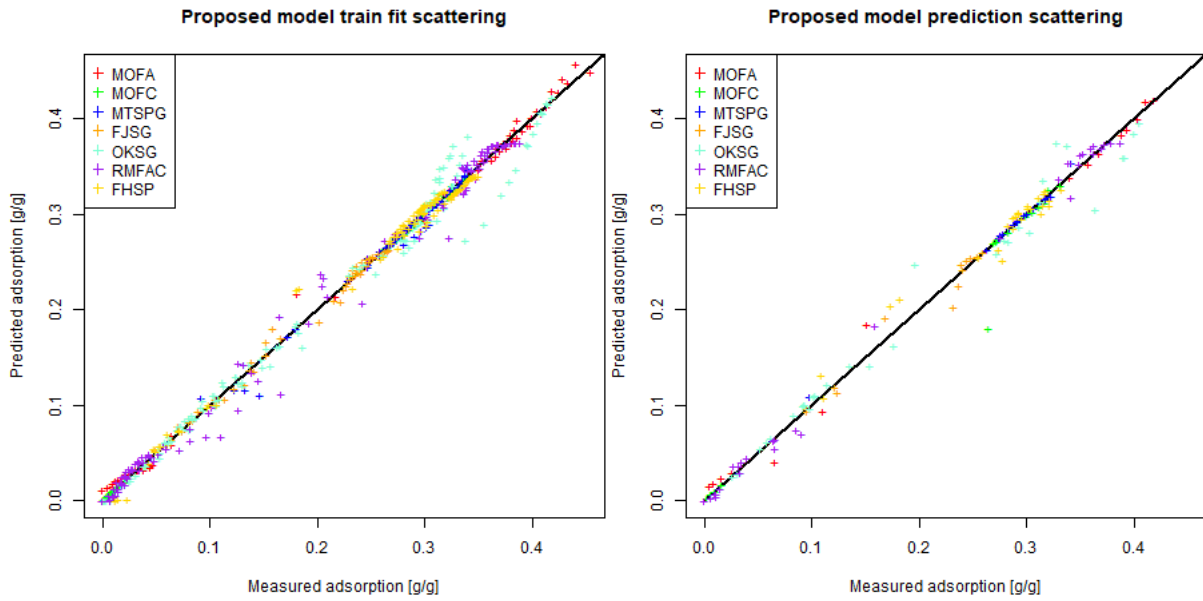


Figure 6. Distribution of pre-calculated *COP*.

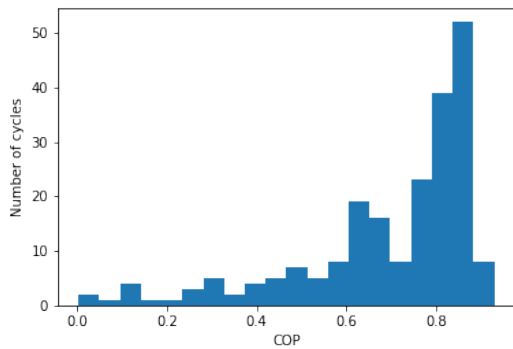
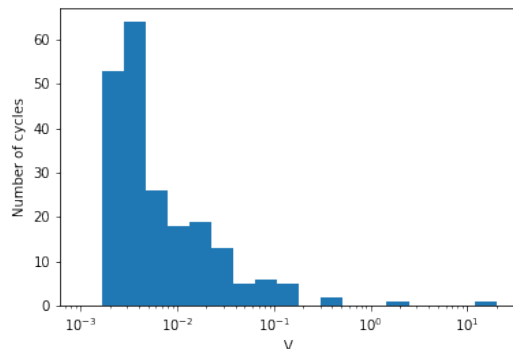


Figure 7. Distribution of pre-calculated *EV*.



As is expected, higher/more positive temperature lifts allow for better thermodynamic performance, including the ones that are generated as a combination of energy needs at different temperatures. Only in few cases the NU of energy was above 1.1 (for ATL below $-15\text{ }^{\circ}\text{C}$) and the NU of exergy was above 3.

It can also be noted how, for some scenarios of mixed heating and cooling (ATL between -5 and 10), extremely compact design are achievable (theoretical minimum energy-specific volumes below $1\text{ mm}^3/\text{J}$, see figure 10). This is the case when one adsorption heat transformer can provide cooling and heating at the same time, which means that the temperature levels are not far from each other (e.g. cooling at $15\text{ }^{\circ}\text{C}$ and heating at $35\text{ }^{\circ}\text{C}$, with ATL of $-1.7\text{ }^{\circ}\text{C}$), but these scenarios are less likely to exist in industry.

Looking at the composition of the optimal solutions, as in Figure 11 and in Figure 12, it is possible to notice that most of the optimal solutions are composed of 3 to 5 adsorption heat transformer. Cascade configurations (where the condenser of one cycle feed the evaporator

Figure 8. Minimum normalized energy use as a function of the averaged temperature lift.

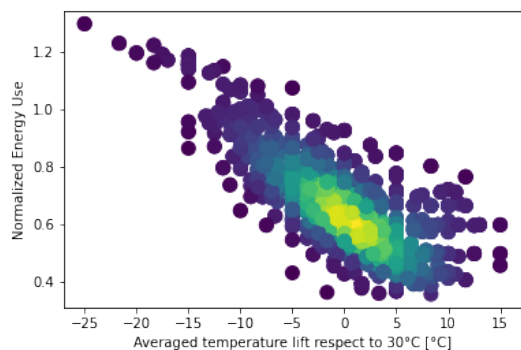


Figure 9. Minimum normalized exergy use as a function of the averaged temperature lift.

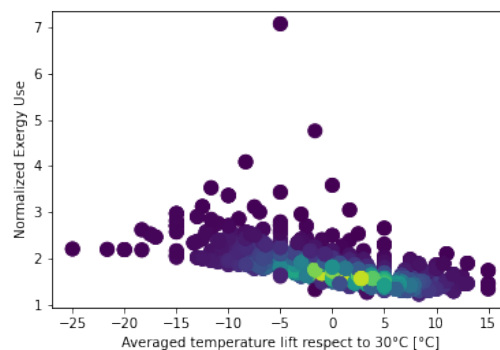
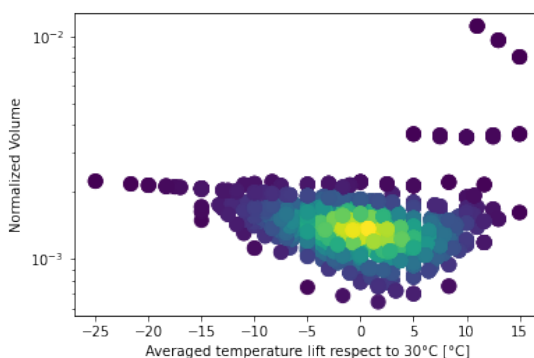


Figure 10. Minimum normalized volume as a function of the averaged temperature lift.



of another cycle) are beneficial when the energy needs happen at very different temperature (e.g. when cooling at 5°C and heating at 55°C are required, as in Figure 13). When energy or exergy consumptions are being minimized, the majority of the adsorption heat transformers use Fahrentheit SAPO34 (FHSP) (for low adsorbate partial pressure cycles) and Al fumarate (MOFA) (for intermediate adsorbate partial pressure cycles), proving that they are the most promising materials for the here studied scenarios. Most of the remaining cycles are using Mitsubishi AQSOA Z02 beads (MTSPG) and Al Isophtalate (MOFC), which means that also these two candidates have many possible applications and should not be discarded. The negligible thermal dependency and hysteresis of the Empa RMF activated carbon (RMFAC) seems to be favorable in exergetic terms, even if the total water capacity is lower than the one of some of its direct competitors.

While these first two indicators are informative about the operational expenditure, having low running costs is often not enough, especially when competing with conventional heat pumps. In the scenarios minimizing the reactor volume, the figure for cycles at intermediate relative pressures change completely: the low density of the MOFs is too penalizing, and almost only the denser zeo-types are used. This emphasize how a screening only based on the adsorption isotherms is not the most efficient, and some parameters representing the integration on the heat exchangers must be included. Using V_{EN} is a good first approximation, but it is important to keep in mind that different material formats (powders, granules, monoliths) provide different packing density according to their shape and size distribution. It is interesting to notice how

Figure 11. Distribution of number of adsorption heat transformers per system for energy and exergy consumption, and for volume minimization.

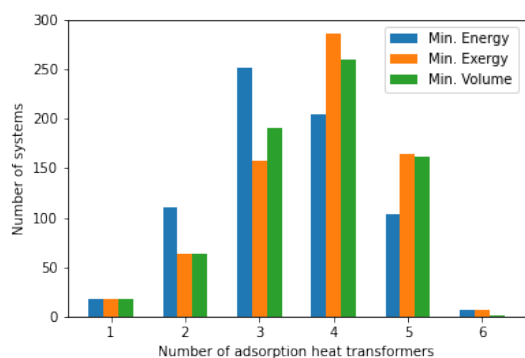


Figure 12. Adsorbent material candidates use for energy and exergy consumption, and for volume minimization.

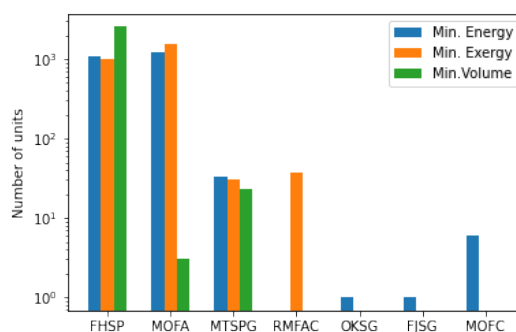
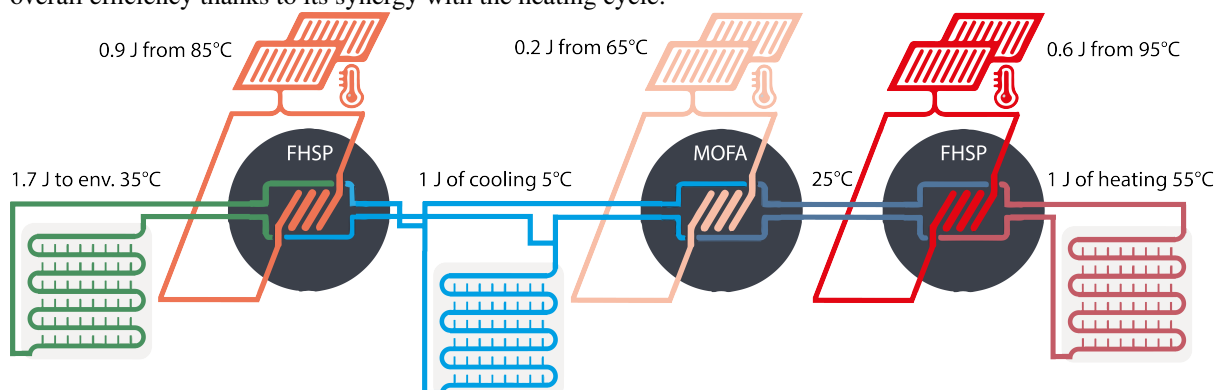


Figure 13. Example of cascade configuration for mixed energy needs (cooling at 5°C and heating at 55°C, with minimum energy use). Part of the cooling needs are satisfied with a less efficient cycle using MOFA, but gaining overall efficiency thanks to its synergy with the heating cycle.



the silica gels, despite their good adsorption capacity, are rarely a good choice because of the adsorption hysteresis and of the broad adsorption peak, both limiting the actual cycled water.

Looking at specific scenarios is the goal of a screening performed by the system designer/developer interested in a specific application. In general, simple energy needs lead to simple solutions. For example, refrigeration at 5°C is most energy-efficiently provided by a single adsorption cycle using Fahrenheits SAPO34 (FHSP) fed by a hot stream at 85°C and discharging energy to a 35°C condenser. This solution, which is thermodynamically challenging, has an ATL of -25 °C and an overall NU of energy of 1.3. The exergy minimization brings to the same choice, as the COP loss using lower temperature hot streams is in this case too big, while if the reactor must have the minimum possible volume, a hot stream temperature of 95°C is preferred.

If the energy needs are more diverse, such as is the case depicted in Figure 13, having multiple reactors is more convenient. If the amount of cooling energy needed does not surpass the needs for heating, the minimum number of adsorption heat transformers is equal to the number of temperature levels of the energy needs. From the illustration, one can appreciate how the NU of energy is minimized thanks to the double use of the Al Fumarate (MOFA) adsorption cycle. This combined heating and cooling scenario is characterized by an ATL of 0 °C and a NU of

energy of 0.85.

The use of energy sources at different temperatures, often recurring in scenarios characterized by complex energy needs, add some complexity to the system, for example spilling some of the hot streams from one reactor to another or having multiple heat generators. Anyway, it brings efficiency improvements also on the generator side (e.g. minimizing the fraction of solar collectors running at high temperatures).

Conclusions

In this work, a reliable and robust methodology to screen and select adsorbent materials for heat transformers was presented. The characterization of tap density, and of specific heat capacity and equilibrium water vapour sorption at different temperatures provided with enough information to evaluate the maximum achievable performances of heating and cooling cycles with respect to energy use, exergy use and volume required.

The equilibrium adsorption data use was improved by the fitting of a novel empirical modification of the Dubinin-Astakhov model, that shows increased significance and accuracy with respect to the original.

Ideal adsorption cycles have been evaluated as a function of adsorbent temperature dependent properties and target system temperatures only. The simulation and optimization of different application scenarios allows to determine the most suitable candidates, as well as some system design insights (e.g parallel/cascade configurations).

In conclusion, the methods presented here proved to be a powerful tools to help material, equipment and system developers to estimate the achievable performances, and to focus the R&D efforts only on the most attractive candidates.

Acknowledgments

This work was performed in the framework of the project *HyCool: Industrial Cooling through Hybrid system based on Solar Heat*, funded by the European Commission H2020 Programme under Grant agreement No. 792073.

References

- [1] Deepesh Sonar, S.L. Soni, and Dilip Sharma. Micro-trigeneration for energy sustainability: Technologies, tools and trends. *Applied Thermal Engineering*, 71(2):790–796, October 2014.
- [2] Augustine Ntiamoah, Jianghua Ling, Penny Xiao, Paul A. Webley, and Yuchun Zhai. CO₂ Capture by Temperature Swing Adsorption: Use of Hot CO₂-Rich Gas for Regeneration. *Industrial & Engineering Chemistry Research*, 55(3):703–713, January 2016.
- [3] Hasan Demir, Moghtada Mobedi, and Semra Ülkü. A review on adsorption heat pump: Problems and solutions. *Renewable and Sustainable Energy Reviews*, 12(9):2381–2403, December 2008.
- [4] Mohamed M. Younes, Ibrahim I. El-Sharkawy, A.E. Kabeel, and Bidyut Baran Saha. A review on adsorbent-adsorbate pairs for cooling applications. *Applied Thermal Engineering*, 114:394–414, March 2017.
- [5] Yury I. Aristov. Novel Materials for Adsorptive Heat Pumping and Storage: Screening and Nanotailoring of Sorption Properties. *Journal of Chemical Engineering of Japan*, 40(13):1242–1251, 2007.

- [6] Vincenza Brancato and Andrea Frazzica. Characterisation and comparative analysis of zeotype water adsorbents for heat transformation applications. *Solar Energy Materials and Solar Cells*, 180:91–102, June 2018.
- [7] Sandra Galmarini, Emanuele Piccoli, Romain Civioc, Sara Madry, Vincenza Brancato, Andrea Frazzica, Thomas Nonnen, Ralph Herrmann, and Matthias Koebel. Measuring protocol for the characterization of adsorber materials. Technical Report Hycool project D4.1, 2019.
- [8] M.M. Dubinin and V.A. Astakhov. Development of the concepts of volume filling of micropores in the adsorption of gases and vapors by microporous adsorbents. page 5, 1971.
- [9] Michał Rozwadowski, Roman Wojsz, Kazimierz E. Wisniewski, and Jan Kornatowski. Description of adsorption equilibrium on type A zeolites with use of the Polanyi-Dubinin potential theory. *Zeolites*, 9(6):503–508, November 1989.
- [10] Mario Llano-Restrepo and Martín A. Mosquera. Accurate correlation, thermochemistry, and structural interpretation of equilibrium adsorption isotherms of water vapor in zeolite 3a by means of a generalized statistical thermodynamic adsorption model. 283(1):73–88, 2009.
- [11] Douglas M. Ruthven. *Principles of adsorption and adsorption processes*. Wiley, 1984.
- [12] W. Wagner and A. Pruß. The IAPWS formulation 1995 for the thermodynamic properties of ordinary water substance for general and scientific use. 31(2):387–535, 2002.
- [13] J. A. Nelder and R. Mead. A simplex method for function minimization. 7(4):308–313.
- [14] F. Pedregosa, G. Varoquaux, A. Gramfort, V. Michel, B. Thirion, O. Grisel, M. Blondel, P. Prettenhofer, R. Weiss, V. Dubourg, J. Vanderplas, A. Passos, D. Cournapeau, M. Brucher, M. Perrot, and E. Duchesnay. Scikit-learn: Machine learning in Python. *Journal of Machine Learning Research*, 12:2825–2830, 2011.
- [15] Christian Sangiorgio and Andreas Ruckstuhl. *Robust Fitting Of Nonlinear Regression Models*, 2005.
- [16] Jens Ammann, Bruno Michel, and Patrick W. Ruch. Characterization of transport limitations in SAPO-34 adsorbent coatings for adsorption heat pumps. *International Journal of Heat and Mass Transfer*, 129:18–27, February 2019.
- [17] Yuriy I. Aristov, Ivan S. Glaznev, and Ilya S. Girnuk. Optimization of adsorption dynamics in adsorptive chillers: Loose grains configuration. *Energy*, 46(1):484–492, October 2012.
- [18] Uwe Bau, Pooya Hoseinpoori, Stefan Graf, Heike Schreiber, Franz Lanzerath, Christian Kirches, and André Bardow. Dynamic optimisation of adsorber-bed designs ensuring optimal control. *Applied Thermal Engineering*, 125:1565–1576, October 2017.
- [19] Stefan Graf, Franz Lanzerath, Alessio Sapienza, Andrea Frazzica, Angelo Freni, and André Bardow. Prediction of SCP and COP for adsorption heat pumps and chillers by combining the large-temperature-jump method and dynamic modeling. *Applied Thermal Engineering*, 98:900–909, April 2016.
- [20] Sheila Samsatli and Nouri J. Samsatli. A general mixed integer linear programming model for the design and operation of integrated urban energy systems. 191:458–479, 2018.
- [21] H. G. Santos and T. A. M. Toffolo. Python - MIP, December 2020.
- [22] Anutosh Chakraborty, Bidyut Baran Saha, Shigeru Koyama, Kim Choon Ng, and Kandadai Srinivasan. Adsorption Thermodynamics of Silica Gel/Water Systems. *Journal of Chemical & Engineering Data*, 54(2):448–452, February 2009.
- [23] Israt Jahan, Md. Amirul Islam, M. L. Palash, Kaiser Ahmed Rocky, Tahmid Hasan Rupam, and Bidyut Baran Saha. Experimental Study on the Influence of Metal Doping on Thermophysical Properties of Porous Aluminum Fumarate. *Heat Transfer Engineering*, pages 1–10, June 2020.

- [24] Björn Nienborg, Stefan Gschwander, Gunther Munz, Dominik Fröhlich, Tobias Helling, Rafael Horn, Helmut Weinsläder, Felix Klinker, and Peter Schossig. Life Cycle Assessment of thermal energy storage materials and components. *Energy Procedia*, 155:111–120, November 2018.
- [25] Kutub Uddin. Specific heat capacities of carbon-based adsorbents for adsorption heat pump application. *Applied Thermal Engineering*, page 10, 2018.
- [26] Engineering Toolbox. Water - Specific Heat (online), 2004.
- [27] Sibnath Kayal, Anutosh Chakraborty, and How Wei Benjamin Teo. Green synthesis and characterization of aluminium fumarate metal-organic framework for heat transformation applications. *Materials Letters*, 221:165–167, June 2018.
- [28] Lukas Huber, Patrick Ruch, Roland Hauert, Gesine Saucke, Santhosh Kumar Matam, Bruno Michel, and Matthias M. Koebel. Monolithic nitrogen-doped carbon as a water sorbent for high-performance adsorption cooling. *RSC Advances*, 6(30):25267–25278, 2016.
- [29] Carsten Schlüsener, Mergime Xhinovci, Sebastian-Johannes Ernst, Alexa Schmitz, Niels Tannert, and Christoph Janiak. Solid-Solution Mixed-Linker Synthesis of Isoreticular Al-Based MOFs for an Easy Hydrophilicity Tuning in Water-Sorption Heat Transformations. *Chemistry of Materials*, 31(11):4051–4062, June 2019.
- [30] G. Restuccia, A. Freni, S. Vasta, and Yu Aristov. Selective water sorbent for solid sorption chiller: experimental results and modelling. *International Journal of Refrigeration*, 27(3):284–293, May 2004.

An analytical design tool for pin fin sorber bed heat and mass exchanger

MJ. Darvish¹, H. Bahrehmand¹ and M. Bahrami^{1*}

¹Laboratory for Alternative Energy Conversion (LAEC), School of Mechatronic Systems Engineering, SFU, BC, CA V3T 0A3

*Corresponding author: mbahrami@sfu.ca

Abstract

This paper proposes a novel closed-form analytical model to predict the sorption performance of a prototype pin fin heat and mass exchanger (PF-HMX), using the Eigen function expansion method to solve the governing energy equation. The proposed transient 2-D solution includes all salient thermophysical and sorption properties, sorbent geometry, operating conditions, and the thermal contact resistance at the interface between the sorber bed heat exchanger and sorption composite. The analytical model validated successfully using the sorption data from a custom-built gravimetric large temperature jump (G-LTJ) test bed.

Keywords: Sorption system, Analytical modeling, Coefficient of performance, Specific cooling power.

Introduction/Background

The heating and cooling systems consumes over 60% of the residential and almost 50% of the commercial building energy [1]. Powered by electricity, vapor-compression systems (VCR) are the most common cooling technologies in the market. And since more than 80% of the global energy– including electrical power generation [2], [3]– is generated from fossil fuels, building heating and cooling systems are major greenhouse gas emitters [4], which leads to catastrophic environmental impact including the climate change.

Furthermore, fluorocarbon-type refrigerants used in VCR systems are not only potent greenhouse gases but also implicated in ozone depletion [5], [6].

Almost 70% of the global primary energy is lost as waste heat [7], with low-grade energies (temperature sources below 100°C) constituting 63% of this untapped energy [7]. Sorption Waste-heat driven cooling/heating systems have the potential to offer a solution to world energy needs and reducing environmental pollutants. Sorption cooling and heating systems (SCHS) have recently drawn immense attention as an alternative technology that enhances the efficiency of energy systems to reduce reliance on fossil fuels for heating and cooling. However, they have not been widely adopted due to following: i) low thermal conductivity and diffusivity of the sorbent composites; ii) low heat and mass transfer due to the inefficiency of existing sorber bed heat exchanger designs; and iii) low operating pressure (near vacuum), all of which lead to large, inefficient, and costly SCHS [8]–[11].

To address some of these challenges, this study evaluates a new PF-HMX sorber bed design, proposed as an alternative to off-the-shelf sorbers. The proposed PF-HMX can provide both high COP and enhanced heat and mass transfer inside the sorber bed. To assess the performance of the proposed PF-HMX, we developed a predictive analytical closed-form model to provide accurate and fast evaluation of SCHS performance as a function of the design, sorption material properties, and operating conditions.

There are several studies in the literature with the focus of developing sorber beds, the specification and performance of these SCHS systems are summarized in table 1, which

includes working pairs, sorber bed HMX design, reported SCP, COP, and MR. However, one can conclude that the literature lack an closed-form solution which includes the geometry of HMX, salient thermophysical and sorption properties as well as operational input parameters and: (i) considers the transient behavior of sorber bed; and (ii) thermal contact resistance at the interface between the sorption material and the HMX.

To enhance the thermal diffusivity of the sorbent material, a consolidated composite, consisting of CaCl₂, silica gel B150, with added natural graphite flakes is prepared. The thermally conductive additive, natural graphite flakes, reduce the active sorbent fraction in the composite creating a need for establishing an optimum composition for specific application, more details can be found in our previous study [12].

To this end, a 2-D analytical solution is developed for a PF-HMX. In addition, using the proposed model, a new PF-HMX is designed, fabricated and validated against the data collected from our custom-built G-LTJ test under a range of operating conditions. The proposed model for PF-HMX is validated against gathered experimental data. Our proposed PF-HMX beds achieved a SCP of 1160 W/kg, a COP of 0.68, with a MR of 3.3, under the operating condition of a sorption chiller: T_{des}=90 °C, T_{ads}=T_{cond}=30 °C and T_{evap}=15 °C.

Performance parameters

SCP is defined as the evaporative cooling rate generated per mass of dry sorbent material, and represents how fast the heat and mass transfer processes take place in the sorber bed, Eq. (1).

$$SCP = \frac{Q_{evap}}{m_{sorb} \tau} = \frac{m_{sorb} \int_{ads} \frac{d\omega}{dt} h_{fg} dt}{m_{sorb} \tau} = \frac{\Delta\omega h_{fg} @T_{evap}}{\tau} \quad (1)$$

where, Q_{evap} is the evaporative cooling energy (J), m_{sorb} is the sorbent mass (kg), ω is the sorbate uptake (g sorbate/g sorbent), h_{fg} is the sorbate enthalpy of evaporation (J/kg), and τ is the cycle time (s).

COP, defined as the ratio of the evaporative cooling energy to the input energy, which is the summation of desorption heat and sensible heat, Eq. (2). COP can be increased by: (i) enhancing the heat and mass transfer rate in the sorber bed, to increase both the evaporative cooling energy and the desorption heat, which overall increases COP, and (ii) decreasing the thermal inertia of the HMX, which reduces the (sensible) heat input needed to perform the temperature swing during the adsorption and desorption cycle.

$$COP = \frac{Q_{evap}}{Q_{input}} = \frac{Q_{evap}}{Q_{sens} + Q_{des}} = \frac{m_{sorb} \int_{ads} \frac{d\omega}{dt} h_{fg} dt}{\int_{des} \left(\left(m_{sorb} (c_{p,s} + \omega c_{p,w}) + m_{HEX} c_{p,HEX} \right) \frac{dT}{dt} - m_{sorb} \frac{d\omega}{dt} h_{ads} \right) dt} \quad (2)$$

where, Q_{evap} is the evaporative cooling energy (J), Q_{input} is the input thermal energy (J), Q_{sens} is the thermal energy required to overcome thermal inertia of the sorber bed HMX (J), Q_{des} is the thermal energy consumed for desorption (J), m_{sorb} is the sorbent mass (kg), m_{HEX} is the mass of HMX (kg), ω is the sorbate uptake (g sorbate/g sorbent), h_{fg} is the sorbate enthalpy of evaporation (J/kg), c_p is the specific heat (J/(kg K)), and T is the sorbent temperature (K).

In order to properly evaluate the performance of sorption cooling system, the MR of sorber bed masses to sorbent material is also considered as follows:

$$MR = \frac{m_{HMX} + m_{sorb} + m_{HTF}}{m_{sorb}} \quad (3)$$

where m_{HMX} is the mass of HMX (kg), m_{sorb} is the sorbent mass (kg), and m_{HTF} is the heat transfer fluid (HTF) mass.

Table 1: A summary the specification and performance of available studies with a reasonable compromise between SCP, COP and MR. * HTF data was not available in the publication.

Ref	Sorption pair	S-HMX	t_{cycle} (min)	SCP (W/kg)	COP	MR
[13]	Coating silica gel + CaCl ₂ (SWS-11)/ water	Aluminum finned tube	10	137	0.15	4.47 *
[14]	Coating AQSOA-FAMZ02/ water	Extruded Aluminum finned-tube heat exchanger		295	0.21	5.37 *
[15]	Loose grain AQSOA-FAM Z02/water	Round tube-fin packed	20	120	0.3	7.86
[15]	Loose grain AQSOA-FAM Z02/water	Round tube-fin packed	20	70	0.45	3.29
[16]	Loose grain LiNO ₃ -Silica KSK/water (SWS-91)	Aluminum finned flat tube	6.4	318	0.176	2.82 *
[17]	Loose grain AQSOA-FAM Z02/water	Aluminum finned flat tube	7	394	0.6	3.61
[18]	Coating zeolite, SAPO- 34/water	Aluminum finned flat tube	5	675	0.24	10
[18]	Loose grain zeolite, SAPO- 34/water	Aluminum finned flat tube	5	498	0.4	4.11
[19]	Coating SAPO- 34/water	Aluminum sintered metal fiber structures soldered on flat fluid channels	10	852	0.4	4.15
[20]	Coating silica gel + CaCl ₂ /water	Aluminum plate-finned HMX	10	1005	0.6	4.7
[21]	Coating silica gel + CaCl ₂ /water	Aluminum finned-tube HMX	10	766	0.55	4

Model development

Based on the general approach reported in our lab's previous publications [20]–[22], a new 2-D analytical solution is proposed to determine the parameters inside the in-line arrangement of pin fin heat/mass exchanger, these include: transient temperature distribution, heat transfer rate, uptake and the sorption performance. Figure 1 shows the solution domain schematically which includes PF-HMX, HTF, and the sorbent material. The assumptions used to develop the model include:

- Two-dimensional, transient heat and mass transfer with constant thermo-physical properties,
- Constant temperature for the HTF, due to the relatively higher heat capacity of the heat transfer fluid [23],
- The boundaries of the sorbent and the fin that are in contact with low pressure refrigerant vapor are assumed to be adiabatic, i.e., due to the low Biot number [24][8], and

- The radiative heat transfer is neglected because of low temperature difference between the sorbent and surrounding (10-20 K).

From these assumptions, the energy equation can be written as follows for both sorbent and HMX fin.

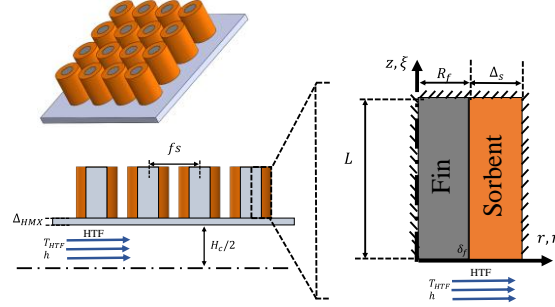


Fig. 1. Schematic of the solution domain consisting of sorbent coating and pin fin heat and mass exchanger, in-line arrangement is shown. For dimensions of the PF-HMX see table 2.

$$\frac{\partial T_i}{\partial t} = \alpha_{i,r} \left(\frac{\partial^2 T_i}{\partial r^2} + \frac{1}{r} \frac{\partial T_i}{\partial r} \right) + \alpha_{i,z} \frac{\partial^2 T_i}{\partial z^2} + \frac{1}{(\rho c_p)_i} G_i(t), T_i(r, z, t), i = s, f \quad (4)$$

$$G_i(t) = \begin{cases} \rho_s H_{ads} \frac{d\omega}{dt}, & i = s \\ 0, & i = f \end{cases} \quad (5)$$

where, T_i is the temperature of the i th layer (K), α is the thermal diffusivity for the i th layer (m^2/s), ρ is the density for the i th layer (kg/m^3), c_p is the specific heat ($J/(kg K)$), r and z are the coordinates, t is time (s), H_{ads} is the enthalpy of adsorption (J/kg), and G_i is the heat generation inside the i th layer and $i=s$ and $i=f$ represent the sorbent and HMX domains, respectively. The boundary conditions are:

$$\frac{\partial T_i(0, z, t)}{\partial r} = 0 \quad (6)$$

$$\frac{\partial T_s(\Delta_s + R_f, z, t)}{\partial r} = 0 \quad (7)$$

$$\frac{\partial T_i(r, L, t)}{\partial z} = 0 \quad (8)$$

$$R = \frac{\Delta_{HMX}}{k_{f,z}} + \frac{1}{h} + TCR \cdot A \quad \left(\frac{K m^2}{W} \right) \quad (9)$$

$$\frac{1}{R} (T_s(r, 0, t) - T_{HTF}) = k_s \frac{\partial T_s(r, 0, t)}{\partial z} \quad (9)$$

$$\frac{1}{R} (T_f(r, 0, t) - T_{HTF}) = k_{f,z} \frac{\partial T_f(r, 0, t)}{\partial z}$$

$$k_{f,r} \frac{\partial T_f(R_f, z, t)}{\partial r} = k_s \frac{\partial T_s(R_f, z, t)}{\partial r} \quad (10)$$

$$-k_{f,r} \frac{\partial T_f(R_f, z, t)}{\partial r} = \frac{1}{TCR \cdot A} (T_f(R_f, z, t) - T_s(R_f, z, t))$$

where, T_i is the temperature of the i th layer (K), Δ_s is the sorbent thickness (m), Δ_{HMX} is the HMX thickness (m), R_f is the fin radius (m), L is the fin height (m), A is the heat transfer area (m^2), k is the thermal conductivity for the i th layer ($W/(m \text{ K})$), h is the convective heat transfer coefficient ($W/(m^2 \text{ K})$), r and z are the coordinates, t is time (s), and TCR is the thermal contact resistance between fin and sorbet.

The initial condition for temperature is

$$T_i(r, z, 0) = T_0 \quad (11)$$

Non-dimensional variables were defined:

$$\begin{aligned} \eta &= \frac{r}{R_f + \Delta_s} & \xi &= \frac{z}{L} & Fo &= \frac{t \alpha_z}{L^2} & \theta_i &= \frac{T_i - T_{HTF}}{T_0 - T_{HTF}} \\ \delta &= \frac{L}{\Delta_s + R_f} & \delta_f &= \frac{R_f}{R_f + \Delta_s} & \mu_r^2 &= \frac{\alpha_r}{\alpha_z} & \mu_s^2 &= \frac{\alpha_s}{\alpha_z} \\ \kappa &= \frac{k_s}{k_{f,r}} & \Lambda &= \frac{R_s + R_f}{k_{f,r} TCR A} & Bi_s &= \frac{L}{Rk_s} & Bi_f &= \frac{L}{Rk_{f,z}} \end{aligned}$$

$$g_i(Fo) = \begin{cases} \frac{H_{ads}}{c_{p,s} (T_0 - T_{fluid})} \frac{d\omega}{dFo}, & i = s \\ 0, & i = f \end{cases}$$

where, θ_i is the dimensionless temperature of the i th layer, Fo (Fourier number) is the dimensionless time, η and ξ are the dimensionless coordinates, and g_i is the dimensionless heat generation inside the i th layer. Using the aforementioned dimensionless variables, the dimensionless energy equation as well as the boundary and initial conditions can be obtained:

$$\frac{\partial \theta_i}{\partial Fo} = (\mu_{i,\eta} \delta)^2 \left(\frac{\partial^2 \theta_i}{\partial \eta^2} + \frac{1}{\eta} \frac{\partial \theta_i}{\partial \eta} \right) + \mu_{i,\xi}^2 \frac{\partial^2 \theta_i}{\partial \xi^2} + g_i(Fo) \quad (12)$$

$$\frac{\partial \theta_i(\eta, 1, Fo)}{\partial \xi} = 0 \quad (13)$$

$$\frac{\partial \theta_f(0, \xi, Fo)}{\partial \eta} = 0 \quad (14)$$

$$\frac{\partial \theta_s(1, \xi, Fo)}{\partial \eta} = 0 \quad (15)$$

$$\frac{\partial \theta_s(\eta, 0, Fo)}{\partial \xi} - Bi_s \theta_s(\eta, 0, Fo) = 0 \quad (16)$$

$$\frac{\partial \theta_f(\eta, 0, Fo)}{\partial \xi} - Bi_f \theta_f(\eta, 0, Fo) = 0$$

$$\frac{\partial \theta_f(\delta_f, \xi, Fo)}{\partial \eta} = \kappa \frac{\partial \theta_s(\delta_f, \xi, Fo)}{\partial \eta} \quad (17)$$

$$-\frac{\partial \theta_f(\delta_f, \xi, Fo)}{\partial \eta} = \Lambda(\theta_f(\delta_f, \xi, Fo) - \theta_s(\delta_f, \xi, Fo))$$

A MATLAB code is developed to calculate the eigenfunctions and eigenvalues in both spatial coordinates along with the Gamma function as a function of Fourier number (dimensionless time). After solving the equations, the dimensionless temperature is acquired:

$$\theta(\eta, \xi, Fo) = \sum_{n=1}^{\infty} \sum_{m=1}^{\infty} \psi_n(\xi) X_{nm}(\eta) \Gamma_{nm}(Fo) \quad (18)$$

The methodology of the solution is presented in Appendix A.

Experimental study

A number of CaCl₂-silica gel composite sorbents with 0-20 wt.% graphite flake contents is prepared. Polyvinyl alcohol (PVA) binder (40,000 MW, Amresco Inc.) is dissolved in water. Following this, CaCl₂ and silica gel (SiliaFlash[®] B150, Silicycle, Inc., Quebec, Canada) and graphite flakes (consisting of both 150 μm fine particles and thin flakes up to 1.3 mm long, Sigma-Aldrich) are added to the aqueous solution. The slurry composites a coated on the designed PF-HMX and oven-dried at 70 °C then cured at 180 °C, each for 4 hour, see Fig. 2 for more details. Thermophysical characteristics of the heat exchanger and sorbent materials with different amount of additives were measured using a transient plane source (TPS), hot disk thermal constants analyzer, as per ISO 22007- 2 (ISO220 07-2, 20 08) (TPS 250 0S, ThermTest Inc., Fredericton, Canada) and described in Table 2 [25], [26]. Sorbent thickness around each fin and fin diameters are measured as 5 mm and 4 mm, respectively. Fig. 3 shows the gravimetric large temperature jump (G-LPJ) test bed custom-built in our lab used to validate the developed analytical solution.

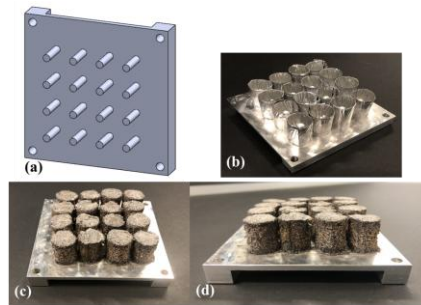


Fig. 2. (a) Pin fin structure designed in SolidWorks to be bolted on top of a copper heat exchanger in the GLTJ test bed, (b) building cylinders around pin fins and fill them with sorbent material. (c, d) PF-HMX coated with the composite sorbent, silica gel, CaCl₂, PVA and graphite flakes.



Fig. 3. (a) Schematic diagram and (b) picture of the G-LTJ test bed.

To simulate the operation of SCHS, HTF was pumped through the PF-HMX and the temperature cycled between 30°C and 67°C for sorption and desorption, respectively. Two four-way valves were used to switch the HTF between the sorber bed and the buffer for desorption and sorption processes. The buffer was used for heat recovery purpose. The sorber bed and the copper PF-HMX were placed inside a vacuum chamber, which was connected to the evaporator/condenser that was maintained at 15 °C. The whole test bed was degassed for five hours using a vacuum pump to dry the sorbent material before the tests. The vacuum chamber was placed on a precision balance (ML4002E, Mettler Toledo) with an accuracy of 0.01 g to measure the mass change due to the sorbate uptake. Five K-type thermocouples with an accuracy of 1.1 °C were passed using a feed-through in the vacuum chamber to measure the sorbent temperature. The instruments were connected to a PC through a data acquisition system and in-house software written in LabVIEW environment. The maximum uncertainties of the measured COP and SCP were estimated to be 8% and 5.7%, respectively. More information on uncertainty analysis can be found elsewhere [26].

Table 2: A summary Graphite flake content in the sorbent, thermophysical properties, geometrical specifications, and SCHS cycle parameters used for the baseline case and model validation.

	Baseline case			Validation with G-LTJ test bed		
	Sorbent	Al fin	Al tube	Sorbent	Al fin	Copper tube
ϕ (wt%)	10	-	-	0-20		
ρ (kg/m ³)	665	2699	2699		2699	8932
c (J/kgK)	1082	909	909		909	386
α (m ² /s)	4.1e-7	9.6e-5	9.6e-5		9.6e-5	1.1e-4
h_{ads} (J/kg)	2.77e6	-	-	2.77e6		1.5
$R_f, \Delta_s, \Delta_{HMX}$ (mm)	$\Delta_s = 2$	$R_f = 2$		$\Delta_s = 5$	$R_f = 2$	
L, H_c, W_c (cm)	$L=2$	$L=1.5$	$H_c=0.6, W_c=1.3$	$L=1.5$	$L=1.5$	$H_c=0.5, W_c=4$
t (min)	15			In Fig. 6		
$TCR.A$ (K m ² /W)	0.0019 [22])					

Model validation

Figure 4 shows the mass change of the sorber bed for the sample with 0 % amount of graphite flakes. Measured mass change of the sorber bed is due to: (i) the water uptake by sorbent material, (ii) fluctuations such as thermal expansion, contraction, and vibration of the flexible hoses, and (iii) density changes of the heat transfer fluid (HTF) due to the temperature swings between adsorption and desorption processes. In order to deconvolute the mass change caused by the water uptake from others, a number of baseline experiments were run under the same operating conditions but with the valve between the sorber bed and the evaporator/condenser kept shut. Consequently, baseline did not include the effect of water uptake. After measuring the baseline signal, the valve was opened and the experiment was repeated; the blue line shows the total mass change of the sorber bed, including water uptake. Subtracting the total mass from the baseline represents the actual water uptake changes.

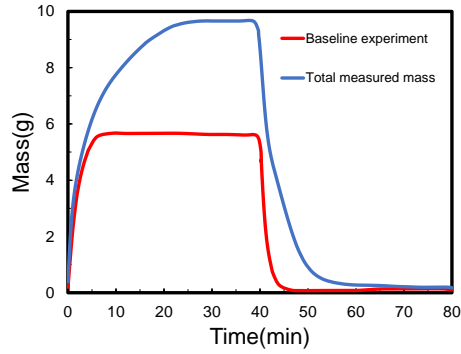


Fig. 4. Mass changes of the sorber bed with 0% graphite flake content in G-LTJ test bed due to the variations in water density and fluctuations during the sorption (30 °C) and desorption (67 °C).

Figure 5 shows variation of average sorbent temperature versus time for varying amounts of graphite flakes. By adding graphite flake, the sorbent thermal diffusivity improves up to 500% [27], which enhances the heat transfer from HMX to the sorbent. For samples with higher amounts of graphite flakes and lower amounts of active material, the heat of sorption decreases.

Figure 6 shows the variation of the water uptake versus time for varying amounts of graphite flakes in the sorbent. In the early stage of sorption (the first 10 to 15 minutes), adding graphite flakes enhances water uptake. As the sorbent approaches saturation, the heat generation rate reduces and the trend starts to reverse. Moreover, a greater amount of graphite flake reduces the amount of active material leading to lower uptake and performance as the sorbent reaches equilibrium. The equilibrium uptakes measured with G-LTJ test bed are in good agreement with thermogravimetric sorption analyzer (TGA) equilibrium data, for more information, see [26]).

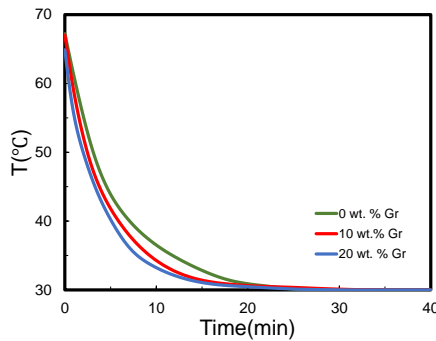


Fig. 5. Variation of average sorbent temperature through the time for different amount of graphite flakes

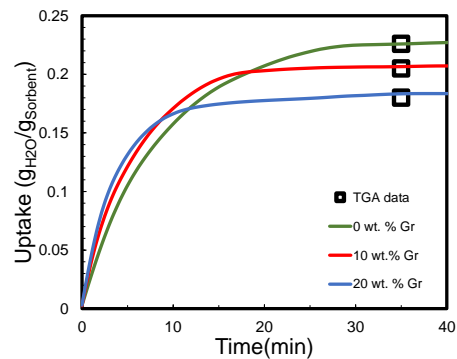


Fig. 6. Effect of graphite flake content on water uptake

Figure 7 shows the effect of graphite flakes on the SCP and COP based on Eqs. (1) and (2). It can be seen that the present analytical model is in a good agreement with the experimental results. Moreover, for small sorption times (the first 10 to 15 minutes), SCP increases 10 to 30% by adding graphite flakes. Thus, during early stages of sorption, the sorption rate and heat generation is high, resulting in a need for higher thermal diffusivity which in turn causes higher uptake. However, over longer periods of time, such as when the sorbent approaches saturation, the need for higher thermal diffusivity reduces as the sorption rate decreases. The trend starts to reverse and the sorbent with higher active material has higher uptake and of course higher SCP.

Additionally, for small sorption time, the sample with higher graphite flakes has higher uptake and thus higher COP. As we approach saturation phase, the sample with smaller amount of additives and greater amount of active material has the highest uptake and COP.

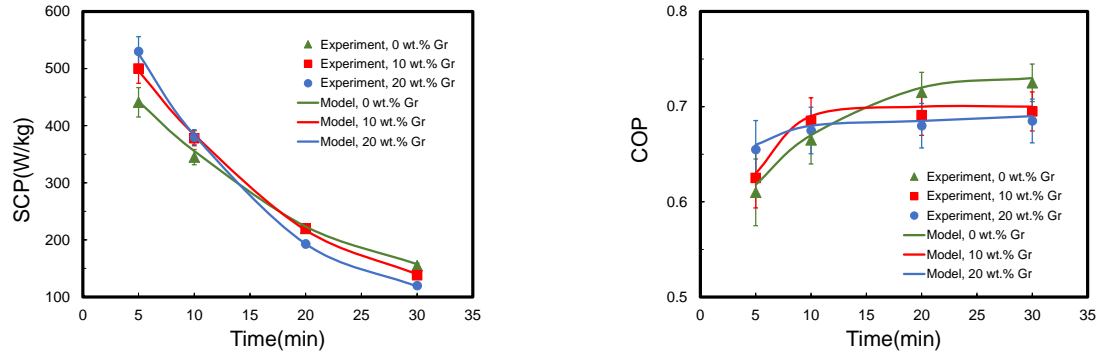


Fig. 7. Comparison between the present analytical model and the experimental data collected from our G-LTJ test bed for 0 and 20 wt% graphite flake content in the sorbent composite.

Performance evaluation

The baseline case is investigated for the operating conditions of the sorption chiller: $T_{des}=90\text{ }^{\circ}\text{C}$, $T_{ads}=T_{cond}=30\text{ }^{\circ}\text{C}$ and $T_{evap}=15\text{ }^{\circ}\text{C}$. SCP, COP, and MR are calculated as the performance metrics based on equations (1), (2), and (3). Note that mass of heat transfer fluid was not available for some studies. The PF-HMX with relatively low MR reaches a SCP of 1160 W/kg and COP of 0.68. Fig. 10 displays the performance of PF-HMX versus state-of-the-art published researches. Note that the composite silica gel/CaCl₂ sorbent used in the PF-HMX, [20] and [21] provide higher SCP and COP. Silica gel/CaCl₂ sorption kinematic occurs over the entire range of relative pressure $0.06 < P/P_0 < 0.4$ which makes it a good candidate for AC applications [26]. Conversely, sorption for zeolite-based materials, such as SAPO-34 and FAM Z02, utilized in [13]–[19] occurs in a narrow range of relative pressure which limits the application to specific operational temperatures.

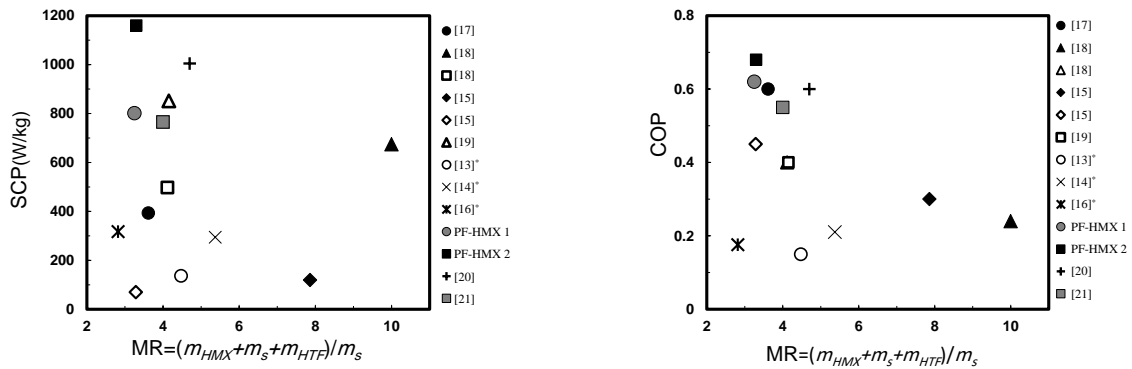


Fig. 8. PF-HMX comparison in terms of the MR, SCP and COP versus the available studies. Fin radius and sorbent thickness of PF-HMX 1 are 2 mm and 5 mm, respectively, while fin radius and sorbent thickness for PF-HMX 2 are 1mm and 2 mm respectively. * HTF data not provided.

Summary/Conclusions

A novel closed-form 2-D analytical model was developed to determine the conjugate heat and mass transfer and performance of PF-HMX. The analytical solution included material properties, operating conditions and all design parameters such as sorbent geometry, HMX geometry, and fluid channel height. The current 2-D model was successfully validated based on experimental results collected from custom-built G-LTJ test bed.

To this end, we compared two arbitrary geometries of PF-HMX with other studies and found that PF-HMX with a relatively low MR could provide high SCP and COP.

Acknowledgements

The authors gratefully acknowledge the financial support of the Natural Sciences and Engineering Research Council of Canada (NSERC) through the Advancing Climate Change Science in Canada (ACCSC) Grant No. ACCPJ 536076-18

Appendix A

Dimensionless energy equation obtained as (12) where

$$\mu_{i,\eta} = \begin{cases} \mu_r, & i = f \\ \mu_s, & i = s \end{cases} \quad (\text{A.1})$$

$$\mu_{i,\xi} = \begin{cases} 1, & i = f \\ \mu_s, & i = s \end{cases} \quad (\text{A.2})$$

Water uptake can be simulated as a function of operating conditions such as pressure and temperature of sorber bed. a linear relationship between water uptake and sorbent temperature is achieved by [12], [22] for each pressure during isobaric desorption and adsorption processes.

Eigen function expansion method is used to solve the dimensionless energy equation and boundary conditions. Based on Eqs. (12)-(18), the following eigenvalue problem can be derived in ξ direction [28], [29].

$$\psi'' + \gamma^2 \psi = 0 \quad (\text{A.3})$$

$$\psi' - Bi \psi = 0 \text{ at } \xi=0 \quad (\text{A.4})$$

$$\psi = 0 \text{ at } \xi=1 \quad (\text{A.5})$$

The following transcendental equation is achieved to calculate the eigenvalues.

$$\gamma \tan(\gamma) = Bi \quad (\text{A.6})$$

The eigenfunction related to each eigenvalue are given as follows.

$$\psi = \cos(\gamma\xi) + \tan(\gamma) \sin(\gamma\xi) \quad (\text{A.7})$$

Furthermore, the following eigenvalue problem can be established in η direction.

$$\frac{d^2 X}{d\eta^2} + \frac{1}{\eta} \frac{dX}{d\eta} + \omega_k^2 X = 0 \quad (\text{A.8})$$

$$\left. \frac{dX}{d\eta} \right|_{\eta=0,1} = 0 \quad (\text{A.9})$$

where,

$$\omega_k^2 = \frac{\lambda r_k - q_k}{P_k}, \quad k = s, f \quad (\text{A.10})$$

$$r_s = \frac{\left((\rho c_p)_s - (\rho H_{ads} a)_s \right) k_z}{(\rho c_p)_f \delta^2} \quad (\text{A.11})$$

$$r_f = \frac{k_{f,z}}{\delta^2} \quad (\text{A.12})$$

$$q_k = (\mu_{k,\eta} \gamma)^2 r_k \quad (\text{A.13})$$

$$q_k = (\mu_{k,\eta} \gamma)^2 r_k \quad (\text{A.14})$$

$$p_f = k_{f,r} \quad (\text{A.15})$$

This is a singular eigenvalue problem because of non-continuous p , r and q . Further, ω_k^2 , depending upon the thermophysical properties and geometrical characteristics of the sorbent and the fin, can be positive, negative or zero. Therefore, there is no simple solution with eigenfunction and transcendental equation for the eigenvalue problem. The approximated solution proposed by [28], [30] is followed in the present paper. The eigenvalue problem is approximated by identically dividing the cylinder (sorbent and fin) into $n-1$ intervals. The finer the division, the better the approximation. The following equations represent the new eigenvalue problem with boundary conditions.

$$\frac{d^2 X}{d\eta^2} + \frac{1}{\eta} \frac{dX}{d\eta} + \omega_k^2 X = 0 \quad (\text{A.16})$$

$$\left. \frac{dX}{d\eta} \right|_{\eta=0} = 0 \quad (\text{A.17})$$

$$X_k = X_{k+1}, \quad k = 2, 3, \dots, n-1 \quad (\text{A.18})$$

$$p_k \frac{dX_k}{d\eta} = p_{k+1} \frac{dX_{k+1}}{d\eta}, \quad k = 2, 3, \dots, n-1 \quad (\text{A.19})$$

$$\left. \frac{dX}{d\eta} \right|_{\eta=1} = 0 \quad (\text{A.20})$$

The following equations are also established to consider TCR as an imaginary layer at the interface between sorbent and the fin.

$$\frac{d^2 X}{d\eta^2} + \frac{1}{\eta} \frac{dX}{d\eta} + \omega_k^2 X = 0 \quad (\text{A.21})$$

$$\omega_k = 0 \quad (\text{A.22})$$

$$p_k \frac{dX}{d\eta} = \frac{R_f + \Delta_s}{TCRA} (X_{k+1} - X_k) \quad (\text{A.23})$$

The following eigenfunction can be achieved for each interval ($\xi_{k-1} < \xi < \xi_k$).

$$X_k(\eta) = X_k(\eta_{k-1}) \frac{J_0(\omega_k \eta) Y_0(\omega_k \eta_k) - J_0(\omega_k \eta_k) Y_0(\omega_k \eta)}{J_0(\omega_k \eta_{k-1}) Y_0(\omega_k \eta_k) - J_0(\omega_k \eta_k) Y_0(\omega_k \eta_{k-1})} \\ + X_k(\eta_k) \frac{J_0(\omega_k \eta_{k-1}) Y_0(\omega_k \eta) - J_0(\omega_k \eta) Y_0(\omega_k \eta_{k-1})}{J_0(\omega_k \eta_{k-1}) Y_0(\omega_k \eta_k) - J_0(\omega_k \eta_k) Y_0(\omega_k \eta_{k-1})}, \quad \omega_k^2 > 0 \quad (\text{A.24})$$

$$X_k(\eta) = X_k(\eta_{k-1}) \text{Log} \frac{\frac{\eta}{\eta_k}}{\frac{\eta_{k-1}}{\eta_k}} + X_k(\eta_k) \text{Log} \frac{\frac{\eta_{k-1}}{\eta_k}}{\frac{\eta}{\eta_k}}, \quad \omega_k^2 = 0 \quad (\text{A.25})$$

$$X_k(\eta) = X_k(\eta_{k-1}) \frac{I_0(\omega_k^* \eta) K_0(\omega_k^* \eta_k) - I_0(\omega_k^* \eta_k) K_0(\omega_k^* \eta)}{I_0(\omega_k^* \eta_{k-1}) K_0(\omega_k^* \eta_k) - I_0(\omega_k^* \eta_k) K_0(\omega_k^* \eta_{k-1})} \\ + X_k(\eta_k) \frac{I_0(\omega_k^* \eta_{k-1}) K_0(\omega_k^* \eta) - I_0(\omega_k^* \eta) K_0(\omega_k^* \eta_{k-1})}{I_0(\omega_k^* \eta_{k-1}) K_0(\omega_k^* \eta_k) - I_0(\omega_k^* \eta_k) K_0(\omega_k^* \eta_{k-1})}, \quad \omega_k^2 < 0 \quad (\text{A.26})$$

$$\omega_k^* = \sqrt{\text{abs}(\omega_k^2)} \quad (\text{A.27})$$

The Eigen functions for each interval can be calculated as follows by substituting abovementioned eigenfunctions into boundary conditions ((A.17)-(A.20)).

$$A_1 X_0 - B_1 X_1 = 0 \quad (\text{A.28})$$

$$B_k X_{k-1} + (A_k + A_{k+1}) X_k - B_{k+1} X_{k+1} = 0, \quad k = 2, \dots, n-1 \quad (\text{A.29})$$

$$-B_n X_{n-1} + A_n X_n = 0 \quad (\text{A.30})$$

where,

$$A_k = p_k \omega_k \left(\frac{J_0(\omega_k \eta_k) Y_1(\omega_k \eta_{k-1}) - Y_0(\omega_k \eta_k) J_1(\omega_k \eta_{k-1})}{J_0(\omega_k \eta_{k-1}) Y_0(\omega_k \eta_k) - J_0(\omega_k \eta_k) Y_0(\omega_k \eta_{k-1})} \right), \quad \omega_k^2 > 0 \quad (\text{A.31})$$

$$A_k = 1, \quad \omega_k^2 = 0 \quad (\text{A.32})$$

$$A_k = p_k \omega_k \left(\frac{I_0(\omega_k^* \eta_k) K_1(\omega_k^* \eta_{k-1}) + K_0(\omega_k^* \eta_k) I_1(\omega_k^* \eta_{k-1})}{I_0(\omega_k^* \eta_{k-1}) K_0(\omega_k^* \eta_k) - I_0(\omega_k^* \eta_k) K_0(\omega_k^* \eta_{k-1})} \right), \quad \omega_k^2 < 0 \quad (\text{A.33})$$

$$B_k = p_k \omega_k \left(\frac{J_0(\omega_k \eta_{k-1}) Y_1(\omega_k \eta_{k-1}) - Y_0(\omega_k \eta_{k-1}) J_1(\omega_k \eta_{k-1})}{J_0(\omega_k \eta_{k-1}) Y_0(\omega_k \eta_k) - J_0(\omega_k \eta_k) Y_0(\omega_k \eta_{k-1})} \right), \quad \omega_k^2 > 0 \quad (\text{A.34})$$

$$B_k = 1, \quad \omega_k^2 = 0 \quad (\text{A.35})$$

$$B_k = p_k \omega_{k+1} \left(\frac{I_0(\omega_k^* \eta_{k-1}) K_1(\omega_k^* \eta_{k-1}) - I_1(\omega_k^* \eta_{k-1}) K_0(\omega_k^* \eta_{k-1})}{I_0(\omega_k^* \eta_{k-1}) K_0(\omega_k^* \eta_k) - I_0(\omega_k^* \eta_k) K_0(\omega_k^* \eta_{k-1})} \right), \quad \omega_k^2 < 0 \quad (\text{A.36})$$

A linear system of homogenous equation formed based on Eqs. (A.28)-(A.30) is derived as follows in order to calculate the eigenfunctions.

$$[K]\{X\} = 0 \quad (\text{A.37})$$

The transcendental equation is obtained to calculate the eigenvalues by equating the determinant of coefficient matrix $[K]$ to zero.

$$\det([K]) = 0 \quad (\text{A.38})$$

Sign-count method, developed by Mikhailov and Vulchanov, is utilized to solve the transcendental equation [28].

Eventually, eigenfunction are evaluated as follows.

$$X_0 = -1 \quad (\text{A.39})$$

$$X_1 = -A_1 / B_1 \quad (\text{A.40})$$

$$X_{k+1} = ((A_k + A_{k+1}) X_k - B_k X_{k-1}) / B_{k+1}, \quad k = 1, 2, \dots, n-1 \quad (\text{A.41})$$

Subsequently, the accuracy of the eigenfunction is evaluated for the last interval. If the required accuracy, $1e-8$ for this study, is not satisfied, then the finer intervals will be chosen based on the algorithm proposed by [30] until it is satisfied.

$$|-B_n X_{n-1} + A_n X_n| \leq \varepsilon_{global}, \quad \varepsilon_{global} \cong \varepsilon_{\max} \cdot n \quad (\text{A.42})$$

To this end, the eigenfunctions in ζ and η directions are evaluated. The last step is to acquire Gamma function. Gamma function, which shows the time variation of θ , can be expanded in the form of infinites series of products of eigenfunctions in ζ and η directions as follows.

$$g_i(Fo) = \sum_{n=1}^{\infty} \sum_{m=1}^{\infty} g_{nm}^*(Fo) \psi_n(\xi) X_{nm}(\eta) \quad (\text{A.43})$$

where, g_{nm}^* can be calculated based on orthogonal property of the eigenfunctions as follows.

$$g_{nm}^*(Fo) = \frac{\int_0^1 \psi d\xi \left(\sum_{k=1}^n r_k \int_{\eta_k}^{\eta_{k+1}} X_k d\eta \right)}{\int_0^1 \psi^2 d\xi \left(\sum_{k=1}^n r_k \int_{\eta_k}^{\eta_{k+1}} X_k^2 d\eta \right)} \quad (\text{A.44})$$

By substituting Eqs. (18) and (A.43) into Eq. (12), the following ordinary differential equation can be obtained for Gamma function.

$$\frac{d\Gamma}{dFo} = g_{nm}^*(Fo) - \lambda\Gamma \quad (\text{A.45})$$

Finally, Gamma function is evaluated as follows.

$$\Gamma = e^{-\lambda Fo} \left(C_{nm} + \int_{Fo'=0}^{Fo} g_{nm}^*(Fo') e^{\lambda Fo'} dFo' \right) \quad (\text{A.46})$$

where,

$$C_{nm} = \frac{\int_0^1 \psi d\xi \left(\sum_{k=1}^n r_k \int_{\eta_k}^{\eta_{k+1}} X_k d\eta \right)}{\int_0^1 \psi^2 d\xi \left(\sum_{k=1}^n r_k \int_{\eta_k}^{\eta_{k+1}} X_k^2 d\eta \right)} \quad (\text{A.47})$$

Nomenclature

A	heat transfer area, m ²	Greek	evap	evaporator
Bi	heat transfer Biot number	λ	eq	equilibrium
c	specific heat capacity, Jkg ⁻¹ K ⁻¹	β	f	fin
Fo	Fourier number	γ	fs	fin spacing
H	height, m	η	HTF	heat transfer fluid
h	convective heat transfer coefficient, Wm ⁻² K ⁻¹	ζ	s	sorbent
H_{ads}	enthalpy of adsorption, J kg ⁻¹	τ		Subscripts
h_{fg}	enthalpy of evaporation, J kg ⁻¹	θ	COP	coefficient of performance
k	thermal conductivity, W m ⁻¹ K ⁻¹	κ	G-LTJ	gravimetric large temperature jump
L	height of adsorbent, m	α	MR	mass ratio
p	pressure, Pa	μ	PF-HMX	pin fin heat and mass exchanger
p_0	saturation pressure, Pa	\mathcal{A}	PVA	polyvinyl alcohol

			conductance		
R	radius, m	ω	adsorbate uptake, (kg adsorbate/kg dry adsorbent)	SCHS	sorption cooling and heating system
Δ	thickness, m	Subscripts		SCP	specific cooling power
t	time, s	0	initial condition	TCR	thermal contact resistance
r	radial coordinate	ads	adsorption	TGA	thermogravimetric sorption analyzer
T	temperature, K	c	channel	TPS	transient plane source
z	coordinate	con d	condenser		
R	thermal resistance, K m ² W ⁻¹	des	desorption		

References:

- [1] D. Üрге-Vorsatz, L. F. Cabeza, S. Serrano, C. Barreneche, and K. Petrichenko, "Heating and cooling energy trends and drivers in buildings," *Renew. Sustain. Energy Rev.*, vol. 41, pp. 85–98, 2015.
- [2] A. A. Askalany, M. Salem, I. M. Ismael, A. H. H. Ali, M. G. Morsy, and B. B. Saha, "An overview on adsorption pairs for cooling," *Renew. Sustain. Energy Rev.*, vol. 19, pp. 565–572, 2013.
- [3] W. Pridasawas, *Solar-driven refrigeration systems with focus on the ejector cycle*, no. 06/55. Department of Energy Technology, Royal Institute of Technology, 2006, 2006.
- [4] J. M. Cullen and J. M. A. Á, "The efficient use of energy : Tracing the global flow of energy from fuel to service," *Energy Policy*, vol. 38, no. 1, pp. 75–81, 2010.
- [5] J. M. Pinheiro, S. Salústio, J. Rocha, A. A. Valente, and C. M. Silva, "Analysis of equilibrium and kinetic parameters of water adsorption heating systems for different porous metal/metalloid oxide adsorbents," *Appl. Therm. Eng.*, vol. 100, pp. 215–226, 2016.
- [6] H. Demir, M. Mobedi, and S. Ülkü, "A review on adsorption heat pump: Problems and solutions," *Renew. Sustain. Energy Rev.*, vol. 12, no. 9, pp. 2381–2403, 2008.
- [7] C. Forman, I. K. Muritala, R. Pardemann, and B. Meyer, "Estimating the global waste heat potential," *Renew. Sustain. Energy Rev.*, vol. 57, pp. 1568–1579, 2016.
- [8] Y. Zhao, E. Hu, and A. Blazewicz, "Dynamic modelling of an activated carbon–methanol adsorption refrigeration tube with considerations of interfacial convection and transient pressure process," *Appl. Energy*, vol. 95, pp. 276–284, 2012.
- [9] W. D. Wu, H. Zhang, and D. W. Sun, "Mathematical simulation and experimental study of a modified zeolite 13X-water adsorption refrigeration module," *Appl. Therm. Eng.*, vol. 29, no. 4, pp. 645–651, 2009.
- [10] A. Sharafian, S. M. N. Mehr, P. C. Thimmaiah, W. Huttema, and M. %J E. Bahrami, "Effects of adsorbent mass and number of adsorber beds on the performance of a waste heat-driven adsorption cooling system for vehicle air conditioning applications," vol. 112, pp. 481–493, 2016.
- [11] E. J. Hu, D. Zhu, X. Sang, L. Wang, and Y. Tan, "Enhancement of Thermal Conductivity by Using Polymer- Zeolite in Solid Adsorption Heat Pumps," *J. Heat Transfer*, vol. 1, no. August, pp. 1991–1993, 1997.
- [12] H. Bahrehmand, M. Ahmadi, and M. Bahrami, "Oscillatory heat transfer in coated sorber beds: An analytical solution," *Int. J. Refrig.*, 2018.

- [13] A. Freni, “An advanced solid sorption chiller using SWS-1L,” vol. 27, pp. 2200–2204, 2007.
- [14] B. Dawoud, P. Höfle, and S. Chmielewski, “Experimental Investigation of the Effect of Zeolite Coating Thickness on the Performance of a novel Zeolite-Water Adsorption Heat Pump Module,” *Proc. Tenth Int. Conf. Enhanc. Build. Oper.*, pp. 1–8, 2010.
- [15] A. Sharafian and others, “Effects of adsorbent mass and number of adsorber beds on the performance of a waste heat-driven adsorption cooling system for vehicle air conditioning applications,” pp. 481–493, 2016.
- [16] Y. I. Aristov, A. Sapienza, D. S. Ovoshchnikov, A. Freni, and G. Restuccia, “Reallocation of adsorption and desorption times for optimisation of cooling cycles Optimisation des cycles de refroidissement par modification des temps d’adsorption et de desorption des dure,” *Int. J. Refrig.*, vol. 35, no. 3, pp. 525–531, 2010.
- [17] A. Sapienza, S. Santamaria, A. Frazzica, and A. Freni, “Influence of the management strategy and operating conditions on the performance of an adsorption chiller,” *Energy*, vol. 36, no. 9, pp. 5532–5538, 2011.
- [18] A. Freni, L. Bonaccorsi, L. Calabrese, A. Capri, A. Frazzica, and A. Sapienza, “SAPO-34 coated adsorbent heat exchanger for adsorption chillers,” *Appl. Therm. Eng.*, vol. 82, pp. 1–7, 2015.
- [19] U. Wittstadt *et al.*, “A novel adsorption module with fiber heat exchangers : Performance analysis based on driving temperature differences,” vol. 110, pp. 154–161, 2017.
- [20] H. Bahrehmand and M. Bahrami, “An analytical design tool for sorber bed heat exchangers of sorption cooling systems,” *Int. J. Refrig.*, vol. 100, pp. 368–379, 2019.
- [21] H. Bahrehmand and M. Bahrami, “Optimized sorber bed heat and mass exchangers for sorption cooling systems,” no. October, 2020.
- [22] H. Bahrehmand, M. Ahmadi, and M. Bahrami, “Analytical modeling of oscillatory heat transfer in coated sorption beds,” *Int. J. Heat Mass Transf.*, vol. 121, pp. 1–9, 2018.
- [23] W. D. Wu, H. Zhang, and D. W. Sun, “Mathematical simulation and experimental study of a modified zeolite 13X-water adsorption refrigeration module,” *Appl. Therm. Eng.*, vol. 29, no. 4, pp. 645–651, 2009.
- [24] N. Wakao and S. Kagei, *Heat and mass transfer in packed beds*, vol. 1. Taylor & Francis, 1982.
- [25] K. Fayazmanesh and M. Bahrami, “Consolidated composite adsorbent containing graphite flake for sorption cooling systems,” 2017.
- [26] H. Bahrehmand, M. Khajepour, and M. Bahrami, “Finding optimal conductive additive content to enhance the performance of coated sorption beds : An experimental study,” *Appl. Therm. Eng.*, vol. 143, no. May, pp. 308–315, 2018.
- [27] H. Bahrehmand, M. Khajepour, and M. Bahrami, “Finding optimal conductive additive content to enhance the performance of coated sorption beds: An experimental study,” *Appl. Therm. Eng.*, vol. 143, no. July, pp. 308–315, 2018.
- [28] R. I. Soloukhin and O. G. Martynenko, “Unified analysis and solutions of heat and mass diffusion,” *International Journal of Heat and Mass Transfer*, vol. 28, no. 9. p. 1791, 1985.
- [29] M. D. Mikhailov and M. N. Özişik, “Transient conduction in a three-dimensional composite slab,” *Int. J. Heat Mass Transf.*, vol. 29, no. 2, pp. 340–342, 1986.
- [30] M. D. Mikhailov and N. L. Vulchanov, “Computational Procedure for Sturm-Liouville Problems,” *J. Comput. Phys.*, vol. 50, pp. 323–336, 1983.

Experimental Investigation of a Gas Driven Absorption Heat Pump and In-Situ Monitoring

Camila Dávila^{1*}, Nicolas Paulus¹ and Vincent Lemort¹

¹University of Liège, Thermodynamics Laboratory, Liège, Belgium

*Corresponding author: cdavila@uliege.be

Abstract

This work describes the methodology used to realize a performance analysis of an ammonia-water condensing gas absorption heat pump. This heat pump shows a nominal heating output of 18,9 kW for outdoor temperature of 7°C and delivery temperature of 35°C, and it is designed for domestic hot water and heating production. The experimental results obtained in the laboratory are contrasted with those obtained from the monitoring of two residential facilities in the northern part of Belgium. The experimental tests were carried out in a climatic chamber to simulate different outside climatic conditions regarding temperature and humidity; different tests conditions were imposed based on a combination of the EN 12309 requirements and typical Belgium weather data. Measures of gas consumption, electrical consumption, water flows and temperatures were collected to compute performance indicators. On the other hand, the monitoring data was analyzed and contrasted with the experimental results to determine the effect of different variables over the system performance. The differences found are described and discussed.

Keywords: Gas Heat Pump, Absorption, Experimental, Monitoring.

Introduction/Background

International commitments related to energy use, environmental impact and decarbonization goals are increasingly restrictive and ambitious. The COP21 objectives signed in 2015 in Paris to limit global warming to 2 K above pre-industrial levels have encourage commitments at both national and regional levels. Without going any further, in Belgium at the end of 2020 the Walloon Region has legally acted that the reduction of its territorial greenhouse gas emissions should reach at least 95% compared to the 1990 levels by the year 2050 [1].

To achieve these goals, a more detailed analysis in terms of energy consumption and final energy use is necessary in order to focalize the efforts. Is in this line that the building sector has been pointed as one of the key areas in the matter; in 2017, the household sector represented 30% of the final use of energy consumption in the European Union (EU), only being surpassed by the industrial sector [2]. Furthermore, 80% of the energy used in the residential sector was destined for domestic hot water (DHW) and space heating (SH) production.

It is here where heat pumps represent an interesting topic. Studies have shown that heat pumps are a good alternative to reduce the energy consumption and CO₂ emissions, of which a significant part is destined to buildings in Europe [3-5]. Between 2005 and 2018, the use of heat pumps in the heating sector in the EU represented an increase in energy consumption of 8.3 Mtoe, surpassed only by the use of solid biomass [6]. Related to this and according to 2016 data, the energy consumption in dwellings in Belgium destined just to space heating and water heating represented 1.52 Mtoe [7], where the consumption of natural gas represented a 45.6% of the total energy consumption followed by electricity consumption (29.7%) [8].

An attractive alternative to traditional appliances is gas absorption heat pumps (GAHP) since thanks to the competitive price of gas, it offers substantial cost and energy savings compared to conventional commercially available systems for water heating [9]. However, the correct integration, sizing, and control of the system is of vital importance to not negatively affect the COP [10].

In this work, an experimental analysis of a gas driven absorption heat pump was conducted. Different outdoor ambient conditions regarding temperature and humidity were emulated in the laboratory to characterize its behavior and to estimate performance indicators. Besides, the system has been installed and monitored quite exhaustively in two residential houses in the northern part of Belgium for the whole year 2020. The results obtained in the laboratory and in the field are compared, finding differences in the behavior of the systems.

Description of the system

Designed for space heating and domestic hot water (DHW) for residential applications, the tested gas absorption heat pump (GAHP) has a nominal heating capacity of 18.9 kW. The system is based on the Water-Ammonia absorption cycle using outdoor air as renewable energy source (low-temperature heat source) and natural gas combustion as high-temperature heat source; the delivered hot water is the medium-temperature heat sink. The working principle of the system is represented in the diagram shown in Figure 1.

To heat the absorbent-refrigerant solution in the Generator (GEN), a Burner (BRN) driven by natural gas is used. The heat delivered to the GEN causes the separation of the two components of the solution by desorption. The desorbed ammonia vapor leaves the GEN and passes through the Rectifier (REC) to remove the last parts of water that could remain. Then it continues to the Condenser (COND), transferring the heat of the refrigerant to the water destined to the Heating Circuit (HC) e.g., radiators, floor heating or others. The water is previously Pre-Heated in a heat exchanger (PH) by the combustion gases and is impulsed by the Water Circulation Pump (WP).

To reduce its pressure, the refrigerant leaving the COND is throttled by means of a restrictor valve and cooled down inside the Pipe in Pipe heat exchanger (PiPHx); then, by means of a second restrictor valve, is brought to the ideal pressure and temperature conditions before entering the Evaporator (EVAP) where the liquid refrigerant is evaporated by taking heat from the surrounding air. Then, the low-pressure vapor ammonia is overheated in the PiPHx before being sent to the Solution Cooled Absorber (SCA), where it meets the poor refrigerant solution coming from the GEN. The pressure of the incoming solution is reduced by a third restrictor valve.

Since the absorption process it is an exothermic reaction, the solution is sent to the Water Cooled Absorber (WCA) where a considerable amount of thermal energy is transferred to the water of the heating circuit. Once the absorption is completed, the solution is pumped back to the GEN using a Solution Pump (SP).

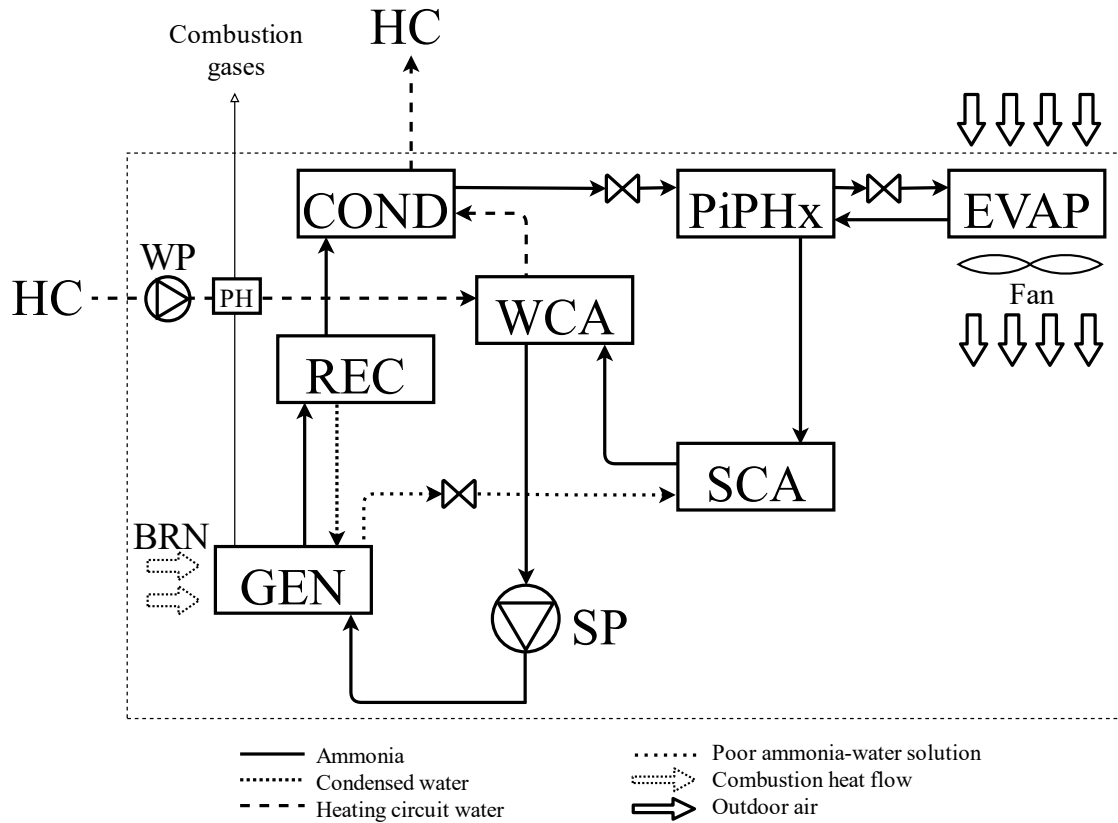


Figure 1. Gas absorption heat pump schematic

Description of the test bench

The system is an outdoor unit, thus, it is installed and the tests are performed in a climatic chamber to vary and control the temperature and humidity conditions. The test bench facilities are shown in Figure 2.

The appliance needs to be supplied by electricity and natural gas, consumptions that are measured. To emulate a heat demand of a house, a heat exchanger is placed in the room adjacent to the climate chamber where the load is regulated by controlling the chilled-water flow rate through the exchanger. The products derived from the operation of the system such as combustion gases, condensate and hot water are removed from the test bench.

The room temperature is decreased by means of an outdoor air-to-water heat pump unit located inside the chamber. The humidity of the room is reduced by water condensation in the evaporators of both units and drawn off of the chamber. Once the temperature and humidity setpoints are reached, a steady state is maintained by means of an electrical heater and a humidifier. These latter are connected to an acquisition system and controlled by a PI controller which receives the signal of temperature and humidity sensors placed at the entrance of the evaporator.

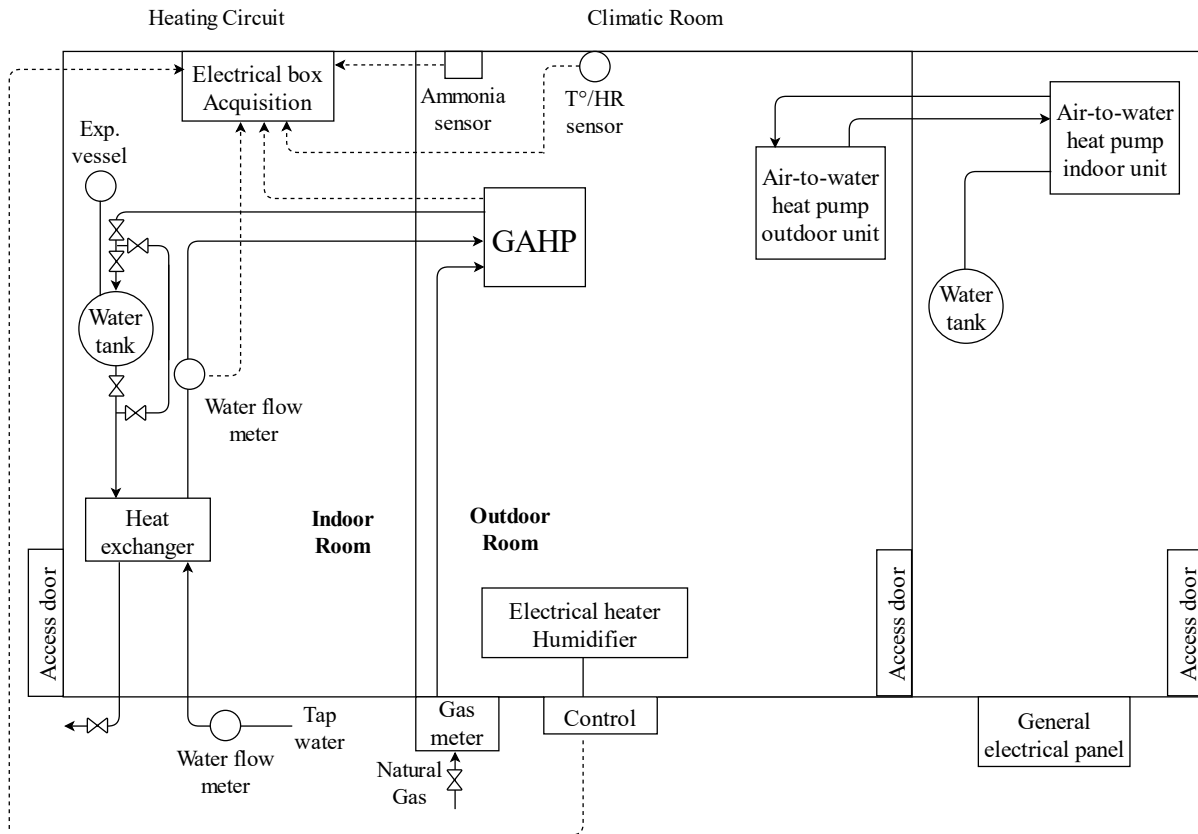


Figure 2. Schematic of the test bench used to characterize the absorption heat pump

In terms of measuring devices, inside the heat pump only surface thermocouples were installed on the different pipes between the components. These thermocouples were placed on an electro-insulating and thermo-conductive sheet, fixed with plastic clamps and insulated at each measurement point to ensure thermal contact and correctly measure the fluid temperature. On the rest of the test bench, in-pipe thermocouples were used. In the cases where the temperature of a large cross-section had to be measured, a grill of thermocouples was used; more precisely, 4 equidistant thermocouples were installed at the fan exhaust and 9 at the evaporator supply. Measurements of gas consumption, water consumption, electrical consumption, room temperature and humidity are also collected.

For caution and since the unit works with an ammonia-water solution that is harmful for health, an ammonia sensor was installed close to the unit to detect leaks and release pipe was installed to extract the ammonia out of the room if necessary. The measuring devices and their characteristics are summarized in Table 1.

Table 1. Measuring devices

Sensor	Type	Accuracy	Number of measure points
Thermocouples	T	± 0.3 K	45
Humidity	Capacitive - wettable	± 2 %	2
Water meter	Volumetric	± 2 % Q_n ; ± 5 % Q_{min}	1
	Magnetic	± 0.5 % from 0.3 to 11.89 m/s	1

Gas meter	Diaphragm	$\pm 0.5 \%$	1
Power meter	Multifunctional	$\pm 0.5 \%$	1
Ammonia sensor	Electrochemical	$\pm 5 \text{ ppm}$	1

Testing conditions

The gas absorption heat pump has certain operating parameters that are supplied by the manufacturer and some of these are modifiable. A display board gives access to different menus and to facilitate the characterization of the system, some of them are changed as described hereunder.

First, it is sought to maintain a constant water temperature difference between the delivery and the inlet of the appliance. To achieve this, the modulation of the circulation pump is activated and the water ΔT° is set to 10 K.

Second, it is necessary to set the permissible delivery and return water temperature range of the appliance to not restrict the system's behavior. In other words, a wide enough water temperature range allows to not operate, for example, at partial load. Therefore, the delivery water temperature range is set between 30°C and 75°C, while the return range goes between 20°C and 30°C.

Third, the control method of the delivery water temperature should be set. This can be done by a variable water setpoint which depends on the outdoor temperature (weather compensated control) or by means of a fixed setpoint. The latter method is used, coinciding with the maximum delivery water temperature set (75°C) and having the option of modifying it if necessary.

Finally, it is possible to establish a power output control of the system allowing the modulation of the burner or based on a "On/Off" behavior. The first option is chosen, having as a consequence a modulation of the gas flow on the burner side, while in the absorption cycle it is reflected in variations in the fan and water circulation pump drive voltage.

The described adjustable parameters configuration is shown in Table 2.

Table 2. Adjustable parameters configuration

Description	Setting
Modulation of circulation pump	Active
Heating circuit water ΔT° setpoint	10 K
Power modulation	Active
Delivery water temperature range	From 30 K to 75 K
Delivery water temperature setpoint	From 45K to 75 K
Return water temperature range	From 20 K to 30 K

The performed test matrix is shown in Table 3. the test campaign is based on the EN 12309 [11] regarding the test conditions at full load refer to the type of appliance (e.g., air-to-water, water-to-water), its application (e.g., low/medium/high temperature), the outdoor heat exchanger conditions referring to dry-wet bulb temperatures and the classification of the climate (e.g., medium, warm, or cold).

To consider the weather conditions to which the appliances are subjected in the field in terms of temperature and humidity, a weather data analysis was made for the cold season from October 2018 to March 2019 based on two local weather stations close to systems [12].

Based on these two aspects, the performed test matrix is shown in Table 3. Here, five outdoor air-dry bulb temperatures and four water delivery temperatures are tested. This base matrix is performed for a relative humidity of 75% since it is the most frequent value obtained from the weather data analysis. Every test is performed at full load on steady state for a period of 20 minutes. The test conditions are monitored throughout the test with a smartphone connected to the appliance besides the test bench data acquisition system.

Table 3. Gas absorption heat pump test matrix

		Water delivery Temperature [°C]			
		35	45	55	65
Outdoor dry bulb Temp.[°C]	12	75%			
	7				
	2				
	-7				
	-10				

Monitoring

The system is installed in two residential houses in the northern part of Belgium. The two houses are considered to be in the same climatical region. These locations have sensors that provide information equivalent to the one obtained in the laboratory to analyze the system's inputs and outputs, allowing to estimate efficiencies and utilization costs among others. The data collected is daily sent to the Cloud for later analysis.

The sites named Brasschaat and Brecht are equally monitored. The used sensors are identical and are placed at the same spots, as can be seen in the installation schemes shown in Figure 3 and Figure 4, respectively.

Both installations count with sensors to measure indoor and outdoor ambient conditions, as well as gas and electric meters to measure the consumptions of the system. A heat meter is installed between the inlet and outlet pipes of the machine to measure the heating energy delivered by the system based on the measurement of the water flow that circulates through the circuit and its respective inlet and outlet temperatures.

The monitored houses count with a water tank for domestic hot water and heat storage. In both sites, the space heating is based on the use of radiators. Additionally, Brasschaat's site has thermal solar panels and an extra buffer for DHW storage, adding complexity to the installation. The heat produced by gas absorption heat pump is directed towards one or the other tank depending on whether the demand is for space heating or DHW.

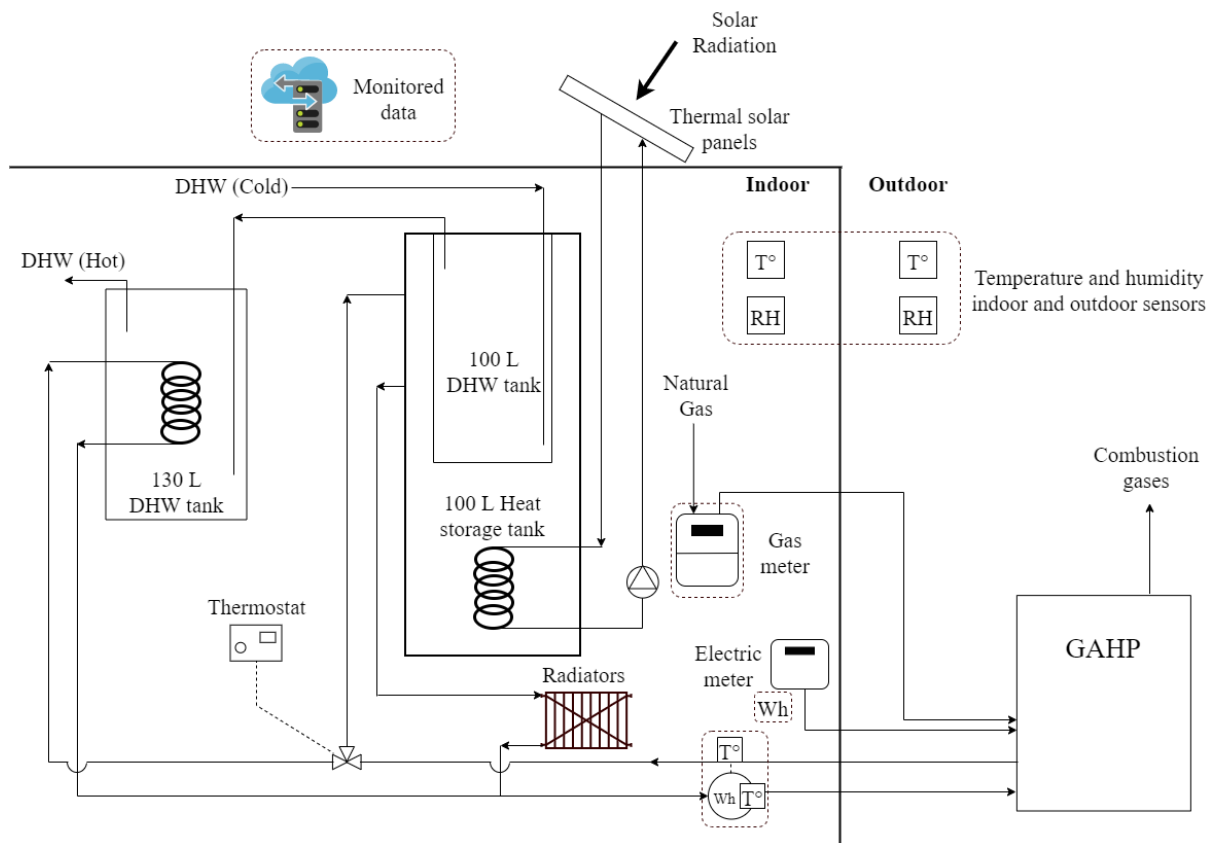


Figure 3. Installation scheme of Brasschaat monitoring site

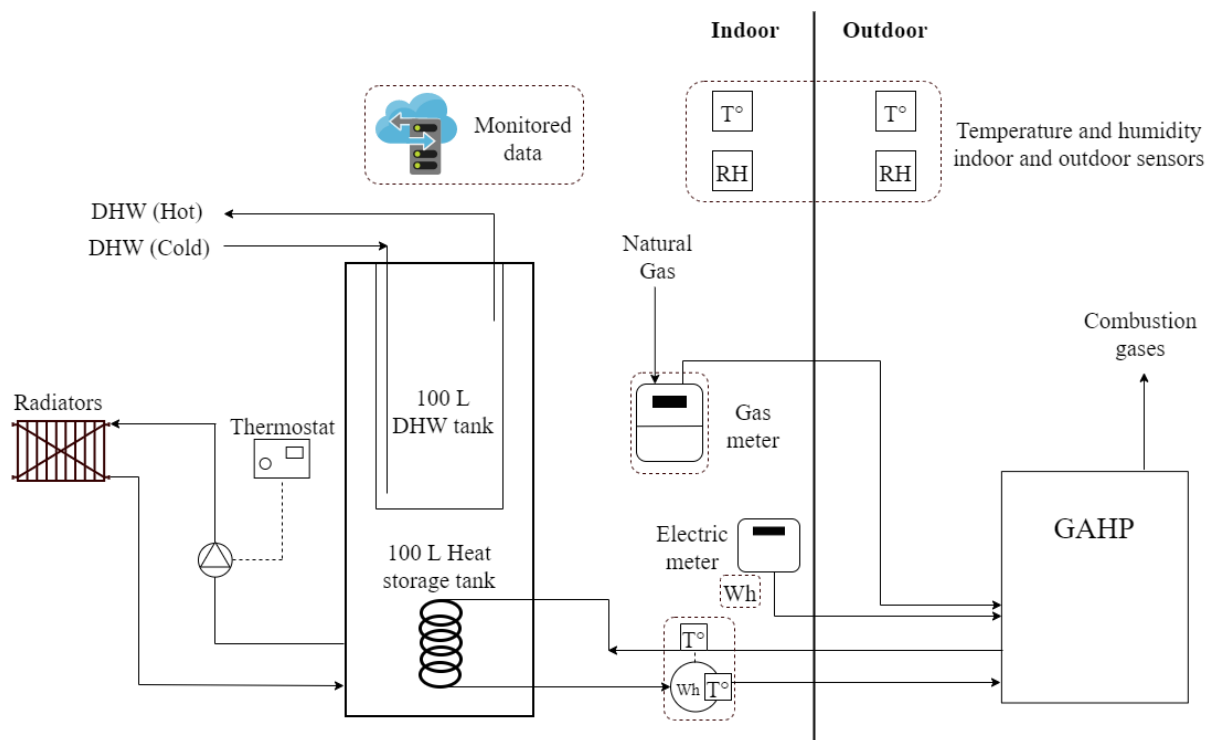


Figure 4. Installation scheme of Brecht monitoring site

The sensors references, their precision and resolution of the acquired data are presented in Table 4.

Table 4. Sensors used at monitored sites

Sensor	Reference	Resolution*	Precision
External temperature and humidity	Weptech Munia	0,1 K 0,1 %	± 0,3 K ± 2 %
Internal temperature and humidity	Weptech Munia	0,1 K 0,1 %	± 0,3 K ± 2 %
Heat counter	Qalcosonic E1	1 kWh 1 L 0,1 K	Accuracy Class 2 [13]
Machine electrical energy counter	Iskraemeco ME162	1 Wh	Accuracy Class 1 [14]
Gas volume counter	Elster BK-G4T	10 L	<1%
Data logger (cloud connection)	Viltrus MX-9	-	-

* *Data logger included*

It is worth mentioning that some control and internal parameters of the systems such as power modulation or temperature setpoint are not remotely controlled or monitored. This means that changes or modifications made by the user or installer could not be communicated, being difficult or impossible to identify only with the data analysis. A constant monitoring is carried out, without guaranteeing that no omissions occurred that could potentially affect the monitoring data and its subsequent analysis.

Results

- **Laboratory**

A valid data collection period is defined on the European standard based on the coefficient of change shown in Equation (1). If this coefficient remains within 2.5% during the data collection period, then the test can be considered as steady state. This coefficient is the difference between the outlet and the inlet temperatures of the heat transfer medium at the indoor room heat exchanger and should be calculated every 5 minutes starting at the end of the previous period ($\tau = 0$).

$$\% \Delta T = \frac{\Delta T_{i(\tau=0)} - \Delta T_{i(\tau)}}{\Delta T_{i(\tau=0)}} * 100 \quad (1)$$

Where $\% \Delta T$ is the coefficient of change, in %; $\Delta T_{i(\tau=0)}$ is the average difference between the outlet and the inlet temperatures for the first 5 min. period; $\Delta T_{i(\tau)}$ is the average difference between the outlet and the inlet temperatures for other 5 min. period than the first 5 min.

In addition, allowable deviation values from the set values are established. This corresponds to $\pm 0.3\text{K}$ for room temperature, $\pm 2\%$ for room mean humidity and $\pm 1\text{K}$ from the setpoint for the depart water temperature.

The *COP* (also called *efficiency* in the monitoring section) for each test was estimated as the ratio between the thermal power output to heat and electric power input as defined in Equation (2).

$$COP = \frac{\dot{Q}_{HC}}{\dot{Q}_{gas} + \dot{W}_{in}} \quad (2)$$

The thermal power output corresponds to that given to the heating circuit \dot{Q}_{HC} while the inputs are the thermal heat obtained from the natural gas combustion \dot{Q}_{gas} and the electric input to the appliance \dot{W}_{in} . The thermal power transferred to the water is defined in Equation (3).

$$\dot{Q}_{HC} = \dot{Q}_{WCA} + \dot{Q}_{cond} + \dot{Q}_{gases} \quad (3)$$

Where \dot{Q}_{WCA} , \dot{Q}_{cond} and \dot{Q}_{gases} are the thermal powers obtained from the water cooled absorber, the condenser, and the combustion gases, respectively.

Since the internal configuration of the system makes it difficult to install sensors between components that allows to measure the previously defined heat inputs individually, it is decided to estimate the heat input transferred to the water as defined in Equation (4).

$$\dot{Q}_{HC} = \dot{m}_{HC,w} * c_{p,w} * (T_{out} - T_{in}) \quad (4)$$

Where $\dot{m}_{HC,w}$ heating circuit water flow, $c_{p,w}$ is the specific heat of water, T_{out} and T_{in} are the outlet and input water temperatures of the system. Similarly, the heat input is defined in Equation (5).

$$\dot{Q}_{gas} = \dot{V}_{gas} * HCV \quad (5)$$

Where \dot{V}_{gas} is the consumed gas flow and *HCV* is the daily average high calorific value. The electric consumption of the appliance \dot{W}_{in} is constantly registered and considered on the results, with maximum variations of 2% between tests and close to 0.35 kW. This consumption includes components such as the fan, oil pump, water circulation pump and sensors.

With these considerations, the results obtained for the test matrix are shown in Table 5. The results are computed meeting the requirements of Equation (1) and are based on the average values of the measurements carried out during a 20-minute test.

Table 5. COP and Thermal Capacity values at a relative humidity of 75%

COP		T° delivery			
		35	45	55	65
Outdoor T°	12	1.45	1.34	1.19	1.05
	7	1.38	1.29	1.13	1.04
	2	1.36	1.21	1.09	0.95
	-7	1.21	1.13	1.02	0.86
	-10	1.16	1.14	0.95	0.86

Th. Capacity [kW]		T° delivery			
		35	45	55	65
Outdoor T°	12	21.11	19.31	16.98	14.82
	7	19.55	18.57	16.30	14.92
	2	20.10	18.01	15.64	13.70
	-7	18.33	16.89	15.13	12.65
	-10	17.36	16.82	14.14	12.66

- **Monitoring**

Both sites were exhaustively monitored during 2020. Their monthly efficiencies for the whole year based on the high calorific value are shown in Figure 5. Unlike laboratory results, here the electrical consumption is not included; its effect, however, will only penalize the displayed values.

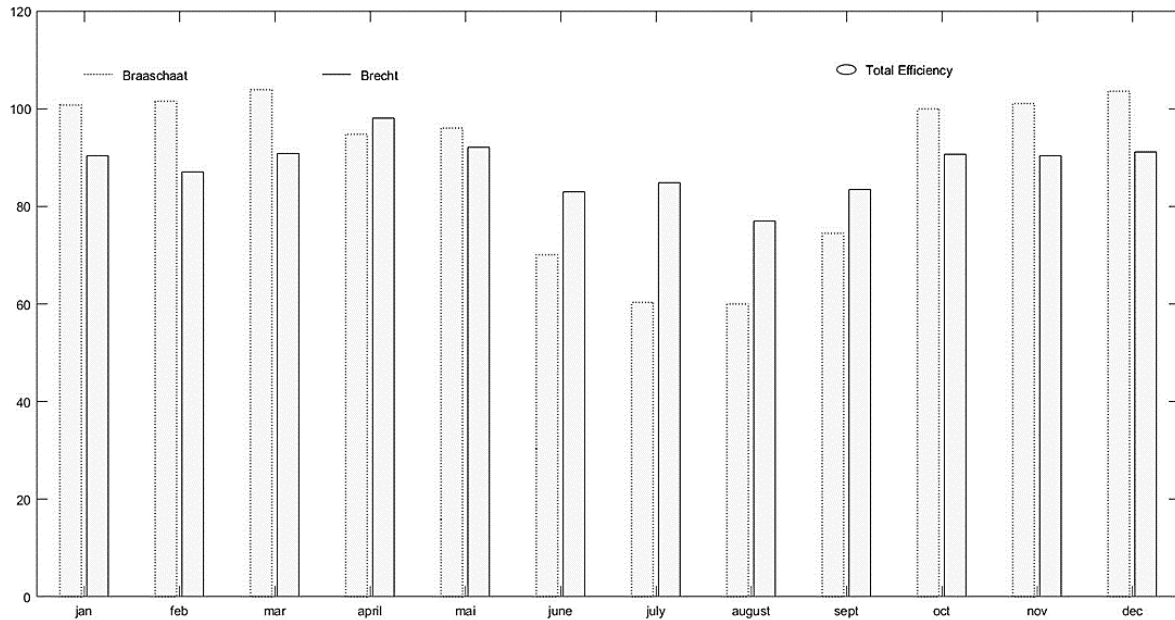


Figure 5. Monitored GAHP's monthly efficiencies

A clear seasonal effect can be observed, showing a penalty in the efficiency during summer that is related to the fact that the systems are less frequently used (no space heating request), generating more on/off cycles to supply only the production of DHW. In this sense, a greater impact is observed in Braaschaat site. This can be partially explained by the coupling of the thermal solar panels and their effect on the working temperature, inducing a change in the behavior of the system. However, these results are far from the ones expected and obtained in the laboratory, especially for winter conditions. Even more, unexpected large differences are observed between the performances of both machines.

To try to explain the differences, an in-depth analysis of the behavior of both systems was carried out. Figure 6 shows the daily thermal production of both sites in relation to their efficiency. Even though Brecht produces more thermal energy compared to Braaschaat, the system is less efficient.

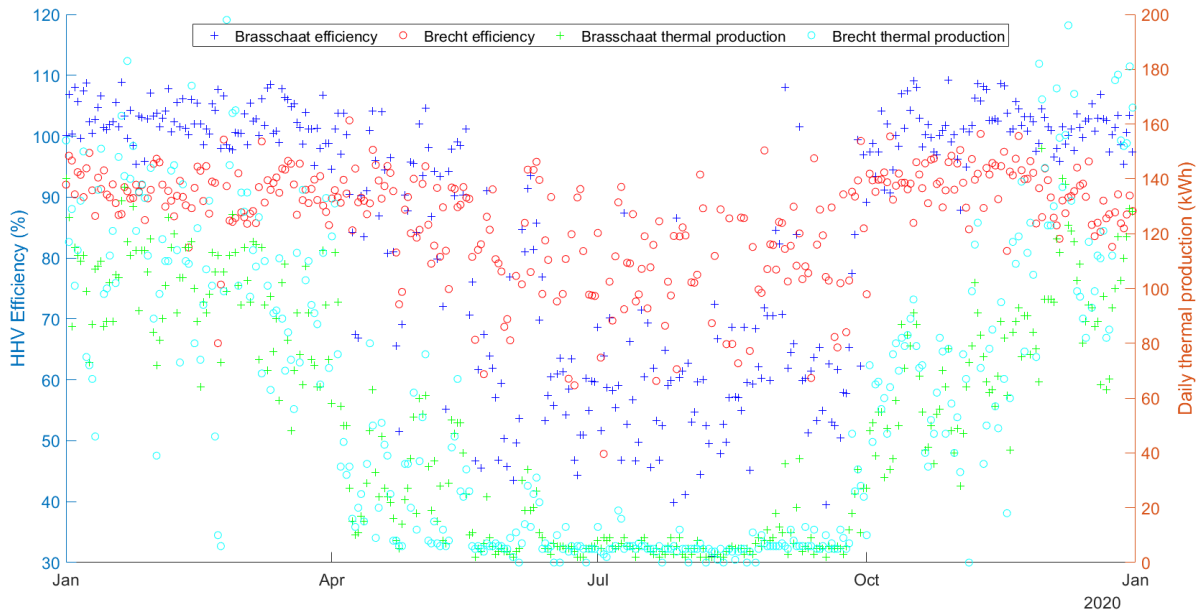


Figure 6. Monitored GAHP's daily thermal production

On the other hand, the daily thermal production is related to the way in which the production of the system is controlled (i.e., On/Off or modulation). Since this information is unknown and is not part of the data collected from the monitoring, a deeper look to try to establish a relationship between the smoothness of the behavior of the system and the electrical consumption is made in Figure 7. Here, Brecht has a higher electrical consumption, thus the machine is working for a longer amount of time which could be related to a smoother behavior; this information though is not conclusive to explain the differences found.

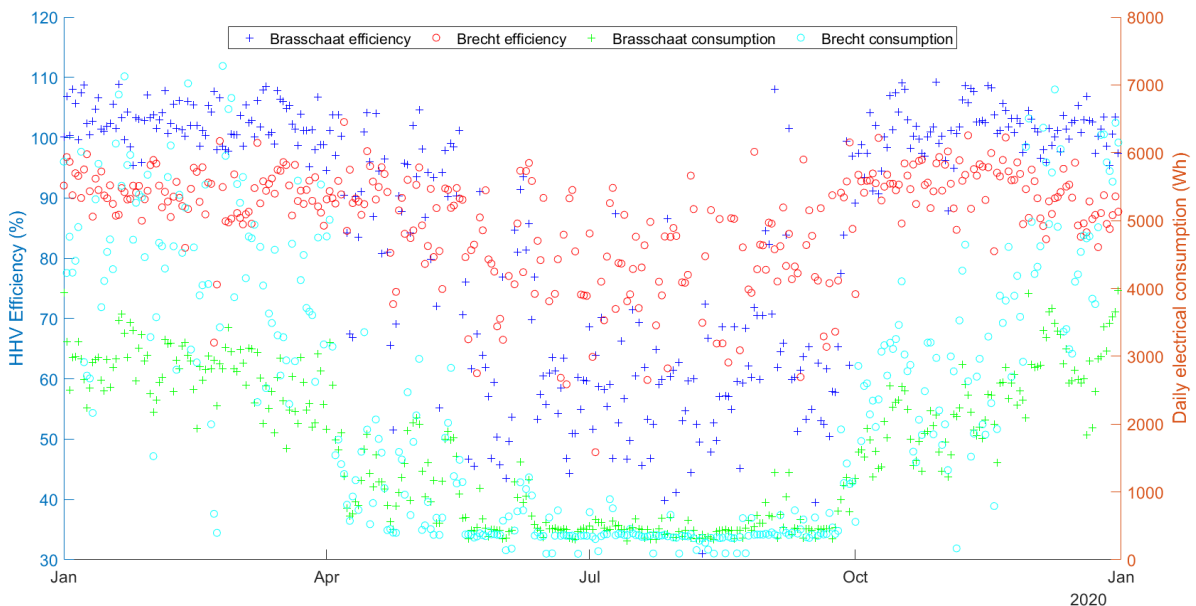


Figure 7. Monitored GAHP's daily electrical consumption

It is noticed that the working temperature of both systems is different as can be seen in Figure 8. Here, it is observed that Brasschaat site does not overpass 40°C of return temperature, while Brecht has a scattered behavior. It is expected that for the temperature range between 30°C and 40°C the systems will operate under similar conditions and therefore, similar efficiency results will be obtained. Despite this, a gap of approximately 10 percentage points is clearly visible.

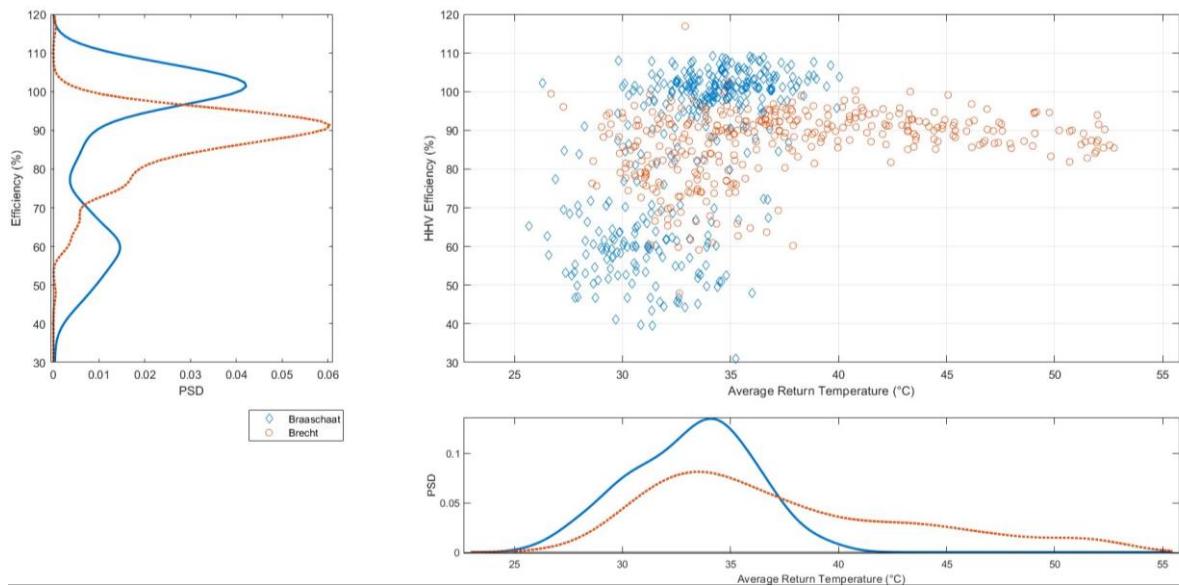


Figure 8. Monitored GAHP's average return temperature

Conclusions

An experimental investigation of a gas absorption heat pump has been conducted where coefficients of performance have been calculated both in the laboratory and in the field, finding discrepancies between them being the latter lower than the former.

The results obtained in the laboratory confirm the expected trends, with an efficiency that increases as the ambient temperature increases and decreases if the water outlet temperature is higher. Besides, the orders of magnitude obtained correspond to those indicated by the manufacturer for the specified conditions. For the monitored systems, a seasonal effect is clearly observed with total efficiency drops during the summer, with both machines showing not negligible differences between them of at least 10 percentage points on their performance values.

Even though the number of machines tested in this study is far from being sufficient to be statistically representative, it is possible to cross-check valid information between laboratory results and on-site monitored data to make a comparison between the three available systems. However, the information obtained by the monitoring data does not allow to provide a conclusive explanation to the observed differences, being necessary to obtain more information regarding the different adjustable settings of the appliances and the quality of the installation.

Even though the conditions in the field are far from being stationary, an attempt has been made to find some small timeframes for which the machines were submitted to almost stationary conditions regarding external temperature, delivery and return temperature, power output and humidity. A comparison has been made by performing a double linear interpolation within the efficiency matrix obtained in the laboratory to fit the field test conditions, obtaining the results shown in Table 6.

Table 6. Steady state field test conditions and efficiency comparison

	Brasschaat	Brecht
Date and time	10/02/2021 – 16h	10/02/2021 – 14h
Duration of the timeframe of stationary conditions	85 min	140 min
Delivery temperature (°C)	51.25	57.77
Return temperature (°C)	39.1	50
Humidity	0.8	0.79
Outdoor temperature (°C)	-1.8	-1.2
Field test COP (HCV)	1.108	0.837
Double linear interpolation COP (HCV)	1.104	1.024

From here, it is possible to establish *a priori* a correlation between the Brasschaat site and the laboratory results for these specific conditions, but not for the Brecht site. Thus, a more detailed analysis of this facility is required to determine what is the cause of the observed discrepancies, highlighting the main role of the correct integration and control of the system in the performance of the latter.

Acknowledgements

The authors thank Gas.be for the financial support to this research project.

References:

- [1] Service public de Wallonie, “20 Fevrier 2014. - Décret "Climat", Moniteur belge du 10-03-2014 page : 20402, 2014.
- [2] European Environment Agency, “Final energy consumption by fuel type and sector” Retrieved from Growth in renewable energy use by technology and sector 2005-2018, 2020.
- [3] N. Aste, R.S. Adhikari, M. Manfren., “Cost optimal analysis of heat pump technology adoption in residential reference buildings” Renewable Energy, 2013.
- [4] M.B. Blarke., “Towards an intermittency-friendly energy system: Comparing electric boilers and heat pumps in distributed cogeneration”, Applied Energy, 2012.
- [5] K.J. Chua, S.K. Chou, W.M. Yang., “Advances in heat pump systems: A review”, Applied Energy, 2010.
- [6] European Environment Agency, “Growth in renewable energy use by technology and sector, 2005-2018”, Retrieved from Final energy consumption by fuel type and sector, 2020.
- [7] European Environment Agency, “Energy consumption by end use per dwelling”, Retrieved from Energy consumption by end use per dwelling, 2016.
- [8] European Environment Agency, “Total final energy consumption by sector in the EU-27, 1990-2010”, Retrieved from Total final energy consumption by sector in the EU-27 1990-2010, 2013.
- [9] Keinath, C. M., & Garimella, S., “An energy and cost comparison of residential water heating technologies”, Energy, 2017.

- [10] Fumagalli, M., Sivieri, A., Aprile, M., Motta, M., & Zanchi, M., “*Monitoring of gas driven absorption heat pumps and comparing energy efficiency on primary energy*”, Renewable Energy, 2017.
- [11] European Standards, “*Gas-fired sorption appliances for heating and/or cooling with a net heat input not exceeding 70 kW*”, 2014.
- [12] WeatherUnderground, “*Weather Underground*”, 2019.
- [13] International Organization of Legal Metrology, “*Water meters intended for the metering of cold potable water and hot water. Part 1: Metrological and technical requirements*”, 2006.
- [14] International Electrotechnical Commission, “*Electricity metering equipment (a.c.) – Particular requirements. Part 21 : Static meters for active energy (classes 1 and 2)*”, 2003.

3D printed adsorption heat transformer

AL-HASNI. Shihab¹, MANGANO. Enzo¹ and Santori. Giulio^{1*}

¹The University of Edinburgh, School of Engineering, Institute for Materials and Processes, Sanderson Building, The King's Buildings, Mayfield Road, EH9 3BF, Edinburgh, Scotland, UK

*Corresponding author: email address (g.santori@ed.ac.uk)

Abstract

One technical issue with sorption heat transformers (SHTs) for cooling (sorption chillers) is their operation in vacuum that needs machined components and skilled labour, which eventually contributes to their high cost of manufacturing. Alternative production methods that reduce the SHT's cost and weight would be advantageous. This investigation proves the adoption of 3D printing of polymers for SHTs. Manufacturing of complex geometries directly from 3D models, ease of production and lightweight are among the key-advantages of 3D printing. In addition, over the next decade, 3D printing costs are expected to drop by 50% to 75%. This experimental investigation intends to seed and set a benchmark for 3D printed plastic miniaturised adsorption chillers. When operated with silica gel, the 3D printed unit results in a maximum coefficient of performance (COP) of 0.57 at a specific cooling power (SCP) of 299 W kg⁻¹, positioning the present design among the best silica gel adsorption chillers demonstrated to date.

Keywords: 3D printing, Stereolithography, Low grade heat, cooling, sustainability

Introduction

Approximately 72% of the primary energy is lost to the environment [3], with 63% of that being waste heat at temperatures below 60°C [4]. This significant amount of untapped waste heat can be recovered for heating and cooling, hence reducing the greenhouse effect and CO₂ emissions. Sorption heat transformers (SHTs) are sustainable technologies can usefully turn ultralow grade heat <60°C into cooling. SHTs show simple design, minimal number of moving parts and in the majority of cases use water as refrigerant. Despite the enormous potential for emissions reduction offered by SHTs when used as chillers or heat pumps, these technologies are still in the preliminary stages of commercialization [6], [7]. SHTs units now on the market are closer to research and development prototypes than commercial devices and they are offered at costs that are incomparably higher than those of vapour compression systems [8], [9]. One technical difficulty with sorption chillers is their operation in vacuum. This necessitates machined components and skilled labour for manufacturing, which ultimately contributes to their high selling price. Because of the strict vacuum requirements, stainless steel parts are often used to construct sorption heat transformers. Therefore, an alternative production strategy to reduce the SHT's cost and weight would be advantageous. This work assesses the use of 3D printing as an alternative production method. The SHT sector could benefit from the drop by 50% to 75% that 3D printing costs are expected to over the next decade [10]. The feasibility of 3D printing vacuum and pressure tight polymer vessels for heat-powered chillers and heat pumps has been previously investigated in [11] that shown how stereolithography (SLA) 3D printing can produce vessels with no pores that meet the SHT's stringent vacuum tightness requirement. Previous research has thoroughly investigated the performance of conventionally manufactured sorption heat transformers [12]–[15]. However, no research has investigated the use of alternative manufacturing methods, such as 3D printing, to produce adsorption chillers. The 3D printed unit in this investigation uses silica gel that is one of the most often used adsorbent materials for adsorption chillers due to its ability to be

regenerated with temperatures $< 60^{\circ}\text{C}$ [16]. This helps to compare the 3D printed unit with the data available from other silica-gel designs produced with conventional methods.

Materials and Methods

Experimental set-up design, manufacture

Three 316L stainless steel water loops (Swagelok, Scotland, United Kingdom) with four solenoid valves (Connexion Developments Ltd, England) are connected to the system's for the purpose of transporting deionized water from the thermostatic baths to the chiller's heat exchangers (RC Racing Radiators, Italy). Rotameters are used to regulate the water flow rate (Nixon Flowmeters, UK, 1.6 % accuracy), as shown in Fig. 1 and Fig. 2. Thermostatic baths (Julabo, UK) are equipped with integrated water pumps that distribute water at three temperatures: cold, intermediate and hot, as illustrated in Fig. 1.

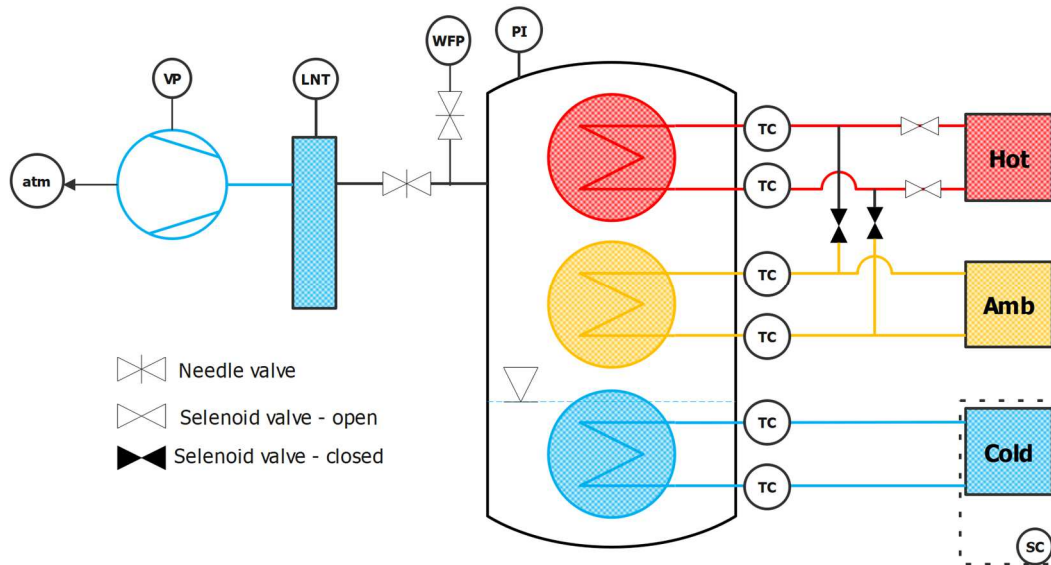


Figure 1: The apparatus used in this study and coupled to the 3D printed adsorption heat transformer. **TC:** Thermocouple temperature sensor; **PI:** Pressure indicator; **WFP:** Water filling point; **LNT:** Liquid nitrogen trap; **VP:** Vacuum pump; **Hot:** Hot water thermostatic bath; **Amb:** Intermediate water temperature thermostatic bath; **Cold:** Cold thermostatic bath; **SC:** Space cooling.

The thermostatic baths maintain three distinct temperatures: desorption at temperature (maintained in this investigation $< 60^{\circ}\text{C}$), adsorption/condensation at $20\text{-}30^{\circ}\text{C}$, and evaporation at $10\text{-}27^{\circ}\text{C}$. Prior to each experiment, the 3D printed adsorption heat transformer is vented using a vacuum pump preceded by a liquid nitrogen trap to protect the vacuum pump's sensitive and expensive components from irreversible damage caused by water vapour. A needle valve is used to maintain vacuum pressure while filling the 3D printed adsorption heat transformer with deionized and bubble-free water. Thermocouples are installed in the centre of the connecting tubes, at the entry and exit of the micro heat exchangers, to monitor the temperature of the entering and exiting heat transfer fluids, respectively. A heavy-duty vacuum sensor is installed to measure the pressure within the 3D printed heat transformer. The T-Type thermocouples (Omega Engineering, USA, 0.4 % accuracy) and pressure indicator (WIKA Alexander Wiegand SE & Co. KG, Germany, 0.25 % accuracy) are controlled by a LabVIEW data acquisition and control programme executed on a PC via a data acquisition board (Advantech Co. Ltd., USA) and the Modbus communication protocol (National Instruments Corp., USA).

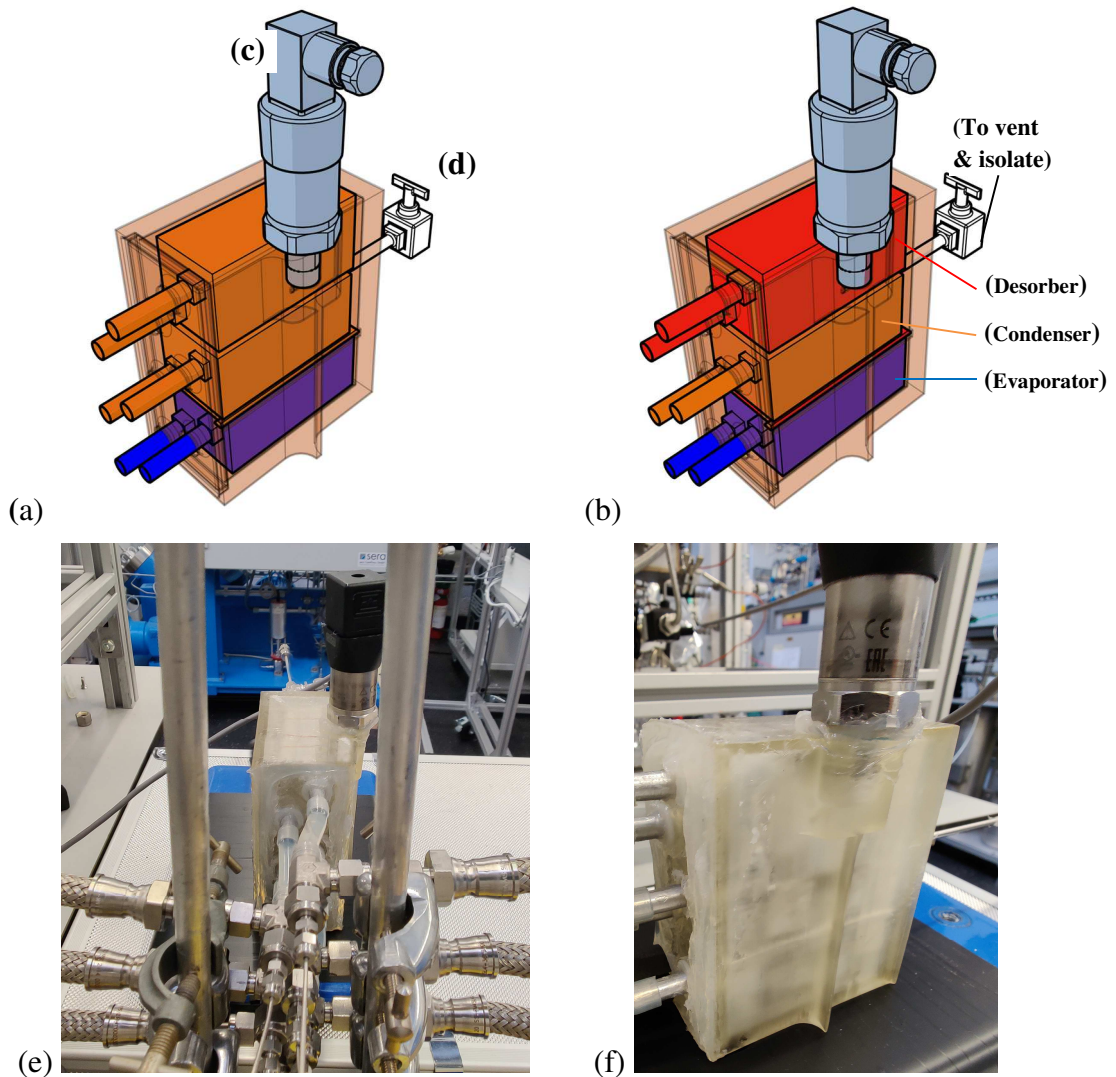


Figure 2: The single-bed miniature sorption heat transformer (a) Adsorption mode;(b) Desorption mode;(c) Heavy duty Vacuum sensor WIKA-S20; (d) Stainless Steel Integral Bonnet Needle Valve Swagelock-SS-OKS2; (e)&(f): Overviews of the real 3D printed adsorption heat transformer under testing. The red colour indicates that the desorber is connected to the heat source, the orange colour indicates that the adsorber/condenser is connected to the cooling source for heat rejection, and the blue colour indicates that the evaporator is connected to the chilled source.

The SL1 commercial SLA 3D printer was used to fabricate all plastic components in this study (Prusa Research, Czech Republic). The microscale SHT displayed in Fig. 2 and Fig. 3a has an internal volume of 355 cm³ and is designed to recover heat between 30 and 60°C. A silicone acetoxo rubber sealant (Dow Corning 732 Multi-Purpose Sealant, USA) is utilised to seal the connection between 3D printed pieces such as the vessel and its front cover. The parameters for the 3D printer used to manufacture the micro-heat transformer as well as the resin specification are reported elsewhere [17]. Prior to conducting performance tests, the water was ultrasonically degassed to eliminate any trapped gas bubbles (Branson 2800 cpxh ultrasonic cleaner 2.8 l, Italy). Another critical step is regeneration of the silica gel prior to filling it into the empty heat exchanger (Fig. 3b), which enables precise mass monitoring for performance evaluation. A standard microwave oven with a medium power setting and a 30 second timer to heat the adsorbent material to 80°C. The adsorber heat exchanger was loaded with adsorption material within 30 minutes.

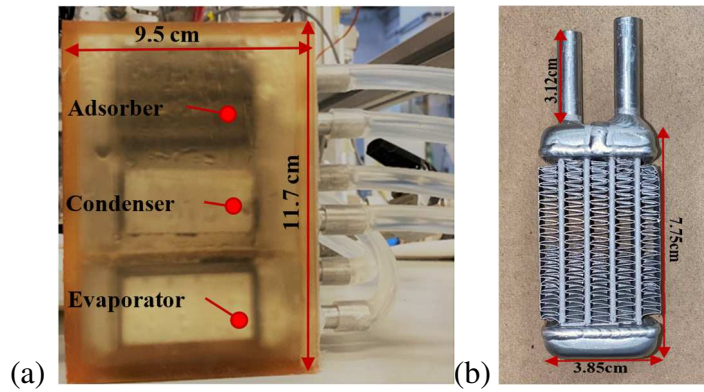


Figure 3: (a) The single-bed miniature heat transformer comprising of evaporator (40.67 g), condenser (45.39 g) and adsorber (47.09 g). The outside dimensions of the 3D-printed micro sorption heat transformer are 11.7 cm X 9.5 cm X 5.4 cm. (b) The outer dimensions of the micro finned heat exchanger employed in this study.

Heat transfer surface area of the empty heat exchanger

The heat transfer surface area of the micro heat exchanger used in this study was accurately determined using a 3D scanning (Einscan Pro, U-create, University of Edinburgh) and the Computer Aided Design software Fusion360, Autodesk. The alignment of the heat exchanger to the Einscan 3D scanner begins with the use of the Einscan turntable. The turntable's 360-degree movement then converts the physical heat exchanger model to a 3D CAD model that can be processed with CAD software using the projected 3D scan rays. The dimension or size of the 3D model was then used to manually verify the designed and obtained dimensions using a Vernier calliper. The 3D scanner precisely sizes the heat exchanger, resulting in a heat transfer area of 0.09295 m^2 , as illustrated in Fig. 4a.

As depicted in Fig. 4b, the Silica-Gel beads are secured inside the micro heat exchanger using a polymer mesh (Plastok Meshes & Filtration Ltd, UK) with a 50% open area. The weight and thermal mass proportions of the micro adsorber are listed in Table 1, which demonstrates that the heat transfer fluid (water) dominates in the thermal mass of the adsorber.

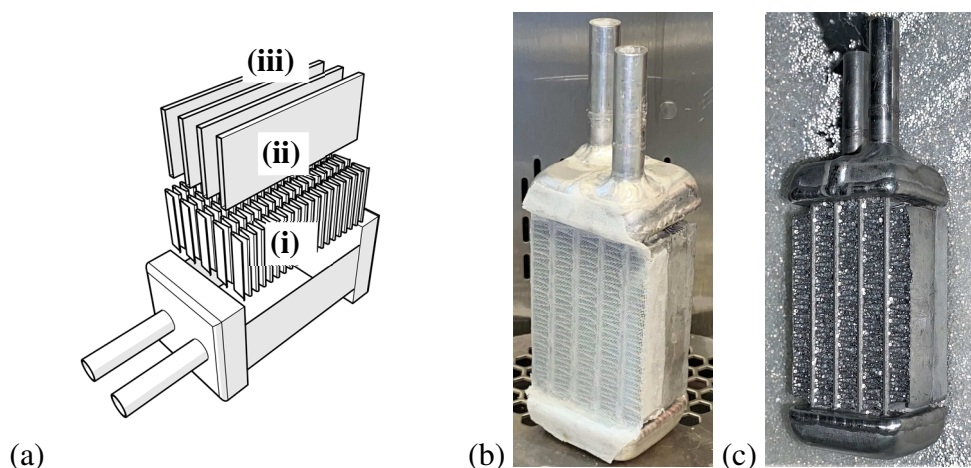


Figure 4: (a) Exploded view of the miniature heat exchanger type and size. (i) base of the miniature heat exchanger with inlet and outlet tubes [0.016876 m^2]; (ii) the miniature heat exchanger fins [0.05433 m^2]; (iii) the heat transfer fluid tubes [0.02174 m^2]. (b) Empty adsorber with bonded mesh. (c) Packed adsorber with silica-gel.

Table (1): Summary of miniature adsorber specifications

Material	Weight [kg]	TM [kJ K ⁻¹]	Thermal mass contribution [%]
Aluminium	0.047	0.043	26%
Water	0.026	0.109	66%
Silica-gel	0.020	0.012	8%
Adsorber	0.093	0.164	

Note: Metal:Adsorbent ratio=2.35

Operation principle of a 3D printed adsorption heat transformer

The classical operation of adsorption chillers happens through four stages:

- 1) isosteric heating: the uptake of the adsorber remains constant during heating;
- 2) desorption and condensation: the uptake decreases at constant pressure;
- 3) isosteric cooling: the uptake of the adsorber remains constant during cooling;
- 4) evaporation and adsorption: the uptake of the adsorber increases during cooling;

The heat transformer depicted in Fig. 2 is a single-bed chiller that produces cold intermittently. However, a second identical unit may be allowed to run in the opposite phase of the first chiller to provide continuous cooling. A significant discrepancy between the operation outlined above and the unit of this investigation is in the stages of operation. The isosteric stages are possible thanks to the separation of evaporator, adsorber and condenser in three distinct vessels. In this investigation, the three units are enclosed in a single vessel, with a consequent change in the cycle thermodynamics. To capture the cooling effect, the tests begin with a fully cold adsorption bed that is allowed to saturate. Following that, the silica-gel is regenerated while cooling and heating water at constant temperature feed the condenser and evaporator inlets. The temperature difference between the heat exchanger's input and output temperature points indicates the amount of energy spent, rejected, or gained.

Evaluation of the performance

The quantity of heating and cooling energy consumed or rejected by a particular heat exchanger connected to the 3D printed adsorption chiller was estimated by accounting for the energy exchanged between the heat transfer fluids (HTF) and metal heat exchangers coupled to the chiller. The Coefficient Of Performance (COP) is defined as the ratio of the cooling effect produced by the evaporator to the total heat input spent throughout the isosteric heating and desorption phases:

$$COP = \frac{\dot{Q}_{evap}}{\dot{Q}_{hot}} \quad (1)$$

Where the cooling effect is as follows:

$$\dot{Q}_{evap} = \dot{m}_{evap} c_{p,w,chill} (T_{evap,in} - T_{evap,out}) \quad (2)$$

Additionally, the total heat input to the device can be determined by the equation:

$$\dot{Q}_{hot} = \dot{m}_{hot} c_{p,w,hot} (T_{hot,in} - T_{hot,out}) \quad (3)$$

The Specific Cooling Power (SCP) can be calculated from:

$$SCP = \frac{(\dot{m}c_p)_{evap} \int_0^{t_{cycle}} (T_{evap,in} - T_{evap,out}) dt}{m_{sorb} t_{cycle}} \quad (4)$$

COP and SCP are dependent on the three inlet temperatures to the evaporator, condenser, and adsorber/desorber. In general, the experimental approach is to hold two inlet temperatures constant while changing the third. This, however, complicates the investigation because two outcomes obtained at in two different sets of temperatures cannot be compared. Núñez et al. overcame this problem by introducing the concept of reduced temperature T_{red} [15]:

$$T_{red} = \frac{T_{cond} - T_{evap}}{T_{hot} - T_{cond}} \quad (5)$$

where (T_{hot} ; T_{cond} ; T_{evap}) are the inflow temperatures of the hot, cold, and chilled water sources connected to the aluminium heat exchangers enclosed inside the vacuum tight 3D printed vessel. T_{red} is a correlation that describes a ratio of the lift force ($T_{cond} - T_{evap}$) to the drive force ($T_{hot} - T_{cond}$). The performance indicators collapse on one single curve when plotted against T_{red} and this is beneficial for system characterisation [7].

Discussion and Results

Pressure and temperature evolution

In a separate study, we demonstrated that SLA 3D printed vessels are vacuum tight by using helium leak testing. SLA can accomplish this result because polymerization occurs homogeneously on a plane and each plane polymerizes while a new layer is forming, resulting in a pore free structure [11]. Fig. 5 depicts the pressure inside the 3D printed adsorption heat transformer during operation, with a leak rate of $2.6 \cdot 10^{-6} \text{ Pa m}^3 \text{ s}^{-1}$ that classifies the unit as vacuum tight [18].

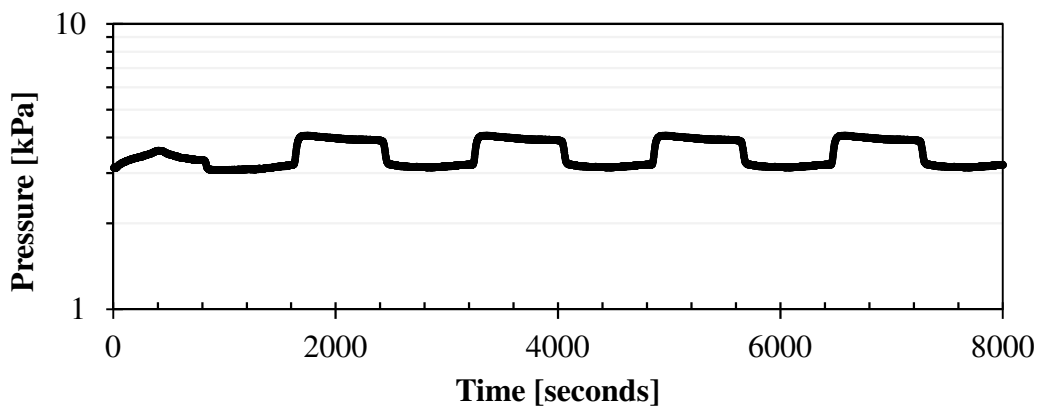


Figure 5: The pressure profile inside the 3D printed adsorption heat transformer at $T_{red} = 0.11$.

The temperature data from the 3D manufactured adsorption chiller at $T_{red} = 0.11$ are shown in Fig. 6. The solid lines in red and yellow indicate the temperature profiles at the adsorber input and outflow, respectively. The maximum desorption temperature was $56 \text{ }^\circ\text{C}$ for longer cycle periods, such as the 800s and 1800s.

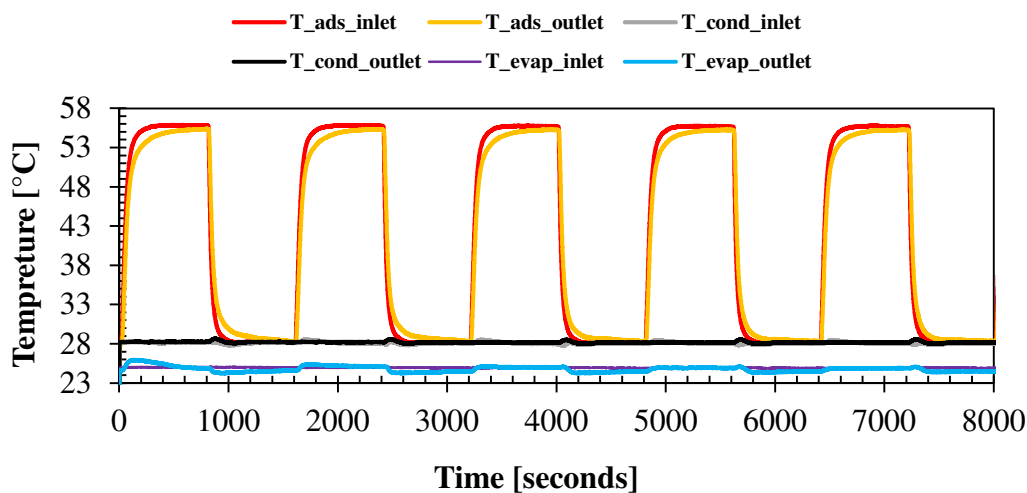


Figure 6: Temperature evolution profiles of the coupled heat exchangers to the 3D printed adsorption heat transformer at $T_{red} = 0.11$.

In steady condition, the adsorber's output temperature reached 56 °C, verifying the high vacuum state and subsequently low heat losses obtained by the 3D printed heat transformer. The grey and black lines are the inlet and outlet temperature profiles of the condenser located beneath the adsorber for converting the hot desorbed water vapour into liquid water. The light blue line is the evaporator outlet temperature, which is cyclic in nature, due to the adsorption/desorption phases, and intermittent due to the presence of a single adsorption bed.

Experimentally measured thermal masses of the adsorber

In [19], Gluesenkamp *et al.* proposed a method to standardise the presentation of data on adsorption chillers with special attention to the thermal mass of the adsorber. They define the thermal mass of the adsorber [kJ K⁻¹] as follows:

$$TM = \rho_{HTF} V_{HTF} c_{HTF} + \sum_{i=1}^N (\rho_{mat,i} V_{mat,i} c_{mat,i}) + m_{sorber} c_{sorber} \quad (6)$$

The physical mass of the adsorber m_{HX} [kg] is composed by the mass of the adsorption material m_{sorb} , of the heat transfer fluid m_{HTF} and of the heat exchanger metal m_{met} :

$$m_{HX} = m_{sorb} + m_{HTF} + m_{met} \quad (7)$$

The dimensionless mass ratio MR [kg_{HX} kg_{sorb}⁻¹], which may be used to compare the bed packing density, is calculated as follows:

$$MR = \frac{m_{HX}}{m_{sorb}} \quad (8)$$

The specific thermal mass STM [kJ kg_{sorb}⁻¹ K⁻¹] is defined as the ratio of the total thermal mass of the adsorber in each control volume to the mass of the sorbent and is:

$$STM = \frac{TM}{m_{sorb}} \quad (9)$$

The establishment of a relationship between commonly accessible and measured quantities such as MR and TM , a less often reported number, is the concept of effective specific heat $c_{effective}$ [kJ kg_{HX}⁻¹ K⁻¹], which is used for comparison among different adsorbers regardless of their design:

$$c_{effective} = \frac{TM}{m_{HX}} \quad (10)$$

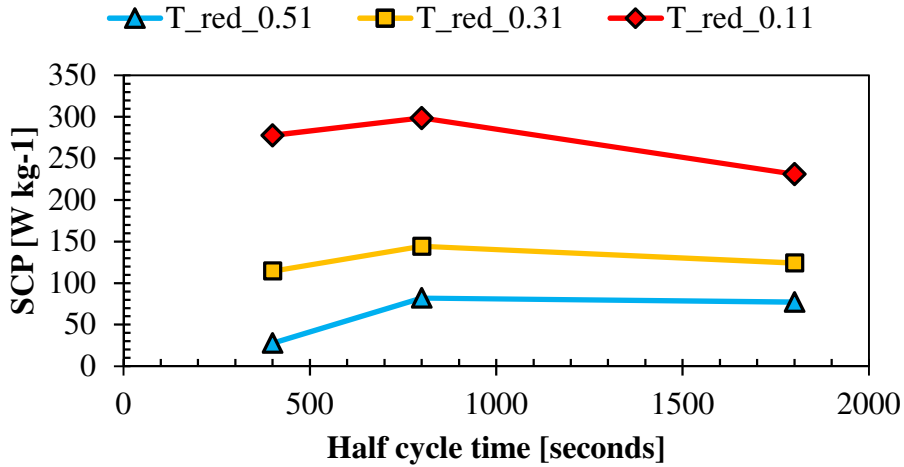
The most common adsorber design consists in packing of adsorbent material in grains between the fins of a heat exchanger. Gluesenkamp *et al.* [19] report a $c_{effective}$ of 1.70 kJ K⁻¹ kg_{HX}⁻¹ for a standard flat tube–fin packed adsorber that compares well with the value of 1.765 of the miniature adsorber used in this investigation. Table 2 reports the details of the thermal mass.

Table 2: Summary of experimentally measured thermal masses.

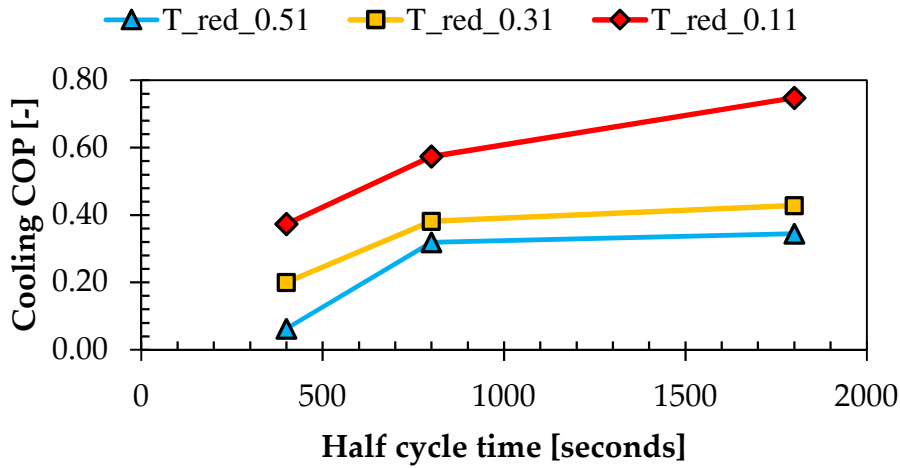
Working Pair	HTF	TM_{total} [kJ K ⁻¹]	m_{sorb} [kg _{sorb}]	m_{HX} [kg _{HX}]	m_{HX}/m_{sorb} [kg _{HX} ¹ kg _{sorb} ⁻¹]	TM/m_{sorb} [kJ K ⁻¹ kg _{sorb} ⁻¹]	$c_{effective}$ [kJ ¹ K ⁻¹ kg _{HX} ⁻¹]	
This study	water/silica-gel	water	0.164	0.020	0.093	4.650	8.206	1.765
Flat tube–fin, packed [19]	water/silica-gel	water	1.92	0.31	1.12	3.58	6.10	1.70

Performance of the 3D printed adsorption heat transformer as a chiller

Using the reduced temperature approach [15], regeneration and ambient temperatures were kept at $T_{hot} = 56$ °C and $T_{cond} = 28$ °C, respectively, while the evaporator inlet temperature was adjusted to achieve *low* $T_{red} = 0.51$, *medium* $T_{red} = 0.31$, and *high* $T_{red} = 0.11$. By using the reduced temperature approach, it is feasible to span the entire performance range with the minimum number of tests.



(a)



(b)

Figure 7: The impact of half cycle time on the performance of a 3D printed adsorption chiller. (a) The specific cooling power (b) The coefficient of performance at various reduced temperatures, respectively.

Fig. 7a depicts the specific cooling power, while the COP is in Fig. 7b as a function of half-cycle time. The results show that half-cycle durations less than 400s are insufficiently informative or comparable to report, as both SCP and COP exhibit low values and too high uncertainties. A short half-cycle of 400s does not allow all the silica gel to regenerate enough to provide a significant cooling effect, with the COP reduction going from 18%-50% its maximum values at long cycle times, depending on the T_{red} .

The SCP of the 3D printed adsorption chiller is highest at half cycle time of 800s with 82 W kg^{-1} at $T_{red} = 0.51$ and 144 W kg^{-1} at $T_{red} = 0.31$. $T_{red} = 0.11$ was determined to have the highest SCP, representing a 48 percent increase above $T_{red} = 0.31$. However, $T_{red} = 0.11$ is descriptive of operational conditions typical of adsorption desalination more than cooling. The SCP decreases steadily at half-cycle time longer than 800s as depicted in Fig. 7a.

Fig. 7b illustrates that the COP of the 3D printed adsorption chiller rises as the half-cycle time increases. Increased cycle time not only helps the adsorber to reach a higher saturation levels during adsorption/desorption, but also enables good regeneration and evaporation temperatures for longer periods. Rather than being lost to the metal or water thermal mass of the heat

exchanger via sensible heat transfer, the whole heat input to the system can be more efficiently used for sorption and desorption.

In adsorption chillers, the sorption rate is higher when the cycle time is shorter, and the SCP decreases as the cycle time increases due to saturation of the sorbent material [9]. This was confirmed by the current investigation. A standard adsorption chiller made of stainless steel consumes an additional 13-15 % of sensible energy to heat the vessel chamber [19], [20]. This parasitic energy loss is eliminated in the 3D printed adsorption chiller, being it made of plastics.

Comparison of performance to the literature in terms of maximum achieved SCP

To boost both cooling capacity and efficiency, a number of characteristics should be considered, including efficiency of heat exchangers [21], high adsorbent working capacity, rapid heat and mass transfer and system compactness [22]. In addition, the presence of residual gases or air significantly impairs the system's overall performance and delays the adsorption process, resulting in a lower SCP [22], [23]. To collocate the results in the bigger context of those achieved in the silica gel chilling sector, Fig. 8 reports the best performance from unit in this study and those achieved in a range other silica gel chillers. Pan *et al.* [24] investigated a modular adsorption chiller experimentally. Their system was highly efficient and affordable. However, given their SCP value of 146 W kg^{-1} , the design appears to be heavy, as one kilowatt of cooling power requires 6.83 kg of silica gel. Alsaman *et al.* [13] experimentally evaluated a solar-powered adsorption chiller with dual desalination and chilling capabilities. Their design delivered a maximum SCP of 113 W kg^{-1} , limited by the overpacking of the adsorber with silica-gel at a ratio of 1.83 adsorbent mass to heat exchanger mass and a bulky iron bed cover that absorbs additional sensible heat. Grisel, Smeding, and Boer [14] developed a silica-gel-water adsorption chiller featuring a 1.4 kg compact plate fin aluminium heat exchanger packed with 1.45 kg of silica-gel, resulting in an exceptional packing ratio of adsorbent mass to heat exchanger mass of one. Their design features a minimal void volume and exceptional vacuum tightness. One of their key outcomes was the maximum SCP of 343 W kg^{-1} , 13% higher than the maximum SCP of 299 W kg^{-1} achieved by the 3D printed unit of this study, likely due to the heat exchanger to mass of adsorbent ratio of the 3D printed adsorber of 2.35.

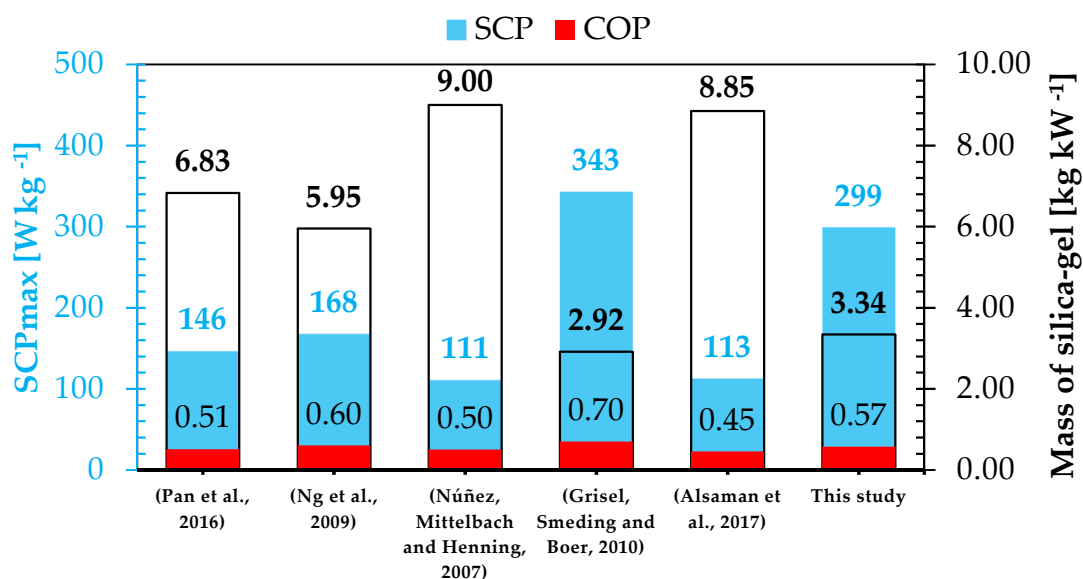


Figure 8: Comparison among the optimal performance proved in various adsorption chiller designs (Silica Gel-Water working pair).

Summary/Conclusions

This investigation has focused on the evaluation of the efficacy of a microscale adsorption chiller manufactured by 3D printing. The investigation showed that the 3D printed adsorption chiller operated stably under high vacuum across the whole set of experiments. By utilising a reduced temperature approach, it was possible to test the whole performance range of the 3D printed silica gel adsorption chiller to have a benchmark and compare it against other designs. The 3D printed adsorption chiller consumes less sensible heat, resulting in a high coefficient of performance of 0.57 at 1800 seconds cycle time, and capable of producing at the same conditions a maximum specific cooling power of 299 W kg^{-1} . These performance indicators are among the best achieved by silica-gel chillers (comparison in Fig. 8), despite the unit operates with one among the highest *adsorber:adsorption-material* mass ratios.

NOMENCLATURE

<i>c_{effective}</i>	Effective specific heat ($\text{kJ}^1\text{K}^{-1}\text{kg}_{\text{HX}}^{-1}$)
<i>cond</i>	Condenser
<i>COP</i>	Coefficient of performance (-)
<i>c_{p,w}</i>	Specific heat water ($\text{kJ kg}^{-1} \text{K}^{-1}$)
<i>evap</i>	Evaporator
<i>hot</i>	Heat source
<i>HTF</i>	Heat transfer fluid
<i>HX</i>	Heat exchanger
<i>in</i>	Inlet
<i>m</i>	Mass (kg)
<i>\dot{m}</i>	Mass flow rate (kg s^{-1})
<i>met</i>	Metal
<i>MR</i>	Mass ratio (-)
<i>out</i>	Outlet
<i>\dot{Q}</i>	Heat flow (W)
<i>SCP</i>	Specific cooling power (W kg^{-1})
<i>sorb</i>	Sorption material
<i>STM</i>	Specific thermal mass ($\text{kJ}^1\text{K}^{-1}\text{kg}_{\text{sorb}}^{-1}$)
<i>T</i>	Temperature ($^{\circ}\text{C}$)
<i>t_{Cycle}</i>	Cycle time (s)
<i>TM</i>	Thermal mass (kJ)
<i>T_{red}</i>	Reduced temperature (-)

References

- [1] “UN Climate Change Conference (COP26) at the SEC – Glasgow 2021.” <https://ukcop26.org/> (accessed Nov. 09, 2021).
- [2] A. A. Askalany, M. Salem, I. M. Ismael, A. H. H. Ali, M. G. Morsy, and B. B. Saha, “An overview on adsorption pairs for cooling,” *Renew. Sustain. Energy Rev.*, vol. 19, pp. 565–572, Mar. 2013, doi: 10.1016/j.rser.2012.11.037.
- [3] M. Luberti, R. Gowans, P. Finn, and G. Santori, “An estimate of the ultralow waste heat available in the European Union,” *Energy*, vol. 238, p. 121967, Jan. 2022, doi: 10.1016/j.energy.2021.121967.
- [4] C. Forman, I. K. Muritala, R. Pardemann, and B. Meyer, “Estimating the global waste heat potential,” *Renewable and Sustainable Energy Reviews*, vol. 57. Elsevier Ltd, pp. 1568–1579, May 01, 2016, doi: 10.1016/j.rser.2015.12.192.
- [5] R. Zevenhoven and A. Beyene, “The relative contribution of waste heat from power plants to global warming,” *Energy*, vol. 36, no. 6, pp. 3754–3762, Jun. 2011, doi: 10.1016/j.energy.2010.10.010.
- [6] F. Meunier, “Adsorption heat powered heat pumps,” *Appl. Therm. Eng.*, vol. 61, no. 2, pp. 830–836, Nov. 2013, doi: 10.1016/J.APPLTHERMALENG.2013.04.050.
- [7] C. Olkis, S. Brandani, and G. Santori, “Cycle and performance analysis of a small-scale

- adsorption heat transformer for desalination and cooling applications,” *Chem. Eng. J.*, vol. 378, p. 122104, Dec. 2019, doi: 10.1016/J.CEJ.2019.122104.
- [8] S. Vasta, V. Palomba, A. Frazzica, G. Di Bella, and A. Freni, “Techno-Economic Analysis of Solar Cooling Systems for Residential Buildings in Italy,” *J. Sol. Energy Eng.*, vol. 138, no. 3, p. 031005, Mar. 2016, doi: 10.1115/1.4032772.
- [9] M. J. Darvish, H. Bahrehmand, and M. Bahrami, “An analytical design tool for pin fin sorber bed heat/mass exchanger,” *Int. J. Refrig.*, Aug. 2021, doi: 10.1016/j.ijrefrig.2021.07.027.
- [10] A. Soo, S. M. Ali, and H. K. Shon, “3D printing for membrane desalination: Challenges and future prospects,” *Desalination*, vol. 520, p. 115366, Dec. 2021, doi: 10.1016/J.DESAL.2021.115366.
- [11] S. AL-Hasni and G. Santori, “3D printing of vacuum and pressure tight polymer vessels for thermally driven chillers and heat pumps,” *Vacuum*, vol. 171, p. 109017, Jan. 2020, doi: 10.1016/j.vacuum.2019.109017.
- [12] K. Thu, A. Chakraborty, B. B. Saha, W. G. Chun, and K. C. Ng, “Life-cycle cost analysis of adsorption cycles for desalination,” *Desalin. Water Treat.*, vol. 20, no. 1–3, pp. 1–10, 2010, doi: 10.5004/dwt.2010.1187.
- [13] A. S. Alsaman, A. A. Askalany, K. Harby, and M. S. Ahmed, “Performance evaluation of a solar-driven adsorption desalination-cooling system,” *Energy*, vol. 128, pp. 196–207, Jun. 2017, doi: 10.1016/j.energy.2017.04.010.
- [14] R. J. H. Grisel, S. F. Smeding, and R. de Boer, “Waste heat driven silica gel/water adsorption cooling in trigeneration,” *Appl. Therm. Eng.*, vol. 30, no. 8–9, pp. 1039–1046, Jun. 2010, doi: 10.1016/j.applthermaleng.2010.01.020.
- [15] T. Núñez, W. Mittelbach, and H. M. Henning, “Development of an adsorption chiller and heat pump for domestic heating and air-conditioning applications,” *Appl. Therm. Eng.*, vol. 27, no. 13, pp. 2205–2212, Sep. 2007, doi: 10.1016/j.applthermaleng.2005.07.024.
- [16] C. Olkis, S. AL-Hasni, S. Brandani, S. Vasta, and G. Santori, “Solar powered adsorption desalination for Northern and Southern Europe,” *Energy*, p. 120942, May 2021, doi: 10.1016/j.energy.2021.120942.
- [17] S. AL-Hasni, C. Olkis, A. Freni, and G. Santori, “A miniature 3D printed sorption heat transformer,” *ISHPC 2021 Proc.*, p. 170, 2020.
- [18] K. Zapfe, “Leak detection,” 2007, doi: 10.5170/CERN-2007-003.227.
- [19] K. R. Gluesenkamp *et al.*, “Experimentally Measured Thermal Masses of Adsorption Heat Exchangers,” *Energies 2020, Vol. 13, Page 1150*, vol. 13, no. 5, p. 1150, Mar. 2020, doi: 10.3390/EN13051150.
- [20] A. Sapienza, V. Palomba, G. Gulli, A. Frazzica, and S. Vasta, “A new management strategy based on the reallocation of ads-/desorption times: Experimental operation of a full-scale 3 beds adsorption chiller,” *Appl. Energy*, vol. 205, pp. 1081–1090, Nov. 2017, doi: 10.1016/J.APENERGY.2017.08.036.
- [21] R. De Boer, S. Smeding, and R. Grisel, “Development and testing of a sorbent filled heat exchanger for use in compact solid sorption cooling systems,” May 2005.
- [22] A. Sapienza, A. Frazzica, A. Freni, and Y. Aristov, “Dramatic effect of residual gas on dynamics of isobaric adsorption stage of an adsorptive chiller,” *Appl. Therm. Eng.*, vol. 96, pp. 385–390, Mar. 2016, doi: 10.1016/J.APPLTHERMALENG.2015.09.031.
- [23] I. S. Girnik and Y. I. Aristov, “Effect of residual air on dynamics of temperature- and pressure-initiated adsorption cycles for heat transformation,” *Appl. Therm. Eng.*, vol. 200, p. 117629, Jan. 2022, doi: 10.1016/J.APPLTHERMALENG.2021.117629.
- [24] Q. W. Pan, R. Z. Wang, L. W. Wang, and D. Liu, “Design and experimental study of a silica gel-water adsorption chiller with modular adsorbers,” *Int. J. Refrig.*, vol. 67, pp. 336–344, Jul. 2016, doi: 10.1016/j.ijrefrig.2016.03.001.

Testing of a falling-film evaporator for adsorption chillers

T. Toppi¹, M. Aprile¹, M. Motta^{1,2}, S. Vasta³, W. Mittelbach⁴ and A. Freni^{2*}

¹Department of Energy, Politecnico di Milano, via Lambruschini 4, 20156, Milano, Italy

²CNR ICCOM – Istituto di Chimica dei Composti Organometallici, Pisa, Italy

³CNR ITAE - Istituto di Tecnologie Avanzate per l'Energia ‘‘Nicola Giordano’’, Messina, Italy

⁴Sorption Technologies GmbH, Freiburg, Germany

*Corresponding author: angelo.freni@pi.iccom.cnr.it

Abstract

The objective of this work is to test and characterize a falling-film evaporator in a lab-scale adsorption test bench realised at Politecnico di Milano labs. Several ad/desorption cooling cycles were performed setting 15 – 20, 25, and 90 °C the heat transfer fluid temperatures for the evaporation, condensation/adsorption and desorption processes respectively. Preliminary evaluation of performance confirmed an evaporation cooling power of 2.5 – 3.5 kW depending on the refrigerant charge level and operating conditions. The overall heat transfer coefficient UA measured was in the range of 620 – 640 W/K.

Keywords: Adsorption chillers, silica gel, water evaporation

Introduction

Adsorption cooling technology is especially interesting in applications where waste heat for driving the adsorption chiller is a widely available energy source (<90°C). Commercial adsorption chillers are based on fixed beds of silica gel, which leads to a larger adsorber. This disadvantage can be compensated employing novel evaporation concepts that can enhance the adsorption chiller overall efficiency [1] and allow for a compact design.

Among the different types of evaporator (flooded, capillary tubes), the falling film concept appears to be the most suitable under typical operating conditions of adsorption chillers, thanks to the superior global heat transfer coefficient [2, 3].

Generally, water is considered as the best working fluid for adsorption chillers and heat pumps, thanks to the high evaporation enthalpy and low environmental impact. On the other hand, the use of water at low evaporation temperature implies low saturation vapor pressure that require special evaporator design to maximize the evaporation rate during the adsorption phase.

Many efforts have been devoted to the study of sub-atmospheric evaporation process in simplified heat exchanger configurations such as smooth tube [4] and flat-plate [5]. These studies focused on falling film [6] and capillary assisted [7] evaporation processes and in general demonstrated the sensitivity of the evaporation rate to different influencing parameters such as filling level, operating conditions, heat exchange surface type [8 -10].

Only few studies have been addressed to the investigation of a full evaporator by means of a real scale test bench able to simulate the adsorption chiller operational mode. Palomba and Frazzica [11] tested an aluminium fin-and-tube heat exchanger by means of a test bench able to achieve evaporation under partially flooded configuration against a condenser. They found that heat transfer fluid temperature and orientation of the heat exchanger significantly affect the evaporation rate. Volmer et al. [12] tested real size copper tube-fin heat exchangers both in thin film and partially flooded evaporation mode. The results showed that some geometric

and process parameters (fin density, fluid flow rate, filling level) strongly influence evaporation performance.

Thimmaiah et al [13] tested a flooded evaporator in a real adsorption heat pump employing AQSOA FAM-Z02 as adsorbent. They found that the utilization of turbulent flow generators inside evaporator tubes and a porous coating on the external surface of evaporator tubes can improve the flooded evaporator performance. Giraud et al. [14] tested a smooth stainless steel plate evaporator in a real adsorption heat pump employing silica gel as adsorbent. Results of experiments indicated high influence of the height of the liquid level on the cooling capacity obtained during the adsorption cycle. Li et al. [15] tested a falling film evaporation on tube bundles in vacuum. Evaporation was obtained against a condenser. According to previous literature research, no falling film evaporators have been exhaustively tested in a real scale adsorption heat pump or chiller. Accordingly, in this work an innovative falling-film evaporator, equipped with a recirculation system to maximize the wetted surface, was tested in a lab-scale adsorption test bench recently realised at Politecnico di Milano labs for evaluating heat transfer performances. Tests have been carried out under realistic operating conditions typical of an adsorption chiller. Evaporation performance have been determined in terms of delivered cooling capacity at different refrigerant charges, external fluid flow rate, evaporation and adsorption temperatures. Additionally, from the experimental data the calculation of the external heat transfer has been performed.

Description of the experimental set-up

An experimental set-up has been built at Politecnico di Milano labs for testing adsorption units and their components. A schematic design of the main system and a photo of the testing setup are shown in Fig. 1a, b. The core of the system consists of a single adsorbent bed, a falling-film evaporator (which geometry is reported in Table 1) equipped with a recirculation pump to improve the heat transfer efficiency and a condenser. The adsorbent bed was made of granular RD silica gel embedded in a finned heat exchanger and was oversized with the purpose of assuring stable working conditions at the evaporator for long periods. The three components are connected by two electric-actuated valves to allow the passage of water vapor enabling the ad/desorption phases. The external sinks/sources consist of three hydraulic circuits (cold-water, hot-water and intermediate circuit) with nominal capacities of 2 kW for evaporator and condenser and 5 kW for the adsorber, with flow rates between 200 and 1000 L/h. The mass flow rates and supply temperature of the three circuits can be set independently based on the required conditions. A schematic layout of the hydraulic circuits and the design of the evaporator are shown in Fig. 2 and 3, respectively. The test bench is also equipped with Pt100 temperature sensors, pressure transducers and flowmeters which uncertainties and operating range are reported in Tab. 2. The resulting efficiency on the measured heat transfer rate are lower than 1.5% for the three circuits. A real time control and data acquisition software for the test bench was realised by means of the LabView™ language.

Taking into consideration that this is a single-bed adsorption cycle, the test bench can work in two modalities: adsorption-evaporation and desorption-condensation. When carrying out the test in the adsorption-evaporation mode, the cold-water circuit provides the needed heat for the evaporation. At the same time, the medium temperature water loop operates as heat sink allowing the heat rejection during the adsorption phase. On the other hand, when working in the desorption-condensation mode, the medium temperature circuit allows the rejection of condensation heat, while the hot water circuit provides the desorption heat to the adsorbent bed. The switching between the phases of the cycle is achieved by means of two-electric actuated valves.

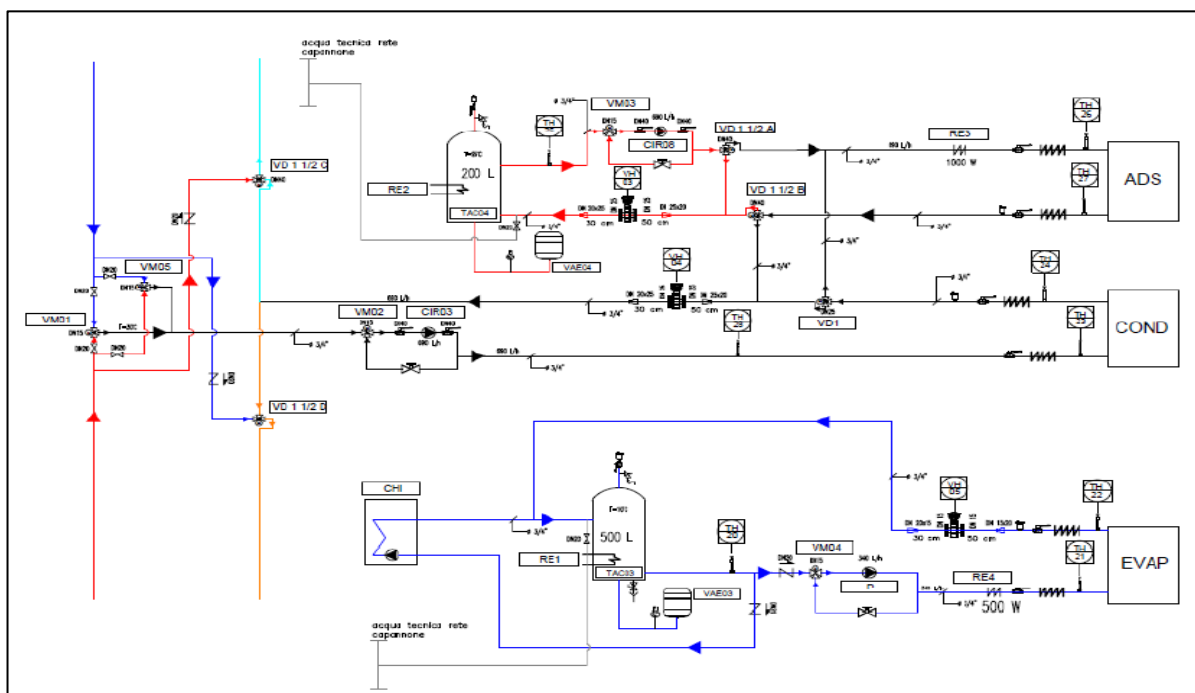
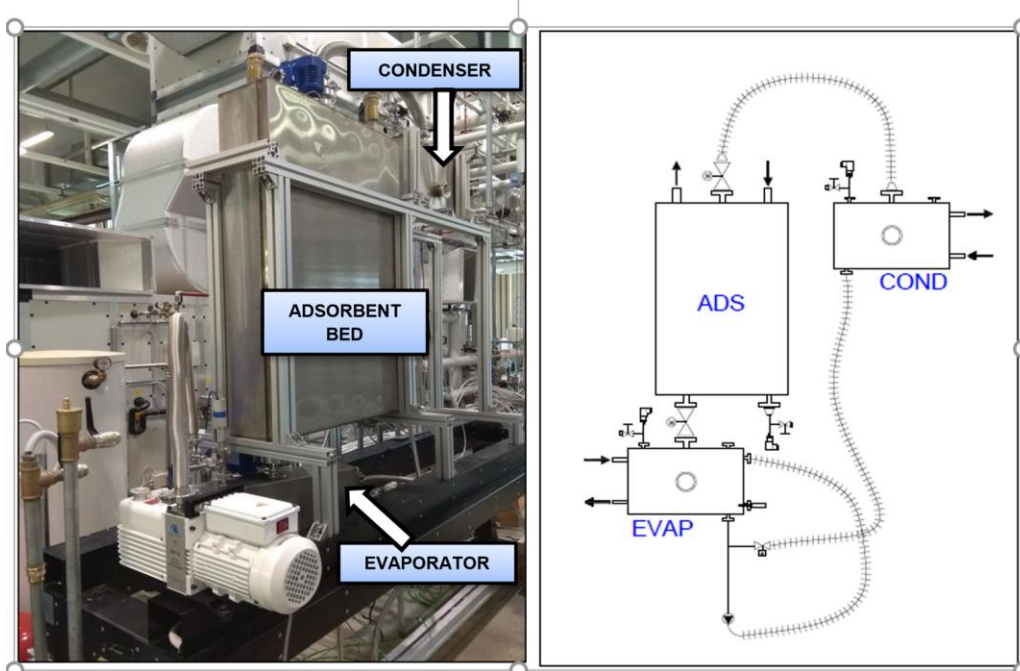


Figure 1a, b – Adsorption test rig schematic and photo

Figure 2 – Hydraulic circuits scheme

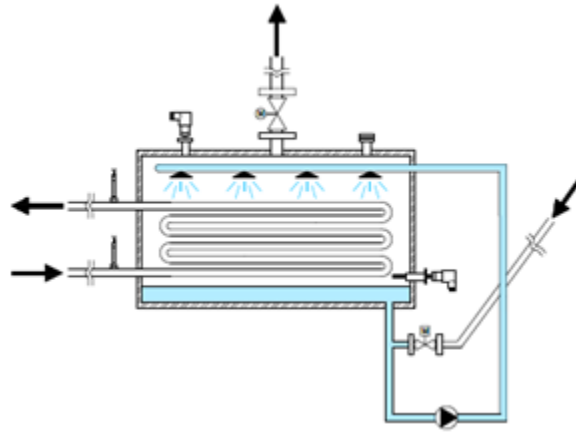


Figure 3 – Evaporator scheme

Table 1. Evaporator parameters

Parameter	Value	Description
a (m)	0.503	evaporator casing width
b (m)	0.113	evaporator casing depth
c (m)	0.283	evaporator casing height
L_{pipe} (m)	5.4191	total length of the evaporator internal pipe
$N^{\circ}C$ (-)	2	number of coils
$N^{\circ}L$ (-)	6	number of levels for each coil
$d_{\text{ext,pipe}}$ (m)	0.016	external base pipe diameter
$d_{\text{int,pipe}}$ (m)	0.015	internal base pipe diameter
h (m)	0.003	fin height
p (m)	0.004	space between consecutive fins
A_{ext} (m ²)	0.7619	external exchange surface of the evaporator internal pipe
A_{int} (m ²)	0.6124	internal exchange surface of the evaporator internal pipe
V_{ref} (m ³)	0.0136	internal volume of the exchanger occupied by the liquid refrigerant

Table 2. Sensors range and accuracy.

Test bench sensors	Measured parameter	Range	Accuracy
Resistance temperature detector Pt 100 1/10 DIN class	Temperature of the water at the inlet/outlet of the component	from -10°C to 100°C	± 0.03°C at 0°C
Pressure transmitter	Pressure inside the component	0 - 20 kPa	0.25% of reading
Magnetic flow meter	Flow rate of the water inside the component	200 - 1000 L/h	always < 0.5% of reading

Test procedure

Considering that the goal of this experimental work is to study the behaviour of an innovative falling-film evaporator for adsorption chillers, the focus has been set mostly on the adsorption-evaporation phase of the cycle. Several tests of this process were carried out with the same heat transfer fluid flow rates (0.4 m³/h for the evaporator and 0.65 m³/h for the adsorbent bed) and the same adsorption bed temperature (25°C), varying both the evaporator inlet water temperature from 15 to 20°C and the initial mass of liquid refrigerant inside the evaporator (from 0.85 to 1.57 kg). Before each test, the incondensable gases were removed by means of a regeneration process at about 90°C under vacuum. The switching from the adsorption to the desorption phases and vice versa was done. A temperature difference between adsorber water inlet and

outlet below 0.2°C was used as criterion for switching from one cycle phase and following phase, with the purpose of beginning the absorption and desorption processes with uniform temperature inside the bed. Moreover, the recirculation pump which circulates the refrigerant on the evaporator was activated as the valve between the evaporator and the adsorption bed opened. This procedure guarantees both uniform initial conditions at the beginning of the tests and repeatable operation.

Experimental results

In the experimental tests the chilled water flow rate inside the evaporator as well as the temperature difference between inlet and outlet of this element were measured. Consequently, the instantaneous heat transfer rate was calculated by applying an energy balance on the evaporator referred to the chilled water side. Moreover, the pressure inside the evaporator is also measured and, based on this measure, the refrigerant saturation temperature was calculated. The overall UA is obtained by dividing the exchanged thermal power by the mean logarithmic temperature difference across the heat exchanger. The hA (referred to the external side of the pipe inside the evaporator) is calculated from the heat transfer rate and the conductive resistance of the pipes and the internal convective resistance.

From Fig. 4, it can be noticed that, as soon as the process starts, the evaporator outlet water temperature decreases rapidly due to the initial intense adsorption process. After this sudden temperature decrease, the profile remains roughly constant with the continuous evaporation of refrigerant. From Fig. 4 it can also be said that, after the initial temperature decrease, there is a sort of plateau section of the profile with an almost constant profile. The maximum temperature difference reached with tests with an inlet water temperature of 20°C is around 7.2°C , while tests with inlet water temperature of 15°C had a maximum temperature difference of 5.5°C . The average pressure value during the plateau section was in the range of $1100\text{ Pa} - 1300\text{ Pa}$. Given the constant inlet temperature, the same path is followed by the heat transfer rate in Fig. 5. Both the calculated external hA and overall UA parameters are reported in Fig. 5 and 6, respectively for the test with 20°C evaporator inlet temperature and evaporator flowrate of $0.4\text{ m}^3/\text{h}$. The average value of the overall UA during the plateau interval is in a range of $620 - 640\text{ W/K}$ while the range for the average external hA is $1040 - 1150\text{ W/K}$. In Fig. 6 it can also be seen the profile of the mass of refrigerant, which smoothly decreases as the test progresses. A possible explanation of the reduction of the hA value can be explained with the reduction of the refrigerant content in the evaporator, which reduces the mass flow rate of recirculated refrigerant due to cavitation and consequently the actual wetted area of the evaporator. Furthermore, the amount of refrigerant inside the evaporator influences the duration of the test. All tests were ensured to begin with a water level below the final tube of the coil to avoid pool boiling and only having falling film evaporation. The duration of each adsorption-evaporation phase increased with the increase of refrigerant mass inside the evaporator.

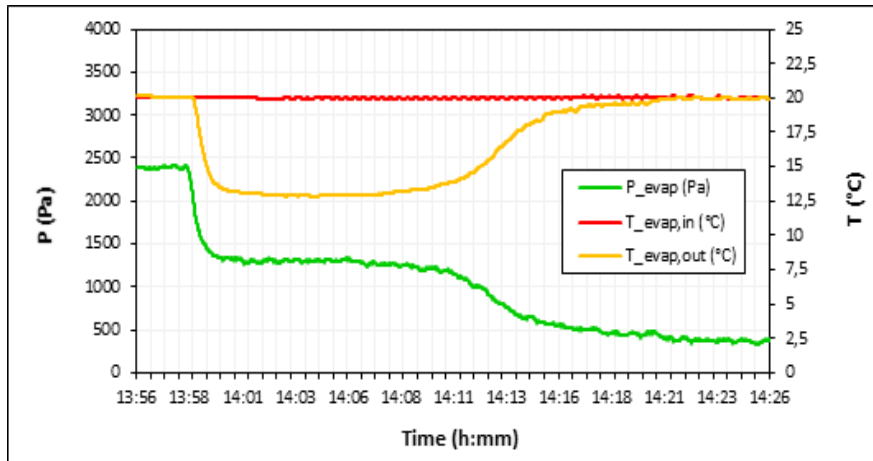


Figure 4 – Pressure-Temperature graph

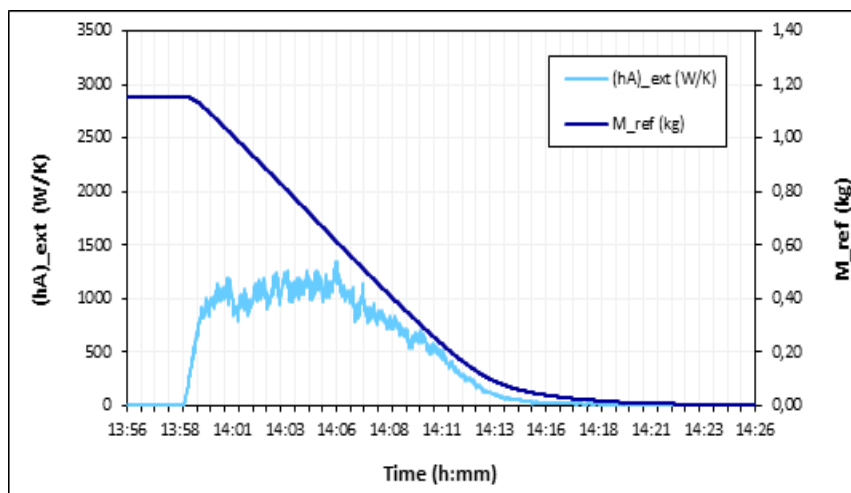


Figure 5 – Overall hA and remaining mass of refrigerant

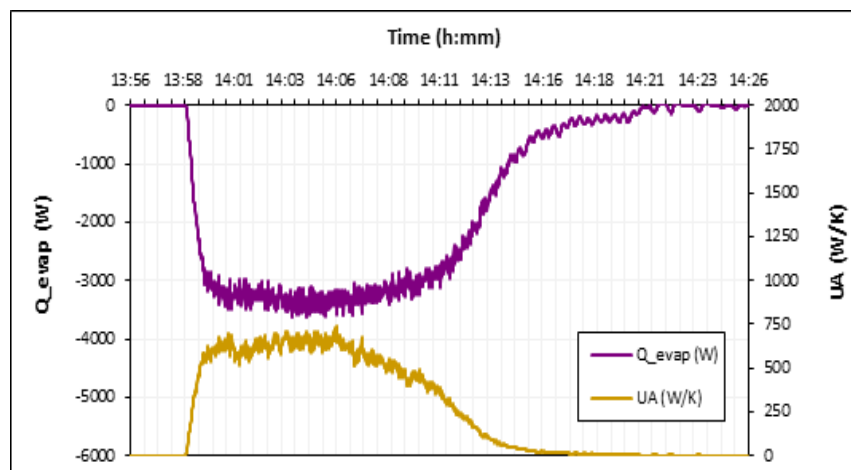


Figure 6 – Overall UA and heat transfer rate

Summary/Conclusions

A falling-film evaporator for adsorption chillers has been tested by a laboratory test-rig with different liquid refrigerant contents (1.57 – 0.85 kg) and different inlet temperatures (15 °C – 20 °C). The cooling capacity obtained in the 15 °C tests is almost 2.5 kW, with an overall UA

coefficient of about 640 W/K and an external hA coefficient of about 1150 W/K. Moreover, in the 20 °C tests, the obtained cooling capacity is around 3.5 kW, with an average overall UA coefficient of about 620 W/K and an external hA coefficient of about 1040 W/K. The hA values is stable during the first phase of the evaporation before decreasing considerably as the process is completed. The reduction of the recirculated refrigerant flow rate is presented as a possible explanation. This will be further investigated with more tests and adding a measure of the recirculated refrigerant mass flow rate to the analysis.

References:

- [1] W. Kalawa, K. Grabowska, K. Sztekler, J. Krzywański, M. Sosnowski, S. Stefański, T. Siwek, and W. Nowak, *Progress in design of adsorption refrigeration systems Evaporators*, EPJ Web of Conferences 213: 02035, 2019.
- [2] G. Ribatski and A.M. Jacobib, *Falling-film evaporation on horizontal tubes—a critical review*, International Journal of Refrigeration 28: 635–653, 2005
- [3] J. Seiler, F. Lanzerath, C. Jansen, A. Bardow. *Only a wet tube is a good tube: understanding capillary-assisted thin-film evaporation of water for adsorption chillers*. Applied Thermal Engineering 147: 571-578, 2019.
- [4] Z.Z. Xia, G.Z. Yang, R.Z. Wang, Experimental investigation of capillary-assisted evaporation on the outside surface of horizontal tubes, Int. Journal of Heat and Mass Transfer, 51 (15–16), 4047-4054, 2008
- [5] F. Giraud, C. Toubanc, R. Rullière, J. Bonjour, M. Clause, Experimental study of water vaporization occurring inside a channel of a smooth plate-type heat exchanger at subatmospheric pressure, Applied Thermal Engineering 106, 180-191, 2016.
- [6] Z.Z. Xia, G.Z. Yang, R.Z. Wang, *Experimental investigation of capillary-assisted evaporation on the outside surface of horizontal tubes*, Int. J. Heat Mass Transf. 51, 4047–4054, 2008
- [7] P.C. Thimmaiah, A. Sharafian, M. Rouhani, W. Huttema, M. Bahrami, *Evaluation of low-pressure flooded evaporator performance for adsorption chillers*, Energy 122, 144–158, 2017
- [8] F. Lanzerath, J. Seiler, Erdogan, H. Schreiber, M. Steinhilber, A. Bardow, *The impact of filling level resolved: Capillary-assisted evaporation of water for adsorption heat pumps*, Applied Thermal Engineering 102, 513–519, 2016.
- [9] L. Schnabel, K. Witte, J. Kowol, P. Schossig, *Evaluation of different evaporator concepts for thermally driven sorption heat pumps and chiller*, Sorption heat pump conf., Padova, Italy (2011), pp. 525-543
- [10] T.P. Cheppudira, A. Sharafian, W. Huttema M. Bahrami, Effects of capillary-assisted tubes with different fin geometries on the performance of a low-operating pressure evaporator for adsorption cooling systems. Appl Energy 171, 2015
- [11] V. Palomba, A. Frazzica, Experimental study of a fin-and-tube heat exchanger working as evaporator in subatmospheric conditions, Applied Thermal Engineering, 175,115336, 2020
- [12] R. Volmer, J. Eckert, G. Földner, L. Schnabel, Evaporator development for adsorption heat transformation devices – Influencing factors on non-stationary evaporation with tube-fin heat exchangers at sub-atmospheric pressure, Renew. Energy., 110, pp. 141-153, 2017
- [13] 1. P.C. Thimmaiah, A. Sharafian, M. Rouhani, W. Huttema, M. Bahrami, Evaluation of low-pressure flooded evaporator performance for adsorption chillers, Energy, 122, pp. 144-158, 2017

- [14] F. Giraud, C. Toubanc, R. Rullière, J. Bonjour, M. Clause, Experimental study of water vaporization occurring inside the channel of a smooth-plate type heat exchanger connected to an adsorber and comparison with trends observed in absorption configuration
- [15] S. W. Li, X.Y. Wu, Z. Luo, R.L. Webb, Falling water film evaporation on newly-designed enhanced tube bundles, *Int J Heat Mass Transf*, 54, pp. 2990-2997, 2011

Experience from the operation of an absorption power cycle with LiBr working fluid and its prospects for future

Vaclav Novotny^{1*}, Jan Spale¹, Jan Pavlicko¹, Jan Novotny¹, Michal Kolovratnik¹

¹Czech Technical University in Prague, Jugoslavských partyzanu 1580/3, 160 00 Prague, Czech Republic

*Vaclav.novotny@cvut.cz

Abstract

Absorption thermodynamic cycles have been proposed not only for cooling but also for power generation. The idea behind the concept is in extracting more heat out of the heat source thanks to working fluid temperature glide and increasing the utilisation efficiency. Most common is the Kalina cycle utilising water-ammonia mixture working fluid. However, other working fluids that may provide further thermodynamic benefits have only rarely been examined experimentally.

Absorption power cycle with LiBr solution working fluid has been proven to theoretically provide superior performance to ORC and Kalina cycle for low temperatures of the heat sources below approximately 120°C. Also, it was identified as suitable even for kW scale systems, for example, as high vapour volume allows for a design of an effective impulse micro turbo-expander. In order to verify the feasibility in real life, a sub-kW scale proof of concept system has been designed.

This work reports on, to the authors' knowledge, the world's first absorption power cycle using salt (LiBr) solution, known so far only from absorption cooling. The system also features a nylon 3D printed turbine. The experimental performance is compared to the theoretical benefits of the cycle, and prospective applications are evaluated. If a standalone waste heat recovery proves unfeasible, the system also offers a possibility of integrating power production to absorption chillers to improve system versatility.

Keywords: Kalina cycle, absorption power cycle, LiBr, proof of concept.

Introduction/Background

The utilisation of low-temperature heat sources, especially of waste heat, efficiently has been a goal of many research activities. Regardless of large potential from low-temperature waste heat (around 100°C and below) conversion into electricity in small distributed power systems, applications of such technologies are, however, very scarce. Reasons are primarily due to poor efficiency and high costs. The traditional method widely considered and applied for higher temperatures, ORC, often doesn't reach sufficient efficiency for commercial application at such low temperatures. Moreover, the requirements for heat rejection rise significantly as the heat source temperature and efficiency decreases, and thus the relative amount of rejected heat against unit of power output rises. The ideal cycle for utilising low temperature is a trilateral cycle, which, thanks to a gradual increase of working fluid temperature during the heat input, minimises the irreversibilities. [1]–[3] Several methods to approach the trilateral cycles have been proposed, including using zeotropic working fluids with a temperature glide during phase change. Absorption power cycles are one of these systems, where many works in the past suggested the use of water-ammonia mixture and several plants were built [4]–[6].

Absorption power cycle (APC) using aqueous salt solutions, particularly LiBr, has been proposed as an alternative to the ORC and Kalina cycle for low-temperature waste heat recovery, providing theoretically higher efficiency [7]. In order to verify actual operation, a proof-of-concept system has been proposed [8]. This system, seen in **Figure 1**, has a nominal heat input of 20 kW of 90°C water and designed power output of around 300 W. In the shell & tube heat exchangers, desorber and absorber, are inserted probes for examination of the working fluid temperature glide during the phase change. Axial partial admission single-stage turbine for expanding steam was selected due to high volumetric flowrates (steam in order of several kPa) and made from nylon by 3D printing and implementing an integrated permanent magnet generator (principle verified in [9]).

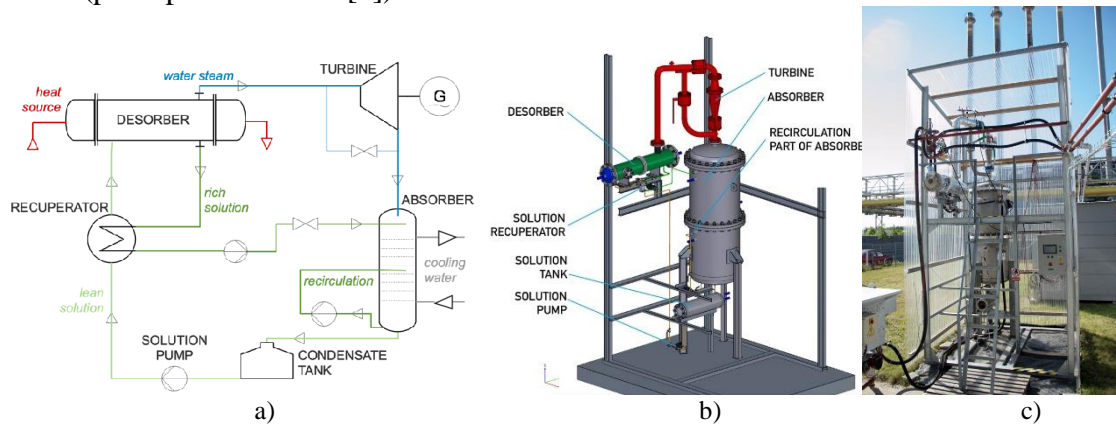


Figure 1: APC experimental rig, (a) schematic diagram, (b) 3D model of the system, (c) photograph of the system

Design review

An experimental system has been proposed to verify the actual applicability and technical feasibility of the APC with LiBr solution. First experimental considerations [10] and trials with water [11] led to the design of a proof of concept system of the cycle with a nominal power output in hundreds of watts. Its design was in detail introduced in [8]. Here the design of the main components is briefly reviewed, followed by details on instrumentation and operation.

Heat Exchangers

After the thermodynamic model based on pinch-points has been made, the obtained value served as a basis for the heat exchanger design. The type of heat exchanger was selected as a flat plate for the recuperator. A horizontal single-pass counter-flow shell & tube exchanger was designed for the desorber, as this concept is common to absorption chillers. The LiBr solution is in the shell with a specified liquid level, meandering between vertical baffles. The tubes and baffles are in the lower part of the exchanger up to the designed liquid level.

The falling film absorber is designed as well as a shell & tube type. The absorber was designed to pursue as much as possible of the counter-flow principle. From the top part with the steam inlet, it consists of rich solution spray nozzles, packing (as from cooling towers) for the adiabatic part of the absorption and helical coils of cooling water with the outlet at the top and inlet at the bottom. About 90% of the required surface area is then repeated under another packing. Spraying nozzles above the coils are using a recirculation stream from the bottom of the absorber. This section serves to promote absorption if needed but can be bypassed and switched off. Note in the overall absorber and desorber design shown in **Figure 2** also the fittings for temperature probe measuring the temperature profile.

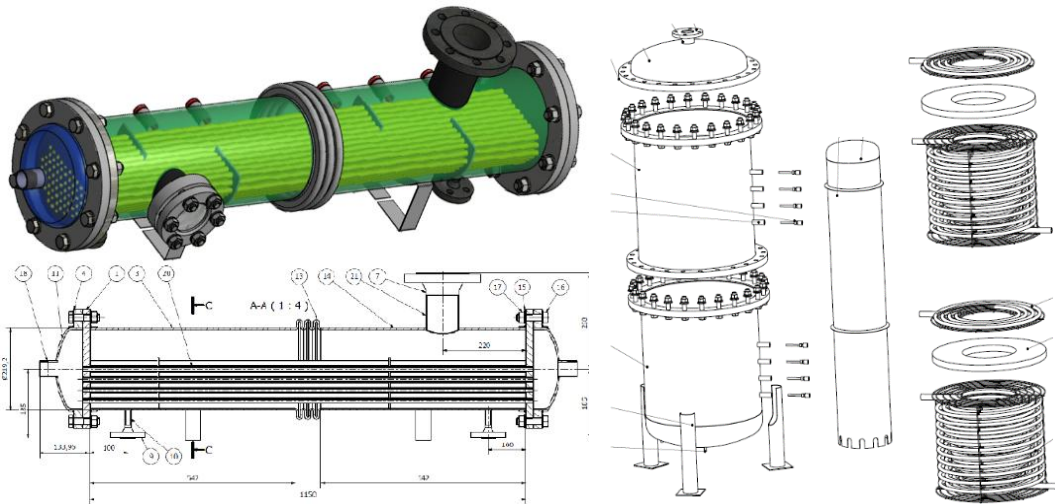


Figure 2: Design of the desorber (left) and the absorber (right) for APC

Turbine

The Turbo-expander concept is chosen due to the large vapour volumetric flowrates in the APC. Following the suggestions of [12], a requirement of low-cost components (lower speed, worse manufacturing tolerances etc.), an axial impulse turbine with partial admission has been designed for this application. The design is based on a 1D mean line model with chosen maximal rotational speed suitable for the generator and its bearings (15 000 rpm) and mean rotor diameter to ensure manufacturability with good tolerances (120 mm). As the loading of the blades and operating temperatures are low, plastic material, which can be even 3D printed, is sufficient for nozzles and rotor buckets. Based on experience in [9], selective laser sintering (SLS) of polyamide powder has been used for manufacturing. The model and drawing in **Figure 3** show that the expander is, for simplicity, designed to be inserted between flanges into the piping. Details of the expander designing procedure and first tests can be found in [13].

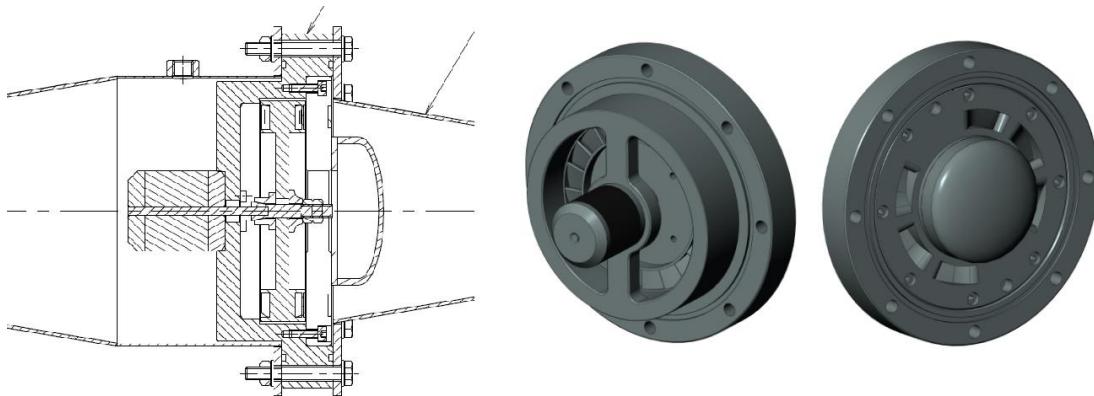


Figure 3: Design of the turbo-expander

Overall system

The experimental proof-of-concept APC system is illustratively shown on a simplified diagram in Figure 1a. As the figure suggests, the design utilises a shell & tube desorber (i.e. steam generator) as well as a shell & tube falling film absorber (LiBr solution flown on the outer surface of helically wound tubes and steam is absorbed). The working fluid in the desorber (steam generator in absorption chillers terminology) undergoes a partial phase change when steam is generated and goes through the expander into the absorber. The rich

solution is routed to the absorber in a separate line via a recuperator. While concepts with counter-flow low volume heat exchangers (as plate type) assume a separator downstream, our design follows a large volume exchanger design which already serves as a separator, as found in standard absorption chillers. Note an additional pump in the rich solution line to overcome potentially excessive pressure losses in the piping and nozzles in the absorber. The steam in the absorber is absorbed into a subcooled liquid solution film flowing on a heat transfer surface where heat is removed into cooling water. In case of insufficient absorption rate additional solution recirculation circuit is considered here with the solution nozzles in the half of the absorber's height.

Major design parameters are summarised in **Table 1**, with details described in [8]. The overall configuration of the system is then clear from a model and photograph in Figure 1b and 1c. Note especially the very low pressures of the turbine inlet and outlet. Also, as the device serves as proof of concept, some components, especially the absorber, are oversized. Finally, the device is built on a two-floor structure so that every part of the system is accessible for commissioning and maintenance.

The main phenomena to be verified by this system are at first of course for the technical feasibility and overall operation, but also actual temperature profile in the heat exchangers with temperature glide (both desorber and absorber have inserted multiple temperature probes along the flow direction) and last but not least feasibility of plastic 3D printed turbo-expanders.

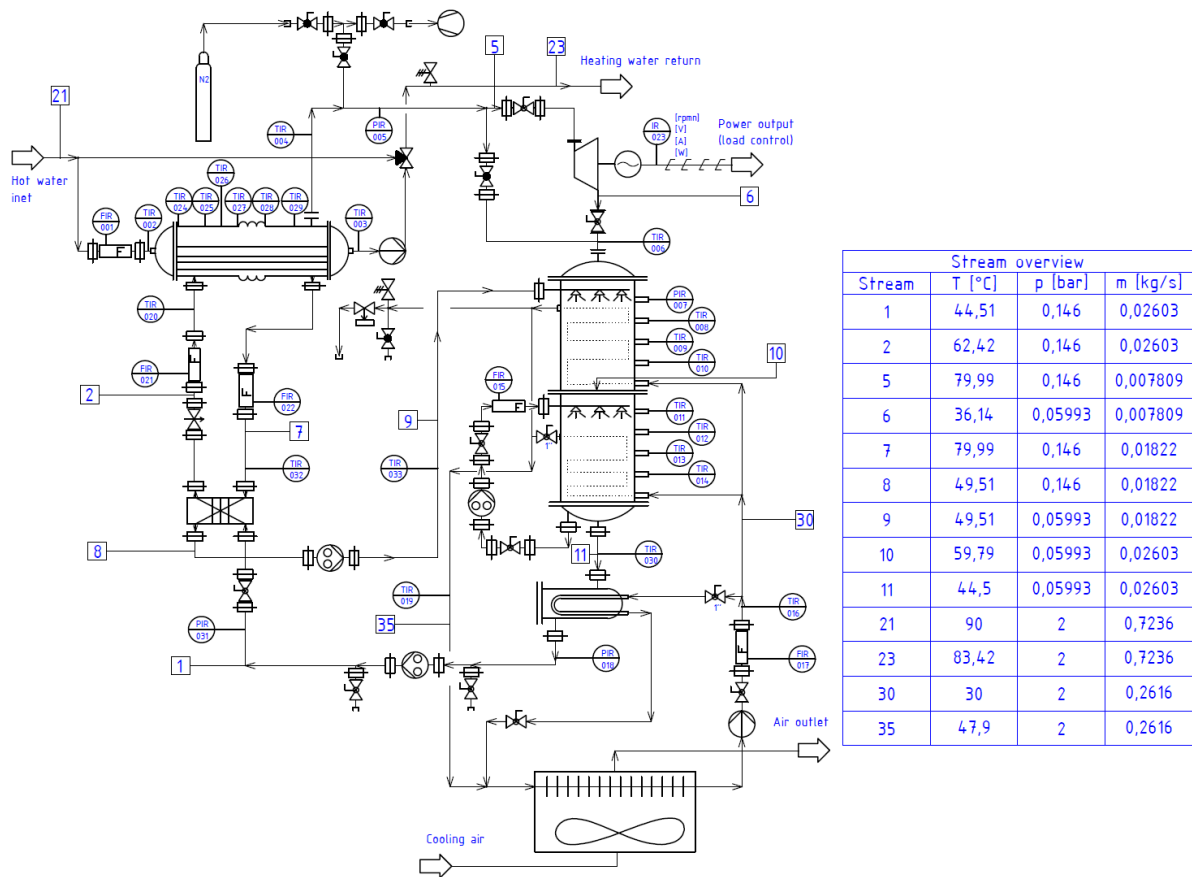
Table 1: Main design parameters of the APC rig

Heat source inlet temperature	T_{hs}	90 °C
Heat input	Q_{in}	20 kW
Cooling water inlet temperature	T_{cw}	30 °C
Working fluid	LiBr+H ₂ O 35% (LiBr wt., lean) / 50% (rich)	
Lean LiBr solution mass flow	\dot{m}_{lean}	0.026 kg s ⁻¹
Vapour mass flow	\dot{m}_{vap}	0.008 kg s ⁻¹
Turbine inlet pressure	p_{HP}	13.38 kPa
Turbine outlet pressure	p_{LP}	5.99 kPa
Turbine isentropic power output	W_{is}	840 W
Turbine design power output	W_{turb}	370 W
Design parasitic load (incl. cooling water pump and fan)	W_{paras}	116.2 W
Design cycle / system efficiency	$\eta_{cycle} / \eta_{system}$	1.9 / 1.3 %

Instrumentation

In the APC rig, most of the measurements were taken and recorded via PLC system AS332T-A with measuring cards for RTD temperature sensors, voltage and current input. Additional temperature sensors for temperature glide were measured via Labview (cRio module). The turbine load was controlled via an in-house built DC load (output current was rectified first) system, which included a PID regulator to keep the required rotational speed. This system also recorded the voltage and current along with rotational speed based on produced AC current frequency. Some details about this method can be found, for example, in [14].

Figure 4 shows a simplified PFID of the APC rig and the position and types of measurements within the system. It also shows design thermodynamic properties in respective streams. The details of the sensors for the measured variables are summarised in **Table 2**.



Stream overview			
Stream	T [°C]	p [bar]	m [kg/s]
1	44,51	0,146	0,02603
2	62,42	0,146	0,02603
5	79,99	0,146	0,007809
6	36,14	0,05993	0,007809
7	79,99	0,146	0,01822
8	49,51	0,146	0,01822
9	49,51	0,05993	0,01822
10	59,79	0,05993	0,02603
11	44,5	0,05993	0,02603
21	90	2	0,7236
23	83,42	2	0,7236
30	30	2	0,2616
35	47,9	2	0,2616

Figure 4: APC experimental rig simplified PFD

Table 2: Test rig sensors and transducers

Parameter	Type	Range	Error
p (kPa)	Ceramic capacitive DMP331	0-400, 0-200	0.35% FS, 0.10% FS
T (°C)	Pt100 RTD (4 wire)	-50 - 200°C	0.5% + 0.3°C
\dot{V} (l min ⁻¹)	Vortex LIQUI-VIEW Base LVB	0.5-10, 3.5-50, 5-85	<1% FS
U (V)	Voltage divider +Arduino A/D	0-60 V	2% + 0.03 V
I (A)	Arduino A/D via U drop (1 block)	0-30 A	2% + 0.02 A
n (RPM)	Electrical frequency via Arduino A/D	2k-100k	~20 rpm (@ 10k rpm)

Operation

Before each test campaign, the system was evacuated, and after it, the rig was filled with nitrogen slightly above ambient pressure to prevent oxygen intrusion and potential corrosion. The tests were performed for ranges of charged solution concentration of 54% (as purchased), then 50%, 45% and 40% and additionally during commissioning with pure distilled water. During the experimental tests, controlling parameters of the cycle were set. The cycle operating with the turbine has two degrees of freedom, speed of the main pump and the rich solution pump. In addition, when the bypass valve was used instead of the turbine, its opening simulated the turbine's swallowing capacity, thus providing another degree of freedom.

The pumps were operated so that the recirculation pump was set to run at a certain constant speed. In contrast, the lean solution pump was (manually) controlled to provide a constant liquid level in the desorber. The opposite method of control has proven to be unreliable. At

certain states, the liquid solution stopped returning to the storage tank. The suspected reason is crystallisation, though there should have been a margin from the limiting concentration. This phenomenon might deserve deeper focus in the future. In addition, the pump's control and long time constant of the system sometimes caused notable departures from steady-state liquid flows. At least partial correction for these discrepancies is provided in the next chapter.

The heat source was a heating water taken as part of the output of biomass-fired ORC units, either a 50 kW version described in [15] or a scaled-up 120 kWth version. Due to the units settings and partly heat losses in the heat input pipes, the heat source temperature was typically between 75 and 85°C, while it could be further decreased by a three-way valve mixing in the return water. Thus, the range of the explored heat source temperature was 67-88°C. The heat sink was provided by a cooling water which rejected the heat into the air in an air cooler, and its temperature depends on ambient conditions. The range of the explored cooling water temperatures was 11-46°C. The range of the explored temperature difference between heat source inlet and cooling water inlet was 38-71K, but bear in mind that the mass flow rates differed as well, between 0.15-0.87 kg/s at the heat source side and 0.27-0.47 kg/s at the cooling water. A sample of recording of the selected data from the operation is in **Figure 5**, with a distinct period of turbine operation, while the bypass was operated at the rest of the time.

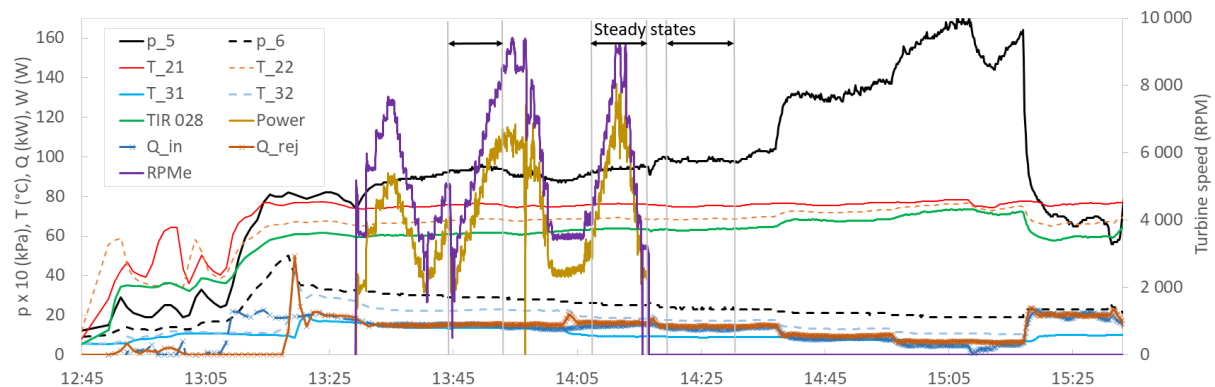


Figure 5: Example of the record of selected parameters from the APC operation with an indication of the selected steady-state periods with and without turbine operation (numbers correspond to the PFID)

Data Evaluation Methods

From the recorded data are selected periods of relatively constant operation, evaluated primarily by the steadiness of the pressure levels. An example of such states selection is in Figure 5. For further evaluation, the average values from these selected periods were obtained, and each value was treated as an operational state.

The mass flow rate cannot be directly evaluated from the volumetric flow rate of the liquid streams. The reason is that the density is a function of LiBr concentration, which is not directly measured. Therefore, the desorber's mass and energy balance equation is used with the inputs, outputs, and measuring point according to **Figure 5a**. The assumption is that the rich solution leaving the absorber is at the saturated temperature; thus, its concentration is given. A slight difference in results is obtained if mass balance is applied to both solution and each fluid component (LiBr and water) or, e.g. energy balance of separation (from calculated 2 phase fluid quality). This difference is also associated with a slight mismatch in either the mass or energy balance of the system. Using the energy balance also helps to smoothen and lower the impact of transient effects affecting the flow rate during cycle control (rising or

falling of desorber liquid level) and volumetric flow rate measurement inaccuracies. Except for solving the mass flow rate, the actual concentrations are also obtained in this calculation.

Another approach has been explored to evaluate the mass flow rate. The first point of the temperature measurement along the desorber length was considered the point of reaching the saturation of the lean solution. This approach would explain the low temperature glide via by concentration difference of the solution. But it has a substantial deviation in mass flow rates. The steam mass flow rate from the evaluated mass balance is more than three times lower than from the energy equation. When concentration data are inserted into the cycle model, lean and rich solution mass flow rates need to be about three times higher than measured. Thus the actual concentration change needs to be higher, and this approach was disregarded.

The resulting graph in **Figure 5b** shows the discrepancy between the steam mass flow rate obtained from the energy balance and the difference from the two measured volumetric flow rates. In order to select data with higher quality, values with relative difference smaller than 40% or absolute difference smaller than 0.015 kg/s were selected. Fluid properties are evaluated from the REFPROP database for water and from a formulation in [16] for the LiBr solution.

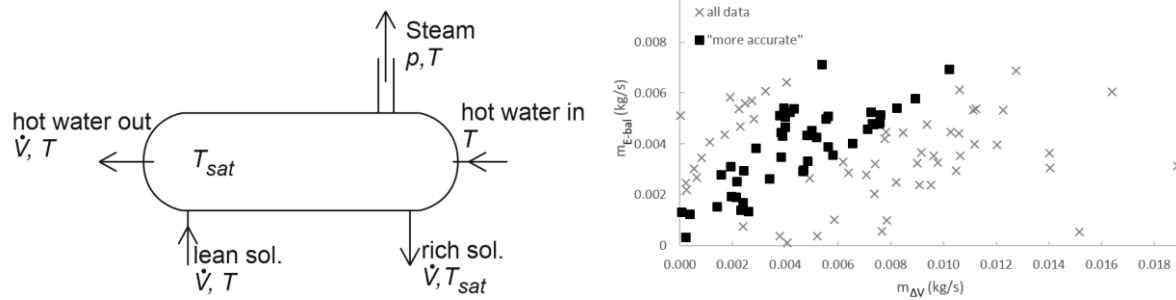


Figure 5: Schematic diagram of desorber parameters used in the evaluation of steam mass flow rate (left) and graph of steam mass flow rate obtained by the difference in measured volumetric flow and from the energy balance

The turbine efficiency is evaluated with respect to the isentropic power. The efficiency is evaluated concerning the produced electrical power output (electrical efficiency) and from the mechanical power output as an isentropic efficiency. As the measured power is in the form of electricity, obtaining mechanical power output has been done using generator efficiency evaluated for each operation state. The generator efficiency is obtained from the characteristics provided by an eCalc¹ tool, which includes performance parameters of a wide range of aeromodelling BLDC motors. This tool was used to obtain torque–rotational speed–efficiency dependencies, which were then applied. Additionally, a nearly constant voltage drop on the rectifier was taken into account.

For the system itself, the important parameter is not just cycle efficiency but also utilisation efficiency (evaluated with respect to heat source heat content). Reference for the utilisation efficiency was taken as cooling water inlet temperature. Only the gross efficiency (excluding all parasitic load) was evaluated at this point. The unit was in most of the time operated with the bypass valve, only simulating the turbine. In order to assess the potential of the cycle in general, a hypothetically achievable expander efficiency of 65% has been assumed as safely realistic for small turbo-expanders [17], [18]. The cycle parameters are then recalculated with this expander efficiency value.

¹ <https://www.ecalc.ch/torquecalc.php>

Experimental Results and Discussion

The experimental performance has been explored mainly from three points of view, regarding parameters of the cycle, the performance of the plastic 3D printed turbo-expand, and actual temperature profiles during the phase change with the temperature glide.

Cycle parameters

The selected and analysed steady states are covering in summary about 20 hours of the APC unit operation (excluding transition states). The resulting cycle and utilisation efficiency for assumed expander efficiency of 65% are plotted for these states in **Figure 6a** as a function of the cycle pressure ratio (PR) and distributed according to the charged LiBr concentration. The operation states recorded as more accurate are highlighted with rich colour. The second graph (**Figure 6b**) shows the same parameters but for actual expander electrical power output (DC after rectification), i.e. including turbine isentropic efficiency, generator efficiency and rectifier diode efficiency (voltage drop) and only the states with turbine operation.

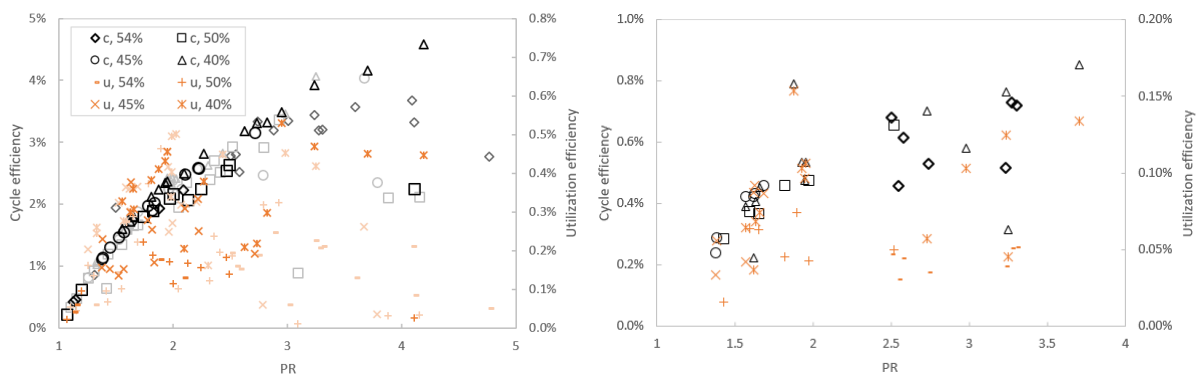


Figure 6: Cycle and utilisation efficiencies as a function of cycle pressure ratio and charged LiBr concentration - with the hypothetical 65% expander efficiency, higher accuracy states in bold (left) and measured parameters with the plastic turbine (right)

The operation points are recorded over a range of heat source and heat sink temperatures and mass flow rates. To generalise the data concerning the temperature potential, **Figure 7a** shows the cycle data points plotted as a function of a temperature difference between the heat source and heat sink inlets. It is not an exhaustive range of possible operation states, but the general trend is that the maximum cycle efficiency is independent of the charged fluid concentration. However, the highest utilisation efficiency is a domain of the lowest explored charged concentration. This is because the low concentration offers a higher space for the concentration change between the lean and rich solution.

The concentration change is furthermore used for plotting the data **Figure 7b**. Here we can see a confirmation of the thermodynamic models that the highest cycle efficiency is associated with lower values of concentration change (but not the very lowest, particular optimum exists). On the other hand, the utilisation efficiency increases with the concentration change with a possible optimum at somewhat higher values. Thus, a drop in utilisation efficiency might come with a further increase in the concentration difference (if the operating conditions allow such a state). This behaviour is further seen in detail for 40% LiBr charge concentration in **Figure 8**, where cases with a low variation between the heat source and sink inlet temperatures were selected.

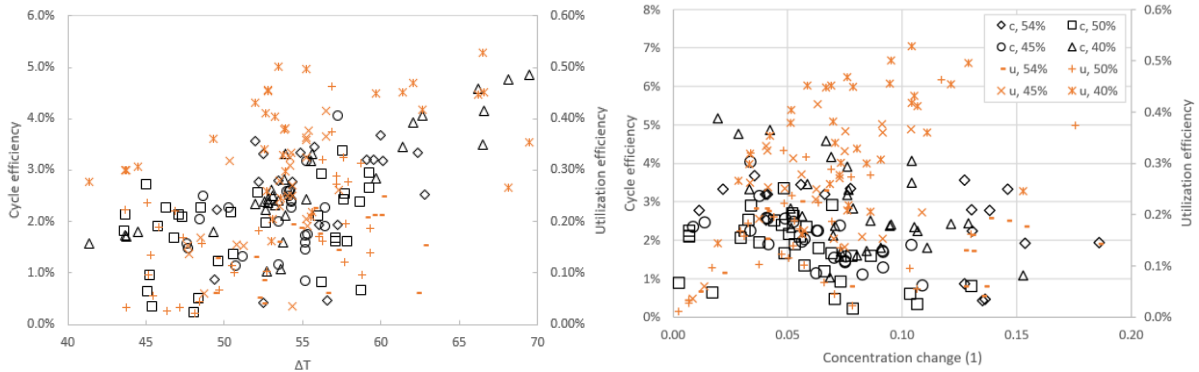


Figure 7: Cycle and utilisation efficiencies as a function of charged LiBr concentration and temperature difference between the heat source and heat sink (left) and of a concentration difference (right), all with the hypothetical 65% expander efficiency

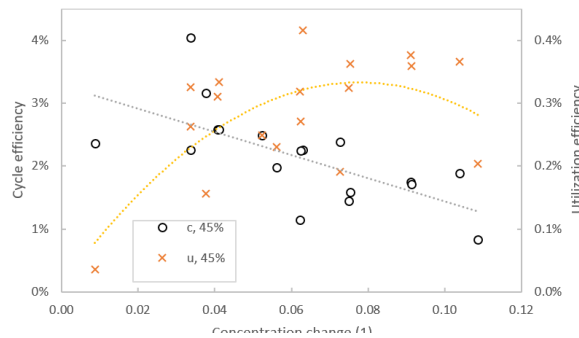


Figure 8: Detail of cycle and utilisation efficiencies as a function of the solution concentration difference for cases with low heat source and sink inlet parameters variation

Temperature glide measurements

One of the objectives of the experiments was to evaluate the temperature glide across the non-isothermal phase change during desorption and absorption, as high temperature change was suggested in the past for waste heat recovery. This glide for several selected operation states is shown for both desorber and absorber in **Figure 9**. The measured temperature in the desorber corresponds to the boiling solution as the probes are placed under the liquid level. The recorded glide is significantly lower than predicted yet still measurable. A certain decrease of the glide was expected due to the large volume shell & tube exchanger with a nearly quiescent pool of the boiling solution in the shell. Interestingly, the glide doesn't differ significantly between the operation states with various solution charge LiBr concentration. However, such a result is in accord with **Figure 7b**, where no clear relation between concentration difference and charge solution concentration has been found. The lowest absolute values for the 40% concentration are caused only by the fact that ambient conditions allowed lower temperatures at these tests.

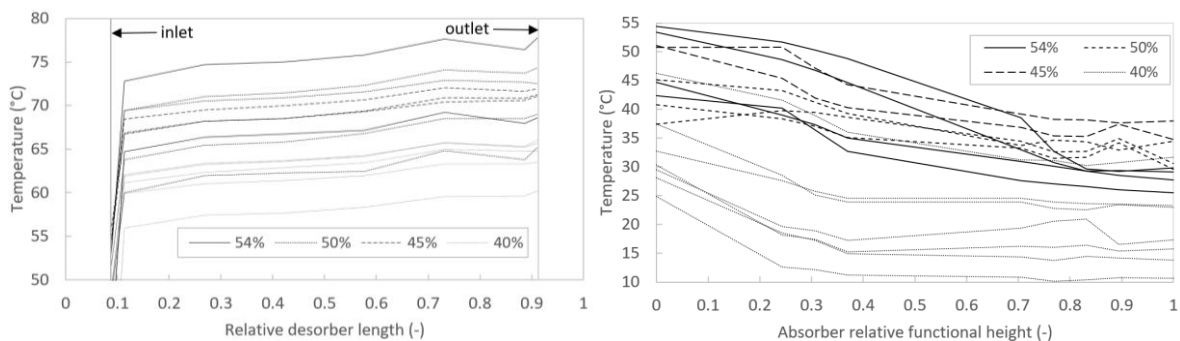


Figure 9: Measured temperature glide profiles in desorber and absorber

In most cases, the absorber had operational only the upper half as the lower half was designed only as a backup if the absorption rate is insufficient. However, the measured temperature might correspond to the low-pressure water vapour as the temperature probes were not always fitted between the cooling coils. Therefore, it is hard to estimate how the sensors are wetted with the liquid solution, and the results need to be taken only as illustrative. The inlet temperature shown is the turbine outlet vapour, while the first point of measurement is after a packing (for adiabatic absorption) and a small portion of cooling coils. Adiabatic absorption may explain the temperature increase in some cases between the inlet and the first measurement. An increase in temperature in the bottom part may be associated with improper wetting by the solution, while the steam has a higher temperature.

The extent of the temperature glide is in theoretical models associated with the concentration change of the solution. Also, the concentration change and temperature glide are related to the cycle PR. These two relationships are shown in **Figure 10**. In the first graph, the general trend of increasing PR with a decrease in concentration change is observed. Several lines can be identified in the trends, each corresponding to the similar heat source and heat sink conditions. The second graph also shows a general trend of increased temperature glide with increased concentration change. However, at any given concentration change, the spread of the glide values is very high. Note the much higher absolute values of measured glide in the absorber, partly associated with measurement of the vapour phase and partly from a better counter-flow operation.

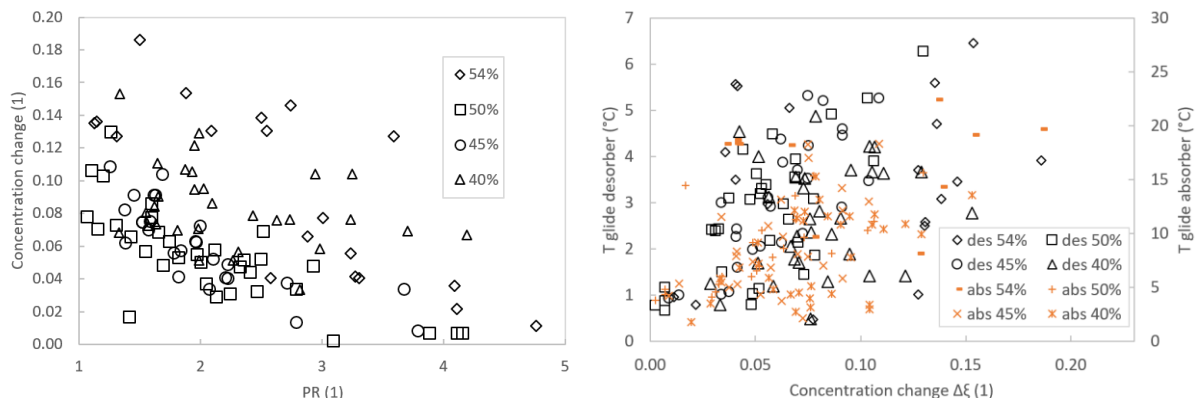


Figure 10: Concentration change as a function of pressure ratio and temperature glide as a function of concentration change for all measured states

Comparison with the design models

For a selected case out of the "more accurate" states, an analysis of parameters and comparison with design models when the operation parameters are fitted back is shown. The design model doesn't work for fully off-design calculation, but it can provide an insight of a performance comparison between design and actual. Desorber analysis and measured data are used to obtain the heat source and heat sink inlet parameters, turbine inlet pressure, lean solution concentration and mass flow rate and absorber outlet temperature. Then, the design model is adjusted, with one input being the actual size of the heat exchangers. A comparison of the main cycle parameters from the design model and measured data is shown in **Table 3**.

Interestingly, at these boundary conditions, the desorber, according to the design model, has worse heat transfer performance, even though the actual LiBr concentration difference is smaller, so the cycle can extract less energy from the heat source. Moreover, the improved heat transfer is regardless of a very tranquil boiling process observed on smooth stainless tubes. On the other hand, the absorber performs worse where the model predicts notably lower pressure and, as a result, a better cycle and utilisation efficiency.

In order to better compare other measured cycle parameters with the modelled ones, a correction factor to the overall heat flux in desorber and mass transfer coefficient in absorber has been determined. Additionally, the concentration and pressure in the absorber do not correspond to the outlet temperature, so the model was extended to solution subcooling at the absorber outlet.

Table 3: Comparison between modelled and measured parameters

Parameter	Unit	design model	corr. model	measured
ζ_{rich}	% LiBr	45.0	47.5	47.5
ζ_{lean}	% LiBr	37.6	37.6	37.6
p_{des}	kPa	9.2	9.2	9.2
p_{abs}	kPa	3.2	4.8	4.8
$CorrF_{des}$	1	0	1.59	n.a.
$CorrF_{abs}$	1	0	0.30	n.a.
ΔT_{des}	K	17.1	13.8	9.5
$\Delta T_{abs,vap-}$	K	6.0	13.4	3.3
$\Delta T_{abs,liq-water}$	K	2.2	2.4	3.3
Q_{in}	kW	11.1	13.5	13.5
$W_{turb,calc}$	W	395	317	317
η_c	%	3.56	2.30	2.30
η_u	%	0.54	0.43	0.43

An essential parameter in the theoretical studies determining the performance in waste heat recovery is the TQ diagram of the heat input. Furthermore, for heat rejection, the shape of the TQ diagram and the related mass flow rate of the cooling fluid relates to the parasitic load. **Figure 11** compares the measured TQ diagrams to the ones from the corrected model. From this comparison, we can see that regardless of baffles for working fluid meandering in the desorber, the solution temperature rises much faster than required. The remaining temperature glide is only moderate. The pinch point then shifts to the point of saturated lean solution from the design point at the heat source inlet.

In the absorber, the vapour temperature corresponds to the saturated solution, while the solution itself on the tube surface is subcooled. The measured temperature profile corresponds to the inlet vapour temperature (lower than theoretical after adiabatic absorption), followed by probably measured vapour temperature before accurately following the modelled liquid solution temperature. This result suggests that the outlet solution is subcooled as it just follows the course of the liquid phase. The actual process doesn't allow the return of the bulk solution temperature back to the saturation temperature.

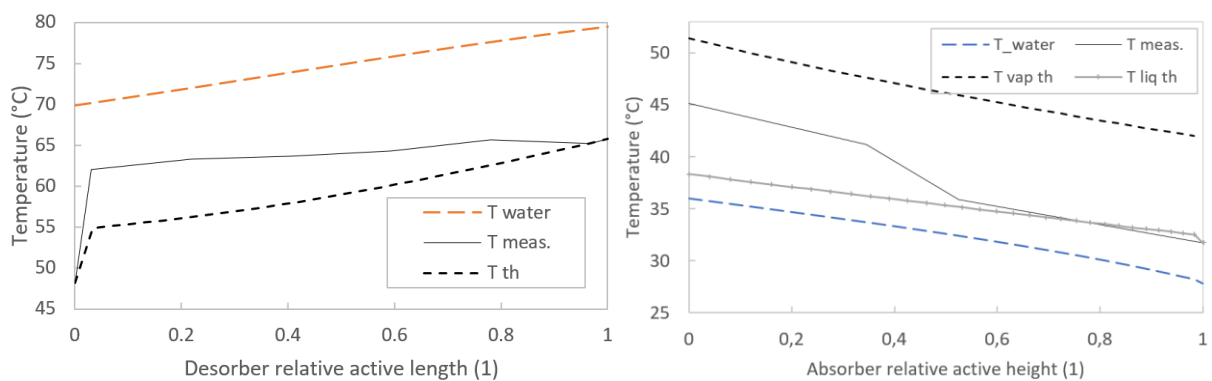


Figure 11: Comparison of measured temperature glide profiles in desorber and absorber with the corrected model

Another deviation from the cycle models is a lower measured vapour temperature exiting the steam generator than corresponds to the saturated mixture temperature (identified by outlet liquid solution). This is illustrated in **Figure 12**, where the theoretical values of pure vapour superheat (saturated solution temperature minus saturated steam temperature at corresponding pressure) are shown with respect to the rich solution concentration. The superheat based on the measured steam temperature is on average 7 K lower, with the spread of the values between 0.5 K and 19 K. Part of the lower temperature can be caused by thermal loss between the desorber and measuring point 1200 mm away. The loss should be nearly constant regardless of the steam mass flow rate, but the data says this is not the case. Adding the spread of the values and mostly constant temperature difference between the actual and the theoretical values suggests another phenomenon that causes departure from the thermal equilibrium. Generation of vapour at a part of the heat exchanger closer to solution inlet can have only partial effect as the measured temperature glide is on average less than 3K.

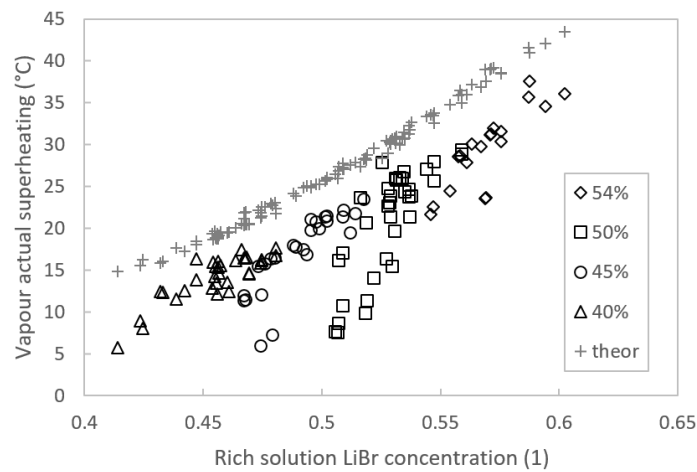


Figure 12: Measured and predicted superheat at the desorber outlet

Turbo-expander performance

Turbine performance is essential as a critical component, and the nature of its operation and a specific approach to the design are assessed separately. During the experiments, the expander was in operation between various pressure levels, with **Figure 13** summarising all experimentally obtained characteristics. During the operation, a resonance frequency and related vibrations caused the turbine speed around 8000 rpm, occasionally around 9000 rpm, to be the limit so that maximum efficiency couldn't be reached. However, the operation of the nylon turbine with an integrated BLDC motor as the generator in the steam environment has been proven. In addition, no issue regarding reliability and components material issue has been observed after the disassembly except for surface corrosion of several steel bolts holding the generator, which did not have any (even zinc) surface treatment.

The detail of turbo-expander operation for only the states selected as more accurate is shown in **Figure 14**. Both figures confirm that the generally expected trend of increasing efficiency with the pressure ratio is valid. Furthermore, even with the poor surface quality of the flow sections, the efficiency is mostly within boundaries provided by different loss models. This shows a high prospect of the plastic 3D printed concept, especially with more advanced design engineering than was adopted for this first proof of concept.

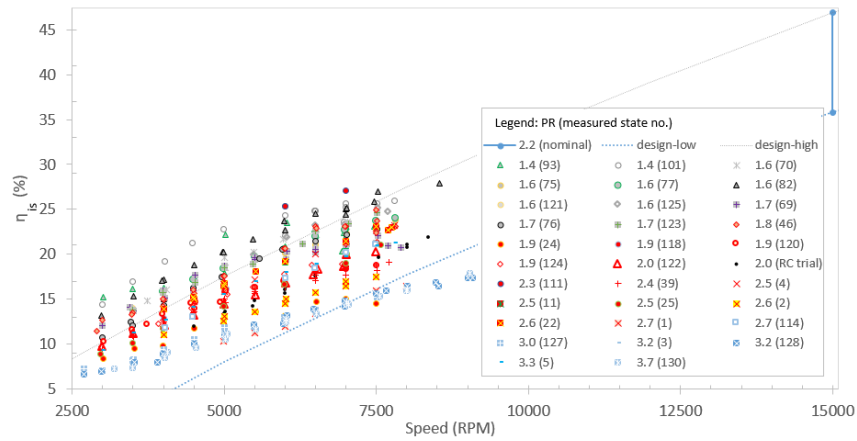


Figure 13: Measured turbine characteristics from APC operation and comparison with design

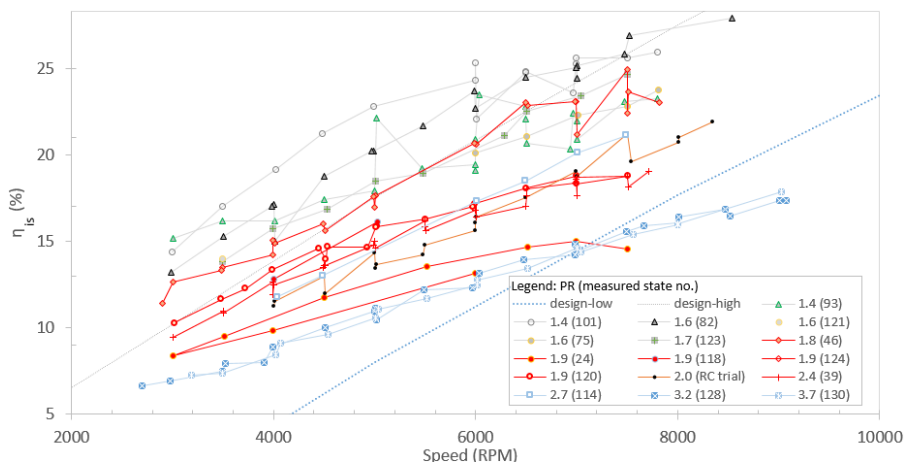


Figure 14: Measured turbine characteristics from APC operation for states with higher accuracy

Conclusions

A proof of concept absorption power cycle unit with LiBr solution working fluid has been built. Experimental performance and results have shown the overall technical feasibility of the concept. This is the first reported operation of a power cycle with a salt solution to the authors' knowledge. A 3D printed plastic turbine has been operated in the system. With the heat source temperature below 90°C, the maximum gross electrical cycle efficiency reached 0.8% and about 150 W. However, with a state of the art turbo-expander, there is a potential for maximal cycle efficiencies of almost 5% and heat source utilisation efficiencies around 0.5%.

Actual behaviour and parameters have shown several important aspects to consider when designing APC systems with LiBr solution. First, the temperature glide has been achieved only at a much smaller extent than it was designed. This is regardless of achieving a large concentration difference of the working fluid.

The performance of the desorber regarding heat transfer turned out better than according to the heat transfer model. The opposite was though the case of the absorber. Further improvement for desorber heat transfer could be in having higher roughness of the heat transfer surface. Still, the applied design of desorber has limited feasibility for the waste heat recovery applications where large temperature glide is essential.

The turbo-expander with the generator has shown over the experimental campaigns no damage both for the nylon components and the generator connected directly to the rotor with the low-pressure steam flowing around. Due to the high volumetric flow rates, it has been proven that the turbine is a suitable expander for APC with LiBr solution, even at very low power outputs. Lower than expected isentropic efficiency reaching about 25% can be significantly improved in future designs by tackling vibrations to allow higher rotational speed, improving the surface quality of flow paths and using better design models with subsequent optimisation. After such modifications, a 3D printed turbine shows a prospect of a cost-effective solution.

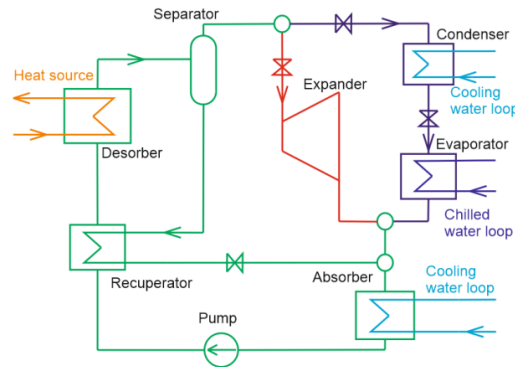


Figure 15: Schematic diagram of proposed combined heat and power absorption system

Even though authors have originally proposed the APC for waste heat recovery, the expander can also be implemented into an absorption chiller as a parallel branch, as shown in **Figure 15**. Such solution can improve utilisation of the absorption system when chiller demand is low, and power demand is high. The technology explored in this work (as 3D printed turbo-expander) can be cost-effectively applied in that manner

Acknowledgements

This work was supported by the Grant Agency of the Czech Technical University in Prague, grant No. SGS18/128/OHK2/2T/12 and SGS21/111/OHK2/2T/12.

References:

- [1] R. DiPippo, *Geothermal power plants : principles, applications, case studies, and environmental impact*. Oxford, UK: Butterworth-Heinemann, 2012.
- [2] Q. An *et al.*, 'Categorisation and analysis of heat sources for organic Rankine cycle systems', *Renew. Sustain. Energy Rev.*, vol. 64, no. October, pp. 790–805, 2016.
- [3] V. Novotny and M. Kolovratnik, 'Absorption power cycles for low-temperature heat sources using aqueous salt solutions as working fluids', *Int. J. Energy Res.*, vol. 41, no. 7, pp. 952–975, 2017.
- [4] A. I. Kalina, 'Method of generating energy', US Patent 4,548,043, 1985.
- [5] S. Macwan, 'THE KALINA CYCLE- A Major Breakthrough in Efficient Heat to Power Generation', in *CHP2013 & WHP2013 Conference and Trade Show*, 2013.
- [6] X. Zhang, M. He, and Y. Zhang, 'A review of research on the Kalina cycle', *Renew. Sustain. Energy Rev.*, vol. 16, no. 7, pp. 5309–5318, Sep. 2012.
- [7] V. Novotny and M. Kolovratnik, 'Absorption power cycles for low-temperature heat sources using aqueous salt solutions as working fluids', *Int. J. Energy Res.*, vol. 41, no. 7, pp. 952–975, Jun. 2017.
- [8] V. Novotný, D. J. Szucs, J. Spale, V. Vodicka, J. Mascuch, and M. Kolovratník, 'ABSORPTION POWER CYCLE WITH LIBR SOLUTION WORKING FLUID- DESIGN OF THE PROOF-OF-CONCEPT UNIT', in *5th International Seminar on ORC Power Systems*, 2019.

- [9] A. P. Weiß *et al.*, 'Customised ORC micro turbo-expanders - From 1D design to modular construction kit and prospects of additive manufacturing', *Energy*, vol. 209, p. 118407, Jul. 2020.
- [10] V. Novotny, J. Mascuch, H. Y. Tsai, and M. Kolovratnik, 'Design of Experimental Rig for Validation of Absorption Power Cycle Concept', *Energy Procedia*, vol. 105, pp. 4990–4996, 2017.
- [11] V. Novotny, D. Suchna, and M. Kolovratnik, 'Experimental rig for LiBr-water absorption power cycle - Design and first experimental results', in *AIP Conference Proceedings*, 2018, vol. 2047.
- [12] A. P. Weiß, 'Volumetric expander versus turbine – which is the better choice for small ORC plants', in *3rd ASME ORC Conference, Brussels (Belgium)*, 2015, pp. 1–10.
- [13] V. Novotny, J. Spale, D. Suchna, J. Pavlicko, M. Kolovratnik, and A. P. Weiß, 'Absorption power cycle with a 3D-printed plastic micro turbo-expander - Considerations, design and first experimental results', in *AIP Conference Proceedings*, 2021, vol. 2323, no. 1, p. 070003.
- [14] J. Spale, V. Novotny, V. Mares, and A. P. Weiß, '3D printed radial impulse cantilever micro-turboexpander for preliminary air testing', in *AIP Conference Proceedings*, 2021, vol. 2323, no. 1, p. 070002.
- [15] J. Mascuch, V. Novotny, V. Vodicka, J. Spale, and Z. Zeleny, 'Experimental development of a kilowatt-scale biomass fired micro – CHP unit based on ORC with rotary vane expander', *Renew. Energy*, 2018.
- [16] D. S. Kim and C. A. I. Ferreira, 'A Gibbs Energy Equation for {LiBr/H₂O} Solutions', in *Proceedings of the 6th IIR Gustav Lorentzen Conference on Natural Working Fluids, Glasgow (UK)*, 2004.
- [17] A. P. Weiss, J. Hauer, T. Popp, and M. Preissinger, 'EXPERIMENTAL INVESTIGATION OF A SUPERSONIC MICRO TURBINE RUNNING WITH HEXAMETHYLDISILOXANE', in *36th Meeting of Departments of Fluid Mechanics and Thermodynamics, 16th conference on Power System Engineering, Thermodynamics & Fluid Flow - PSE 2017*, 2017.
- [18] A. P. Weiß, T. Popp, G. Zinn, M. Preißinger, and D. Brüggemann, 'A micro-turbine-generator-construction-kit (MTG-c-kit) for small-scale waste heat recovery ORC-Plants', *Energy*, vol. 181, pp. 51–55, Aug. 2019.

Testing of a Carbon-Ammonia Gas-Fired Heat Pump

S.J. Metcalf^{1*}, A.M. Rivero-Pacho¹ and R.E. Critoph¹

¹School of Engineering, University of Warwick, Coventry, UK

*Corresponding author: steven.metcalf@warwick.ac.uk

Abstract

The aim of the work is to develop a gas-fired heat pump as a domestic gas boiler replacement, with 10 kW heat output and a seasonal gas utilisation efficiency (GUE, the ratio of heat output to gross calorific value of gas used) of 1.2. It is a two-bed carbon-ammonia adsorption heat pump with heat and mass recovery. The generators are a low-cost monolithic carbon – aluminium fin laminate design. Testing of the machine has revealed that the generators do not adsorb and desorb at the expected rate which limits the heat output to 7.7 kW and the COP (the ratio of heat output to heat input) to 1.27. This would translate to a GUE of only 1.12 including the anticipated gas burner efficiency. The cause of the slow adsorption rate has been identified as blockage of the beds by carbon powder and work is underway to rectify it.

Keywords: adsorption, heat pump, active carbon, ammonia

Introduction/Background

Fossil fuel boilers providing space heating and domestic hot water production are responsible for a significant proportion of global CO₂ emissions. Whilst the ultimate aim may be to replace them with electric heat pumps operating on renewably generated electricity, in many countries this would require a significant upgrade or even total replacement of the electrical grid in order to meet the demand created. In the interim period gas-fired heat pumps offer a more efficient alternative to gas boilers. Longer term they may even become renewable with the introduction of hydrogen or biogas into gas grids, and would reduce the amount of renewable gas that would need to be generated.

Several companies, universities and research establishments are developing gas-fired heat pumps with the aim of replacing domestic gas boilers [1-5] and the state-of-the-art is reviewed in the recent IEA Annex 43 report on 'Fuel Driven Sorption Heat Pumps' [6]. Systems using water as a refrigerant [1, 2] must operate with evaporating temperatures above 0°C which precludes the use of an air-source, necessitating a solar assisted or ground source for the evaporator at higher capital cost. Systems using ammonia refrigerant can operate with an air-source at lower cost and with a wider range of applicability. Ammonia-water absorption systems have a typical GUE of around 1.4-1.5 [3, 4]. Ammonia-salt adsorption systems are under development [5] with similar target GUE to the absorption systems, but the salt reactions are sensitive to the temperature conditions and reaction rates can limit the power density, adversely affecting the size and capital cost of the system.

Whilst active carbon has a lower concentration swing than salts (resulting in lower COP and GUE), physical adsorption is less sensitive to temperature conditions and so can operate over a wider range of conditions. It is also not limited by reaction rates, only heat transfer, and it is possible to highly compact the adsorbent without affecting mass transfer. These factors should enable more compact and lower cost systems to be constructed. Work has been ongoing at Warwick to develop an adsorption generator of sufficiently low cost for application to a domestic gas-fired heat pump. Previous designs using plates [7] and micro-

tubes [8] could not reach the desired price point due to manufacturing complexity and so a finned tube design has been developed as shown in Figure 1. The design incorporates a 10 mm O.D. stainless steel tube with a 400 mm long, 25 mm across-the-flats hexagonal carbon-aluminium laminate. There is a wire type ‘turbulator’ insert on the inside of the tube to increase the heat transfer coefficient. The carbon layers are 3 mm thick and the aluminium fins are 0.2 mm thick. These dimensions were decided upon as part of a previous study [9] which used a computational model of the generator to investigate the effect on COP and power density of varying these parameters. 19 such tubes are packed in a hexagonal array inside each generator. This number was chosen to achieve the target heat output of 10 kW at a GUE of 1.2 according the model predictions in [9]. The manufacturing process for these tube modules can be highly automated and should therefore be low cost.



Figure 1: Carbon-aluminium fin laminate over a 10 mm O.D. stainless steel tube

Methodology

The proof of concept system is shown in Figure 2. For ease of control of test parameters and to focus development on the heat pump itself, the heat input is provided by an electric heater and the evaporator uses glycol as the heat transfer fluid controlled by a circulator bath (the final machine would be air-source to ensure wide applicability). Two further refrigerated circulator baths are used to reject the heat output from the condenser and the cooler (which rejects the heat of adsorption).

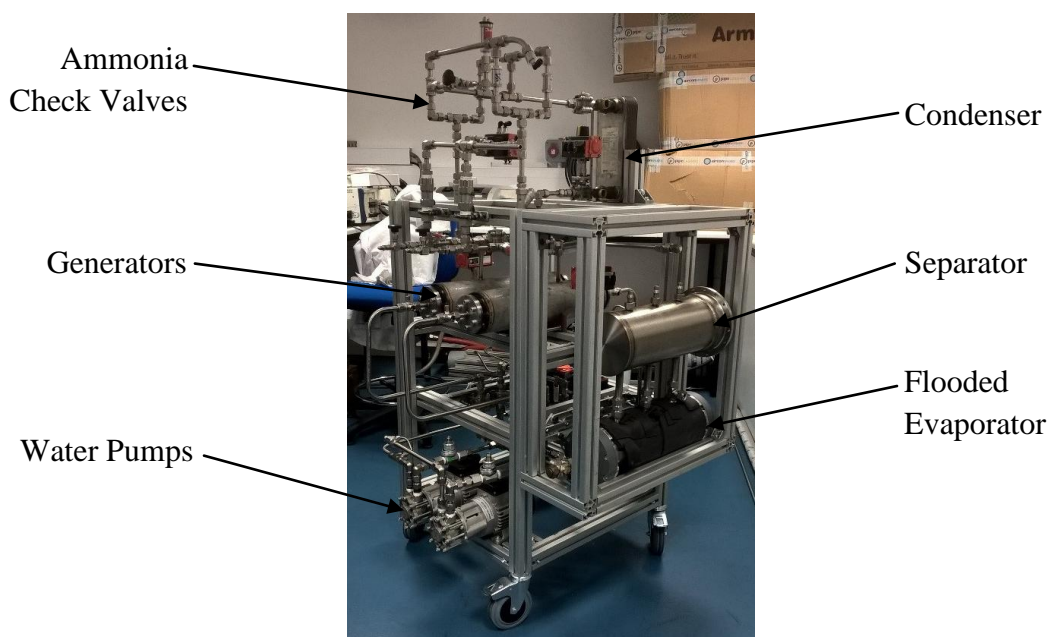


Figure 2: Proof of concept carbon-ammonia heat pump (prior to insulation)

Assuming that the eventual system has a gas burner efficiency of 80% and that a further 10% of the gross gas input could be recovered directly to the load, the target COP to achieve a GUE of 1.2 is 1.375 ($0.8 \times 1.375 + 0.1 = 1.2$).

The mass flow rate of water to the condenser and cooler and from the high temperature heat input are measured with Coriolis meters with an accuracy of $\pm 0.1\%$. The inlet and outlet temperatures are measured with PT100 temperature sensors calibrated to $\pm 0.1^\circ\text{C}$. This enables the heat inputs and outputs to be measured with an accuracy of $\pm 50\text{W}$.

The water flow to the beds is controlled by pneumatically operated ball valves for low pressure drop and a high switching speed. The mass recovery process is carried out by opening a pneumatically operated ball valve connecting the ammonia side of the two generators at the end of each half cycle. The ammonia flow between the generators and the condenser and evaporator is controlled by ball type spring check valves. The liquid ammonia from the condenser is collected in a 0.5 litre receiver vessel. Once full, a ball valve between the receiver and condenser is closed and a solenoid valve to the evaporator is opened and the liquid emptied into the evaporator. This process occurs approximately 2-4 times per cycle depending on the operating conditions.

Discussion and Results

Table 1 shows the results from selected cycles with two different heat input temperatures and evaporating temperatures and with varied cycle times. The maximum COP is only 1.249 despite the favourable condensing temperature and is below the target of around 1.375. Measurement of the ammonia flow rate to and from the generators using Coriolis meters has revealed that the rate of adsorption and desorption is lower than expected, but especially the adsorption. Cycle times are longer than predicted, leading to lower than expected power output and lower COP (since the losses become more significant). The tube modules were put through a large temperature jump test before installation and performed as expected in both adsorption and desorption and so the only course of action was to partially dismantle one of the generators to try to determine the cause of the problem.

Table 1: Test results with varied cycle time, evaporating temperature and high temperature heat input (no mass recovery)

T_{HT} [$^\circ\text{C}$]	T_{evap} [$^\circ\text{C}$]	T_{cond} [$^\circ\text{C}$]	Cycle time [s]	Heating Power [W]	High Temp (HT) Heat Input [W]	COP
160	6 – 15	37 – 41	552	6614	5295	1.249
160	6 – 15	37 – 41	612	5899	4722	1.249
140	5 – 10	36 – 40	342	7599	6277	1.211
140	5 – 10	36 – 40	462	7089	5751	1.233
140	-6 – -1	34 – 39	342	6531	5724	1.141
140	-6 – -1	34 – 39	462	6119	5273	1.160
160	-6 – -1	34 – 39	342	7721	6752	1.143
160	-6 – -1	34 – 39	462	7177	6186	1.160

Part of the shell and a few of the outer tubes of one of the generators were cut away for investigation, as shown in Figure 3. It was discovered that the passages between the tube modules had become blocked with carbon powder. A spacing of approximately 1.5 mm was allowed for between each module, but this had become completely filled with carbon and the passage of ammonia obstructed to the modules in the centre and lower part of the generators.

The effect during adsorption is more pronounced due to the lower gas density and therefore higher gas velocity. There is also a lower driving pressure difference available during adsorption due to the closer spacing of isosteres at lower temperature.

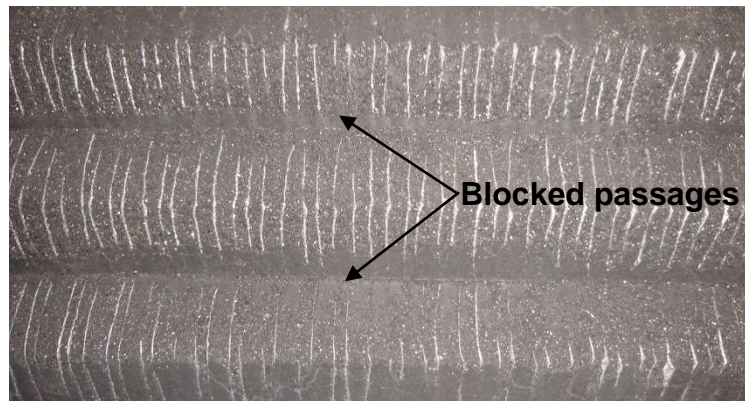


Figure 3: Shell cut away from a generator revealing blockage of ammonia passages.

The outer layer of carbon on each module is relatively fragile after release from the mould and it is believed that it is this carbon which has blocked the passages. The modules do not appear to be continually deteriorating and it is believed that once this fragile outer layer is removed, the modules should be stable and not lose any further material.

Before dismantling one of the generators, tests were carried out with mass recovery to determine if the benefits were as predicted by computational models. The results are shown in Table 2 in comparison to a cycle without mass recovery.

Table 2: Effect of mass recovery

Mass Recovery?	Heating Power [W]	High Temp (HT) Heat Input [kW]	COP	Ammonia mass change per cycle per generator [g]
No	6614	5295	1.249	363
Yes	6740	5312	1.269	443

The effect of mass recovery on COP and power output is in line with model predictions and increases the COP from 1.249 to 1.269. This would correspond to a GUE of $1.269 \times 0.8 + 0.1 = 1.12$.

Summary/Conclusions

Testing of a finned tube design of carbon-ammonia adsorption generator has revealed that the flow rate of ammonia during adsorption and desorption is lower than expected, limiting power output and COP. The cause has been determined to be blockage of the ammonia flow passages within the generators by loose carbon material. It is believed that the deterioration is not continual and further work is underway to reconstruct the generators with the blockage removed.

Acknowledgements

This work was supported by the UK EPSRC grants ‘i-STUTE’ EP/K011847/1 and ‘4S-DHW’ EP/N021304/1 and by the UK government department BEIS grant LCHTIF1021 ‘Gas Adsorption Heat Pump’.

Nomenclature

cond	Condenser
COP	Coefficient of performance
evap	Evaporator
GUE	Gas utilisation efficiency
HT	High temperature
T	Temperature

References:

- [1] Wittstadt, U., Földner, G., Vasta, S., Volmer, R., Bendix, P., Schnabel, L., Mittelbach, W, Adsorption Heat Pumps and Chillers – Recent Developments for Materials and Components, 12th IEA Heat Pump Conference, 2017
- [2] Földner, G., ADOSO – Gas Adsorption Heat Pump with a Crystalline Zeolite Heat Exchanger and a Novel Evaporator-condenser Device, German Federal Ministry of Economic Affairs and Energy (BMWi) Project. URL: <https://www.ise.fraunhofer.de/en/research-projects/adoso.html>
- [3] Aprile M, Scoccia R, Toppi T, Guerra M, Motta M. Modelling and experimental analysis of a GAX NH₃-H₂O gas-driven absorption heat pump. *Int J Refrig.* 2016;66:145–55
- [4] Garrabrant, M., Stout, R., Blaylock, M., Keinath, C., Residential and Commercial Capacity Absorption Heat Pumps for Space and Domestic Water Heating Applications, 12th IEA Heat Pump Conference, 2017.
- [5] Blackman C, Bales C, Thorin E. Experimental Evaluation and Concept Demonstration of a Novel Modular Gas-Driven Sorption Heat Pump, 12th IEA Heat Pump Conference, 2017.
- [6] Albers et. al., Fuel Driven Sorption Heat Pumps, IEA Annex 43 Final Report, Heat Pump Centre, ISBN 978-91-89167-50-6.
- [7] Z. Tamainot-Telto, S.J. Metcalf, R.E. Critoph, Novel compact sorption generators for car air conditioning, *International Journal of Refrigeration*, 2009.
- [8] S.J. Metcalf, A.M Rivero-Pacho, R.E. Critoph, Performance Map of an Ammonia-Carbon Adsorption Heat Pump, *2016 Heat Powered Cycles Conference*, Nottingham, UK, 2016.
- [9] A.M. Rivero-Pacho, R.E. Critoph, S.J. Metcalf, Modelling and development of a generator for a domestic gas-fired carbon-ammonia adsorption heat pump, *Renewable Energy*, 110, pp. 180-185, 2017

Ammonia-Salt Reactions for Heat Pumping and Thermal Transforming Applications

S. Hinners^{1*}, G. H. Atkinson¹, R. E. Critoph¹ and M. Van der Pal²

¹ Sustainable Thermal Energy Technologies (STET) Research Group, School of Engineering, The University of Warwick, Coventry, CV4 7AL, UK

² TNO Energy Transition, Westerduinweg 3, 1755 LE Petten, Netherlands

* Corresponding author: S.Hinners@warwick.ac.uk

Abstract

Work to produce resorption machines has been performed at The University of Warwick (Warwick) by testing and analysing candidate sorbent salts. A heat transfer and reaction kinetics model has been designed to predict the ammonia sorption behaviour of the salt (a composite of salt and expanded natural graphite) and to calculate a value for the specific mean power per volume of the composite. Simulations from the model predict the salt behaviour well, but preliminary results show that heat transfer resistance between the composite salt and the metallic heat transfer surface significantly reduces the power output per litre of sorbent. To be considered for integration into future heating networks, improving the heat transfer in the sorbent reactor is key to producing an effective and compact resorption machine, which can be used in the upgrading of waste heat or for heat pumping.

Keywords: adsorption; ammonia; desorption; heat; heat pump; resorption; thermal transformer; thermochemical; waste heat

Introduction

The UK government is trialling the use of hydrogen for heating homes with demonstration homes to be built in Gateshead and plans for low carbon fuels (biogas and hydrogen) to replace fossil fuels in both industry and domestic settings [1]. Key to achieving these goals will be an increase in efficiency of heating systems, which can improve running costs and energy utilisation. Resorption systems using ammonia-salt reactions have long been of interest and could provide these developments. Resorption heat pumps will have a marked efficiency improvement versus a condensing boiler, with potential coefficients of performance of 1.6. The two-bed format of resorption means that systems are simple in design, making manufacture and development more affordable than sorption systems with condensers and evaporators. Thermal transformers can utilise low grade waste heat that would otherwise be emitted to atmosphere, returning steam to an industrial process. Both thermal transformers and heat pumps can be a key part of heating and cooling networks for improved heating integration and heat recovery.

Work at Warwick has focussed on developing resorption systems by characterising a number of salts with Large Temperature Jump (LTJ) testing, and matching results to a heat transfer and reaction kinetics simulation model. The tests mimic the salt reaction behaviour in conditions similar to a real machine. The results have enabled reaction kinetics for ammonia-salt reactions to be modelled, identifying Clapeyron lines for the onset of reaction, estimating a single accurate heat of reaction (for adsorption and desorption), and identifying model parameters to characterise the performance of the composite salt.

The LTJ experiment tests a composite salt adsorbent (halide salt in an expanded graphite matrix) in a small heat exchanger, with a temperature controlled heat transfer fluid which initiates the sorption reactions. The primary reactor was designed hosting the composite salt inside a tube ('tube-side'), and later, a secondary reactor was manufactured to test the material on the outside of a tube ('shell side'), which has been key to explore the heat transfer into and out of the material.

Material Preparation

The halide salts selected for test are impregnated in an Expanded Natural Graphite (ENG) sheet. The salts are impregnated into an ENG matrix to address conductivity issues, swelling or agglomeration of the pure salt. The resultant composite exhibits the characteristics favoured for a chemisorption machine, mainly rapid heating and cooling, and good salt distribution in the matrix. Preparation is described by Hinners and Critoph [2].

The ENG is a SIGRATHERM[®] graphite lightweight board (ECOPHIT[®] L10/1500 10 mm thick) and samples are cut from sheet to two different profiles. Disks to fit a 10.8 mm tube bore, Figure 1 (a), are used for the tube side reactor and rings with a 12.7 mm internal diameter (to fit over a ½" OD tube) and 35 mm outer diameter are used in the shell side reactor. The disks (or rings) are dried in an oven for 30 minutes at 200 °C, weighed, Figure 1 (b), and then submerged in a salt solution. The strength of the salt solution predominantly determines the salt uptake. The disks in solution are placed under vacuum for 24 hours, Figure 1 (c), removed and finally dried in an oven to evaporate the water resulting in the final composite samples, Figure 1 (d). The composite sample mass is measured and compared with the pure ENG mass to determine the salt uptake.

The composite samples produced and tested in this work were manufactured using a waterjet cutting method. However, mechanical cutting of the ENG sheet is being investigated to improve the thermal contact between the composite salt and heat transfer surface area, aiming to improve heat transfer in a proof-of-concept resorption heat pump or thermal transformer. Mechanical cutting uses custom designed hole saws, such that ENG samples can be made quickly with minimal material wastage and a *smooth* finish. Initial samples prepared by mechanical cutting have no apparent reduction in performance or salt uptake.

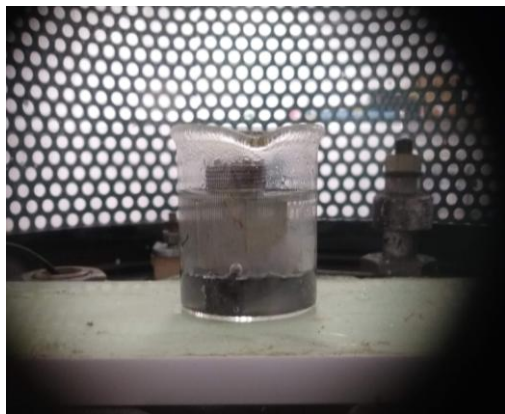
In this work, Low Temperature Salts (LTS) and High Temperature Salts (HTS) are investigated for heat pumping and thermal transformation applications. Manganese chloride (MnCl₂) is reviewed for the HTS in both heat pumping and thermal transforming. The LTSs for a resorption heat pump require a desorption reaction at low ammonia vapour pressures and this is the limiting stage in the cycle. Ammonium chloride (NH₄Cl), sodium bromide (NaBr) and barium chloride (BaCl₂) have been identified as potential candidates. For thermal transformers calcium chloride (CaCl₂) is likely to be the low temperature salt; when paired with manganese chloride, calcium chloride will desorb at around 80 °C (low grade waste heat temperature) and manganese chloride will adsorb above 100 °C at the same pressure.



(a)



(b)



(c)



(d)

Figure 1. (a) Dried ENG disk samples (central hole drilled for thermocouple access and gas transport) (b) the mass of the disks is measured (c) ENG disks submerged in salt solution under vacuum conditions and (d) the final composite samples.

Experimental Method

The LTJ technique pioneered by Aristov and Dawoud [3], has been used to assess composite salt behaviour. Experiments involve placing composite samples inside a ‘unit-cell’ sorbent reactor connected to an ammonia expansion vessel, with the composite salt placed on either the tube side, or shell side, depending on the reactor geometry. A silicone oil heat transfer fluid flows through the reactor, which is supplied from two temperature controlled baths at different temperatures. By controlling the flow through the reactor from each bath, through a valve manifold, a temperature ‘jump’ up or down, imposes conditions that imitate the dynamic conditions of a real machine and initiate an adsorption, or desorption reaction as illustrated by Hinners and Critoph [2].

An example of a tube side LTJ setup is shown in Figure 2, with the key components on the ammonia side and the heat transfer fluid (HTF) connections shown. The tube side reactor is a double pipe heat exchanger. Figure 3 shows the shell side reactor for reference. The shell reactor was developed to further evaluate the composite salt performance in the shell side of the double pipe heat exchanger geometry, the design is presented in detail by Hinners et al. [reference pending]

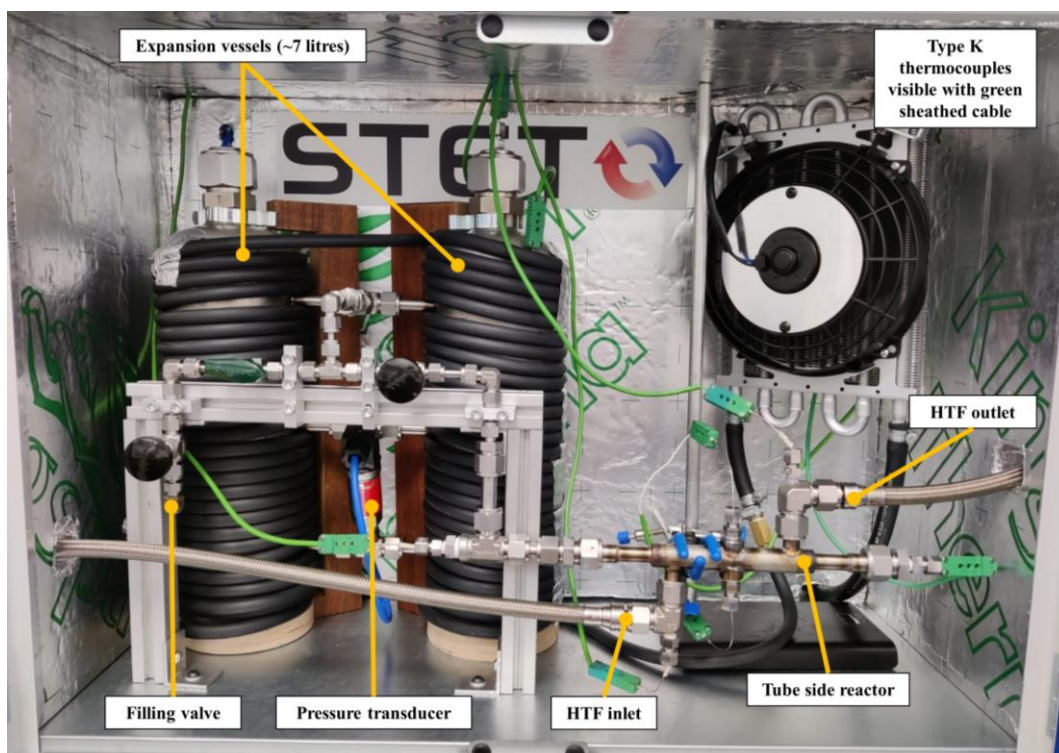


Figure 2. The Large Temperature Jump (LTJ) experimental setup, with the tube side reactor configuration.

The LTJ rig can be modified to estimate the heat of reaction by disconnecting the expansion vessels. Unlike the LTJ test, the temperature must change very slowly, tracking along the isostere and for simplicity is termed an Isosteric Temperature Change (ITC) test. The slow nature of the ITC together with the lack of significant sorption when on the isostere reduces the hysteresis and gives a single value for the enthalpy. A cycle (desorption and adsorption) using the ITC test method takes several hours (typically 10 hours to heat and cool by 15°C), whereas with the LTJ testing method, a cycle completes in minutes (typically 10-30 minutes).

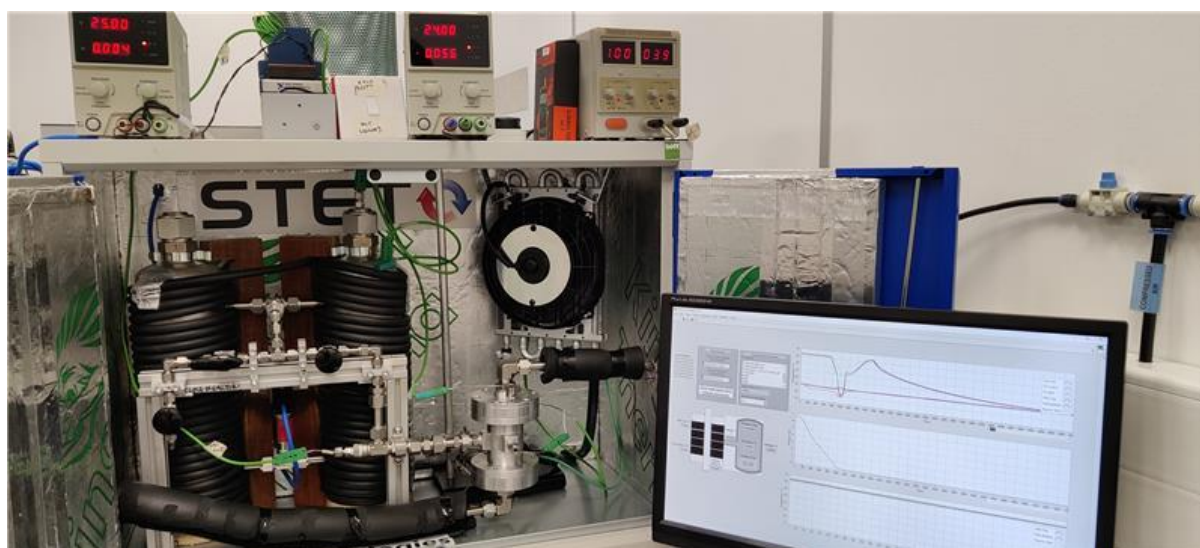


Figure 3. The Large Temperature Jump (LTJ) experimental setup, with the shell side reactor configuration. The LabVIEW program can also be seen on the screen.

Pressure readings for the system and temperature measurements of the reactor, using sensors connected to an NI CompactDAQ and linked to a LabVIEW interface, allow an

understanding of the kinetics of the composite salt to be observed in real-time. For the ITC test, the temperature and pressure isostere data, is used to obtain an accurate heat of reaction.

For the LTJ recorded data, the temperature and pressure is used to find separate adsorption and desorption equilibrium lines, which illustrate the onset of reaction as described by the Clapeyron equation (equation 2) where: ΔH is the reaction enthalpy change; ΔS is the reaction entropy change; R_0 is the universal gas constant, 8.413 [J/(mol·K)]; and T is the temperature. ΔH and ΔS are obtained through LTJ testing.

The LTJ results also are the basis for a semi-empirical heat transfer and reaction kinetics model developed by Critoph et al. [*reference pending*], based on a linear form advancement equation summarised by Mazet, Amouroux and Spinner [4] Equation 1.

$$\frac{dX}{dt} = (1 - X)^n A \frac{(p_{eq} - P)}{p}, \quad (1)$$

Where: X is the advancement of the reaction (0 to 1); p is the pressure; p_{eq} is the equilibrium pressure; and A and n are constants. Critoph et al. developed the advancement model into a physical adsorbent ‘mass based’ model, considering the mass of adsorbate in each ‘state’ during the reaction. p_{eq} in Equation 1 is calculated from the Clapeyron equation:

$$\ln(p_{eq}) = -\frac{\Delta H}{R_0 T} + \frac{\Delta S}{R_0}, \quad (2)$$

The adsorption and desorption equilibrium lines from equation 2 will have different values for ΔH . To abide by the first law of thermodynamics the value for the heat of reaction must be near to equal (with the difference as a function of hysteresis temperature). Therefore the estimated heat of reaction ΔH_{react} from the ITC is used within an energy balance.

The model was implemented in MATLAB[®] and the simulated outputs matched to the experimentally obtained data through the fine-tuning of five key modelling parameters: the thermal conductivity of ENG, wall heat transfer coefficient (characterised by an ammonia gas gap between the reactor wall and composite sample), fraction of salt accessible to gas (active fraction), and the two reaction rate constants (A and n) in Equation 1, which are different for adsorption and desorption. This is detailed by Hinners et al. [*reference pending*]

Experimental tests were conducted across a pressure range of interest for applications in resorption heat pumping and thermal transforming, predominantly 0.5-10 bar. The validity of the model output was tested by comparing with collected experimental data at different pressures and for different driving temperatures during a temperature jump cycle. On completion of testing, the constants in equation 2 were obtained and through modelling, the five key parameters identified, which allow predictions of the performance of the composite salt to be made.

The simplicity of the LTJ rig allows the testing configuration to be adapted and changed easily, allowing for different reactor geometries and dimensions that might be used in real machines. The shell side system also provides a basis to quickly test different ENG sample ring sizes around a ½” tube. The intention of the work is that following model validation / characterisation of the composite salt behaviour, the model can be used to optimise the design of a full-size reactor (e.g. in a ‘shell side’ configuration of a shell and tube reactor, the tube

diameter and pitch). A ‘unit-cell’ reactor can quickly be manufactured for a confirmatory LTJ test, testing the model predictions.

Results and Discussion

To summarise the tests, firstly an LTJ test is a quick method to identify isothermal reaction onset, understand dynamic behaviour and to calculate equilibrium lines. Secondly, an ITC test allows an accurate prediction of the heat of reaction to be made. Finally, the semi-empirical MATLAB® model outputs can be matched to recorded pressure and temperature measurements from LTJ tests, allowing the tested salts to be characterised and subsequently the composite salts simulated for different geometries (shell or tube side) with applications in thermal transforming and heat pumping.

Large Temperature Jump Experiments

An example of a barium chloride composite salt test (in tube side) is shown in Figure 4. Referring to Figure 4, unique characteristics such as the superheat region during the desorption reaction (peak prior to the isothermal region) and the hysteresis between the adsorption and desorption reactions (with different isothermal reaction temperatures at the same pressure), are clearly visible from the LTJ results. These characteristics are not exhibited when running the same samples through the ITC testing method, or with Rubotherm magnetic suspension balance measurements. The results illustrate the additional detail gained in understanding the dynamic performance of the candidate salts when tested in this manner.

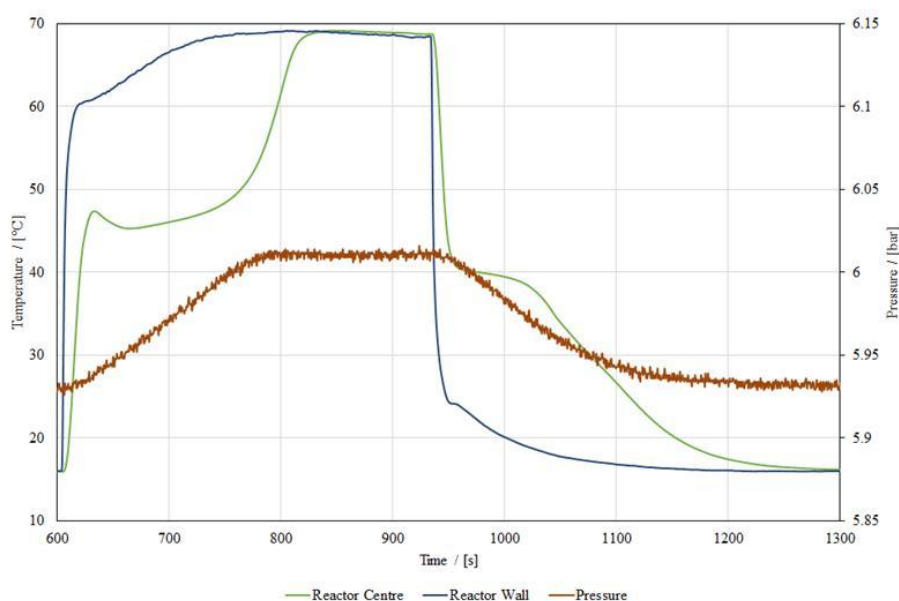


Figure 4. Barium chloride LTJ cycle with a desorption followed by an adsorption reaction. Reactor centre and reactor wall temperatures are measured from the left-hand y axis and the pressure from the right-hand y axis.

Equilibrium ‘points’ are measured during the isothermal phase change regions in the LTJ data, with ‘points’ recorded at different tested pressures. The points are plotted on a $\ln(p)$ vs. $-1/T$ graph and form the working equilibrium lines for the onset of each reaction. These working equilibrium lines were found for all tested salts and an example of the equilibrium lines for manganese chloride are shown in Figure 6 (grey is adsorption and yellow is desorption).

However, during analysis of some salts and also visible in Figure 6, hysteresis is present between the adsorption and desorption reaction, often with deviations in the heat of reaction (slope) between the two lines. To address these issues an ITC test is conducted.

Isosteric Temperature Change Experiments

The ITC test, is a different application of the LTJ rig. The premise of the test is that if the expansion vessels are disconnected and the system volume is small, the proceeding reaction causes a large pressure rise. Under these conditions it is possible to slowly track the equilibrium line up and then down without significant desorption or adsorption. In effect, the slower the heating and the less the gas void volume, the less hysteresis is seen, with the ultimate conclusion that to leave the system to reach equilibrium at a number of points (at infinite time) a single line would be followed in both directions. The ITC method collects tens of thousands of data points and the adsorption and desorption lines are very nearly parallel, which allows a single value for the enthalpy to be calculated based on the Clausius-Clapeyron function.

Figure 5 shows an example of an ITC output for a manganese chloride composite sample over a series of heating and cooling cycles, showing a large pressure rise and clear repeatability during the test. Figure 6 shows the data from Figure 5 plotted on a $\ln(p)$ vs. $-1/T$ graph (orange for adsorption and blue for desorption) and although hysteresis is still present, the adsorption and desorption lines are parallel with a single value for the heat of reaction, calculated from an average of both line gradients.

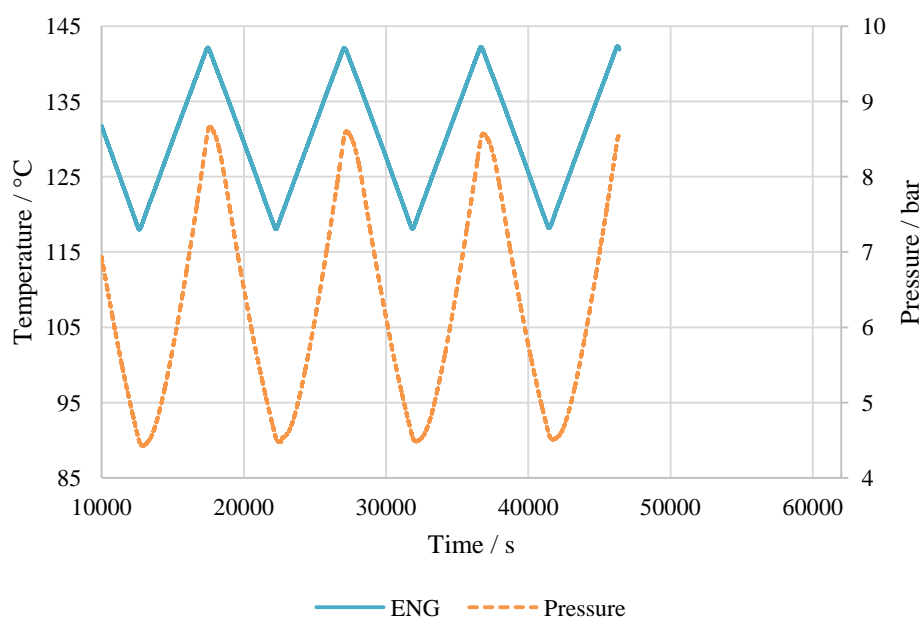


Figure 5. ITC data output for manganese chloride. The solid line shows the composite sample cycling temperature (left hand y axis) and the dashed line the pressure change (right hand y axis).

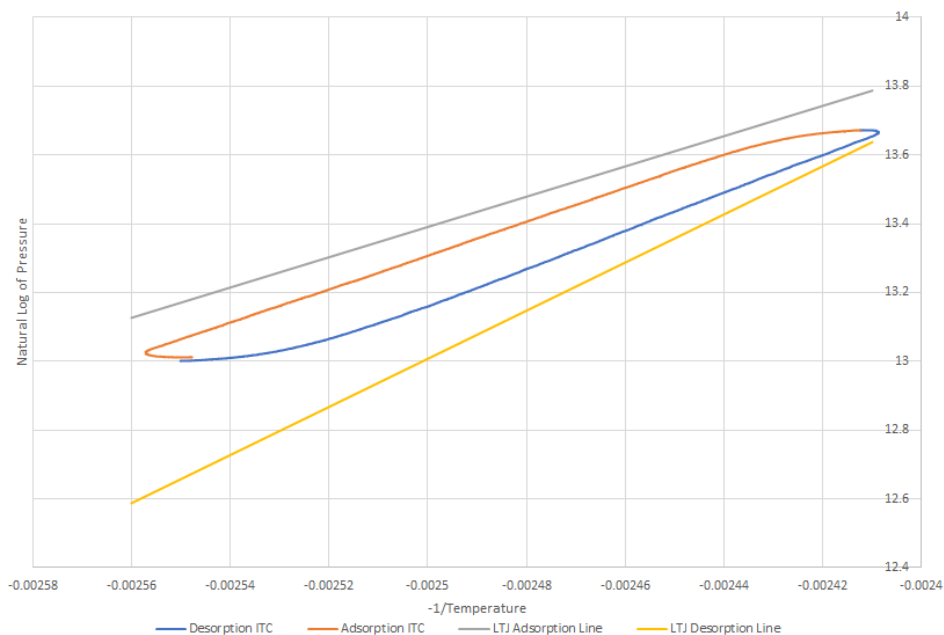


Figure 6. $\ln(p)$ versus $-1/T$ plot of ITC data from Figure 5 with the LTJ result lines, showing the difference in equilibrium data obtained from the LTJ and ITC testing methods.

MATLAB[®] Model Outputs

An example of the MATLAB[®] model output is shown in Figure 7 for a BaCl_2 sample at 8 bar during a desorption reaction. By matching the modelling constants (thermal conductivity of ENG, wall heat transfer coefficient, active fraction and the two reaction rate constants A and n) and using the experimentally obtained equilibrium data (from a combination of LTJ and ITC testing), the reaction onset, isothermal phase change temperature and reaction duration can be predicted. The simulated model output is matched to the experimental data and the model is validated by running both adsorption and desorption reactions across the tested experimental pressure range, ensuring a suitable match [*reference pending*].

The resulting matched simulation data can then be used to predict performance for different reaction driving temperatures and for different reactor geometries, as well as predict the power outputs from the reaction, see Discussion.

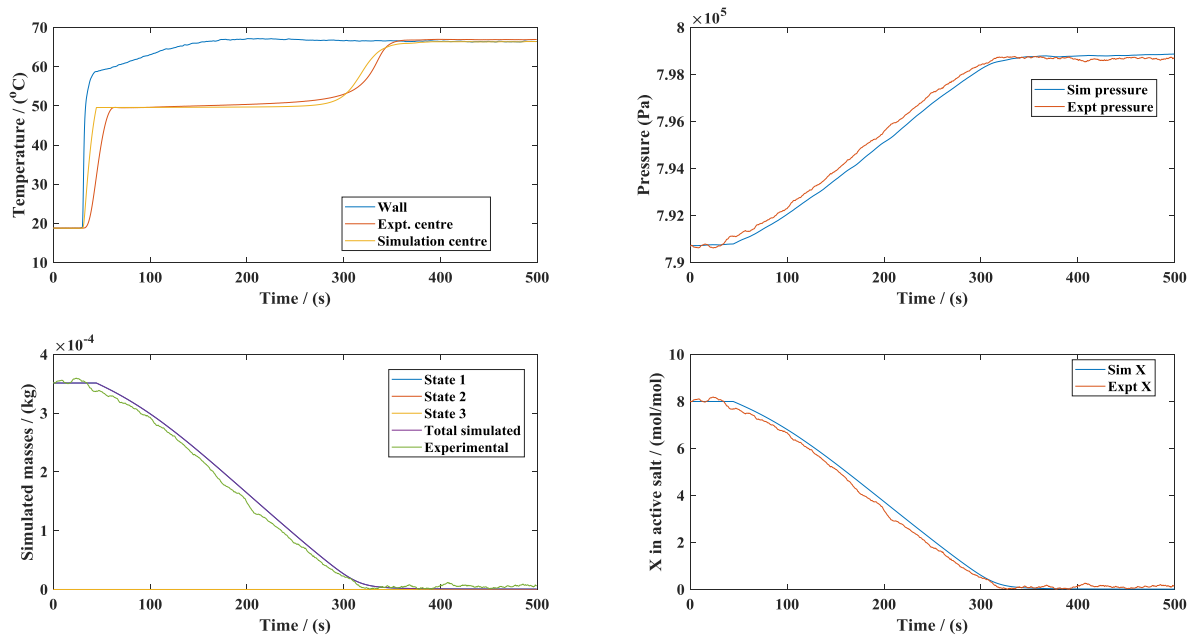


Figure 7. Example of the model output for a BaCl_2 (8/0 reaction) sample at 8 bar during a desorption reaction, comparing the simulated (sim) with the experimental (expt) data for a tube side reactor configuration.

Discussion

Of the five modelling constants, identifying the heat transfer coefficient or ‘gap’, between the composite salt and the stainless-steel tube (for the tube side reactor, the contact is to the internal surface of a 1/2” tube and for the shell side reactor, the contact is the external surface of a 1/2” tube) is crucial to matching the temperature rise seen in the experimental data. The importance of the ‘gap’ is highlighted when the physical significance is considered, as a ‘gap’ represents a thermal resistance between a heat transfer surface and the sample, reducing the efficacy of the ‘unit-cell’ reactor to heat and cool the samples quickly during test — the larger the gap, the greater the resistance and the poorer the heat transfer into and out of the sample. Given the reactions are heat transfer limited (shown by the linear pressure rise during testing) ensuring good heat transfer across the tube-to-sample interface is critical to performance.

Experimental tests conducted in both the tube and shell side configurations, highlighted the model effectiveness as shown by Hinners et al. [*reference pending*]. An example of the shell side model output is shown in Figure 8 (a), with good matching of the temperature and pressure profiles, and Figure 8 (b) shows the specific mean power output during the reaction. Detailed shell side information and results can be found in [*reference pending*].

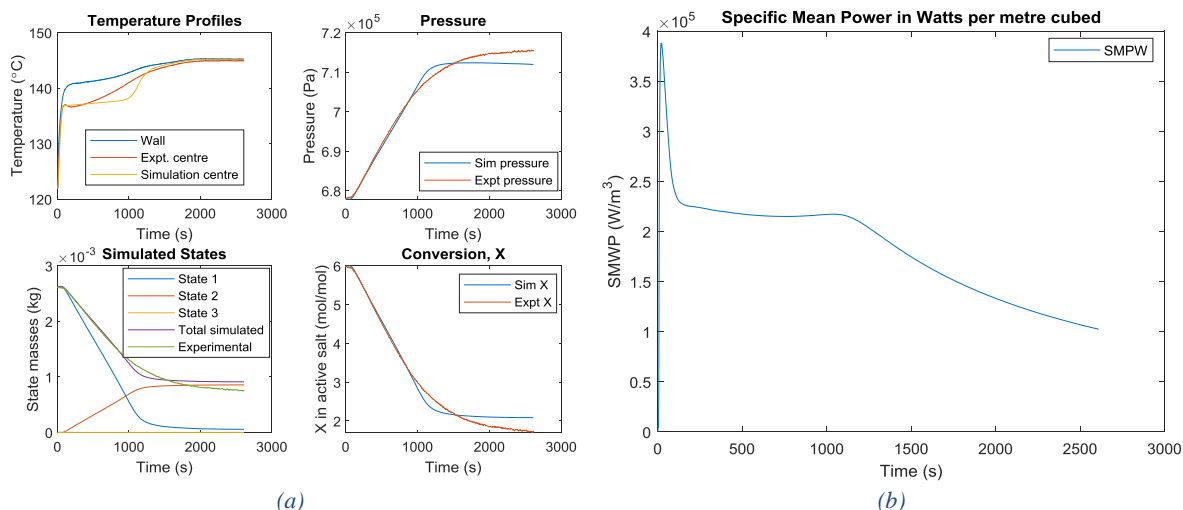


Figure 8. (a) Temperature and pressure plots for a manganese chloride shell side test and (b) the specific mean power output during the reaction.

With the model providing good estimation of results, the model has been developed to be able to simulate different diameters of composite samples, in shell or tube side configuration. By comparing the mean power per volume, an optimised reactor design can be produced. This is derived by optimising for the highest peak Specific Mean Power (SMPW) in W/m^3 or kW/litre . An effective resorption system target is to provide 1 kW per litre, which is the aim when investigating different reactor geometries.

Figure 8 (a) shows experimental data and model outputs for a manganese chloride shell side sample at 7 bar. Figure 8 (b) shows the SMPW calculated from the experimental data. The results are lower than the target SMPW and highlights two main challenges. First, in Figure 8 (a), although the oil temperature is provided at a temperature 10 °C above the equilibrium (akin to a designed driving temperature for a transformer), the wall temperature is held down by the phase change in the salt, suggesting the heat transfer from the fluid to the wall is limiting. Second is the value for the peak SMPW, Figure 8 (b) which is below 0.4 MW/m^3 (0.4 kW/l). When the model is used to simulate a temperature jump, a higher SMPW is predicted with a reduced ‘gap’ size, i.e. a better heat transfer between material and the wall. To realise a proof-of-concept machine, the peak SMPW value will be improved by increasing the heat transfer from the fluid to the wall, reducing the ‘gap’ between the composite salt and tube, and optimising the outer radii and/or inner pipe size.

Future work will focus on improving the heat transfer by fitting the composite samples tighter to the tube to improve the heat transfer and using high pressure water (rather than silicone oil) as the heat transfer fluid. Fluid side inserts will also be used to increase the heat transfer coefficient from fluid to tube, by increasing turbulence. Initial results are promising for the development of a bench-scale test rig and steps are already being taken to improve the heat transfer by improved material cutting as described in the material preparation section. Methods to fit shell side rings with a smaller inner diameter are also being trialled. Small reductions in the metal-ENG gap will have a large effect in improving the heat transfer, and therefore producing a 2kW scale resorption system with a SMPW of 1 kW/l should be achievable.

Conclusions

Salt testing and analysis has been successful and a MATLAB[®] model has been developed which predicts the performance of the adsorbent material (salt impregnated in ENG). The model has been extended to simulate different geometries, changing parameters to find an optimal design. Preliminary results from experimental test show the specific mean power per cubic metre is lower than the simulated target value of 1 kW/l, but issues with heat transfer have been identified and work is ongoing to increase heat transfer between the composite salt and tube, as well as tube and heat transfer fluid. A test system will soon be produced showing the efficacy of the composite and resorption systems for integrated heating networks.

Acknowledgements

This work has been supported by two EPSRC projects: EP/V011316/1, 'Sorption Heat Pump Systems' in support of Mission Innovation Challenge 7: Affordable Heating and Cooling, and EP/R045496/1, Low Temperature Heat Recovery and Distribution Network Technologies (LoT-NET).

Thanks go to Charles Joyce for his technical guidance and manufacture of materials and widgets needed for testing.

References

- [1] A.-M. Trevelyan, "Say Hy to the home of the future," ed. BEIS: Department for Business, Energy & Industrial Strategy 2021.
- [2] S. Hinners and R. E. Critoph, "Modelling the Ammoniation of Barium Chloride for Chemical Heat Transformations," *Energies*, vol. 12, no. 23, p. 4404, 2019. [Online]. Available: <https://www.mdpi.com/1996-1073/12/23/4404>.
- [3] Y. I. Aristov, B. Dawoud, I. S. Glaznev, and A. Elyas, "A new methodology of studying the dynamics of water sorption/desorption under real operating conditions of adsorption heat pumps: Experiment," *International Journal of Heat and Mass Transfer*, vol. 51, no. 19–20, pp. 4966-4972, 9// 2008, doi: <http://dx.doi.org/10.1016/j.ijheatmasstransfer.2007.10.042>.
- [4] N. Mazet, M. Amouroux, and B. Spinner, "ANALYSIS AND EXPERIMENTAL STUDY OF THE TRANSFORMATION OF A NON-ISOTHERMAL SOLID/GAS REACTING MEDIUM," *Chemical Engineering Communications*, vol. 99, no. 1, pp. 155-174, 1991/01/01 1991, doi: 10.1080/00986449108911585.

2 references pending upon acceptance for publication.

Extended Frequency Response Analysis for Loading and Temperature Dependent Heat and Mass Transfer Evaluation in Adsorbent Coatings

E. Laurenz^{1*}, G. Földner¹, A. Velte¹ and L. Schnabel¹

¹ Fraunhofer Institute for Solar Energy Systems (ISE), Heidenhofstr. 2, D-79110 Freiburg, Germany

*Corresponding author: eric.laurenz@ise.fraunhofer.de

Abstract

The combination of heat and mass transfer (HMT) phenomena and sorption equilibria are governing the adsorption dynamics. Their thorough understanding is crucial for the improvement of power density on appliance level. HMT phenomena are often difficult to distinguish, especially regarding the dependency on loading and temperature, i.e. the thermodynamic state of the adsorbent. In this contribution a frequency response (FR) analysis extended by manometrical equilibrium measurements is presented as a novel method for measuring both, adsorption equilibrium and HMT, in a single measurement for the example of an aluminium fumarate coating with water as refrigerant. This includes the direct measurement of the adsorption equilibrium derivatives for adsorption enthalpy evaluation. The thermal conductivity of the samples was identified as about 0.07 W/(m K), and the LDF time constant between 0.1 and 3 s⁻¹ at 40 °C with a U-shaped loading dependency and an Arrhenius-type temperature dependency. The heat transfer coefficient h for the contact between coating and support was identified to $\geq 4 \times 10^3$ W/(m²K). The method is validated by comparing a measured large temperature jump experiment to the results from a non-linear simulation informed solely by these parameters obtained from the new FR-based method.

Keywords: adsorption dynamics; heat and mass transfer; frequency response analysis; adsorption equilibrium, adsorption enthalpy; aluminium fumarate; metal organic framework

Introduction

The increase of volume specific cooling power – thus reduction of specific costs – while keeping a reasonably high COP is one of the major development challenges for adsorption chillers [1]. Further performance increase can be reached through model based design and optimization which is more cost-effective than empiric trial-and-error prototyping of adsorption heat exchangers (Ad-HX) [2]. However, model based design requires detailed knowledge of a) relevant physical heat and mass mechanisms and the corresponding transfer coefficients, b) the adsorption equilibria, c) the adsorption enthalpy and d) the specific heat capacities, allowing for models with explicit dependency on design parameters like heat exchanger geometry, layer thicknesses and particle sizes. In this work we propose a comprehensive approach to gain most of this data from small representative Ad-HX cut-outs based on the FR analysis [3, 4].

As example material we use aluminium fumarate, a metal–organic framework (MOF) that exhibits adsorption equilibrium properties fitting well to low-driving-temperature applications [5] like data centre cooling driven by heat yielded from water cooled CPUs [6].

Discussion and Results

Sample plates (5x5 cm²) were coated ($A_{ct} = 18.9$ cm²) with different thicknesses (140, 240, 610 μm) and placed on a temperature-controlled plate in a variable-volume vacuum chamber.

The integrated measurement procedure consists of absolute adsorption equilibrium measurements by manometric uptake measurements, differential adsorption equilibrium measurements by small step-wise volume and temperature variations around an equilibrium point, and thermal frequency response measurements at the same equilibrium point through sinusoidal volume variations while measuring pressure and surface-temperature responses.

The measured FR, i.e. amplitude and phase shift at different variation, could be well reproduced with a Laplace-transformed model with 1-D-discretised heat transfer and LDF-simplified micro level mass transfer. This allowed to identify the loading and temperature dependent transport parameters (Figure 1). Macropore mass transfer and thermal contact resistance to the support showed to be irrelevant for the overall dynamics. Adsorption equilibrium and enthalpy results were published recently [4], detailed FR results will be available in due course [3].

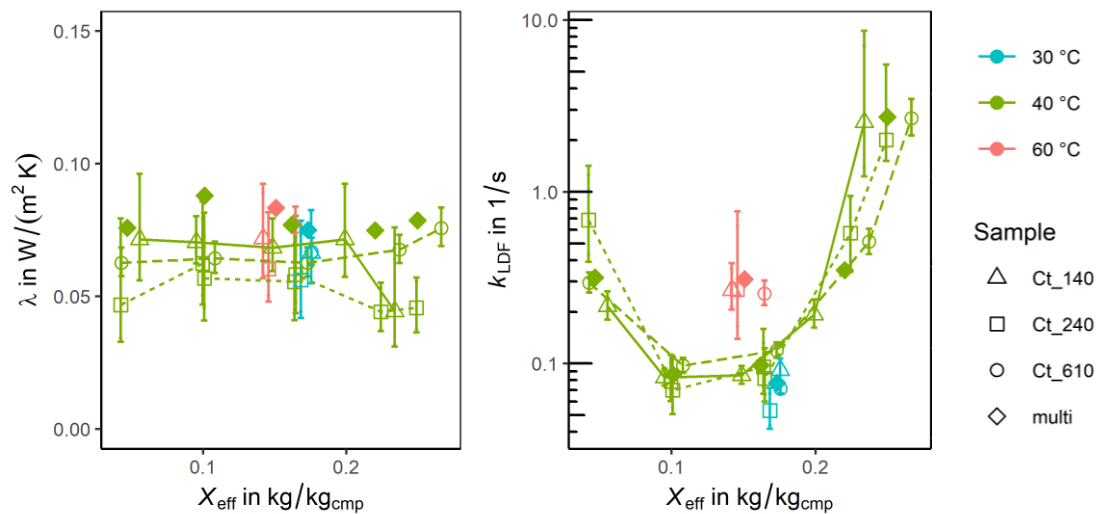


Figure 1: Estimated thermal conductivity λ and micro-level LDF-coefficient k_{LDF} over X_{eff} , the loading with respect to the dry coating mass for different coating thicknesses. Lines are only meant as guides to the eye.

Conclusions

The extended FRA was developed as a new method for the evaluation of heat and mass transfer parameters in an unprecedented resolution of the temperature and loading dependency. As the underlying models explicitly include geometrical parameters, the results may be directly used for design and optimisation of Ad-HX for adsorption heat pumps and chillers.

References

- [1] L. Schnabel, G. Földner, A. Velte, E. Laurenz, P. Bendix, H. Kummer, U. Wittstadt, in *Innovative Heat Exchangers* (Eds: H.-J. Bart, S. Scholl), Springer International Publishing, Cham **2018**.
- [2] S. Graf, S. Eibel, F. Lanzerath, A. Bardow, *Energy Technol.* **2020**, 1901130. DOI: 10.1002/ente.201901130.
- [3] E. Laurenz, G. Földner, A. Velte, L. Schnabel, G. Schmitz, *International Journal of Heat and Mass Transfer* **2021**, *accepted*.
- [4] E. Laurenz, G. Földner, L. Schnabel, G. Schmitz, *Energies* **2020**, *13 (11)*, 3003. DOI: 10.3390/en13113003.
- [5] D. Lenzen, J. Zhao, S.-J. Ernst, M. Wahiduzzaman, A. Ken Inge, D. Fröhlich, H. Xu, H.-J. Bart, C. Janiak, S. Henninger, G. Maurin, X. Zou, N. Stock, *Nature communications* **2019**, *10 (1)*, 3025. DOI: 10.1038/s41467-019-10960-0.

- [6] T. Wilde, M. Ott, A. Auweter, I. Meijer, P. Ruch, M. Hilger, S. Kuhnert, H. Huber, in *Proceedings 2017*.

Control of solution flow rate in single stage absorption chillers

Stefan Petersen^{1*}, Walther Hüls Güido¹

¹TU Berlin, Institut für Energietechnik, Sek. KT2, Marchstraße 18, 10587 Berlin
Tel: +49 30 314 25183, Fax: +49 30 314 22253

*stefan.petersen@tu-berlin.de

Abstract

Recent achievements in design, process and operation control of water-lithium bromide absorption chillers have opened the operation field in terms of allowed temperature range of external circuits, especially for the heat sink (cooling water circuit). This broad operating conditions are process challenging, but can lead to a significant increase in energy efficiency, improving thermal and electric energy expenses. One main challenge is the duty of the solution pump. Hydraulic net curve of solution cycle is not any more as constant as it has been before. Pressure head may vary by a factor of three or even four. Consequently, by using state of the art constant speed pumps, the solution volume and mass flow varies according to the actual operation condition, such as temperatures, loads, etc. Mass/ volume flowrates of the solution, may violate process restrictions, but even if not, thermally reasonable values will only be matched coincidentally.

Improvements may be achieved by diverging the state-of-the-art constant speed pump by one to control solution flowrate. Investigations in a solution flow control by means of solution heat exchanger effectiveness ϵ_{SHX} is proposed in this paper. Based on three to four temperature probes to analyse ϵ_{SHX} in real time is very cost effective and easy to adapt. In a first lab test phase a reasonable ϵ_{SHX}^{set} is identified and differences to state of the art fixed solution pumps are analysed. Thermal efficiency (COP) of the absorption chiller increments in a range of 15%. Electricity savings in the same range as COP improvements are predictable, and observed within a field test cooling system, including reject heat device, pumps, and further heat pump related peripherals. Thermal efficiency improvements of the chiller as much as electrical energy savings on system level overcome the expectations. Particular challenges near to borderline operation conditions can be solved by dynamic adaptations of minimum and maximum control limits of the pump speed.

Keywords: sorption, cooling, heating, efficiency, solution heat exchanger, COP, strategy

Nomenclature					
A	heat exchange surface	m ²	\dot{V}	volume flow rate	m h ⁻³
ACU	Absorption cooling unit		W	Heat capacity flow rate	kW K ⁻¹
AHU	Absorption heating unit				
C	control signal/speed of pump	%	<i>Sub- and superscripts</i>		
COP	coefficient of performance		0	rated value	
c _p	specific heat capacity	kJ kg ⁻¹ K ⁻¹	A	Absorber	
L	electrical power	kW	C	Condenser	
ϵ	heat exchanger effectiveness		D	Desorber	
\dot{m}	Massflow	kg/s	E	Evaporator	
p	Pressure	mbar	Cl	cooler	
\dot{Q}	heat flow rate	kW	h, c	hot, cold	
SFC	solution flow control		i, o	inlet, outlet	
SHX	solution heat exchanger		set	set value	
t	temperature	°C	th	thermal	
U	overall heat transfer coefficient	kW m ⁻² K ⁻¹	x	placeholder for component	

Introduction and Motivation

Latest developments in absorption chiller technology allow reject heat operation temperatures above 40°C or even 45°C in operation. As consequence this facilitate operation with dry reject heat devices instead of wet cooling towers [1], avoiding water consumption and legionella problems. In addition, using dry reject heat devices offers a significant potential of energy savings of the heat sink in part load operation [2, 3]. Meanwhile, reject heat temperatures of 45°C or even up to 60°C is increasing interest of usage as heat pump [4]. Requested heat sink temperature and volume flow needs to be controlled dynamically during operation to achieve energy savings, which can be realized by using enhanced control systems [5, 6].

State of the art absorption chillers using lithium bromide as solvent do need at least one pump to overcome pressure difference ($\Delta p_{DA} = p_C - p_E$) and physical height between absorber (A) and desorber (D) to circulate solution flow as shown in figure 1. Transport of strong solution from desorber to absorber may be forced by same pressure difference, supported by height difference if the absorption chiller/heating unit ACU/AHU is well designed. The lower vessel pressure p_E (dominated by the evaporator) is more or less determined by external outlet temperature of the evaporator as much as p_C is directly depending on external condenser temperature level. Considering exponential increase of equilibrium pressure with increase in temperature, the pressure difference is dominated by the latter and therefore correlating mainly with pressure p_C . Electric consumption for the pump is at least for lithium bromide ACU/AHU normally neglectable. For the ACU used in these investigations it is in the range of 0.2 to 0.5 ‰ of nominal cooling load capacity \dot{Q}_E^0 , accordingly less than 1% of electricity consumption of an installation including brine pumps and reject heat cooler.

While state of the art ACU are often combined with wet cooling towers, providing most of the time stable cooling water temperature, e.g. 29.5 °C, solution flow rate could be assumed to be nearly constant. Heading for more efficient cooling systems, using system strategies as provided in the above mentioned literature, cooling water temperature will vary in between operation limits of the ACU. In cooling mode Bee and Bumblebee chillers allow operation with cooling water inlet temperatures between 18°C and 42°C (47°C if moderate chilled water temperatures are present), while in heating mode temperature up to 60°C is feasible. Correspondingly, upper vessel pressure levels p_C vary from 20 to 100 mbar in cooling mode ACU and from 80 to 200 mbar in heat pump mode AHU. Having a solution pump, running at fixed speed, the solution flow rate will change significantly in accordance with the load curve of the pump by correlated differences to Δp_{DA} .

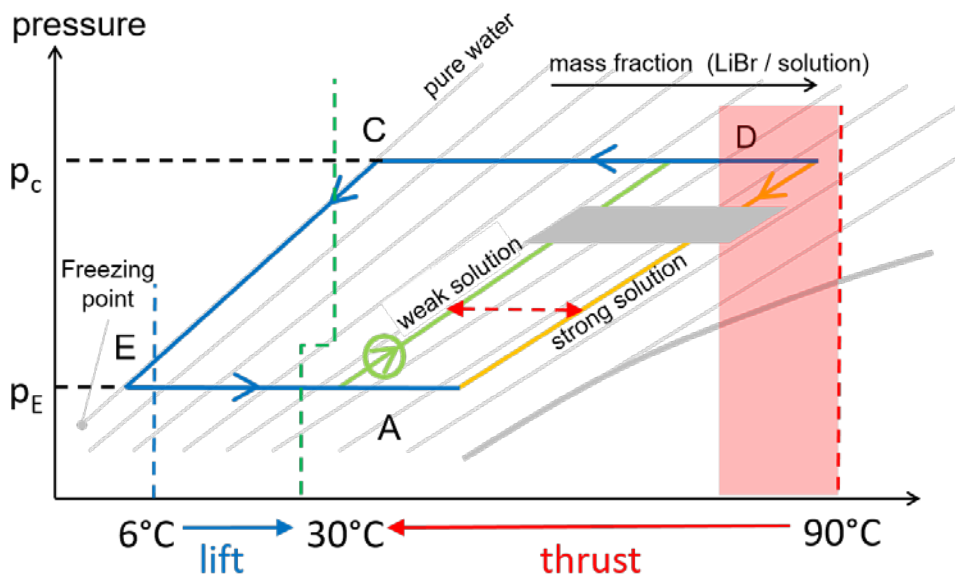


figure 1: single effect absorption process in Dühring diagram (H₂O-LiBr)

Lithium bromide solution in single stage absorption chillers exchange heat in three heat exchangers (see also figure 1). Main heat exchangers are the desorber (D) and the absorber (A). The desorber may be flooded or fall film tube bundle heat exchanger while the absorber is mostly designed as fall film tube bundle. Normally solution flow rate is determined by the ACU/AHU capacity and tube bundles are constructed to ensure a good wetting with thin films to ensure good UA values in absorber and desorber. In combination with a spraying or droplet system to feed solution on the surface of these heat exchangers, there may be a range of tolerable volume flow rate as effects of wetting and film thickness with increasing volume flow have opposing and therefore often a compensative effect around maximum of UA. Moreover, small differences in good practices volume flowrates for absorption and desorption heat exchangers will enlarge the range of tolerable general volume flows to gain best cooling performance of real existing chillers. The solution heat exchanger (SHX), shown in figure 1 as a grey box is introduced to reach a better thermal coefficient of performance (COP) of the overall process. Mostly it is a plate heat exchanger in counter flow regime, offering better UA values than tube bundle heat exchanger and being more compact and cheaper in production. The layout and dimension are determined after fixing all other heat exchangers and solution flow rate in nominal rating conditions. Consequently, following statements can be determined:

- I. Reasonable solution flow rate for rated operation conditions of ACU or AHU is not limited to one exact value but a range.
- II. Solution pumps running at fixed speed do not deliver constant volume flow if Δp_{DA} may change and/or fluid properties, such as density, are varying.
- III. Amount of heat exchanged in SHX will be directly determined by T_{Si} , and therefore by temperature of high temperature heat source (t_2), T_{Wi} , and therefore by temperature of heat sink (t_1), solution flow rate and difference of solution heat flows on each side of the SHX.
- IV. COP of ACU/AHU is strongly dependent on efficiency ϵ_{SHX} and capacity of SHX \dot{Q}_{SHX} .

As operation conditions (t_1 and t_2 maybe even \dot{V}_1 and \dot{V}_2) are modulated to match operating demands (\dot{Q}_E, t_{E0}^{set}), effects of II and III (respectively IV) to COP will only result coincidentally to gain reasonable good cooling capacity and COP figures of the process. As a matter of truth effects may reinforce and lower cooling capacity and COP. A change in thermal COP will not only influence the amount of heat needed for a particular amount of cooling but moreover the amount of electricity consumption within a cooling system, especially for the reject heat device / cooler. Results of a theoretical calculation are shown in figure 2. The COP for stable cooling load of 20kW, fixed chilled, cooling and heating temperatures was calculated to 0.64. A variation of ambient temperature is undertaken. Deviations for COP, between 0.57 and 0.72, all reasonable values found in field installations, are analysed to their influence on electricity demand of the cooler L_{Cl} . Absorption chiller and cooler data are taken from an installation with rated full load of 40 kW. An increase in COP by 0.08 (64-62%) saves. up to 14% of electricity consumption at 27°C [7].

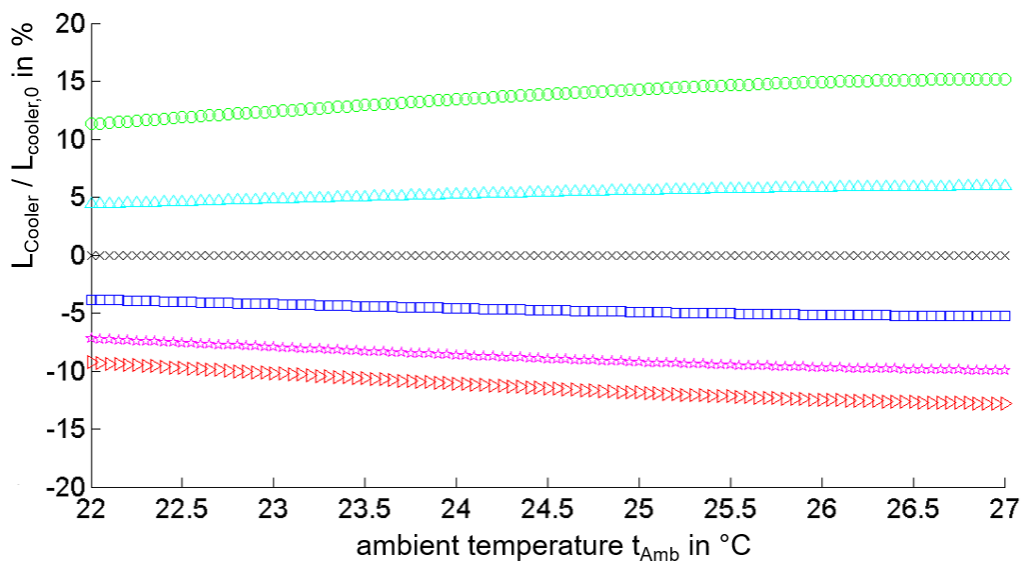


figure 2: Effect on el. consumption of cooler by thermal COP of chiller for different ambient temperatures [6]

Solution mass / volume flowrate, defined for rated conditions (see statement I), can and should be controlled in part- and overload to enable the process at its best. First constraint is, to have a speed-controlled solution pump installed. If so, following insight offers a solution to achieve proposed savings, already in the second, enhanced version.

Condition / statement III directly influences the heat exchanger efficiency. For counter flow heat exchangers with constant heat capacity flows this is defined by quotient of temperature difference of lower heat capacity flow to the temperature difference of the inlets (maximum temperature difference around heat exchanger). Operated as solution heat exchanger (SHX) efficiency is defined by equation 1:

$$\epsilon_{SHX} = \frac{T_{Si} - T_{So}}{T_{Si} - T_{Wi}} \quad (1)$$

Typical heat exchanger efficiencies for rating conditions are in the range of 80 to 95%. In a favourable layout / operation of process design, weak solution may be heated up to equilibrium temperature before entering the desorber. The strong solution may be cooled down to equilibrium temperature at absorber inlet, latter to avoid desorption and necessity of resorption within the absorber. Additional heat exchanger (absorber) surface and/or lower cooling

capacity will consequently be the result, as less absorber area is available to absorb steam from evaporator. Hence, this should be avoided. Boundary condition to calculate ϵ_{SHX} (constant heat capacity flowrates) will be violated if two phase flow occurs. This may happen on both sides but is more often observed for weak solution when the temperature is increased above equilibrium temperature. Even if two phase flow may increase partially the U value of SHX, a decrease of UA is more probable as consequence of dry out of heat exchanger surface. To detect the general appearance, the pseudo heat exchanger effectiveness ϵ_{SHX}^{ps} (in addition to heat exchanger effectiveness) as defined in equation 2 can be determined as followed:

$$\epsilon_{SHX}^{ps} = \frac{T_{Wo} - T_{Wi}}{T_{Si} - T_{Wi}} \quad (2).$$

Both effectiveness have a strong correlation to each other. If only sensible heat exchange is present a correlation factor can be predicted. Accordingly, calculations do not match theory if at least on one side of the heat exchanger latent heat effects are present. This topic will be discussed later on, improving the first concept.

Brief overview of feasible solution flow control (SFC) strategies

As mentioned in the introduction, external temperature and/or volume flowrates specially in the heat sink circuit affects the pressure levels in the upper and lower chamber and therefore Δp_{DA} , having an effect on the solution flowrate. Thus, SFC seems to be a worthfull approach.

Depending on type and number of available sensors, controlling the solution flowrate (due controlling the solution pump speed) can regulate the process with regard to thermal efficiency (COP) or cooling/heating performance (\dot{Q}_E or \dot{Q}_1) by guarantying a wetting of the heat exchanger surfaces in a propitious range. The following process variables are possible set targets:

- I. pressure difference Δp_{DA} ,
- II. volume or mass flowrate of the weak (\dot{V}_W or \dot{m}_W) or strong solution (\dot{V}_S or \dot{m}_S),
- III. difference of mass fraction between strong and weak solution ($\xi_S - \xi_W$), corresponding to the cooling/heating capacity (\dot{Q}_E or \dot{Q}_1),
- IV. pump head pressure or sump pressure in absorber or desorber,
- V. SHX hot side temperature difference ($T_{Si} - T_{Wo}$),
- VI. SHX cold side temperature difference ($T_{So} - T_{Wi}$),
- VII. SHX efficiency ϵ_{SHX} (see eq. 1)

Each of these targets require a different measurement setup. Measuring temperatures is convenient regarding technical (e.g. vacuum tightness) and economic issues. Pressure sensors are between 20% and 100% more expensive than temperature sensors and mass or volume flowrate measuring devices are even 10 to 15 times more expensive.

The control concept I can be easily implemented. The required pressures can either be directly measured or calculated from the measured temperatures using equilibrium data. However, using this methodology considers nor the cooling/heating capacity neither difference in mass fraction of strong and weak solution. Concepts II and III build on each other. If the volume flow of the weak solution \dot{V}_W is available, this is certainly the most stable type of control, but it is also cost-intensive. Since the cooling capacity is usually available within DAQ and/or control system, it may only be necessary to make it accessible to the solution pump controller.

Consequently, a load-dependent variation of \dot{V}_W^{set} can also be used to increase thermal efficiency by keeping solution mass flow at good levels for a high SHX effectiveness as much as a good wetting of de- and absorber.

Concept IV essentially pursues the location of the solution in the solution circuit, as well as ensuring enough pressure in the feed line of the pump. This concept similar to concept I does not consider the cooling/heating capacity and the COP but ensures pump safety in the first line. Due to part load changes in hold up of solution in the circuit, there may only be a minimum level / value being used to provide against dry out of the pump. In conditions, where mass fraction of salt is low, as it will occur during part load operation at low temperatures on high temperature heat source (desorber). Solution hold up is high under these conditions and solution mass flow will be maximal. Consequently, ϵ_{SHX} will be at a low level, as much as UA values of absorber and desorber due to film thickness. Again reasonable good cooling capacity and/or COP will only be matched coincidentally.

Concepts V to VII aim to regulate the solution cycle in such a way that the SHX can maintain an effectiveness ϵ_{SHX} according to its purpose. Highly different heat capacity flows W_S and W_W may be prevented. Undercooling and overheating at the desorber, but also at the absorber inlet can be forced and/or prevented. Using three to 4 temperature sensors is comparable cheap and safe in terms of maintenance and vacuum tightness.

First results

An energy efficient and cooling capacity enhancing control strategy for solution cycle in absorption process shall be cost effective, durable (corrosion, vacuum, etc.) and avoid crucial operation conditions due to crystallization. The best results, according to experimental studies of the authors, are reached by controlling the solution flow rate (SFC) \dot{V}_W , according to concept VII. The target variable is the heat exchanger effectiveness ϵ_{SHX} of the solution heat exchanger (SHX) as published in [7].

The difference between a constant speed control C_W^{set} (s. star marker symbol) and a constant weak solution volume flowrate \dot{V}_W^{set} (s. circle marker symbols) is presented in figure 3. The ordinate scale relates the actual to the nominal solution flowrate \dot{V}_W / \dot{V}_W^0 . The abscissa corresponds in all three figures a broad field of operation shown as the absorber inlet

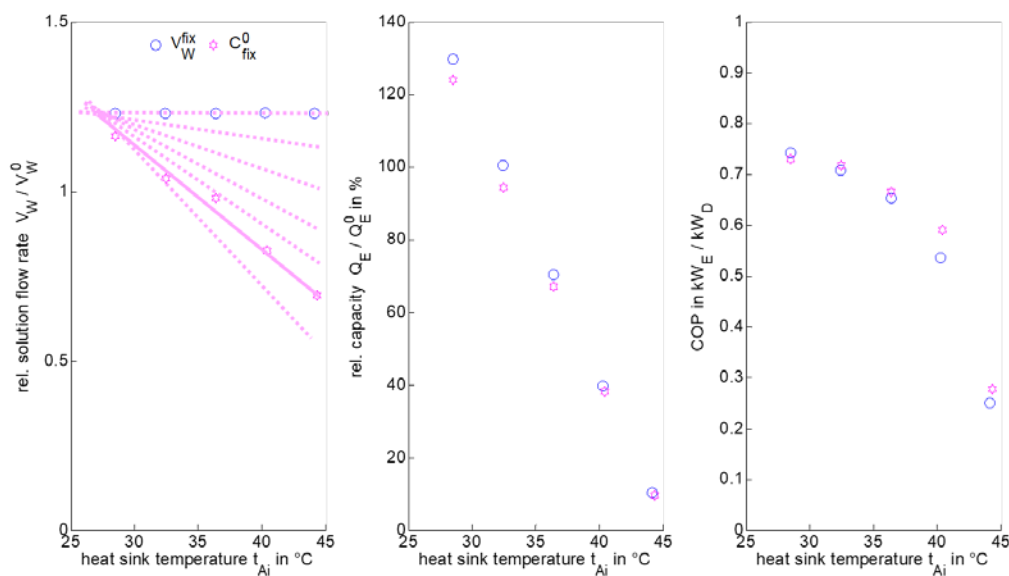


figure 3: Operation field of a weak solution pump by different absorber inlet temperatures t_{Ai}

temperature between 25-45°C. Further conditions were held constant (e.g. desorber inlet temperature $t_{Di}=90^{\circ}\text{C}$ and the evaporator inlet temperature $t_{Ei}=13^{\circ}\text{C}$). It is shown that the solution flowrate decreases to approximately 50% at a temperature $t_{Ai}=45^{\circ}\text{C}$ compared to measurements at $t_{Ai}=25^{\circ}\text{C}$ if the pump speed is hold constant. The figure in the middle shows the result in cooling power, the ordinate shows again a relative cooling power to the design cooling power of a specific location (\dot{Q}_E / \dot{Q}_E^0). Increasing the temperature t_{Ai} seem to have several effects i.e. in the wetting of the heat exchanger bundle, wetting thickness, undercooling and overheating among others. However, all effects compensate in a way that the cooling power seems to have a low correlation to the different solution volume flowrates \dot{V}_W . For low cooling temperatures $t_{Ai}=28^{\circ}\text{C}$ it seems that the higher volume flowrate \dot{V}_W turns in a slightly higher cooling power \dot{Q}_E . A lower volume flowrate \dot{V}_W is in turn slightly favorable for the efficiency of the process COP (s. Figure 3 on the right-hand side). Both a constant speed control and volume flowrate are operation lines for constant control modes. Other pump types and sizes will have different outcomes to solution flowrate as indicated by the magenta dotted lines on the left-hand side of figure 3. Drawback in the cooling power \dot{Q}_E or efficiency COP can be assumed. Thus, the importance to operate in between the constant operation modes with SFC is strengthen.

As the inlet temperature of strong solution (T_{Si}) to the SHX and the inlet temperature of the weak solution (T_{Wi}) are mostly defined by driving heat and reject heat temperatures, strong solution outlet temperature (T_{So}) is constrained by operation condition, mainly depending on \dot{V}_W and ϵ_{SHX} (see also equation 1). Hence T_{Si} can be used to control \dot{V}_W for reaching an ϵ_{SHX}^{set} . Measurement with four different values of ϵ_{SHX}^{set} and one at nominal flow rate are shown in figure 4. While results of \dot{V}_W in a range of 50% to 150%, depending on ϵ_{SHX}^{set} , cooling capacity seems mostly independent / unaffected. \dot{V}_W varies by $\pm 10\%$, for defined ϵ_{SHX}^{set} and a variation of reject heat inlet temperature t_{Ai} . Strongly promising is the effect on thermal COP.

Running a chiller with an active SFC not only under lab and steady state conditions (figure 4), but in field operation lead to significant increase in COP as shown in figure 5. An increase of mean COP during operation time, 0.68 without SFC to 0.75 with SFC, is achieved.

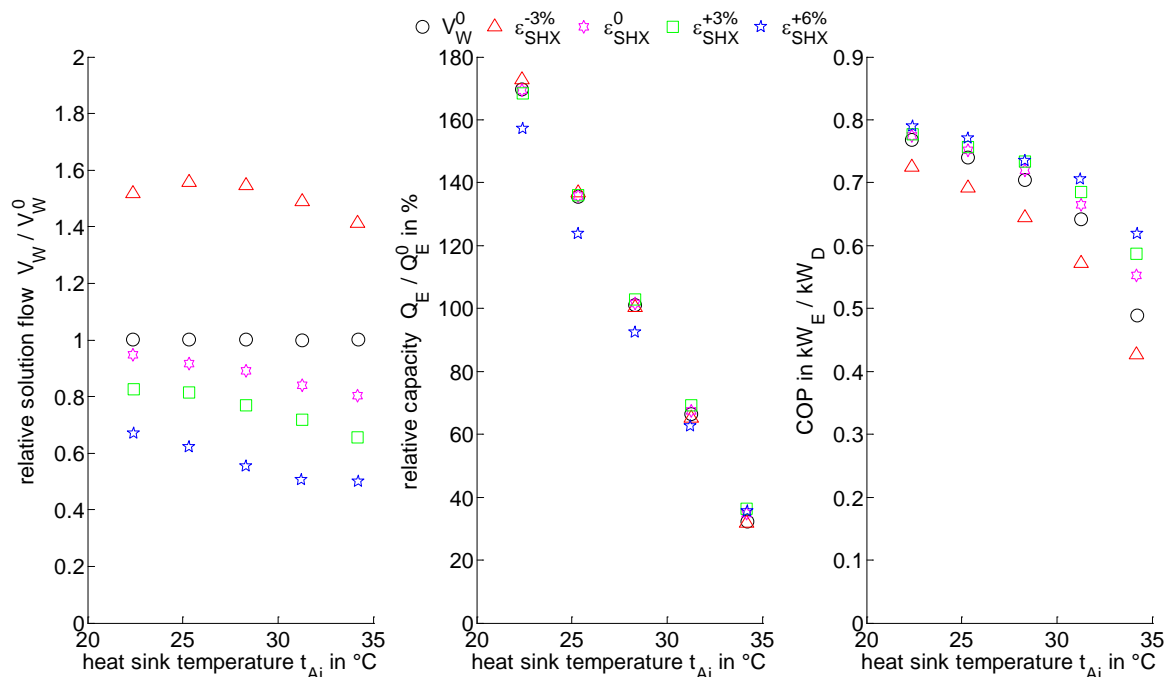


figure 4: typical chiller conditions, solution flow, cooling capacity and COP

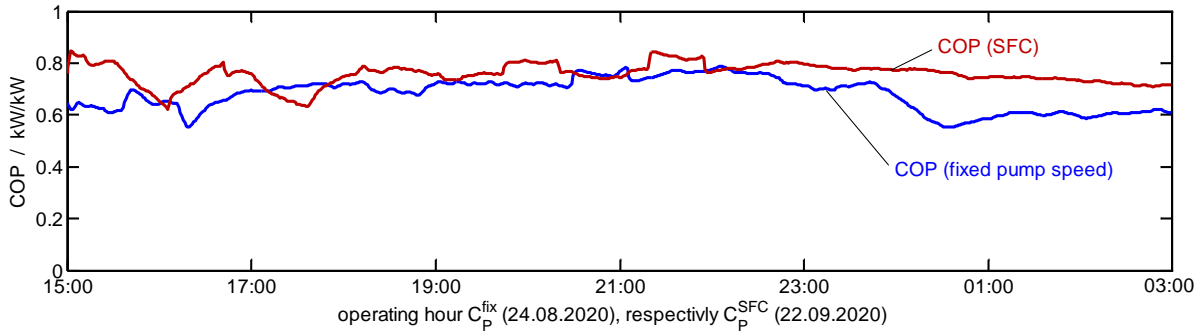


Figure 5: full operation day with and without SFC

Hence savings of driving heat, rejected heat and savings of electricity, mainly due to lower amount of heat to be rejected, are gained. Expectations, as mentioned and calculated in the motivation chapter are fulfilled.

Latest improvements

In contrary to unambiguous measurements and deviated results shown in figure 4 and figure 5, figure 6 shows a campaign of lab measurement at conditions, comparable to industrial heat pump conditions or hot climate cooling conditions for single stage ACU. Low temperature heat source is operated at t_{Ei} of 20°C with heat sink temperatures (t_{Ai}) of 37°C. At t_{Ai} of 44°C t_{Ei} is set to be as high as 30°C. High temperature heat source starts at t_{Ai} of 37°C with 80°C and reaches 100°C, corresponding to highest values of t_{Ai} . Both heat sources have linear slope related to increase of heat sink temperature. As shown in figure 6 the COP is strongly effected by set values of ϵ_{SHX}^{set} at low temperatures of t_{Ai} . COP varies around middle value of 0.65 with ± 0.1 , which is an increase by 40% between $\epsilon_{SHX}^{-2\%}$ and best values. At high temperature values of heat sink, former reasonable

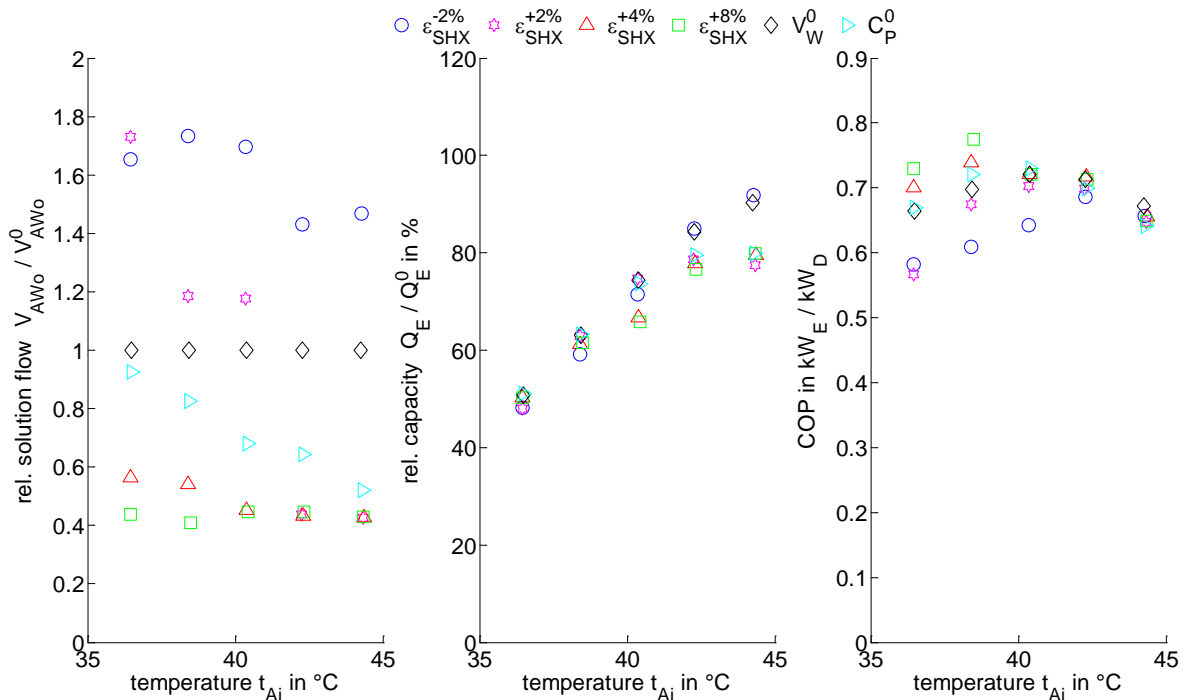


figure 6: typical heat pump conditions, solution flow, capacity and COP

set values of $\epsilon_{SHX}^{+2\%}$ or higher suffer a significant lack of capacity in comparison to others. One may guess, that wetting of absorber or desorber are crucial at the low amounts of solution mass flow, but these have not been lower than shown in figure 4. If $\epsilon_{SHX} < \epsilon_{SHX}^{set}$ is calculated, C_{PW} is forced to decrease. If calculated ϵ_{SHX} is below ϵ_{SHX}^{set} C_W will be decreased to lower \dot{V}_W , accordingly ϵ_{SHX} should increase to match ϵ_{SHX}^{set} . If boiling occurs reduction of C_W will have the contrary effect on ϵ_{SHX} and boiling will even occur earlier, limiting effective SHX surface and decrease therefore ϵ_{SHX} furthermore. SFC strategy in its simple, first algorithm will decrease solution mass flow, limited by the inherent minimal flowrate, ensuring reasonable overall heat transfer ratio and wetting area of desorber and absorber, but provoking and reinforcing upper mentioned superheating within the SHX. Hence, superheating needs to be detected. Various possibilities are available to determine superheating if solution mass fraction and or solution volume flowrate would be available, but are mostly not. Another option is provided by analysing

- deviation of ϵ_{SHX} to ϵ_{SHX}^{set} (figure 7, left side),
- comparison of ϵ_{SHX} to ϵ_{SHX}^{ps} ,
- or deviation of ϵ_{SHX}^{exp} to ϵ_{SHX}^{ps} . (figure 7, right side and figure 8).

Data, already presented in figure 6 are used to plot figure 7. Once, when boiling in SHX occurs, ϵ_{SHX} and ϵ_{SHX}^{set} are diverging significantly, see left side of figure 7, where ϵ_{SHX} is plotted (normalized by ϵ_{SHX}^0). Same effect can be detected by calculation ϵ_{SHX}^{ps} as shown in figure 7, right side. Effectiveness ϵ_{SHX} and ϵ_{SHX}^{set} are already used to control speed of solution pump (C_W). Hence, not to use one and the same figure to control and at the same time limit speed of solution pump ϵ_{SHX}^{ps} maybe the better option.

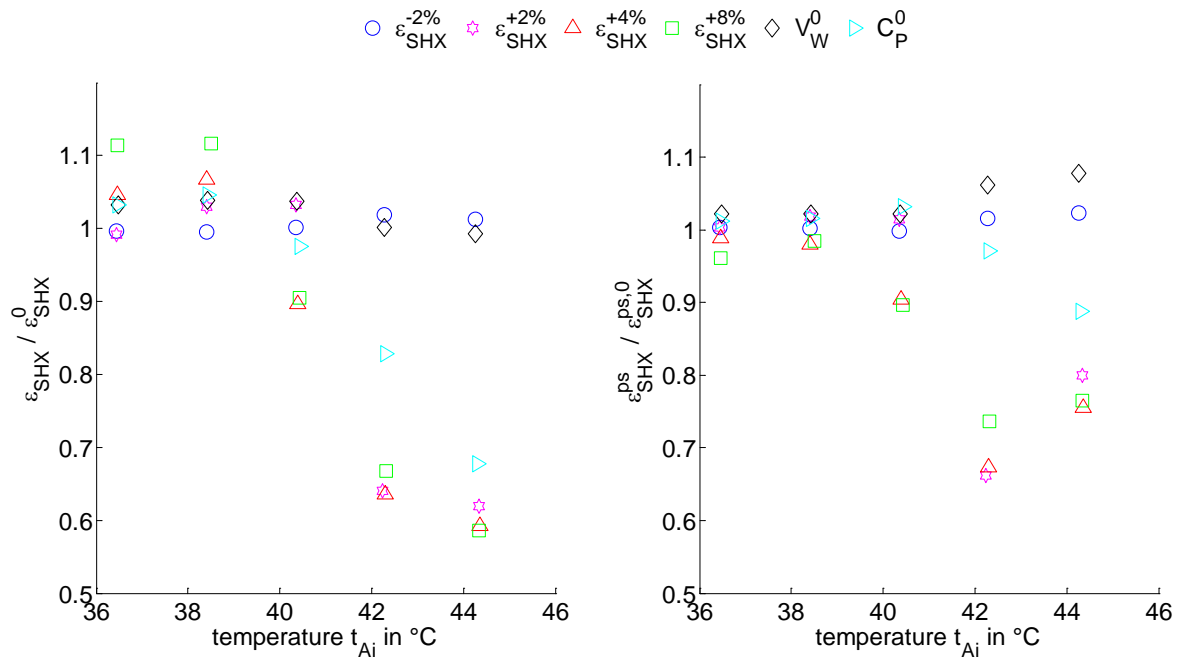


figure 7: evaluation on effectiveness of SHX to control limits of C_{PW}

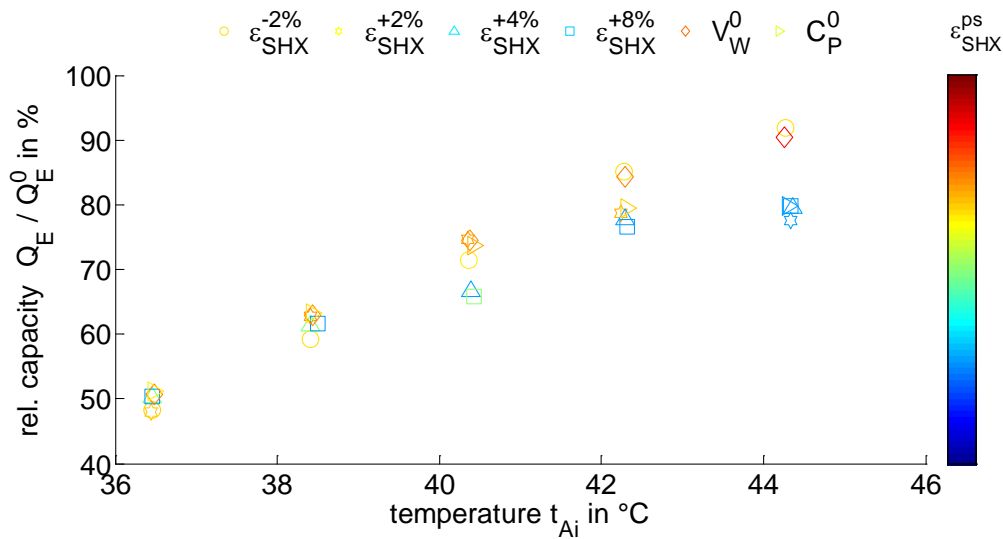


figure 8: introducing minimum allowed ϵ_{SHX}^{ps} to set C_{PW}^{min}

Post processing of upper measurement runs, adapting limitations to pump speed by minimum set values for ϵ_{SHX}^{ps} , is presented in figure 8. Correspondingly, ϵ_{SHX}^{ps} increase from blue to red (scatter colour). Maintaining a set value of $\epsilon_{SHX}^{+4\%}$ in combination with C_{PW}^{min} to match at least yellow coloured ϵ_{SHX}^{ps} will ensure high COP (see also figure 4, right) and reasonable cooling capacity values at moderate t_{Ai} and high capacity without lack in COP at high values of t_{Ai} (compare also figure 6).

Summary/Conclusions

Driving heat and electricity savings were achieved by activating solution flow control (SFC) in operation of single stage absorption chillers. The strategy is applicable to new chillers but can also be retrofitted in most of know absorption chillers in a cost-effective way. Savings on electricity consumption of reject heat device can easily overcome 10% or more of yearly consumption only by SFC, which has been proven in a first field test. The results have been valid for a certain level of low heat sink temperature and corresponding concentrations. SFC is based on real time evaluation of solution heat exchanger (SHX) effectiveness.

Other than the given values of operation conditions may have destabilized the pump control due to boiling in SHX. Operating same chillers in totally different operating conditions, compared to first lab and prototype installation runs, showed up some negative side effects with inherent reinforcement. Measured values of solution heat exchanger effectiveness where irritated by superheating in SHX and a violation of constraints of rules to calculate efficiency. In contrary to its aim, solution flow strategy was reacting contrary to its best. To overcome reinforcement two methodologies are introduced, using either deviation of measured to expected effectiveness or a minimum value of allowed pseudo effectiveness of solution heat exchanger to limit minimum of solution pump speed. Increasing latter one in occurrence of superheating, which is detected by mentioned methodologies secure from reinforcement and moreover allow to maintain solution volume flowrate to maximize capacity as well as thermal efficiency of the chiller.

It is foreseen to implement the enhanced strategy to field installation and different chillers within upcoming projects.

Acknowledgements

The authors acknowledge financial support by “ EnEff: Wärme” Projects 03ET1171A and 03ET1583 grant funded by the Federal Ministry for Economic Affairs and Energy (BMWi).

Moreover, we would like to thank our colleagues and Prof. Felix Ziegler for his long and enduring support, his questions and positive critics, which accompanied and empowered us, not limited to this paper.

Thanks also to chiller manufacturer W.Bälz & Sohn GmbH & Co for offering the results of our work to the market.

Supported by:



Federal Ministry
for Economic Affairs
and Energy

on the basis of a decision
by the German Bundestag

References:

- [1] S. Petersen, et al. Absorption technology for low temperature heat sources. Final Project Report FKZ 03ET1171(A-D), TU Berlin, FG Maschinen u. Energieanlagentechnik, 2019.
- [2] W. Hüls, W. Lanser, S. Petersen, F. Ziegler. Performance of absorption chillers in field tests. Elsevier. Applied Thermal Engineering 2018-02 134 Pp. 353-359.
- [3] C. Paitazoglou, W. Hüls, J. Albers, and S. Petersen. Betriebsführungsstrategien zur Steigerung der elektrischen Energieeffizienz bei der thermischen Kälteerzeugung. DKV Proceedings, III.21, Aachen, Nov 2018. DKV. ISBN: 978-3-932715-96-9.
- [4] S. Hunt, S. Petersen, F. Ziegler, C. Henrich. Experimental proof of concept for a water/LiBr single stage absorption heat conversion system as a house connection station. HPC Proceedings, Pp. 280-286. Bayreuth, Sep. 2018. ISBN 978-0-9563329-6-7
- [5] J. Albers. Improved Solar Operation Control for a Solar Cooling System of an IT Center. Applied Sciences, 10:3354, 2020.
- [6] S. Petersen, et al. Efficient absorption cooling for low district heating return temperatures, DHC Proceedings, Nottingham, Sep 2021,
- [7] S. Petersen, W. Hüls, C. Paitazoglou. Regelung des Lösungsumlaufs von einstufigen Absorptionskälteanlagen zur Effizienzsteigerung im Betrieb. DKV Proceedings, paper-ID AII.1.14, 2020. DKV. ISBN: 978-3-932715-96-9.

Composite “LiCl/Vermiculite” for Adsorption Thermal Batteries: Giant acceleration of methanol sorption due to the adsorbent modification

S. Strelova^{1,2}, L. Gordeeva^{1*}, A. Grekova¹ and Yu. Aristov¹

¹Boreskov Institute of Catalysis, Ac. Lavrentiev av. 5, Novosibirsk, Russia

²Novosibirsk State University, Pirogova str. 2, Novosibirsk, Russia

*Corresponding author: gordeeva@catalysis.ru

Abstract

The specific power of an Adsorption Thermal Battery (ATB) is often limited by slow adsorption. This paper aims to develop a new method for accelerating sorption dynamics and to study a modified composite sorbent LiCl/Vermiculite, specialized for ATB. The new sorbent is characterized by outstanding methanol uptake, heat storage capacity and advanced specific power.

Keywords: Adsorption thermal battery, Adsorption dynamics, Methanol, LiCl/vermiculite, Promoting additive, Aluminium oxide.

Introduction

Adsorption thermal batteries (ATB) driven by low-temperature waste and solar heat present energy and environment-saving alternative to conventional compression and absorption chillers and heat pumps and provide cooling, heating, and heat storage [1]. The performance of ATB strongly depends on the properties of the adsorbent. Nowadays, a large number of various porous materials have been proposed as water and methanol sorbents for ATB [2], among which there is a family of Composites "Salt confined inside Porous Matrixes" (CSPMs), demonstrating a large sorption capacity and steep sorption isotherms. Sorption of water and alcohols vapor on CSPMs involves several mechanisms: (i) adsorption on the surface of the matrix at low relative humidity (the impact of this mechanism is minor and usually does not exceed 0.03-0.05 g/g); (ii) gas-solid reaction of salt S with vapor V leading to the formation of the solid complex according to equation $S + nV = S \cdot nV$; (iii) deliquescence of the complex $S \cdot nV$ and absorption of the vapor by formed solution [3]. The confined salt is the major sorbing component, whereas the matrix serves as a media for dispersing the salt and providing efficient heat and mass transfer [4]. Composites based on macroporous matrixes with a high porosity may contain a large salt amount and, hence, exhibit high capacities of water and methanol sorption [5].

Recently, a LiCl/Vermiculite (LiCl/V) composite has been proposed as a methanol sorbent for ATB. It ensures the outstanding methanol uptake (up to 2 g/g) and heat storage capacity (1.0-1.5 kJ/g) under conditions of typical ATB cycles [6]. However, the practical use of this composite is hindered by poor adsorption and, particularly, desorption dynamics, which strongly reduce the ATB specific power. This could be caused by the following reasons:

- slow chemical reaction between the salt and vapor [7], which is especially typical for large crystals of the salt, stabilized in matrix's macropores [5];
- hindered crystallization of the salt/solvate solid phases from solution, which requires a strong solution supersaturation [8];
- low thermal conductivity of vermiculite due to its extra-high porosity [9].

This work focuses on the desorption acceleration by means of modifying the vermiculite surface with aluminium oxide as a promoting additive. For this purpose, we, first, studied the methanol sorption/desorption dynamics on the neat LiCl/V to elucidate factors limiting the sorption rate. Then, modified composites LiCl/Al₂O₃/Vermiculite were synthesized and comprehensively characterized by a set of complementary physical-chemical methods (SEM,

XRD, BET, DSC). The effect of aluminium content on methanol sorption dynamics was also investigated.

Experimental

Synthesis of the composites

The expanded vermiculite ($S_{sp} = 5.9 \text{ m}^2/\text{g}$, $V_p = 2.7 \text{ cm}^3/\text{g}$, $d_{av} = 6.5 \text{ }\mu\text{m}$) was used as a host matrix for the composite synthesis. LiCl (Aldrich, 99 %) and $\text{Al}(\text{NO}_3)_3 \cdot 9\text{H}_2\text{O}$ (ACROS ORGANICS, 99%) were used as delivered. The composites were prepared by a dry impregnation method [6]. For the preparation of the modified composites (Fig. 1), the dried vermiculite was impregnated with an aqueous $\text{Al}(\text{NO}_3)_3$ solution, held in ammonia vapor above an aqueous ammonia solution for 24 h, dried at $160 \text{ }^\circ\text{C}$ for 2 h, and calcinated at $575 \text{ }^\circ\text{C}$ for 48 h to form aluminum oxide. Then the composite LiCl/ Al_2O_3 /vermiculite was prepared by the dry impregnation of the Al_2O_3 /vermiculite matrix. The LiCl and Al_2O_3 contents of the composites are presented in Table 1.

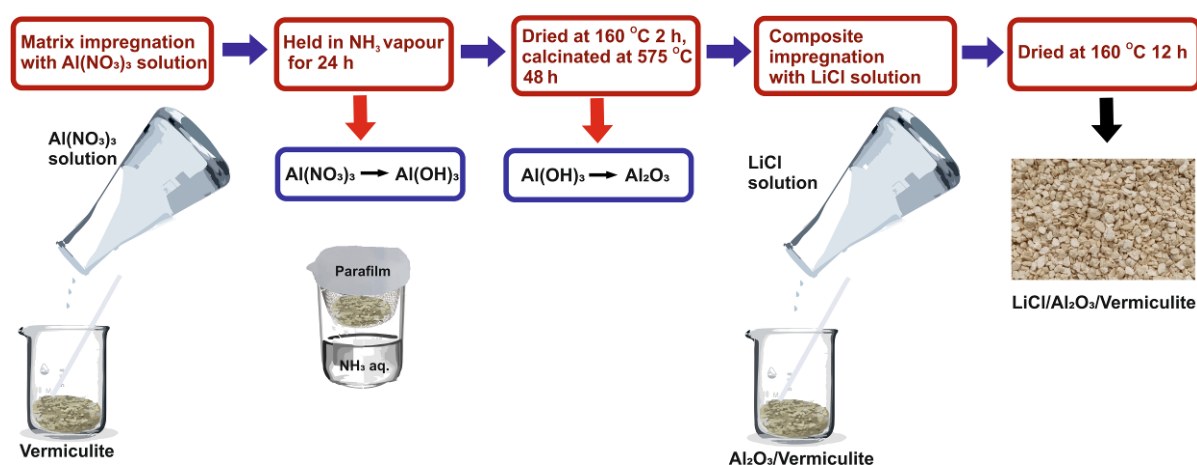


Fig. 1. Scheme of the LiCl/ Al_2O_3 /vermiculite composite synthesis.

Table 1. Composition and textural characteristics of the prepared composites.

Sorbent	Name	LiCl content, wt. %	Al_2O_3 content, wt. %	S_{sp} , m^2/g	V_p , cm^3/g
LiCl/vermiculite	LiCl/V	38.0	0	1.9	1.4
LiCl/ Al_2O_3 (2.5%)/vermiculite	LiCl/2.5 Al_2O_3 /V	39.4	2.5	4.9	1.15
LiCl/ Al_2O_3 (5.8%)/vermiculite	LiCl/5.8 Al_2O_3 /V	38.4	5.8	5.0	1.3
LiCl/ Al_2O_3 (8.9%)/vermiculite	LiCl/8.9 Al_2O_3 /V	37.9	8.9	7.5	1.2

Characterization

The texture characteristics (specific surface area) of the composites were determined by low-temperature nitrogen adsorption using a Quantachrome© Nova 1200e analyzer. The specific pore volume V_p was evaluated as moisture capacity upon immersion in water. The characteristics of the porous structure of the prepared composites are presented in Table 1. The morphology of the prepared composites was characterized by the SEM technique using a scanning electron microscope Jeol JSM-6460 LV.

The phase composition of the composites and its transformation during methanol adsorption were characterized *in situ* by XRD analysis by a Siemens D-500 diffractometer with Cu K_{α} radiation. The high temperature *in situ* experiments were conducted using an X-ray reactor chamber installed at the diffractometer. The sample was placed in a camera-reactor of the diffractometer, heated up to $T = 160$ °C in a helium flow, and a diffraction pattern of the dry sample was recorded. Then camera-reactor with the sample was cooled to $T = 18$ °C in a helium flux. After cooling, helium saturated with methanol vapor in a temperature-controlled saturator was introduced in the chamber. The methanol pressure was adjusted by change of the saturator temperature from -13.6 to +15 °C with a step of 3-5 °C. The sample was kept at constant pressure for 1–2 h, and the diffraction pattern was recorded.

The phase transformations of LiCl/V saturated with methanol upon heating were studied by DSC analysis using a differential scanning calorimeter NETZSCH DSC 204 F1 Phoenix. A sample was placed in a crucible, saturated with methanol by adding the fixed methanol amount to the sample, and tightly closed with a lid. The methanol content of the prepared samples was expressed as the number of n moles of methanol to one salt mole. Two samples saturated with methanol up to $n = 0.9$ and 2.8 mole/mole were prepared. The samples were held for 16 h to distribute methanol in the sample evenly. The samples were studied at a temperature from -33 to 57 °C, with preliminary isothermal exposure for 10 min at -33°C.

Sorption dynamics measurements

The dynamics of methanol sorption was studied with a volumetric set-up, consisting of three main parts: a measuring cell with the studied adsorbent, a buffering vessel and a condenser/evaporator with liquid methanol [10]. An adsorbent bed was composed of loose grains of 0.4-0.5 mm size placed on the metal support surface in the measuring cell. A thin plastic ring was used to fix constant the contact surface area $S = 2.27$ cm² between the adsorbent and the support. The mass of sorbent equaled 40 mg.

Dynamics of methanol sorption on the composites was studied by a Large Pressure Jump (LPJ) method [11]. The sorption/desorption processes were initiated by a jump/drop of the methanol pressure. At the same time, temperature T of the metal support was maintained constant with an accuracy of ± 0.1 °C by a thermal bath. An absolute pressure transducer MKS Baratron PR4300 recorded the pressure evolution $P(t)$ each 0.25-60 s with an accuracy of $\pm 0.15\%$. The measuring cell and buffering vessel were filled with methanol vapor from the evaporator to reach the initial adsorption pressure P_{in} , and then the evaporator was disengaged. After setting the adsorption equilibrium, the measuring cell was disconnected from the buffering vessel. For adsorption runs, the buffering vessel was filled with methanol vapor from the evaporator to reach the methanol pressure $P = P_{fin} + \Delta P$. For desorption, methanol vapor was drawn off the buffering vessel to the pressure of $P = P_{fin} - \Delta P$ mbar. For starting the adsorption/desorption, the measuring cell was connected to the buffering vessel, which led to the methanol pressure jump/drop. The methanol adsorption/desorption on/from the sample resulting in the gradual change of the methanol pressure $P(t)$ to the final (equilibrium) pressure P_{fin} .

The pressure change $\Delta P(t)$ was used to calculate the methanol uptake/release $\Delta w(t)$ and the dimensionless conversion $q(t)$ as:

$$\Delta w(t) = \frac{(P(t) - P_0)VM}{RTm} \quad (1)$$

$$q(t) = \frac{\Delta w(t)}{\Delta w_{fin}} \quad (2)$$

where $P(t)$ and P_0 – current and initial pressure, respectively, V – the rig volume, M – the molar mass of methanol, T – temperature, R – the universal gas constant, m – the adsorbent mass, Δw_{fin} – the final uptake change. The accumulated error in the absolute methanol loading was $\pm 10^{-3}$ g/g that led to the accuracy of the differential methanol loading equaled to $\pm 3\%$.

The boundary conditions during sorption runs were selected based on the isosteric chart of methanol sorption on the LiCl/V [6]. For studying the effect of the temperature/pressure on the sorption dynamics, the ad/desorption runs were carried out between two isosteres with the maximum uptake $n_1 = 4.2 \pm 0.2$ (mole CH₃OH)/(mole LiCl) and the minimum uptake $n_2 = 0.10 \pm 0.05$ (mole CH₃OH)/(mole LiCl) for all runs (Fig. 2, Table 2).

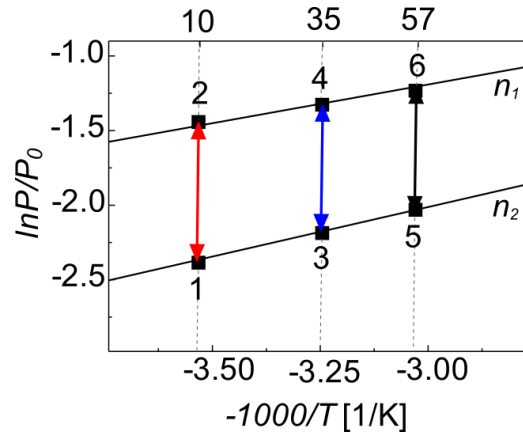


Fig. 2. Isosteres n_1 and n_2 of methanol sorption and studied adsorption and desorption runs on P - T diagram.

Table 2. Boundary conditions of the kinetic tests.

$T, ^\circ\text{C}$	Run	Adsorption		Desorption		
		P_{in}, mbar	P_{fin}, mbar	Run	P_{in}, mbar	P_{fin}, mbar
10.0	1→2	6.7	17.2	2→1	17.2	6.7
35.0	3→4	30.8	72.8	4→3	72.8	30.8
57.2	5→6	96.6	214.6	6→5	214.6	96.6

Sorption equilibrium measurements

The methanol sorption isotherms were measured by the volumetric method with the same experimental rig at temperatures 10 and 35°C and pressures of 0.1 to 70.0 mbar. Methanol adsorption was initiated by consecutive small jumps in the methanol vapor pressure above the sample. The uptake was calculated according to equation (1).

Discussion and Results

LiCl/vermiculite

Methanol sorption dynamics

An initial part of kinetic curves of methanol sorption (Fig. 1a) and desorption (Fig. 1b) for LiCl/V composite obey the exponential equation:

$$q = 1 - \exp(-t/\tau), \quad (3)$$

where τ is the characteristic time (Table 3). At larger conversion $q > 0.6$ and 0.3 for sorption and desorption runs, respectively, deceleration for sorption and strong rate reduction for

desorption are observed. For the sorption runs, curves measured at different temperatures and pressures (runs 1-2, 3-4, and 5-6 in Fig. 2) are very close to each other (Fig. 3a): the characteristic times τ_{ad} and $\tau_{ad0.8}$ corresponding to the conversion $q = 0.8$ vary in the range 4.0-5.1 and 14-20 min, respectively (Table 3). Thus, the sorption kinetics weakly depends on the temperature in the range 10.0-57.2 °C and the pressure in the range 17.2-214.6 mbar. Similar behavior is observed for the initial part of the desorption runs ($\tau_{des} = 6.5$ -13.2 min). On the contrary, at $q > 0.5$, the desorption dramatically decelerates, especially at lower temperature and pressure (Fig. 3b) so that the characteristic time $\tau_{des0.8}$ varies from 137 to 550 min. The sorption always occurs much faster than desorption; e.g., at $T = 57.2^\circ\text{C}$, the time $\tau_{0.8}$ equals 14 and 137 min for sorption and desorption, respectively (Table 3). This can be attributed, at least partially, to higher methanol pressure P_{fin} during sorption runs.

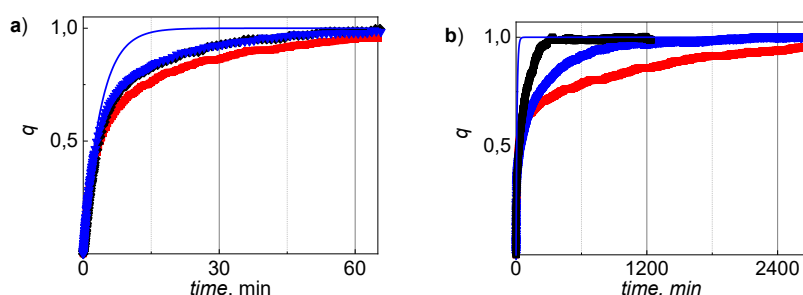


Fig. 3. Kinetic curves of the methanol sorption on (a) and desorption from (b) the LiCl/V at $T = 10\text{ }^\circ\text{C}$ (■), $35\text{ }^\circ\text{C}$ (▼), and $57\text{ }^\circ\text{C}$ (◆). Line – exponential approximation at $T = 35\text{ }^\circ\text{C}$.

Table 3. Characteristic times τ and $\tau_{0.8}$ of the adsorption and desorption runs (the error equals $\pm 10\%$ for all runs) for LiCl/V.

T, °C	Adsorption			Desorption		
	Run	τ_{ad} , min	$\tau_{ad0.8}$, min	Run	τ_{des} , min	$\tau_{des0.8}$, min
10.0	1→2	4.0±0.3	20±2	2→1	13.2±1.3	550±425
35.0	3→4	4.0±0.2	15±1.5	4→3	8.5±0.5	312±12
57.2	5→6	5.1±0.2	14±1	6→5	6.5±0.6	137±20

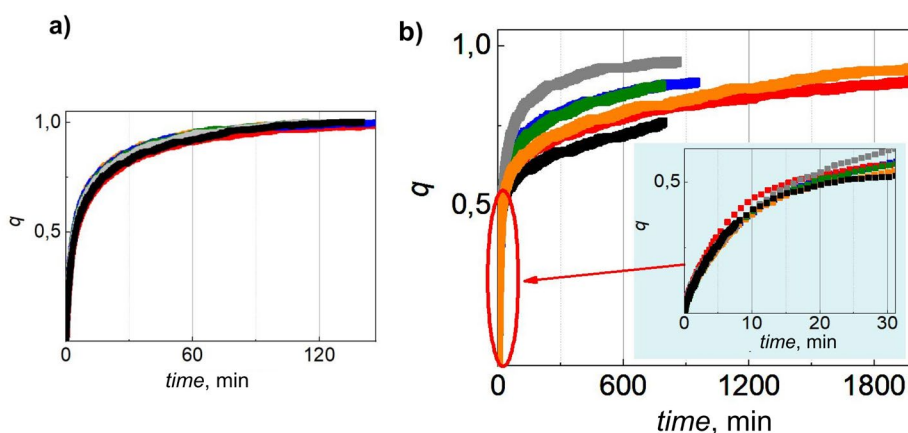


Fig. 4. Reproducibility of kinetic curves of the methanol sorption on (a) and desorption from (b) the LiCl/V at $T = 10\text{ }^\circ\text{C}$. Different runs are indicated with various colours.

It is important to note that, at $q > 0.5$, the desorption kinetic curves are poorly reproducible while the adsorption curves are perfectly reproducible in the whole conversions range (Fig. 4), although the error in measuring both curves is the same (Table 3). Yet, the characteristic desorption time $\tau_{des0.8}$ for curves measured with the same batch under the same conditions varies from 124 to 975 min. Such data scatter is typical for dehydration kinetics of crystalline hydrates in bulk [12]. It is caused by a random nucleation nature of the salt and its hydrates. It was shown in [13] that for dehydration of $\text{NiSO}_4 \cdot 7\text{H}_2\text{O}$, the time of first nucleus appearance varies from 495 to 1920 min under the same conditions. The nucleation stage is commonly very slow, resulting in a long induction period always observed in dehydration reactions [14]. It is not surprising that similar effects were observed during the formation of salt (hydrates) in the macropores of vermiculite, in which the salt solution/hydrates behave similarly to those in bulk.

Thus, the desorption curves have a fast part at $q < 0.5$ and a slow part at larger conversion. The latter part is temperature and pressure-dependent and becomes much slower at lower temperature and pressure (Fig. 3b). The methanol desorption from these composites might involve the following processes:

1. Release of methanol vapor from the LiCl-methanol solution inside the pores at $n > 3$ mol $\text{CH}_3\text{OH}/\text{mol LiCl}$.
2. Crystallization of solid complexes $\text{LiCl} \cdot n\text{CH}_3\text{OH}$ ($n = 1$ and 3), known for the bulk system LiCl - methanol [15].
3. Their decomposition toward a neat LiCl.

The initial "fast" part of the experimental kinetic curves can be assigned to the methanol desorption from the solution. Further desorption involves crystallization of the complexes $\text{LiCl} \cdot n\text{CH}_3\text{OH}$ and LiCl. This process is complex and includes nucleation and crystal growth stages. Thus, at $q > 0.5$, the methanol desorption in the LiCl/V macropores can be hindered by the mentioned processes. For revealing the rate-control process, the change in phase composition of the "LiCl – methanol" system during the desorption, was studied by XRD *in situ* and DSC techniques.

The XRD patterns measured *in situ* during methanol sorption on the composite LiCl/V at $T = 160^\circ\text{C}$ exhibit symmetrical peaks (Fig. 5) that can be assigned as (111), (200), (220), (311), (222) reflexes of a cubic lattice (space group Fm-3m) of LiCl (JCPDS No. 74-1972). Cooling the composite down to $T = 18^\circ\text{C}$ at helium flow results in appearance of additional reflexes at $2\theta = 33.5, 41.2, 47.5, 48.0, 59.4,$ and 60.2 , attributed to the formation of monohydrate $\text{LiCl} \cdot \text{H}_2\text{O}$ (space group $\text{P}4_2/\text{nmc}$; JCPDS 73-1273). It is formed via the reaction of LiCl with the residual water vapor in helium flow. Increasing methanol pressure results in lessening the reflexes of both LiCl and $\text{LiCl} \cdot \text{H}_2\text{O}$. At $P_{\text{CH}_3\text{OH}} > 40$ mbar, the sample becomes X-ray amorphous. No reflexes, which could be referred to $\text{LiCl} \cdot n\text{CH}_3\text{OH}$ ($n = 1, 3$) complex, are observed during methanol sorption. Therefore, the crystalline complexes $\text{LiCl} \cdot \text{CH}_3\text{OH}$ or $\text{LiCl} \cdot 3\text{CH}_3\text{OH}$ do not form at $T = 18^\circ\text{C}$ in the vermiculite pores, and the salt transforms directly into a "LiCl – methanol" solution.

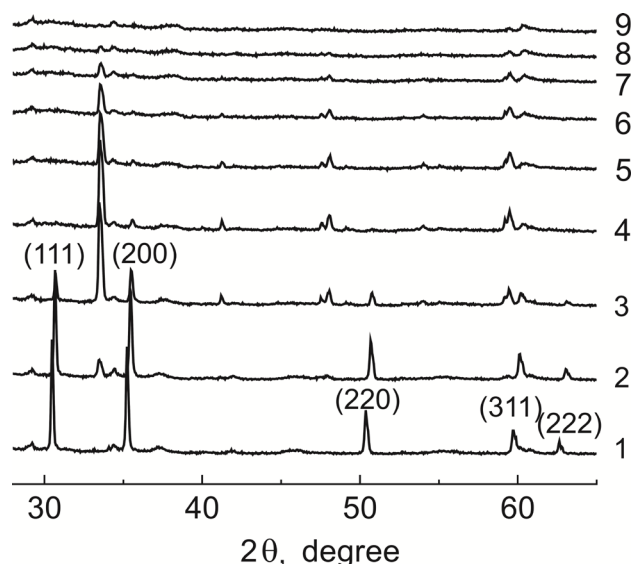


Fig. 5. XRD *in situ* pattern of LiCl/V measured at $T = 160^\circ\text{C}$ (1), 18°C (2) in a helium flow, at $T = 18^\circ\text{C}$ (3-9) in the helium flow saturated with methanol vapor. $P_{\text{CH}_3\text{OH}} = 15.8$ (3), 23.0 (4), 28.1 (5), 32.0 (6), 39.8 (7), 54.1 (8), and 72.8 (9) mbar.

The DSC curve for the system $\text{LiCl}\cdot n\text{CH}_3\text{OH}$ confined to the vermiculite macropores and saturated with methanol up to $n = (2.8 \pm 0.1)$ mole $\text{CH}_3\text{OH}/\text{mole LiCl}$ has an endothermic peak with the onset temperature 4°C (Fig. 6a). This peak can be related to the melting of a crystalline complex $\text{LiCl}\cdot 3\text{CH}_3\text{OH}$ inside the pores. The melting enthalpy is estimated to be $125 \pm 15 \text{ J/g}$, which is essentially smaller than the enthalpy of monohydrate $\text{LiCl}\cdot\text{H}_2\text{O}$ melting (212 J/g) [16]. No peak is detected for the $\text{LiCl}\cdot 0.9\text{CH}_3\text{OH}/\text{vermiculite}$ (Fig. 6b), which indicates no formation of the crystalline complexes $\text{LiCl}\cdot\text{CH}_3\text{OH}$ in the vermiculite pores. This is in line with the equilibrium curve of methanol sorption on LiCl/V, which has only one steep increase of the uptake from $n \approx 0$ to $n \approx 3 \text{ mol/mol}$ [6].

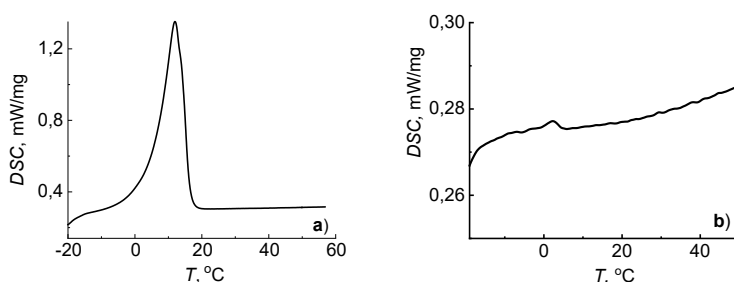


Fig. 6. DSC curves for $\text{LiCl}\cdot n\text{CH}_3\text{OH}/\text{Vermiculite}$ at $n = 2.8$ (a) and 0.9 (b).

Thus, the DSC data confirm the XRD results and demonstrate that no crystalline complexes form in the macropores of LiCl/V under the test conditions at $T = 10.0\text{-}57.2^\circ\text{C}$. Indeed, a complex $\text{LiCl}\cdot 3\text{CH}_3\text{OH}$, detected in bulk “LiCl – methanol” solution, melts inside the pores at the lower temperature (4°C). Consequently, the slowdown of desorption at $q > 0.5$ is most likely due to LiCl crystallization from its solution in methanol.

The crystallization in pores is expected to occur through heterogeneous nucleation on the pore wall as it requires lower activation energy [17]. The evaporation from the solution droplet located on the wall is faster near the droplet edge, where the heat flux is larger [18]. This results in faster evaporation and higher supersaturation near the edge. Accordingly, the nuclei first form in the vicinity of the contact line “drop – substrate” (so-called “coffee-stain” effect [18]). It was revealed for aqueous solutions of NaCl [19], LiBr [20], CaCl_2 [21], and

CaSO₄ [22]. The nuclei rapidly grow, neighboring crystals associate together, forming the crystallization front, which moves to the droplet center, forming a crust on the droplet surface. Further desorption involves the methanol transport through the crust, or through defects and cracks in it, and the desorption rate slows down dramatically [23].

Consequently, the most probable reason for the methanol desorption deceleration at $q > 0.5$ might be the slow heterogeneous nucleation of anhydrous LiCl and/or the formation of the crystalline crust of LiCl on the surface of the solution, which slows down vapor transport (Fig. 7).

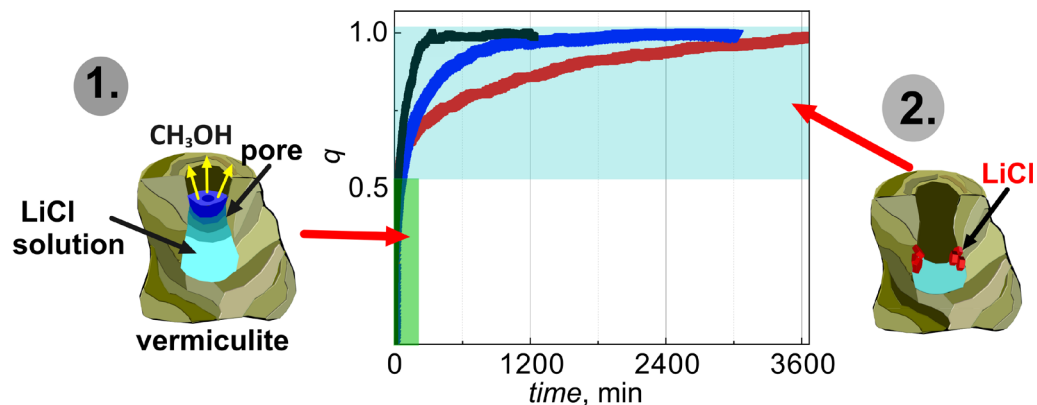


Fig. 7. Schematics of the proposed mechanism of methanol desorption from LiCl/V: (1) fast desorption from LiCl-methanol solution at $n > 3$; (2) slow formation of crystalline LiCl from the solution at $n < 3$.

It might be expected that modification of the vermiculite by highly dispersed additives could create new centers of the salt nucleation, facilitate this process and accelerate the methanol desorption. It was shown in [24] that Li⁺ cations specifically adsorbed on the alumina surface form anchored complexes Li⁺-Al₂O₃, which could be additional centers for LiCl nucleation. Moreover, the formation of a large number of smaller LiCl crystals might reduce the mass transport resistance through the LiCl crust. In the hope of accelerating methanol desorption, the vermiculite surface was modified by 2.5, 5.8, and 8.9 wt.% of dispersed alumina (Al₂O₃). The obtained porous matrixes Al₂O₃/vermiculite were loaded with LiCl by dry impregnation. For new composites LiCl/Al₂O₃/vermiculite (LiCl/Al₂O₃/V), their equilibrium and kinetics of methanol sorption/ desorption were comprehensively studied.

LiCl/Al₂O₃/vermiculite composites

Characterization

The SEM-images show that the surface morphology for the neat vermiculite, LiCl/V, and LiCl/Al₂O₃/V composites is similar (Fig. 8). No salt crystals were detected on the external surface of the grains for LiCl/V, LiCl/5.8Al₂O₃/V and LiCl/8.9Al₂O₃/V. Consequently, the salt is confined to the vermiculite macropores. The surface of the modified LiCl/Al₂O₃/V composites is somewhat more friable.

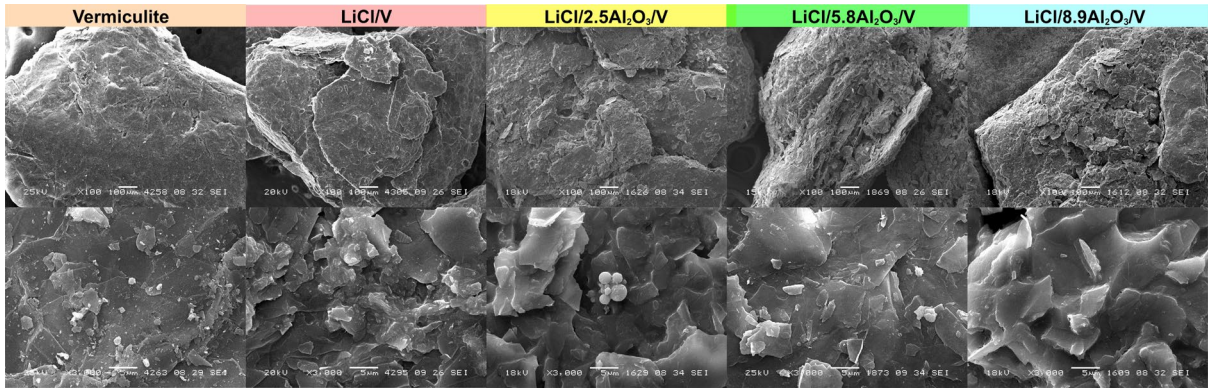


Fig. 8. SEM images of the neat vermiculite, LiCl/V and LiCl/Al₂O₃/V composites.

The powder XRD patterns of the LiCl/Al₂O₃/V composites (Fig. 9) are similar to those of LiCl/V and exhibits symmetrical peaks that correspond to a LiCl cubic lattice (space group Fm-3m) (JCPDF No. 74-1972). No crystalline Al₂O₃ was detected as it forms a highly dispersed X-ray amorphous phase inside the vermiculite pores. The size of coherently scattering domains equals 90-100 nm for all composites. Some of the basal vermiculite reflexes are retained, but their intensity significantly decreases after the modification. It could be due to a change in the layered structure of vermiculite during the composite synthesis.

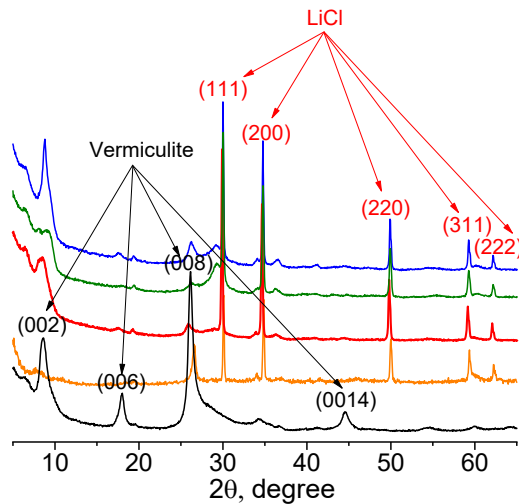


Fig. 9. XRD in situ pattern of vermiculite (black line), LiCl/V (orange line), LiCl/2.5Al₂O₃/V (red line), LiCl/5.8Al₂O₃/V (green line) and LiCl/8.9Al₂O₃/V (blue line) measured at $T = 160^\circ\text{C}$

Thus, SEM and XRD analysis show that the Al₂O₃ additive results in only small changes in the morphology and phase composition of the confined LiCl.

Methanol sorption dynamics

The kinetic curves of methanol sorption on and desorption from the modified composites are presented in Fig. 10. The initial parts of kinetic curves also obey the exponential equation (3).

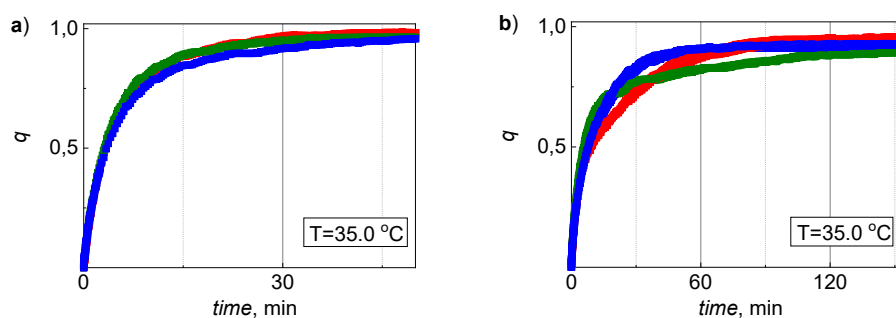


Fig. 10. Kinetic curves of the methanol sorption on (a) and desorption from (b) the LiCl/Al₂O₃/V composites with the Al₂O₃ content 2.5 (■), 5.8 (■) and 8.9 (■) wt.% at 35 °C.

The kinetic curves of methanol sorption on the modified composites are very close, thus, the characteristic time τ_{ad} varies in the range 4.3-5.0 min and $\tau_{ad0.8} = 9.4$ -14.3 min (Table 4). The methanol desorption slightly accelerates at the larger alumina content; the characteristic time $\tau_{des0.8}$ reduces from 46.3 min to 27.5 min at $T = 35$ °C and $P = 72.8 \rightarrow 30.8$ mbar.

Kinetic curves of methanol sorption and desorption measured for LiCl/Al₂O₃/V at various T and P are shown in Fig. 11.

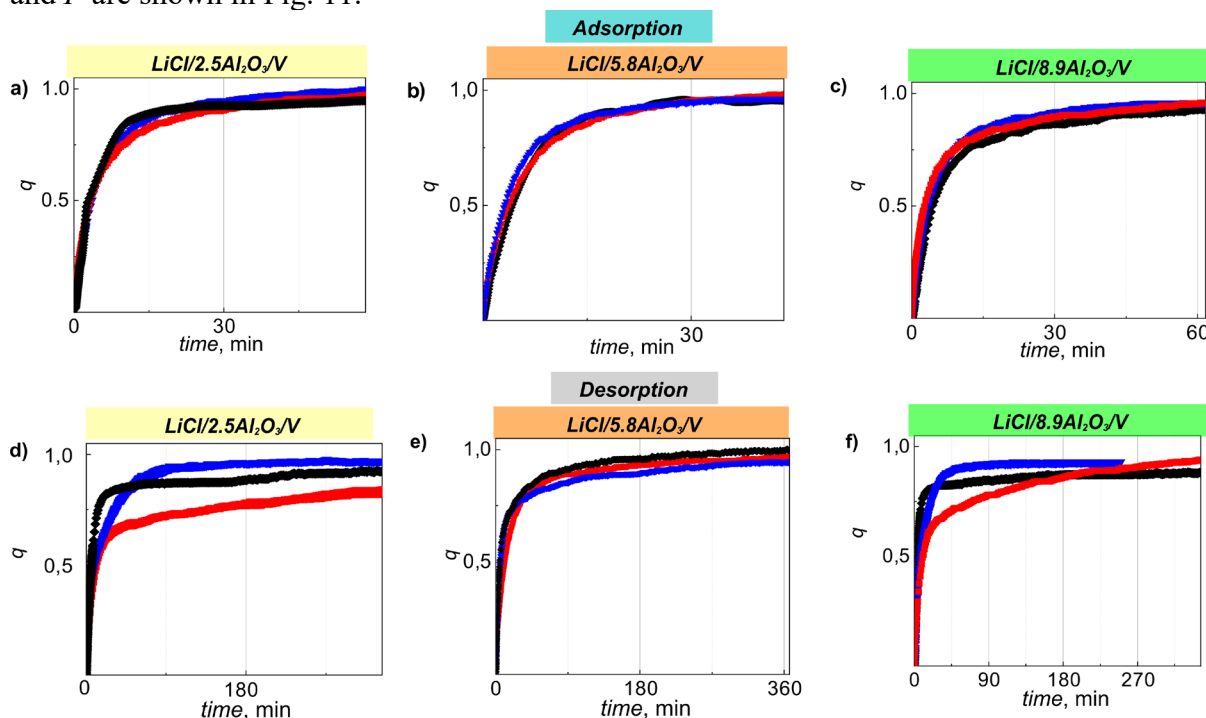


Fig. 11. Kinetic curves of the methanol sorption on (a, b, c) and desorption from (d, e, f) the LiCl/Al₂O₃/V with the Al₂O₃ content 2.5 (a, d), 5.8 (b, e) and 8.9 (c, f) wt.% at $T = 10$ °C (■), 35 °C (▼) and 57 °C (◆).

The kinetic curves of methanol sorption (Fig. 11 a, b, c) are close to each other for all the modified composites, and only slightly depends on T and P . On the contrary, the methanol desorption from LiCl/Al₂O₃/V is dependent on process conditions and becomes slower at a lower temperature and pressure (Fig. 11 d-f), (Table 4). In contrast to unmodified LiCl/V, the kinetic curves of methanol desorption for all modified LiCl/Al₂O₃/V are *well reproduced*. Apparently, this is due to the fact that the introduction of Al₂O₃, whose surface groups can serve as additional nucleation centers, accelerates this process, and the nucleation of LiCl is no longer the stage that determines the rate of methanol desorption.

Table 4. Characteristic times τ and $\tau_{0.8}$ of the methanol adsorption and desorption for the LiCl/Al₂O₃/V composites (the error equals $\pm 10\%$ for all the runs).

T, °C	Adsorption			Desorption		
	Run	τ_{ad} , min	$\tau_{ad0.8}$, min	Run	τ_{des} , min	$\tau_{des0.8}$, min
LiCl/2.5Al ₂ O ₃ /V						
10	1→2	5.1	17	2→1	11.5	255
35	3→4	4.6	11	4→3	6.5	42
57	5→6	5.5	17	6→5	6.3	28
LiCl/5.8Al ₂ O ₃ /V						
10	1→2	4.0	11	2→1	9.0	47
35	3→4	4.3	9	4→3	5.7	46
57	5→6	5.8	10	6→5	6.1	34
LiCl/8.9Al ₂ O ₃ /V						
10	1→2	4.3	16	2→1	10.3	110
35	3→4	5.0	14	4→3	7.3	27
57	5→6	5.8	21	6→5	5.5	15

Let us compare kinetic curves of methanol sorption and desorption for modified composites LiCl/Al₂O₃/V and unmodified LiCl/V under various conditions (Fig. 12). The kinetic curves of the methanol sorption on the modified and neat composites coincide; hence, the modification does not affect the sorption dynamics. It seems that the sorption kinetics is determined by vapor transfer in the sorbent grains and heat transfer between the metal substrate and the sorbent layer and, likely, in the sorbent layer. Small additions of Al₂O₃ do not affect these processes.

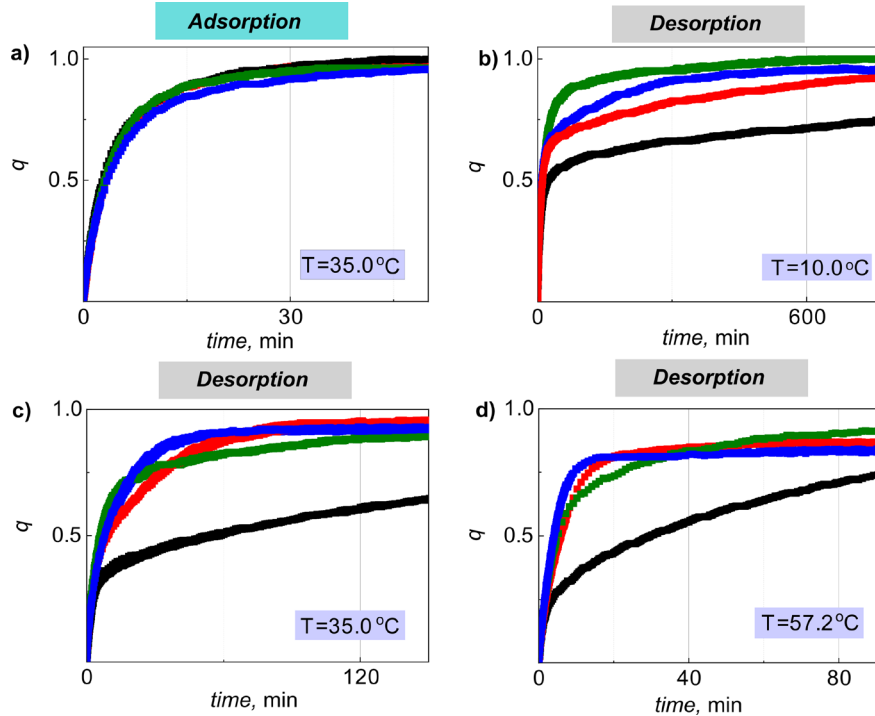


Fig. 12. Kinetic curves of the methanol sorption on (a) and desorption from (b, c, d) LiCl/V (■) and LiCl/Al₂O₃/V with the Al₂O₃ content 2.5 (■), 5.8 (■) and 8.9 (■) wt.% at $T = 10$ °C (b), 35 °C (a, c), and 57 °C (d).

In contrast, the methanol desorption occurs much faster on modified composites that is the *main finding* of this study. The initial part of the desorption curves at $q < 0.5$ are quite close for the modified LiCl/Al₂O₃/V and unmodified LiCl/V composites. Under these conditions (at $n > 3$ mol CH₃OH/mol LiCl), methanol desorbs from the LiCl-methanol solution confined to the pores; this corresponds to the "fast" desorption. Further desorption is much faster for the modified composites. For LiCl/5.8Al₂O₃/V, at $T = 10.0$ °C and $P = 17.2 \rightarrow 6.74$ mbar, the characteristic time $\tau_{des0.8}$ decreases by a factor of 12. A similar tendency is observed at all temperatures and pressures for all modified composites (Tables 3, 4). Thus, the vermiculite modification by small additives of finely-dispersed Al₂O₃ is deemed to promote effectively the LiCl nucleation by forming Li⁺-Al₂O₃ complexes anchored to the vermiculite surface (Fig. 13).

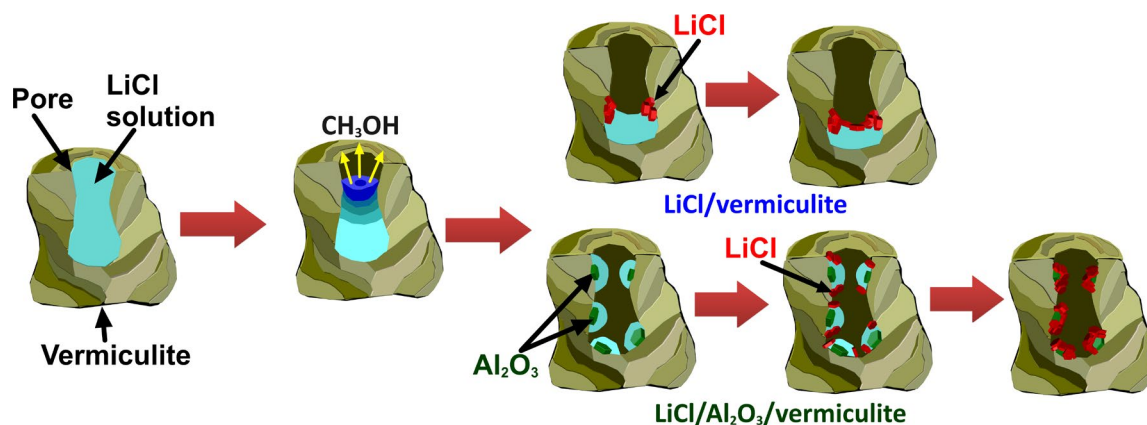


Fig. 13. Scheme of the salt nucleation in the macropores of the LiCl/V and LiCl/Al₂O₃/V composites.

The anchored complexes Li⁺-Al₂O₃ on the vermiculite surface facilitate the salt nucleation, which results in forming a larger number of tiny salt crystals in the modified composite LiCl/Al₂O₃/V compared to the pristine LiCl/V composite. This leads to low super-saturation of the salt solution, fast nucleation and strong acceleration of the methanol desorption.

Thus, the modification of the vermiculite surface by dispersed Al₂O₃ is a powerful tool for accelerating the methanol desorption without reducing the methanol sorption capacity of the composite (see below).

Methanol sorption equilibrium

For studying the effect of the Al₂O₃ additive on the methanol adsorption equilibrium of the composites involved, the isotherms of methanol sorption/desorption were measured for LiCl/5.8Al₂O₃/V. They are presented in Fig. 14 as a function of the adsorption potential $\Delta F = RT \ln(P/P_0(T))$, where $P_0(T)$ is the saturation pressure of methanol vapor at temperature T . A steep uptake rises from $n = 0$ to 3 mol/mol is observed at $\Delta F = 4.5 \pm 0.1$ kJ/mol. This step can be attributed to the formation of LiCl·3CH₃OH, which immediately deliquesces and continues absorbing methanol vapor at decreasing ΔF . The characteristic curve of methanol sorption on the modified composite is close to that for the pristine LiCl/V. The uptake reaches 1.2 g/g, which corresponds to an energy storage capacity of 1.6 kJ/g. Thus, the modification of the vermiculite surface by the Al₂O₃ additive does not change the equilibrium in the confined system "LiCl – methanol" and, hence, its' heat storing capacity.

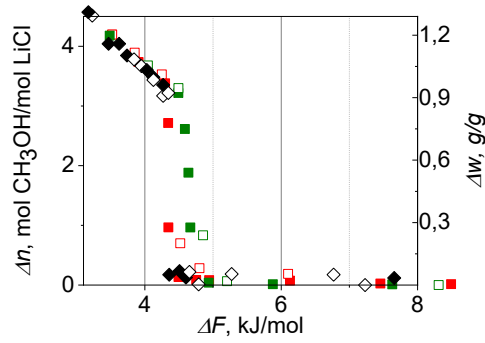


Fig. 14. Characteristic curve of methanol sorption on LiCl/5.8Al₂O₃/V at $T = 10$ (■, □) and 35°C (■, □). Open symbols – desorption, solid symbols – sorption.

Specific power of adsorption heat storage cycle

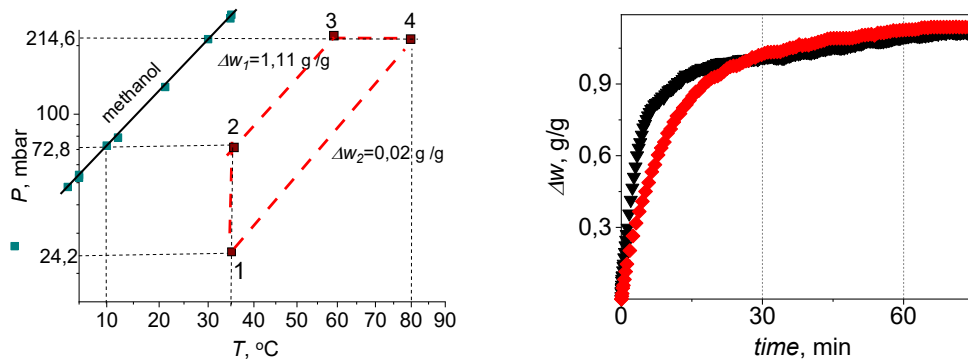


Fig. 15. Boundary conditions of a seasonal heat storage cycle (a) [6] and kinetic curves of the methanol sorption (◆) and desorption (▼).

Table 5. Boundary conditions of the analyzed seasonal heat storage cycle.

Sorption			Desorption		
$T_{ad}, ^\circ\text{C}$	$P_{in.ad}, \text{mbar}$	P_{ad}, mbar	$T_{in.des}, ^\circ\text{C}$	$T_{des}, ^\circ\text{C}$	P_{des}, mbar
35	24.2	72.8	57	80	214.6

For evaluating the specific power of a seasonal heat storage cycle using LiCl/5.8Al₂O₃/V, the adsorption kinetics was studied under conditions of the typical heat storage cycle (Fig. 15a, Table 5) [6]. The specific power $W_{0.8}$ was estimated according to equation

$$W_{0.8} = 0.8 \cdot \Delta w_{fin} \cdot \Delta H_{ad} / \tau_{0.8} \quad (4)$$

where Δw_{fin} is the final uptake variation, ΔH_{ad} is the heat of methanol sorption estimated as 42 kJ/mol [6], $\tau_{0.8}$ is the time related to $q = 0.8$. It is shown that $W_{0.8}$ reaches 1.05 and 1.6 kW/kg for the heat release and heat storage stages, respectively. The obtained powers exceed appropriate values for the neat composite 1.5 and 4 times [6].

Summary

The methanol sorption/desorption dynamics was comprehensively studied for the composite sorbent LiCl/vermiculite. The desorption dynamics is found to be strongly decelerated due to the slow LiCl nucleation on the vermiculite surface and/or sluggish methanol transport through the formed LiCl layer. A novel method for intensifying the sorption dynamics through the composite modification is suggested: the LiCl/V composite is modified by the aluminium oxide

additive, which allows desorption to be significantly accelerated. The characteristic time $\tau_{des0.8}$, corresponding to the 80% conversion decreases by a factor of 2-12 for composites with 2.5-8.9 wt.% Al_2O_3 at $T = 10.0\text{-}57.2$ °C and $P = 6.74\text{-}96.6$ mbar. Such a strong acceleration can be stemmed from enhanced nucleation of the LiCl phase on the Al_2O_3 surface in the vermiculite macropores. This allows the specific cycle power to be increased by factors of 1.5 and 4 for the heat release and heat storage stages, respectively. Thus, the large heat storage capacity, advanced specific power, and low cost make the new composite LiCl/ Al_2O_3 /V promising methanol sorbent for adsorption heat storage applications.

Acknowledgements: This work was partially supported by the Russian Foundation for Basic Research (grant no. 18-58-80047 BRICS) and the Ministry of Science and Higher Education of the Russian Federation within the governmental order for Boreskov Institute of Catalysis (project AAAA-A21-121011390006-0).

References:

- [1] Wang, R., Wang, L., Wu, J., *Adsorption Refrigeration Technology: Theory and Application*, John Wiley & Sons, 2014.
- [2] Shabir, F., Sultan, M., Miyazaki, T., Saha, B. B., Askalany, A., Ali, I., Zhou, Y., Ahmad, R., Shamshiri, R. R., “Recent updates on the adsorption capacities of adsorbent-adsorbate pairs for heat transformation applications”, *Renewable and Sustainable Energy Reviews*, 2020.
- [3] Gordeeva, L. G., Aristov, Yu. I., “Composites ‘salt inside porous matrix’ for adsorption heat transformation: a current state-of-the-art and new trends”, *International Journal of Low-Carbon Technologies*, 2012.
- [4] Palomba, V., Frazzica, A., “Recent advancements in sorption technology for solar thermal energy storage applications”, *Solar Energy*, 2019.
- [5] Aristov, Yu. I., Restuccia, G., Tokarev, M. M., Buerger, H. D., Freni, A., “Selective water sorbents for multiple applications. 11. CaCl_2 confined to expanded vermiculite”, *Reaction Kinetics and Catalysis Letters*, 2000.
- [6] Grekova, A. D., Strelova, S. V., Gordeeva, L. G., Aristov, Yu. I., ““LiCl/vermiculite-Methanol” as working pair for adsorption heat storage: Adsorption equilibrium and dynamics”, *Energy*, 2019.
- [7] Galwey, A. K., Brown, M. E., *Thermal decomposition of ionic solids: chemical properties and reactivities of ionic crystalline phases*, Elsevier, 1999.
- [8] Mullin, J. W., *Crystallization*, Elsevier, 2001.
- [9] Low, N. M., “The thermal insulating properties of vermiculite”, *Journal of thermal insulation*, 1984.
- [10] Gordeeva, L. G., Aristov, Yu. I., “Composite sorbent of methanol “LiCl in mesoporous silica gel” for adsorption cooling: dynamic optimization”, *Energy*, 2011.
- [11] Girnuk, I. S., Aristov, Yu. I., “A HeCol cycle for upgrading the ambient heat: The dynamic verification of desorption stage”, *Applied Thermal Engineering*, 2019.
- [12] Lyakhov, N. Z., Boldyrev, V. V., “Kinetics and mechanism of the dehydration of crystal hydrates”, *Russian Chemical Reviews*, 1972.
- [13] Garner, W. E., Southon, W. R. “404. Nucleus formation on crystals of nickel sulphate heptahydrate”, *Journal of the Chemical Society (Resumed)*, 1935.
- [14] Rae, W. N., “LXXXVII. — A period of induction in the dehydration of some crystalline hydrates”, *Journal of the Chemical Society, Transactions*, 1916.

- [15] Data G., 2005 Gesellschaft Deutscher Chemiker licensed to MDL Information Systems GmbH; 1988–1999: Gmelin Institut fuer Anorganische Chemie und Grenzgebiete der Max-Planck-Gesellschaft zur Foerderung der Wissenschaften, vol. Li: S, 2000.
- [16] Voigt, W., Zeng, D., “Solid–liquid equilibria in mixtures of molten salt hydrates for the design of heat storage materials”, Pure and Applied Chemistry, 2002.
- [17] Diao, Y., Myerson, A. S., Hatton, T. A., Trout, B. L., “Surface design for controlled crystallization: The role of surface chemistry and nanoscale pores in heterogeneous nucleation”, Langmuir, 2011.
- [18] Deegan, R. D., Bakajin, O., Dupont, T. F., Huber, G., Nagel, S. R. Witten, T. A., “Capillary flow as the cause of ring stains from dried liquid drops”, Nature, 1997.
- [19] Misyura, S. Yu., “Different modes of heat transfer and crystallization in a drop of NaCl solution: The influence of key factors on the crystallization rate and the heat transfer coefficient”, International Journal of Thermal Sciences, 2021.
- [20] Kuznetsov, G. V., Misyura, S. Yu., Volkov, R. S., Morozov, V. S. “Marangoni flow and free convection during crystallization of a salt solution droplet”, Colloids and Surfaces A: Physicochemical and Engineering Aspects, 2019.
- [21] Misyura, S. Yu., “The crystallization behavior of the aqueous solution of CaCl₂ salt in a drop and a layer”, Scientific reports, 2020.
- [22] Shahidzadeh, N., Schut, M. F., Desarnaud, J., Prat, M., Bonn, D., “Salt stains from evaporating droplets”, Scientific Reports, 2015.
- [23] Nakoryakov, V. E., Misyura, S. Y., Elistratov, S. L., “Nonisothermal desorption of droplets of complex compositions”, Thermal Science, 2012.
- [24] Johnson, S. B., Scales, P. J., Healy, T. W., “The binding of monovalent electrolyte ions on α -alumina. I. Electroacoustic studies at high electrolyte concentrations”, Langmuir, 1999.

Composite sorbents Salt/MIL-101(Cr) for atmospheric water harvesting

I.O. Krivosheeva^{1,2}, M.V. Solovyeva¹, Yu. Aristov¹ and L.G. Gordeeva^{1*}

¹ Borekov Institute of Catalysis, Novosibirsk, Ac. Lavrentiev Novosibirsk State University,

² Novosibirsk State University, Novosibirsk, Pirogova str. 2, 630090, Russia

*Corresponding author: gordeeva@catalysis.ru

Abstract

Nowadays, the Adsorption method for atmospheric Water Harvesting (AWH) is considered a promising heat-driven technology for potable water supply in arid regions. This research focuses on novel composite sorbents based on hygroscopic salts placed inside pores of MIL-101(Cr). They have been developed keeping in mind AWH applications. The composites based on LiCl, LiBr, CaCl₂, and Ca(NO₃)₂ were synthesised and comprehensively studied by SEM, XRD, N₂ adsorption, and TG methods. The main findings are: (i) CaCl₂/MIL-101(Cr) demonstrates high specific water productivity of 0.52-0.59 g_H₂O/g_composite per cycle under conditions of Saudi Arabia and the Sahara Desert, which exceeds the appropriate values for other known adsorbents; (ii) the water adsorption on the composite cannot be presented as a linear combination of the adsorption on the components; a synergistic effect is revealed. The performance of AWH employing CaCl₂/MIL-101(Cr) was evaluated in terms of the fractions of water extracted and collected and the specific energy consumption, demonstrating its high potential for AWH.

Keywords: Potable water harvesting from the atmosphere, Adsorption, MIL-101(Cr), Composite “salt/matrix”.

Introduction/Background

In 2015, the United Nations General Assembly adopted the 2030 Agenda for Sustainable Development that features “Ensure availability and sustainable management of water and sanitation for all” as one of global the Sustainable Development Goals to provide the people’s wellbeing and protecting the environment [1,2]. With the rapidly growing population, industry and agriculture, potable water shortage is one of the pressing global challenges of our time. Nowadays, 2.2 billion people lack access to safely managed drinking water, and more than 4.2 billion people lack sanitation [3]. Climate change is exacerbating the situation, with increasing disasters such as floods and droughts. It is estimated that two-thirds of the population will live in water-stressed countries by 2025 [4].

Although most of the earth’s surface is covered with water, only 2.5% of these resources is fresh water. It worth also noting that current freshwater sources (rivers, lakes, and groundwater) are becoming increasingly polluted from human impact and insufficient to meet the growing demand [5]. Nowadays various water purification technologies such as desalination [4], filtration [6], reverse osmosis [7], multistage distillation [8], and solar water purification [9] have been developed to utilize seawater or wastewater. However, these technologies are energy intensive and are mainly inappropriate to use in arid landlocked regions with limited infrastructure [10,11,12].

Instead, the atmosphere contains 12,900 km³ of moisture which is accessible everywhere regardless of geographical conditions. Therefore, atmospheric moisture is considered a rich renewable source of fresh water and opens up a new path to solving the current global issue of potable water scarcity. Moreover, the natural hydrologic cycle enables a sustainable atmospheric humidity supply [13]. In this context, the technology of Adsorptive Water Harvesting from the atmosphere (AWH) is considered a promising method for decentralized

water supply for domestic and sanitation purposes in arid and remote areas with no natural water sources (sea, rivers, lakes, underground water, etc.), the areas affected by natural disasters, war zones, and areas with heavily chemically/biologically contaminated water supply [11].

The AWH is essentially based on the fact that the absolute air humidity in arid areas demonstrates just a small variation during a day, while the air temperature and the Relative Humidity (RH) fluctuations are wide [14,15]. The AWH process includes two stages: a) sorption of water vapor in an adsorber in the night-time when the air RH is high, and b) heat-driven desorption of the stored water with its subsequent condensation in the day-time. The adsorbent properties are the key element of AWH, which strongly affect the system performance. Recently, a family of crystalline solids - metal-organic frameworks (MOFs) - have aroused interest in the scientific community as promising adsorbents for AWH systems [16,17]. MOFs stand out among the other porous materials by their extremely high porosity and specific surface area and modular construction, which allows regulating the structure and composition of these compounds and, as a consequence, tuning the adsorption properties. A number of MOFs (MIL-101(Cr) and MIL-100(Cr, Al, Fe) [16, 18], MOF-841 [19], Co₂Cl₂BTDD [20], MOF-801 [21], MOF-303 [22] etc.) have recently been suggested for AWH. Among them, MIL-101(Cr) shows the highest water uptake (> 1.0 g/g) and excellent stability towards water [23]. However, the capacity of most MOFs at low RH is low due to their weak affinity to water vapor, which hinders the implementation of MOFs-based AWH under climatic conditions of arid regions. Inorganic salts placed inside porous matrices is another class of sorbents used for AWH [24, 25], which possess a high adsorption capacity and a quite strong affinity for water. The main shortage limiting their use in open AWH systems is a possible leakage of the aqueous salt solution, formed during the water adsorption, out of the pore space [26], which can cause a deterioration of the adsorbent and corrosion of metal details of the adsorber.

In this work, we modified the MIL-101(Cr) structure with ions of a number of inorganic salts to create additional adsorption centers and increase the affinity of the adsorbent to water vapor. A large pore volume of MIL-101(Cr), its open porosity and narrow pore size distribution promote the salt solution formed during water adsorption to remain inside pores, thus overcoming the main disadvantages of the composite sorbents. Therefore, this research is devoted to the development of the novel composite sorbents based on inorganic hygroscopic salts (LiCl, LiBr, CaCl₂, and Ca(NO₃)₂) inside pores of MIL-101(Cr) for AWH technology as well as the study of the impact of the salt chemical nature on sorption properties of the composites. Then, the properties of the composite CaCl₂/MIL-101, chosen as sorbent the most promising for AWH in arid climate, are studied in more detail. The potential of AWH system employing this composite is estimated in terms of the fractions of water extracted and collected, and the specific energy consumption in arid climate conditions of the Sahara Desert and Saudi Arabia regions.

Discussion and Results

Effect of the salt chemical nature

The composites salt/MIL-101 (salt = LiCl, LiBr, CaCl₂, Ca(NO₃)₂) were synthesised by a dry impregnation method. The salt content $C_s = 17, 32, 16-39$ and 17 wt%, for LiCl/MIL-101, LiBr/MIL-101, CaCl₂/MIL-101, Ca(NO₃)₂/MIL-101, respectively. Their water vapor adsorption equilibrium was studied by TG method.

The water adsorption isobars of the prepared salt/MIL-101(Cr) composites are presented as a function of the uptake versus adsorption potential $\Delta F = RT \ln(P_0/P)$ in Fig. 1. The data on water adsorption on the pristine MIL-101(Cr) taken in [23] are presented for comparison. MIL-

MIL-101(Cr) shows a minor uptake at the adsorption potential $\Delta F > 2.3$ kJ/mol, followed by a sharp jump at a narrow ΔF -range from 1.5 to 2.3 kJ/mol. On the contrary, the isobars for the composites are smooth curves indicating di-variant adsorption equilibrium with water vapor. The water uptake on the composites salt/MIL-101(Cr) significantly exceeds that for the pristine MIL-101(Cr) at $\Delta F > 2.0$ kJ/mol (Fig. 1), which indicates that at the high ΔF , the salt mainly adsorbs water vapor. Thus, the modification of MIL-101(Cr) by the hygroscopic salts allows the affinity of MIL-101(Cr) for water to be enhanced significantly.

The CaCl_2 and LiBr - based composites show the highest uptake w ΔF (Fig. 1). The $\text{Ca}(\text{NO}_3)_2/\text{MIL-101}(\text{Cr})$ and $\text{LiCl}/\text{MIL-101}(\text{Cr})$ composites exhibit much lower water adsorption capacity. Taking into account the toxicity of Li and a high price, the $\text{CaCl}_2/\text{MIL-101}(\text{Cr})$ was selected as the most promising material for the AWH and is further studied in more detail.

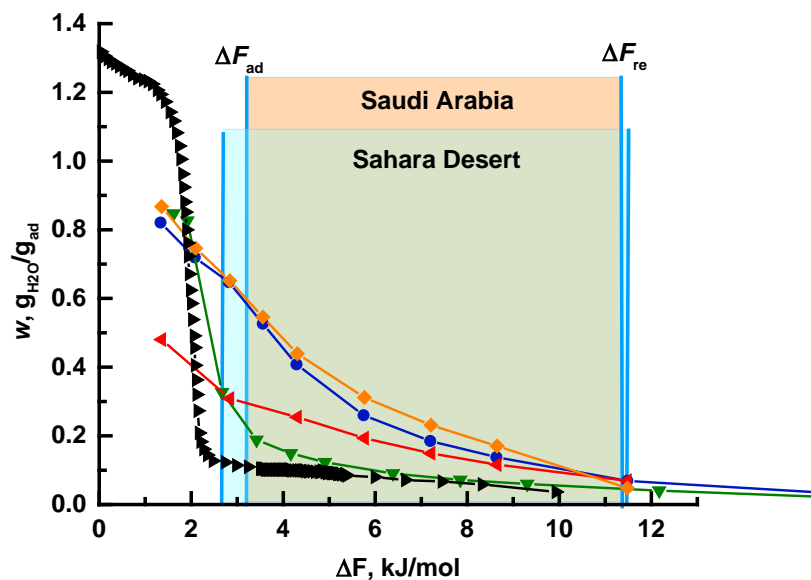


Figure 1. Water adsorption isobars on the pristine MIL-101 (\blacktriangleright) and the composites $\text{CaCl}_2/\text{MIL-101}$ (\bullet), $\text{Ca}(\text{NO}_3)_2/\text{MIL-101}$ (\blacktriangledown), $\text{LiBr}/\text{MIL-101}$ (\blacklozenge), $\text{LiCl}/\text{MIL-101}$ (\blacktriangleleft) at $P = 25$ mbar. The blue bars represent the values of ΔF_{ad} and ΔF_{re} at $T_{re} = 80$ °C of AWH cycle under climatic conditions of Saudi Arabia and the Sahara Desert as reference arid regions.

Composites $\text{CaCl}_2/\text{MIL-101}(\text{Cr})$

Characterization

The structure of the composites with a CaCl_2 content of 16-39 wt. % was studied by powder XRD, SEM and nitrogen low-temperature adsorption. The XRD patterns of $\text{CaCl}_2/\text{MIL-101}(\text{Cr})$ composites with different salt content show reflexes similar to the parent MIL-101 that confirms no structural deformation of MIL-101 during the composite synthesis (Fig. 2). The gradual decrease in the reflexes intensity is observed at larger salt content, which can be attributed to the smaller MIL-101(Cr) content. The diffraction peaks of crystalline CaCl_2 are absent, which may be caused by an ultra-dispersed state of CaCl_2 confined to the small pores of the MIL (29 and 36 Å [23]).

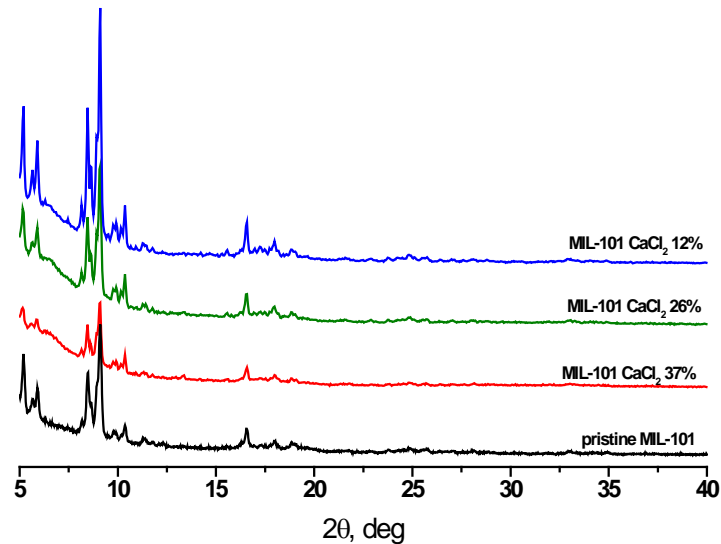


Figure 2. PXRD-patterns of $\text{CaCl}_2/\text{MIL-101}(\text{Cr})$ composites with salt content of 12% (blue), 26% (red) and 37% (black).

The confinement of CaCl_2 in MIL-101 pores results in a significant decrease in both the specific surface area (S_{sp}) and the pore volume (V_{p}) (Table 1). The theoretical pore volume $V_{\text{p,th}}$ was calculated for the composites assuming that the salt is completely deposited inside pores according to the expression:

$$V_{\text{p,th}} = V_{\text{p,MIL}}(1 - C_s) - C_s \rho_s, \quad (1)$$

Where $V_{\text{p,MIL}}$ is the pore volume of the pristine MIL, and ρ_s is the density of CaCl_2 (Table 1). The $V_{\text{p,th}}$ is essentially larger than experimentally measured that can be attributed to the partial blocking of the MIL pores by CaCl_2 particles inside pores.

Table 1. Texture characteristics of $\text{CaCl}_2/\text{MIL-101}$ composites: specific surface area S_{sp} and total pore volume V_{p} of MIL-101(Cr) and $\text{CaCl}_2/\text{MIL-101}$ composite.

Sample	S_{sp} [m^2/g]	V_{p} [cm^3/g]	$V_{\text{p,th}}$ [cm^3/g]
MIL-101(Cr)	2650	2.00	2.00
$\text{CaCl}_2/\text{MIL-101}_{16}$	1805	1.07	1.6
$\text{CaCl}_2/\text{MIL-101}_{29}$	1075	0.84	1.3
$\text{CaCl}_2/\text{MIL-101}_{39}$	555	0.57	1.0

SEM images of the composites (Fig. 3) show that CaCl_2 crystallites are not observed on the surface of MOFs particles. The crystals morphology of the composites with the low salt content 16 and 29% are similar to the pristine MIL-101(Cr) (Fig. 3). The shape of the crystals of the composite with a high CaCl_2 content of 39% is somewhat deformed and smoothed.

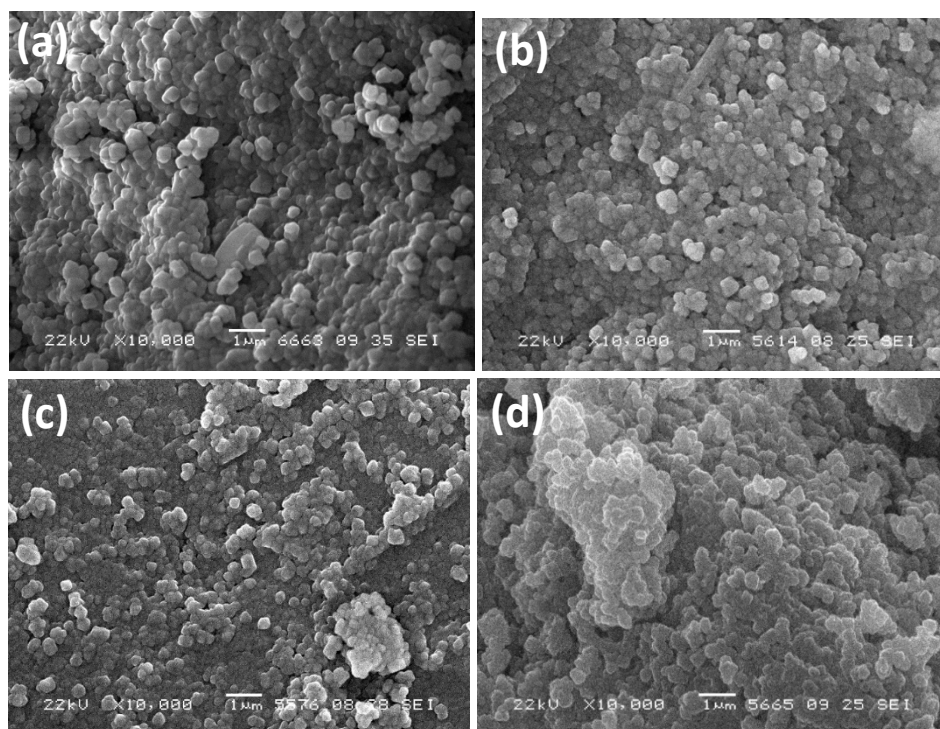


Figure 3. SEM images of the pristine MIL-101(Cr) (a) and $\text{CaCl}_2/\text{MIL-101(Cr)}$ composites with CaCl_2 content of 16% (b), 29% (c) and 39% (d).

Water adsorption on $\text{CaCl}_2/\text{MIL-101(Cr)}$ composite

Water adsorption isobars for $\text{CaCl}_2/\text{MIL-101(Cr)}$ are gradual curves with the uptake continuous decreasing in a temperature range of 25-130°C (Fig. 4 a). No plateau corresponding to the formation of the crystalline hydrates $\text{CaCl}_2 \cdot n\text{H}_2\text{O}$ ($n = 1, 2, 4$) typical of the bulky “ $\text{CaCl}_2 - \text{H}_2\text{O}$ ” system is observed. The system is divariant over the whole uptake range. This agrees well with the data on water vapor sorption on the CaCl_2 inserted into small pores of microporous silica gel KSM [27]. Due to the nano-dispersed state of CaCl_2 it forms XRD-amorphous phase with di-variant adsorption equilibrium with water vapor.

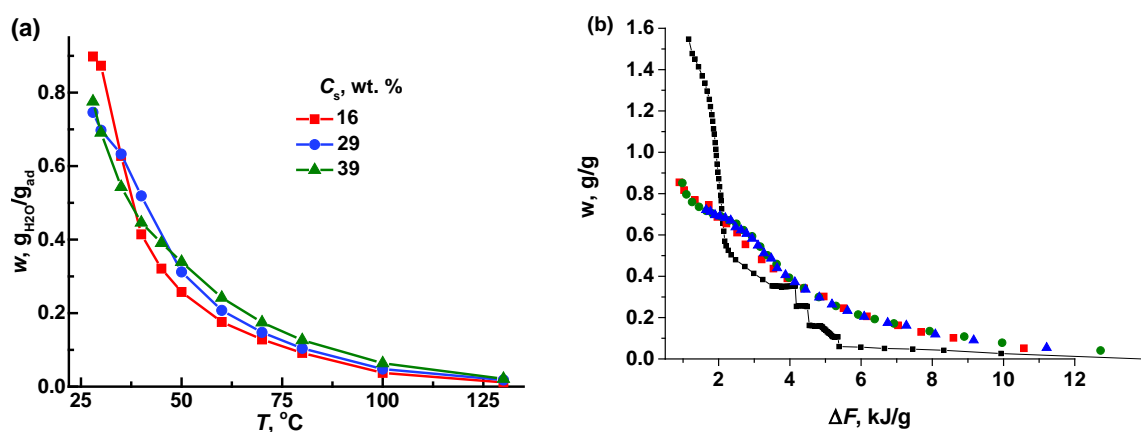


Figure 4. Water adsorption isobars on composites $\text{CaCl}_2/\text{MIL-101(Cr)}$ at $P = 20$ mbar (a). The characteristic curves of water adsorption on the composite $\text{CaCl}_2(29\%)/\text{MIL-101(Cr)}$ at $T = 25.0$ (●) 35 (◆) 45 °C (▲) and theoretical curve, calculated according to eq. 1 (■) (b).

The increase in the salt content results in the uptake growth at $T > 40 \pm 5^\circ\text{C}$, which agrees with the literature data on water adsorption on the composite sorbents [26]. It indicates that the salt impact in the composites adsorption ability at a high temperature is dominant. The opposite behavior is observed at $T < 40 \pm 5^\circ\text{C}$. For the composite with the smallest CaCl_2 content $C_s = 16\%$, the uptake is superior to that for composites with the larger salt content. It is quite surprising because, according to the literature data [26], the uptake rises gradually with increasing salt content, because namely the salt is the main sorbing component of the composite. A probable reason for such behavior could be the following. According to Fig. 1, the water uptake on the pristine MIL-101(Cr) rises sharply due to capillary condensation in the mesopores at $\Delta F \leq 2.3 \text{ kJ/g}$, which corresponds to $T < 39^\circ\text{C}$ at $P = 20 \text{ mbar}$. This temperature is in a good agreement with the abovementioned temperature of $40 \pm 5^\circ\text{C}$. Probably, at a lower temperature, the capillary condensation mainly contributes to the water sorption on the composite. The pore volume of the composites diminishes at increasing salt content (Table 1), consequently, the uptake on the composites with a smaller salt content is higher.

Interestingly that the isobars of water uptake on the composites does not coincide with theoretical adsorption curve calculated as a linear combination of adsorption w_s and $w_{\text{MIL-101}}$ on the bulky CaCl_2 and MIL-101(Cr), respectively, taken with appropriate coefficients equal to their contents in the composite:

$$w_{\text{th}} = w_s \cdot C_s + w_{\text{MIL-101}} \cdot (1 - C_s). \quad (1)$$

At $\Delta F > 2.1 \text{ kJ/g}$, the salt is the main sorbing component, and the experimental uptake exceeds the linear combination. On the contrary, at $\Delta F < 2.1 \text{ kJ/g}$, the composite uptake is essentially smaller than the linear combination. Thus, the synergistic effect of hygroscopic salt and MIL-101(Cr) matrix in the process of water adsorption on the $\text{CaCl}_2/\text{MIL-101(Cr)}$ composites was revealed. At high ΔF -values, water vapor is mainly sorbed by CaCl_2 , and its sorption ability is significantly enhanced due to nano-dispersion inside the MIL pores. At low ΔF , the sorbing ability of aqueous CaCl_2 solution inside the MIL pores decreases, and the capillary condensation in mesopores mainly contributes to the sorption. Therefore, the uptake of the composites is reduced. It is very profitable for AWH because it prevents the aqueous salt solution from leaking out of the MIL pores at decreasing ambient temperature.

For $\text{CaCl}_2(29 \text{ wt. \%})/\text{MIL-101(Cr)}$, the water vapor isotherms are measured at the temperature range $25\text{-}45^\circ\text{C}$. When presented as a function of ΔF , they merge into one characteristic curve (Fig. 4b); thus, the water sorption follows the Polanyi principle of temperature invariance [28]. The isosteres of water vapor adsorption plotted in the $\ln(P) - 1/T$ coordinates (Fig. 5a) allow the isosteric sorption heat ΔQ_{adoc} to be calculated according to the Clausius – Clapeyron equation:

$$\ln P = Q_{\text{is}}/(RT) + \text{Const} . \quad (2)$$

It equals $44 \pm 4 \text{ kJ/mol}$ at the water uptake w from 0.08 to 0.70 g/g that is close to the latent heat of water condensation $L = 43.0\text{-}43.6 \text{ kJ/mol}$ at $T = 25\text{-}45^\circ\text{C}$.

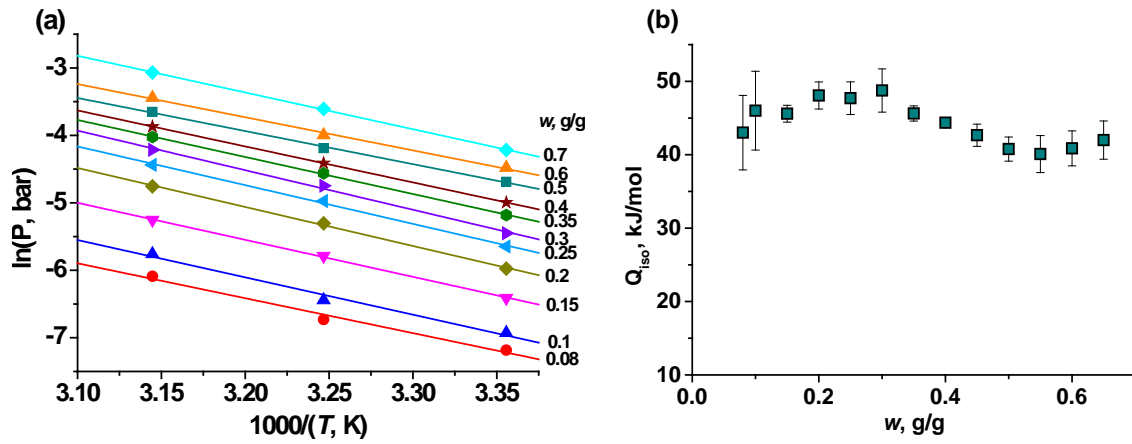


Figure 4. Isotheres (a) and isosteric heat ΔQ_{iso} of water sorption (b) on $CaCl_2(29\%)/MIL-101(Cr)$.

The performance of AWhA employing $CaCl_2/MIL-101(Cr)$ composite

The equilibrium adsorption data for $CaCl_2(29\%)/MIL-101(Cr)$ are used to evaluate the performance of AWH employing this sorbent under climatic conditions of Saudi Arabia (Riyad-Old) and the Sahara Desert as the reference arid regions. The values of adsorption potential ΔF_{ad} and ΔF_{re} , corresponding to the operating conditions during the AWhA regeneration stages were calculated as:

$$\Delta F_{ad} = -RT_n[\ln P_{am}/P_0(T_n)] = -RT_{re}[\ln P_{out.re}/P_0(T_{re})] \quad (3)$$

$$\Delta F_{re} = -RT_{re}[\ln P_{am}/P_0(T_{re})] = -RT_n[\ln P_{out.ad}/P_0(T_n)]. \quad (4)$$

where T_n is the average minimum night temperature, T_{re} is the regeneration temperature, and P_{am} is the water vapor pressure in the ambient air. The climatic data are collected from the Meteororm database (Table 2).

Table 2. Climatic data for Riyadh-Old (Saudi Arabia) and the Sahara desert

Region	T_n , °C	RH_n , %	T_d , °C	RH_d , %	P_{am} , mbar	ΔF_{ad} , kJ/mol	ΔF_{re} , kJ/mol at $T_{re}=80^\circ\text{C}$	Δw , g/g
Dry season (July)								
Saudi Arabia	28.1	26.3	36.7	16.5	10.1	3.2	11.3	0.52
Sahara	22.6	31.3	30.4	21.2	9.3	2.7	11.5	0.59
Humid season (January)								
Saudi Arabia	8.5	74.1	16.3	45.1	8.3	0.8	11.9	0.80
Sahara	5.1	50.6	14.9	27.2	4.5	1.6	13.7	0.73

The maximum specific water productivity per cycle, or the net uptake variation $\Delta w = w(\Delta F_{ad}) - w(\Delta F_{re})$ reaches 0.52 and 0.59 at $T_{re} = 80^\circ\text{C}$ for the Saudi Arabia and Sahara regions during the dry season (July) (Fig. 1). During the humid season (January), it rises to 0.73 g/g due to the increase in the ambient RH. That exceeds the appropriate values for known adsorbents, suggested for AWH (Figure 6). It is worth noting that at $\Delta F_{re} = 11.3$ kJ/mol, the uptake does not exceed $w = 0.06$ g/g (Fig. 1). Thus the adsorbent can be regenerated almost completely at a low temperature of 80°C , easily available when using simple solar collectors.

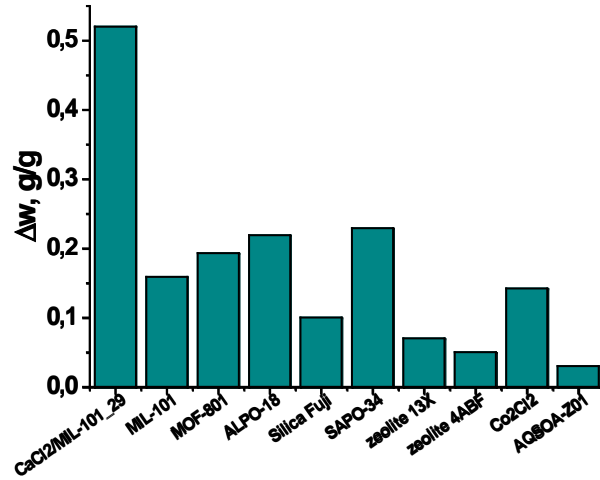


Figure 6. Specific water productivity per cycle Δw for various adsorbents used for the AWHA process in Saudi Arabia at $T_{reg}=80^{\circ}\text{C}$.

Water extraction and collection fractions

Along with the net variation per cycle Δw , the fractions of water extracted from the air during adsorption (δ_{ex}) and collected during condensation (δ_{col}) are also the crucial indexes of the AWH performance. They determine the air volume to be passed through the adsorbent bed to get 1 L of the water, and, consequently, the electricity consumption for the adsorber blowing [15]. They can be calculated as:

$$\delta_{ex} = (P_{am} - P_{out.ad})/P_{am} = 1 - P_{out.ad}/P_{am} \quad (5)$$

$$\delta_{col} = [P_{out.re} - P_0(T_d)]/P_{out.re} = 1 - P_0(T_d)/P_{out.re}, \quad (6)$$

where P_{am} is the partial pressure of water vapor in the ambient air; $P_{out.ad}$ is the water vapor pressure in the outlet air during the adsorption stage; $P_{out.re}$ is the water vapor pressure in the outlet air during the regeneration stage; $P_0(T_d)$ is the saturated vapor pressure at the daytime air temperature T_d . The values of $P_{out.ad}$ and $P_{out.re}$ are evaluated for a fixed bed adsorber based on the following assumption (Fig. 7): The residence time is sufficient for the sorption equilibrium to be reached. Thereby, the vapor pressures $P_{out.re}$ and $P_{out.ad}$ in the outlet air are assumed to be equilibrium with the adsorbent layer nearby the adsorber outlet.

As the water vapor sorption on $\text{CaCl}_2(29\%)/\text{MIL-101}(\text{Cr})$ follows the Polanyi principle of temperature invariance, each isoster (Fig 7 right) corresponds to a definite ΔF -value, $w = f(\Delta F)$. Then the following expressions can be written [15]:

$$\Delta F_{ad} = -RT_n[\ln P_{am}/P_0(T_n)] = -RT_{re}[\ln P_{out.re}/P_0(T_{re})] \quad (7)$$

$$\Delta F_{re} = -RT_{re}[\ln P_{am}/P_0(T_{re})] = -RT_n[\ln P_{out.ad}/P_0(T_n)] \quad (8)$$

and the fractions δ_{ex} and collected δ_{col} can be evaluated from eqs. (5)-(8).

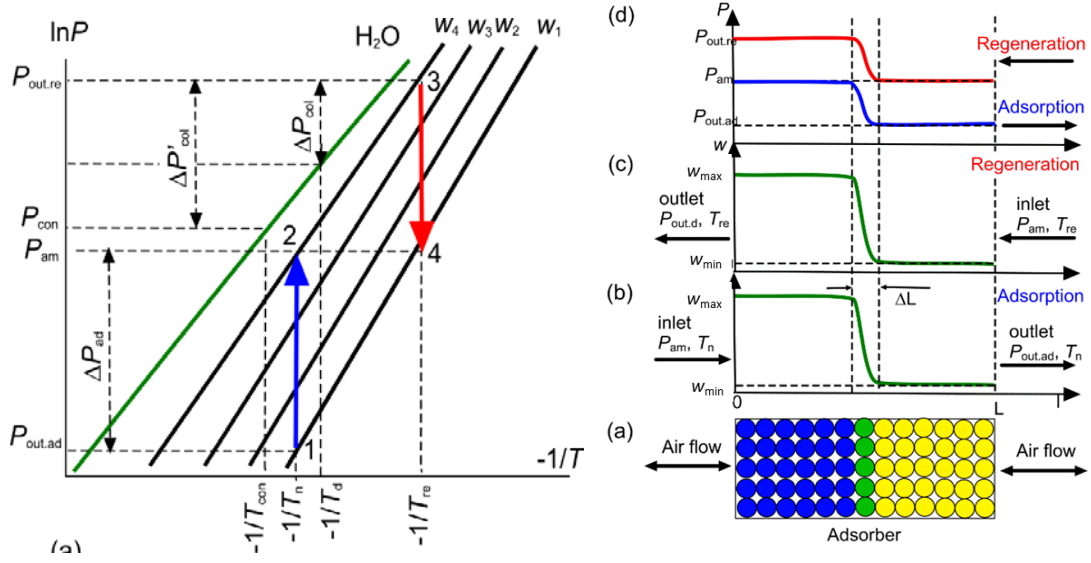


Figure 7. Scheme of a fixed-bed flowing adsorber and distribution of water uptake (b, c) and vapour partial pressure (d) along the adsorber (left). Adsorption isosters $w_1 - w_4$ and water-vapor equilibrium line in the Clausius-Clapeyron diagram. Arrows denote changes in the water uptake during the adsorption and desorption stages of the AWEA process (right).

The high fraction $\delta_{ex} = 0.95$ can be reached in the dry season using $\text{CaCl}_2(29\%)/\text{MIL-101}(\text{Cr})$ under climatic conditions of Saudi Arabia (Table 3). It rises to $\delta_{ex} = 0.98$ during the humid (wet) season due to the increased ambient air humidity (Table 3). The collected water fraction δ_{col} for the condenser cooled by the ambient air at the daytime temperature T_d , at $T_{re} = 80-100^\circ\text{C}$, grows from 0.61 to 0.83 and to 0.94-0.97 during the dry and humid seasons. This is due to the fact that the temperature T_d , at which condensation occurs, is lower in winter than in summer. It should be noted that this fraction can be enhanced significantly by a realization of the so-called semi-open cycle when the outlet air is returned in the adsorber again to promote more effective desorption/condensation [29].

Table 3. Fractions δ_{ex} and δ_{col} for the $\text{CaCl}_2(29\%)/\text{MIL-101}(\text{Cr})$ composite under climatic conditions of Saudi Arabia region

δ_{ex}	δ_{col}		
Humid season (January)			
	$T_{re}, ^\circ\text{C}$		
0.98	80	90	100
	0.94	0.96	0.97
Dry season (July)			
0.95	0.61	0.75	0.83

Specific thermal energy consumption

An important characteristic of AWH system is the specific energy consumption Q_{sp} for water production, which is calculated as

$$Q_{sp,pr} = \Delta w \cdot \Delta H_{ads} + (C_{pad} + w_{ads} \cdot C_{pH_2O}) \cdot (T_{re} - T_d) / (\Delta w \cdot \delta_{col}), \quad (9)$$

where C_{pad} is the adsorbent specific heat; C_{pH_2O} is the water specific heat ($4.21 \text{ J}/(\text{g} \cdot \text{K})$); Q_{is} is the isosteric adsorption heat ($44 \text{ kJ}/\text{mol}$ as the average value in the range $w = 0.1 - 0.7 \text{ g}/\text{g}$); Δw is the specific mass of water exchanged in the AWEA cycle; w_{ads} is the water uptake at ΔF_{ad} .

The adsorbent specific heat is calculated as a linear combination of the specific heat $C_p(\text{MIL})$ of MIL-101(Cr) and C_{ps} of CaCl_2 , $C_p(\text{comp}) = C_p(\text{MIL})(1 - C_s) + C_{ps}C_s = 0.70 \text{ J}/(\text{g}\cdot\text{K})$. The specific energy consumption Q_{sp} ranges from 3.4 to 4.4 kJ/ g_{H2O} at $T_{re} = 80\text{-}100^\circ\text{C}$ during the dry season. During the humid season, Q_{sp} falls to 2.9-3.0 kJ/g_{H2O} owing to the significant increase in the net uptake variation Δw (Table 2) and the fraction δ_{col} (Table 3). Since the values obtained are higher than the heat of water vaporization, the AWhA energy consumption is higher than the energy consumption for water desalination. However, in arid regions, renewable solar energy for adsorbent regeneration is available in abundance. Therefore, the obtained values of specific energy consumption for water production are quite acceptable. Accordingly, the AWhA method is promising for arid regions remote from sources of salt water.

Summary/Conclusions

In this research, the novel composite sorbents based on inorganic hygroscopic salts inside pores of MIL-101(Cr) are developed to increase the MIL water vapor capacity in climatic conditions of arid areas. The composition, structure, morphology, and water adsorption properties of the $\text{CaCl}_2/\text{MIL-101(Cr)}$ composites are studied. It is shown that the salt presence does not lead to structural changes in MIL-101. The salt crystals on the MIL-101(Cr) surface are not found. They are located inside the pores, which leads to a decrease in the specific surface area and pore volume. The synergistic effect of the confined salt and the matrix that is the water adsorption enhancement is found. The most promising composite is $\text{CaCl}_2/\text{MIL-101}$, with the salt content 29%. It demonstrates the high specific water productivity 0.52-0.73 g_{H2O}/g per cycle under conditions of the arid climates typical for Saudi Arabia, which exceeds the appropriate values for known adsorbents. The use of $\text{CaCl}_2/\text{MIL-101(Cr)}_{29}$ composite for AWhA allows getting the fractions of water extracted $\delta_{ex} = 0.95\text{-}0.98$ and collected $\delta_{col} = 0.39\text{-}0.97$ at the regeneration temperature 70-100°C and the condenser cooled by ambient air. The average isosteric water adsorption enthalpy ΔH_{ads} calculated from isosteres is $44 \pm 4 \text{ kJ/mol}$. The AWhA technology is promising for arid regions remote from sources of saltwater due to the availability of renewable thermal energy sources for adsorbent regeneration. The high potential of the developed composites for AWhA encourages us for further detailed study of their water adsorption properties and the feasibility of AWhA employing these MOFs.

Acknowledgements

This work was partially supported by Russian Foundation for Basic Research (project no. 18-29-04033) and by the Ministry of Science and Higher Education of the Russian Federation within the governmental order for Boreskov Institute of Catalysis (project AAAA-A21-121011390006-0).

References:

-
- [1] United Nations (2015) Resolution adopted by the General Assembly on 25 September 2015, Transforming our world: the 2030 Agenda for Sustainable Development.
 - [2] "Goal 6 Targets". United Nations Development Programme. Archived from the original on 19 February 2018. Retrieved 16 November 2017.
 - [3] Progress on household drinking water, sanitation and hygiene 2000-2017: Special focus on inequalities (PDF). United Nations Children's Fund (UNICEF) and World Health Organization (Report). New York. June 2019. p. 138. ISBN 978-92-415-1623-5.
 - [4] Elimelech, M., Phillip, W. A. "The future of seawater desalination: energy, technology, and the environment", Science, 2011, 333, 712-717.

-
- [5] Vörösmarty, C. J., Green, P., Salisbury, J., Lammers, R. B. “Global Water Resources: Vulnerability from Climate Change and Population Growth”, *Science*, 2000, 289, 284 – 288.
- [6] Jiao, M., Yao, Y., Chen, C., Jiang, B., Pastel, G., Lin, Z., Wu, Q., Cui, M., He, S., Hu, L. “Highly Efficient Water Treatment Via a Wood-Based and Reusable Filter”, *ACS Mater. Lett.* 2020, 2, 430– 437,
- [7] Fritzmann, C., Löwenberg, J., Wintgens, T., Melin, T. “State-of-the-Art of Reverse Osmosis Desalination” *Desalination*, 2007, 216, 1– 76.
- [8] Alsehli, M., Choi, J.-K., Aljuhan, M. A “Novel Design for a Solar Powered Multistage Flash Desalination”, *Sol. Energy*, 2017, 153, 348– 359,
- [9] Zhao, F., Guo, Y., Zhou, X., Shi, W., Yu, G. “Materials for Solar-Powered Water Evaporation”, *Nat. Rev. Mater.* 2020, 5, 388– 401.
- [10] Hamed, A.M., Aly, A.A., Zeidan, E.B. “Application of solar energy for recovery of water from atmospheric air in climatic zones of Saudi Arabia” *Nat. Resour.* 2011, 2, 8–17.
- [11] Tu, Y., Wang, R., Zhang, Y., Wang, J. “Progress and Expectation of Atmospheric Water Harvesting” *Joule*, 2018, 2, 1452– 1475
- [12] Pinto, F.S., Marques, R.C. “Desalination projects economic feasibility: a standardization of cost determinants” *Renew. Sustain. Energy Rev.* (2017), 78, 904–915.
- [13] Oki, T., Kanae, S. “Global Hydrological Cycles and World Water Resources”, *Science*, 2006, 313, 1068– 1072,
- [14] Bar, E., “Extraction of water from air – an alternative solution for water supply”, *Desalination*, 2004, 165, 335-338.
- [15] Gordeeva, L.G., Solovyeva, M.V., Sapienza, A., Aristov, Yu.I. “Potable water extraction from the atmosphere: Potential of MOFs”, *Renewable Energy*, 2020, 148, 72-80.
- [16] Seo, Y.-K., Yoon, J. W., Lee, J. S., Hwang, Y. K., Jun, C.-H, Chang, J.-S., Wuttkee, S., Bazin, P., Vimont, M., Daturi, M., Burrelly, S., Liewellyn, P. L., Horcajada, P., Serre, C., Ferrey, G. “Energy-efficient dehumidification over hierarchically porous metal-organic frameworks as advanced water adsorbents”, *Adv. Matter.*, 2012, 24, 806-810.
- [17] Kalmutzki, M. J., Diercks, C. S., Yaghi, O. M. “Metal-Organic Frameworks for Water Harvesting from Air”, *Adv. Mater.* 2018, 30, 1704304.
- [18] Trapani, F., Polyzoidis, A., Loebbecke, S., Piscopo, C.G. “On the general water harvesting capability of metal-organic frameworks under well-defined climatic conditions”, *Microporous Mesoporous Mater.*, 2016, 230, 20-24.
- [19] Furukawa, H., Gandara, F., Zhang, Y.-B., Jiang, J., Queen, W.L., Hudson, M.R., Yaghi, O.M., “Water adsorption in porous Metal-Organic frameworks and related materials”, *J. Am. Chem. Soc.*, 2014, 136, 4369e4381.
- [20] Rieth, A.J., Yang, S., Wang, E.N., Dinca, M., “Record Atmospheric Fresh Water Capture and Heat Transfer with a Material Operating at the Water Uptake Reversibility Limit”, *ACS Cent. Sci.*, 2017, 3, 668–672.
- [21] Kim, H., Yang, S., Rao, S.R., Narayanan, S., Kapustin, E.A., Furukawa, H., Umans, A.S., Yaghi, O.M., Wang, E.N. “Water harvesting from air with metalorganic frameworks powered by natural sunlight”, *Sci. Rep.*, 2017, 356, 430-434.
- [22] Xu, W., Yaghi, O.M. “Metal-organic frameworks for water harvesting from air anywhere, anytime”, *ACS Central Science*, 6 (2020) 1348-1354.
- [23] Akiyama, G., Matsuda, R., Sato, H., Hori, A., Takata, M., Kitagawa, S. “Effect of functional groups in MIL-101 on water sorption behavior”, *Micropor. Mesopor. Mater.*, 2012, 157, 89-93.
- 24 Aristov, Yu.I., Tokarev, M.M., Gordeeva, L.G., Snytnikov, V.N., Parmon, V.N. “New composite sorbents for solar-driven technology of fresh water production from the atmosphere”, *Solar Energy*, 1999, 66, 165-168.

-
- [25] Ji, G., Wang, R.Z., Li, L. X. “New composite adsorbent for solar-driven fresh water production from the atmosphere”, *Desalination*, 2007, 212, 176–18.
- [26] L. G. Gordeeva, Yu. I. Aristov, Composites “salt inside porous matrix” for adsorption heat transformation: a current state of the art and new trends, *Int. J. Low Carbon Technol.* 7 (2012) 288-302.
- [27] Aristov, Yu.I., Tokarev, M.M., Cacciola, G., Restuccia, G. “Selective water sorbents for multiple applications: 2. CaCl₂ confined in micropores of the silica gel: sorption properties”, *React. Kinet. Cat. Lett.*, 1996, 59, n 2, 335-342.
- [28] Polanyi, M. “Theories of the adsorption of gas”, *Trans. Faraday Soc.*, 1932, 28, 16.
- [29] Wang, J. Y., Wang, R. Z., Wang, L. W., Liu, J. Y. “A high efficient semi-open system for fresh water production from atmosphere”, *Energy*, 2017, 138, 542-551.

Assessment of an adsorption based solar heating system for domestic heating applications in Ladakh

Sai Yagnamurthy

School of Engineering, University of Warwick

sai.yagnamurthy@warwick.ac.uk

Abstract

In an attempt to contribute to the sustainable heating solutions for the cold arid region of Ladakh, a solar powered adsorption heating system is numerically studied for performance assessment. An adsorbent integrated tubular collector design is considered, which can be integrated into the roof tops of domestic spaces for capturing and radiating solar thermal energy into the room without the requirement of any auxiliary electric power. Maxsorb-III activated carbon is selected as the adsorbent with methanol as the adsorbate. The key design features of the collector design for maximising the heat flux into the room are presented. An optimum outer radius of 1.5 cm is evaluated for the maximum annual heat transfer into the room, with the daily average flux reaching up to 44.1 W/m^2 . The novel design presented in this study could pave way for further optimisation in design parameters and operating procedures for maximising sustainable heating.

Keywords: adsorption, solar thermal, space heating, Ladakh, thermal storage

Introduction

Adsorption working pairs have gained prominence for cooling and heat pumping applications, due to their ability to capture low grade thermal energy and having lesser maintenance issues. Apart from cooling, adsorption based working pairs are seen to offer among the highest energy densities in thermal storage applications [1]. Yan et al. [1] experimentally studied a resorption based heat storage system with the sorption working pair of $\text{MnCl}_2\text{-SrCl}_2/\text{NH}_3$ and observed an energy storage density of up to 261.35 kWh/m^3 with a charging temperature requirement of 177°C . N'Tsoukpoe et al. [2] studied 45 salt hydrates for low temperature thermochemical heat storage application through TGA/DSC analysis. They have identified $\text{Sr.Br}_2.6\text{H}_2\text{O}$ to be the most promising pair with an energy density of 133 kWh/m^3 and a desorption temperature requirement of 105°C . For solar based domestic heating applications, further lower desorption temperatures ($<90^\circ\text{C}$) are desired for the various non-concentrating solar heating collectors widely employed for these applications [3]. Kohler and Muller [4] studied various alcohol-activated carbon pairs for a low grade solar thermal energy based heating application and identified activated carbon-methanol pair to be offering the best efficiency of 40% with the desorption temperature of 350 K.

Activated carbon-methanol has been amongst the most preferred working pairs for adsorption cooling application owing to the low regeneration temperature requirements. Various researchers have developed single bed solar powered ice making systems employing activated carbon-methanol pair and have realized cooling without the necessity of any auxiliary power requirement. Pons and Guilleminot [5] developed one of the earliest designs of a flat plate solar ice maker using carbon-methanol pair, yielding a solar COP of 0.12 for a typical day in August in the location of Paris. Similar solar COP values (0.12-0.14) have been observed by other researchers with the carbon-methanol pair in the literature [6,7], with ice production of 4-5kg

per m² of the collector area. In the recent years, tubular collector designs [8–10] have gained prominence over that of the flat plate designs for ice making applications, owing to the better vacuum sealing provided by the former design. The effectiveness of the tubular collector design is yet to be explored for heating applications.

In the present study, solar powered room heating employing activated carbon-methanol pair is envisaged for the cold arid region of Ladakh in India. The region receives the highest solar radiation of about 7-7.5 kWh/m²/day, while also being among the coldest regions in the country with the peak winter temperatures reaching up to -28°C [11]. A tubular collector design is envisaged for the application, which can be fitted into the roof for capturing and radiating solar thermal energy into the room. Optimisation of the tubular diameter is further carried out through numerical simulations for maximizing the heating potential of the collector unit.

System description

Working pair: Maxsorb-III activated carbon has been chosen as the adsorbent with methanol as the adsorbate. The key thermophysical adsorption properties of the pair are shown in Table 1 [12]. The adsorption properties of the pair are evaluated using D-R equation described in Sharkawy et al. [13].

Table 1. Maxsorb-III thermophysical properties [12]

Bulk density (ρ_{ads})	310 kg/m ³
Skeletal volume (V_{sk})	4.5×10 ⁻⁴ m ³ /kg
Micropore volume ($V_{micropore}$)	1.71×10 ⁻³ m ³ /kg
Particle radius (r_p)	70µm

Collector design: A stainless steel tubular collector design is considered with the adsorbent material placed inside the tubes and the inner annulus of the adsorbent material being used for refrigerant transport, as described by Qasem et al. [10]. The tube length is oriented along the collector tilt, which is considered to be at 34.15° corresponding to the latitude of Ladakh. The tubes are covered by a single glazing glass cover on the top and insulated on the sides, whose properties are given in Table 2. The bottom surface of the collector is exposed to the room to radiate heat into it.

The condenser/evaporator design is ignored in the present evaluation and the corresponding saturation pressure of condensation and evaporation are evaluated from the ambient temperature during desorption and adsorption processes respectively.

Further, it is of utmost importance to minimise the heat dissipation to the ambient from the collector. For this purpose, the glass cover is considered to be covered by an opaque cover from 12 PM to 6AM of the subsequent day.

Room: The room is considered to be maintained at 15°C with apertures in the roof for the tubular collector to radiate heat from its back side. No air infiltration is considered through the aperture opening.

Table 2. Collector parameters

Glass transmissivity (τ)	0.9
Tube absorptivity (α)	0.9
Side insulation heat transfer coefficient (U_s)	0.15 W/ K
Opaque cover heat transfer coefficient	0.38 W/ K
Collector tilt (β)	34.15°
Tube inner radius (R_i)	0.005 m

Weather data: The solar radiation, ambient temperature and wind speed of the location are obtained from the National Solar Radiation Database (NSRDB) [14].

Mathematical modeling

A distributed parameter model has been used for modelling the mass and energy balance in the tubular collector using Matlab™ software. The continuity, momentum, and energy conservation equations are considered after eliminating the non-significant terms based on a scaling analysis described by Mitra et al. [15].

Equation (1) shows the continuity equation after neglecting the non-significant density variation term.

$$\frac{\partial(\rho_{\text{vapor}}vr)}{r \partial r} + \rho_{\text{ads}} \frac{\partial w}{\partial t} = 0 \quad (1)$$

Where ρ_{vapor} is the density of refrigerant vapor, v is the velocity of the diffusing vapor, ρ_{ads} is the density of adsorbent and w is the concentration of the adsorbent.

The momentum equation across the bed is given by the Darcy equation as shown in equations (2), (3) and (4).

$$\frac{\partial P}{\partial r} = -\frac{\mu}{\lambda} V \quad (2)$$

$$\text{where } \lambda = \frac{\varepsilon^3 r_p^2}{37.5(1-\varepsilon)^2} \quad (3)$$

$$\text{and } \varepsilon = 1 - \rho_{\text{ads}}(V_{\text{sk}} + V_{\text{micropore}}) \quad (4)$$

where P is the pressure of refrigerant vapor, μ is the viscosity of refrigerant vapor, λ is the permeability of the bed, ε is the permeability of the bed and r_p is the particle radius of the adsorbent.

The energy balance across the bed is given by equation (5) after eliminating the non-significant convective term. The heat of adsorption (Q_{st}) is obtained from the Clausius-clapeyron equation as described in [16].

$$\frac{1}{r} K \frac{\partial(r \frac{\partial T}{\partial r})}{\partial r} + \rho_{\text{ads}} Q_{\text{st}} \frac{\partial w}{\partial t} = (\rho C_p)_{\text{ads}} \left(1 + w \frac{(C_p)_l}{(C_p)_{\text{ads}}} \right) \frac{\partial T}{\partial t} \quad (5)$$

Where K is the thermal conductivity of the bed, T is the temperature of the bed, $(C_p)_l$ is the specific heat capacity of the refrigerant liquid. The adsorption kinetics of the bed ($\frac{\partial w}{\partial t}$) are computed from the correlation given by Passos et al. [17].

The energy balance for the collector steel tube is given by equation (6) which takes into account the incident solar radiation and various heat losses from the tube.

$$(mC_p)_{\text{steel}} \frac{dT_{\text{steel}}}{dt} = I(\tau\alpha) - 0.5(U_t + U_b + U_s)A_{\text{actual}}(T_{\text{steel}} - T_{\text{ambient}}) - KA_{\text{internal}} \frac{\partial T}{\partial r} \Big|_{R_o} \quad (6)$$

$$A_{\text{actual}} = N_{\text{tubes}} \times 2\pi R_o \quad (7)$$

$$A_{\text{internal}} = 2\pi R_i \quad (8)$$

$$U_b = k_{\text{air}} \times 0.27Ra^{0.25} \quad (9)$$

$$Q = U_b(T_{\text{steel}} - T_{\text{room air}}) \quad (10)$$

Where A_{actual} is the surface area of the tubes per unit area of aperture area and A_{internal} is the internal surface area of the tube. The heat loss coefficient for the top surface (U_t) is computed from the correlation given in [18] for the local weather conditions, for 6AM to 12PM. For the rest of the hours, U_t is substituted with the opaque heat transfer coefficient value of 0.38 W/K. The back heat loss coefficient U_b is computed from the correlation for natural heat transfer coefficient for downward facing surfaces given in [19].

Discussion and Results

The heat radiated per unit area of the collector into the room is evaluated for various outer radii of the tubes. It has been estimated that the optimum outer radius yielding the highest daily average heat transfer rate over the year is 0.015m. Figure 1 shows the variation of the average daily heat transfer rate per unit area of the collector for a typical day in the month of January. For lower outer radii than 0.015m, the mass of the adsorbent reduces per unit area of the collector which further reduces the heat storage capacity of the collector. At higher outer radii, the maximum temperature attained by the tubular collector reduces due to the increasing adsorbent mass, which reduces the heat transfer rate to the room. Further, the temperature and pressure gradients of the adsorbent within the tube increase with increasing outer radius as shown in Figure 2 and Figure 3 respectively. Figure 2 shows that the maximum temperature at 12 noon occurs at the outermost radius of the bed due to the heating of the steel outer surface with incident radiation. Figure 3 shows that the maximum pressure also occurs at the outermost radius due to the desorption phenomenon, with the refrigerant vapor radially diffusing inwards into the annular space of the tube.

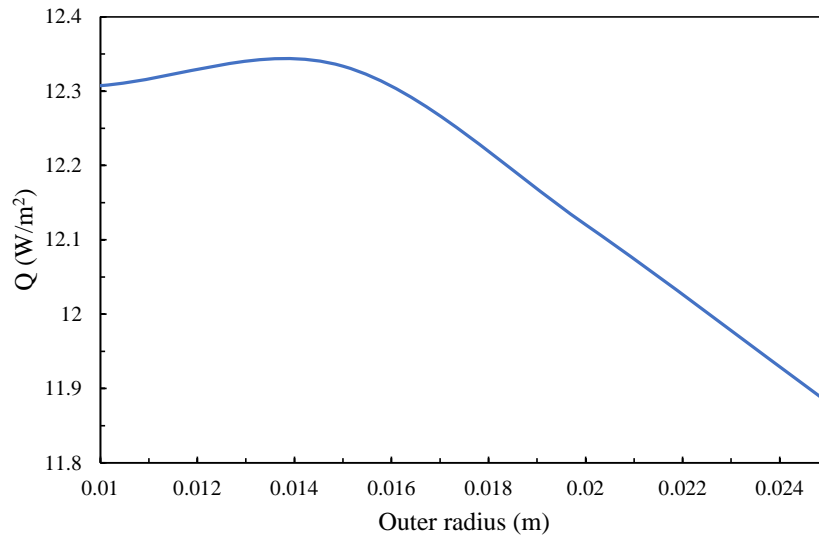


Figure 1. Heat transfer flux variation with outer radius for a typical day in January

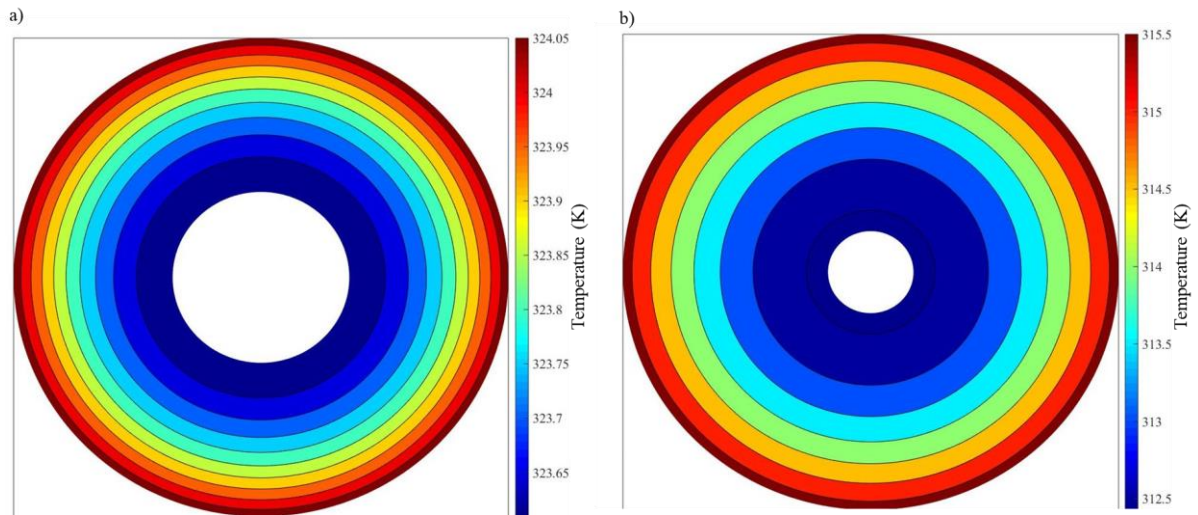


Figure 2. Temperature distribution within adsorbent for a) Outer radius of 1.5 cm and b) Outer radius of 3 cm at 12PM for a typical day in January

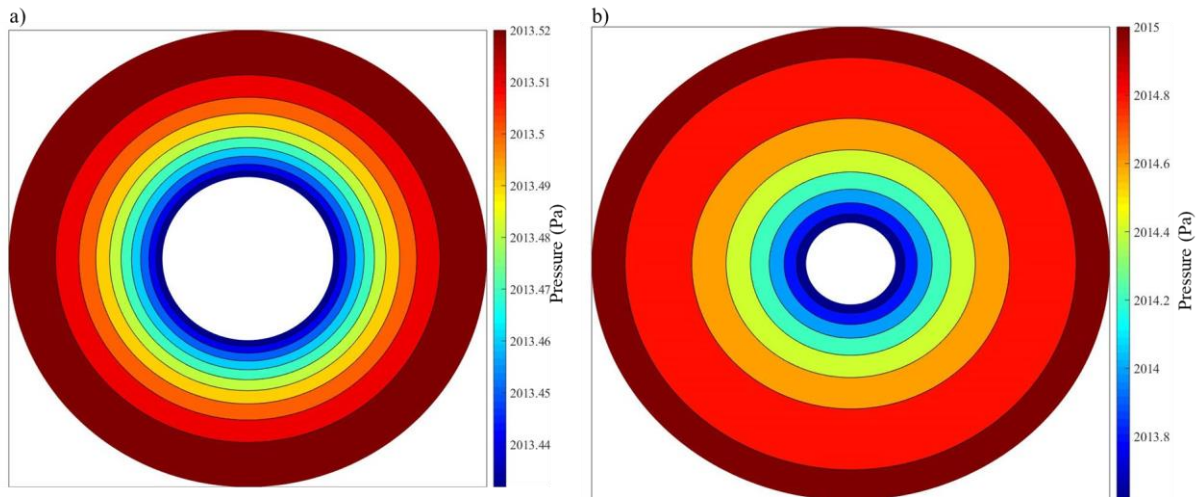


Figure 3. Pressure distribution within adsorbent for a) Outer radius of 1.5 cm and b) Outer radius of 3 cm at 12PM for a typical day in January

Figure 4 shows the heat flux from the collector for a typical day in January. It can be seen that the heat flux value increases until 12PM and follows a decreasing trend for the subsequent hours of the day. This can be understood from the increasing solar radiation flux incident on the collector until 12PM followed by which it is covered by the opaque cover. The temperature of the bed and the steel tube rise accordingly resulting in an increase of heat flux to the room. This is followed by the covering of the glass plate with an opaque surface, resulting in the decrease of tube and bed temperature.

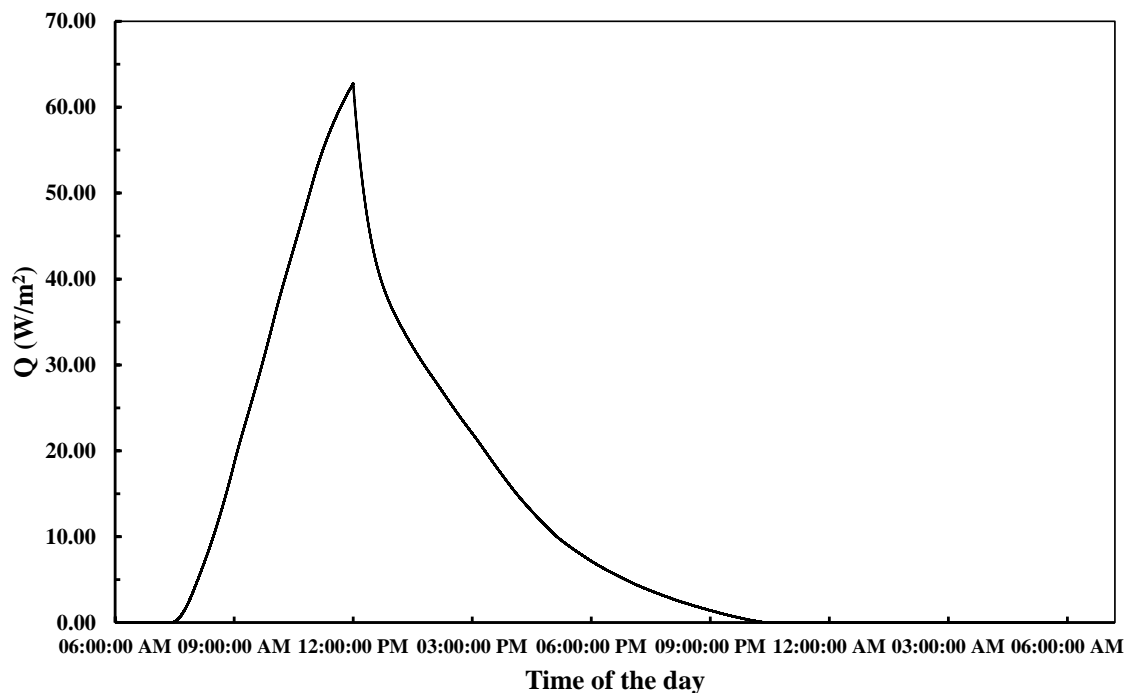


Figure 4. Heat flux variation over a typical day in the month of January

Figure 5 shows the average concentration profile variation of the bed. It can be seen that the concentration of the bed starts reducing from 8AM with the increase of solar flux incident on the collector and the rise in temperature of the bed. The concentration of the bed is seen to drop until 12PM due to the desorption phenomenon. After 12PM, the bed's temperature reduces due

to heat dissipation to the room resulting in the adsorption phenomenon commencing until 11 PM, where the bed reaches the saturation limit. The valve to the evaporator is shutoff to prevent any further desorption until the opaque cover is removed off the glass sheet the subsequent day. Figure 6 shows the corresponding bed temperature variation. It can be seen that the rate of bed temperature decrease is lower than that of its increase, owing to the low heat transfer coefficient of the room air and slower adsorption kinetics in comparison to that of the desorption phenomenon.

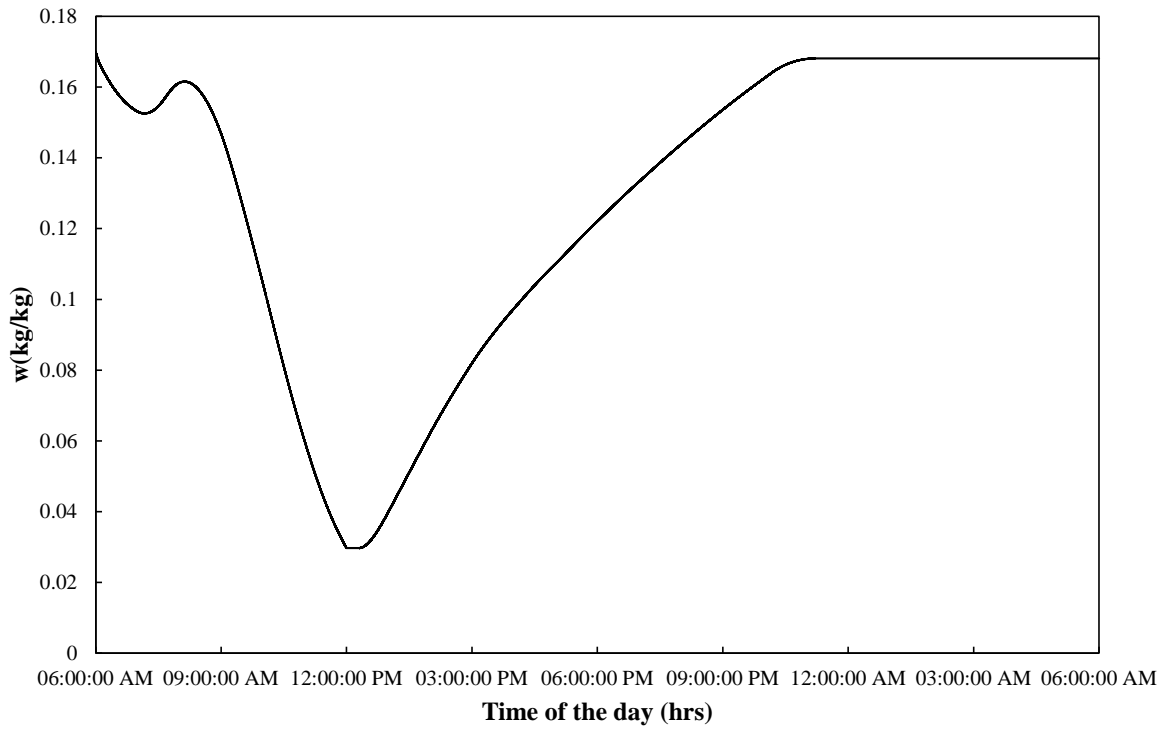


Figure 5. Bed concentration variation over a typical day in the month of January

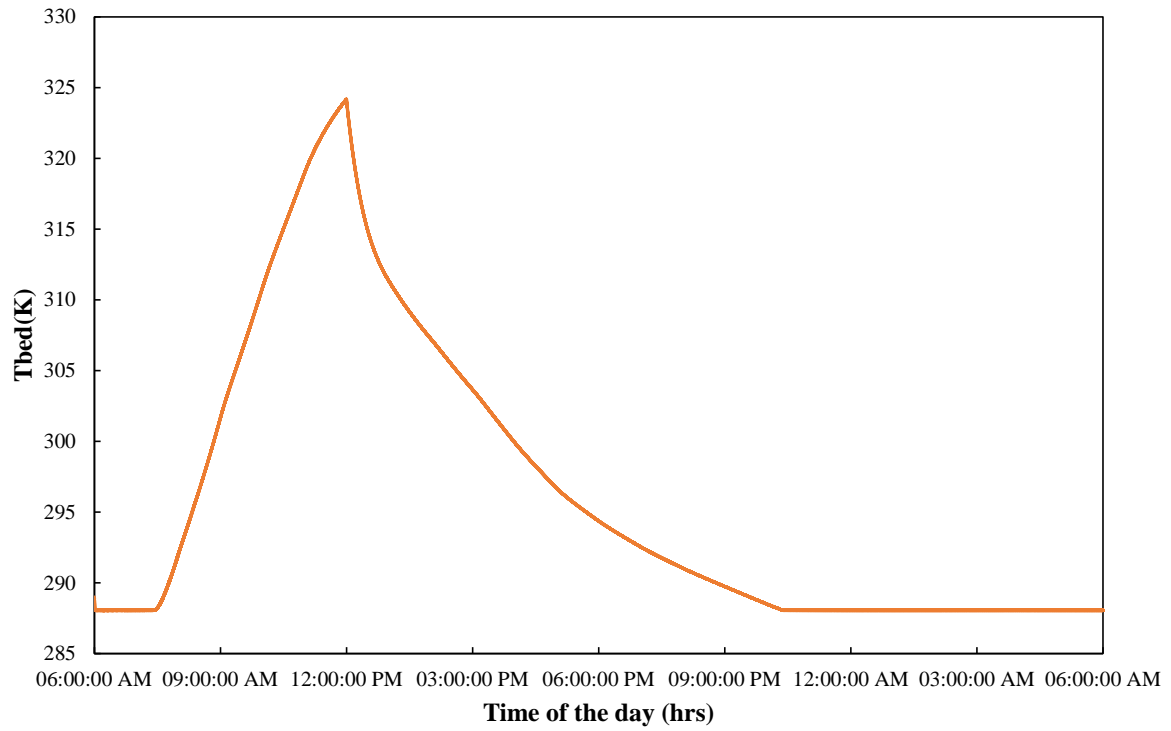


Figure 6. Bed temperature variation over a typical day in the month of January

The annual variation of the daily average heat flux is shown in Figure 7. It can be seen that the trend of the daily average flux is very much inline with that of the daily solar insolation, with the highest value of 44.1 W/m^2 in July.

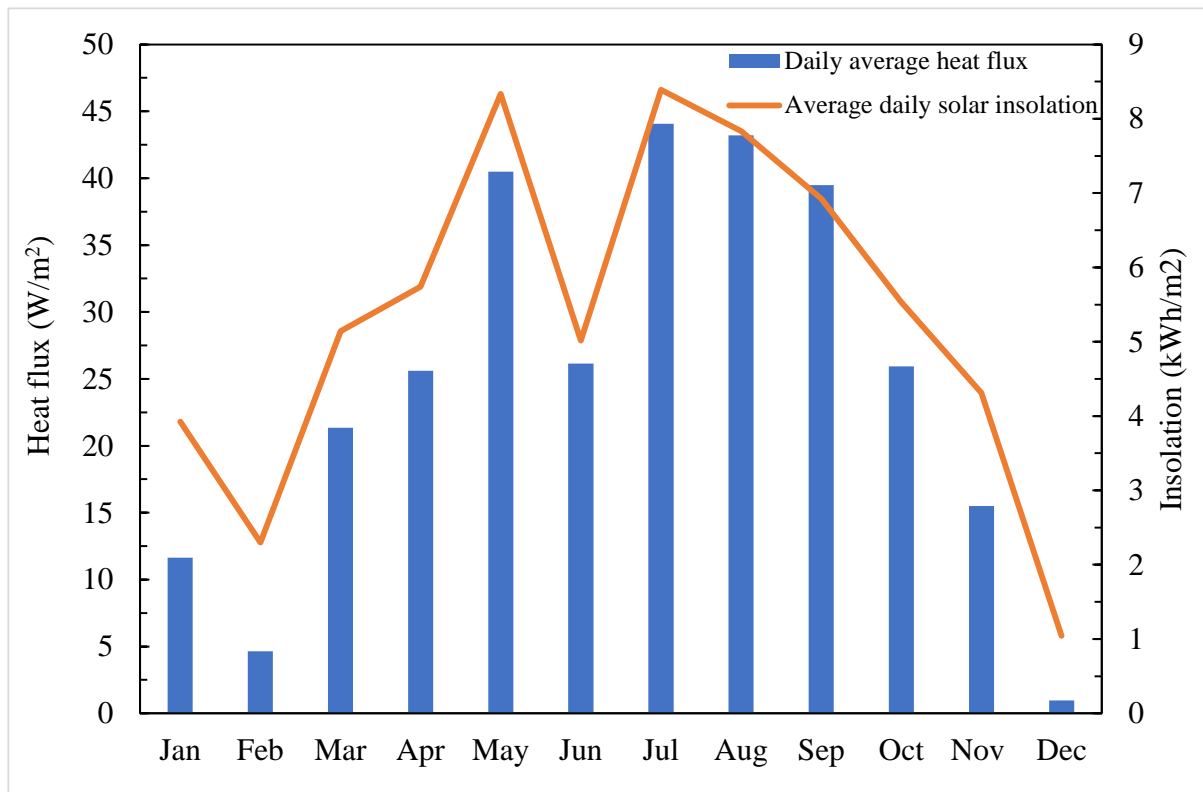


Figure 7. Annual variation of daily average heat flux and solar insolation values

Summary

The present study evaluates the performance of a tubular collector integrated adsorption system for a solar powered domestic heating application in the cold arid region of Ladakh. The prominent features of the tubular collector design *viz.*, removal of back covering for room air heating and un-exposing of the glass cover after 12 PM, have been considered for performance evaluation. The optimum outer radius yielding the maximum annual heating flux into the room has been identified through a distributed parameter modelling of the system under the local weather conditions. The optimised collector design is observed to be capable of radiating heat into the room at 15°C for over 11 hours in the coldest month of January with the ambient temperatures reaching up to -28°C. The study could be further extended to study the impact of thermal comfort due to enhanced mean radiant temperature of the room as well as a techno-economic analysis for a better optimisation of various design parameters.

References

- [1] T. Yan, H. Zhang, N. Yu, D. Li, Q.W. Pan, Performance of thermochemical adsorption heat storage system based on MnCl₂-NH₃ working pair, *Energy*. 239 (2022) 122327. <https://doi.org/10.1016/J.ENERGY.2021.122327>.
- [2] K.E. N'Tsoukpoe, T. Schmidt, H.U. Rammelberg, B.A. Watts, W.K.L. Ruck, A systematic multi-step screening of numerous salt hydrates for low temperature thermochemical energy storage, *Appl. Energy*. 124 (2014) 1–16. <https://doi.org/10.1016/J.APENERGY.2014.02.053>.
- [3] B. Weyres-Borchert, B.-R. Kasper, B.I. FIZ Karlsruhe, *Solare Wärme Technik - Planung*

- Hausanlage., (2015).
- [4] T. Kohler, K. Müller, Storage of low grade solar thermal energy by adsorption of organics, *AIP Conf. Proc.* 1850 (2017) 080014. <https://doi.org/10.1063/1.4984435>.
- [5] M. Pons, J.J. Guillemot, Design of an Experimental Solar-Powered, Solid-Adsorption Ice Maker, *J. Sol. Energy Eng.* 108 (1986) 332. <https://doi.org/10.1115/1.3268115>.
- [6] M. Li, R.. Wang, Y.. Xu, J.. Wu, A.. Dieng, Experimental study on dynamic performance analysis of a flat-plate solar solid-adsorption refrigeration for ice maker, *Renew. Energy.* 27 (2002) 211–221. [https://doi.org/10.1016/S0960-1481\(01\)00188-4](https://doi.org/10.1016/S0960-1481(01)00188-4).
- [7] M. Li, H.B. Huang, R.Z. Wang, L.L. Wang, W.D. Cai, W.M. Yang, Experimental study on adsorbent of activated carbon with refrigerant of methanol and ethanol for solar ice maker, *Renew. Energy.* 29 (2004) 2235–2244. <https://doi.org/10.1016/j.renene.2004.04.006>.
- [8] A.P.F. Leite, M.B. Grilo, R.R.D. Andrade, F.A. Belo, F. Meunier, Experimental thermodynamic cycles and performance analysis of a solar-powered adsorptive icemaker in hot humid climate, *Renew. Energy.* 32 (2007) 697–712. <https://doi.org/10.1016/j.renene.2006.03.002>.
- [9] W. Chekirou, A. Chikouche, N. Boukheit, A. Karaali, S. Phalippou, Dynamic modelling and simulation of the tubular adsorber of a solid adsorption machine powered by solar energy, *Int. J. Refrig.* 39 (2014) 137–151. <https://doi.org/10.1016/j.ijrefrig.2013.11.019>.
- [10] N.A.A. Qasem, M.A.I. El-Shaarawi, Thermal analysis and modeling study of an activated carbon solar adsorption icemaker: Dhahran case study, *Energy Convers. Manag.* 100 (2015) 310–323. <https://doi.org/10.1016/j.enconman.2015.04.054>.
- [11] P. Santra, Scope of Solar Energy in Cold Arid Region of India at Leh Ladakh, *Ann. Arid Zone.* 54 (2016). <http://epubs.icar.org.in/ejournal/index.php/AAZ/article/view/63046> (accessed December 19, 2021).
- [12] B.B. Saha, A. Chakraborty, S. Koyama, S.H. Yoon, I. Mochida, M. Kumja, C. Yap, K.C. Ng, Isotherms and thermodynamics for the adsorption of n-butane on pitch based activated carbon, *Int. J. Heat Mass Transf.* 51 (2008) 1582–1589. <https://doi.org/10.1016/J.IJHEATMASSTRANSFER.2007.07.031>.
- [13] I.I. El-Sharkawy, M. Hassan, B.B. Saha, S. Koyama, M.M. Nasr, Study on adsorption of methanol onto carbon based adsorbents, *Int. J. Refrig.* 32 (2009) 1579–1586. <https://doi.org/10.1016/J.IJREFRIG.2009.06.011>.
- [14] Home - NSRDB, (n.d.). <https://nsrdb.nrel.gov/> (accessed December 19, 2021).
- [15] S. Mitra, N. Aswin, P. Dutta, Scaling analysis and numerical studies on water vapour adsorption in a columnar porous silica gel bed, *Int. J. Heat Mass Transf.* 95 (2016) 853–864. <https://doi.org/10.1016/j.ijheatmasstransfer.2015.12.011>.
- [16] M.J. Rupa, A. Pal, B.B. Saha, Activated carbon-graphene nanoplatelets based green cooling system: Adsorption kinetics, heat of adsorption, and thermodynamic performance, *Energy.* 193 (2020) 116774. <https://doi.org/10.1016/j.energy.2019.116774>.

- [17] E.F. Passos, J.F. Escobedo, F. Meunier, Simulation of an intermittent adsorptive solar cooling system, *Sol. Energy.* 42 (1989) 103–111. [https://doi.org/10.1016/0038-092X\(89\)90137-0](https://doi.org/10.1016/0038-092X(89)90137-0).
- [18] J. a. Duffie, W. a. Beckman, W.M. Worek, *Solar Engineering of Thermal Processes*, 4th ed., 2003. <https://doi.org/10.1115/1.2930068>.
- [19] Y. Cengel, M. Boles, *Heat Transfer A practical Approach*, McGraw - Hill. (2002) 932. https://books.google.com/books/about/Heat_Transfer.html?id=nrbfpSZTwsK (accessed December 21, 2021).

Stacked adsorption module with aluminium composite foil: Simulation and experimental evaluation of a novel concept

E. Laurenz^{1*}, M. Linke¹, A. Velte¹, R. Volmer¹, J. Weise² and G. Földner¹

¹Fraunhofer Institute for Solar Energy Systems ISE,
Heidenhofstr. 2, 79110 Freiburg, Germany

²Fraunhofer Institute for Manufacturing Technology and Advanced Materials IFAM,
Wiener Strasse 12, 28359 Bremen, Germany

*Corresponding author: eric.laurenz@ise.fraunhofer.de

Abstract

Adsorption chillers, heat pumps and heat upgraders are important technologies for the valorisation of waste heat and the decarbonisation of heating and cooling. However, available solutions lack compactness and high costs. A novel concept of an adsorption module with water as refrigerant is based on polymer-aluminium-polymer composite foils as integrated vacuum encapsulation and heat exchanger surface. Inspired by classical plate heat exchanger the concept allows for the usage of low-cost materials, a simplified manufacturing procedure and easy scalability. Stability-critical vacuum feedthroughs of heat exchanger tubes are inherently avoided by reducing the vacuum part to so-called adsorption cells. An innovative copper fibre TiAPSO-34 composite is employed as adsorbent layer allowing for high adsorption dynamics. In this contribution we present preliminary results of the manufacturing procedure and experimental results. For the design process the method of effective thermal resistance has been employed. Alongside results of a transient FEM simulation of heat and mass transfer processes provides insights into internal mechanisms and optimization potential.

Keywords: Adsorption chiller, Aluminium composite foil, TiAPSO-34, Adsorption cell, Plate heat exchanger, simulation

Introduction

Adsorption heat transformation (chillers, heat pumps, heat upgraders) is an important technology for the valorisation of waste heat and the decarbonisation of heating and cooling [1]. In principle, they allow to use the working potential of a heat flow dropping from a higher to a lower temperature to lift another heat flow from a lower to a higher temperature in cycling operation. The common realisation of adsorption heat transformers consists of two “conventional” heat exchangers introduced in a tight vessel with a pure refrigerant atmosphere, the adsorption module, with an external set of valves, connectors and a control unit. In the adsorption module the heat exchangers are the adsorption heat exchanger covered with an adsorption material or composite [2] and the evaporator/condenser [1]. Despite its popularity, this concept has limitations like stability issues of the vacuum feedthroughs, undesired condensation of working fluid on the vessel walls and reduced scalability.

Here, we present a novel concept consisting of layered adsorption cells arranged to a plate-heat-exchanger-type of configuration (**Figure 1**). This concept has several advantages, like the reduction of vacuum conditions to the encapsulated inner part of the adsorption cells which avoids any feedthrough and inherently avoids undesired condensation.

The adsorption cells consist of a copper adsorbent composite layer (cite Velte et al), a highly porous thermal separator and a copper mesh as evaporator/condenser, which all is encapsulated by a polymer aluminium composite foil commonly used for pouch battery cells in a special manufacturing procedure.

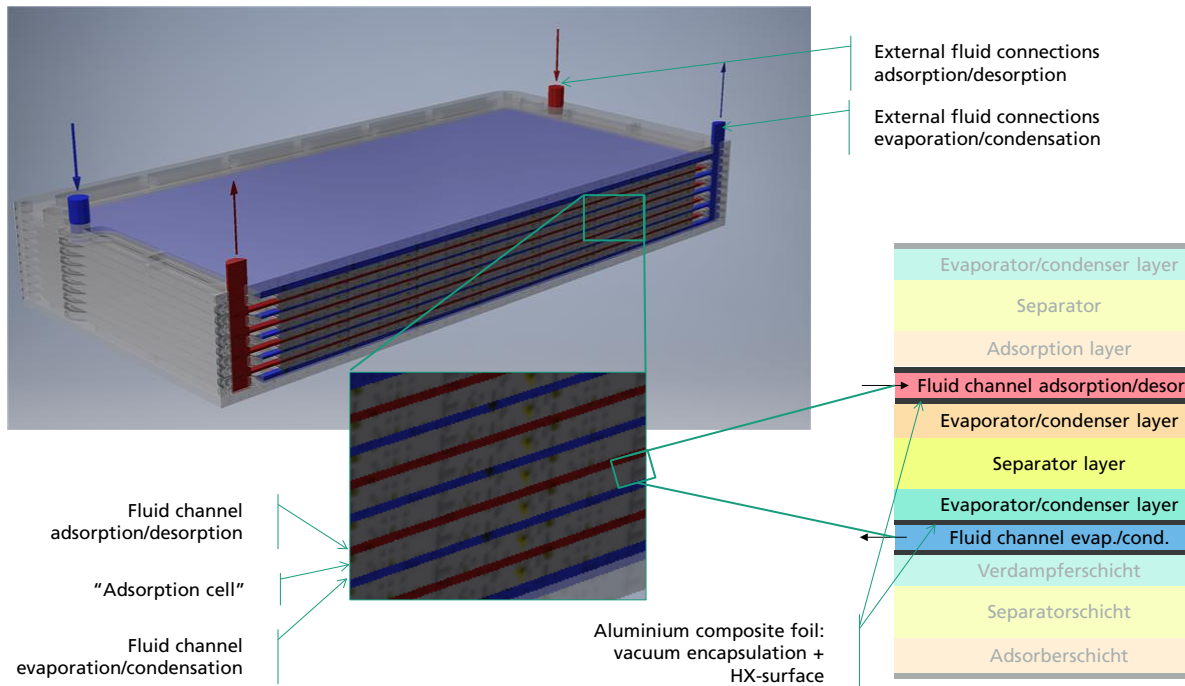


Figure 1: Schematic sketch of the investigated concept: The adsorption module consists of a set of stacked vacuum-encapsulated adsorption cells in a plate-heat-exchanger-type arrangement. The adsorption cells contain a pure refrigerant atmosphere with all parts of a classical adsorption chiller in different layers.

For the design process the novel method of effective thermal resistance was employed [3]. A 2D-simulation model has been implemented in COMSOL representing a longitudinal cut through an adsorption cell. The model consists of heat transfer with heat conduction and source/sink terms for adsorption/desorption and evaporation/condensation and the mass transfer considering viscous flow and Knudsen diffusion and again, source/sink terms for adsorption and evaporation/condensation.

Discussion and Results

The manufacturing procedure was successfully applied. Experimental results are pending and will be presented at the conference. Based on preliminary modelling results and under inlet temperature conditions of 80/35/15 °C for desorption, adsorption/condensation and evaporation, respectively, a COP of 0.38 and a specific cooling power of 160 W/l with respect to the active volume (cell and fluid channel) and of 44 W/l with respect to the external dimension of the small-scale test module.

References

- [1] L. Schnabel, G. Földner, A. Velte, E. Laurenz, P. Bendix, H. Kummer, U. Wittstadt, in *Innovative Heat Exchangers*, Springer International Publishing. Cham **2018**.
- [2] K. R. Gluesenkamp, A. Frazzica, A. Velte, S. Metcalf, Z. Yang, M. Rouhani, C. Blackman, M. Qu, E. Laurenz, A. Rivero-Pacho, S. Hinners, R. Critoph, M. Bahrami, G. Földner, I. Hallin, *Energies* **2020**, *13* (5), 1150. DOI: 10.3390/en13051150.
- [3] E. Laurenz, Frequency response analysis of heat and mass transfer in adsorbent composites and simplified performance estimation for heat transformation, *Doctoral Dissertation*, TUHH **2021**.

Thermal operation map for the mechanical discharging process of the Lamm-Honigmann Energy Storage

E. Thiele^{1*}, F. Ziegler²

¹Technische Universität Berlin, Institut für Energietechnik, Marchstr. 18, 10587 Berlin

Corresponding author: e.thiele@tu-berlin.de

Abstract (12-pt Times New Roman)

The Lamm-Honigmann (LAHMA) energy storage is a sorption based Pumped Thermal Electricity Storage (PTES) that can be charged and discharged arbitrarily with both heat and electrical power. The mechanical charging and discharging processes of this storage are characterized by an internal heat transfer between the main components Absorber/Desorber and Evaporator/Condenser that is driven by the working fluid mass transferred between those components with help of an expansion or compression device respectively.

In this paper, a thermal operation map for the mechanical discharging process is developed from energy balances in order to predict power output depending on the system state, that is in particular defined by the mass flow rate of vapor and the salt mass fraction. The conducted method is applied for the working fluid pair LiBr/H₂O. This thermal map is especially useful for dimensioning of the expansion machine and for the development of control strategies for the storage.

In a first step, a thermal efficiency is defined to account for second order losses due to the internal heat transfer. E.g. for discharging from a salt mass fraction of 0.7 to 0.5 (kg LiBr)/(kg sol.) at a temperature of 130°C, it is found that the reversible shaft work output is reduced by 1.1 – 2.9%/K driving temperature difference. For lower operating temperatures the reduction is larger, e.g. at 80°C the efficiency loss due to heat transfer rises to 3.5%/K for a salt mass fraction of 0.5 (kg LiBr)/(kg sol.).

In a second step, a quasi-stationary assumption leads to the thermal operation map from which the discharging characteristics can be found. E.g. at an operating temperature of 130°C for a constant power output of 0.4 kW/m² heat exchanger area at volumetric and inner machine efficiencies of $\eta_i = \eta_{vol} = 0.8$ and for an overall heat transfer coefficient of 1500 W/(K m²), the mass flow rate has to rise continuously from 1.5 to 4.2 g/(s m²) while the thermal efficiency is reduced due to this rise and due to dilution of the sorbent from 97% to 83%. For this discharging scenario, the corresponding discharge time is 4.4(min. · m²)/(kg salt). This results in an exergetic storage density of around 29 Wh/kg of salt mass in the absorber.

Besides those predictions for arbitrary discharging szenarios, the derived thermal map is especially useful for dimensioning of the storage system and for the development of control strategies. It has to be noted, that the operation map does not illustrate the transient behavior of the system, but its quasi-stationary state. However, it will be shown, mathematically, that the system tends to return to this state when disturbed.

Keywords: thermochemical energy storage, absorption storage, storage and conversion, Carnot Battery, Thermal Operation Map, Control strategy, storage efficiency, storage power.

Nomenclature

χ	vapor quality
ΔT	driving temperature difference (K)
η	energetic efficiency
λ_q	
Θ	fitted parameter (%/K)
ξ	mass fraction ($\frac{\text{kg working fluid}}{\text{kg sorbant}}$)
a, b, c, d	parameters of the diff. eq.
A	area (m ²)
c_p	isobaric heat capacity ($\frac{\text{kJ}}{\text{kg}}$)
d	differential operator
f	variable coeff. of the diff. eq. ($\frac{K^2}{s}$)
g	variable coeff. of the diff. eq. ($\frac{K^2}{s}$)
h	specific enthalpy ($\frac{\text{kJ}}{\text{kg}}$)
Δh_A	sorption enthalpy ($\frac{\text{kJ}}{\text{kg}}$)
Δh^{lv}	evaporation enthalpy ($\frac{\text{kJ}}{\text{kg}}$)
k	heat transfer coefficient ($\frac{\text{W}}{\text{K m}^2}$)
m	mass (kg)
p	pressure (Pa)
P^t	shaft power (W)
R	universal gas constant ($\frac{\text{kJ}}{\text{kg K}}$)
s	specific entropy ($\frac{\text{kJ}}{\text{kg}}$)
T	temperature (K)
q	specific heat ($\frac{\text{kJ}}{\text{kg}}$)
Q	heat (kJ)
v	specific volume ($\frac{\text{m}^3}{\text{kg}}$)
w^t	specific shaft work ($\frac{\text{kJ}}{\text{kg}}$)
x	salt mass fraction ($\frac{\text{kg salt}}{\text{kg sorbant}}$)
Z	compressibility ($\frac{\text{kJ/kg}}{\text{kJ/kg}}$)

Abbreviations

H2P	heat to power
P2P	power to power
A	ab-/adsorber
D	desorber
E	evaporator
EM	expansion machine
C	condenser
CM	compression machine
P	component parts/periphery
sol.	solution

Indices

'	saturated liquid
"	saturated vapor
S	storage
A	ad-/absorbant
eq	equilibrium
ch	charge
dis	discharge
comp	compression
exp	expansion
rev	reversible limit
isen	isentropic
poly	polytropic
vol	volumetric
htf	heat transfer fluid
i	inlet
o	outlet
h	particulate
p	homogeneous

Introduction

Energy storage plays a key role on the way to decarbonized energy systems relying on renewable sources. The Lamm-Honigmann-process (LAHMA) is a thermo-chemical energy conversion and storage process that was originally invented to drive fireless locomotives. Two patents were issued in the 19th century using different working fluid pairs: by Moritz Honigmann in 1883 ([1],[2]), and by Emile Lamm in 1870 [3]. The process is based on the principle of vapor pressure depression of an un-loaded ad-/absorbent, compared to the pure working fluid. The stored energy can be retrieved in the form of heat, cold or mechanical work, as well [4]. The combination of storage and conversion renders the process unique and favorable for an optimized use of transient renewable energy and waste heat.

However, the concept was rarely investigated in the last century¹ but recent experimental work by Jahnke ([6]) has proven the potential of the process to be used as stationary energy storage. In [6] the focus lies on the experiments performed on the prototype, the plausibility of the results and on the identification of the peculiarities of the prototype (e.g. heat losses, thermal masses, chosen process configuration, the inefficient expansion device). Those peculiarities are not necessarily representative for the general concept but their influence on the figures of merit is large. Thus, the efficiency for conversion of thermal to mechanical energy and the storage density were low (0.2% compared to calculated 13% conversion efficiency and 0.2 Wh/kg compared to 12 Wh/kg if the expansion device would work isentropically and thermal heat losses would be neglected), but reasons could be identified and the adaption of the experimental set-up is work in progress.

In [7] the author has investigated theoretical efficiencies of the storage system for different storage materials but without accounting for different discharging scenarios in terms of arbitrary power output. So, there is still a need for a fundamental theoretical understanding of the system independent of its dedicated realization (e.g. size, working fluid pair, temperature level, configuration, expansion/compression device used) and for arbitrary discharging scenarios, that enables general system analysis and optimization and facilitates system scale-up and development of operation and control strategies.

A known approach for understanding the operational behavior of hydraulic systems consisting of pumps and piping is that of the systems operational line, indicating the required pressure head in the system in dependence of working fluid mass flow rate. Combined with the pumps operational line the volume flow rate in the system can be predicted, or the correct pump sizing for the volume flow rate required be chosen. Inspired by this method, a thermal operational field for the mechanical discharging process of the system that can later be matched with the operational field of any expansion device, will be developed. The derived equations are applied for the working fluid pair LiBr/water and storage characteristics are conducted from the results.

Storage Cycle description

As already mentioned the Lamm-Honigmann storage concept has different realizations depending on the form of energy to store or extract. For a detailed description of the thermal charging and discharging refer to e.g. [7] and [4].

The basic system consists of a water heat exchanger (HX), that can work either as condenser (c) or as evaporator (E), and a solution HX, that can work as an absorber or as a desorber. The mechanical charging and discharging processes are shown in figure 1 in a Van't Hoff diagram. The state point of the water heat exchanger (blue circle) is always on the vapor pressure line of

¹for more detailed historical background refer to e.g. [5]

pure water, whereas the solution heat exchanger (green circle) changes between the isosteres of the rich (discharged) and poor (charged) solution.

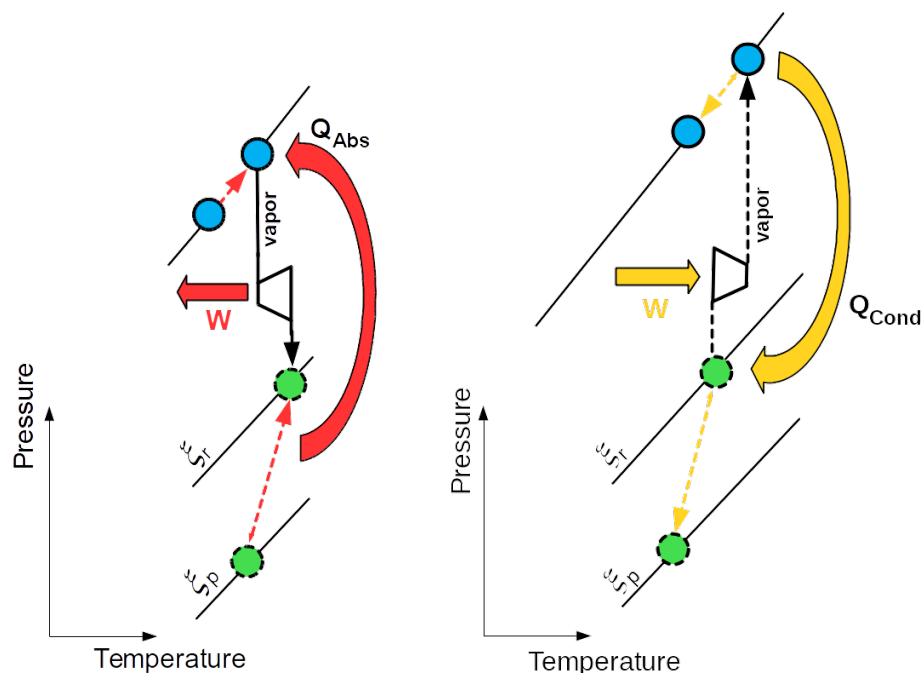


Figure 1. mechanical discharging phase (left) and charging phase (right)[7]

In [7] mechanical charging and discharging are described as follows (direct citation):

- (1) *Discharging (figure 1, left):* The water heat exchanger works as evaporator, the sorption heat exchanger works as absorber. The evaporator has a slightly lower temperature than the absorber to enable the heat transfer. Water vapor from the evaporator is passed through an expansion machine to produce mechanical work W . The expanded water vapor is absorbed by the LiBr-solution in the absorber and the heat of absorption Q_{Abs} is used to evaporate more water. This goes on until the LiBr-solution is so diluted that the vapor pressure difference is not sufficient anymore to supply the desired mechanical power or torque. As the energy released when the water is absorbed is higher than the energy required for evaporation of that water (for the common physisorptive systems the ratio is around 1.1 . . . 1.2) the entire system heats up during discharge.
- (2) *Charging: (figure 1, right)* The sorption heat exchanger works as desorber. The LiBr-solution is regenerated by the input of heat from the water heat exchanger working as condenser Q^{Cond} . The desorbed water vapor is compressed to condenser pressure level and liquefied in the condenser.

Solution field geometry

The usable pressure potential during discharging depends on the salt mass fraction and temperature in the absorber (storage temperature T_S) and can be calculated using equilibrium property data of the working fluid pair. The driving temperature difference for the heat transfer $\Delta T_{dis} = T_S - T_E$ will reduce this pressure potential (and thus the useful enthalpy difference). This effect is illustrated in a Van't Hoff diagram in figure 2.

In figure 3 the useful (discharging) isentropic enthalpy differences Δh_{isen} of the water vapor

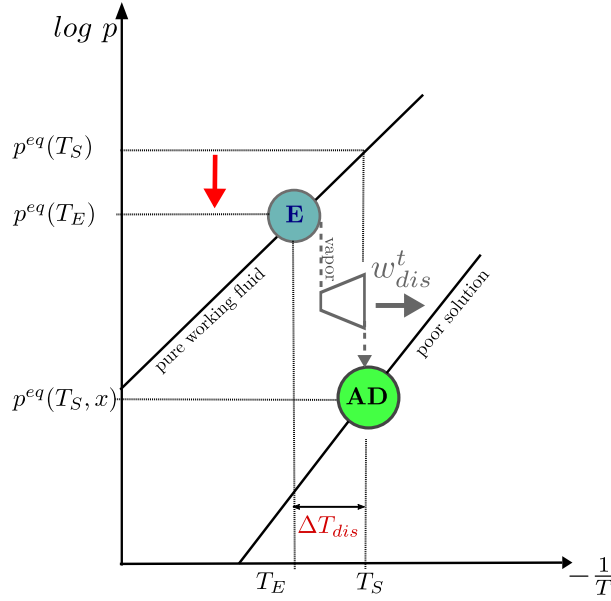


Figure 2. influence of driving temperatures on usable pressure ratio.

are drawn over working fluid mass fraction $\xi = 1 - x$ and driving temperature difference ΔT for different storage temperatures T_S (temperature of the absorber/desorber) They are defined as:

$$\Delta h_{isen,dis} = h''(T_E) - h(s''(T_E), p^{eq}(T_S, x)) \quad (1)$$

$$(2)$$

Obviously the isentropic enthalpy difference depends linearly on the driving temperature difference ΔT . As the value of ΔT is actually specific to the HX design and process operation and is not a working fluid specific nor process inherent property, its influence on the usable isentropic enthalpy difference will be expressed by a thermal efficiency:

$$\eta_{th,dis} := \frac{\Delta h_{isen,dis}(\Delta T_{dis}, x, T_S)}{w_{rev,exp}^t(T_S, x)} \quad (3)$$

where the reversible shaft work $w_{rev}^t(T_S, x)$ equals the isentropic enthalpy difference if $\Delta T = 0$ (infinite HX area).

Considering the linearity of the relation between Δh_{isen} and ΔT observed in figure 3, the thermal efficiencies can be fitted according to eq. 4 with the proportionality factor $\Theta(T_S, x)$ in unit K^{-1} , that depends on storage temperature and salt mass fraction.

$$\eta_{th,dis} = 1 - \Theta_{dis} \Delta T_{dis} \quad (4)$$

A 3-D fit of the proportionality factor $\Theta_{dis} = f(T_S, x)$ is shown in figure 4 on the right. The symbols represent calculated values for Θ_{dis} at driving temperatures between $\Delta T = 1 \dots 10K$ for $T_S = 80 \dots 140^\circ C$ and $x = 0.5 \dots 0.7$ kg salt/kg sol. and represent the data base for the shown polynomial fit. The corresponding fit function is:

$$\Theta_{dis}(T_S, x) = \left[2.42 - 1.62 \cdot \frac{(1-x)}{x_N} - 1.31 \cdot \frac{T_S}{T_{S,N}} + 8.89 \cdot \left(\frac{(1-x)}{x_N} \right)^2 - 8.52 \cdot \frac{(1-x)}{x_N} \cdot \frac{T_S}{T_{S,N}} + 2.91 \cdot \left(\frac{T_S}{T_{S,N}} \right)^2 \right] \% \quad (5)$$

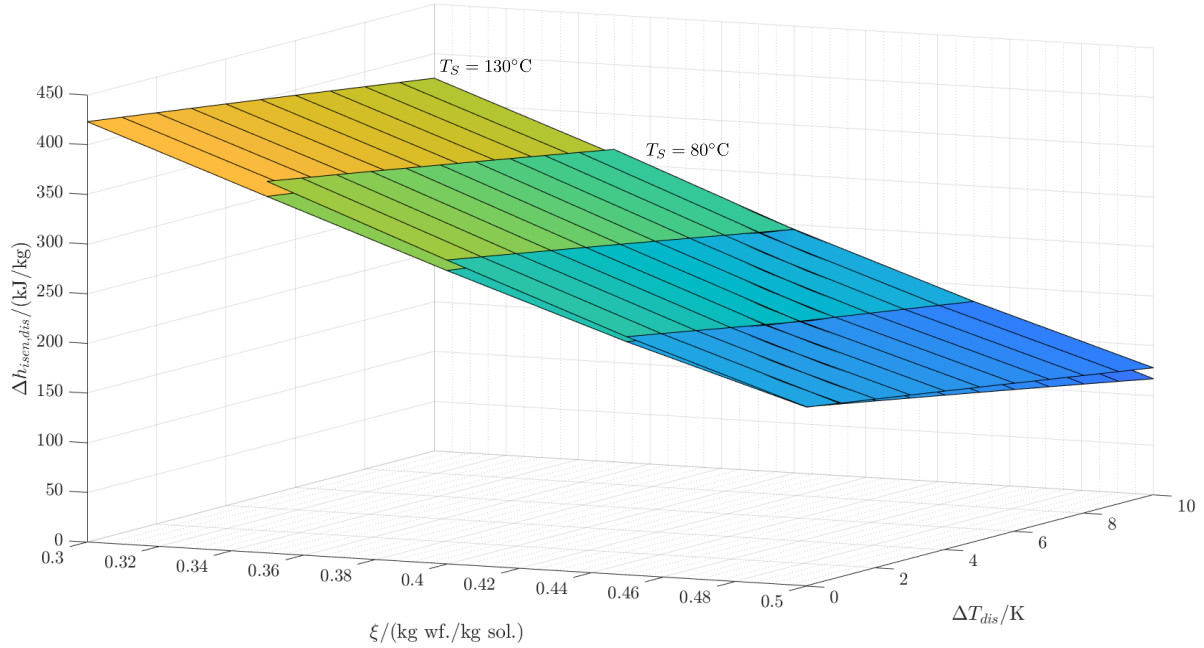


Figure 3. isentropic enthalpy difference Δh_{isen} over working fluid mass fraction and driving temperature difference.

with the normalization factors $x_N = 0.5$ kg salt/kg sol. and $T_{S,N} = 413.15$ K.

On the left side of figure 4 the thermal efficiencies for discharging is shown in dependence of the corresponding driving temperature difference for different working fluid mass fractions; and in the middle of figure 4 for different storage temperatures. The symbols represent the calculated values from enthalpy data. The lines are the corresponding functions of η_{th} (eq. 4) with the fitted proportionality factor Θ (eq. 5). Obviously the match of fitted and calculated data is accurate. The figure shows, that e.g. for a storage temperature of 130°C and a salt mass fraction of 0.5 kg salt/kg sol., the thermal efficiency for discharging drops about 3%/K temperature difference.

Guiding differential equations of the discharging process

Instationary energy balances for heat exchangers and stationary balance for the expansion device are made under the following assumptions:

- the working fluids in the heat exchangers are in thermodynamic equilibrium
- no vapor phase is present within the heat exchangers (the vapor is immediately absorbed by the liquid in the absorber/leaves immediately the evaporator)
- the liquids in the heat exchangers are ideally mixed (retention time in the solution circuit is neglected, temperature is distributed equally); static pressure differences are negligible
- the liquids are ideal and $du = dh$ holds true
- heat and pressure losses in the connecting pipes are negligible
- the component itself is at the same temperature as the respective working fluid contained

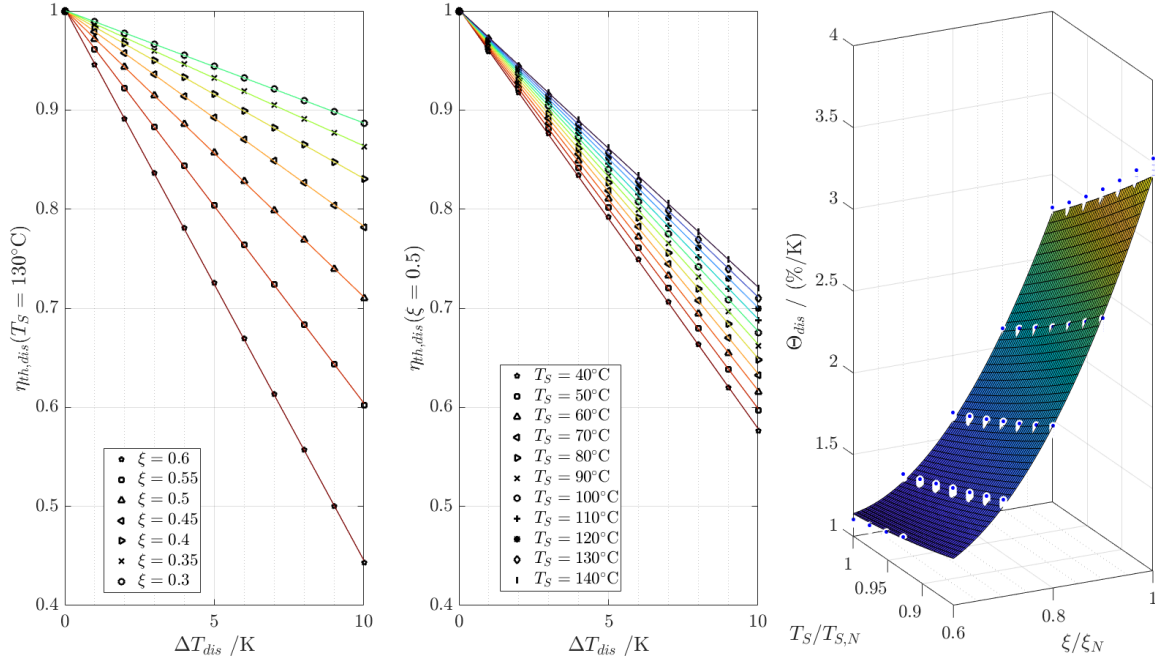


Figure 4. thermal efficiency η_{th} for discharging for a storage temperature of $T_S = 130^\circ\text{C}$ (left) and for a working fluid mass fraction of $x = 0.5$ kg wf/kg sol (middle); calculated proportionality factor Θ_{dis} (equation 5) on the right.

This leads to the following relation between the driving temperature difference for the heat exchange and the mass flow rate that is exchanged between evaporator and absorber (discharging). The underlying equations can be found in Appendix and .

$$\begin{aligned} \frac{d\Delta T_{dis}(t)}{dt} = & - \left(\frac{1}{C_A} + \frac{1}{C_E} \right) kA \cdot \Delta T_{dis}(t) + \left(\chi \Delta h^{lv} \left(\frac{1}{C_A} + \frac{1}{C_E} \right) + \frac{l_A}{C_A} \right) \dot{m}(t) \\ & - \frac{P_{dis}^t(t)}{C_A} - \frac{c_{p,E}}{C_A} \Delta T_{dis}(t) \cdot \dot{m}(t) + \frac{\dot{Q}_{loss,E}}{C_E} - \frac{\dot{Q}_{loss,A}}{C_A} \end{aligned} \quad (6)$$

whereby (see for definition of efficiencies):

$$P_{dis}^t(t) = \dot{m}(t) \cdot \eta_{vol,EM} \cdot w_{dis}^t \quad (7)$$

$$= \dot{m}(t) \cdot \eta_{vol,EM} \cdot w_{rev,exp}^t(x(t), T_A) \cdot \eta_{i,EM} \cdot \eta_{th,dis}(x(t), T_A, \Delta T_{dis}(t)) \quad (8)$$

$$\begin{aligned} & \frac{d\Delta T_{dis}(t)}{dt} \quad (9) \\ = & - \underbrace{\left[(c_{p,E} - \Theta \cdot w_{rev,exp}^t \cdot \eta_{vol,EM} \cdot \eta_{i,EM}) \frac{1}{C_A} \cdot \dot{m}(t) + \left(\frac{1}{C_A} + \frac{1}{C_E} \right) kA \right]}_{f(t) := a \cdot \dot{m}(t) + b} \Delta T_{dis}(t) \\ & + \underbrace{\left(\frac{l_A - w_{rev,exp}^t \cdot \eta_{vol,EM} \cdot \eta_{i,EM}}{C_A} + \chi \Delta h_E^{lv} \left(\frac{1}{C_E} + \frac{1}{C_A} \right) \right) \dot{m}(t) + \frac{\dot{Q}_{loss,E}}{C_E} - \frac{\dot{Q}_{loss,A}}{C_A}}_{g(t) := c \cdot \dot{m}(t) + d} \quad (10) \end{aligned}$$

The inhomogeneous differential equation of first order with variable coefficients can be solved

using variation of constants. Its general solution is:

$$\Delta T_{dis}(t) = \Delta T_{dis,h}(t) + \Delta T_{dis,p}(t) \quad (11)$$

$$= e^{-\int f(t)dt} \left(c_i + \int \frac{g(t)}{e^{-\int f(t)dt}} dt \right) \quad (12)$$

$$= e^{-F(t)} \left(c_i + \int g(t) \cdot e^{F(t)} dt \right) \quad (13)$$

with integration constant c_i , and $F(t)$ being the primitive of $f(t)$.

Another important differential equations connects the salt mass fraction and the mass flow rate:

$$\dot{m}(t) = \frac{dm_A}{dt} = \frac{d \frac{m_{salt}}{x}}{dt} = -m_{salt} \cdot \frac{1}{x^2} \frac{dx}{dt} \quad (14)$$

$$\dot{m}(t)dt = -m_{salt} \frac{1}{x^2} dx \quad (15)$$

It is required for calculation of discharge times.

In the following sections the specific solution of eq. 13 for a constant vapor mass flow rate and a linear rising and falling vapor mass flow rate will be discussed exemplary for discharging. It will be shown that the system tends to a quasi-static state, that is $\frac{d\Delta T}{dt} = 0$ and the validity of a model based on this quasi-static state will be discussed by comparing it to the dynamic model.

Constant vapor mass flow

For a constant vapor mass flow $\dot{m}(t) = \dot{m}_c$ and a constant salt mass fraction x , the coefficients of the differential equation are constants as well ($f(t) = f$; $g(t) = g$) and the analytical solution is:

$$\Delta T_{dis}(t) = (\Delta T_{dis0} - \frac{g}{f}) \cdot e^{-f \cdot t} + \frac{g}{f} \quad (16)$$

It should be noted, that the heat capacities of the working fluids $c_{p,E}$, $c_{p,A}$, the enthalpy of dilution l_A and the heat losses in the HX's are dependent on absolute temperature, that is not necessarily constant. However for the working fluid pair in question the change in absolute temperature is small during discharging (e.g. compare simulations in [8]) and its influence on the working fluid properties and heat losses is negligible.

Actually, the salt mass fraction will not be constant neither. As soon as there is a vapor mass flow between evaporator and absorber the salt mass fraction in the absorber and the water mass in the evaporator will change, and therefore C_A and C_E . Same holds true for the reversible shaft work w_{rev}^t that changes with pressure ratio and for the heat of dilution l_A . That means $a = a(x(t))$, $b = b(x(t))$, $c = c(x(t))$ and $d = d(x(t))$.

However, if the working fluid reservoir is large enough compared to the vapor mass flow rate (corresponding to long discharge times), the change in salt mass fraction is very small, and so its contribution to the dynamic behavior, as will be shown later.

Equation 16 shows, that the initial temperature difference ΔT_{dis0} increases or decreases exponentially towards the value of $\frac{g}{f}$ in case that $f > 0$. The value $\frac{g}{f}$ can be interpreted as the ratio of heat rate used or produced within the components to the heat transferred between the components per K temperature difference when the system is in its rest position, where $\frac{\Delta T_{dis}}{dt} = 0$ and:

$$\Delta T_{dis} = \Delta T_{dis,R} = \frac{g}{f} = \frac{a \cdot \dot{m} + b}{c \cdot \dot{m} + d} \quad (17)$$

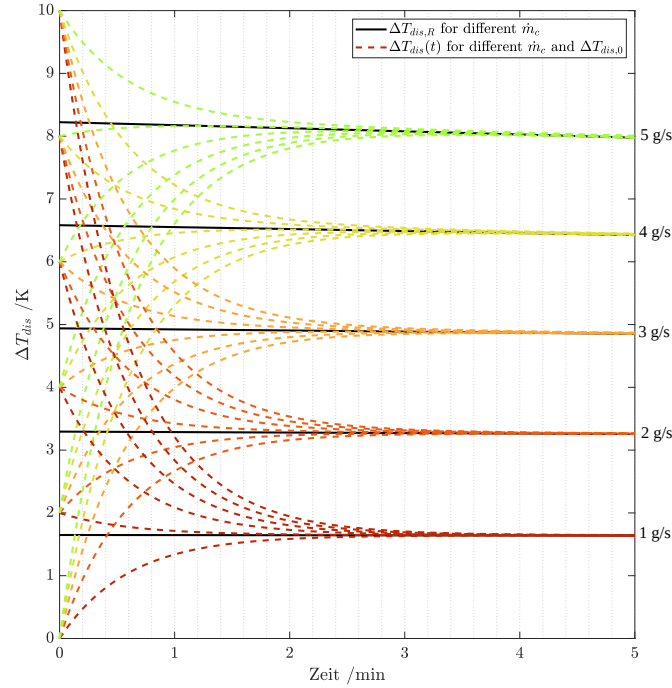


Figure 5. Driving temperature difference over time for different constant vapor mass flow rates \dot{m}_{const} (1, 2, 3, 4 and 5 g/s represented as dotted lines in different colors) and different start values $\Delta T_{dis,0}$ (0, 2, 4, 6, 8 and 10 K represented as dotted lines with the same colors). The solid black lines represent the rest position $\Delta T_{dis,R}$ corresponding to each \dot{m}_{const} .

In figure 5, equation 16 is plotted for different mass flow rates and different starting conditions of ΔT_{dis} , and with the parameters and start values reflected in table 1 which correspond to the pilot plant at TU Berlin (see [6]) when neglecting thermal masses of periphery ($C_{EP/AP} = 0$) and the heat losses to the environment ($\dot{Q}_{loss,EC/AD} = 0$).

The rest positions $\Delta T_{dis,R}$ corresponding to different constant mass flow rates are plotted in black lines. Their change in time (due to change in salt mass fraction) is rather small. E.g. for the largest mass flow rate of 5 g/s, which corresponds to the double nominal value, the change in corresponding $\Delta T_{dis,R}$ is $< 0.2\text{K}$ ($< 2.5\%$) after 5 min. The dotted lines show the change in driving temperature difference for different start values of ΔT_{dis} at different constant mass flow rates. It can be seen that the rest position is always reached within 3 min, even for the double of the nominal mass flow rate. The quasi-stationary solution $\frac{\Delta T_{dis}}{dt} = 0$ of the mathematical model is only accurate for the specific start conditions but is always reached in some minutes for a wide range of start conditions. In order to achieve useful operation conditions for the storage, it is required that $f > 0$. If this is not the case, the driving temperature difference would rise exponentially although the mass flow rate is constant and no rest position would be achieved. The pressure potential would shrink continuously and the process stop fast. Thus, it has to be:

$$\frac{\Theta \cdot w_{rev,exp}^t \cdot \eta_{vol} \cdot \eta_{i,EM} \cdot \dot{m}}{C_A} < kA \cdot \left(\frac{1}{C_A} + \frac{1}{C_E} \right) \quad (18)$$

For the working fluid pair LiBr/water at the operating conditions investigated here: we can estimate, that $\Theta_{dis} < 5 \text{ %/K}$ (compare figure 4) and that $w_{rev}^t < 500 \text{ kJ/kg}$ (compare figure 3) and therefore

$$(\Theta_{dis} \cdot w_{rev,exp}^t \cdot \eta_{vol} \cdot \eta_{i,EM} < 2.5 \text{ kJ/kg}) < (c_{p,E} > 4 \text{ kJ/kg}).$$

Table 1. constant model parameters

parameter	value
heat transfer coefficient kA	1500 W/K
inner efficiency of EM $\eta_{EM,i}$	0.8
volumetric efficiency of EM $\eta_{vol,EM}$	0.8
quality of produced water vapor χ	1
storage temperature T_{AD}	130°C
mass of LiBr	30 kg
mass of water	60 kg
salt mass fraction at start x_0	0.7
design mass flow rate \dot{m}_N	2.5 g/s

That means, $f > 0$ is fulfilled for all mass flow rates and even in absence of internal heat transfer ($kA = 0$) and for a given mass flow rate, the quasi-stationary working point after eq. 17 is always reached in finite time.

But, if the heat transfer capability kA is too small, the driving temperature difference of rest position, that corresponds to a given mass flow rate, might actually be too large and never be reached before the entire available pressure potential is gone (and the storage is already discharged). In this case the quasi-stationary solution is out of the physical boundaries of the modeled system.

Therefore f should not only be positive but more specifically the parameters a and b should be large in order to achieve sufficiently small values of ΔT_R for a given mass flow rate on the one hand, and to lower the time constant and achieve small values of Δt between two quasi-stationary working points on the other hand.

That means, large heat exchanger area, large heat transfer coefficient, and a working fluid with large heat capacity and small Θ_{dis} are not only favorable for a large thermal efficiency but also for the quasi-stationary operation of the system. Obviously, larger mass flow rates will lower the time constants aswell but have a negative effect on the thermal efficiency.

Linear rising or falling vapor mass flow

The solution for constant mass flow rate is useful for a basic understanding of the systems behavior but does not reflect at all realistic operation conditions. In order to control storage power output, the mass flow rate will have to be adjusted continuously. Therefore solutions of the differential equation will be analyzed for mass flow rates rising or falling linearly. For a vapor mass flow rising or falling linear with time

$$\dot{m}(t) = \mu \cdot t + \dot{m}_0 \quad (19)$$

the variable coefficients are

$$f(t) = \underbrace{a \cdot \mu \cdot t}_{\alpha} + \underbrace{a \cdot \dot{m}_0 + b}_{\beta} \quad (20)$$

$$g(t) = \underbrace{c \cdot \mu \cdot t}_{\gamma} + \underbrace{c \cdot \dot{m}_0 + d}_{\delta} \quad (21)$$

and the analytical solution is:

$$\Delta T_{dis}(t) = e^{-\left(\frac{1}{2}\alpha \cdot t^2 + \beta \cdot t\right)} \left[\Delta T_{dis0} - \left(\underbrace{\frac{\delta}{\beta}}_{>0} - \underbrace{\frac{\gamma}{\beta^2}}_{\text{sign}(\mu)} \right) \right] + \left(\underbrace{\frac{g(t)}{f(t)}}_{>0} - \underbrace{\frac{\gamma}{f(t)^2}}_{\text{sign}(\mu)} \right) \quad (22)$$

In figure 6 equation 22 is plotted for different start conditions of driving temperature difference and mass flow rate and different change rates of the mass flow rate. It can be seen that a negative change rate leads for any start value of the driving temperature difference ΔT_{dis} to a positive difference of the asymptotic value of ΔT_{dis} compared to the corresponding rest position $\Delta T_{dis,R}$, and a positive change rate leads to a negative deviation from its corresponding rest position. The thermal part of the system is slow, it requires time to adapt to changing conditions.

It can also be stated that the deviation from the rest position is larger, the larger the absolute change rate of the mass flow rate. However, even for a quite fast change rate of 0.01 g/s^2 , which corresponds to a time smaller than 5 min to reach the design mass flow rate of $\dot{m}_D = 2.5 \text{ g/s}$ starting from 0 g/s , the deviation from the corresponding rest position is $< 1\text{K}$.

So, it can be concluded that the rest position ($\frac{d\Delta T_{dis}}{dt} = 0$) can represent the storage operation conditions (for a long discharge time and a response time that is large enough). Then, to a certain mass flow rate through the system, there is a corresponding driving temperature difference for the heat exchange, and vice versa.

Knowing the solution field geometry presented in section the mechanical power retrieved from the storage can be calculated in dependence of vapor mass flow rate and salt mass fraction. And that is what is called the thermal operation map of the storage, here.

Operation maps

The mechanical power output of the system in its rest position ($\frac{d\Delta T_{dis}}{dt} = 0$) is (for a size independent representation it is divided by the heat exchanger area A):

$$\begin{aligned} \frac{P_{dis,R}^t}{A} = & - \left(1 + \frac{C_A(x)}{C_E(x)} \right) k \cdot \Delta T_{dis,R} + \left(\chi \Delta h^{lv} \left(1 + \frac{C_A(x)}{C_E(x)} \right) + l_A(x) - c_{p,E} \Delta T_{dis,R} \right) \frac{\dot{m}}{A} \\ & + \frac{\dot{Q}_{loss,E} \frac{C_A(x)}{C_E(x)} - \dot{Q}_{loss,A}}{A} \end{aligned} \quad (23)$$

The thermal masses of evaporator and absorber are divided by the salt mass of the storage and the influence of thermal mass of periphery is neglected for simplicity (for the equations with thermal mass of periphery, see). Then, the derived thermal map is valid for all storage sizes (in terms of capacity).

$$\begin{aligned} \frac{C_{A/D}(x)}{C_{E/C}(x)} &= \frac{c_{p,A} \cdot m_{A/D}(x)}{c_{p,E/C} \cdot m_{E/C}(x)} \\ &= \frac{c_{p,A}}{c_{p,E/C}} \frac{1}{\frac{x}{x_{discharged}} - 1} \end{aligned} \quad (24)$$

Storage discharge time is calculated by integrating the differential equation connecting the salt mass fraction and the mass flow rate (eq. 15). If the system is in its rest position the mass flow rate only depends on demanded power and salt mass fraction, not on time, so that the variables

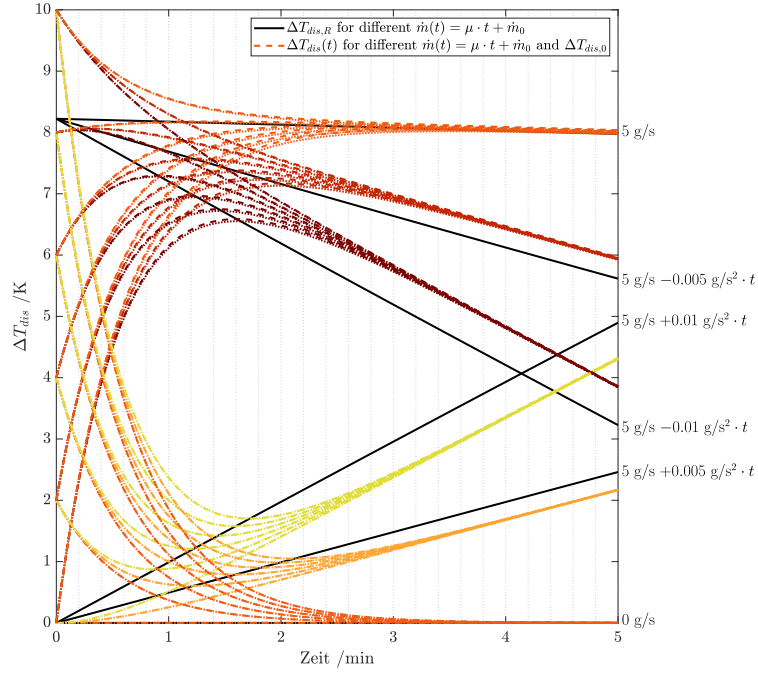


Figure 6. Driving temperature difference over time for different vapor mass flow rates $\dot{m}(t) = \mu \cdot t + \dot{m}_0$ ($\mu = -0.01; -0.005; 0; 0.005; 0.01 \text{ g/s}^2$ and $\dot{m}_0 = 0; 5 \text{ g/s}$ represented as dotted lines in different colors) and different start values $\Delta T_{dis,0}$ (0, 2, 4, 6, 8 and 10 K represented as dotted lines with the same colors for each $\dot{m}(t)$). The solid black lines represent the rest position $\Delta T_{dis,R}(t)$ corresponding to each $\dot{m}(t)$.

can be separated:

$$\int dt = -m_{salt} \int \frac{1}{x^2} \frac{1}{\dot{m}(x)} dx \quad (25)$$

For a discharge with constant mass flow the right side of the integral can be solved analytically, so the time (multiplied by the HX area and per salt mass) for discharging to a salt mass fraction of x is:

$$\Delta t_{dis} \frac{A}{m_{salt}} = \frac{1}{\frac{\dot{m}_c}{A}} \cdot \left(\frac{1}{x} - \frac{1}{x_{charged}} \right) \quad (26)$$

For a discharge with constant power output, the integral on the right side is solved numerically using the tangential-trapezoidal rule with 401 lattice points. The required mass flow for the given power output has to be calculated iteratively from the 2 dimensional system of nonlinear equations 17 and 23. This was done in matlab by the fsolve function with a function tolerance of $1 \cdot 10^{-3}$.

Combining equations 23, 17 and 24 and using the proposed solutions for eq. 25 a map as shown in figure 7 can be found for a certain storage temperature, here for $T_S = 130^\circ\text{C}$. One color in the rainbow corresponds to a certain salt mass fraction of the solution. The larger the mass flow rate at a certain salt mass fraction, the larger is the mechanical power output (left abscissa). Lines of constant thermal efficiency η_{th} are shown additionally. Thermal efficiency rises with salt mass fraction and declines with mass flow rate.

On the right abscissa the time for a full discharge is shown per mass of salt and HX area. The corresponding curves represent a discharging scenario with constant mass flow rate (bottom ordinate) and with constant power output (top ordinate).

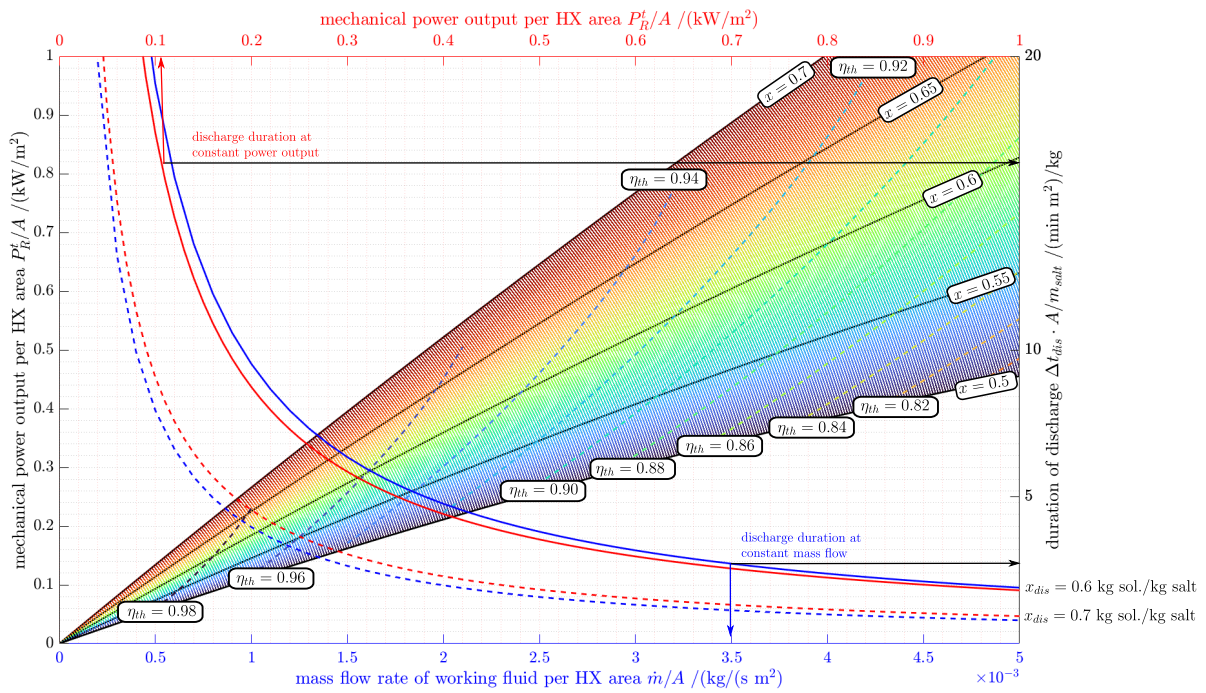


Figure 7. Operation map of the discharging process for the parameters reflected in table 1. Colored dotted lines show the power output (left abscissa) in dependence of the vapor mass flow rate (bottom ordinate) for different salt mass fractions. Lines of constant thermal efficiencies are dashed. The blue lines show the discharge time (right abscissa) for different constant vapor mass flows (bottom ordinate), and the red lines show the discharge times for different constant power outputs (top ordinate); full line for full discharge/dashed line for half discharge.

Discussion

Deduced storage characteristics

Assuming a good agreement of the quasi-stationary model with reality (experimental validation is in progress), the mathematical analysis shows a very quick response time of the system towards its new rest position when disturbed. Obviously, the storage can deliver a certain power very quickly, due to the fact that the entire system is at a similar temperature level at any time. This is an out-standing characteristic for a thermal storage system that stores electrical energy. Common *Pumped Thermal Energy Storage* systems are based e.g. on Brayton, Joule, Clausius-Rankine or Air liquefaction cycles working at two distinguished temperature levels during charging/discharging.

The thermal map shows further storage characteristics quite clearly:

- the thermal efficiency of the process is very sensitive to the vapor mass flow rate
- the lower the mass flow rate, the larger is the thermal efficiency - as usual, there is a trade-off between power and energy density and efficiency
- for a constant power output, the mass flow rate has to rise along discharging, with the consequence of declining thermal efficiency
- so, discharging with constant power is thermally more efficient - therefore, the discharge time for constant power is always larger than that for constant mass flow
- for a constant power input, the mass flow rate has to decline along charging, with the consequence of rising thermal efficiency

Model validity

Critical model assumptions The model is held as general as possible in order to make it universal, so certain effects in a real application are not modeled at all. A critical assumption in the model is the ideal mixing within the HX, especially for the AD. In the AD the liquid solution has a changing density depending on the salt mass fraction. The liquid being more dense (having a larger salt mass fraction) will tend to occupy the ground level of the AD or associated liquid storage tanks. This would be the liquid that has not yet absorbed vapor during discharging (flowing into the film absorber). The value of this modeling error depends on the realization of the AD and its connection with the liquid storage tanks.

Another critical assumption is that of thermodynamic equilibrium. Effects of superheating or subcooling in the liquid or gas phases will occur in a real application. However, the amount will depend on the realization: the heat exchanger design, the working fluid pair and heat transfer fluid used, and volume flows applied.

Constant model parameters The parameters reflected in table 1 are assumed to be constant. In reality, the expansion machine efficiency will definitely change with changing pressure ratio and changing rotational speed (speed control would be required for controlling the power output). Again, the amount depends on the machine that is used. Looking at the equations, they have a large influence on the power output/input but a small influence on the quasi-stationary ΔT and \dot{m} .

Depending, on the working fluid pair and the significance of heat losses, the storage temperature will change. However, as the heat of dilution is in the same order of magnitude as the expansion machine work, and the heat losses are insignificant, temperature change will be small and slow.

The other constants do, usually, not change in reality.

Summary/Conclusions

The derived method makes it possible to easily assess the interdependency of mass flow rate and driving temperature difference, and therefore predict storage behaviour for arbitrary power output and for arbitrary expansion machine types.

The mathematical analysis has shown that for a storage system, where absorber and evaporator are directly coupled and where the model assumptions reflected in section are applicable, the mechanical discharging process can reasonably be assumed to be quasi-stationary (meaning that $\frac{d\Delta T_{dis}}{dt} = 0$) if the change in mass flow rate is rather small. Then, the derived thermal operation map is valid independently of starting conditions of the system and the thermal map and the underlying equations can be used for general system analysis and optimization.

Some important storage characteristics were derived, most importantly, that the thermal storage efficiency is very sensitive to the exchanged vapor mass flow rate. Thus, the larger the power density of the storage system, the lower is the thermal efficiency.

Furthermore, the shown map and underlying equations can be used to:

- dimension the storage components (heat exchanger, expansion device, liquid storage tanks)
- conduct economic analysis to find the optimal heat exchanger size for different energy production scenarios (e.g. long or short-term reserves)
- develop a model based control strategy for the power output of the storage

References

- [1] Moritz Honigmann. Utilization of exhaust-steam. Specification forming part of Reissued Patent No. 10.675, United States Patent Office, 1885.
- [2] Moritz Honigmann. Verfahren zur Entwicklung gespannten Dampfes durch Absorption des abgehenden Maschinendampfes in Aetznatron oder Aetzkali. Patent No. 26234, Kaiserliches Patentamt, 1883.
- [3] E. Lamm. Improvement in ammoniacal-gas engines. Patent No.105 581, United States Patent Office, 1870.
- [4] Anna Jahnke, Felix Ziegler, and Michael Karow. Re-evaluation of the Honigmann-process: Thermo-chemical heat store for the supply of electricity and refrigeration. In *Proceedings of the Heat Powered Cycles Conference, Berlin, Germany*, 2009.
- [5] Elisabeth Thiele. *The Lamm-Honigmann thermochemical energy storage*, in: *Encyclopedia of Energy Storage*. elsevier, 2022.
- [6] Anna Jahnke. *Untersuchung des Honigmann-Prozesses zur thermochemischen Energiespeicherung*. Doctoral thesis, Technische Universität Berlin, Berlin, 2019.
- [7] Elisabeth Thiele, Anna Jahnke, and Felix Ziegler. Efficiency of the lamm-honigmann thermochemical energy storage. 19, 2020.
- [8] Anna Jahnke, Lia Strenge, Christian Fleßner, Niklas Wolf, Tim Jungnickel, and Felix Ziegler. First Cycle simulations of the Honigmann process with LiBr/H₂O and NaOH/H₂O as working fluid pairs as a thermochemical energy storage. 8, 2013.

Appendix

Energy balances

The entire system is shown in figure 8 and the single components in figures 9, 10 and 11.

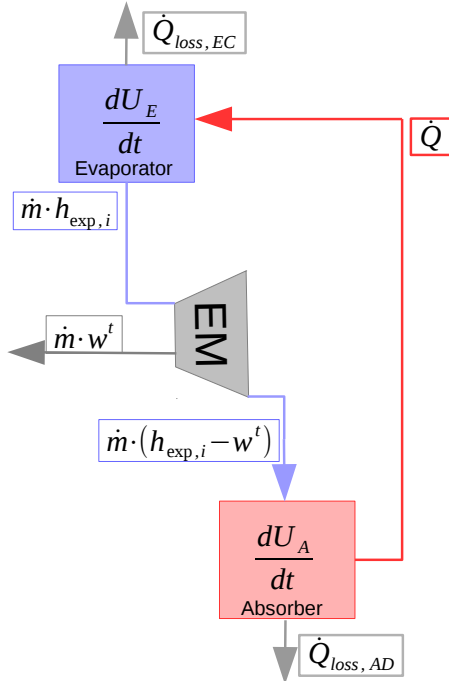


Figure 8. mechanical discharging

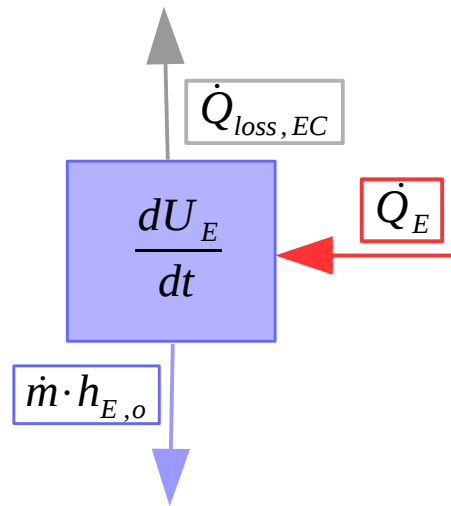


Figure 9. evaporator balance

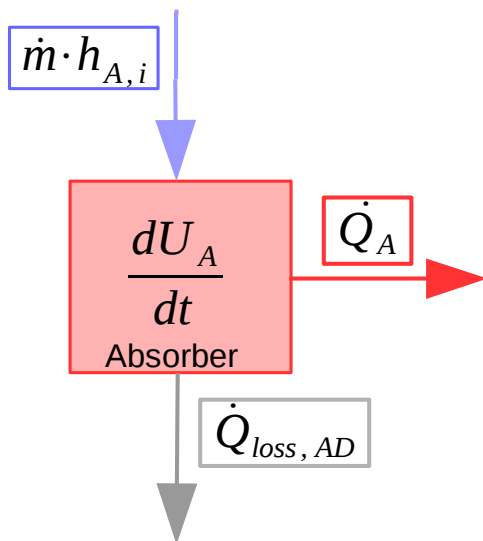


Figure 10. absorber balance

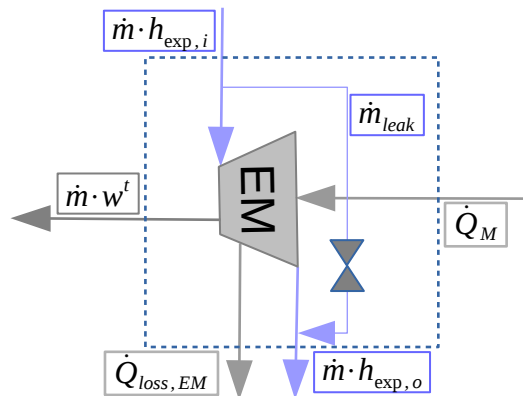


Figure 11. expansion machine balance

Evaporator(E)

$$\frac{dU_E}{dt} = \dot{Q}_E - \dot{m} \cdot h_{E,o}(T_E, \chi) - \dot{Q}_{loss,E} \quad (27)$$

with χ the vapor quality of the escaping mass flow.

The internal energy of the evaporator consists of the internal energy of the working fluid within the component and the internal energy of the component itself and connected periphery

$dU_{E,P} = C_{E,P}dT_E$ (pipes and walls etc.):

$$\frac{dU_E}{dt} = \frac{dm_E}{dt} \cdot h_E(T_E) + m_E \frac{dh_E(T_E)}{dt} + C_{E,P} \frac{dT_E}{dt}, \quad (28)$$

with h_E being the enthalpy of the liquid working fluid in the E.

Inserted into eq. 27 and with $\dot{m} = -\frac{dm_E}{dt}$ and $dh_E = c_p dT_E$, we find for the heat flow into the component:

$$\dot{Q}_E = \dot{m} (h_{E,o}(T_E, \chi) - h_E(T_E)) + \underbrace{(m_E \cdot c_{pE} + C_{E,P})}_{C_E(x)} \frac{dT_E}{dt} + \dot{Q}_{loss,E} \quad (29)$$

As the mass of working fluid in the E depends on the salt mass fraction in the A, the thermal mass C_E is a function of x .

With the definition of the vapor quality χ the output enthalpy in eq. 29 can be replaced by:

$$h_{E,o}(T_E, \chi) = \chi \cdot h''(T_E) + (1 - \chi) \cdot h'(T_E), \quad (30)$$

and as $h_E = h'(T_E)$ we find:

$$\dot{Q}_E = \dot{m} \cdot \chi \Delta h^{lv} + C_E(x) \frac{dT_E}{dt} + \dot{Q}_{loss,E} \quad (31)$$

Absorber

$$\frac{dU_A}{dt} = \dot{m} \cdot h_{A,i} - \dot{Q}_A - \dot{Q}_{loss,A} \quad (32)$$

The internal energy of the A is composed analogously to that of the E with the only difference that the working fluid is the liquid sorbate.

$$\frac{dU_A}{dt} = \frac{dm_A}{dt} \cdot h_A(T_A, x) + m_A \frac{dh_A(T_A, x)}{dt} + C_{A,P} \frac{dT_A}{dt} \quad (33)$$

h_A is the enthalpy of the liquid sorbate.

Inserted into eq. 32 and with $\dot{m} = \frac{dm_A}{dt}$, we find for the heat flow out of the A:

$$\dot{Q}_A = \dot{m} (h_{A,i} - h_A(T_A, x)) - m_A \frac{dh_A(T_A, x)}{dt} - C_{AP} \frac{dT_A}{dt} - \dot{Q}_{loss,A} \quad (34)$$

The working fluid in the E has a lower temperature than the working fluid in the A. Between those two temperatures the heat capacity can be set constant, so that:

$$h_E(T_A) - h_E(T_E) = c_{pE} (T_A - T_E) \quad (35)$$

together with the definition of the solution enthalpy:

$$l(T_A, x) := \underbrace{h'(T_A)}_{\text{sat. enthalpy of liquid water}} - \underbrace{h_A^{eq}(x, T_A)}_{\text{equ. enthalpy of solution}} + x \underbrace{\frac{\partial h_A^{eq}(x, T_A)}{\partial x}}_{\text{excess enthalpy}}, \quad (36)$$

and with $h'(T_A) = h_E(T_A)$, the enthalpy difference in the brackets behind the mass flow rate in eq. 34 can be written as:

$$\begin{aligned} h_{A,i} - h_A(T_A, x) \\ = h_{A,i} - h_E(T_E) + h_E(T_E) - h_A(T_A, x) \end{aligned} \quad (37)$$

$$\begin{aligned} = h_{A,i} - h_E(T_E) + l(T_A, x) - x \frac{\partial h_A(T_A, x)}{\partial x} \\ - c_{pE}(T_A - T_E) \end{aligned} \quad (38)$$

Using the differential for the enthalpy of the absorbate:

$$\frac{dh_A(T_A, x)}{dt} = \frac{\partial h_A(x, T_A)}{\partial x} \frac{dx}{dt} + \frac{\partial h_A(x, T_A)}{\partial T_A} \frac{dT_A}{dt} \quad (39)$$

$$= \frac{\partial h_A(x, T_A)}{\partial x} \frac{dx}{dt} + c_{pA}(x) \frac{dT_A}{dt} \quad (40)$$

eq. 34 can be written as:

$$\begin{aligned} \dot{Q}_A = \dot{m} \left(h_{A,i} - h_E(T_E) + l(T_A, x) - x \frac{\partial h_A(T_A, x)}{\partial x} - c_{pE}(T_A - T_E) \right) \\ - m_A \left(\frac{\partial h_A(x, T_A)}{\partial x} \frac{dx}{dt} + c_{pA}(x) \frac{dT_A}{dt} \right) - C_{AP} \frac{dT_A}{dt} - \dot{Q}_{loss,A} \end{aligned} \quad (41)$$

whereas the terms with the partial differentials of the solution enthalpy can be canceled out because (see also eq. 15):

$$m_A \cdot dx = -x \cdot dm_A = -x \cdot \dot{m} \cdot dt. \quad (42)$$

It follows:

$$\begin{aligned} \dot{Q}_A = \dot{m} (h_{A,i} - h_E(T_E) + l(x, T_A) - c_{pE} \Delta T_{dis}) \\ - \underbrace{(m_A \cdot c_{pA}(x) + C_{AP})}_{C_A(x)} \frac{dT_A}{dt} - \dot{Q}_{loss,A} \end{aligned} \quad (43)$$

with $\Delta T_{dis} := T_A - T_E$.

Expansion Machine

$$\frac{dU_{EM}}{dt} = \dot{m}(h_{Exp,i} - w^t - h_{Exp,o}) \quad (44)$$

Adiabatic expansion is assumed, so that $\delta \dot{Q}_M = 0$ and $\dot{Q}_{loss,EM} = 0$. The expansion device is small compared to the large heat exchangers with working fluid and storage reservoir. For that reason and simplicity, changes of the internal energy within the expansion device are neglected. Note, that w^t is not the measured mechanical work w_{mech}^t here, but:

$$w_{dis}^t = \frac{w_{mech}^t}{\eta_{mech}} = w_{rev,exp}^t \cdot \eta_{i,EM} \cdot \eta_{th} \quad (45)$$

$$(46)$$

For the enthalpy at the outlet we find:

$$h_{Exp,o} = h_{Exp,i} - w^t - \frac{\dot{Q}_{loss,EM}}{\dot{m}} \quad (47)$$

with $\delta q_M := \frac{\dot{Q}_M}{\dot{m}}$.

Efficiencies $\eta_{i,EM}$ is the inner efficiency of the expansion machine and $\eta_{vol,EM}$ is the volumetric efficiency respectively, defined as the ratio of mass flow excluding the inner machine leakages to the mass flow including them (compare figure 11):

$$\eta_{vol,EM} = \frac{\dot{m}}{\dot{m} + \dot{m}_{leak}} \quad (48)$$

The inner machine efficiency is defined as the ratio of real shaft work w^t to isentropic enthalpy difference along the machine Δh_{isen} :

$$\eta_{i,EM} = \frac{w_{dis}^t}{\Delta h_{isen,dis}} \quad (49)$$

$$(50)$$

Combined energy balance of absorber and expansion machine

The expanded vapor directly flows into the absorber, such that

$$h_{Exp,o} = h_{A,i}.$$

Combining eq. 47 and 43, we find:

$$\begin{aligned} \dot{Q}_A = & \dot{m} (h_{Exp,i} - h_E(T_E) + l(x, T_A) - c_{pE} \Delta T_{dis} - w^t) \\ & - C_A(x) \frac{dT_A}{dt} + \delta \dot{Q}_M - \dot{Q}_{loss,A} - \dot{Q}_{loss,EM} \end{aligned} \quad (51)$$

The vapor from the evaporator directly enters the expansion machine, such that

$$h_{Exp,i} = h_{E,o}(T_E, \chi).$$

Eq. 51 can be written as follows:

$$\begin{aligned} \dot{Q}_A = & -P^t + \dot{m} \cdot (\chi \Delta h^{lv} + l_A(x, T_A) - c_{pE} \Delta T_{dis}) \\ & - C_A(x) \frac{dT_A}{dt} + \delta \dot{Q}_M - \dot{Q}_{loss,A} - \dot{Q}_{loss,EM} \end{aligned} \quad (52)$$

Deduction of the guiding differential equations

In case of a directly coupled system, we find:

$$\dot{Q}_A = \dot{Q}_E = \dot{Q}_{dis} \quad (53)$$

Using the heat transfer characteristic of the system:

$$\dot{Q}_{dis} = k \cdot A \cdot \Delta T_{dis} \quad (54)$$

We find for the A balance (eq. 52):

$$\frac{dT_A}{dt} = -\frac{k \cdot A}{C_A(x)} \Delta T_{dis} + \frac{\chi \Delta h^{lv}(T_E) + l_A(x, T_A) - c_{p,E} \Delta T_{dis}}{C_A(x)} \dot{m} - \frac{P^t}{C_A(x)} - \frac{\dot{Q}_{loss,A}}{C_A(x)} \quad (55)$$

and from the E balances (eq. 31):

$$\frac{dT_E}{dt} = \frac{k \cdot A}{C_E(x)} \Delta T_{dis} - \frac{\chi \Delta h^{lv}(T_E)}{C_E(x)} \dot{m} - \frac{\dot{Q}_{loss,E}}{C_E(x)} \quad (56)$$

The guiding differential equation for ΔT_{dis} can be found by subtracting eq. 56 from 55 and replacing the power output:

$$P^t = \dot{m} \cdot \eta_{vol} \cdot w_{rev}^t(x(t), T_A) \cdot \eta_{i,EM} \cdot \eta_{th} \quad (57)$$

Normalization of Thermal masses with salt mass

$$\frac{C_A(x)}{m_{salt}} = \frac{C_{A,P}}{m_{salt}} + c_{p,A} \frac{1}{x} \quad (58)$$

$$\frac{C_E(x)}{m_{salt}} = \frac{C_{E,P}}{m_{salt}} + c_{p,E} \left(\underbrace{\frac{1}{x_{discharged}} - \frac{1}{x_{charged}}}_{\frac{m_{water}}{m_{salt}}} + 1 - \frac{1}{x} \right) \quad (59)$$

The ratio of thermal masses of the periphery to the entire salt mass $\frac{C_{A/E,P}}{m_{salt}}$ should get smaller the larger the storage is. However, it will be neglected here - so, we assume a rather large system with a small surface to volume ratio. For very small plants this should not be neglected.

Thermodynamic Evaluation of an Experimental WHR ORC Test Rig with Quasi-Impulse Cantilever Turbine

T. Popp^{1*}, A. P. Weiß², F. Heberle¹, P. Streit² and D. Brüggemann¹

¹ Chair of Engineering Thermodynamics and Transport Processes (LTTT), Center of Energy Technology (ZET), University of Bayreuth, Universitätsstraße 30, 95447 Bayreuth, Germany

² Center of Excellence for Cogeneration Technologies (CECoGen), Technical University of Applied Sciences Amberg-Weiden, Kaiser-Wilhelm-Ring 23, 92224 Amberg, Germany

*Corresponding author: tobias.popp@uni-bayreuth.de

Abstract

Organic Rankine Cycle (ORC) Systems are a commonly used technology for recovering the low temperature waste heat in energy intensive industries. ORCs are generally designed for one operating point, which is often the maximum available thermal power of the upstream industry process. However, these processes tend to fluctuate in mass flow rate, temperature or even both. Therefore, the design of the ORC based on the maximum power of the waste heat leads not necessarily to the optimum concerning the energy yield. In the present paper, an experimental ORC test rig running at different operating points is evaluated under thermodynamic criteria. These analyses are focused on the performance of the main ORC components in design and off-design conditions. Special emphasis is put on the effect of the decreasing turbine inlet pressure in part load due to a fixed swallowing capacity of the deployed Quasi-Impulse Cantilever turbine. An outlook how to cope with the reduced ORC performance in part load under technical aspects is given.

Keywords: Organic Rankine Cycle, Thermodynamic Evaluation, Waste Heat Recovery, Cantilever Turbine

Introduction/Background

For recovering the waste heat of industrial processes, often Organic Rankine Cycles are the means of choice due to the possibility of exploiting low and medium temperature heat sources. Generally, all components of the ORC are designed for one operating point of the upstream process and only little attention [1,2] is paid on the off-design performance of the ORC. However, this design approach may not lead to the maximum energy yield. Depending on the process, the mass flow rate, the temperatures or even both can fluctuate significantly [3, 4]. For these volatile waste heat profiles, the total energy yield of the ORC plant may not be achieved by designing for the maximum power, due to the off-design performance of the different components of the WHR plant. Thus, to enable a more advanced design approach for the cycle, the characteristic off-design behavior of the various ORC components should be taken into account. In this context, the authors perform a thermodynamic evaluation of an experimental ORC plant located at the Center of Energy Technology at the University of Bayreuth.

Already other authors performed thermodynamic evaluations of experimental ORC test rigs with various heat sources [5–11], some of them even in off-design operation. Bianchi et al. [5] for instance performed a thermodynamic analysis of a ORC test rig with the working fluid R134a and a special radial piston expander (up to 1.15 kW) as expansion machine. They used an electrical boiler as heat source, which created a maximal inlet temperature of 90 °C for the heat transfer fluid (water). The paper shows off-design characteristics of every important component (pump, evaporator, expander & turbine) of the cycle. The research team observed

a maximum expander efficiency of approx. 43%, whereas the maximum value for the gross and net cycle efficiencies achieved 4.5 and 2.2%, respectively. Carraro et al. [6] experimentally investigated a biomass-fired micro-ORC system with an scroll expander (up to 2.53 kW) and R245fa as working fluid. By means of the biomass-firing, thermal oil in the intermediate cycle was heated to a temperature of max. 155 °C. The authors showed the influence of a variation of the heat source (thermal oil) temperature and mass flow rate as well as a variation of the mass flow rate of cooling water on the cycles' performance. A maximum electric efficiency of the cycle of 7.3% was observed. With 150 °C as thermal oil temperature, the researchers achieved an expander efficiency of 57%. Unamba et al. [10] analyzed a ORC test bench with an electric oil heater as heat supply, an scroll expander (1 kW_{el}) as expansion machine and R245fa as working fluid. Oil temperatures in the range of 120-140 °C and working fluid mass flow rates between 0.0088 kg/s and 0.0337 kg/s were investigated. An exergetic analysis for the components of the cycles was performed, showing that the highest exergy destruction occurs in the evaporator, the second highest in the expander. A thermal efficiency of maximum 6% was achieved for the described test bench. Wang et al. [11] performed experimental investigations on a small-scale ORC test bench with scroll expander (3 kW_{el}) and the working fluid R123. Using a natural gas burner, exhaust gas was generated, which was afterwards mixed with air and served the direct evaporator as heat source. For 15 steady-state operation points, they performed an analysis of the thermodynamic inlet and outlet conditions of the cycle's main components. The research group paid special attention to the data fluctuation. They detected the largest fluctuation amplitude at the pump outlet, due to the applied diaphragm pump.

All the aforementioned publications have a closer look at the thermodynamic behavior of experimental test rigs, which use a volumetric expander (often a scroll expander) as expansion machine. The investigated heat source temperatures are rather low, which also favors the application of volumetric expanders. There are only few publications in literature, which show the thermodynamic behavior of the entire WHR plant with a "high-temperature" ORC fluid. Mascuch et al. [12] show operational data of a biomass-fired ORC module applying direct evaporator and the working fluid hexamethyldisiloxane (MM). Their in-house developed rotary vane expander generates a maximum power of 2 kW_{el}. The publication rather focuses on experiences of field operation. Uusitalo et al. [13] perform an analysis on a small-scale ORC test bench, which uses the exhaust gases from a Diesel engine as heat source. Their investigations are focused on the operational behavior of the applied supersonic radial turbine, which is mounted on one shaft with the main pump. A maximum electrical power output of 6 kW was measured.

From the authors' point of view, there is a lack of experimental results concerning the (off-design) energy balance of ORCs with a high-temperature fluid and a turbine as expansion machine. In this paper, a thermodynamic evaluation of design and off-design characteristics of all main components of the ORC, namely pump, evaporator (combination of preheater, evaporator and superheater), turbine and condenser is presented. By varying the working fluid amount in the plant, different condensing pressures were implemented. Combining this approach with a variation of working fluid mass flow rate (50-100%) enabled the thermodynamic evaluation of the ORC plant in a wide range of pressure ratios.

The test rig at the University of Bayreuth (see Figure 1) is designed to exploit the waste heat in the exhaust gas of an upstream industry process, simulated by a propane gas burner. It uses the high-temperature working fluid hexamethyldisiloxane (MM) at a design pressure level of 6 bar ($T_{turbine,in} = 176$ °C) to generate an electrical power output of approx. 12 kW by means of a Quasi-Impulse Cantilever turbine (see [14]). For heat rejection, an intermediate water/glycol circuit with an air-cooler located outside the building is used. The thermal power fed into the ORC can be varied. Hence, the ORC can be operated with mass flow rates lower

than design (down to 50%). Since a turbine is used as expansion machine, reduced mass flow rate leads to reduced turbine inlet pressure (i.e. evaporation pressure). Thus, the influence of a decreasing upper cycle pressure in part load on the cycles' overall performance is studied and the operational behavior of the various components is analyzed.

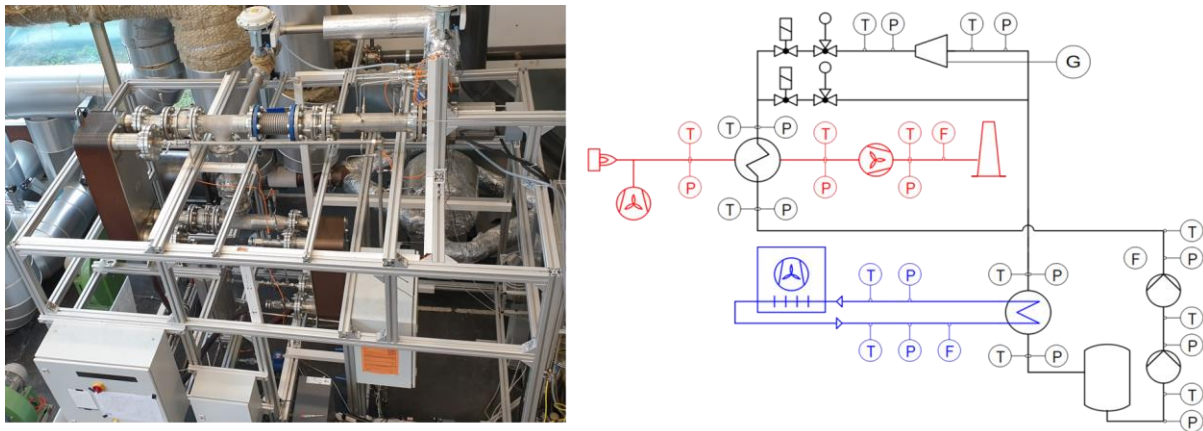


Figure 1: Photograph (left) and R&I scheme (right) of the experimental ORC plant at the University of Bayreuth

In Table 1, an overview of the main components of the experimental test rig is given. Since it was designed for waste heat profiles occurring in industry, a propane gas burner is used to simulate the waste heat of the upstream process. For pumping the low-pressure fluid at the required pressure level, two pumps are applied. The piston diaphragm pump was reused from a former plant. To fit the boundary conditions of the current plant, an additional centrifugal pump as booster pump is required to avoid cavitation. For preheating, evaporating and overheating, a Plate & Shell heat exchanger from the manufacturer GESMEX is used. For the sake of simplicity, in the following, this heat exchanger is referred to as “evaporator”. As expansion machine, a Quasi-Impulse Cantilever turbine is used, which was already presented in previous publications [14,15]. The plate heat exchanger serving as condenser was provided by ALPHA LAVAL. An air cooler outside the building is used to cool the intermediate water/glycol cycle, which serves as cold supply for the condenser.

Table 1: Main components of the ORC test rig

Component	Type
Heat supply	Propane gas burner
Pumps	Centrifugal & piston diaphragm pump
“Evaporator”	Plate & Shell type heat exchanger
Expander	Quasi-Impulse Cantilever turbine
Condenser	Plate heat exchanger
Cold supply	Air cooler

Already in previous publications [14–17], data generated with test rig was published by the authors, focusing on characterizing different turbine types. To enable solving the energy

balance for the whole system, the research plant was equipped with additional measurement sensors. For all sensors, it was ensured that the measurement range fits to the measurement task to minimize the measurement error as far as possible. In the following, the equations used for calculating the efficiencies of the main components are listed. For calculating the thermodynamic properties of the working fluid as well as those of the exhaust gas, the REFPROP Data Base, Version 9.1 [18] is used.

The pump efficiency is calculated as the ratio of hydraulic power added to the working fluid and the electrical power consumption of the two pumps.

$$\eta_{pump} = \frac{\dot{V}_{ORC} \cdot \Delta p_{pump}}{P_{el,pump}} \cdot 100\% \quad (1)$$

Where \dot{V}_{ORC} is the volumetric flow rate of the liquid working fluid (MM), Δp_{pump} the pressure difference over the two pumps and $P_{el,pump}$ the electrical power, consumed by the two pumps. The evaporator efficiency is defined as the ratio of the enthalpy flux absorbed from the high-pressure working fluid and the enthalpy flux delivered by the exhaust gas. For calculating the enthalpy fluxes of the exhaust gas, the composition (H₂O and CO₂) was measured by means of an FTIR analyzer. The contents of the remaining components were calculated based on CO₂ content and the corresponding chemical reactions.

$$\eta_{evaporator} = \frac{\dot{H}_{ORC,EV,out} - \dot{H}_{ORC,EV,in}}{\dot{H}_{EG,in} - \dot{H}_{EG,out}} \cdot 100\% \quad (2)$$

With $\dot{H}_{ORC,EV,in}$ & $\dot{H}_{ORC,EV,out}$ being the inlet and outlet enthalpy fluxes of the high-pressure working fluid at the evaporator (EV) and $\dot{H}_{EG,in}$ & $\dot{H}_{EG,out}$ representing the exhaust gas enthalpy fluxes.

For evaluating the turbine, the total-to-static isentropic efficiency is used. To avoid the determination of a too optimistic efficiency, the turbine outlet temperature is not used to calculate the turbine efficiency. Instead, based on a known efficiency behavior of the electronics (generator & power electronics), the turbine shaft power can be calculated based on the electrical power output. This approach was already used in previous publications of the authors [14–17].

$$\eta_{turbine} = \frac{\frac{P_{el,turbine}}{\eta_{electronics}}}{\dot{m}_{ORC} \cdot \Delta h_{is,turbine}} \cdot 100\% \quad (3)$$

$P_{el,turbine}$ is the electrical power at the outlet of the feed-in unit, $\eta_{electronics}$ the aforementioned efficiency of generator and power electronics, \dot{m}_{ORC} the mass flow rate of the working fluid and $\Delta h_{is,turbine}$ the isentropic enthalpy drop over the turbine.

The efficiency of the condenser was calculated as the heat flux added to the cooling water (CW) in relation to the enthalpy flux difference, produced by condensing the low-pressure working fluid in the condenser (CD).

$$\eta_{condenser} = \frac{\dot{m}_{CW} \cdot c_{p,CW} \cdot \Delta T_{CW}}{\dot{H}_{ORC,CD,in} - \dot{H}_{ORC,CD,out}} \cdot 100\% \quad (4)$$

With \dot{m}_{CW} as the mass flow rate of cooling water, $c_{p,CW}$ as isobaric heat capacity of the cooling water and ΔT_{CW} as temperature difference of the cooling water over the condenser. $\dot{H}_{ORC,CD,in}$

and $\dot{H}_{ORC,CD,out}$ represent the inlet and outlet enthalpy fluxes of the low-pressure working fluid at the condenser.

Besides the evaluation of the design and off-design performance of every main component of the cycle, another objective of the present paper is to evaluate the energy conversion chain of the cycle (see Figure 2), beginning with the available exergy flux of the exhaust gas and ending with the electrical power output of the turbine (or feed-in unit respectively). In this context, the waste heat recovery efficiency is evaluated in design and off-design condition.

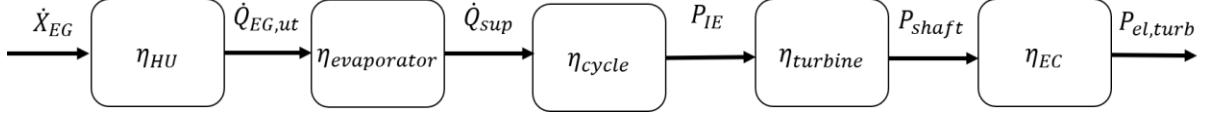


Figure 2: Energy conversion chain of the ORC

The first step of the energy conversion chain is described by the heat utilization rate η_{HU} . It represents the ratio of utilized exhaust gas heat flux $\dot{Q}_{EG,ut}$ and the exergy flux \dot{X}_{EG} available from the exhaust gas (reference temperature 20 °C).

$$\eta_{HU} = \frac{\dot{Q}_{EG,ut}}{\dot{X}_{EG}} \cdot 100\% = \frac{\dot{H}_{EG,in} - \dot{H}_{EG,out}}{\dot{X}_{EG}} \cdot 100\% \quad (5)$$

As in the denominator of Equation (2), $\dot{H}_{EG,in}$ and $\dot{H}_{EG,out}$ are the inlet and outlet enthalpy fluxes of the exhaust gas at the evaporator.

The evaporator efficiency $\eta_{evaporator}$ sets the heat flux supplied to the ORC in relation to the utilized exhaust gas heat flux. It is calculated in the same manner as in Equation (2).

$$\eta_{evaporator} = \frac{\dot{Q}_{sup}}{\dot{Q}_{EG,ut}} \cdot 100\% = \frac{\dot{H}_{ORC,EV,out} - \dot{H}_{ORC,EV,in}}{\dot{H}_{EG,in} - \dot{H}_{EG,out}} \cdot 100\% \quad (6)$$

To calculate the thermodynamic efficiency of the cycle η_{cycle} , the ratio of isentropic expansion work P_{IE} and supplied heat flux \dot{Q}_{sup} is built.

$$\eta_{cycle} = \frac{P_{IE}}{\dot{Q}_{sup}} \cdot 100\% = \frac{\dot{m}_{ORC} \cdot \Delta h_{is,turbine}}{\dot{H}_{ORC,EV,out} - \dot{H}_{ORC,EV,in}} \cdot 100\% \quad (6)$$

Where P_{IE} is calculated from the mass flow rate of the working fluid \dot{m}_{ORC} and the isentropic enthalpy drop over the turbine $\Delta h_{is,turbine}$.

The turbine efficiency describes the amount of thermodynamically available power that is converted into shaft power. Numerator and denominator equal those of Equation (3).

$$\eta_{turbine} = \frac{P_{shaft}}{P_{IE}} \cdot 100\% \quad (7)$$

As already mentioned above, the efficiency of the electrical chain η_{EC} (EC, generator and feed-in unit) is known from individual measurements. It describes the amount of shaft power available as electrical power after the last energy conversion step.

$$\eta_{EC} = \frac{P_{el,turb}}{P_{shaft}} \cdot 100\% \quad (8)$$

To evaluate the efficiency of the waste heat recovery process, the waste heat recovery efficiency is defined as follows:

$$\eta_{WHR} = \frac{P_{el,turb}}{\dot{X}_{EG}} \cdot 100\% \quad (9)$$

It describes the share of the available exhaust gas exergy eventually available as electrical power at the end of the energy conversion chain.

Discussion and Results

In previous publications, the authors already showed extensive experimental results concerning the off-design efficiency of the Quasi-Impulse Cantilever turbine [14,17]. However, the remaining components of the cycle were not yet analyzed in detail. In the present paper, besides more detailed turbine investigations, characteristic curves of the heat exchangers and the pumps are provided.

In Figure 3, the efficiency characteristics of all main components of the ORC for a mass flow rate down to 50% of the design (0.320 kg/s) are shown. The data points derive from a measurement campaign with 7 measurement days in total, outliers were thereby ignored. By increasing the amount of fluid in the test rig, the condensing pressure was intentionally increased. Hence, a broad data basis, even for high condensing/turbine outlet pressures, occurring at higher ambient temperatures in the summer, was created. Per measurement day, a variation from 50 to 100% working fluid mass flow rate was performed. The variation of the working fluid mass flow rate also results in a slight variation of the condensing pressure, but the predominant effect stems from the MM filling quantity. For each mass flow rate, the rotational speed of maximum efficiency was searched for the turbine. Table 1 shows the considered operating points during the measurement campaign. From this table, the approximately linear correlation between mass flow rate and turbine inlet pressure becomes obvious.

Table 1: Considered operation points during the measurement campaign

$\frac{\dot{m}_{ORC}}{\dot{m}_{ORC,Design}}$ (%)	\dot{m}_{ORC} (g/s)	$\dot{Q}_{EG,ut}$ (kW)	$p_{turbine,in}$ (bar)
50	160	96	3.2
60	192	114	3.8
70	224	132	4.4
80	256	150	5.0
90	288	168	5.6
100	320	186	6.2

In Figure 3 (a), the pump efficiency in dependency of the ORC mass flow rate is shown. As discussed above, the piston diaphragm main pump was reused from a former project, which leads to the necessity of an additional booster pump to meet the required boundary conditions without cavitation. The additional energy demand of the booster pump explains the rather low total pump efficiency of approx. 30% at design point. In general, the measurement data shows a good reproducibility and the shape of the curve matches the expectations.

In Figure 3 (b), the evaporator efficiency is shown as function of the MM mass flow rate. Interestingly, the Plate & Shell heat exchanger shows a weak dependency on the cold sides' mass flow rate. The highest efficiency of approx. 83% was reached at design mass flow rate.

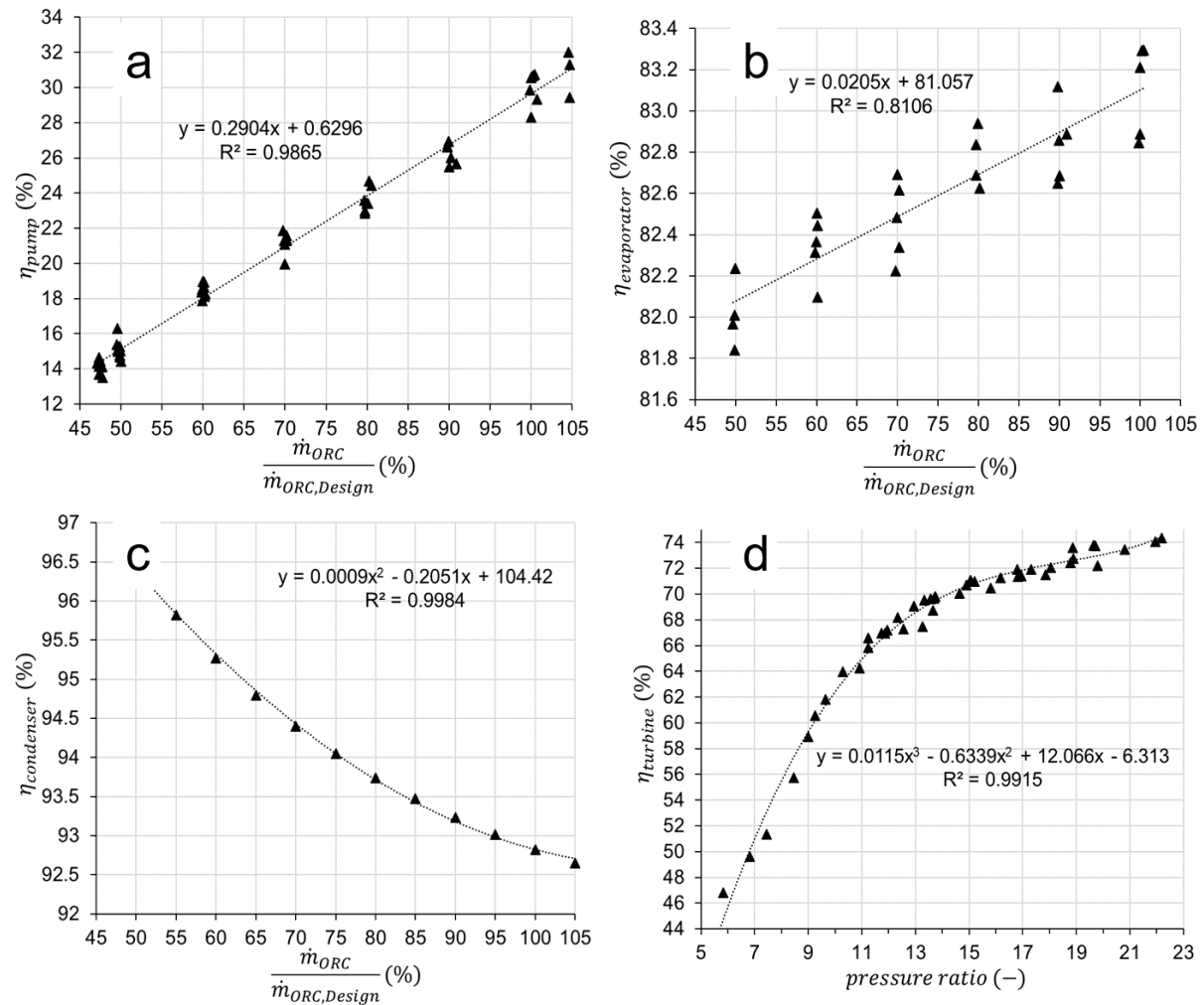


Figure 3: Pump (a), evaporator (b) and condenser (c) efficiency as function of working fluid mass flow rate, isentropic turbine efficiency (d) as function of pressure ratio

The condenser efficiency in dependency of the working fluid mass flow rate is depicted in Figure 3 (c). To create this graph, firstly, a fit for the heat flux added to the cooling water was derived from the measurement data. Secondly, the fit for the cooling water heat flux was divided by a fit for the condensing of the low-pressure fluid. This enables the derivation of a quite clear trend, despite the rather low temperature differences in the cooling water, which result in a strong scattering of the heat added to the cooling water. Looking at the graph, a minimal condenser efficiency of approx. 92.5% can be observed at 105% mass flow rate.

In Figure 3 (d), the total-to-static isentropic turbine efficiency is analyzed. In contrast to the other 3 graphs, it shows the turbine efficiency as function of the pressure ratio, not the mass

flow rate. From the performed experiments, it could clearly be deduced, that the isentropic turbine efficiency does not depend on the working fluid mass flow rate. The obtained isentropic efficiency as function of the total-to-static pressure ratio complements previously published data [14]. In contrast to the former publications, a much broader range of pressure ratios (down to approx 5.5, design 18.75) could be achieved in the measurements. The reproducibility of the turbine efficiency is remarkable. Even when targeting the same pressure ratio with different inlet pressures i.e. mass flow rates, the resulting turbine efficiency is almost identical. For a small highly-loaded turbine with a power output of about 12 kW_{el}, the measured peak efficiency of approx. 74% is certainly satisfactory.

In the following, the 5 steps of the energy conversion chain, as well as the waste heat recovery efficiency are, analyzed. The analysis has to be split in 2 different chapters. In the first chapter, those energy conversion steps mainly depending on the working fluid mass flow rate are discussed. In the second chapter, the influence of the pressure ratio on the remaining conversion steps is shown.

Figure 4 depicts the heat utilization rate, the evaporator efficiency and the efficiency of the electrical chain in dependency of the mass flow rate percentage. The heat utilization rate improves slightly from 89% to 93% moving from 50% mass flow rate to 100%. The reproducibility is very good. As already discussed above, the evaporator efficiency shows only a weak dependency on the mass flow rate of the working fluid. The efficiency of the electrical chain is mainly affected by the electrical power output of the feed-in unit. Hence, it obviously increases with rising mass flow rates. In addition, the efficiency of the electrical chain highly depends on the pressure ratio of the turbine, because it also has a strong impact on the electrical power output. This is why a rather broad range of efficiencies of the electrical chain can be observed for the same mass flow rate.

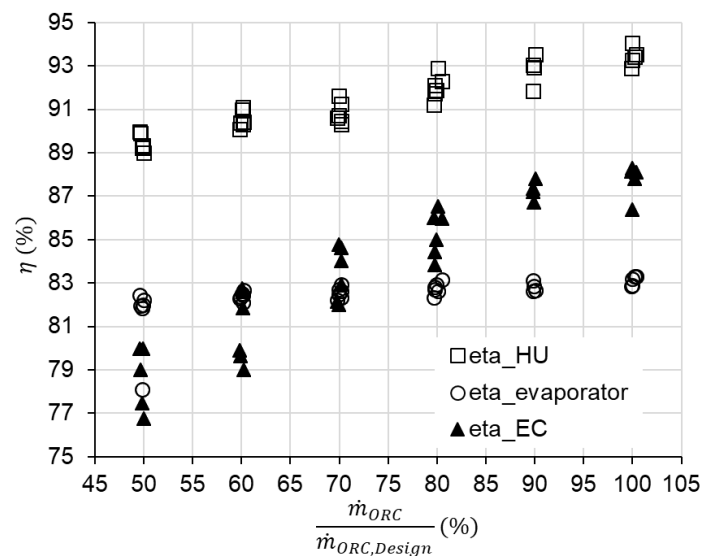


Figure 4: Heat utilization rate, evaporator efficiency and efficiency of the electrical chain as a function of the mass flow rate percentage

In contrast to the efficiencies shown above, the cycle efficiency and the turbine efficiency mainly depend on the pressure ratio. The applied Cantilever turbine has a fixed geometry and therefore a theoretically constant swallowing capacity (for an ideal gas). This means that an increase in mass flow rate is associated with an increase in turbine inlet pressure and (for a constant condensing outlet pressure) also in pressure ratio. As already discussed, the same pressure ratio can be achieved by different combinations of mass flow rate and condensing pressure, resulting in the same turbine efficiency. As becomes obvious from Figure 5, also the

cycle efficiency is not affected by a variation in mass flow rate but just from the pressure ratio. A higher pressure ratio leads to a higher available isentropic enthalpy drop for the turbine.

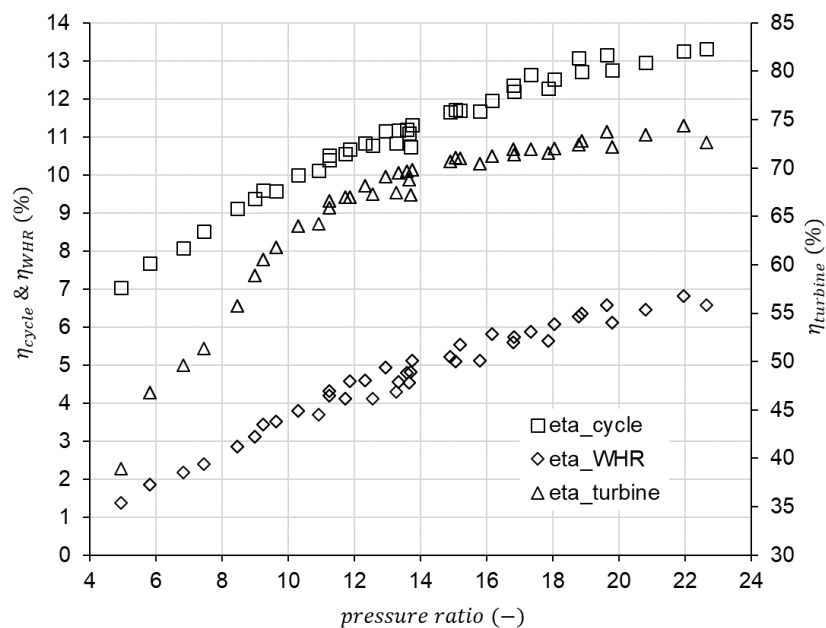


Figure 5: Heat utilization rate, evaporator efficiency, turbine efficiency, efficiency of the electrical chain, cycle efficiency and waste heat recovery efficiency as function of the pressure ratio

Based on the shown analysis of the different partial efficiencies, it becomes obvious that the effects of the pressure ratio on the cycle and turbine efficiency (Figure 5) clearly outweigh the effects of dependencies on the mass flow rate in Figure 4. Moving from pressure ratio 22 to 6 the waste heat recovery efficiency drops from approx. 7% to just about 2% (Figure 5). As a result, it can be stated, that the waste heat recovery efficiency of the analyzed ORC test rig mainly depends on the available pressure ratio.

This result is of high significance for performance of ORCs in waste heat recovery applications with fluctuating heat sources. A decrease in waste heat power is associated with a lower ORC mass flow rate and, for turbines with a fixed swallowing capacity, therefore a drop in turbine inlet pressure. Consequently, the pressure ratio decreases and the waste heat recovery efficiency significantly deteriorates. In another publication [19], the authors already described possibilities to cope with the circumstance of fluctuating heat sources e.g. different storage technologies or buffering by means of an intermediate cycle. When designing a new WHR ORC plant, another possibility would be using the above shown characteristics in conjunction with the present heat source fluctuation of the upstream process and simulating the best compromise design point. However, the authors follow a different approach:

A turbine, which managed to hold its inlet pressure constant by adapting the swallowing capacity smart to the available heat/working fluid mass flow rate, would be able to prevent or at least counteract this efficiency deterioration at off-design heat fluxes of the upstream process. The development of a turbine with adjustable swallowing capacity is subject of current and future research activities of the authors [19].

Summary/Conclusions

By thorough experimental investigations, detailed off-design characteristics of heat exchangers, the feed pump as well as the turbine were provided. Especially the performance map for the turbine efficiency in a very broad range of pressure ratio may be a valuable contribution for the simulation community. From the presented experimental results, it became obvious that the off-design performance of the components leads in part load to a significant decrease of the overall waste heat recovery efficiency of the plant. Particularly the changing upper process pressure, due to the turbine's fixed swallowing capacity, has a strong influence on the off-design behavior of the cycle as well as its components. Thus, the authors are currently developing a turbine with adjustable swallowing capacity. In consequence, the upper pressure of the cycle will be kept constant and thereby the off-design behavior of cycle will be significantly improved.

Acknowledgements

The work presented in this paper was conducted within the frame of the BFS project (AZ-1344-18) “*TurboSmart – adaptive Mikroexpansionsturbine für die Energierückgewinnung*”. The authors want to thank the Bavarian Research Foundation (BFS) for their financial support.

References:

- [1] Manente, G., Toffolo, A., Lazzaretto, A., and Paci, M., “An Organic Rankine Cycle off-design model for the search of the optimal control strategy,” *Energy*; Vol. 58, 2013, pp. 97–106. doi: 10.1016/j.energy.2012.12.035.
- [2] Schuster, S., Markides, C. N., and White, A. J., “Design and off-design optimisation of an organic Rankine cycle (ORC) system with an integrated radial turbine model,” *Applied Thermal Engineering*; Vol. 174, 2020, p. 115192. doi: 10.1016/j.applthermaleng.2020.115192.
- [3] Pili, R., Romagnoli, A., Spliethoff, H., and Wieland, C., “Techno-Economic Analysis of Waste Heat Recovery with ORC from Fluctuating Industrial Sources,” *Energy Procedia*; Vol. 129, 2017, pp. 503–510. doi: 10.1016/j.egypro.2017.09.170.
- [4] Jiménez-Arreola, M., Pili, R., Wieland, C., and Romagnoli, A., “Analysis and comparison of dynamic behavior of heat exchangers for direct evaporation in ORC waste heat recovery applications from fluctuating sources,” *Applied Energy*; Vol. 216, 2018, pp. 724–740. doi: 10.1016/j.apenergy.2018.01.085.
- [5] Bianchi, M., Branchini, L., Casari, N., Pascale, A. de, Melino, F., Ottaviano, S., Pinelli, M., Spina, P. R., and Suman, A., “Experimental analysis of a micro-ORC driven by piston expander for low-grade heat recovery,” *Applied Thermal Engineering*; Vol. 148, 2019, pp. 1278–1291. doi: 10.1016/j.applthermaleng.2018.12.019.
- [6] Carraro, G., Bori, V., Lazzaretto, A., Toniato, G., and Danieli, P., “Experimental investigation of an innovative biomass-fired micro-ORC system for cogeneration applications,” *Renewable Energy*; Vol. 161, 2020, pp. 1226–1243. doi: 10.1016/j.renene.2020.07.012.
- [7] Kosmadakis, G., Manolakos, D., and Papadakis, G., “Experimental investigation of a low-temperature organic Rankine cycle (ORC) engine under variable heat input

- operating at both subcritical and supercritical conditions,” *Applied Thermal Engineering*; Vol. 92, 2016, pp. 1–7. doi: 10.1016/j.applthermaleng.2015.09.082.
- [8] Manolakos, D., Kosmadakis, G., Ntavou, E., and Tchanche, B., “Test results for characterizing two in-series scroll expanders within a low-temperature ORC unit under partial heat load,” *Applied Thermal Engineering*; Vol. 163, 2019, p. 114389. doi: 10.1016/j.applthermaleng.2019.114389.
- [9] Peris, B., Navarro-Esbrí, J., Molés, F., González, M., and Mota-Babiloni, A., “Experimental characterization of an ORC (organic Rankine cycle) for power and CHP (combined heat and power) applications from low grade heat sources,” *Energy*; Vol. 82, 2015, pp. 269–276. doi: 10.1016/j.energy.2015.01.037.
- [10] Unamba, C. K., White, M., Sapin, P., Freeman, J., Lecompte, S., Oyewunmi, O. A., and Markides, C. N., “Experimental Investigation of the Operating Point of a 1-kW ORC System,” *Energy Procedia*; Vol. 129, 2017, pp. 875–882. doi: 10.1016/j.egypro.2017.09.211.
- [11] Wang, T., Liu, L., Zhu, T., and Gao, N., “Experimental investigation of a small-scale Organic Rankine Cycle under off-design conditions: From the perspective of data fluctuation,” *Energy Conversion and Management*; Vol. 198, 2019, p. 111826. doi: 10.1016/j.enconman.2019.111826.
- [12] Mascuch, J., Novotny, V., Spale, J., Vodicka, V., and Zeleny, Z., “Experience from set-up and pilot operation of an in-house developed biomass-fired ORC microcogeneration unit,” *Renewable Energy*; Vol. 165, 2021, pp. 251–260. doi: 10.1016/j.renene.2020.11.021.
- [13] Uusitalo, A., Turunen-Saaresti, T., Honkatukia, J., and Dhanasegaran, R., “Experimental study of small scale and high expansion ratio ORC for recovering high temperature waste heat,” *Energy*; Vol. 208, 2020, p. 118321. doi: 10.1016/j.energy.2020.118321.
- [14] Weiß, A. P., Popp, T., Müller, J., Hauer, J., Brüggemann, D., and Preißinger, M., “Experimental characterization and comparison of an axial and a cantilever micro-turbine for small-scale Organic Rankine Cycle,” *Applied Thermal Engineering*; Vol. 140, 2018, pp. 235–244. doi: 10.1016/j.applthermaleng.2018.05.033.
- [15] Weiß, A. P., Novotný, V., Popp, T., Zinn, G., and Kolovratník, M., “Customized Small-Scale ORC Turbogenerators- Combining a 1D-Design Tool, a Micro-Turbine-Generator-construction-kit and Potentials of 3D-Printing,” *ORC2019*, 2019.
- [16] Weiß, A. P., Hauer, J., Popp, T., and Preißinger, M., “Experimental investigation of a supersonic micro turbine running with hexamethyldisiloxane,” *16th conference on Power System Engineering, Thermodynamics & Fluid Flow: PSE 2017*, AIP Publishing, 2017, p. 20050.
- [17] Weiß, A. P., Novotný, V., Popp, T., Streit, P., Špale, J., Zinn, G., and Kolovratník, M., “Customized ORC micro turbo-expanders - From 1D design to modular construction kit and prospects of additive manufacturing,” *Energy*; Vol. 209, 2020, p. 118407. doi: 10.1016/j.energy.2020.118407.
- [18] Lemmon, E. W., Huber, M. L., and McLinden, M. O., “NIST Standard Reference Database 23: Reference Fluid Thermodynamic and Transport Properties-REFPROP,

Version 9.1,” [online], <https://www.nist.gov/publications/nist-standard-reference-database-23-reference-fluid-thermodynamic-and-transport#>.

- [19] Streit, P., Popp, T., Winkler, J., Scharf, R., and Weiß, A. P., “Numerical and Experimental Investigation of Different Technologies for Adjusting the Swallowing Capacity of a Cantilever ORC Turbine,” *19th Conference on Power System Engineering*, AIP Publishing, 2021.

Parametric simulation of a solar coupled heat pump system

G.E. Dino^{1*}, A. Frazzica¹, D. Chèze², A. Gabaldón³, D. Ntimos⁴, G. Tardioli⁴, F. Fuligni⁵

¹Consiglio Nazionale delle Ricerche, Istituto di Tecnologie Avanzate per le Energie. Salita Santa Lucia Sopra Contesse 5, Messina (Italy)

²Univ Grenoble Alpes, CEA, LITEN, INES, F-38000 Grenoble (France)

³Fundación CARTIF, Parque Tecnológico de Boecillo, Boecillo 47151, Valladolid, Spain

⁴Integrated Environmental Solutions, R&D Ireland, Castleforbes House, Castleforbes Road, Dublin 1, Dublin, Ireland

⁵RINA Consulting SpA, Via Cecchi, 6, Genova, Italy

* giuseppe.dino@itae.cnr.it

Abstract

Increasing studies about climate change and CO₂ emissions levels, as well as international agreements, are leading toward a decarbonization of the overall energy system. Heating and cooling for civil and residential application covers 55% of EU primary energy demand. On this frame the solar coupled technologies offer interesting perspectives in terms of primary energy savings and emissions reduction. The SunHorizon project (H2020 Project GA818329) aims to analyse the performance of building-integrated solar and HPs solutions. Within this project a parametric study showing the performance of a sun-coupled system that integrates solar technology and innovative thermally driven heat pump was carried out. The simulations, performed by commercial software IESVE and TRNSYS, show promising results by achieving a remarkable range of primary energy savings (from 18% to 57%) and greenhouse gas emission reduction (from 24% to 57%).

Keywords: Solar, Adsorption, Heat pump, Efficiency.

Introduction

Heating and cooling (H&C) for civil and residential application covers 55% of EU primary energy demand [1]. Despite several projects and ambitious strategic plans were adopted with the aim to increase the renewable energy production, H&C demand is still mostly met by fossil fuels, with natural gas having the main share. Conversely, there is a growing tendency that aims at the electrification of the building heating and cooling systems. Indeed, other options are in principle available, such as solar thermal, biomass, biogas, synthetic natural gas, and a combination of them, that might be an effective solution to reach a 100% renewable system by 2050 [2]. It has to be considered that, while electrification has the potential to supply all heating demand, other low-carbon options may serve only some of the overall building demand [3]. The development of efficient technologies is a priority for the actual energy policy; moreover, substantial research efforts are devoted to study complex systems in which new and efficient technologies based on renewable sources can interact with the great support of artificial intelligence and predictive models [4]. Solar thermal energy plays a key role in the renewable energy production that can be fully exploited through direct utilisation of heat produced or by coupling solar technologies with H&C systems [5]. Within thermally driven solar cooling technologies, sorption and hybrid systems show promising result in terms of efficiency, adaptability, and exploitation of solar thermal energy sources [6].

The SunHorizon project (H2020 Project GA818329) aims to analyse and test in real life application the performance of building-integrated solar and HPs solutions in terms of total primary energy (PE) savings, increase of Renewable Energy Ratio (RER), cost reduction (optimized size, installation cost reduction etc.) and reliability (lifetime and reduced maintenance).

In this framework, a dynamic parametric analysis was carried out by considering the application of a sun-coupled system on an existing building. Four novel technologies analysed in the SunHorizon project were integrated in the model: the BH20 thermal compressor heat pump from the company BOOSTHEAT (BH), the Hybrid adsorption/compression chiller from FAHRENHEIT (FAHR), the high-vacuum flat thermal panels from TVP SOLAR (TVP) and the high stratification thermal energy storage from RATIO THERM (RT). The combination of these technologies constitutes technology package 5 (TP5), which one out of the 5 technology combinations that are applied in the project. A first set of simulation of SunHorizon systems (Technology package 3) has been performed

Materials and method

The simulation of the whole system is performed through two different dynamic softwares: IESVE (Integrated Environmental Solutions) for the building simulation and TRNSYS for heating and cooling system. Since no co-simulation between the two software is possible yet, an independent simulation protocol is used. First, the IESVE simulation is run in order to obtain the heating and cooling loads from the building model, then its results are used as input for the heating and cooling plant simulated in TRNSYS. In order to evaluate the main achievements obtained by the new system in terms of Primary Energy saving (PES) and Greenhouse Gas saving (GHG) two different systems were simulated: the baseline one, equipped with existing heating and cooling technologies and, the SunHorizon system, equipped with a novel solution that foresees the integration of solar technologies with innovative heat pumps and chillers. Furthermore, a parametric analysis was carried out on the SunHorizon system, in order to assess the optimal solar field size.

The simulated technology system has been applied to a SunHorizon demonstrator. The chosen building is a SunHorizon demo-site, it is located in Sant Cugat del Vallès (SPAIN) and it consists of tertiary building (owned by the Municipality) with different spaces for cultural activities (Figure 1). The building is composed by two parts, built in two stages:

1. the first one was built in October 1996
2. the second one was built in February 2006 and represents the demo building in which the SunHorizon solution is applied (Figure 2).

Table 1: properties of the construction structures

Construction type	Area m ²	U-Value (W/m ² K)	G-Value
External wall	412.57	0.25	
Roof	96.85	0.33	
Exposed floor	853.85	0.22	
Door	26.34	2.17	
Internal ceiling/Floor	378.73	3.4	
Internal partition	497.77	1.08	
External window	284.62	1.9	0.41

The simulated portion of the building is indicated with red line in Figure 2, the total floor area is 806 m², the evaluated total net volume for space conditioning is 3400 m³. The simulations were run considering the following conditioning seasonal schedules:

- Heating: from 1st January to 1st April and from 1st November to 31st December
- Cooling: from 1st June to 1st October

Three different climate conditions were considered to better evaluate the performances of the innovative system (Figure 3): Barcelona (*Csa* climate, according Köppen-Geiger classification), Madrid (*Csa-Bsk* climate), Nurnberg (*Cfb* climate). Standard Meteoronorm weather files were implemented in both simulations. The mentioned locations will host demo-sites for other applications in SunHorizon project, so a weather monitoring station has been installed on demo buildings as part of the project, results of the present simulations will be compared with data retrieved from the demo sites. Since Barcelona is the closest location to Sant Cugat, it is considered as the reference climate for nominal sizing of existing heating and cooling equipment.

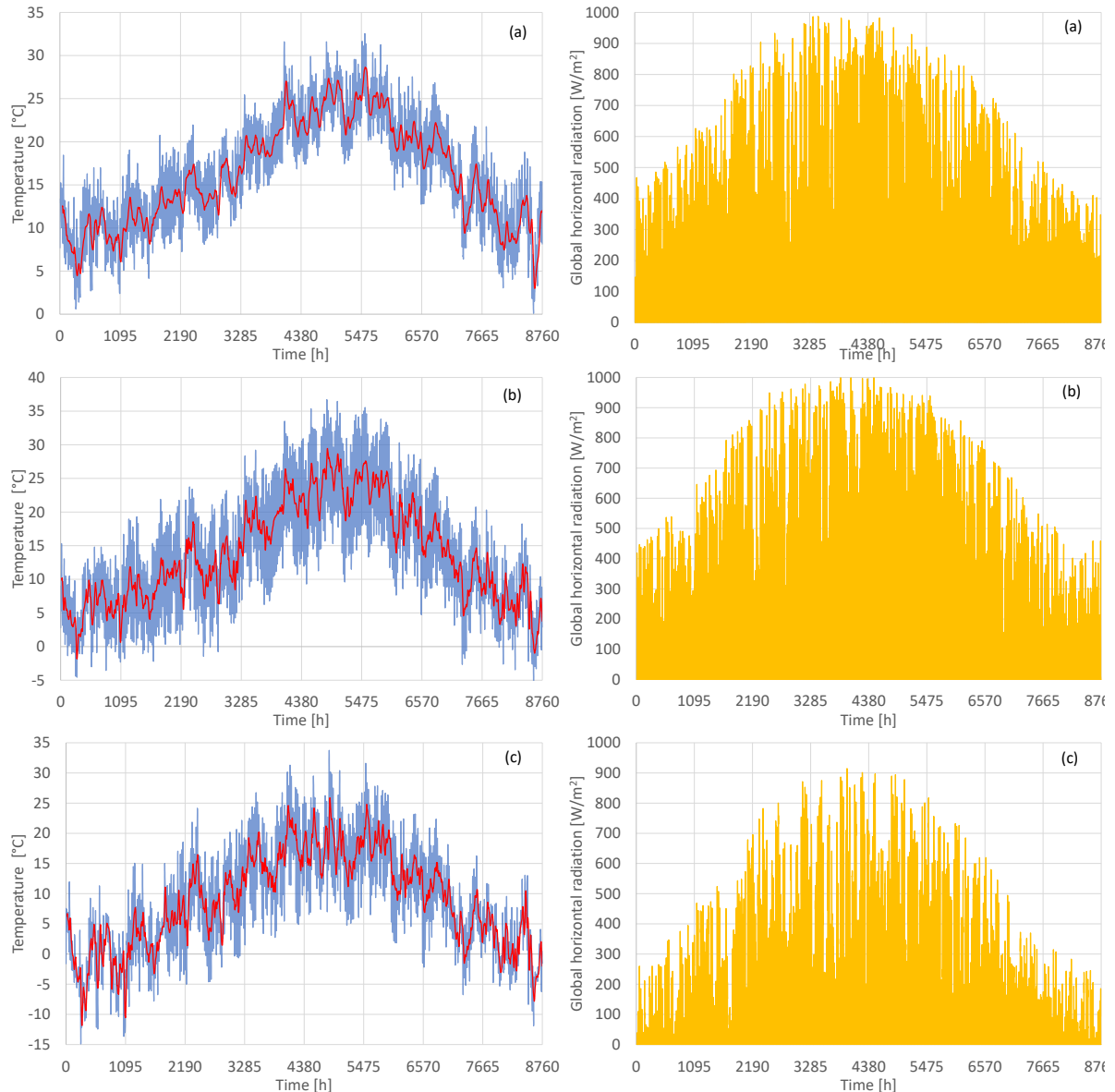


Figure 3: temperature and solar radiation trend for the three selected locations. (a) Barcelona, (b) Madrid, (c) Nurnberg

IESVE building envelope simulation

The dynamic simulation of the building has been performed through IESVE software, it allows an accurate geometric reproduction of the envelope and will be used in the next steps of SunHorizon project for demand and supply prediction and optimizing the control [7]. The ideal load profiles were calculated by considering an ideal heating and cooling system with unlimited capacity. The selected set-points are 21 °C for space heating and 25°C for cooling. These are valid for all the conditioned spaces. DHW use has not been considered for the evaluation of heating and cooling loads. Humidity control has been set between 45% and 55%. The obtained thermal loads profiles were used as inputs for TRNSYS simulation.

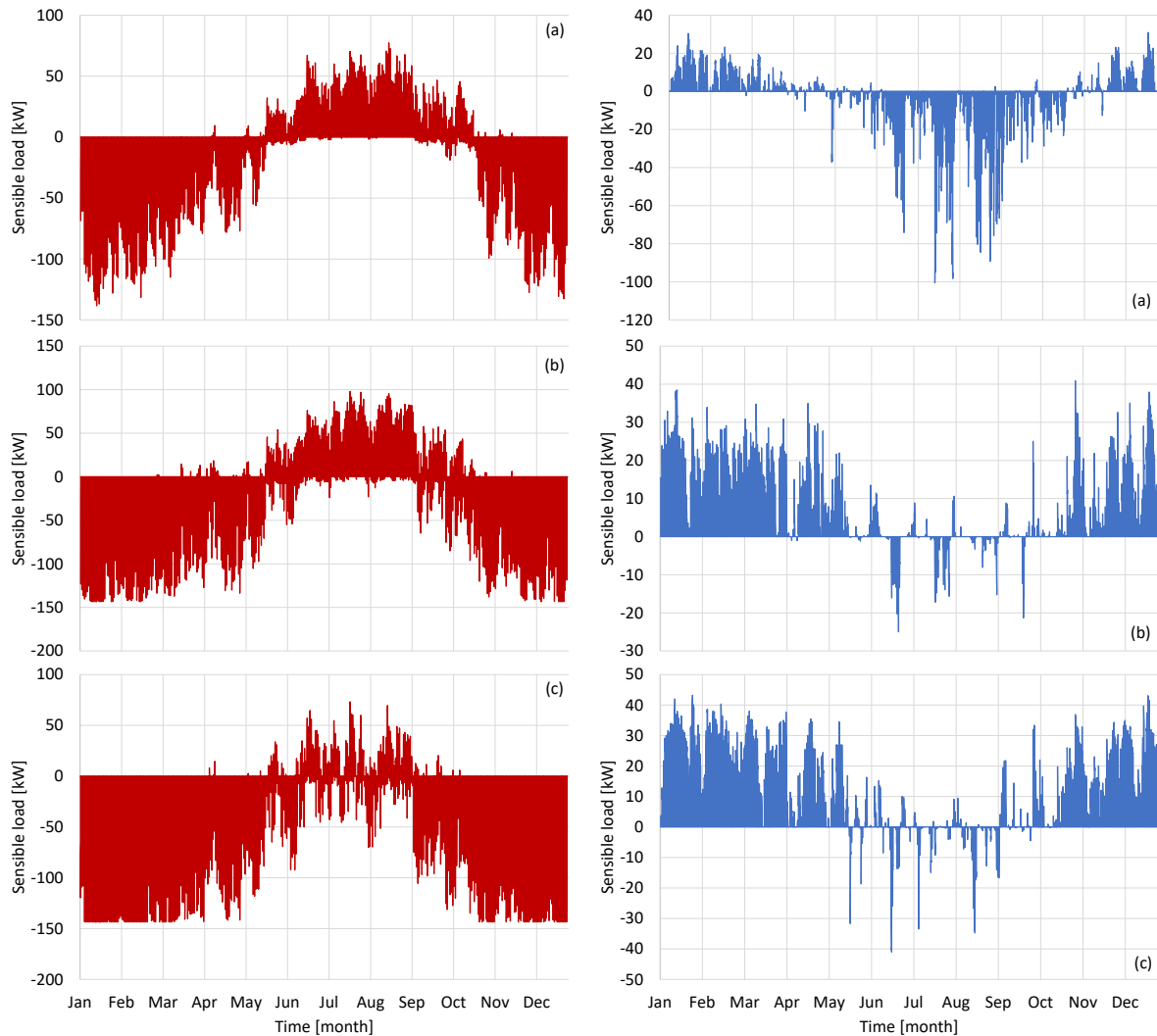


Figure 4: sensible and latent thermal load for the three selected locations - (a) Barcelona, (b) Madrid, (c) Nurnberg

TRNSYS model implementation

Once the heating and cooling loads have been calculated by IESVE, the air conditioning systems were simulated by TRNSYS (Transient System Simulation Tool). First, a reference system was simulated to obtain the primary energy consumption baseline: this was carried out by simulating the existing technology systems installed in the Sant Cugat building. An air to water heat pump (AWHP) supplies heating and cooling to an air handling unit that has two coils: the first one is hydronic and controls the temperature, and the second one is electric and manages the relative humidity. The AWHP is characterized by the following nominal capacities: heating 96.3kW, cooling 93.6kW. Since these values are referred to Sant Cugat location (and Barcelona weather file), they were scaled to adapt the system to the different locations (Madrid and Nurnberg).

Two different models were created to avoid computational burdening: one for cooling operation and one for heating. TRNSYS model (Figure 5) is divided into three sections: the ventilation loop (green continuous line), the hydronic loop (blue continuous line) and controls. The IESVE sensible and latent loads were provided as input in Type 9 (data reader of txt files) and delivered to Type 690 that converts them to temperatures and humidity. Furthermore, the

ventilation air coming from ventilation loop is set as input for type 690. With this method the entire building is conditioned and considered as a single thermal zone.

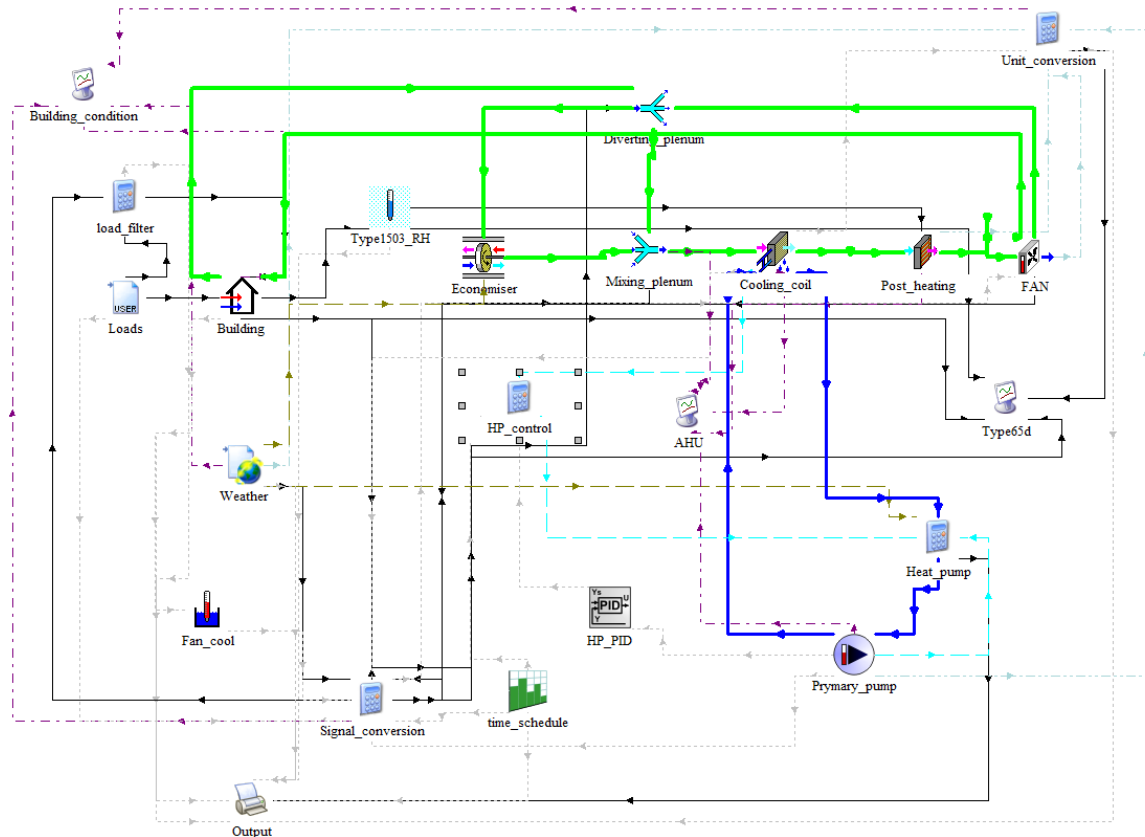


Figure 5: Overall view of the baseline system TRNSYS model

The ventilation loop includes the air handling unit (AHU), the building and the fan controls. AHU model was built by implementing each individual component. Two different TRNSYS types for heating and cooling coils were implemented since each one has only one operating function (heating or cooling). The ratio between exhaust air and fresh air on the controlled dump was set on fixed values: 60% for fresh air and 40% for recirculating air. The ventilation loop is composed by the following types:

- Type 760: economiser heat exchanger
- Type648: mixing section
- Type 508a: cooling coil (only summer operation)
- Type 753d: heating coil (only winter operation)
- Type 930: post heating electrical coil
- Type 662: intake/recovery fan
- Type 148a: Controlled dump

The hydronic loop includes the AWHP, the AHU coils, the circulating pump and the HP/pump controllers. The existing heat pump modelling is described in the dedicated paragraph, it provides both heating and cooling. The hydronic loop components are:

- Type 508a: cooling coil (only summer operation)
- Type 753d: heating coil (only winter operation)
- Type 654: circulating pump
- Calculator that models AWHP

The control strategy is summarized in Table 2

Table 2: control strategy for the baseline TRNSYS model

Component	Signal logic
Time schedule	All the system is operated between 06:00 a.m. and 10:00 p.m every day
AWHP	The heat pump has 4 power levels as retrieved from the datasheet: 0%-37%-63%-100%. A PID controller attempts to maintain the outlet water set-point: 40°C for heating and 7°C for cooling. The signal generated from PID controller can assume values between 0 and 1, it is converted on a discrete signal to obtain the fixed power levels.
AHU control dump	40% fixed recirculation air ratio
AHU fan (type 662)	The fan is controlled by an on/off logic through a simple thermostat that monitors the indoor air temperature and has the following settings: 21°C for heating mode and 25°C for cooling mode.

The SunHorizon system under this study (TP5) replaces the heat pump included in the reference one. TP5 is composed by the TVP high vacuum solar panel field, the RT high stratification storage tank, the FAHR hybrid adsorption-compression chiller and the BH thermal compression heat pump. The main concept of the proposed system is to maximize the exploitation of the solar source during heating and cooling system, furthermore, the innovative FAHR hybrid chiller will produce cooling in summer (Figure 6) and the BH thermal compression heat pump will integrate heating during winter (Figure 7). The electrical post-heating coil in AHU is replaced by a hydronic one.

The FAHR hybrid chiller is composed by two units connected in parallel: a thermally driven adsorption chiller and a vapour compression one. The sorption chiller exploits the heat source and produces chilled water (LT) by using water (R718) as refrigerant, the electrical energy consumption is due only to the auxiliary pumps since the process is operated without electrical compressor. This module contains an adsorber and an evaporator equipped with the refrigerant (R718) on its surface. The evaporation heat is supplied from process water coming from AHU. Due to the adsorption process, the refrigerant vapour flows in the direction of the adsorber. The surface of the adsorber is coated with SAPO 34 that operates as adsorbent material. The refrigerant vapour accumulates on this adsorbent, whereby the heat is released exothermically. This is dissipated to the environment by a “re-cooling” water flow (MT) that heats up and is cooled by a dry-cooler external unit. If the adsorbent is saturated with refrigerant vapour, the water molecules must be expelled from the adsorbent allowing the adsorption process starting again. The internal controller switches over the circuits of the integrated hydraulic group so that the hot water of the driving circuit (HT) flows through the adsorber and thus becomes the desorber. At the same time, the evaporator becomes a condenser, as water from the re-cooling circuit flows through it.

The BH thermal compression heat pump is composed by a novel CO₂ – gas fired heat pump. This system implements the natural gas to activate a thermal compression cycle at high temperatures without mechanical power transmission rather than directly power the heaters. Unlike a volume compressor where power is transmitted by mechanical, this thermal compressor does not have a working piston but a displacer piston. The innovative thermal compressor is composed by a displacer piston and exploits the heat supplied by the gas burner for the direct CO₂ compression working at pressure levels that range between 40 and 100 bars

Cooling mode

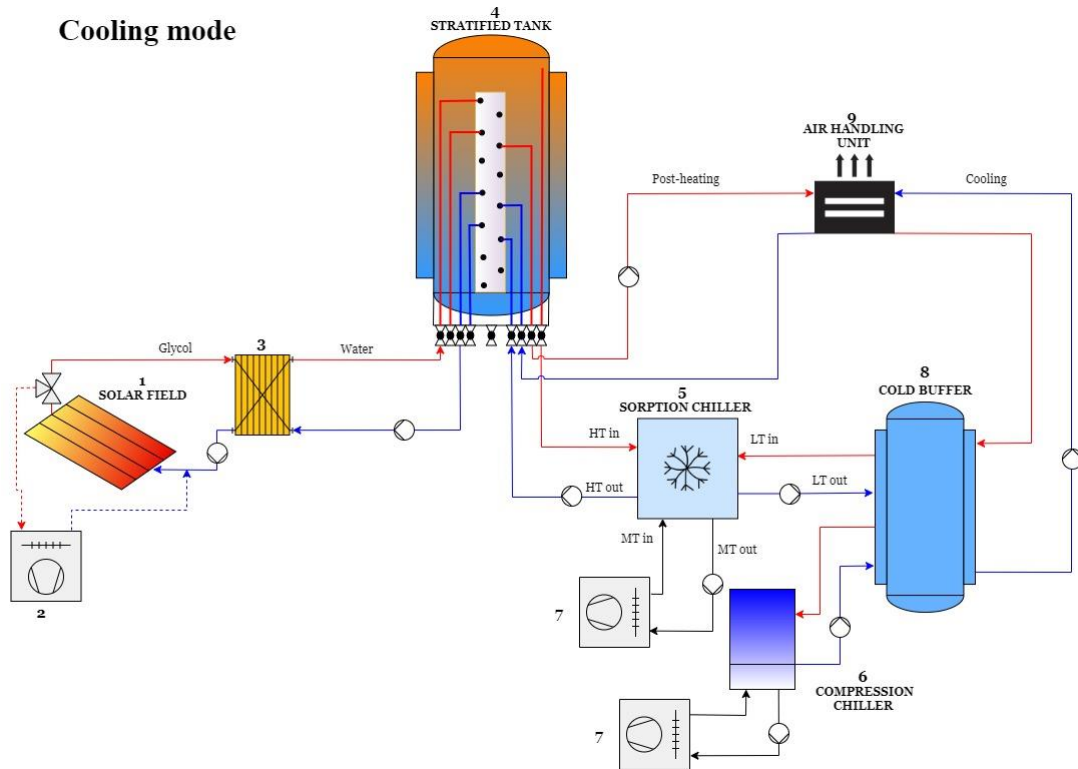


Figure 6: layout of the SunHorizon system in cooling mode

Heating mode

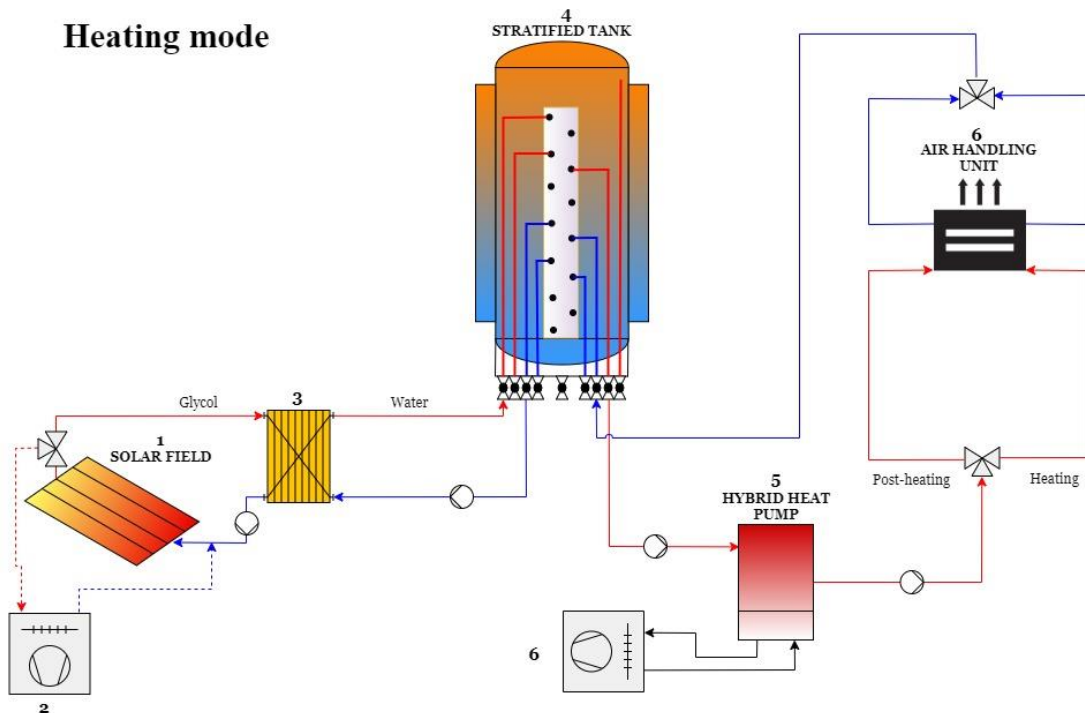


Figure 7: layout of the SUNHORIZON system in heating mode

The TVP solar field produces hot water with a set point of 95°C in summer and 50°C in winter. An internal control of TRNSYS solar panel type539 attempts to keep the collector outlet as close to the user-specified temperature as possible by varying the flowrate if the collector is gaining energy; while the collector is shut off (flowrate = 0) if it is losing energy. The higher temperature set-point during summer operation is due to the hot water demanded by FAHR adsorption module, which requires a temperature range between 70°C and 95°C for HT circuit.

During winter, the temperature is maintained to the temperature set point required by AHU. If the outlet temperature rises up to the set-point, a safety dry-cooler will operate (unit n.2 in Figure 6) to avoid super-heating and stagnation.

The hot water produced by solar field is stored in the RT high stratification storage tank equipped with a novel internal stratification device that allows to increase the vertical temperature gradient inside the tank. The HT adsorption input is derived from the upper part of the buffer tank; the post heating is derived from a lower port. A control stops the adsorption chiller if the temperature outlet from the chiller is less than 5°C. The water to water vapour compression chiller produces chilled water at a lower thermal level than the sorption one, a control modulates power until the temperature outlet is greater than 5°C, then it turns off the component. The hot water for the post-heating coil is delivered directly from the storage tank.

During winter, hot water derived from the top of the tank flows inside the BH thermal compression heat pump that turns on only if the temperature is under the set-point required from AHU (40°C). Then the hot water is delivered to the heating and post-heating coils.

The SunHorizon macro is composed by the following types:

- Type 539 Flat plate solar collector.
- Type 91 Heat exchanger with constant effectiveness
- Type 511 Dry cooler (used for adsorption re-cooler and electrical vapour compression chiller, for solar field it is used as safety cooler)
- Type 340 RT Stratification tank, non-standard type
- Type 534 Cylindrical storage tank
- Type 5837 BH thermal compression heat pump, non-standard type
- Calculator to model the adsorption and vapour compression chiller as specified in the dedicated paragraph.

Parametric analysis

A parametric analysis was carried out by varying the solar field size for each location. The nominal size was chosen by considering the total heat request composed by: adsorption chiller and post-heating in summer, heating and post-heating supply in winter. This configuration is unbalanced when there is no equal heat request for summer and winter operations as occurs for all the selected locations. For example, in hot climate as Barcelona, the heat request for supplying the adsorption unit is prevalent if compared to the winter heating demand; the optimal size of the system is therefore calibrated on summer demand, with a resulting high amount of heat wasted to the environment. Conversely, in Nurnberg the high winter heating demand leads to an over-production of heat in summer that must be rejected by the solar safety dry-cooler. In the parametric analysis the solar field size was reduced by 30%, all the other components remained unchanged to investigate the effect of the solar field as main energy supply. The total solar field area (Table 3) was obtained by reducing the nominal size by a value closes to 30% considering that only strings composed by 10 solar panels could be added or removed.

Table 3: Solar field sizes for parametric analysis

Location	Sunhorizon nominal size (SH)	Sunhorizon reduced size (SH_30%)
Barcelona	156.8 m ²	117.6 m ²
Madrid	117.6 m ²	78.4 m ²
Nurnberg	98 m ²	78.4 m ²

For each scenario the following nominal sizes of components were considered:

- volume of storage tank: 10 m³;
- 2 adsorption units (hybrid chiller) for a total nominal power up to 40 kW (in nominal conditions, 85°C HT- 27 °C MT – 15°C LT);
- 2 vapour compression units (hybrid chiller) for Barcelona and Madrid and 1 unit for Nurnberg with a nominal cooling capacity of 42 kW (for a single unit);
- a different nominal BH size for each location: 50 kW for Barcelona, 100 kW for Madrid and 200 kW for Nurnberg

Finally, three simulations were run for each location: reference system, SunHorizon nominal system, SunHorizon reduced configuration, for nine total simulations.

Chiller model implementation in TRNSYS

A common approach suggested by [8] was used in order to define the performance of the chillers implemented in both models (reference system and SunHorizon one). A set of equations based on data retrieved from technical datasheet was implemented to calculate the heating and cooling capacity and the COP. The equations were obtained by a regression analysis carried out on the performance maps that lets to determine the overall performances of the examined unit through the operating temperatures. A non-linear polynomial expression was obtained both for the air to water chiller implemented in the reference system (1) and water to water unit of the FAHR hybrid one implemented in SunHorizon system (2):

$$f(T_{air}, T_{w_{out}}) = a + b * T_{air} + c * T_{w_{out}} + d * T_{air}^2 + e * T_{air} * T_{w_{out}} \quad (1)$$

$$f(T_{w_{ev}}, T_{w_{cond}}) = a + b * T_{w_{ev}} + c * T_{w_{cond}} + d * T_{w_{ev}}^2 + e * T_{w_{ev}} * T_{w_{cond}} \quad (2)$$

A linear model that considers the three operating temperatures (HT-high temperature, MT-re-cooling temperature, LT-cooling temperature) was obtained for the FAHR adsorption unit implemented in the SunHorizon system (3):

$$f(HT_{in}, MT_{in}, LT_{in}) = a + b * HT_{in} + c * MT_{in} + d * LT_{in} \quad (3)$$

The model predictors were evaluated by statistical evaluation parameters (Table 4). High values of R² (close to 1) and low values of root mean square error (RMSE) show the predictor's reliability.

Table 4: predictors evaluation parameters for the implemented statistical correlations

		R ²	RMSE
Air to water heat pump (reference model)	Heating capacity	0.9998	0.3352 kW
	Cooling capacity	0.9994	0.4367 kW
	Electrical power (heating)	0.9925	0.4448 kW
	Electrical power (cooling)	0.9994	0.1074 kW
FAHR Water to water chiller (Sunhorizon model)	Cooling capacity	0.9989	0.1811 kW
	Electrical power	0.998	0.05084 kW
FAHRA dsorption chiller (Sunhorizon model)	Cooling capacity	0.973	0.886 kW
	COP	0.86	0.0334

Results and discussion

The simulation results were aggregated in key performance indicators (KPI) in order to evaluate and quantify the performances of the SunHorizon single technologies and combined system [9].

The KPIs for the overall system are the f_{PES} (total Primary energy Saving factor) and $f_{sav,GHG}$ (Greenhouse Gas saving factor) defined as reported in (4) and (5), the subscripts “bs” and “SH” indicates respectively the baseline system and the SunHorizon system.

$$f_{PES} = 1 - \frac{\sum PE_{SH}}{\sum PE_{bs}} \quad (4) \quad f_{sav,GHG} = 1 - \frac{\sum GHG_{SH}}{\sum GHG_{bs}} \quad (5)$$

In (4) $\sum PE$ is the sum of total primary energy contributions for each energy carrier obtained as $\sum_i Q_i * PEF_i$ (6) where Q_i is the total amount of final energy (FE) delivered for a specific energy carrier and PEF_i the corresponding total Primary Energy Factor, expressed in kWh_{PE}/kWh_{FE}. In the simulated system, electricity and natural gas are the only energy carriers involved, the considered primary energy factors are, respectively, 1.896 kWh_{PE}/kWh_{FE} and 1.1 kWh_{PE}/kWh_{FE}[10]. Similarly, in (5) $\sum GHG$ is the sum of greenhouse gas emissions for each energy carrier obtained as $\sum_i Q_i * GHGF_i$ (7) where Q_i is the total amount of final energy for a specific energy carrier and $GHGF_i$ the corresponding Greenhouse Gas Emission Factor, expressed in gCO₂/kWh_{FE}. For electricity and natural gas were considered respectively 420 gCO₂/kWh_{FE} and 220 gCO₂/kWh_{FE}. [11].

Furthermore, KPIs are also calculated at technology level. For TVP panel the following KPIs were considered:

- the global efficiency that expresses the fraction of useful energy produced by the solar panels for the whole simulated period on the solar radiation collected by the gross area of the panel: $\eta_{TVP}^{gross} = \int \frac{Q_{TVP} dt}{G_{col} * A_{TVP}^{gross}} dt$ (8) where: Q_{TVP} is the instantaneous thermal power output expressed in kW, G_{col} is the specific solar irradiation on the collector plane expressed in kW/m², A is the solar gross surface area;
- the solar thermal fraction that expresses the contribution of the solar system over the total heat input of the system for a considered period, in this case only for winter:

$f_{sol,th} = \int \frac{\dot{Q}_{TVP} dt}{\dot{Q}_{sys} dt}$ (9) where \dot{Q}_{TVP} is the instantaneous thermal power output expressed in kW and \dot{Q}_{sys} is the thermal energy output from other technologies summed to \dot{Q}_{TVP} ;

- the fraction of energy rejected to the environment because of lack of request and overheating of solar circuit $f_{sol,waste} = \int \frac{\dot{Q}_{DryC} dt}{\dot{Q}_{TVP} dt}$: (10) where \dot{Q}_{TVP} is the instantaneous thermal power output expressed in kW and \dot{Q}_{DryC} is the instantaneous thermal power rejected to the environment

For BH gas driven heat pump the following KPIs were considered only for winter operation mode:

- Seasonal Gas Utilization Efficiency (SGUE), that expresses the gas utilization efficiency to provide a useful output, calculated as the ratio of the overall heating energy to the overall gas consumption: $SGUE = \int \frac{\dot{Q}_{BH,h} dt}{\dot{Q}_f dt}$ (11) where $\dot{Q}_{BH,h}$ is the thermal energy output (heating) from the Boostheat unit obtained from Type 5837 and \dot{Q}_f is the final energy consumption (natural gas) in kW obtained from the same TRNSYS type;
- seasonal Performance Factor (SPF) that expresses the efficiency factor of the unit in primary energy terms. It considers the total amount of primary energy used to produce a useful output, including electricity associated to pumps, auxiliaries, etc. of the BH unit, and the gas consumption: $SPF_{BH} = \frac{\int \dot{Q}_{BH,h} dt}{(\int \dot{E}_{BH} dt)PEF_{tot,cr} + (\int \dot{Q}_{BH} dt)PEF_{tot,cr}}$ (12) where $\dot{Q}_{BH,h}$ is the thermal power output (heating) from the BH unit obtained from Type 5837, \dot{E}_{BH} is the total electrical power consumption (included the auxiliaries) and \dot{Q}_{BH} is the final power consumption (natural gas) in kW obtained from the same TRNSYS type, PEF_i is the total Primary Energy Factors for each energy carrier considered.

Finally, the following KPIs were considered for FAHR adsorption unit:

- Seasonal Electric Efficiency Ratio (SEER) that expresses the energy efficiency ratio of a heat pump, air conditioner or comfort chiller, in cooling mode, calculated as the cooling demand divided by the associated energy consumption to provide that cooling demand throughout a specific period (in this case the entire cooling period): $SEER = \frac{\int \dot{Q}_{FAHR,c} dt}{\int \dot{E}_{FAHR} dt}$ (13) where $\dot{Q}_{FAHR,c}$ is the thermal power output (cooling) from the FAHR adsorption unit and \dot{E}_{FAHR} is the electric power consumption, since it is a thermally driven adsorption unit, the electrical energy consumption is due only to auxiliaries (pumps and dry cooler)
- Seasonal Performance Factor (SPF) that expresses the efficiency factor of the unit in primary energy terms. It considers the total amount of primary energy used to produce a useful output, including electricity associated to pumps, auxiliaries, etc. of the FAHR unit and other energy carrier's consumption: $SPF_{FAHR} = \frac{\int \dot{Q}_{FAHR,c} dt}{(\int \dot{E}_{FAHR} dt)PEF_{tot,cr} + (\int \dot{Q}_{FAHR} dt)PEF_{tot,cr}}$ where $\dot{Q}_{FAHR,c}$ is the thermal power output (cooling) from the FAHR adsorption unit and \dot{E}_{FAHR} is the electric power consumption, and \dot{Q}_{FAHR} is the heating power consumption that in this case is entirely supplied by the solar renewable source, for this reason the PEF_i for this component is considered as 1.

In Table 5 the KPIs resume the main results of the performed parametric simulations.

Table 5: KPIs resulting from the parametric simulation. SH is the system considering the nominal SunHorizon size for TVP solar fields, SH30% is the scenario that foresees the reduction of the solar field size by 30%

KPI		Barcelona	Madrid	Nurnberg
f_{PES}	Summer	SH - 45% SH30% - 44%	SH - 35% SH30% - 34%	SH - 28% SH30% - 27%
	Winter	SH - 71% SH30% - 59%	SH - 33% SH30% - 25%	SH - 18% SH30% - 17%
	Global	SH - 57% SH30% - 51%	SH - 33% SH30% - 28%	SH - 19% SH30% - 18%
$f_{sav,GHG}$	Summer	SH - 45% SH30% - 44%	SH - 35% SH30% - 34%	SH - 28% SH30% - 27%
	Winter	SH - 72% SH30% - 61%	SH - 37% SH30% - 30%	SH - 24% SH30% - 23%
	Global	SH - 57% SH30% - 52%	SH - 36% SH30% - 31%	SH - 25% SH30% - 24%
η_{TVP}^{gross}	Summer	SH - 51.6% SH30% - 52%	SH - 53% SH30% - 53.9%	SH - 45.6% SH30% - 46%
	Winter	SH - 53.5% SH30% - 56.1%	SH - 55% SH30% - 55.9%	SH - 48.2% SH30% - 47.8%
	Global	SH - 52% SH30% - 54%	SH - 54% SH30% - 55%	SH - 46% SH30% - 47%
$f_{sol,th}$	Winter	SH - 87% SH30% - 73%	SH - 36% SH30% - 26%	SH - 7% SH30% - 5%
$f_{sol,waste}$	Summer	SH - 24% SH30% - 12.3%	SH - 19.3% SH30% - 5.8%	SH - 33% SH30% - 24.8%
	Winter	SH - 10.5% SH30% - 3.9%	SH - 5.1% SH30% - 0.3%	SH - 0% SH30% - 0%
	Global	SH - 17% SH30% - 8%	SH - 13% SH30% - 4%	SH - 22% SH30% - 17%
SGUE	Winter	SH - 144% SH30% - 146%	SH - 133% SH30% - 134%	SH - 148% SH30% - 148%
SPF_{BH}	Winter	SH - 1.21 SH30% - 1.22	SH - 1.14 SH30% - 1.15	SH - 1.23 SH30% - 1.23
SEER	Summer	SH - 6.19 SH30% - 5.90	SH - 4.99 SH30% - 4.41	SH - 6.31 SH30% - 6.12
SPF_{FAHR}	Summer	SH - 0.33 SH30% - 0.33	SH - 0.32 SH30% - 0.30	SH - 0.34 SH30% - 0.33

The results clearly highlight the reduction of PE and GHG for all the examined cases with reference to baseline system. The parametric analysis shows that the reduction of TVP field size by 30% doesn't affect the f_{PES} and $f_{sav,GHG}$ indicators if considered for a whole operating year that includes both heating and cooling seasons. But, the analysis of the cited indicators for each single season shows a relevant decrease when the solar field is reduced. The advantages of a sun-coupled system as proposed in the present simulation are better underlined in hot climates than in colder ones, as shown by the decrease of f_{PES} and $f_{sav,GHG}$ when moving from hot to cold climates.

The efficiency of the high vacuum TVP panels is stable when moving from summer to winter operation, showing slight differences with a range between 45.6% and 53.9%. Decreasing the solar field size induces a small increase in efficiency. Conversely, the solar covering $f_{sol,th}$ is more remarkable in hot climates, whereas in cold climates as Nurnberg it tends to be negligible. The energy wasted to the environment is considerably reduced when reducing the TVP solar field size with great differences between winter and summer operation. Nevertheless, the electricity needed to drive the drycooler of the TVP field is negligible in comparison with the PE benefits obtained in winter time.

The parametric analysis didn't affect the performance indicators of BH and FAHR that for all cases maintained constant values with slight changes for each location. The high performances achieved in terms of SGUE and SEER are due to the novel technology that, being thermally driven, excludes the electrical energy consumption that has a great impact in the indicator calculation. The low values of SPF_{FAHR} if compared with SPF_{BH} are due to the introduction of solar energy in the denominator of the indicator, as heat consumption needed to serve the cooling demand.

Finally, the parametric analysis shows that the reduction of solar field shows a slight difference when passing from SH reference case to SH30%. This variation could produce relevant effects on economic evaluations. In this paper the economic aspects were not considered but the performed analysis gives useful perspectives also on this point of view.

Conclusions

The SunHorizon project proposes innovative sun coupled technologies and systems. In this framework, a parametric analysis was carried out by considering the application of a sun-coupled system on an existing building. The study was extended to three different climates (Barcelona, Madrid and Nurnberg) and the effects of the variation of TVP solar field was analysed. A dynamic simulation was performed first through IESVE software to evaluate the building loads, then TRNSYS was used to simulate a baseline reference system and the SunHorizon one. The simulations show remarkable results in terms of PES (from 18% to 57%) and GHG reduction (from 24% to 57%). The reduction of solar field doesn't have a relevant effect on these indexes. Each technology was evaluated by calculating specific KPIs and, the results show promising outcomes in terms of efficiency and, consequently, energy savings. A future economic analysis will take into account the results of the present study, furthermore, it will be enriched by the data coming from the first experimental campaigns that will be carried out on the demo-sites.

Acknowledgments



The SunHorizon Project has received funding from the European Union's Horizon 2020 Research and Innovation Programme under Grant Agreement N. 818329

References

- [1] "Policy brief Energy efficiency trends in buildings," 2018.

- [2] Palomba V. et al., “Implementation of a solar-biomass system for multi-family houses: Towards 100% renewable energy utilization,” *Renewable Energy*, vol. 166, (Apr. 2020), pp. 190–209. <https://doi.org/10.1016/j.renene.2020.11.126>
- [3] Sheikh I. and Callaway D., “Decarbonizing space and water heating in temperate climates: The case for electrification,” *Atmosphere*, vol. 10, no. 8, (Aug. 2019), p. 435. <https://doi.org/10.3390/atmos10080435>
- [4] Paradeshi L. et al., “Performance studies of R433A in a direct expansion solar-assisted heat pump,” *International Journal of Ambient Energy*, vol. 41, no. 3, (Feb. 2020), pp. 262–273. <https://doi.org/10.1080/01430750.2018.1451369>
- [5] Palomba V. et al., “Solar-Assisted Heat Pumps and Chillers,” in *Handbook of Climate Change Mitigation and Adaptation*, New York, NY: Springer New York, 2021, pp. 1–54. https://doi.org/10.1007/978-1-4614-6431-0_116-1
- [6] Tzivanidis C. and Bellos E., “A comparative study of solar-driven trigeneration systems for the building sector,” *Energies*, vol. 13, no. 8, (Apr. 2020), p. 2074. <https://doi.org/10.3390/en13082074>
- [7] “Sun coupled innovative Heat pumps D5.1-Prediction models and demand characterization,”
- [8] Dino G. E. et al., “Experimental characterization of an innovative hybrid thermal-electric chiller for industrial cooling and refrigeration application,” *Applied Energy*, vol. 281, (2021), p. 116098. <https://doi.org/10.1016/j.apenergy.2020.116098>
- [9] Cartif M. A. C. et al., “Work Package 2 Sun coupled innovative Heat pumps,” (2019).
- [10] “Conversion Factors | SEAI Statistics | SEAI,” Available: <https://www.seai.ie/data-and-insights/seai-statistics/conversion-factors/> [Accessed: 06 May 2021]
- [11] “EN ISO 52000-1:2017,” Available: http://store.uni.com/catalogo/en-iso-52000-1-2017?josso_back_to=http://store.uni.com/josso-security-check.php&josso_cmd=login_optional&josso_partnerapp_host=store.uni.com [Accessed: 06 May 2021]

CO₂ Power Cycle Assessment for Low Grade Waste Heat Recovery

V. Wolf^{1*}, E. J. Rabadàn Santana¹ and S. Leyer¹

¹University of Luxemburg, 2 Avenue de l'Université, 4365 Esch-sur-Alzette, Luxembourg

*Corresponding author: veronika.wolf@uni.lu

Abstract

Organic Rankine Cycles for waste heat recovery have become more and more popular in the last year since the environmental awareness or society has risen. A possibility of employing supercritical carbon dioxide (sCO₂) within the Rankine cycle is discussed among academia and industry recently due to its low ozone depletion potential and good heat transfer characteristics. Numerous modifications of the power cycle layout were proposed, reheated expansion, recuperation and intercooled compression among them. These modifications are often adjusted to a certain application, often for medium-grade waste heat within temperatures from 240-480 °C. Since low-grade waste heat (< 240 °C) represents the major portion of excess heat globally, the authors concentrate on very low temperatures for recovery. This temperature range is hard to recover due to the small temperature gap of heat source and heat sink leading to a poor efficiency of the Rankine Cycle. To enhance the great potential in turning low grade waste heat into usable energy, this work assesses various ORC architectures for a defined waste heat source (60-100 °C) and heat sink (20 °C) which form a standardized base and thus enable a comparison. In the first place, sCO₂ cycle architectures from literature are examined via the commercial software EBSILON in order to implement the cycle setup with its original operational parameters. Secondly, the predefined low-grade heat source is implemented into the cycle. The cycle architecture is then assessed regarding efficiency, mass flow and pressure. As a final point, the cycle architectures are ranked in terms of performance within the low-grade waste heat sector. Results show that recuperation of heat within the cycle enhances the cycle performance from source temperatures greater than 80 °C whereas intercooled compression negatively affects the efficiency. For the temperature region from 60-80 °C, the conventional configuration without any modifications operated most efficiently. When source temperature becomes higher, reheated expansion positively affects the system performance. The authors deliver a road map of thermodynamic efficiencies of sCO₂ cycle architectures for low-grade waste heat recovery up to 100 °C which might be beneficial for designers of such power cycles.

Keywords: Waste heat recovery, power generation, low temperature, ambient air, supercritical CO₂, Rankine cycle, cycle configuration

Introduction/Background

With increasing global energy demand, efficient and economic use of heat grows more important. Especially since large amounts of waste heat is produced during the conversion of primary energy into secondary energy, e.g. electricity. [1]. The 63% thereof is reported to be low grade with temperatures smaller than 240 °C [1]. A problem for thermodynamic cycles associated with low grade waste heat is the narrow temperature difference between heat source and heat sink resulting in a big challenge for the cycle efficiency.

Supercritical carbon dioxide (sCO₂) power cycles show great potential to recover low-grade waste heat because of good heat transfer characteristics due to the low critical temperature of

CO₂ at 30.98 °C and a pressure of 73.77 bar [2]. In comparison to conventional ORC refrigerants, carbon dioxide is chemically stable and less toxic [3]. Accordingly, the study focuses on low-grade heat sources recovered by a sCO₂ power cycle.

The basic power cycle configuration with a compressor, heater, turbine and cooler has been widely studied. Ahmadi et al. [4] using solar energy as a heat source and Amini et al. [5] recovered low grade waste heat from combined-cycle power plant. Xia et al. [6] added an ejector to solve the condensation problem of CO₂ under the higher temperature heat sink.

Meanwhile, many studies focus on the optimization of sCO₂ power cycles by modifying the cycle architecture. Hafei et al. [7] report an increased work output when adding reheated expansion to the basic cycle. In this configuration, the high pressure CO₂ is expanded to a medium pressure in a first stage, then reheated, and finally expanded to the lower cycle pressure. Tuo [8] found that a reheated expansion can improve the performance with lower turbine inlet temperatures and higher maximum cycle pressure. Chen et al. [9] concluded that a power cycle with reheated expansion is most effective in utilizing low-grade waste heat from vehicle exhaust gas.

A power cycle with intercooled compression was studied by Olumayegun et al. [4] for a gas turbine exhaust stream. When modifying a power cycle with intercooled compression, the CO₂ compression process is split into several smaller compression stages and the fluid is cooled in between these stages in order to lower the necessary compression energy. Nassar et al. [10] developed an individual main compressor and recompression compressor for a CO₂ power plant. They also employed a regenerator within the cycle to transfer heat from the low pressure part of the cycle into the high pressure part. This reduces the cooling load significantly. Also Kim et al. [11] examined the combination of intercooled compression and regeneration and found that this arrangement is highly efficient with less CO₂ mass flow necessary.

Another cycle modification that has been applied by numerous authors is the split flow configuration. In order to enhance the system performance, the working fluid is divided into sub streams, which are finally merged again in another point in the system. The split position can occur in different points of the system. Li et al. [12] investigated the split flow before the compression of the working fluid and merged the CO₂ again before condensation. With this configuration, the net power output could be enhanced by 11.60% compared to the basic power cycle setup. Kim et al. [13] also report an enhanced cycle efficiency by 10.5% with a split flow before compression. Another point where the working fluid can be divided is before the expansion process. Padilla et al. [14] separated the CO₂ before the turbine, where as one section is directed upstream and merged with the stream before heating. This means that a small part of the working fluid is expanded one time while the major part is expanded one time. This configuration achieved the same thermal efficiency than a power cycle with one recuperator.

A system configuration with split flow before heating was modelled by Walnum et al. [15]. A bottoming cycle for offshore oil and gas installations with a split of the CO₂ stream before the heater and a merge after the turbine was investigated. In this configuration, CO₂ showed 16% less power output than steam as working fluid.

Summarizing the findings in literature, there is an immense diversity of system layouts in power cycle architectures. Applicable modifications in the system layout are not limited so that several modifications can be combined, for example split flow and recuperation as studied by Cespri et al. [16]. In addition, the number of recuperators can be increased,

depending on the available thermal energy in the system. Where as a combination of cycle modification leads to a more complex system bigger in size.

Previous studies show that cycle modifications lead to changes in the cycle efficiency. All publications mentioned above are tailor made to the specific application. Especially the waste heat temperature and operational conditions strongly depend on the particular application. Consequently, the stated efficiencies of the findings above cannot be compared with each other as they rest upon different boundary conditions. Hence, a comprehensive study of the optimal cycle configuration for a given temperature rang is missing. This work provides a systematic assessment and comparison of different cycle architectures for a waste heat source temperature range between 60 to 100 °C. The before mentioned different cycle configurations are modelled with EBSILON Professional solver and a performance optimization as function of the system pressure ratio, mass flow and specific work output is performed.

Methodology

Uniform operational conditions for the cycle comparison are defined as follow: The Rankine Cycle has a full condensation of the CO₂. The waste heat source is air, which provides temperatures between 60-100 °C (333.15-373.15 K) at ambient pressure and a mass flow rate of 1000 kg/s. The heat sink is ambient air, which is assumed at a mean annual temperature of 20 °C (293.15 K). The mass flow is adjusted to ensure a full condensation of the working fluid. Isentropic efficiency of turbo machinery (pump and turbine) are set to be 80%. The effectiveness of the heat exchanger is 95% [17]. The different power cycle configurations are implemented in EBSILON® Professional [18], a commercial simulation software for power plants. It uses REFPROP database [19] for fluid properties, which employs the Span-Wagner equation of state for CO₂ [20].

Firstly, the power cycle architectures with their original operational conditions as stated in literature were modelled in EBSILON. Only when the setup and results matched with the publication, the previously specified uniform operational conditions were applied. Each power cycle architecture is compared in terms of the thermodynamic efficiency n_{th} :

$$n_{th} = \frac{\dot{W}_{net}}{\dot{Q}_{in}} \quad (1)$$

\dot{Q}_{in} is the waste source heat flux absorbed by the heat exchanger(s) and \dot{W}_{net} is the net power output:

$$\dot{W}_{net} = \dot{W}_{Turbine} - \dot{W}_{Pump} \quad (2)$$

In Eq. (2), the turbine output power $\dot{W}_{Turbine}$ and pump input power \dot{W}_{Pump} are calculated via the following formulas:

$$\dot{W}_{Pump} = \frac{(h_{2,is} - h_1)}{\eta_{Pump}} \quad (3)$$

$$\dot{W}_{Turbine} = (h_3 - h_{4,is}) * \eta_{Turbine} \quad (4)$$

In Eqs. (3) and (4), the numbers in subscript of the specific enthalpies h represent the state points in the system as shown in Figure 1.

The theoretic Carnot efficiency η_{Carnot} is calculated with the temperatures of the heat sink (here: ambient air) T_{Cold} and the heat source (waste heat temperature) T_{hot} :

$$\eta_{Carnot} = 1 - \frac{T_{Cold}}{T_{hot}} \quad (5)$$

With Eq. (5), an idealistic Carnot efficiency of 12.0% to 21.4% can be reached for the given temperature difference of 20°C and 60°C or 100 °C, respectively.

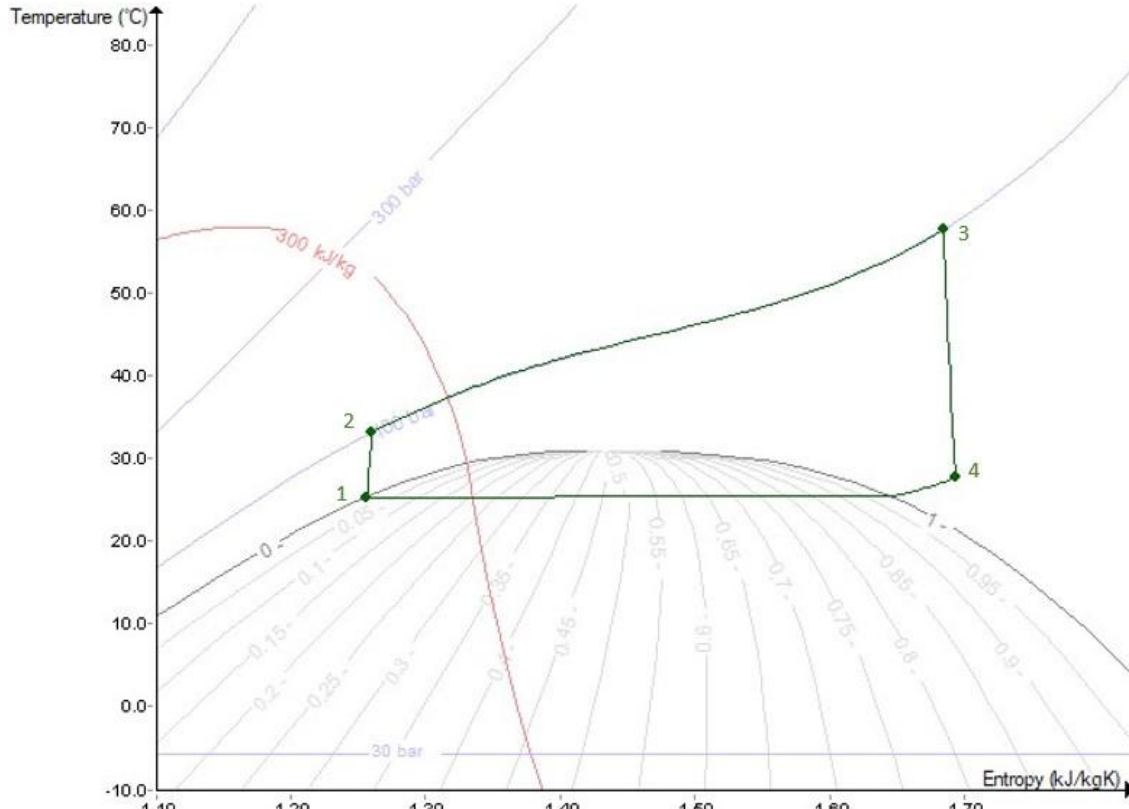


Figure 1: TS diagram of basic power cycle configuration

With every iteration in waste heat temperature, the thermodynamic efficiency is optimized by pressure ratio:

$$r_p = \frac{P_{High}}{P_{Low}} \quad (6)$$

In Eq. (6), P_{High} denotes the high pressure part and P_{Low} denotes the low pressure part of the power cycle. With more compression and expansion stages, the highest and lowest pressures are denoted.

The validation process was framed in a way that the original cycle layout from publication was modelled with its stated operational parameters. After reaching accordance of the obtained results with published ones, the previously defined uniform parameters for the cycle assessment were applied to the power cycle layouts. The outcome of the comparative study with unified conditions is shown in the next chapter.

Discussion and Results

Figure 2 displays the basic cycle configuration and the corresponding efficiency in comparison to the Carnot efficiency. The difference of the basic and Carnot cycle efficiency

are diverging with increasing heat source temperature. It can be seen that the gain of efficiency with rising heat source temperature is rather flat in comparison to the ideally reachable efficiency. The efficiency shown in Figure 2 results are based on an optimization of the pressure ratio to obtain a maximum net power output. For a waste heat source of 60°C, the optimization of cycle pressure ratio is illustrated in Figure 3. One can see that it exists a maximum (optimum) pressure ratio in the parabolic shaped efficiency curve. It is observed that this shape is not unique for this basic system configuration example, but for all modelled configurations. If parameters like heat source temperature or system configurations are changed, the amplitude of the curve changes as well. Whereas for an increase of waste heat sources, a proportional rising amplitude towards higher efficiency can be observed and the maximum is shifted to the right towards a higher pressure ratio. A change in system configuration causes the curve to either augment or descent, depending on the specific modification. The subsequent cycle configurations will be compared to this basic cycle configuration, as it serves as initial point for modifications. Thus, only with this cycle configuration, a comparison is legitimate and it can be analysed, whether a modification in the cycle architecture leads to a higher efficiency.

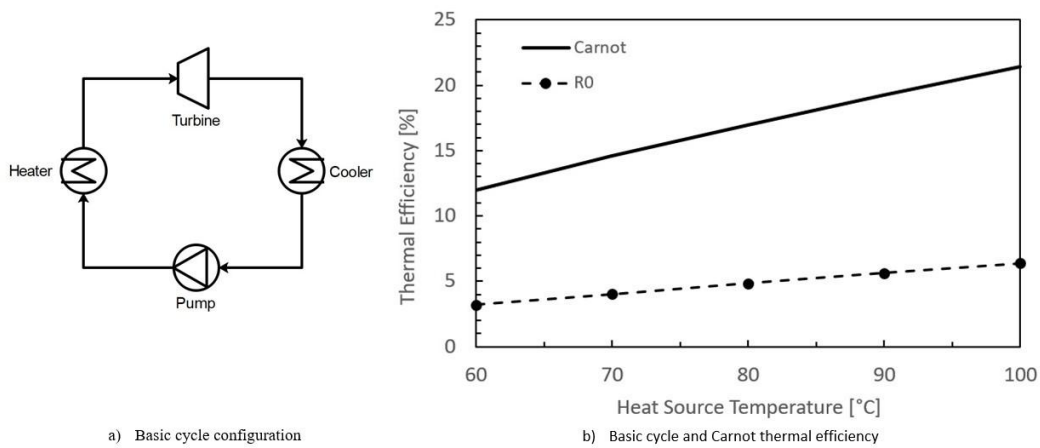


Figure 2: basic cycle configuration and efficiency

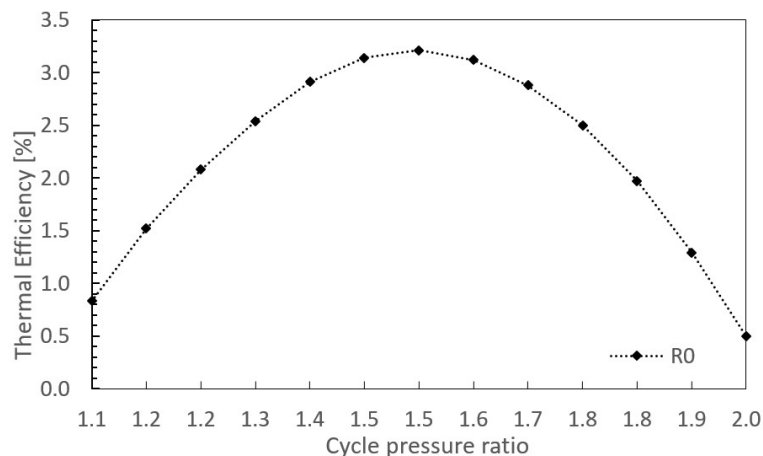
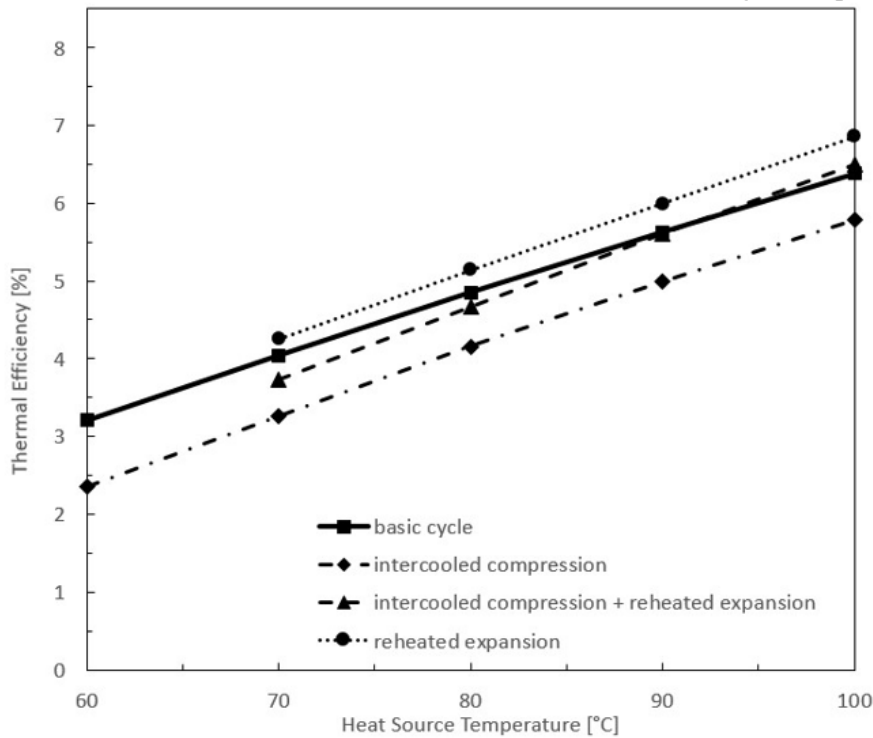
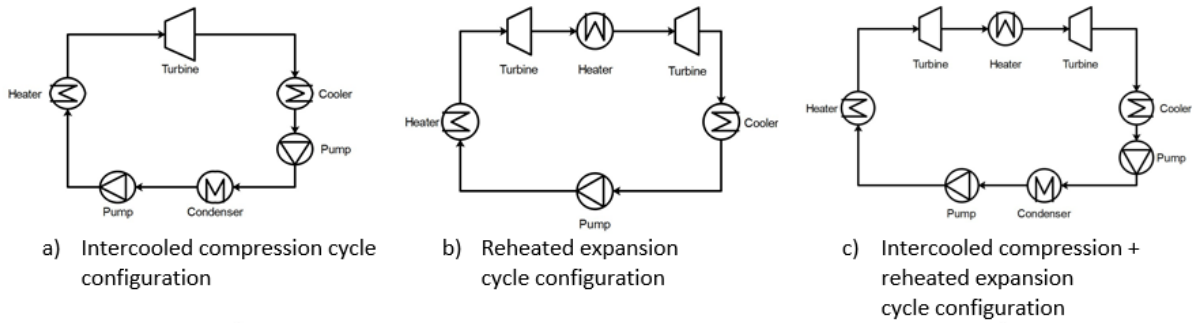


Figure 3: Cycle efficiency of basic cycle configuration in terms of pressure ratio

The modification of intercooled compression possesses two pumps and two coolers as shown in Figure 4a. Here, two steps of compression are displayed as simulated in EBSILON. The

benefit of intercooled compression is in general, that a fluid requires less compression work when its specific energy content is lower. For the case of low-grade heat sources, there is only a small temperature gap between turbine exit temperature and condensation temperature. Thus, the benefit of intercooled compression cannot be exploited at low waste heat source temperatures. A comparison between the efficiencies of the basic cycle and intercooled compression cycle is shown in Figure 4d: One can see that intercooled compression affects the cycle efficiency negatively by one percentage point. Towards higher temperatures, the efficiency curve gets closer to the basic cycle efficiency and thus, there exists a point from which the addition of intercooled compression to the cycle enhances the efficiency. Within the modelling process, it was calculated that this break-even point of the two efficiency lines is at 440°C. Thus, for low-grade waste heat sources less than 100°C, intercooled compression is not beneficial.

The principle of reheated expansion is the separation of the expansion process into several steps (Figure 4b), derived from the idea to achieve an isothermal like expansion of the fluid. A two-step expansion is modelled in this work. Generally, more steps are also possible. In the first expansion step, the working fluid is expanded to an intermediate pressure between high-pressure side and low-pressure side. Then, it follows another heat input and an expansion to the low cycle pressure.



d) Thermal efficiencies of basic, intercooled compression and reheated expansion cycle

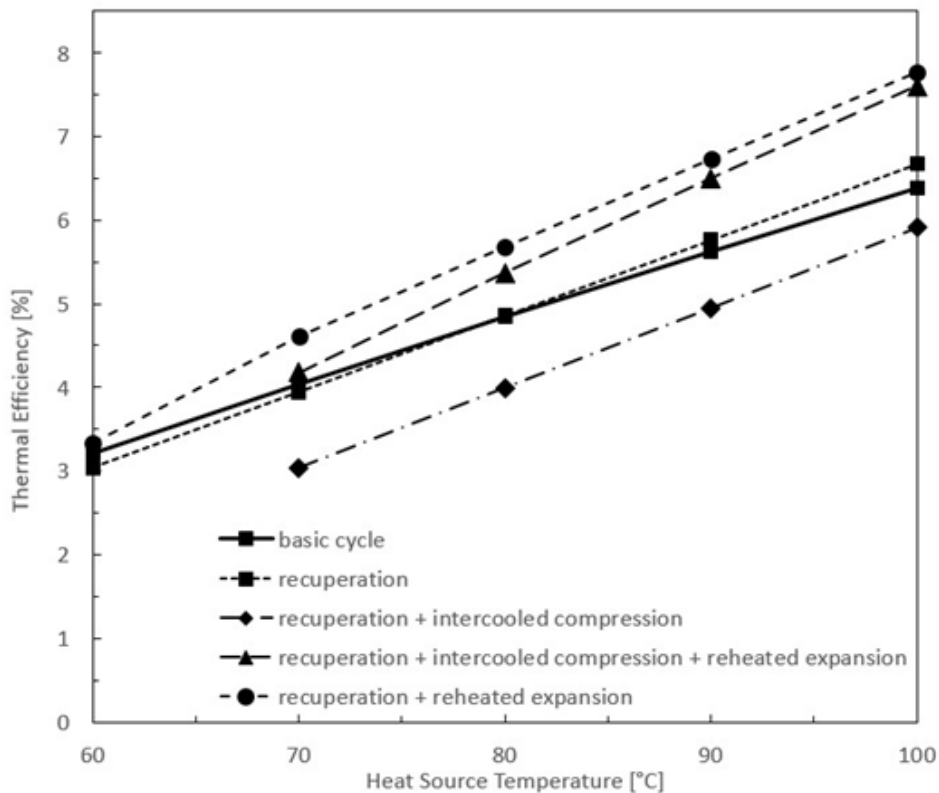
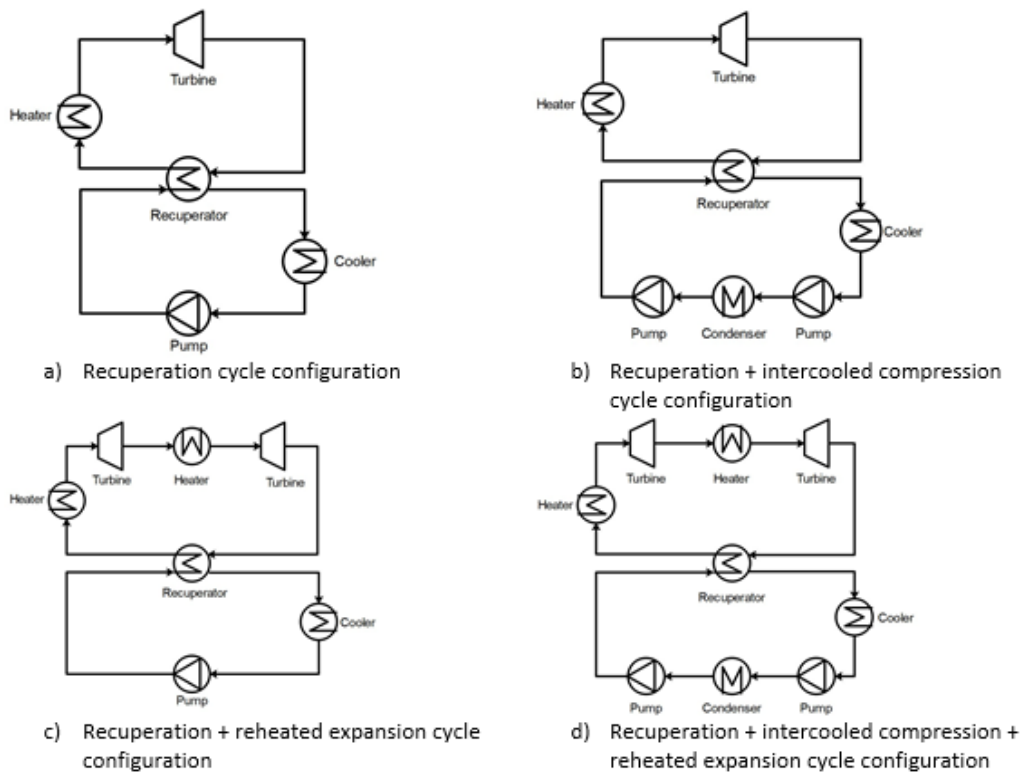
Figure 4: intercooled compression and reheated expansion cycle configurations and efficiencies

Figure 4d shows the resulting thermal efficiencies with respect to different heat source temperatures. Note that for the reheated expansion configuration, an implementation at a waste heat source temperature as low as 60°C was not possible: At low source temperatures, the maximum possible cycle pressure is also lower. Thus, the cycle pressure ratio is small at it was not possible to find an intermediate pressure, at which the fluid could be expanded a second time without condensation within the second turbine. Modelling could be started at a source temperature of 70°C with only little benefit over the basic configuration. At this point, reheated expansion improves the efficiency by 0.3 percentage points. The efficiency plots are diverging towards higher source temperatures with the reheated expansion configuration having a steeper rise of efficiency than the basic system layout. At a source temperature of 100°C, reheated expansion contributes to a 0.7 percentage points higher cycle efficiency. Thus, reheated expansion becomes more significant with rising waste heat temperatures.

The power cycle configuration shown in Figure 4c combines the modifications of intercooled compression and reheated expansion. Its efficiency plot (Figure 4d) is relatively close to the efficiency of the basic cycle. This results from the combination of reheated expansion, which

enhances the cycle efficiency and intercooled compression, which decreases the cycle efficiency for low temperatures. It is found that a source temperature of 60°C is too low for this configuration and it could not be implemented as the small pressure ratio impedes the addition of reheated expansion. At 90°C, there is a turning point where this combination of modifications outperforms the basic configuration. There is a trend towards a greater efficiency gain in higher waste heat temperatures.

Figure 5a shows a system configuration that employs one recuperator to transfer heat from the expanded fluid to preheat the compressed fluid prior to the heater. The benefit from adding a recuperation step is the reduction of the the heat discharge to the heat sink. Consequently, the thermal energy at turbine exit does not have to be removed by the cooler, but can be transferred to the high pressure side of the power cycle. Figure 5d displays the resulting efficiency with regards to the waste heat source temperature. For temperatures as low as 60°C and 70°C, an additional recuperator step degrades the cycle efficiency. In order for a regenerator to function, the temperature of the working fluid after the turbine must be higher than after compression. For waste heat temperatures of 60°C and 70°C, these temperatures were nearly equal so that no thermal energy could be transferred. In order to employ a regenerator, the cycle pressure ratio changes, which leads to a lower net power output. Only from source temperatures greater than 80°C, the optimum cycle pressure ratio is not affected by the recuperator and a gain of efficiency can be achieved. The efficiency curve of the recuperation configuration in Figure 5e is noticeably steeper than the basic system line. Thus, a greater efficiency benefit with higher source temperature can be observed.



e) Thermal efficiencies of recuperation, intercooled compression and reheated expansion cycle

Figure 5: recuperation with modifications configurations and efficiencies

A grouping of intercooled compression and recuperation (Figure 5b) decreases the efficiency for source temperatures lower than 80°C (Figure 5e). Altogether, the combination of the two modifications results in a very low cycle efficiency which can be explained by the observation from Figure 4: intercooled compression and reheated expansion cycle configurations

and efficiencies where intercooled compression negatively affected the cycle efficiency at temperatures until 80°C.

Already from very low waste heat source temperatures, the combination of recuperation and reheated expansion (Figure 5c) outperforms the basic configuration. While for 60°C, the difference between their efficiencies is rather small (0.1 percentage points), the difference in efficiency grows rapidly with increasing heat source temperature (Figure 5e). At a waste heat source temperature of 100°C, the difference in efficiency already represents 1.4 percentage points.

Observing from Figure 5e, the combination of recuperation, intercooled compression and reheated expansion (Figure 5d) is one of the most complex cycle architectures in this study. The cycle configuration was modelled with nine components, where intercooled compression and reheated expansion have two stages each. Numerical results showed that this system layout is less attractive than the combination of recuperation and reheated expansion due to the negative influence of intercooled compression. For temperatures as low as 60°C, it was not possible to model the system due to temperature and pressure restrictions: the temperature difference between recuperator outlet and cooler inlet are only a few degree Celsius. From a source temperature greater than 70°C, this configuration shows a steep rise in efficiency with increasing waste heat source, which is steeper than the slope of recuperation reheated expansion combination.

The presented system layout in Figure 6a is a split flow configuration. The CO₂ stream is split before heating and merges before the second stage of heat addition. Because this cycle architecture employs two heat exchangers for heating, the heat source can be exploited more efficiently than in other configurations. Figure 6c shows the numerical results for split flow configurations. For the configuration with split flow before heating, an implementation for a waste heat source temperature of 60°C was not possible because of the recuperator step. From source temperatures greater than 70°C, it can be noticed that this cycle architecture outperforms the basic configuration.

The split flow before heating and expansion configuration (Figure 6b) separates the CO₂ mass flow before heating and merges it after the expansion process. In the resulting efficiencies (Figure 6: split flow configurations and efficiencies), the recuperator step prohibited an implementation of this architecture for a waste heat source of 60°C. Overall, this cycle configuration has a rather poor efficiency at very low heat source temperatures with no major positive influence on the cycle efficiency in comparison to the basic system, although it contains almost double the amount of components.

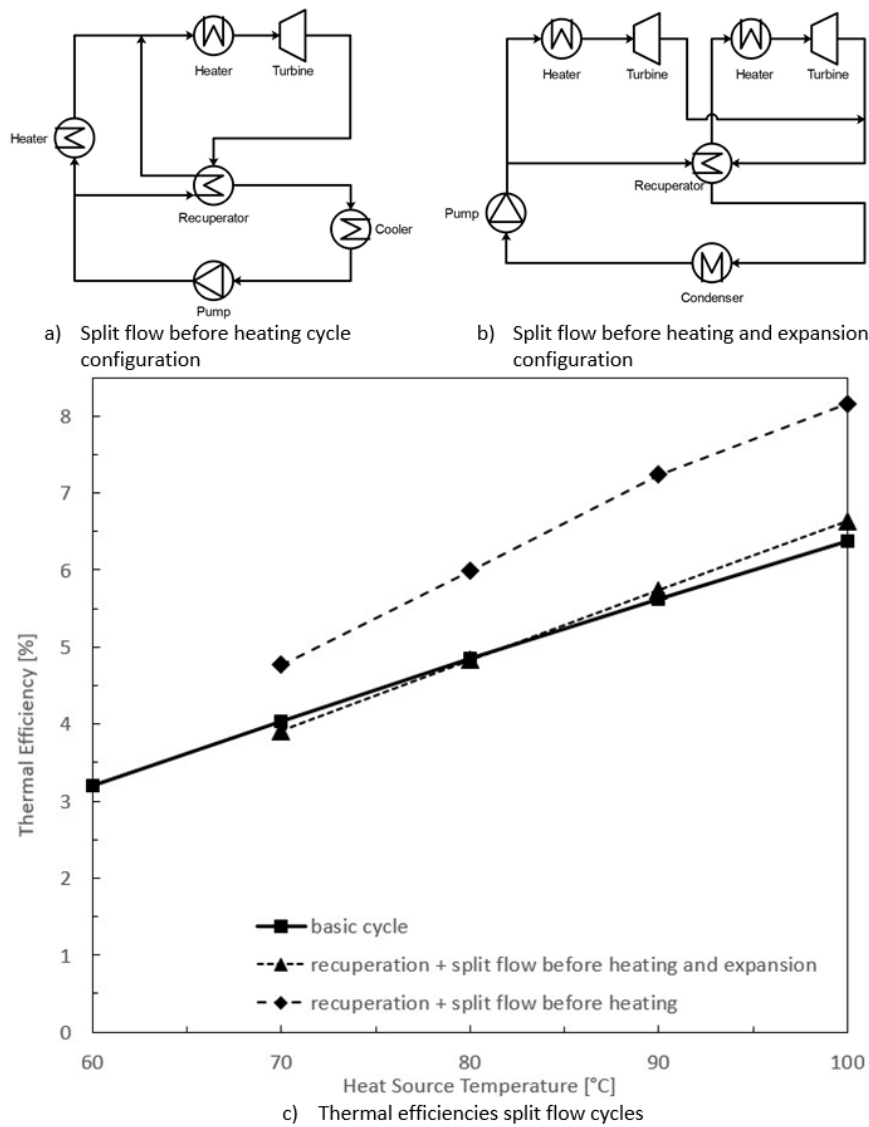


Figure 6: split flow configurations and efficiencies

Figure 7 shows the result from previous sections consolidated in one plot. It can be seen that the applied cycle modifications affect the thermal efficiency only in a minor percentage range for very low heat source temperatures. A maximum difference of 1.4 percentage points is noticed at a heat source temperature of 100°C between the basic cycle and the system with split flow before heating. This is because of the second heat exchanger for extraction of the waste heat source.

System layouts with intercooled compression are constantly lower than the basic cycle efficiency. All plots of system architectures with a recuperator show a steeper rise in efficiency than systems without recuperation. However, recuperation is suitable for source temperatures greater 80°C. Furthermore, one can see that only few cycle architectures are relevant for waste heat temperatures of 60°C and 70°C whereas the conventional power cycle plays the dominant role.

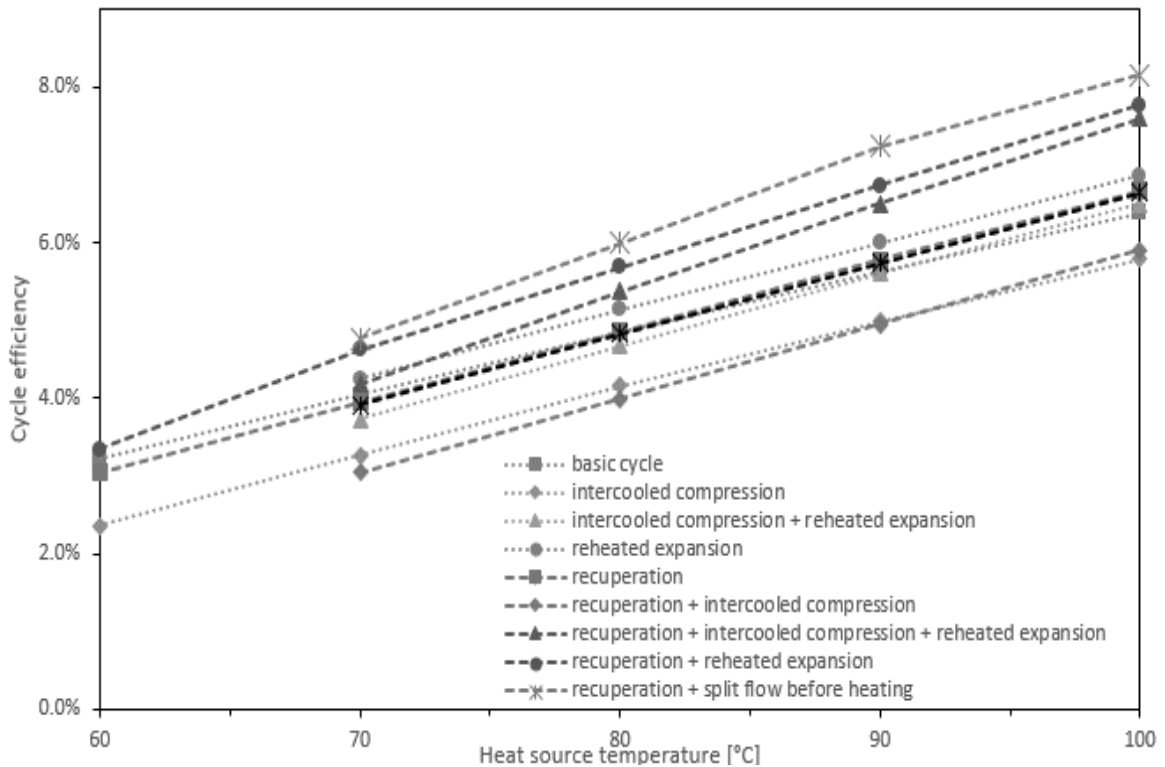


Figure 7: efficiencies of cycle architectures with respect to heat source temperature

Summary/Conclusions

The comparison of the sCO₂ cycle architectures revealed that the basic configuration performs best at heat source temperatures as low as 60°C to 80°C. For this sector, the small temperature range between heat source and heat sink limits the amount of applicable cycle modifications. Cycle modifications like recuperation start to be beneficial for temperatures above 80°C. Recuperation also contributes to a steeper gradient of the efficiency and results in diverging slopes of recuperative and basic system. Split flow before heating performed best within this comparative study above heat source temperatures of 80°C. With a system efficiency of 8.16 percent, 1.4 percentage points higher than the basic system performance. The modification with reheated expansion proved to enhance the thermal efficiency by 0.7 percentage points, which is small for low-grade waste heat. For rising waste heat temperatures, the benefit becomes greater. Intercooled compression decreased the thermal efficiency constantly by approximately 1 percentage point whereas for waste heat temperatures greater than 192°C, intercooled compression enhances the system performance.

In conclusion, the challenge to recover waste heat from sources with temperatures lower than 100°C can be addressed by sCO₂ cycles. However, the small operation temperature range excludes several cycle architectures involving measures that were found to be beneficial for higher operation temperature. For the design of such systems, the basic cycle configuration is recommended especially for source temperature slower than 80 °C. For source temperatures higher than 80 °C measures like recuperation can be considered. However, the efficiency gain needs to be compared to the increased complexity of the cycle and the related investment cost.

Acknowledgement

The authors would like to express their gratitude to the Luxembourg National Research Fund (FNR) for the financial support. The project has been conducted under the grand AFR 12541056.

References

- [1] Forman C, Muritala IK, Pardemann R, Meyer B. Estimating the global waste heat potential. *Renewable and Sustainable Energy Reviews* 2016;57:1568–79.
- [2] Li M, Wang J, Li S, Wang X, He W, Dai Y. Thermo-economic analysis and comparison of a CO₂ transcritical power cycle and an organic Rankine cycle. *Geothermics* 2014;50:101–11.
- [3] J. Calm, G. Hourahan. Refrigerant data summary; 2001.
- [4] Ahmadi MH, Mehrpooya M, Abbasi S, Pourfayaz F, Bruno JC. Thermo-economic analysis and multi-objective optimization of a transcritical CO₂ power cycle driven by solar energy and LNG cold recovery. *Thermal Science and Engineering Progress* 2017;4:185–96.
- [5] Amini A, Mirkhani N, Pakjesm Pourfard P, Ashjaee M, Khodkar MA. Thermo-economic optimization of low-grade waste heat recovery in Yazd combined-cycle power plant (Iran) by a CO₂ transcritical Rankine cycle. *Energy* 2015;86:74–84.
- [6] Xia J, Wang J, Zhou K, Zhao P, Dai Y. Thermodynamic and economic analysis and multi-objective optimization of a novel transcritical CO₂ Rankine cycle with an ejector driven by low grade heat source. *Energy* 2018;161:337–51.
- [7] Mirkhani N, Amini A, Ashjaee M. Thermo-economic analysis of transcritical CO₂ cycles with bounded and unbounded reheats in low-temperature heat recovery applications. *Energy* 2017;133:676–90.
- [8] Hanfei T. 5_268_2011_Parametric-analysis-of-reheat-co2-transcritical-pc-LTHS. 2nd International Conference on Environmental Engineering and Applications 2011.
- [9] Chen Y, Lundqvist P, Platell P. Theoretical research of carbon dioxide power cycle application in automobile industry to reduce vehicle's fuel consumption. *Applied Thermal Engineering* 2005;25(14-15):2041–53.
- [10] Nassar A, Moroz L, Burlaka M, Pagur P, Govoruschenko Y. Designing supercritical CO₂ power plants using an integrated design system. *Proceedings of ASME 2014 Gas Turbine India Conference* 2014.
- [11] Kim MS, Ahn Y, Kim B, Lee JI. Study on the supercritical CO₂ power cycles for landfill gas firing gas turbine bottoming cycle. *Energy* 2016;111:893–909.
- [12] Li X, Huang H, Zhao W. A supercritical or transcritical Rankine cycle with ejector using low-grade heat. *Energy Conversion and Management* 2014;78:551–8.
- [13] Kim YM, Kim CG, Favrat D. Transcritical or supercritical CO₂ cycles using both low- and high-temperature heat sources. *Energy* 2012;43(1):402–15.
- [14] Padilla RV, Too YCS, Benito R, McNaughton R, Stein W. Thermodynamic feasibility of alternative supercritical CO₂ Brayton cycles integrated with an ejector. *Applied Energy* 2016;169:49–62.
- [15] Walnum HT, Nekså P, Nord LO, Andresen T. Modelling and simulation of CO₂ (carbon dioxide) bottoming cycles for offshore oil and gas installations at design and off-design conditions. *Energy* 2013;59:513–20.
- [16] Crespi F, Gavagnin G, Sánchez D, Martínez GS. Supercritical carbon dioxide cycles for power generation: A review. *Applied Energy* 2017;195:152–83.
- [17] Meggitt PLC. Heatric PCHE - Performance and Efficiency.
- [18] Steag System Technologies. EBSILON Professional for the design of power plants.
- [19] National Institute of Standards and Technology. REFPROP: NIST Reference Fluid Thermodynamic and Transport Properties Database.
- [20] R. Span, W. Wagner. A New Equation of State for Carbon Dioxide Covering the Fluid Region from the Triple-Point Temperature to 1100 K at Pressures up to 800 MPa. *Journal of Physical and Chemical Reference Data* 1996;25.6:1509.

Design, Build and Initial Testing of a Novel Energy Management System

T. Weller^{1*}, M. Johnson¹, F. Trebilcock², S. Lecompte³ and D. Bauer¹

¹German Aerospace Center, Pfaffenwaldring 38-40, 70569 Stuttgart, Germany

²Tecnalia Research & Innovation, Area Anardi 5, Azpeitia, Guipuzkoa 20730, Spain

³Ghent University, Faculty of Engineering and Architecture, Department of Electrical Energy, Metals, Mechanical Constructions & Systems, Ghent 9000, Belgium

*Corresponding author: Thilo.Weller@dlr.de

Abstract

A compressed heat energy storage (CHEST) system is a novel energy management system based on Rankine cycles. The design and build of a first lab-scale CHEST system is for many reasons a very complex process. On the one hand, the individual components such as the high temperature heat pump, organic Rankine cycle and thermal energy storage must be able to perform efficiently under a wide range of operating conditions, and on the other hand, these components have to be able to operate together as a highly transient overall system. This work gives an overview on the design and initial testing of the individual prototypes and the challenges of combining them to a novel energy management system.

Keywords: high temperature heat pump, organic Rankine cycle, thermal energy storage, Carnot battery, power-heat-power.

Introduction/Background

Efficient energy storage and sector coupling are important key elements in future energy scenarios. Using a specific kind of Carnot battery based on Rankine cycles, both elements are combined. The so-called CHEST system, discussed by Steinmann [1], consists of a high temperature heat pump (HTHP), a high temperature thermal energy storage (HT-TES) and an organic Rankine cycle (ORC), which as a system is coupled to a smart district heating network and to renewable sources. The goal of the CHESTER system, a variant of the CHEST system, is to provide a flexible electricity and heat dispatchment with discontinuous energy input from renewable sources. A simplified flow diagram with the main components of the CHESTER system is shown in Figure 1.

In charging mode, thermal energy from renewable sources is converted to high temperature heat by the HTHP. The electric compressor of the heat pump is driven by surplus electricity from the power grid at times of low demand. The high temperature heat is stored in the storage system, which is a cascade of a latent heat thermal energy storage (LH-TES) and a sensible heat thermal energy storage (SH-TES). On demand, the high temperature heat can be converted back into electrical energy by the ORC. During discharging, the working fluid of the ORC is preheated by the SH-TES and evaporated in the LH-TES. The operating modes of the CHESTER system can be varied in a wide range. With this, depending on the ratio between input and output of heat and electrical energy, a flexible and demand-oriented energy supply can be provided. Within the framework of the European Union H2020 project CHESTER, this system is being analysed and developed, including the design, build and experimental testing of the first lab-scale CHESTER system. The aim is to provide proof of

function for the CHESTER concept and to gain real experience with system characteristics and dynamics.

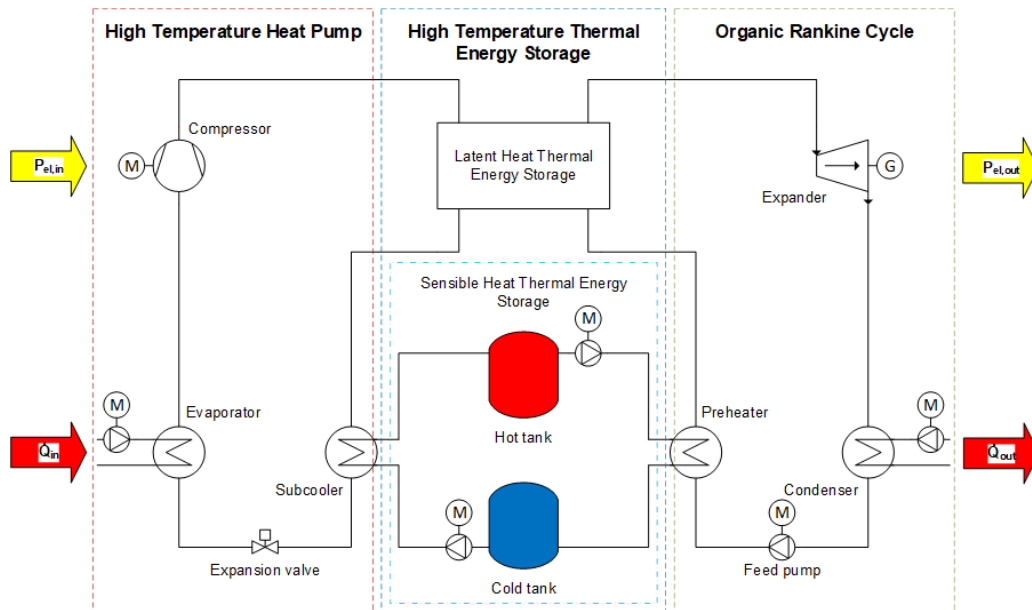


Figure 1: Simplified flow diagram of a CHESTER system

The lab-scale system is designed for an electrical output power of 10 kW_e and also combines the main CHESTER system components HTHP, ORC and HT-TES. In contrast to the CHESTER concept and a large-scale version of the system, the lab-scale system is connected to a temperature-controlled heat source and -sink instead of a smart district heating network. The heat source consists of an electric flow heater with a capacity of 100 kW, which is connected to the evaporator of the HTHP via a water circuit. The water temperature can be controlled by a three-way valve. Thus, in charging mode, the evaporator can be supplied with hot water in a temperature range between 50 °C-100 °C. At the ORC condenser, the thermal energy is dissipated to a cooling water network. The heat sink is controlled by a three-way valve, with which it is possible to regulate the cooling water during discharging, with temperatures from uncooled down to 17 °C possible.

As discussed by Trebilcock et al [2], the performance of a CHESTER system integrated into a smart district heating network was investigated for six different operating modes using several different software programs. Based on the generated data, general design parameters for the lab-scale system could be derived. In [3] and [4], the thermodynamic performance of HTHP and an ORC using different refrigerants were analyzed. Under consideration of the CHESTER project constraints and in order to ensure a high efficiency under a wide range of boundary conditions, R1233zd(E) for the HTHP prototype and R1336mzz(E) for the ORC prototype were identified as suitable working fluids. Phase change materials (PCMs) for LH-TES must have high cycle stability, should not cause corrosive reactions with the storage components and have to match the required temperature range(s) of the application. An overview of suitable PCMs for process heat applications in the temperature range 120 °C to 250 °C is given by Bauer et al [5]. For the LH-TES prototype of the lab-scale system, a eutectic mixture of potassium nitrate and lithium nitrate with a melting temperature of 133 °C was selected. After the preliminary definition of general design parameters, performance maps for the HTHP and ORC were calculated and a nominal operating point for charging and discharging was determined. Another design criterion is that the built components need to physically fit in the available laboratory space. With all these aspects in mind, the design was

defined and the prototypes were manufactured. Individual testing of these novel components prior to system operation delivers information regarding the performance maps and constraints of each of the prototypes and will be used in the development of the system operation performance maps and experimental characterization campaign.

High Temperature Heat Pump

The HTHP lab prototype is a water-to-water heat pump designed to operate at evaporating temperatures between 70 and 100 °C and condensing temperatures up to approximately 150 °C.

The prototype consists of a single stage vapour compression refrigeration machine with a dedicated subcooler. A special high temperature single piston reciprocating compressor was considered in this prototype. A suction-line accumulator was implemented in order to protect the compressor from liquid entering the admission, as well as an oil separator system in the discharge line in order to ensure the proper return of the lubricant to the compressor. On the water side, three independent water loops for the evaporator, condenser and subcooler were integrated, each of them including all the necessary auxiliary components such as pumps, valves, flow switches and instrumentation required for the proper and safe operation of the heat pump. The condenser substitutes the functionality of the LH-TES in the lab-scale CHESTER system for this dedicated characterization campaign.

For the control of the suction superheating, a fast response electronic expansion valve was considered. A complete in-house control algorithm was developed and implemented in a control system for controlling and monitoring the HTHP. Everything was mounted within a control cabinet with its own touch panel for easy operation of the unit. Once the experimental characterization campaign finished, the unit was mounted on a self-supporting steel frame structure prepared for the transport of the HTHP for integration into the lab-scale system, as shown in Figure 2.



Figure 2: Overview of the HTHP unit with/without the protective casing

The working fluid considered in this prototype is the R1233zd(E). It is a hydro-chloro-fluoro-olefin (HCFO), which is an alternative refrigerant with low global warming potential (GWP) when compared to the conventional fluids. It is a non-flammable liquid with a boiling point of 15.1 °C (at atmospheric pressure) and critical temperature of 165.6 °C.

The main component of the HTHP is the compressor. This is a single piston reciprocating type compressor and can operate at a maximum internal temperature of 215 °C. It is equipped

with a permanent magnet synchronous motor that can provide a wide range of motor speeds while achieving high efficiencies. The motor's maximum operating temperature is 110 °C, and it is continuously cooled by means of a water jacket cooling circuit. The compressor's speed variation and monitoring are performed by means of a 15 kW Siemens Sinamics inverter drive unit. The crankcase holds up to 7.5 l of lubricant and is equipped with an internal oil circuit, an oil filter and two electric 1 kW preheaters.

The main characteristics of the HTHP unit are presented in Table 1.

Table 1: HTHP main characteristics

Property	Quantity
Type	Water-to-water, single stage with subcooler
Operating range	Heat source: 70-100 °C; Heat sink: 100-150 °C
Heating capacity*	Condenser: 35 kW / Subcooler: 25 kW approx.
Compressor	Reciprocating, Single Piston. Model HBC511 from Viking Heat Engines©. 15 kW Siemens© inverter drive unit
Heat exchangers	Plate heat exchangers from SWEP©
Expansion device	Electronic expansion valve – Siemens© MVL661
Control	Programmable logic controller (PLC) with integrated touch panel

* Heat source: water inlet at 90 °C; Heat sink: water outlet at 138 °C approx.; Subcooler: water inlet/outlet at 55/129 °C approx.

In the characterization of the HTHP unit, a total number of 50 tests were conducted between August and October of 2020. The experimental campaign consisted of two phases: a first set of tests for the characterization of the operating conditions required in the charging mode of the HT- TES and a second set of tests for further characterizing the HTHP performance curve.

For the first testing phase, stable condensing conditions were defined. Therefore, fixed condensing temperatures around 137 °C were analysed. Three different evaporator water inlet temperatures were considered (70, 80 and 90 °C), as well as three different compressor speeds (800, 1100 and 1500 rpm). The subcooler was analysed over a wide range of operating conditions, however it always provided enough cooling of the liquid refrigerant in order to keep the liquid line below 80 °C, and therefore protect all electronic devices in this part of the system (solenoid and expansion valves, mainly). In all the tests, the subcooler water outlet temperature was kept as close to the condensing temperature as possible (i.e.: 130 °C).

For the extended tests performed to further characterize the HTHP performance curve, the evaporator and subcooler water inlet temperatures were fixed at 80 °C and 60 °C, respectively. The compressor was operated at two different speeds, 1100 and 1500 rpm, while the condensing temperature was varied from 100 °C to almost 150 °C in steps of 10 Kelvin.

Figure 3 shows an overview of the experimental tests performed at different condenser outlet water temperatures for a wide range of heat source temperatures.

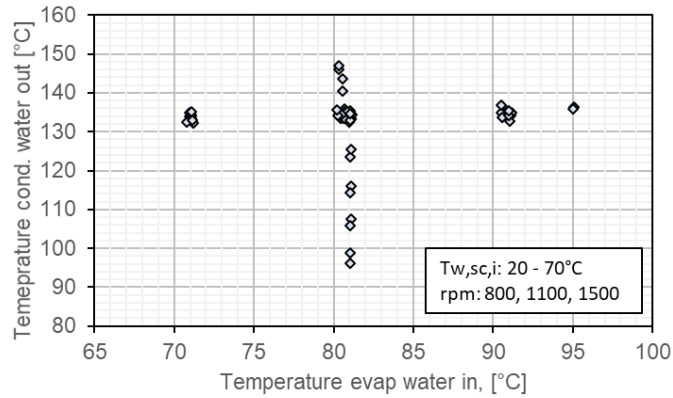


Figure 3: HTHP test mapping

In general terms, the HTHP operated satisfactorily along the experimental characterization phase. Heating capacities in the condenser between 22.5 to 44.5 kW were achieved when operating at 1500 rpm, while values ranging from 17.3 to 31.5 kW were observed when operating at 1100 rpm. In the case of the subcooler, heating capacities of around 10 to 20 kW were usually achieved, with some extreme points where values up to 30 kW were observed. The heat capacities for different operating points are presented in Figure 4.

In regard to the HTHP performance, net coefficient of performance (COP) values that ranged from 3.56 to 6.10 were achieved at motor speeds of 1500 rpm, while at 1100 rpm the net COP resulted in values approximately 15 % higher, ranging from 4.12 to 6.92.

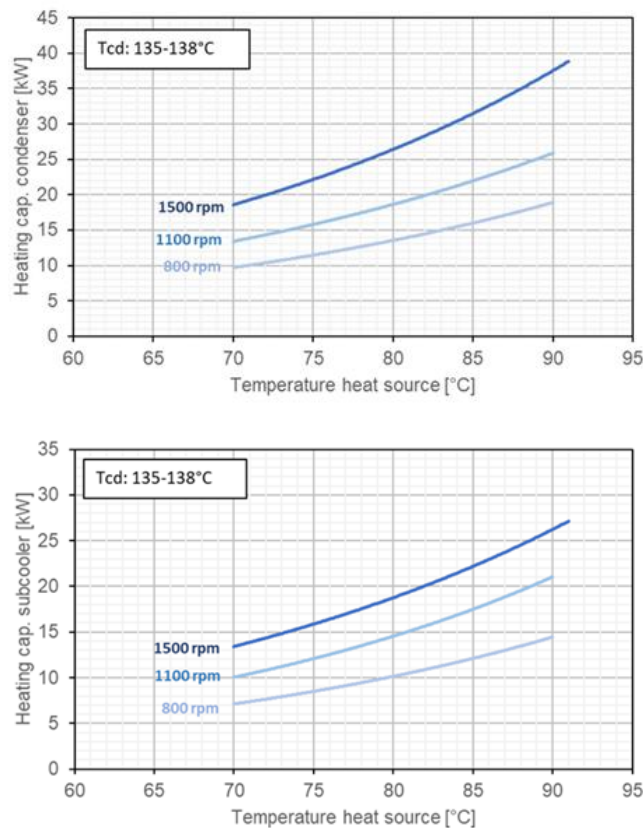


Figure 4: HTHP heating capacity for tests at 800, 1100 and 1500 rpm

From the experimental characterization campaign, it can be concluded that the objectives required within the CHESTER project in order to provide a HTHP capable of operating at high evaporating and condensing temperatures were achieved. The HTHP prototype uses an environmentally friendly low-GWP refrigerant and was able to provide heat at condensing temperatures as high as 148 °C. When working at nominal point conditions, the unit achieved thermal capacities of around 35 kW and 25 kW in the condenser and subcooler, respectively. As the HTHP benefits from the high degree of sensible heat used within the system, COP values ranging from 3 up to almost 7 were achieved. Therefore, the heat pump's expected performance was validated for the different operating conditions required.

Organic Rankine Cycle

The aim is to build a lab-scale CHESTER system that is capable of delivering around 10 kW_e power output. This defines the capacity of the ORC prototype that has to be designed and manufactured. To achieve this goal, a preliminary analysis and design of the ORC prototype system was carried out to define the most appropriate working fluid for the experiments and also the sizing and characteristics of the individual components. Furthermore, the concept of variable valve timing is investigated to optimize the built-in volume ratio for the specific working conditions of the CHESTER system. The resulting system is shortly presented in this work. Finally, some preliminary results of the experimental investigations are shared.



Figure 5: ORC prototype experimental test rig

Figure 5 shows the final experimental test-rig. It consists of a piston expander, plate heat exchangers as condenser and evaporator, bypass valve over the expander, liquid receiver and a membrane pump. It is fully instrumented with pressure and temperature sensors over the main components and a Coriolis flow meter after the pump. The working fluid used is R1336mzz(E).

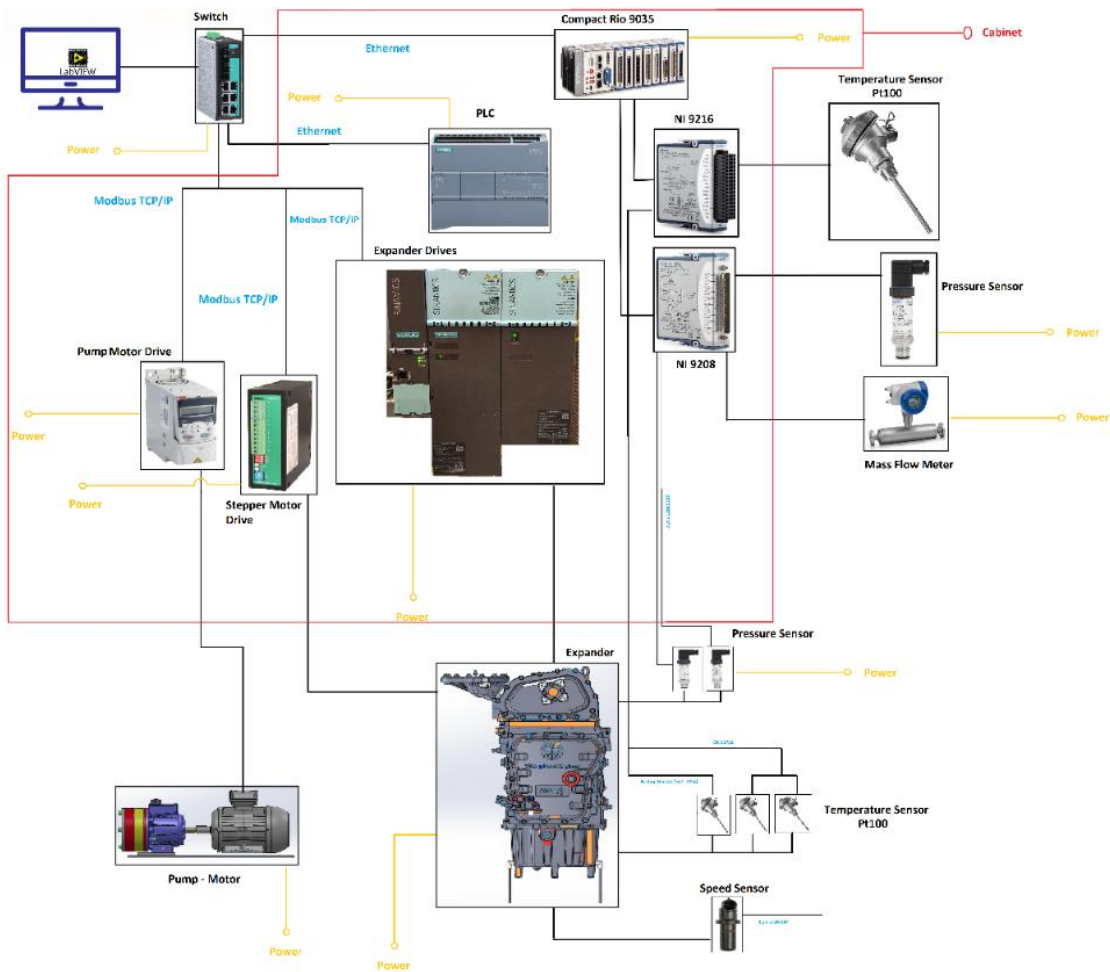


Figure 6: A schematic of the control system architecture for the ORC test rig

Figure 6 represents a schematic of how the different control systems are connected. It also shows the flow of information from the sensors to the data and measurement acquisition system. All the devices are connected to a network switch to facilitate communication of data over a computer network. The switch itself is not mounted inside the cabinet. The switch is connected to a National Instruments (NI) chassis (NI CompactRIO), which is an embedded controller that reads signals from the individual NI modules mounted on the chassis. These NI modules are then connected to pressure and temperature sensors, the mass flow meter and the speed sensor for the piston movement. A Siemens PLC is used to control the expander drives and also the motor drives for the pump and the stepper motor. The control operating loop in LabView is shown in Figure 7.

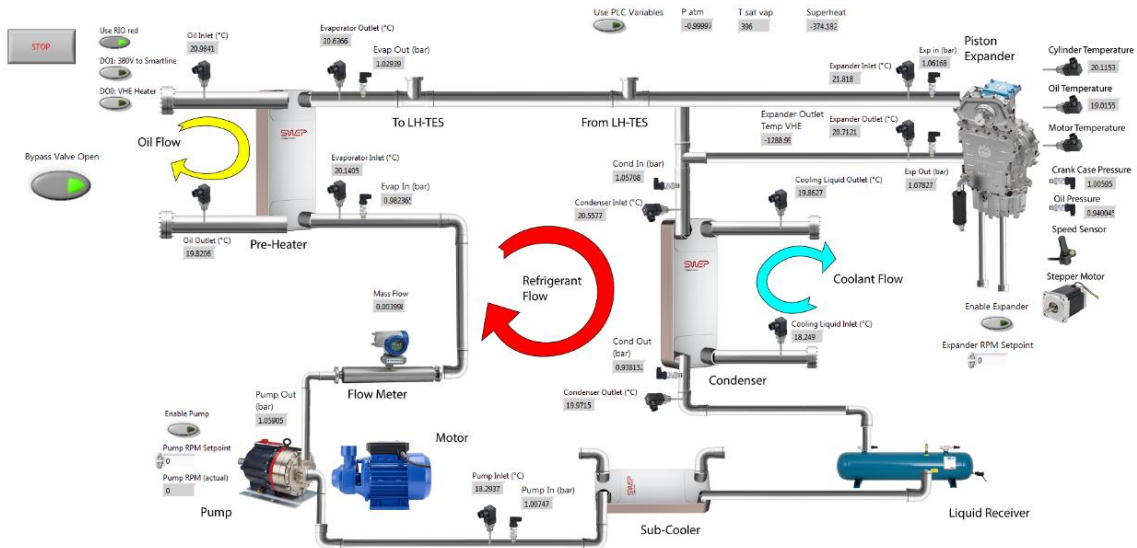


Figure 7: LabView front panel interface indicating the state of the refrigerant at a given location

The limits of the experimental campaign are given in Table 2.

Table 2: Factors under consideration and corresponding limits

Factors	Levels	
	Minimum limit	Maximum limit
RPM expander	800	1500
RPM pump	600	1100
Volume flow coolant (m ³ /h)	7	13.4
T coolant (°C)	20	50
T oil (°C)	125	135
Mass flow oil (kg/s)	1.5	3
Valve opening (degrees)	84	170

The preliminary results of the experimental campaign are shown in Figure 8. In total, 86 operating conditions are measured. The vertical line in the right figure indicates a change in working fluid charge. Left of the line, the system was charged with too much working fluid leading to a large subcooling (up to 20 °C). The measurements to the right correspond to an optimal charged system with subcooling of around 5 °C. A maximum power output of 8.14 kWe was achieved for a working fluid mass flow rate of 6.0 kg/s. The optimal pressure ratio is indicated to be higher than 6; this is typically achieved for expander rotational speeds between 1000 and 1200 rpm. Furthermore, for the investigated conditions a valve position of around 150 ° gives the highest power output.

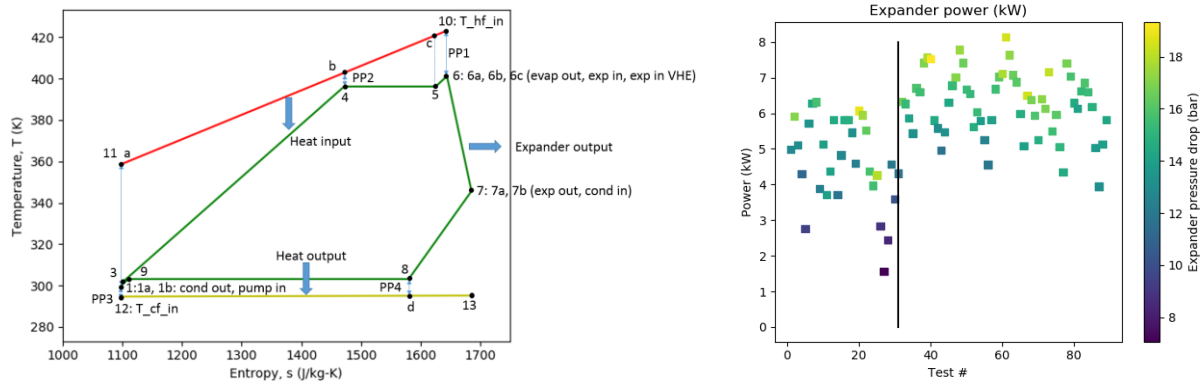


Figure 8: Example Ts diagram from the experiments (left), full dataset plotted in function of power and expander pressure difference (right)

High Temperature Thermal Energy Storage

The HT-TES is located between the HTHP and the ORC, coupling these two circuits and thereby creating the CHESTER system. The key component of the storage system is a LH-TES unit. This is designed as a vertical shell and tube heat exchanger embedded in the PCM. This allows for condensation and evaporation of the working fluids in the tubes at small temperature differences with respect to the melting temperature of the PCM on the shell side in order to minimize entropy generation in the system. Figure 9 shows the T-s diagrams for the charging (HTHP circuit, left) and discharging (ORC circuit, right) modes. The upper temperature plateaus indicate the evaporation temperatures, while the lower plateaus indicate the condensation temperatures. The melting temperature of the PCM, shown with the dotted line at 133 °C, has a constant temperature difference to the isothermal evaporation temperature, which is a general advantage of latent heat storage technology.

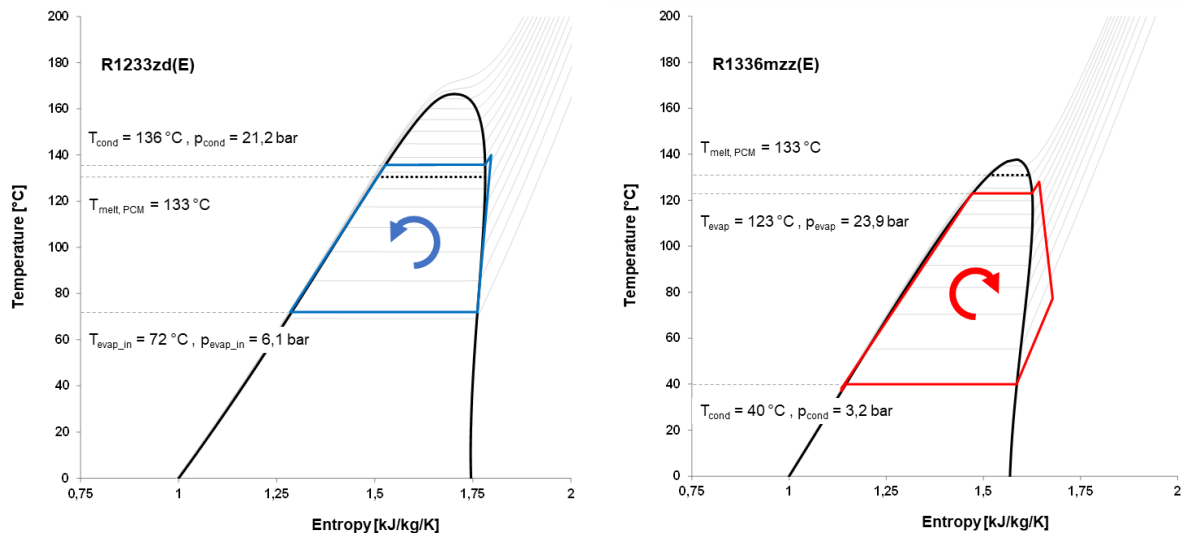


Figure 9: T-s diagram with charging mode using HTHP (left) and discharging mode using ORC (right) of the lab-scale CHESTER system at nominal point conditions

For the LH-TES, a novel dual-tube heat exchanger storage concept has been developed. This dual-tube concept was necessary to separate the charging and discharging circuits. These use different working fluids and operating conditions, and as novel systems the HTHP and ORC systems could be independently optimized. Moreover, migration of refrigerant and lubricant

is avoided, as well as a reduction in the number of two- and three-way valves achieved. This reduces costs and simplifies the control systems.

Axial aluminium fins connect the two tube systems and are immersed in the PCM storage media. These improve the heat transfer between the PCM and the working fluid in the heat exchanger tubes, since nitrate salts generally have a low thermal conductivity of about 0.5 W/m/K [6]. In the desired temperature range, aluminium is a suitable fin material due to its compatibility with nitrate salts and low volumetric costs as well as high thermal conductivity and formability. The fin design was thermodynamically analysed and optimized, also considering manufacturing and cost constraints. The challenge is to obtain an extrudable fin shape, to avoid far-removed areas in the PCM volume and to achieve a low fin fraction. After the design was defined and refined for manufacturing, fin profiles were built and attached to the tubes. Figure 10 shows the two-dimensional temperature distribution over the cross-section of the dual tube heat exchanger during charging, obtained from a thermodynamic analysis, and a dual tube assembly consisting of two fin segments and two steel tubes.

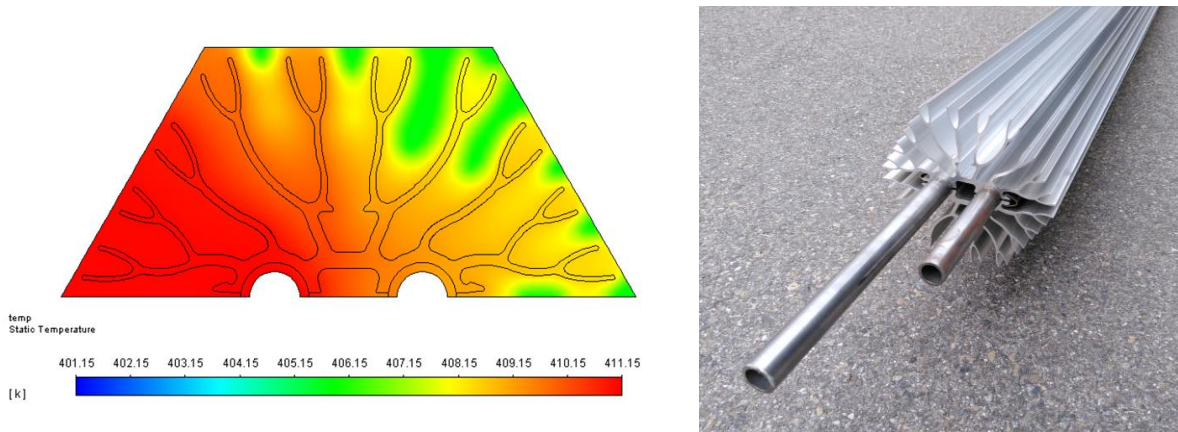


Figure 10: Simulated temperature distribution over the cross-section during charging (left) and dual tube assembly (right)

The dual-tubes assemblies are connected to the headers and integrated into the storage containment. The heat exchanger is immersed vertically within the storage material. This allows for density changes and simplified flow during evaporation and condensation of the refrigerants. Similarly, volume change in the PCM during phase change from solid to liquid or reverse is allowed for by the axial fins. A technical drawing of the final storage design and an image of the LH-TES unit within the manufacturing process are depicted in Figure 11.

In charging mode, the working fluid of the HTHP is condensed while flowing through the vertical heat exchanger in the LH-TES from top to bottom. Thermal energy is transferred from the working fluid over the steel tubes and aluminium fins to the PCM, which melts. Conversely, in discharging mode, the working fluid of the ORC enters the heat exchanger at the bottom. Due to the driving temperature difference, heat is transferred back from the PCM to the working fluid and the working fluid evaporates while flowing to the top. The PCM solidifies as thermal energy is extracted from the LH-TES. The PCM volume in the storage containment is under atmospheric pressure throughout the entire process.



Figure 11: Technical drawing of the final storage design (left) and LH-TES during manufacturing (right)

For the experimental prototype testing, temperature sensors were placed on and around several dual-tubes as well as in selected areas of the PCM volume. After assembly in the laboratory, the LH-TES was thermally insulated and equipped with an electrical trace heating system to minimize heat losses during downtimes. The design parameters of the LH-TES unit are summarized in Table 3.

Table 3: As-built design parameters of the LH-TES unit

Property	Quantity
Storage capacity	approx. 160 kWh
Heat exchanger type	Tube bundle with separate circuits for charging and discharging
Heat exchanger configuration	Vertical tube pairs integrated into the PCM volume and connected to the headers
Effective tube length	3 m
Storage material (PCM)	Eutectic of KNO_3 - LiNO_3 (63% - 37%)
PCM mass	approx. 4400 kg

After condensing in the LH-TES, the working fluid of the HTHP, during charging of the storage system, flows to the SH-TES. Here, sensible heat is dissipated by subcooling the working fluid and stored in the SH-TES. During discharging of the HT-TES, this stored thermal energy is used to preheat the working fluid in the ORC circuit before it is evaporated in the LH-TES. The SH-TES is designed as two-tank system with a hot and a cold tank. Due to its high specific heat capacity and low costs at the necessary operating conditions, water is used as the storage medium. During operation, hot tank water temperatures are above 100 °C; to prevent the storage medium from evaporating, both tanks are equipped with a nitrogen

pressure control system, keeping the SH-TES at 5 bar. A schematic and an image of the SH-TES tanks can be seen in Figure 12. In charging mode, water is pumped from the cold tank through the subcooler of the HTHP, heated and stored in the hot tank. The volume change is thereby compensated by the nitrogen pressure control system. During discharging, water from the hot tank flows to the preheater heat exchanger of the ORC and back to the cold tank, as shown in Figure 1.

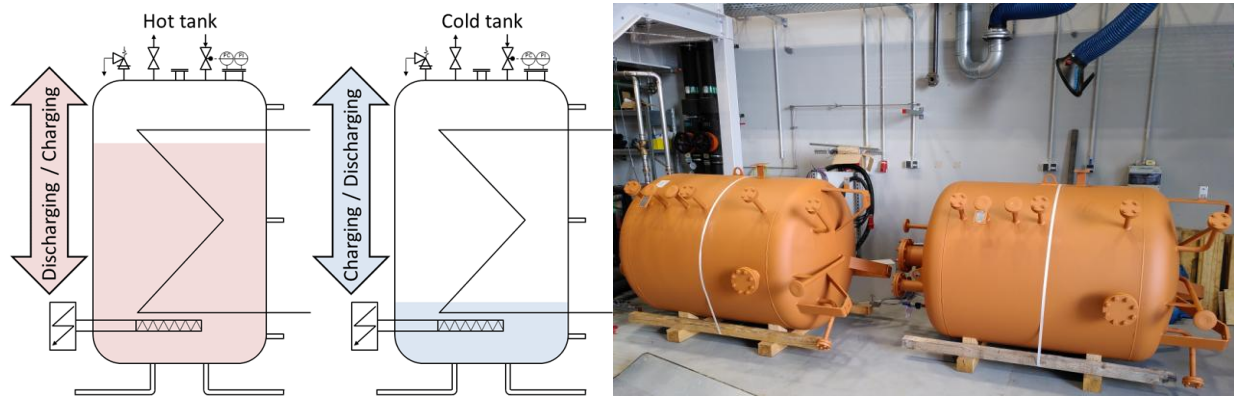


Figure 12: SH-TES tanks as a schematic (left) and after manufacturing (right)

In addition, both tanks are fitted with electric immersion heaters and internal heat exchangers, which are connected to a cooling water network. Thus, the water temperature can be adjusted between the charging and discharging process in order to generate reproducible results within the experimental analysis of the lab-scale system and increase the parameter testing range. The design parameters of the SH-TES tanks are given in Table 4.

Table 4: Technical specifications of the SH-TES

Property	Quantity
Storage capacity	approx. 210 kWh
Storage type	Two-tank system with a hot and a cold tank
Storage material	Water
Temperature range	40-135 °C
Tank volume	2 m ³ each

Before integrating the HT-TES into the overall CHESTER system, the LH-TES unit has to be analysed on its own. For this purpose, the storage was connected to a stand-alone steam infrastructure designed for evaporation and condensation of organic fluids in a wide range of operating parameters. In order to determine the LH-TES characteristics, a test matrix for charging and discharging at different flow rates and pressures was developed. Another goal is to study the behaviour of the storage component for different operating modes and to validate the numerical models used during the design process. Currently, the test setup is being prepared and results are expected in the upcoming months.

Summary/Conclusions

A lab-scale CHESTER system connecting a HTHP and an ORC via a HT-TES has been designed and built and will be tested in the coming months. This system allows for flexible management of energy with fluctuating renewable sources being dispatched at times of demand. This novel system combines a HTHP operating at condensation temperatures up to 148 °C, an ORC that operates optimally at off-design conditions and a dual-tube LH-TES cascaded with a

SH-TES, allowing for testing of a wide range of system parameters. The testing campaigns for the HTHP and ORC have been successfully conducted and presented, providing a basis for the performance maps of the lab-scale CHESTER system. The HTHP, HT-TES and ORC prototypes will now be connected for full system characterization.

Acknowledgements

The authors gratefully acknowledge the support of the European Union's Horizon 2020 research and innovation program through the Compressed Heat Energy Storage for Energy from Renewable sources (CHESTER) project (Grant agreement No. 764042).

References:

- [1] Steinmann W.-D., *The CHEST (Compressed Heat Energy Storage) concept for facility scale thermo mechanical energy storage*, Energy, 69:543-552, 2014.
- [2] Trebilcock F., Ramirez M., Pascual C., Weller T., Lecompte S., Hassan A. H., *Development of a Compressed Heat Energy Storage System Prototype*, Presented at IIR Rankine Conference, 2020, Glasgow, UK.
- [3] Corberán J. M., Hassan A. H., Payá J., *Thermodynamic analysis and selection of refrigerants for high temperature-heat pumps*, 25th IIR International Congress of Refrigeration, 2019, Montreal, Canada.
- [4] Pillai A., Kaya A., De Paepe M., Lecompte S., *Technical challenges in the design and integration of an organic Rankine cycle in a Carnot battery*, 5th International Seminar on ORC Power Systems, 2019, Athens, Greece.
- [5] Bauer T., Laing D., Steinmann W.-D., Kröner U., Tamme R., *Screening of phase change materials for process heat applications in the temperature range 120 to 250 °C*, Eurosun, 2008, Lisbon, Portugal.
- [6] Mehling H., Cabeza L. F., *Heat and cold storage with PCM*, Springer, 2008.

An Improved Thermodynamic Model for Supersonic Ejectors

A. Metsue^{1,2*}, R. Debroeyer¹, S. Poncet², Y. Bartosiewicz¹

¹Université catholique de Louvain
(UCLouvain), Institute Mechanics, Materials, and Civil Engineering (iMMC), Louvain-la-Neuve, 1348 Belgium

²Mechanical Engineering Department, Université de Sherbrooke, 2500 boulevard de l'Université,
Sherbrooke. (QC) J1K 2R1, Canada

*Corresponding author: antoine.metsue@uclouvain.be

Abstract

Ejector design relies heavily on the use of thermodynamic models. Indeed, such simplified models allow to assess ejector performance without the need of time-consuming experiments or advanced numerical simulations. Those models remain however limited by the strong and sometimes arguable assumptions they require. Most notably, the Fabri-choking has been the prevalent criterion used to calculate on-design ejector operation. However, the compound-choking has recently demonstrated to yield better matching with experimental results and appears to be an attractive alternative to the Fabri-choking. The present work aims at building, based on this assumption, a new on- and off-design thermodynamic model for supersonic ejectors using the compound-choking theory. First, the model is laid out and the integration of the compound-choking criterion is explained. The link between Fabri- and compound-choking is clarified by comparing the model with its Fabri-choking counterpart. Then, the characteristic curves are calibrated onto R134a and air experimental data. Finally, an analytical study is performed to show that imposing the compound-choking is actually equivalent to maximizing the mass flow rate within the ejector.

Keywords: Supersonic ejector; real gas; compound-choking; Fabri-choking; thermodynamic modeling.

Introduction

Much as they may offer a compelling alternative to traditional compression devices, ejectors are nonetheless characterized by complicated fluid dynamics, and some of the mechanisms at play within the ejector remain insufficiently understood, which hinders the performance of the global system [1]. Though the most straightforward approach to acquire data might be to perform experiments, such a strategy would not be economically advantageous as it would require too much time and material resources [2]. Instead, numerical methods seem to be the most profitable way to generate results, and *thermodynamic* models are the easiest and fastest way to give a first rough appreciation of ejector performance and/or to design them.

Ejectors are passive devices composed of a primary nozzle embedded into a larger secondary nozzle. They are used to suck and compress fluids. In the case of a supersonic ejector, the primary stream reaches sonic conditions in the near vicinity of the primary nozzle throat. The flow is consequently said to be *choked*, because the mass flow rate is independent of the downstream conditions. Complex turbulent mixing phenomena then occur in the mixing chamber; the primary stream transfers a part of its energy and momentum to the secondary stream through viscous shearing and suction into the low pressure jet [3]. During this process, the flow goes through a series of oblique shock waves that interact with the shear layer, thus re-compressing the fluid [4].

Because ejectors are used as entrainment devices, a convenient quantity to characterize their performance is their entrainment ratio $\omega = \dot{m}_s/\dot{m}_p$. To outline the different regimes of an

Nomenclature

Alpha numeric symbols

\dot{m}	Mass flow rate [$kg.s^{-1}$]
A	Area [m^2]
a	Speed of sound [$m.s^{-1}$]
D	Diameter [m]
G	Mass flux [$kg.m^{-2}.s^{-1}$]
h	Specific enthalpy [$J.kg^{-1}$]
M	Mach number [-]
p	Pressure [Pa]
R	Specific gas constant [$J.(kg.K)^{-1}$]
s	Specific entropy [$J.(kg.K)^{-1}$]
T	Temperature [K]
V	Velocity [$m.s^{-1}$]
x	Horizontal coordinate [m]

Subscripts

0	Stagnation conditions
2	Diffuser inlet
c	Setpoint back pressure
d	Diffuser outlet
e	Primary nozzle exit
<i>guess</i>	Gussed value
h	Hydraulic

is	Isentropic conditions
m	Mixed flow
max	Maximum
N	Normal shock
out	Outlet conditions
p	Primary flow
pol	Polytropic
s	Secondary flow
sat	Saturated vapour conditions
t	Primary throat
w	Wall
y	Hypothetical throat

Superscripts

*	Critical conditions
---	---------------------

Greek letters

β	Compound-flow indicator [m^2]
ϵ	Error tolerance [-]
η	Efficiency [-]
γ	Heat capacity ratio [-]
ω	Entrainment ratio [-]
ρ	Density [$kg.m^{-3}$]
τ	Shear stress [$kg.m^{-1}.s^{-2}$]

ejector, it is convenient to draw its characteristic curves, which depict the evolution of the entrainment ratio as a function of the back-pressure p_{out} . Depending on the operating conditions and on the internal geometry of the ejector, the secondary flow might become choked as well [5]. One may typically define the *critical* pressure p_{out}^* as the pressure at which the ejector transitions from on-design (ω constant wrt. p_{out}) to off-design (ω decreases with p_{out}). If the back-pressure is increased above a threshold value referred to as the *breakdown pressure*, the primary flow reverses back into the suction chamber. This case corresponds to a malfunction of the ejector. The interested reader can refer to the recent reviews of Besagni *et al.* [6] and Ameer *et al.* [7, 8] for more details about the applications, functioning and modeling of supersonic ejectors.

The first one-dimensional mathematical model of an ejector was introduced by Keenan *et al.* [9] in 1950. It was based on the application of mass, momentum and energy conservation equations, with the use of isentropic flow relations. This model has been used as a theoretical basis in ejector design since then. Munday and Bagster [10] later proposed modifications to the model of Keenan *et al.* [9]. Their theory assumed that the two streams conserve their integrity up until a particular downstream section in the mixing chamber. It was postulated that an hypothetical throat is formed by the primary flow and the ejector wall and that the secondary stream reaches a sonic velocity at that particular location (Fig. 1). The two streams then mix at constant pressure. This phenomenology is somewhat related to the *choked secondary flow* pattern that was discovered experimentally by Fabri and Siestrunk [11] in 1958. Since the presence of an hypothetical throat constitutes the basis of numerous mathematical models, the choking mechanism associated with this regime is often referred to as *Fabri-choking* [12].

Based on those early works, a number of first generation thermodynamic models were proposed. However, those models could only predict the ejector performance at critical mode operation. Thus, in 2013, Chen et al. [13] introduced a model to predict the ejector performance under critical and sub-critical operational regimes. Their model was also based on the presence of an hypothetical throat inside the constant area duct. For the sub-critical operating regime, this hypothesis was conserved.

As pointed out by Lamberts et al. [14], the *Fabri-choking* is used as the foundation of most thermodynamic ejector models, including the aforementioned ones [2, 10, 15, 16]. However, the Fabri-choking has only been experimentally observed once, by Lamberts et al. [12]. In addition, significant discrepancies remain between experiments and model predictions. Hence, the Fabri-choking is not necessarily representative of the actual phenomena occurring inside of a double-choked ejector. In their article, Lamberts et al. [14] described a new choking theory for perfect gas based on the early work of Bernstein et al. [17] about the so-called *compound-choking* theory. This theory [14] for perfect gas ejectors was then extended to real gas ejectors by Fang [18] and Metsue [19] for CFD and thermodynamic modeling purposes, respectively. Very recently, Croquer et al. [20] also validated the compound-choking for single-phase gas refrigerants using both approaches.

In the present work, the compound-choking theory developed by Fang [18] is used for the first time to build a *real gas* thermodynamic model for both on- and off-design operating regimes. First, the ejector model is presented, along with the solving algorithm. The model of Chen et al. [2] is modified to integrate the compound-choking theory. Then, the new model is used to shed light on the relationship between the Fabri-choking and compound-choking criteria. It is then calibrated on experimental data for supersonic ejectors working with R134a and air, and the results are discussed. Lastly, it is demonstrated that using the compound-choking criterion is actually equivalent to maximizing the total mass flow rate within the ejector working with a perfect gas. The paper ends by some conclusions and future views.

Discussion and Results

Over the numerous thermodynamic models published in the literature, the model of Chen et al. [2] is preferred as a basis for the present research, with some improvements. First, the primary flow is solved by maximizing the mass flow rate instead of imposing a Mach number M equal to unity at the throat, which constitute the primary definition of a choked flow. Most notably, the secondary flow is using the compound-choking theory, instead of the Fabri-choking theory commonly adopted by thermodynamic models.

The flow within an ejector is quite complex and thus often requires the use of assumptions in order to solve the flow swiftly, which is the essence of thermodynamic models. The main assumptions used in the present work are :

1. The flow is one dimensional, steady and adiabatic. The inlet (primary and secondary) and outlet velocities are supposed to be negligible.
2. Friction losses along the walls and within the shear layer between the primary and secondary streams are taken into account through isentropic efficiencies (Fig.1): η_p for the primary nozzle (sections $0 \rightarrow e$); $\eta_{p,y}$ for the friction losses undertaken by the primary flow within the mixing chamber (sections $e \rightarrow y$); η_s for the friction losses undertaken by the secondary flow within the mixing chamber (sections $0 \rightarrow y$) and η_d for the diffuser (sections $2 \rightarrow d$). The mixing losses between the primary and secondary streams are taken into account by means of a loss coefficient η_m (sections $y \rightarrow m$).

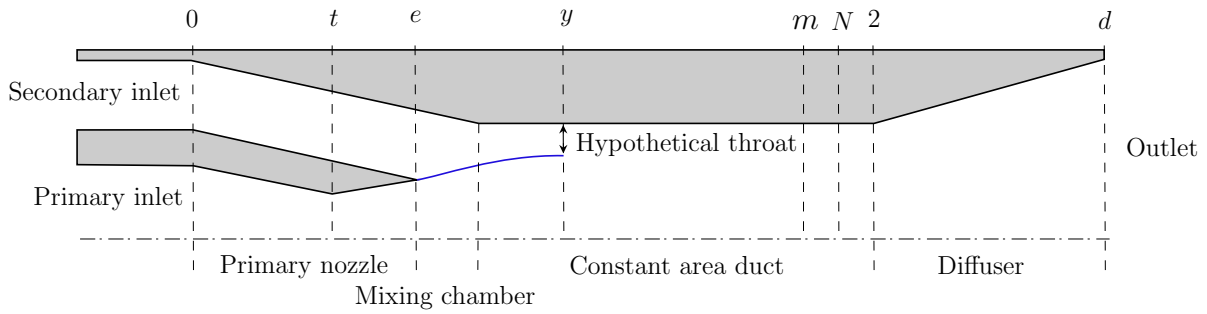


Fig. 1: Schematic diagram of the ejector model (top half).

3. Real gas properties are retrieved from the tabulated database COOLPROP available in the Python library.
4. Primary and secondary streams do not start mixing up until a particular section –that will be referred to as *mixing section*– located inside the constant area duct. At that location, both pressures are assumed to be equal. The location of the particular section at which the mixing phenomenon begins is the location of the hypothetical throat that is well described in the literature [21]. This section is *compound-choked* if the ejector is working under critical regime.

A schematic of the ejector, along with the notations that will be used in the following is shown in Fig. 1. Since the primary flow is assumed to be choked, the primary mass flow rate \dot{m}_p is constant and does not depend on any downstream quantity (i.e. it only depends on the primary stagnation conditions). The primary flow expands in the primary nozzle, and then further more in the mixing chamber until it reaches section y . The secondary flow is also –separately– expanded upon section y , and then only the mixing process starts. In other words, the two flows are essentially independent up until reaching section y . It is important to note that the position of the mixing section y is assumed to lie within the constant area section, whether or not the ejector is working in the on- or off-design regime. Then, the two flows start to mix at constant pressure, and are assumed to be completely mixed upon section m . If the flow is supersonic at section m , it consequently goes through a normal shock at section N , located in the constant area section as well. The flow thus reaches the diffuser inlet –section 2– at a subsonic speed. It then further expands in the diffuser, where the flow velocity is further decreased and the pressure recovered.

The flow in the primary nozzle can be solved from the stagnation conditions and the isentropic efficiency governing the flow in this part. For the sake of conciseness, the thorough derivation of the computation algorithm will not be presented here, as for a nozzle the equations are well known. In order to solve the flow, the hypothesis of choked primary flow has to be used. The classical way to impose such a condition is to set the Mach number to unity at the nozzle throat. Although this is the approach taken in the model of Chen et al. [2], one prefers here to impose the choking condition by the maximization of the mass flux. This approach presents two advantages. First, one does not require to know the speed of sound at the throat for the computation of the primary mass flow rate, which can sometimes be problematic for two-phase flows. Then, if one considers a non-isentropic expansion, the sonic section is not actually located at the geometric throat of the nozzle, but rather at a certain distance downstream. Imposing a Mach number equal to unity at the throat would consequently lead to an error in the computation of the primary mass flow rate. By rather directly maximizing the mass flow rate, this problem is avoided and the physical definition of a choked flow is preserved. Indeed, in the case of an

isentropic nozzle flow, it can be shown that maximizing the mass flux is equivalent to imposing $M = 1$ at the throat. The mass flux (i.e. the mass flow rate per unit area) is defined as :

$$G = \rho V. \quad (1)$$

Following an expansion from the primary stagnation conditions, one can compute G as a function of the primary pressure p_p . Then, from the maximum mass flow rate per unit area $G_{p,max}$ and the throat area of the nozzle $A_{p,t}$, one can find the mass flow rate for the choked primary nozzle by:

$$\dot{m}_p = G_{p,max} A_{p,t}. \quad (2)$$

The throat thermodynamic state is then fully solved, as $G_{p,max}$ provides the knowledge of the throat pressure $p_{p,t}$, which can later be used to find the throat enthalpy $h_{p,t}$ by using the definition of the isentropic efficiency η_p . The nozzle exit conditions are found by further expanding the flow from the known state at the throat. Knowing the exit section area $A_{p,e}$, the exit state of the fluid is found by using the mass and total enthalpy conservation equations.

The on-design conditions at section y (i.e. the mixing section) can be found using the compound-choking criterion for real gas derived in [20], i.e.:

$$\beta = p_y \left(\frac{A_{p,y}}{\rho_{p,y} V_{p,y}^2} (1 - M_{p,y}^2) + \frac{A_{s,y}}{\rho_{s,y} V_{s,y}^2} (1 - M_{s,y}^2) \right) = 0, \quad (3)$$

where the secondary flow properties at section y are computed from the secondary inlet conditions and using the prescribed value of p_y (please refer to Croquer et al. [20] for more details). Once the value of p_y is found with sufficient precision (i.e. $\beta \leq \epsilon$, with ϵ the error tolerance), all properties at section y are known, and the secondary mass flow rate can be computed, which allows to determine the on-design entrainment ratio $\omega = \dot{m}_s / \dot{m}_p$. Fig. 2 shows the flowchart of the on-design operation computational algorithm. Note that the procedure to compute the critical back pressure will be presented hereafter. One now proposes to review the off-design part of the model, which implies solving the flow up until the ejector exit section d . This part of the model also allows one to compute the critical back pressure, that is at the on-off-design interface. Under sub-critical operation, the ejector performance depends on downstream conditions (i.e. the back pressure p_{out}). Indeed, if the ejector is operating in the off-design regime, information will travel from the end of the diffuser up to the mixing section. This will have the effect of rising the mixing pressure p_y compared to when the ejector works in the on-design operation, therefore modifying the secondary mass flow rate. The entrainment ratio will thus be dependant on the back pressure. As a reminder, the condition for the ejector to be in on-design regime is given by:

$$p_{out} < p_{out}^*, \quad (4)$$

where p_{out}^* is the critical back pressure. Hence, the critical back pressure has to be computed to assess the operating regime. First, the thermodynamic states and velocities of the primary and secondary flows are computed using the on-design model, that is, using the compound-choking theory. Then, properties are computed at section m , that is the particular section located inside the constant area duct at which primary and secondary flows are assumed to be completely mixed. State m therefore constitutes one single state, without any distinction between the two flows.

As was noted by the authors, the model of Chen et al. [2] does not ensure mass conservation between sections y and m . Therefore, the assumption of constant mixing pressure in [2] is

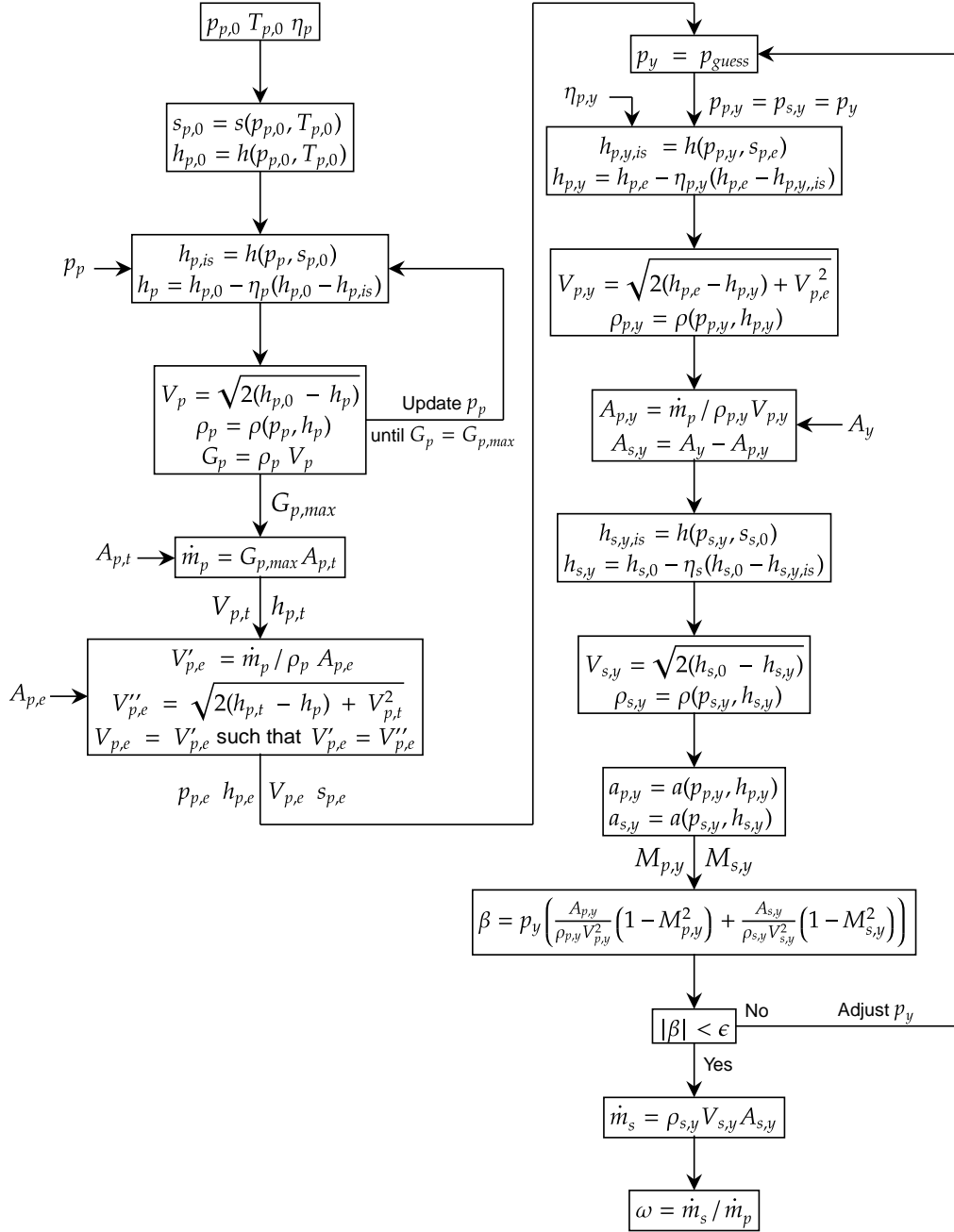


Fig. 2: Flowchart of the model for on-design operations using the compound-choking criterion (see Fig.1 for the notations).

here lifted and replaced by the mass conservation equation. This implies that an additional term has to be added to the momentum conservation equation, to take into account the pressure difference between sections m and y . State m is therefore defined by four equations, that are, the equations for the conservation of mass and total enthalpy, an equation of state provided by COOLPROP and the momentum conservation equation where one applies the mixing efficiency η_m to model mixing related losses:

$$V_m = \eta_m \frac{\dot{m}_p V_{p,y} + \dot{m}_s V_{s,y} + (p_y - p_m) A_y}{\dot{m}_p + \dot{m}_s}. \quad (5)$$

Note at this point that η_m does not need to be a linear function of p_{out} as it was the case for the model of Chen et al. [2]. Instead η_m is assumed to be constant.

After the mixing, the flow may or may not be supersonic. Therefore, if the flow is supersonic at section m , it was chosen to re-compress it through a single normal shock located at the end of the constant area duct (section N). Note that sections m , N and 2 are virtually at the same location, but were drawn separately in Fig. 1 for the sake of readability. The flow across the eventual shock is solved by applying, once again the mass, momentum and total enthalpy conservation equations, as is commonly done. State 2 being then fully defined, the last step is to solve the flow within the diffuser. To this end, the classical definition of the diffuser isentropic

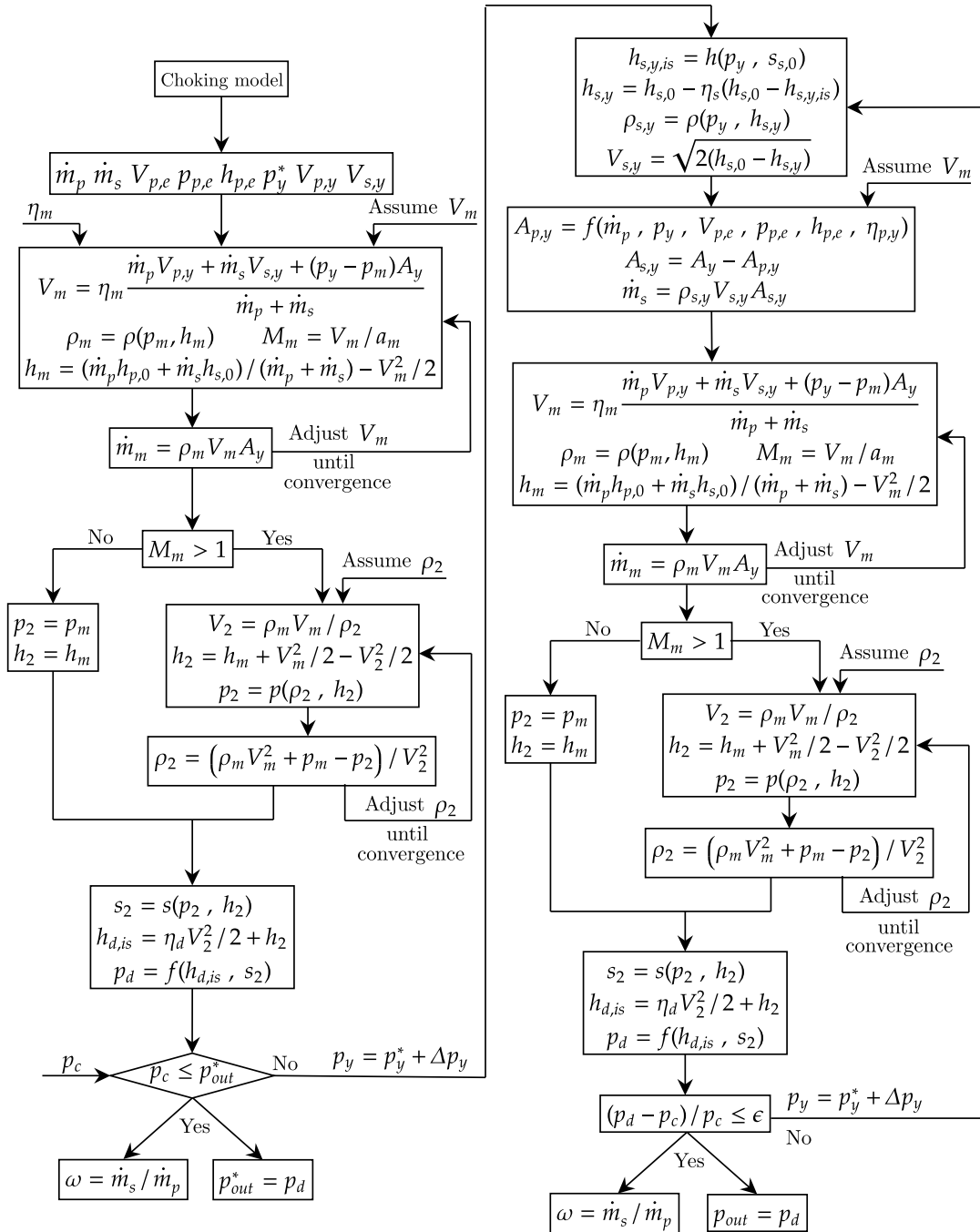


Fig. 3: Flowchart of the model for off-design operations (see Fig.1 for the notations).

efficiency η_d is used along with the total enthalpy conservation equation. One has:

$$p_d = p(h_{d,is}, s_2) \quad \text{with} \quad h_{d,is} = h_2 + \eta_d \frac{V_2^2}{2}, \quad (6)$$

where one also used the fact that the end pressure for the isentropic expansion is the same as that of the non-isentropic one. If the ejector is double-choked, the computed pressure p_d actually corresponds to the critical back pressure p_{out}^* , and if the ejector is under sub-critical regime, $p_d = p_{out}$.

For a given back pressure p_c , one can now determine if the ejector works in the on- or off-design regime. For the latter case, the pressure at the end of the diffuser must match the back pressure, which requires to solve the flow in an iterative way until finding the pressure p_y that satisfies :

$$\frac{p_d - p_c}{p_c} < \epsilon, \quad (7)$$

with ϵ the error tolerance. As mentioned previously, the mixing pressure p_y gets higher as the back pressure gets higher when the ejector is working in the off-design regime. Pressure p_y is therefore updated at each iteration until satisfying Eq. (7). Fig. 3 summarizes the computation algorithm of the new off-design model.

It is now proposed to explain in more details the link between Fabri-choking and compound-choking. To do that, the air ejector geometry of the test bench at Université catholique de Louvain and considered by Lamberts et al. [12, 14] is modeled for $p_{p,0}/p_{s,0} = 4.5$ and with

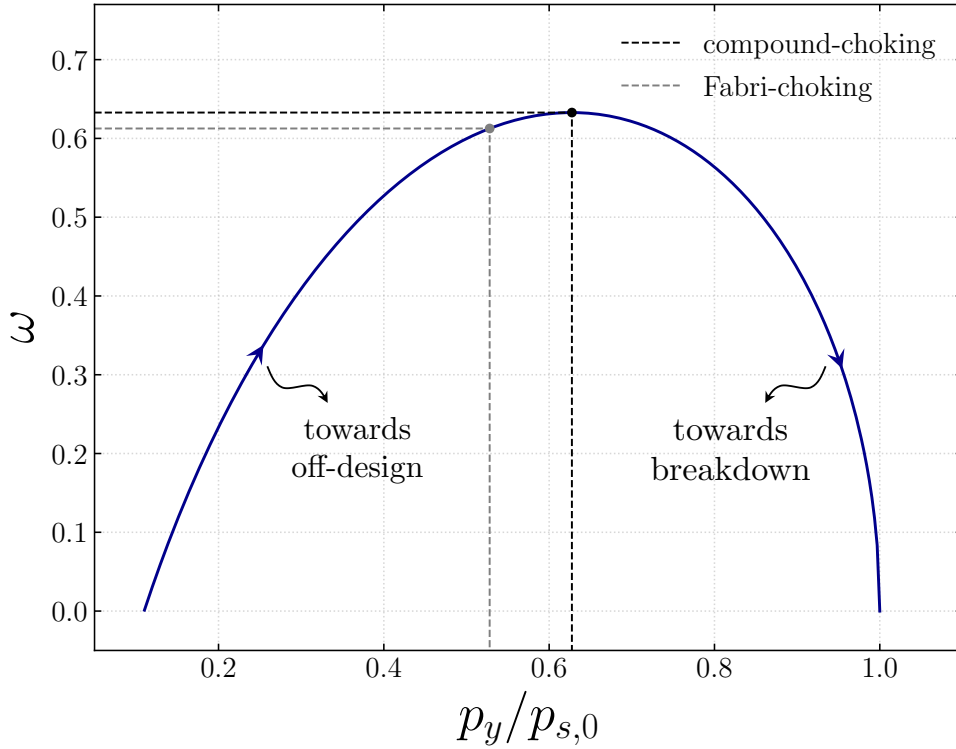


Fig. 4: Comparison between Fabri-choking and compound-choking for $p_{p,0}/p_{s,0} = 4.5$. The working fluid is air and $\eta_m = 0.92$. The positions of the critical conditions have been highlighted on the curve with black (compound) and grey (Fabri) dots.

$\eta_m = 0.92$. All other efficiencies are set to 1. Fig. 4 presents the evolution of the entrainment ratio as a function of the mixing pressure. As a reminder, ω can be computed as a function of the mixing pressure and the stagnation conditions only. Then, the positions of the critical conditions can be located for both choking criteria. Those are represented by dots on the curve. One can now clearly see why the compound-choking criterion systematically predicts higher entrainment ratios than the Fabri-choking criterion. Indeed, the entrainment ratio predicted by the compound-choking is located exactly at the maximum of the curve. This means that, if the transformations are isentropic until the mixing section, satisfying the compound-choking criterion will lead to the maximization of the total mass flow rate within the ejector. Indeed, since the primary flow is choked, maximizing ω is equivalent to maximizing \dot{m}_s and therefore $\dot{m}_p + \dot{m}_s$.

On the other hand, the Fabri-choking mixing pressure at the critical condition p_y^* is slightly lower than that of the maximum, and as one gets further into the off-design part of the characteristic curves, the mixing pressure p_y gets higher. Hence, starting from the Fabri-choking critical point (Fig. 4) and following the curve towards the right, one eventually reaches the maximum (i.e. the compound-choking critical point). By the same token, it is the authors understanding that other thermodynamic models based on the Fabri-choking criterion should logically present overshoots. Note that those spurious overshoots will be observed and further discussed in the following.

Next, it is proposed to calibrate the model onto R134a and air experimental data. To calibrate the characteristic curves for ejectors working with R134a, the experimental data of Garcia del Valle et al. [22] are used as reference. Three different geometries were presented in the original article. However, they differ only in shape; the areas at the sections of interest (Fig. 1) are equal. For this reason, only one ejector can be modeled using the present 0-D model. The relevant ejector dimensions are thus $D_t = 2.0$ [mm], $D_e = 3.0$ [mm] and $D_y = 4.8$ [mm]. The stagnation conditions for the experiments are $(T_{sat})_{p,0} = 84.38^\circ\text{C}$ and $(T_{sat})_{s,0} = 10^\circ\text{C}$ with a superheating of 10°C . It was found that an accurate calibration could be performed by using only three parameters, that are, $\eta_p = 0.977$, $\eta_s = 0.89$ and $\eta_m = 0.813$. The value of $\eta_{p,y}$

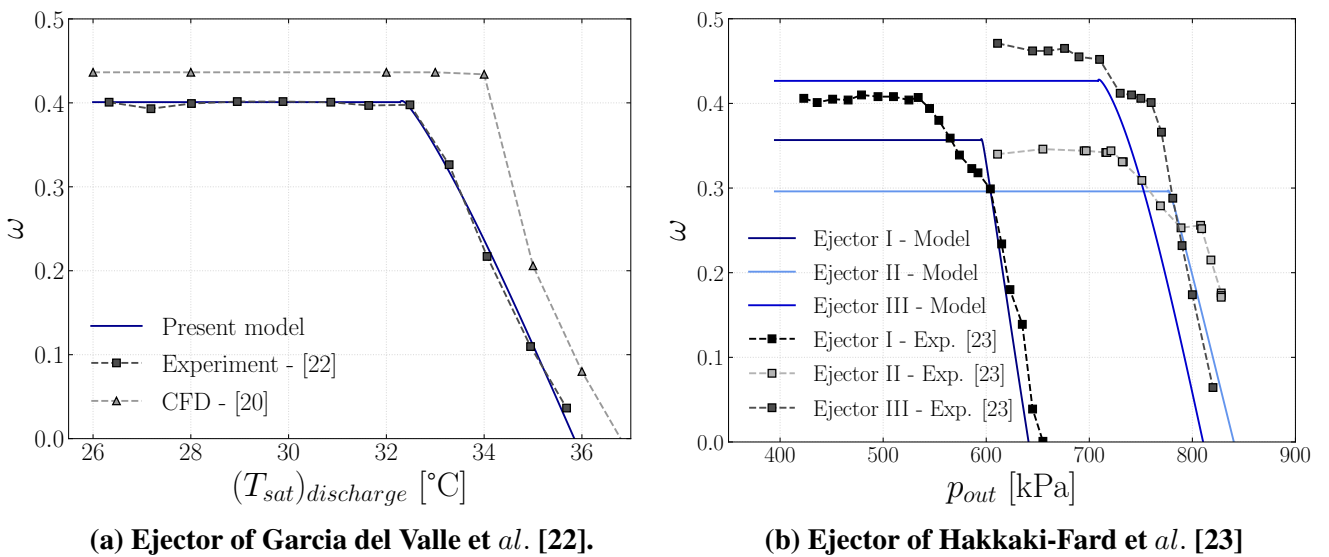


Fig. 5: Characteristic curves obtained for R134a with $\eta_p = 0.977$, $\eta_s = 0.89$ and $\eta_m = 0.813$. Comparison between the present thermodynamic model and CFD/experimental data.

and η_d are thus maintained to 1. Note that these values appear to be plausible for real ejectors. Indeed, the primary nozzle flow is almost isentropic and the secondary flow slightly less due to the more complex geometry. The most limiting factor remains the mixing efficiency. Fig. 5a shows the results of the calibration, along with the CFD results obtained by Croquer *et al.* [20]. The model fits quite well the experimental data of Garcia del Valle *et al.* [22], even better than the CFD results that tend to overestimate the entrainment ratio.

To determine if the calibration stays accurate for other geometries and operating conditions, one proposes to plot the characteristic curves for the ejectors of Hakkaki-Fard *et al.* [23] using the calibration parameters found for the ejector of Garcia del Valle *et al.* [22]. The three ejector geometries (Ejectors I, II and III) and associated operating conditions that were tested experimentally can be found in the original article of Hakkaki-Fard *et al.* [23]. Fig. 5b shows the results for the three ejectors. One can observe that, although the model does not predict the entrainment ratio as accurately as for the ejector of Garcia del Valle *et al.* [22], it nevertheless gives a good approximation. The model appears to underestimate the on-design entrainment ratio, but the off-design part of the characteristic curves seems to fit quite nicely. More precisely, the slopes of the off-design curves are quite accurate, and the model even overlaps the experiments for Ejector I.

As a last step, it is proposed to perform an analytical study on the compound-choking criterion in the frame of non-isentropic perfect gas flows. The aim is to demonstrate the connection between the compound-choking criterion and the maximization of the mass flow rate within an ejector, which could be put in parallel with the definition of choking in the classical sense, i.e. for a simple nozzle.

First, one may develop the equations for non-isentropic nozzle flows for perfect gases. In order to obtain an analytical solution for this problem, one will consider a polytropic efficiency, noted η_{pol} defined as:

$$\eta_{pol} = \frac{dh}{dh_{is}}, \quad (8)$$

since one only deals with expansions. In the previous sections, isentropic efficiencies were used because these are more suited for global transformations. However, these two types of efficiencies (isentropic and polytropic) can be linked and have the same global effect. The conservation equations in a control volume can be written as:

$$\frac{d\rho}{\rho} + \frac{dV}{V} + \frac{dA}{A} = 0, \quad (9)$$

$$\rho V dV + dp + 4\tau_w \frac{dx}{D_h} = 0, \quad (10)$$

$$dh_0 = dh + V dV = 0. \quad (11)$$

After some algebra that will not be presented here for the sake of conciseness, one may obtain the differential equation linking the Mach number to the cross-section area:

$$\frac{dM}{M} \frac{1 - \frac{(\eta_{pol}-1)(\gamma-1)}{\eta_{pol}} M^2 - 1}{1 + \frac{\gamma-1}{2} M^2} = \frac{dA}{A}. \quad (12)$$

The throat is defined as the location in the nozzle where $dA = 0$ and this last equation shows that this will occur for a Mach number $M_t = \sqrt{\frac{\eta_{pol}}{\eta_{pol} + \gamma(1-\eta_{pol})}}$ which is different from unity

when $\eta_{pol} < 1$. This means that, as soon as the flow becomes non-isentropic, the flow does not reach sonic conditions at the throat when it is choked but somewhere further down the divergent. When the flow is considered to be non-isentropic, one can thus not use the unity Mach number at the throat as choking condition.

Next, the compound-choking criterion is re-defined so as to take losses into account via the polytropic efficiency. One considers a flow with several separate streams under the following assumptions:

1. The flow is one dimensional, steady-state and adiabatic.
2. There is no mixing between streams.
3. The pressure is constant between streams at each cross section.
4. The transverse pressure gradient caused by the streamline curvature is negligible.

One may then define, after some algebra, the compound indicator β similarly to what was done by Bernstein *et al.* [17]:

$$\beta = \frac{\frac{dA}{dx}}{\frac{d(\ln(p))}{dx}}, \quad (13)$$

$$= \sum_i \frac{A_i}{\gamma_i M_i^2} (\eta_{pol,i} - M_i^2 (1 - (\eta_{pol,i} - 1)(\gamma_i - 1))), \quad (14)$$

$$= \sum_i \frac{A_i}{\gamma_i} \left[\eta_{pol,i} \left(\frac{1}{M_i^2} - 1 \right) - \gamma_i (1 - \eta_{pol,i}) \right]. \quad (15)$$

This expression can be verified to match the expression from Bernstein *et al.* [17] for the case $\eta_{pol,i} = 1$. It can be shown through a compound wave analysis that this indicator must be equal to 0 for the compound flow to be choked.

From the compressible flow theory, when a flow is choked, its mass flow rate is maximized. Hence, if the compound-choking is the actual choking mechanism, it should be equivalent to maximizing the mass flow rate within the ejector. Since the primary mass flow rate is fixed, as the primary flow is itself choked in the primary nozzle, maximizing the mass flow rate in the ejector is equivalent to maximizing the secondary mass flow rate. Since the choking criteria (Fabri- or compound-choking) are destined at finding the pressure at the mixing section p_y such that the ejector is choked, the mass flow rate has to be maximized with respect to this pressure. To this end, the derivative of \dot{m}_s with respect to p_y can be computed. One may find:

$$\begin{aligned} \frac{\partial \dot{m}_s}{\partial p_y} = \frac{\dot{m}_s}{A_{s,y} p_y} & \left[\frac{A_{s,y}}{\gamma_s} \left(\eta_{pol,s} \left(1 - \frac{1}{M_{s,y}^2} \right) - \gamma_s (\eta_{pol,s} - 1) \right) \right. \\ & \left. + \frac{A_{p,y}}{\gamma_p} \left(\eta_{pol,p} \left(1 - \frac{1}{M_{p,y}^2} \right) - \gamma_p (\eta_{pol,p} - 1) \right) \right]. \end{aligned} \quad (16)$$

This last expression can be compared to the expression of the compound-choking indicator β obtained in Eq. (15), taken for 2 streams at section y :

$$\frac{\partial \dot{m}_s}{\partial p_y} = - \frac{\dot{m}_s}{A_{s,y} p_y} \beta. \quad (17)$$

Thus, it shows that applying the compound-choking criterion, i.e. $\beta = 0$ to an ejector is similar to maximizing the total mass flow rate within this ejector. More fundamentally, this shows

that the choking mechanism at play in a supersonic ejector is the compound-choking. Indeed, the flow within a device is choked if the mass flow rate is maximized. Since maximizing the mass flow rate and applying the compound-choking criterion yield the same result, both must be equivalent.

To demonstrate the improvement that constitutes the compound-choking, one proposes to compare characteristic curves obtained using the compound-choking as defined by Eq. (3) with the curves obtained by maximising the mass flow rate at critical conditions. This is done by calibrating the model onto experimental data obtained using the air ejector test bench at Université catholique de Louvain. Using Eq. (3) (Fig. 6a), one can observe that the spurious overshoot that was previously mentioned in the case of the Fabri-choking curves is also present in the compound-choking curves. This is actually due to the fact that, as explained in Croquer *et al.* [20], the compound-choking criterion as expressed in Eq. (3) is not rigorously correct if one considers non-isentropic flows. Fig. 6b shows the corrected version of the characteristic curves. Obtaining those corrected curves is actually rather straightforward, as one only needs to locate the maximum of the overshoot (in this case, in Fig. 6a), which indicates the location of the critical point and therefore of the on-design plateau. Note however that $\eta_s = 0.71$ in Fig. 6b for a better fitting of the experimental data.

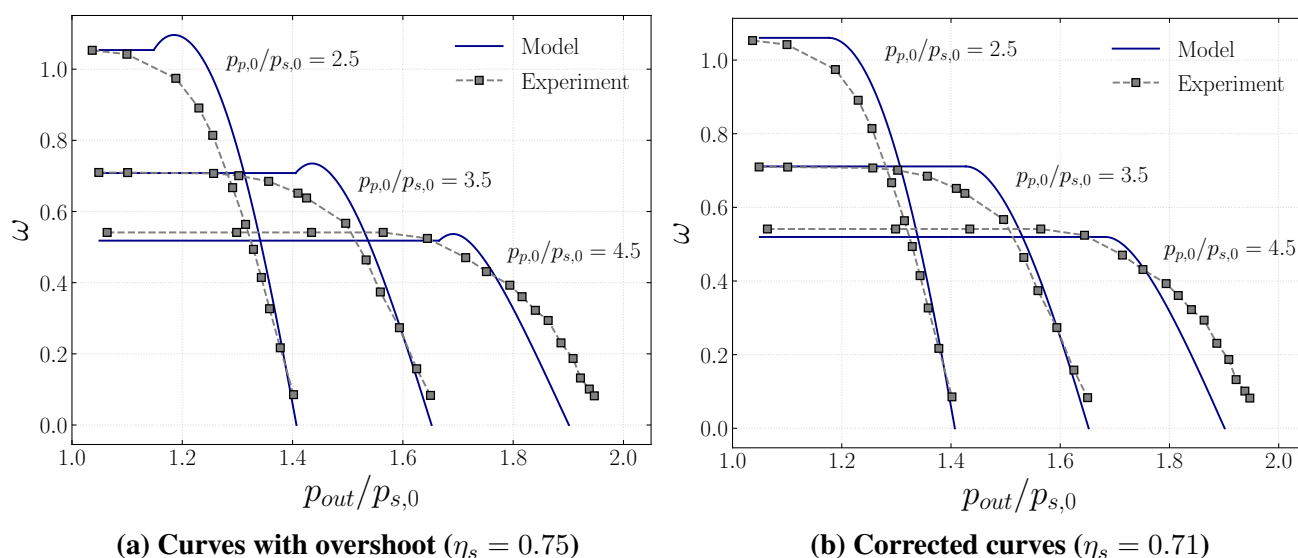


Fig. 6: Characteristic curves obtained for the air ejector test bench of Université catholique de Louvain with $\eta_p = 0.977$ and $\eta_m = 0.95$. Comparison between the present thermodynamic model and new experimental data.

Conclusions

In this paper, a new real gas thermodynamic model was presented. It can be calibrated by means of multiple efficiencies. Although the model was only validated in the case of single-phase ejectors, it is foreseen to use this model for two-phase ejectors as well. This will be the subject of further studies.

First, a modified version of the model of Chen *et al.* [2] was implemented. As opposed to most models that can be found in the literature, it uses the compound-choking criterion derived from the theory of Bernstein *et al.* [17], successfully applied to explain the choking mechanism in supersonic ejectors by Lamberts *et al.* [14, 24], and further developed in the frame of real gas ejectors by Fang [18] and Metsue [19]. Rather than assuming constant mixing

pressure and using a variable mixing efficiency as in the model of Chen et al. [2], the mass conservation equation was re-introduced into the mixing model. The decrease in performance in the off-design regime is thereby modeled by pressure effects within the constant area duct. The new model was then used to perform an analysis on the connections between the Fabri-choking and the compound-choking. Despite the fact that the Fabri-choking seems to be the most straight-forward approach to model ejector entrainment limitation, it actually does not lead to the maximization of the mass flow rate within the device, which is in contradiction with the definition of a choked flow.

The model was validated for single-phase R134a (ejectors of Garcia del Valle et al. [22] and Hakkaki-Fard et al. [23]) and air (ejector of Université catholique de Louvain) flows. A good fitting ability was obtained for both fluids by using only three fitting parameters.

Lastly, an analytical study on the compound-choking criterion in the frame of non-isentropic perfect gas ejector flows showed that the use of the compound-choking criterion leads to the maximization of the total mass flow rate within the ejector. This is in accordance with the definition of choking for a simple nozzle (i.e. the maximization of the mass flow rate).

Future works include the validation of the present model for two-phase ejector predictions, especially those working with CO₂. The objective will be then to couple it to a model for a transcritical CO₂ heat pump and to assess the benefit of integrating an ejector on the performance of the whole cycle.

Acknowledgments

A.M. and S.P. would like to thank the support of the NSERC chair on industrial energy efficiency established at Université de Sherbrooke with Hydro-Québec (Laboratoire des technologies de l'énergie in Shawinigan), Natural Resources Canada (CanmetEnergy in Varennes) and Emerson Canada.

References

- [1] G. Besagni. Ejectors on the cutting edge: The past, the present and the perspective. *Energy*, 170:998 – 1003, 2019.
- [2] W. Chen, C. Shi, S. Zhang, H. Chen, D. Chong, and J. Yan. Theoretical analysis of ejector refrigeration system performance under overall modes. *Applied Energy*, 185:2074 – 2084, 2017.
- [3] S. Rao and J. Gopalan. Observations on the non-mixed length and unsteady shock motion in a two dimensional supersonic ejector. *Physics of Fluids*, 26, 2014.
- [4] A. Bouhanguel, P. Desevaux, and E. Gavignet. Flow visualization in supersonic ejectors using laser tomography techniques. *International Journal of Refrigeration*, 34:1633–1640, 2011.
- [5] X. Chen, S. Omer, M. Worall, and S. Riffat. Recent developments in ejector refrigeration technologies. *Renewable and Sustainable Energy Reviews*, 19:629–651, 2013.
- [6] G. Besagni, R. Mereu, and F. Inzoli. Ejector refrigeration: A comprehensive review. *Renewable and Sustainable Energy Reviews*, 53:373 – 407, 2016.
- [7] Z. Aidoun, K. Ameer, M. Falsafioon, and M. Badache. Current advances in ejector modeling, experimentation and applications for refrigeration and heat pumps. Part 1: Single-phase ejectors. *Inventions*, 4:15, 2019.
- [8] Z. Aidoun, K. Ameer, M. Falsafioon, and M. Badache. Current advances in ejector modeling, experimentation and applications for refrigeration and heat pumps. Part 2: Two-phase ejectors. *Inventions*, 4:16, 2019.

- [9] J. H. Keenan, E. P. Neumann, and F. Lustwerk. An investigation of ejector design by analysis and experiment. *Journal of Applied Mechanics*, 72:299–309, 1950.
- [10] J. T. Munday and D. F. Bagster. A new ejector theory applied to steam jet refrigeration. *Industrial & Engineering Chemistry Process Design and Development*, 16:442–449, 1977.
- [11] J. Fabri and R. Siestrunk. Supersonic air ejectors. volume 5 of *Advances in Applied Mechanics*, pages 1 – 34. Elsevier, 1958.
- [12] O. Lamberts, P. Chatelain, and Y. Bartosiewicz. Numerical and experimental evidence of the Fabri-choking in a supersonic ejector. *International Journal of Heat and Fluid Flow*, 69:194 – 209, 2018.
- [13] W. Chen, M. Liu, D. Chong, J. Yan, A. B. Little, and Y. Bartosiewicz. A 1D model to predict ejector performance at critical and sub-critical operational regimes. *International Journal of Refrigeration*, 36:1750 – 1761, 2013.
- [14] O. Lamberts, P. Chatelain, N. Bourgeois, and Y. Bartosiewicz. The compound-choking theory as an explanation of the entrainment limitation in supersonic ejectors. *Energy*, 158:524 – 536, 2018.
- [15] I.W Eames, S Aphornratana, and H Haider. A theoretical and experimental study of a small-scale steam jet refrigerator. *International Journal of Refrigeration*, 18:378 – 386, 1995.
- [16] B.J. Huang, J.M. Chang, C.P. Wang, and V.A. Petrenko. A 1-D analysis of ejector performance. *International Journal of Refrigeration*, 22:354 – 364, 1999.
- [17] A. Bernstein, W. H. Heiser, and C. Hevenor. Compound-Compressible Nozzle Flow. *Journal of Applied Mechanics*, 34:548–554, 1967.
- [18] Y. Fang. *Advanced numerical simulations of two-phase CO₂ ejectors*. PhD thesis, Université catholique de Louvain, Université de Sherbrooke, 2019.
- [19] A. Metsue. An improved thermodynamic model for supersonic ejectors. Master’s thesis, Université catholique de Louvain, 2020.
- [20] S. Croquer, Y. Fang, A. Metsue, Y. Bartosiewicz, and S. Poncet. Compound-choking theory for supersonic ejectors working with real gas. *Energy*, in press.
- [21] S. He, Y. Li, and R.Z. Wang. Progress of mathematical modeling on ejectors. *Renewable and Sustainable Energy Reviews*, 13:1760 – 1780, 2009.
- [22] J. García del Valle, J.M. Saíz Jabardo, F. Castro Ruiz, and J.F. San José Alonso. An experimental investigation of a R-134a ejector refrigeration system. *International Journal of Refrigeration*, 46:105 – 113, 2014.
- [23] A. Hakkaki-Fard, Z. Aidoun, and M. Ouzzane. A computational methodology for ejector design and performance maximisation. *Energy Conversion and Management*, 105:1291 – 1302, 2015.
- [24] O. Lamberts. *Choking and mixing phenomena in supersonic ejectors*. PhD thesis, Université Catholique de Louvain, 2018.

Propane-isobutane mixtures in heat pumps with higher temperature lift: an experimental investigation

J. Quenel^{1*}, M. Anders¹ and B. Atakan¹

¹ University of Duisburg-Essen, Thermodynamics, Lotharstr. 1, 47057 Duisburg, Germany

*Corresponding author: julian.quenel@uni-due.de

Abstract

The shift towards renewable energies leads to an increased interest in heat pumps, not only for floor heating at temperatures around 40 °C, but also for providing hot water at higher temperatures (> 60 °C). To reach the goal of a climate neutral process it is important to use working fluids with a low global warming potential (GWP). Zeotropic mixtures are discussed to potentially increase the coefficient of performance (COP) of a heat pump compared to pure fluids. This is examined here for mixtures of two refrigerants. The present work experimentally analyses a compression heat pump process of such fluids; five mixtures of propane and isobutane are investigated here. The influence of composition, compressor speed, inlet temperature of the working fluid into the evaporator and the inlet temperature of the secondary fluid water into the condenser are researched. Besides the COP, the exergetic losses of the components are evaluated, to find possibilities for improvements. It is shown that the COP for a temperature lift of 33 °C are above 3 for the mixtures, while at a higher temperature lift of 53 °C the COP is around 2. Furthermore, a strong impact of the compressor efficiency on the process was found. This leads to the fact that the advantage of zeotropic refrigerant mixture building is often limited by the operating characteristics of the compressor.

Keywords: thermal heat pump, hydrocarbon refrigerants, refrigerant mixtures, higher temperature lift.

Introduction/Background

Heat pumps gain importance due to the shift towards renewable energies and the shift from chemical to electrical heating. At the same time, the fluorocarbons have to be replaced as working fluids, due to their global warming potential (GWP) [1]. Natural refrigerants like hydrocarbons are an option to replace them. Hydrocarbons are investigated as working fluids [2], due to their low GWP and their high availability. Further, zeotropic refrigerant mixtures are a good way to achieve lower exergetic losses in heat exchangers. While heat pumps are mainly used for low temperature lifts, the interest in higher temperature heat pumps (HTHP) rises [3], which provide secondary fluid exit temperatures of 50 °C to 100 °C. For example, the warm water distribution with a needed temperature of around 60 °C is a possible application for an HTHP. With them, higher efficiencies of energy usage and lower CO₂ emissions in the domestic section can be reached, when the electrical energy is provided from renewables.

In the field of water heating Zhang et al. [4] evaluated the COP of a process depending on the pipe length of the heat exchangers and the refrigerant amount. They used ambient air as the heat source and R22 as the refrigerant. The temperature of the secondary fluid was increased to 55 °C and the COP showed a strong dependency on the temperature of the ambient air and the charge of the system.

The authors Chaichana et al [5] compared the hydrocarbons propane, propene, isobutane, and n-butane as refrigerants for a solar-powered heat pump for the provision of hot water, varying the evaporation and condensing temperature. The mass flow rates, operating pressures,

compressor inlet temperatures and COP were compared. Propane and propene showed good performance in their study for condensing temperatures of up to 70 °C.

The authors Chang et al [6] also compared the pure fluids isobutane, n-butane, propane and propene. They considered the zeotropic mixtures of isobutane/propane and n-butane/propane. The substances were compared in a test plant at low secondary fluid temperatures of 21.1 °C in the condenser and 8.3 °C in the evaporator. The mixture isobutane/propane (mass ratio 50/50) led to a 7 % higher coefficient of performance compared to the reference case with R22. The mixture of n-butane/propane (mass ratio 75/25) increased the COP by about 11 %.

Park et al [7] investigated propane and propene as pure refrigerants as well as the mixture of these two substances, also as an alternative to R22. In addition, a ternary mixture of propane/propene/DME was measured. They found an increase in the COP for each used refrigerant except for pure propane, with the ternary mixture showing the highest increase of 5.7 %.

Bamigbetan et al [8] investigated a cascade heat pump that can provide energy at 115 °C to use residual heat. This heat pump cascade was operated with propane and butane and has a heating capacity of 20 kW. They concluded that this heat pump cascade with an average COP of 3.1 at a temperature range of 58-72 °C is a better alternative than electric heating or a gas boiler.

As mentioned in the reviews [2-3], the experimental study of HTHP especially with hydrocarbons was not carried out often, but is promising like the brief literature review showed. Thus, the present work evaluates propane/isobutane mixtures as working fluids, using heat from water at environmental conditions and delivering secondary fluid enthalpy flows at 40 °C or 60 °C.

The used simple compression heat pump system consists of a compressor, an evaporator, a condenser, an expansion valve, and a refrigerant reservoir. The simplified process is shown in Figure 1.

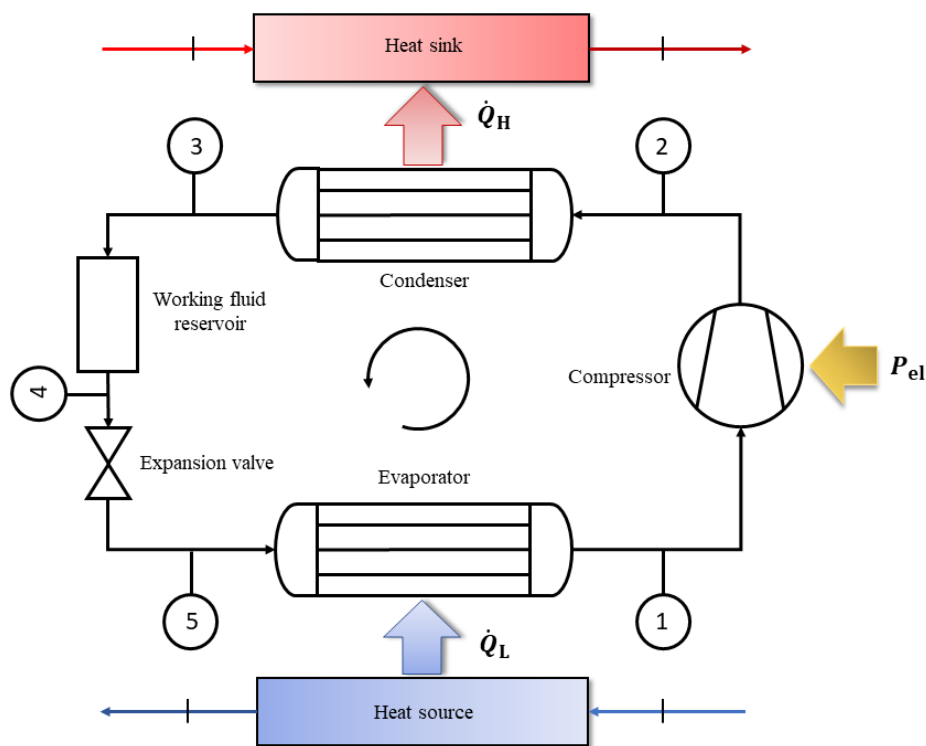


Fig 1: Schematic View of the used compression heat pump.

Water was used as the secondary fluid in the heat exchangers, its temperature can be elevated up to 60 °C, although this was varied in the experiments. In the evaporator, water with an inlet temperature of 17 °C was used throughout. A semi-hermetic reciprocating compressor with a maximum power consumption of 2.2 kW increases the pressure. In the reference case, it rotates at a speed of 1500 min⁻¹ and can be varied between 1050 min⁻¹ and 2100 min⁻¹. The throttling is realised with the help of a needle valve. This creates a controllable pressure drop, which, due to the fine adjustment of the needle valve, ensures a wide range of refrigerant utilisation. The evaporator is a double-tube heat exchanger with an inner tube diameter of 10 mm (wall thickness: 1 mm) and an inner diameter of the outer tube of 16 mm. This results in an annular gap of 2 mm in which the water flows. The evaporator has a length of 14 m. The condenser is also a double-tube heat exchanger with an annular gap of 2 mm and an inner tube diameter of the outer tube of 19 mm. The condenser has a total length of 22 m.

For monitoring and evaluating the processes, 6 pressure sensors and a total of 38 temperature sensors are installed in the system. The pressure sensors are located at the inlet and the outlet of the main components of the system (evaporator, compressor, condenser and expansion valve). A temperature sensor is also installed at each of these points. The temperatures of the inlets and outlets and the mass flow of the secondary fluid are also recorded. The remaining temperature sensors are installed in the heat exchangers. Thus, the temperature profile inside the heat exchangers can be recorded and evaluated, regarding the temperature glide.

The present work deals with the influence of the mixture composition of propane and isobutane, the evaporator inlet temperature, the compressor speed, and the condenser inlet temperature of water. For this purpose, these parameters were varied while the inlet temperature of the secondary fluid into the evaporator and the temperature difference of the water in the condenser were kept constant. The process values set in this way are shown in Table 1.

Table 1: Investigated process boundary conditions.

Parameter	Used values
Mole fraction isobutane, $x_{C_4H_{10}}$	0, 0.25, 0.5, 0.75, 1
Compressor speed, n_{Comp}	1500 min ⁻¹ , 1050 min ⁻¹
Working fluid inlet temperature evaporator, $T_{Evap, in}$	0 °C, 4 °C, 8 °C
Secondary fluid inlet temperature evaporator, $T_{Evap, sf, in}$	17 °C
Secondary fluid inlet temperature condenser, $T_{Cond, sf, in}$	40 °C, 60 °C
Secondary fluid temperature difference condenser, $\Delta T_{Cond, sf}$	10 °C
Secondary fluid outlet temperature condenser, $T_{Cond, sf, out}$	50 °C, 70 °C
Temperature lift, T_{Lift}	33 °C, 53 °C

The temperature lift is defined as the effective total temperature difference achieved between the evaporator inlet and the condenser outlet temperature of the secondary fluid. Thus, the temperature lifts are 33 °C and 53 °C.

The target mole fractions of 0.25, 0.5 and 0.75 that are filled into the system, did not correspond to the mixtures circulating during operation. These differed somewhat because the more volatile propane accumulated in the gas phase of some parts of the system, such as the refrigerant reservoir. So, the circulating mixture contains a higher amount of isobutane. The composition of the circulating mixture was determined with the help of the assumption that the

expansion valve is isenthalpic and thus the mole fractions could be calculated iteratively with the data from RefProp, until the enthalpy of a composition before and after the expansion valve were the same.

In the following, the most important equations necessary for the evaluation of the experimental data will be discussed. The COP is defined as the ratio of the determined heat flow rate transferred to the secondary fluid to the consumed compressor power:

$$\text{COP } \varepsilon_H = \frac{\dot{Q}_{\text{H,sec. fluid}}}{\dot{P}_{\text{el}}} \quad (\text{Eq. 1})$$

To analyse the process details, the exergetic losses are examined. These are generally determined by the difference between incoming and outgoing exergy flow. The exergies, neglecting kinetic and potential energy, are given by:

$$\dot{E}_i = \dot{m}_i \cdot (h_i - h_u - T_u \cdot (s_i - s_u)) \quad (\text{Eq. 2})$$

An ambient (subscript: u) temperature of 25 °C and an ambient pressure of 1 bar were used in this work as dead state. Using Eq. 2, the incoming and outgoing exergy flow can be determined for each component and the difference can be calculated as exergy destruction.

Various efficiencies can be defined for the compressor to characterise it. In the present work, on the one hand the electro-mechanical compressor efficiency is used with:

$$\eta_{\text{Comp}} = \eta_{\text{Comp,el}} \cdot \eta_{\text{Comp,mech}} = \frac{P_{\text{Comp,working fluid}}}{P_{\text{Comp,el}}} \quad (\text{Eq. 3})$$

It represents the ratio of the power delivered to the fluid and the power consumed by the compressor and takes the mechanical and electrical losses in the compressor into account. On the other hand, the global compressor efficiency is defined, which considers all losses including the isentropic efficiency of the compressor:

$$\eta_{\text{Comp,global}} = \eta_{\text{Comp,el}} \cdot \eta_{\text{Comp,mech}} \cdot \eta_{\text{Comp,is}} \quad (\text{Eq. 4})$$

To analyse the volumetric compressor efficiency, the delivery ratio is defined as the quotient of the effective volumetric flow rate into the compressor and the geometrically highest possible volumetric flow rate:

$$\lambda_{\text{Comp}} = \frac{\dot{V}_{\text{Comp,in}}}{\dot{V}_{\text{theoretical}}} \quad (\text{Eq. 5})$$

The refrigerant mass flow was determined from the energy balance across the evaporator, which was assumed to be adiabatic because of the small temperature difference to the environment. Thus, the mass flow can be calculated from:

$$\dot{m}_{\text{working fluid}} = \dot{m}_{\text{Evap,sec. fluid}} \cdot \frac{(h_{\text{Evap,sec. fluid,in}} - h_{\text{Evap,sec. fluid,out}})}{(h_{\text{Evap,working fluid,in}} - h_{\text{Evap,working fluid,out}})} \quad (\text{Eq. 6})$$

Discussion and Results

First, the influence of the mixture composition, the compressor speed and the temperature lift on the COP is shown for different operating points. In Fig. 2 the COP is plotted as a function of the isobutane mole fraction for four combinations of compressor speed and temperature lift. The evaporator inlet temperature is 4 °C for all points.

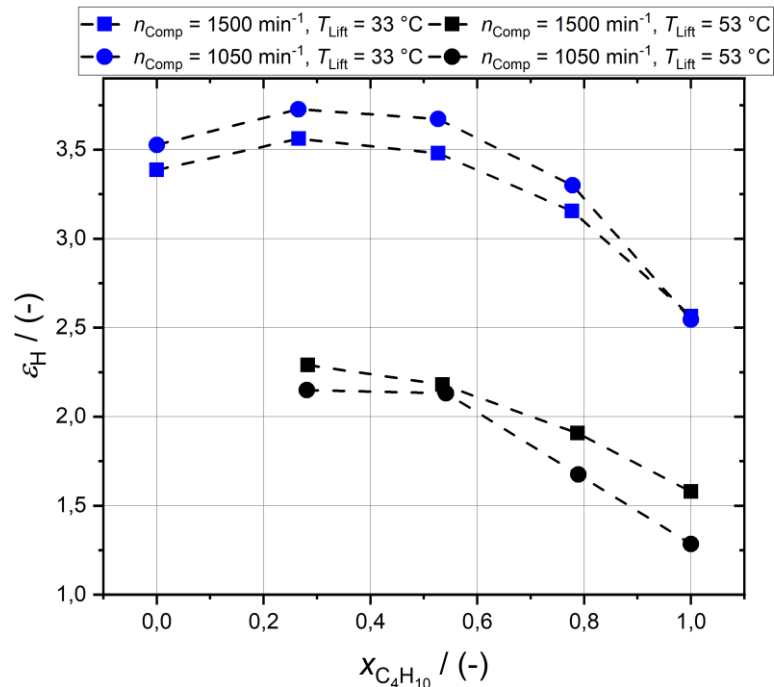


Fig 2: COP ϵ_H depending on the mole fraction of isobutane for $T_{Evap, in} = 4 \text{ }^\circ\text{C}$.

The values for pure propane (mole fraction of 0) could not be recorded, because the maximum pressure in the system exceeded the limit of 20 bar for a temperature lift of 53 °C. A COP between 2.54 and 3.73 are found for the lower temperature lift of 33 °C. These COPs are higher than those for a higher temperature lift, where values between 1.28 and 2.29 are observed. Pure isobutane leads throughout to the lowest COPs; the highest COPs are found for mole fraction of 0.25. Like mentioned before, the circulating mole fraction differed from 0.25 and was determined to be 0.267. The COP for pure propane as refrigerant is higher than for pure isobutane, the latter COPs always being the lowest of a series. The lower COPs for higher temperature lifts are as expected from the Carnot efficiency.

The use of the zeotropic mixture increases the COP compared to the pure refrigerants. This can be attributed to the temperature glide that occurs with mixtures, leading to a better matching between working fluid temperatures and secondary fluid temperatures. This reduces the exergy losses in the heat exchangers, as will be discussed later. With the rising temperature glide, the temperature difference between refrigerant and secondary fluid is lower and, in addition, the pressure ratio in the compressor decreases. As an example, the measured temperature glides in the condenser are plotted in Fig. 3 as a function of the isobutane mole fraction for a compressor speed of 1500 min^{-1} and an evaporator inlet temperature of 4°C.

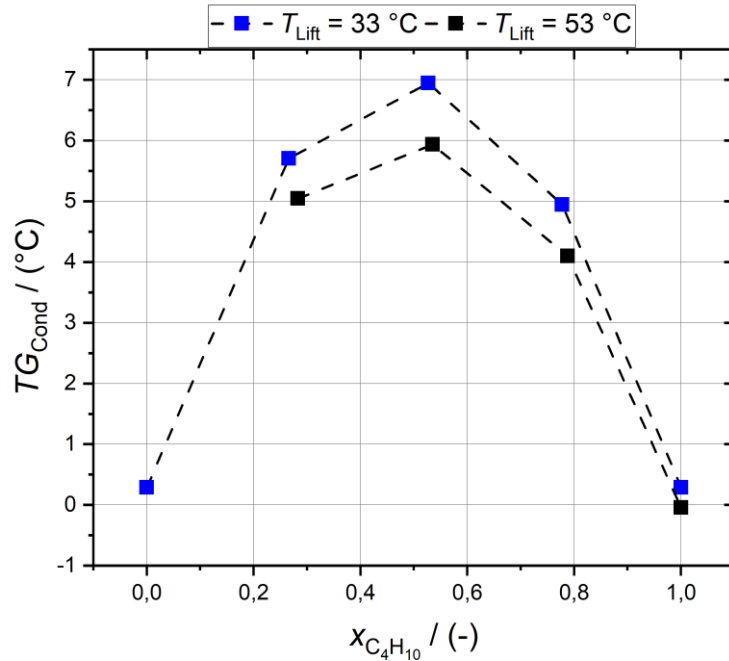


Fig 3: Temperature glide in condenser depending on isobutane mole fraction at $T_{Evap, in} = 4^{\circ}C$ and $n_{Comp} = 1500 \text{ min}^{-1}$ for both temperature lifts.

As expected from theory and the fluid properties, the highest temperature glide is found at a fraction of 0.527. It is $5.94^{\circ}C$ for a temperature lift of $53^{\circ}C$ and $6.95^{\circ}C$ for $33^{\circ}C$. The small, but not vanishing temperature glide for the pure fluids is caused by the pressure drop in the condenser. In general, the temperature glide is larger at lower temperature lifts of the heat pump ($33^{\circ}C$ here), because the condensation pressure is lower and thus the difference between boiling point and dew point is increased. In general, higher temperature glides leads to higher COPs, due to the lower exergy losses. By comparing Fig. 3 and Fig. 2, it can be noticed that the operating point with the highest COP is not at the mixture with the highest temperature glide, but at a mole fraction of 0.267. This is, because the positive effect of the temperature glide is superimposed by the variation in compressor efficiency with composition; this is another important influencing variable.

To examine the influence of the compressor, the change of the COP with the compressor speed can be considered first by regarding Fig. 2 once more. It is seen that the influence of the compressor speed is changing between the low and the high temperature lift. For a high temperature lift the COP increases for the lower speed, while for the $33^{\circ}C$ lift, the opposite behaviour is observed, and the coefficient is reduced. The increase of the COP can be explained by a reduction in the losses in the compressor, e.g., smaller piston speeds and thus lower friction losses lead to higher efficiencies in the compressor. To take a closer look at the opposing behaviour, Table 2 shows the compressor efficiency from Eq. 3 working with the pure fluids as a function of the compressor speed and the evaporator inlet temperature at a temperature lift of $33^{\circ}C$.

Table 2: Electro-mechanical compressor efficiencies with the pure fluids for two $T_{\text{Evap, in}}$ and compressor speeds for $T_{\text{Lift}} = 33 \text{ }^\circ\text{C}$.

Fluid	Propane	Propane	Isobutane	Isobutane
n_{Comp} (min ⁻¹)	1050	1500	1050	1500
$T_{\text{Evap, in}}$ (°C)	η_{Comp} (-)	η_{Comp} (-)	η_{Comp} (-)	η_{Comp} (-)
0	0.953	0.958	0.715	0.792
4	0.982	0.959	0.792	0.823

Table 2 shows that the electro-mechanical compressor efficiencies are higher for propane than for isobutane. The efficiencies for propane are in a narrow range between 0.95 and 0.982, while for isobutane the variation is larger with values between 0.71 and 0.82. Furthermore, an increase in the evaporator inlet temperature leads to an increase in the compressor efficiency. The opposing behaviour of the heat pump running with propane and isobutane with decreasing compressor speeds also gets clear. For example, at an evaporator inlet temperature of 4 °C, the efficiency for propane increases by 2.34 % from 0.959 to 0.982, when the compressor speed is reduced. For isobutane the efficiency decreases by 3.91 % from 0.823 to 0.792. Such changes in the compressor efficiency directly influence the COP of the process. It gets clearer if \dot{P}_{el} from Eq. 1 is expressed with the total compressor efficiency:

$$\text{COP } \varepsilon_H = \eta_{\text{Comp, total}} \cdot \frac{\dot{Q}_{\text{H, sec. fluid}}}{\dot{m}_{\text{working fluid}} \cdot (h_{\text{Comp, out}} - h_{\text{Comp, in}})} \quad (\text{Eq. 7})$$

In addition to this direct influence on the COP through the efficiency, the operating characteristics also influence the mass flow rate and thus the process. To examine this influence, the refrigerant mass flowrate, the density at the inlet of the compressor and the delivery ratio of the compressor for a temperature lift of 33 °C are given in Table 3.

Table 3: Data for the refrigerant mass flow rate, the delivery ratio and the density at the compressor inlet depending on the isobutane mole fraction at $n_{\text{Comp}} = 1500 \text{ min}^{-1}$ and $T_{\text{Lift}} = 33 \text{ }^\circ\text{C}$

x_{C4H10} (-)	$\rho_{\text{Comp, in}}$ (kg/m ³)	$\dot{m}_{\text{working fluid}}$ (kg/s)	λ_{Comp} (-)
0	9.75	0.0110	0.7299
0.267	8.09	0.0092	0.7312
0.527	6.59	0.0074	0.7225
0.778	5.26	0.0057	0.6979
1	4.15	0.0044	0.6763

With increasing isobutane mole fraction, the density of the mixture entering the compressor, as well as the refrigerant mass flow rate, decreases. This occurs almost linearly with the increase in isobutane content. The delivery ratio of the compressor is non-linear. It has a maximum of 0.7312 for an isobutane fraction of 0.267 and decreases slightly towards pure propane and stronger towards pure isobutane. A high delivery ratio means a better utilisation of the compressor in term of the effective volumetric flow rate compared with the theoretically reachable volume flow rate (see Eq. 5). Also, a lower pressure ratio is obtained for high λ_{Comp} . These two facts, in turn, lead to a higher compressor efficiency.

The high delivery ratio at a mole fraction of 0.267 and the slight decrease in refrigerant mass flow rate lead to a high COP. Especially the refrigerant mass flow directly influences the coefficient via the heat flow rate in the condenser. To underline this fact, the heat transfer per mass of working fluid in the condenser is shown in Fig. 4 for one example as a function of isobutane amount.

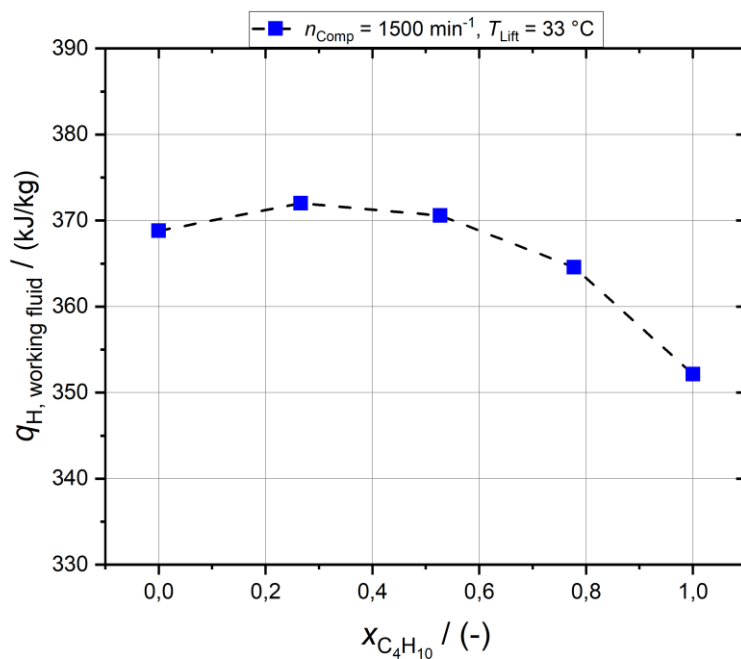


Fig 4: Specific heat in the condenser depending on the isobutane mole fraction at $n_{\text{Comp}} = 1500 \text{ min}^{-1}$, $T_{\text{Lift}} = 33 \text{ °C}$ and $T_{\text{Evap, in}} = 4 \text{ °C}$.

The course of the heat transfer per mass of working fluid in the condenser with increasing isobutane content is similar to the course at the same conditions in Fig. 2. In both figures the maximum is at a mole fraction of 0.267 and decreases slightly towards pure propane and stronger with more isobutane. This behaviour can be explained by the condensation enthalpy of the respective mixture. This enthalpy makes up the largest part of the heat transfer to the secondary fluid in the condenser. The condensation enthalpies associated with the temperature glides shown in Fig. 3, and the heat flows in the condenser (related to the working fluid) are shown in Table 4. The boundary conditions are the same as in Fig. 4

Table 4: Condensation enthalpy, heat flow in the condenser and temperature glide depending on the isobutane mole fraction at $n_{\text{Comp}} = 1500 \text{ min}^{-1}$, $T_{\text{Lift}} = 33 \text{ }^{\circ}\text{C}$ and $T_{\text{Evap, in}} = 4 \text{ }^{\circ}\text{C}$.

$x_{\text{C}_4\text{H}_{10}}$ (-)	Δh_{Cond} (kJ/kg)	\dot{Q}_{H} (kW)	TG ($^{\circ}\text{C}$)
0	288.55	4.06	0.286
0.267	310.15	3.41	5.706
0.527	315.92	2.73	6.947
0.778	312.29	2.07	4.946
1	300.94	1.53	0.2902

In Table 4 it can be seen that the condensation enthalpy increases with rising temperature glide up to the maximum at a mole fraction of 0.527 with 315.92 kJ/kg. The enthalpy for a mole fraction of 0.267, however, is not far below, with a value of 310.15 kJ/kg, while the propane enthalpy of evaporation is 288.55 kJ/kg. The heat flow in the condenser decreases with increasing isobutane mole fraction due to the decreasing mass flow (see table 3), with the maximum heat flow rate for pure propane. Thus, for pure propane, the heat flow does not rise sufficiently to compensate the larger obtained mass flow. With a mole fraction of 0.527, the condensation enthalpy and the temperature glide are at maxima, but the mass flow rate is low, due to the lower density of the mixture. The result is that the mixture with an isobutane fraction of 0.267 condenser heat flow rate per mass is highest and the nominator of the COP is largest.

Finally, the fluid dependent specific exergy losses of all components are shown in order to illuminate their influence on the entire process and to find the components with the highest potential for improvements. The specific exergy losses depending on the isobutane mole fraction for a compressor speed of 1500 min^{-1} , a temperature lift of $33 \text{ }^{\circ}\text{C}$ and an evaporator inlet temperature of $4 \text{ }^{\circ}\text{C}$ are shown exemplarily in Fig. 5.

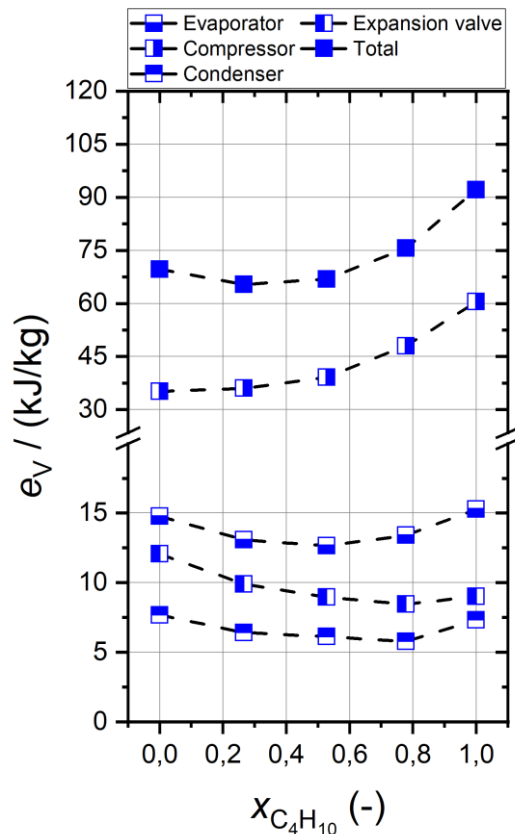


Fig 5: Specific exergy loss depending on the isobutane mole fraction at $n_{Comp} = 1500 \text{ min}^{-1}$, $T_{Lift} = 33 \text{ }^\circ\text{C}$ and $T_{Evap, in} = 4 \text{ }^\circ\text{C}$.

It is seen that the total specific exergy losses are in the range between 65 kJ/kg and 92 kJ/kg. The lowest exergy loss is found for a mole fraction of 0.267 and the highest for pure isobutane. The losses with pure propane and with a mole fraction of 0.5 are only slightly above the minimum. The condenser losses are lowest, with values between 5.8 kJ/kg and 7.7 kJ/kg. The component with the next highest losses is the expansion valve (8.5 kJ/kg - 12.1 kJ/kg). The evaporator leads to slightly higher losses of 12.6 kJ/kg to 15.3 kJ/kg, while the compressor conducts to largest losses between 35 kJ/kg and 60 kJ/kg. As expected for a temperature glide, the specific exergy losses in the condenser are highest for the pure refrigerants. In comparison, the compressor has a very high share of at least 50.4 % up to 65.67 % of the exergy losses. The decreasing refrigerant mass flow with increasing isobutane fraction, is the reason for the rising losses because of the decreasing global compressor efficiency, which in turn increases the specific exergy loss in the compressor [9]. Due to this high share of exergy losses, the compressor is one of the most important components of the process with a high potential for improvements.

Conclusions

Experimental results for the fluid dependence of the performance of a compression heat pump system with temperature lifts of 33 °C and 53 °C are presented, which can also be used for providing hot water. The performance was investigated as a function of evaporator inlet temperature, compressor speed and isobutane mole fraction in a propane/isobutane refrigerant mixture. The use of this zeotropic mixture has a positive effect on the process due to the temperature glide and the associated higher condensation enthalpy. The higher condensation enthalpy leads to higher heat flows in the condenser, resulting in higher COPs. But the effect is not as high as expected, because it turns out that the compressor performance worsens for mixtures and thus the compressor is identified as the most important component. It influences the COP

directly via the compressor efficiency and also indirectly via the delivery ratio or the mass flow rate, both being composition dependent. The results showed a direct relationship between high compressor efficiencies and higher COP, and that the mixture with the highest delivery rate was the mixture with the highest COP. Furthermore, the analysis of the specific exergy losses of the individual components showed that the compressor accounts for a share of the total losses between 50 % and 66.67 %. In this way, on the one hand, the compressor can limit the benefits of a zeotropic mixture due to lower efficiencies and operating characteristics, and on the other hand, it represents a great opportunity to improve and optimise such heat pump processes. From this it gets clear that using constant compressor efficiencies in cycle calculations for different fluid mixtures will not lead to reliable results.

References:

- [1] United Nations Environment Programme UNEP, *Montreal Protocol on Substances that Deplete the Ozone Layer*, 1987.
- [2] K. Harby. Hydrocarbons and their mixtures as alternatives to environmental unfriendly halogenated refrigerants. *Renewable and Sustainable Energy Reviews*, 73:1247-1264, 2017.
- [3] C. Arpagaus et al. High temperature heat pumps: Market overview, state of the art, research status, refrigerants, and application potentials. *Energy*, 152:985-1010, 2018.
- [4] Zhang et al. System optimization and experimental research on air source water heat pump water heater. *Applied Thermal Engineering*, 27:1029-1035, 2007.
- [5] Chaichana et al. Natural working fluids for solar-boosted heat pumps. *International Journal of Refrigeration*, 26:637-643, 2003.
- [6] Chang et al. Performance and heat transfer characteristics of hydrocarbon refrigerants in a heat pump system. *International Journal of Refrigeration*, 23:232-242, 2000.
- [7] Park et al. Performance of alternative refrigerants for residential air-conditioning applications. *Applied Energy*, 84:985-991, 2009.
- [8] Bamigbetan et al. The development of a hydrocarbon high temperature heat pump for waste heat recovery. *Energy*, 173:1141-1153, 2019.
- [9] Venzik. Experimentelle Untersuchung des Fluideinflusses auf die Thermodynamik der Wärmepumpe: Kohlenwasserstoffe und deren Gemische. *University Duisburg-Essen*, 2019

Failure detection in a water treatment system of a biomass CHP

G.Prokhorskii^{1,2}, C.Stegh^{1,2}, V.Seiler^{1,2}, M.Netzer³ and M.Preißinger^{1,2*}

¹illwerke vkw Endowed Professorship for Energy Efficiency, Research Center Energy, Vorarlberg University of Applied Sciences, Hochschulstraße 1, 6850 Dornbirn, Austria

²Josef Ressel Centre for Intelligent Thermal Energy Systems, Vorarlberg University of Applied Sciences, Hochschulstraße 1, 6850 Dornbirn, Austria

³Bertsch Energy GmbH & Co KG Vorarlberg, 6700 Bludenz, Austria

*Corresponding author: markus.preissinger@fhv.at

Abstract

To keep energy systems in an optimal state it is necessary to ensure proper maintenance and optimized operation. Both of these goals can be achieved with implementation of predictive maintenance. Based on sensor data, it is a perfect option to fulfil diagnostics and prognostic tasks, and optimize long time operation of the power plant. Prediction of failures and outlier detection methods are the basis of predictive maintenance. Several outlier and failure detection algorithms have been presented so far, but still have limitations concerning implementation. We propose a predictive maintenance approach for a water treatment system of a power plant of BERTSCHEnergy. We investigate methods for failure detection and find that only a combination of data-driven and knowledge-based leads to the desired result.

Keywords: Predictive maintenance, expert system, power plant, water treatment, failure prediction, intelligent thermal energy systems.

Introduction

Biomass power plants are complex systems in which components do not work independently from each other. It is therefore difficult to achieve proper maintenance by solely focusing on conventional maintenance in intervals or based on thresholds. Instead, it is necessary to predict failures of all components reliably to provide stability of the working cycle, achieve high availability and reliability, and improve the efficiency of power plant units. Often, it is a problem for the operator to detect certain issues like deterioration of water quality or blocking of fuel supply chain and to locate promptly the equipment which was involved in this process. One step to cost-efficient operation is to perform corrective and predictive maintenance of power plants [1]. Its integration can ensure enhanced reliability, enhanced safety, and reduced maintenance costs. Moreover, predictive maintenance might eliminate breakdowns by 70-75%, reduce breakdown time by 35-45%, and increase production by 20-25% [2].

Prediction of failures and outlier detection methods are the basis of predictive maintenance. Several outlier and failure detection algorithms have been presented so far. Qi et al. [3] implemented the original Grubbs' method and modified Grubbs' method based on median and median absolute deviation [4]. Hubballi et al. [5] proposed the nearest neighbor-based outlier detection algorithm (NDoT), evaluated this method experimentally, and compared results with a classical outlier detection method LOF (Local Outlier Factor). In turn, LOF was described by Breunig et al. [6]. Wang and Mao [7] applied the Gaussian process for process monitoring and process control, and moreover developed several detection algorithms and implemented all of them on both synthetic and real-life datasets. Chow et al. [8] implemented a k-means clustering algorithm for the real-time industrial process at a wastewater treatment plant. A lot of algorithms such as principal component analysis (PCA), partial least squares (PLS), smallest

half volume (SHV), resampling by half-mean (RHM) have been applied for outlier detection and compared between each other [9].

Despite the numerous studies on anomaly detection just a few of all predictive maintenance approaches have been implemented so far. One study describes data screening for use in anomaly detection and predictive maintenance applications [10]. Also, authors classified a working regimes of the mill fan system in a coal fired power plant with use of a rule based model in [11]. Agarwal et al. [12] show a very simple data-driven approach based on only one sensor of amount of neutron flow with a very specific problem of data variation of this sensor. Wang and Liu [13] described the knowledge- and data driven approach which are related to only one small piece of equipment. Moleda et. al [14] implemented the algorithm for predicting failures in feed water pump and compared them with other usable algorithms. As the schemes of the power plants are individual, parts of these papers are highly specialized. In turn, our goal is the prediction of failures in a biomass fired power plant and the development of an intellectual reporting system.

Background

The object of our research is a makeup water treatment system of a biomass fired power plant with a nominal electric power output of 8.1 MW or 40.5 MW firing capacity. The water treatment system sustains continuous flow of fresh clean water to power plant. If the process fails, the quality of make up water will deteriorate and may decrease the power output of the power plant. If the failure mode lasts longer than the water storage tanks can compensate, the power plant has to be shut down or expensive equipment might be damaged. This motivates to choose the right water treatment at the stage of planning and to sustain the continuous operation of the process.

The water treatment system in Fig.1 consists of a water softening stage with two Na-cation exchangers and two reverse osmosis (RO) units that form the first desalination stage, electrodeionization (EDI) as a second desalination stage, and lastly a water polishing stage with two mixed-bed filters (MBF).

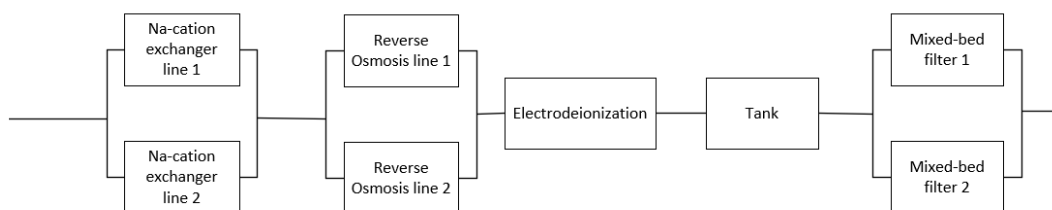


Figure 1. Flow chart of the water treatment system

After the mixed-bed filter, the polished water enters the deaerator and is then directed as feed water to the boiler (Fig.2(left)). The main part of it goes to the drum, the other one goes to the steam superheater (Fig.2(right)). Hence, impurities from water treatment system go directly to superheater surfaces and turbine blades; expensive repairs and equipment downtime would arise from that.

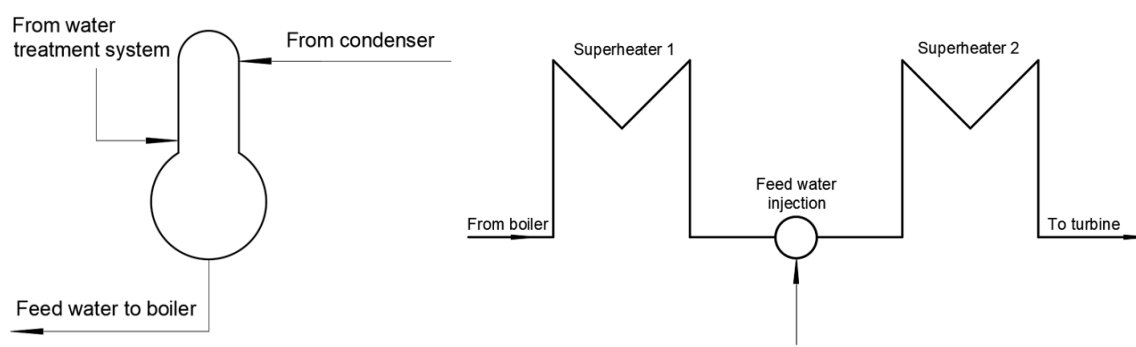


Figure 2. Path of the additional water: deaerator (left), steam line (right)

To avoid such impurities, the mixed-bed-filters are set to a maximum conductivity of $0.1 \mu\text{S}/\text{cm}$. This threshold value is ensured by cation and anion layers of exchanging resin. Positively and negatively charged impurities go from the water to the resin. The lifetime of the mixed-bed filters varies with the water quality it is supplied with. So, if all stages upstream the mixed-bed filters work properly the expected lifetime of the unit is six months.

However the conductivity sensor downstream MBF in Fig.3 represents several time periods of up to three weeks when the threshold value is exceeded by up to a factor 50, leading to a maximum conductivity of $5 \mu\text{S}/\text{cm}$. Hence, the lifetime of the mixed-bed filter is reduced to less than one month.

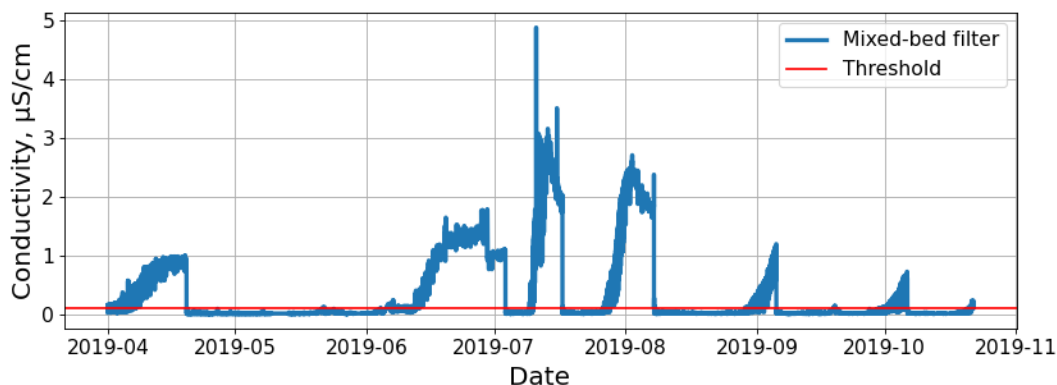


Figure 3. Mixed-bed filter lifecycle

To prevent this behaviour in our system and give valuable insights for predictive maintenance in thermal power plants, we want to answer the following research question:

How is it possible to reduce malfunction of the water treatment system by using a multimodal approach for failure prediction?

To answer this question, we analyze historical data of the system components upstream of the MBF, identify dependencies and develop an intelligent reporting system.

Methods

According to Montero Jimenez et.al [2] the first two steps of predictive maintenance are historical data collection and data pre-processing (see Fig.4). As the power plant investigated doesn't

have an automated cloud-based data acquisition and analyzing system, operational data has to be exported manually.

Our raw data set contains 156 sensors with data collection started in August 2017. In a first step, we preprocessed the data to a common format. We used Jupyter Notebook/Lab as a Python [15] environment as framework and pickles as common file format. Pickles are used for serializing and de-serializing Python object structures, also called marshalling or flattening.

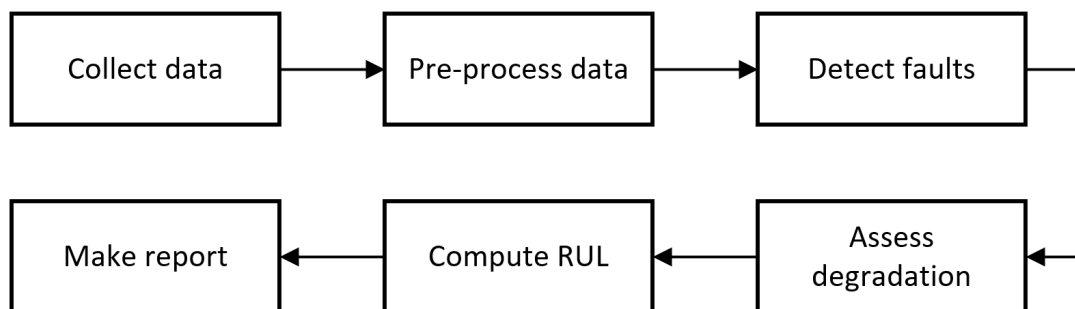


Figure 4. Predictive maintenance diagram (adapted from Jimenez et al.[2])

The third step is the combination of the next three points: fault detection, assessment of degradation and computation of remaining useful lifetime (RUL).

Fault detection methods in predictive maintenance are divided into three categories: Knowledge-based (KB), Data Driven (DD) and Physics-based (PB). Knowledge-based models hinge on experiences expressed by rules, cases, etc. Data-driven models use data accumulated over the years of operation. Physics-based models use the laws of physics to estimate ageing of components. All of these methods can be used separately or in combination. In Fig.5 the simple scheme of predictive maintenance methods is represented. Thus, it is possible to combine all of these methods according the needs of the problem given.

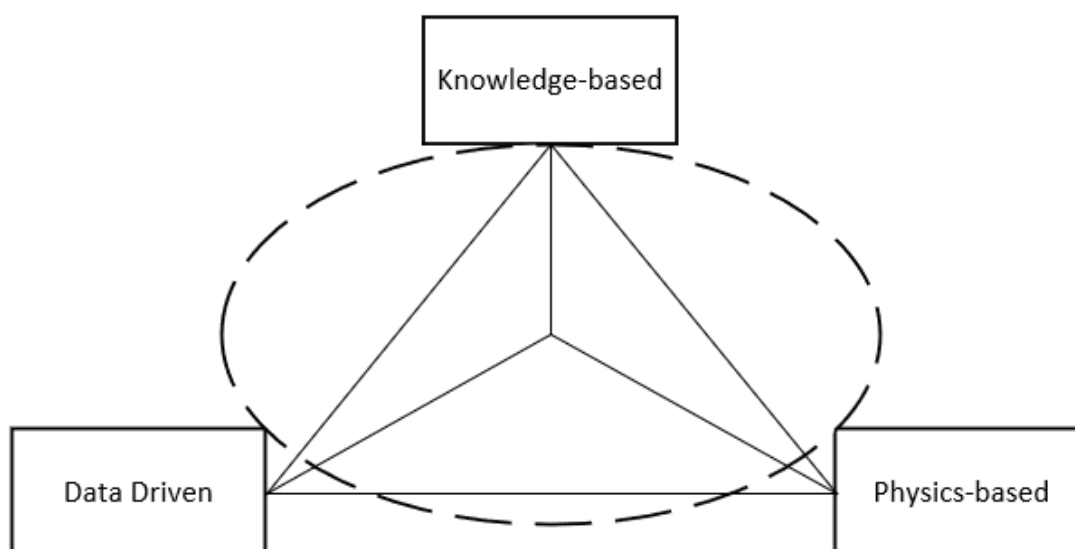


Figure 5. Predictive maintenance methods (adapted from Jimenez et al.[2])

Results and Discussion

Based on a broad historical data set, we first focused on a data-driven solution. However, typical failure detection algorithms as LOF [6], Grubbs, and modified Grubbs methods [3], etc. require steady sensor signal. In Fig.6 we can see 6-month data of conductivity after each water purifying stage. Blue color represents the measured conductivity, red color demonstrates the required conductivity threshold. It is obvious that mostly the data is not steady, instead, it has strong fluctuation due to various peaks.

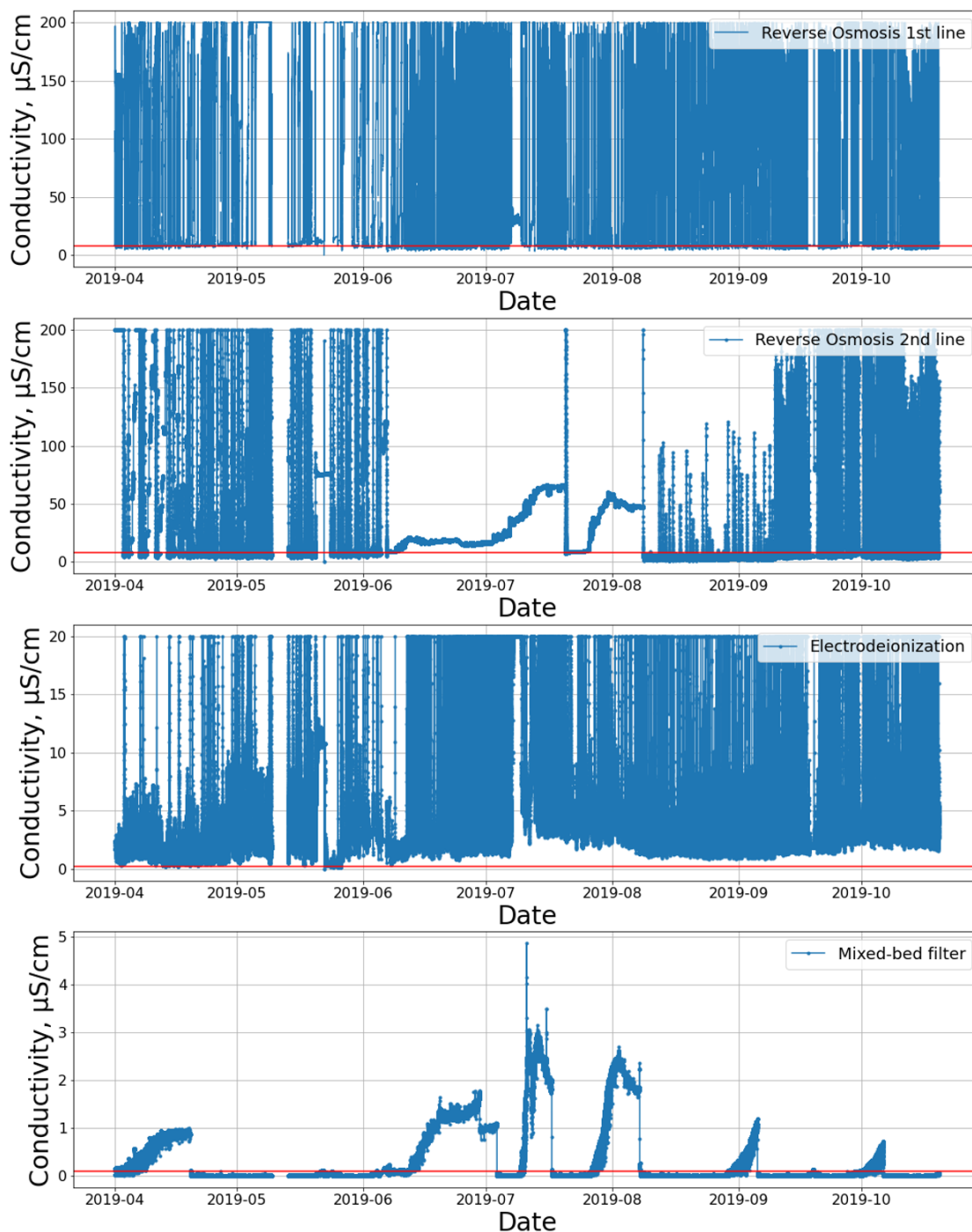


Figure 6. Conductivity after each stage of the water treatment system

Furthermore, the long-term trend in Fig.6 of the data shows:

- RO1 shows a strong fluctuation with values distributed between 0 $\mu\text{S}/\text{cm}$ and 200 $\mu\text{S}/\text{cm}$ where 200 $\mu\text{S}/\text{cm}$ is the upper limit of the sensor.
- RO2 shows the same fluctuation but in a period of two month the conductivity is steady, but constantly above the threshold.
- EDI also shows fluctuation of conductivity. These peaks correlate with the peaks of conductivity in RO1 and RO2. Whereas the conductivity during the whole period exceeds the threshold.
- MBF data are steady values due to the tank upstream that provides continuous flow. This leads to a clear trend when the conductivity is above and when it is below the threshold.

Although a pure data-driven approach seems not to be the right choice for the long-term trend, analyzing the data within a short period of several hours, a first correlation can be identified. In Fig.7 blue and red color represent conductivity after RO1 and RO2 respectively and black color the water flow of the WTS. This figure clarifies that the peaks in conductivity are associated with the water flow through the water treatment system. Moreover, the data show that peaks alternate. This can indicate an interchangeable working pattern of the RO system.

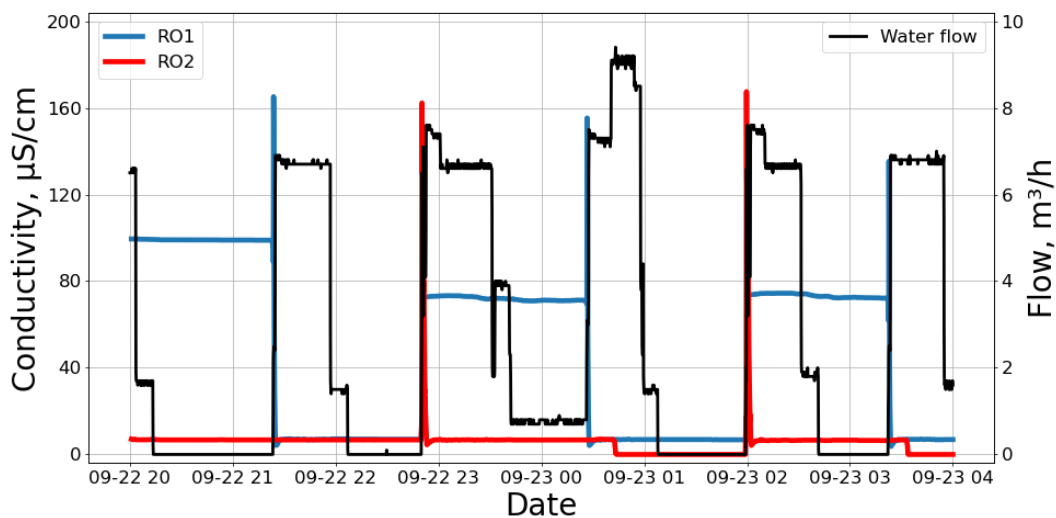


Figure 7. Reverse Osmosis short-term data

Still, the correlation can not be expressed as algorithm and it is necessary to develop a combination of knowledge-based and data-driven predictive maintenance models. First of all, in Fig.8 blue and red lines represent a flow of concentrate of RO1 and RO2 respectively and black color is the water level of the tank. The use of expert knowledge helps to understand that if the water level drops lower than 3000 mm in the water tank, an operational cycle in the WTS is started. Moreover, a flow of concentrate above the threshold value of 1 t/h signals that the unit was turned on. Several important notes can be drawn:

- the RO lines work in cycles.
- an algorithm controls the RO lines and it decides to switch the RO lines on or off.
- an algorithm shuts down the line if the conductivity which is provided by the equipment is higher than it should be.
- conductivity about 200 $\mu\text{S}/\text{cm}$ at the beginning of the cycles is not a problem, because during first three minutes the conductivity stabilization process happens.

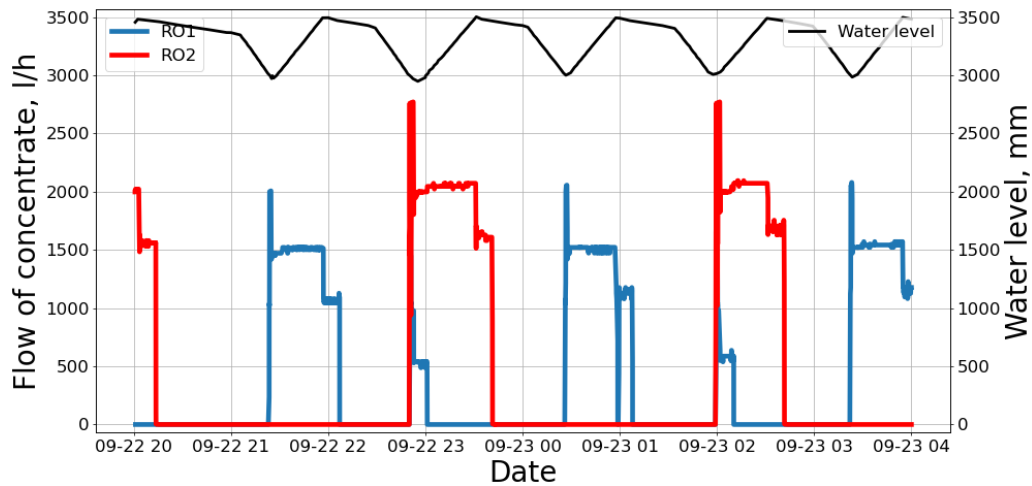


Figure 8. Flow of concentrate short-term data

Having analysed the data, the ultimate goal is to distinguish between normal behaviour shown and anomalies that might lead to serious damage of equipment. In other words: we want to identify short-problems that might cause long-term problems.

To do so, we combine Fig.7 and Fig.8 and analyze the flow of concentrate in correlation to the conductivity for RO1 and RO2 (Fig.9). In a period of 24 hours the flow of concentrate indicates that RO1 is switched on five times (1-5), RO2 is switched on four times (A-D). However, analysing the conductivity, it is obvious that for RO2, all four attempts (A-D) to reduce the conductivity fail as the conductivity remains at around 32 $\mu\text{S}/\text{cm}$.

For RO1 a problem after switching on occurs in two cases (1,4) which is indicated by an increase in conductivity. However, all other periods of operation (2,3,5) work properly and keep the conductivity low. Integrating the expert knowledge from the industrial partner, such behaviour is classified as normal as it can occur once in a while that switching of the RO line fails. Therefore, within an automated monitoring system an algorithm to detect anomalies in RO operation has to be based on two rules (rule 1 and 2):

- if switching an RO line fails once or twice in a row, the behaviour is classified as normal.
- if switching an RO line fails more that twice in a row, an alert to the plant operator has to be given so that long-term problems are avoided.

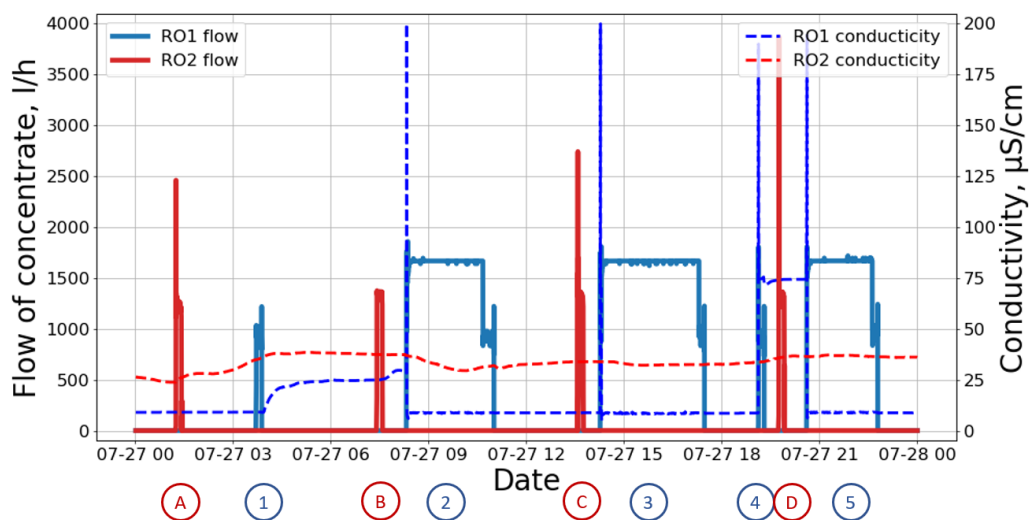


Figure 9. Short-term problem

Having developed the expert rules to identify short term problems it is necessary to analyze the influence of the short-term behaviour on long-term operation. Therefore, as it was stated above we apply a pre-processing rule (rule 3) for skipping the first three minutes of each operational cycle to pass the stabilization behavior, and then analyze the integrated mean conductivity of each cycle. The operational cycles are classified into three groups and displayed in Fig.10:

- operational cycles with normal behaviour (green)
- operational cycles with one or two anomalies in a row (orange)
- operational cycles with more than two anomalies in a row (red)

Based on this classification, many anomalies of class 2 (orange) are identified although the mixed-bed filter fulfills the threshold value. Additional data analysis leads to a solution on this aspect: if we exclude all operational cycles with a duration of less than 650 s (grey colored) which do not influence the long-term behaviour (rule 4), Fig.11 gives a clear correlation between short term problem and long-term behaviour.

In the first part of Fig.11, short-term problems (orange and red crosses) are frequently occurring mostly in RO1 and also sometimes in RO2. Furthermore, EDI seems not to work properly until December 2019 leading to several serious peaks in conductivity after the mixed-bed filter. From January 2020 on, only few problems larger than 650s (orange) occur, all other problems have a duration of less than 650s (grey) and it is obvious that they do not influence the EDI and the mixed-bed filter.

Hence, the combination of a data driven and a knowledge driven approach is successful to identify short-term problems and extend them to long-term behaviour.

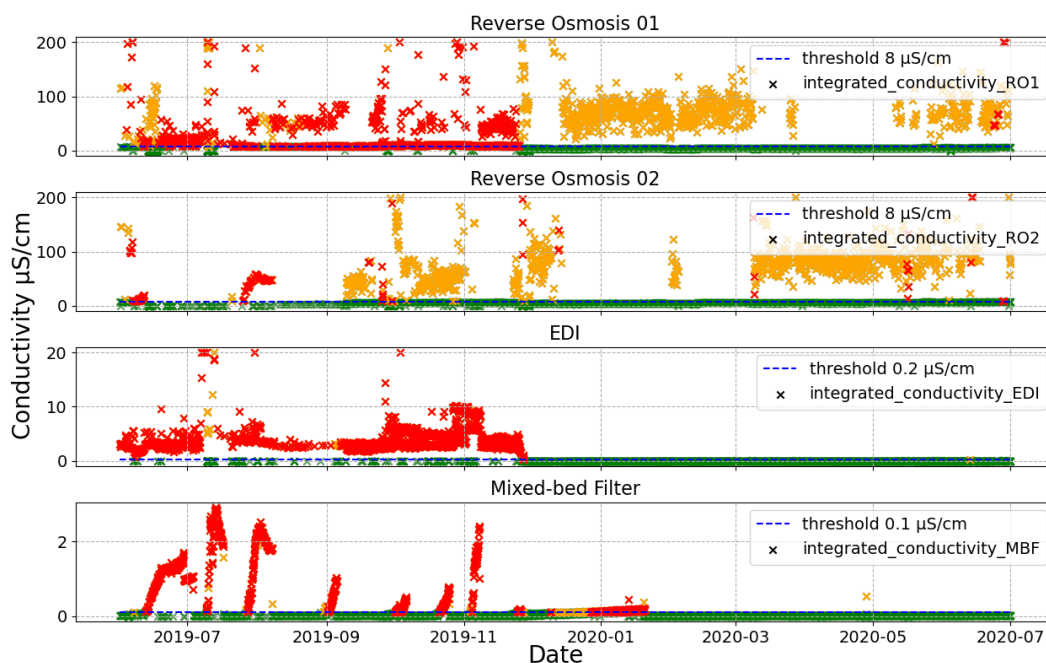


Figure 10. WTS with rules 1-3

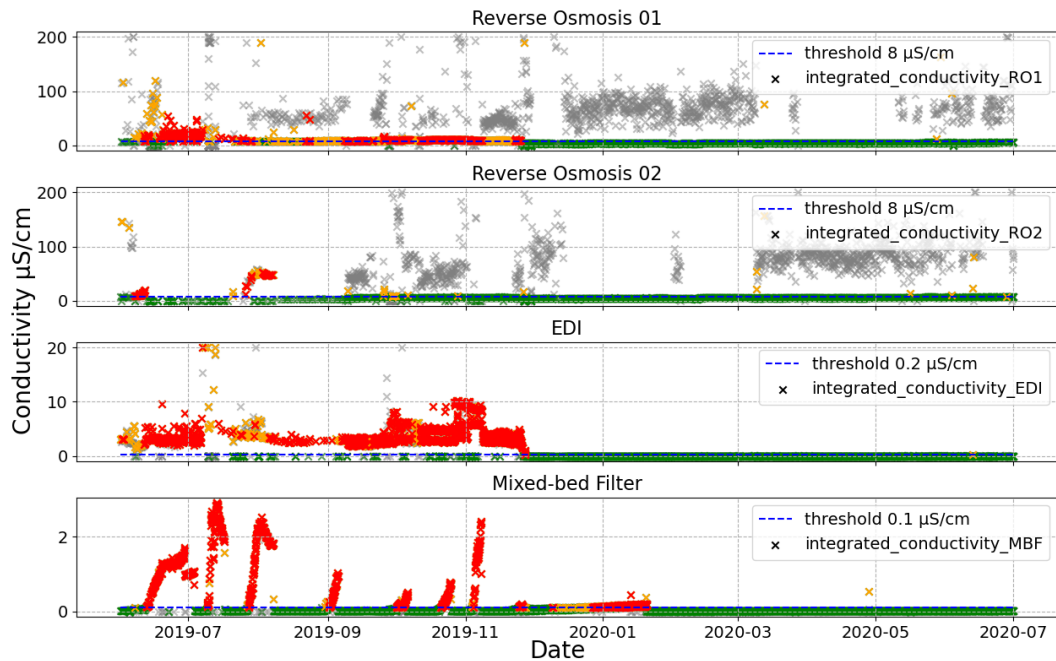


Figure 11. WTS with rules 1-4

Lastly, it is our goal to use this information to calculate the remaining useful lifetime(RUL) of the mixed bed filter (Fig.12). This is the first step to apply our method to predictive maintenance. To calculate the RUL it is necessary to know what is the current status of the equipment unit (what happened before) and to predict what will be in the future. Therefore, we implemented a simple knowledge-based rule (rule 5) to estimate the days until the next regeneration.

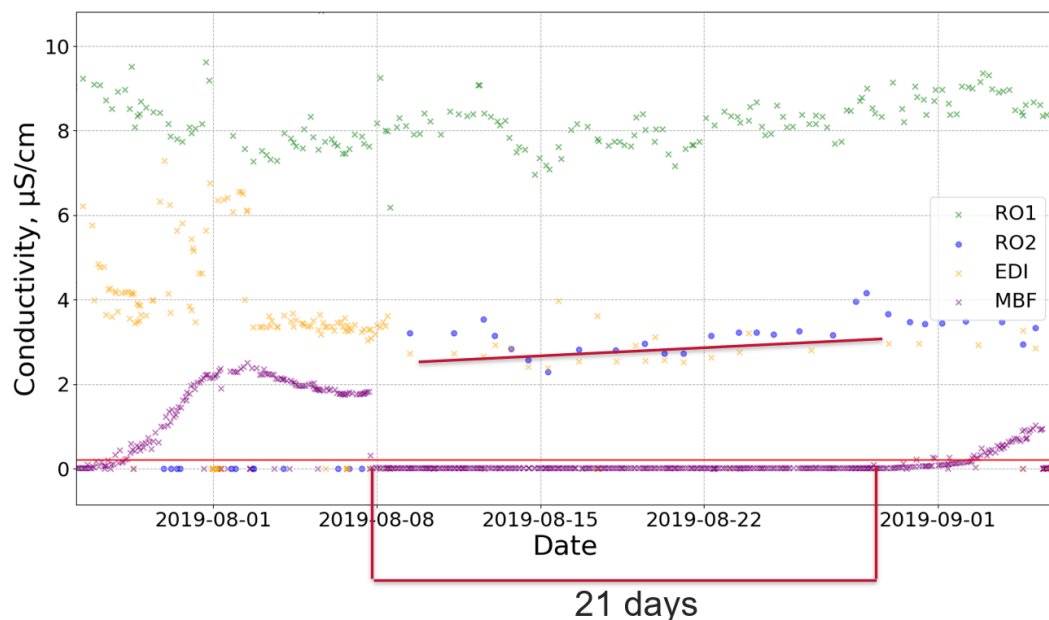


Figure 12. RUL expression (rule 5)

As it was stated in the background chapter, the mixed-bed filter has a certain capacity. After the capacity is exhausted water goes through MBF without purification. This can cause problems with power plant equipment due to deposits in boiler heating surfaces and turbine blades.

Especially if something will happen with the equipment upstream MBF the quality of make-up water will deteriorate very fast. With Eq.1 we can calculate the capacity of the MBF.

$$C = \int_0^{N_{days}} \lambda(t) dt \quad (1)$$

To calculate the number of days until the next breakout, we have to take an average conductivity of EDI during the considering period. Then we need to equate two capacities and then determine the number of days N_2 with Eq.2. In our project, we estimate the required water quality on the level of 0.2 $\mu\text{S}/\text{cm}$ (required conductivity in the inlet of MBF) and the required duration of the operation 180 days (technical specs of MBF).

$$\begin{aligned} C_1 = C_2 &\Rightarrow \lambda_1 \cdot (N_1 - 0) = \lambda_2 \cdot (N_2 - 0) \\ 0.2 \cdot 180 &= \lambda_2 \cdot N_2 \\ N_2 &= 36/\lambda_2 \end{aligned} \quad (2)$$

For the example shown in Fig.12 this simple formula gives 15 days as a result. So that means that our monitoring system shows problems with the Mixed-bed filter, the plant operator has 15 days to fix the problem before the capacity is exhausted. This is a very simple approach but it allows to get a rough estimation of the number of days before the next break down.

The last step is the creation of the report. It will include the key results of fault detection and RUL estimation: how many and what type of anomalies have been found; estimation of the breakdown point; etc. These aspects will help the plant operator to detect faults way earlier than so far and to act as soon as possible.

Summary and Conclusions

Predictive maintenance is one of the most crucial directions in industrial research, whereas the interest will grow further in future. The predictive maintenance technique which was considered and showed on the example of the water treatment system is the first approach in a series of researches based on a broad collection of data from a biomass power plant. Here, we tried the methods which can help to reduce malfunction of the water treatment system, how the data fits for this task, and which methods we can use in the future. Our method is simple and straightforward but it meets our goals. It clearly describes the process from the beginning (data acquisition) until the end (the report tool) with a simple example.

Moreover, our research give us a valuable result: to be successful in predictive maintenance approaches, based on real power plant data one has to use multimodal methods. Otherwise, the methods which are based only on one type of knowledge fail due to misunderstanding, lack of knowledge and a lot of assumptions.

Acknowledgment

The financial support by the Austrian Federal Ministry for Digital and Economic Affairs and the National Foundation for Research, Technology and Development, and the Christian Doppler Research Association are gratefully acknowledged.

References

- [1] Hardik A. Gohel, Himanshu Upadhyay, Leonel Lagos, Kevin Cooper, and Andrew Sanzetenea. Predictive Maintenance Architecture Development for Nuclear Infrastructure using Machine Learning. *Nuclear Engineering and Technology*, page S1738573319306783, January 2020.

- [2] Juan José Montero Jimenez, Sébastien Schwartz, Rob Vingerhoeds, Bernard Grabot, and Michel Salaün. Towards multi-model approaches to predictive maintenance: A systematic literature survey on diagnostics and prognostics. *Journal of Manufacturing Systems*, 56:539–557, July 2020.
- [3] Minfang Qi, Zhongguang Fu, and Fei Chen. Outliers detection method of multiple measuring points of parameters in power plant units. *Applied Thermal Engineering*, 85:297–303, June 2015.
- [4] Frank E. Grubbs. Procedures for Detecting Outlying Observations in Samples. *Technometrics*, 11(1):1–21, February 1969.
- [5] Neminath Hubballi, Bidyut Kr. Patra, and Sukumar Nandi. NDoT: Nearest Neighbor Distance Based Outlier Detection Technique. In Sergei O. Kuznetsov, Deba P. Mandal, Malay K. Kundu, and Sankar K. Pal, editors, *Pattern Recognition and Machine Intelligence*, volume 6744, pages 36–42. Springer Berlin Heidelberg, Berlin, Heidelberg, 2011. Series Title: Lecture Notes in Computer Science.
- [6] Markus M. Breunig, Hans-Peter Kriegel, Raymond T. Ng, and Jörg Sander. LOF: identifying density-based local outliers. In *Proceedings of the 2000 ACM SIGMOD international conference on Management of data - SIGMOD '00*, pages 93–104, Dallas, Texas, United States, 2000. ACM Press.
- [7] Biao Wang and Zhizhong Mao. Outlier detection based on Gaussian process with application to industrial processes. *Applied Soft Computing*, 76:505–516, March 2019.
- [8] Christopher W.K. Chow, Jixue Liu, Jiuyong Li, Nick Swain, Katherine Reid, and Christopher P. Saint. Development of smart data analytics tools to support wastewater treatment plant operation. *Chemometrics and Intelligent Laboratory Systems*, 177:140–150, June 2018.
- [9] Leo H. Chiang, Randy J. Pell, and Mary Beth Seasholtz. Exploring process data with the use of robust outlier detection algorithms. *Journal of Process Control*, 13(5):437–449, August 2003.
- [10] Ping Li, Jiru Chu, and Rui Han. *Research on the Screening Method of Predictive Maintenance Monitoring Equipment in Nuclear Power Plant*. IEEE, 2020. Pages: 128-31 Publication Title: 2020 Prognostics and Health Management Conference (PHM-Besancon). Proceedings INSPEC:19688406.
- [11] Petia Koprinkova-Hristova, Lyubka Doukovska, and Peter Kostov. Working regimes classification for predictive maintenance of mill fan systems. In *2013 IEEE INISTA*, pages 1–5, Albena, Bulgaria, June 2013. IEEE.
- [12] Kapil Agarwal, Durga Toshniwal, Pramod K. Gupta, Vikas Khurana, and Pushp Upadhyay. *Anomaly Detection and Similarity Search in Neutron Monitor Data for Predictive Maintenance of Nuclear Power Plants*. IEEE, 2013. Pages: 29-34 Publication Title: 2013 2nd International Conference on Advanced Computing, Networking and Security (ADCONS) INSPEC:14042880.
- [13] Xiao Wang and Han Liu. A Knowledge- and Data-Driven Soft Sensor Based on Deep Learning for Predicting the Deformation of an Air Preheater Rotor. *IEEE Access*, 7:159651–159660, 2019.
- [14] Marek Moleda, Alina Momot, and Dariusz Mrozek. Predictive Maintenance of Boiler Feed Water Pumps Using SCADA Data. *Sensors*, 20(2):571, January 2020.
- [15] Wes McKinney. *Python for Data Analysis*. O'Reilly Media, 1 edition, 2012.

Theoretical investigation of the potential of capillary heat exchangers in heat pumps

M. Aps^{1*}, F. Durmus¹ and B. Atakan¹

¹Thermodynamic, University of Duisburg-Essen, Duisburg, Germany

*michael.aps@uni-due.de

Abstract

Heat pumps gain importance, due to the shift towards renewables. One possibility to increase their coefficient of performance (*COP*) is to use the exergy available in the condensed fluid prior to throttling. Here capillaries are investigated which act also as heat exchangers for subcooling behind the condenser of a heat pump. The influence of geometric parameters of double-tube heat exchangers on pressure drop, heat transfer and fluid velocity are investigated theoretically for different working fluids. The focus is particularly on selecting the geometries of the heat exchanger in such a way that no evaporation occurs. It turns out that this approach is promising for the refrigerants propane, isobutane and butane, leading to an increase in the *COP* of more than 25 %, while the geometry has to be chosen carefully, to avoid evaporation in the capillary, due to too large pressure drops.

Keywords: Capillary heat exchanger, throttle, heat pump, natural refrigerants

Introduction

Anthropogenic climate change requires a change in global energy conversion, both in the industrial and the private sector. Heat pumps can be used to convert electrical energy from renewables to heat, which is useable within private households. In Germany, heat pumps are the preferred choice for new buildings, where they already have a share of over 40 % [1]. A further improvement of the Coefficient of Performance (*COP*) will be needed and one approach is investigated here. Also, the Kigali amendments to the Montreal protocol decided to phase out established refrigerants such as hydrofluorocarbons (HFC, e.g. R134a) [2]. Hydrocarbons can be used instead, and the *COP* can theoretically be increased using the temperature glide of their zeotropic mixtures in order to reduce the exergy loss in the condenser [3]. Other opportunities to increase the *COP* exist by controlling the process. In various publications, particular attention is paid to the degree of superheating and subcooling. A comparison between the effects of subcooling and superheating was carried out in [4]. It turned out that subcooling provides a promising approach. Subcooling can enhance heat pump performance up to an optimal value depending on differing operation points. Corberan and coworkers find control methodologies for optimal subcooling and tested them theoretical and experimentally [5]. As a possible alternative the exergy of the secondary fluid can also be increased with heat exchangers constructed with capillaries as sub-coolers in heat pumps. Increasing the *COP* with an additional sub-cooler behind the condenser was already performed by Pitarch et al [6] in experiments, but they did not examine a simultaneous pressure loss. This uses some of the exergy destructed in the throttle for a further heat transfer to the secondary fluid. The pressure loss (Δp) depends on the capillary length (l), the density (ρ), the velocity (u_i) according to (2) and the discharge coefficient (ζ) and is described with

$$\Delta p = \zeta \frac{l}{d_i} \frac{\rho u_i^2}{2}. \quad (1)$$

This pressure loss with simultaneous heat transfer for such single-phase flows have to be investigated. If the pressure-drop of the refrigerant is high enough, a throttle may even become obsolete. The modified process scheme, with an ordinary compression heat pump with a capillary heat exchanger, is shown in Figure 1.

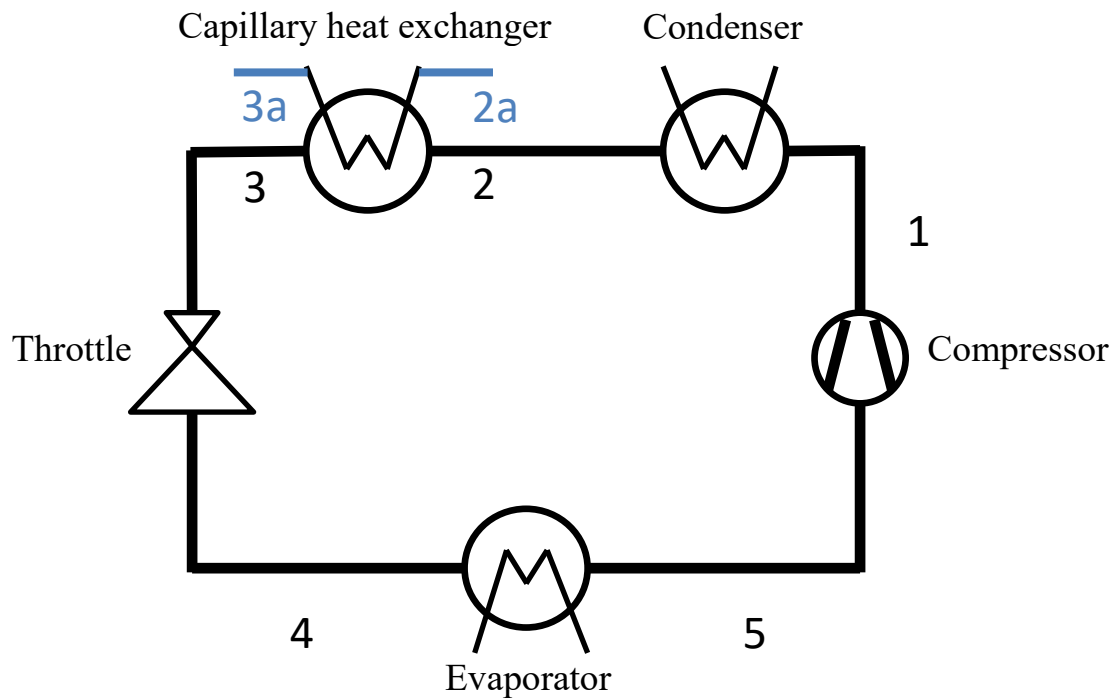


Figure 1: Heat pump process with a capillary heat exchanger

However, when the pressure drop is regarded, which often cannot be avoided, the acceleration of the fluids up to sonic speed has to be avoided and it is unclear how pressure drop and heat transfer rate correlate. At a constant mass flow (\dot{m}) and diameter (d_i), the local velocity (u_i) in the capillary depends only on the density (ρ):

$$u_i = \frac{4\dot{m}}{\pi d_i^2 \rho} \quad (2)$$

Also, a strong pressure drop can lead to an evaporation, increasing the pressure drop further, which has to be avoided.

In this work the dependence of the combined heat transfer and pressure drop in subcooling is investigated for the three alkanes butane, isobutane, and propane as function of geometry and entrance temperatures. Since, the pressure drop normally takes place in a throttle, a pressure drop in the capillary heat exchanger is no additional loss; this should be kept in mind. The investigation relies on modelling the system.

The system was modelled using python to calculate the heat flows, pressure drops and fluid velocity profiles. The density and other fluid properties, are needed for such calculations and the evaluation. The library CoolProp, which is non-commercial and freely available, is used for their calculation [7]. The influence of capillary lengths and diameters on pressure, speed and heat transfer are investigated theoretically here.

The capillary behind the condenser can either be used for preheating the secondary fluid before entering the condenser or to provide a second heated mass flow for a different application. The process is most efficient, when the minimum approach temperature ΔT between refrigerant and secondary fluid at the condenser outlet approaches 0 K [8]. By replacing the throttle in the process, the input parameters of the evaporator (condition 4, see Figure 1) remain similar, compared to the case without capillary leading to an unchanged power consumption of the compressor ($P_{electric}$). With the additional heat flow of the capillary ($\dot{Q}_{Capillary}$) and the heat flow of the condenser ($\dot{Q}_{condenser}$), the COP for the heat pump is increased accordingly

$$COP = \frac{\dot{Q}_{condenser} + \dot{Q}_{Capillary}}{P_{electric}} \quad (3)$$

The Nusselt correlations from Stephan [9] and Gnielinski [10,11] were used to determine the convection coefficients. The determination of pressure losses is based on the established equations of Prandtl and v. Karman and were taken from the VDI Wärmeatlas [12]. Inside the capillary, correlations for turbulent flows are used. Laminar flows or flows in the transition region occur in the annular gap of the capillary heat exchanger.

In order to select relevant conditions, the experimental inlet conditions from a heat pump are selected, which was running with all three fluids [13]. The mass flow rates, pressure levels, and the exit conditions of the working fluid, leaving the condenser were selected as input condition for the capillary. For all following calculations 12 m was chosen for the maximum length of the capillary. The heat pump aims to heat water from a temperature of 10°C (condition 2a) to 60 °C (condition 3a, see Figure 1). The water mass flow is regarded as variable to reach this target. For three different natural refrigerants (butane, isobutane and propane), the capillary diameter is investigated. A diameter is deemed to be optimal, when a) the length of the capillary is near 12 m, b) the heat transfer is high, c) the pressure drop is near the pressure drop which is normally achieved with the throttle, and d) without evaporation within the capillary. The hydraulic diameter of the countercurrent double-tube heat exchanger is set to 4 mm. The experimental setup is documented in the experimental work of Venzik et al. [13]. The common setup for the calculations is summarized in Table 1.

Table 1: Calculation parameters, input and output

Name	Input data for calculation	Comment
Refrigerant mass flow	variable	from experimental data
Refrigerant inlet pressure	variable	from experimental data
Refrigerant outlet pressure	variable	calculated
Refrigerant inlet temperature	variable	from experimental data
Refrigerant outlet temperature	variable	calculated
Water mass flow	variable	fixed, to reach exit temperature
Inlet and outlet water pressure	1.5 bar	fixed
Inlet water temperature	10 °C	fixed
Exit water temperature	60 °C	fixed
Capillary length	max. 12 m	calculated
Hydraulic diameter	4 mm	fixed
Inner diameter capillary	variable	fixed, so that no boiling occurs
Refrigerant	butane, isobutane or propane	fixed
Compressor performance	fixed for each refrigerant	from experimental data, compressor performance is assumed to be constant

Discussion and Results

Diameters fulfilling the conditions listed above are throughout between 2 and 3 mm. For butane, even capillaries with a length of less than 12 m are sufficient to throttle to a pressure of about 3 bar. The calculated temperature and pressure curves for the refrigerant butane and the resulting water temperatures are shown in Figure 2.

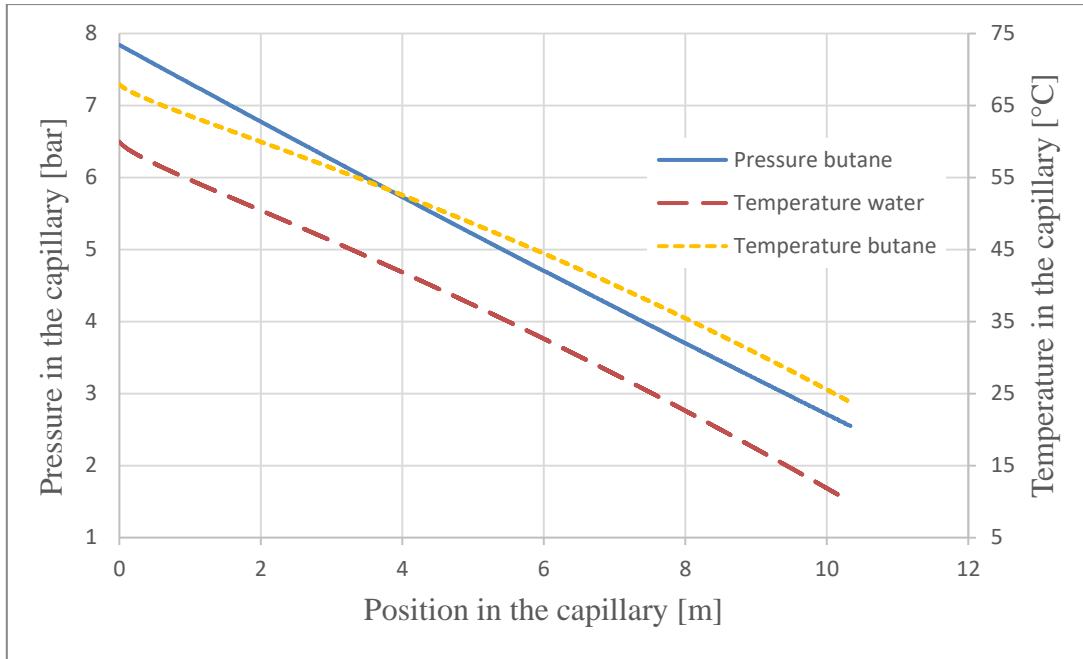


Figure 2: Pressure and temperature in a capillary with an inner diameter of 2.2 mm, butane mass flow of $5.1 \frac{g}{s}$ and a water mass flow of $3.21 \frac{g}{s}$

A water mass flow of $3.21 \frac{g}{s}$ can be heated from 10 °C to 60 °C in the capillary. At the same time, the refrigerant is throttled to a pressure of 2.6 bar. The transferred heat flow rate is 671 W under these conditions, the heat transferred in the experiment with negligible subcooling was 2435 W. When the inner diameter of the capillary is reduced and all other parameters are kept constant, sudden evaporation occurs inside the capillary. This results in a large increase of velocity and very high pressure drops, so that the capillary blocks the flow. This case is shown in Figure 3.

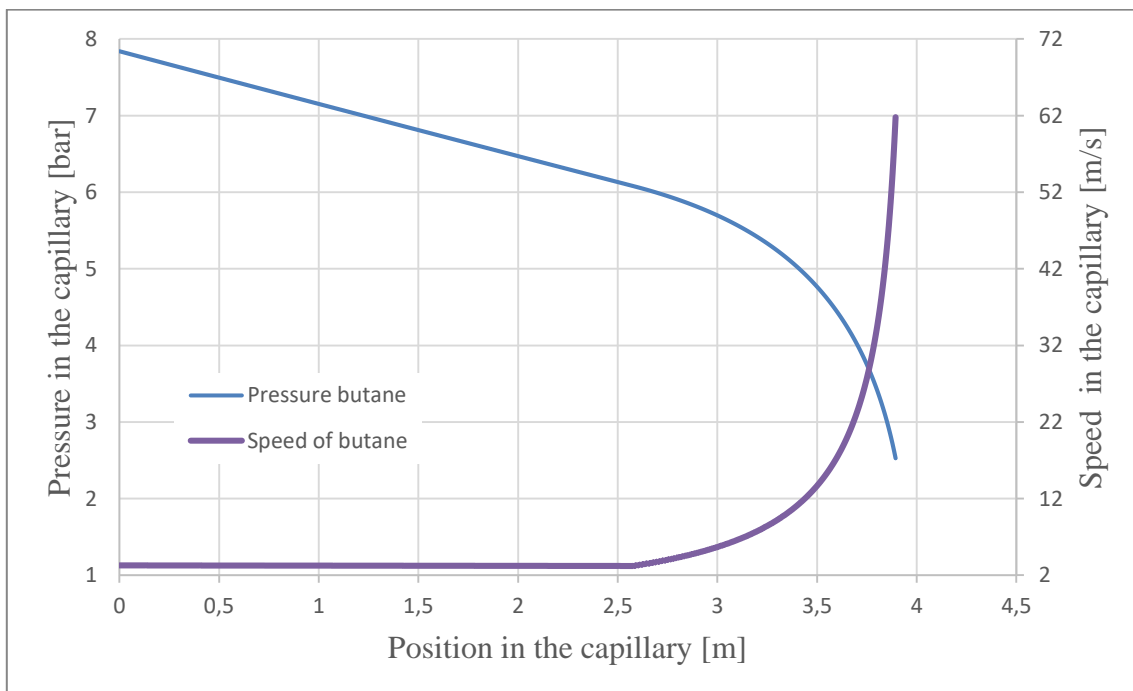


Figure 3: Pressure drop and rising velocity if boiling occurs in the capillary of 2.1 mm inner diameter

The phase change is not found at the end of the capillary, but already at a length below 4 m. With the same water and butane mass flow and at a capillary diameter of 2.1 mm, water can only be heated from 48.39 °C to 60 °C. Therefore, the transferred heat flow rate drops by 70%. This case will not be examined in the further course, as it is unwanted. For inner diameters below 2.2 mm, the water mass flow rate has to be reduced, in order to reach 60°C, before the pressure loss gets too high. This limits the transferred heat flow rate, because the maximum capillary length of 12 m cannot be used. To analyse the influence on the transferred heat flow rate, the inner diameter of the capillary is varied in steps of 0.1 mm. The results are shown in Table 2 and Figure 4.

Table 2: Calculations for different inner diameters in the capillary for butane

Inner Diameter (di) of the capillary	2.1 mm	2.2 mm	2.3 mm	2.4 mm	2.5 mm	2.6 mm
Pressure butane entry	7.84 bar					
Pressure butane exit	2.90 bar	2.60 bar	3.05 bar	4.04 bar	4.79 bar	5.36 bar
Length of the capillary	7.22 m	10.36 m	11.92 m	11.93 m	11.95 m	11.98 m
Speed butane exit	3.00 m/s	2.71 m/s	2.46 m/s	2.26 m/s	2.08 m/s	1.92 m/s
Temperature butane entry	67.5 °C					
Temperature butane exit	30.63 °C	24.13 °C	21.62 °C	21.33 °C	21.03 °C	20.73 °C
Mass flow of butane	5.9 g/s					
Mass flow of water	2.8 g/s	3.15 g/s	3.32 g/s	3.34 g/s	3.36 g/s	3.38 g/s
Heat flow rate transferred in capillary	565 W	659 W	694 W	698 W	703 W	707 W
Heat flow rate transferred in condenser	1973 W					
Compressor performance	798 W					

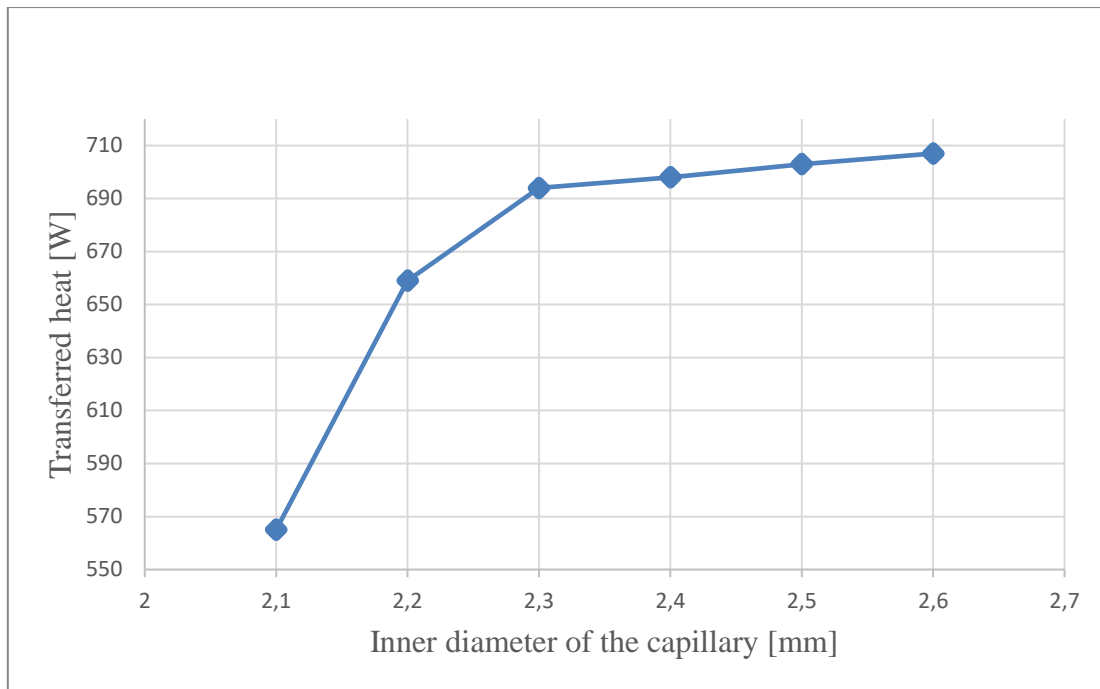


Figure 4: Transferred heat for the refrigerant butane with conditions from Table 2

From Table 2 and Figure 4 it is seen that the transferred heat flow rate rises with the inner diameter of the capillary, until the maximum length of the capillary is reached. The slope drops for larger diameters. The heat flow rate increases only slightly, because with increasing diameter the flow velocity drops reducing the convection coefficient, which is in part counterbalanced by the increasing heat transfer area. This trend will continue until butane is cooled to the water temperature of 10 °C. The maximum achievable enthalpy difference for butane, when cooled to 10°C would be 857 W, which would also be the reachable limit. The pressure loss will sink, with diameter according to (1) due to the lowered flow speed and the transition to laminar flow. Beyond an inner diameter of 2.3 mm, the heat flux rate only changes slightly, while the pressure drop is in the target regime. At an inner diameter of 6.5 mm the maximum heat flow rate of 753 W is reached. If the inner diameter is increased further the heat flow rate will sink, because the convection coefficient is too low and the compensation through a higher transmission area is too low. It is possible to increase the heat transfer at lower diameters around 2.3 mm. The limiting factor is convection coefficient in the annular gap. To increase it, the hydraulic diameter must be lowered and the water mass flow should stay constant.

For isobutane and propane, we observe similar results as for butane. However, the pressure levels are quite different now. An optimal utilization of the maximum capillary length of 12 m is achieved with an inner capillary diameter of 2.0 mm for isobutane and for 1.9 mm propane. The curves of temperatures and pressures vs. capillary length are similar to those of butane in Figure 2. The comparison of the transmitted heat flow rate and the pressure losses for all three refrigerants is shown in Figure 5. All conditions and results are shown for isobutane in Table 3 and for propane in Table 4. The maximum transferred heat flow rate in the capillary is highest for propane, followed by butane and isobutane. But this by itself is not sufficient to assess the improvements in the heat pump cycle, since the heat flow rates of the unmodified heat pumps without the capillary, also differ, as can be seen in the three tables.

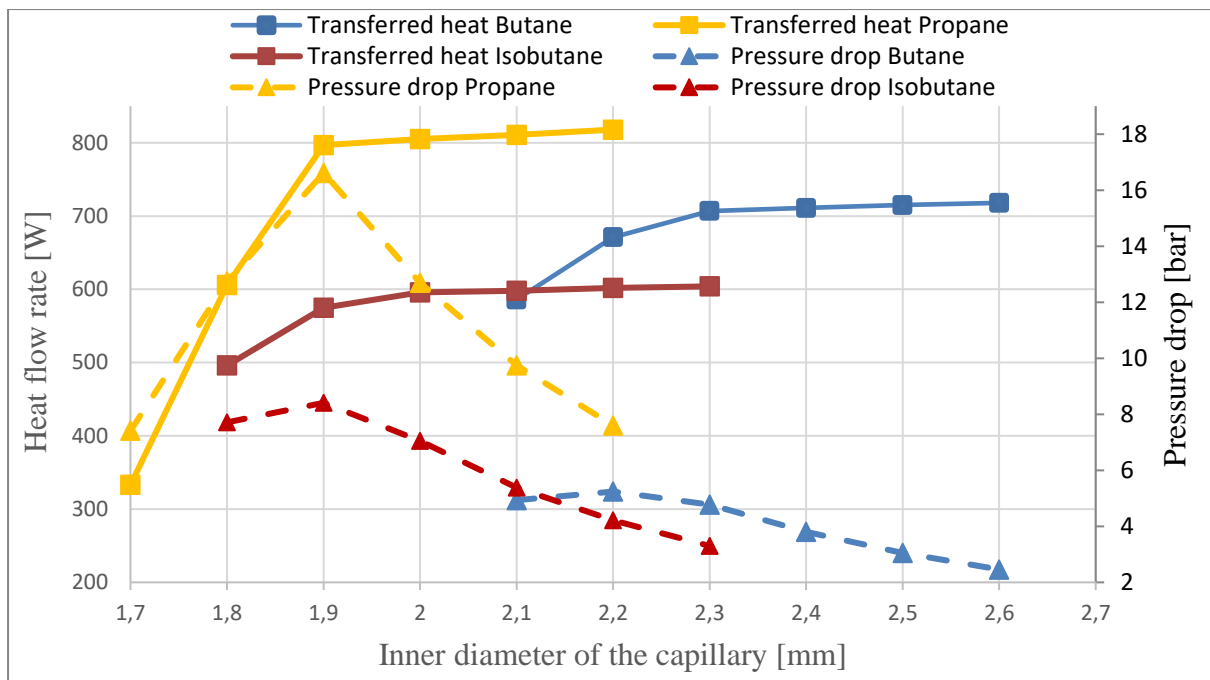


Figure 5: Comparison of the transferred heat and pressure losses as a function of the inner capillary diameter for 3 refrigerants

Table 3: Calculations of different inner diameters in the capillary for isobutane

Inner Diameter (di) of the capillary	1.8 mm	1.9 mm	2.0 mm	2.1 mm	2.2 mm	2.3 mm
Pressure isobutane entry	11.59 bar					
Pressure isobutane exit	3.88 bar	3.18 bar	4.54 bar	6.21 bar	7.38 bar	8.29 bar
Length of the capillary	7.29 m	10.78 m	11.98 m	11.90 m	11.99 m	11.94 m
Speed isobutane exit	3.45 m/s	3.05 m/s	2.74 m/s	2.48 m/s	2.26 m/s	2.07 m/s
Temperature isobutane entry	68.0 °C					
Temperature isobutane exit	28.36 °C	21.53 °C	19.68 °C	19.47 °C	19.09 °C	18.89 °C
Mass flow of isobutane	4.8 g/s					
Mass flow of water	2.37 g/s	2.75 g/s	2.85 g/s	2.86 g/s	2.88 g/s	2.89 g/s
Heat flow rate transferred in capillary	496 W	575 W	596 W	598 W	602 W	604 W
Heat flow rate transferred in condenser	1458 W					
Compressor performance	454 W					

Table 4: Calculations of different inner diameters in the capillary for propane

Inner Diameter (di) of the capillary	1.7 mm	1.8 mm	1.9 mm	2.0 mm	2.1 mm	2.2 mm
Pressure propane entry	25.9 bar	25.9 bar	25.9 bar	25.9 bar	25.9 bar	25.9 bar
Pressure propane exit	18.49 bar	13.16 bar	9.28 bar	13.21 bar	16.15 bar	18.3 bar
Length of the capillary	2.71 m	6.56 m	11.79 m	11.91 m	11.95 m	11.98 m
Speed isobutane exit	5.9 m/s	4.95 m/s	4.28 m/s	3.85 m/s	3.48 m/s	3.16 m/s
Temperature propane entry	68.0 °C	68.0 °C	68.0 °C	68.0 °C	68.0 °C	68.0 °C
Temperature propane exit	51.33 °C	35.91 °C	24.4 °C	26.68 °C	23.15 °C	22.65 °C
Mass flow of propane	6 g/s	6 g/s	6 g/s	6 g/s	6 g/s	6 g/s
Mass flow of water	1.59 g/s	2.90 g/s	3.81 g/s	3.85 g/s	3.88 g/s	3.91 g/s
Heat flow rate transferred in capillary	333 W	606 W	797 W	805 W	811 W	818 W
Heat flow rate transferred in condenser	2142 W	2142 W	2142 W	2142 W	2142 W	2142 W
Compressor performance	781 W	781 W	781 W	781 W	781 W	781 W

For all refrigerants the pressure drop rises until the maximum length is reached at a certain diameter. The transmitted heat has its highest increase up to this point and increases only slightly with larger inner diameters. For larger diameters the tube length remains at the maximum and pressure drop and fluid velocity get smaller. The calculations show that higher pressure levels always require capillaries of smaller diameters. This is only applicable if the other parameters are kept constant. For these refrigerants subcooling of about 1 K is reached after the capillary. The operating point of the compressor remains the same because the capillary has nearly the same output parameters like the throttle. The additional transferred heat at the highest pressure drop of Figure 5 is taken to calculate the new *COP* according to (3). The relative change in *COP* is shown together with the COPs in Figure 6. It is seen that a remarkable improvement of up to 40 % is possible, when the exergy in the fluid leaving the condenser is further used.

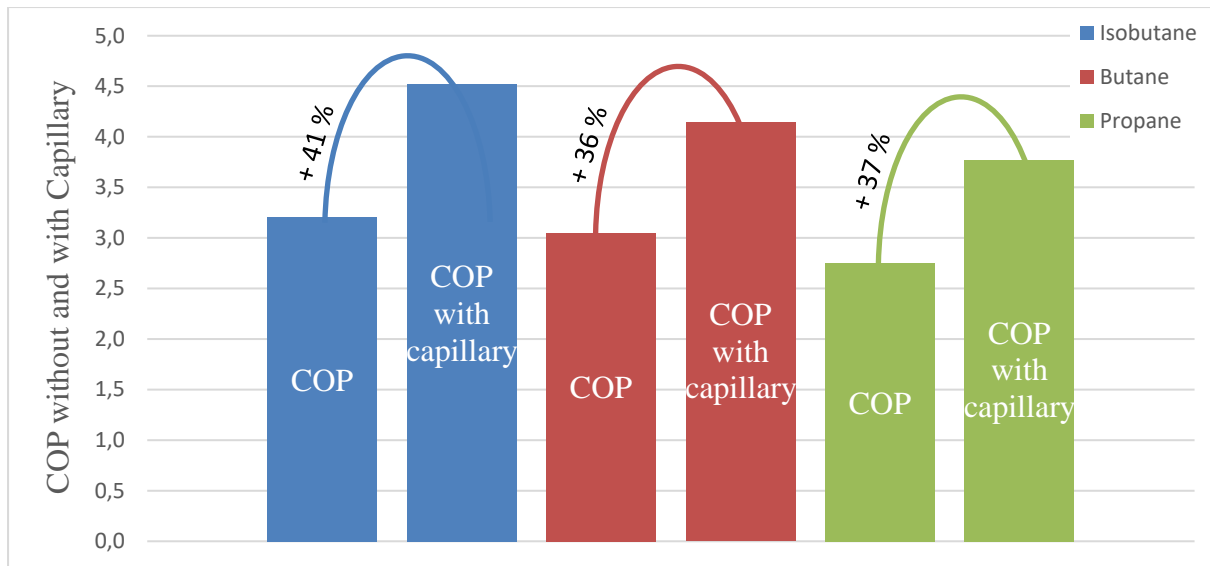


Figure 6: Measured COP without capillary and calculated COP with capillary

Conclusions

An approach to improve the COP of compression heat pumps was investigated in order to use the exergy available in the fluid leaving the condenser. Since a pressure drop is generally accepted by using a throttle, a capillary heat exchanger can be used with a similar pressure drop, leading to high fluid velocities and high convection coefficients. The pressure drop in such a capillary does not lead to additional losses, while the temperature level of the fluid is used for heating. The remaining part of the heat pump remains unchanged. The temperature, pressure and velocity curves within the capillary were calculated for three fluids. A lower limit for the capillary diameter is given due to fluid evaporation, which has to be avoided. For larger diameters, it turns out that when only a maximum capillary length is acceptable, that the diameter should be selected such that a maximum acceptable pressure drop in the cycle is reached, in accordance with the pressure level of the evaporator.

The comparison of the additionally transferred heat and pressure losses for three natural refrigerants show that such a process is quite favorable. The additional heat transfer from the refrigerant without additional power consumption of the compressor causes an increase of the COP by more than 27%. This shows the potential for the use of capillaries as heat exchangers. The calculated heat transfer and pressure drops were calculated using standard correlations, often having error margins of 15-30%, thus the results have to be validated experimentally.

References

- [1] Statista, Anteil der Wärmepumpen im Neubau in Deutschland bis 2019 | Statista, [May 13, 2021], <https://de.statista.com/statistik/daten/studie/237364/umfrage/bedeutung-der-waermepumpen-im-neubau-in-deutschland/>.
- [2] E.A. Heath, Amendment to the Montreal Protocol on Substances that Deplete the Ozone Layer (Kigali Amendment), *Int. leg. mater.* 56 (2017) 193–205.
- [3] B. Zühlsdorf, J.K. Jensen, S. Cignitti, C. Madsen, B. Elmegaard, Analysis of temperature glide matching of heat pumps with zeotropic working fluid mixtures for different temperature glides, *Energy* 153 (2018) 650–660.
- [4] E. Hervás-Blasco, E. Navarro-Peris, F. Barceló-Ruescas, J.M. Corberán, Improved water to water heat pump design for low-temperature waste heat recovery based on subcooling control, *International Journal of Refrigeration* 106 (2019) 374–383.
- [5] E. Hervas-Blasco, M. Pitarch, E. Navarro-Peris, J.M. Corberán, Study of different subcooling control strategies in order to enhance the performance of a heat pump, *International Journal of Refrigeration* 88 (2018) 324–336.
- [6] M. Pitarch, E. Navarro-Peris, J. González-Maciá, J.M. Corberán, Experimental study of a subcritical heat pump booster for sanitary hot water production using a subcooler in order to enhance the efficiency of the system with a natural refrigerant (R290), *International Journal of Refrigeration* 73 (2017) 226–234.
- [7] I.H. Bell, J. Wronski, S. Quoilin, V. Lemort, Pure and Pseudo-pure Fluid Thermophysical Property Evaluation and the Open-Source Thermophysical Property Library CoolProp, *Industrial & engineering chemistry research* 53 (2014) 2498–2508.
- [8] M. Pitarch, E. Hervas-Blasco, E. Navarro-Peris, J. González-Maciá, J.M. Corberán, Evaluation of optimal subcooling in subcritical heat pump systems, *International Journal of Refrigeration* 78 (2017) 18–31.
- [9] K. Stephan, Wärmeübergang bei turbulenter und bei laminarer Strömung in Ringspalten, *Chemie Ingenieur Technik* 34 (1962) 207–212.
- [10] V. Gnielinski, Corrigendum to “On heat transfer in tubes” [*International Journal of Heat and Mass Transfer* 63 (2013) 134–140], *International Journal of Heat and Mass Transfer* 81 (2015) 638.
- [11] V. Gnielinski, On heat transfer in tubes, *International Journal of Heat and Mass Transfer* 63 (2013) 134–140.
- [12] P. Stephan, S. Kabelac, M. Kind, D. Mewes, K. Schaber, T. Wetzel, *VDI-Wärmeatlas*, Springer Berlin Heidelberg, Berlin, Heidelberg, 2019.
- [13] V. Venzik, Experimentelle Untersuchung des Fluideinflusses auf die Thermodynamik der Wärmepumpe: Kohlenwasserstoffe und deren Gemische, 2019.

Predictive maintenance in thermal power plants: a systematic literature survey

M. Preißinger^{1,2*}

¹illwerke vkw Endowed Professorship for Energy Efficiency, Research Center Energy,
Vorarlberg University of Applied Sciences, Hochschulstraße 1, 6850 Dornbirn, Austria

²Josef Ressel Centre for Intelligent Thermal Energy Systems,
Vorarlberg University of Applied Sciences, Hochschulstraße 1, 6850 Dornbirn, Austria

*Corresponding author: markus.preissinger@fhv.at

Abstract

The main goals of power plant operators are high availability and high profitability. Absolute run time and performance thus have to be maximized. One crucial aspect is the choice of proper maintenance strategies. In a systematic literature survey, we analyse recent achievements for predictive and condition-based maintenance strategies. We describe our research questions, our search strategy as well as inclusion, exclusion and quality criteria. Altogether, we intend to identify research trends as well as gaps for predictive maintenance in thermal power plants.

Keywords: predictive maintenance, power plant, thermal, systematic review, intelligent thermal energy system.

Introduction

Profitability of power plants depends on the chosen maintenance strategy. May it be possible for plant operators to focus for some components on corrective maintenance taking place after a failure occurs, preventive and time-based maintenance that take place before a failure occurs are preferred. The advantages of predictive maintenance were already addressed clearly in the nineties by Fresco and Subudhi [1] who claimed that “*preventive and predictive maintenance programs, including failure trending and root cause analysis, together with the development of an integrated maintenance database, can significantly improve the management of ageing degradation and the safety of nuclear plant operations*”.

Despite the clear advantage, computational power probably prevented a widespread use of predictive maintenance. Increased digitization in the last two decades now enables predictive and condition-based maintenance for whole subsystems in the power plant and not only for single components. In this case, multimodal approaches have to be developed. Figure 1 shows that predictive maintenance is even possible without proper modeling of the system itself, although high-quality models in the background still lead to higher quality of the maintenance approach [2].

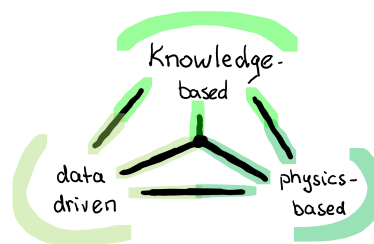


Figure 1. Methods for predictive maintenance adapted from Montero Jimenez et al. [3]

Our goal is to perform a systematic literature review on predictive maintenance in thermal power plants to identify research trends as well as gaps in literature. The literature survey follows the approach of Kitchenham [4].

Methods

The following planning protocol is considered:

Research questions

- Q1: Is predictive maintenance applied in thermal power plants for single components or for whole subsystems?
- Q2: Are physics-based, knowledge-based or data-driven approaches applied or are even multimodal approaches applied?
- Q3: Is the data used from real power plants or is it synthetic data?
- Q4: Do real implementations in thermal power plants exist?

Databases used

Research articles and reviews are searched in two common databases: Web of Science and ScienceDirect. IEEE Xplore is excluded cause the publications cover mostly electric systems.

Exclusion criteria

- EC1: Work that does not address predictive maintenance methodically.
- EC2: Work that is not related to thermal systems.
- EC3: Organisational aspects (paper not available anymore, etc.).

Quality criteria

- QC1: Publications that are based on real power plant data.
- QC2: Publications that address whole subsystems instead of just single components.
- QC3: Publications that apply a multimodal approach.

Execution

The literature survey is executed on November 5th, 2020 by searching for commonly used terms in title (TI), abstract (AB) and author specified keywords (AK):

- Web of Science: (TI OR AB OR AK)=(predictive AND maintenance AND “power plant”)
- ScienceDirect: title-abstr-key(“predictive”AND “maintenance”AND “power plant”)

Results and Discussion

Quantitative Analysis

The survey led to 134 publications in Web of Science and 72 publications in ScienceDirect. Removing duplicates, a total of 195 publications are identified. A first analysis shows that 130 publications have to be excluded based on the exclusion criteria defined in the methods chapter.

According to Figure 2, 105 papers are excluded as they do not cover predictive maintenance methodically (EC1). Some typical topics that are found during the initial search but excluded based on EC1 are: papers that cover predictive control but not predictive maintenance (e.g. [5, 6, 7]); papers describing pure online monitoring systems (e.g. [8, 9]); papers that deal with human errors during plant operation (e.g. [10, 11, 12]); papers that focus on sensors only (e.g. [13, 14]); papers with pure failure analysis without linkage to predictive maintenance (e.g. [15]); and papers that just explain the idea of expert systems [16]. The main reason why

those paper were found by the search strategy is that predictive maintenance is mentioned as challenge in the abstract/introduction or as future work in the conclusion. Concerning exclusion criteria 2 (no thermal energy system), the excluded papers are mainly related to renewable energies like PV systems (e.g. [17, 18, 19]). The only paper that is excluded based on exclusion criteria 3 is the paper of Piety and Pardue [20] as it just describes a commercial computer-based system for predictive maintenance but is not a scientific contribution.

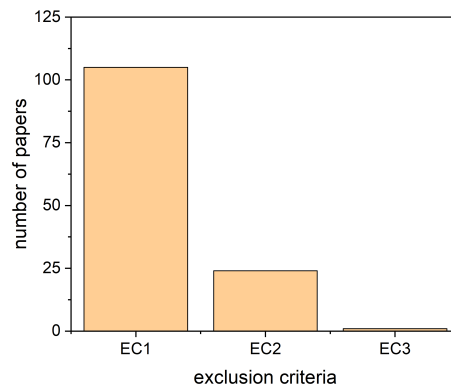


Figure 2. Number of publications excluded based on the three exclusion criteria applied

Hence the survey leads to 65 papers that has to be included in the systematic review. Table 1 summarizes all papers investigated including the answers to the relevant research questions. A list of excluded papers is found in Appendix A.

Table 1. Included papers sorted alphabetically on 1st author

Paper	RQ 1	RQ 2	RQ 3	RQ 4	full paper
Ajah et al. [21]	subsystem	DD	real	?	yes
Alamaniotis et al. [22]	subsystem	MM (KB/DD)	real	no	yes
Anghel [23]	single comp.	MM (KB/DD)	?	?	no
Anonymous [24]	?	?	real	yes	no
Atlason et al. [25]	single comp.	DD	real	no	yes
Auge et al. [26]	single comp.	MM (KB/DD/PB)	real	yes	yes
Ayodeji and Liu [27]	single comp.	MM (PB/DD)	real	?	yes
Barbero et al. [28]	single comp.	MM (PB/DD)	synthetic	no	yes
Basseville et al. [29]	subsystem	MM (KB/DD/PB)	real	no	yes
Bogard et al. [30]	single comp.	?	real	yes	no
Carneiro et al. [31]	single comp.	DD	real	no	yes
Choi et al. [32]	single comp.	DD	real	?	yes
Civerchia et al. [33]	subsystem	DD	real	yes	yes
Cooper [34]	?	?	?	?	no
David and Mercusot [35]	single comp.	DD	real	yes	no
Deliang et al. [36]	single comp.	DD	real	no	no
Fallbright and David [37]	single comp.	DD	real	?	yes
Hang-Rung and Ten-Der [38]	single comp.	MM (PB/DD)	real	?	no
Hashemian [39]	single comp.	?	real	?	no
Hashemian and Bean [40]	single comp.	MM (KB/DD)	real	?	yes
Hashemian [41]	single comp.	DD	real	no	yes
Hashemian [42]	subsystem	DD	real	no	yes
Hastings [43]	?	?	real	yes	no
Hui et al. [44]	single comp.	MM (KB/DD)	real	yes	no
Humphreys [45]	single comp.	DD	real	yes	no

Table 1. Included papers sorted alphabetically on 1st author - continued -

Paper	RC 1	RC 2	RC 3	RC 4	full paper
Ji-wei et al. [46]	single comp.	MM (KB/DD)	real	?	no
Kerastas and Leah [47]	single comp.	?	real	yes	no
Khalaquzzaman et al. [48]	subsystem	KB	real	?	yes
Kiaee and Tousi [49]	subsystem	MM (KB/DD)	real	?	yes
Kingston [50]	single comp.	?	real	yes	no
Klaer and Burch [51]	single comp.	MM (PB/DD)	real	yes	yes
Koprinkova-Hristova et al. [52]	single comp.	DD	real	no	yes
Lin et al. [53]	single comp.	?	real	yes	no
Lin and Holbert [54]	single comp.	MM (PB/DD)	real	no	yes
Liu and Zio [55]	single comp.	DD	real	no	yes
Lu and Jiang [56]	subsystem	PB	synthetic	no	yes
Lv et al. [57]	single comp.	DD	real	no	yes
Mackey and Fenner [58]	single comp.	DD	real	yes	no
Martorell et al. [59]	single comp.	MM (KB/DD)	real	no	yes
Mathews et al. [60]	subsystem	MM (PB/DD)	real	no	yes
Matusheski [61]	?	?	?	?	no
McCorkell and D'Isidoro [62]	subsystem	MM (PB/DD)	?	?	no
McElroy and Fruchtman [63]	single comp.	DD	?	?	no
Medina-Oliva et al. [64]	subsystem	KB	real	?	yes
Mo et al. [65]	subsystem	MM (KB/DD/PB)	real	no	yes
Naumov et al. [66]	subsystem	DD	real	yes	yes
Nwobi-Okoye and Igboanugo [67]	subsystem	DD	real	no	yes
Olano et al. [68]	single comp.	MM (PB/DD)	real	yes	yes
Oluwasegun and Jung [69]	single comp.	DD	real	no	yes
Petherus et al. [70]	single comp.	DD	real	no	yes
Petre-Lazar et al. [71]	single comp.	MM (PB/DD)	real	?	no
Pugh and Huff [72]	single comp.	KB	real	yes	yes
Ramakrishna [73]	single comp.	?	?	?	no
Rebenstorf [74]	single comp.	DD	real	yes	yes
Remy et al. [75]	single comp.	MM (PB/DD)	real	no	yes
Sharma [76]	?	?	?	?	no
Shugars and Scheibel [77]	single comp.	(MM (PB/DD)	real	no	no
Teshima et al. [78]	single comp.	?	real	yes	no
Tsoutsanis et al. [79]	subsystem	MM (PB/DD)	real	?	yes
Tsoutsanis et al. [80]	subsystem	MM (PB/DD)	real	?	yes
van Niekerk et al. [81]	single comp.	DD	real	no	yes
Verda [82]	subsystem	MM (PB/DD)	real	no	yes
Wilson and Fraey [83]	single comp.	PB	synthetic	no	yes
Yam et al. [84]	single comp.	DD	real	no	yes
Zhang et al. [85]	subsystem	MM (KB/DD)	real	no	yes

For 24 out of these 65 papers, only the abstract is available. This happens especially for papers published before 2000 (15 out of 20). For papers published from 2000 onward only 9 out of 45 papers just have an abstract online. Generally, the number of papers increases since the 70s gradually but not exponentially as in other research fields. An overview on availability and volume is given in Figure 3 and Figure 4.

In a next step, the remaining 65 papers are classified according to the four research questions. Figures 5-8 lead to the following quantitative conclusions:

- The majority of papers deal with single components (43) instead of subsystems (17), whereas for a minority the specific application remains undefined (5).
- A pure data driven approach (22) is more likely than a pure knowledge-based (3) or a pure physics-based approach (2).

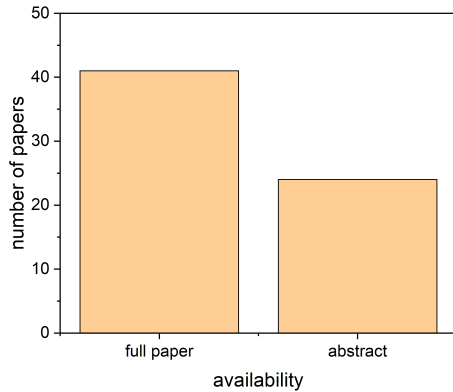


Figure 3. Availability of abstracts and full papers of the 65 papers included

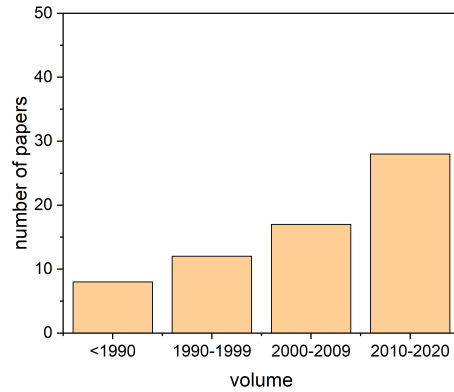


Figure 4. Volume of the 65 papers included

- Multimodal approaches always include a data-driven approach, either in combination with a physics-based approach (15) or with a knowledge-based approach (7).
- Only 3 papers include a data-driven, knowledge-based and physics-based approach.
- The majority of papers use real data (55), synthetic data does not play a role in research (only 3 papers).
- Only 18 papers report a first implementation in a real system. For 26 papers, results are drawn without implementation, for 21 papers this research question remains unanswered.

This first quantitative analysis clearly shows a lack of knowledge concerning implemented multimodal approaches. To narrow the focus of further research, the quality criteria are analysed separately and in combination. According to Figure 9, 15 papers investigate real data and a subsystem, whereas only 2 of the 15 report an implementation. The combination of real data and a multimodal approach leads to 22 paper including 4 papers with an implementation. Investigation of a subsystem and a multimodal whereas the data type is synthetic or unclear account for 9 papers without any including an implementation. Lastly, 8 papers fulfill all three quality criteria, however, none of these papers report an implementation.

To summarize the results of Figure 9, the following shortcomings are identified in the literature:

1. Available methods are hardly implemented in real power plants, especially if multimodal approaches are reported.
2. Analysis subsystems based on multimodal approaches seems to be challenging and is not covered enough in the scientific field.

Qualitative Analysis

Motivation for predictive maintenance

The early days of predictive maintenance end of the seventies beginning of the eighties are connected to the nuclear industry. Their main motivation were regulatory organizations that forced plant operators to reduce costs and, therefore, the electricity price for end users [62]. The change in plant operation from merit to baseload after necessary refurbishments was also a driver of predictive maintenance [34]. Even in this time, artificial intelligence (AI) was already mentioned [30] although progress in computing systems was just about to start. In the late nineties, a similar effect concerning regulatory aspects occurred: the deregulation of the electricity market. Again, plant operators were forced to reduce their costs, this time not from the

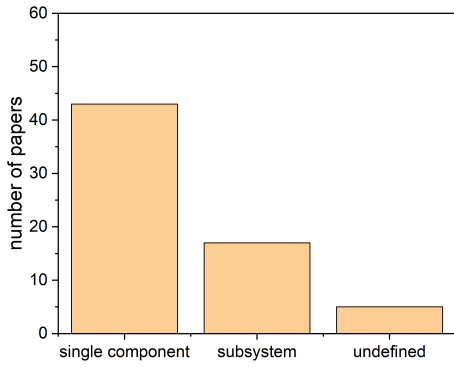


Figure 5. Share of papers for research question 1

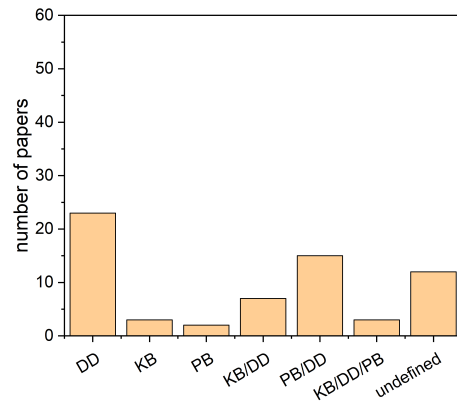


Figure 6. Share of papers for research question 2

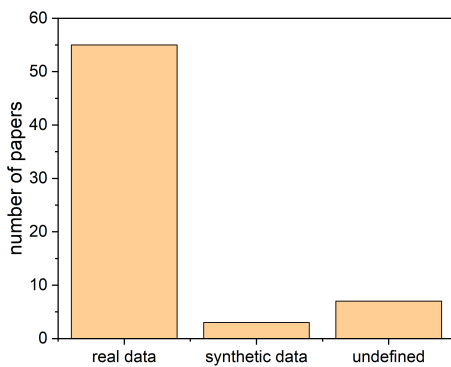


Figure 7. Share of papers for research question 3

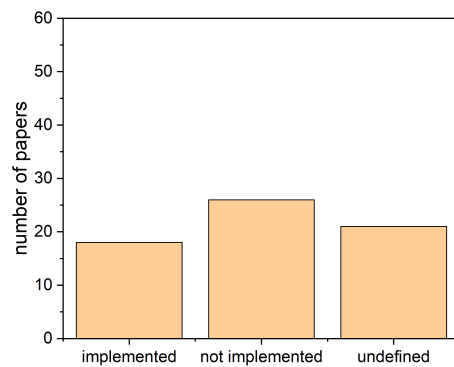


Figure 8. Share of papers for research question 4

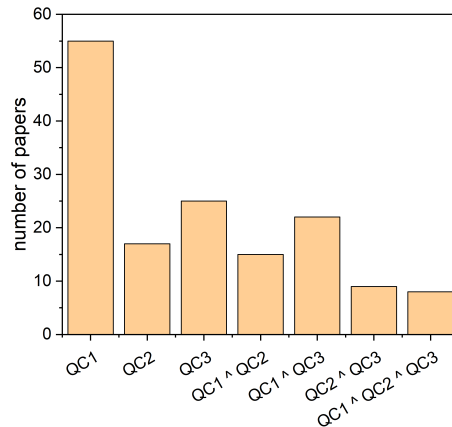


Figure 9. Number of papers for each quality criteria separately and in combination

regulatory organizations but from the market itself and predictive maintenance was a promising option again [61]. In the last several years, also coal fired power plants (e.g. [60]), gas fired power plants (e.g. [79, 80]), micro-gas turbines (e.g. [49]) and solar thermal power plants (e.g. [68]) are reported as case studies for predictive maintenance. However, as the quantitative analysis showed, a widespread utilization is still not achieved.

Papers that fulfill all quality criteria

The eight papers that fulfill all three quality criteria are summarized subsequently and chronically sorted from the beginning of this research field to the present.

Basseville et al. [29] focus on statistical methods for fault detection and diagnosis, but they set this data-driven approach in relation to expert knowledge and physical modeling. They provide a general approach to monitoring condition-based maintenance in which they always focus on a “signature” first. A signature in their sense means a “*parametric characterization of the plant, should it be a model or a network, based on the physics or not*”. Their main goal is to detect and evaluate slight deviations from the original signature. To do so, they cover four steps.

1. By learning from data recorded during normal operation, they intend to come up with an in site identification of the signature.
2. In the detection step new data is compared to the original signature and it has to be decided if the original signature still describes the new data conveniently.
3. In a next step, insufficiently described behaviour can be isolated as a failure based on the data, the models, and the expert knowledge.
4. Based on the results, it is possible to optimize sensor location if necessary and design a holistic monitoring system.

The four steps are applied on two examples: 1) Vibration monitoring of turbo-alternators and 2) Monitoring system for the combustion of gas turbines. The authors conclude that a pure data-driven approach is not purposeful as a crucial aspect is the decision, if a discrepancy between two signatures is significant. This can only be answered by a physical/black-box model or by expert knowledge. A combination of all three approaches seems to be promising for early warning and isolation of small faults.

Verda [82] investigates a prognosis procedure for a gas turbine in combination with a heat recovery system. Although the method is basically intended to allow for a calculation of performance degradation based on fuel impact, it is relevant for predictive maintenance as well as a main step of the method is anomaly detection. A simplified thermodynamic model that related products and resources for each component is combined with real measurement data.

Tsoutsanis et al. [79] model an engine including compressor, turbine and power turbine in Matlab/Simulink with a validation via PROOSIS. The foundation of their research are compressor performance map data which are fitted by elliptical curves and later on implemented in the dynamic model of the gas turbine. Maintenance issues come into place by diagnosing compressor fouling using transient data. Within the paper, steady-state, transient and degraded operating conditions are analysed and it is presented how the injection of degradation into the performance analysis can help to transform a performance model to a diagnostics model. It is noteworthy that the initial coefficients for the elliptical curves can be set without expert knowledge, so the model described is a combination of physical modeling and a data-driven approach. To sum up, the paper gives a valuable insight into a tool for improved conditions monitoring and diagnostics with the use case of gas turbine power plants.

Tsoutsanis et al. [80] also deal with the detection and forecasting of compressor fouling and turbine erosion in a follow-up paper. The authors once again use a combination of a physics-based and a data-driven approach. They extend their former work [79] by a calculation of the remaining useful lifetime (RUL) and use the method of sliding windows to evaluate performance in certain time periods. Quantitatively, they can estimate the RUL for a one-month prediction window with a relative error of less than 10 % for two different prediction models. To calculate the fuel impact with different anomalies, two different approaches are

presented. In one approach, the reference condition is set as initial point, in the other approach, the operating conditions are set as initial conditions (“*backward procedure*”). This approach as well can be applied without expert knowledge as it is based on a physics-based and a data-driven approach.

Zhang et al. [85] use a knowledge-based and data-driven approach and apply it to a subsystem in a coal fired power plant. Compared to the other papers presented, they focus on time-lagged correlations that are very promising in the context of thermal and, therefore, often sluggish systems. To come up with a predictive maintenance model, the authors start with the original sensor data stream. In a next step, curve regression is realized via k-means clustering or G-SEM-based curve registration. The results lead to PCA (principal component analysis) feature extraction which finally gives effective features and failure recorders. They analyzed a data set with sampling rate of 1/3 minutes and an overall period of roughly 1.5 years (July 2014 to January 2016). With their approach the authors manage to overcome some challenges of high-dimensional data and time-lagged correlation and present a method how to reduce training time of predictive maintenance assuring at the same time a high accuracy of the prediction.

Mo et al. [65] deal with the influence of the control units during or after degradation of subsystems on the efficiency of large gas turbine. In a first part, authors focus on the degradation models that focus on the control system and the component degradation path. In a next step, meta-heuristic algorithms are applied to find the optimal maintenance strategy. Here, a strong connection to cost analysis via Monte Carlo simulation is available. The optimization step is based on a combination of genetic algorithms and the simulated annealing. The ultimate goal of the work is a guide for practitioners that combines the data- and physics-driven approach with some expert knowledge to come up with a maintenance strategy that includes deterioration effects. Finally, the authors state that their approach can be adapted to many other engineering fields like wind farms or industry.

Mathews et al. [60] deal with maintenance issues of the condenser subsystem in a coal fired power plant based on a semi-empirical thermohydraulic model that is calibrated with actual data. A crucial aspect of this paper is the integration of the subsystem condenser into the framework of the whole power plant so that interactions can be identified. E.g. the influence of condenser fouling on maintenance aspects and on the efficiency of the power plant are investigated. To do so, simplifications have to be made to keep the system manageable: the boiler and the condenser are modeled as single components although many boilers and many cooling towers are operated in the power plant. However, simplification is justified based on expert knowledge. As the integrated simulation relies on the model itself, the authors ensured a thorough verification of the model based on real data. The model can then be used in combination with expert knowledge for decision-making or scenario investigations. The concept itself can be applied to other subsystems of thermal power plants or to evaluate any change to any component.

Kiaee and Tousi [49] present a holistic framework for the modeling of gas path prognostics and integrate aging modeling and fault modeling. Their main contribution is a vector-based deterioration index. This index describes the relationship between the performance parameters of every single component with different fault models and physical age. Hence, the approach is based on physical modeling, whereas measured data is used to feed these models. With expert knowledge it is then possible to assess degradation holistically and deduce time periods for maintenance issues. The model was tested in the framework of a 100 kW micro-turbine. In a first compressor degradation model it was shown that some degradation mechanism even lead to higher efficiency but to a decrease in lifetime. Both is caused by the higher temperature

due to the degradation of the compressor. This shows the necessity of analysing subsystems instead of single components in thermal power plants as a lot of interconnections between the components exist. For a certain compressor fouling mode the authors analysed the time span between maintenance measures and concluded that maintenance and inspection requirements are far higher if the deterioration of single components are integrated in an overall analysis of the subsystem.

Papers that fulfill two quality criteria with an implementation

As mentioned already, none of these eight papers has an implementation in a thermal power plant. Therefore, the four papers that are multimodal with real data including an implementation are investigated shortly with a focus on the implementation part.

Auge et al. [26] presented an optimization of the maintenance strategy of a nuclear reactor cooling piping system. They focus on the ageing of materials and structures as they are identified as a main thread for seaside nuclear power plants. Hence, they implemented different monitoring systems and analysed the data in the software SIMEO Manager™.

Their main conclusion with respect to the client gives three aspects:

1. potential economical gain of several million euros
2. extended life cycle of infrastructure
3. no negative influence on safety level

Klaer and Burch [51] give a rough overview on the implementation of supersonic flow meters for the detection of condenser fouling to avoid tube sheets plug up. The system was successfully tested in two coal fired power plants with a power of more than 700 MW and low RPM GMP pumps. With their system, the customer Kansas City Power & Light Company was able to switch the maintenance strategy from preventive maintenance (time scheduled) to predictive maintenance (specific need).

Hui et al. [44] report an implementation of a predictive maintenance system in a power plant in Tianjin, China. The remarkable aspect of this publication is the fact that it integrates on-site data management with remote expert diagnosis. Details on the implementation cannot be give as only the abstract is available.

Olano et al. [68] report an inspection system for a solar thermal power plant in Spain. The system measures the temperature of the receiver tube glass surface by infrared thermography. The system allows to inspect the complete solar field for the 50 MW power plant in about four days. Their software combines configuration parameters (like plant, solar field, tube, etc.) with inputs (like IR video, meteorological parameters, etc.). After processing they compare the results with historical data resulting in alerts and an improved O&M strategy. They conclude that with periodic inspections, predictive maintenance is possible based on the reported system.

Some other implementation are reported for the nuclear industry [24, 26, 30, 35, 43, 45, 58, 72], however, mostly only abstracts are available. This is probably do to the high security measures for data and results from nuclear industry.

Critical remarks on the selection of final papers

It is noteworthy to mention, that a certain bias might have influenced the selection of the paper due to the fact that for some paper only the abstract is available. For publications with the full paper available, it happened that the abstract sounded promising but the paper had to be excluded based on the exclusion criteria. Vice versa it was possible that a promising abstract for which the full paper was not available was still included in the 65 publications. One example

is the publication of McElroy et. al [63] who use the phrase “*power plant*” in the abstract but “*electric devices*” are also mentioned. Therefore, it was hard to decide whether to take the publication into the final selection or not. Another example McCorkell et al. [62] who writes about predictive maintenance but it remains unclear whether the paper is dealing with this topic methodical or not. The mentioned three phases are an indicator for “yes” but without the full paper it is not possible to be 100 % sure. Also the paper of Matusheski [61] is a critical case as the research questions can not be answered based on the abstract, however a “*practical guide*” to predictive maintenance is promised in the abstract. The even bigger challenge is to distinguish between a pure data-driven approach or a physical model in the background (especially for vibration analysis, e.g. [47]). Therefore, papers with just the abstract available should be handled with care.

Summary and Conclusion

Predictive maintenance is a vital research field also for thermal power plants. In total, 195 publications are found with the applied search strategy, however, applying our exclusion criteria, only 65 papers are classified based on our research questions and quality criteria. It is obvious that the main driver of predictive maintenance was the nuclear industry. But although it was clearly stated in literature that the progress in predictive maintenance can make a huge improvement in reliability of power plants (see Fresco and Subudhi [1]), it got quiet for a long time. However, in the light of increasing computational power and decreasing costs, predictive maintenance is gaining interest in other thermal energy systems as well. The main, trends, gaps and necessities for further research are:

- In the advent of increasing computational power, pure data-driven approaches are applied more and more. However, multimodal approaches should be favoured to exploit the whole potential of predictive maintenance.
- Investigation of single components is easier to apply and also to implement but the investigation of subsystems are important in complex systems like thermal power plants.
- Approaches that are implemented in real power plants and also well documented are rare. Most implemented approaches are only rudimentarily described.
- Thermal power plants based on renewable energies should be covered in more detail. This includes e.g. solar thermal, geothermal or biomass fired power plants. Profitability of these power plants in future energy systems could be enhanced.
- The combination of online monitoring systems, expert knowledge applied as rule based systems and suitable methods from data sciences can be a promising future research field.

Last but not least, it seems that the framework conditions for the application of predictive maintenance in general and even for complex systems like thermal power plants are better than ever before. It can therefore be hoped that science and industry jointly turn the high potential of predictive maintenance into real applications.

Acknowledgement

The financial support by the Austrian Federal Ministry for Digital and Economic Affairs and the National Foundation for Research, Technology and Development and the Christian Doppler Research Association is gratefully acknowledged.

References

- [1] A. Fresco and M. Subudhi. Managing aging in nuclear power plants: insights from NRC's maintenance team inspection reports. *Nuclear Safety*, 35(1):142–9, June 1994.
- [2] Andrea Cortinovis, Mehmet Mercangöz, Tarun Mathur, Jan Poland, and Marcel Blauermann. Nonlinear coal mill modeling and its application to model predictive control. *Control Engineering Practice*, 21(3):308–320, March 2013.
- [3] Juan José Montero Jimenez, Sébastien Schwartz, Rob Vingerhoeds, Bernard Grabot, and Michel Salaün. Towards multi-model approaches to predictive maintenance: A systematic literature survey on diagnostics and prognostics. *Journal of Manufacturing Systems*, 56:539–557, July 2020.
- [4] Barbara Kitchenham. Procedures for Performing Systematic Reviews. Technical Report TR/SE-0401, Software Engineering Group, Department of Computer Science, Keele University, Keele, UK, July 2004.
- [5] E. G. Cojocar, J. M. Bravo, M. J. Vasallo, and D. Marin. A binary-regularization-based model predictive control applied to generation scheduling in concentrating solar power plants. *Optimal Control Applications and Methods*, 41(1):215–38, February 2020.
- [6] Uduakobong E. Ekpenyong, Jiangfeng Zhang, and Xiaohua Xia. An improved robust model for generator maintenance scheduling. *Electric Power Systems Research*, 92:29–36, November 2012.
- [7] M. V. Kothare, B. Mettler, M. Morari, P. Bendotti, and C.-M. Falinower. Linear parameter varying model predictive control for steam generator level control. *Computers & Chemical Engineering*, 21:S861–6, 1997.
- [8] H. M. Hashemian. Automated Maintenance Technology to be Embedded in Small Modular Reactor Designs. *Transactions of the American Nuclear Society*, 109(2):2265–8, 2013.
- [9] H. M. Hashemian. Integrated online condition monitoring system for nuclear power plants. *Kerntechnik*, 75(5):231–42, September 2010.
- [10] Jaewhan Kim, Jinkyun Park, Wondea Jung, and Ji Tae Kim. Characteristics of test and maintenance human errors leading to unplanned reactor trips in nuclear power plants. *Nuclear Engineering and Design*, 239(11):2530–2536, November 2009.
- [11] Jaewhan Kim and Jinkyun Park. Reduction of test and maintenance human errors by analyzing task characteristics and work conditions. *Progress in Nuclear Energy*, 58:89–99, July 2012.
- [12] Mahendra Prasad and A.J. Gaikwad. Human error probability estimation by coupling simulator data and deterministic analysis. *Progress in Nuclear Energy*, 81:22–29, May 2015.
- [13] J. T. Kim, S. H. Seong, C. K. Lee, S. Hur, N. Y. Lee, and S. J. Lee. Flow-accelerated corrosion monitoring through advanced sensors. *Proceedings of the SPIE - The International Society for Optical Engineering*, 5634(1):404–15, February 2005.
- [14] H. M. Hashemian, C. J. Kiger, G. W. Morton, and B. D. Shumaker. Wireless sensor applications in nuclear power plants. *Nuclear Technology*, 173(1):8–16, January 2011.
- [15] H. F. Martz and R. R. Picard. On comparing PRA results with operating experience. *Reliability Engineering & System Safety*, 59(2):187–99, February 1998.
- [16] F. Pons and B. Georgel. Ultrasonic and eddy current imaging: signal processing for defect visualization [nuclear power plants]. *Bulletin de la Direction des Etudes et Recherches, Serie A*, 3-4:19–28, 1985.
- [17] Patrick de Mars, Aidan O'Sullivan, and Ilkka Keppo. Estimating the impact of variable renewable energy on base-load cycling in the GB power system. *Energy*, 195:117041, March 2020.

- [18] Ravinesh C. Deo and Mehmet Şahin. Forecasting long-term global solar radiation with an ANN algorithm coupled with satellite-derived (MODIS) land surface temperature (LST) for regional locations in Queensland. *Renewable and Sustainable Energy Reviews*, 72:828–848, May 2017.
- [19] Ananda S. Vaka and Prabal Talukdar. Novel inverse heat transfer technique for estimation of properties and location-specific process parameters of roof-mounted solar PV plants. *Thermal Science and Engineering Progress*, 19:100657, October 2020.
- [20] K. R. Piety and E. F. Pardue. A new approach for implementing a computer-based predictive maintenance program. *IEEE Transactions on Nuclear Science*, NS-32(1):1005–6, February 1985.
- [21] A.N. Ajah, P.M. Herder, J. Grievink, and M.P.C. Weijnen. Hierarchical markov reliability / availability models for energy & industrial infrastructure systems conceptual design. In W. Marquardt and C. Pantelides, editors, *Computer Aided Chemical Engineering*, volume 21, pages 1753–1758. Elsevier, January 2006.
- [22] Miltiadis Alamaniotis, Austin Grelle, and Lefteri H. Tsoukalas. Regression to fuzziness method for estimation of remaining useful life in power plant components. *Mechanical Systems and Signal Processing*, 48(1):188–198, October 2014.
- [23] V. Anghel. Simulation for cavitations failures at predictive maintenance in Cryogenic nuclear plant. *WSEAS Transactions on Systems and Control*, 1(1):49–53, November 2006.
- [24] Anonymous. Recorders help avoid forced outages. *Electrical World*, 188(6):70–1, September 1977.
- [25] R.S. Atlason, O.P. Geirsson, A. Elisson, and R. Unnthorsson. Geothermal wellhead maintenance: A statistical model based on documented Icelandic experience. *Geothermics*, 53:147–153, January 2015.
- [26] L. Auge, B. Capra, M. Lasne, O. Bernard, P. Benefice, and R. Comby. Risk management and maintenance optimization of nuclear reactor cooling piping system. *Journal de Physique IV (Proceedings)*, 136:263–71, November 2006.
- [27] A. Ayodeji and Yong-kuo Liu. PWR heat exchanger tube defects: trends, signatures and diagnostic techniques. *Progress in Nuclear Energy*, 112:171–84, April 2019.
- [28] Javier Barbero, Juan Blázquez, and Oscar Vela. Bubbles in the sensing line of nuclear power plant pressure transmitters: the shift of spectrum resonances. *Nuclear Engineering and Design*, 199(3):327–334, July 2000.
- [29] M. Basseville, A. Benveniste, and Q. Zhang. Decision Versus Identification Issues in Fault Detection/Isolation for Predictive Maintenance. *IFAC Proceedings Volumes*, 27(8):1063–1068, July 1994.
- [30] W. T. Bogard, S. S. Palusamy, and W. Ciaramitaro. Apply automation to diagnostics, predictive maintenance in plants. *Power*, 132(5):27–32, May 1988.
- [31] A. L. G. Carneiro, A. A. da Silva, and A. B. R. Upadhyaya. Incipient fault detection of motor-operated valves using wavelet transform analysis. *Nuclear Engineering and Design*, 238(9):2453–9, September 2008.
- [32] Woosung Choi, Byeng D. Youn, Hyunseok Oh, and Nam H. Kim. A Bayesian approach for a damage growth model using sporadically measured and heterogeneous on-site data from a steam turbine. *Reliability Engineering & System Safety*, 184:137–150, April 2019.
- [33] Federico Civerchia, Stefano Bocchino, Claudio Salvadori, Enrico Rossi, Luca Maggiani, and Matteo Petracca. Industrial Internet of Things monitoring solution for advanced predictive maintenance applications. *Journal of Industrial Information Integration*, 7:4–12, September 2017.
- [34] P. Cooper. Predictive maintenance following power plant rehabilitation. *International Power Generation*, 9(5):15–17, June 1986.

- [35] J. David and M. Mercusot. Monitoring of rotating machines in a nuclear plant by vibratory techniques. *Revue Generale Nucleaire*, 1:27–30, February 1992.
- [36] Zeng Deliang, Liu Jiwei, Liu Jizhen, Liu Yu, and Xie Xie. Application of Wavelet Multi-scale Analysis for Wear Characteristics. *Proceedings of the CSEE*, 32(23):126–31, August 2012.
- [37] J. Fallbright and D. R. David. Predictive maintenance can prevent motor failures. *Power Engineering*, 101(10):46, 48, 53–4, October 1997.
- [38] Lin Hang-Rung and Jane Ten-Der. Applying weibull distribution to maintenance strategies for power plants. *Monthly Journal of Taipower's Engineering*, 728(98):9–20, April 2009.
- [39] H. M. Hashemian. On-line maintenance of nuclear plant I&C systems for operation beyond 40 and 60 years. *Transactions of the American Nuclear Society*, 100:493–4, 2009.
- [40] H. M. Hashemian and W. C. Bean. State-of-the-Art Predictive Maintenance Techniques*. *IEEE Transactions on Instrumentation and Measurement*, 60(10):3480–92, October 2011.
- [41] H.M. Hashemian. Wireless sensors for predictive maintenance of rotating equipment in research reactors. *Annals of Nuclear Energy*, 38(2):665–680, February 2011.
- [42] H.M. Hashemian. On-line monitoring applications in nuclear power plants. *Progress in Nuclear Energy*, 53(2):167–181, March 2011.
- [43] M. Hastings. Rising to the challenge [nuclear power plant maintenance]. *International Power Generation*, 19(1):21–2, January 1996.
- [44] Deng Hui, Wang Tai-yong, and Zhang Ying. Research of open condition monitor system based on predictive maintenance. *Computer Engineering and Applications*, 45(14):231–3, May 2009.
- [45] R. L. Humphreys. Life extension through predictive maintenance. *Transactions of the American Nuclear Society*, 49:329–30, 1985.
- [46] Liu Ji-wei, Zeng De-liang, Jiang Xin-jun, Yang Xiang-dong, and Liu Qian. Abstracting trend component of wear characteristics based on wavelet transform. *Journal of North China Electric Power University*, 38(2):37–42, March 2011.
- [47] J. Kerastas and R. Leah. Same data, more value: multivariate sensor signal monitoring. *Sensors*, 21(3):33–6, March 2004.
- [48] M. Khalazqzaman, Hyun Gook Kang, Man Cheol Kim, and Poong Hyun Seong. A model for estimation of reactor spurious shutdown rate considering maintenance human errors in reactor protection system of nuclear power plants. *Nuclear Engineering and Design*, 240(10):2963–2971, October 2010.
- [49] Mehrdad Kiaee and A.M. Tousi. Vector-Based Deterioration Index for Gas Turbine Gas-Path Prognostics Modeling Framework. *Energy*, page 119198, November 2020.
- [50] J. Kingston. Vibration monitoring raises Finnish efficiency. *Modern Power Systems*, 11(10):51–55, October 1991.
- [51] H. Klaer and T. Burch. A multiple path to ultrasonic optimization [multiple-path ultrasonic transit-time flowmeter]. *InTech*, 54(1):22–6, January 2007.
- [52] P. D. Koprinkova-Hristova, M. B. Hadjiski, L. A. Doukovska, and S. V. Belorehski. Recurrent Neural Networks for Predictive Maintenance of Mill Fan Systems. *Kwartalnik Elektoniki i Telekomunikacji*, 57(3):401–6, 2011.
- [53] J. Lin, K.-T. Tsai, and H. Lin. Predictive maintenance for the vibration of rotary machine in the Ta-Lin power plant. *Monthly Journal of Taipower's Engineering*, 598:1–7, June 1998.
- [54] Kang Lin and Keith E. Holbert. Blockage diagnostics for nuclear power plant pressure transmitter sensing lines. *Nuclear Engineering and Design*, 239(2):365–372, February 2009.

- [55] Jie Liu and E. Zio. SVM hyperparameters tuning for recursive multi-step-ahead prediction. *Neural Computing and Applications*, 28(12):3749–63, December 2017.
- [56] Lixuan Lu and Jin Jiang. Analysis of on-line maintenance strategies for -out-of-standby safety systems. *Reliability Engineering & System Safety*, 92(2):144–155, February 2007.
- [57] You Lv, Fang Fang, Tingting Yang, and Carlos E. Romero. An early fault detection method for induced draft fans based on MSET with informative memory matrix selection. *ISA Transactions*, 102:325–334, July 2020.
- [58] W. Mackey and R. Fenner. Vibration monitoring system enhances troubleshooting. *Power Engineering*, 103(9):41–2, 44, September 1999.
- [59] S. Martorell, A. Muñoz, and V. Serradell. An approach to integrating surveillance and maintenance tasks to prevent the dominant failure causes of critical components. *Reliability Engineering & System Safety*, 50(2):179–187, January 1995.
- [60] I. Mathews, E.H. Mathews, J.H. van Laar, W. Hamer, and M. Kleingeld. A simulation-based prediction model for coal-fired power plant condenser maintenance. *Applied Thermal Engineering*, 174:115294, June 2020.
- [61] R. L. Matusheski. Predicting success [power station maintenance]. *Power Engineering*, 101(2):26, 28–30, February 1997.
- [62] T. E. McCorkell and J. D. D’Isidoro. Engineered maintenance [nuclear reactors]. *Transactions of the American Nuclear Society*, 45:563–5, 1983.
- [63] A. J. McElroy and I. Fruchtman. Use statistical analysis to predict equipment reliability [in power stations]. *Power*, 135(10):39, 42, 45–6, October 1991.
- [64] Gabriela Medina-Oliva, Alexandre Voisin, Maxime Monnin, and Jean-Baptiste Leger. Predictive diagnosis based on a fleet-wide ontology approach. *Knowledge-Based Systems*, 68:40–57, September 2014.
- [65] Huadong Mo, Giovanni Sansavini, and Min Xie. Performance-based maintenance of gas turbines for reliable control of degraded power systems. *Mechanical Systems and Signal Processing*, 103:398–412, March 2018.
- [66] S. A. Naumov, A. V. Krymskii, M. A. Lipatov, and D. N. Skrabatun. Experience in Use of Remote Access and Predictive Analytics for Power Equipment’s Condition. *Therm. Eng.*, 65(4):189–199, April 2018.
- [67] Chidozie Chukwuemeka Nwobi-Okoye and Anthony Clement Igboanugo. Performance appraisal of gas based electric power generation system using transfer function modelling. *Ain Shams Engineering Journal*, 6(2):541–551, June 2015.
- [68] X. Olano, A. Garcia de Jalon, D. Perez, J. Garcia Barberena, J. Lopez, and M. Gaston. Outcomes and features of the inspection of receiver tubes (ITR) system for improved O&M in parabolic trough plants. *AIP Conference Proceedings*, 2033:030011 (9 pp.)–030011 (9 pp.), November 2018.
- [69] Adebena Oluwasegun and Jae-Cheon Jung. The application of machine learning for the Prognostics and Health Management of control element drive system. *Nuclear Engineering and Technology*, page S1738573319308654, May 2020.
- [70] V. Petherus, W. Nirbito, and H. Nurhantoko. Application of predictive maintenance technique with vibration monitoring method for analysis of damage trend and damage diagnosis at make up water pump on PLTGU installation. *AIP Conference Proceedings*, 2088:050003 (9 pp.)–050003 (9 pp.), March 2019.
- [71] Petre-Lazar, B. Sudret, F. Foct, L. Granger, and L. Dechaux. Service life estimation of the secondary containment with respect to rebar corrosion. *Journal de Physique IV (Proceedings)*, 136:201–12, November 2006.

- [72] R. Pugh and R. Huff. Transfer of infrared thermography predictive maintenance technologies to Soviet-designed nuclear power plants: experience at Chernobyl. *Proceedings of the SPIE - The International Society for Optical Engineering*, 3700:300–10, 1999.
- [73] K. Ramakrishna. Development of computerized on-line vibration monitoring, analysis and assessment systems for power plant machinery. *International Journal of COMADEM*, 4(2):5–12, April 2001.
- [74] G. W. Rebenstorf. A Wireless Vibration Monitoring System. *Power Engineering*, 113(9):52, 54, 56–52, 54, 56, September 2009.
- [75] Emmanuel Remy, Franck Corset, Stéphane Despréaux, Laurent Doyen, and Olivier Gaudoin. An example of integrated approach to technical and economic optimization of maintenance. *Reliability Engineering & System Safety*, 116:8–19, August 2013.
- [76] H. C. Sharma. Computer aided maintenance management system of large thermal power plants. *Indian Journal of Power and River Valley Development*, 40(12):460–7, December 1990.
- [77] H. G. Shugars and J. R. Scheibel. On-line vibration monitoring of turbines, pumps and fans: recent results of research. *Transactions of the American Nuclear Society*, 46(1):30–1, 1984.
- [78] H. Teshima, T. Koizumi, T. Usami, T. Fujiyama, and R. Taniguchi. A monitoring system for roller bearings for rotary machines. *Mitsubishi Denki Giho*, 54(7):487–91, 1980.
- [79] Elias Tsoutsanis, Nader Meskin, Mohieddine Benammar, and Khashayar Khorasani. A component map tuning method for performance prediction and diagnostics of gas turbine compressors. *Applied Energy*, 135:572–585, December 2014.
- [80] Elias Tsoutsanis, Nader Meskin, Mohieddine Benammar, and Khashayar Khorasani. A dynamic prognosis scheme for flexible operation of gas turbines. *Applied Energy*, 164:686–701, February 2016.
- [81] J.L. van Niekerk, P.S. Heyns, M.P. Hindley, and C. Erasmus. Estimation of high energy steam piping degradation using hybrid recurrent neural networks. *International Journal of Pressure Vessels and Piping*, 186:104127, September 2020.
- [82] Vittorio Verda. Prediction of the fuel impact associated with performance degradation in power plants. *Energy*, 33(2):213–223, February 2008.
- [83] D.S. Wilson and J.L. Frarey. Automated machinery surveillance and diagnostics. *Progress in Nuclear Energy*, 1(2):723–733, January 1977.
- [84] R. C. M. Yam, P. W. Tse, L. Li, and P. Tu. Intelligent predictive decision support system for condition-based maintenance. *International Journal of Advanced Manufacturing Technology*, 17(5):383–91, 2001.
- [85] Shouli Zhang, Chen Liu, Shen Su, Yanbo Han, and XiaoHong Li. A feature extraction method for predictive maintenance with time-lagged correlation-based curve-registration model. *International Journal of Network Management*, 28(5):e2025 (15 pp.)–e2025 (15 pp.), October 2018.

Appendix A: List of excluded publications, sorted alphabetically on 1st author

- (1) P. Abbott, Optimizing power plant maintenance, *Power*. 148 (2004) 26, 28–30.
- (2) T. Aldemir, S. Guarro, D. Mandelli, J. Kirschenbaum, L.A. Mangan, P. Bucci, M. Yau, E. Ekici, D.W. Miller, X. Sun, S.A. Arndt, Probabilistic risk assessment modeling of digital instrumentation and control systems using two dynamic methodologies, *Reliability Engineering & System Safety*. 95 (2010) 1011–39.
- (3) A. Almasi, Power Plant Condition Monitoring, *Power Engineering*. 115 (2011) 7 pp.-7 pp.
- (4) V. Anghel, New conceptual method in maintenance with application in cryogenics pilot plant (CPP), *WSEAS Transactions on Environment and Development*. 2 (2006) 968–72.
- (5) S. Anvari, H. Taghavifar, R.K. Saray, S. Khalilarya, S. Jafarmadar, Implementation of ANN on CCHP system to predict trigeneration performance with consideration of various operative factors, *Energy Conversion and Management*. 101 (2015) 503–514.
- (6) N. Aretakis, I. Roumeliotis, G. Doumouras, K. Mathioudakis, Compressor washing economic analysis and optimization for power generation, *Applied Energy*. 95 (2012) 77–86.
- (7) W. Asvapoositkul, S. Treeutok, A simplified method on thermal performance capacity evaluation of counter flow cooling tower, *Applied Thermal Engineering*. 38 (2012) 160–167.
- (8) R.S. Atlason, R. Unnthorsson, G.V. Oddsson, Innovation and development in geothermal turbine maintenance based on Icelandic experience, *Geothermics*. 56 (2015) 72–78.
- (9) N.N. Aung, E. Crowe, X. Liu, Development of self-powered wireless high temperature electrochemical sensor for in situ corrosion monitoring of coal-fired power plant, *ISA Transactions*. 55 (2015) 188–194.
- (10) M. Basseville, A. Benveniste, B. Gach-Devauchelle, M. Goursat, D. Bonnacase, P. Dorey, M. Prevosto, M. Olagnon, In situ damage monitoring in vibration mechanics: diagnostics and predictive maintenance, *Mechanical Systems and Signal Processing*. 7 (1993) 401–423.
- (11) J.A. Becerra Villanueva, F. Jiménez Espadafor, F. Cruz-Peragón, M. Torres García, A methodology for cracks identification in large crankshafts, *Mechanical Systems and Signal Processing*. 25 (2011) 3168–3185.
- (12) A. Benato, A. Stoppato, S. Bracco, Combined cycle power plants: A comparison between two different dynamic models to evaluate transient behaviour and residual life, *Energy Conversion and Management*. 87 (2014) 1269–1280.
- (13) M. Bevilacqua, M. Braglia, The analytic hierarchy process applied to maintenance strategy selection, *Reliability Engineering & System Safety*. 70 (2000) 71–83.
- (14) J.E.T. Bistline, J.H. Merrick, Parameterizing open-source energy models: Statistical learning to estimate unknown power plant attributes, *Applied Energy*. 269 (2020) 114941.
- (15) J. Blaney, L. Tingley, Digital power (digital bus technology in power plant) , *InTech*. 55 (2008) 56–8, 60, 62.
- (16) C. Boccaletti, P. Di Felice, E. Santini, Integration of renewable power systems in an Antarctic Research Station, *Renewable Energy*. 62 (2014) 582–591.
- (17) S.Z. Boksteen, J.P. van Buijtenen, R. Pecnik, D. van der Vecht, Bayesian calibration of power plant models for accurate performance prediction, *Energy Conversion and Management*. 83 (2014) 314–324.
- (18) G. Bongioví, A. Häußler, Progresses in the structural assessment of the central region of a HELIAS 5-B breeding blanket half sector, *Fusion Engineering and Design*. 159 (2020) 111620.
- (19) S.M. Bragg-Sitton, J.P. Holloway, Autonomous reactor control using model based predictive control for space propulsion applications, *Annals of Nuclear Energy*. 33 (2006) 1368–1378.
- (20) Y. Cao, Y. He, H. Zheng, J. Yang, An alarm method for a Loose Parts Monitoring System, *Shock and Vibration*. 19 (2012) 753–61.
- (21) J. Cardoso, V. Silva, D. Eusébio, Techno-economic analysis of a biomass gasification power plant dealing with forestry residues blends for electricity production in Portugal, *Journal of Cleaner Production*. 212 (2019) 741–753.
- (22) A.F.A. Castanheira, J.F.P. Fernandes, P.J.C. Branco, Demonstration project of a cooling system for existing PV power plants in Portugal, *Applied Energy*. 211 (2018) 1297–1307.
- (23) K.H. Chan, E.J. Dozal-Mejorada, X. Cheng, R. Kephart, B.E. Ydstie, Predictive control with adaptive model maintenance: Application to power plants, *Computers & Chemical Engineering*. 70 (2014) 91–103.
- (24) A. Chockie, K. Bjorkelo, Effective maintenance practices to manage system aging, 1992.
- (25) F. Chuang, Y. Lu-qing, Y. Ren, L. Yong-qian, C. Mu-hua, Predictive maintenance for hydropower plant based on MAS and ANN, *Proceedings of the CSEE*. 25 (2005) 81–7.
- (26) M. Chun-xiao, Important parameters required in point inspection of equipment, *Electric Power*. 38 (2005) 90–2.
- (27) J.G. Clark, M.D. Fitzgerald, Thermographic applications for industrial/utilities predictive maintenance, *Proceedings of the SPIE - The International Society for Optical Engineering*. 581 (1986) 128–32.
- (28) E.G. Cojocar, J.M. Bravo, M.J. Vasallo, D. Marin, A binary-regularization-based model predictive control applied to generation scheduling in concentrating solar power plants, *Optimal Control Applications and Methods*.

41 (2020) 215–38.

- (29) A. Cortinovis, M. Mercangöz, T. Mathur, J. Poland, M. Blaumann, Nonlinear coal mill modeling and its application to model predictive control, *Control Engineering Practice*. 21 (2013) 308–320.
- (30) J. Cunningham, Future proof (predictive maintenance), *Professional Engineering*. 21 (2008) 40–40.
- (31) P. de Mars, A. O’Sullivan, I. Keppo, Estimating the impact of variable renewable energy on base-load cycling in the GB power system, *Energy*. 195 (2020) 117041.
- (32) R.N. De Mesquita, D.K.S. Ting, E.L.L. Cabral, B.R. Upadhyaya, Classification of steam generator tube defects for real-time applications using eddy current test data and self-organizing maps, *Real-Time Systems*. 27 (2004) 49–70.
- (33) R.C. Deo, M. Şahin, Forecasting long-term global solar radiation with an ANN algorithm coupled with satellite-derived (MODIS) land surface temperature (LST) for regional locations in Queensland, *Renewable and Sustainable Energy Reviews*. 72 (2017) 828–848.
- (34) V.S. Deshpande, J.P. Modak, Maintenance strategy for tilting table of rolling mill based on reliability considerations, *Reliability Engineering & System Safety*. 80 (2003) 1–18.
- (35) U.E. Ekpenyong, J. Zhang, X. Xia, An improved robust model for generator maintenance scheduling, *Electric Power Systems Research*. 92 (2012) 29–36.
- (36) G. Espinosa-Paredes, A. Nuñez-Carrera, A.L. Laureano-Cruces, A. Vázquez-Rodríguez, E.-G. Espinosa-Martinez, Emergency management for a nuclear power plant using fuzzy cognitive maps, *Annals of Nuclear Energy*. 35 (2008) 2387–2396.
- (37) A. Fresco, M. Subudhi, Managing aging in nuclear power plants: insights from NRC’s maintenance team inspection reports, *Nuclear Safety*. 35 (1994) 142–9.
- (38) D.A. Fynan, K.-I. Ahn, Implicit Treatment of Technical Specification and Thermal Hydraulic Parameter Uncertainties in Gaussian Process Model to Estimate Safety Margin, *Nuclear Engineering and Technology*. 48 (2016) 684–701.
- (39) E. Gallestey, A. Stothert, M. Antoine, S. Morton, Model predictive control and the optimization of power plant load while considering lifetime consumption, *IEEE Transactions on Power Systems*. 17 (2002) 186–91.
- (40) J.R. Gossner, P. Vyas, B. Kouvaritakis, A.W. Morris, Application of cautious stable predictive control to vertical positioning in COMPASS-D tokamak, *IEEE Transactions on Control Systems Technology*. 7 (1999) 580–7.
- (41) Y. Guo, S. Sheng, C. Phillips, J. Keller, P. Veers, L. Williams, A methodology for reliability assessment and prognosis of bearing axial cracking in wind turbine gearboxes, *Renewable and Sustainable Energy Reviews*. 127 (2020) 109888.
- (42) M. Hanel, R. Escobar, Influence of solar energy resource assessment uncertainty in the levelized electricity cost of concentrated solar power plants in Chile, *Renewable Energy*. 49 (2013) 96–100.
- (43) D. Harman, Wising up to get Smart, *Nuclear Engineering International*. 46 (2001) 32–3.
- (44) H.M. Hashemian, Research Reactor Reliability Improvement and Aging Management, *Transactions of the American Nuclear Society*. 101 (2009) 587–9.
- (45) H.M. Hashemian, Integrated online condition monitoring system for nuclear power plants, *Kerntechnik*. 75 (2010) 231–42.
- (46) H.M. Hashemian, Automated Maintenance Technology to be Embedded in Small Modular Reactor Designs, *Transactions of the American Nuclear Society*. 109 (2013) 2265–8.
- (47) H.M. Hashemian, C.J. Kiger, G.W. Morton, B.D. Shumaker, Wireless sensor applications in nuclear power plants, *Nuclear Technology*. 173 (2011) 8–16.
- (48) H.M. Hashemian, C.J. Kiger, J.C. Seibel, B.D. Shumaker, M.A. Feltus, Wireless technologies for nuclear facilities, *Transactions of the American Nuclear Society*. 100 (2009) 208–10.
- (49) G. Hauck, C. Truempi, P. Stockert, Installing Predictive Vibration Monitors, *Power Engineering*. 113 (2010) 4 pp.-4 pp.
- (50) R. Hinckley, R. Thorpe, Thermal Barrier Coatings in Gas Turbines, *Advanced Materials & Processes*. 171 (2013) 52–3.
- (51) I. Ikemoto, K. Kanda, Nuclear power under the clean development mechanism, *Progress in Nuclear Energy*. 37 (2000) 89–94.
- (52) P. Isasi-Vinuela, J.M. Molina-Lopez, A. Sanchis de Miguel, Unsupervised neural network for forecasting alarms in hydroelectric power plant, 1997.
- (53) A. Ito, Y. Tennichi, H. Hanaoka, Thermal power generation supervisory/control system, *Hitachi Review*. 44 (1995) 25–30.
- (54) P.-X. Jiang, F.-Z. Zhang, R.-N. Xu, Thermodynamic analysis of a solar-enhanced geothermal hybrid power plant using CO₂ as working fluid, *Applied Thermal Engineering*. 116 (2017) 463–472.
- (55) G. Kahraman, Y. Taşgın, Research of thermal performance by metallographic investigation of stator winding solder region in hydroelectric power plants, *Engineering Failure Analysis*. 97 (2019) 311–321.

- (56) M.E. Kantor, H.F. Menzel, R.W. Schlicht, Engineering tests during the initial operation of the peach bottom HTGR, *Nuclear Engineering and Design*. 7 (1968) 297–311.
- (57) J.T. Kim, S.H. Seong, C.K. Lee, S. Hur, N.Y. Lee, S.J. Lee, Flow-accelerated corrosion monitoring through advanced sensors, *Proceedings of the SPIE - The International Society for Optical Engineering*. 5634 (2005) 404–15.
- (58) J. Kim, J. Park, Reduction of test and maintenance human errors by analyzing task characteristics and work conditions, *Progress in Nuclear Energy*. 58 (2012) 89–99.
- (59) J. Kim, J. Park, W. Jung, J.T. Kim, Characteristics of test and maintenance human errors leading to unplanned reactor trips in nuclear power plants, *Nuclear Engineering and Design*. 239 (2009) 2530–2536.
- (60) K. Kim, W.-P. Chang, K.-J. Yoo, S.-H. Lee, C.-B. Lee, RETRAN-03 simulation of a multiple failure event at Kori Unit 2, *Nuclear Technology*. 122 (1998) 125–31.
- (61) M.V. Kothare, B. Mettler, M. Morari, P. Bendotti, C.-M. Falinower, Linear parameter varying model predictive control for steam generator level control, *Computers & Chemical Engineering*. 21 (1997) S861-6.
- (62) S.E. Kuehn, Reliability-centered maintenance trims nuclear plant costs, *Power Engineering*. 96 (1992) 23–8.
- (63) S.E. Kuehn, Reliability-centered maintenance trims costs. II, *Power Engineering*. 96 (1992) 30–2.
- (64) P.H. Kvam, J.G. Miller, Discrete predictive analysis in probabilistic safety assessment, *Journal of Quality Technology*. 34 (2002) 106–17.
- (65) M.A. Lanius, Infrared applications for steam turbine condenser systems, *Proceedings of the SPIE - The International Society for Optical Engineering*. 4020 (2000) 107–14.
- (66) A.S.A. Latiff, M. Musa, Z. Anhar, S. Illias, M.H. Ani, Slagging of coal blends: comparison between pre-blended and in furnace blend, *IOP Conference Series: Materials Science and Engineering*. 864 (2020) 012115 (12 pp.)-012115 (12 pp.).
- (67) W.L. Lavalley, R.W. Carr, S.N. Hale, Elements of a total MOV maintenance program, *Transactions of the American Nuclear Society*. 59 (1989) 62–62.
- (68) J.B. Leger, B. Iung, A. Ferro De Beca, J. Pinoteau, An innovative approach for new distributed maintenance system: application to hydro power plants of the REMAFEX project, *Computers in Industry*. 38 (1999) 131–148.
- (69) D. Lehnen, M. Demmer, Requirements on structural maintenance in power plants, *VGB Powertech*. 91 (2011) 50–5.
- (70) D. Lehnen, T. Kloker, J. Meyer, P. Holdt, Experience with protection and restoration measures on reinforced concrete structures, *VGB Powertech*. 88 (2008) 43–7.
- (71) F. Leonard, On the use of statistics and kriging to the monitoring of hydro generating units at Hydro-Quebec, *RAIRO-APII-JESA Journal European Des Systemes Automatises*. 30 (1996) 407–36.
- (72) T.U. Marston, F. Gelhaus, R. Burke, Advanced maintenance research programs, *Transactions of the American Nuclear Society*. 49 (1985) 46–7.
- (73) H.F. Martz, R.R. Picard, On comparing PRA results with operating experience, *Reliability Engineering & System Safety*. 59 (1998) 187–99.
- (74) J. Matsumura, N. Uwazumi, H. Iida, Recently developed features of control technology in thermal power plants, *Hitachi Review*. 32 (1983) 315–20.
- (75) D.A. Mauney, Fully quantitative predictive maintenance/inspection planning optimization for utility/plant components, *Proceedings of the SPIE - The International Society for Optical Engineering*. 2947 (1996) 48–58.
- (76) S. Mazzoni, G. Cerri, L. Chennaoui, A simulation tool for concentrated solar power based on micro gas turbine engines, *Energy Conversion and Management*. 174 (2018) 844–854.
- (77) M. Mercangoez, J. Poland, Coal Mill Modeling for Monitoring and Control (Extended Abstract), *IFAC Proceedings Volumes*. 44 (2011) 13163–13166.
- (78) J. Mitchem, Automated calibration aids smooth turnover of new plants, *IEEE Instrumentation & Measurement Magazine*. 7 (2004) 26–9.
- (79) J.M. Molina, P. Isasi, A. Berlanga, A. Sanchis, Hydroelectric power plant management relying on neural networks and expert system integration, *Engineering Applications of Artificial Intelligence*. 13 (2000) 357–369.
- (80) M. Mori, H. Matmura, Kansai takes a predictive approach to degradation problems (nuclear plants), *Nuclear Engineering International*. 35 (1990) 40–2.
- (81) K. Moriyama, A. Kanaya, J. Kusumoto, K. Koba, T. Kamisasanuki, T. Imazato, K. Nakashima, Estimation of material properties and maintenance of pressure parts of thermal power plant boilers under long-term service of 300,000 hours, *Materials Science and Engineering: A*. 510–511 (2009) 142–148.
- (82) A. Morris, B. Cacciapuoti, W. Sun, The role of hardness on condition monitoring and lifing for high temperature power plant structural risk management, *Measurement*. 131 (2019) 501–12.
- (83) R.W. Morris, J.M. Fife, Using probabilistic methods to define reliability requirements for high power inverters, *Proceedings of the SPIE - The International Society for Optical Engineering*. 7412 (2009) 74120G (10 pp.)-74120G (10 pp.).

- (84) W.T. Motley, Lean thinking redefines O&M practices, *Power*. 148 (2004) 72–5.
- (85) L. Mubaraali, N. Kuppuswamy, R. Muthukumar, Intelligent fault diagnosis in microprocessor systems for vibration analysis in roller bearings in whirlpool turbine generators real time processor applications, *Microprocessors and Microsystems*. 76 (2020) 103079.
- (86) F. Muller, H. Eickhoff, Efficient monitoring and diagnosis for hydro powerplants, *International Journal on Hydropower & Dams*. 3 (1996) 31–4.
- (87) N. Murugan, R.S. Parmar, S.K. Sud, Effect of submerged arc process variables on dilution and bead geometry in single wire surfacing, *Journal of Materials Processing Technology*. 37 (1993) 767–780.
- (88) N. Nakagawa, F. Inanc, A. Frishman, R.B. Thompson, W.R. Junker, F.H. Ruddy, A.R. Dulloo, J.M. Beatty, N.G. Arlia, On-line NDE and structural health monitoring for advanced reactors, *Key Engineering Materials*. 321–323 (2006) 234–9.
- (89) J. Naser, R. Shankar, Equipment early fault detection, diagnostics, and prognostics: building on on-line monitoring experience, invited, *Transactions of the American Nuclear Society*. 92 (2005) 73–4.
- (90) S.-V. Oprea, A. Bara, D. Preotescu, L. Elefterescu, Photovoltaic Power Plants (PV-PP) Reliability Indicators for Improving Operation and Maintenance Activities. A Case Study of PV-PP Agigea Located in Romania, *IEEE Access*. 7 (2019) 39142–57.
- (91) S.-V. Oprea, A. Bâra, Ultra-short-term forecasting for photovoltaic power plants and real-time key performance indicators analysis with big data solutions. Two case studies - PV Agigea and PV Giurgiu located in Romania, *Computers in Industry*. 120 (2020) 103230.
- (92) C. Paes Salomon, C. Ferreira, W.C. Sant’Ana, G. Lambert-Torres, L.E. Borges da Silva, E.L. Bonaldi, L.E. de Lacerda de Oliveira, B. Silva Torres, A study of fault diagnosis based on electrical signature analysis for synchronous generators predictive maintenance in bulk electric systems, *Energies*. 12 (2019) 1506 (16 pp.)-1506 (16 pp.).
- (93) L. Pentecost, T. Weir, Cable testing pays off at Scan Onofre, *Nuclear Engineering International*. 36 (1991) 42, 44–5.
- (94) H.F. Perla, J.G. Stampelos, W.C. Gekler, Accommodating performance effectiveness uncertainty in evaluation of proposed maintenance, *Transactions of the American Nuclear Society*. 46 (1984) 663–5.
- (95) K.R. Piety, E.F. Pardue, A new approach for implementing a computer-based predictive maintenance program, *IEEE Transactions on Nuclear Science*. NS-32 (1985) 1005–6.
- (96) F. Pons, B. Georgel, Ultrasonic and eddy current imaging: signal processing for defect visualization (nuclear power plants), *Bulletin de La Direction Des Etudes et Recherches, Serie A*. (1985) 19–28.
- (97) M. Prasad, A.J. Gaikwad, Human error probability estimation by coupling simulator data and deterministic analysis, *Progress in Nuclear Energy*. 81 (2015) 22–29.
- (98) B. Raj, G.J. Abraham, V.R. Raju, Engineering approach to corrosion management, *Transactions of the Indian Institute of Metals*. 54 (2001) 285–316.
- (99) M. Ralph, Spotting electrical problems with IR thermography, *Plant Engineering*. 63 (2009) 25–6.
- (100) L.R. Ranganath, B. Krishna, A.K. Singh, M.D. Kudale, Model and Desk Studies for Feasibility of Sea Route in a Complex Estuary, *Aquatic Procedia*. 4 (2015) 49–56.
- (101) M.B. Reksono, I.M. Miasa, Vibration Analysis For Reducing Excessive Vibration Level on Gas Turbine Generator (GTG) 100 MW in Cogeneration Power Plant, *Journal of Physics: Conference Series*. 1351 (2019) 012083 (9 pp.)-012083 (9 pp.).
- (102) C. Ren-Rong, L. Bok-Mun, G. Yi-Yi, Improving energy efficiency & a case study for power plant, *Monthly Journal of Taipower’s Engineering*. 734 (2009) 11–18.
- (103) L.C. Ribeiro, E.L. Bonaldi, L.E.L. de Oliveira, L.E.B. da Silva, C.P. Salomon, W.C. Santana, J.G.B. da Silva, G. Lambert-Torres, Equipment for Predictive Maintenance in Hydrogenerators, *AASRI Procedia*. 7 (2014) 75–80.
- (104) J. Sanahuja, C. Toulemonde, Numerical homogenization of concrete microstructures without explicit meshes, *Cement and Concrete Research*. 41 (2011) 1320–9.
- (105) Y. Shi, Y. Zhu, R.K. Mehta, J. Du, A neurophysiological approach to assess training outcome under stress: A virtual reality experiment of industrial shutdown maintenance using Functional Near-Infrared Spectroscopy (fNIRS), *Advanced Engineering Informatics*. 46 (2020) 101153.
- (106) R.B. Shirley, C. Smidts, M. Li, A. Gupta, Validating THERP: Assessing the scope of a full-scale validation of the Technique for Human Error Rate Prediction, *Annals of Nuclear Energy*. 77 (2015) 194–211.
- (107) T. Shoji, Materials Ageing Degradation Programme in Japan and Proactive Ageing Management in NPP, *EPJ Web of Conferences*. 51 (2013) 04001 (33 pp.)-04001 (33 pp.).
- (108) D.J. Smith, Computer aided design and engineering leads the way, *Power Engineering*. 91 (1987) 12–18.
- (109) D.J. Smith, Artificial intelligence-today’s new design and diagnostic tool, *Power Engineering*. 93 (1989) 26–30.

- (110) D.J. Smith, Improved valve and pump designs hiking plant performance, *Power Engineering*. 107 (2003) 32–6.
- (111) P.P. Stancavage, BWR performance for longevity, *Transactions of the American Nuclear Society*. 55 (1987) 510–12.
- (112) A. Stoppato, A. Mirandola, G. Meneghetti, E. Lo Casto, On the operation strategy of steam power plants working at variable load: Technical and economic issues, *Energy*. 37 (2012) 228–236.
- (113) R. Swanenkamp, Fuel management: natural gas/fuel oil, *Power*. 140 (1996) 11–16, 18.
- (114) K. Ting, Y.P. Ma, The evaluation of erosion/corrosion problems of carbon steel piping in Taiwan PWR nuclear power plant, *Nuclear Engineering and Design*. 191 (1999) 231–43.
- (115) H. Utsuno, T. Sakuma, Best estimate BWR transient analysis with TRACG assessment using data from BWR startup tests and LOCA integral tests, *Journal of Nuclear Science and Technology*. 35 (1998) 607–20.
- (116) A.S. Vaka, P. Talukdar, Novel inverse heat transfer technique for estimation of properties and location-specific process parameters of roof-mounted solar PV plants, *Thermal Science and Engineering Progress*. 19 (2020) 100657.
- (117) P. van Eeten, T. Bräuer, V. Bykov, A. Carls, J. Fellinger, J.P. Kallmeyer, Features and analyses of W7-X cryostat system FE model, *Fusion Engineering and Design*. 96–97 (2015) 369–372.
- (118) F. Verrilli, S. Srinivasan, G. Gambino, M. Canelli, M. Himanka, C. Del Vecchio, M. Sasso, L. Glielmo, Model predictive control-based optimal operations of district heating system with thermal energy storage and flexible loads, *IEEE Transactions on Automation Science and Engineering*. 14 (2017) 547–57.
- (119) L. Wang, Y. Zeng, J. Zhang, W. Huang, Y. Bao, The criticality of spare parts evaluating model using artificial neural network approach, 2006.
- (120) W.-C. Wang, Laboratory investigation of drying process of Illinois coals, *Powder Technology*. 225 (2012) 72–85.
- (121) T.Y.C. Wei, M.C. Regalbuto, J.F. Krebs, Y.S. Park, A.S. Hebden, H. Ley, Feasibility testing of the IGENPRO reactor plant operator advisory system with the ANL UREX+ facility for diversion detection, *Transactions of the American Nuclear Society*. 98 (2008) 163–4.
- (122) H. Wilson, The impact of plasma physics on the timescale to a tokamak fusion power plant, *Philosophical Transactions of the Royal Society A (Mathematical, Physical and Engineering Sciences)*. 377 (2019) 20170435 (14 pp.)-20170435 (14 pp.).
- (123) D. Wu, S. Liu, L. Zhang, J. Terpenney, R.X. Gao, T. Kurfess, J.A. Guzzo, A fog computing-based framework for process monitoring and prognosis in cyber-manufacturing, *Journal of Manufacturing Systems*. 43 (2017) 25–34.
- (124) R.N. Wurzbach, Developing a comprehensive training curriculum for integrated predictive maintenance, *Proceedings of the SPIE - The International Society for Optical Engineering*. 4710 (2002) 341–52.
- (125) K. Yamamura, S. Fujimura, T. Ota, T. Ishikawa, T. Saito, Y. Arai, T. Shinano, A statistical model for estimating the radiocesium transfer factor from soil to brown rice using the soil exchangeable potassium content, *Journal of Environmental Radioactivity*. 195 (2018) 114–125.
- (126) N. Yamashita, M. Iwasaki, K. Dozaki, N. Soneda, Industry practice for the neutron irradiation embrittlement of reactor pressure vessels in Japan, *Journal of Engineering for Gas Turbines and Power*. 132 (2010) 102919 (8 pp.)-102919 (8 pp.).
- (127) P. Yvon, F. Carre, Structural materials challenges for advanced reactor systems, *Journal of Nuclear Materials*. 385 (2009) 217–22.
- (128) W. Zapletal, G. Albert, W. Baumkirchner, R. Doppler, H. Nyvelt, W. Westerthaler, Monitoring and diagnosis system for strategic maintenance methods in hydro power plant, *Elektrotechnik Und Informationstechnik*. 113 (1996) 126–32.
- (129) P. Zayicek, S.M. Shepard, Investigation of an IR technique for detection of wall thinning in service water piping, *Proceedings of the SPIE - The International Society for Optical Engineering*. 3056 (1997) 242–7.
- (130) C. Zinoni, L. Janvier, B. Symoens, Qualification Strategy of New Technologies for Safety Instrumentation in Harsh Radiation Environments, *IEEE Transactions on Nuclear Science*. 65 (2018) 1661–6.

A Steam Rankine Cycle Pilot Plant for Distributed High Temperature Waste Heat Recovery

F. Raab^{1*}, H. Klein², F. Opferkuch¹

¹Technische Hochschule Nürnberg Georg Simon Ohm, Distributed Energy Conversion and Storage,
Fürther Str. 246b, 90429 Nürnberg, Germany

²Technische Universität München, Institute of Plant and Process Technology,
Boltzmannstraße 15, 85748 Garching, Germany

*Corresponding author: florian.raab@th-nuernberg.de

Abstract

Although the Steam Rankine Cycle (SRC) technology with water as working fluid has its techno-economic optimum in large, centralized plants, this technology can also be used in distributed Waste Heat Recovery (WHR) systems. This paper describes a pilot SRC plant, which on the one hand represents the state of the art in distributed small-scale WHR using water and on the other hand can be used to test new or further developed apparatus and equipment. The technology used, special aspects in the operation of SRC plants in the lower power range and measurements of the overall system are presented. Finally, an outlook on the future research and development of the system in terms of compactness, efficiency and economic operation is given.

Keywords: Steam Rankine Cycle, SRC, Pilot Plant, Waste Heat Recovery, WHR

Introduction/Background

In large, centralized thermal power plants, the SRC, with water as working fluid, is state of the art. At high temperatures and pressures, such plants can achieve the currently highest efficiencies in the conversion of heat to electricity and are involved in more than half of the world's electricity generation [1]. Applied research and development in recent decades has achieved thermal system efficiencies of up to 45 % with live steam parameters of up to 620 °C and 280 bar [2]. The economic optimum of this technology lies in large centralised power plants with high availability. For the WHR in distributed small-scale plants, the Organic Rankine Cycle (ORC) technology, with organic working fluids instead of water, is state of the art, as it can be operated efficiently and economically even at lower temperatures. Various manufacturers worldwide offer ORC systems with different working fluids for a wide range of applications, temperatures and power classes that can be operated economically [3, 4]. However, working fluids used in ORCs are often toxic, flammable, carcinogenic, have a high Global Warming Potential or Ozone Depletion Potential or tend to decompose at higher temperatures [5, 6], which is why an adequate WHR is not applied in several processes.

Water, on the contrary, as a non-toxic, affordable and widely available working fluid, offers many advantages in the areas of environmental protection, occupational health and safety. From a thermodynamic point of view, an SRC process with water as working fluid could achieve comparable system efficiencies only at higher waste heat temperatures [7, 8]. These high temperatures occur in many distributed energy conversion processes in various heat flow rates. In addition to natural gas, biogas and hydrogen Internal Combustion Engines (ICEs), which will continue to provide a reliable baseload supply in the future. High temperature waste heat in solid oxide fuel cells and volatile waste heat from mobile applications such as ships, trains and trucks, as well as industrial manufacturing processes [9] are therefore potential use cases for the SRC. Additionally, in processes with existing steam networks such as marine,

food processing, laundries and hospitals, the SRC can convert the high exergy of fuels into flexibly usable electrical energy, while the remaining thermal power from the heat sink could still be used to produce steam and heat for other processes.

SRC plant technology in the lower power range has not been developed significantly in recent years due to a lack of market incentives. Furthermore, challenges exist in the apparatus design of the steam generator, turbine, condenser and pump due to high required levels of superheating, comparatively low mass flows, high volume increase at phase transition and high evaporation enthalpies. This results in the particular apparatuses becoming bigger or less efficient than in the ORC [10]. Gewald et al. conclude in their investigations of WHR that a more detailed examination of process parameters and overall economics is required to make a well-reasoned and meaningful decision for or against SRC [11].

The research group of Distributed Energy Conversion and Storage at the TH Nürnberg designed and constructed a SRC pilot plant called “MicroRankine” with water as working fluid, which converts the thermal energy contained in the exhaust gas of an ICE in electrical energy. The experimental setup, which represents the state of the art in small-scale distributed SRC technology, enables system testing of the overall design and the investigation and measurement of new or further developed apparatus and equipment.

MicroRankine Pilot Plant

The steam generator of the MicroRankine plant is fired by flue gas from a sewage gas ICE, which flows adjustable in counter current through the economizer, the fire tube boiler and the superheater. The Jenbacher JMS 312 GS-B.L ICE of this pilot plant has a nominal electrical power of 526 kW_{el}, an exploitable thermal power of 316 kW_{th} at 81 °C from the cooling system and 247.6 kW_{th} at 451 °C from the 2,797 kg/h flue gas stream, when cooled down to 170 °C [12]. The composition of the sewage gas and the waste gas of the engine at lambda 1.64 are shown in Table 1. Calculated properties of the exhaust gas for the measured in- and outflow parameters of the steam generator are shown in Table 2. The material data of the specific pure substances were calculated with REFPROP [13]. The density and isobaric heat capacity of the exhaust gas mixture were calculated by the respective mass fractions and molar masses, the conductivity and viscosity with the mixing rule according to Wilke [14].

Table 1: Sewage gas and exhaust gas composition

	sewage gas	exhaust gas
T [°C]	20	451
H ₂ O [m%]	1.5	7.5
N ₂ [m%]	1.5	68.7
O ₂ [m%]	0.5	9.4
Ar [m%]	0.04	1.17
CO ₂ [m%]	57.9	12.9
CH ₄ [m%]	38.5	0.3

Table 2: Calculated properties of the exhaust gas

T [°C]	429.4	156.5
p [bar(a)]	1.032	1.016
ρ [kg/m ³]	0.50	0.81
c _p [J/kg/K]	1169.8	1090.6
η [Pa·s]	3.26E-05	2.25E-05
λ [W/m/K]	0.053	0.034

The evaporator consists of an economizer, a steam boiler and a superheater. The water at up to approx. 16 bar(a) is preheated in the cross flow economizer almost to saturation, with the water flowing through 32 serial tubes made of P250GH with an outer diameter of 33.7 mm, an inner diameter of 27.9 mm and a length of 1.0 m. The exhaust gas flows around the finned tubes. The preheated water flows into the steam boiler, where the exhaust gas flows through the 176 parallel tubes made of P250GH with an outer diameter of 26.9 mm, an inner diameter of 22.3 mm and a length of 3.0 m. The water evaporates at the outside of the tubes. The filling

volume in operation is approx. 1,400 l. Finally, the saturated steam is superheated in the superheater to a maximum of 431 °C, while the exhaust gas flows around the 168 tubes made of 1.457 with an outer diameter of 33.7 mm, an inner diameter of 28.5 mm and a length of 0.8 m, the steam flows through 12 parallel strings of 14 tubes each in cross flow.

In order to be able to evaluate different turbine operating conditions, the live steam temperature can be lowered by means of a controllable injection cooling, which at the same time increases the mass flow. To avoid droplet impact in the turbine due to insufficient mixing of the superheated steam and the subcooled droplets, the steam first flows through an approx. 11 m long live steam section and a mist eliminator until it then flows into the turbine.

The current turbine consists of four Laval nozzles in which the pressure is released and the steam hits a two-stage Curtis turbine wheel at supersonic velocity, where the kinetic power is converted into mechanical shaft power. The shaft, which is directly attached to the turbine wheel and on which both the permanent magnets of the generator and the magnetic bearings are mounted, rotates at a maximum speed of 36,000 rpm [15].

The expanded steam condenses in an *Airec Compact 72-C-100-T* asymmetric brazed plate condenser made from 1.4404 with 100 parallel plates [16]. The heat in the condenser is transferred to the river water cooling system of the sewage treatment plant, allowing variable exhaust steam pressures of a minimum of 0.08 bar(a) to be realized. Due to the polluted river water and the lack of possibility to clean the condenser, an intermediate circuit transfers the thermal energy to the river water via a screwed plate heat exchanger. After the condenser, the working fluid is stored in a hotwell with approx. 150 l in operation state.

From the hotwell, the water is pumped back up to operating pressure by a *LEWA type LDD* piston membrane-type metering pump [17], where it first cools the turbine jacket and then flows into the preheater.

A total of 18 temperature measuring points, which are relevant for the balancing and evaluation of the apparatuses, 12 pressure measuring points and 7 flow meters are installed in the plant. To monitor the water quality, in addition to two sampling points, through which the chemical parameters can be identified with the help of portable measuring instruments and laboratory tests, automated measuring instruments are installed. In parallel with a conductivity sensor in the steam boiler, sensors are installed before the pump in which the electrical conductivity, the pH-value, the oxygen content and the redox potential are measured [18]. From these four parameters and the actual temperature, the iron content can be concluded [19].

The measuring points in the plant are shown in the simplified process flow diagram in Figure 1. The gas and water side high temperature measuring points at over 400 °C are accurate to at least ± 1.1 K, at temperatures around 200 °C to ± 0.59 K and the other temperature measuring points to ± 0.20 K. The pressure sensors are accurate to ± 1 %, the flow sensors in the circuit are accurate to ± 0.5 % and the flow measurement in the exhaust gas is accurate to at least ± 1 %.

The system is controlled by a Programmable Logic Controller and with the help of a Human Machine Interface, various operating points can be approached and measured data can be exported. The internal consumption of the pumps, the control system and the voltage converters are also recorded.

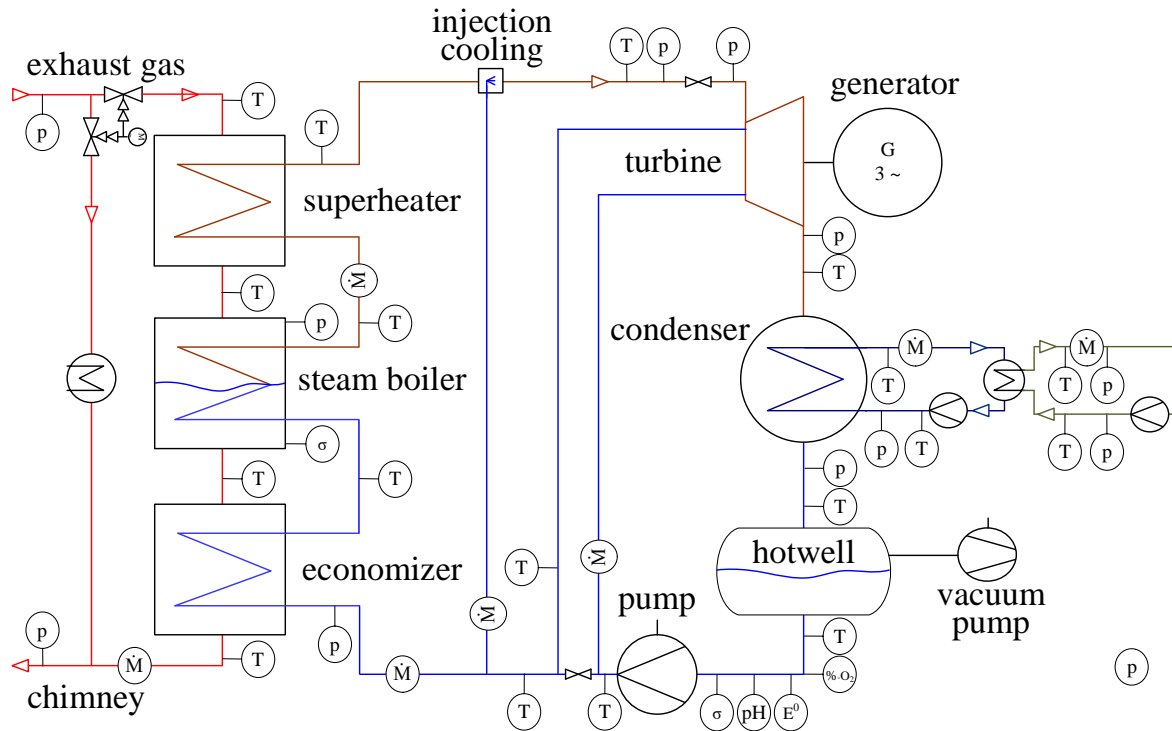


Figure 1: Simplified process flow diagram of the MicroRankine pilot plant with measuring positions

A picture of the pilot plant as it is set up at the sewage treatment plant in Nürnberg is shown in the following Figure 2.



Figure 2: MicroRankine pilot SRC plant at the sewage treatment plant in Nürnberg

Discussion and Results

The measurement data of the thermodynamic parameters in a steady state are displayed in Figure 3. The plant's internal consumption in this operating condition totals $1.28 \text{ kW}_{\text{el}}$, $0.31 \text{ kW}_{\text{el}}$ of which is for the feedwater pump. The efficiency of the generator at full load is determined to 95 %, the efficiency of the inverter to 94.3 %. The overall pump efficiency in this operation point is 31.3 % and the isentropic turbine efficiency at a rotational speed of 36,000 rpm is 56.8 %. The vacuum pump needs an additional power of $1.31 \text{ kW}_{\text{el}}$ when pulling vacuum. The heat flux transferred from the exhaust gas is $215.9 \text{ kW}_{\text{th}}$, and the power of the turbine after the converter is $31.7 \text{ kW}_{\text{el}}$, resulting in an overall gross plant efficiency of 14.7 % and net efficiency of 14.1 %.

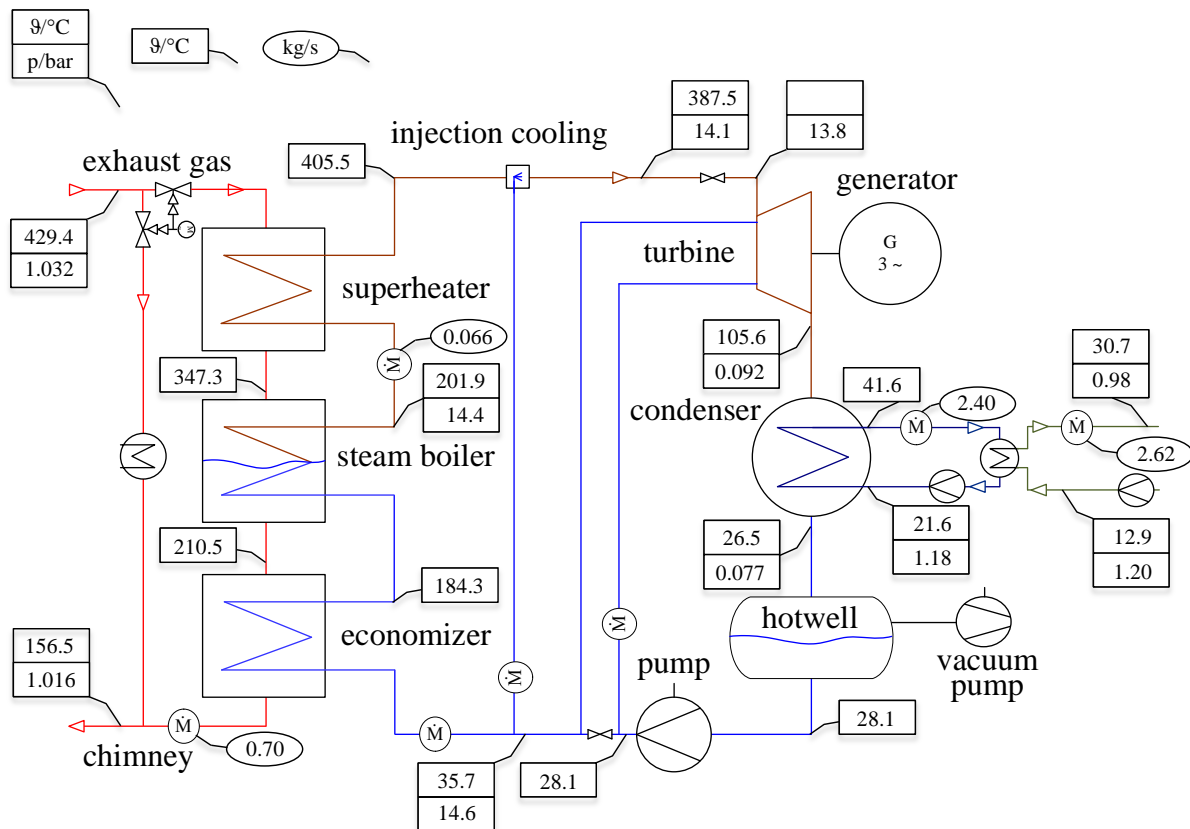


Figure 3: Thermodynamic measurement data of the MicroRankine plant in steady state

The large evaporator surface, that is not ideally insulated, causes a calculated heat flux of 8.5 kW_{th} that is lost to the environment in this case. Due to the long live steam mixing distance, 2.5 kW_{th} is lost between the steam generator and the steam turbine.

As a result of the high number of flanges, which make the pilot plant very flexible in design, the volume under vacuum between the turbine and the pump is not perfectly tight. However, even with a largely welded system, total vacuum tightness cannot be achieved. In the Micro-Rankine system, the vacuum pump always operates for some seconds when the pressure after the condenser exceeds a certain value. The exhaust pressures of the turbine and after the condenser increase over time and decrease rapidly again after activation of the vacuum pump. The temperatures after the condenser and after the hotwell decrease over time and increase rapidly when the vacuum pump is active. These trends over a period of 7.5 h are shown in Figure 4. It can be seen that the vacuum pump, and thus the proportion of air in the system, in the case considered hardly noticeably affects the turbine performance. The temperature after the condenser reaches the saturation temperature for a while after the vacuum pump is activated. The hotwell with its approx. 150 l buffers this circumstance and thus protects the pump from cavitation.

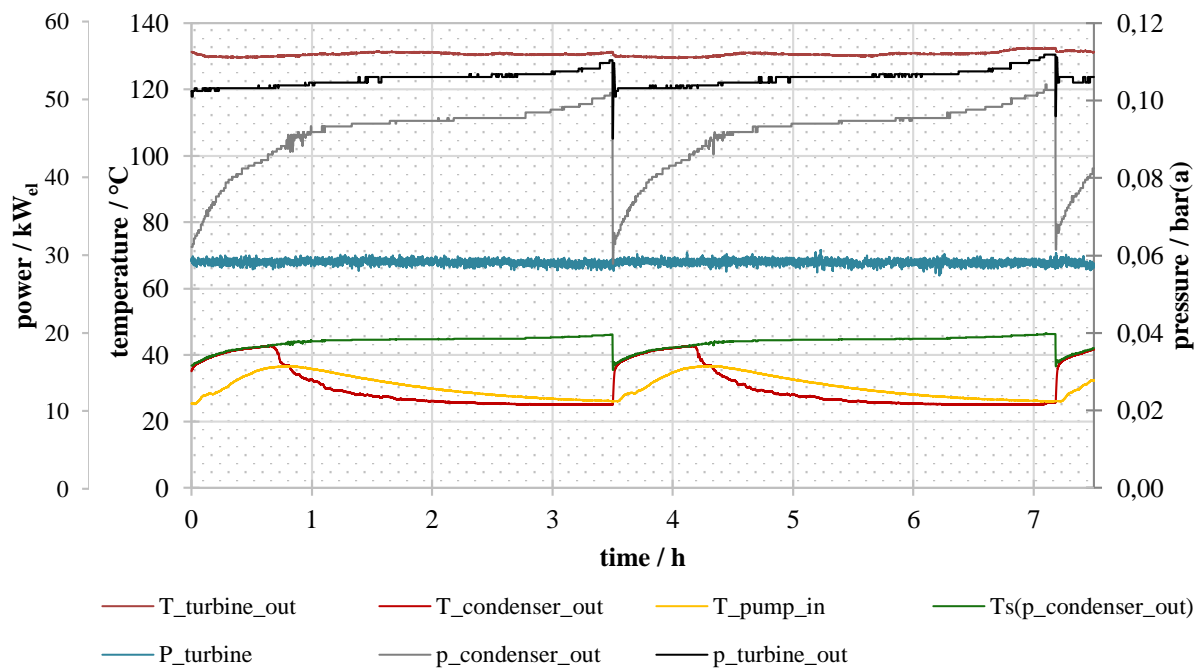


Figure 4: Exhaust turbine and condenser pressure and temperature, pump inlet temperature, saturation temperature after condenser and turbine power in continuous operation at approx. 30,000 rpm

Since the steam boiler and the economizer are made of unalloyed steel, the water quality must be checked regularly in the hermetic system to prevent corrosion. The plant was filled with fresh, deionized water for the following series of measurements. Figure 5 shows the course of conductivity, oxygen and pH-value in the steam boiler in black lines, as well as after the condenser in grey lines.

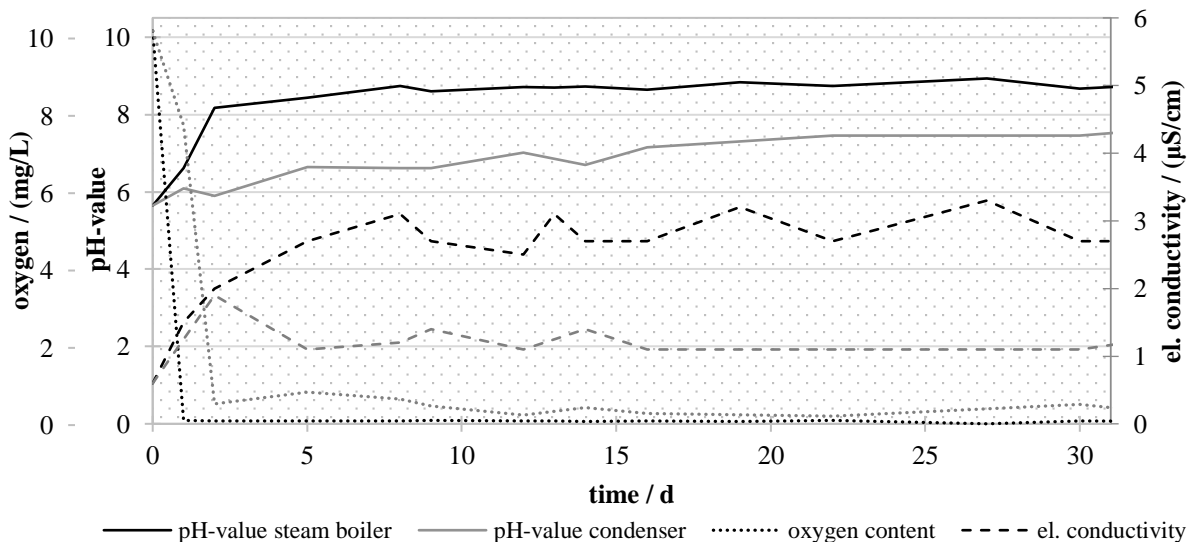


Figure 5: pH-value, oxygen content and electrical conductivity of the water in the steam boiler and after the condenser applied over time

It can be seen that the oxygen brought into the system via the fresh water largely disappears after a few days. The evaporator serves as a degasser and the oxygen is removed from the system via the vacuum pump. In the first days after filling the plant with deionized water, the vacuum pump starts more frequently. The conductivity in the steam generator is always slightly

higher than in the condenser, since the evaporation leaves all impurities in the boiler. The pH-value in the steam generator stabilizes at approx. 8.7 and in the condenser at 7.2. To protect the steam boiler, an alkalizing agent must be introduced into the system in the future to raise the pH-value, alternatively the system must be made completely of stainless steel.

The evaporator itself, with its net weight of almost four tons and the 1,400 l of water it contains, represents an energy store that can be used, on the one hand, to store and flatten volatile waste heat from industrial processes, for example. On the other hand, in the event of a blackout, such a boiler can be used to maintain the power supply until motor-driven emergency generators are started up. Especially in an infrastructure where a steam network is available anyway, e.g. in hospitals, this SRC technology could be adapted to the existing steam boiler and keep indispensable equipment in operation in case of emergency. A heating failure was simulated with the MicroRankine system, the turbine power, the live steam temperature and the pressure decreasing with time are shown in Figure 6. Over a period of approx. 25 minutes, the turbine still supplies electrical power.

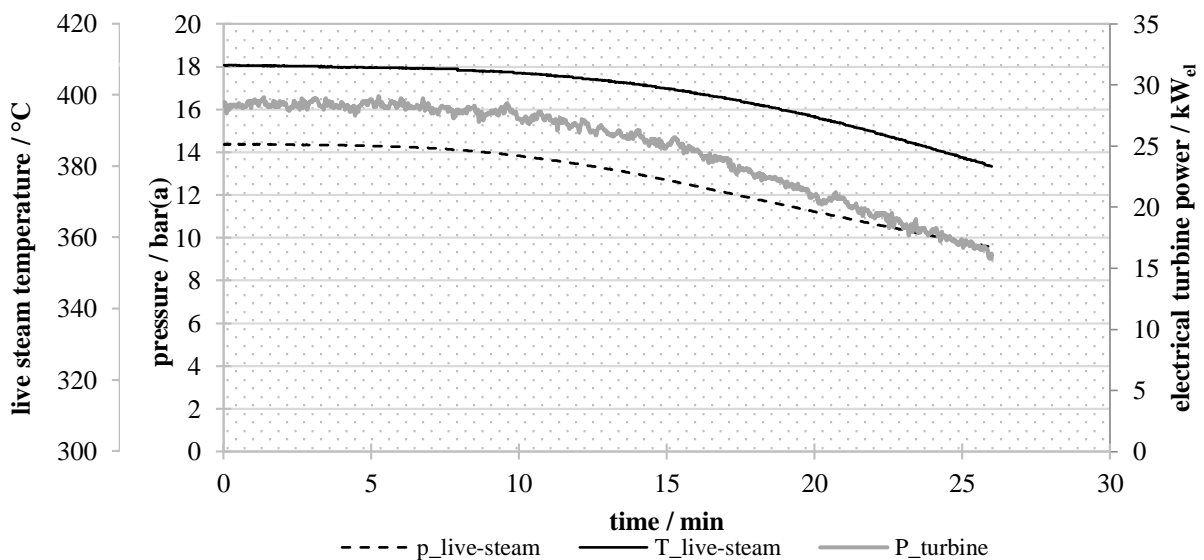


Figure 6: Turbine power, live steam temperature and pressure in case of heating failure of the MicroRankine plant applied over time

Summary/Conclusions and Outlook

With the MicroRankine pilot plant, the state of the art in distributed small-scale SRC technology is represented and the feasibility of scaling down large SRC power plants is proven. In current system tests a low-maintenance and reliable continuous operation of the individual components and the overall system is investigated. In transient experiments and simulations, the system behaviour of the plant will be investigated depending on volatile heat loads, condensation and ambient temperatures. A current research project of the TH Nürnberg with partners from industry and applied science aims to develop a compact and economically optimized plant design for different applications. In detail, a once-through steam generator, an optimized steam turbine, an improved condenser and a standardized and modularized plant concept for waste heat in the area of 200 to 2,000 kW_{th} are to be developed. This will enable a sustainable, safe and economic operation, where high temperature waste heat can be converted into electrical energy and district heating as required. The developed apparatuses are to be investigated in the MicroRankine pilot plant under real operating conditions and tested in continuous operation.

Acknowledgements

The majority of the MicroRankine pilot plant was funded by the Federal Ministry of Education and Research as part of the FH-Invest 2016 program. The authors highly appreciated this funding. The micro steam turbine was kindly provided to the TH Nürnberg by the SIEMENS AG, which always supported the system design process. Special thanks belongs to the Stadtentwässerung und Umweltanalytik Nürnberg, which provided the space and the waste heat of the ICE and supported the project both financially and practically, which made the presented work possible.

References

- [1] Sönnichsen, N., *Distribution of electricity generation worldwide in 2018, by energy source*, International Energy Agency, 2020.
- [2] Strauß, K., *Kraftwerkstechnik. Zur Nutzung fossiler, nuklearer und regenerativer Energiequellen*, Springer Berlin Heidelberg, 2009.
- [3] Tartière, T., Astolfi, M., *A World Overview of the Organic Rankine Cycle Market*, Energy Procedia, 2017.
- [4] Vélez, F., Segovia, J., Martín, M., Antolín, G., Chejne, F., Quijano, A., *A technical, economical and market review of organic Rankine cycles for the conversion of low-grade heat for power generation*, Renewable and Sustainable Energy Reviews, 2012.
- [5] Grob, J., *Arbeitsmittelauswahl, Messdatenanalyse und Modellüberprüfung eines Hochtemperatur-Organic-Rankine-Cycle*, Dissertation, Universität Bochum, 2013.
- [6] Dai, X., Shi, L., Qian, W., *Review of the Working Fluid Thermal Stability for Organic Rankine Cycles*, J. Therm. Sci, 28, 2019.
- [7] Zhang, X., Wu, L., Wang, X., Ju, G., *Comparative study of waste heat steam SRC, ORC and S-ORC power generation systems in medium-low temperature*, Applied Thermal Engineering, 2016.
- [8] Vankeirsbilck, I., Vanslambrouck B., Gusev S., de Paepe M., *Organic Rankine cycle as efficient alternative to steam cycle for small scale power generation*, 8th International Conference on Heat Transfer, Fluid Mechanics and Thermodynamics, 2011.
- [9] Panayiotou, G. P., Bianchi, G., Georgiou, G., Aresti, L., Argyrou, M., Agathokleous, R., Tsamos, K. M., Tassou, S. A., Florides, G., Kalogirou, S., Christodoulides, P., *Preliminary assessment of waste heat potential in major European industries*, Energy Procedia, 2017.
- [10] Shu, G., Li, X., Tian, H., Liang, X., Wei, H., Wang, X., *Alkanes as working fluids for high-temperature exhaust heat recovery of diesel engine using organic Rankine cycle*, Applied Energy, 2014.
- [11] Gewalt, D., Siokos, K., Karellas, S., Spliethoff, H., *Waste heat recovery from a landfill gas-fired power plant*, Renewable and Sustainable Energy Reviews, 2012.
- [12] GE Jenbacher GmbH & Co OG, *Technische Beschreibung BHKW JMS 312 GS-B.L.*, 2004
- [13] Lemmon, E. W., Huber, M. L., McLinden, M. O., *NIST Reference Fluid Thermodynamic and Transport Properties REFPROP*. The National Institute of Standards and Technology (NIST), 2007.
- [14] Wilke, C. R., *A Viscosity Equation for Gas Mixtures*. J Chem Phys, 1950.
- [15] Kraus M., Deichsel M., Opferkuch F., Hirsch P., Heckel C., *Hermetic 40-kW-Class Steam Turbine System for the Bottoming Cycle of Internal Combustion Engines*, ASME Turbo Technical Conference and Exposition GT 2016, 2016.
- [16] Airec AB, *Compact 72*, 2017.
- [17] LEWA GmbH, *LEWA type LDD*, 2018.
- [18] Zargari, M., Opel, O., Wiegand, M., *Vermeidung von Korrosion in hydraulischen Systemen*, DKV-Tagung Bremen, 2017.
- [19] Opel, O., *Detektion von Verockerungsprozessen und Korrosion/Belagbildung in Brunnen und Leitungssystemen mithilfe des Redoxpotentials*, Dissertation, Leuphana Universität Lüneburg, 2012.

Experimental Development of Additively Manufactured Turboexpanders towards an Application in the ORC

Jan Spale^{1,*}, Vaclav Novotny¹, Jan Novotny¹, Andreas P. Weiß^{1,2}, Michal Kolovratnik¹

¹Czech Technical University in Prague, Jugoslavských partyzanu 1580/3, 160 00 Prague, Czech Republic

²University of Applied Sciences Amberg-Weiden, Center of Excellence for Cogeneration Technologies, Kaiser-Wilhelm-Ring 23, 92224 Amberg, Germany

* Corresponding author: Jan.Spale@cvut.cz

Abstract

Widespread application of distributed energy systems using thermodynamic cycles is hindered by the absence of efficient and cost-effective expanders. 3D printing offers an interesting option for customization and low cost manufacturing of turboexpander components, especially for low temperature machines which may operate with plastic materials. This work provides an introductory comprehensive experimental research of the performance of an air turboexpander with components being manufactured by various 3D printing methods and from different plastic materials and from stainless steel by DMLS method for reference. The flow components were investigated on a purpose-built pressurized air test rig. The highest obtained isentropic efficiency was around 40% with nylon components from the SLS method, but surprisingly also FDM method had shown outstanding performance. The SLA method, leaving a rather glassy surface and having the best resolution, ended up in our cold air trials poorly, and its brittleness had appeared to be a serious issue for practical applications.

Keywords: 3D printing, additive manufacturing, turbomachinery, polymer materials, surface roughness

Introduction

The large expansion of distributed micro-scale energy systems based on low-temperature thermal cycles has a bottleneck in the performance, efficiency and cost of the expanders. Turboexpanders have the potential to provide high performance in comparison to volumetric ones [1], but they typically suffer from high costs inflicted by complex shapes increasing manufacturing costs and thus are not economically feasible for small series or even prototype and single-piece production.

Additive manufacturing (AM) might be a potential solution to this cause as it both decreases the development time and the production cost of the turbine wheel. AM can also reduce the number of separate parts by printing the entire wheels in whole. Plastic materials, furthermore, provide an interesting possibility for such low-temperature applications. One of the typical drawbacks of the additively manufactured blades is a poor surface roughness in the as-made state. This one puts in the question of how extensive the post-processing has to be to achieve suitable performance. [2] A detailed overview of the application and opportunities of different AM technologies for turbomachinery can be then found in a precedent review study of the author's collective. [3]

This work first further provides an updated version of the review of the additive manufacturing for micro turboexpanders. Then, the experimental method of investigation of the performance of several axial 3D printed impulse turbines made of plastic is described. The performance is investigated for the as-printed state of the components by various technologies (FDM, SLS, SLA and MJF - FDM – fused deposition modelling, SLS – selective laser sintering, SLA – stereolithography, MJF – multi-jet fusion). The results are then presented for each of the manufacturing technology and finally reported in a generalized summary.

Review of additive manufacturing for micro turboexpanders

As ORC micro turboexpanders are most likely not going to be ever produced in large series and customization is key for quality performance, a possibility to effectively tailor the turboexpander design to the desired operating conditions of the cycle is a necessity. That comes with increased costs mainly on the two fronts: i) the turbomachinery design and ii) the manufacturing of the designed turbine. The design part is tackled usually by specialized design tools that can easily vary and customize the turbine in a specific area of boundary conditions. [2] Cost-effective manufacturing of single-piece produced small-scale turbines was not possible until the last decade since AM technology allowed to produce technically feasible and sufficient products while being a cost-effective option in comparison with conventional manufacturing technologies.

A brief overview of the state-of-the-art of AM for turbomachinery follows. For a more detailed and thorough review, a fellow reader is referred to the author’s collective previous work. [4] Summary of the possible additive manufacturing methods and their division according to ISO/ASTM 52900:2015 terminology is presented on a tree chart in Figure 1.

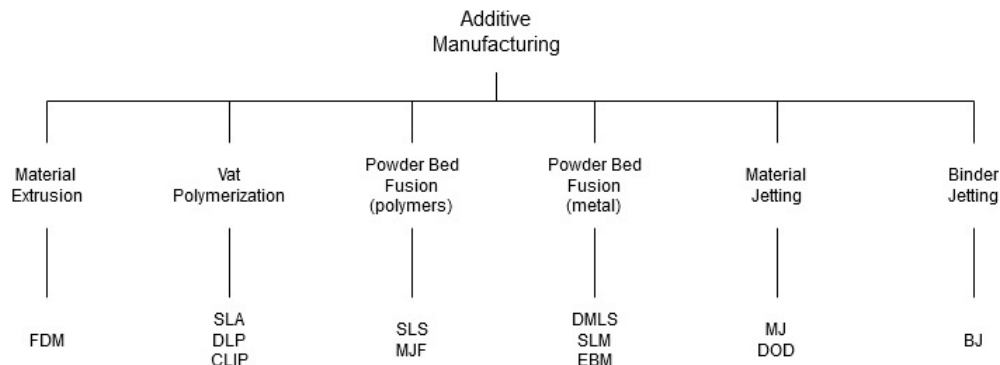


Figure 1 A tree chart of additive manufacturing technologies according to ISO/ASTM 52900:2015

Additive manufacturing has found its way towards large-scale turbines and major industrial manufacturers but not as a manufacturing technology for entire wheels or blades, but rather repairs, maintenance and overhaul of the current machines. [5] Another great trend in the AM for turbomachinery is 3D printing of wind turbine blades for the small and micro scale machines. This is though beyond the scope of interest of this paper as it discusses only turbomachinery components of thermodynamic cycles. [6]

The authors see the further interesting potential of some of the above-mentioned technologies also for small to micro scale low temperature applications, as plastics can be utilized and lower stage loading is usually obtained. Based on the literature review as well as on in-house tests, an overview of AM applicability for micro turboexpanders was created and presented in Table 1. A very brief analysis of each AM method, which was used for the experimental tests and its applicability for turbomachinery with relevant references on

experimental investigations available in the literature, follows. For the complete overview, a fellow reader is referenced to the review paper of the author's collective [4]

Table 1 Summary of AM technologies for small turbines

Technology	Possible applications	Materials	Maximum temperature	Advantages	Drawbacks
FDM	Low demand parts, other parts with limits	ABS, Ultra ABS, PETG	~100 °C	Cheap, widely available	Rough surface, needs supports, anisotropic mechanical properties
SLS	Any parts	Nylon, carbon, TPU, PP	~80 °C	Cheap, no supports, good accuracy	Limited T ~80 °C
SLA	Stationary parts	Resins	>200 °C	Good resolution and surface quality	Very expensive, needs supports, problems with fine features
DMLS	Flow components	Metals (steel, Al, Ti)	>1000 °C	Most available metal AM technology	Expensive, sensitive to fine-tuning, rough surface in as-printed, needs supports
MJF	Any parts	Nylon based composites	~80 °C	Cheap, no supports, best tolerances, fastest	Limited T ~80 °C; domain of HP company only
EBM	Flow components	Metals (steel, Al, Ti)	>1000 °C	Fast, well-tuned properties	Very expensive

Stereolithography (SLA)

Stereolithography is based on a functional principle of UV curing of a liquid resin. Most of the resins have a temperature limit of around 70 °C, which significantly reduces its potential for turbomachinery applications, but special high-temperature resins that can withstand temperatures up to 290°C for low loaded parts exist. The glossy surface similar to glass, high precision of the prints and low layer thickness suggest good applicability for turbomachinery. Furthermore, there are various references for this technology in relation to turbomachinery, especially for small scale cold aerodynamic tests and models in fluid dynamics research. [7]–[10]

Fused Deposition Modelling (FDM)

Fused Deposition Modelling is certainly the most common AM technology amongst private applications and is widespread at the market for reasonable prices. Nonetheless, the quality of its prints is usually not able to fulfil requirements and criteria for turbomachinery operation since the print inhomogeneity is rather large. The minimum layer thickness is a number of times higher than for SLA, and thermal effects cause large deterioration of accuracy, support structures are needed and leave burrs, circular tolerances are poor and surface quality is quite rough and requires additional treatment. Concerning the materials and their temperature resistance, FDM prints can sustain temperatures of over 80°C and exceptionally above 100°C (Ultra ABS material). Again, numerous references for the FDM technology application for technology were found in the literature, especially in micro scale for nozzles or vanes operated with cold air. [10], [11]

Selective Laser Sintering (SLS)

Selective Laser Sintering is an AM method based on selective sintering of a polymer powder usually nylon powder and composite mixtures by a high-power laser. This technology provides an interesting option for small-scale turbomachinery since the height of individual layers start from very low thickness (around 50 μm). Together with no need for supporting structures, it provides decent surface quality, even without further polishing and with sufficient circular tolerances of the rotor wheels. The temperature resistance of the materials is usually around 80-100°C and a bit over 100°C for composite materials. No turbomachinery applications nor references have been found in the literature which is to the utmost of interest to the authors as its features, such as accuracy, rigidity, price and surface quality, make SLS a truly promising technology for small to micro-scale low-temperature turbomachinery applications.

Very similar technology to SLS is HP's *Multi Jet Fusion* (MJF), which also belongs to the polymer powder bed fusion family of the AM methods, and it also uses nylon as the main material. The main difference between MJF and SLS is the heat source. SLS uses a laser to scan and sinter each cross-section, while MJF uses ink as a fusing agent, which is dispensed on the nylon powder and thus promotes the absorption of infrared light. An infrared energy source then passes over the building platform and fuses the inked areas. This technology has the advantages of SLS technology and is cheaper per printed piece. Also, the dimensional accuracy as measured on the 120mm rotor wheel was the highest amongst all of the AM methods. This makes this technology promising for prototyping of turbine flow components for cold aerodynamic testing.

Direct Metal Laser Sintering (DMLS)

Direct Metal Laser Sintering technology is presented as one of the major AM technologies, which works on a similar principle as SLS, but with metal powders. The minimal layer height is similar to SLS, but the support structures are necessary, and the resulting surface roughness is very high. Altogether these factors limit the application for turbomachinery in the as-printed state. On the other hand, most references have been found for this AM technology in the literature. The possibility to print cooling channels directly without drilling has been successfully explored for high temperature turbochargers for automotive. [12], [13] A small radial turboexpander for Organic Rankine cycle (ORC) was manufactured by SLS method by the author's collective from Indonesian Institute of Sciences. The aluminium-silicon (AlSi) powder was used for the sintering of the rotor wheel. [14] Finally, a research team from Auckland have modelled, and successfully 3D printed a ultra-micro gas turbine rotor of several watts of mechanical power output using DMLS with Ti64 alloy powder. [15]

Material Jetting (MJ)

Material jetting is a group of AM technologies that utilize layer-by-layer photopolymerization of the materials solidified by UV curing such as SLA, but this technology allows for different materials to be used within the same printed part. The printer dispenses and jets the material from a nozzle of the movable print head onto the build platform where these droplets of material are cured by the UV light. Support structures are a necessity for these parts and these are often made of a material that can be later removed by melting or peeling off. This also differs the MJ technology from the SLA, which inherently must use the same material for the supports and for the printed part.

A very similar experimental investigation to the one of the authors of this paper was conducted by researchers from the University of Birmingham. [16] The authors have manufactured the flow components using PolyJet technology (MJ with wax support

structures) and also performed cold aerodynamic testing in a similar setup, evaluating the overall isentropic efficiency on several pressure ratios and rotational speeds. Moreover, the authors were also studying the effect of varying the blade length of the additively manufactured stator and rotor wheels. The experimental study validated a CFD analysis of the fluid flow. Results showed that the 8 mm blade height micro-scale axial turbine using a rotational speed of 16000RPM achieved the best performance in terms of power output of around 800W and isentropic efficiency of 47.1%, with almost a 15% deviation from the CFD results.

Experimental method

Various combinations of rotor and stator wheel were tested to investigate several tasks. For the first generation, the combinations were made from stators and rotors made by DMLS, SLS, FDM and in two versions of chord length short chord and long chord. The DMLS stator wheels were tested with different finishing methods and with added support features to investigate these effects on the turbine performance.

For the second generation, there were three variants of nozzle segment manufacturing methods SLA, SLS and DMLS - and three variants for the rotor - SLA, SLS and MJF. All combinations of the manufacturing methods, both for the nozzles and rotors were investigated. Detailed information regarding the first and second generation designs follow.

Proof-of-concept first generation turboexpander

This proof-of-concept 1st gen turboexpander was designed to operate with air and 30 kJ/kg enthalpy head at a design pressure ratio of 1.4. The low design pressure ratio was chosen for the sake of a safe operation of the machine and not to run into high rotational speed and fluid speeds, respectively. The final design of the first-generation proof-of-concept experimental turbomachine is displayed in Figure 2. The geometrical parameters and the design procedures of this turbine are then extensively discussed in [17]. The midspan diameter was chosen as 120 mm and the design rotational speed of 15 000 rpm.

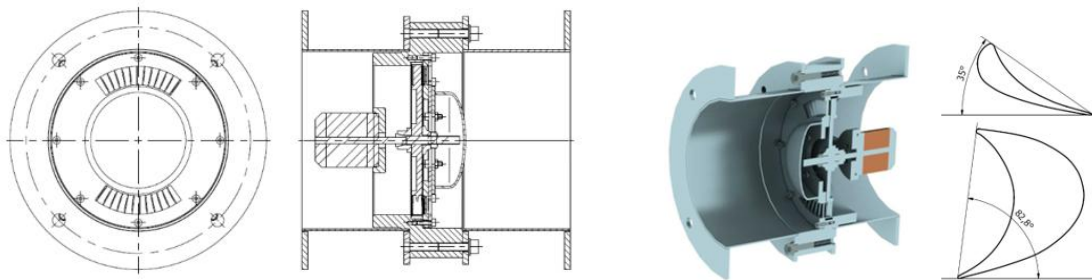


Figure 2 Design of the first-generation proof-of-concept turboexpander and detail of guide vane and rotor blade shapes S-90-12A and R-26-17A; source [17]

The flow components of the micro turboexpanders of the first generation were designed according to the methodology and loss correlations for large scale steam turbines from the 1950s. The first generation was designed in two variations: *long* and *short* chord. These two differ in the number of blades in the stator and rotor wheel and as the name indicates, in the chord length, with approximately the same pitch to chord ratio.

The main goal of the first generation was to prove that the concept is reliable and gives valid data for isentropic efficiency evaluation of turbine assemblies with flow components

made of several different materials and AM technologies. These AM technologies differ in the resulting surface roughness, geometrical precision and strength of the material, and the goal was to evaluate these effects on the overall efficiency of the turbomachine. In Figure 3 are shown the details of the blading of the 1st gen stator wheels.



Figure 3: Investigated 1st gen stator wheels, from the left – DMLS as-printed short chord stator, DMLS polished long chord stator and DMLS stator with the functional supports, SLS long chord, SLS short chord, FDM long chord

The values of surface roughness of the blades are summarized in Table 2. The surface roughness measurements were performed inside the channel on the pressure side of the blade in the fluid flow direction, and the total values were averaged from five measurements with the lowest and the highest values of Ra left out, the accuracy of the roughness meter is declared as 10% of the measured Ra value.

The lowest Ra was measured for the polished stainless steel DMLS blades and the highest for the same blades in the as printed state. The plastic wheels were without any post processing, and the same goes for the stators as well as the rotors. A variation of the DMLS stator wheel with *functional supports* (as recommended by the manufacturer) was tested. These supports were added for improved print quality, and the goal was to experimentally verify what will be the impact on the overall turbine performance with these extra features.

Table 2 The surface roughness of the first-generation stator blades, measured inside the channel in the fluid flow direction

AM technology	Value	Units
Selective Laser Sintering (SLS, nylon)	5	µm
Fused Filament Extrusion (FDM, ABS)	7.1	µm
Laser Powder Bed Fusion (DMLS, stainless steel) - as printed	20	µm
Laser Powder Bed Fusion (DMLS, stainless steel) - polished	0.9	µm

During the experiments, the 1st generation turboexpanders were operated with only one admitted stator nozzle for long chord stator wheels and 3 nozzles for short chord wheels (equal to the degree of admission e of 6.7 %) with an aim to reduce the power output and the cost and size of the power electronics.

Second generation micro turboexpander

As a next step forward in the research of additively manufactured micro turboexpanders towards an ORC application, another geometry of the rotor and stator nozzles were designed specifically for the hexamethyldisiloxane and with supersonic convergent-divergent Laval nozzles. The second generation turbine assembly is displayed in the drawings and a cross-section in Figure 4. These flow components were designed in a way that it would also be possible to test this combination with pressurized air in the same test rig as the first-generation turbine and verify the possibility to transfer the results obtained from the cold aerodynamic testing of the AM flow components to the hot-fired ORC tests.

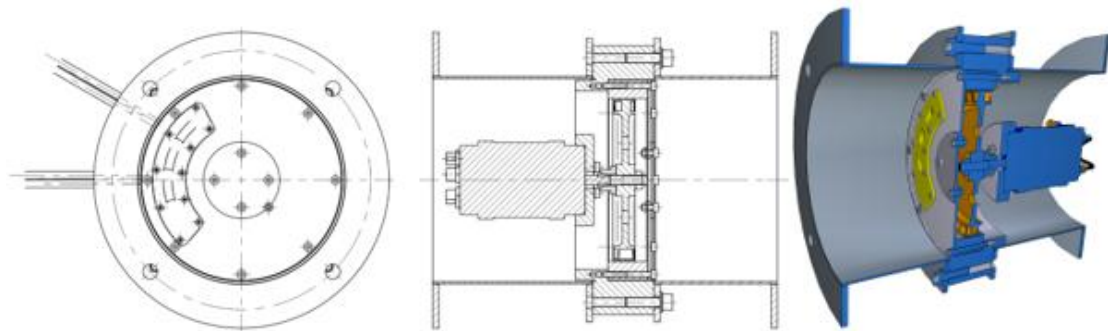


Figure 4 Design of the second-generation ORC turboexpander and a cross-sectional view of the model

This second generation also featured improved sealing and fitting of the assembly, which significantly reduced lead time for changing the flow components. With pressurized air though, the second generation of course operated in highly off-design condition, and the results yield from these experiments cannot be fully compared with the first gen.

Experiments with the second-generation design were more focused onto gaining experience operating the turbine and also to compare various combinations of AM methods and materials for 3-D printing with different surface quality and geometrical precision.

The nozzle segments and rotor wheels that were experimentally investigated are shown in Figure 5. Note the apparent drilling holes from the dynamic balancing (G 1.2 ISO 1940-1 precision) of the rotor wheels and that the SLA wheel on the left is after an accident.

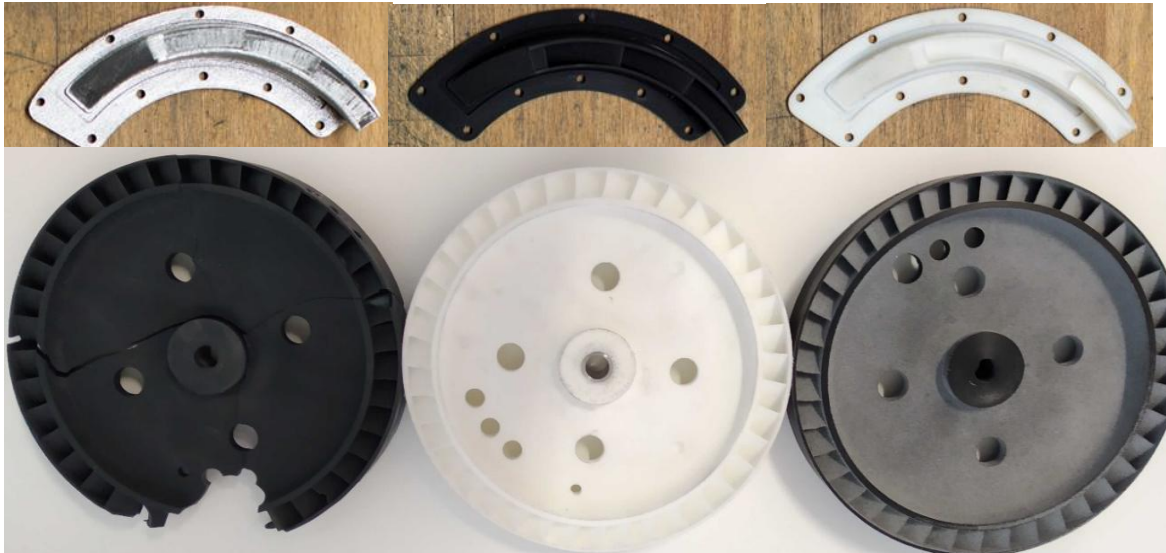


Figure 5 Second generation stator nozzles (upper image) and rotor wheels (lower image); from upper left to lower right – DMLS stainless steel, SLS nylon, SLA resin, SLA resin (shattered), SLS nylon, MJF nylon

Again, as for the 1st gen turboexpanders, the surface roughness of the nozzles was measured and with the same procedure. The results of the surface roughness measurement are reported in Table 3.

Table 3 The surface roughness of the second-generation nozzle elements, measured inside the channel in the fluid flow direction

AM technology	Value	Units
Selective Laser sintering (SLS, nylon)	5.7	µm
Stereolithography (SLA, resin)	5.4	µm
Laser Powder Bed Fusion (DMLS, stainless steel) - polished	3.1	µm

Description of the test rig and experimental data acquisition and evaluation methodology

The main objective of the experiment was to test various additive manufacturing methods and their feasibility for turbomachinery, respectively, how their accuracy of the prints, mechanical properties and the surface roughness affects the overall isentropic efficiency of the machine.

To perform such experiments, some equipment of the test rig was designed and built with a configuration according to Figure 6 exclusively for this purpose. The measurements were conducted at the Test bench for compressed air drives and technology (PDLT) at OTH Amberg-Weiden.

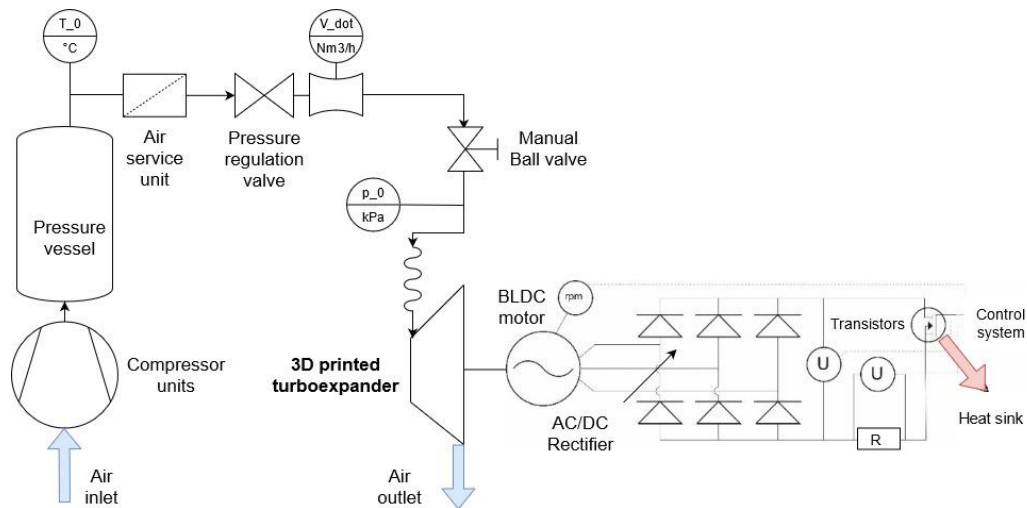


Figure 6 Schematics of the test rig configuration

Apart from the turboexpander itself, an electrical device that serves as an integrated instrumentation and control system but also as a variable load and a heat sink was developed. All the electrical components were fitted into a frame that is easily transportable and mobile. The rotor of the turboexpander is directly coupled to the BLDC motor operating in the generator regime. A three-phase alternating current is produced by the generator. It is then rectified, and the overall voltage is measured. A calibrated precise resistor is used for current measurement by measuring the voltage drop. The generator speed and electrical parameters are measured. The rotational speed is measured from the generated phase-voltage frequency, which is directly proportional to the generator rotational speed by fixed periods per revolution. For the details regarding the measurement devices and data acquisition procedure, a fellow reader is referenced to [18].

The raw data are processed to evaluate the isentropic efficiency of each turbine assembly at steady states for any given rotational speed with a certain rpm step ramping up to the maximum rpm and slowing down. These values are then averaged. The thermodynamic properties of air are calculated using the fluid properties database REFPROP. The electrical efficiency of the generator (Turnigy SK3-6364-245) is calculated by the TorqueCalc tool at eCalc website¹ as a function of rotational speed and torque. An assumption of equal efficiency in the motor and generator regime is presumed for the same mechanical power output on the shaft and the efficiency of the generator. The iteration loop for generator efficiency calculation was automated using GoalSeek function and bilinear interpolation. From the measured value of mechanical power and calculated isentropic power, one can obtain the final value of the isentropic efficiency at each steady state of each assembly at a given pressure ratio. The mechanical losses in bearings are included in the generator efficiency.

Discussion and Results

This chapter presents the results from the cold aerodynamic experimental campaign of the first and second generation additively manufactured axial impulse micro turboexpanders. There were various tasks to be performed and phenomena to be studied and analyzed from the experimental trials.

¹ <https://www.ecalc.ch/torquecalc.php>

In total, over 20 experimental campaigns were conducted at the test rig; each for four pressure ratios (PR 1.3-1.6) by varying the inlet pressure of the compressed air; ergo over 80 efficiency curves were measured in a region of 3000 to 12000 rpm with a step of approximately 500 rpm.

First generation results and discussion

For the 1st gen turboexpander experiments, eight combinations of rotor and stator wheels are presented. For the 1st generation wheels, it is apparent that there is a significant difference in between the assemblies depending not only on the manufacturing method, the material and the resulting surface roughness but also on the short or long chord version of the stator wheel.

Initially, the suitability of either a long or short chord stator wheel was assessed. These two were designed to study the impact that the length of the chord and the number of blades, respectively, the Reynolds number effect would yield in this microturbine design. This has been studied on the selective laser sintered flow components. The results of this analysis are shown in Figure 7a, and it is apparent that the assembly with a stator wheel with a longer chord and lower number of blades was significantly better in performance at all pressure ratios compared to the stator wheel with a shorter chord. This has also been confirmed for other configurations with long chord stator wheels.

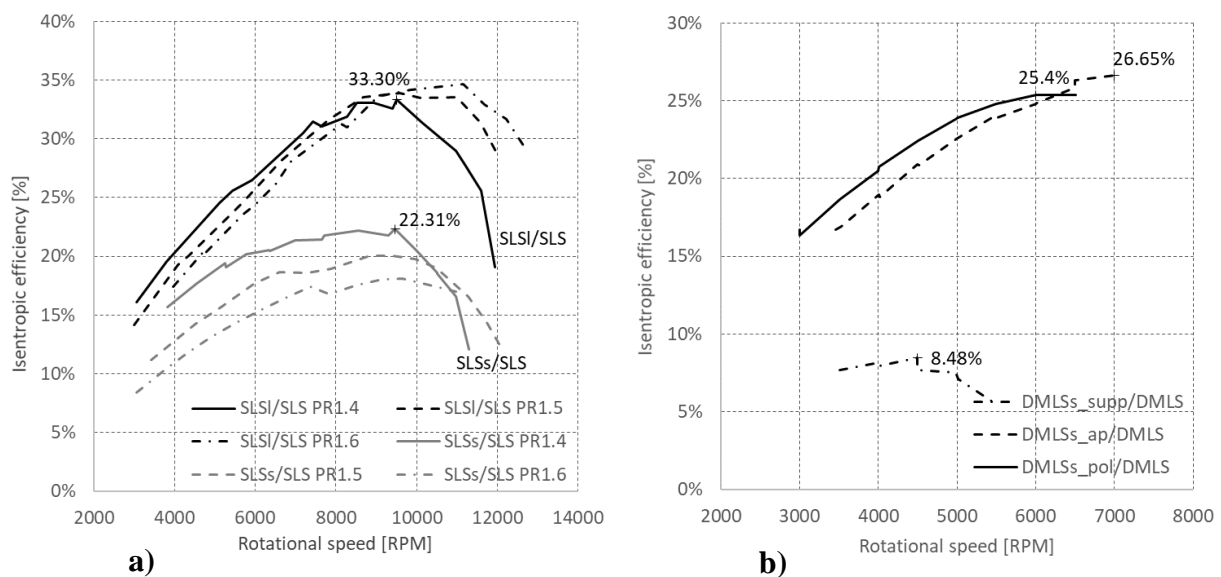


Figure 7 a) Experimental comparison of the long and short chord SLS stator wheel (rotor also SLS) at different PRs; **b)** Effect of the surface roughness on the isentropic efficiency at PR 1.4; stator DMLSs with various post processing

The authors argue that it may be caused by several effects; one being that for the long chord stator, only one nozzle segment was admitted by the pressurized air but three nozzle segments for the short chord ones. Therefore, the profile losses caused by the surface roughness are higher and also since there is a finite width of the trailing edge of the blades, some mixing of the streams occurs at the outlet. Also, as the nozzle channel is longer for the long chord stators, the flow is fully attached to the nozzle geometry, and the shape of the nozzle directs the fluid flow at design outlet angle, which might not be the case for the rather short chord lengths. Finally, the geometrical precision and accuracy of the AM

method for the short chord blade, relatively to the chord length, is much higher and the blades may not be shaped precisely according to the design.

One of the other tasks was to investigate the effect of the friction losses of the DMLS steel flow components with different finishing methods and to compare the impact that improving the surface roughness has on the overall isentropic efficiency of the turbomachine. In Figure 3, the as printed DMLS stator wheel, polished stator wheel and the stator wheel with functional supports as suggested by the manufacturer is shown. This effect is displayed in Figure 7b, where the supports have proven to be beneficial from the manufacturing point of view, but as anticipated, completely unusable from the aerodynamic viewpoint. Also, it is apparent, that especially in the region of low rotational speed, the polished nozzle surface improves the isentropic efficiency by a significant margin, which diminishes with increasing RPM.

At the low Reynolds number region during the low rotational speed, the increased surface roughness may act as a turbulator which interrupts the large laminar viscous sublayer near the blade surface, which improves the overall performance due to lower profile losses. As the turbine operating point moves towards higher rotational speed, the flow gets into a fully turbulent region in which the effect of the high surface roughness is adverse. However, it is this high rotational speed region, in which the as printed stator assembly is superior in performance when compared to the polished one. This goes against the prediction, and the authors suggest conducting another experimental campaign with these two assemblies to verify this observation.

The next effect that was studied was the effect of the partial admission on the turbine performance and the validity of the correlation for the ventilation losses (see equation below) originally adopted from [19].

$$P_V = 0.925 \cdot \left[(1 - e) \rho_3 \cdot \left(\frac{n}{60} \right)^3 \cdot D_{\text{mid}}^4 \cdot 4.5 \cdot h_{\text{rotout}} \right]$$

This has been experimentally verified by performing measurements first for a single partial admission segment (one nozzle) and then for double the arc (two nozzles). The ventilation loss model should reflect the twofold increase in partial admission, and the experimental results would match the estimate from the 1-D model. The results can be observed in Figure 8b, and it is apparent that doubling the partial admission arc, the maximum efficiency point moves towards higher rotational speed and also increases by 7 % points, this is most likely caused by that the design degree of admission of the turbine was 34% and in other cases for the 1st gen trials, the turbines were operated with only 6.7 % degree of admission. Doubling it then moves the turboexpander closer to its design point, and it goes in hand with an increase of isentropic efficiency.

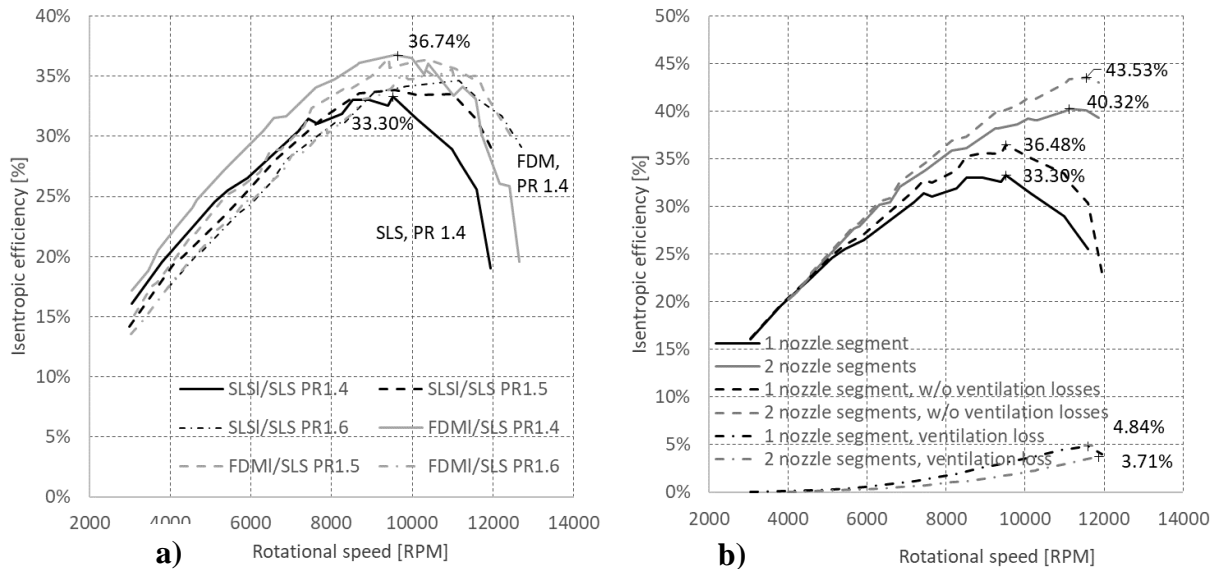


Figure 8 a) Comparison of FDM and SLS (long chord) stator wheels and the effect of 3-D printing methods on the isentropic efficiency; both with SLS rotor; measured at three different PRs; **b)** Effect of the partial admission on the ventilation loss correlation and turbine performance; both stator and rotor - selective laser sintered (SLS, long chord stator)

Furthermore, the operation of the turbine and especially the rotational speed control was remarkably improved when adopting double partial arc admission. The authors consider this to be a result of balancing a counterforce by adding an additional fluid stream since the double partial arc admission was realized by adding an additional admitted nozzle at 180° on the opposite to the other nozzle.

Since the results of isentropic efficiency without ventilation loss are quite different to each other, at these small power and very low partial arc admission, it appears as not directly applicable, respectively another effect associated with partial admission arc extent is present or the nature of rough printed parts and extremely low partial admission does not allow to use the applied correlation.

Next on the list was the comparison of FDM and SLS stator wheels, especially the effect of different surface roughness and surface nature of each 3-D printing method. FDM components are distinguished by the specific layer-by-layer structure, which is the result of the manufacturing procedure, and it increases the roughness of the surface especially in the direction perpendicular to the build direction.

In this case, the layer structure was indeed built perpendicularly to the flow path, so it was anticipated that this FDM stator wheel would yield worse performance compared to the more uniform and less rough SLS stator wheel. However, the latter was the case, as one can observe in Figure 8a, and perhaps as a result of the same effect as with the DMLS steel stators, the rougher the surface of the nozzles, the higher was the performance. Contradictory to the expected behaviour, despite having a rougher surface by 40 % compared to the SLS, the turbine assembly with FDM stator wheel was superior in terms of isentropic efficiency for any measured pressure ratios.

In spite of being the most affordable and common 3-D printing technology, ultimately and quite surprisingly, the FDM manufacturing method turned out to achieve the best values of isentropic efficiencies amongst all of the measured 1st gen turbine assemblies (excluding the double admission experiment). This conclusion, however, should not be adopted to other turboexpanders without at least a preliminary assessment of the fluid flow regime.

Finally, the effects of surface treatment such as sanding, polishing, metal plating, or chemical treatment of the plastic 3-D printed parts have not been analyzed despite the potential it may bring to the turboexpander performance. This may be considered a potential for future work.

Second generation results and discussion

As the 2nd gen turboexpander was designed to operate with hexamethyldisiloxane, and also the flow components were designed according to that, the goal was to identify how transferable are the cold aerodynamic tests for an ORC turbine design. Additionally, and similarly to the 1st gen tests, various additive manufacturing technologies were used for the nozzle segments and rotor wheels. The effect of the resulting surface roughness on the isentropic efficiency and also the operational parameters of the turbines were investigated and compared amongst the AM methods. Some of the AM methods were also adopted for the 1st gen wheel (SLS and DMLS), and some of them were new (SLA, MJF). In total, nine combinations of nozzle segments and rotor wheels were measured, differing only in the material and AM method, not in the number of blades or nozzle segments nor the degree of admission.

Contrary to the 1st gen experiments, a very narrow band of isentropic efficiencies in between 25 and 30 % was obtained for different AM technologies. Moreover, the turboexpanders showed rather flat behaviours of their efficiency curves with increasing rotational speed and especially with an increasing pressure ratio. The highest overall isentropic efficiency was measured for the pair of SLS nozzle segments and SLS rotor wheel, again despite having the highest surface roughness of the measured nozzle segments. This combination was superior at any measured pressure ratio but only by a small margin compared to the rest of the nozzle/rotor combinations. This can also be seen in the efficiency chart in Figure 9 for the design pressure ratio.

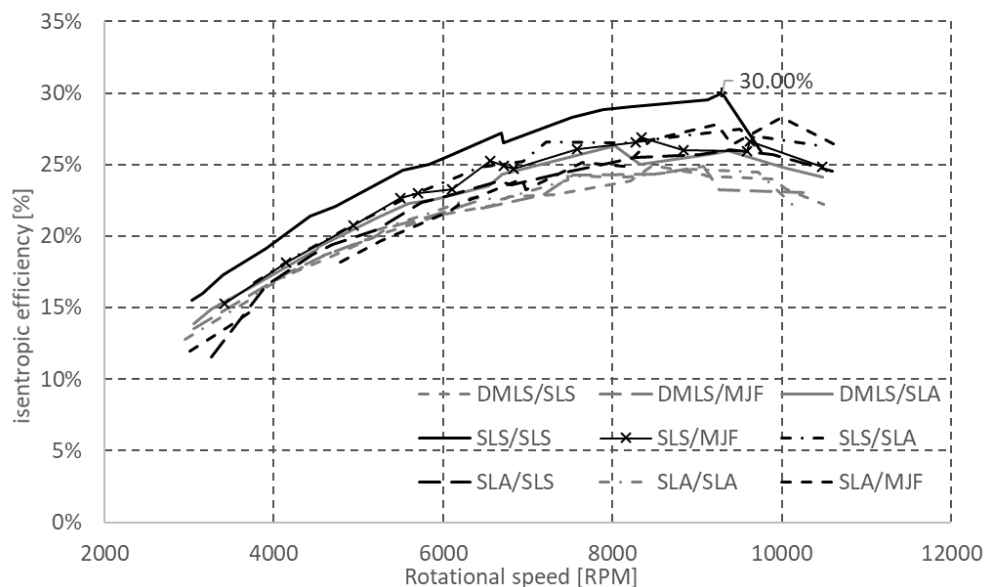


Figure 9 Second generation design, different AM methods stator/rotor; pressure ratio of 1.4

From the operational standpoint, it was also an overarching goal amongst all of the experiments to evaluate the effect of geometrical inaccuracies of the AM flow components on the assembly, fitting, sealing and safe operation of the turbines. Some mechanical issues were observed as well, mostly as a result of a dynamic runout of the rotor wheel caused by the inhomogeneity of the additive manufactured part and also by the overhung rotor concept, which resulted in further dynamic imbalance and finally bending the shaft. Issues with an inaccuracy of some of the manufacturing methods were also observed, most apparent for the SLA manufacturing technology. The inaccuracies negatively affected the fitting and assembly of the parts. Also, some problems with a different rate of thermal expansion of the plastic wheels and the aluminium stator frame occurred, which lead to troubles with exchanging the prototyped stator wheels.

Summary/Conclusions

This paper brought an insight into the problematics of additive manufacturing and especially its potential for turbomachinery. This potential was experimentally verified by cold aerodynamic testing. Various aspects such as geometrical precision, accuracy, surface roughness, inhomogeneity or material integrity of the 3D printed flow components and their respective impacts on the turboexpander performance were investigated on a test rig built specifically for that purpose.

Furthermore, the results from the experimental campaign with four different additive manufactured (FDM, SLS, SLA and MJF) plastic flow components are reported within the scope of this work. The highest obtained efficiency was around 40% with nylon components from SLS method. Each of the AM methods are finally evaluated based on the authors' experience from the experimental campaign within Table 4. The conclusions drawn from the cold air testing will then be transferred towards implementing additively manufactured parts in the development of an ORC turboexpander.

Table 4 Evaluation of the four investigated plastic additive manufacturing methods based on experience from the experiments

Technology	FDM	SLS	SLA	MJF
Accuracy	-	+	-	++
Homogeneity	-	+	+	++
As printed surface roughness	-	+	++	+
Price per part printed	++	+	-	++
Mechanical properties	-	+	-	+
Durability	-	+	-	+
Measured efficiency	++	++	-	+
Overall performance	-	+	-	++

Acknowledgements

This work has been supported by project SGS21/111/OHK2/2T/12 Micro-scale turbines for distributed energy systems.

References

- [1] A. P. Weiß, "Volumetric expander versus turbine – which is the better choice for small ORC plants," in *3rd ASME ORC Conference, Brussels (Belgium)*, 2015, pp. 1–10.

- [2] A. P. Weiß *et al.*, “Customized ORC micro turbo-expanders - From 1D design to modular construction kit and prospects of additive manufacturing,” *Energy*, p. 118407, Jul. 2020.
- [3] V. Novotny, J. Spale, B. B. Stunova, M. Kolovratnik, M. Vitvarova, and P. Zikmund, “3D Printing in Turbomachinery: Overview of Technologies, Applications and Possibilities for Industry 4.0,” in *ASME Turboexpo 2019*, 2019.
- [4] V. Novotny, J. Spale, B. B. Stunova, M. Kolovratnik, M. Vitvarova, and P. Zikmund, “3D printing in turbomachinery: Overview of technologies, applications and possibilities for industry 4.0,” in *Proceedings of the ASME Turbo Expo*, 2019, vol. 6.
- [5] W. (Siemens P. and G. division) Meixner, “Additive Manufacturing Breakthrough with 3D printed Gas Turbine Blades,” 2017. [Online]. Available: <https://www.siemens.com/press/pool/de/pressemittelungen/2017/power-gas/PR2017020154PGEN.pdf>.
- [6] K. Bassett, R. Carriveau, and D. S.-K. Ting, “3D printed wind turbines part 1: Design considerations and rapid manufacture potential,” *Sustain. Energy Technol. Assessments*, vol. 11, pp. 186–193, Sep. 2015.
- [7] K. Rahbar, S. Mahmoud, R. K. Al-Dadah, N. Moazami, and S. A. Mirhadizadeh, “Development and experimental study of a small-scale compressed air radial inflow turbine for distributed power generation,” *Appl. Therm. Eng.*, vol. 116, pp. 549–583, 2017.
- [8] A. M. Al Jubori, F. N. Al-Mousawi, K. Rahbar, R. Al-Dadah, and S. Mahmoud, “Design and manufacturing a small-scale radial-inflow turbine for clean organic Rankine power system,” *J. Clean. Prod.*, vol. 257, p. 120488, 2020.
- [9] M. Meier, W. Gooding, J. Fabian, and N. L. Key, “Considerations for Using Additive Manufacturing Technology in Centrifugal Compressor Research,” *J. Eng. Gas Turbines Power*, pp. 1–10, 2019.
- [10] I. Hernandez-Carrillo, C. Wood, and H. Liu, “Development of a 1000 W organic Rankine cycle micro-turbine-generator using polymeric structural materials and its performance test with compressed air,” *Energy Convers. Manag.*, vol. 190, no. December 2018, pp. 105–120, 2019.
- [11] J. E. Grady *et al.*, “A Fully Nonmetallic Gas Turbine Engine Enabled by Additive Manufacturing Part I: System Analysis , Component Identification , Additive Manufacturing , and Testing of Polymer Composites,” no. May, 2015.
- [12] Y. Zhang, T. Duda, J. A. Scobie, C. M. Sangan, C. D. Copeland, and A. Redwood, “Design of an Air-Cooled Radial Turbine: Part 1 — Computational Modelling,” in *Volume 8: Microturbines, Turbochargers, and Small Turbomachines; Steam Turbines*, 2018, p. V008T26A013.
- [13] Y. Zhang, T. Duda, J. A. Scobie, C. M. Sangan, C. D. Copeland, and A. Redwood, “Design of an Air-Cooled Radial Turbine: Part 2 — Experimental Measurements of Heat Transfer,” in *Volume 8: Microturbines, Turbochargers, and Small Turbomachines; Steam Turbines*, 2018, p. V008T26A014.
- [14] M. Arifin, B. Wahono, E. Junianto, and A. D. Pasek, “Process manufacture rotor radial turbo-expander for small scale organic Rankine cycles using selective laser melting machine,” *Energy Procedia*, vol. 68, pp. 305–310, 2015.
- [15] R. D’souza and R. N. Sharma, “An experimental study of an ultra-micro scale gas ‘Turbine,’” *Appl. Therm. Eng.*, vol. 163, p. 114349, Dec. 2019.
- [16] K. M. Khalil, S. Mahmoud, and R. K. Al- Dadah, “Experimental and numerical investigation of blade height effects on micro-scale axial turbines performance using compressed air open cycle,” *Energy*, vol. 211, p. 118660, 2020.
- [17] V. Novotny *et al.*, “Design and manufacturing of a metal 3D printed KW scale axial turboexpander,” in *Proceedings of the ASME Turbo Expo*, 2019, vol. 8.
- [18] J. Spale, V. Novotny, V. Mares, and A. P. Weiss, “3D Printed Radial Impulse Cantilever Micro-Turboexpander for Preliminary Air Testing,” *AIP Conf. Proc.*, 2021.
- [19] C. Pfleiderer and H. Petermann, *Strömungsmaschinen*. Springer-Verlag, 7. Auflage , 2004.

Artificial Neural Network based marine diesel engine modelling

Joseba Castresana^{a*}, Gorka Gabiña^a, Leopoldo Martin^b, Zigor Uriondo^b

^a AZTI, Marine Research, Basque Research and Technology Alliance (BRTA) - Txatxarramendi ugarte
0-48395, Sukarrieta

^bDepartment of Thermal Engineering, University of the Basque Country UPV/EHU, Alameda Urquijo s/n
48013 Bilbao, Spain

Abstract

Condition based maintenance (CBM) is one of the most effective instruments to avoid failures in marine diesel engines. If engine performance is accurately predicted by a model, deviations between real-modelled results might be good indicators when a certain failure is about to happen in the real engine. On this basis, data-driven modelling techniques offer high accuracy and low calculation times being able to predict engine performance in real-time applications. In this contribution, Artificial Neural Networks (ANN) were used to fully model a YANMAR-6HYM-WET diesel engine, predicting 31 performance parameters (i.e cylinder exhaust gas temperatures, oil temperatures etc.) and validating the model with real engine tests. Among the results, a faulty sensor was identified during the training phase of the ANN. All the 31 predicted performance parameters showed mean absolute percentage errors below 7.5%. Exhaust gas temperature, torque and cooling water system temperature predictions showed highest accuracy levels, while air pressure measurements in turbocharger outlets and engine inlet showed highest error levels due to their small range of variation. Prediction accuracy was discussed among different parameters, analysing the robustness of the designed ANN when predicting multiple outputs. Finally, different procedures were presented to consider parameters with highest error levels in fault detection or diagnosis systems.

Keywords

- Marine diesel engine
- Engine modelling
- Artificial Neural Network
- Multiple Parameter Prediction

***Corresponding author:** Joseba Castresana Larrauri

Phone: +34 667183668

Email: jcastresana@azti.es

Email addresses: ggabina@azti.es; leopoldo.martin@ehu.es; zigor.uriondo@ehu.es

Nomenclature

CBM	Condition-Based Maintenance	HC	Hydrocarbons
ANN	Artificial Neural Networks	CO₂	Carbon dioxide
SFOC	Specific Fuel Oil Consumption	BTE	Brake thermal efficiency
T_{exh}	Exhaust gas temperature	ISO	International Organization for Standardization
BSFC	Brake specific fuel consumption	TC	Turbo-compressor
CNG	Compressed Natural Gas	MSE	Mean Squared Error
NO_x	Nitrogen oxides	MAPE	Mean Absolute Percentage Error
CO	Carbon monoxide	R	Regression coefficient

Introduction

Marine transport has a pivotal role in global trade, and it accounted for 46% of the value of the goods exported from and 56.2% imported to the European Union in 2019, being the most used mean of goods transport [1]. In the same year, 1355 incidents were registered in the European Union fleet, among which 295 were caused by propulsion loss [2]. In this context, condition-based maintenance is becoming a fundamental instrument to avoid failures in marine diesel engines and reduce the number of incidents given by propulsion issues. Some authors assume that the mean cost of a failure replacement is 10 time higher than that for a preventive replacement [3], so preventive maintenance is interesting in safety and economic terms.

On this basis, engine performance prediction is fundamental to detect deviations that may indicate early failures. Engine modelling techniques have thus become a subject of particular concern in recent years [4]. Many research works have focused on thermodynamic modelling techniques to simulate engine performance. Some authors have developed theoretical assessments to ascertain different performance parameters [5, 6]. Others have preferred to use different software for thermodynamic simulation [7-10]. According to Albrecht et al [11], computational time may depend on the dimensionality of the model, but in spite of choosing low dimensional thermodynamic models, calculation time may be too high for real time applications as stated by Castresana et al. [12].

With the aim of reaching high prediction accuracy levels and low time calculations, machine learning techniques have been widely used in the last decade. Cai et al. [13] used Support Vector Machine for engine subsystem state classification. Atmanli et al. [14] used response surface methodology to reach optimum alternative fuel blends. Some authors have also compared different machine learning techniques to reach optimum models. Flett and Bone [15] compared five different machine learning classification techniques for valve train fault detection, concluding that Naïve Bayes gave the best overall performance in terms of detection and classification accuracies. Moosavian et al. [16] compared K-nearest neighbour and artificial neural networks for fault detection on a main engine journal bearing, studying different architectures and concluding ANN with

5 neurons in hidden layer gave best overall performance. Most recently, Xu et al. [17] demonstrated that combining different data-driven models the performance of a wear detection system could be enhanced.

ANNs offer high robustness and accuracy levels, being one of the most used diesel engine modelling techniques in the last decade [4]. Part of the ANN research has focused on the classification of different faulty situations of the engine. Srihari et al. [18] identified worn-out gear case and cracked tooth case by using a multilayer feed forward neural network. Liu et al. [19] developed a misfire detection model by using artificial neural network models.

Apart from being applied to classify among different engine faults, artificial neural networks have been widely used to predict engine performance parameters. Parlak et al. [20] studied the ability of an ANN to predict SFOC and T_{exh} , proving that a well-trained network could be fast and accurate enough to evaluate diesel engine parameters. Yusaf et al. [21] predicted brake power, torque, BSFC and exhaust emissions for a CNG/diesel dual-fuel and compared the results to pure diesel fuelled results, concluding lower maximum power and emissions (NO_x , CO and CO_2) for dual-fuelled case.

Artificial Neural Networks provide great advantages in certain research fields as it is diesel engine operation whilst using alternative fuels. As mentioned before, these are data-driven modelling techniques, so the network does not necessarily have to know about alternative fuel chemical reactions to give accurate results. This has led many research works to focus on engine ANN modelling while using alternative fuels [22-24]. Besides, this has resulted in many other studies predicting emission parameters by using ANN [25-27]

Concerning the marine field, ANN has been used by many authors to model marine diesel engines. Basurko et al. [28] predicted 15 performance parameters with an ANN comparing predicted values to real values to identify different faults in marine operational environment. Noor et al. [29] compared ANN and mathematical model accuracies when predicting brake power, BSFC, BTE, volumetric efficiency, T_{exh} and NO_x in a 6-cylinder marine diesel engine. They concluded that ANN was a reliable prediction tool in terms of accuracy levels, showing better overall performance than the mathematical model.

Many of the previous studies selected few input/output parameters for their Neural Networks without a previous correlation study. In this context, some authors carried out the selection by pure trial and error. For instance, Porteiro et al. [30] concluded after several attempts that coolant temperature and oil temperature were unnecessary for their model, removing them from the input vector. Alternatively, Roy et al. [31] used the Pearson Correlation Coefficient to examine the correlation between different parameters to choose the most relevant ones for the neural network input and outputs. Jafari et al. [32] carried out a combination of correlation matrix, Principal Component Analysis and Hierarchical clustering to ascertain the correlations between parameters from different groups of a six-cylinder diesel engine.

Furthermore, most of the existing studies have not dealt with multiple output models, considering reduced output quantities in the majority of the contributions. Lazakis et al. [33] conducted a fault detection system based on solely T_{exh} prediction. Shailaja et al. [26] predicted CO, NO_x and HC only including 3 different outputs for their model. Higher output dimension models could be found in [31, 34] with 5 outputs, [29] with 6 and [35] with 8 outputs. Nevertheless, none of the presented studies included more than 10 outputs with some exceptions [28]. Some authors even designed separate ANNs for each output when higher output dimensions were presented [36].

In the present study, a YANMAR-6HYM-WET marine diesel engine is fully modelled, predicting 31 performance parameters throughout the whole engine. Prediction accuracy is discussed for different parameters predicted by the network, identifying which ones have stronger correlation with the engine performance. Likewise, it is concluded which parameters should be included in a fault detection system and which ones should be avoided in order to avoid misclassifications.

Materials and methods

Testing bench and equipment

The engine used for the experimental trials is a YANMAR-6HYM-WET six-cylinder marine diesel engine. This engine has twin turbochargers and is cooled with sea water; its characteristics are shown in Table 1. The engine load is controlled using a hydraulic brake which allows the user to manually change the load from 0% to 100% of the engine capacity. The acquisition system used to measure and acquire engine performance parameters is a National Instruments Compact FieldPoint which is directly connected to a Labview data acquisition software. Once the data is recorded, it is exported and pre-processed in Python3 to be introduced in the artificial neural networks.

Table 1 YANMAR-6HYM-WET engine characteristics

Parameter	Value	Unit
Manufacturer	YANMAR	[-]
Type of cycle	4 stroke medium speed	[-]
N cylinders	6	[-]
Nominal speed	2084	Rpm
Nominal power	424	kW
Compression ratio	15.18	[-]
Bore	132.9	mm
Stroke	165	mm
Air charge	Turbocharged	[-]

Figure 1 shows the engine scheme used for experimental trials. In total, 27 temperature and 7 pressure parameters were measured throughout the whole engine, as well as ambient conditions, engine torque and fuel consumption. Different colours were applied depending on the fluid measured by each sensor, according to the main colours set for different fluids in ISO14726 [37]. Table 2 shows the uncertainties of the different data

acquisition systems used in the experimental trials. Engine trials were carried out varying engine load from 0% to 100%. The acquired data base was used to train, validate and test the proposed Artificial Neural Network to later discuss accuracy among the different predicted parameters.

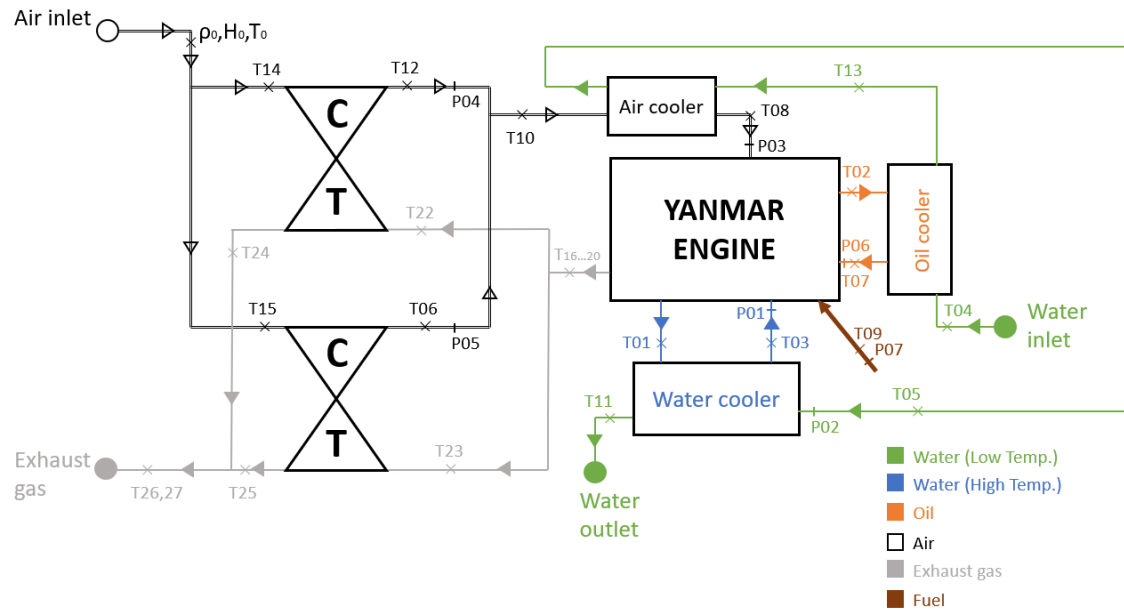


Figure 1 YANMAR-6HYM-WET engine data acquisition scheme

Table 2 Measuring instruments and uncertainties

ID	Unit	Instrument	Uncertainty
T01, T05, T09, T10, T13	[°C]	Pt100 temperature sensor	± 0.3 °C
T02, T03, T04, T06, T07, T08, T11, T12, [T14,...,T27]	[°C]	K Type Thermocouple	± 4%
ρ0,H0,T0	[kg/m ³], [%], [°C]	HD2001.1 meteorological station	ρ0: ±0.5mbar H0: ±1.5% T0: ±0.3%
P01, P02	[bar]	Pressure transmitter SEN 9601 B055	±0.5%
P06, P07	[bar]	Pressure transmitter SEN 9601 B075	±0.5%
P03, P04, P05	[bar]	Pressure transmitter KTP-D-F1	±0.25%
Engine speed	[rpm]	Kistler encoder Type 2614B	± 0.05%
Piston Position	[°]	Kistler encoder Type 2614B	± 0.02°
Torque	[Nm]	Kistler 4502A50RA	< 0.07%
Fuel consumption	[Kg/h]	Instrument: KRAL OME13flow metre	± 0.1%

Artificial Neural Network model

Artificial Neural Networks were selected to model the engine used in this case of study. Concretely, Feed Forward ANN were used for the simulation. As mentioned by Fine [38], the neural networks methodology enables to design nonlinear systems accepting large numbers of inputs, based solely on input-output relationships. Therefore, a medium speed diesel engine was set on different load conditions so as to acquire a database to train validate and test a Feed Forward Neural Network. Thus, 400 data samples of 40 different parameters (8 inputs and 32 outputs) were measured throughout the whole load spectrum of the engine. Data partition was 70%, 15% and 15% for training, validation and testing respectively, and 20 samples were randomly selected from testing data to analyse testing results visually. Figure 2 shows the ANN scheme proposed in this study, presenting selected inputs and outputs for the model.

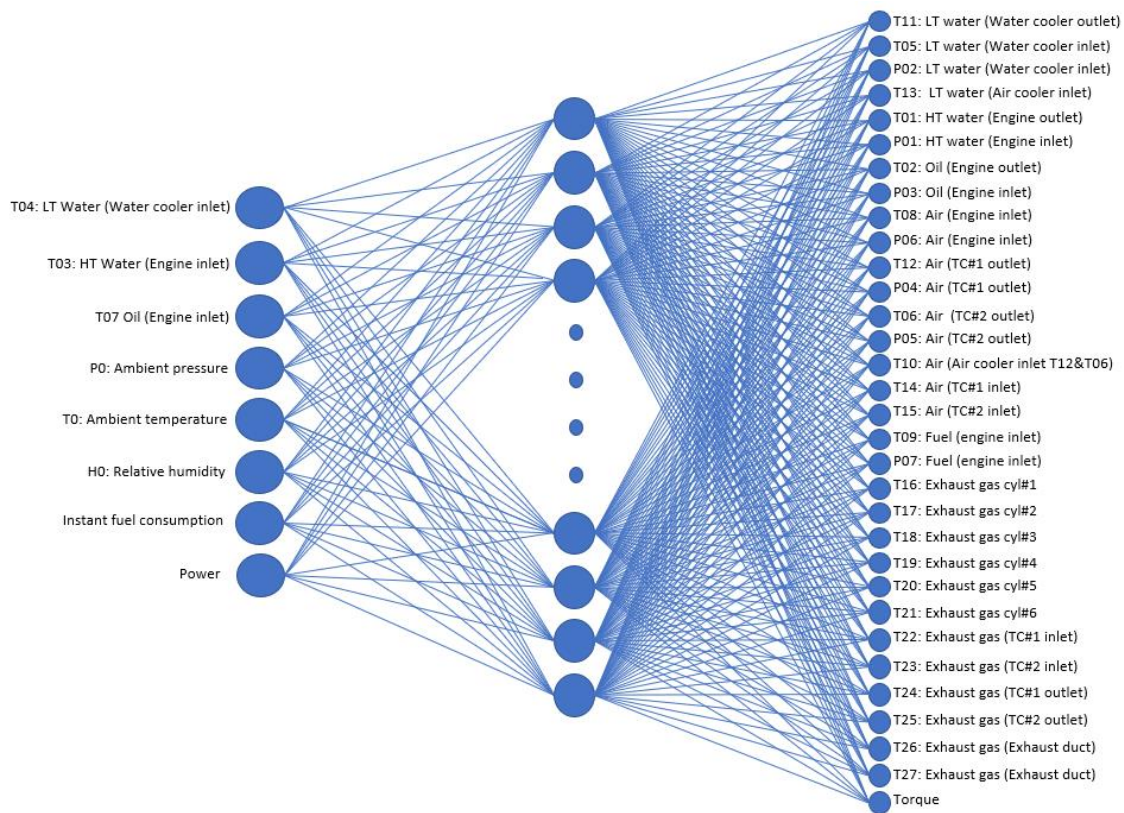


Figure 2 ANN scheme

The ANN was designed and implemented in Matlab, which in contrast to other ANN design methodologies allowed to select Levenberg-Marquardt algorithm for network training. This is a high order gradient based optimization algorithm, which was selected by Rezaei [39] as the most suitable training algorithm after being compared to other 12 training algorithms. Concerning transfer functions, hyperbolic tangent sigmoid and pure linear were selected for hidden and output layers respectively. Before optimizing the ANN structure, the network was proved with 25 neurons in hidden layer to analyse at first sight whether data was pre-processed successfully. Figure 3a shows the training phase regression in the first attempt. Target values near 0 and 1 presented many different outputs, which is represented as two vertical lines of points in these two target values.

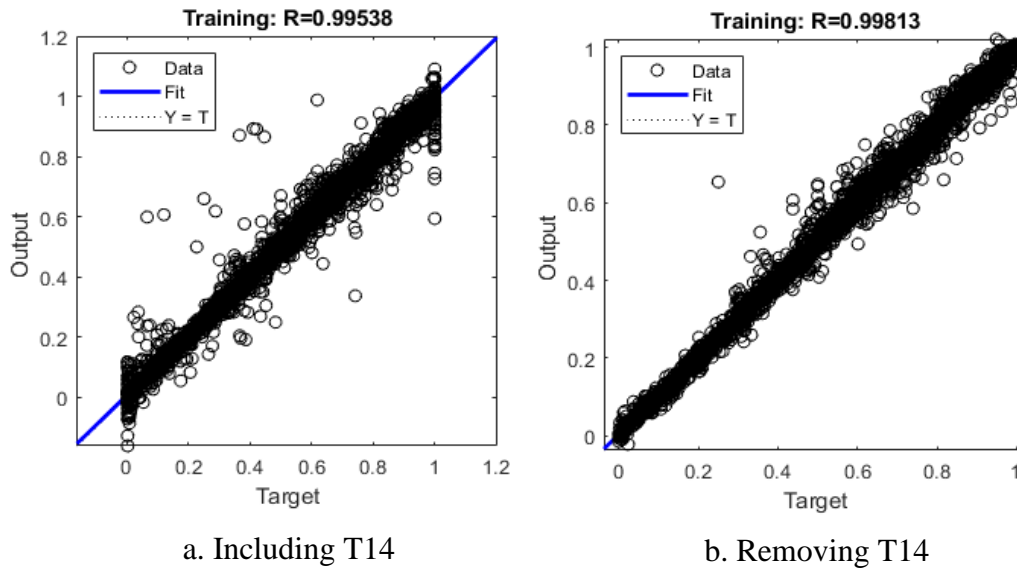


Figure 3 Training regression before and after removing T14

Thus, this means that the ANN did not properly predict target values of 0 and 1 for some parameters. However, after revising the existent database, it was found that sensor T14 (Air temperature in TC#1 inlet) was broken during the engine tests, giving wrong values throughout the tests. Therefore, T14 was removed from the existing database, and the ANN was again proved with the same structure but not including T14, resulting in the training regression presented in Figure 3b. It is observed that the mentioned two vertical lines disappeared, resulting in an increased training regression value. Once it was checked that no other sensors gave incorrect values, number of neurons in hidden layer was determined by analysing validation MSE and R values for different hidden layer configurations. Yang et al. [40] and Noor et al [41] followed analogue methodologies to ascertain optimum training learning rate and neuron number in hidden layer respectively. Figure 4 shows validation MSE and R values for different neuron numbers in hidden layer.

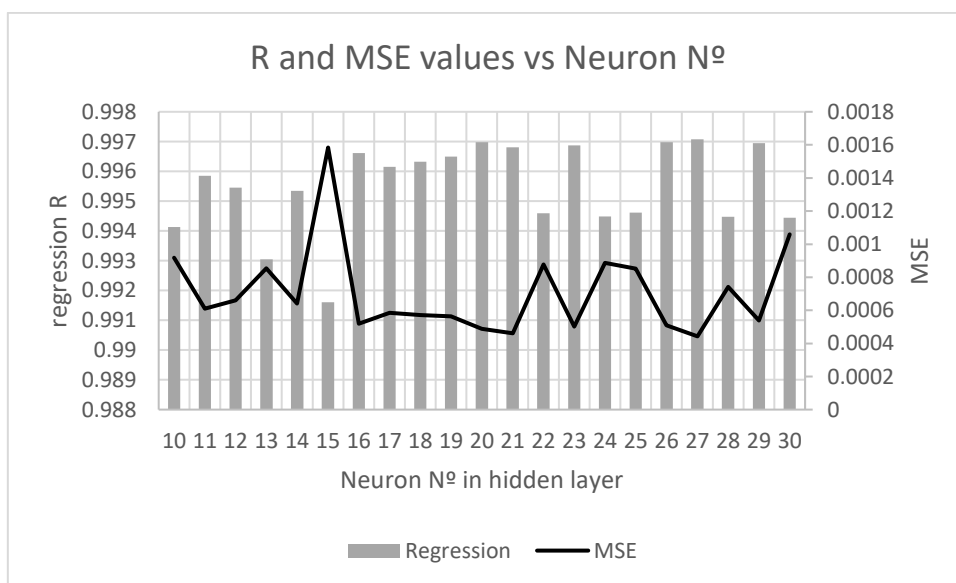


Figure 4 Validation R and MSE values for different neuron numbers in hidden layer

Neuron number of 27 presented highest R and lowest MSE values; it was therefore selected as the neuron number for hidden layer.

Results

As seen in section 2, training regression showed values near 1, which induced that outputs predicted at the end of the training phase were near their respective target values. As mentioned in this section, 15% of data was reserved for testing. With the aim of visually analysing the accuracy of each parameter prediction, 20 samples were randomly selected from the testing data, to show whether output values match target values in different parameter predictions. Accuracy levels change depending on each parameter, so this should be considered when applying this kind of models to a diagnosis or fault detection process. Figure 5 and 6 show ANN predictions for exhaust gas temperature in cylinder 1 (T16) and air temperature in the air cooler inlet (T10) respectively.

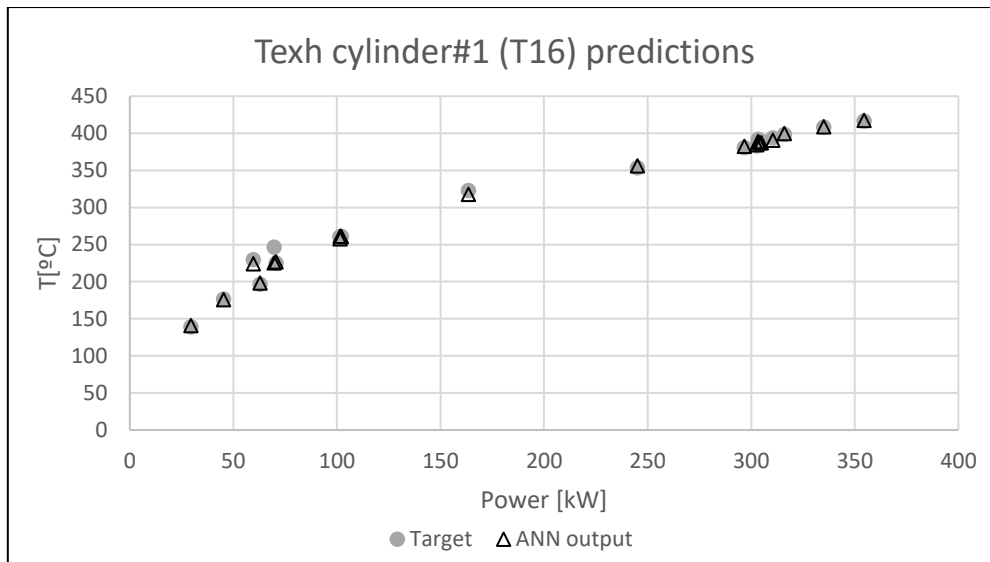


Figure 5 ANN predictions and target values for T_{exh} cylinder1

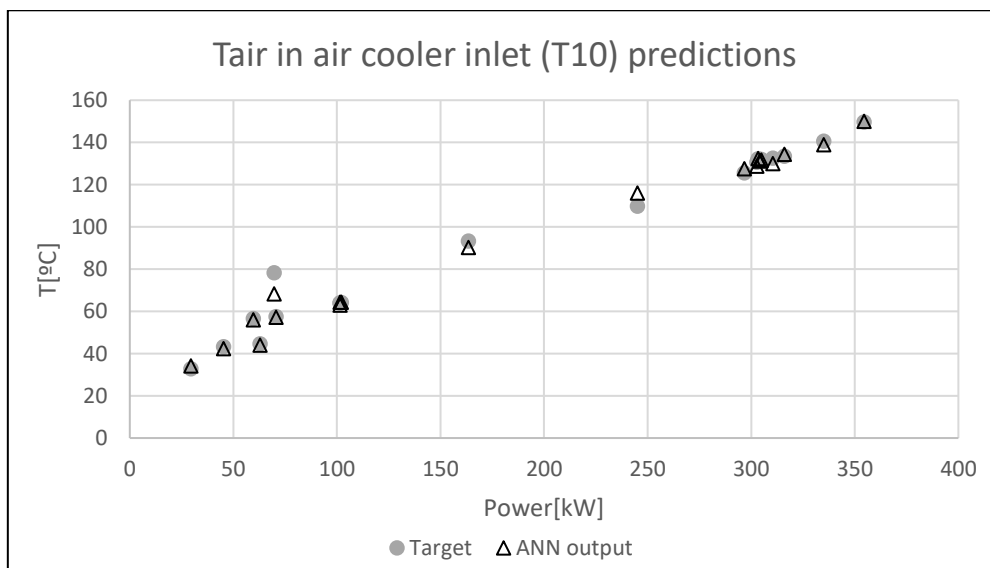


Figure 6 Air cooler inlet air temperature ANN predictions and target values

Except for a few out-layers in each case, both parameters are predicted with high accuracy levels for different engine loads. Nevertheless, in fault identification applications incipient faults may be identified by observing deviations between ANN predictions and the target values, so out-layers may be avoided to prevent misclassifications. Likewise, minimum error levels should be required to include a parameter in this kind of preventive maintenance applications. Therefore, in this case of study an error analysis was conducted to evaluate the accuracy level for each parameter. Thus, Mean Absolute Percentage Error was selected to carry out the mentioned analysis in the 20 testing samples. This error equation calculates the mean of the relative percentage error for a n number of predictions. Equation 1 shows the cited mathematical expression.

$$MAPE = \frac{1}{n} \sum_{i=1}^n \frac{|t_i - y_i|}{t_i} \quad (1)$$

y_i is the predicted output for the sample i and t_i is its respective target value. n is the number of samples, which is 20 in this case of study. Therefore, MAPE was calculated for the 20 sample predictions of the 31 predicted parameters. Figure 5 shows MAPE values calculated for all parameters predicted in the 20 testing samples. Different colours are used following the colour code used in Figure 1 for different fluids. Likewise, abbreviations used for each parameter correspond to the parameters shown in Figure 1.

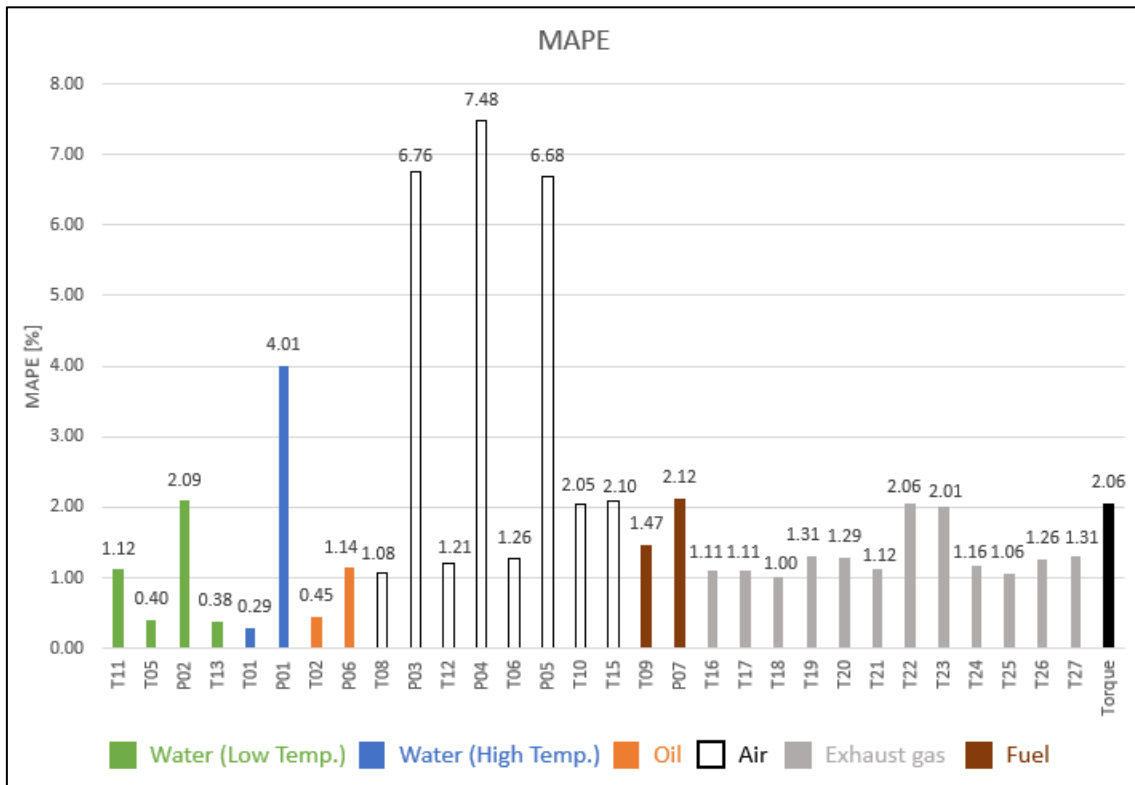


Figure 7 MAPE values for different parameter predictions in testing data

Highest MAPE values correspond to pressure parameters. Parameters P04 and P05 represent pressures in discharges of turbochargers 1 and 2 respectively. MAPE values shown for these two parameters are two of the highest in the whole engine (7.48% and 6.68% respectively). On the contrary, the temperature parameters measured in the same points T12 and T06, present much lower MAPE values with 1.21% and 1.26% respectively. The rest of temperature errors remain below 2.10% for the air system of the engine. This suggests that it may not be a problem of the air system itself, but the relation between measured pressures and engine performance; this issue will be later treated in discussion section.

The other highest error parameters correspond to the rest of the pressure measurements. Engine inlet air pressure P03 shows 6.76% MAPE error, which is notably higher than the 1.08% MAPE value of engine inlet air temperature prediction T08. High temperature water pressure measured in engine inlet P01 also presents relatively high MAPE value when being compared to others with 4.01%. In general terms, the 7 pressure measurements present the highest MAPE values, which will be later object of discussion. On the other hand, exhaust gas temperatures show good agreement between model predictions and real target values, which induces a strong correlation between this parameters and engine performance. The same happens with low temperature water system temperatures and air system temperatures. Torque prediction presents 2.06% MAPE value, which at first sight may be lower considering that power is an input for the model. However, the relation between these two variables would depend on the engine speed which did not remain constant during engine tests.

Discussion

In the present case of study, the capability of an artificial neural network to predict multiple engine parameters was demonstrated with a marine diesel engine operating in real conditions. Despite facing different load conditions ranging from 0 to 100% in the engine, the model was able to predict all parameters within MAPE values below 7.5%. Castresana et al. showed different ANN structures used for engine performance and emission predictions [12]. It was seen that almost all studies considered less than 10 outputs when predicting engine performance and emission parameters, with few exceptions [28]. In this contribution, 31 different parameters were predicted throughout the whole engine, analysing the robustness of the ANN to fully simulate a medium speed marine diesel engine. Furthermore, the prediction accuracy of different parameters will be discussed in the next section, analysing their applicability to real engine diagnosis processes.

Relative percentage errors reached by other authors vary depending on each ANN model. For instance, Sinaga et al. [42] reached relative errors between 0.2244-0.3577% when predicting only two outputs: torque and fuel consumption. Other studies which considered higher output dimensions also showed higher MAPE values. Javed et al. [43] reached 4.963% MAPE overall value when considering 8 different parameters as outputs. After conducting a comparison between different training algorithms and ANN structures, they concluded that Levenberg Marquardt with 16 neurons in hidden layer gave the best

results. In this case of study, 27 was the number of neurons in hidden layer, which is reasonable since much more inputs and outputs are considered in comparison to their model.

In the present study, exhaust gas temperatures through engine cylinders and exhaust ducts showed the lowest MAPE values. Thus, one of the reasons for this phenomenon is the strong correlation between exhaust gas temperatures and engine performance. This has led many authors to include this parameter as an output in their studies, reaching different error levels depending on each ANN modelling approach. Cay et al. [36] reached 3.14% for T_{exh} prediction, however, one specific ANN was developed for each of the four predicted outputs. Likewise, Parlak et al. [20] predicted specific fuel consumption and exhaust gas temperature, reaching 2.36% MAPE value for T_{exh} prediction. The error levels reached in this study for the different exhaust gas temperatures are in the range of the mentioned studies despite being predicted all at once with other 19 parameters, which induces a good model performance. Nevertheless, there have also been some studies with lower error levels when predicting exhaust gas temperatures. Noor et al. [41] reached 0.58% MAPE value for T_{exh} prediction in a marine diesel engine by using an ANN trained by Levenberg Marquardt. In the same study, 2.78% MAPE value was reached for torque prediction. Hence, comparing them to the present study it can be seen how in their study T_{exh} showed higher accuracy levels while torque showed lower accuracy levels in the same model. Besides, this fact reveals the dependency of the model accuracy not only on the model structure itself but also on the parameter being predicted. All in all, T_{exh} predictions showed high exactitude in the present paper, becoming an important and reliable parameter to be included in condition-based maintenance applications.

It was seen that pressure measurements gave much higher error values than temperature measurements in some cases. This in part is due to the small range in which some pressures changed. In case of air duct measurements, pressure values ranged from -0.02 up to 1.45 bar (manometric pressure), which means that an error of 0.1 bar would induce an error of 6.8%. On the other hand, other pressure measurements such as oil pressure in engine inlet P06 reached up to 5 bars, having a wider range in measurements. If MAPE value is observed for this parameter, 1.14% was reached, which is relatively low in comparison to other parameters. It was thus proved that low acquirement range was causing increased MAPE values in air pressure measurements.

When observing threshold values for faulty conditions set in other studies, it is concluded that these parameters may lead to misclassifications. For instance, Basurko et al. [28] established threshold values from 5 to 8% for different faulty conditions. In this study, MAPE values reached for air pressure measurements were in that range, which would cause errors in fault classification. Considering that MAPE values presented in Figure 7 are mean values for 20 testing samples, it may also happen that P01 (high temperature water pressure in engine inlet), which reached MAPE values of 4.01%, may also induce misclassifications in some specific points. Therefore, in case of P01, P03, P04 and P05, two different approaches may be carried out: i) avoid them in order to prevent misclassifications; ii) set higher thresholds for these parameters when designing the fault identification system. The second approach would be very interesting in some specific fault detection applications such as turbocharger faulty condition identification. When a turbocharger does not work properly, there may be a decrease in the outlet pressure which

would result in a big deviation between the model and the real engine. In this kind of faulty situations these parameters could be very helpful even if their threshold values were bigger than in other parameters.

Additionally, in this study there were some parameters that showed high accuracy levels not because of their strong correlation with engine performance but because of their low variation through engine tests. This is the case of fuel temperature T09 which did not show a clear correlation with respect to input parameters; however, as it did not change throughout engine tests, prediction accuracy level was relatively high. The same happened to fuel pressure, which changed only 0.13 bar from lowest to highest engine loads. Even if they may not provide as much information as other highly correlated parameters, these parameters may be included in a diagnosis process, as if they were much deviated from their constant trends they may be good indicators for a upcoming faulty situation.

Conclusions and future work

In the present study, a six-cylinder medium speed marine diesel engine was modelled by a unique Artificial Neural Network. 31 different performance parameters were predicted by using 8 inputs employing real engine test data to train, validate and test the designed model. Among the results, the identification of a damaged sensor was carried out by analysing the training error of the model, discarding one parameter due to erroneous sensor lectures. The rest of the parameters were predicted with high accuracy levels, which led to relatively low Mean Absolute Percentage Errors when conducting the error analysis. Those parameters which presented highest error values were presented in discussion section, proposing different procedures when applying them to a diagnosis or fault detection system in diesel engines. From the present case of study, the following conclusions can be drawn:

- A faulty sensor was identified during the training phase of the ANN.
- 31 outputs were predicted for variable engine conditions by introducing 8 input parameters, reaching overall MAPE values under 7.5% for any predicted output parameter.
- Engine torque, exhaust gas temperatures and cooling water system temperatures proved to have strong correlation with engine performance, showing low MAPE values for testing data.
- Turbo-chargers outlet and engine inlet air pressure parameters gave the highest MAPE values, while it may be caused by their low range of variation. These parameters were proposed to be discarded or treated with higher threshold values for specific faults when applying diagnosis methodologies.

Future works may implement this kind of models to a fault detection system. Firstly, the accuracy level for different parameters should be studied, considering the results obtained in this study. After a proper model adjustment, different threshold values may be implemented for each fault type, considering measurement and model errors to avoid misclassifications. Afterwards, faults could be studied to see whether deviations between modelled and real values could properly represent incipient faults. Furthermore, once an effective fault detection system was developed, on-board implementations would be the last step, analysing whether these data-driven methods are effective in real vessel propulsion fault detection applications.

Acknowledgments

The work behind this contribution has been funded by Basque Government. J. Castresana is being benefited from a grant of the Department of Economic Development and Infrastructures. The authors also want to thank the Department of Thermal Engineering and Nautical and Naval Machines of the University of the Basque Country.

References

- [1] Eurostat, International trade in goods by mode of transport, in, 2020.
- [2] E.M.S.A. EMSA, Learning From Accidents Through EMCIP (European Marine Casualty Information Platform), EMSA, (2018).
- [3] W. Wang, B. Hussin, T. Jefferis, A case study of condition based maintenance modelling based upon the oil analysis data of marine diesel engines using stochastic filtering, *International Journal of Production Economics*, 136 (2012) 84-92.
- [4] G. Sujesh, S. Ramesh, Modeling and control of diesel engines: A systematic review, *Alexandria engineering journal*, 57 (2018) 4033-4048.
- [5] F. Payri, P. Olmeda, J. Martín, A. García, A complete 0D thermodynamic predictive model for direct injection diesel engines, *Applied Energy*, 88 (2011) 4632-4641.
- [6] J. Benajes, P. Olmeda, J. Martín, R. Carreño, A new methodology for uncertainties characterization in combustion diagnosis and thermodynamic modelling, *Applied Thermal Engineering*, 71 (2014) 389-399.
- [7] M. Altosole, U. Campora, M. Figari, M. Laviola, M. Martelli, A diesel engine modelling approach for ship propulsion real-time simulators, *Journal of Marine Science and Engineering*, 7 (2019) 138.
- [8] D. Khan, M.Z. Gül, Zero-dimensional modelling of a four-cylinder turbocharged diesel engine with variable compression ratio and its effects on emissions, *SN Applied Sciences*, 1 (2019) 1162.
- [9] D.D. Ion, N. Anisor, Single cylinder diesel engine performances estimation using AVL boost software, in: *Proceedings of the 12th WSEAS international conference on Neural networks, fuzzy systems, evolutionary computing & automation*, World Scientific and Engineering Academy and Society (WSEAS), 2011, pp. 173-176.
- [10] V.V. Pham, V.V. Le, A modelling technique of the intake and exhaust systems of a medium speed marine diesel engine, in: *AIP Conference Proceedings*, Vol. 2207, AIP Publishing LLC, 2020, pp. 030003.

- [11] A. Albrecht, O. Grondin, F. Le Berr, G. Le Sollicec, Towards a stronger simulation support for engine control design: a methodological point of view, *Oil & Gas Science and Technology-Revue de l'IFP*, 62 (2007) 437-456.
- [12] J. Castresana, G. Gabiña, L. Martin, Z. Uriondo, Comparative performance and emissions assessments of a single-cylinder diesel engine using artificial neural network and thermodynamic simulation, *Applied Thermal Engineering*, (2020) 116343.
- [13] C. Cai, X. Weng, C. Zhang, A novel approach for marine diesel engine fault diagnosis, *Cluster Computing*, 20 (2017) 1691-1702.
- [14] A. Atmanli, E. Ileri, N. Yilmaz, Optimization of diesel–butanol–vegetable oil blend ratios based on engine operating parameters, *Energy*, 96 (2016) 569-580.
- [15] J. Flett, G.M. Bone, Fault detection and diagnosis of diesel engine valve trains, *Mechanical Systems and Signal Processing*, 72 (2016) 316-327.
- [16] A. Moosavian, H. Ahmadi, A. Tabatabaefar, M. Khazaei, Comparison of two classifiers; K-nearest neighbor and artificial neural network, for fault diagnosis on a main engine journal-bearing, *Shock and Vibration*, 20 (2013) 263-272.
- [17] X. Xu, Z. Zhao, X. Xu, J. Yang, L. Chang, X. Yan, G. Wang, Machine learning-based wear fault diagnosis for marine diesel engine by fusing multiple data-driven models, *Knowledge-Based Systems*, 190 (2020) 105324.
- [18] P. Srihari, K. Govindarajulu, K. Ramachandra, A method to improve reliability of gearbox fault detection with artificial neural networks, *International Journal of Automotive and Mechanical Engineering*, 2 (2010) 221-230.
- [19] B. Liu, C. Zhao, F. Zhang, T. Cui, J. Su, Misfire detection of a turbocharged diesel engine by using artificial neural networks, *Applied Thermal Engineering*, 55 (2013) 26-32.
- [20] A. Parlak, Y. Islamoglu, H. Yasar, A. Egrisogut, Application of artificial neural network to predict specific fuel consumption and exhaust temperature for a diesel engine, *Applied Thermal Engineering*, 26 (2006) 824-828.
- [21] T.F. Yusaf, D. Buttsworth, K.H. Saleh, B. Yousif, CNG-diesel engine performance and exhaust emission analysis with the aid of artificial neural network, *Applied Energy*, 87 (2010) 1661-1669.
- [22] P. Madane, R. Panua, Investigation of Performance of jatropha oil on diesel engine using Artificial Neural Network Model, *International Journal of Computational Intelligence & IoT*, 2 (2019).
- [23] B. Ghobadian, H. Rahimi, A. Nikbakht, G. Najafi, T. Yusaf, Diesel engine performance and exhaust emission analysis using waste cooking biodiesel fuel with an artificial neural network, *Renewable energy*, 34 (2009) 976-982.
- [24] B. Işcan, ANN modeling for justification of thermodynamic analysis of experimental applications on combustion parameters of a diesel engine using diesel and safflower biodiesel fuels, *Fuel*, 279 (2020) 118391.
- [25] Ü. Ağbulut, M. Ayyıldız, S. Sarıdemir, Prediction of performance, combustion and emission characteristics for a dual fuel diesel engine at varying injection pressures, *Energy*, (2020) 117257.
- [26] M. Shailaja, A.S.R. Raju, Neural Network—Based Diesel Engine Emissions Prediction for Variable Injection Timing, Injection Pressure, Compression Ratio and Load Conditions, in: *Emerging Trends in Electrical, Communications and Information Technologies*, Springer, 2017, pp. 109-122.
- [27] H. Taghavifar, H. Taghavifar, A. Mardani, A. Mohebbi, S. Khalilarya, S. Jafarmadar, Appraisal of artificial neural networks to the emission analysis and prediction of CO₂, soot, and NO_x of n-heptane fueled engine, *Journal of cleaner production*, 112 (2016) 1729-1739.

- [28] O.C. Basurko, Z. Uriondo, Condition-Based Maintenance for medium speed diesel engines used in vessels in operation, *Applied Thermal Engineering*, 80 (2015) 404-412.
- [29] C.W.M. Noor, R. Mamat, A.N. Ahmed, Comparative study of artificial neural network and mathematical model on marine diesel engine performance prediction, *International Journal of Innovative Computing, Information and Control* Volume 14, Issue 3, June 2018, Pages 959-969, (2018).
- [30] J. Porteiro, J. Collazo, D. Patiño, J.L. Míguez, Diesel engine condition monitoring using a multi-net neural network system with nonintrusive sensors, *Applied Thermal Engineering*, 31 (2011) 4097-4105.
- [31] S. Roy, R. Banerjee, P.K. Bose, Performance and exhaust emissions prediction of a CRDI assisted single cylinder diesel engine coupled with EGR using artificial neural network, *Applied Energy*, 119 (2014) 330-340.
- [32] M. Jafari, P. Verma, T.A. Bodisco, A. Zare, N.C. Surawski, P. Borghesani, S. Stevanovic, Y. Guo, J. Alroe, C. Osuagwu, Multivariate analysis of performance and emission parameters in a diesel engine using biodiesel and oxygenated additive, *Energy conversion and management*, 201 (2019) 112183.
- [33] I. Lazakis, Y. Raptodimos, T. Varelas, Predicting ship machinery system condition through analytical reliability tools and artificial neural networks, *Ocean Engineering*, 152 (2018) 404-415.
- [34] S. Roy, R. Banerjee, A.K. Das, P.K. Bose, Development of an ANN based system identification tool to estimate the performance-emission characteristics of a CRDI assisted CNG dual fuel diesel engine, *Journal of Natural Gas Science and Engineering*, 21 (2014) 147-158.
- [35] S. Channapattana, A.A. Pawar, P.G. Kamble, Optimisation of operating parameters of DI-CI engine fueled with second generation Bio-fuel and development of ANN based prediction model, *Applied Energy*, 187 (2017) 84-95.
- [36] Y. Cay, A. Çiçek, F. Kara, S. Sağıroğlu, Prediction of engine performance for an alternative fuel using artificial neural network, *Applied Thermal Engineering*, 37 (2012) 217-225.
- [37] I.O.f.S. ISO, ISO 14726:2008 Ships and marine technology — Identification colours for the content of piping systems, in, 2008.
- [38] T.L. Fine, *Feedforward neural network methodology*, Springer Science & Business Media, 2006.
- [39] J. Rezaei, M. Shahbakhti, B. Bahri, A.A. Aziz, Performance prediction of HCCI engines with oxygenated fuels using artificial neural networks, *Applied Energy*, 138 (2015) 460-473.
- [40] F. Yang, H. Cho, H. Zhang, J. Zhang, Y. Wu, Artificial neural network (ANN) based prediction and optimization of an organic Rankine cycle (ORC) for diesel engine waste heat recovery, *Energy conversion and management*, 164 (2018) 15-26.
- [41] M.N. CW, M.Y. MH, I. CK, N. MM, Prediction of marine diesel engine performance by using artificial neural network model, (2016).
- [42] N. Sinaga, Optimization and prediction of motorcycle injection system performance with feed-forward back-propagation method Artificial Neural Network (ANN), (2016).
- [43] S. Javed, Y.S. Murthy, R.U. Baig, D.P. Rao, Development of ANN model for prediction of performance and emission characteristics of hydrogen dual fueled diesel engine with *Jatropha Methyl Ester* biodiesel blends, *Journal of Natural Gas Science and Engineering*, 26 (2015) 549-557.

Algorithm-Based Optimization for Energy-Efficient Operation of Refrigeration Systems

J. Bentz*¹, T. Hamacher², C. Schweigler¹

¹CENERGIE - Center for Energy-Efficient Buildings and Districts
Munich University of Applied Sciences, 80335 Munich, Germany

²Chair of Renewable and Sustainable Energy Systems
Technical University Munich, 85748 Garching, Germany

*joerg.bentz@hm.edu

Abstract

In refrigeration systems, a set of devices is applied for the provision of cooling, for the transfer of reject heat to ambient and for circulation of the respective heat carrier fluids. Aiming at energy-efficient operation of the entire system, a complex optimization exercise is given, characterized by the number of degrees of freedom and the interdependence of the different components. In order to form a realistic model of the system, the operating characteristics of all system components must be modelled in sufficient quality. In order to achieve sufficiently exact representation of the real system, e.g. for part load operation, a nonlinear optimization including higher-order component models has to be applied. Overall, a considerable effort for the development and application of a mathematical optimization is required in order to cope with the complexity of typical refrigeration systems. Within the framework of this study, a method is shown to set up a pre-configured algorithm-based optimization tool which can be applied for smaller refrigeration systems.

Keywords: Refrigeration Systems, Energy Efficiency, Performance, Modelling, Optimization

Introduction

Several interdependencies occur when chillers are operated in conjunction with their peripherals like heat rejection units, pumps and other refrigeration units. An example is shown in **Fig. 1**. An optimal set of operating parameters is essential for finding the most efficient point of operation, providing a reduction of the power consumption. A mathematical optimization procedure (**Fig. 2**) is needed to find the best constellation of the parameter values [1]. For this purpose, the operating characteristics of all system components must be modeled in sufficient quality. During the last decade powerful optimization tool, based on non-linear correlations have become available, allowing for appropriate description of the components [7]. Overall, a considerable effort has to be undertaken for the configuration and application of a mathematical optimization for complex refrigeration systems. Examples have been given by [5] and [9].

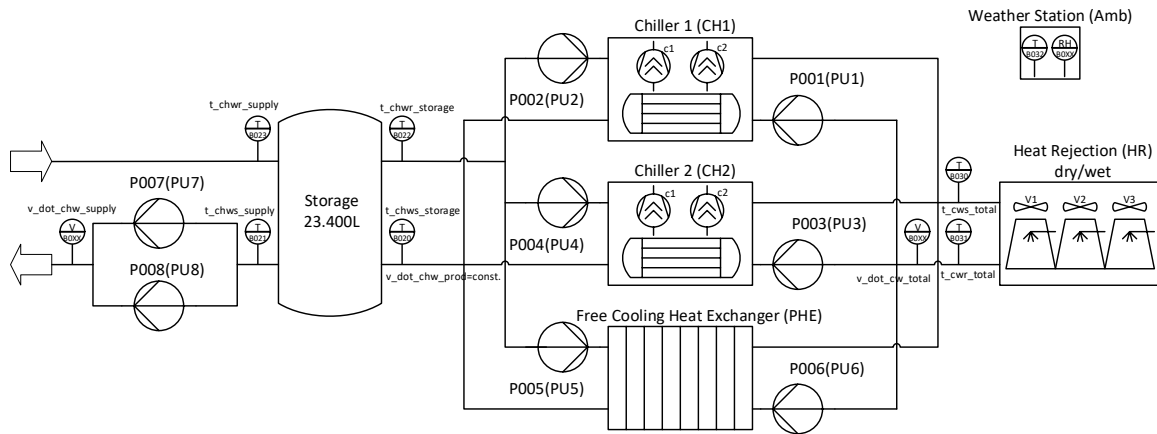


Figure 1: Schematic of sample refrigeration plant

Methodology: Optimization Procedure

Modeling and Simulation

As basis for the algorithm-based optimization of the refrigeration supply system, the individual components (see **Fig. 1**) were mapped using rigorously simplified physical models [2]. These simplified component models have been validated with reference to both exact physical models and real operating data. With the help of the validated models, the individual components have been simulated across their entire operating envelope, forming an artificial performance map. With the help of this simulation database, it was possible to create polynomials by linear regression, which depict the operating characteristics of all components. Due to their simple mathematical structure, these polynomials are well suited for implementation within an equation-based optimization algorithm. The polynomial representation offers two significant advantages. On one hand, enormous computational effort can be saved and on the other hand, the coefficients of the polynomials can easily be adapted by comparison to real operating data.

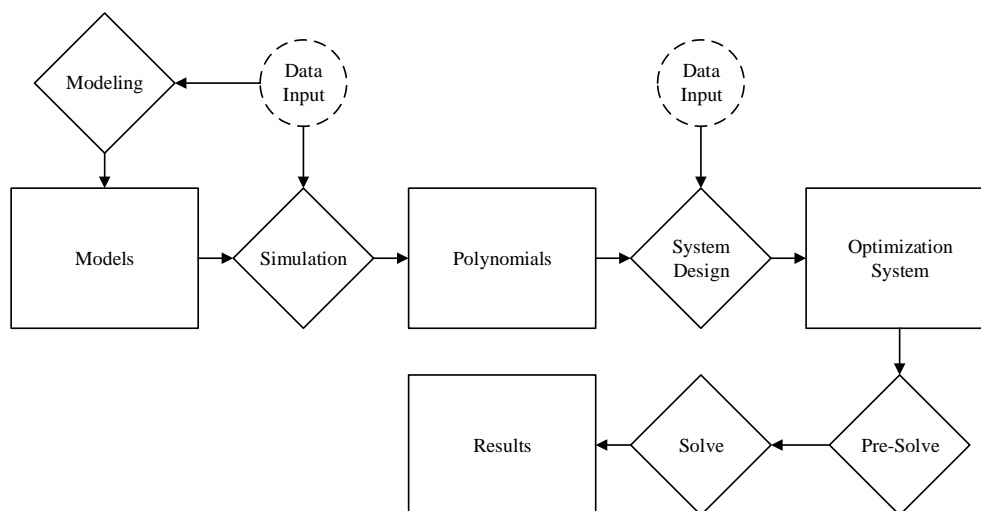


Figure 2: Data flow of the optimization procedure

System Design for Optimization

Mixed integer non-linear programming (MINLP) with the general form (1) was selected to include the switch-on and switch-off states and the non-linear behavior of the system components.

$$\begin{aligned} \min \quad & f(x, y) \\ \text{s. t.} \quad & g(x, y) \leq 0 \\ & x \in X \\ & y \in Y \text{ integer} \end{aligned} \quad (1)$$

Where the function $f \in \mathbb{R}$ is a nonlinear objective function and $g \in \mathbb{R}$ are possibly nonlinear constraint functions. Most algorithms require the functions f and g to be continuous and differentiable, but some may even allow for singular discontinuities. The variables x and y are the decision variables, where y is required to be integer valued. The sets $X \in \mathbb{R}$ and $Y \in \mathbb{R}$ are bounding restrictions on the variables. In addition to the integer requirements on variables, other kinds of discrete constraints are commonly used. Computational tractability significantly depends on whether the functions $f(x, y)$ and $g(x, y)$ are convex or not [3].

Objective function

The objective of the optimization is the minimization of the total electrical consumption of the reference system (**Fig. 1**) over all designated time steps (2).

$$\min W_{el,total} = \sum_{t=0}^T P_{el,t} * \Delta T \quad (2)$$

The current total power demand $P_{el,t}$ originates from 3 different groups of consumers (3),

$$P_{el} = \sum_{i=1}^I P_{el_ch,i} + \sum_{j=1}^J P_{el_ct,j} + \sum_{k=1}^K P_{el_pu,k} \quad (3)$$

where $\sum_{i=1}^I P_{el_ch,i}$ is the sum of the electric power of all chillers in the system, $\sum_{j=1}^J P_{el_ct,j}$ represents all active heat rejection components and $\sum_{k=1}^K P_{el_pu,k}$ the total electric power consumption of all pumps.

To optimize the discrete switching of the components or the change of operation modes, a set of decision variables x is introduced. See **Table 1**. In the following section, the discrete variables and continuous polynomials of **Table 2** will be combined, creating the complete set of equations for the objective function. The involved parameters and variables for the polynomials can be found in **Table 3**.

In typical refrigeration supply system, the energy demand is dominated by the electric power of the chillers P_{el_ch} (4), which is the sum of both chillers $P_{el_ch_1}$ and $P_{el_ch_2}$. The power supply to the chillers is only switched on during active cooling mode ($x_i = 1$). In the free cooling mode, the power consumption is eliminated by the decision variable ($x_i = 0$). Furthermore it is necessary to decide if only one chiller shall be activated ($x_j = 0$ or if both chillers operate at the same time ($x_j = 1$). If only one chiller is active, the decision variable x_k serves for selection of chiller 1 or 2 respectively, having in mind that both chillers may have different operating characteristics.

$$P_{el_ch} = x_i \cdot (x_j \cdot (x_k \cdot P_{el_ch_1} + (1 - x_k) \cdot P_{el_ch_2}) + (1 - x_j) \cdot (P_{el_ch_1} + P_{el_ch_2})) \quad (4)$$

Following the selection of the chillers, for the case of two-stage units the decision process continues with the choice of the compressors inside the chillers (5-6). This is necessary, since the compressors themselves can also have different operating characteristics. Again, the system states

comprise the operation of one ($x_l/x_n=1$) or two ($x_l/x_n=0$) compressors. As stated earlier, the performance of all components, i.e. in this case the electric demand of the chillers ($P_{el_ch_{x,x}}$), is represented by polynomials. A complete list of all polynomials can be found in **Table 2**. The involved variables and parameters are given in **Table 3**.

$$P_{el_ch_1} = x_l \cdot (x_m \cdot P_{el_ch_{1,1}} + (1 - x_m) \cdot P_{el_ch_{1,2}}) + (1 - x_l) \cdot (P_{el_ch_{1,1/1,2}}) \quad (5)$$

$$P_{el_ch_2} = x_n \cdot (x_o \cdot P_{el_ch_{1,1}} + (1 - x_o) \cdot P_{el_ch_{1,2}}) + (1 - x_n) \cdot (P_{el_ch_{1,1/1,2}}) \quad (6)$$

The procedure continues with the heat rejection plant (P_{el_ct}) (7). Here the fans for activation of the air flow are the second important power consumers in the system. Also for the heat rejection plant a decision tree is implemented. With the help of the decision variable (x_p) it is chosen if the plant is operated dry ($x_p=1$) or wet ($x_p=0$).

$$P_{el_ct} = x_p \cdot P_{el_ct_{dry}} + (1 - x_p) \cdot P_{el_ct_{wet}} \quad (7)$$

The dry ($P_{el_ct_{dry}}$) and wet ($P_{el_ct_{wet}}$) operation modes also have significantly different characteristics and are therefore modeled by individual expressions (8-9). With permutations of the decision variables x_q and x_r for the dry operation and x_s and x_t for the wet operation it is possible to whether one, two or three fans are active.

$$P_{el_ct_{dry}} = x_q \cdot x_r \cdot P_{ct_{dry,1}} + (1 - x_q) \cdot x_r \cdot P_{ct_{dry,2}} + (x_q \cdot (1 - x_r) \cdot P_{ct_{dry,3}}) \quad (8)$$

$$P_{el_ct_{wet}} = x_s \cdot x_t \cdot P_{ct_{wet,1}} + (1 - x_s) \cdot x_t \cdot P_{ct_{wet,2}} + (x_s \cdot (1 - x_t) \cdot P_{ct_{wet,3}}) \quad (9)$$

The pumps of the system (P_{el_pu}) are clustered into three groups (10). The pumps for the chillers ($P_{el_pu_{ch}}$), the pumps for the free cooling mode ($P_{el_pu_{fc}}$) and the pumps for the supply of the consumer ($P_{el_pu_{supply}}$). The pumps for the chillers and the free cooling alternate with the decision variable (x_i). The supply pumps are always active.

$$P_{el_pu} = x_i \cdot P_{el_pu_{ch}} + (1 - x_i) \cdot P_{el_pu_{fc}} + P_{el_pu_{supply}} \quad (10)$$

The pumps for the chillers ($P_{el_pu_{ch}}$) are switched simultaneously with the respective chillers, expressed by their decision variables (x_j, x_k) (11). In addition, the electric demand of the pumps for each chiller ($P_{el_pu_{ch1}}$) (12) and ($P_{el_pu_{ch1}}$) (13) is represented by polynomials for the chilled water pumps ($P_{el_pu_{chw,x}}$) and the cooling water pumps ($P_{el_pu_{cw,x}}$).

$$P_{el_pu_{ch}} = x_j \cdot (x_k \cdot P_{el_pu_{ch1}} + (1 - x_k) \cdot P_{el_pu_{ch2}}) + (1 - x_j) \cdot (P_{el_pu_{ch1}} + P_{el_pu_{ch2}}) \quad (11)$$

$$P_{el_pu_{ch1}} = P_{el_pu_{chw,1}} + P_{el_pu_{cw1}} \quad (12)$$

$$P_{el_pu_{ch2}} = P_{el_pu_{chw,2}} + P_{el_pu_{cw,2}} \quad (13)$$

The pumps ($P_{el_pu_{fc}}$) (14) for the free cooling mode are only active when free cooling is applied. Then the polynomials ($P_{el_pu_{chw,fc}}$) and ($P_{el_pu_{cw,fc}}$) are considered for the chilled water pump and the cooling water pump respectively.

$$P_{el_pu_{fc}} = P_{el_pu_{chw,fc}} + P_{el_pu_{cw,fc}} \quad (14)$$

For the chilled water supply to the consumer a pair of redundant pumps is applied with electric demand ($P_{el_pu_{supply}}$), as described in (15). The polynomials ($P_{el_pu_{supply,1}}$) and ($P_{el_pu_{supply,2}}$) are selected with the decision variable (x_u). The switching of these pumps is not a matter of efficiency, but operational hours or availability of the components can be taken into account.

$$P_{el_pu_{supply}} = x_u \cdot P_{el_pu_{supply,1}} + (1 - x_u) \cdot P_{el_pu_{supply,2}} \quad (15)$$

Additional expressions

To support all polynomials (**Table 2**) with all involved variables and parameters (**Table 3**), in some cases it is necessary to use additional expressions (16-19). These equations are essential for the description of the cold water storage tank. At first the chilled water flow (\dot{V}_{stor}) to through the storage needs to be calculated. This is done by calculating the difference between the chilled water flow provided by the chillers (\dot{V}_{chw}) and the chilled water flow to the customer (\dot{V}_{supply}) (16). Where \dot{V}_{chw} is constant and \dot{V}_{supply} varies according to the load. With this information it is possible to determine the cooling load ($\dot{Q}_{0,stor}$) which is transferred to the storage (17). Where CP_{chw} and RHO_{chw} are constants, T_{chws} is a parameter and T_{chwr} a variable to satisfy the energy balance, as stated in (21). Finally, the total cooling energy to be produced by the chillers is determined (18). ($\dot{Q}_{0,produce}$) is obtained by the sum of cooling energy supplied to the customer ($\dot{Q}_{0,supply}$) and the cooling energy loaded or unloaded to or from the storage ($\dot{Q}_{0,stor}$). With this result, the rejected heat (\dot{Q}_1) of the system is expressed by the sum of the produced cooling load ($\dot{Q}_{0,produce}$) and the electrical power consumption of the chillers (P_{el_ch}) (19).

$$\dot{V}_{stor} = \dot{V}_{chw} - \dot{V}_{supply} \quad (16)$$

$$\dot{Q}_{0,stor} = \dot{V}_{stor} \cdot CP_{chw} \cdot RHO_{chw} \cdot (T_{chwr} - T_{chws}) \quad (17)$$

$$\dot{Q}_{0,produce} = \dot{Q}_{0,supply} + \dot{Q}_{0,stor} \quad (18)$$

$$\dot{Q}_1 = \dot{Q}_{0,produce} + P_{el_ch} \quad (19)$$

Constraints

In order to satisfy underlying physical principles and operational requirements, e.g. restrictions and limits given by the system and the used equipment, it is necessary to apply constraints for the optimization of the operating variables of the system. In case of the given example of a modular cooling system, constraints can be divided into two groups. The general constraints contain the

restrictions which are always active. And so-called disjunctions are used to specify the constraints which are only valid under certain circumstances.

General constraints

One prominent constraint is the restriction of the cooling water return temperature (T_{cwr}) (20) which is directly bound to the ambient air temperature (T_{amb}). Its optimization strongly affects the efficiency of the whole system. In order to obtain the lower limit of (T_{cwr}) the minimal closest approach temperature (ΔT_{ct}) of the heat rejection unit has to be taken into account.

$$T_{cwr} \geq T_{amb} + \Delta T_{ct} \quad (20)$$

The constraints shown in (21-22) ensure the energy balance of the chilled water and cooling water cycles. Where (T_{chws}) is the given set point parameter for the chilled water supply temperature and (T_{chwr}) the optimized chilled water return temperature. For each time step, optimization yields a consistent result for (T_{chwr}) and (\dot{V}_{chw}), based on current values of the parameter ($\dot{Q}_{0,supply}$) and fluid properties (cp_{chw}) and (ρ_{chw}). The same procedure is applied for the cooling water return temperature (T_{cwr}).

$$T_{chwr} = \frac{\dot{Q}_{0,supply} \cdot 3600}{\dot{V}_{chw} \cdot cp_{chw} \cdot \rho_{chw}} + T_{chws} \quad (21)$$

$$T_{cwr} = T_{cws} - \frac{\dot{Q}_1 \cdot 3600}{\dot{V}_{cw} \cdot cp_{cw} \cdot \rho_{cw}} \quad (22)$$

Disjunctions

As already mentioned above, the disjunctions contain the constraints only active on certain circumstances. They are organized by defining numbered disjunctions which contain the different disjuncts.

Disjunction 1 is containing the different constraints for active cooling (disjunct 1) (23-24) and free cooling (disjunct 2) (25-26). In (23) the decision variable (x_i) is forced to be “true” while in (24) a lower limit for (T_{cws}) is given, taking into account the minimal temperature lift of the chiller dT_{Lift} , governed by the pressure ration of the chiller (Δp_{ch}). In (25) the decision variable x_i is forced to be “false”, which allows the chilled water supply temperature (T_{chws}) to be equal to the cooling water return temperature (T_{cwr}) in (26) plus a temperature difference of ΔT_{fc} . In this free cooling mode, the heat rejection plant covers the cooling load of the customer without contribution of active cooling. dT_{fc} represents the driving temperature difference for the heat transfer between cooling water and chilled water in the separating heat exchanger.

Disjunction 1: disjunct 1

$$x_i = true \text{ (active cooling)} \quad (23)$$

$$T_{cws} \geq T_{chws} + \Delta T_{Lift}(\Delta p_{ch}) \quad (24)$$

Disjunction 1: disjunct 2

$$x_i = false \text{ (free-cooling)} \quad (25)$$

$$T_{cwr} = T_{chws} - \Delta T_{fc} \quad T_{chws} = T_{cwr} + \Delta T_{fc} \quad (26)$$

The disjunction 2 is handling the switching between the dry operation ($x_i = true$) (27) and the wet operation ($x_i = false$) (28) of the heat rejection plant. This disjunction is necessary, because it is essential to ensure a freeze protection at ambient temperatures (T_{amb}) lower than 5°C. This is done by a forced deactivation by the disjunct 2 in (29).

Disjunction 2: disjunct 1

$$x_i = true \text{ (dry operation)} \quad (27)$$

Disjunction 2: disjunct 2

$$x_i = false \text{ (wet operation)} \quad (28)$$

$$\text{If } T_{amb} < 5 \text{ Then disjunct 2 = deactivated} \quad (29)$$

Variables and Polynomials

The polynomials p of d variables x and degree $n = (n_1, \dots, n_d)$ are linear combinations of monomials (30),

$$p(x) = \sum_{k \leq n} c_k x^k \quad \text{with } x^k = x_1^{k_1} \dots x_d^{k_d} \quad (30)$$

with coefficients $c_k \in \mathbb{R}$ and $c_n \neq 0$. The polynomial represents a sum over the multi-indices k (non-negative integer vectors).

Table 1: discrete variables and parameters

Name	Designation	Type
x_i	switching between free-cooling and active cooling	var
x_j	switching between 1 or 2 chiller operation mode	param
x_k	switching between chiller 1 and chiller 2	param
x_l	switching between 1 or 2 compressor operation mode of chiller 1	param
x_m	switching between compressor 1 and compressor 2 of chiller 1	param
x_n	switching between 1 or 2 compressor operation mode of chiller 2	param
x_o	switching between compressor 1 and compressor 2 of chiller 2	param
x_p	switching between dry and wet operation of cooling tower	var
x_q, x_r	switching between 1, 2 or 3 ventilators in dry operation	param
x_s, x_t	switching between 1, 2 or 3 ventilators in wet operation	param
x_u	switching between both consumer supply pumps	param

Table 2: list of polynomials with involved parameters and variables

dependent variables	independent variables	Order
$P_{el_ch_i}$	$T_{chws}, T_{cws}, \dot{V}_{chw}, \dot{V}_{cw}, \dot{Q}_0$	2nd

$P_{el_ct,i}$	$T_{cws}, T_{amb}, RH_{amb}, \dot{V}_{cw}, \dot{Q}_1$	3rd
$P_{el_pu_chw,i}$	\dot{V}_{chw}	3rd
$P_{el_pu_cw,i}$	\dot{V}_{cw}	3rd
$P_{el_pu_supply,i}$	\dot{V}_{supply}	3rd

Table 3: continuous variables, parameters and expressions

Name	Designation	Unit	Type
optimized variables			
T_{chwr}	temperature chilled water return	°C	var
T_{cws}	temperature cooling water supply	°C	var
T_{cwr}	temperature cooling water return	°C	var
\dot{V}_{cw}	volume flow cooling water	m ³ /h	var
\dot{V}_{supply}	volume flow consumer supply water	m ³ /h	var
Parameters for Optimization: Input parameters, defining the demand and the given situation of operation			
$\dot{Q}_{0,supply}$	actual refrigeration supply energy to consumer	kW	param
T_{chws}	temperature chilled water supply	°C	param
\dot{V}_{chw}	volume flow chilled water	m ³ /h	param
T_{amb}	temperature ambient air	°C	param
RH_{amb}	relative humidity ambient air	-	param
Constraints (Limits for variation of optimized variables)			
Δp_{ch}	minimal pressure difference for the chillers	-	param
ΔT_{ct}	heat rejection, closest approach temperature: minimal temperature difference between T_{cwr} and T_{amb}	K	param
ΔT_{fc}	temperature difference between T_{chws} and T_{cwr}	K	param
expressions depending on variables			
\dot{V}_{stor}	volume flow through storage	m ³ /h	expr
$\dot{Q}_{0,produce}$	actual refrigeration supply produced	kW	expr
$\dot{Q}_{0,stor}$	actual refrigeration supply stored	kW	expr
\dot{Q}_1	actual heat rejection energy	kW	expr
P_{el_ch1}	electrical power consumption of chiller 1	kW	expr
P_{el_ch2}	electrical power consumption of chiller 2	kW	expr
P_{el_ct}	electrical power consumption of cooling tower	kW	expr
P_{pu_ch1}	electrical power consumption of pumps for chiller 1	kW	expr
P_{pu_ch2}	electrical power consumption of pumps for chiller 2	kW	expr
P_{pu_fc}	electrical power consumption of pumps for free cooling	kW	expr
P_{pu_supply}	electrical power consumption of consumer pumps	kW	expr

Pre-Solving and Solving

The optimization procedure is implemented with the help of the mathematical tool box Pyomo [6]. The optimization model is solved by the Baron Solver [8]. Pyomo supports the formulation and analysis of mathematical models for complex optimization applications. This capability is commonly associated with commercial algebraic modeling languages (AMLs) such as AIMMS, AMPL and GAMS. Pyomo offers a rich set of modeling and analysis capabilities and it provides

access to these capabilities within Python, a high-level programming language with a large set of supporting libraries.

Prior to the final solving by the baron solver, a so called pre-solve process is performed. For the given specific example, the general disjunctive programming (GDP) module is used. Here the disjunctions in the model are transformed into continuous mathematical formulations. This is done by Pyomo, using a BigM-Method [4]. The Big-M method tackles the problem by transforming the original problem with adding some auxiliary variables, to guarantee the existence of an initial feasible solution. However, not being part of the original problem, finally all auxiliary variables must be equal to zero in the optimal solution of the modified problem. In order to guide the optimizer towards this annihilation, the Big-M method adds the auxiliary variables to the objective function and weights them with a high value of the penalty factor M (“big-M”).

The pre-solved model is then transferred into the AML, which can be processed by the Baron solver. So the model is sent to Baron and then returned back to Pyomo after a solution is found. The solution can then be further examined. See Chapter Discussion and Results.

Discussion and Results

Although the optimization system ENOS offers the opportunity to optimize all previously mentioned variables, the real system under consideration is in some cases limited in its operational freedom. In contrast to the flexible activation of the pair of two-stage chiller units, characterized by the discrete variables x_j to x_o , the initiation of the two compressors inside each chiller is governed by a rule-based control algorithm. Therefore, the binary switching variables were transformed into parameters, reducing the degrees of freedom for the optimization.

The optimization was then carried out over a series of 120 time steps (5 days in 1 hour steps) in the month June, which is an appropriate time horizon for taking into account the storage capabilities of the system. For each time step the external operating conditions are characterized by the parameters (T_{Amb} , RH_{Amb} and P_{Amb}). The target cooling capacity is given by (Q_o). The ambient air parameters were taken from test reference year (TRY) data for the location Munich for the 1st-5th of June. For the purpose of clarity, a period with high variation of the ambient weather conditions has been chosen. The temporal profile of the cooling capacity has been generated by observing historic load data of the reference system.

In order to assess the the potential for energy saving by different measures, the ENOS optimization procedure has been applied in different settings. Apart from a global, i.e. simultaneous, optimization of all variables, the impact of variation of single variables has been investigated. The results are shown in **Table 4** and **Figure 3**.

Table 4: observed optimization cases

optimized variables	description	electrical energy consumption [kWh] / savings
none	Reference operation of the system	25.952 / 0%
T_{CWR}	Optimization of the cooling water return temperature	20.154 / 22%
\dot{V}_{CW}	Optimization of the cooling water flow	25.556 / 1,5%
Storage	Optimization with the use of the storage	25.411 / 2%
dry/wet	Optimized dry or wet operation of cooling tower	25.644 / 1,2%
combined	Optimization of all cases in parallel	18.172 / 29,9%

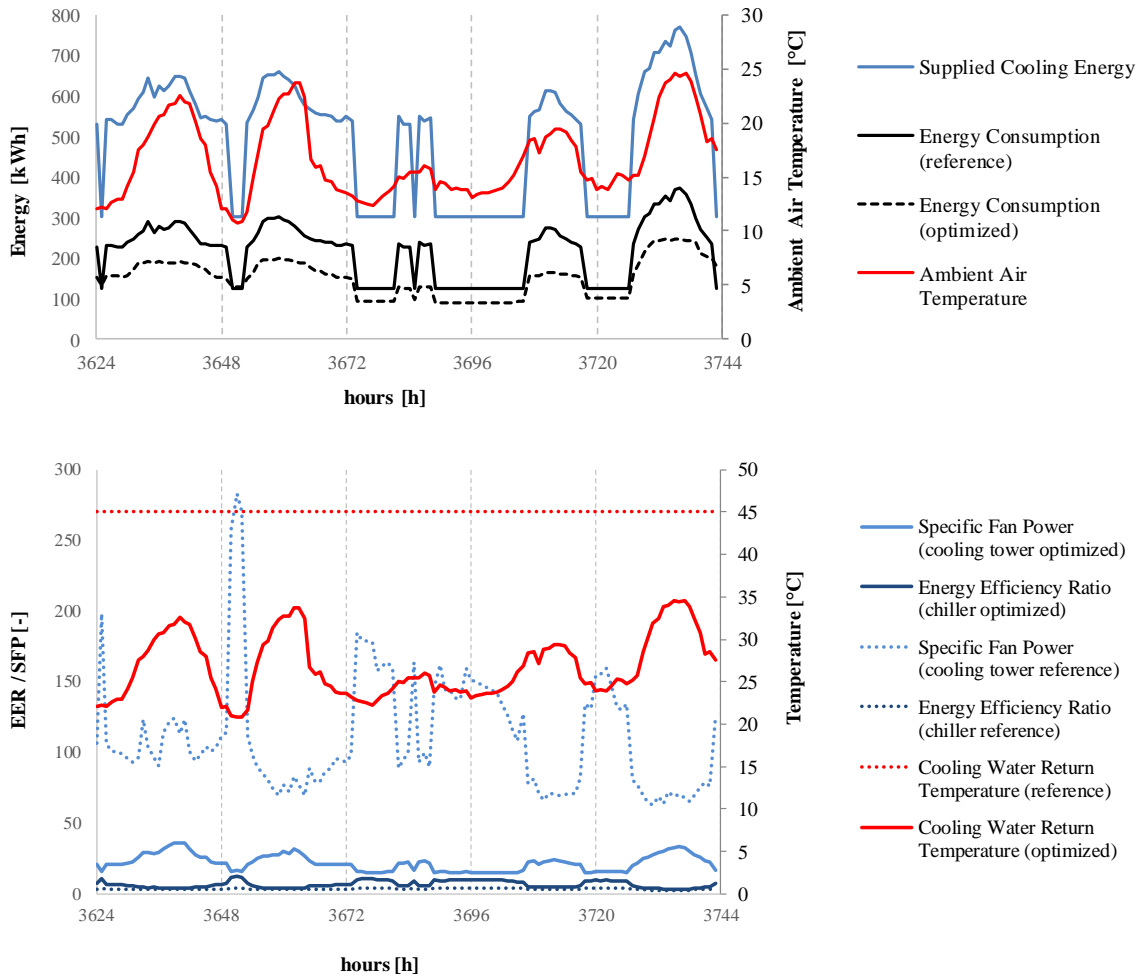


Figure 3: Optimization results of 120 optimized time steps

For the reference operation of the system, the optimized variables have been set to the standard values which are defined and controlled by the building control system. So the cooling water return temperature T_{CWR} was set to 45°C, which is the design point for the cooling tower. The volume flow of the cooling water \dot{V}_{CW} was chosen to be 100 m³/h, corresponding to the design point of the cooling water pumps. The storage was not taken into account, since in reference operation the storage is only used as hydraulic switch. The switching of dry and wet operation mode of the heat rejection plant has been disabled. Only wet operation has been allowed, since the control system of the reference systems strictly activates the wet operation mode when the ambient temperature T_{Amb} is greater than 5°C.

Comparing the reference operation with the optimized operation using all degrees of freedom simultaneously, a massive saving of electric consumption by 29,9% could be achieved. As can be read from the results for the optimization cases with only one free variable, the largest impact results from the optimization of the cooling water return temperature T_{CWR} (**Figure 3**, bottom section). By optimum setting of the cooling water temperature for each individual time step according to the currently given ambient conditions, an energy saving of 22% is reached. The reason for this massive reduction of electrical power consumption is found in a substantial improvement of the energetic efficiency of the chiller, expressed by the energy efficiency ratio ($EER=Q_0/P_{el,ch}$), resulting from the lowering of the cooling water return temperature. During active cooling the EER varies between about 3 and 6, showing an increasing trend when the cooling water temperature drops. In return for the gain in EER, the specific fan power for

ventilation of the heat rejection unit increases strongly. Yet, even when the fan power is doubled, a reduction of the total power demand of chiller and heat rejection unit can be reached, because the connected ratings of the chiller and the heat rejection unit differ by a factor of roughly 10. In free cooling mode with deactivated chillers, the EER reaches values above 10, as a result of the parasitic power demand of circulating pumps and heat rejection unit.

Optimization of all other variables yields substantially lower savings. The best effect may be expected from the use of a cold storage. Using stored cooling energy during high ambient air temperature is an effective operation strategy, allowing for reduced operation of the chiller under unfavourable operating conditions. For the given system configuration, a reduction of only 2% of the energy input is achieved by the utilization of the storage, limited by the small storage volume. With increasing the size, higher energysavings are possible. The optimization of the cooling water flow rate (1,5% savings) and the selection of the dry and wet operation of the heat rejection unit (1,2% savings) had a comparatively minor impact on the energy demand of the system. Interestingly, when optimizing each variable individually, the sum of all savings is lower than when a global optimization of all variables is performed in parallel. This gives an indication, that when maximum freedom for the optimization of the operation of the system is provided, the beneficial interaction of all variables allows for maximum reduction of the energy consumption.

Summary/Conclusion

A method has been presented how refrigeration supply systems can be modeled and optimized with limited mathematical effort. The system configuration and the function of the individual components, such as refrigeration systems and cooling towers are described using higher-order mathematical models. The search for the optimum set of operating parameters is then carried out by means of software applications, so-called solvers. During optimization all secondary conditions are taken into account. Discontinuities, resulting from the modularity of the system with on/off-switching of components and selection of distinct operating modes, is handled by the use of integer-type decision variables.

For a typical operating period of a cooling system of a hospital building with a cooling capacity of 3,2 MW, a simultaneous optimization of all free variables has been performed. Compared to operation with fixed values of the operating parameters, about 30 % of the power consumption can be saved. Largest impact is found for the optimum setting of the cooling water temperature, followed by the utilization of a cold storage.

This approach is easily adaptable to other cooling supply systems, which makes it a perfect basis for further application in the field.

References

- [1] Belotti, P., Kirches, C., Leyffer, S., Linderoth, J., Luedtke, J., and Mahajan, A. 2012. *Mixed-Integer Nonlinear Optimization* ANL/MCS-P3060-1112. ARGONNE NATIONAL LABORATORY, Argonne, Illinois 60439.
- [2] Bentz, J., Loistl, F., and Schweigler, C. 2019. Algorithmus-gestützte Betriebsoptimierung von Kälteversorgungssystemen. In *Deutsche Kälte-Klima-Tagung*.
- [3] Bussieck, M. R. and Vigerske, S. 2010. MINLP Solver Software. In *Wiley Encyclopedia of Operations Research and Management Science*, J. J. Cochran, L. A. Cox, P. Keskinocak, J. P. Kharoufeh and J. C. Smith, Eds. John Wiley & Sons, Inc, Hoboken, NJ, USA. DOI=10.1002/9780470400531.eorms0527.
- [4] Cococcioni, M. and Fiaschi, L. 2020. The Big-M method with the numerical infinite M. *Optim Lett.*

- [5] D'Antonio, M., Moray, S., McCowan, B., and Epstein, G. 2005. Optimization of Industrial Refrigeration Plants. Including a Case Study at Stonyfield Farm Yogurt. *ACEEE Summer Study on Energy Efficiency in Industrie* 2005.
- [6] Hart, W. E., Laird, C. D., Watson, J.-P., Woodruff, D. L., Hackebeil, G. A., Nicholson, B. L., and Siirola, J. D. 2017. *Pyomo. Optimization Modeling in Python*. Springer.
- [7] Hunting, M. 2015. *Solving mixed-integer nonlinear programming (MINLP) problems*.
- [8] Sahinidis, N. 2019. *BARON: UsersManual*. The Optimization Firm.
- [9] Thiem and M, S. 2017. *Multi-modal on-site energy systems. Development and application of a superstructure-based optimization method for energy system design under consideration of part-load efficiencies*. Dissertation, Technische Universität München.

Optimal volume fraction of support material in a heat transfer-enhanced composite for thermochemical energy storage

S. Funayama^{1*}, T. Harada², H. Takasu¹ and Y. Kato¹

¹Laboratory for Advanced Nuclear Energy, Institute of Innovative Research,
Tokyo Institute of Technology,

2-12-1-N1-22, O-okayama, Meguro-ku, Tokyo, 152-8550, Japan

²Department of Chemical Science and Engineering, School of Materials and Chemical
Technology, Tokyo Institute of Technology,

2-12-1-N1-29, O-okayama, Meguro-ku, Tokyo 152-8550, Japan

*Corresponding author: funayama.s.aa@m.titech.ac.jp

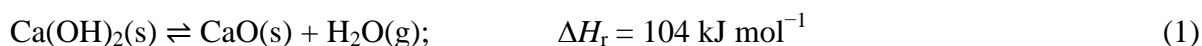
Abstract

The dehydration of calcium hydroxide (Ca(OH)₂) and hydration of calcium oxide (CaO) can potentially be utilized for high-temperature thermal energy storage because of its reversibility, high energy density, and inexpensive storage materials. However, for low thermal conductivities of pure Ca(OH)₂/CaO, it is required to develop composite materials by employing a support material with a high thermal conductivity. In this study, we focused on the volume fraction of the support material, and investigated the optimal fraction that maximizes the heat output rate of the composite by numerical analysis. The results showed that the optimal volume fraction of the support material decreases with increasing thermal conductivity of the support. This study also showed that the optimal fraction could be approximately within 10 vol% for the support material with a thermal conductivity of 100 W m⁻¹ K⁻¹. The results of this study will be applied to future development of heat transfer-enhanced composites for thermochemical energy storage.

Keywords: Thermochemical energy storage, Calcium hydroxide, Heat transfer enhancement, Numerical analysis.

Introduction

Thermochemical energy storage (TCES) using calcium hydroxide (Ca(OH)₂) and calcium oxide (CaO) has recently received attention as a suitable technology for high-temperature (400–600°C) thermal energy storage. The reversible gas-solid reaction that the TCES uses is described in **Equation 1**:



The forward reaction is an endothermic reaction called the dehydration of Ca(OH)₂, and the reverse reaction is an exothermic reaction called the hydration of CaO. The dehydration and hydration are used for heat storage process and heat output process, respectively.

Pure Ca(OH)₂/CaO materials have low thermal conductivities of approximately between 0.1–0.4 W m⁻¹ K⁻¹ [1,2]. Thus, we need to develop composite materials using high thermal

conductivity support materials [3,4]. The mixing ratio of the support material is an important design variable of a composite [5]. This study aimed to investigate the optimal volume fraction of the support material that maximizes the heat output rate of the composite through a numerical analysis of CaO hydration in a packed bed reactor.

Numerical analysis methods

A two-dimensional numerical analysis was performed for the cylindrical packed bed reactor used in a previous study (**Figure 1**) [4]. The reaction bed has a diameter of 48 mm and a height of 50 mm. In this study, we used the assumptions that (1) the domain is continuum and homogeneous; (2) the volume of the material is constant; (3) effective thermal conductivity during a hydration is constant; (4) pressure drop is negligible; (5) density and specific heat of the bed is constant for the reaction bed.

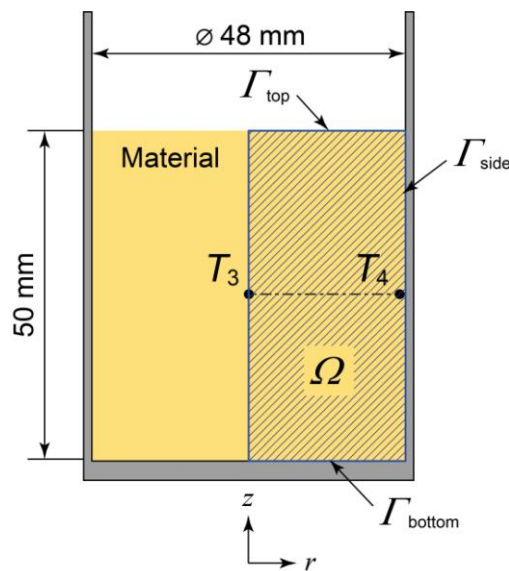


Figure 1 A two-dimensional model of the packed bed reactor. The computational domain (Ω) corresponds to the hatched area.

The heat conduction equation and reaction rate equations were used as the governing equations:

$$\rho c_p \frac{\partial T}{\partial t} = \lambda_{\text{eff}} \nabla^2 T + Q \frac{\partial x_{\text{h,local}}}{\partial t}, \quad (2)$$

where ρ [kg m^{-3}], c_p [$\text{J K}^{-1} \text{kg}^{-1}$], T [K], λ_{eff} [$\text{W m}^{-1} \text{K}^{-1}$], Q [J m^{-3}], $x_{\text{h,local}}$ [-], t [s] denotes density, specific heat, absolute temperature, effective thermal conductivity, energy density of the bed, local conversion of the hydration of CaO, and hydration time, respectively. This study used the rate equations Schaube *et al.* derived [6]. The mass balance equation was ignored in this study to focus on the heat conduction in the reaction bed.

The effective thermal conductivity of a composite bed was assumed to be described with a linear correlation using the weighted thermal conductivities of a pure CaO bed ($0.4 \text{ W m}^{-1} \text{K}^{-1}$) and support material ($1\text{--}100 \text{ W m}^{-1} \text{K}^{-1}$):

$$\lambda_{\text{eff}} = \lambda_{\text{CaO bed}}(1 - \phi) + \lambda_{\text{support}}\phi, \quad (3)$$

where ϕ [-] denotes the volume fraction of the support material. The energy density of the composite bed is described using the energy density of a pure CaO bed, $Q_{\text{CaO bed}}$ [MJ L⁻¹] (0.5–1.6 MJ L⁻¹ [7,8]):

$$Q = Q_{\text{CaO bed}}(1 - \phi). \quad (4)$$

The initial temperature of the reaction bed was set 350°C for the domain, and a temperature of 350°C was set on the boundaries of the top, side, and bottom of the bed.

The governing equations subject to the initial and boundary conditions were implemented using OpenFOAM[®] (-v1806).

The global conversion of the reaction bed during a hydration is calculated using the local conversions:

$$x_{\text{h,global}} = \frac{1}{V_{\text{bed}}} \int_{\Omega} x_{\text{h,local}} dV, \quad (5)$$

where V_{bed} [m³] is the volume of the reaction bed. The heat output rate of the bed is defined with the following equation:

$$w_{\text{h}} = Q \frac{x_{\text{h,global}}}{t}. \quad (6)$$

The optimal volume fraction of support materials that maximizes the heat output rate at 5 min was investigated in this study.

Results and Discussion

The validation of the numerical analysis model was conducted using an experimental data of a pure Ca(OH)₂ pellet bed [9]. **Figure 2** shows a numerical result using the measured bed thermal conductivity of 0.18 W m⁻¹ K⁻¹, and energy density of 1.0 MJ L⁻¹. The computed temperature agrees well with the measured center temperature for 60 min, and the computed conversion also shows good agreement with the experimental data.

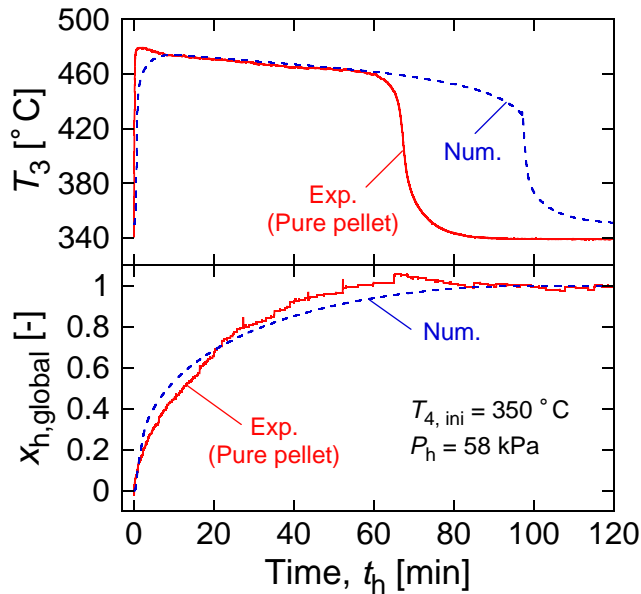


Figure 2 The center temperature and global conversion of the reaction bed.

The heat output rates at 5 min computed with different thermal conductivities between 1–100 $\text{W m}^{-1} \text{K}^{-1}$ are shown in **Figure 3**. When the thermal conductivity of the support is 100 $\text{W m}^{-1} \text{K}^{-1}$, a composite with a 5–10 vol% support material could have a maximum heat output rate of 4.8 kW L-bed^{-1} , which was approximately 2 times higher than the rate of the pure CaO bed.

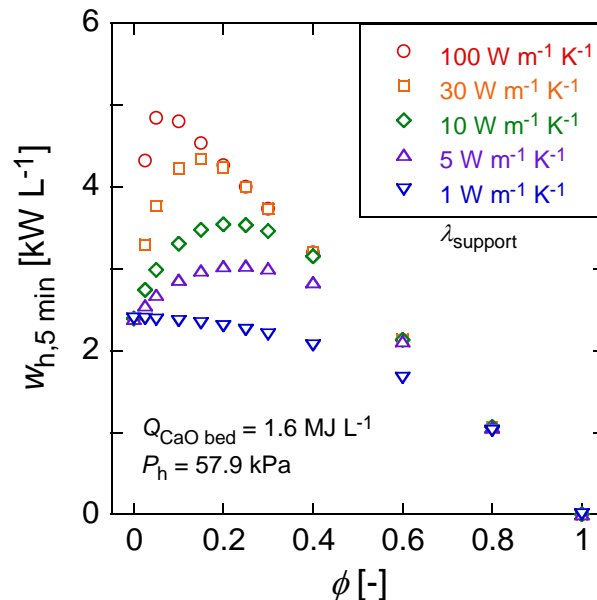


Figure 3 The heat output rate at 5 min with different thermal conductivities of the support.

Figure 4 shows the heat output rates at 5 min computed with different energy densities of the CaO bed between 0.5–1.6 MJ L^{-1} . The result shows that the optimal volume fraction increases as the energy density of the CaO bed increases. When the density is 1.6 MJ L^{-1} , the optimal fraction could be at 20 vol%.

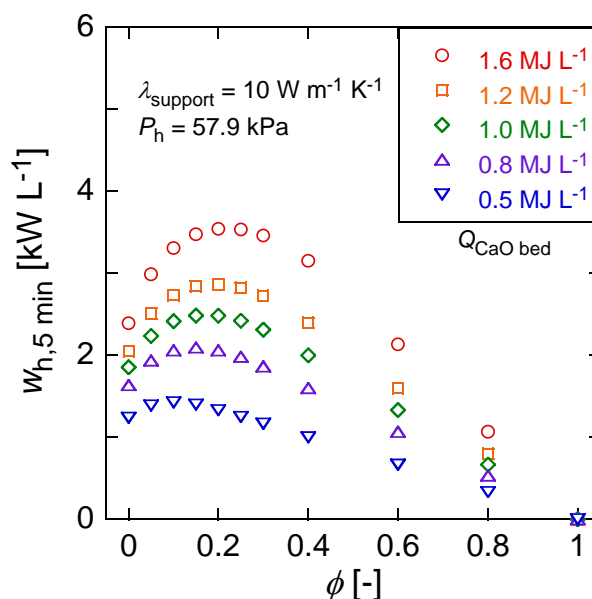


Figure 4 The heat output rate at 5 min with different energy densities of the CaO bed.

We admit that the numerical model uses a simplified series of governing equations to focus on the heat conduction in the reaction bed. Future studies will address the mass transfer of water vapor, in particular for compressed CaO beds with high energy densities, and effects of the density and specific heat of the reaction bed to improve the prediction of the optimal volume fraction of the support material in a composite.

Conclusions

This study investigated the optimal volume fraction of high thermal conductivity supports in composite materials for thermochemical energy storage. It was shown that a composite that contains 5–10 vol%-support material with a thermal conductivity of $100 \text{ W m}^{-1} \text{ K}^{-1}$ has a heat output rate of $4.8 \text{ kW L-bed}^{-1}$, which is approximately 2 times higher than the rate of a pure CaO bed. The numerical results will be applied to future development of heat transfer-enhanced composites for thermochemical energy storage.

Acknowledgements

I would like to thank Professor Yasunori Okano and Mr. Keisuke Nishida at Osaka University, and Mr. Dmitrii Kuzmenkov at MEPHI for the support of numerical studies.

References:

- [1] Ogura, H., Miyazaki, M., Matsuda, H., Hasatani, M., Yanadori, M., Hiramatsu, M., “Experimental study on heat transfer enhancement of the solid reactant particle bed in a chemical heat pump using $\text{Ca}(\text{OH})_2/\text{CaO}$ reaction”, *Kagaku Kogaku Ronbunshu.*, 17 (1991), 916–923.
- [2] Schaube, F., Wörner, A., Tamme, R., “High temperature thermochemical heat storage for concentrated solar power using gas–solid reactions”, *J. Sol. Energy Eng.*, 133 (2011), 031006.

- [3] Funayama, S., Takasu, H., Zamengo, M., Kariya, J., S.T. Kim, S.T., Kato, Y., “Composite material for high-temperature thermochemical energy storage using calcium hydroxide and ceramic foam”, *Energy Storage*, 1 (2019), e53.
- [4] Funayama, S., Takasu, H., Kim, S.T., Kato, Y., “Thermochemical storage performance of a packed bed of calcium hydroxide composite with a silicon-based ceramic honeycomb support”, *Energy*, 201 (2020), 117673.
- [5] Balat, M, Spinner, B., “Optimization of a chemical heat pump: Energetic density and power”, *Heat Recover. Syst. CHP.*, 13 (1993), 277–285.
- [6] Schaube, F., Koch, L., Wörner, A., Müller-Steinhagen, H., “A thermodynamic and kinetic study of the de- and rehydration of $\text{Ca}(\text{OH})_2$ at high H_2O partial pressures for thermo-chemical heat storage”, *Thermochim. Acta.*, 538 (2012), 9–20.
- [7] Schmidt, M., Linder, M., “Power generation based on the $\text{Ca}(\text{OH})_2/\text{CaO}$ thermochemical storage system – Experimental investigation of discharge operation modes in lab scale and corresponding conceptual process design”, *Appl. Energy.*, 203 (2017), 594–607.
- [8] Kamiya, H., Ito, Y., Yamauchi, T., Mochizuki, M., Itahara, H., Shimazu, T., “Development and factory verification of the high-energy density thermochemical storage system”, *AIP Conf. Proc.* (2020), 2303.
- [9] Funayama, S., Takasu, H., Zamengo, M., Kariya, J., Kim, S.T., Kato, Y., “Performance of thermochemical energy storage of a packed bed of calcium hydroxide pellets”, *Energy Storage*, 1 (2019), e40.

Piston compressors driven by isobaric expansion heat engines

A. Kronberg*, M. Glushenkov

Encontech B.V. TNW/SPT, PO box 217, 7500 AE Enschede, The Netherlands

*Corresponding author e-mail: info@encontech.nl

Abstract

Compression of gases or vapors in reciprocating compressors involves multiple energy conversion steps. These steps include converting of energy of different fluids (steam, combustion products, water or wind) to shaft power, generation of electricity, feeding the electricity to an electric motor through electrical networks, transformers, frequency converters, and eventually driving the compressor kinematics. Direct compression of a gas or vapor by another fluid (referred to as vapor) is an attractive alternative to the current compression methods. Besides the elimination of the multiple energy conversion steps and associated equipment this old compression concept permits to use sustainable, abundantly available low grade heat sources instead of fossil fuels. Isobaric expansion heat engines offer an interesting opportunity for efficient vapor driven compression processes without the use of electricity. The purpose of this paper is to assess the feasibility of this method, in which compressor piston is directly actuated by a vapor of arbitrary parameters. Thermodynamic analysis performed shows that the efficiency of vapor use in the simplest compressor schemes applied in the past is inherently low. In order to eliminate this drawback different new vapor driven compressor configurations are proposed and evaluated using the same approach. These configurations include multistage vapor driven compression, reuse of the driving vapor and the use of force transmission between the compressor and driver pistons. It is shown that the proposed configurations can significantly improve the efficiency of vapor use and can be a valuable alternative to existing compression technologies.

Keywords: Compression, heat-driven compressor, isobaric expansion, renewable energy, low-grade heat.

Introduction

Energy consumption by compressors is substantial. For instance, compressed air systems alone account for 10% of industrial electricity consumption in the USA and the EU [1, 2]. An increase in electricity demand from residential and commercial air conditioning by 2050 is expected to be comparable to adding the European Union's entire electricity consumption. Air conditioning will represent 12.7% of electricity demand by the middle of the century, compared to almost 9% now [3]. Therefore, any improvements in the cost and efficiency of compression processes are of great interest.

Reciprocating, or piston compressors, are the best known and most widely used compressors of the positive displacement type [4]. Although piston compressors are simple in principle, all the used arrangements include massive and expensive kinematic components (piston, piston rod, crosshead, crankshaft, crankcase, flywheel, and gearbox).

Most piston compressors are driven by electric motors. Different heat engines (steam or gas turbines, piston engines) are also used as drivers of reciprocating compressors [4, 5, 6]. Generally, the heat engines convert the energy of different fluids (steam, combustion products, water or wind) to shaft power. This shaft power, in turn, is converted into electricity, which is fed to the electric motor through electrical networks, transformers, frequency converters, etc. The electric motor drives the compressor kinematics which performs work on the compressed fluid (gas or vapor). Ultimately, the energy of a primary fluid is transferred to the energy of the compressed fluid in such a complex multistage way.

There are also compression technologies in which one fluid is compressed directly by another one. Gas (liquid-gas) ejectors [7], wave pressure exchangers [8], free piston diesel compressors [9, 10, 11, 12] and steam compressors [6] are among them. These methods eliminate kinematic transmission and multiple energy conversion steps. However, the efficiencies of gas ejectors and wave pressure exchangers are rather low. Free-piston diesel compressors proved to possess some very attractive features. However, they did not gain widespread commercial success. No reports of serious lacks or flaws in the concept explaining this can be found [13].

A direct steam-driven air compressor is one of the earliest compressor types. It is actuated by a steam engine of the reciprocating type with a direct connection between the piston of the compressor and that of the steam engine so that both pistons move as a unit [6]. The idea of steam-driven compressors goes back to the first heat engines invented by Savery and Newcomen for water pumping more than 300 years ago [14, 15, 16]. Probably the first steam driven compressors were blast furnace bellows for the production of lead copper and iron in the mid-18th century [17].

Steam-driven compressors are similar to steam pumps although the processes are different, and in contrast to steam pumps they are almost unknown [5]. To date, no application has been found for this compression technology. The last mention of operating steam driven air compressors we found is a compressor instruction pamphlet from the Westinghouse Air Brake Company [18] that is 100 years old.

The practical implementation of the concept of steam or (more generally heat driven) reciprocating compressor depends on the availability of an energy efficient heat engine. So-called isobaric expansion (IE) engines, which directly convert heat to mechanical energy in the form of a high pressure fluid (liquid or vapor) have the potential to revive the steam-driven compression concept. The isobaric expansion technology was introduced in [19], although it was previously studied under different names and for various applications [20, 21, 22, 23, 24, 25]. With their hydraulic or pneumatic power output, the IE engines are ideal for pumping and compression applications. The impact of this method can be significant because, in addition to eliminating multiple energy conversions and associated equipment, they allow replacing primary fossil energy sources with abundantly available low-grade heat, even at temperatures below 100 °C.

The energy efficiency of heat driven IE engine-pumps has been studied both theoretically and experimentally [19, 26, 27]. However, according to our knowledge, studies of compression processes in which a compressible fluid acts as an actuating agent are absent in the literature; the interesting system proposed in [28] has not been evaluated properly as the used assumptions violate both momentum and energy conservation. Recent publications on this topic, [29, 30], do not differentiate between compression and pumping, which can lead to gross errors.

The purpose of this paper is to assess the feasibility of a direct transfer of energy from one compressible fluid to another one as it occurs in the steam-driven reciprocating piston compressor. In the processes under consideration, the compressor piston is driven directly by the piston of a heat engine (driver) using a working fluid of arbitrary parameters. Any fluid (gas, liquid, supercritical fluid or fluid undergoing phase transition) can be considered as the actuating or driving agent. In the following part of the present work, we will use the terms vapor or driving fluid to refer to all possible fluids.

The question of how the driving vapor is generated (i.e. heat engine process) is not considered. Therefore, this analysis is equivalent to the analysis of the energy efficiency of a steam-driven compressor operating on an open cycle. In the case of a closed cycle, the overall process efficiency is also determined by the engine process which is beyond the scope of the present work.

A thermodynamic analysis of the efficiency of vapor use (defined as work performed by the driver per unit mass of vapor) is performed. At first, the simplest compressor schemes are considered. In these schemes the compressor piston is rigidly connected to another piston accommodated in a cylinder, called in this paper driver. It is found that in such schemes the direct transfer of energy from one fluid to another is inherently inefficient since the energy of the driving vapor is largely spent on the compression of the driving vapor itself.

In order to eliminate the drawback of simple vapor driven compressors different new vapor driven compressor configurations are proposed and evaluated using the same approach. These configurations include multistage vapor driven compression, reuse of the driving vapor and the use of force transmission between the compressor and driver pistons.

Basic vapor driven compressors

Two basic schemes of single- and double-acting direct vapor driven compressors are shown in Figure 1. They consist of a compressor cylinder and a driver cylinder provided with pistons that are coupled by a connecting rod. The driver cylinder is combined with a vapor generation circuit (shown in the single acting scheme) consisting of a heater **H**, recuperator **R**, cooler **C** and feed pump **P**. The driver together with the vapor circuit forms an IE heat engine. Its operation is described in [19]. The heat engine replaces the electric motor or internal combustion engine and the crank mechanism of the conventional piston reciprocating compressors.

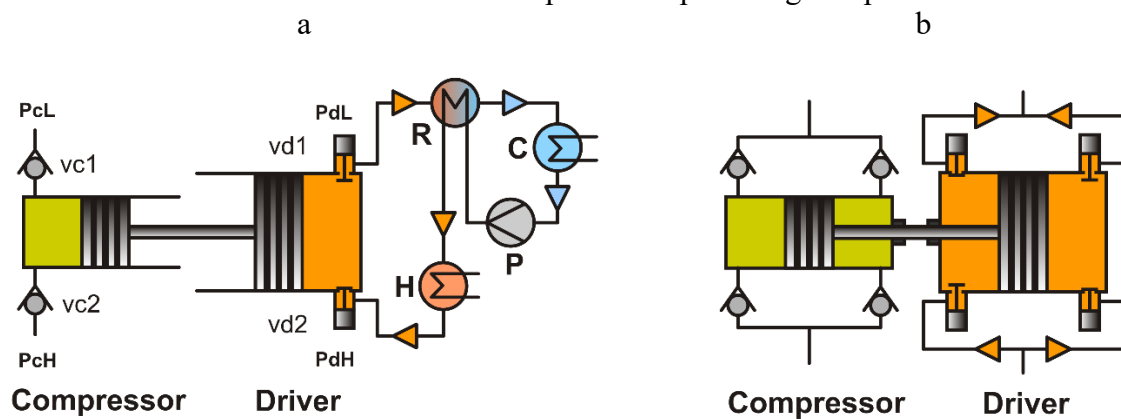


Figure 1. Basic schemes of vapor-driven compressors: a – single acting; b – double acting.

In the case of the single-acting unit (Figure 1a) both the compression and actuation occur on one side of the compressor and driver pistons. In the double-acting type unit (Figure 1b) compression and actuation take place on both sides of the pistons. In the case of the single-acting unit, the pressures on the outer surfaces of the pistons are usually constant ambient pressure, whereas for the double-acting system they are intake and discharge pressures of the compressor and driver, respectively.

The pistons are free in the sense that their movement is controlled only by the fluid forces acting upon them. The driver piston is actuated by vapor generated in the vapor circuit. The reciprocating motion of the driver piston in each scheme is transformed into the reciprocating motion of the compressor piston.

The processes in the compressor and driver can be explained for the single acting scheme, Figure 1a, as follows. Let us assume that initially the compressor cylinder is filled with the compressed fluid at its intake or low pressure P_{cL} and the volume of the cylinder is maximal V_{c0} . During the compression step the discharge valve of the driver $vd2$ is closed; the driving fluid is supplied to the driver through the intake valve $vd1$. The pressure of the driving fluid is transmitted through the driver piston and connecting rod to the compressor piston. As a result

pressure in the compressor increases from the initial/intake or low pressure P_{cL} to the final/discharge or high pressure P_{cH} and then the compressed fluid under influence of the driving fluid at its maximum pressure P_{dH} is discharged from the compressor through the outlet check valve $vc2$ at constant high pressure P_{cH} . After that the inlet valve of the driver $vd1$ closes, the outlet valve $vd2$ opens and pressure of the driving fluid in the driver drops from P_{dH} to the low driver pressure P_{dL} . Due to equalization of the forces acting on the pistons, they move a little to the right so that a small amount of the compressed fluid remaining in the compressor (mainly in the intake and discharge valves) expands and its pressure decreases to the intake pressure P_{cL} ; simultaneously part of the driving fluid is pushed out of the driver through the discharge valve $vd2$. After that the compressor intake stroke begins during which pressure in the compressor remains constant. Simultaneously the rest of the driving fluid discharges from the cylinder through the valve $vd2$ at constant pressure P_{dL} . At the end of the compressor intake and the driver discharge stroke the system returns to the initial state and the system is ready for the cycle to be repeated.

As in the case of steam piston engines the crucial problem is to find a method to supply the driving vapor to the power cylinder (driver), providing the highest work. If the pistons of the compressor and driver are coupled by a mechanism such as a crank gear with a massive flywheel acting as energy storage, the solution is well known: a certain amount of steam is to be injected at high pressure during an initial stage of piston movement, after which the intake valve closes and the supplied steam expands further adiabatically. However, this method will not be satisfactory in the case of low-inertia, directly coupled pistons (low mass or low reciprocation frequency), as shown in Figure 1. A large difference in the forces acting on the compressor and driver pistons, especially at the beginning of the compression stroke, results in an uncontrollable acceleration of the pair of pistons, fluid to be compressed and excessive consumption of the driving vapor. Therefore, to avoid detrimental piston acceleration, the pressure change in the driver should correspond to the variable pressure in the compressor.

Ideally, the pistons move without acceleration (except for the top and bottom dead points). Technically, such an operation can be achieved if the characteristic time of the pressure rise in the driver is lower than the characteristic time of the force equalization in the compressor and driver. In addition, appropriate sizes of the compressor and driver pistons and the high and low pressures of the driving fluid should be selected for the compression process.

For the double-acting compressor-driver combination forward and back strokes of the pistons are identical. In this case, taking into account the forces acting on the pistons, it is possible to obtain a relation between the areas of the pistons and the pressures that allow the compression cycle to be carried out:

$$\frac{A_c}{A_d} = \frac{P_{dH} - P_{dL}}{P_{cH} - P_{cL}} \quad (1)$$

The maximum pressure of the driving fluid P_{dH} can be higher than that obtained from Eq. 1. However, this is not justified from the energy efficiency standpoint in view of unnecessary consumption of the driving fluid at the end of the compression stroke. The minimum pressure of the driving fluid P_{dL} can be lower than that obtained from Eq. 1, however, such an operation would require a controlled discharge valve of the driver to maintain the driving fluid pressure at a level that is necessary for uniform movement of the pistons.

A remarkable feature of a double-acting unit is that for any given values of low and upper pressures in the compressor P_{cL} and P_{cH} , arbitrary values of low and upper pressures in the driver P_{dL} and P_{dH} can be used.

For the single-acting compressors, shown in Figure 1a, the requirements towards the low and upper pressures in the driver are different. In this case, the relation between the pressures conforming the condition of the uniform piston movement is

$$(P_c - P_a)A_c = (P_d - P_a)A_d \quad (2)$$

where P_a is the ambient pressure.

Eq. 2 places a restriction on the driver pressure range for given compressor pressures. This can be understood considering a high-pressure process when ambient pressure can be neglected. In this case the forward and back piston strokes will be performed if $P_{dH}A_d \geq P_{cH}A_c$ and $P_{dL}A_d \leq P_{cL}A_c$ accordingly. From these requirements it follows that the driver pressure ratio should be not less than the compressor pressure ratio: $\frac{P_{dH}}{P_{dL}} \geq \frac{P_{cH}}{P_{cL}}$. However, for many practically interesting applications the pressure ratio in the compressor $r_c = \frac{P_{cH}}{P_{cL}}$ is much higher than the available pressure ratio in the driver $r_d = \frac{P_{dH}}{P_{dL}}$, especially within the scope of the current research focused on the low temperature difference applications of the IE engines.

The restriction on the pressure of the driving fluid in the single-acting scheme can be avoided using a modified, more flexible, scheme shown in Figure 2a.

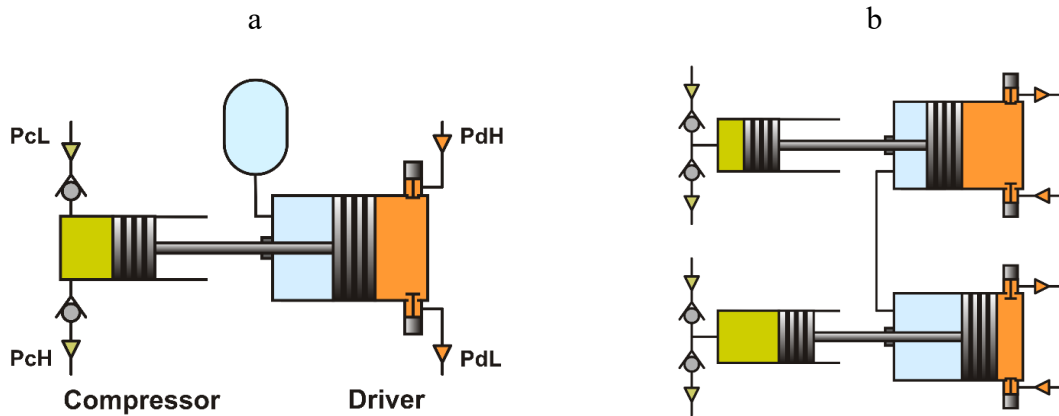


Figure 2. Modified single-acting schemes: with a receiver (a) and duplex scheme (b).

In this improved scheme there is a large volume accumulator or receiver with a specified pressure P_r which becomes an additional process parameter. Taking it equal to

$$P_r = \frac{P_{dL}(P_{cH} - P_a) - P_{dH}(P_{cL} - P_a)}{P_{cH} - P_{cL}} \quad (3)$$

allows for using any low and upper pressures in the driver, P_{dL} and P_{dH} , for given values of low and upper pressures in the compressor, P_{cL} and P_{cH} . It can be shown that in this case Eq. 1 also becomes valid.

The scheme with the receiver, Figure 2a, is a useful theoretical configuration. Better functionality can be achieved by using the duplex design, Figure 2b. Duplex is a combination of two identical machines operating in counterphase, both auxiliary chambers of which (in blue) are connected by a pipe. If the auxiliary chambers are filled with a gas at the pressure P_r needed in the receiver, they function as a large receiver without compression/expansion of the gas inside them. The auxiliary chambers can also be used for the lubrication, draining of working fluid leakages through the seals etc. An auxiliary chamber(s) can also be arranged in the compressor cylinder.

Having in mind the modified scheme, Figure 2, in the following analysis of the process efficiencies there is no need to distinguish single-acting and double acting schemes. For any given pressures in the compressor arbitrary low and upper pressures in the driver can be applied.

Efficiency of driving vapor use in basic vapor driven compressors

In this paper, the efficiency of vapor generation in the heat engine is not considered; it is assumed that driving vapor with a certain temperature and pressure is available. The focus of the study is on the efficiency of vapor use in the driver when it is applied for compression processes with different compression ratios either adiabatically or isothermally.

For the purpose of simple analysis, the following usual assumptions are made consistent with thermodynamic analysis:

- The process in the compressor is either adiabatic or isothermal.
- The process in the driver is adiabatic.
- The driver performs only useful work on the compression.
- Minimum volumes of the compression and driving cylinder are zero (no dead volume).
- Temperature and pressure of the fluids in the driver and compressor are uniform.
- Mechanical friction between moving and stationary parts in contact is negligible.
- Inertia of the pistons, piston rods and the fluids is negligible; this is justified for IE engines operating at low frequencies.
- Cross-sectional area of the piston rods is much smaller than the area of the pistons.
- Compressed and driving fluid are ideal gases; the ratios of the heat capacities at constant pressure and constant volume of the driving and compressed gases, γ_c and γ_d , were taken equal to 1.4 unless otherwise indicated.

To characterize the process we introduce a vapor use efficiency defined as the useful work performed by the driver per cycle per unit mass of the consumed vapor m_{d0} :

$$w = \frac{W_{c0}}{m_{d0}} \quad (4)$$

In Eq. 4 the useful work is designated as the work of the compressor per cycle, $W_{c0} = \oint P_c dV_c$, which is equal to the work of the driver, $W_{d0} = \oint P_d dV_d$, under the assumptions made.

The mass of the consumed vapor depends on its temperature at the end of compression stroke, T_{de} , and can be calculated as

$$m_{d0} = \rho_d(T_{de}, P_{dH})V_{d0} \quad (5)$$

where $\rho_d(T_{de}, P_{dH})$ and V_{d0} are the vapor density and its volume at the end of the compression stroke.

The specific work w can easily be calculated if the load on the driver piston is constant during the forward and back strokes of the piston. Such a constant load is realized in the limiting case when the compressor operates as an ideal pump. In this case the driver performs the maximum possible work, $W_{dmax} = (P_{dH} - P_{dL})V_{d0}$, because the pressure of the driving vapor is maximal during the compression piston stroke and minimal during the discharge piston stroke. From the energy balance equation it follows that temperature of the driving vapor at the end of the compression/pumping stroke is T_{dH} . Therefore, $m_{p0} = \rho_d(T_{dH}, P_{dH})V_{d0}$ and the specific work of the driver operating as an actuator of the ideal pump is

$$w_p = \frac{W_{dmax}}{m_{p0}} = \frac{P_{dH} - P_{dL}}{\rho_d(T_{dH}, P_{dH})} \quad (6)$$

w_p of Eq. 6 is taken as the benchmark for the comparison of the efficiencies of the driver in this paper. Thus the relative efficiency of vapor use is defined as

$$\alpha = \frac{w}{w_p} = \frac{\rho_d(T_{dH}, P_{dH})}{\rho_d(T_{de}, P_{dH})} \frac{W_{c0}}{(P_{dH} - P_{dL})V_{d0}} \quad (7)$$

α or T_{de} can be obtained from the energy balance for the compression stroke which in case of adiabatic process is:

$$(H_d(T_{dH}, P_{dH}) - U_d(T_{de}, P_{dH}))m_{d0} = W_{dc} \quad (8)$$

where H_d and U_d are specific enthalpy and internal energy of the driving vapor, and W_{dc} is the work of the driver in the compression stroke. Eq. 8 takes into account that the driving vapor enters the driver cylinder at temperature T_{dH} and pressure P_{dH} .

W_{dc} can be expressed through the work per cycle, $W_{d0} = W_{c0}$, and the discharge work of the driving vapor, $-P_{dL}V_{d0}$:

$$W_{dc} = W_{c0} + P_{dL}V_{d0} \quad (9)$$

From Eqs. 1, 5, 8, 9 and the fluid state equation ($\phi(\rho, P, T) = 0$) T_{de} and all other process characteristics can be obtained, if the work W_{c0} is known. Important qualitative conclusions can be drawn from these simple equations: for the highest specific work, Eq. 4, the internal energy at the end of the compression stroke $U_d(T_{de}, P_{dH})$ should be as low as possible, and the useful work W_{c0} as large as possible. Using Eq. 4 and taking into account that the highest rate of the pressure change with the volume occurs at adiabatic expansion, one can prove that the Rankine cycle has the maximum steam use efficiency.

The equations above can readily be treated if both the compressed and driving fluid are the ideal gasses. In this case enthalpy, internal energy, density and specific heats, c_p and c_v , are

$$H_d(T, P) = c_p T, \quad U_d(T, P) = c_v T, \quad \rho_d(T, P) = \frac{P\mu}{RT} \quad (10)$$

$$c_p = \frac{R\gamma_d}{\mu(\gamma_d - 1)}, \quad c_v = \frac{R}{\mu(\gamma_d - 1)}, \quad \gamma_d = \frac{c_p}{c_v} \quad (11)$$

in which R is the gas constant and μ is the molecular mass of the driving vapor.

Combining these equations with Eqs. 4, 5, 8 and 9 the temperature of the gas at the end of the compression stroke and the efficiency of gas use can be obtained:

$$\frac{T_{de}}{T_H} = \frac{\gamma_d r_d}{\gamma_d + (r_d - 1) \left[\frac{\omega_{c0}}{r_c - 1} (\gamma_d - 1) + 1 \right]}, \quad \alpha = \frac{\omega_{c0}}{r_c - 1} \frac{T_{de}}{T_{dH}} \quad (12)$$

where $r_c = \frac{P_{cH}}{P_{cL}}$ and $r_d = \frac{P_{dH}}{P_{dL}}$ are the pressure ratios of the compressor and driver, and $\omega_{c0} = \frac{W_{c0}}{P_{cL}V_{c0}}$ is the dimensionless compressor work. In case of adiabatic and isothermal compressions the dimensionless compressor works are:

$$\omega_{c0,ad} = \frac{\gamma_c}{\gamma_c - 1} \left(r_c^{\frac{\gamma_c - 1}{\gamma_c}} - 1 \right), \quad \omega_{c0,isothermal} = \ln(r_c) \quad (13)$$

where γ_c is the ratio of the heat capacities at constant pressure and constant volume of the compressed gas.

Figure 3 shows the calculated efficiency of driving gas use.

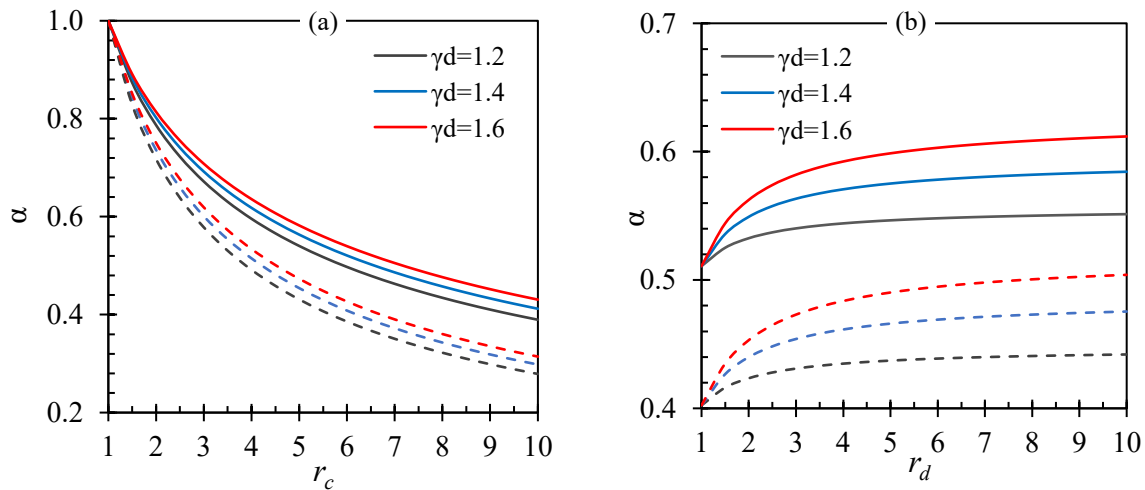


Figure 3. Efficiency of the driving gas use as a function of the pressure ratio in the compressor at $r_d = 3$ (a) and driver at $r_c = 5$ (b) and different γ_d ; solid lines – adiabatic compression, dashed lines – isothermal compression, $\gamma_c = 1.4$.

The results obtained show that the efficiency of the driving gas use depends strongly on the properties of the gases, γ_c and γ_d , and on the pressure ratios in the compressor and driver. For practically interesting compression processes (r_c is not close to 1) the efficiency of vapor use is much less than the efficiencies of vapor use in vapor-driven pumps. The pressure ratio in the compressor r_c has the major effect on the efficiency. It drops rapidly with r_c and increases with the pressure ratio in the driver r_d . The reason for the low efficiency is that a significant fraction of the energy of the driving gas supplied to the driver is spent on the compression of the driving gas that is already present in the driver.

It should be noted that although the dependence of the efficiency on the driver pressure ratio r_d is not strong, operation with r_d approaching 1 is impractical, since in this case the work done approaches zero.

The relative position of the red, blue and grey lines in Figure 3 is explained by the fact that the temperature elevation of the driving fluid with larger γ_d during the compression stroke is higher and the density is lower. Accordingly, the consumption of the driving gas with higher γ_d is lower whereas the efficiency of its use is higher.

Isothermal compression is preferred over adiabatic compression in conventional compression processes because the compression work is lower. For vapor driven compression, this advantage is diminished, see Figure 3, because the driver piston is less loaded when compression is isothermal.

Based on the results obtained, several modified methods of vapor-driven compression can be proposed. These methods are presented below.

Multistage compression

When multiple compressor cylinders are connected in series and a gas or vapor is compressed in stages the arrangement is referred to as a multistage or stage compressor. If compression ratio is high, the compression is carried out in more than one step [6].

In almost all multi-stage applications the compressed gas or vapor will be cooled between stages because with intercooling, the compression more closely approximates an isothermal compression with resulting lower power requirement [6].

The simplest scheme of two-stage vapor driven compression with intercooling is presented in Figure 4. In this scheme each driver piston is actuated by the same vapor source. A difference compared to the conventional scheme is that the compressor pistons are actuated by a driving vapor and not by an electric motor or IC engine through a crank mechanism. In addition, it is important to note that the main reason for multistage vapor-driven compression is to improve efficiency of vapor use rather than a considerable temperature rise and a reduction of the compression work. Therefore processes without intercooling could also be of interest.

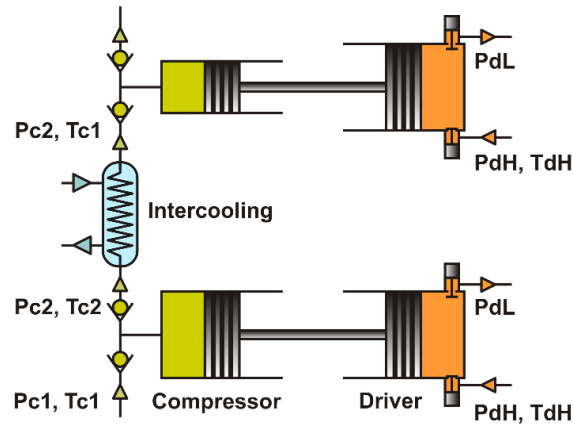


Figure 4. Scheme of two-stage vapor-driven compressor.

The multistage vapor driven compression process can be studied using the same approach as in the previous section. Figure 5 shows examples of efficiency of the driving gas use for one-, two- and three-stage compression. The results presented in Figure 5 were obtained for adiabatic compression under assumption that the compressor pressure ratio is the same in all stages.

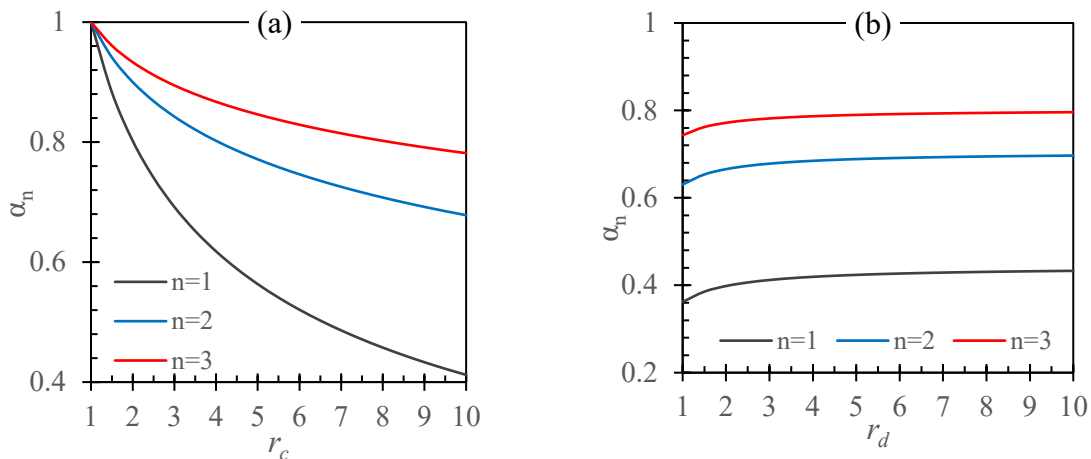


Figure 5. Efficiency of the driving gas use for one, two and three stage compression as a function of the compressor pressure ratio (a), $r_d = 3$ and driver pressure ratio (b), $r_c = 10$.

Significant improvement of the efficiency is observed when the number of stages increases, especially if two stage compression is used instead of single stage compression. The efficiency increases with the number of stages and in the limit of large number of stages its value approaches 1. In this case pressure changes in the compressor and driver at each stage are negligible and the process is the same as in an ideal pump.

The efficiency is the same for processes with and without intercooling because in case of the ideal gases it is determined by the pressure ratios in the compressor and driver and the heat

capacities. However, intercooling reduces the driving gas consumption as the compression work is reduced. This effect is significant at high compressor pressure ratio.

It can be shown that, in addition to improving the efficiency, stage compression permits substantially reduce the total volume of the drivers, especially for processes with intercooling. For practically interesting pressure ratios the total volume of the drivers can be reduced several times. It is interesting that the total volume of the compressors and drivers can decrease with the number of stages at certain process parameters.

Compression with driving vapor reuse

Vapor in the driver at the end of the compression stroke is a valuable energy source. Its pressure is equal to the initial pressure P_{dH} and its temperature is higher than the initial temperature T_{dH} . Therefore, one of the ways to improve efficiency of the driving vapor use is to reuse the vapor that is in the driver at the end of compression stroke. A difference compared to the basic method, Figures 1 and 2, is that, the driving vapor at the end of the compression stroke is not discharged from the driver to the vapor circuit (specifically to the recuperator, Figure 1a) but used for initial, or intermediate, compression in another compressors. The vapor from the vapor circuit of the heat engine is used only in the final compression phase.

Many different schemes utilizing the driving vapor reuse principle can be proposed. As an example, a simple scheme of a single stage compression processes with vapor reuse is shown in Figure 6. It includes two drivers, two compressors and two 3-way valves. A description of the process can be started at the initial moment when driver 1 is at the end of the compression stroke and is filled with high pressure, hot driving vapor (P_{dH}, T_{dH}), Figure 6a. Driver 2 at this moment is in the end of its discharge stroke and does not contain driving vapor. Valve 1 is closed whereas valve 2 opens and communicate the drivers. As a result, driver 2 performs compression in compressor 2 until the pressure forces on the driver 2 and compressor 2 pistons equalize, Figure 6b. Thus, at this phase of the process, compression in compressor 2 occurs with vapor from driver 1. Then valve 2 closes and the driving vapor from its original source (heat engine) is delivered to driver 2 through valve 1 to accomplish the compression stroke in compressor 2, Figure 6c. Then, or simultaneously, driving vapor remaining in driver 1 is discharged and compressor 1 is filled with the fluid to be compressed, Figure 6d. After that process repeats with the interchanged functions of compressor 1 - driver 1 and compressor 2 - driver 2.

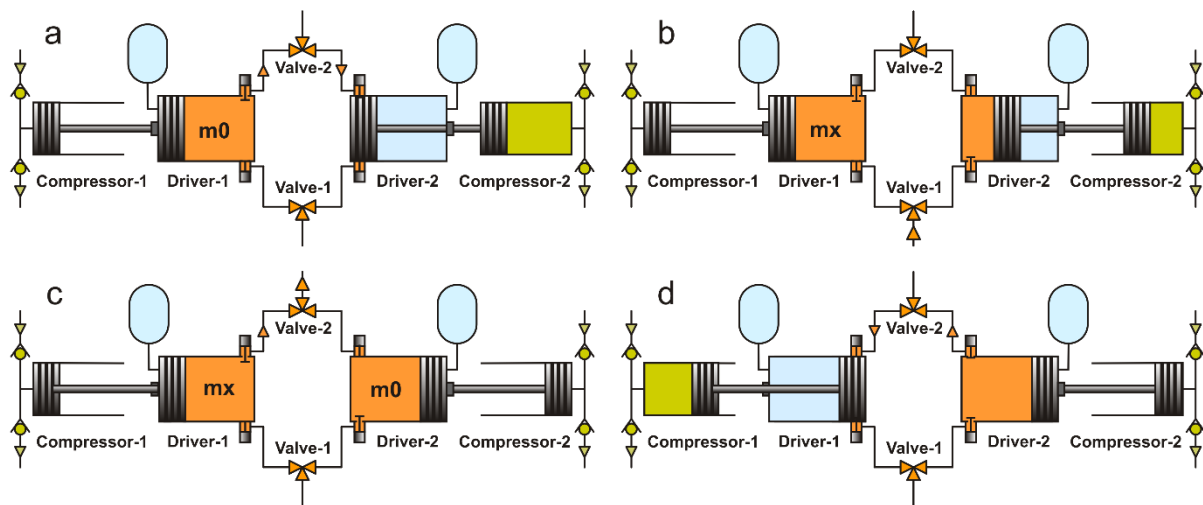


Figure 6. Scheme of single stage vapor driven compression with vapor reuse; different phases of the process are shown.

Taking into account the advantages of multistage vapor driven compression a logical step is to apply the idea of vapor reuse for multistage compression processes. Figure 7 shows an example of two-stage scheme with vapor reuse. At first stage the fluid is compressed from the low pressure P_{CL} to some intermediate pressure in compressor 1. Then partly compressed fluid is displaced to compressor 2 where it is compressed till the desired pressure P_{CH} . The drivers operate in the same way as in the scheme shown in Figure 6. The fluid from compressor 1 can be displaced to compressor 2 directly or through an intercooler as in Figure 7.

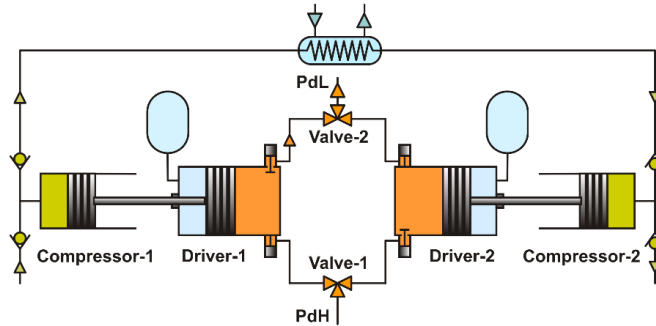


Figure 7. Scheme of two-stage vapor driven compression with vapor reuse.

Figure 8 shows the calculated efficiencies for different processes: without driving gas reuse (basic scheme), and with driving gas reuse in the one- and two-stage compression as a function of the pressure ratios in the compressor and driver.

The results presented were obtained using the same approach as in the previous sections, although with slightly more complex mathematics. A significant increase in efficiency is seen due to the reuse of driving gas. Two-stage compression with reuse of the driving gas offers the efficiency very near to the efficiencies of vapor driven pumping process. Remarkably that at low compressor pressure ratio the efficiency becomes even higher than in case of operation as the ideal pump.

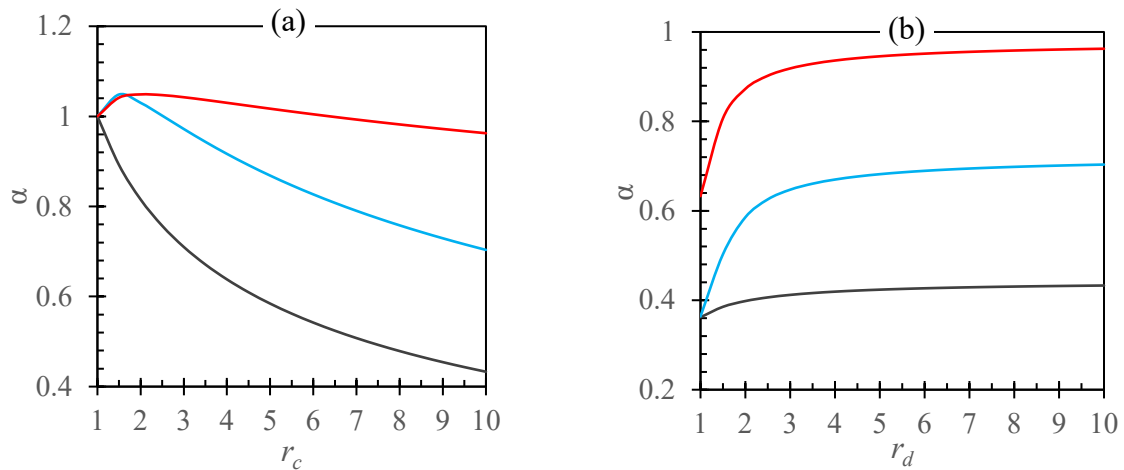


Figure 8. Efficiency of the driving gas use as a function of the compressor (a) and driver (b) pressure ratio: grey lines - basic compression scheme, blue lines - single-stage with gas reuse, red lines - two-stage with gas reuse; $r_d = 10$ (a), $r_c = 10$ (b).

Vapor driven compression with force transmission

From the analysis of the basic vapor driven compression processes it follows that the rising pressure of the driving vapor during compression stroke is the reason of low vapor use efficiency. One of the possible methods to avoid significant pressure rise in the driver and

improve its efficiency is to connect the piston rods through a mechanical linkage (kinematic transmission) to manage forces and movement of the pistons.

A massive flywheel in combination with a crank gear is well-known linkage mechanism used in different machines e.g. in reciprocating piston compressors driven by an electric motor or IC engines. This method can also be applied in vapor driven compressors as e.g. is shown in Figure 9a. In this case, some part of power delivered by driver in an initial period of the compression cycle is accumulated by a flywheel (shown in blue in Figure 9a) and then is used in a final period of the compression piston stroke. If the intake valve of the driver is open and does not create a resistance to the driving vapor flow the pressure in the driver will be constant and equal to its maximum pressure P_{dH} . As a result, the vapor use efficiency will be the same as in case of an ideal pump.

Many mechanisms for force transmission can be proposed, which help to increase the efficiency of vapor use without using the effect of energy storage. One of such methods was proposed in [31] to equalize the variable forces between the steam actuated power piston and the saline water pump piston in a reverse osmosis system.

Mathematically the presence of a mechanical linkage can be expressed by an equation relating the forces $F_c(x)$ and $F_d(y)$ on the compressor and driver piston:

$$F_d(y) = Tr(x)F_c(x) \quad (14)$$

In these equation x and y are positions of the pistons in the compressor and driver and the transmission function $Tr(x)$ is expressed as a function of x . Obviously, choosing $Tr(x)$, one can achieve any desired balance of the forces.

We will briefly illustrate the concept of force transmission using as an example a simple lever mechanism shown in Figure 9b. The transmitting function in this case expressed through the angle between the driver piston rod and the lever is $ctg(\varphi)$.

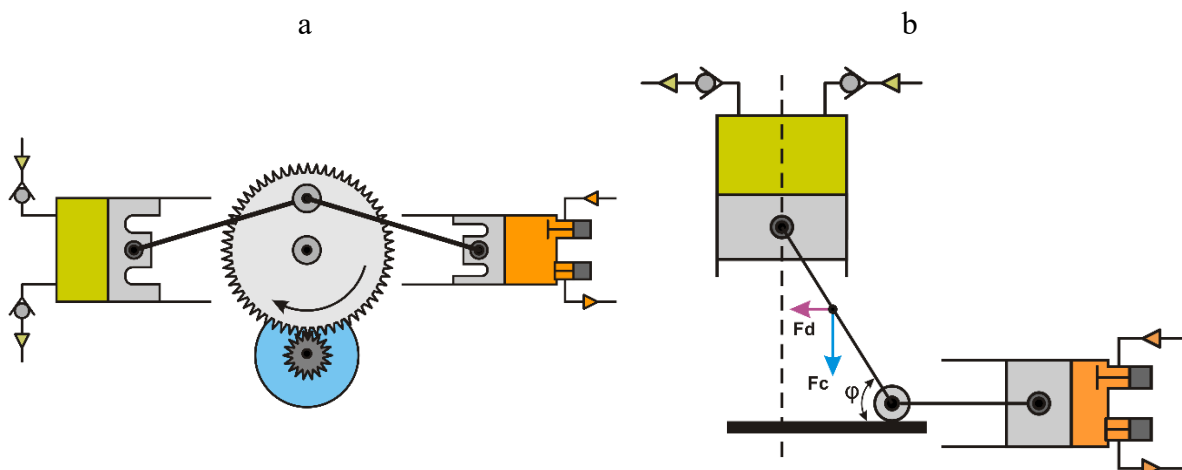


Figure 9. Schemes of vapor driven compressor with mechanical linkages between the pistons.

Figure 10 shows an example of the calculated vapor use efficiency in the case of double acting piston-driver arrangements when the angle φ changes in the range $20^\circ - 70^\circ$.

Gain in the efficiency due to the transmission is clearly seen. An additional advantage of the transmission is that the improved efficiency is achieved with smaller driver volume as the pressure span in the driver becomes narrower, close to the maximum pressure.

Generally the analysis of the systems with a transmission is more complicated than without it. Not every transmission can provide a balance of the forces and uniform piston movement. In the example above even a minor force on the driver piston will result in acceleration of the both

pistons if the angle φ approaches 90° and $ctg(\varphi)$ tends to zero. Also the ambient pressure or pressure in the receiver become an additional process parameters in case of single acting scheme. These important details are beyond the scope of this paper.

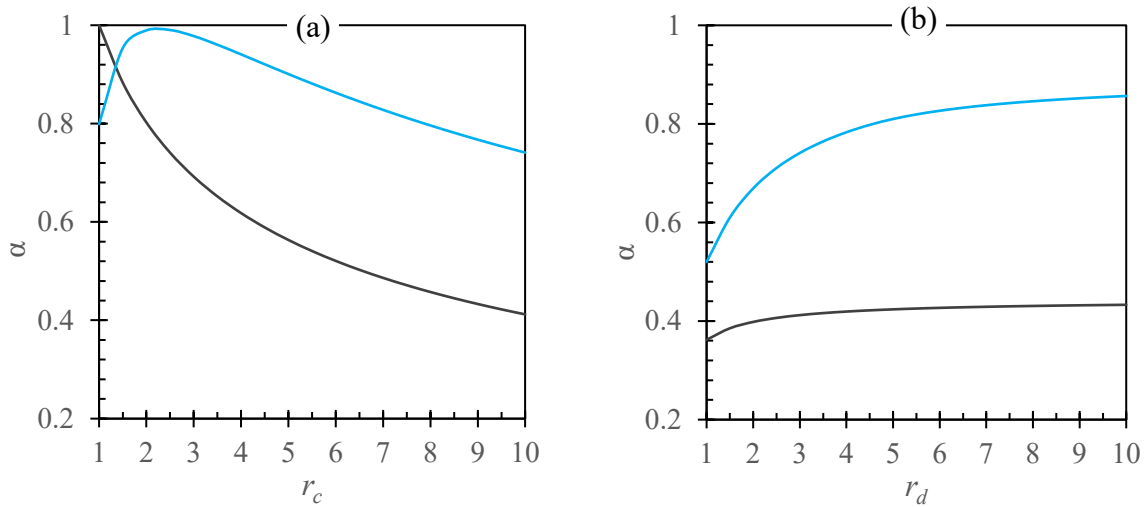


Figure 10. Efficiency of the driving gas use without (grey lines) and with (blue lines) transmission as a function of the pressure ratios in the compressor, $r_d = 10$ (a) and driver $r_c = 10$ (b).

Discussion and conclusions

In the known steam driven compressors [18] the steam was supplied to the compressor from a boiler and exhausted to atmosphere. Therefore thermal efficiency of the compressor was determined by the steam use efficiency introduced in this paper, Eq. 4 or 7, because the supplied heat was directly proportional to the mass of the generated steam.

The results obtained in this paper for the simplest schemes might explain why such steam driven compressors are not used. The use of closed steam cycles, shown in Figure 1a, will not help to improve their thermal efficiency because heat regeneration in case of steam is very poor as explained e.g. in [32]. However, if a regenerative heat engine is used and the steam is replaced by a fluid with thermodynamic properties allowing efficient heat regeneration, see [26], it can be expected that processes with low vapor use efficiency might be feasible.

Inefficient use of the driving vapor manifests in the higher temperature of vapor exhausted from the driver. In the case of ideal gases this temperature is determined by Eq. 12. The increased temperature offers additional potential for improved heat recovery in the recuperator of the IE engine. This problem requires further detailed investigation accounting for thermodynamic properties of the driving fluid.

This paper presents how, if necessary, the disadvantages of the schemes with low vapor use efficiency can be eliminated with the proposed above methods – multistage vapor driven compression, vapor reuse, force transmission or combination of thereof – and other methods. With these methods the vapor use efficiency can become comparable with the efficiency in pumping processes. Which of them is preferable depends on technical complexity and eventually on the economics.

Overall, the results presented in this paper show the significant potential of the heat driven compression concept and the need for further research. This concepts is especially attractive because it allows the of low-grade heat sources ($<100^\circ\text{C}$) which cannot be effectively used with existing technologies.

Acknowledgements

This publication was made possible by NPRP grant # [NPRP11S-1231-170155] from the Qatar National Research Fund (a member of Qatar Foundation). The findings achieved herein are solely the responsibility of the authors.

References

- [1] "Assessment of the Market for Compressed Air Efficiency Services," US department of Energy, Report prepared for Oak Ridge National laboratory and Lawrence Berkeley National laboratory by Xenergy Inc, [Online]. Available: <https://www.energy.gov/sites/prod/files/2014/05/fl6/newma>.
- [2] R. Saidur, N. Rahim and M. Hasanuzzaman, "A review on compressed-air energy use and energy savings," *Renewable and Sustainable Energy Reviews*, vol. 14, p. 1135–1153, 2010.
- [3] C. Bryant, "Air conditioning is the world's next big threat," [Online]. Available: <https://www.renewableenergyworld.com/2019/07/02/air-conditioning-is-the-worlds-next-big-threat/#gref>.
- [4] H. P. Bloch and J. J. Hoefner, *Reciprocating compressors: operation and maintenance*, Butterworth-Heinemann, 1996.
- [5] R. N. Brown, *Compressors: Selection and Sizing*, 3rd edition, Elsevier Science & Technology Books, 2005.
- [6] B. F. Dodge, *Chemical Engineering Thermodynamics*, New York and London: McGRAW-HILL, 1944.
- [7] B. M. Tashtoush, M. A. Al-Nimr and M. A. Khasawneh, "A comprehensive review of ejector design, performance, and applications," *Applied Energy*, vol. 240, pp. 138-172, 2019.
- [8] P. Akbari, "A Review of Wave rotor technology and its application," *Journal of Engineering for Gas Turbines and Power*, vol. 128, no. October, pp. 717-735, 2006.
- [9] R. P. Pescara, "Motor compressor apparatus". US Patent 1,657,641, 1928.
- [10] R. P. Pescara, "Motor compressor of the free piston type". US Patent 2,241,957, 1941.
- [11] H. O. Farmer, "Free-piston compressor-engines," *Proc. Inst. Mech. Eng.*, vol. 156, p. 253–271, 1947.
- [12] W. T. Toutant, "The Worthington-Junkers free-piston air compressor," *Journal of the American Society of Naval Engineers*, vol. 64, no. 3, p. 583–594, 1952.
- [13] R. Mikalsen and A. P. Roskilly, "A review of free-piston engine history and applications," *Applied Thermal Engineering*, vol. 27, no. 14-15, pp. 2339-2352, 2007.
- [14] H. E. Keeney, *Steam consumption of pumping machinery. Thesis*, University of Illinois, June 1900.
- [15] J. G. Mair, "Experiments on a direct-acting steam-pump," *Minutes of the Proceedings of the Institution of Civil Engineers*, vol. 86, no. 4, pp. 293-302, 1886.
- [16] J. B. Crocker, "Direct-acting pump". US Patent 571,751, 24 November 1896.
- [17] "Steam power during the Industrial Revolution," [Online]. Available: https://en.wikipedia.org/wiki/Steam_power_during_the_Industrial_Revolution.
- [18] Westinghouse steam driven air compressors. Single stage type, Pittsburgh, PA: Westinghouse air brake co, 1919.

- [19] M. Glushenkov, A. Kronberg, T. Knoke and E. Y. Kenig, "Isobaric Expansion Engines: New Opportunities in Energy Conversion for Heat Engines, Pumps and Compressors," *Energies*, vol. 11, no. 1, p. 154, 2018.
- [20] C. N. Markides and T. C. B. Smith, "A dynamic model for the efficiency optimization of an oscillatory low grade heat engine," *Energy*, vol. 36, no. 12, p. 6967–6980, 2011.
- [21] R. Solanki, A. Galindo and C. N. Markides, "Dynamic modelling of a two-phase thermofluidic oscillator for efficient low grade heat utilization: Effect of fluid inertia," <https://doi.org/10.1016/j.apenergy.2011.01.007>," *Applied Energy*, vol. 89, no. 1, p. 156–163, 2012.
- [22] A. Date and A. Akbarzadeh, "Theoretical study of a new thermodynamic power cycle for thermal water pumping application and its prospects when coupled to a solar pond," *Applied Thermal Engineering*, vol. 58, no. 1–2, pp. 511–521, 2013.
- [23] M. Glushenkov and A. Kronberg, "Regenerative Heat to Mechanical Energy Converter with Dense Working Fluid," in *Proceedings of the 16th International Stirling Engine Conference*, Bilbao, Spain, 24 – 26 September 2014, 177–186.
- [24] C. J. W. Kirmse, O. A. Oyewunmi, A. I. Taleb, A. J. Haslam and C. N. Markides, "A two-phase single-reciprocating-piston heat conversion engine: Non-linear dynamic modelling," *Applied Energy*, vol. 186, p. 359–375, 2017.
- [25] O. A. Oyewunmi, C. J. W. Kirmse, A. J. Haslam, E. A. Müller and C. N. Markides, "Working-fluid selection and performance investigation of a two-phase single-reciprocating-piston heat-conversion engine," *Applied Energy*, vol. 186, p. 376–395, 2017.
- [26] S. Roosjen, M. Glushenkov, A. Kronberg and S. Kersten, "Binary mixtures as working fluids for low temperature waste heat recovery systems with isobaric expansion technology," in *Heat Powered Cycles Conference 2021*, Bilbao, 19 - 22 September 2021.
- [27] M. Glushenkov and A. Kronberg, " Experimental study of an isobaric expansion engine-pump," in *Heat Powered Cycles Conference*, Bilbao, 19 - 22 September 2021., 2021.
- [28] S. Aphornratana and T. Sriveerakul, "Analysis of a combined Rankine–vapour–compression refrigeration cycle," *Energy Conversion and Management*, vol. 51, p. 2557–2564, 2010.
- [29] A. K. Sleiti, "Isobaric Expansion Engines Powered by Low-Grade Heat - Working Fluid Performance and Selection Database for Power and Thermomechanical Refrigeration.," *Energy Technology 2020*, vol. 8, 2020.
- [30] A. K. Sleiti, W. A. Al-Ammari and M. Al-Khawaja, "Analysis of Novel Regenerative Thermo-Mechanical Refrigeration System Integrated With Isobaric Engine," *Journal of Energy Resources Technology - Transactions of the ASME*, vol. 143, no. 5, p. 052103, 2021.
- [31] P. A. Davies, "A solar-powered reverse osmosis system for high recovery of freshwater from saline groundwater," *Desalination*, vol. 271, pp. 72–79, 2011.
- [32] A. Kronberg, M. Glushenkov, T. Knoke and E. Y. Kenig, "Theoretical limits on the heat regeneration degree," *International Journal of Heat and Mass Transfer*, vol. 161, no. 11, pp. 1–10, 2020.

Annual energy analysis of a trigeneration solar system using radiative cooling in Mediterranean climate

M. Noro^{1*}, S. Mancin¹ and R. Riehl²

¹Dept. of Management and Engineering – University of Padova – stradella San Nicola 3 – 36100 Vicenza - Italy

²National Instit. for Space Research – Av. dos Astronautas 1758, São José dos Campos, SP 12227-010 – Brazil

*Corresponding author: marco.noro@unipd.it

Abstract

Radiative cooling with the outer space as a natural heat sink can be very useful in order to widely diffuse the standard of Nearly Zero Energy Building in Mediterranean climate. Despite it is a well-known passive technique, it is not so commonly used due to low power density and long payback periods. Recently, the integration of a radiative cooler into a solar photovoltaic/thermal collector is gaining increasing interest in research as a solution to overcome these drawbacks. In this study, the energy performance of a system converting solar energy into electricity and heat during daytime and offering cooling energy at night is assessed on the basis of a validated model of a trifunctional photovoltaic–thermal–radiative cooling module. The key energy performance indicators are analysed by varying the main parameters of the system such as spectral emissivity of the selective absorber plate and cover, and thermal insulation thickness. The annual performance analysis is performed for a typical residential building and climate of the Mediterranean area.

Keywords: cogeneration, Mediterranean climate, photovoltaic/thermal, radiative cooling.

Introduction

Even if extensive application of insulation is reducing energy demand for new and refurbished buildings, heating demand remains high in more diffused existing buildings, particularly in temperate zones [1]. On the other hand, cooling energy demand is increasing especially in milder climates, due to the global climate change, and to the reduced capacity of more insulated buildings to waste energy [2]. As a matter of fact, in the last decades, more efficient heating and cooling systems have becoming desirable to reduce the conventional energy demand from fossil fuels or electricity, such as condensing boilers, heat pumps, open and closed cycle sorption systems, solar thermal, and electrical technologies.

Despite nowadays solar energy is not the most widely used renewable energy in the world [3], it is considered the most promising one for the sustainable development of modern society. Solar thermal collectors that produce hot water or air, and photovoltaic modules that produce electricity are the most diffused solar technologies. As it is well known, the thermal efficiency of a solar thermal collector highly depends on its photothermal conversion efficiency and heat loss [4]. In particular, it relies on its spectral absorptivity in the solar heating (SH) band (0.2-3 μm range) and on the radiative heat loss in the middle and far infrared band ($> 3 \mu\text{m}$). Starting from the beginning of this century, a series of improvements regarding the solar thermal collectors have been proposed. Higher performance selective coatings were developed, with an absorptivity of approximately 0.95 and an emissivity of as low as 0.05 [5] [6]. Thus, a first-order thermal loss coefficient of $1 \text{ W m}^{-2} \text{ K}^{-1}$ or even less is now the standard value in solar thermal collectors largely available on market.

Concerning the solar conversion to electricity, not all wavelengths of the incoming radiation are usefully converted into electricity in PV cells: commercially available single junction PV cells have an electrical efficiency varying between 6% to 25% (under optimum operating conditions and depending on the semiconductor material), whereas the rest of the solar radiation is dissipated as heat [7]. This is due to the band-gap energy of the semiconductor material. For example, crystalline silicon PV cells can utilize the entire visible spectrum plus some part of the infrared spectrum, but the energy of all other wavelengths (far infrared and higher energy radiation) cannot be converted into electricity and unfortunately is dissipated by the cell as thermal energy. The main drawback is that the PV module can reach temperatures as high as 40 °C above ambient; this causes an increased intrinsic carrier concentration which tends to increase the dark saturation current of the p–n junction. The main effect is the decreasing of the available maximum electrical power, typically 0.2–0.5% for every 1 °C rise in the PV module temperature for crystalline silicon cells. Another critical issue for improving the performance of PV systems is maintaining a homogeneous low temperature distribution across the string of cells.

The well-known main idea to face the issues just described is to increase the electrical production of PV by decreasing the normal operating cell temperature by cooling the panel by a liquid (or air). Thus, PhotoVoltaic/Thermal technology (PVT) aims at using the same area both for producing electricity and heat. This also implies to have higher global efficiency with an enhanced use of solar incoming energy [8] [9].

Besides the direct conversion of solar radiation into thermal and electrical energy, solar thermal cooling was one of the first studied technologies aftermath the 1973 energy crisis for the cooling of buildings. In spite of many successful pilot plants, this technology has not taken off yet. Over and over, intergovernmental organizations [3] or multi-stakeholder governance groups [10] recommended the development of solar cooling. The fact is that the last recording of installations worldwide reached only 1200 plants in 2014, most in Europe [11]. The system appears expensive and complex. Moreover, in temperate climates, the ab/adsorption chiller is utilized only in summer, so that the investment cost is even less advisable. Moreover, the progressive cost reduction of PV panels occurred in the first decade of the present century, highlighted a possible competition between solar PV cooling systems, where PV panels drive a compression chiller. The further impressive PV price reduction of the last decade seems to close definitively the game, and now the competition of solar electrical cooling in terms of overall cost is rather with conventional air-conditioning [12].

Radiative Cooling (RC) can be considered a viable alternative to solar thermal and solar PV cooling. It is a renewable energy technology that uses the high spectral transmittance of the atmosphere in the so-called “atmospheric window” band (8-13 μm , the “RC band”) to extract heat from a collector by radiative heat exchange with cold outer space [13]-[15].

The cooling performance of a radiative cooler is positively affected by the clearness of the atmosphere and the spectral emissivity in the RC band of the cooling surface. In fact, the cooling surface should have the lowest possible spectral absorptivity (that is, emissivity) in the bands excluding the RC band to maintain the surface temperature as low as possible. In the last years, daytime RC has also been successfully achieved thanks to the development of materials science in micro-nano scale that allows to further strengthen the spectral selectivity of RC coatings [16] [17].

As a matter of fact, the spectral selectivity of the SH coating and RC coating are incompatible: the former features extremely low emissivity in the middle and far infrared bands, particularly in and the RC band, the latter features low absorptivity in the SH band. As a consequence, solar collectors can be used only during the daytime, when most of the

radiative coolers normally cannot run. Furthermore, the solar heat collector is more useful in spring, autumn, and winter, when the RC collector is of less value than summer. Finally, the RC collector shows a cooling power density lower (in the range of 40-80 W m⁻²) than the vapor compression refrigeration system; thus, the payback period of SH and RC systems is still long due to all these characteristics.

For such reasons, it is worth to analyse a system set-up by integrated diurnal solar thermal and photovoltaic (PVT) and nightly RC functions into one single collector. Such a system would extend the operation time of conventional solar installations until night-time while eliminating the cost disadvantages of stand-alone RC collectors. Moreover, it would feature an increased overall efficiency and seasonal adaptability.

Some authors have already studied SH-RC system [18]-[22]. They developed a mathematic model that considers the spectral radiant distribution of the coating and atmosphere. Numerical calculations were performed to investigate the heating and cooling performance of the hypothetical spectrally selective SH-RC surface by comparing it with three other typical surfaces. They also investigated a trifunctional photovoltaic–photothermic–radiative cooling (PVT-RC) collector, and a practical-scale testing system was built to verify the effectiveness of the numerical model [23]-[25].

In all those studies, the authors investigated numerically and experimentally some key performance indicators of the system, such as its diurnal thermal efficiency under different ambient temperatures, inlet temperature, and solar irradiance, as well as its nocturnal cooling power under different inlet temperatures and sky conditions. Surfaces with different spectral selectivity were also tested. However, only a parametric analysis of the PVT-RC and SH-RC collectors were made, and no annual energy performance of the whole system was evaluated. The originality of the present study is the application of the mathematical model of the PVT-RC module in a Trnsys project in order to simulate the annual performance of the system to face the loads (heating, cooling, domestic hot water (DHW), and electricity) of a residential building in a typical Mediterranean climate. The annual performance of the hybrid system was evaluated to investigate its electricity, heat, and cooling energy outputs, efficiency, and load factor, both in specific and total terms. Such analysis was carried out varying different key structural parameters such as cover emissivity, collector plate emissivity, and thermal insulation thickness.

Methods

The building and the loads

A model of a residential building was realized [26], and simulations performed using Trnsys were performed to create a heating and cooling demand. The single family detached house has two floors, a total volume of 363.5 m³ and the first and second floor cover an area of 77 m² and 58 m², respectively. The main entrance has an orientation to the north and a portico to the south; a wall of the living room is oriented to the west.

A DHW load profile consumption was generated using a free tool of Trnsys called the Domestic Hot Water load profile generator, with a daily DHW demand of approximately 200 l at 40 °C. Data for electricity demand was taken from [26] in terms of average hourly electrical consumption of a household for the main uses (fridges and freezer, lighting, dishwasher and washing machine, multimedia tools). The annual total energy demands for the house located in Trapani (Italy, 38 °N, with a Csa climate according to Koppen classification, i.e., temperate with dry summer climate with a hot summer – the hottest month has a mean temperature above 22 °C) for space heating, DHW, cooling, and electricity were

approximately 2860 kWh, 2727 kWh, 2008 kWh, and 2120 kWh, respectively, based on test reference year data [27]. Figure 1 summarizes the monthly energy demand to show how the hourly energy demand changes between the colder and hotter seasons.

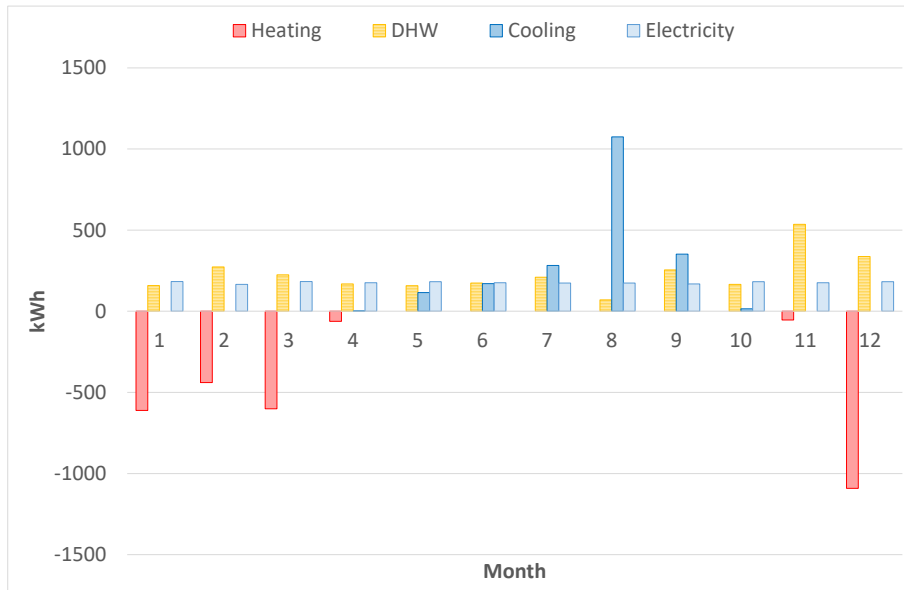


Figure 1 – Heating, cooling, DHW, and electricity energy needs for the residential building in Trapani (Italy)

Spectral characteristics of different surfaces

To compare the energy performance of the plant in different cases, in this paper we considered three surfaces for the collector plate with different spectral characteristics in terms of absorptivity (i.e., emissivity), and two surfaces for the cover with different spectral characteristics in terms of transmittance (Figure 2). Therefore, in this study, six different configurations are evaluated in terms of energy performance, given by the combination of the three collector plates and the two covers.

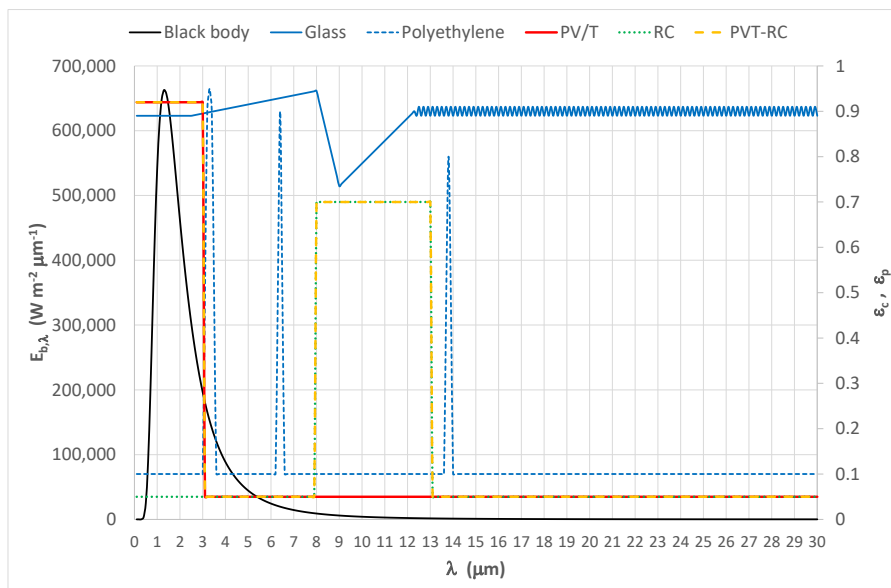


Figure 2 – Spectral properties of the black body (spectral radiation power at 2200 K, left y-axis) and of the collector plate (PVT, RC, PVT-RC) and transparent cover (Glass, Polyethylene) (emissivity, right y-axis) ([22] [25])

Figure 2 reports the spectral emissivity of a typical PVT collector (high spectral absorptivity in the SH band, red continuous line), for a typical radiative cooler (high spectral emissivity in the RC band, dotted green line), and for a PVT-RC collector that has high spectral absorptivity (i.e., spectral emissivity) in the SH and RC bands (hatched yellow line). Accordingly, in this study, we considered a spectrally selective PVT-RC surface with an average absorptivity of 0.92 (i.e., nearly the same as that of the real SH surface) in the SH band, an average emissivity of 0.70 (i.e., nearly the same as that of the real RC surface) in the RC band, and an average absorptivity (emissivity) of 0.05 (i.e., nearly the same as that of the real SH surface) in other bands.

Concerning the transparent cover, the glazing one is commonly applied in PVT collectors, but it is not properly suitable for RC as it is “opaque” to the mid and long wave infrared radiation. On the other hand, the polyethylene film acts as the cover of the RC device for its high transmissivity in most bands as it is transparent in the RC band, but it features low mechanical resistance to adverse meteorological phenomena [20]. In the present study, both a 6 μm thick polyethylene film and a 2.8 mm thick glass served as the cover of the different collectors considered. The reason is that even if the direct heat exchange between the plate and the cold sky is inhibited, the plate can firstly dissipate heat to the glass cover by heat radiation and convection, and then the glass cover exchanges heat to the sky by radiative cooling. As a matter of fact, the cooling capacity can be considered effective thanks to the high long-wave absorptivity and emissivity on both sides of the glass cover. Moreover, the cooling capacity of a PVT collector can be considered as an unexpected additional bonus, so a lower cooling performance with respect to the modified PE film-based PVT-RC collector is acceptable. The transmittance characteristics of both the low-density polyethylene film and the glass are reported as absorptivity (i.e., the complement to one of the transmittances assuming a very low reflection coefficient of 0.01) in Figure 2.

The schematic diagram of the PVT-RC collector model is shown in Figure 3 [24]. It has a flat-plate structure, with overall dimensions of 2000 mm \times 1000 mm \times 80 mm. A 1964 mm \times 964 mm \times 0.4 mm aluminum plate served as the baseplate, which is fully covered by a 0.3 mm thick layer of black Tedlar–polyester–Tedlar (TPT). A total of 72 mono-crystalline silicon PV cells, with an area of 1.12 m², were laminated onto the black TPT surface. An encapsulation layer of transparent TPT was placed above the PV cells and the black TPT. Two glue layers of ethylene–vinyl–acetate (EVA) were fixed between the aluminum plate and the TPTs. A 40 mm high air gap was set between the cover and the PVT-RC panel. Seven copper water tubes, each with an inner diameter of 8 mm and an external diameter of 10 mm, were welded in parallel at the backside of the aluminum plate. A 40 mm thick layer of glass fiber was adopted as the back insulator of the collector.

The collector was set to a tilt angle suitable to optimize the solar radiation collection during the year (27.9° in Trapani, TR) with an unobstructed view of the sky. A simplified schematic of the plant is reported in Figure 4, where only the heating energy is reported for simplicity. In Table I the main variables are reported. The full description of the mathematical model of the collector is described in the full references [18]-[25], and it is not reported here for the sake of brevity.

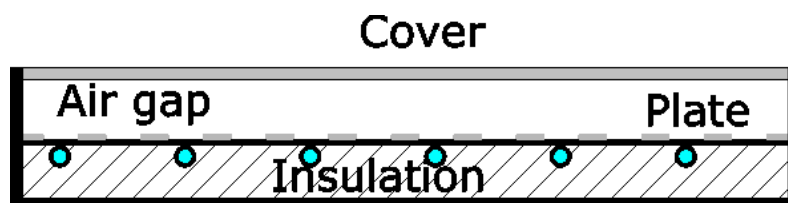


Figure 3 – Cross-section view of the collector modelled. The cover can be Glass or Polyethylene, the plate can be with PVT, RC, or PVT-RC spectral characteristics

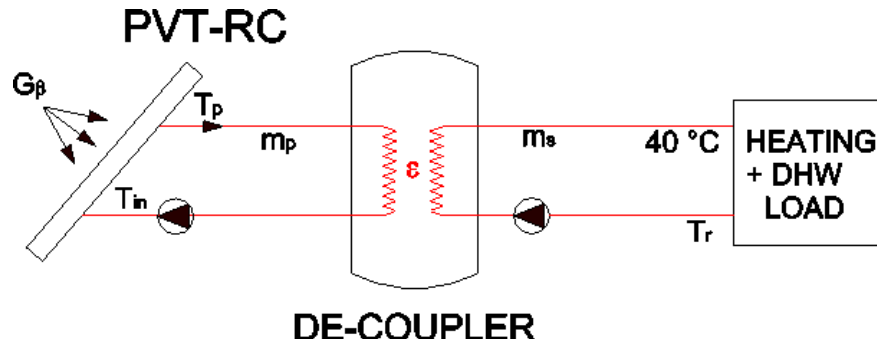


Figure 4 – Simplified functional diagram of the solar plant (only heating energy is reported)

Table I – Values of the main variables of Figure 4

Variable (unit)	Value
Primary circuit specific mass flow rate (m_p) ($\text{kg h}^{-1} \text{m}^{-2}$)	60
Secondary circuit specific mass flow rate (m_s) ($\text{kg h}^{-1} \text{m}^{-2}$)	20
Collector area (m^2)	10
Distance cover-plate ($d_{p,c}$) (mm)	40
Insulation thickness (d_b) (mm)	40
Insulation thermal conductivity (k_b) ($\text{W m}^{-1} \text{K}^{-1}$)	0.04
Reflectance of the cover (ρ_c)	0.01
Reflectance of the plate (ρ_p)	0.10
Transmittance (τ_c) - Polyethylene	0.90
Transmittance (τ_c) - Glass mid and far infrared (night)	0.10
Transmittance (τ_c) - Glass near infrared (day)	0.90
Reference electrical efficiency of the solar cells (η_{ref})	16.0%
Temperature coefficient of the solar cells (B_r) (K^{-1})	0.0045
Efficiency of the heat exchanger (ϵ)	0.8

Results and Discussion

Based on the validated mathematic model, the main temperatures of the glass-covered PVT-RC module during two typical 24-hours periods were investigated. The water flow rate was set to $0.017 \text{ kg s}^{-1} \text{ m}^{-2}$ ($60 \text{ kg h}^{-1} \text{ m}^{-2}$), and the initial water temperature in the tank was set equal to 10°C at the starting time. The evaluation is reported in Figure 5 for two different seasons, 17th January and 17th August, in terms of temperature of the glass cover T_c and the collector plate T_p , together with air temperature T_a , collector inlet water temperature T_{in} , and heat exchanger return water temperature T_r (see also Figure 4).

As shown in Figure 5, the ambient air temperature remains relatively stable at around 20°C during night-time and 25°C during daytime in July (11°C and 16°C respectively, in January), while the wind velocity fluctuates significantly with an average value of about 2.8 m s^{-1} in July (12.6 m s^{-1} in January). The temperature of both the glass cover and the plate decreases by several degrees below the ambient temperature in July as a consequence of the radiative sky cooling that determines the temperature change of the PVT-RC module at night. The temperature of the glass cover reduces averagely by 3.5°C as it is the thermal emitter of the

PVT-RC module, and it exchanges heat to the sky. The plate decreases its temperature by around 2 °C by exchanging heat to the sky indirectly through radiation to the glass cover. If a low-density PE film is used as a long-wave transparent cover, the temperature of the plate decreases during the night by around 5 °C, and it is averagely lower than the ambient temperature by 13 °C, compared to 6 °C obtained with a glass cover.

The same analysis on a typical PVT module exhibits only a slightly higher T_p with respect to PVT-RC, in the order of 4 °C: it is interesting to observe that a typical PVT module, without any structural modification, features an additional not negligible cooling potential during the night time which can be suitably used.

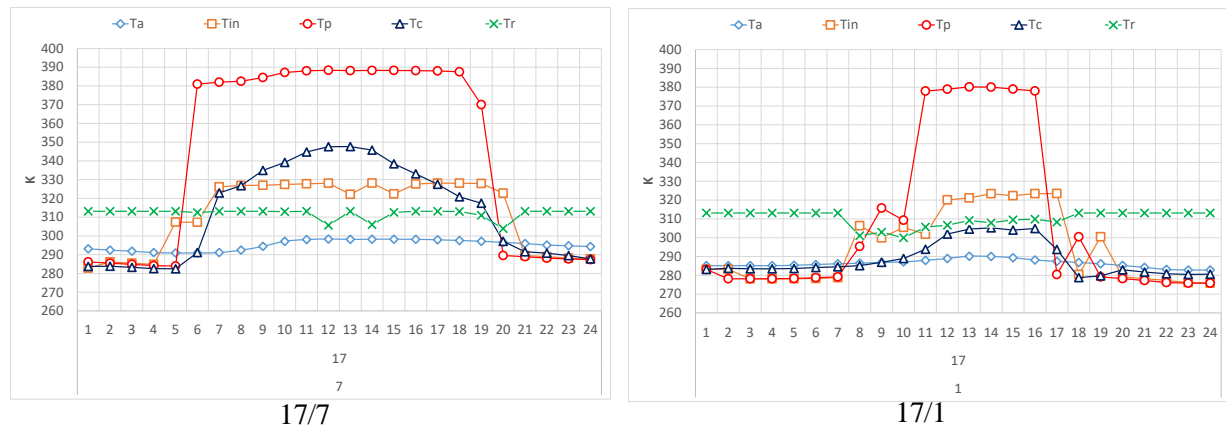


Figure 5 – Temperature of the cover (T_c), plate collector (T_p), outdoor air (T_a), collector inlet (T_{in}), and return from the loads (T_r) for the Glass-PVT-RC configuration

The monthly electricity, heat, and cooling energy gained by the different solutions were determined by accumulating the daily energy gains. In Figure 6, the maximum electricity (E_{PVT}) and thermal energy ($Q_{out,heat}$) were achieved in June and July, respectively, for all cases. This is due to the greatest total solar irradiance received in June with a lower average air temperature with respect to July, thus allowing a greater electrical efficiency in June and a better thermal efficiency in July. The values range from 25.6 kWh m⁻² for the Glass-PVT-RC to 30.6 kWh m⁻² for Polyethylene-PVT for E_{PVT} , and from 55 kWh m⁻² for Polyethylene-PVT to 111.1 kWh m⁻² for Glass-PVT-RC for $Q_{out,heat}$.

However, the minimum electricity and heat outputs were observed in January for all solutions (14.9 kWh m⁻² for Polyethylene-PVT for thermal energy and 7.9 kWh m⁻² for Glass-PVT-RC for electricity), during which the total solar irradiance was the poorest.

For the night-time cooling performance, the monthly cooling energy generally experienced a gradual decrement from January to July and then a successive increment during the other months of the year. The system generated the highest monthly cooling energy in winter (30.5 kWh m⁻² for the Polyethylene-PVT-RC system in December and around 20 kWh m⁻² for the Glass-PVT system in January) and the lowest in summer (22.2 kWh m⁻² and 13.8 kWh m⁻² in August respectively). Hence, the system can provide considerable cooling energy during summer that allows to cover the whole cooling load of the building in a passive and environment-friendly manner (only the Glass-PVT solution covers 87.6% of the cooling load). Moreover, introducing an energy storage component, such as phase-change material (PCM), could be a viable solution both in a long-term period (cooling energy in winter can be reserved for use the following summer [28]) and in a short-term period (the PCM could be employed to save cooling energy in the night-time and release it for use the following day when cooling demands are greater [29]).

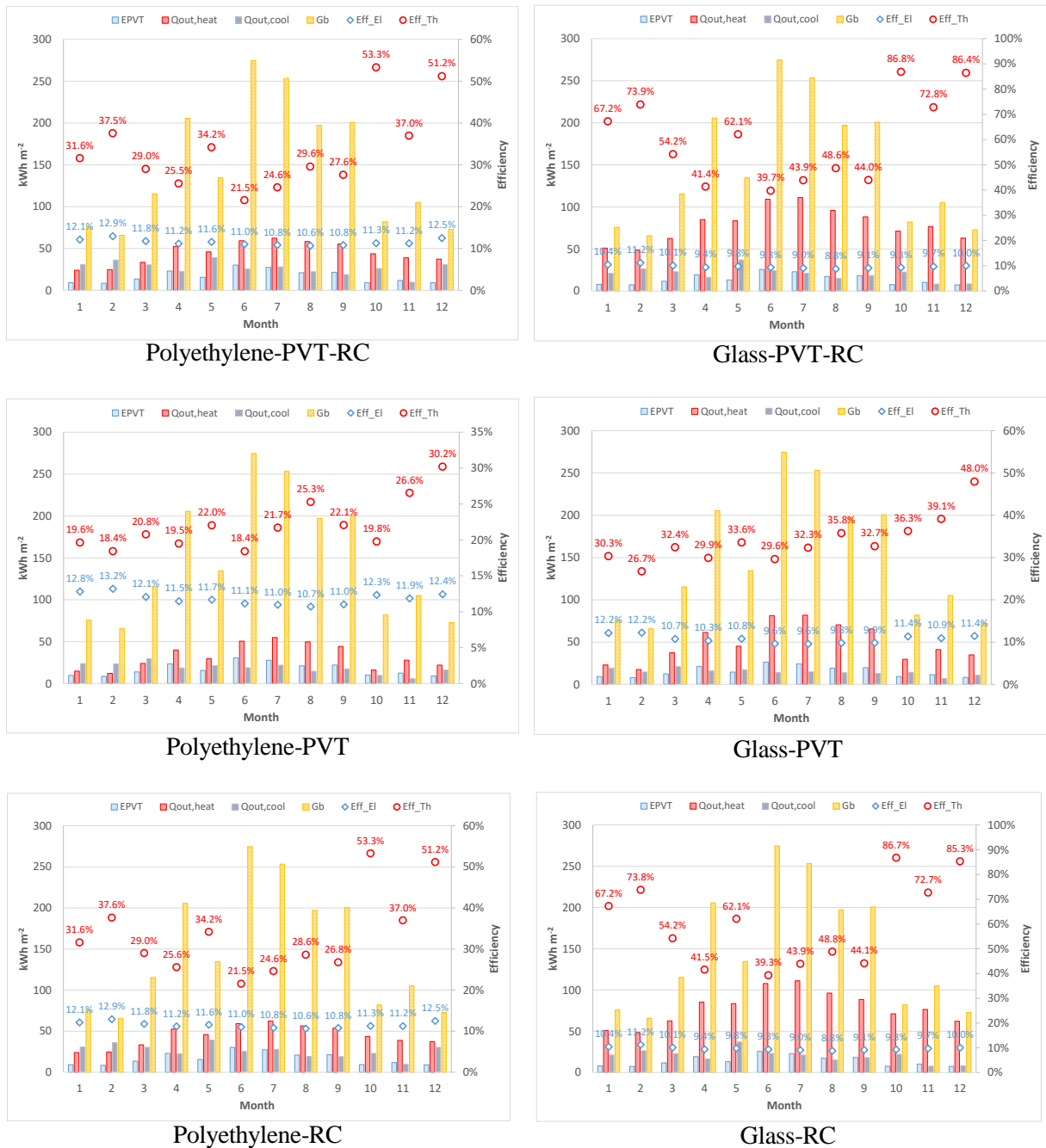


Figure 6 – Monthly energy production (electricity- E_{PVT} ; thermal energy- $Q_{out,heat}$; cooling energy- $Q_{out,cool}$), solar radiation (G_{β}), thermal and electrical efficiency (Eff_{Th} , Eff_{EI}) for the different solutions (40 mm insulation thickness)

The effects of insulation thickness on the daytime and night-time performance of the Glass-PVT-RC system were investigated as well. The electrical, thermal, and cooling specific energy production, and electrical/thermal efficiencies for a greater insulation thickness (100 mm) are depicted in Figure 7 on monthly base. Electrical efficiency decreased with an increase in insulation thickness, above all during summer. By contrast, the thermal efficiency improved with an increase in insulation thickness, above all in winter. A thicker insulation layer led to a lower heat loss and a higher PV module temperature, thus enhancing the solar thermal efficiency

while deteriorating the PV efficiency. A further increase in insulation layer thickness would have a reduced impact in relative terms.

The 100 mm insulation layer suppressed the cooling loss of the Glass-PVT-RC system. Then, a higher cooling energy gain was determined, above all during summer. The cooling energy capacity increased from 2419 kWh to 3201 kWh with an increase in insulation thickness from 0.04 m to 0.10 m.

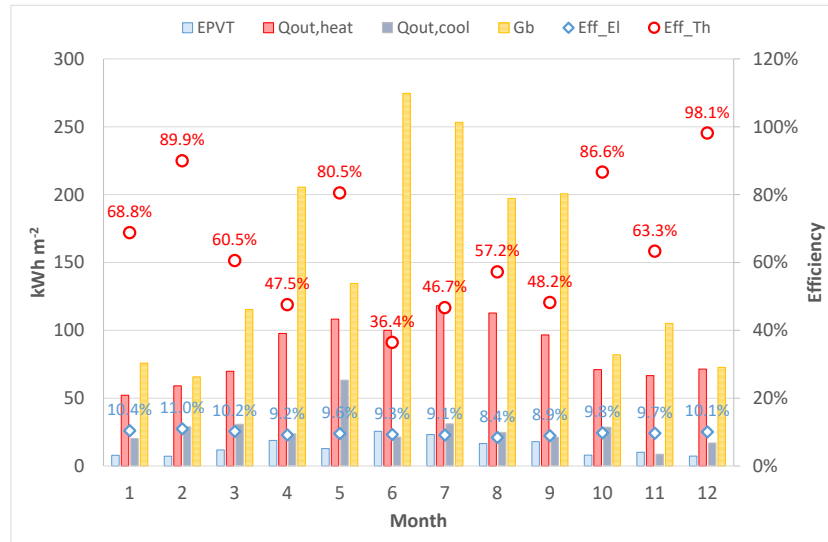


Figure 7 – Monthly energy production (electricity- E_{PVT} ; thermal energy- $Q_{out,heat}$; cooling energy- $Q_{out,cool}$), solar radiation (G_{β}), thermal and electrical efficiency (Eff_{Th} , Eff_{El}) for the Glass-PVT-RC solution with 100 mm insulation thickness

Table II - Annual results in terms of energy production, efficiencies and load factors

		Polyethylene-PVT-RC	Glass-PVT-RC	Polyethylene-PVT	Glass-PVT	Polyethylene-RC	Glass-RC	Glass-PVT-RC*
E_{PVT}	kWh	2003	1686	2049	1844	2002	1685	1676
$Q_{out,heat}$	kWh	5355	9455	3865	5897	5320	9443	10238
$Q_{out,cool}$	kWh	3200	2419	2219	1760	3144	2392	3201
G_{β}	kWh	17827	17827	17827	17827	17827	17827	17827
η_e		11.2%	9.5%	11.5%	10.3%	11.2%	9.5%	9.4%
η_t		30.0%	53.0%	21.7%	33.1%	29.8%	53.0%	57.4%
E_{load}	kWh	2121	2121	2121	2121	2121	2121	2121
$Q_{heating+DHW}$	kWh	5586	5586	5586	5586	5586	5586	5586
$Q_{cooling}$	kWh	2008	2008	2008	2008	2008	2008	2008
$\frac{E_{PVT}}{E_{load}}$		94.4%	79.5%	96.6%	87.0%	94.4%	79.5%	79.0%
$\frac{Q_{out,heat}}{Q_{heating+DHW}}$		95.9%	100.0%	69.2%	100.0%	95.2%	100.0%	100.0%
$\frac{Q_{out,cool}}{Q_{cooling}}$		100.0%	100.0%	100.0%	87.6%	100.0%	100.0%	100.0%

* With $d_b=100$ mm

Electrical, thermal, and cooling energy gains of the different systems are reported in Table II in terms of annual performance. The last three rows of the table report the load factors, that is, the ratio between the useful energy produced by the collector (electric, thermal, and cooling) and the respective load of the building. If the solutions are compared on the base of electricity production, Polyethylene-PVT collector is the best one (2049 kWh with an annual average electrical efficiency of 11.5%). Instead, if the comparison is made on the base of thermal energy, Glass-PVT-RC allows the best performance, even with an increased insulation thickness (10238 kWh, 57.4% thermal efficiency). As a result, Glass-PVT-RC with a thicker insulation layer is the best solution in terms of both overall efficiency (electric+thermal) and cooling energy capacity (3200 kWh, slightly better than the Polyethylene-RC collector).

A further comparison was made on the basis of the no-renewable primary energy (PE) consumed to satisfy the (eventual) parts of the loads not fully covered by the collectors, and the primary energy saving (PES) with respect to a reference solution (a natural gas fired condensing boiler, an air-water electric vapour compression chiller, and electricity from the grid). In order to conduct such a comparison, reference efficiencies were fixed for electricity ($\eta_{el,sp}=51.3\%$) and thermal energy ($\eta_{th,sp}=95.2\%$) of the separate production on the base of the primary energy factors as defined by Italian Decree DM 26/06/2015: $f_{P,nren}$ (natural gas) = 1.05; $f_{P,nren}$ (electricity from the grid) = 1.95. An energy efficiency ratio of 3 was set for the cooling energy production by the conventional chiller.

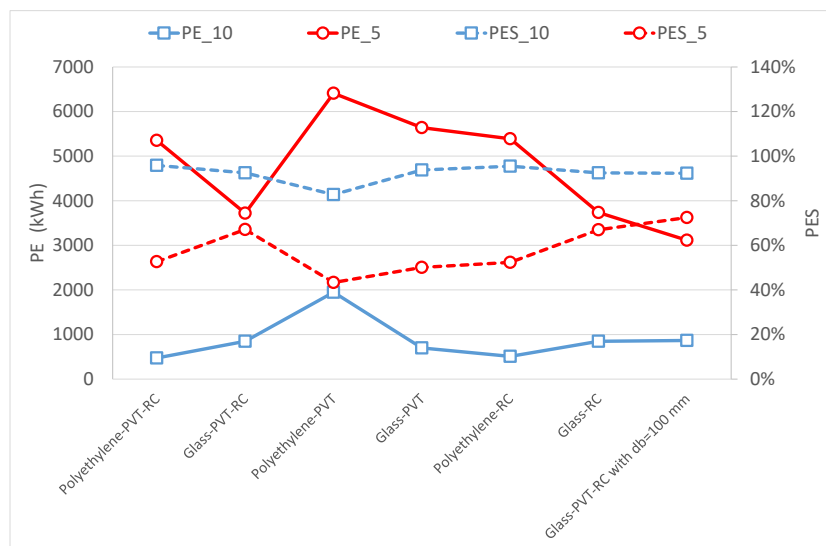


Figure 8 – Annual PE consumption and PES with respect to the reference solution

As reported in Figure 8, the best solutions are the Polyethylene-PVT-RC and Polyethylene-RC, that is, the ones that allow the best electrical and thermal energy load factors. They both have a PES greater than 95% and a PE consumption around 500 kWh. Instead, the collector with Polyethylene cover and PVT plate spectral emissivity features the worst performance in terms of PE (1950 kWh) and PES (82.8%). Moreover, it is interesting to note that the typical PVT module allows a performance quite similar to the best ones, as it features a PE consumption of 700 kWh and a PES of 93.8%.

An increase of solar collector's area indeed would increase the PES and reduce the PE consumption, but again Polyethylene-PVT-RC and Polyethylene-RC solutions would be the best. Instead, Figure 8 reveals that a decrease of the collector's area to 5 m^2 would make the Glass-PVT-RC solution the most effective one, even with a thicker insulation layer.

Conclusions

The study here reported numerically investigated different configurations of a hybrid PVT-RC system on the base of a mathematical model, which was previously validated against experimental data. The annual performance of the systems in a typical Mediterranean climate on the base of the test reference year and the electric, heating, DHW and cooling loads of a residential building was evaluated. The results of the annual performance investigation suggest that the maximum and the minimum heat gain are obtained in July and February, respectively (1111 kWh and 486 kWh for the most performing configuration, Glass-PVT-RC). The maximum and minimum electricity production are performed in June and February, respectively, and they amount to 306 kWh and 87 kWh for the most effective solution (Polyethylene-PVT). The peak and lowest cooling gains of the system are expected in May and November, reaching 393 kWh and 97 kWh for the Polyethylene-PVT-RC solution, respectively.

Glass-PVT-RC is the best solution in terms of both overall efficiency (electric+thermal) and cooling energy capacity, even better if with a thicker insulation layer: the annual electrical, heat and cooling gains of this system are 1676, 10238 and 3200 kWh, correspondingly. Nevertheless, the typical Glass-PVT module allows a performance quite similar to the best ones.

In summary, the proposed Glass-PVT-RC collector can serve as a promising cooling-heating-power system and can be applied to face buildings' electricity, heat, and cooling energy needs. It can cover a great part of energy load in an environment-friendly manner by coupling the collector with the inherent heating, ventilation, and air conditioning system in buildings. A typical Glass-PVT collector can serve in this scope as well with an interesting primary energy saving. As a further development of this study, a more comprehensive analysis will be developed by considering a multisource renewables-based plant, e.g., with multisource heat pump, in different climates to evaluate the effect of the latter on the performance of the system.

References

- [1] Lazzarin, R., "Heat pumps and solar energy: A review with some insights in the future", *International Journal of Refrigeration* 2020; 116:146–160.
- [2] Lazzarin, R., "Renewable energy technologies in air conditioning: State-of-the-art and perspectives", *Refrigeration Science and Technology - Proceedings "25th IIR International Conference of Refrigeration, ICR 2019"*, Montréal, 2019-August, pp. 130-141, Manuscript ID: 1846.
- [3] IEA (2020), *World Energy Outlook 2020*, IEA, Paris <https://www.iea.org/reports/world-energy-outlook-2020>
- [4] Yang, H., Wang, Q., Huang, X., Li, J., Pei, G., "Performance study and comparative analysis of traditional and double-selective-coated parabolic trough receivers", *Energy* 2017; 145:206-16.
- [5] Dan, A., Barshilia, H.C., Chattopadhyay, K., Basu, B., "Solar energy absorption mediated by surface plasma polaritons in spectrally selective dielectric-metal-dielectric coatings: a critical review", *Renew Sustain Energy Rev* 2017; 79:1050-77.
- [6] Ning, Y., Wang, W., Wang, L., Sun, Y., Song, P., Man, H., et al., "Optical simulation and preparation of novel Mo/ZrSiN/ZrSiON/SiO₂ solar selective absorbing coating", *Sol Energy Mater Sol Cell* 2017; 167:178-183.
- [7] Bauer, G.H., *Photovoltaic Solar Energy Conversion*, Springer, ISBN 978-3-662-46683-4, 2015.

- [8] Theodore, L., *Heat transfer applications for the practicing engineer*, John Wiley & Sons: New Jersey, 2011.
- [9] Chow, T.T., “A review on photovoltaic/thermal hybrid solar technology”, *Applied Energy* 2010; 87:365-379.
- [10] AA. VV., *Renewables 2020 - Global Status Report*, ISBN 978-3-948393-00-7, <https://www.ren21.net/gsr-2020/>.
- [11] Montagnino, F.M., “Solar cooling technologies. Design, application and performance of existing projects”, *Solar Energy* 2017; 154:144-157.
- [12] Lazzarin, R., Noro, M., “Past, present, future of solar cooling: Technical and economical considerations”, *Solar Energy* 2018; 172:2-13.
- [13] Raman, A.P., Anoma, M.A., Zhu, L., Rephaeli, E., Fan, S., “Passive radiative cooling below ambient air temperature under direct sunlight”, *Nature* 2014; 515(7528):540-544.
- [14] Zhai, Y., Ma, Y., David, S.N., Zhao, D., Lou, R., Tan, G., et al. “Scalable-manufactured randomized glass-polymer hybrid metamaterial for daytime radiative cooling”, *Science* 2017; 355(6329):1062-1066.
- [15] Vall, S., Castell, A., “Radiative cooling as low-grade energy source: a literature review”, *Renew Sustain Energy Rev* 2017; 77:803-820.
- [16] Gentle, A.R., Smith, G.B., “A subambient open roof surface under the Mid-Summer sun”, *Adv Sci* 2015; 2(9):1500119.
- [17] Kou, J.-l., Jurado, Z., Chen, Z., Fan, S., Minnich, A.J., “Daytime radiative cooling using near-black infrared emitters”, *ACS Photon* 2017; 4(3):626-630.
- [18] Zhao, B., Hu, M., Ao, X., Pei, G., “Conceptual development of a building-integrated photovoltaic–radiative cooling system and preliminary performance analysis in Eastern China”, *Applied Energy* 2017; 205:626–634.
- [19] Hu, M., Zhao, B., Ao, X., Zhao, P., Su, Y., Pei, G., “Field investigation of a hybrid photovoltaic-photothermic-radiative cooling system”, *Applied Energy* 2018; 231:288–300.
- [20] Zhao, B., Hu, M., Ao, X., Chen, N., Pei, G., “Radiative cooling: A review of fundamentals, materials, applications, and prospects”, *Applied Energy* 2019; 236:489–513.
- [21] Suhendri, Hu, M., Su, Y., Darkwa, J., Riffat, S., “Implementation of Passive Radiative Cooling Technology in Buildings: A Review”, *Buildings* 2020; 10:215.
- [22] Hu, M., Zhao, B., Ao, X., Su, Y., Wang, Y., Pei, G., “Comparative analysis of different surfaces for integrated solar heating and radiative cooling: A numerical study”, *Energy* 2018; 155:360-369.
- [23] Hu, M., Zhao, B., Li, J., Wang, Y., Pei, G., “Preliminary thermal analysis of a combined photovoltaic-photothermic-nocturnal radiative cooling system”, *Energy* 2017; 137:419-430.
- [24] Hu, M., Zhao, B., Ao, X., Ren, X., Cao, J., Wang, Q., Su, Y., Pei, G., “Performance assessment of a trifunctional system integrating solar PV, solar thermal, and radiative sky cooling”, *Applied Energy* 2020; 260:114167.
- [25] Hu, M., Zhao, B., Ao, X., Suhendri, Cao, J., Wang, Q., Riffat, S., Su, Y., Pei, G., “An analytical study of the nocturnal radiative cooling potential of typical photovoltaic/thermal module”, *Applied Energy* 2020; 277:115625.
- [26] Vialetto, G., Noro, M., Rokni, M., “Innovative household systems based on solid oxide fuel cells for the Mediterranean climate”, *International Journal of Hydrogen Energy* 2015; 40(41):14378-14391.
- [27] Sicily. Weather reference year. (Italian) CTI – Comitato Termotecnico Italiano.
- [28] Mancin, S., Noro, M., “Reversible Heat Pump Coupled with Ground Ice Storage for Annual Air Conditioning: An Energy Analysis”, *Energies* 2020; 13(23):6182.

- [29] Righetti, G., Lazzarin, R., Noro, M., Mancin, S., “Phase Change Materials embedded in porous matrices for hybrid thermal energy storages: Experimental results and modelling”, *International Journal of Refrigeration* 2019; 106:266-277.

Algorithmic optimisation of the electrical power output of a low-cost, multicore thermoacoustic engine with varying resonator pressure

F. Huntingford^{1*}, W. Kisha¹

¹Faculty of Engineering, University of Nottingham, UK, NG7 2RD

*Corresponding author: eayfh3@nottingham.ac.uk

Abstract

Incorporating thermoacoustic engines (TAEs) into clean cooking stoves offers to reduce rural energy poverty while cutting morbidity associated with smoke inhalation. TAEs are used to generate electricity from the waste heat of a cooking fire to provide power for lighting and personal devices. This study investigated the effect of TAE mean pressure using a numerical model of a twin-core, asymmetrically heated TAE. Automation code was developed to allow the numerical model to be optimised using the Nelder-Mead algorithm to maximise electrical power output at each mean pressure. The parameters available for optimisation were the length and position of two side volumes (stubs). A maximum electrical output of 59.63 W was determined at 2.2 bar mean pressure. This is a 90% increase on the original numerical model. Simulation-based optimisation, as performed in this study, is identified as being universally applicable to the design of TAEs.

Keywords: thermoacoustic, DeltaEC, simulation-based optimisation

1. Introduction

The 7th United Nation's Sustainable Development Goal is to "Ensure access to affordable, reliable, sustainable and modern energy for all" [1]. Despite significant advancements in energy technologies, progress is rapidly required if this global energy target is to be met by 2030. Cooking and electricity generation in rural areas are two sectors that require particular attention in developing countries.

In 2016, some 2.8 billion people used polluting open fires or simple, solid-fuel stoves to cook [2]. This statistic has a significant overlap with the 13% of the global population who have no access to electricity [1]. When solid fuels combust, they emit gaseous and particulate pollutants which were attributable to 1.8 million deaths in 2017 [3].

The SCORE (Stove for Cooking, Refrigeration and Electricity) project (www.score.uk.com) is an initiative established in 2007 to incorporate electricity generation into efficient cooking stoves. Adding this secondary function to clean cooking stoves has the potential to increase their uptake, as the device is more attractive to the entire household. Small scale, domestic electricity production enables the powering of lighting and personal electronics. Furthermore, the efficient use of resources for multiple purposes has the potential to reduce fossil fuel use and decrease greenhouse gas emissions.

The stove under development uses a travelling-wave thermoacoustic engine (TAE) to convert waste heat from solid fuel combustion into electricity. This technology has been identified as a potential low cost, low maintenance alternative to more mature electricity generating techniques [4]. Both these advantages are due to the fact that these engines have very few moving parts. Riley [4] concluded that thermoacoustic electricity generation incorporated into a stove is more cost-effective than community-sized solar and wind technologies, but more expensive than hydropower. However, hydropower installation is limited by local geography.

Prototypes have been produced by the SCORE program, but to date they fall short of the design target of 100 W of electricity generation. Multi-core TAEs are being considered to address this shortfall [5]. Despite higher complexity, they have been shown to have a lower onset temperature [6] and increased power output [7].

2.2 Selected opportunities for performance increase

Thermoacoustic theory indicates that increasing the mean pressure in a given thermoacoustic system will also increase acoustic power. This is indicated by the dimensionless group [14] :

$$\frac{\dot{E}}{p_m A a} \quad (1)$$

Where \dot{E} is the acoustic power, p_m is mean pressure, A the cross sectional-area of the regenerator and a the speed of sound.

Pressurisation to the order of 100 Bar is used in some applications [15], however, high pressurisation is not an option for a low-cost TAE due to the cost of manufacture. The investigation of electrical power output at slightly elevated pressure will determine economic feasibility, considering the manufacturing cost penalty. Pressurisation to moderate pressure (5 bar) is possible using a bicycle pump.

Chen, et al. [5] found that by increasing the mean pressure of a TAE from atmospheric to 1.51 bar resulted in a 45% increase in power output. Their simulations showed that an increase to 2.1 bar would further increase performance but they were limited by the structural integrity of the prototype to experimentally validate this. Riley [11] experimented with increasing pressure in a demonstration TAE which found a peak in developed electrical output at 2 bar.

Mean pressure is a confounded variable with many acoustic parameters of a TAE [12]. The position and length of two side-volumes (stubs) located on the TAE loop also influence the acoustic field and can be adjusted to maximise performance [16]. These parameters can be tuned to maximise electrical output for each mean pressure.

The process of tuning the stub parameters to manipulate the acoustic field has been approached in several ways. Abdoulla-Latiwish and Jaworski [13] increased and decreased the dimensions of each component individually until a maximum output was found. Yu, et al. [17] selected the position for their stub experimentally, acknowledging there was room for improvement. They found that introducing a tuning stub to their prototype increased electrical output by 10-15% and reduced onset temperature by 40-50°C.

The tuning process is ideally repeated after each major design revision of a TAE, and therefore methods to streamline this process are desirable. Currently this is a time-consuming process involving manual manipulation of the design parameters in simulation software. Automated control of the simulation software will allow for the use of optimisation algorithms, resulting in a faster process and higher confidence in an optimal configuration. Automation also allows for fast sampling of a design with changing parameters, allowing for detailed insights into parameter interactions.

2.3 Simulation-based Optimisation

The field of simulation based optimisation has advanced in recent years to become widespread with regards to computational fluid dynamics and finite element analysis [18].

Design of Experiments (DOE) is an established tool for maximising the amount of information gained from a study while minimizing required data collection [19]. DOE specifies that parameters are varied simultaneously, and the response measured allowing convenient identification of parameter effects and relationships. A DOE approach is excellent for establishing relationships over a small input space but suffers limitations when the scale and dimensionality of the input space increase due to the number of sample points required.

A local search is an alternative to finding a global optimal solution, at the sacrifice of the information and insights gained from a global search (DOE or otherwise). Local search algorithms incrementally change parameters in the hope of improving the solution until some criteria is met, such as time elapsed or convergence. However, little to no information on parameter effects is gained and the solution may converge to a local optimum.

The Nelder-Mead method [20] is a popular numerical method for simulation-based optimisation. Various modifications and hybridisations are used for component design e.g. topology optimisation [21]; and system design e.g. nuclear reactor core design [22] and low energy building design [23]. This method is well suited to working with expensive-to-evaluate, ‘black-box’ functions due to the minimal number of function evaluations needed and the fact that no gradient information of the objective function is required [24]. The Nelder-Mead method is considered heuristic due to the problem of explicitly proving convergence of an optimal solution [25].

3. Methodology

This paper investigates the relationship between electrical power output and mean operating pressure. The results are obtained by simulation.

3.1 DeltaEC Model

The behaviour of TAEs is complicated to model analytically due to interacting acoustic and thermal physics. It is therefore required to numerically simulate the engine behaviour. DeltaEC [26] is a program used by researchers to design and evaluate the performance of thermoacoustic devices. The TAE under investigation by this paper is the asymmetrically heated, twin-core SCORE stove prototype, pictured in Figure 2a). A model of this TAE has been developed and validated in DeltaEC [27], of which the layout is shown in Figure 2b). The majority of the dimensions of the system are defined by either previous design processes or premanufactured parts and can be found in a thesis by Chen, et al. [5]. The engine receives 2.5 kW of heat input, with 40% of the heat applied to core 1 and 60% of the heat applied to core 2. The current model outputs 31.4 W of electrical power [27].

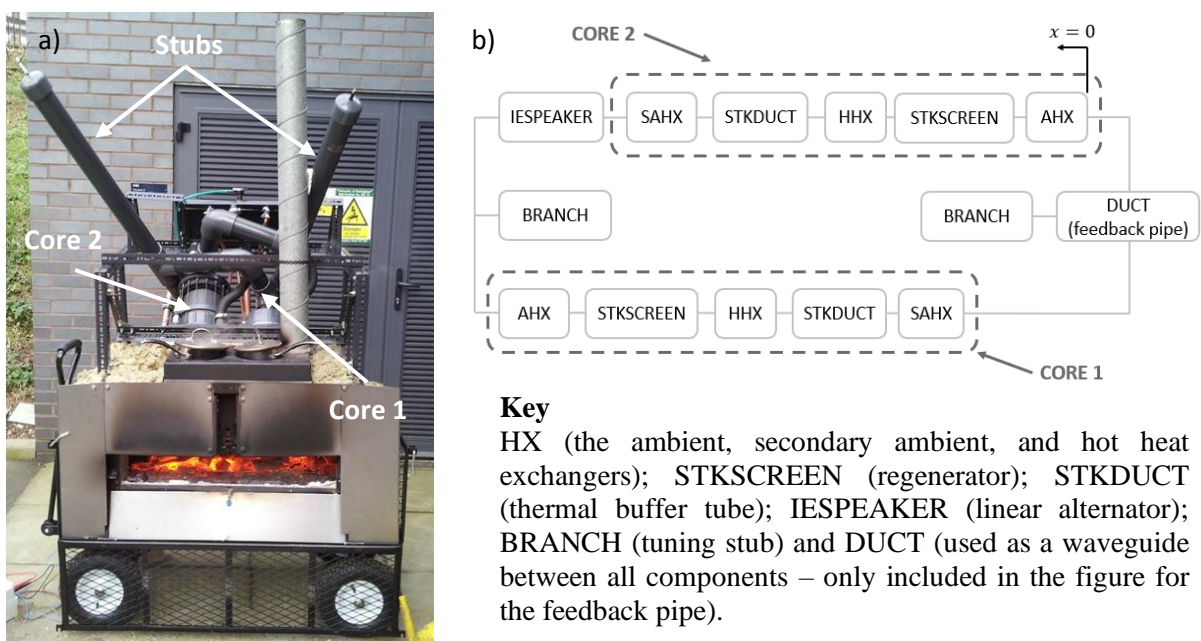


Figure 2. a) Twin core TAE prototype [28] b) Schematic of the twin core TAE.

The boundary conditions for the DeltaEC model are:

- Pressure magnitude and phase are matched at the start and end of the loop.
- Volumetric velocity magnitude and phase are matched at the start and end of the loop.
- The temperature after the thermal buffer tube is ambient.
- The phase of the electrical impedance of the alternator is forced to 180° i.e., purely resistive.

3.2 Optimisation Constraints

Design freedom to improve the DeltaEC model was given to five parameters: the position and length of two stubs (BRANCH in Figure 2b) as well as the mean pressure. The length of each stub is initially considered in terms of the imaginary component of its acoustic impedance, $Im(Z)$, as this is the quantity defined in DeltaEC. An approximation of equivalent length is then determined using the equations detailed by Yu, et al. [29]:

$$\frac{1}{3}\rho_M\omega^2l^2 - A_{stub}\omega Im(Z)l - \rho_M a^2 = 0 \quad (2)$$

Where ρ_M is the mean density of the working gas; ω is the angular frequency of the acoustic wave in the engine; A_{stub} is the cross-sectional area of the tuning stub; l is the length of the stub; $Im(Z)$ is the imaginary part of the impedance of the stub; and a is the speed of sound. All these values are available from the DeltaEC model.

The parameters were bounded as shown in Table 1 where the position (x) is consistent with Figure 2b.

Table 1. Parameters with design freedom and their associated bounds.

Parameter	Lower Bound	Upper Bound	Reasoning
Im(Z) Stub 1	-3.5 MPa.s/m ³	-0.5 MPa.s/m ³	Estimated from experience of corresponding stub length
Im(Z) Stub 2	-3.5 MPa.s/m ³	-0.5 MPa.s/m ³	
Stub 1 Position (x)	0.924 m	4.124 m	Position of speaker and Core 1
Stub 2 Position (x)	0.267 m	0.817 m	Position of Core 1 and Core 2
Mean Pressure	Atmospheric	5 bar	Max pressure achievable with bicycle pump

In this study, TAE performance is defined by the electrical power output from the loudspeaker (IESPEAKER in Figure 2b). Electrical power developed by the loudspeaker is influenced by the electrical load resistance. Finding the load resistance that maximises electrical power output is known as load matching. Load matching is applied in this study when comparison between sample points is required.

3.3 Automated Sampling of DeltaEC

Automation of DeltaEC is achieved using the set of python modules ‘pywinauto’, that enable automation of the Windows graphical user interface. Python was chosen as the language for automation due to the availability of a large library of useful modules, and the ease of learning for a beginner. In all cases the automation was performed on an Intel i7 processor at 1.8 GHz.

Sampling of a DeltaEC model requires a tailored approach due to the obligation of slowly incrementing parameters from one sample point to the next, in order to maintain

convergence. DeltaEC uses a guess-target shooting routine for each run with the guesses updated from the results of the previous run. Incrementing the parameters by small amounts ensures the guesses are suitably accurate. This ‘travel’ between sample points is a chokepoint in the automation code because inputting new parameters and running DeltaEC is relatively slow. Faster sampling of the model was achieved by saving converged models and keeping a log. The log is then consulted after choosing a new sampling point, in order to select the model with parameters closest to the desired sampling point. The parameters in the log are scaled to account for differing units, and the Chebyshev distance between scaled parameters is used to define ‘closeness’. The Chebyshev distance is the greatest of the differences along each dimension. This metric is also used to calculate the number of increments required for a particular travel between sample points. For the case when sample points are known in advance, the sample points are ordered by solving the travelling salesman problem with Chebyshev distance in order to minimise travel distance and therefore minimise the time taken for automation.

3.4 Pilot Study (Design of Experiments Approach)

Firstly, the DOE approach to optimisation was attempted by performing an initial full factorial experiment. Each parameter was assigned 4 levels as a compromise between resolution and data acquisition speed. In the case of this study, with 5 parameters each set at 4 levels the initial experiment had 1024 sample points. The automated process to gather this data took 12 hours and only 30 of the sample points resulted in a converged solution. This corresponds to one evaluation of the model per 42 seconds. Data analysis is complicated by the non-converged sample points. A value of 0 W output is assigned to non-converged treatments, however other missing data representations could be used such as Not-a-Number (NaN). If these zero values are included in analysis, then any relationship is highly skewed. Whereas if the data is limited to converged treatments only, the sample becomes biased. The non-converged results can be included using missing-not-at-random (MNAR) statistical techniques [30], but the process is very involved and available conclusions are limited with a high level of uncertainty. The portion of the data that is MNAR makes this a worthless task. Smaller experiments could be designed using fractional factorial designs but the problem of a large proportion of non-converged sample points would remain.

In conclusion, global sampling using DOE techniques is not feasible for optimisation of DeltaEC models due to the large number of sample points required to resolve the small region of convergence and the associated high run time. However, this experiment did serve to identify the region of interest where the model converges.

3.5 Main Study (Nelder-Mead Optimisation)

Secondly, a local optimisation was performed. In this case the mean pressure was varied manually before optimisation of the stub parameters was performed. This allows comparison of the performance of tuned engines at different mean pressures.

The Nelder-Mead scheme was chosen over other derivative-free, local optimisation schemes due to its ease of implementation using the SciPy module [31]. The particular implementation of the method is based on the paper by Gao and Han [32] and adapted to accept parameter bounds based on the paper by Luersen, et al. [33]. The implementation of a bounded search is critical as the dimensions of some components of the TAE are constrained.

Non-reliance on gradient information is essential for DeltaEC where a large area of the input space will result in a non-converged solution. Optimisation algorithms often estimate the gradient in the absence of an analytical gradient via finite difference methods or by monitoring elementary operations during the computation process [18]. However, gradient

estimation in the region of discontinuities (such as the non-converged region in a DeltaEC model) is not meaningful. The Nelder-Mead algorithm has been shown to be insensitive to small imprecisions or stochastic effects in the evaluated function [34], however this is unlikely to be significant for numerical simulation.

It was found that the choice of load resistor (load matching) was primarily dependant on mean pressure. As each optimisation process occurs at a constant pressure, only the final, optimised model is load matched using Brent's Method (a scalar optimisation algorithm) implemented in SciPy.

4. Discussion and Results

4.1 Optimisation

Initially, the TAE models with mean pressures of atmospheric, 2,3,4 and 5 bar were optimised. A further four pressures were investigated to determine the peak electrical output to a tolerance of ± 0.1 bar. All optimisations proceeded for a maximum of 200 samples with convergence defined as a change in less than 0.05 W between iterations. This condition was reached in 4 out of the 9 optimisations. However, reaching this convergence condition was not critical due to the heuristic nature of the search. It was judged that improvement after 200 iterations would be insignificant. The flat nature of the model near the optimum poses a problem for convergence as the sensitivity to convergence tolerance is high.

Figure 3 shows the typical progression of the optimisation algorithm. It is seen that the rate of improvement of the electrical output is slow beyond 100 iterations. Beyond this point only small improvements are made despite significant changes in the parameters.

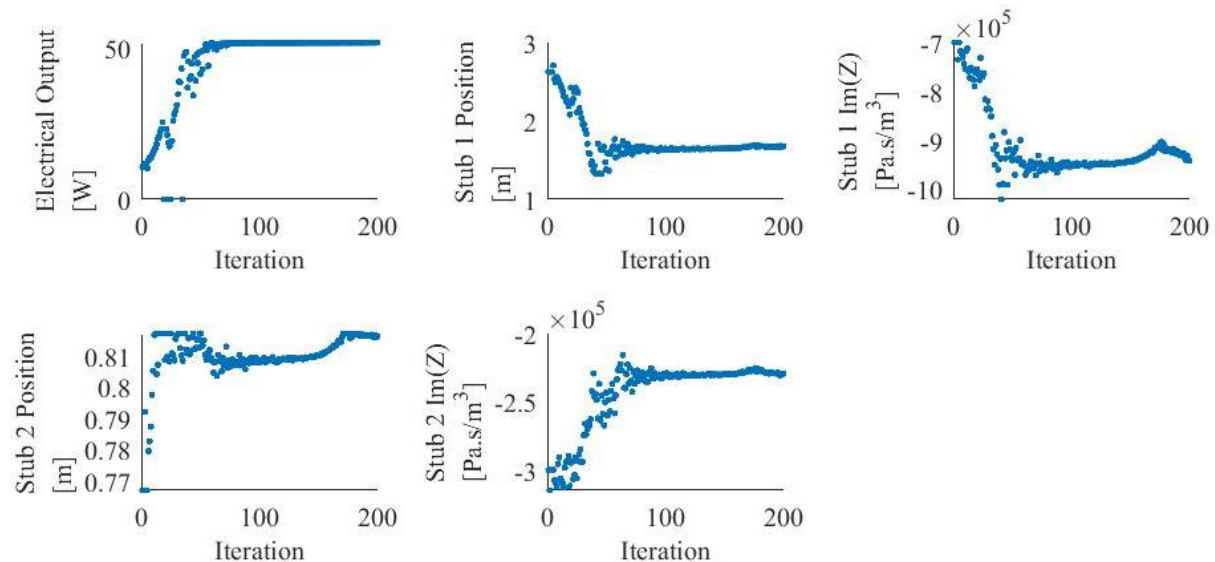


Figure 3. Progression of the Nelder-Mead optimisation algorithm for a mean pressure of 3 bar. Stub position is consistent with distance, x in Figure 2b.

Automation with the Nelder-Mead algorithm required a mean of 28 seconds per sample of the model. This is less than the DOE approach due to the shorter 'travel' required between sample points.

The relationships between optimal stub parameters and mean pressure is shown in Figure 4. Note that each of the contour plots are formed by linear interpolation from 9 data points. The length of both stubs increases with pressure, whereas the positions of stubs do not show a trend with respect to pressure. This lack of trend can be explained by the starting parameter

setting for each optimisation. The number of iterations required before significant improvement slows is partly determined by the proximity of the starting parameter settings to the optimum parameter settings. The large variation in stub parameters after this point was not accounted for when completing the optimisation and consequently the effect of initial parameter settings obscures any trend.

The effect of initial conditions could be negated by using the Globalised Restart Nelder Mead (GBNM) algorithm [35]. This enhancement involves repeatedly running the Nelder-Mead algorithm from randomly selected starting points. However, this method cannot easily be implemented in the case of DeltaEC as the limits of the sample space compatible with convergence would need to be known in advance, in order to select feasible starting points.

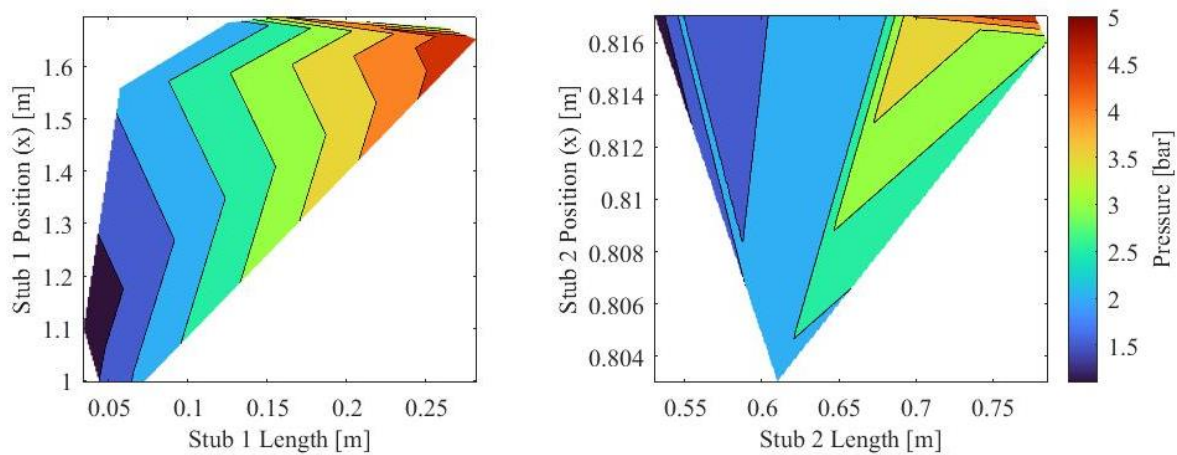


Figure 4. Contour plots for the optimal stub parameters with varying mean pressure.

4.2 Power Output

The relationship between pressure and electrical power output is shown in Figure 5a. Figure 5a also shows the acoustic power at the loudspeaker. Acoustic power continuously increases with mean pressure confirming theory (Equation 1). However, electrical power output reaches a maximum of 59.63 W at 2.2 bar. This power output is an increase of 16.14 W compared to the tuned engine at 1 atmosphere mean pressure.

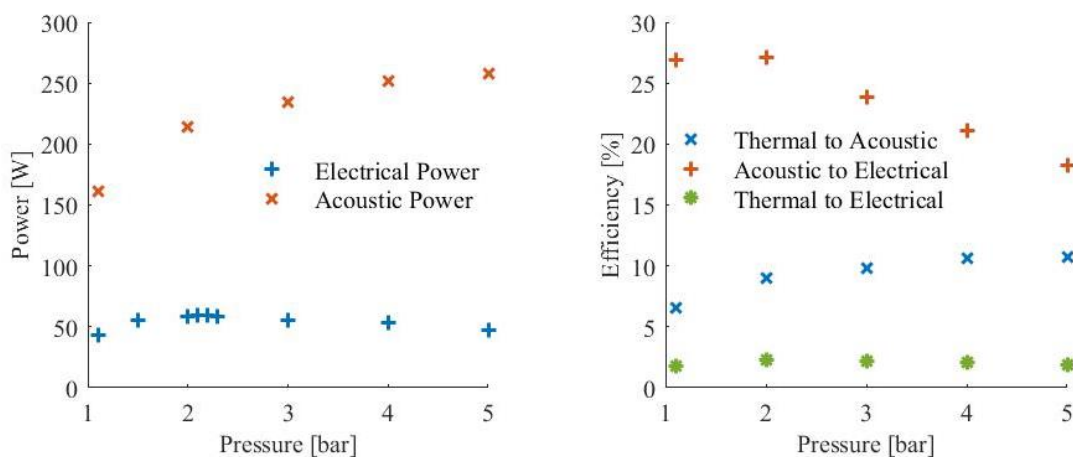


Figure 5. a) Acoustic and electrical power developed by the TAE with varying mean pressure. b) Efficiencies of the TAE with varying mean pressure

A significant (90%) improvement has been made in theoretical power output. However, it cannot be explicitly proven that the DeltaEC model has been fully optimised within the parameter boundaries due to the nature of the algorithm used. Future work is required to experimentally validate these results. The experimental results are likely to produce lower powers than DeltaEC due to the absence of effects in the numerical model such as mass streaming and thermal radiation [26]. Kisha, et al. [27] reported a decrease in power from the numerical model to experiment of 27-32% and Riley [11] reported decreases of 30%.

Figure 5b shows the efficiency of various power conversions in the engine. Thermal to acoustic efficiency increases with pressure whereas acoustic to electrical efficiency has a peak in the region of 2 bar. This corresponds to the peak in thermal to electric efficiency of 2.385% at 2.2 bar. This is similar to numerical simulations of comparable TAEs, achieving thermal to electric efficiency of 2.4% [29] and 2.5% [13].

The eventual decrease in acoustic to electrical efficiency indicates that the power extracted by the loudspeaker is not proportional to the acoustic power at the loudspeaker. The decrease in acoustic power extracted can be attributed to at least two factors:

1. Decreasing volumetric velocity

The acoustic power removed from the TAE is a function of acoustic parameters either side of the loudspeaker. This is described by Equation 3 [36]:

$$P = \frac{1}{2} |U_1| \{p_1 \cos(\theta_a) - p_2 \cos(\theta_b)\} \quad (3)$$

U is volumetric velocity, p is pressure and θ is phase angle. The subscripts 1 and 2 refer to the position adjacent to the loudspeaker on the side of high and low acoustic power, respectively. θ_a is the phase angle between p_1 and U_1 , θ_b is the phase angle between p_2 and U_1 . Plotting both components of Equation 3 (Figure 6) shows that a decreasing volumetric velocity is responsible for decreasing power despite an increasing pressure difference.

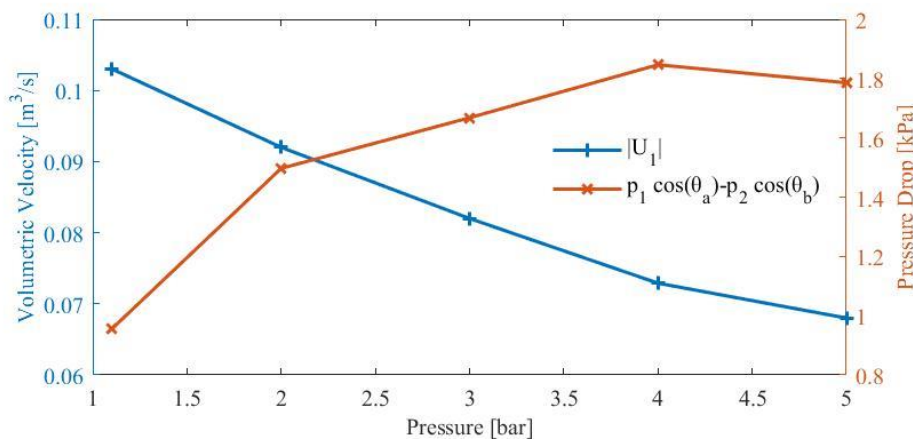


Figure 6. Volumetric velocity and pressure drop across loudspeaker.

The decrease in volumetric velocity is explained using the following one-dimensional, first order differential equation derived from decoupling the second order ‘wave equation’ [8]. The equation presented omits viscous or thermal relaxation losses.

$$dU = -\left(\frac{i\omega A}{\gamma p_m} p\right) dx \quad (4)$$

U is volumetric velocity, p is pressure, ω is frequency, A is cross sectional area, x is length and γ is the ratio of specific heats. The subscript m refers to mean. Equation 4 shows that the change in volumetric velocity over a length, dx decreases with increasing mean pressure.

2. Decreasing operating frequency

One of the conditions for maximising the efficiency of the loudspeaker is to operate it at the frequency corresponding to its mechanical resonance [12]. The resonance of the loudspeaker is 77.19 Hz, whereas the operating frequency of the TAE decreases from 75.21 Hz at 1 bar to 71.52 Hz at 5 bar. Therefore, the contribution of resonance to efficiency decreases with increasing pressure. Riley [11] relates operating frequency as a function of feedback pipe length and parasitic volume. Feedback pipe length is kept constant and therefore it is postured that increasing stub length is partly responsible for the decrease in frequency. The length of the feedback pipe may be optimised to raise the frequency closer to 77.19 Hz, however this will have competing effects elsewhere.

4.3 Acoustic Field

Table 2 details the positions of selected components with major influence on the acoustic field. The position (x) is measured from the ambient temperature side of regenerator 2 as shown in Figure 2b.

Table 2. Positions of key components in the TAE. The position (x) is consistent with Figure 2b.

Key component	Label in Figures 7 to 11	Position (x [m])
Regenerator 2	a	0.038
Loudspeaker	b	0.267
Stub 2	c	0.803-0.817
Regenerator 1	d	0.845
Stub 1	e	1.100 - 1.696
Feedback Loop	n/a	0.924 - 4.124

Select acoustic fields of the tuned engine at three representative pressures are presented (Figures 7 to 11) for the purpose of providing context to the trends in acoustic and electrical power output with changing pressure. The vertical lines correspond to the position or range of positions where a component is situated, as described in Table 2.

The implication of changes in pressure, volumetric velocity and phase difference on acoustic power can be explained using Equation 5, which describes time-averaged acoustic power produced in a length, dx , of channel [12]. This equation describes the acoustic power gradient along x , in terms of pressure, p ; volumetric velocity, U ; phase difference between p and U , φ ; specific viscous resistance, r_v ; specific thermal resistance, r_k ; and specific gain, g .

$$\frac{d\dot{E}}{dx} = -\frac{r_v}{2}|U|^2 - \frac{1}{2r_k}|p|^2 + \frac{1}{2}Re[gpU\cos(\varphi)] \quad (5)$$

Acoustic power (Figure 7) increases at higher mean pressures in accordance with Equation 1. The regenerators (a,d) augment acoustic power and the loudspeaker (b) diminishes it. The stubs (c,e) have little effect on acoustic power. Acoustic power decreases between components because of viscous losses and thermal relaxation (terms 1 and 2 of Equation 5). This can be seen in the feedback loop ($x = 0.924$ to 4.124) as a decreasing gradient. The rate of acoustic power loss in the feedback loop is higher at 1 bar (4.57 W/m) than at 5 bar (2.80 W/m). This indicates that decreasing volumetric velocity magnitude (Figure 9) is the

dominant effect over increased pressure magnitude (Figure 8) contributing to power loss (Equation 5) in this area of the TAE.

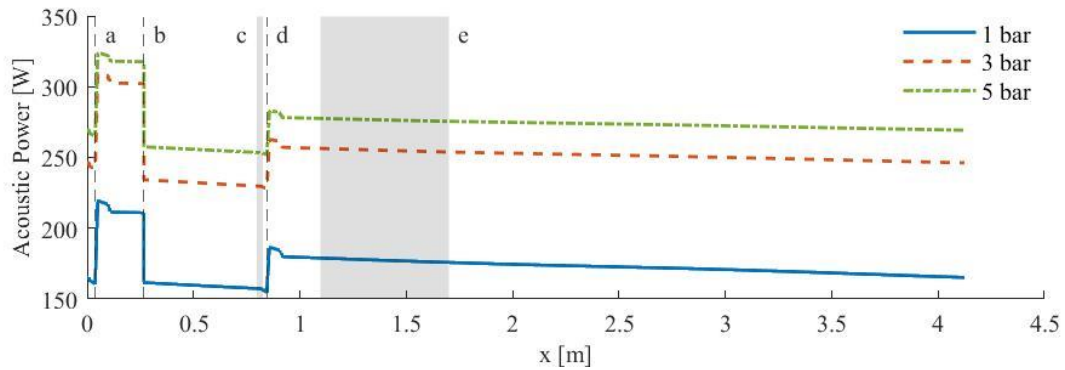


Figure 7. Variation of the acoustic power with position in the TAE for selected mean pressures.

In Figure 8, pressure amplitude increases with mean pressure as expected. Pressure amplitude drops at both regenerators (a,d) as a result of viscous losses. The pressure drop across the loudspeaker (b) indicates the acoustic power removed. The stubs (c,e) have little effect on the local pressure magnitude.

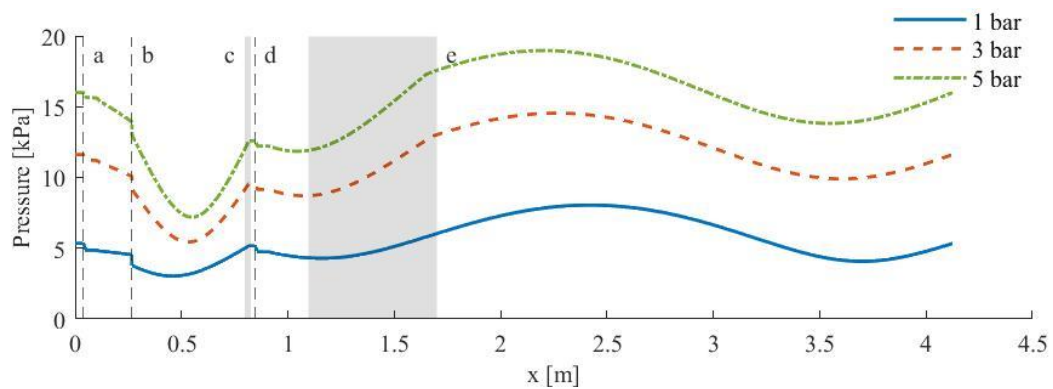


Figure 8. Variation of pressure amplitude with position in the TAE for selected mean pressures

The pressure standing-wave ratio (PSWR) shows minor variation with changing mean pressure. The median value is 2.655 across all mean pressures with a standard deviation of 0.0263. This indicates a significant standing wave in the feedback loop resulting in a decrease in efficiency. A PSWR of less than 1.8 is considered good for this type of TAE [11].

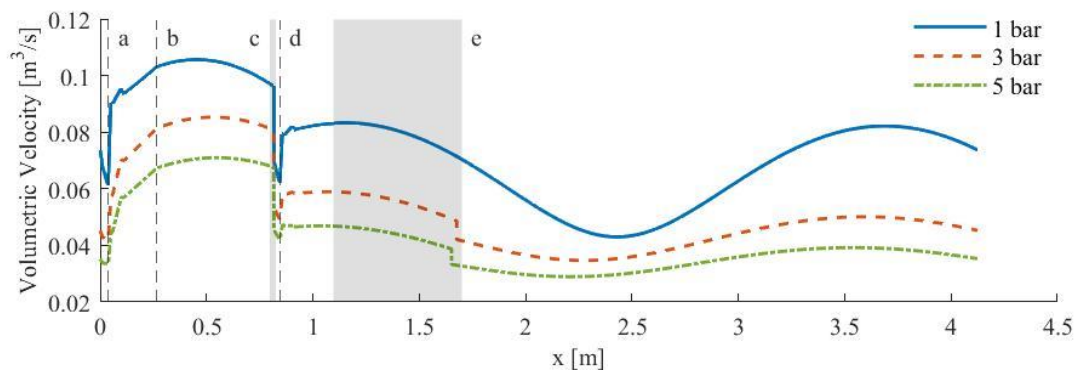


Figure 9. Variation of volumetric velocity magnitude with position in the TAE for selected mean pressures.

In Figure 9, volumetric velocity shows a decreasing trend with increased mean pressure. This results in efficiency increases within the TAE as viscous losses are reduced. However, it contributes to a decreasing electrical power output as described in Section 4.1. The position of the loudspeaker (b) is a compromise in maximising pressure amplitude (decreasing x) and maximising velocity amplitude (increasing x). A sharp increase in velocity occurs in the region of the two regenerators (a,d) as the flow accelerates due to the heat addition and resulting expansion. Both stubs (c,e) cause a decrease in volumetric velocity. The drop at stub 2 (c) results in an increase in efficiency as viscous losses in the regenerator are reduced as a result of the decreased entry velocity. Stub 1 (e) acts to adjust the position of the velocity nodes such that velocity is low entering regenerator 2 (a).

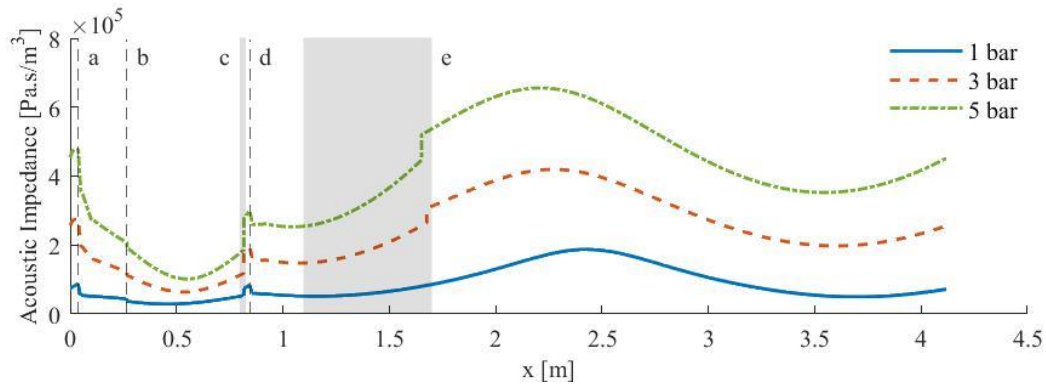


Figure 10. Variation of acoustic impedance magnitude with position in the TAE for selected mean pressures.

In Figure 10, acoustic impedance shows a trend of increasing with increasing mean pressure. This is a desirable trait at the regenerators as an increase in impedance within the regenerators reduces viscous losses [12]. The stubs (c,e) both increase acoustic impedance as a result of decreasing volumetric velocity and negligible pressure change. The magnitude of this impedance change increases with a higher mean pressure. The regenerators (a,d) decrease impedance due to increased velocity and the loudspeaker (b) decreases acoustic impedance due to the decreased pressure.

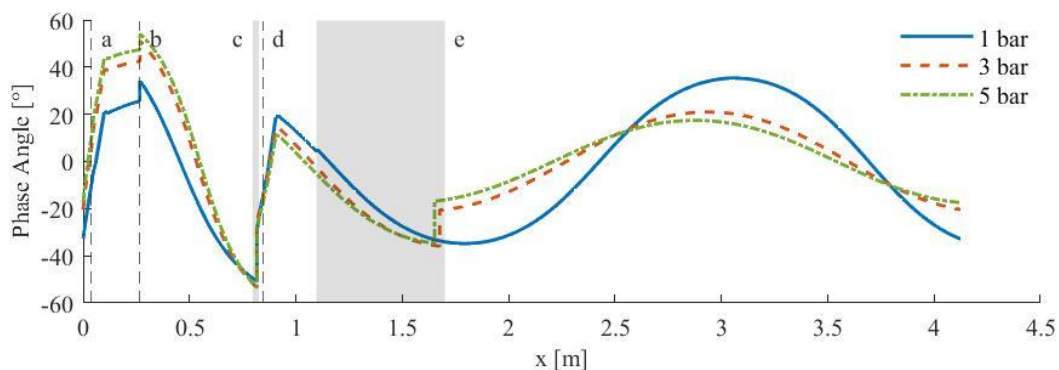


Figure 11. Variation of the phase difference between pressure and volumetric velocity with position in the TAE for selected mean pressures.

Figure 11 shows the action of both stubs to increase regenerator efficiency. Both stubs act to move the phase difference at the succeeding regenerator closer to zero, thereby maximising the acoustic power gain (term 3, Equation 5). However, a trend in this action is not discernible with changing mean pressure. A higher pressure results in greater phase difference at the loudspeaker (b) but decreased phase difference in the feedback loop, indicating a better travelling wave condition.

Onset temperature difference for both regenerators decreases with increasing pressure. The values for regenerator 1 decreased from 120°C to 67°C, whereas the values for regenerator 2 decreased from 184°C to 121°C. The onset temperature is a measure of acoustic matching between components, with a lower temperature indicating better matching [11].

4.4 Optimisation via Surrogate Modelling

The local search employed in this paper is limited by 1) the inability to quantify optimality of the local solution, 2) the limited information on main and interaction parameter effects, and 3) the lack of guarantee of a global solution. Surrogate modelling is a type of supervised machine learning [37] that aims to create a numerical model to approximate a simulation output. This numerical model can then be employed to perform optimisation as well as sensitivity and risk analysis. It is identified as an effective approach to working with DeltaEC to further understand parameter interactions and optimise if necessary. The process starts with an initial, global sample (training sample) based on DOE sampling schemes. In this case performing a global DOE is more acceptable due to the greater reward of a surrogate model and the significantly reduced number of required sample points – as the initial goal is not to resolve the optimum. An iterative approach is then used to approximate the data with a model and intelligently identify more sample points in order to improve the model (active learning). This approach is identified as being highly efficient (least number of function evaluations, most information recovered) however the implementation is a subject for future work. A particular nuance of applying this approach to DeltaEC is accepting non-converged sample points. This problem can be addressed by the imputation approach detailed by Forrester, et al. [37].

5. Conclusions

This numerical study shows that increasing the mean pressure in a twin-core, asymmetrically heated thermoacoustic engine increases electrical power output. The maximum electrical output is 59.63 W achieved at 2.2 bar mean pressure. However, these simulation results need to be verified experimentally. Cost analysis is required to determine if the hardware and manufacturing costs required for a 2.2 bar mean pressure TAE are acceptable. The peak in electrical power output is a result of a decrease in both volumetric velocity and operating frequency at increased mean pressure. The development of automation techniques for DeltaEC enables the use of algorithmic optimisation allowing for quick determination of optimal parameters considering system level parameter interactions. This is especially applicable for tuning the acoustic field using side branched volumes (stubs). This type of algorithmic optimisation could be applied to any continuous design parameter(s) of a TAE. The automated approach developed for this study allows fast data gathering from a DeltaEC model and may be adapted for other design studies. Optimisation by surrogate modelling is one such approach recommended for future studies.

Acknowledgements

The author would like to thank Greg Swift for help using Python to automate DeltaEC.

References

- [1] United-Nations, "Sustainable Development Goals," 2018. [Online]. Available: <https://unstats.un.org/sdgs/report/2018/goal-07>
- [2] WHO. "Global health observatory data repository." WHO. (accessed 2020).
- [3] K. K. Lee *et al.*, "Adverse health effects associated with household air pollution: a systematic review, meta-analysis, and burden estimation study," *The Lancet Global Health*, Article vol. 8, no. 11, pp. e1427-e1434, 2020, doi: 10.1016/S2214-109X(20)30343-0.

- [4] P. H. Riley, "Affordability for sustainable energy development products," *Applied Energy*, Article vol. 132, pp. 308-316, 2014, doi: 10.1016/j.apenergy.2014.06.050.
- [5] B. M. Chen, P. H. Riley, Y. A. Abakr, K. Pullen, D. B. Hann, and C. M. Johnson, "Design and development of a low-cost, electricity-generating cooking Score-Stove™," *Proceedings of the Institution of Mechanical Engineers, Part A: Journal of Power and Energy*, Article vol. 227, no. 7, pp. 803-813, 2013, doi: 10.1177/0957650913498733.
- [6] T. Biwa, D. Hasegawa, and T. Yazaki, "Low temperature differential thermoacoustic Stirling engine," *Applied Physics Letters*, Article vol. 97, no. 3, 2010, Art no. 034102, doi: 10.1063/1.3464554.
- [7] K. De Blok, "Multi-stage traveling wave thermoacoustics in practice," in *19th International Congress on Sound and Vibration 2012, ICSV 2012*, 2012, vol. 2, pp. 1573-1580.
- [8] N. Rott, "Damped and thermally driven acoustic oscillations in wide and narrow tubes," *Zeitschrift für angewandte Mathematik und Physik ZAMP*, Article vol. 20, no. 2, pp. 230-243, 1969, doi: 10.1007/BF01595562.
- [9] A. Bodrov, M. Zhang, R. Shuttleworth, and M. F. Iacchetti, "Sensorless Control of a Linear Generator for Energy Harvesting Applications," in *2019 12th International Symposium on Linear Drives for Industry Applications, LDIA 2019*, 2019, doi: 10.1109/LDIA.2019.8770976.
- [10] M. A. G. Timmer and T. H. Van Der Meer, "Optimizing bidirectional impulse turbines for thermoacoustic engines," *Journal of the Acoustical Society of America*, Article vol. 147, no. 4, pp. 2348-2356, 2020, doi: 10.1121/10.0001067.
- [11] P. H. Riley, "Designing a low-cost electricity-generating cooking stove for high-volume implementaion," 2014.
- [12] G. W. Swift, *Thermoacoustics: A Unifying perspective for some engines and refrigerators* (Thermoacoustics: A Unifying Perspective for Some Engines and Refrigerators). 2002.
- [13] K. O. A. Abdoulla-Latiwish and A. J. Jaworski, "Two-stage travelling-wave thermoacoustic electricity generator for rural areas of developing countries," *Applied Acoustics*, Article vol. 151, pp. 87-98, 2019, doi: 10.1016/j.apacoust.2019.03.010.
- [14] J. R. Olson and G. W. Swift, "Similitude in Thermoacoustics," *Journal of the Acoustical Society of America*, Article vol. 95, no. 3, pp. 1405-1412, 1994, doi: 10.1121/1.408581.
- [15] Z. Wu, G. Yu, L. Zhang, W. Dai, and E. Luo, "Development of a 3kW double-acting thermoacoustic Stirling electric generator," *Applied Energy*, Article vol. 136, pp. 866-872, 2014, doi: 10.1016/j.apenergy.2014.04.105.
- [16] A. Al-Kayiem and Z. Yu, "Using a side-branched volume to tune the acoustic field in a looped-tube travelling-wave thermoacoustic engine with a RC load," *Energy Convers. Manage.*, Article vol. 150, pp. 814-821, 2017, doi: 10.1016/j.enconman.2017.03.019.
- [17] Z. Yu, A. J. Jaworski, and S. Backhaus, "A low-cost electricity generator for rural areas using a travelling-wave looped-tube thermoacoustic engine," *Proceedings of the Institution of Mechanical Engineers, Part A: Journal of Power and Energy*, Article vol. 224, no. 6, pp. 787-795, 2010, doi: 10.1243/09576509JPE864.
- [18] A. Gosavi, "Simulation-Based Optimization: An Overview," in *Simulation-Based Optimization: Parametric Optimization Techniques and Reinforcement Learning*, A. Gosavi Ed. Boston, MA: Springer US, 2015, pp. 29-35.
- [19] J. Antony and J. Antony, *Design of Experiments for Engineers and Scientists*. Jordan Hill, UNITED KINGDOM: Elsevier, 2003.
- [20] J. Nelder and R. Mead, "A Simplex Method for Function Minimization," *Comput. J.*, vol. 7, pp. 308-313, 1965.
- [21] H. Ghiasi, D. Pasini, and L. Lessard, "Constrained globalized Nelder-Mead method for simultaneous structural and manufacturing optimization of a composite bracket," *Journal of Composite Materials*, Article vol. 42, no. 7, pp. 717-736, 2008, doi: 10.1177/0021998307088592.
- [22] W. F. Sacco, H. A. Filho, N. Henderson, and C. R. E. de Oliveira, "A Metropolis algorithm combined with Nelder-Mead Simplex applied to nuclear reactor core design," *Annals of Nuclear Energy*, Article vol. 35, no. 5, pp. 861-867, 2008, doi: 10.1016/j.anucene.2007.09.006.

- [23] Z. Romani, A. Draoui, and F. Allard, "Metamodeling the heating and cooling energy needs and simultaneous building envelope optimization for low energy building design in Morocco," *Energy and Buildings*, Article vol. 102, pp. 139-148, 2015, doi: 10.1016/j.enbuild.2015.04.014.
- [24] A. Gosavi, "Parametric Optimization: Stochastic Gradients and Adaptive Search," in *Simulation-Based Optimization: Parametric Optimization Techniques and Reinforcement Learning*, A. Gosavi Ed. Boston, MA: Springer US, 2015, pp. 71-122.
- [25] J. C. Lagarias, J. A. Reeds, M. H. Wright, and P. E. Wright, "Convergence properties of the Nelder-Mead simplex method in low dimensions," *SIAM Journal on Optimization*, Article vol. 9, no. 1, pp. 112-147, 1998, doi: 10.1137/S1052623496303470.
- [26] J. Clark, W. Ward, and G. Swift, "Design environment for low-amplitude thermoacoustic energy conversion (DeltaEC)," *Journal of the Acoustical Society of America*, vol. 122, pp. 3014-3014, 2007.
- [27] W. Kisha, P. H. Riley, J. McKechnie, and D. Hann, "The Influence of Heat Input Ratio on Electrical Power Output of a Dual-Core Travelling-Wave Thermoacoustic Engine," presented at the 8th Heat Powered Cycles Conference, University of Bayreuth, Germany, 2018.
- [28] P. H. Riley, "SoFo Executive Meeting," ed, 2012.
- [29] Z. Yu, A. J. Jaworski, and S. Backhaus, "Travelling-wave thermoacoustic electricity generator using an ultra-compliant alternator for utilization of low-grade thermal energy," *Applied Energy*, Article vol. 99, pp. 135-145, 2012, doi: 10.1016/j.apenergy.2012.04.046.
- [30] J. L. Schafer and J. W. Graham, "Missing data: Our view of the state of the art," *Psychological Methods*, Article vol. 7, no. 2, pp. 147-177, 2002, doi: 10.1037/1082-989X.7.2.147.
- [31] K. J. Millman and M. Aivazis, "Python for Scientists and Engineers," *Computing in Science & Engineering*, vol. 13, no. 2, pp. 9-12, 2011, doi: 10.1109/MCSE.2011.36.
- [32] F. Gao and L. Han, "Implementing the Nelder-Mead simplex algorithm with adaptive parameters," *Computational Optimization and Applications*, Article vol. 51, no. 1, pp. 259-277, 2012, doi: 10.1007/s10589-010-9329-3.
- [33] M. A. Luersen, R. Le Riche, and F. Guyon, "A constrained, globalized, and bounded Nelder-Mead method for engineering optimization," *Structural and Multidisciplinary Optimization*, Article vol. 27, no. 1-2, pp. 43-54, 2004, doi: 10.1007/s00158-003-0320-9.
- [34] R. R. Barton and J. S. Ivey, "Nelder-Mead Simplex Modifications for Simulation Optimization," *Management Science*, vol. 42, no. 7, pp. 954-973, 1996.
- [35] M. A. Luersen and R. Le Riche, "Globalized Nelder-Mead method for engineering optimization," *Computers & Structures*, vol. 82, no. 23, pp. 2251-2260, 2004/09/01/ 2004.
- [36] Z. Yu, P. Saechan, and A. J. Jaworski, "A method of characterising performance of audio loudspeakers for linear alternator applications in low-cost thermoacoustic electricity generators," *Applied Acoustics*, Article vol. 72, no. 5, pp. 260-267, 2011, doi: 10.1016/j.apacoust.2010.11.011.
- [37] A. I. J. Forrester, A. Sóbester, and A. Keane, *Engineering Design via Surrogate Modelling*. Wiley, 2008.

Electro Deionization for treatment of Condensate of Steam Bottoming Cycles

M. Mazzetti* and G. Skaugen

Sintef Energy Research, Kolbjørn Heijes vei 1D, 7034 Trondheim, Norway

*Corresponding author: marit.mazzetti@sintef.no

Abstract

This paper studies the operational reliability of electro-deionization (EDI) condensate treatment systems. The rationale is to investigate whether EDI would be a technology with high enough operational reliability to be installed on offshore oil and gas platforms as part of a steam bottoming cycle for power production. A survey was made of land-based power plants that operate steam cycles where EDI is used for the water purification. A questionnaire was sent out to the plants and followed up with telephone interviews. The study found that the EDI systems installed in land-based power plants have high operational reliability and therefore may be suitable for installation in offshore power plants.

Keywords: Electro Deionization, EDI, Steam Bottoming Cycle, Condensate, Offshore

Introduction/Background

Oil and gas production is powered by gas turbines which cause high CO₂ emissions. Today the oil and gas industry account for a quarter of the total emissions in Norway[1]. In order to reduce these emissions more combined cycle steam plants can be installed on offshore oil and gas production platforms and reduce CO₂ emissions by up to 25 % [2][3]. However, high weight, operational reliability and operational expense have been detrimental factors to widespread implementation [3]. An illustration of a gas turbine with a steam cycle attached is shown in Figure 1.

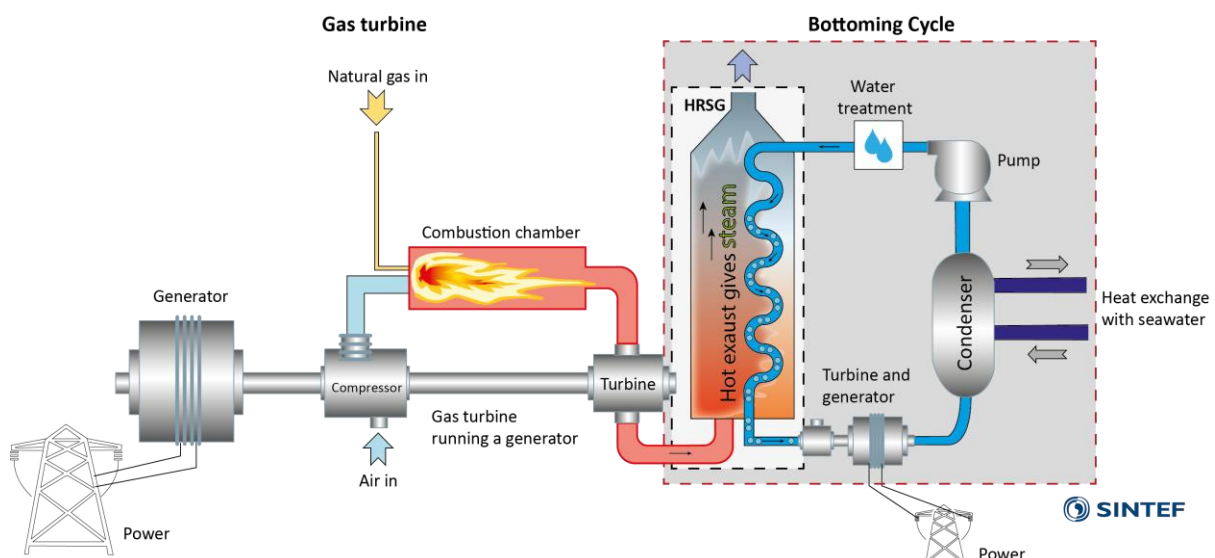


Figure 1: Illustration of gas turbine with steam bottoming cycle attached.

In the steam cycle heat is recovered from the exhaust of the gas turbine in the Heat Recovery Steam Generator (HRSG). The steam produces extra power in a steam turbine/generator set before it is condensed by heat exchange with seawater. It then goes through a water treatment step purifying the condensate before it is pumped back into the HRSG. Over the last few years several research projects, COMPACTS[4] and COMPACTS2[5] have been conducted to determine ways to design lower weight steam bottoming cycles so that they can be implemented on more platforms offshore. Significant weight reduction of over 50% has been achieved for the bottoming cycle[6]. In addition to weight reduction, a key enabler for more widespread installation of steam cycles offshore is lower operational expense and better operational reliability of the steam cycles. Here the condensate purification process is an important factor. Offshore bottoming cycle systems have strict demands for make-up water purification. As fresh water is a limited resource offshore, makeup water must be produced from sea water through desalination and further purification e.g. through ion exchange mixed bed demineralization [7].

Traditional purification processes on land-based steam cycles involve pre-treatment followed by beds of ion exchange resin for metals and minerals polishing. Frequent regeneration of the ion exchange resin and testing of the water quality is needed to ensure that the ion exchange resin beds are not exhausted. It is labour intensive to manually monitor and maintain such a system. Therefore, it is of interest to investigate alternative water purification technologies with lower operational involvement and maintenance requirements such as electro-deionization (EDI). In addition, ion exchange technology is quite heavy while EDI plants are very compact[8]. By replacing ion exchange with EDI a weight reduction can therefore be achieved. The disadvantage of EDI is a 5 % increase in water consumption as water concentrated in impurities is continuously rejected during the EDI purification process.

EDI is a continuous process of removing ionized and ionizable species from feedwater using DC power. EDI originated in the late 1950s at Argonne National Labs[9]. The first EDI devices were made by commercial companies in the late 1980s. The main applications for the main producers such as E-Cell, SnowPure and IonPure are in plants requiring ultra-high purity water such as electronics, pharmaceuticals and power production.

In an EDI cell, an ion exchange resin is packed between a cationic and an anionic membrane creating a deionization chamber. Charged ions are pulled off the resin and drawn to the respective oppositely charged electrodes. The strong ions are removed from the water into the concentration chambers[10]. The plants need minimum maintenance[9].

One major advantage is that EDI utilizes chemical free regeneration. Therefore regeneration downtime is eliminated and storage and handling of acid and lye are avoided[8] reducing operational costs.

Today there are three steam cycles installed on offshore platforms on the Norwegian Continental Shelf (NCS). They all have traditional ion exchange resin beds for purification of the condensate. Switching from ion exchange to EDI would simplify the operation of the offshore steam cycles and eliminate handling of chemicals as well as increase compactness and reduce weight. However, since there is no experience with using EDI technology for offshore steam cycles, its operational reliability must therefore be determined.

In this study the operational reliability and life-time expectancy of EDI systems already installed on land-based power plants were therefore characterized in order to investigate whether the technology is sufficiently operationally reliable for offshore applications.

Method

A survey was made of existing power plants having EDI systems installed to obtain information about their operational reliability. A questionnaire was sent to operators of EDI equipment in industrial and power plants and followed up with telephone interviews. Contact was also made with the main vendors of EDI systems in the Nordic countries and Europe to determine what the operational experience and operational reliability is for the onshore systems.

The questionnaire contained the following questions:

1. What is application for the EDI system?
2. What is the input water?
3. What is yield (flow rate) in m³/h?
4. What is the conductivity?
5. How long has the EDI system been in operation?
6. Who was the manufacturer of the EDI cells?
7. What is the maintenance requirements for the cells?
8. Have the cells failed during the operation, if so when and how many times?
9. Have there been many leaks?
10. Is there any downtime of the system?
11. Temperature of water?

Results and Discussion

Operational reliability of EDI systems

In Norway there are three larger size land-based power plants which have steam cycles installed for power production from excess heat. They all use EDI for the purification of the condensate for the steam cycle. A short summary of facts obtained from interviews with operators or vendors at each site follows.

Power Plant A: The water steam cycle consisted of a three- pressure HRSG boiler, deaerator, steam turbines, condenser, condensate and feedwater pumps and was in operation from 2007-2014.

The EDIs installed there required no maintenance attention nor modifications. They seemed to be running very stable over the 7 years they were in operation. A half-yearly check of the electrical connections and a measurement of the electric current over each cell was a part of the maintenance programme.

In case of a long-term preservation, it is crucial that the EDIs are stored as is, in fully wet condition. During the first long-term preservation, due to a poor power market, one of the

EDIs was partly drained. The mentioned EDI did therefore not work properly after this incident, and it was exchanged with the spare EDI already installed in the skid.

Power Plant B: This is a waste incineration-based power plant. It produces 95 GW annually of electricity as well as delivers heat to the district heating network. It has been operating since 2010.

This power plant has an EDI system. Here one cell has been exchanged once during ten years of operation. The reason for failure was incoming water quality.

Power Plant C: A steam turbine produces power from the waste heat from the off-gases from metals production. The turbine was installed in 2012 and has an annual production of 340 GWh of power. The system consists of a coarse filter, a carbon filter a fine filter, an RO and then the EDI. The flow rate of the filter is 18 m³/h divided on 2 cells, so the EDI cells are operating in parallel. It has been relatively operationally reliable. Both EDI cells have recently been exchanged after 7 years of operation.

EDI has been used as treatment technology for the condensate of steam cycles at several Norwegian, Swedish and Danish land-based power plants in the period 1998-2021. A summary of the plants reviewed in this study and their years of operation is shown in Table 1. The number of EDI failures are taken as a measure of operational reliability and are shown for each plant over the period running.

Table 1: Operational reliability of EDI systems installed in Nordic power and incineration plants with steam cycles.

Plant	Yield (m ³ /hr)	Years in Operation	# EDI failures	Comment
Incineration	3.8	5	0	1 leak
Power plant	11	7	1	
Power plant		10	1	
Power plant	15	10	3	Failure due to contamination of incoming water
Power plant		23	0	
Power plant		19	0	
Power plant	18	9	2	Both cells exchanged after 7 years

Based on interviews with the operators and the results shown in Table 1, it is estimated that EDI cells will run 5-7 years or longer before they fail and have to be exchanged. There was one exception found to this conclusion; in one case there was three failures of the EDI. In this particular case there was water from a rusty tank with particles flowing into the EDI that destroyed it.

The feedback from operators indicated that the contamination build-up and loss in performance of the cell is slow. The faults that occur to EDI systems are a slow rise in conductivity, slow rise in pressure drop or reduction in flow as well as minor leakages.

Therefore the switch out of the cell can be part of scheduled maintenance. It is also common to have a backup cell on-site so that the cell can easily be switched out without any need for unplanned downtime in plant operations.

Leaks

As can be seen from the results, leaks have not been a significant problem among those surveyed. Most operators have not experienced any leaks. A few of the outfits have had one leak.

Water Quality

The results of the surveys clearly show that the incoming water quality is crucial to the life time of the units. The EDI system requires a consistent feed of pure incoming water that has been treated by RO or being of equivalent quality. The other factor is storage of units in the event of a shut down, they have to be stored in water. If they drain, they stop working properly afterwards.

Maintenance

The feedback from the questionnaires was that the EDI installed in the plants required little maintenance attention nor modifications during their years of operation. The regular monitoring consists of regular checks of the voltage in relation to electric current and checks of the online-conductivity. A half-yearly check of the electrical connections and a measurement of the electric current over each cell was reported as part of the maintenance programme.

Range of Operational Temperature

The systems surveyed were operating over a range of water temperatures from 7-35°C. The max water temperature that the EDI can operate with is 40°C. One of the reference cases operated at 35°C showing that it works well to run at higher temperatures. The condensate temperature is important in the steam cycle since it affects what condenser pressure is possible and also if a supercooler is needed in the system.

Summary/Conclusions

In this study interviews have been made with several facilities that run EDI water purification systems in power plants as well as experienced vendors who have installed hundreds of EDI systems. Based on the interviews the following conclusions can be made:

- EDI technology requires very little follow up and no regular maintenance
- EDI cells require a consistent feed of pure incoming water that has been treated by RO or being of equivalent quality. The incoming water quality is crucial to the lifetime of the unit. If water quality is reduced it can cause build-up of impurities in the EDI and clogging and gradual loss of performance to where the cell must be exchanged.
- The average expected life-time of an EDI cell is 5- 7 years.

- The switching out of cells can be planned as part of scheduled maintenance as there is a gradual loss in performance and not acute failure. The EDI therefore does not cause unplanned production stops.
- Leaks are not a significant problem. The operators interviewed in this study reported little or no leaks. If there were any leaks they were at the beginning of the operating period. Most outfits did not have problems with leaks.

This study shows that EDI is an operationally reliable technology in steam cycle power plants where there is rare that failure occurs which results in shut down of water production. The typical lifetime of an EDI system is 5-7 years. The faults that occur are slow rise in conductivity, slow rise in pressure drop or reduction in flow as well as minor leakages. These systems should therefore be suited for offshore applications. Online monitoring of conductivity and pressure drop can be used to predict when the cell must be replaced.

Acknowledgements

The authors acknowledge the COMPACTS2 partners: ConocoPhillips Scandinavia AS, Equinor Energy AS, NTNU, SINTEF and the Research Council of Norway, strategic Norwegian research program PETROMAKS2 (#280713) for their support.

References:

- [1] Norsk Petroleum. Emissions to air, 2020. <https://www.norskpetroleum.no/en/environment-and-technology/emissions-to-air/>.
- [2] Mazzetti MJ, Neksa P, Walnum HT, Hemmingsen AKT. Energy-Efficiency Technologies for Reduction of Offshore CO₂ Emissions. *Oil Gas Facil* 2014;3:89–96. <https://doi.org/10.2118/169811-PA>.
- [3] Nord L, Bolland O. Steam bottoming cycles offshore - Challenges and possibilities. *J Power Technol* 2012;92:201--207.
- [4] COMPACTS. Compact Offshore Steam Cycles 2018. <https://www.sintef.no/compacts>.
- [5] COMPACTS2. Compact Offshore Steam Cycles2, 2021, www.sintef.no/COMPACTS2.
- [6] Mazzetti, M.J., Hagen, B., Skaugen, G., Lindqvist, K., Lundberg, S, Kristensen OA. Achieving 50% Weight Reduction of Offshore Steam Bottoming Cycles. *Energy*, Volume 230, 2021, 120634.
- [7] Kloster P. Reduction of emissions to air through energy optimisation on offshore installations. *Int. Conf. Heal. Saf. Environ. Oil Gas Explor. Prod.*, 2000. <https://doi.org/10.2523/61651-ms>.

- [8] <https://www.eurowater.com/water-treatment-plants/electrodeionization>.
- [9] <https://en.wikipedia.org/wiki/Electrodeionization>.
- [10] <https://www.lenntech.com/library/edi/edi.htm>.

Solar tower plant extra electricity production potential by means of harnessing excess solar energy

U. Oyarzabal^{1*}, A. Erkoreka¹, I. Gomez-Arriaran¹, D. Novales¹, B. Herrazti²

¹Department of Thermal Engineering, Faculty of Engineering of Bilbao, University of the Basque Country (UPV/EHU), Avda. Urquijo s/n 48013 Bilbao, Spain.

²Department of Mechanical Engineering, SENER Ingeniería y Sistemas S.A., Avda. Zugazarte 56, 48930 Getxo, Spain

*Corresponding author: unaioiar92@gmail.com

Abstract

Currently, one of the renewable energy sources capable of combating global climate change is solar energy. Among all renewable energy sources, concentrated solar power is the only one with which we can store energy in order to be able to match the production of electricity with the current demand. For all these reasons, any change applicable to this type of plant is considered very interesting in order to increase its electricity production and thus put an end to the discussion that questions the maturity of this type of technology.

The most developed CSP plants at the moment are central tower and parabolic trough plants. This type of plant is designed for an optimal LCOE (Levelized Cost of Electricity) value with the intention of achieving a balance between the investment of the plant and the production expected to be obtained from it. For this reason, in central tower plants, there are days (mainly in summer) when the hot molten salt tank is saturated and therefore, it is not possible to make use of all the solar irradiation that could be projected by the heliostats that constitute the solar field.

This problem does not exist in parabolic trough plants that use thermal oil as heat transfer fluid, but it does in solar tower plants because the heat transfer fluid is molten salts, a mixture of sodium nitrate 60% - potassium nitrate 40% whose freezing temperature is 243 °C due to impurities. For the safety of the plant, it is avoided to introduce water below 260 °C into the economizer.

This article will study how to solve this problem in order to be able to generate more MW of electricity throughout the year at the sacrifice of the plant's performance at certain times. To do this, a new way of operating the plant in off-design modes will be analysed in order to make use of the extra solar energy that currently no central tower plant is capable of harnessing.

All data used throughout this study are based on the world's first commercial central tower plant, Gemasolar. In order to study the potential of this new way of operating the plant, the Thermoflex software has been used. More specifically, to analyse the effect of lowering the salts outlet temperature of the Steam Generation System (SGS) on the overall performance of the plant.

In order to carry out this new way of operating the plant, the inlet temperature of the feedwater to the economizer will be lowered below 260 °C (currently, this inlet temperature is always set above 260 °C so that the salts cannot drop below this temperature and thus avoid possible freezing problems). All the calculations made during this study are easily extrapolated to the rest of the central tower plants in the world.

Once the optimal way to use this extra energy had been studied and the value of this extra annual energy quantified, an economic analysis was carried out. No constraints based on grid limitations for electricity export or possible tariff impacts have been considered for the analysis. The conclusion is that the potential annual extra electricity production for Gemasolar could be 1,657.6 MWh/year, which represents almost 1.6% of extra electricity production potential for a power plant that annually generates about 100 GWh/year. A simple payback period of 5.4 years is obtained when applying the proposed strategy based on a 50€/MWh electricity price.

Keywords: Solar Tower Power, molten salts, extra solar energy, vapor power cycle off-design operation

Introduction/Background

Nowadays, climate change is the most concerning environmental problem and its main cause is considered to be greenhouse gas emissions [1]. Global society is concerned about the negative effects of CO₂ emissions, derived mainly from the disproportionate use of fossil fuels in developed countries. To reduce such emissions to a zero emitting society, it is necessary to urgently renovate the world's energy system by substituting fossil fuel based resources with renewable sources, such as eolic, hydraulic and solar, among others [2, 3].

One of the main sources of renewable energy that has been benefited by the worldwide purpose to reduce CO₂ emissions is solar energy [4]. Two main technologies have been developed for the production of electricity from solar radiation: Photovoltaic and Solar Thermal Concentrated Solar Power (CSP). Logically, this technology should be developed in locations with high availability of direct solar radiation, such as North Africa, the Middle East, Southern Europe, China, Southern USA and Australia, among others [5]. In contrast with photovoltaic, CSP power plants can be equipped with molten salts energy storage tanks and can shift electricity production to the desired hours of the day [6].

Within this type of technology there is the parabolic trough, a mature and proven technology, but there is also the central tower technology, which is the one that will be studied in this article. Among others, these are some of the advantages of the solar tower power technology when compared to other CSP technologies:

1. This technology enables the cycle to operate with a higher maximum superheated steam temperature (up to 560 °C) in comparison with other CSP technologies, resulting in a higher efficiency of the vapor power cycle.
2. If storage exists, solar energy capture is independent from electricity production. The most common way to store thermal energy is by means of molten salts tanks [7], which are a mixture of sodium nitrate (60%) and potassium nitrate (40%), with a theoretical freezing point of 223 °C. [8]. In practice, due to the impurities in the salt mixture, crystallization occurs at higher temperatures and the freezing temperature considered when solar tower power plants are designed is usually between 240-245 °C. In this paper, the practical freezing point temperature of the salts will be considered to be 242 °C.
3. The scalability of the power of the plant (plants up to 200 MWe) [9, 10].

During the design of a solar tower power plant, it is very important to pay special attention to the sizing of the solar field (or heliostat field), since it is the part of the plant that requires the greatest investment, and in order to obtain the optimum value of the Levelized Cost of Electricity [11-13]. One of the main parameters for designing solar field sizing is the available Direct Normal Irradiance (DNI). The Direct Normal Irradiance is the part of solar radiation that reaches the earth's surface with a well defined path and could be redirected against a specific area of the solar receiver [14, 15]. It is also essential to know the detailed distribution of the daily DNI in [Wh/m²] in order to find out the exact amount of radiation that can be exploited by the plant every moment of the day. A summer day with clouds and clear spells, and multiple sudden variations in the DNI, can have the same total daily available solar energy as a clear winter day with a lower but more stable DNI; yet the production of electricity will be higher on the clear winter day [16, 17].

In solar tower power plants, the TES system is usually composed of two molten salts tanks: The cold tank (290°C - 300°C) and the hot tank (560°C) [18]. During the hours of solar radiation, a greater mass flow rate of salts than demanded by the steam power cycle is pumped to the tower (see Figure 2). In this way, depending on the sizing of the plant, some of the thermal energy is converted into electricity in the power block, while the rest of the thermal energy is stored in the tank of hot salts.

It is important to mention that, during the year, there are a considerable number of days when the daily DNI is higher than the one considered as the design parameter. This occurs because, as mentioned before, the heliostat field is sized for the optimum value of the Levelized Cost of Electricity on a yearly basis and, consequently, although the solar field has the optimum size for the specific location, it is oversized for some completely sunny summer days. During these sunny summer days, several heliostats are usually defocused to avoid overheating the receiver and its structural failure. On these days, even operating the power block at full capacity, the hot tank is usually completely filled when there are still sunny hours available (see an example of TES storage saturation in Figure 1). As a result, during these days, the excess radiation will be wasted.

As far as we know, there is no literature related to how this extra solar energy in an installation with a molten salt receiver could be exploited by modifying the plant operating conditions in this situation. The objectives of this research are to study the off-design operating conditions required for a solar tower power plant to exploit this extra solar energy and propose a general methodology to estimate the extra yearly electricity production potential regarding the said unexploited solar energy.

The methodology proposed in this work is applied in a practical manner to the central tower plant Gemasolar, located in the province of Sevilla (Spain), using available published data. The articles referring to this plant [19, 20] show different graphs where the DNI of different days, together with the power generated and the charge and discharge of the tanks of molten salts, can be seen (Figure 1 shows the performance on a completely sunny summer day). In Figure 1, the effect of the saturation of the TES can be perfectly appreciated; as a result of the excessive available DNI, the plant is not capable to exploit it completely. The 'STORAGED

ENERGY' line grows until the moment the hot tank is full and saturation occurs; then, the line becomes horizontal. From that moment, the mass flow rate of the salts from the receiver to the hot tank is equal to the mass flow rate that is pumped to the power block (see Figure 2). In this manner, even if there is available DNI, the 'SOLAR FIELD POWER' line drops drastically, just to cover the power block heat input requirements [20].

The goal of this article, in order to be able to exploit the solar radiation that cannot be currently absorbed by the plant due to the saturation of the storage capacity, is to propose and evaluate a modification in the existing Gemasolar plant. The concept would include a new shell and tube molten salts - feedwater heat exchanger located upstream (water side) of the currently existing economizer, which would reduce the temperature of the cold salts below the design temperature (see 'supercooler' in Figure 4). Although thermodynamically feasible, the technical solution to properly conduct this heat exchange must be studied in detail to avoid the risk of freezing within the proposed heat exchanger. This heat exchanger would permit the power block electrical power output to increase by closing some of the steam turbine bleeds, thus increasing the power block heat absorption by cooling the molten salts below the design operation temperature. This also increases the TES capacity of the plant, since the temperature difference between the hot and cold tanks is now greater. This new solution, although it reduces the cycle thermal efficiency under these off-design steam power cycle operation conditions, will increase the electricity production. In order to be able to operate in this way, the turbine extractions for the feedwater preheaters should be partially or completely closed, using a by-pass in the preheaters, as can be seen in Figure 3. As previously pointed out, this operating mode implies a decrease in the thermodynamic efficiency of the power cycle, but the solar energy that is lost by saturation of the TES would now be used to produce electricity, thus increasing the global electricity production.

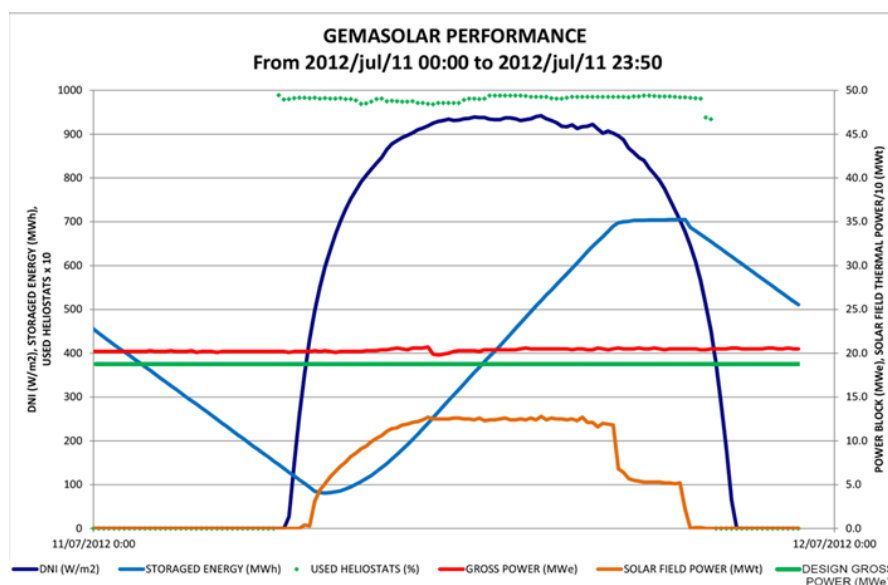


Figure 1- Actual daily evolution of the main operation parameters of the Gemasolar solar tower power plant during a completely sunny summer day (11th July 2012). Data presented in detail by SENER in SOLAR PACES conference in 2012 [19]

The extra electricity potential estimation methodology can be extrapolated to any existing or new solar tower power plant with a considerable variation of the DNI, radiation daily hours and radiation angle through the year.

Gemasolar was the first commercial plant in the world to use a central tower molten salts receiver and a TES (Thermal Energy Storage) system. Figure 2 represents the design plant operation principle. Likewise, as mentioned above, the economizer is fed with feedwater at 260°C. This temperature is higher than the practical freezing temperature of the molten salts (242°C) to avoid the risk of freezing within the economizer and therefore having to stop the plant.

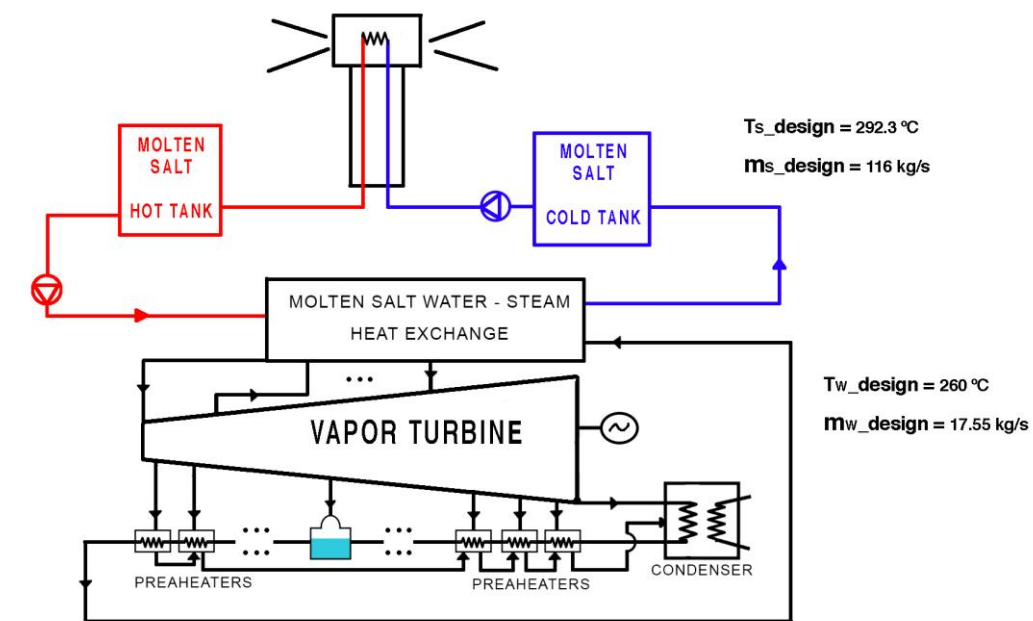


Figure 2- Schematic of the actual Gemasolar solar tower power plant

Gemasolar power plant is sized for a specific design DNI profile so that the power block may operate in nominal conditions for 24 hours per day thanks to the TES system. The design DNI of the plant can be estimated based on the steam power cycle's main performance parameters and the design daily operating hours of the power plant.

First of all, we find out the thermal power in MW that the steam power cycle needs to be able to generate the design gross electrical power. This value will be the quotient between the design gross electrical power and the design gross electric efficiency of the vapor power cycle (see Eq. (1)). Then, the design heat input to the vapor power cycle (\dot{Q}_{th_design}) in MWh to generate the design gross electrical power uninterruptedly over the 24 hours must be calculated as in Eq. (2).

$$\dot{Q}_{th_design} = \frac{W_{e_design}}{\eta} \quad [MW] \quad (1)$$

where \dot{Q}_{th_design} is the design gross thermal power input to the vapor power cycle, W_{e_design} is the design gross electrical power and η is the gross design electric efficiency.

$$Q_{th_design} = \dot{Q}_{th_design} \cdot 24 \quad [\text{MWh}] \quad (2)$$

Q_{th_design} can be represented as a function of the total area of the mirrors of the heliostat field, the daily DNI solar energy and a certain factor, F. This F factor represents the daily averaged capacity of the plant for transferring the DNI available in the solar field mirrors area to the salts and is calculated as the quotient between the daily thermal MWh transmitted to the salts and the daily DNI solar energy available in the mirrors. Then, the value of the daily design DNI ($\sum_{i=1}^{N=24} DNI_{design_i}$) in [MWh/m²] of Gemasolar is obtained from Eq. (3). Note that $\sum_{i=1}^{N=24} DNI_{design_i}$ is calculated on an hourly basis in Eq. (3).

$$Q_{th_design} = A_{mirror} \cdot F \cdot \sum_{i=1}^{N=24} DNI_{design_i} \quad [\text{MWh}] \quad (3)$$

A_{mirror} refers to the total area of mirrors [m²], F is the factor that represents the percentage of DNI solar radiation energy in the mirrors that ends up in the salts during the plant operation for clear days [-] and $\sum_{i=1}^{N=24} DNI_{design_i}$ is the plant DNI for the design day in [MWh/m²].

Having calculated the design DNI and converted it to [Wh/m²], it is possible to calculate the available extra DNI solar energy quantity not exploited by the plant under the design operating conditions for each day of the year. Based on the annual hourly DNI solar radiation at the plant location, the available daily DNI solar energy can be obtained for each of the 365 days of the year using Eq. (4):

$$DNI_{day} = \sum_{i=1}^{N=24} DNI \left(\frac{\text{Wh}}{\text{m}^2} \right)_i \quad [\text{Wh/m}^2] \quad (4)$$

where DNI_{day} refers to the daily available DNI.

Then, the total DNI solar energy available in the mirrors (Q_{mirror}) can be calculated for each day of the considered year using Eq. (5), note that Eq. (5) requires the DNI_{day} in [MWh/m²]. Then, using Eq. (6), it is possible to obtain the daily averaged available DNI solar radiation power ($\overline{Q_{mirror}}$).

$$Q_{mirror} = A_{mirror} \cdot DNI_{day} \quad [\text{MWh}] \quad (5)$$

$$\overline{Q_{mirror}} = \frac{Q_{mirror}}{24 \text{ h}} \quad [\text{MW}] \quad (6)$$

The daily averaged heat power the plant is capable of transmitting to the salts ($\overline{Q_{salts}}$) can then be calculated by Eq. (7) for each day of the year. The daily averaged F factor can be very variable due to sunny days with cloudy spells, and its calculation for those types of days is a very complex task. However, for completely sunny days with the plant operating without incidences, the daily averaged F factor is very stable throughout the year. The latter is fundamental to this research, since only completely sunny summer days have the potential to produce extra electricity and, thus, the F factor can be considered similar for all those days.

Even if this factor is very sensitive, mainly to sudden DNI variations due to clouds, based on the analysis of the real operation data of the Gemasolar power plant, it has been checked that the F factor for completely sunny days is very stable. An average value of 0.416 has been obtained from the analysis of a set of randomly chosen, completely sunny days where the plant has been operated without incidence. However, for some completely sunny days' operation, the F factor has been close to 0.45.

$$\overline{Q_{salts}} = F \cdot \overline{Q_{mirror}} \quad [\text{MW}] \quad (7)$$

Now that the daily averaged thermal power in salts ($\overline{Q_{salts}}$) has been estimated for all the days of the year, it is possible to foresee how many days of the year have the potential to produce more electricity than the design day. Since it is averaged daily and the plant is sized to operate 24h/day, $\overline{Q_{salts}}$ already represents the potential thermal power input to the power cycle and, thus, the days with potential to produce more electricity than the design day can be identified by simply searching for days with $\overline{Q_{salts}} > \dot{Q}_{th_design}$.

It is not straightforward to convert the available daily averaged $\overline{Q_{salts}}$ into gross electric power by using Eq. (1) since, on the days where $\overline{Q_{salts}} > \dot{Q}_{th_design}$, the power block must be operated under off-design conditions and thus, depending on the available $\overline{Q_{salts}}$, the off-design power cycle gross electric efficiency ($\eta_{\text{off-design}}$) will be different. However, once these $\eta_{\text{off-design}}$ values are available, the daily gross electricity production for all the days of the year where $\overline{Q_{salts}} > \dot{Q}_{th_design}$ can be obtained through Eq. (8).

$$W_{e_day} = \overline{Q_{salts}} \cdot \eta_{\text{off-design}} \cdot 24 \text{ h} \quad \left[\frac{\text{MWh}}{\text{day}} \right] \quad (8)$$

If we want to calculate the extra electricity production of these completely sunny summer days, we need the design daily electricity production of the Gemasolar power plant ($W_{e_day_design}$). This can be obtained by multiplying the design gross electric power of the plant by 24 hours, as done in Eq. (9).

$$W_{e_day_design} = \dot{W}_{e_design} \cdot 24 \text{ h} \quad \left[\frac{\text{MWh}}{\text{day}} \right] \quad (9)$$

Finally, using Eq. (10), the daily extra electricity production of the days where $\overline{Q_{salts}} > \dot{Q}_{th_design}$ can be calculated with respect to the design day.

$$W_{e_extra} = W_{e_day} - W_{e_day_design} \quad \left[\frac{\text{MWh}}{\text{day}} \right] \quad (10)$$

Moreover, for the complete year:

$$W_{e_extra_annual} = \sum W_{e_extra} \quad \left[\frac{\text{MWh}}{\text{year}} \right] \quad (11)$$

where $W_{e_extra_annual}$ is the total extra electricity potential production for the whole year.

To understand the implications in the plant operation and estimate the off-design gross electric efficiencies for the days where $\overline{Q_{salts}} > \dot{Q}_{th_design}$, it is necessary to define the best off-design operating strategies for the Gemasolar power cycle. No literature has been found about the best off-design operating strategies to take advantage of the available extra solar energy on completely sunny days for solar tower power plants. Thus, based on the current plant operation analysis, based on published data and our expertise on steam power cycle design, construction and operation, three main strategies have been considered:

Strategy A: increase the salts mass flow rate through the steam generation system of the power cycle to produce a higher steam mass flow rate without closing any of the steam turbine bleeds. Under this type of operation, the salts leave the steam generation system at a higher temperature than the design temperature. The latter slightly increases the power cycle off-design thermal efficiency due to a higher average hot temperature of the heat power supplied to the power cycle, but also increases the cold tank temperature. Increasing the cold tank temperature decreases the thermal storage capacity of the TES system. Considering the TES capacity of the Gemasolar power plant, this strategy can be used for completely sunny days where $\overline{Q_{salts}} \leq 1.064 \cdot \dot{Q}_{th_design}$. In other words, if the daily available DNI is up to 6.4% higher than the design DNI, this strategy permits the Gemasolar power plant to operate 24 hours a day up to 106.4% of the design heat input to the cycle without saturating the TES system.

Strategy B: this strategy is similar to strategy A, but now the steam turbine bleeds should be partially closed, starting from the highest pressure bleed towards the lowest pressure bleed in order to maintain the outlet salts temperature from the steam generation system at its design temperature, $T_{scold} = 292.3 \text{ }^\circ\text{C}$ (see Figure 2). This strategy slightly reduces the power cycle off-design efficiency, but is limited by two aspects; on the one hand, for days where $\overline{Q_{salts}}$ is considerably higher than the \dot{Q}_{th_design} it requires the salts mass flow rates, which could be impossible to pump using the existing pumping systems, and would generate an excessive pressure loss in some equipment. For the Gemasolar power plant, the design salts mass flow rate is 116.0 kg/s and the actual maximum salts mass flow rate is calculated to be around 125.8 kg/s. The second aspect limiting this strategy is the TES saturation; as stated above for strategy A, considering the TES capacity of the Gemasolar power plant, strategy B can be used for completely sunny days where $\overline{Q_{salts}} \leq 1.084 \cdot \dot{Q}_{th_design}$. If $\overline{Q_{salts}}$ is 8.4% higher than \dot{Q}_{th_design} capturing all the available DNI will not be possible due to the saturation of the TES system.

Strategy C: for completely sunny summer days where $\overline{Q_{salts}}$ is considerably higher than \dot{Q}_{th_design} there is a third strategy that will allow the capture of all the available DNI by closing the steam turbine bleeds until the cold salts exit temperature from the steam generator is cold enough to allow the total capture of all the available DNI. This strategy would

produce moderate decreases in the thermal efficiency of the power cycle due to a lower average hot temperature for the heat input to the cycle. This strategy is thermodynamically limited by the salts freezing temperature (around 242 °C), but in practice, to prevent local freezing risks on the economizer's possible cold surfaces, the introduction of feedwater below the salts freezing temperature is avoided. Thus, for Gemasolar, when $\overline{Q_{salts}} > 1.084 \cdot \dot{Q}_{th_design}$, the only strategy for permitting further capture and use of the available extra DNI is a combined operation of strategy A or B with C. Thanks to strategy C, the cold tank temperature will be lower than the design temperature while maintaining the hot tank at 560°C and this will permit the TES system capacity to be increased in parallel with a higher electricity power production in the power cycle.

The most efficient solution that would permit the total exploitation of all the available DNI over the whole year is obtained when strategies A and C are properly combined. Strategy A should be used alone for all the days when $1 \cdot \dot{Q}_{th_design} \leq \overline{Q_{salts}} \leq 1.064 \cdot \dot{Q}_{th_design}$. In fact, the Gemasolar power plant is currently using this strategy on completely sunny summer days, as those presented in Figure 1. There, it can be seen that the gross electric production is 20 MWe instead of the design 18.7 MWe. At this point, the mass flow rate of the salts is already in its current possible maximum of 125.8 kg/s. Thus, for days where $\overline{Q_{salts}} > 1.064 \cdot \dot{Q}_{th_design}$ the maximum possible mass flow rate of salts will be maintained and the steam turbine bleeds should be properly closed thanks to the by-passes made to the preheaters, as seen in Figure 4.

The off-design operation electric efficiencies of the power cycle of Gemasolar have been carried out using the Thermoflex software and based on the Thermoflex model used to design the Gemasolar steam power cycle. Thermoflex is a computer simulator for designing power cycles that can also simulate the designed cycles under different off-design conditions [21].

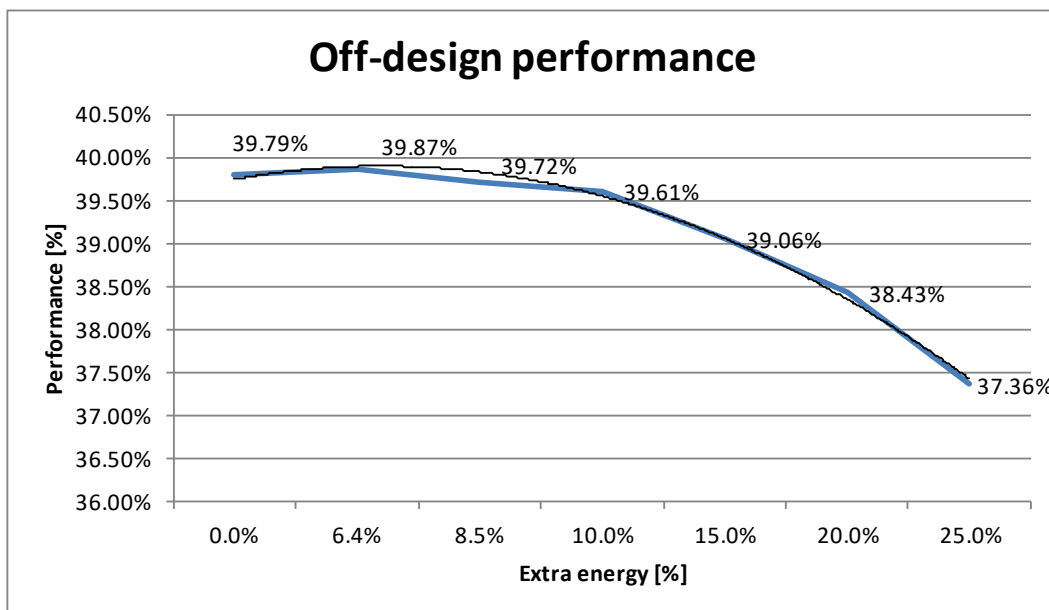


Figure 3- Off-design gross electric efficiency curve used to calculate Eq. (8).

Discussion and Results

In practice, to apply strategies B and C, two main modifications should be performed to the power cycle. First of all, to permit the closure of the different steam turbine bleeds, the existing preheaters of the Gemasolar power cycle should be given the possibility of a bypass. For example, to completely close the highest pressure bleed, it would be sufficient to bypass the feedwater, as in Figure 4. The second variation would be the inclusion, prior to the actual economizer, of a feedwater-molten salts heat exchanger (namely the ‘supercooler’ in Figure 4) to permit the heat exchange between the cold feedwater that has bypassed the preheaters and that permits the molten salts to cool down to below the design exit temperature from the steam generating system.

Even if strategy B has finally not been considered for taking advantage of the extra available DNI on the completely sunny days, it is more interesting to show the simulation results of strategies B and C in Tables 1 and 2 respectively. Strategy B, on its own, permits the sole effect of increasing the salts mass flow rate while maintaining the steam generation system salts inlet and outlet temperatures at the design conditions on the power cycle gross electric efficiency to be analyzed. It is necessary to partially close the highest pressure turbine bleed under this operation strategy. While strategy C, on its own, permits the sole effect of decreasing the exit temperature of the salts from the steam generator system on the power cycle gross electric efficiency, while maintaining the mass flow rate at the design value, to be analyzed.

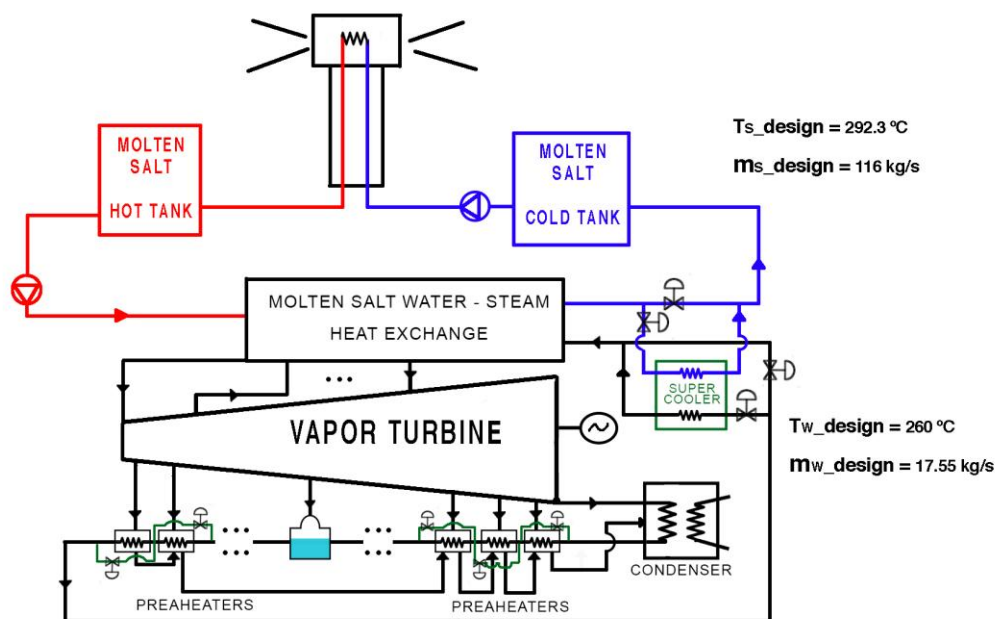


Figure 4- Schematic of the Gemasolar solar tower power plant including the super cooler previous to the economizer and the preheater bypasses for turbine bleeds closure.

Table 1- Strategy B simulation outputs. Extra energy represents the extra available DNI in % with respect to the design case. $T_{in,s}$ and $T_{out,s}$ are the inlet and outlet temperatures of the salts from the steam generation system considering the Figure 4 supercooler within the steam generation system. m_s is the salts mass flow rate and η is the off-design gross electric efficiency of the Gemasolar power cycle for each simulated case.

Simulation number	Extra Energy (%)	$T_{in,s}$ (°C)	$T_{out,s}$ (°C)	m_s (kg/s)	η (%)
1	5%	560 °C	292.1 °C	121.8 kg/s	39.74%
2	10%	560 °C	292.1 °C	127.6 kg/s	39.71%
3	15%	560 °C	292.1 °C	133.4 kg/s	39.69%
4	20%	560 °C	292.1 °C	139.2 kg/s	39.64%
5	25%	560 °C	292.1 °C	145 kg/s	39.63%

Table 2- Strategy C simulation outputs

Simulation number	Extra Energy (%)	$T_{in,s}$ (°C)	$T_{out,s}$ (°C)	m_s (kg/s)	η (%)
1	5%	560 °C	278.9 °C	116 kg/s	39.41%
2	10%	560 °C	265.31 °C	116 kg/s	38.66%
3	15%	560 °C	251.91 °C	116 kg/s	38.12%

Analyzing Tables 1 and 2, it is obvious that the strategy of increasing the mass flow rate is better than the Strategy C, from the gross electric efficiency point of view. The day of the year with the highest available DNI would allow 24% Extra Energy ($\overline{Q_{salts}} = 1.24 \cdot \dot{Q}_{th_design}$) as compared to the design DNI day. Such an excess of available DNI would be impossible to exploit using just one of the two strategies. Strategy B is limited by the actual salts pump maximum mass flow rate (125.8 kg/s) and by the actual TES system storage capacity. Strategy C, on its own, is limited to exploiting as much as 18.8% of the extra energy; at that point, salts would be leaving the steam generation system at 242 °C and some crystallization would start to happen within the salts.

The proposed operating strategy maximizes the extra electricity production of the power cycle. This operating strategy is a combination of strategies A and C, as presented in Table 3.

For extra energy availability, up to 6.4% ($\overline{Q_{salts}} \leq 1.064 \cdot \dot{Q}_{th_design}$), the strategy would be to increase the mass flow rate of the salts without closing any of the steam turbine bleeds (the exit temperature of cold salts from the steam generator will be higher than the design and therefore the thermal efficiency too, see Table 3). This operation mode, according to the available data, is nowadays being used, whenever possible, in the operation of the Gemasolar power plant. Figure 1 shows how, during the whole day of 11th July 2012, even if the Gemasolar plant has been operating the 24 hours at 20 MWe, the TES system has become

saturated at about 17:00, thus not exploiting a considerable amount of the available DNI before the sunset.

For days with higher DNI availability, such as the 11th July 2012, where there is potential for $\overline{Q_{salts}} > 1.064 \cdot \dot{Q}_{th_design}$, strategy C and A should be combined. In this manner, the mass flow rate of the salts will be maintained at its maximum (125.8 kg/s) and the steam turbine bleeds should start to be closed to reduce the salts exit temperature from the steam generator system, thus permitting 100% use of all the available extra energy. Table 3 shows how this combination potentially permits up to 25% of the extra energy ($\overline{Q_{salts}} = 1.25 \cdot \dot{Q}_{th_design}$) to be exploited, with an exit salts temperature of 248.2 °C and an incoming feedwater temperature to the super cooler of just 133.2 °C.

Table 3- Proposed operating strategy by mixing strategies A and C. $T_{in,w}$ and $T_{out,w}$ are the inlet and outlet temperatures of the feedwater from the control volume formed by the actual economizer plus the Figure 3 supercooler. m_w is the feedwater mass flow rate towards the super cooler and η is the off-design gross electric efficiency of the Gemasolar power cycle for each simulated case.

Simulation number	Extra Energy (%)	$T_{in,s}$ (°C)	$T_{out,s}$ (°C)	$T_{in,w}$ (°C)	$T_{out,w}$ (°C)	m_s (kg/s)	m_w (kg/s)	η (%)
Design	0%	560 °C	292.3 °C	260.2 °C	308.9 °C	116 kg/s	17.55 kg/s	39.79%
1	6.4%	560 °C	297.1 °C	263.7 °C	313.4 °C	125.8 kg/s	18.88 kg/s	39.87%
2	8.4%	560 °C	292.1 °C	250.9 °C	312.0 °C	125.8 kg/s	18.76 kg/s	39.72%
3	10%	560 °C	288.0 °C	241.0 °C	311.0 °C	125.8 kg/s	18.69 kg/s	39.61%
4	15%	560 °C	274.9 °C	205.9 °C	307.4 °C	125.8 kg/s	18.47 kg/s	39.06%
5	20%	560 °C	261.5 °C	169.7 °C	303.7 °C	125.8 kg/s	18.31 kg/s	38.43%
6	25%	560 °C	248.2 °C	133.2 °C	300.0 °C	125.8 kg/s	18.17 kg/s	37.36%

Analyzing the salts mass flow rate and the feedwater mass flow rate, it can be stated that the off-design strategies provide a suitable operational strategy to avoid excessive mass flow rates through the power cycle equipment. Furthermore, the maximum mass flow rates for salts and water occur with the 6.4% extra energy case, and this situation is already being used in Gemasolar. Of course, due to the total closure of three of the steam turbine bleeds, the outlet mass flow rate through the lower pressure turbine increases considerably (up to 33% for the 25% extra energy case when compared to the design case). Unless considered in the design phase of the equipment, the increase of 33% in the steam mass flow rate through the steam turbine low pressure bodies could be unacceptable. For these calculations, no upper limitations in the increase of flow and power in the related equipments (steam turbine, pumps, heat exchangers) have been considered.

Once the operational strategy for operating the Gemasolar power plant has been developed and analyzed, it is possible to calculate the potential extra electricity production of the Gemasolar power plant for a typical year using Eq. (4) to Eq. (11). Of course, it is necessary to obtain the typical meteorological data (mainly hourly DNI radiation) of the plant location. For that purpose, the programme METEONORM has been used [22].

The resulting annual extra energy is 3,722.4 MWh/year with reference to the initial design conditions of the plant (using the design value of $W_{e_design} = 18,735$ MWe for Eq. (9)). In addition, as can be seen in Figure 1, the Gemasolar plant already operates as in the case of Table 1 with up to an extra energy of 6.4%. Thus, if we use the actual maximum of $W_{e_design} = 19,990$ MWe for Eq. (9), it can be seen that an extra electricity production of 1,657.6 MWh/year is still exploitable. For these results, no constraints have been considered regarding grid limitation to the exportation of electricity, in terms of maximum power nor operating hours.

Figure 5 shows how the potential of electricity generation varies when the F factor increases from 0.39 to 0.45. The difference in extra annual electricity might be up to 2,674.9 MWh/year between the two extreme values considered in this parametric study. Note that the study of Figure 5 is based on the use of the actual maximum of $W_{e_design} = 19,990$ MWe for Eq. (9).

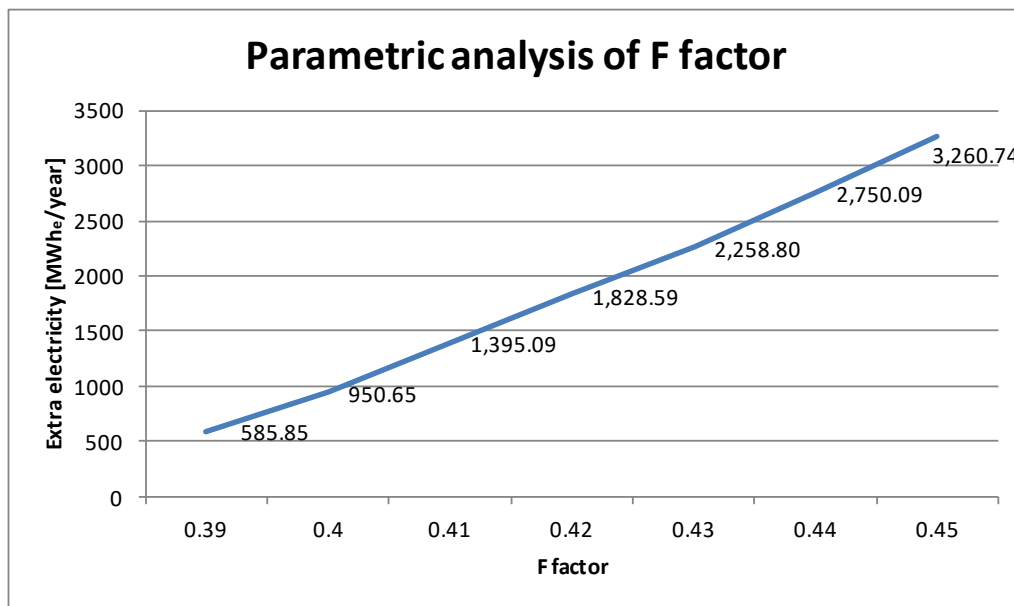


Figure 5- Parametric analysis of the potential annual electricity production regarding the F factor

The parametric study of the potential yearly income due to the exploitation of the available extra solar energy has been done in the range between 50 €/MWh and 200 €/MWh. Figure 6 shows the annual potential income variation (assuming an F factor of 0.416) regarding the possible electricity prices. Note that the study of Figure 6 is also based on the use of the actual maximum of $W_{e_design} = 19,990$ MWe for Eq. (9).

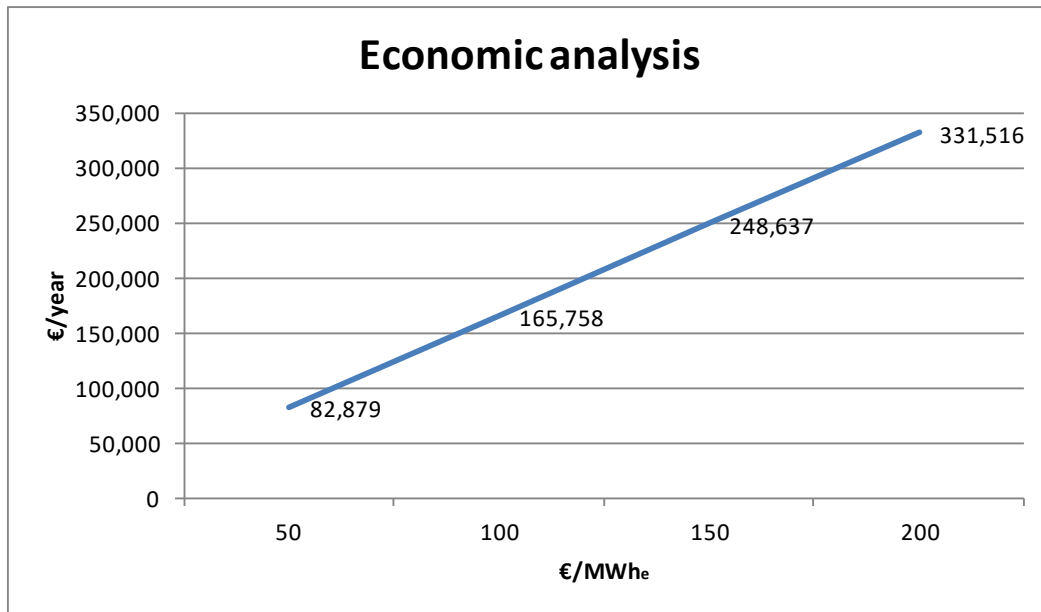


Figure 6- Parametric study of the potential extra income due to the yearly extra electricity production regarding the electricity price

To take advantage of the extra availability of DNI on completely sunny days, it will be necessary to look at the forecast for the next day to know if there will be extra DNI availability or not. It is assumed that, at the end of the day, the hot salts tank is always full. Based on the DNI forecast for the following day, the temperature to which the cold salts tank must be cooled during the night operation will be calculated. This is done because, with the expected DNI for the next day, it could be possible to lower the temperature of the cold salts to a certain temperature below their current design temperature (see Table 3 operation modes), thus increasing electricity production and taking advantage of the next day's extra energy availability.

Thanks to this operation, the next day would start with the cold salts tank with the temperature sufficiently low as to be able to capture 100% of the high DNI day. During the day, the plant will also operate as during the night, producing the cold salts at a lower temperature than the design; thus the plant will be able to take advantage of this extra energy during the day and refill the tank of hot salts at the end of the day up to 560 °C, while still avoiding the saturation of the TES system. If there has been an error with the weather forecast, the plant operation can be adjusted during the day to exploit 100% of the DNI, ending the day with the hot tank completely full of salts at 560 °C.

Summary/Conclusions

This study analyzes the potential of central tower solar power plant with molten salts to exploit the yearly extra available DNI radiation of completely sunny summer days. The case study is based on the existing operating plant Gemasolar using published data. The procedure presented in this article can be extrapolated to any other solar tower power plant. The main conclusions of the study are as follows:

- (1) Thanks to the proposed methodology, it is possible to identify the number of days of a typical year in which the available DNI solar energy is greater than the design DNI solar energy for solar tower plants. The proposed methodology also proposes a power cycle off-design operation strategy to optimally exploit this available extra DNI solar energy. By simulating the power cycle under the proposed strategy, it is possible to obtain the off-design gross electric efficiencies that make it possible to quantify the total potential extra annual electricity production.
- (2) The potential annual extra electricity production for the Gemasolar plant would be about 1,657.6 MWhe/year. This is 1.6% of extra electricity production potential for a power plant that annually generates about 100 GWhe/year. In any case, the extra electricity production is very sensitive to the F factor of the plant, which represents the daily averaged capacity of the plant to transfer the DNI available in the solar field mirrors area to the salts. Using the upper limit of the F factor for the Gemasolar plant, the annual extra electricity production could be as much as 3,260.7 MWhe/year (about 3.3% extra annual electricity production).
- (3) Analyzing the probable costs of the modifications required to apply the proposed operating strategies and the price of the sold extra electricity production, simple payback periods below 5.4 years are obtained for electricity prices of 50€/MWhe. Since all the solar tower plants sell the electricity at over 90€/MWhe, the proposed system seems to be economically interesting.
- (4) The main limitations for the sizing and profitability of this concept in an existing plant like Gemasolar come from the individual limitations of the existing equipment involved in this new operating mode (steam turbine, generator, salts pumps...). For the numerical calculations in the specific analysis of the Gemasolar plant, certain, reasonable assumptions have been made about the overcapacity of the equipment with respect to their nominal operating point. Obviously, for a new plant, this operating mode should be foreseen at the design phase and the equipment involved sized accordingly.

Acknowledgements

This work has been carried out in collaboration with the Engineering company 'SENER Ingeniería y Sistemas' under the direction of Dr. Erkoreka and Dr. Gómez-Arriaran, both of them professors of the Thermal Engineering Department of the Faculty of Engineering of Bilbao, and also under the direction of Borja Herrazti, engineer of the Department of Mechanical Engineering of SENER.

References:

- [1] B. Lin, J. Zhu, The role of renewable energy technological innovation on climate change: Empirical evidence from China, *Science of The Total Environment* 659 (2019) 1505-1512.
- [2] K. Chang, Emissions reduction targets and wealth distribution effects through interprovincial emissions trading scheme in China, *Energy Procedia* 159 (2019) 539-544.

- [3] H. Holmberg, S. Siitonen, T. Laukkanen, M. Tuomaala, T. Niskanen, Comparison of Indirect CO₂-emissions of Different Renewable Transport Fuels, *Energy Procedia* 72 (2015) 19-26.
- [4] F. Wang, S. Deng, J. Zhao, J. Zhao, G. Yang, J. Yan, Integrating geothermal into coal-fired power plant with carbon capture: A comparative study with solar energy, *Energy Conversion and Management* 148 (2017) 569-582.
- [5] B. Sweerts, F.D. Longa, B. van der Zwaan, Financial de-risking to unlock Africa's renewable energy potential, *Renewable and Sustainable Energy Reviews* 102 (2019) 75-82.
- [6] J.M. Alemany, B. Arendarski, P. Lombardi, P. Komarnicki, Accentuating the renewable energy exploitation: Evaluation of flexibility options, *International Journal of Electrical Power & Energy Systems* 102 (2018) 131-151.
- [7] A. Iranzo, C. Suárez, J. Guerra, Mixing enhancement in thermal energy storage molten salt tanks, *Energy Conversion and Management* 168 (2018) 320-328.
- [8] W. Pu, N. Yang, C. Yue, S. Bai, Y. Chen, Simulation on direct contact heat transfer in gas-molten salt bubble column for high temperature solar thermal storage, *International Communications in Heat and Mass Transfer* 104 (2019) 51-59.
- [9] Santos, José J. C. S., J.C.E. Palacio, A.M.M. Reyes, M. Carvalho, A.J.R. Freire, M.A. Barone, Chapter 12 - Concentrating Solar Power, *Advances in Renewable Energies and Power Technologies* (2018) 373-402.
- [10] O. Behar, A. Khellaf, K. Mohammedi, A review of studies on central receiver solar thermal power plants, *Renewable and Sustainable Energy Reviews* 23 (2013) 12-39.
- [11] J.A. Aguilar-Jiménez, N. Velázquez, A. Acuña, R. Cota, E. González, L. González, R. López, S. Islas, Techno-economic analysis of a hybrid PV-CSP system with thermal energy storage applied to isolated microgrids, *Solar Energy* 174 (2018) 55-65.
- [12] C. Parrado, A. Marzo, E. Fuentealba, A.G. Fernández, 2050 LCOE improvement using new molten salts for thermal energy storage in CSP plants, *Renewable and Sustainable Energy Reviews* 57 (2016) 505-514.
- [13] C. Silinga, P. Gauché, Scenarios for a South African CSP Peaking System in the Short Term, *Energy Procedia* 49 (2014) 1543-1552.
- [14] M.C. Kotti, A.A. Argiriou, A. Kazantzidis, Estimation of direct normal irradiance from measured global and corrected diffuse horizontal irradiance, *Energy* 70 (2014) 382-392.
- [15] O. Behar, A. Khellaf, K. Mohammedi, Comparison of solar radiation models and their validation under Algerian climate – The case of direct irradiance, *Energy Conversion and Management* 98 (2015) 236-251.
- [16] S. Moreno-Tejera, M.A. Silva-Pérez, L. Ramírez-Santigosa, I. Lillo-Bravo, Classification of days according to DNI profiles using clustering techniques, *Solar Energy* 146 (2017) 319-333.
- [17] J. Alonso-Montesinos, J. Polo, J. Ballestrín, F.J. Batlles, C. Portillo, Impact of DNI forecasting on CSP tower plant power production, *Renewable Energy* 138 (2019) 368-377.
- [18] S. Benammar, A. Khellaf, K. Mohammedi, Contribution to the modeling and simulation of solar power tower plants using energy analysis, *Energy Conversion and Management* 78 (2014) 923-930.
- [19] E. García, R. Calvo, One year operation experience of Gemasolar plant, *Solar Paces* (2012).
- [20] S. Relloso, E. García, Tower Technology Cost Reduction Approach after Gemasolar Experience, *Energy Procedia* 69 (2015) 1660-1666.
- [21] Thermoflow Inc. Thermoflex 27.
- [33] Meteotest. Meteonorm 7 V1.11.24422.

Modelling of a Food Processing Plant for Industrial Demand Side Management

P. Wohlgenannt^{1,2}, G. Huber¹, K. Rheinberger¹, M. Preißinger¹, P. Kepplinger^{1*}

¹Josef Ressel Centre for Intelligent Thermal Energy Systems, Villwerke vkw Endowed Professorship for Energy Efficiency, Research Center Energy, Vorarlberg University of Applied Sciences, Hochschulstrasse 1, 6850 Dornbirn, Austria

²Faculty of Engineering and Science, University of Agder, 4879 Grimstad, Norway

*Corresponding author: peter.kepplinger@fhv.at

Abstract

Industrial demand side management has shown significant potential to increase the efficiency of industrial energy systems via flexibility management by model-driven optimization methods. We propose a grey-box model of an industrial food processing plant. The model relies on physical and process knowledge and mass and energy balances. The model parameters are estimated using a predictive error method. Optimization methods are applied to separately reduce the total energy consumption, total energy costs and the peak electricity demand of the plant. A viable potential for demand side management in the plant is identified by increasing the energy efficiency, shifting cooling power to low price periods or by peak load reduction.

Keywords: Grey-box Model, Processed Food Plant, Industrial Demand Side Management, Intelligent Thermal Energy System

Nomenclature

Physical Quantities

α	absorptance
\dot{m}	mass flow rate (kg/s)
\dot{Q}	heat transfer rate (W)
η	thermal efficiency
ε	coefficient of performance
ξ	mass flow ratio
C	thermal capacity (J/K)
c	specific thermal capacity (J/(kg K))
h	specific enthalpy (J/kg)
k	overall heat transfer coefficient (W/K)
P	power (W)
p	pressure (bar)
T	temperature (K)
t	time (s)

Further Symbols

π	price function (€/kWh)
N	number of differential equations
N_P	number of process steps
N_T	number of time steps

Subscripts and Abbreviations

∞	ambient
----------	---------

B	building envelope
B2 ∞	building envelope to ambient
B2P	building envelope to production hall
C	chiller
El	electric
end	end value
F	feed water tank
G	gas
H,C	cooling hall
H,P	production hall
i	discrete time step index
P	product
P2C	production hall to cooling hall
S	steam
S,B	boiler steam
S,E	exhaust vapour
S,F	feed water tank steam
S,H,P	production hall steam
S,P	product steam
W,F	feed water
W,O	osmosis water
W,R	raw water
W,S	softened water

Introduction and Background

Demand side management (DSM) is a promising approach to increase energy system efficiency and to enable the integration of renewable energies into the existing power grid [1]. To reach the full potential of DSM, application in all three consumer sectors is necessary: residential, commercial and industrial. So far, researchers have focused on the residential and the commercial sector [2]. Four main challenges of industrial DSM were identified by Zhang and Grossmann [3]: 1) accurate modelling of operational flexibility; 2) integration of production and energy management; 3) optimization across multiple time scales; 4) decision making under uncertainty.

For the realization of DSM, thermal energy storages are showing a high potential with the ability to shift electric loads from high demand to low demand hours [4, 5, 6]. Arteconi and Polonara [7] reviewed demand side management in refrigeration applications. Different DSM categories (energy efficiency, energy storage and demand response) are discussed and the potential of DSM with chillers and heat pumps in combination with active or passive energy storages is shown.

Shafiei et al. [8] proposed a non-linear model of a supermarket refrigeration system for DSM. They focused on estimating the power consumption of the chillers while estimating the cold reservoirs as well. As DSM method, direct load control is used.

Mueller et al. [9] modelled a set of large industrial freezer warehouse units to act as flexible loads in a smart grid setting. As DSM method, power reference tracking is used. Disturbances like the weather were neglected. The chillers were controlled via temperature set points, a direct compressor control was not implemented. The authors successfully have shown that large freezer systems can be used as flexible loads.

Kepplinger et al. [10] presented an overview of different DSM approaches. Autonomous demand side management methods were applied to different areas such as electric vehicle charging, battery storage systems or domestic hot water storages. In [11], Kepplinger et al. proposed a grey-box modelling approach based on energy and mass balances for thermal systems and DSM methods for optimal predictive control.

We contribute to the first main challenge by proposing a grey-box model of a real industrial plant to serve as the basis for DSM algorithms. In contrast to the papers mentioned above, we present a model of a real processed food plant including the food production process and the refrigeration systems. A linear temperature model is set up such that the effect of controlling the electric power of both chillers can be simulated, making the model well suited for optimization and DSM methods. As only limited data of this system is available via data acquisition, simplifications are made and a grey-box modelling approach is applied. Using methods from Kepplinger et al. [11], the system is described via energy balances, and the parameters are estimated using a predictive error method. As proof of concept, optimal predictive control of the chillers under three DSM scenarios is evaluated: 1) minimization of the total energy consumption; 2) minimization of the total energy costs under real-time pricing; 3) peak load reduction.

Methods

Figure 1 shows a simplified sketch of the plant. The building is divided into three subparts, the production hall, the cooling hall and the thermal mass of the building envelope. The system temperatures are depended on the heat loss of these production lines, the outside temperature, the radiation of the sun and the extracted heat by the two chillers. The first chiller is used for

cooling the production hall and the second one is used for cooling the product in the cooling hall. In this chapter, the production process is first described. Next, the models of the steam boiler and the chillers are described, which serve as inputs for the thermal model. Finally, the analytical solution of the energy balances of the thermal model is used to formulate different optimization-based DSM strategies.

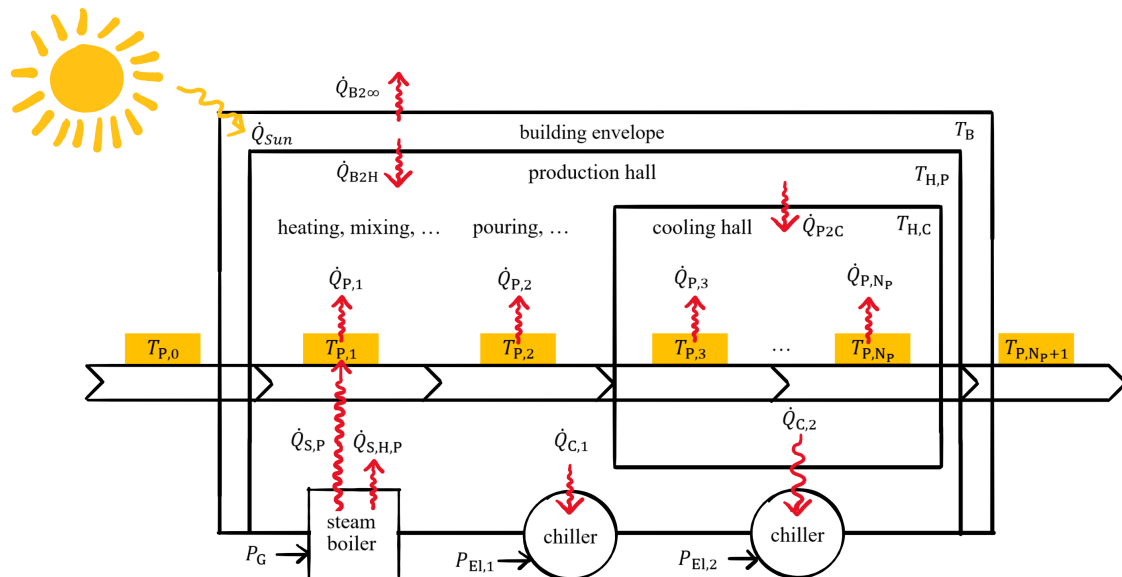


Figure 1. Processed food plant.

The production of processed food is described in detail elsewhere [12, 13, 14]. Here, this batch process is simplified into three different stages: 1) steam ($\dot{Q}_{S,P}$) heats the product to approximately 90 °C (range: 70-130 °C) and served ingredients are mixed in; 2) the fluid product is poured into molds and transported to the cooling room while it cools down; 3) the product is cooled down to approximately 5 °C for storing.

A steam boiler plant provides the steam needed. Figure 2 shows the main components and mass flows in the steam generation system. Only the freshwater ($\dot{m}_{W,R}$) and the steam produced by the boiler ($\dot{m}_{S,B}$) are known by measurement. Therefore a model of the steam generation system is created to estimate the steam \dot{m}_S , which is available for production. Due to the direct steam heating of the product, the amount of condensate can be assumed to be negligible as most of the steam is generated from freshwater. First, the freshwater is filtered with a reverse osmosis system, next, Ca^{++} and Mg^{++} ions are filtered out of the remaining permeate ($\dot{m}_{W,O}$). Then softened water ($\dot{m}_{W,S}$) can be used for steam generation. In a feed water tank, the softened water is heated up from $T_{W,S}=12$ °C to $T_F=105$ °C to achieve full degassing of O_2 and CO_2 . Exhaust vapour ($\dot{m}_{S,E}$) is released to the surroundings. The steam boiler heats the feed water ($\dot{m}_{W,F}$) to $T_B=175$ °C and $p_B=9$ bar with natural gas (\dot{Q}_G). A part of the feed water is used for desalination and blowdown. The resulting steam ($\dot{m}_{S,B}$) is in part used for the heating of the feed water tank ($\dot{m}_{S,F}$), and mostly for production (\dot{m}_S).

The feed water tank is assumed to be in steady-state conditions, i.e. $\dot{m}_{S,E}$ being constant. Enthalpies for the states of the fluid, i.e. $h_{W,S}$, $h_{W,F}$ and h_S , are taken from literature [15]. All

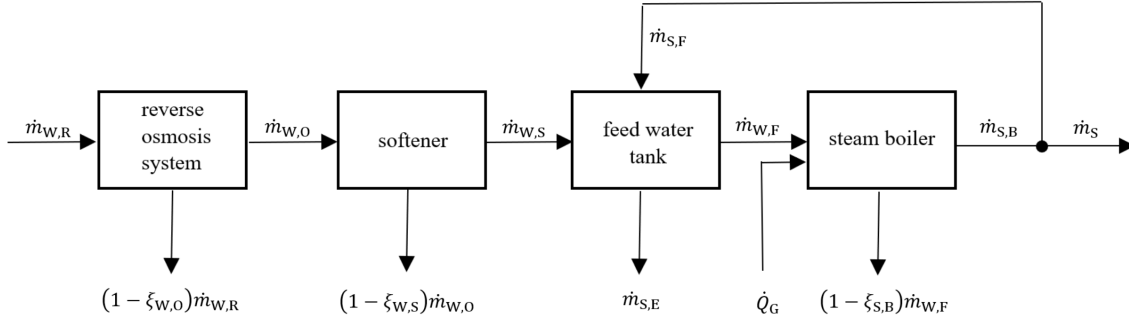


Figure 2. Steam generation system.

mass flows can then be derived from \dot{m}_s using mass and energy balances as follows:

$$\dot{m}_{w,o} = \dot{m}_{w,R}\xi_{w,o} \quad (1)$$

$$\dot{m}_{w,s} = \dot{m}_{w,o}\xi_{w,s} \quad (2)$$

$$\dot{m}_{w,F} + \dot{m}_{s,E} = \dot{m}_{w,s} + \dot{m}_{s,F} \quad (3)$$

$$\dot{m}_{s,B} = \dot{m}_{w,F}\xi_{s,B} \quad (4)$$

$$\dot{m}_{s,B} = \dot{m}_s + \dot{m}_{s,F} \quad (5)$$

$$\dot{m}_{w,F}h_{w,F} + \dot{m}_{s,E}h_{s,E} = \dot{m}_{w,s}h_{w,s} + \dot{m}_{s,F}h_s \quad (6)$$

$$\dot{m}_{w,F}h_{w,F} + \dot{Q}_G = \dot{m}_{s,B}h_s \quad (7)$$

$$\dot{Q}_G = \eta P_G \quad (8)$$

During times of no production, i.e. $\dot{m}_s = 0$, $\dot{m}_{s,E}$ can be calculated. Typical values for $\xi_{w,o}$, $\xi_{w,s}$ and $\xi_{s,B}$ and the thermal efficiency η of a steam boiler are provided in literature [16]. Using \dot{m}_s , the heat flow available for production (\dot{Q}_s), the heat flow of the steam to the product ($\dot{Q}_{s,P}$) and the heat flow of the steam to the production hall ($\dot{Q}_{s,H,P}$) can be calculated by

$$\dot{Q}_s = \dot{m}_sh_s, \quad (9)$$

$$\dot{Q}_{s,P} = \dot{Q}_s\xi_{s,P}, \text{ and} \quad (10)$$

$$\dot{Q}_{s,H,P} = \dot{Q}_s\xi_{s,H,P}, \text{ where} \quad (11)$$

$$0 \leq \xi_{s,P} + \xi_{s,H,P} \leq 1, \quad (12)$$

$$0 \leq \xi_{s,P} \leq 1, \text{ and} \quad (13)$$

$$0 \leq \xi_{s,H,P} \leq 1. \quad (14)$$

Knowing the temperature of the product before and after heating, $\xi_{s,P}$ can be estimated. $\xi_{s,P}$ and $\xi_{s,H,P}$ sum up to less than 100 %, because the excess steam is used to heat offices via a thermal storage.

The cooling power of the chillers is calculated by using the linearized coefficients of performance (COPs) ε_1 and ε_2 :

$$\dot{Q}_{C,1} = P_{El,1}\varepsilon_1 \quad (15)$$

$$\dot{Q}_{C,2} = P_{El,2}\varepsilon_2 \quad (16)$$

$$\varepsilon_1(T_\infty) = a_1T_\infty + b_1 \quad (17)$$

$$\varepsilon_2(T_\infty) = a_2T_\infty + b_2 \quad (18)$$

The influence of the sun is modelled via the absorbed radiation of the sun ($\alpha\dot{Q}_{\text{Sun}}$) which heats the thermal capacity of the building envelope. The heat transfer rates from the building envelope to production hall and the surroundings are modelled via a single heat transfer coefficient to reflect convection.

Combing this, the energy balances for Figure 1 can be written as:

$$\dot{T}_{\text{B}}(t) = \frac{1}{C_{\text{B}}} \left[\alpha\dot{Q}_{\text{Sun}}(t) + k_{\text{B}2\infty}(T_{\infty}(t) - T_{\text{B}}(t)) + k_{\text{B}2\text{P}}(T_{\text{H,P}}(t) - T_{\text{B}}(t)) \right] \quad (19)$$

$$\begin{aligned} \dot{T}_{\text{H,P}}(t) = & \frac{1}{C_{\text{H,P}}} \left[\dot{Q}_{\text{S,H,P}}(t) - \dot{Q}_{\text{C},1}(t) + k_{\text{B}2\text{P}}(T_{\text{B}}(t) - T_{\text{H,P}}(t)) + k_{\text{P}2\text{C}}(T_{\text{H,C}}(t) - T_{\text{H,P}}(t)) \right. \\ & \left. + \sum_{n=1}^2 k_{\text{P},n}(T_{\text{P},n}(t) - T_{\text{H,P}}(t)) \right] \end{aligned} \quad (20)$$

$$\dot{T}_{\text{H,C}}(t) = \frac{1}{C_{\text{H,C}}} \left[-\dot{Q}_{\text{C},2}(t) + k_{\text{P}2\text{C}}(T_{\text{H,P}}(t) - T_{\text{H,C}}(t)) + \sum_{n=3}^{\text{N}_{\text{P}}} k_{\text{P},n}(T_{\text{P},n}(t) - T_{\text{H,P}}(t)) \right] \quad (21)$$

$$\dot{T}_{\text{P},n}(t) = \begin{cases} \frac{1}{C_{\text{P},n}} \left[\dot{Q}_{\text{S,P}}(t) + k_{\text{P},n}(T_{\text{H,P}}(t) - T_{\text{P},n}(t)) \right], & n = 1 \\ \frac{1}{C_{\text{P},n}} k_{\text{P},n}(T_{\text{H,P}}(t) - T_{\text{P},n}(t)), & n = 2 \\ \frac{1}{C_{\text{P},n}} k_{\text{P},n}(T_{\text{H,C}}(t) - T_{\text{P},n}(t)), & 3 \leq n \leq \text{N}_{\text{P}} \end{cases} \quad (22)$$

Assuming $\dot{Q}_{\text{Sun}}(t)$, $\dot{Q}_{\text{C},1}(t)$, $\dot{Q}_{\text{C},2}(t)$, $\dot{Q}_{\text{S,H,P}}(t)$, $\dot{Q}_{\text{S,P}}(t)$ and $T_{\infty}(t)$ to be constant in each time interval of the batch process, this defines a system of first-order inhomogeneous linear differential equations with constant coefficients:

$$\dot{\mathbf{T}}(t) = \mathbf{A} \cdot \mathbf{T}(t) + \mathbf{b} \quad (23)$$

$$\forall t \in [t_i, t_{i+1}] \quad (24)$$

This system of differential equations can be solved using the eigenvectors \mathbf{v}_n and the eigenvalues λ_n of the matrix \mathbf{A} , expressing $\mathbf{T}(t)$ by coefficient functions $f_n(t)$ and by coefficients g_n ,

$$\mathbf{T}(t) = \sum_{n=1}^N f_n(t) \mathbf{v}_n \text{ and} \quad (25)$$

$$\mathbf{b} = \sum_{n=1}^N g_n \mathbf{v}_n. \quad (26)$$

The solution for this system of equations is given by

$$f_n(t) = f_n(0)e^{\lambda_n t} - \frac{g_n}{\lambda_n}(1 - e^{\lambda_n t}). \quad (27)$$

This analytical solution allows for the calculation of the system dynamics forward in time for a single time interval and can be discretized assuming piecewise constant parameters on N_{T} intervals of duration Δt . The discretized model is used as the basis for the parameter estimation via a prediction error method and the formulation of the optimization problems.

Assuming that the production hall and the cooling hall are controlled via P-controllers, the parameters of the model are estimated by minimizing the quadratic error of the measured and the simulated cooling powers.

Optimal chiller control can be achieved by solving a linear optimization problem. Assuming the price function π and the uncertainties (steam, mass flow of the product, radiation of the sun and outside temperature) to be perfectly known in advance, the optimization problem, which minimizes the total costs for cooling, can be formulated as follows, keeping the production hall and the cooling hall temperature in a set temperature band:

$$\min_{P_{\text{El},1}, P_{\text{El},2}} \sum_{i=1}^{N_T} (P_{\text{El},1}^{(i)} + P_{\text{El},2}^{(i)}) \pi^{(i)} \quad (28)$$

$$\text{s.t. } \forall i \in [1, \dots, N_T] : \quad (29)$$

$$\dot{\mathbf{T}}^{(i)}(t) = \mathbf{A}^{(i)} \cdot \mathbf{T}^{(i)}(t) + \mathbf{b}^{(i)} \quad (30)$$

$$0 \leq P_{\text{El},1}^{(i)} \epsilon_1 \leq \dot{Q}_{\text{max},1} \quad (31)$$

$$0 \leq P_{\text{El},2}^{(i)} \epsilon_2 \leq \dot{Q}_{\text{max},2} \quad (32)$$

$$T_{\text{H,P,min}} \leq T_{\text{H,P}}^{(i)} \leq T_{\text{H,P,max}} \quad (33)$$

$$T_{\text{H,C,min}} \leq T_{\text{H,C}}^{(i)} \leq T_{\text{H,C,max}} \quad (34)$$

$$T_{\text{H,P}}^{(N_T)} = T_{\text{H,P,end}} \quad (35)$$

$$T_{\text{H,C}}^{(N_T)} = T_{\text{H,C,end}} \quad (36)$$

Using a constant price $\pi = 1$, the energy minimization problem is solved fulfilling the same constraints (29-36),

$$\min_{P_{\text{El},1}, P_{\text{El},2}} \sum_{i=1}^{N_T} (P_{\text{El},1}^{(i)} + P_{\text{El},2}^{(i)}). \quad (37)$$

To solve the peak load reduction problem, using the same constraints (29-36), the following objective function is defined,

$$\min_{P_{\text{El},1}, P_{\text{El},2}} \max_i P_{\text{El},1}^{(i)} + P_{\text{El},2}^{(i)}. \quad (38)$$

The objective function (38) can be linearized by introducing auxiliary variables.

Results and Discussion

Only limited data from the real factory is available. The electric power consumption of both chillers, the COP of one chiller, the mass flows \dot{m}_W and \dot{m}_S , the states (temperature or pressure) of the steam boiler systems and the production quantity per day are known. For the outside temperature and the direct radiation of the sun, data from a weather station nearby is used [17].

Table 2 shows the steam boiler parameters estimated.

$\xi_{W,O}$	$\xi_{W,S}$	$\xi_{S,B}$
0.75	0.97	0.90

Table 1. Estimated steam boiler parameters.

The COP of the first chiller is fitted with linear regression from measured data and the COP of the second chiller is calculated using its datasheet [18]. Both are linearized around the operation temperature set point of 20°C.

	a	b
chiller 1	-0.10000	33.6150
chiller 2	-0.03723	14.7674

Table 2. Estimated chiller parameters.

Using equations (1-8), all heat and mass flows of the steam boiler are calculated from $\dot{m}_{S,B}$, as shown in the left subplot of Figure 3. For better visibility, the data is filtered by applying a moving average filter (window length 3.75 h for $\dot{m}_{S,B}$ and 7.5 h for $\dot{m}_{W,R}$). $\dot{m}_{S,B}$ denotes the measured boiler steam. \dot{m}_S can be used for production and $\dot{m}_{S,F}$ is lead back to supply the feed water tank. The model is validated by comparing the calculated quantity of freshwater to the recorded values as shown in the right subplot of Figure 3 and resulting in a root mean square error of 0.12 kg/s.

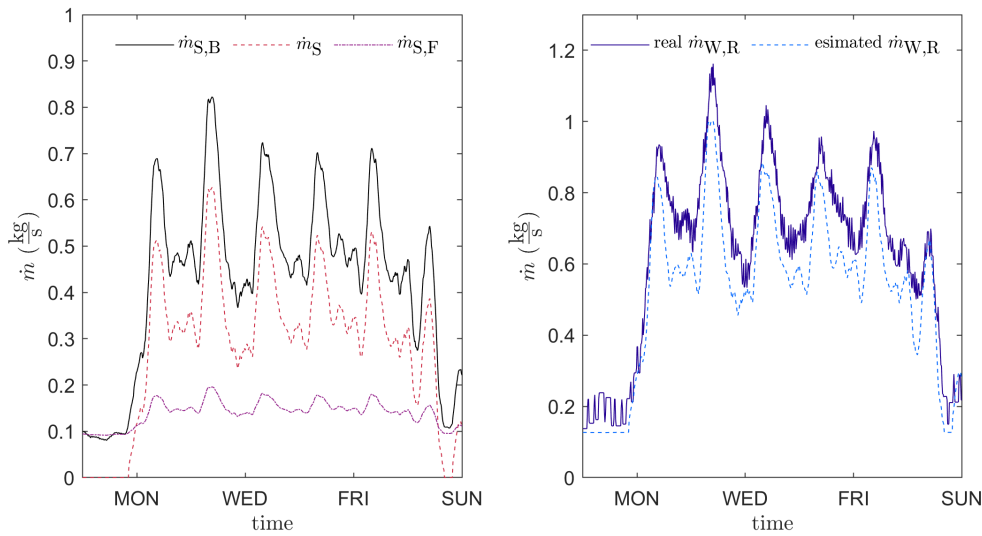


Figure 3. Mass flows of the generated steam, comparison of the estimated and the measured freshwater.

The data is preprocessed to create a single week dataset consisting of average weekdays and average weekends. This data is used to determine the model parameters and the DSM potential. The product mass flow is estimated from the mass flow of the steam, assuming a direct proportion.

The model parameter identification is done using Matlab's [19] *lsqcurvefit* routine. The value of the specific thermal heat coefficient of the product is taken from literature [20]. First the heat transfer coefficients of the product ($k_{P,n}$) and the production steam rate $\xi_{S,P}$ are fitted such that the heating and cooling time of the product fit measurements. Then, the remaining heat transfer coefficients and thermal capacities from Table 3 are fitted by minimizing the quadratic errors of both chiller powers. The sun has a delayed effect on the system, which is accounted for by the thermal capacity of the building envelope C_B . Given temperature bands for the production and the cooling hall, both flexibilities can roughly be estimated using the thermal capacities $C_{H,P}$ and $C_{H,C}$. As time interval $\Delta t=30$ min and as process step number $N_P=18$ are chosen resulting in a total process time of 9 hours for producing (1 h) and cooling (8 h) for a batch of product and up to 18 possible parallel processes, which are time-shifted by multiples of Δt .

The control of the chillers is simulated with two P-controllers. Figure 4 compares the simulated

parameter	value
$C_{H,P}$	$3.9 \cdot 10^8 \frac{J}{K}$
$C_{H,C}$	$9.6 \cdot 10^7 \frac{J}{K}$
C_B	$1.6 \cdot 10^9 \frac{J}{K}$
$c_{P,n}$	$3270 \frac{J}{kg K}$
$k_{B2\infty}$	$1.3 \cdot 10^4 \frac{W}{K}$
k_{B2P}	$1.3 \cdot 10^4 \frac{W}{K}$
k_{P2C}	$3.0 \cdot 10^3 \frac{W}{K}$
$k_{P,n}$	$0.35 \frac{W}{kg K} \cdot m_{P,n}$
α	0.98
$\xi_{S,P}$	0.35
$\xi_{S,H,P}$	0.05

Table 3. Estimated model parameters.

to the real cooling powers and shows the temperature profile of the production hall and the cooling hall. Figure 5 shows the temperature of a batch of product during the process.

Three different DSM algorithms are applied to the model: 1) an energy-efficient strategy minimizes the total electric power consumption by shifting cooling power to increase the system efficiency 2) a real-time pricing (RTP) strategy minimizes the costs of the electric power by shifting cooling power to low price periods; 3) a peak load reduction strategy minimizes the peak electricity demand. For RTP, the EXAA spot market price [21] is used. The temperature band for the production hall and the cooling hall are chosen to be [15°C, 25°C] and [-6°C, 4°C], respectively. The optimization problems are solved using Matlab's [19] *fmincon* routine for a simulation period of one week. The computations last approximately two days on a laptop with an Intel Core i5 10th Gen. processor.

Table 4 and Figure 6 show the optimal predictive control of the chillers during the different operation modes simulated. As expected, during the energy-efficient mode the temperatures are near the upper boundary to reduce the needed cooling power. Shifting of the cooling power to high chiller efficiency periods during the night can not be observed, because this would have decreased the system efficiency due to the lower temperatures and thereby increased heat flows to the surroundings. The energy reduction also results in a cost reduction. The RTP-driven operation mode reduces the costs by shifting cooling power to low price periods during the night and avoiding price peaks during the day. The costs for the first chiller are reduced by 17 % and the costs of the second chiller are reduced by 10 %. The higher cost reduction achieved by the production hall chiller is due to the high thermal capacity of the production hall. The amount of precooling in the cooling hall is often limited by the cooling hall capacity, as can be seen in the temperature profile when the temperature reaches the lower limit. Due to the better coefficient of performance of the chillers during the night, this mode also reduces the total energy consumption. Finally, a peak load reduction of 21 % is achieved by precooling during the night.

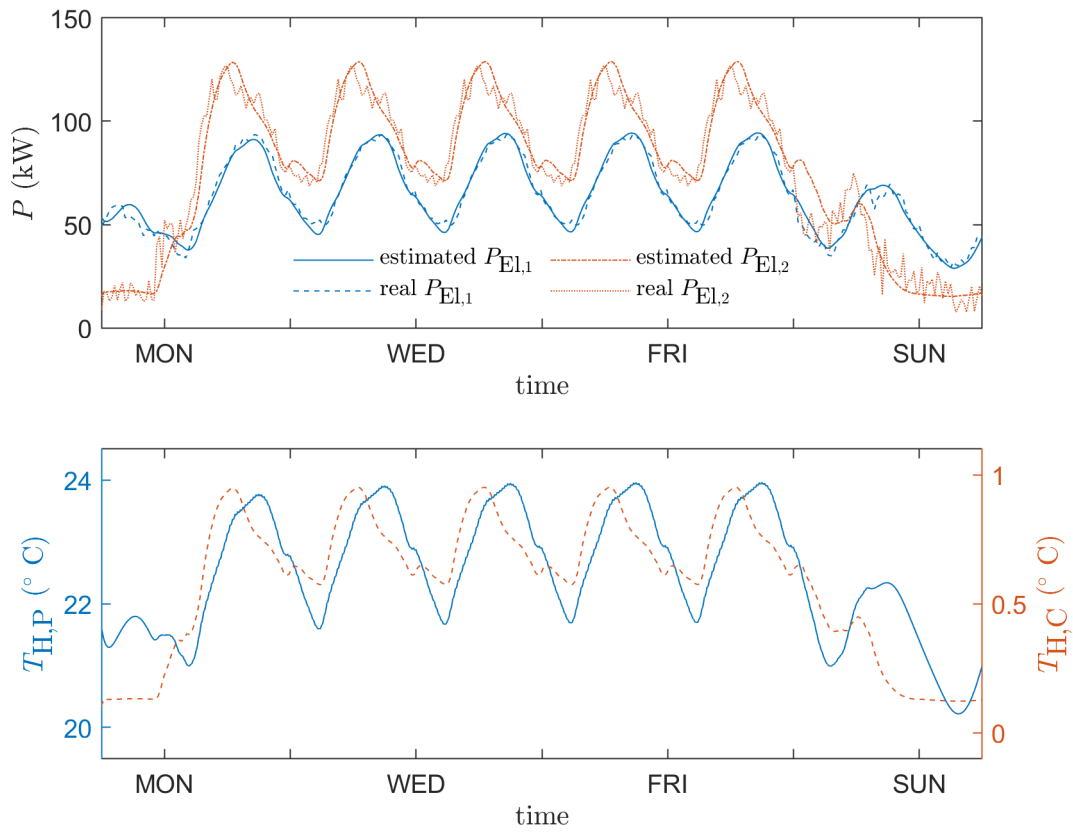


Figure 4. Comparison of the estimated and measured cooling powers (top), temperature profiles of the production hall and the cooling hall (bottom).

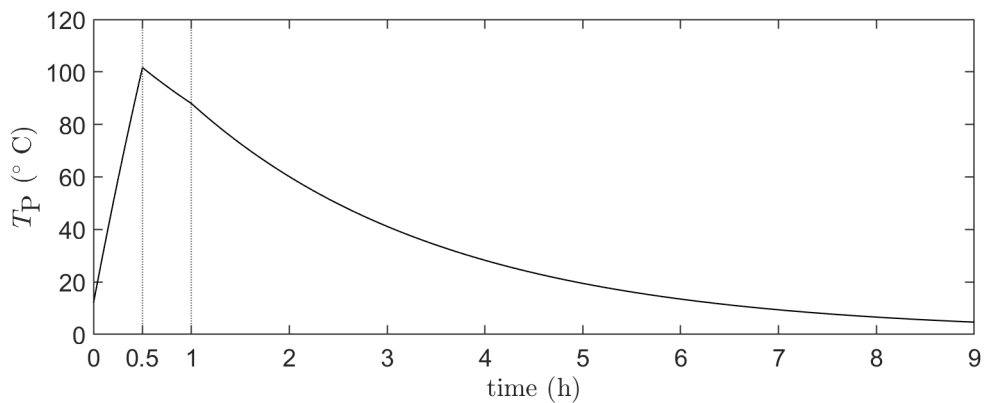


Figure 5. Temperature profile of product during the batch process. The vertical lines indicate the different steps during the batch process, starting with the heating and mixing, next the pouring, and, finally, the cooling.

operation mode	reference	energy-efficient DSM	RTP-driven DSM	peak load reduction
total	23.74 MWh	22.71 MWh	23.42 MWh	23.90 MWh
energy per week	10.77 MWh	10.19 MWh	10.65 MWh	11.32 MWh
chiller 1	12.96 MWh	12.52 MWh	12.77 MWh	12.58 MWh
chiller 2	773 €	743 €	668 €	785 €
total	343 €	328 €	283 €	370 €
chiller 1	430 €	415 €	386 €	415 €
chiller 2	217 kW	216 kW	271 kW	171 kW
total				

Table 4. Optimization results for one simulated week.

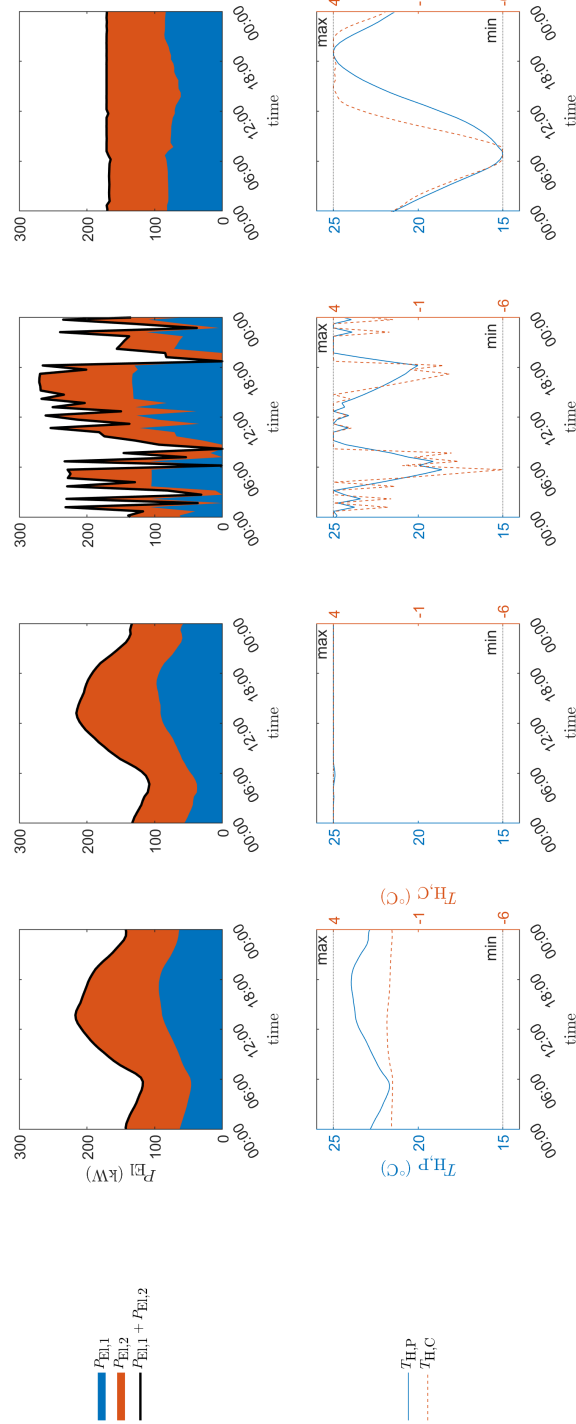


Figure 6. Optimization results for one simulated week, showing the electric power consumption of the two chillers (top) and the production and cooling hall temperatures (bottom). Form left to right: reference case, energy-efficient DSM, RTP-driven DSM, and peak load reduction.

Conclusion and Outlook

A grey-box model of a real industrial food processing plant has been created, whose model parameters were identified by a predictive error method. The method proposed solved the first main challenge of industrial DSM by providing a suitable model. The model was used for optimization-based DSM in a simulation study of one week using Matlab. Austrian day-ahead prices were used for an RTP-driven optimization showing a cost reduction of 14 %. An energy-efficient strategy was able to reduce the energy consumption by 4 % by increasing the temperature to the upper boundary of the allowed range. The peak load could be reduced by 21 % by precooling during the night. Based on the promising DSM potential, future measurements should be established to improve the quality of the estimation of the system dynamics. In further work, this model can be used as the basis for more efficient optimization methods and should deal with challenges like optimization across multiple time scales and decision making under uncertainty.

Acknowledgements

The financial support by the Austrian Federal Ministry for Digital and Economic Affairs and the National Foundation for Research, Technology and Development and the Christian Doppler Research Association is gratefully acknowledged.

References

- [1] P. Palensky and D. Dietrich. Demand side management: Demand response, intelligent energy systems, and smart loads. *Transactions in Industrial Informatics*, 7:381–388, 2011.
- [2] M. Shafie-khah and P. Siano. Comprehensive review of the recent advances in industrial and commercial dr. *Transactions in Industrial Informatics*, 15:3757–3771, 2019.
- [3] Q. Zhang and I. E. Grossmann. Planning and scheduling for industrial demand side management: Advances and challenges. *Alternative Energy Sources and Technologies: Process Design and Operation*, pages 383–414, 2016.
- [4] A. Arteconi et al. State of the art of thermal storage for demand-side management. *Applied Energy*, 93:371–389, 2012.
- [5] V. V. Tyagi and D. Buddhi. PCM thermal storage in buildings: A state of art. *Renewable and Sustainable Energy Reviews*, 11(6):1146–1166.
- [6] B. Alimohammadisagvand et al. Cost-optimal thermal energy storage system for a residential building with heat pump heating and demand response control. *Applied Energy*, 174:275–287, 2016.
- [7] A. Arteconi and F. Polonra. Demand side management in refrigeration applications. *International Journal of Heat and Technology*, 35:58–63, 2017.
- [8] S. Shafiei et al. Modeling supermarket refrigeration systems for demand-side management. *Energies*, 6(2):900–920, 2013.
- [9] F. L. Mueller et al. Power reference tracking of a large-scale industrial freezer system for ancillary service delivery. In *Innovative Smart Grid Technologies Europe (ISGT EUROPE), 2013 4th IEEE/PES*.
- [10] P. Kepplinger et al. Autonomes demand side management verteilter energiespeicher. *e & i Elektrotechnik und Informationstechnik*, 2019.
- [11] P. Kepplinger et al. Active demand side management with domestic hot water heaters using binary integer programming. In *e-nova*, volume 17, 2013.
- [12] R. Kapoor and L. Metzger. Process cheese: Scientific and technological aspects - a review. *Comprehensive Reviews in Food Science and Food Safety*, 7:194–214, 2008.

- [13] R. Heiss. *Lebensmitteltechnologie - Biotechnologische, chemische, mechanische und thermische Verfahren der Lebensmittelaufbereitung*. Springer-Verlag, Berlin, GER, 4.ed edition, 1991.
- [14] Y. Edelby. *Strukturierungsmechanismen bei der Herstellung von Analog- und Schmelzkäse*. PhD thesis, Technische Universität Berlin, Berlin, GER, 2014.
- [15] M. Moran et al. *Fundamentals of engineering thermodynamics*. John Wiley & Sons, Inc, seventh edition edition.
- [16] *Planungshandbuch Dampfkessel*. Viessmann Group, Allendorf, GER.
- [17] CDC, CDC - Climate Data Center Austria. <https://cdc.dwd.de/portal/>. [Online; accessed 10-Nov-2020].
- [18] *Climaveneta - air cooled liquid chillers*. Climaveneta S.p.A., Italy, 2006.
- [19] Matlab Release 2020a. The Mathworks, Inc., Natick, MA.
- [20] A. Pajonk et al. Heat transfer study and modeling during emmental ripening. *Journal of Food Engineering*, 57:249–255, 2003.
- [21] EXAA, EXAA - Energy Exchange Austria. <https://www.apg.at>. [Online; accessed 5-May-2021].

A Cloud-Based Flexibility Estimation Method for Domestic Heat Pumps

C. Baumann¹, G. Huber¹, M. Preißinger¹, and P. Kepplinger^{1*}

¹Josef Ressel Centre for Intelligent Thermal Energy Systems,
Illwerke vkw Endowed Professorship for Energy Efficiency, Research Center Energy,
Vorarlberg University of Applied Sciences, Hochschulstrasse 1, 6850 Dornbirn, Austria

*Corresponding author: peter.kepplinger@fhv.at

Abstract

Flexibility estimation is the first step necessary to incorporate building energy systems into demand side management programs. We extend a known method for temporal flexibility estimation from literature to a real-world residential heat pump system, solely based on historical cloud data. The method proposed relies on robust simplifications and estimates employing process knowledge, energy balances and manufacturer's information. Resulting forced and delayed temporal flexibility, covering both domestic hot water and space heating demands as constraints, allows to derive a flexibility range for the heat pump system. The resulting temporal flexibility lay within the range of 24 minutes and 6 hours for forced and delayed flexibility, respectively. This range provides new insights into the system's behaviour and is the basis for estimating power and energy flexibility - the first step necessary to incorporate building energy systems into demand side management programs.

Keywords: flexibility estimation, heat pump, intelligent thermal energy systems.

Introduction

Flexibility estimation of building energy systems (BES) provides the basis for residential demand side management (DSM), which manages consumption to improve overall system efficiency [1]. Chen et al. [1] classify and discuss reliable methods for DSM with thermal energy storages (TES) to provide flexibility in buildings, concluding division of flexibility into positive and negative components as essential.

A typical configuration of BES for DSM studied in literature comprise heat pump (HP) systems for space heating (SH) [2] or domestic hot water (DHW) supply [3], which exhibit flexibility via building mass and thermal energy storage [4, 5]. Arteconi et al. [2] analyzed HPs with radiators, underfloor heating and TES, depicting influences on the building occupant's thermal comfort. Underfloor heating (high thermal inertia) maintained the thermal comfort even without TES, whereas radiators (low thermal inertia) made the inclusion of a TES necessary. Kepplinger et al. [3] investigated a cost-optimization-driven domestic hot water heater (DHW) by taking user thermal comfort and reduced sensor information for state estimation into account [6]. Results showed energy and cost savings compared to alternatively night-tariff switched DHWHs [3]. D'hulst et al. [4] showed that DHWH with TES show the highest potential of all household appliances for DSM to provide the most stable flexibility over time. Hewitt et al. [5] stated, that the role of HPs cannot be underestimated in an effort to integrate greater amounts of electricity since the dynamics of even relatively simple buildings already allows a degree of thermal management.

However, to benefit from the potentials reported, flexibility estimation has to be provided at low technological and economic costs [7]. Finding an optimal integration solution with the lowest cost, potential flexibility should already be considered in planning phase of the HP system; for scalable solutions and broader knowledge about flexibility use, HP pools should be considered

[7, 8]. Different flexibility estimation and assessment methods are discussed in literature [4, 8, 9, 10, 11, 12], but rarely applied to settings of real-world implementation, struggling with reduced sensor information [6]. Several studies in literature quantify flexibility, but a unique definition still does not exist; but it is clear that the inclusion of DSM becomes increasingly important [9, 8]. Arteconi et al. [8] also illustrate that flexibility is mostly characterized by: amount of power change, duration of change, rate of change, response time, shifted load, and maximal hours of load shifted. Additionally, they assess the potential during operation time with the occurrence of specific events like demand response control signals, where the most relevant parameters are temporal flexibility, power capacity, and energy shifted.

Similar to Arteconi et al. [8], Fischer et al. [10] introduce characteristic flexibility parameters like maximum power, mean power, shiftable energy, duration time, and regeneration time for a heat pump pool, suggesting duration of activation and regeneration as new flexibility parameters to get insights on shifting cycles. Nuytten et al. [11] separate flexibility estimation into a forced and delayed component, where depending on BES including TES, has an almost linear influence on flexibility. Thereby, no distinction between SH and DHW was made. Stinner et al. [12] distinguish between temporal, power and energy flexibility including average and cycle flexibilities, which makes aggregating flexibilities on a higher level possible, e.g. district level or electrical grid. In summary, the literature shows a gap, where the distinction of flexibility between DHW and SH operation is neglected and real-world implementation, struggling with reduced sensor information is rarely considered. We adapt the method proposed by Stinner et al. [12] to estimate the temporal flexibility of a real-world heat pump system supplying SH and DHW based on historical cloud data available to a heat pump manufacturer and operator.

Methodology

According to Stinner et al. [12], temporal flexibility can be divided into forced and delayed temporal flexibility. The former refers to the maximum operation time of the HP until the storage is fully charged, the latter to the time until full depletion of the storage. We adapt this method to derive a combined forced and delayed flexibility range (Figure 1, bottom). A real-world heat pump system with stratified storage for DHW and SH is considered (Figure 1, top). Due to usual cost reductive measures, the system comes without all needed pressure, temperature, power and flow metering. Instead, our approach only uses a given compressor's map of characteristics and those sensors which are needed for operation. Measurements available include evaporation temperature, flow temperature, DHW temperature, SH temperature, and operation times. These reduced information forces us to make assumptions on the calculation of electrical power P_{el} , cooling power \dot{Q}_{cool} , DHW demand \dot{Q}_{DHW} and SH demand \dot{Q}_{SH} (Figure 1, middle). On the one hand, determining electrical power and cooling power by using the compressor's map of characteristics, on the other hand determining DHW and SH demand by using process knowledge and forward calculation. The proposed method not only can be transferred to other heat pump systems but also provides the basis for a cloud-based system to estimate the flexibility of a fleet of heat pumps. In the following sections, the necessary steps are explained in more detail.

Defining operation times for DHW and SH via compressor run time sensors allows distinguishing the specific operation mode. The heat pump either is operated to supply heat for DHW or SH, also it might be switched off, i.e., the total set of discrete-time steps $\mathcal{T} = \{t_1, \dots, t_n\}$ can be divided into disjoint subsets,

$$\mathcal{T} = \mathcal{T}_{DHW} \sqcup \mathcal{T}_{SH} \sqcup \mathcal{T}_{OFF}. \quad (1)$$

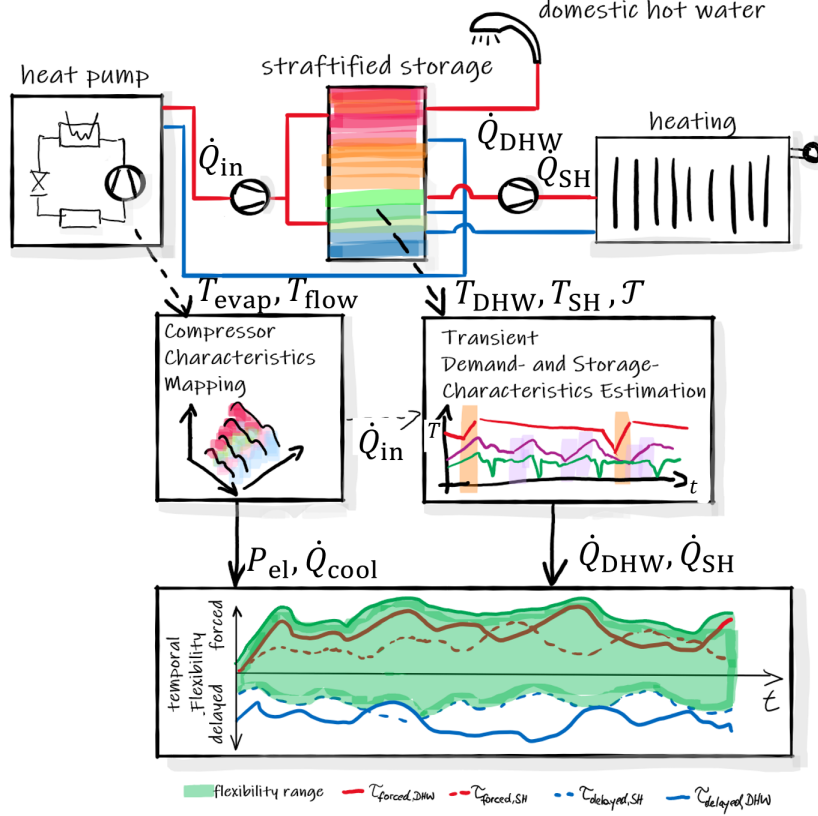


Figure 1. Schematic of the method proposed to derive a temporal flexibility estimation.

To easily formulate relationships for both operation modes, we refer to the subscript 'MODE', e.g., T_{MODE} can refer to T_{SH} or T_{DHW} .

Polynomial approximation of the compressor's map of characteristics is used to calculate the cooling power \dot{Q}_{cool} and electrical power P_{el} of the compressor, as no power or energy meter is available. The required power is estimated by using the foregoing estimated operation times \mathcal{T} for MODE and polynomials are given by the manufacturer. The power polynomials require condensation temperature T_{cond} and evaporation temperature T_{evap} for the estimation. Since the condensation temperature is not recorded by measurement, the flow temperature is used as an estimate of the condensation temperature, i.e. $T_{cond} \approx T_{flow}$. the coefficients $C_0 - C_9$ of the polynomials to estimate electric power and cooling power are provided by the manufacturer,

$$P_{el,MODE} = C_0 + C_1 T_{evap} + C_2 T_{flow} + C_3 T_{evap}^2 + C_4 T_{evap} T_{flow} + C_5 T_{flow}^2 + C_6 T_{evap}^3 + C_7 T_{flow} T_{evap}^2 + C_8 T_{evap} T_{flow}^2 + C_9 T_{flow}^3, \quad (2)$$

$$\dot{Q}_{cool,MODE} = C_0 + C_1 T_{evap} + C_2 T_{flow} + C_3 T_{evap}^2 + C_4 T_{evap} T_{flow} + C_5 T_{flow}^2 + C_6 T_{evap}^3 + C_7 T_{flow} T_{evap}^2 + C_8 T_{evap} T_{flow}^2 + C_9 T_{flow}^3. \quad (3)$$

Then, at each timestep t , the heating power \dot{Q}_{in} for both modes of operation, DHW and SH, can be calculated as follows:

$$\dot{Q}_{in,MODE}(t) = P_{el,MODE}(t) + \dot{Q}_{cool,MODE}(t). \quad (4)$$

Determination of heat transfer characteristics $(UA)_{\text{DHW}}$ and $(UA)_{\text{SH}}$ of the TES, as well as the thermal storage capacities C_{DHW} and C_{SH} are based on the hydraulic scheme provided by the manufacturer. Assuming a perfectly stratified storage enabled through stratification switches leads to the following energy balances for each operation mode:

$$\frac{C_{\text{MODE}}dT}{dt} = \dot{Q}_{\text{in,MODE}}(t) - \dot{Q}_{\text{loss,MODE}}(t) - \dot{Q}_{\text{dem,MODE}}(t). \quad (5)$$

We assume the heat transfer from the heat pump to the storage to take place in the specific storage layer and no overlapping of the two storage layers at all times.

TES capacities C_{DHW} and C_{SH} are determined, identifying the shortest heating period, for which losses are assumed to be negligible and no demand occurs:

$$C_{\text{MODE}} = \frac{\sum_{t_1}^{t_2} \dot{Q}_{\text{in,MODE}}(t)\Delta t}{T_{\text{MODE}}(t_2) - T_{\text{MODE}}(t_1)}, \text{ where} \quad (6)$$

$$(t_1, t_2) = \arg \min_{t_1, t_2 \in \mathcal{T}_{\text{MODE}}} t_2 - t_1, \text{ such that} \quad (7)$$

$$T_{\text{MODE}}(t_2) = T_{\text{up,MODE}}, \quad (8)$$

$$T_{\text{MODE}}(t_1) = T_{\text{low,MODE}}, \quad (9)$$

$$\dot{Q}_{\text{in,MODE}}(t) > 0 \forall t \in [t_1, t_2]. \quad (10)$$

Here $(T_{\text{up,MODE}}$ and $T_{\text{low,MODE}}$) refer to the upper and lower set point temperature, respectively.

Analogously in equation (15), heat transfer characteristics $(UA)_{\text{DHW}}$ and $(UA)_{\text{SH}}$ have been determined, by using maximum duration non-heating periods, assuming to reflect no demand,

$$(UA)_{\text{MODE}} = \frac{\sum_{t_1}^{t_2} \dot{Q}_{\text{loss,MODE}}(t)\Delta t}{T_{\text{MODE}}(t_2) - T_{\infty}}, \text{ where} \quad (11)$$

$$(t_1, t_2) = \arg \max_{t_1, t_2 \in \mathcal{T}_{\text{OFF}}} t_2 - t_1, \text{ such that} \quad (12)$$

$$T_{\text{MODE}}(t_1) = T_{\text{up,MODE}}, \quad (13)$$

$$T_{\text{MODE}}(t_2) = T_{\text{low,MODE}}, \quad (14)$$

$$\dot{Q}_{\text{in,MODE}}(t) = 0 \forall t \in [t_1, t_2]. \quad (15)$$

Reformulating equation (5) with parameters $(UA)_{\text{MODE}}$ and C_{MODE} allows determining the demand as follows:

$$\begin{aligned} \dot{Q}_{\text{dem,MODE}}(t) &= \dot{Q}_{\text{in,MODE}}(t) - (UA)_{\text{MODE}}(T_{\text{MODE}}(t) - T_{\infty}(t)) \\ &\quad - C_{\text{MODE}}(T_{\text{MODE}}(t + \Delta t) - T_{\text{MODE}}(t)), \forall t \in \mathcal{T}_{\text{MODE}}. \end{aligned} \quad (16)$$

The maximum available TES capacity is determined as:

$$E_{\text{max,MODE}} = C_{\text{MODE}}\Delta T_{\text{MODE}} = C_{\text{MODE}}(T_{\text{up,MODE}} - T_{\text{low,MODE}}). \quad (17)$$

To estimate the maximum heating power for the present mode of operation, the highest value in data is chosen:

$$Q_{\text{max,MODE}} = \max_{t \in \mathcal{T}_{\text{MODE}}} \dot{Q}_{\text{in,MODE}}(t)\Delta t. \quad (18)$$

Stinner et al. [12] define the forced temporal flexibility as the period for each time step where the power surplus of the heat pump working at maximum power, will be enabled to fully charge the in-situ located TES from a fully discharged state. To this end, heating demand, heat loss and generated heat (Figure 2, left). Hence, repeating this process for every time step t with an assumed discharged TES at the beginning, the forced temporal flexibility $\tau_{\text{forced,MODE}}(t_0)$ can be determined by solving:

$$\sum_{t=t_0}^{\tau_{\text{forced,MODE}}(t_0)} Q_{\text{max,MODE}} - Q_{\text{dem,MODE}}(t) - Q_{\text{loss,MODE}}(t) \stackrel{!}{\geq} E_{\text{max,MODE}}. \quad (19)$$

In the same way, the delayed temporal flexibility is defined as the period the heat pump can be switched off until the full energetic depletion of the TES is reached from a fully charged state. Heat demand and heat losses lead to the depletion of the TES (Figure 2, right). Repeating this process for every time step t , the delayed temporal flexibility $\tau_{\text{delayed,MODE}}(t_0)$ can be determined by solving:

$$\sum_{t=t_0}^{\tau_{\text{delayed,MODE}}(t_0)} Q_{\text{dem,MODE}}(t) + Q_{\text{loss,MODE}}(t) \stackrel{!}{\geq} E_{\text{max,MODE}} \quad (20)$$

Comparing the heat generated $Q_{\text{in,MODE}}$ and the heat demand $Q_{\text{dem,MODE}}$ including storage losses $Q_{\text{loss,MODE}}$, allows to calculate the forced and delayed temporal flexibility for each time step, resulting in a function $\tau_{\text{forced}}(t)$ and $\tau_{\text{delayed}}(t)$, respectively. The feasible operation has to take into account both constraining demands, resulting in the combined flexibility range (Figure 1, bottom). Since generated heat input is operation mode dependent, both thermal capacities are exploited. Hence, both forced flexibilities accumulate to a combined forced temporal flexibility where the function describes the upper bound of the flexibility range. Opposing, delayed temporal flexibility as lower bound of the flexibility range takes the minimum available time of both DHW and SH into account. Assuming the decision for full energetic depletion of the chosen storage capacity, only one limit can be exploited at a time, otherwise comfort and system boundaries will be violated.

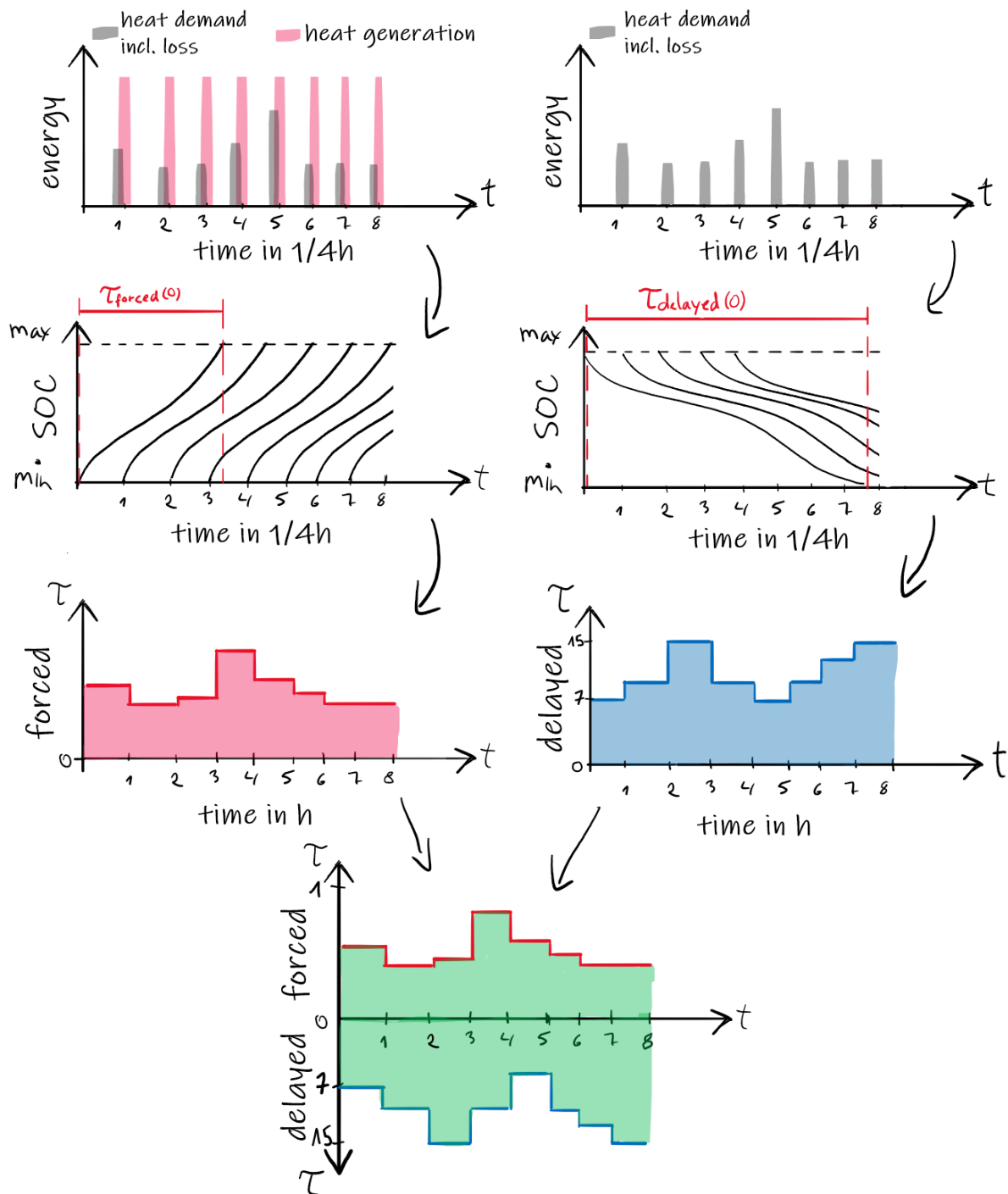


Figure 2. Schematic of the estimation methodology for forced (left) and delayed (right) temporal flexibility, according to Stinner et al. [12].

Example & Results

Applying the methodology to a real-world heat pump system, the specifics of the system, including the hydraulic scheme and sensor positions, have to be taken into account. We investigate a Weider Weitrona SW151 brine/water heat pump including a stratified storage with a capacity of 1000 litres for DHW and SH, based in Vorarlberg, Austria, showing significant seasonal variation. (Figure 1, top).

Assuming a perfect stratification through stratification switches leads to the determination of the thermal capacity of 2.3 kWh for DHW and 4.6 kWh for SH, respectively. Analogously, the heat transfer characteristic $(UA)_{\text{MODE}}$ could be determined with 0.7 W/K for DHW and 0.9 W/K for SH, respectively.

Based on that, iterative calculation of heat demand and heat loss for DHW and SH is implemented and lead to the necessary profiles. Eventually, the determination of maximum thermal storage capacity and maximum possible heating power provides the basis for the forced and delayed temporal flexibility estimation. The temporal flexibility estimation is based on a data set of one year.

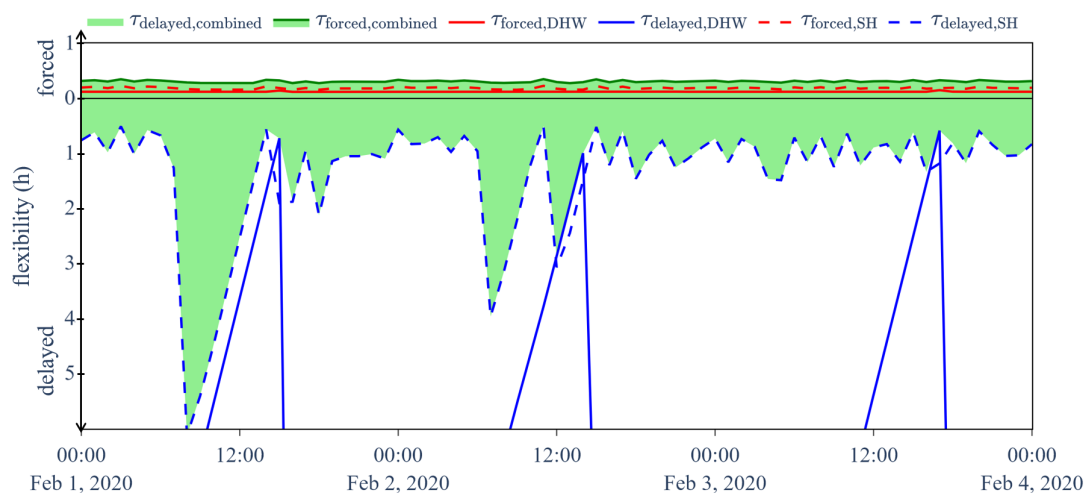


Figure 3. Determined forced and delayed temporal flexibility for DHW-, SH- and the combined mode. Forced temporal flexibility (red) and delayed temporal flexibility (blue) shown for DHW/SH mode (solid/dashed). Combined temporal flexibility range (green area) derived by boundary conditions of forced and delayed temporal flexibility of DHW and SH.

Determined forced and delayed flexibility for DHW and SH are depicted for three consecutive days in winter (Figure 3). Combined forced flexibility is derived by an accumulation of forced flexibility for DHW and SH, shown as green curve. Thus, a maximum combined forced flexibility of 24 minutes can be determined. The possible forced flexibility range lay within 0 and 24 minutes. Analogously, finding the minimum available delayed flexibility of DHW and SH leads to the opposing maximum available delayed flexibility of the combined system. In the time series of the three consecutive days, a maximum delayed flexibility of 6 hours can be determined. The possible delayed flexibility range lays within 0 and 6 hours. Derived from these two ranges, the overall range lay within 24 minutes forced and 6 hours of delayed flexibility.

While Figure 3 is taking different operation modes into account and shows the combined result, Figure 4 takes the whole year calculation of combined forced and delayed flexibility into account, comparing three consecutive days of winter, summer and transition season. For forced flexibility, peak times during the winter season, followed by intermediate flexibilities of transition and summer period, are observed. Hence, the lowest forced flexibilities are available during summer, where the demand for SH is lowest. Opposing, delayed flexibility is highest during the transition season. The decreased potential is identified in winter, continued by the summer season. Contrary to peak flexibility, the highest delayed base flexibility is identified

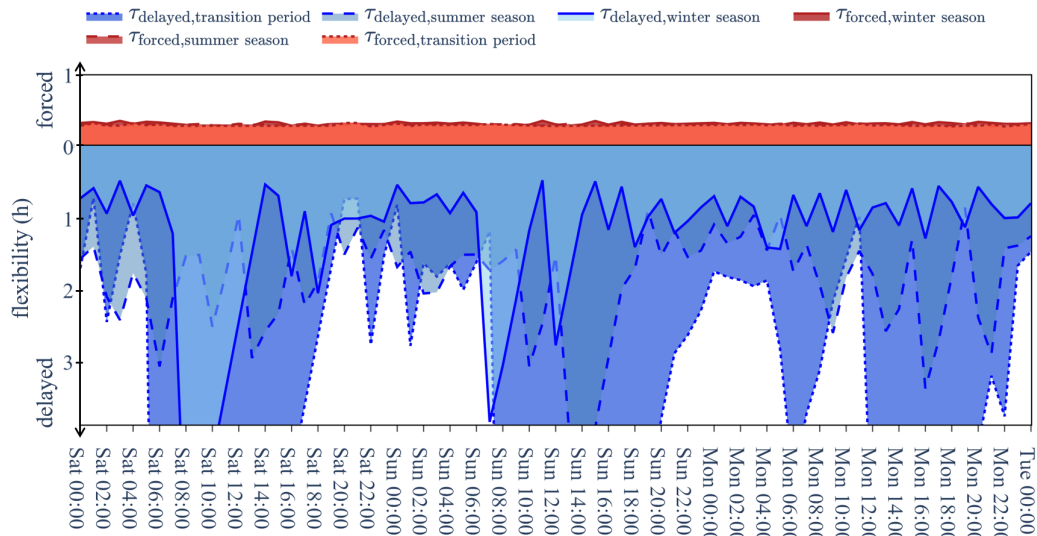


Figure 4. Comparison of the temporal flexibility range of three consecutive days during winter (solid), summer (dashed) and in the transition period (dotted) marked as forced (red) and delayed flexibilities (blue).

during summer season, followed by the transition and winter period. Comparing the amount of possible flexibility in the example investigated, delayed flexibility shows a tremendously higher potential than the forced operation.

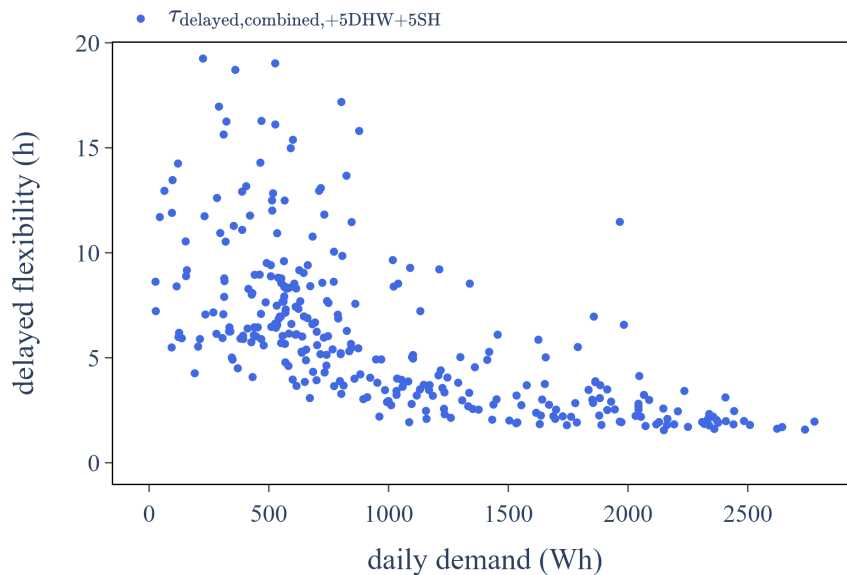


Figure 5. The daily mean of delayed temporal flexibility plotted against daily sum of DHW & SH demand over a one year period.

Considering possible forced and delayed flexibility in more detail, four different scenarios for DHW and SH temperature spreads (+5K) are investigated: reference case, +5DHW, +5SH and +5DHW+5SH. Since forced and delayed flexibility show contrary flexibility characteristics due

to heat demand, the relation between the daily mean of flexibility and the daily sum of DHW and SH demand over a one year period is investigated. A decrease in the available delayed flexibility correlates with rising demand (Figure 5). Consequently, the highest flexibilities are found for days only showing little tap events within the range from 200 to 800 Wh.

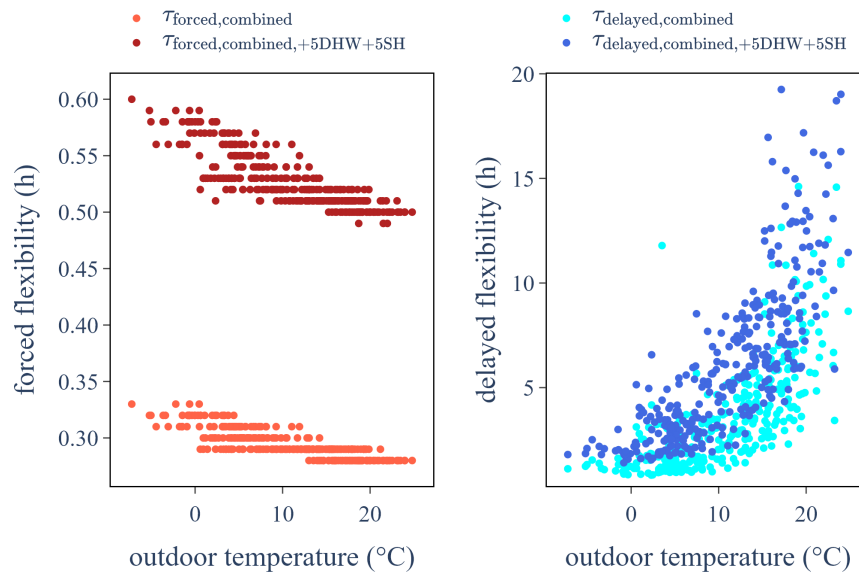


Figure 6. Left: The daily mean of combined forced temporal flexibility plotted against the daily mean of outdoor temperature over a one year period. Right: The daily mean of delayed temporal flexibility plotted against the daily mean of outdoor temperature over a one year period.

Figure 6 left refers to the forced flexibility, showing two of the scenarios investigated. The daily mean of forced flexibility is plotted against the daily mean of outdoor temperature over a one year period. A decrease in the available forced flexibility with rising outdoor temperatures independently from the scenarios is shown. Taking the same decay in every scenario into account, a linear offset factor can be observed: 1.2 for +5DHW, 1.6 for +5SH and 1.8 for +5DHW+5SH (Figure 7, left). Hence, the increase of the combined temperature spread +5DHW+5SH leads to the highest potential. Comparison of the +5DHW and the +5SH scenario shows a higher flexibility per Kelvin in the SH scenario, which is derived by higher thermal capacity.

In contrast to forced flexibility, an increase in the available flexibility with rising outdoor temperatures can be observed (Figure 6, right). For delayed flexibility, low SH use is related to higher outdoor temperatures and provides more available capacity. The highest flexibility of the investigated scenarios is observed in the combined +5DHW+5SH scenario. Taking the same increase in every scenario into account, an exponential offset factor can be observed: 1.1 for +5DHW, 1.6 for +5SH and 1.7 for +5DHW+5SH (Figure 7, right).

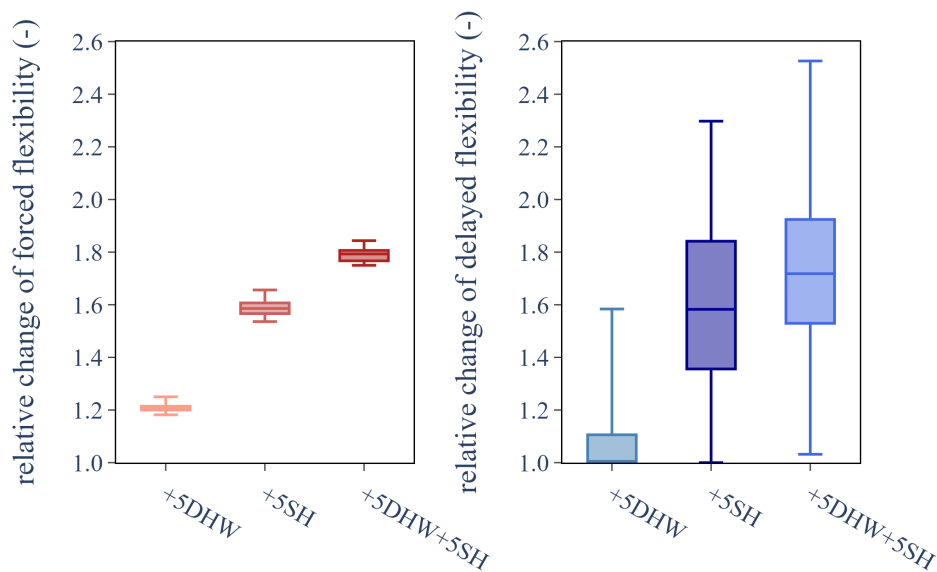


Figure 7. Box-plots of the relative change of forced (left) and delayed (right) temporal flexibility of different scenarios considered.

Discussion

Setup dependent thermal capacities and heat demand behaviour of DHW and SH decide on the flexibility characteristic of the system. In the real-world application, forced and delayed temporal flexibility showed quite different behaviour on demand. While forced flexibility rose with high demand, delayed flexibility showed a decrease. Since SH demand and thermal capacity dominated over the DHW case, forced and delayed temporal flexibility have been strongly dependent on seasonal variations. Depending on the sizing of thermal capacities in other system configurations, this may vary. Thus, an intelligent forecast of demand can lead to highly reliable flexibility forecast and use.

Delayed temporal flexibility showed a significantly higher potential in all cases and scenarios. Thus, in further application of flexibility range, an absolute difference of forced and delayed flexibility has to be considered.

Additionally, the calculation of the relative change of flexibility showed that minor increments of the limiting storage temperatures can lead to high improvements in forced and delayed flexibility. Exemplary for the +5SH scenario, an increment of 5 Kelvin led to an improvement of factor 1.6 in forced and delayed flexibility.

Conclusion

An extended method for flexibility estimation based on historical cloud data of a real-world heat pump system has been presented. The method proposed, relied on robust simplifications and estimates, employing process knowledge, energy balances and manufacturer's information. Resulting forced and delayed temporal flexibility, covering both, domestic hot water and space heating demands as constraints, allowed to derive a flexibility range for the heat pump system.

The simulation was conducted for an entire year. Forced and delayed temporal flexibility of each operation mode were calculated, deriving the combined flexibility, as well as the flexibility

range. In the reference case, the derived flexibility range lay within 24 minutes of forced and 6 hours of delayed temporal flexibility. The best-case scenario of three additionally investigated scenarios enhanced forced temporal flexibility by factor 1.8, delayed flexibility by about 1.7, respectively.

The proposed flexibility estimation method not only provides insights into the system's behaviour, it also enables the estimation of possible flexibility improvements and provides the basis for a cloud-based system to estimate the flexibility of a fleet of heat pumps. As temporal flexibility range is the basis for estimating power and energy flexibility, which is the first step necessary to incorporate building energy systems into demand side management programs, this work should be further extended.

Acknowledgement: The financial support by the Austrian Federal Ministry for Digital and Economic Affairs and the National Foundation for Research, Technology and Development and the Christian Doppler Research Association is gratefully acknowledged. The authors are grateful to the project partner Weider Wärmepumpen GmbH for the support and providing the real data.

References

- [1] Yongbao Chen, Peng Xu, Jiefan Gu, Ferdinand Schmidt, and Weilin Li. Measures to improve energy demand flexibility in buildings for demand response (DR): A review. *Energy and Buildings*, 177:125–139, 2018.
- [2] A. Arteconi, N.J. Hewitt, and F. Polonara. Domestic demand-side management (DSM): Role of heat pumps and thermal energy storage (TES) systems. *Applied Thermal Engineering*, 51(1):155–165, 2013. 00141.
- [3] Peter Kepplinger, Gerhard Huber, and Jörg Petrasch. Autonomous optimal control for demand side management with resistive domestic hot water heaters using linear optimization. *Energy and Buildings*, 100:50–55, 2015.
- [4] R. D'hulst, W. Labeeuw, B. Beusen, S. Claessens, G. Deconinck, and K. Vanthournout. Demand response flexibility and flexibility potential of residential smart appliances: Experiences from large pilot test in belgium. *Applied Energy*, 155:79–90, 2015.
- [5] Neil J Hewitt. Heat pumps and energy storage – the challenges of implementation. *Applied Energy*, 89(1):37–44, 2012.
- [6] Peter Kepplinger, Gerhard Huber, Markus Preißinger, and Jörg Petrasch. State estimation of resistive domestic hot water heaters in arbitrary operation modes for demand side management. *Thermal Science and Engineering Progress*, 9:94–109, 2019.
- [7] David Fischer and Hatef Madani. On heat pumps in smart grids: A review. *Renewable and Sustainable Energy Reviews*, 70:342–357, 2017. 00005.
- [8] Alessia Arteconi and Fabio Polonara. Assessing the demand side management potential and the energy flexibility of heat pumps in buildings. *Energies*, 11(7), 2018.
- [9] John Clauß. Control strategies for building energy systems to unlock demand side flexibility – a review. *IBPSA Building Simulation 2017, San Francisco, 7-9 August 2017*, 2017.
- [10] David Fischer, Tobias Wolf, Jeannette Wapler, Raphael Hollinger, and Hatef Madani. Model-based flexibility assessment of a residential heat pump pool. *Energy*, 118:853–864, 2017.
- [11] Thomas Nuytten, Bert Claessens, Kristof Paredis, Johan Van Bael, and Daan Six. Flexibility of a combined heat and power system with thermal energy storage for district heating. *Applied Energy*, 104:583–591, 2013.

- [12] Sebastian Stinner, Kristian Huchtemann, and Dirk Müller. Quantifying the operational flexibility of building energy systems with thermal energy storages. *Applied Energy*, 181:140–154, 2016.

Numerical Investigation of Desiccant Cooling Using Aluminium Fumarate Metal Organic Framework Material

Andrew N. Aziz^{1,2*}, Saad Mahmoud¹, Raya Al-Dadah¹, Ibrahim Albaik¹

¹School of Engineering, University of Birmingham, Edgbaston, Birmingham, B15-2TT

²City of Scientific Research and Technological Applications, SRTA-City, New Borg El Arab City, 21934 Alexandria, Egypt

*Corresponding Author: anm900@student.bham.ac.uk

Abstract

Desiccant cooling systems are effective in controlling moisture content in supply air. They do not use any ozone-depleting coolants and consume less energy as compared with the vapor compression systems. The desiccant wheel and the adsorbent material used are key components that affect the performance of desiccant cooling system. Metal Organic Frameworks (MOFs) are meso-porous materials with exceptionally high porosity, large surface area (up to 5500m²/g) and superior water uptake capacity compared to silica gel. In this work, 1D numerical model of a desiccant wheel was developed using MATLAB software to predict the effect of adsorbent material on the performance of the desiccant wheel in terms of moisture removal and Coefficient of Performance. Results showed that using aluminium fumarate MOF improves the desiccant wheel ability to remove moisture from the air by 54%, lowers the relative humidity for process air by 10%, and raises the relative humidity for regeneration by 20% compared to silica gel highlighting the potential of MOF materials for desiccant cooling.

Keywords: modelling, desiccant, MOF, aluminium fumarate.

Introduction

Most of current cooling systems use vapor compression technology which suffers from high electricity consumption and uses environmentally damaging refrigerants. Evaporative cooling has major advantages like typically uses less than 10% of the electricity than conventional air conditioning, it uses no refrigerants, supplies 100% fresh cool air, it has low carbon dioxide footprint with simple engineering, and can significantly reduce the temperature on hot days. But the main disadvantage of evaporative cooling is that it is only applicable in dry atmospheres, it is not successful in the areas where ambient humidity is high [1-2]. Desiccant cooling systems have been considered as an efficient method of controlling moisture content in supply air. They do not use any ozone-depleting coolants and consume less energy as compared with the vapor compression systems. Therefore, the integration of desiccant and evaporative cooling will significantly improve the cooling performance and avoid the impact of high ambient air humidity. Currently desiccant cooling systems utilise silica gel as the adsorbent material on the desiccant wheel which has limited water uptake thus reducing the performance of the system. Metal Organic Frameworks (MOFs) are meso-porous materials with exceptionally high porosity, large surface area (up to 5500m²/g) and superior water uptake capacity compared to silica gel [3].

Understanding how desiccant wheel works and the factors that determine its effectiveness is critical to improve the performance of the desiccant wheel in terms of moisture removal and

the coefficient of performance. Beccali et al. [4] developed a simplified model to predict the performance of rotary desiccant wheels by fitting experimental data obtained from the industry, to produce correlations for predicting the air outlet temperature and absolute humidity. This model is used to predict the performance of three different types of desiccant rotors made using various types of solid desiccants (Type I, II and III). Zhang et al. [5] used heat and mass transfer equations to model honeycombed rotary desiccant dehumidifier. The numerical results were compared to experimental ones showing good agreement with maximum deviation of 3.5% and 6% for humidity and temperature respectively. Ge et al. [6] developed a mathematical model to estimate the performance of silica gel haloid compound desiccant wheel to determine the best operating conditions. In the genetic algorithm used, two scenarios were considered for the objective function: first, specific adsorption energy, and second, the humidity ratio of process air. Zouaoui et al. [7] developed a model to study the performance of open solid desiccant air cooling systems with direct and/or indirect humidification. Their results revealed that the desiccant method covers the latent load, while direct and/or indirect humidification covers the sensible load. Koronaki et al. [8] made a thermodynamic analysis of an open cycle solid desiccant cooling system using Artificial Neural Network. They showed that their neural network model could adequately predict dehumidification capability and outlet desiccant conditions under a variety of climatic conditions. Shanmuga et al. [9] developed a TRNSYS-MATLAB simulation model for desiccant cooling system where Transys software was used to estimate the energy required by buildings and the solar desiccant based evaporative cooling model done by MATLAB. Diglio et al. [10] developed a 1-D numerical simulation of a rotary desiccant wheel using COMSOL for process and regeneration operations. Bellemo et al. [11] developed a 2-D steady-state model of desiccant wheels using Engineering Equation Solver. Chung et al. [12] optimised a desiccant wheel speed and area ratio of regeneration to dehumidification as a function of regeneration temperature to improve the performance the desiccant wheel for cooling application and concluded that the moisture removal capability of the wheel is critical to the system overall performance. Kapteijn et al. [13] carried out a review and showed that MOF material has higher water uptake compared with SAPO-34 thus can be used for humidity control applications.

In this work, a 1-D mathematical model was developed using finite difference implicit method to simulate the moisture removal and the coefficient of performance for a desiccant wheel using aluminium fumarate MOF material and silica gel.

Model description

Figure 1 shows the details of the desiccant wheel used in this model where dehumidification process of air occurs between points (1) and (2) through the red section while the regeneration process occurs in the reverse direction through the blue part. Channel dimensions and operating conditions for process air are shown in Figure 1(b) and presented in table 1.

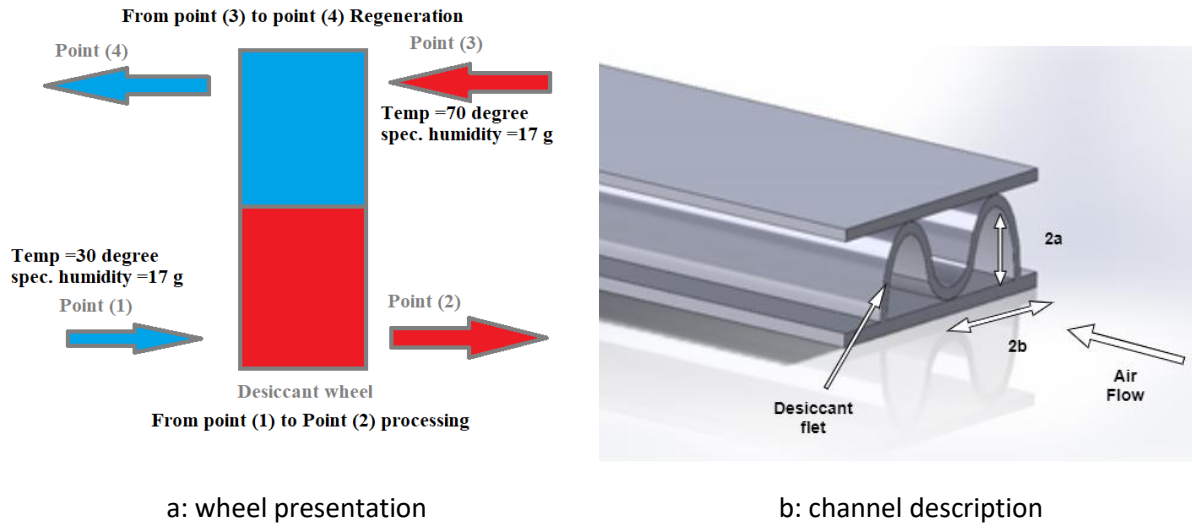


Figure 1: Wheel and air flow passage presentation

Table 1: physical channel dimensions and operating conditions for process air.

Desiccant width (Lw)	0.1 [m]
Channel height (a)	0.0018 [m]
Channel pitch (b)	0.0032 [m]
Desiccant thickness (δd)	0.00025 [m]
Air density (ρ_a)	1.016 [kg/m ³]
Specific heat of air (C_{pa})	1005 [kJ/kg/K]
Thermal conductivity of air (K_a)	0.175 [W/mK]
Specific heat of water vapours (C_{pv})	1864 [kJ/kg/K]
Nusselt number (Nu)	2.45
Sher wood number (Sh)	2.5
Atmospheric Pressure (P)	1.01325×10^5 [Pa]
Facial air velocity (u)	2 [m/s]

The desiccant wheel channel geometric equations are:

$$A_f = 2 \times a \times b \tag{1}$$

$$A_t = 0.5 \times (2a + \delta d) \times (2b + \delta d) \tag{2}$$

$$p_e = 2b + 2\sqrt{b^2 + (a\pi)^2} \times \frac{3 + (\frac{2b}{a\pi})^2}{4 + (\frac{2b}{a\pi})^2} \quad (3)$$

$$D_h = \frac{4 \times A_f}{p_e} \quad (4)$$

Where A_f is cross sectional area of air flow passage, A_t is the total cross-sectional area of one channel, p_e represents the perimeter of flow passage for one channel, and D_h is the hydraulic diameter.

The conservation of moisture in the air could be stated as [14]:

$$\rho_a d_e \left(\frac{\partial Y_p}{\partial t} + u \frac{\partial Y_p}{\partial x} \right) = K_y (Y_d - Y_p) \quad (5)$$

The energy conservation for the air is given as:

$$\rho_a C_{pa} d_e \left(\frac{\partial T_p}{\partial t} + u \frac{\partial T_p}{\partial x} \right) = h (T_d - T_p) + K_y C_{pv} (Y_d - Y_p) (T_d - T_p) \quad (6)$$

Desiccant moisture conservation is determined by:

$$\delta d \rho_d \left(\frac{\partial W}{\partial t} - D_e \frac{\partial W}{\partial x^2} \right) = K_y (Y_p - Y_d) \quad (7)$$

Desiccant energy conservation can be written as follows:

$$\left(\frac{\partial T_d}{\partial t} - \frac{K_d}{C_{pd} \rho_d} \frac{\partial T_d}{\partial x^2} \right) \times \delta d \cdot \rho_d \cdot C_{pd} = h (T_p - T_d) + q_{st} \cdot K_y \times (Y_p - Y_d) + C_{pv} K_y \times (T_p - T_d) (Y_p - Y_d) \quad (8)$$

Where Y_d is the adsorbent material equilibrium uptake expressed as a function of the desiccant relative humidity as:

$$Y_d = 0.62188 \times \frac{P_v}{P_{atm} - P_v} = 0.62188 \times \frac{RH_d}{(P_{atm} - P_{vs}) - RH_d} \quad (9)$$

The effective diffusivity (D_e) is determined as [15]:

$$D_e = D_s \times \frac{1.6 \times 10^{-6}}{\tau} e^{(-0.974 \times 10^{-6} \times \frac{q_{st}}{T_d})} \quad (10)$$

Where q_{st} is adsorption heat given as;

$$q_{st} = A = h_{fg} [1 + 0.2843 e^{(-10.28W)}] \quad (11)$$

Where h_{fg} is the latent heat of evaporation for water and is given by:

$$h_{fg} = (2504.4 - 2.4425 T_d) \times 1000 \quad (12)$$

The desiccant relative humidity for Silica Gel and Aluminium fumarate is given by equations 13 and 14 respectively:

$$RH_d = 0.0078 - 0.0579*W + 24.16551*W^2 - 124.478*W^3 + 204.226*W^4 \quad (13)$$

$$RH_d = -138.41*W^4 + 159.67*W^3 - 55.534*W^2 + 7.0476*W - 0.0399 \quad (14)$$

Figure 2 shows the isotherm curve used as equilibrium condition in the model where the maximum water uptake that can be adsorbed from air is 0.54 kgwater/kgAF.

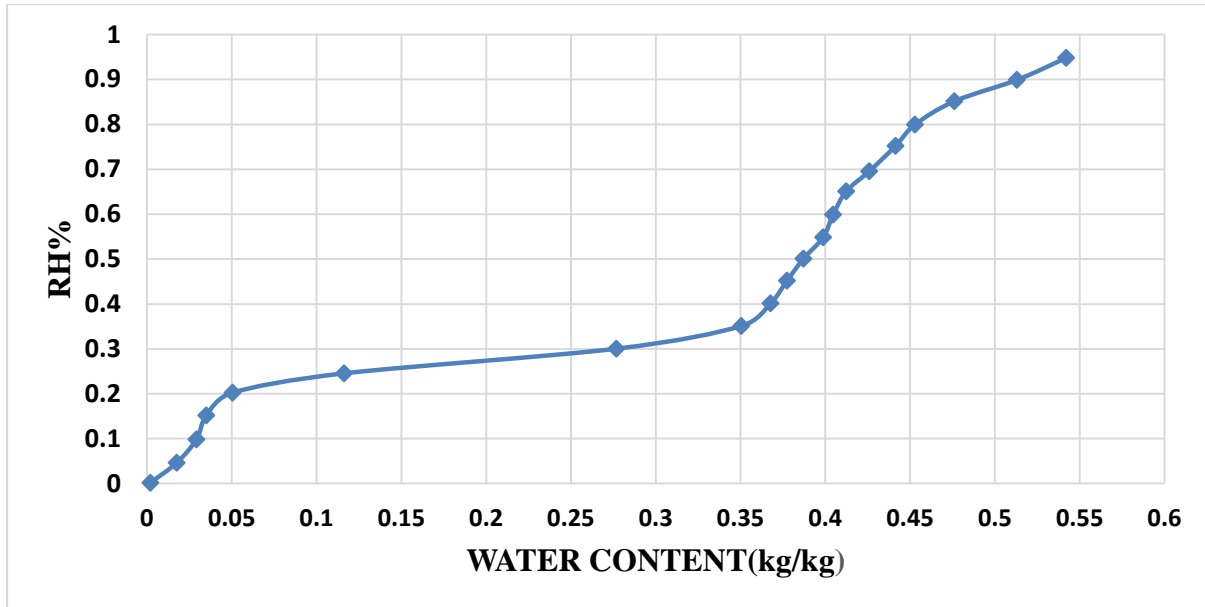


Figure 2: Isotherm curve for aluminium fumarate

The model boundary conditions are as follow:

$$\frac{\partial T_d}{\partial x} \Big|_{x=0} = \frac{\partial T_d}{\partial x} \Big|_{x=L_w} \quad (15)$$

$$\frac{\partial Y_d}{\partial x} \Big|_{x=0} = \frac{\partial Y_d}{\partial x} \Big|_{x=L_w} \quad (16)$$

The initial conditions used in this modelling include the initial temperature of the air and desiccant (T_{p0} and T_{d0}), the water content in desiccant (W_0) and the humidity ratio of the air and desiccant (Y_{p0} and Y_{d0}). Figure 3 shows a flow diagram of the developed mathematical model and table 2 lists the thermophysical properties of silica gel and aluminium fumarate adsorbent materials.

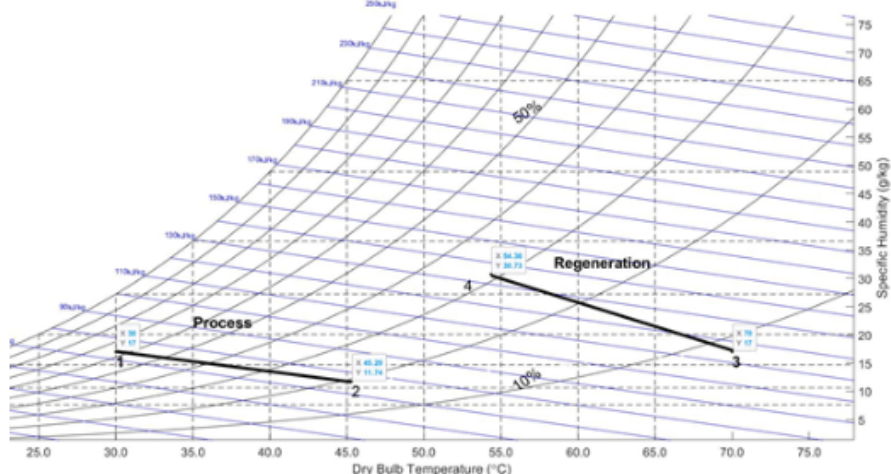
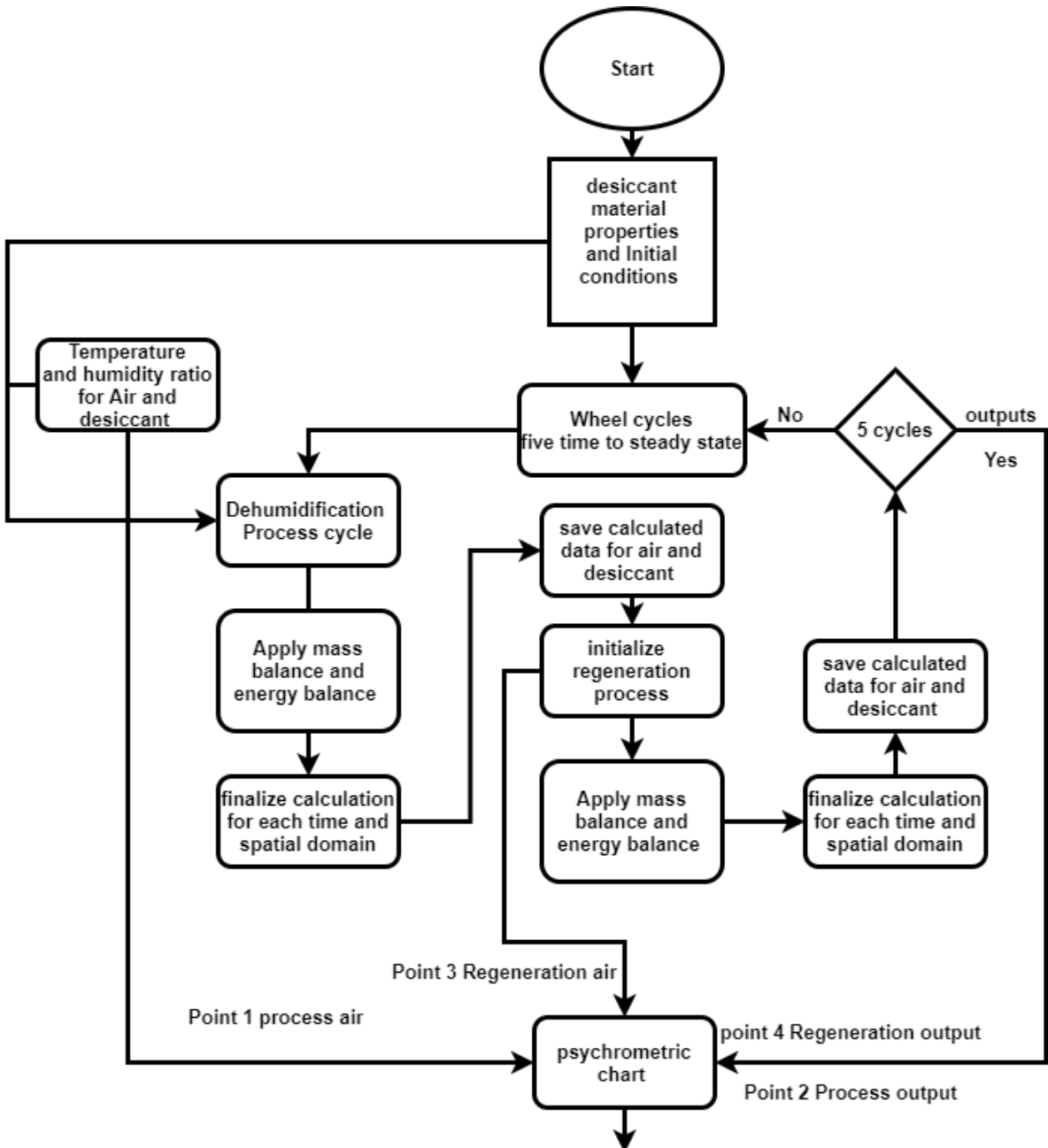


Figure 3: Model flow chart

Table 2: Model inputs

Material	Density (ρ_d)	Thermal conductivity (K_d)	Specific heat (C_{pd})	Surface diffusivity	Porosity	Maximum water content	solid tortuosity (τ)
Silica gel	550	0.175	921	1.6e-10[16].	0.4	0.34	2.8[17]
Aluminum fumarate	520	0.08+1.4E-4Tbed [18].	970	3.63e-14 [19].	0.67	0.54	2.8

Model validation

Figure 4, and Figure 5 compare the model predicted moisture removal output at various air flow velocity and various inlet humidity compared with those predicted by Yadav’s model [16] for silica gel. From figure 4, it can be seen that the average deviation in moisture removal is 7.6 % and the maximum error is 8.4 % while figure 5 shows maximum deviation of 10% and average deviation of 7.7%.

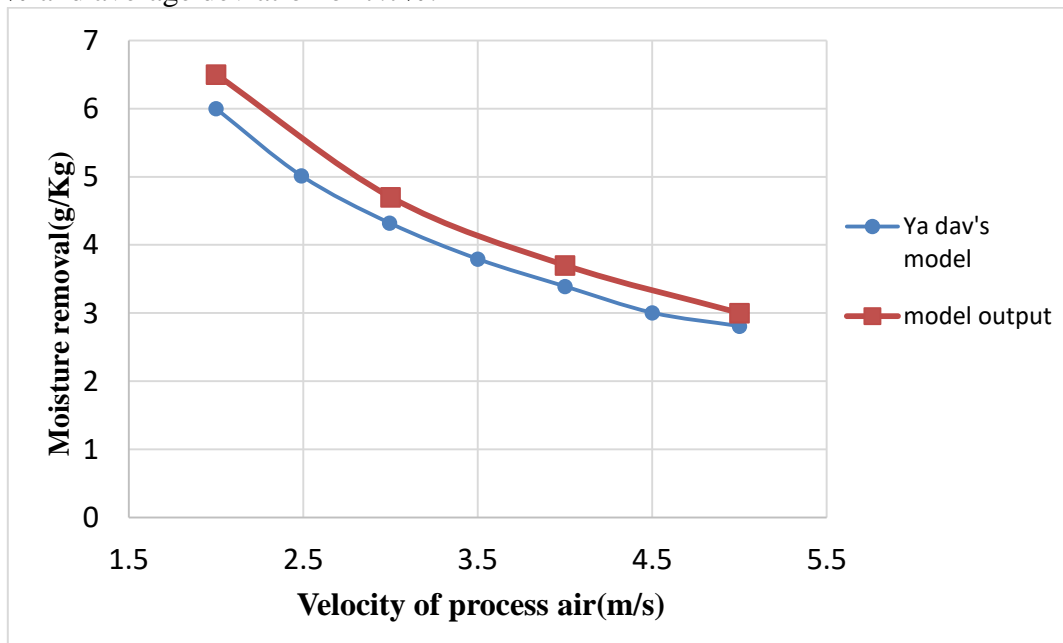


Figure 4: Inlet velocity change vs moisture removal

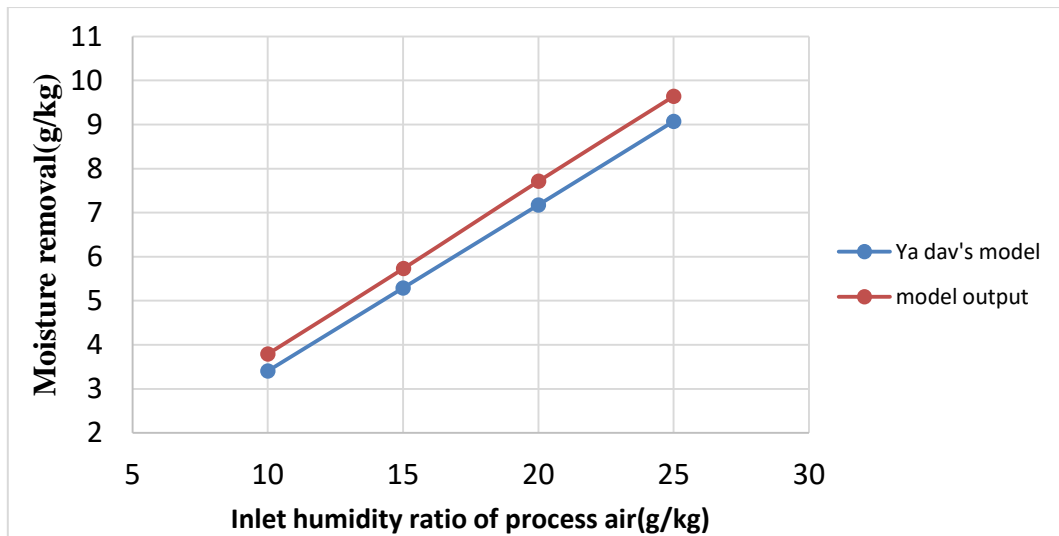


Figure 5: Inlet humidity change vs moisture removal

Results and Discussion

Table 3 shows the predicted COP for desiccant wheels using silica gel and aluminium fumarate, which were 0.3684 and 0.6591, respectively. These results were due to aluminium fumarate, having a larger capability for adsorbing water than silica gel. The ambient temperature at point 1 as input in the model was 30 degrees Celsius, with a specific humidity of 17 grams of water in the air. The operational parameters for regeneration air at point 3 were 70 degrees Celsius and 17 grams of specific humidity. In the processing of silica gel, the temperature is raised from 30 to 45.29 degrees Celsius, and the temperature for aluminium fumarate is changed from 30 to 44.97 degrees Celsius, which represents a slight decrease compared to silica gel by about 0.32 oC. In the regeneration process, however, the two materials perform similarly in terms of temperature change, falling from 70 oC to 54.36 oC for silica gel and 54.46 for aluminium fumarate, respectively, in contrast to the specific

Table 3: Model results for both regeneration and dehumidification processes

Material	Initial air temp. (°C)	Initial specific humidity	Output air temp. (°C)	Output specific humidity (g/kg)	Initial air temp. (°C)	Initial specific humidity	Output air temp (°C)	Output specific humidity (g/kg)	COP For desiccant wheel	Moisture removal (Grams)
	Process		Process		Regeneration		Regeneration			
	Point 1	Point 1	Point 2	Point 2	Point 3	Point 3	Point 4	Point 4		
Silica gel	30	17	45.29	11.74	70	17	54.36	30.73	0.3684	13.73
aluminium fumarate	30	17	44.97	4.349	70	17	54.46	47.28	0.6591	30.28

humidity change at point 4 of 30.73 and 47.28

for silica gel and aluminium fumarate respectively. This means that aluminium fumarate outperforms silica gel by 16.55 grams. From table 3, the moisture removal for aluminium fumarate is higher than the moisture removal for silica gel by 45 % at the same operating conditions.

Figure 6 shows the psychrometric chart for the de-humification (1-2) and regeneration processes (3-4) across the desiccant wheel using silica gel where the relative humidity at point 2 is lower than 20% while the relative humidity at point 4 is 30 %. Figure 7 shows the de-humification (1-2) and regeneration processes (3-4) across the desiccant wheel using aluminium fumarate where the relative humidity at point 2 is lower than 10% while the relative humidity at point 4 is 50 %.

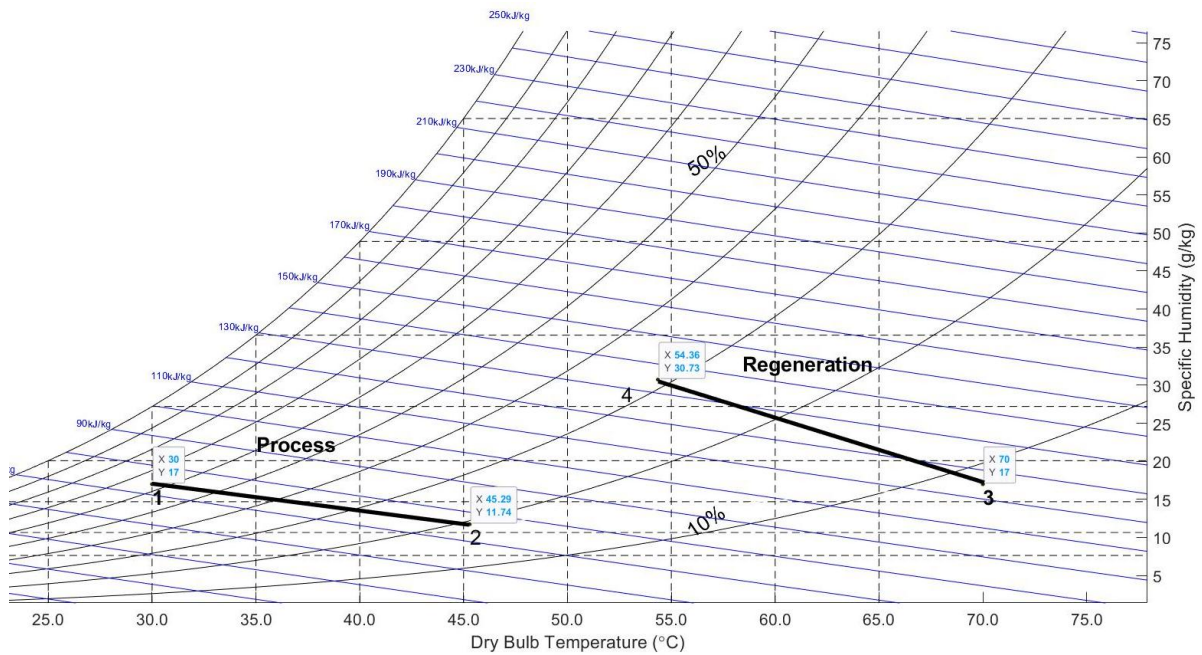


Figure 6: psychrometric representation for aluminium fumarate

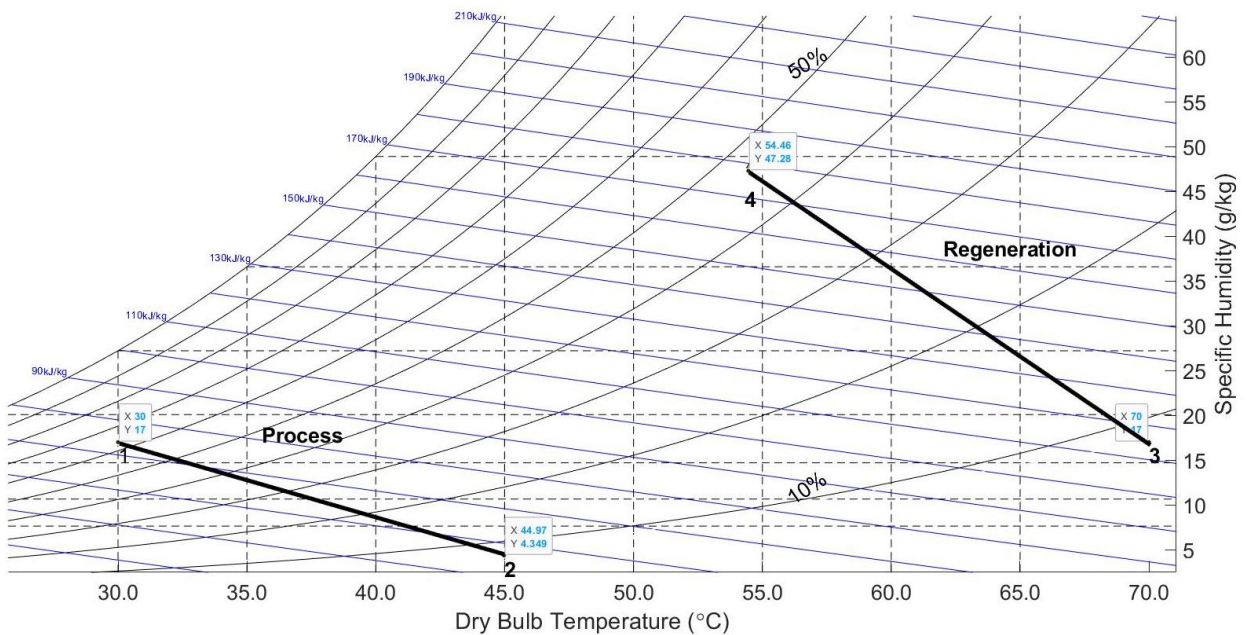


Figure 7: psychrometric representation for aluminium fumarate

Conclusions

Desiccant cooling offers many advantages compared to vapour compression cooling systems where the desiccant wheel is a key component and affects the performance of such system. Also, the use of adsorbent materials in the desiccant when will have major impacts on its performance in terms of the moisture removal from the air. In this work, a numerical model for a desiccant wheel was developed using MATLAB to predict the wheel's performance using aluminium fumarate MOF compared to silica gel. The model was validated against published data for silica gel showing maximum deviation in moisture removal of less than 10%. Results showed that using aluminium fumarate improves the desiccant wheel ability to remove moisture from the air by 54%, lowers the relative humidity for process air by 10%, and raises the relative humidity for regeneration by 20% compared to silica gel. The results show the potential of using aluminium fumarate MOF for desiccant cooling.

Acknowledgements

The authors acknowledge the sponsorship of Newton-Mosharfa fund for enabling this PhD project.

References

- [1] S. E. Reviews et al., “*Evaporative Cooler Integrated Design and Retrofit of Buildings*,” 2018.
- [2] J. Steven Brown and P. A. Domanski, “*Review of alternative cooling technologies*,” *Appl. Therm. Eng.*, vol. 64, no. 1–2, pp. 252–262, 2014.
- [3] R. AL-Dadah, S. Mahmoud, E. Elsayed, P. Youssef, and F. Al-Mousawi, “*Metal-organic framework materials for adsorption heat pumps*,” *Energy*, vol. 190, p. 116356, 2020.
- [4] M. Beccali, F. Butera, R. Guanella, and R. S. Adhikari, “*Simplified models for the performance evaluation of desiccant wheel dehumidification*,” *Int. J. Energy Res.*, vol. 27, no. 1, pp. 17–29, 2003.
- [5] X. J. Zhang, Y. J. Dai, and R. Z. Wang, “*A simulation study of heat and mass transfer in a honeycombed rotary desiccant dehumidifier*,” *Appl. Therm. Eng.*, vol. 23, no. 8, pp. 989–1003, 2003.
- [6] T. S. Ge, F. Ziegler, and R. Z. Wang, “*A mathematical model for predicting the performance of a compound desiccant wheel (A model of compound desiccant wheel)*,” *Appl. Therm. Eng.*, vol. 30, no. 8–9, pp. 1005–1015, 2010.
- [7] A. Zouaoui, L. Zili-Ghedira, and S. Ben Nasrallah, “*Open solid desiccant cooling air systems: A review and comparative study*,” *Renew. Sustain. Energy Rev.*, vol. 54, pp. 889–917, 2016.
- [8] I. P. Koronaki, E. Rogdakis, and T. Kakatsiou, “*Thermodynamic analysis of an open cycle solid desiccant cooling system using Artificial Neural Network*,” *Energy Convers. Manag.*, vol. 60, pp. 152–160, 2012.
- [9] K. Sudhakar, M. S. Jenkins, S. Mangal, and S. S. Priya, “*Modelling of a solar desiccant cooling system using a TRNSYS-MATLAB co-simulator: A review*,” *J. Build. Eng.*, vol. 24, no. March, p. 100749, 2019.
- [10] G. Heidarinejad, H. P. Shahri, and S. Delfani, “*The effect of geometrical characteristics of desiccant wheel on its performance*,” *Int. J. Eng. Trans. B Appl.*, vol. 22, no. 1, pp. 63–65, 2009.
- [11] L. Bellemo, B. Elmegaard, M. R. Kærn, W. B. Markussen, and L. O. Reinholdt, “*Formulation and validation of a two-dimensional steady-state model of desiccant wheels*,” *Sci. Technol. Built Environ.*, vol. 21, no. 3, pp. 300–311, 2015.

- [12] J. D. Chung, D. Y. Lee, and S. M. Yoon, “*Optimization of desiccant wheel speed and area ratio of regeneration to dehumidification as a function of regeneration temperature,*” *Sol. Energy*, vol. 83, no. 5, pp. 625–635, 2009.
- [13] X. Liu, X. Wang, and F. Kapteijn, “*Water and Metal-Organic Frameworks: From Interaction toward Utilization,*” *Chem. Rev.*, vol. 120, no. 16, pp. 8303–8377, 2020.
- [14] T. S. Ge, Y. Li, R. Z. Wang, and Y. J. Dai, “*A review of the mathematical models for predicting rotary desiccant wheel,*” *Renew. Sustain. Energy Rev.*, vol. 12, no. 6, pp. 1485–1528, 2008.
- [15] J. Y. San and S. C. Hsiau, “*Effect of axial solid heat conduction and mass diffusion in a rotary heat and mass regenerator,*” *Int. J. Heat Mass Transf.*, vol. 36, no. 8, pp. 2051–2059, 1993.
- [16] A. YADAV, “*EVALUATION AND OPTIMIZATION OF DESICCANT WHEEL PERFORMANCE,*” no. 209423, 2011.
- [17] R. H. Mohammed, O. Mesalhy, M. L. Elsayed, and L. C. Chow, “*Novel compact bed design for adsorption cooling systems: parametric numerical study,*” *Int. J. Refrig.*, 2017.
- [18] E. M. E. A. Hussein, “*NUMERICAL AND EXPERIMENTAL EVALUATION OF ADVANCED METAL- ORGANIC FRAMEWORK MATERIALS FOR ADSORPTION HEAT PUMPS,*” 2018.
- [19] J. Lee, K. J. Bae, and O. K. Kwon, “*Performance Investigation of a Two-Bed Type Adsorption Chiller with Various Adsorbents,*” pp. 1–16, 2020.

Solar cooling system for a buildings using parallel ejectors

M. Falsafioon¹, M. Poirier¹ and P. Simard¹

¹ CanmetENERGY, Natural Resources Canada, 1615 Lionel-Boulet Blvd., Varennes, Québec, Canada J3X 1S6

*Corresponding author: mehdi.falsafioon@canada.ca

Abstract

This paper presents the field testing of a solar thermal plant combined with an ejector-compression system for building's space cooling applications. The thermal plant uses solar parabolic collectors that focus a large area of sunlight towards a tube where circulating oil captures the energy. This energy activates the ejector system, which produces a cooling effect. The ejector system is integrated into the CanmetENERGY Research Centre's building such as to cover part of its air conditioning load, thus allowing to decrease the electrical consumption of the main building's chiller. The current manuscript presents design and operation characteristics of the ejector cooling loop, including the usage of multiple ejectors with different capacities in order to improve the flexibility and the number of hours of operation for this type of system. Performance data and recommendations for performance improvement are discussed as well.

Keywords: Solar cooling; Ejector Technology; Parabolic Collectors;

Introduction

Solar ejector cooling systems have raised a lot of interest in the recent years in the scientific community, but there is very few published data on full scale installations. For one, concentrated thermal solar collectors are useful to provide medium temperature energy (e.g. 80 °C to 140 °C), that can be used for different building and process applications. In view to test this technology in real operating conditions for building operations, the CanmetENERGY Research Centre in Varennes (QC, Canada) installed an array of solar parabolic collectors on its roof. In winter, the heat is used to assist in the heating of the building. In summer, the solar energy is used for space cooling. Among the different heat-driven cooling technologies, the vapor ejector technology allows for gas compression using thermal energy instead of electricity [1-3]. This offers the opportunity to decrease the electrical consumption of the cooling system by eliminating the compressor. In addition, an ejector does not have any moving parts and its configuration is simple and cost effective enough to build. This paper presents the solar ejector cooling system built and tested at the CanmetENERGY Research Centre in Varennes, along with the analysis of some results obtained with two ejectors having different capacity, as well as their energy efficiency.

Solar thermal plant description

The solar thermal plant consists of eight rows of parabolic collectors installed on the roof of CanmetENERGY's building as shown in Fig. 1. Each row is made of 12 metres of polished aluminum that are called "mirrors". Absorber tubes are installed at the focal point of the parabolic collectors where the solar beams are concentrated. The absorbing tubes are embedded in partial vacuum glass tubes, which help reduce the convective heat loss to the ambient air. A secondary fluid (thermal oil) circulates inside the absorbing tubes to collect the thermal energy. All mirrors and absorbers are installed on pivoting structures. An automatic tracking system allows for the optimal orientation of the mirrors at all times. A pyrliometer measures direct sunlight and transfers the data to the tracking system. An

inclinometer also helps with the precise positioning of the mirrors. Table 1 shows the features of the parabolic collectors, and the rated power and efficiency of the thermal solar collectors.

Table 1: Dimensions and capacity of the solar power plant.

Width of the mirrors	Area reported per row	Number of rows	Total light receiving area	Rated [†]	
				Power	Efficiency
1.18 m	14.1 m ²	8	112.8 m ²	55 kW	0.49

†: At 1000 W/m².

There are normally two possibilities for the orientation of the parabolic collectors: north-south axis and east-west axis. A north-south arrangement maximizes solar gain in summer, while an east-west arrangement maximizes solar gain in winter. For the demonstration project, the collectors were oriented in a north-south axis to maximize solar gain in summer, to favour the operation of the ejector system for building cooling purposes. The collectors are constantly moved throughout each day to track the sun's path.



Fig. 1: Pictures showing one row of parabolic solar collectors (left) and the solar power plant (right).

The thermal oil used to collect solar thermal energy is stored in a 500 litre tank. A pump is employed to circulate the oil to the collectors and to the building, either for heating in winter or to the ejector system for cooling in summer. The solar thermal plant is activated when there is a minimum direct sunshine irradiance of 200 W/m². The collectors cannot use diffuse radiation from the sun. Before carrying the heat to the building, the oil temperature has to warm up to its set point, which is 90 °C for both the heating mode in winter and the cooling mode in summer. As shown in Fig. 2, three-way valves direct the oil to the appropriate heat exchanger. The control system of the plant turns off the collectors when direct sunshine irradiance falls below 200 W/m². The preheating time to warm the 500 litres of oil to 90 °C is about 100 minutes when the irradiance is 200 W/m². The maximum oil temperature is set to 135 °C and when this temperature is reached, some or the entire eight rows of solar collectors are automatically closed in order to prevent overheating of the oil.

Ejector system description

The R-134a refrigerant is used in the ejector system. Ejector operation consists in using a high pressure primary vapor stream mass flow rate (m_1) and expanding it in a supersonic nozzle to entrain and exchange energy with a secondary vapor stream mass flow rate (m_2). The two streams are fully mixed and then compressed inside a diffuser at the end of ejector.

A high pressure refrigerant pump circulates the liquid refrigerant from a refrigerant receiver to a heat exchanger, identified as "Generator" in Fig. 2. Once there, the solar thermal energy provided by the circulating oil allows for the complete evaporation of the refrigerant. A secondary R-134a liquid stream flows from the tank to an expansion valve before reaching the evaporator, where the refrigerant evaporates by collecting heat from the glycol loop of the building's air conditioning system. The vapor refrigerant exiting the ejector is sent to an air condenser that rejects the condensing energy of the R-134a to the outside air, and the liquid refrigerant is returned to the receiver. Finally, a heat exchanger identified below as "Regenerator" is used to recover part of the thermal energy of the vapor refrigerant exiting the ejector to preheat the liquid refrigerant going to the generator, in order to increase the energy efficiency of the cooling system.

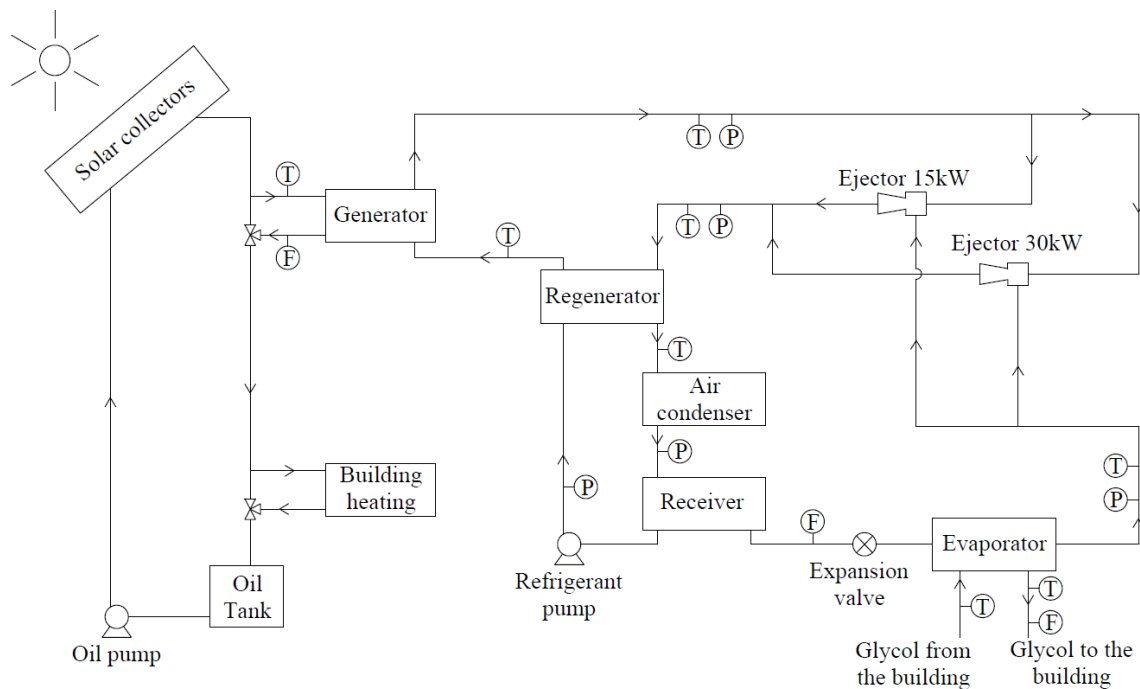


Fig. 2: Schematic of the prototype.

The prototype includes two ejectors of different capacities: 15 kW and 30 kW (Fig. 2) representing the nominal thermal energy requirements at the generator to drive each ejectors. A 1-D thermodynamic model as well as CFD simulations were employed to design the two ejectors and ensure maximum performance at the design point. Figure 3 shows a schematic of the designed ejectors along with their dimensions in Table 2. Utilizing two different ejectors with different capacities provides more flexibility and allows a higher number of hours of operation considering that the energy collected from the solar panels is not constant, but rather varies. Hence, three operating capacities are possible: a low capacity of 15 kW by using the smaller ejector, a medium one of 30 kW by using the larger ejector, and a higher one of 45 kW when both ejectors are used simultaneously. A control strategy was developed and implemented such that the appropriate operating capacity is selected based on the oil temperature, which is a function of the available solar energy.

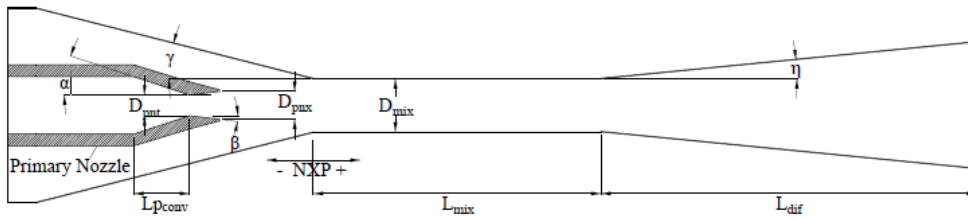


Fig. 3: Schematic of an ejector including geometrical parameters.

Table 2: Ejector Dimensions (all dimensions are in millimetres).

Capacity	α	β	γ	η	D_{pnt}	D_{pnx}	D_{mix}	NXP	L_{pconv}	L_{mix}	L_{dif}
15 kW	10.0°	6.5°	14.2°	3.1°	3.06	4.19	7.08	-16.4	13.5	36.8	172
30 kW	10.0°	6.5°	14.2°	3.1°	4.33	5.92	10.01	-23.0	19.2	54.6	145

The building air conditioning system is using a conventional chiller system located in the mechanical room. This chiller cools a glycol loop that, in turn circulates in all parts of the building to meet the cooling load. The ejector cooling system receives the glycol stream returning from the building upstream of the chiller, when the glycol is at its highest temperature. The ejector cooling system cools the glycol upstream of the chiller, thus reducing its electrical consumption.

The prototype is equipped with pressure, temperature and flow measurements allowing for mass and energy balance for the refrigerant, the oil and the glycol loops. A data acquisition system provides the values of all instruments, at two-second intervals. The performance of the ejector cooling prototype is evaluated using the cooling capacity ($Q_{cooling}$) and the compression ratio, defined by the two equations below:

$$Q_{cooling} = m_{gly} \cdot C_{p_{gly}} \cdot (T_{in} - T_{out})_{gly} \quad (1)$$

$$\text{Compression ratio} = P_{out} / P_2 \quad (2)$$

Where m_{gly} is the glycol mass flow rate, $C_{p_{gly}}$ is the glycol specific heat capacity, T_{in} and T_{out} are the glycol inlet and outlet temperatures at the evaporator, P_{out} is the ejector outlet pressure, and P_2 is the ejector secondary inlet pressure, which is also the evaporation pressure. To operate the prototype, the first step is to start the solar power plant in order to warm up the oil. A minimum oil temperature of 100 °C is necessary for the ejector cooling system to operate. At that moment, the cooling system refrigerant pump can be started and set at a primary pressure of 3000 kPa. The glycol is then allowed to flow to the evaporator, and the air condenser fan can be switched on. The expansion valve is set in a position allowing the refrigerant temperature in the evaporator to be about 1 °C below the leaving glycol temperature.

Results and discussion

Figure 4 presents typical results of the $Q_{cooling}$ and compression ratio for the two ejectors operated independently, calculated based on summer 2019 collected data. Fig. 4a shows that the 15 kW ejector produced a cooling effect of about 6 kW for a nominal thermal energy consumption of 15 kW, which corresponds to a thermal efficiency of 40% (which is roughly what is expected from thermally driven ejector cooling system). Fig. 4b shows, however, that

the 30 kW ejector produced a cooling effect of about 9 kW for a nominal thermal energy consumption of 30 kW, which corresponds to a thermal efficiency of 30%. The lower efficiency in Fig. 4b is due to the higher compression ratio of about 2.0, compared to about 1.8 in Fig. 4a. The compression ratio results from a combination of the evaporation pressure, which is a function of the glycol temperature coming from the building, and the condensation pressure, which is a function of the outside air temperature. Thus, the compression ratio fluctuates from day to day and also throughout the day, which continuously influences the cooling effect from the ejectors.

The cooling system's electrical coefficient of performance (COP_e) is the ratio between the cooling capacity (kW) and the electrical consumption (kW). The following three components consume a significant amount of electricity: the oil pump, the refrigerant pump and the three air condenser fans. The oil pump has a fixed average consumption of 1.5 kW; the refrigerant pump consumes 0.4 kW for the 15 kW ejector, and 0.6 kW for the 30 kW ejector; and all three air condenser fans consume 1 kW each. Since two fans were used, for the most part, the electricity consumption of the air condenser is assumed to be 2 kW. This leads to an electrical coefficient of performance of 1.5 for the 15 kW ejector, and of 2.2 for the 30 kW ejector. Results are summarized below in Table 3. The use of a more efficient oil pump would improve the COP_e . Moreover, setting-up the ejector-cooling system differently so that the condensation heat is rejected into the ground, thus eliminating the electrical consumption of the air condenser, would also greatly improve the COP_e .

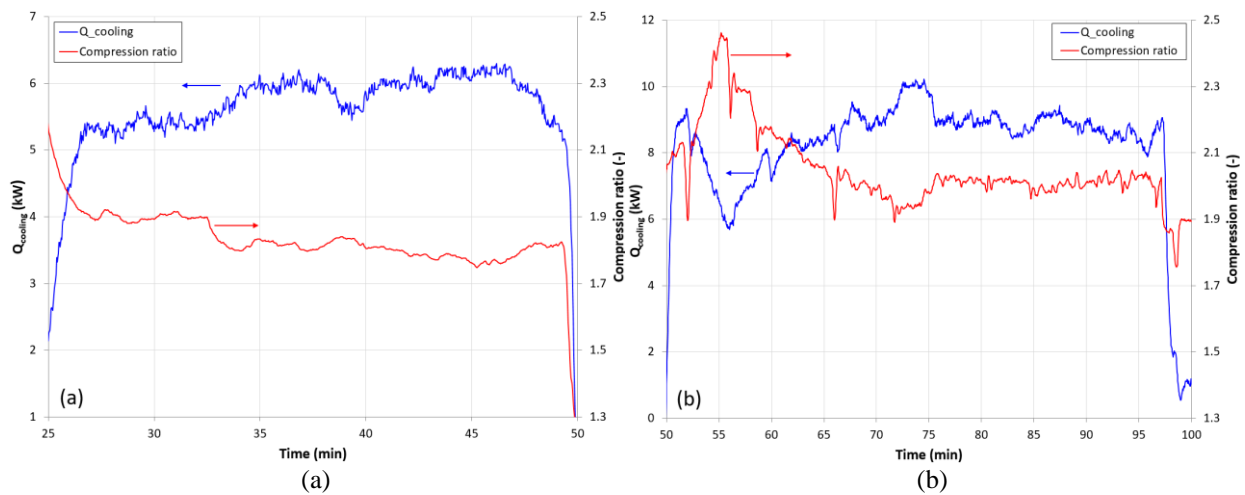


Fig. 4: Typical results of $Q_{cooling}$ and the Compression ratio for the two ejectors operated independently; (a) 15 kW ejector and (b) 30 kW ejector.

Table 3 - Cooling capacity, electrical consumption and electrical COP.

Ejector	Electrical consumption			$Q_{cooling}$ (kW)	COP_e (-)
	Fans (kW)	Refrigerant Pump (kW)	Oil Pump (kW)		
15 kW	2	0.4	1.5	6	1.5
30 kW	2	0.6	1.5	9	2.2

Conclusions

The testing of a solar ejector cooling system prototype in a real environment setting allowed to confirm the potential of such system to decrease the electrical consumption of an institutional building's main air conditioning system. This demonstration project allowed as well to confirm that a multi-ejector arrangement is an appropriate strategy to deal with fluctuation of solar irradiance over the operating time. The two installed ejectors of different capacity (15 kW and 30 kW), operated according to the solar thermal energy input, and both demonstrated good thermal efficiency ranging from 30% to 40%. Ways to increase the electrical COP of the solar ejector cooling system could be investigated further. They include the adoption of a system allowing to reject the heat into the ground, instead of an air condenser.

Acknowledgements

The Government of Canada through the Office of Energy Research and Development (OERD) of Natural Resources Canada provided the funding for this project.

References:

- [1] Sarbu I, Sebarchievici C. *Review of solar refrigeration and cooling systems*. Energy and Buildings 2013;**67**:286–297.
- [2] Abdulateef JM, Sopian K, Alghoul MA, Sulaiman MY. *Review on solar-driven ejector refrigeration technologies*. Renewable and Sustainable Energy Reviews 2009;**13**:1338–1349.
- [3] Anand S, Gupta A, Tyagi SK. *Solar cooling systems for climate change mitigation: A review*. Renewable and Sustainable Energy Reviews 2015;**41**:143–161.

Vortex Tube Thermodynamic Model Operating with Two-Phase Fluids

A. Mansour^{1*}, J. Lagrandeur¹, S. Poncet¹

¹Mechanical Engineering Department, Université de Sherbrooke,
2500 boulevard de l'Université, Sherbrooke (QC), J1K 2R1, Canada

*Corresponding author: ahmed.mansour@USherbrooke.ca

Abstract (12-pt Times New Roman)

A thermodynamic model is presented to estimate the vortex tube energy separation in terms of enthalpies of hot and cold exits. The model is a modified version of a previously developed model for real gases. It is validated using two-phase propane and evaluates the cold exit enthalpy with a maximum difference error of 1.78 % and 5.95 % for the hot exit enthalpy. The model is also implemented in a parametric analysis using transcritical carbon dioxide to study how the energy separation behaves using two-phase fluids. As the liquid forms inside the vortex tube, the energy separation stays significant even though it declines as the inlet flow quality decreases. Finally, if the inlet flow quality is high enough, the flow of both hot and cold exits can be in two-phase conditions.

Keywords: Vortex tube, Two-phase, Carbon dioxide, Thermodynamic model.

Introduction

The vortex tube is a simple device aiming at separating a fluid into two streams. One is usually separated at a lower enthalpy (or in many cases temperature) than the inlet enthalpy and the other at a higher enthalpy (temperature). This phenomenon is known as energy (temperature) separation. The device was invented by Ranque in the 1930s [1]. However, it became more popular when Hilsch [2] improved the design and provided more understanding of its working mechanism. Because of its simplicity, low maintenance quality and its intriguing mechanism, the interest has been increasing over the years to understand the mechanism behind the energy separation and to diversify its potential applications.

The vortex tube typically consists of multiple inlet nozzles leading to a main vortex chamber and a tube with two exits, the cold exit and the hot exit. The most popular configurations of the vortex tube are the counter-flow and the parallel-flow. However, in the recent years, the research is more focused on counter-flow vortex tubes due to their better performance [3]. The major difference between both is the location of the cold and hot exits. Both exits are located on one side in parallel-flow vortex tubes, meanwhile for counter-flow vortex tubes, each is located on opposite side of the other. In a counter-flow vortex tube, the fluid enters through tangential nozzles, generating a flow with high swirl velocity in the vortex chamber. The flow then separates into core cold stream and periphery hot stream throughout the tube.

Even though most studies used air as the working fluid, the research community is now shifting towards testing various other working fluids that may be needed for different applications of the vortex tube. Thakare and Parekh [4] conducted a numerical study using air, nitrogen, carbon dioxide (CO₂) and oxygen. They concluded that nitrogen provides the maximum temperature difference between hot and cold exits, while carbon dioxide offers the least temperature difference. Aydın and Baki [5] performed experimental trials with three gases: air, oxygen and nitrogen. For every inlet pressure tested, nitrogen proved to provide the optimum cold temperature difference, while air showed the least. Wang and Suen [6] presented a comparison between air and two refrigerants used in refrigeration and air conditioning cycles: R134a and R600. For

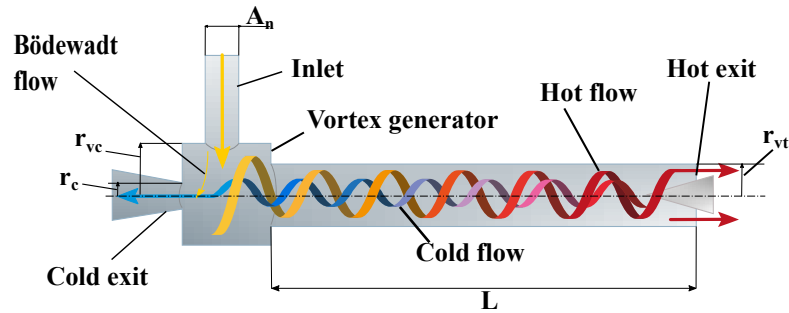


Figure 1. Schematic view of a counter-flow vortex tube.

either cooling or heating in terms of exit temperatures, air showed a clear superiority over both refrigerants for every cold mass fraction tested. Both refrigerants presented marginal difference in heating, while R600 exhibited a better cooling effect than R134a. Kırmacı *et al.* [7] made an exergy analysis using oxygen, nitrogen and argon. They conducted their experiments under a pressure range of 150 – 700 kPa for different numbers of inlet nozzles and a fixed cold mass fraction of 0.5. Based on their results, argon exhibited the highest exergetic efficiency for every nozzle number and at all inlet pressures. On the other hand, nitrogen showed the maximum exergy losses among other gases even though air showed the lowest exergy efficiency. Liang *et al.* [8] used a numerical model (ANSYS Fluent) to simulate a vortex tube using $\text{CO}_2\text{-CH}_4$ mixtures at different molar fractions of CO_2 . They concluded that cold temperature difference and cooling power are better as the CO_2 fraction decreases. However, the coefficient of performance decreases with CO_2 fraction reduction.

On the other hand, the studies handling incompressible or two-phase flows are still quite scarce, due to the degradation in the energy separation performance that might happen. Balmer [9] used a commercial vortex tube to test the temperature separation using liquid water as a working fluid. Their experiments concluded that a temperature separation of up to 20 degrees is possible given that the inlet pressure is high enough (20–50 MPa). Collins and Lovelace [10] performed experiments to evaluate the performance of the vortex tube using two-phase propane. They studied not only the temperature separation but also carried out an energy separation analysis represented in the study of the exit enthalpies. Using a fixed value of inlet pressure, they stated that above an inlet vapor mass quality of 0.8, a significant temperature separation still exists. On the other hand, as the quality decreases below 0.8, the temperature difference between both cold and hot exits becomes insignificant even though the energy separation is still maintained with a substantial enthalpy difference between both exits.

Many thermodynamic models have been proposed to predict the vortex tube performance [11]. Liew [12] developed a model based on the perfect gas assumption where the length to diameter ratio is restricted to be larger than 20. He developed the model based on a simplified radial momentum equation, the ideal gas law and the isentropic flow assumption in the inlet. He also adopted a combination of two reasons for the occurrence of energy separation. The first is the presence of the radial pressure gradient due to the centrifugal force. He explained that gas pockets expand and compress between the vortex tube periphery and core while transporting energy. The second is the higher kinetic energy in the periphery flow that transforms into heat. It predicted temperatures with an average error of around 1.1% compared to the experimental data. As an improvement over Liew's model [12], Lagrandeur *et al.* [13] extended the model by considering the effects of inlet nozzles' friction and the Bödewadt boundary layer in the

inlet plane, which greatly improved the predictions at low cold mass fractions. It was validated with the air experimental data of Camiré [14] and they showed that it greatly outperforms the predictions of Liew's model [15].

The analytical models developed previously were dependent on the ideal gas assumption. However, these models are not suitable to work with real gases nor at high pressure conditions. Mansour *et al.* [16] presented a model tackling this problem. Their model uses the virial EoS and CoolProp to account for the deviation from the ideal gas assumption. The model was validated using air, CO₂ and R134a and was compared to the ideal gas model of Lagrandeur *et al.* [13]. Both models showed a similar prediction of exit temperatures for air. However, the real gas model exhibited a significant enhancement over the ideal gas model for exit temperatures predictions for CO₂ and R134a.

In this study, a modification to the thermodynamic real gas model of Mansour *et al.* [16] is carried out. The goal of this modification is to broaden the capability of the model to evaluate the energy separation performance of vortex tubes working with two-phase fluids. The model is validated with the experimental data of Collins and Lovelace [10] and a parametric study is executed to assess the vortex tube performance operating under transcritical CO₂ heat pump conditions.

Thermodynamic Model

In this section, the two-phase fluid model development process is described in details. The model is similar to that of Mansour *et al.* [16] with some modifications to expand its operating scope to include two-phase fluids.

Just after the inlet nozzles expansion, Mansour *et al.* [16] calculates the pressure and density distributions along the inlet plane depending on the virial EoS and the isothermal inlet plane assumption. As long as the fluid behaves as a gas, this methodology proved to be efficient in the evaluation of exits' temperatures. However, as the expanded flow moves into the two-phase region, the virial EoS becomes invalid. In addition, there is not enough information on whether the isothermal assumption holds when operating with two-phase fluids. Hence, an isentropic inlet plane flow assumption is adopted and the momentum equation is solved numerically to obtain the pressure and density distributions. The isentropic flow assumption was also utilized by Deissler and Perlmutter [17] for vortex tube turbulent flow depending their assumption on meteorological observations of isentropic relation between pressure and temperature for atmospheric altitude change. Moreover, Mischner and Bepalov [18] adopted the same assumption with suggesting the use of isentropic efficiency dealing with perfect gas.

As a first step, several reasonable assumptions are taken into consideration to facilitate the derivation process:

- Steady state flow
- A much higher swirl velocity in comparison to the axial ($u_\theta \gg u_z$) and radial ($u_\theta \gg u_r$) components in the inlet plane
- The axial derivative is neglected compared to the radial one ($\frac{\partial}{\partial r} \gg \frac{\partial}{\partial z}$)
- Isentropic process in the inlet nozzles and along the inlet plane
- Isobaric cold exit flow
- Presence of a forced vortex
- Negligible velocity at the hot exit

The model aims at predicting the exit enthalpies (temperatures) of the vortex tube, and in order to achieve this, the following parameters are taken as inputs to the model:

- Total inlet (P_{0in}) and exit (P_h and P_c) pressures
- Cold mass fraction (μ_c), which is the cold exit to inlet mass flow rates ratio (\dot{m}_c/\dot{m}_{in})
- Total inlet specific enthalpy (h_{0in})
- Radii of vortex tube (r_{vt}), vortex chamber (r_{vc}) and cold exit (r_c)

The most challenging section in the model is to develop an equation connecting the flow properties at the nozzles exit to the cold exit flow properties, and that explains most of the assumptions implemented in the inlet plane. Otherwise, the nozzles flow is solved using the isentropic acceleration assumption while the hot exit properties are computed using the energy equation.

Accounting for the above mentioned assumptions and the continuity equation, a simplified radial momentum equation writes:

$$\frac{\partial P(r)}{\partial r} = \frac{u_\theta^2 \rho(r)}{r} \quad (1)$$

where P , r , u_θ and ρ are the static pressure, radius, swirl velocity and density, respectively. To handle the density term in Eqn. (1), the virial equation of state (EoS) is used instead of the perfect gas law. The implementation of the virial EoS opens the possibility of operating with real gases and at high pressures. In the present model, the pressure series expansion of the virial EoS is utilized:

$$\frac{PV_m}{RT} = 1 + B^*P + C^*P^2 + D^*P^3 + \dots \quad (2)$$

where V_m , T and R are the fluid's molar volume, static temperature and universal gas constant. B^* , C^* , \dots , called virial coefficients, are temperature-dependent.

The second integral term of Eqn. (1) is the swirl velocity. Liew [12] derived a mathematical correlation of the inlet plane swirl velocity based on experimental and numerical tests. Based on his study, the flow is in a forced vortex state from the vortex tube center up to its radius (r_{vt}). However, if there is a vortex chamber, the velocity becomes almost constant in it:

$$u_\theta(r) = \begin{cases} \omega_e r & 0 < r < r_{vt} \\ \omega_e r_{vt} & r_{vt} < r < r_{vc} \end{cases} \quad (3)$$

where ω_e is the rotation rate at the nozzles exit. Combining both Eqns. (2) and (3) into Eqn. (1), the pressure in the resultant equation can then be integrated between the cold exit (P_c at $r = 0$) and the nozzles exit (P_{in} at $r = r_{vc}$) to get:

$$\ln\left(\frac{P_{in}}{P_c}\right) + B^*(P_{in} - P_c) + \frac{C^*}{2}(P_{in}^2 - P_c^2) = \frac{\omega_e^2 r_{vt}^2}{R_s T_{in}} \left(\frac{1}{2} + \ln\left(\frac{r_{vc}}{r_{vt}}\right)\right) \quad (4)$$

where T_{in} and R_s are the nozzles exit static temperature and the specific gas constant, respectively.

To evaluate the exit enthalpies (temperatures) of the vortex tube, the following procedure is followed:

1. Using the inlet total properties (P_{0in} and h_{0in}), the entropy (s_{in}) is calculated.

2. Assuming a value for ω_e , the inlet static enthalpy (h_{in}) is evaluated:

$$h_{in} = h_{0in} - \frac{\omega_e^2 r_{vt}^2}{2} \quad (5)$$

3. Using the isentropic nozzles flow assumption, a value for the static pressure (P_{in}) is obtained.
4. Using Eqn. (4) and since every term is known, P_{in} is recalculated and compared to the one obtained from the previous step. The iteration process is continued on ω_e until a difference error between both pressure values is less than 0.5 %.
5. To proceed with the following steps, density distribution ($\rho(r)$) along the inlet plane, has to be calculated. This step is the major difference with Mansour et al.'s [16] study. To calculate $\rho(r)$, they used the virial EoS which is not suited for two-phase fluids. Hence, another iteration process is performed using Eqn. (6), which is just a reorganized version of Eqn. (1). The right hand side can be computed accurately. However, for the left hand side, a final integration value of pressure is assumed and with the isentropic inlet plane flow assumption, the density is computed and the integration is solved numerically:

$$\int_{P_c}^{P(r)} \frac{\partial P(r)}{\rho(r)} = \int_0^r \frac{u_\theta^2 \partial r}{r} \quad (6)$$

6. The axial cold exit velocity is uniformly computed:

$$u_z = \frac{\dot{m}_c}{\int_0^{2\pi} \int_0^{r_c} \rho(r) r \partial r \partial \theta} \quad (7)$$

where \dot{m}_c is the cold mass flow rate and θ is the rotational angle.

7. Benefiting from the isentropic inlet plane flow and the input P_c , the cold exit static enthalpy (h_c) is computed.
8. The cold exit total enthalpy is calculated using the following equation:

$$h_{0c} = h_c + \frac{u_z^2}{2} + \frac{u_z}{\dot{m}_c} \int_0^{2\pi} \int_0^{r_c} \frac{u_\theta^2(r)}{2} \rho(r) r \partial r \partial \theta \quad (8)$$

9. Using the calculated value of h_{0c} from Eqn. (8) and P_c , the total cold exit temperature (T_{0c}) is computed.
10. On the other side, the hot exit total enthalpy is calculated using the conservation of energy:

$$h_{0h} = \frac{h_{0in} - \mu_c h_{0c}}{(1 - \mu_c)} \quad (9)$$

11. Finally, the hot exit temperature (T_{0h}) is computed using the knowledge of both h_{0h} and P_h .

Lagrandeur et al. [13] considered the frictional losses in inlet nozzles and the Bödewadt boundary layer as improvements to the model developed by Liew [12]. In this study, the Bödewadt boundary layer flow is taken into account. It has proved to be important for low cold mass fractions. The approximated Eqn. (10) developed by Gutsol [19] is used as a simple representation of the Bödewadt boundary layer mass flow rate escaping from the inlet to the cold exit.

$$\dot{m}_{bl} = 25 r_c \rho(r_c) \sqrt{[(r_{vt} - r_c) \nu \omega_e r_{vt}]} \quad (10)$$

where ν is the fluid kinematic viscosity.

For the inlet frictional losses, they are not considered here, since the equations used to recalculate the properties are dependent upon the ideal gas law and there is no knowledge by the authors of the existence of similar equations for real gases or two-phase flows [20]. In addition, the nozzles' friction is only a minor contribution to the exergy consumed in vortex tubes using air [21].

Moreover, a correction factor of h_{0h} is used to prohibit it from approaching infinity when the value of μ_c approaches 1 in Eqn. (9). Lagrandeur et al. [21] suggested a similar factor applied to the cold exit temperature before using the conservation of energy to calculate the hot exit temperature. The equation suggested for the correction factor writes:

$$h_{0h} = h_{0h@μ=0.1} - (h_{0h@μ=0.1} - h_{0u}) \tanh [A(1 - \mu_c)] \quad (11)$$

$h_{0h@μ=0.1}$ is the hot exit enthalpy calculated by Eqn. (9) at a cold mass fraction of 0.1, h_{0u} is the cold exit enthalpy computed by Eqn. (8) and A is a scaling factor that controls the transition value between 0 and 1 of the tanh function and is equal to 1.5. Finally, h_{0c} is recalculated to comply with the conservation of energy.

Results and Discussion

This section discusses the validation process of the model with two-phase propane experimental data. Then, the model is utilized to perform a parametric analysis using carbon dioxide as a working fluid. Phenomena noticed with CO₂ are compared to those observed by Collins and Lovelace [10] in their experiments. Hence, the conclusion will be deduced on whether two-phase CO₂ exhibits similar behaviour as a two-phase propane or not. The selection of CO₂ is based on the fact that transcritical CO₂ vortex tube is part of a heat pump system simulated within the same project.

Table 1. Operating parameters of the two-phase propane experiments of Collins and Lovelace [10].

Parameter	Value
P_{0in} (MPa)	0.791
P_c (MPa)	0.103
P_h (MPa)	0.173 - 0.191
\dot{m}_{in} (g/s)	1.44 - 1.79
r_{vt} (mm)	2.78
r_c (mm)	1.015

Initially, the model is validated with the experimental data of Collins and Lovelace [10]. Their two-phase propane data are suitable to test the ability of the model to predict the energy separation. Table 1 displays the operating and geometrical parameters of their vortex tube. These values are used as input parameters in the model.

Table 2 shows the discrepancies on exit enthalpies between the experiments of Collins and Lovelace [10] and the present model, for eight data points, which represent every point falling

Table 2. Exit enthalpies ($kJ \cdot kg^{-1}$). Comparison between the present thermodynamic model and the experiments of Collins and Lovelace [10].

Test	Inlet			Cold exit				Hot exit		
	x_{0in}	h_{0in}	μ_c	x_c	$h_{0c,exp}$	$h_{0c,model}$	Error (%)	$h_{0h,exp}$	$h_{0h,model}$	Error (%)
1	0.58	451	0.80	0.77	428	434	1.46	544	511	5.95
2	0.69	488	0.79	0.85	464	468	0.99	578	556	3.74
3	0.71	493	0.79	0.89	480	473	1.39	544	561	3.27
4	0.8	525	0.77	0.94	503	501	0.25	599	599	0.11
5	0.81	531	0.78	0.97	515	507	1.45	589	606	2.96
6	0.82	531	0.79	0.98	518	508	1.78	577	607	5.27
7	0.84	541	0.77	0.97	516	515	0.12	621	617	0.57
8	0.89	557	0.82	1.03	540	535	0.81	632	643	1.82

within the range of two-phase flow ($x_{in} < 1$). The model provides very good predictions compared to the experiments. It evaluates the cold exit enthalpy with an average error of 1.03 % and a maximum of 1.78 % only. Meanwhile for the hot exit enthalpy, the error rises slightly into an average of 2.96 % and a maximum of 5.95 %. Based on these presented data, there is no clear trend on discrepancies' variation. The independent variable that is significantly changing is the inlet flow quality (x_{in}), and regardless, the differences with experiments seem to be independent of the change with x_{in} .

Table 3. Operating and geometrical conditions of the parametric analysis.

Parameter	Value
P_c (MPa)	1
P_h (MPa)	4
T_{0in} (K)	330
\dot{m}_{in} (g/s)	40
r_{vt} (mm)	3.15
r_c (mm)	1.45

The second part of this section presents a parametric analysis using the thermodynamic model with CO₂. To perform this analysis, Table 3 exhibits the fixed parameters used in this study. P_c and P_h are selected to ensure a transcritical expansion in the vortex tube and to provide a high energy separation, while \dot{m}_{in} was selected as a compliance with a typical heat pump mass flow rate order of magnitude [22]. The geometrical parameters, r_{vt} and r_c , are the same as those used by Zhu [23].

Figs. 2, 3 and 4 present the variations of both cold and hot exits' enthalpies with the cold mass fraction for different inlet pressures: 8 MPa, 11 MPa and 14 MPa. The figures also exhibit the difference between hot and cold enthalpies for each condition (above each bar). The first observation is the consistent rise of h with the increase of μ_c , which is a typical energy separation behaviour noticed in different studies [10, 18]. The second significant observation is that if P_{0in} increases, the difference between hot and cold enthalpies declines. This is coincident with what is noticed in Table 4: as P_{0in} increases, x_{in} decreases. Therefore, as the flow quality at the inlet decreases, the energy separation also declines. The explanation can be that some of the liquid droplets, due to their small size, gets evaporated during the energy separation process. Therefore, the drop in enthalpies is noticed. However, even though the quality reaches around

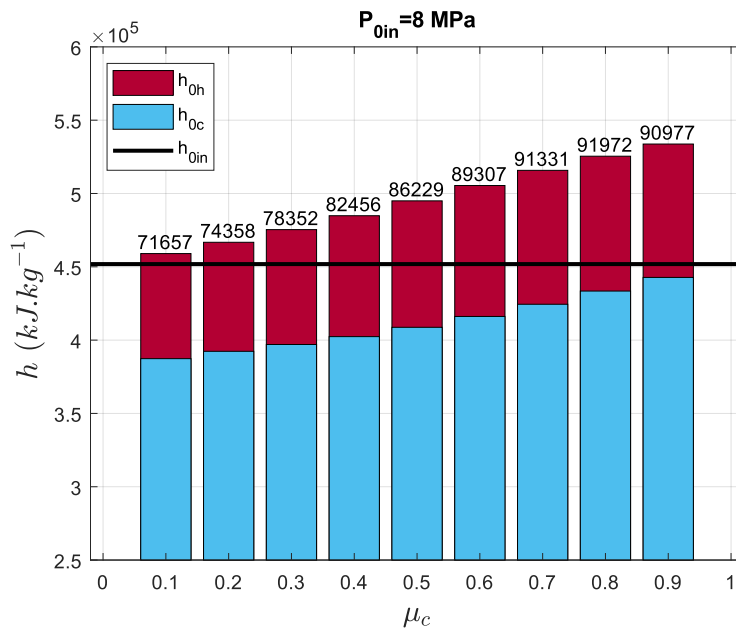


Figure 2. Variation of hot and cold exit enthalpies with the cold mass fraction for an inlet pressure of 8 MPa.

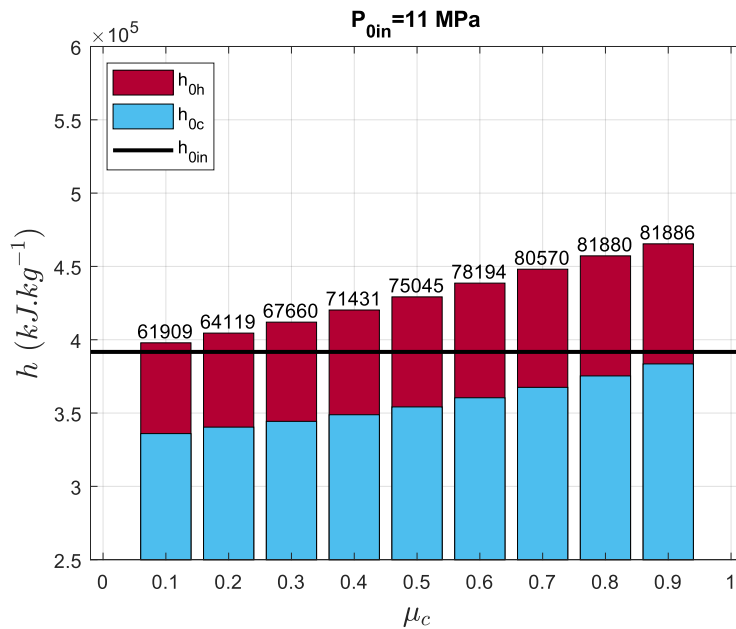


Figure 3. Variation of hot and cold exits' enthalpies with the cold mass fraction for an inlet pressure of 11 MPa.

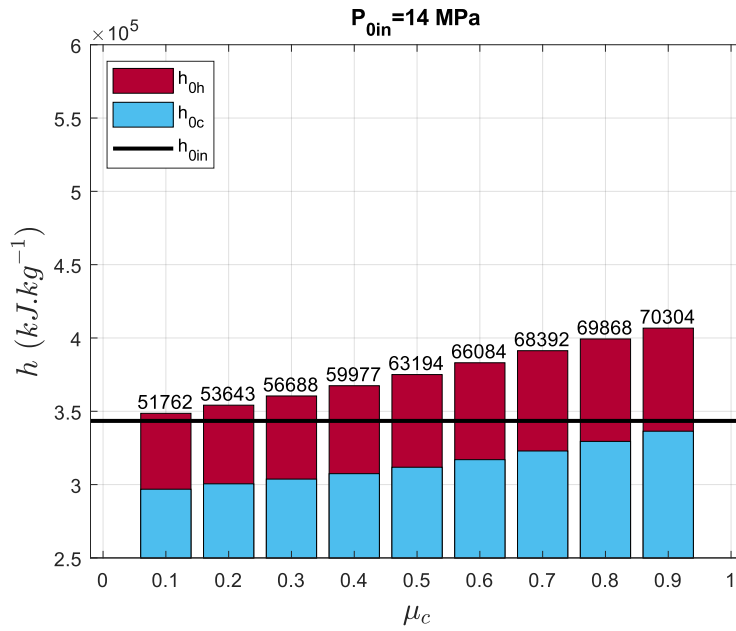


Figure 4. Variation of hot and cold exit enthalpies with the cold mass fraction for an inlet pressure of 14 MPa.

0.5, the energy separation is still possible. This is in agreement with Collins and Lovelace's conclusion [10].

Table 4 also indicates that the flow qualities at the exits (x_c and x_h) are significantly affected by the quality of the inlet flow, especially the cold exit quality. The table presents the maximum and minimum qualities corresponding to the lowest and highest cold mass fractions, respectively, for both exits. As the inlet quality decreases, the quality of both exits also decreases. A remarkable observation is at $x_{in} = 0.91$, the quality of the cold exit is lower. This is mainly due to the assumption of the isentropic expansion from the nozzles exit down to the vortex tube core (isentropic inlet plane). This trend will be only observable whenever x_{in} is high as the opposite is noticed for $x_{in} = 0.69$ and $x_{in} = 0.53$. A final conclusion that can be extracted from the table is that as x_{in} keeps on decreasing and μ_c is low enough, liquid droplets can be noticed from the hot exit side. This is why Collins and Lovelace [10] operated at high cold mass fractions so that the flow from the hot exit could be purely vapor and could be measured with only pressure and temperature sensors.

Table 4. Inlet and exits flow qualities and their variation with inlet pressure.

P_{0in} (MPa)	8	11	14
x_{in} (-)	0.91	0.69	0.53
x_c (-)	0.84-0.88	0.69-0.71	0.57-0.58
x_h (-)	1	0.86-1	0.68-0.9

Conclusions

A modified version of the thermodynamic real gas model of Mansour *et al.* [16] was introduced to deal with two-phase flow conditions inside the vortex tube. The model was validated with the experimental data of Collins and Lovelace [10] using propane and a fairly good agreement

was obtained for all conditions in terms of both cold and hot exit enthalpies. In addition, a short parametric analysis was performed to validate, compare and study the phenomena discussed by Collins and Lovelace [10], however, using carbon dioxide. Carbon dioxide was selected for this study as it will be used as a vortex tube refrigerant in a heat pump system for further future studies. The most significant finding is that as the liquid forms due to expansion in the vortex tube, the device still holds its capability to produce energy separation.

Acknowledgments

The authors would like to thank the support of the NSERC chair on industrial energy efficiency established at Université de Sherbrooke in 2019 and funded by Hydro-Québec (Laboratoire des technologies de l'énergie), Natural Resources Canada (CanmetEnergy-Varenes) and Emerson Commercial and Residential Solutions.

References

- [1] G. J. Ranque, "Experiments on expansion in a vortex with simultaneous exhaust of hot air and cold air," *Journal de Physique et le Radium*, vol. 4, no. 7, pp. 112–114, 1933.
- [2] R. Hilsch, "The use of the expansion of gases in a centrifugal field as cooling process," *Review of Scientific Instruments*, vol. 18, no. 2, pp. 108–113, 1947.
- [3] U. S. Gupta, M. K. Joshi, and C. B. Pawar, "Experimental performance evaluation of counter flow vortex tube," *Journal of Environmental Research And Development*, vol. 7, no. 1A, pp. 496–502, 2012.
- [4] H. R. Thakare and A. Parekh, "Computational analysis of energy separation in counter—flow vortex tube," *Energy*, vol. 85, pp. 62–77, 2015.
- [5] O. Aydın and M. Baki, "An experimental study on the design parameters of a counterflow vortex tube," *Energy*, vol. 31, no. 14, pp. 2763–2772, 2006.
- [6] Z. Wang and K. Suen, "Numerical comparisons of the thermal behaviour of air and refrigerants in the vortex tube," *Applied Thermal Engineering*, vol. 164, no. 114515, 2020.
- [7] V. Kırmacı, O. Uluer, and K. Dincer, "An experimental investigation of performance and exergy analysis of a counterflow vortex tube having various nozzle numbers at different inlet pressures of air, oxygen, nitrogen, and argon," *Journal of Heat Transfer*, vol. 132, no. 12, 2010.
- [8] F. Liang, H. Wang, and G. Tang, "Temperature separation characteristics of CH₄–CO₂ binary gas mixture within a vortex tube," *International Journal of Thermal Sciences*, vol. 161, no. 106726, 2021.
- [9] R. T. Balmer, "Pressure-driven Ranque-Hilsch temperature separation in liquids," *Journal of Fluids Engineering*, vol. 110, no. 2, pp. 161–164, 1988.
- [10] R. L. Collins and R. B. Lovelace, "Experimental study of two-phase propane expanded through the Ranque-Hilsch tube," *Journal of Heat Transfer*, vol. 101, no. 2, pp. 300–305, 1979.
- [11] J. Lagrandeur, S. Poncet, and M. Sorin, "Review of predictive models for the design of counterflow vortex tubes working with perfect gas," *International Journal of Thermal Sciences*, vol. 142, pp. 188–204, 2019.
- [12] R. Liew, *Droplet behaviour and thermal separation in Ranque-Hilsch vortex tubes*. PhD thesis, Technische Universiteit Eindhoven, the Netherlands, 2013.
- [13] J. Lagrandeur, S. Poncet, M. Sorin, and M. Khennich, "Thermodynamic modeling and artificial neural network of air counterflow vortex tubes," *International Journal of Thermal Sciences*, vol. 146, no. 106097, 2019.
- [14] J. Camiré, "Experimental investigation of vortex tube concepts," Master's thesis, University of British Columbia, Vancouver, Canada, 1995.

- [15] R. Liew, J. C. H. Zeegers, J. G. M. Kuerten, and W. R. Michalek, “Maxwell’s demon in the Ranque-Hilsch vortex tube,” *Physical Review Letters*, vol. 109, no. 054503, 2012.
- [16] A. Mansour, J. Lagrandeur, and S. Poncet, “Thermodynamic modeling of vortex tubes working with real gases,” in *Canadian Society for Mechanical Engineering International Congress*, vol. 4, June 2021.
- [17] R. Deissler and M. Perlmutter, “Analysis of the flow and energy separation in a turbulent vortex,” *International Journal of Heat and Mass Transfer*, vol. 1, no. 2, pp. 173–191, 1960.
- [18] J. Mischner and V. Bepalov, “Zur Entropieproduktion im Ranque–Hilsch–Rohr,” *Forschung im Ingenieurwesen*, vol. 67, no. 1, pp. 1–10, 2002.
- [19] A. F. Gutsol, “The Ranque effect,” *Physics-Uspekhi*, vol. 40, no. 6, pp. 639–658, 1997.
- [20] F. White, *Fluid mechanics*. McGraw-Hill series in mechanical engineering, McGraw Hill, 2011.
- [21] J. Lagrandeur, S. Croquer, S. Poncet, and M. Sorin, “Exergy analysis of the flow process and exergetic optimization of counterflow vortex tubes working with air,” *International Journal of Heat and Mass Transfer*, vol. 152, no. 119527, pp. 1–17, 2020.
- [22] S. Taslimi Taleghani, M. Sorin, S. Poncet, and H. Nesreddine, “Performance investigation of a two-phase transcritical CO₂ ejector heat pump system,” *Energy Conversion and Management*, vol. 185, pp. 442–454, 2019.
- [23] J. Zhu, “Experimental investigation of vortex tube and vortex nozzle for applications in air-conditioning, refrigeration, and heat pump systems,” Master’s thesis, University of Illinois, Urbana-Champaign, USA, 2015.

Nomenclature			
Acronym		ω	Rotational speed ($rad.s^{-1}$)
CO ₂	Carbon dioxide	ρ	Density ($kg.m^{-3}$)
EoS	Equation of State	B^*	Pressure expansion second virial coefficient ($m.s^2.kg^{-1}$)
Indices		C^*	Pressure expansion third virial coefficient ($m^2.s^4.kg^{-2}$)
0	Total (stagnation) condition	h	Specific enthalpy ($J.kg^{-1}$)
θ	Tangential	P	Pressure (Pa)
c	Cold exit	R	Universal gas constant ($J.mol^{-1}.K^{-1}$)
e	Nozzle exit	r	Radius (m)
h	Hot exit	R_s	Specific gas constant ($J.kg^{-1}.K^{-1}$)
m	Molar	s	Specific entropy ($J.kg^{-1}.K^{-1}$)
r	Radial	T	Temperature (K)
vc	Vortex chamber	u	Velocity ($m.s^{-1}$)
vt	Vortex tube	V	Volume ($m^3.mol^{-1}$)
z	Axial	x	Vapor quality (–)
Symbol			
\dot{m}	Mass flow rate ($kg.s^{-1}$)		
μ	Mass fraction (–)		
ν	Fluid kinematic viscosity ($m^2.s^{-1}$)		

Design and experimental validation of a R290 dual-source reversible heat pump prototype

X. Peña^{1*}, L. Alonso¹, J. Iturralde¹ and A. Agirre¹

¹Tecnalia, Energy and Environment Division, Area Anardi, 5, Azpeitia E20730, Spain

*Corresponding author: xabier.pena@tecnalia.com

Abstract

The R290 based dual source heat pump (DSHP) has a specifically designed dual source heat exchanger (DSHX), able to work as a condenser or evaporator, exchanging heat with brine coming from geothermal boreholes, directly with air or against both simultaneously in a smart way without complicate control strategies and the requirement of secondary water loops is avoided.

Predictive models have been developed for the DSHX working as condenser or evaporator with Propane (R290) as refrigerant. The models developed enable us to face the dimensioning and simulation of DSHX evaporator and condenser using brine or air as heat source/sink.

This study presents the experimental results of a dual-source 10 kW reversible heat pump prototype, tested in a climatic chamber in all the possible working modes. The experimental campaign has served to validate the models developed for designing the DSHX.

Keywords: Dual-source heat pump, Heat pump, Dual-source Heat Exchanger, Experimental validation, Propane, R290.

Introduction/Background

The geothermal heat pumps require a proper sizing of the installation and dimensioning of the boreholes. An enlargement of the installation required due to an increase of heating/cooling demands leads to a higher quantity of boreholes. If the geothermal installation is not properly enlarged, risk of saturation is plausible. In addition, the drilling cost of the boreholes is something to be considered when an expansion of the installation is proposed. On the other hand, a properly designed geothermal installation in combination with a clever heat pump could achieve high COP/EER values and therefore a reduction of the electrical consumption in comparison with aérothermal heat pumps.

Aérothermal installations are cheap but the achieved COP/EER depends on the ambient temperature changes; therefore, so does electricity consumption.

With the aim of combine the benefits of both worlds in a unique device dual source heat pumps (DSHP) were developed. Commercially, dual source heat pumps (DSHP) are water/water HP which use alternatively water coming from geothermal boreholes or from a secondary 'air to water' heat exchanger (fan-coil). This strategy complicates the operation of the heat pump. Some researchers tried to develop a DSHP implementing the dual source/sink: water and air, directly into the heat pump design.

Cai et al. 2017 [1], have numerically analysed an indirect DSHP having in parallel an air source evaporator and PV/T panels. The key problem identified is that the distribution of the refrigerant fluid in the two evaporators strongly affect the performance of the DSHP, and it depends on the environmental conditions.

Dynamic modelling and energy performance analysis of a Dual source Heat pumps using both, a plate heat exchanger or fin and tube heat exchanger alternatively based on a combination of

3-way valves in the refrigerant circuit was developed by Grossi et al., 2018 [2]. They concluded that DSHP can be suggested for the replacement of conventional ground coupled heat pumps in presence of undersized BHEs when a significant modification of the building energy demand occurs. In addition, they pointed out that energy losses linked to the defrost cycles are avoided using DSHP-s.

Corberan et al. 2018 [3], tested and characterized a DSHP prototype, it was an outdoor ‘plug & play’ unit, working with R32 refrigerant and including a variable speed compressor. Their development considered that the dual-source heat exchange was accomplished by means of two independent parallel heat exchangers. Although in principle, two heat exchangers in parallel could be used simultaneously, during the experimental campaign realized that it was extremely difficult to control the amount of refrigerant distributed between them and thus only one source was used at a time. It was concluded that the DSHP system would be able to reach efficiencies close to the Ground Source HP system (yearly SPF_4 around 3.6) with half the length of boreholes.

Based on a similar concept of “air-source” and “water-source” evaporators, connected in series and operated alternatively, Besagni et al., 2019 [4], carried out a field study of a R410A based dual-source Heat pump using solar PVT panel’s refrigeration water or air as heat source. In the present study PVT panels were able to support the “water-source” evaporator of the DSHP in the winter/spring seasons and support the production of DHW in the summer season. According to the author, compared with a “baseline” air-to-water heat pump a reduction of 15.4% daily averaged energy consumptions was achieved. As previously mentioned, the possibility of avoiding defrost cycles was mentioned, as well, in the present study.

In addition, the refrigeration brine/water coming from a PVT panel combined with air was used in the experimental and analytical study of an innovative integrated dual-source evaporator for solar-assisted heat pumps by Simonetti et al., 2019 [5]. An Indirect Solar-Assisted, R410A based, Heat Pump (I-SAHP) with an Integrated Dual-Source Evaporator was tested by them. Different configurations of the dual source evaporator were tested but, in all configurations, air is the heat transfer medium from the water to the refrigerant, therefore there is not direct exchange between the refrigerant and the brine/water coming from the PVT panel. They claim that the system proposed has higher COP in comparison with a standard Air-Source Heat Pump (ASHP), with a relative improvement of 14% maximum.

Lazzarin et al. 2020 [6], develop a performance analysis based on dynamic simulation by Trnsys of the plant designed for a refurbished building, based on water-water geothermal heat pump based on R410A, combined with glazed PVT panels. The most efficient solution is the alternative 60 m² PVT + 300 m boreholes. They claimed that, increasing the solar field to a certain extent permits to reduce the ground field extension with better performances and lower costs.

The current work focuses on the integration between a reversible R290 heat pump and a specially designed dual source heat exchanger (DSHX) which allows a combination of different sources/sinks, for cooling and heating. Direct heat exchange in between the refrigerant and air or brine coming from the boreholes is produced in the same unit, i.e. the Dual Source Heat eXchanger (DSHX). The DSHX developed in the frame of Tri-HP project is able to do combine both sources/sinks in a smart way without complicate control strategies and the requirement of secondary water loops is avoided. Being a reversible heat pump the DSHX acts as evaporator in space heating/DHW working mode or as a condenser in space cooling working mode.

Not only dual installations are going to benefit from the currently developed dual source heat pump (DSHP), but district or local cooling-heating networks as well could benefit with the possibility of using both sources/sinks, e.g. for compensating the ring that it is decompensated because unexpected demands, and so on.

Design of the Dual Source Heat Pump (DSHP) prototype

The interest in propane as refrigerant is increasing during the last years due to its thermodynamic and transport properties. Being a natural refrigerant with very low global warming potential (GWP=3), its main handicap is the issue of being flammable (A3 classified by ASHRAE). Lately, there are many heat pump manufacturers which include propane heat pumps among their products, or which are working on development of heat pumps using this natural refrigerant.

The prototype incorporates scroll inverter technology in order to improve the efficiency, adapting the performance to different operating conditions and minimizing the part load losses. Based on the compressor availability for the required 10 kW R290 DSHP, the selected compressor is model YHV0461U-9E9-ABK (R290) provided by Emerson.

Inclusion of a DSH was decided in order to make use of the high compressor discharge temperatures for DHW generation. Based on the working conditions, Alfa Laval's CB30 unit was selected, with 16 plates.

Regarding the internal unit or the Space Conditioning Heat eXchanger (SCHX), of the reversible DSHP, the AC30 with 40 plates was selected, working either as evaporator or condenser depending on the operation mode. The AC30 unit includes unremovable integrated refrigerant distributor in S3 (refrigerant inlet in cooling duty, outlet in heating duty). It is normally used in reversible heat pumps, since the AC30 should not give any trouble in heating duty, considering that the outlet refrigerant is subcooled and therefore the pressure drop created by the distribution holes is just negligible.

Electronic expansion valve (EEV) model EXL-B1G/ EXL-125 supplied by Emerson was implemented in the prototype in order to keep control of the superheat. In addition, the 4 way valve in order to achieve the switching between cooling mode and heating mode by changing the flow path of refrigerant was included. Selected valve model was the SHF-20D-46-02, based on the refrigerant circuit lines' diameter (mainly suction and discharge 3/4" and 1/2" respectively) and on the required capacity for both cooling and heating modes.

Considering that the critical component of the present DSHP prototype is the Dual Source Heat eXchanger (DSHX), a thorough description of the mentioned component is going to be presented in a specific section.

Design of the Dual Source Heat eXchanger (DSHX) prototype

In order to design a DSHX able to work as evaporator and condenser, and in each case able to exchange heat with both heat source/sinks, air and water/brine coming from geothermal boreholes; a design which fulfils with the heat exchange surface's requirements for each of the four different working modes has been developed. In order to perform the design, four different design tools have been defined for determining the capacity of each DSHX working mode and its required heat exchanging surface.

With the aim of developing the four dimensioning tools, deterministic models have been implemented in EES (Engineering Equation Solver) [7] based on geometry of air source heat exchangers or coils, for air source/sink evaporator/condenser and on coaxial tube heat exchangers' geometry for geothermal source/sink evaporator/condenser.

In the following subsections each of the deterministic models developed are described and the correlations used for determining the refrigerant and secondary fluid heat transfer coefficients are presented.

Air source condenser dimensioning tool

The developed model has been divided in 3 different zones: the desuperheating zone, the two-phase zone and the subcooling zone. The addition of the required heat exchange surfaces for each zone is going to be the surface of the total heat exchanger derived from the defined geometry. Therefore, a percentage of the total surface is dedicated to desuperheating, another percentage is dedicated to condensing and the last percentage until 100% to subcooling. The subprogram will calculate which percentage corresponds to each of the defined zones based on working conditions.

The DSHX model working as an air condenser has been developed using the ϵ -NTU method for each of the zone's in which the model has been subdivided. In addition, the energy balances in the coil have been implemented in each of the subprograms (Desuperheating/Condensing/Subcooling) in both tube and external or air side, as well as in the tube wall.

Regarding the Heat Transfer Coefficient (HTC) of the air side, the correlation proposed by Wang et al. [8] was selected and the HTC validated against a reference HX calculation software.

On the other hand, for the calculation of the sensible HTC of the refrigerant side in the desuperheating and subcooling zones, the following correlations have been implemented depending on the flow regime (laminar, transitional or turbulent):

- In laminar regime ($Re < 3.000$), the HTC has been determined by the correlation proposed by Shah and London [9].
- In turbulent regime the implemented correlation for Re numbers in between 3.000 and 10.000 is the one proposed in the VDI heat Atlas [10].
- For transitional flow an interpolation between the results obtained for laminar flow and turbulent flow ($3.000 < Re < 10.000$) correlations has been carried out in agreement with the strategy proposed by Nellis and Klein [11].
- Finally, for turbulent regimes with Reynolds numbers higher than 10.000 the Dittus-Böelter [12] correlation has been used.

For the calculation of the HTC in the condensing zone the correlation recently proposed by Shah [13][14] has been implemented.

Finally, two more procedures have been defined in the model in order to calculate the pressure drop trough the coil in the air and in refrigerant side. The model uses the correlations proposed by Wang et al. [8] for the air side and the correlation proposed by Ould Didi, Kattan and Thome [15], for two phase pressure drop on the tube side.

Air sink evaporator dimensioning tool

The developed model has been divided in two different zones, the two-phase zone and the superheating zone. The sum of the required heat exchange surfaces for each zone is going to be the surface of the total Heat exchanger derived from the defined geometry. Therefore, a percentage of the total surface is dedicated to evaporating and the rest of the surface to superheating. The subprogram will calculate which percentage corresponds to each of the defined zones based on working conditions.

A dehumidifying coil normally removes both moisture and sensible heat from entering air. In the DSHX working as evaporator, the air cooled is a mixture of water vapour and dry air gases. Both lose sensible heat when in contact with a surface cooler than the air. The removal of latent heat

through condensation occurs only on the portions of the coil where the surface temperature is lower than the dew point of the air passing over it.

When the coil starts to remove moisture, the cooling surfaces carry both the sensible and latent heat load. As the air approaches saturation, each degree of sensible cooling is nearly matched by a corresponding degree of dewpoint decrease. The latent heat removal per degree of dew-point change is considerably greater. A subprogram has been defined in which the coil under completely dry and completely wet regimes has been simulated according to the air and refrigerant streams input conditions and the physical properties of the selected coil. Calculation of the efficiency of fins in both dry and wet regimes has been taken into account in the present model. The efficiency of fins has been calculated using Bessel functions according to [16]. The dry coil calculation has been developed using the ϵ -NTU method.

On the other hand, for the calculation of wet coil different methods have been tested; but finally, a modified version of the model proposed in [17] has been implemented. That method is based on mean logarithmic temperature difference (LMTD) and on the mean effective difference in air enthalpy between airstream and surface (LMHD). In addition, the energy balances in the evaporator are implemented in the subprogram in both tube and external or air side, as well as in the tube wall.

This model is based on ϵ -NTU and LMTD and LMHD equations and uses Braun's [18] hypothesis to simulate the behaviour of the evaporator's air side. A procedure has been defined in order to implement the Braun's hypothesis, which generally leads to an error less than 5% of the total energy rate.

The evaporator has been discretised in 2 zones: an evaporation and a superheating zone. For the sensible heat transfer, the same correlations described for the calculation of sensible zones of the condenser model have been implemented (see previous section). On the other hand, the correlations proposed by Mishima et al. [19] and Shah [20] have been implemented for the evaporation zone. It should be mention that the results obtained by both correlations are in agreement.

In addition, in order to calculate the HTC of the air side, the correlation proposed by Wang et al. [8] has been selected for both wet and dry regimes. Finally, as in air source condenser case, two more procedures have been defined in the model in order to calculate the pressure drop trough the coil in the air side, and for the two-phase pressure drop in tube side.

Ground source condenser dimensioning tool

As in case of the air source condenser dimensioning tool, the developed model has been divided in three different zones: the desuperheating zone, the two-phase zone and the subcooling zone. The sum of the required heat exchange surfaces for each zone is going to be the surface of the total heat exchanger derived from the defined geometry. Therefore, a percentage of the total surface is dedicated to desuperheating, another percentage is dedicated to condensing and the last percentage until 100% to subcooling. The subprogram will calculate which percentage corresponds to each of the defined zones based on working conditions. In case of the ground source dimensioning tool, the heat exchange will take place in a coaxial tube HX, but the dimensioning should be in agreement with the number of tubes, circuits diameters, etc. of the air source heat exchanger.

The method employed in order to calculate the three subprograms included in the ground source condenser dimensioning tool is the ϵ – NTU (effectiveness – Number of Transfer Units). The ϵ – NTU is considered the most suitable method when the available inputs are the streams' supply conditions and the geometry of the heat exchanger, and the objective is to obtain the exhaust

conditions of each stream. The method is implemented combined with energy balances on both sides (Refrigerant/Brine) and on the wall.

The correlations implemented for the calculation of the HTC in the refrigerant side in the desuperheating and subcooling zones, are previously described in the air source condenser section. In addition, the same correlations have been implemented for the Brine/Water side.

On the other hand, for in tube condensing HTC, the correlation proposed by Shah [13] [14] has been employed as in the case of the air source condenser dimensioning tool. Finally, two more procedures have been defined in the model in order to calculate the pressure drop through the coaxial Heat exchanger in the Brine side, using the classical theory of Darcy Weisbach with the friction factor proposed on ref [22] and for the two phase pressure drop on the external tube side of the coaxial HX the proposed by Ould Didi, Kattan, Thome [15] based on Friedel's correlation.

Ground sink evaporator dimensioning tool

The developed model has been divided in two different zones the, the two-phase zone and the superheating zone, as in the case of the air source evaporator dimensioning tool. The sum of the required heat exchange surfaces for each zone is going to be the surface of the total heat exchanger derived from the defined geometry. Therefore, a percentage of the total surface will be dedicated to evaporating and the rest of the surface to superheating. The subprogram will calculate which percentage corresponds to each of the defined zones based on working conditions.

As in the case of the ground source condenser dimensioning tool the method employed in order to calculate the two subprograms included in the ground source evaporator dimensioning tool is the ϵ -NTU (effectiveness –Number of Transfer Units).

In order to obtain the sensible heat transfer coefficient for the refrigerant side in the superheating zone and in the brine side, the correlations implemented depending on the flow regime are already presented in the air sink evaporator's section.

On the two-phase zone, as in case of the air source evaporator dimensioning tool, the correlations proposed by Mishima et al. [19] and Shah [20] have been implemented.

Finally, two more procedures have been defined in the dimensioning tool in order to calculate the pressure drop through the coaxial heat exchanger in the refrigerant and in the brine side. In the procedures the modification of the Friedel correlation proposed by Ould Didi, Kattan and Thome [15] has been used for the two-phase pressure drop calculation. The classical theory of Darcy-Weisbach has been implemented using the friction factor proposed on [22] in order to obtain the pressure-drop on the tube side.

Geometry of manufactured first DSHX prototype

The selected geometry, which fulfils the design requirements, manufactured by Koxka group, is detailed in the following paragraph:

Tube pitch= 55E-3 (m); Row pitch= 27.5E-3 (m); Tube length= 0.9 (m); External tube's outer diameter= 15.875E-3 (m); Internal tube's outer diameter= 9.52E-3 (m); External tube thickness= 0.38E-3 (m); Internal tube thickness= 0.78 E-3 (m); Number of tubes per row= 16; Number of rows= 6; Number of circuits= 6; Fin pitch= 2.5 E-3 (m); Fin thickness= 0.11E-3 (m).



Figure 1. Dual source Heat exchanger (DSHX) prototype

Experimental campaign, Results and discussion

DSHP in cooling mode using air as heat sink

In cooling-air working mode, the DSHX acts as air dissipated condenser. Therefore, the SCHX works as evaporator in the dual source heat pump. The heat pump was tested for different ambient temperatures 27 °C, 35 °C and 45 °C, chilling water from 12 °C-7 °C and from 23 °C -18 °C, at its nominal operating point with compressor working at 70 rps and at different partial loads at 40, 50, and full load 90 rps. The EER and cooling power for testing points at different compressor speeds (rps) and SCHX and DSHX supply streams temperatures are presented in the following Figures.

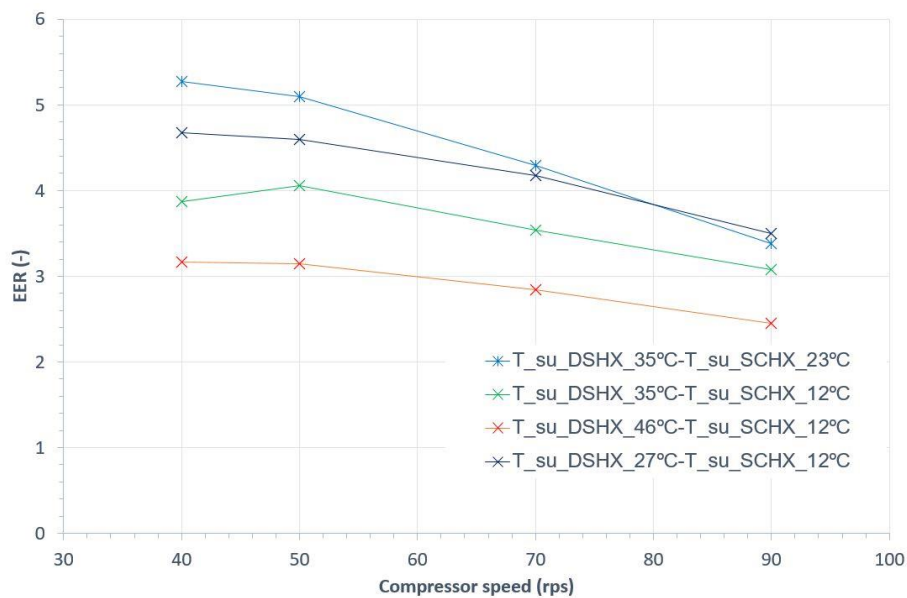


Figure 2. EER, for DSHP at different compressor speeds (rps). Obtained for different SCHX and DSHX supply streams temperatures.

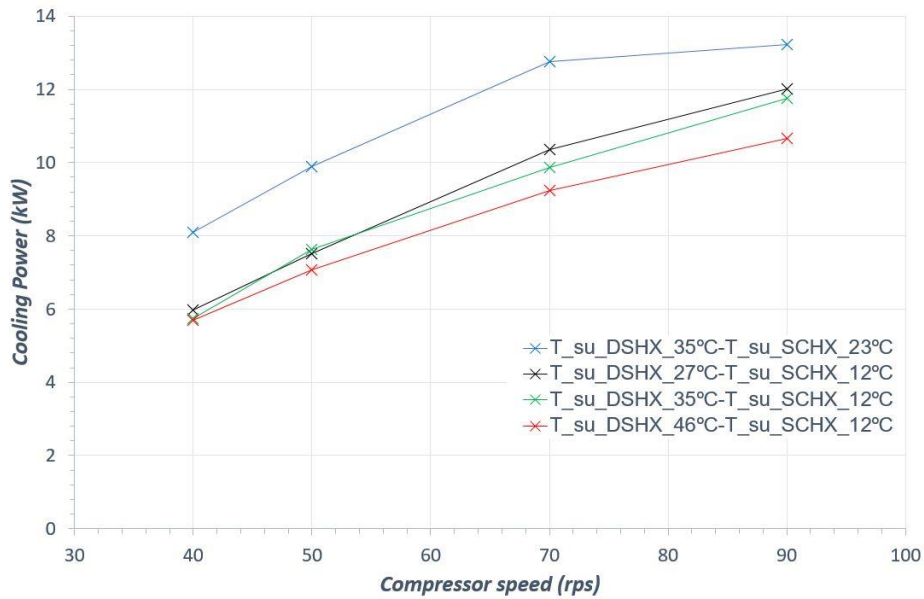


Figure 3. Cooling power, for DSHP at different compressor speeds (rps). Obtained for different SCHX and DSHX supply streams temperatures.

In figure 4, it could be seen the deviation between the condenser capacity estimated by the dimensioning tool and the experiment one. The deviation is below 10 % for all of the testing points. Therefore, the numerical model can be used for predicting the capacity of the DSHX as air source condenser. The model tends to slightly over-predict the behavior of the DSHX in air condenser mode, but differences below 10 % are acceptable.

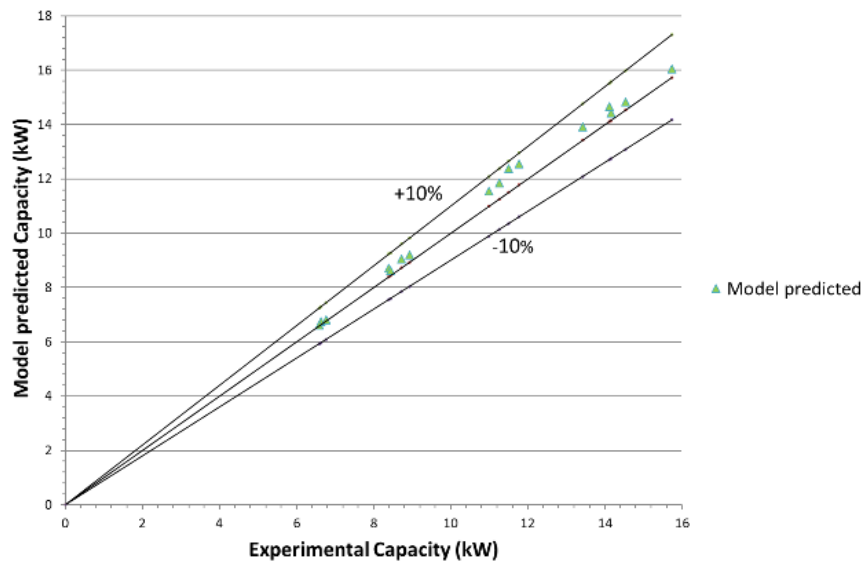


Figure 4. Heat capacity deviation between predictive model and real behaviour of the DSHX working as air cooled condenser.

DSHP in heating mode using air as heat source

At heating mode, the DSHX acts as an evaporator, therefore the SCHX works as a condenser and the DSHP is producing space heating. Based on testing points defined, the DSHP was tested for 7 °C ambient air temperature, producing warm water from 30 °C to 35 °C, from 40 °C to 45 °C, from 47 °C to 55 °C and from 52 °C to 60 °C. The testing campaign was developed with the

compressor at its nominal operating point, 70 rps and at different partial loads: 50 rps, 60 rps and 90 rps (full load). The testing points at different conditions are presented in the following figures.

Due to an abnormal refrigerant pressure drop on the DSHX, the achieved COP and SCHX power values are lower than expected in heating mode. This aspect related to the pressure drop in the evaporator is a critical point discovered during the testing campaign. Values below 0.5 bar were expected, i.e. experimental values are around 4 times higher. Consequently, the evaporation temperature was lower than expected. Values of pressure drop up to 1.9 bar were achieved at highest compressor speed. These values are unacceptable and as a result the difference between suction and discharge pressure in the compressor is elevated up to 4 K.

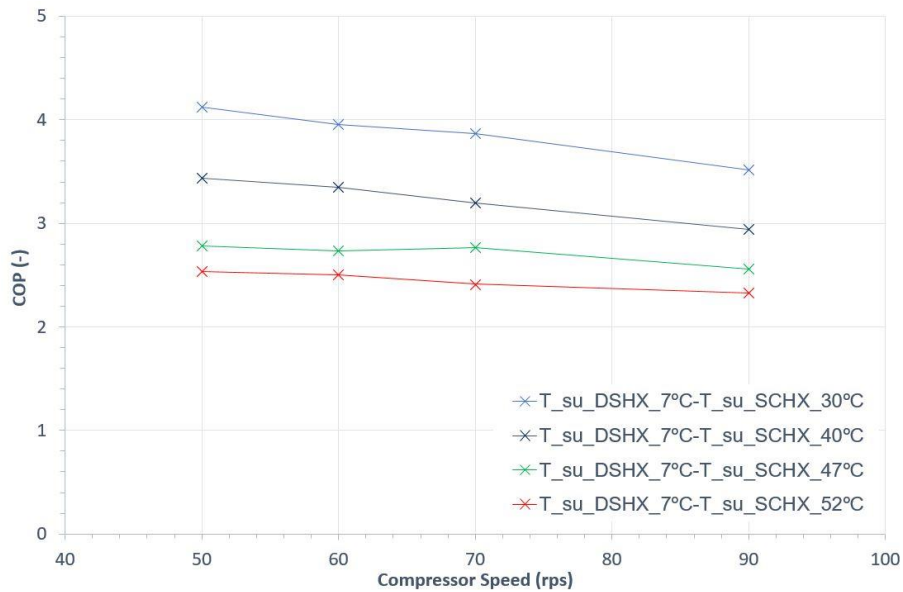


Figure 5. COP achieved by DSHP for different compressor speeds (rps). In different SCHX working conditions.

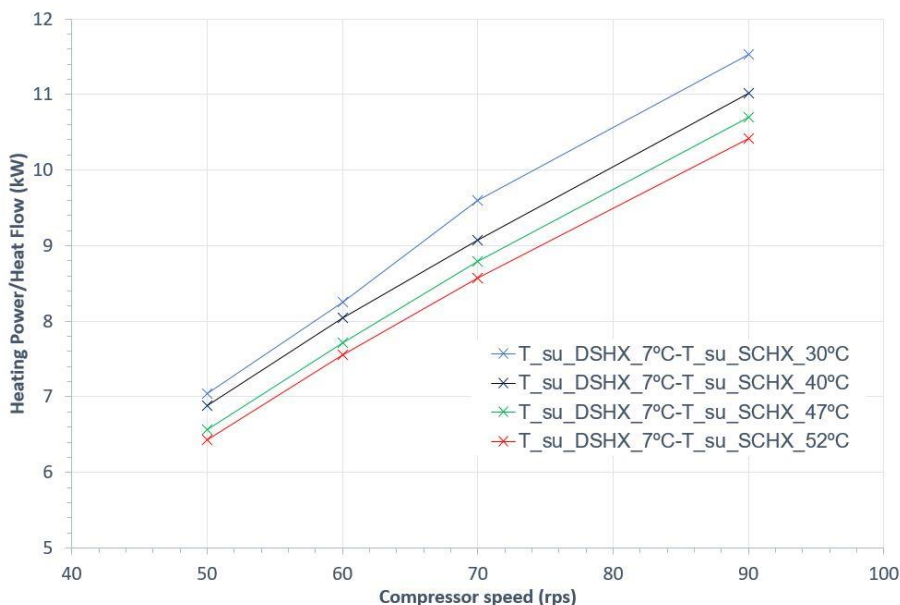


Figure 6. Heat flow achieved by DSHP for different compressor speeds (rps). In different SCHX working conditions.

Taking into account that at the condensing mode, the values of refrigerant pressure drop inside the coaxial tubes were lower than 10 kPa, and at evaporation mode these values increase up to 190 kPa, it is clear that the origin of that huge pressure drop falls on the only circuit difference in

between the evaporator and condenser modes, i.e. the distributor. Apparently, an incorrect selection of the mentioned distributor was made by the manufacturer.

In figure 7, the deviation between the DSHX capacity estimated by the dimensioning tool and the experimental results can be observed. The deviation is below 10 % for all of the testing points. Therefore, the numerical model can be used for predicting the capacity of the DSHX as air source evaporator. It should be mentioned that the capacity obtained from the thermodynamic model was obtained introducing the refrigerant pressure drop values obtained experimentally

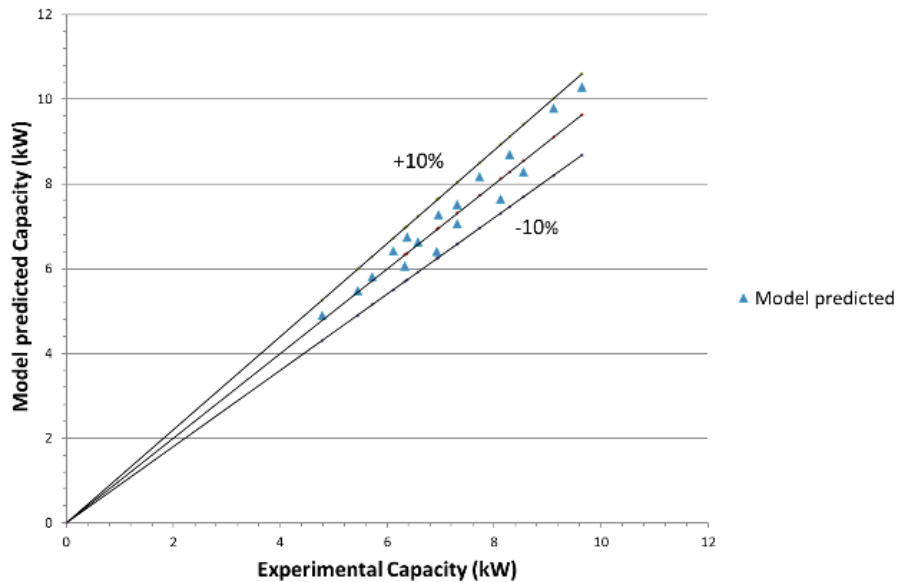


Figure 7. Capacity deviation between predictive model and real behaviour of the DSHX working as air evaporator.

DSHP in cooling mode using water as heat sink

Furthermore, the DSHP working as a water-water chiller, with the DSHX working as a condenser using brine or water from the geothermal boreholes was experimentally tested. In the present case, the SCHX works at evaporator mode.

The DSHP was tested for different water sink (rejection) temperatures, i.e. 25 °C and 30 °C. A cold-water supply from 12 °C to 7 °C was analyzed. The compressor speed varied from its nominal operating point at 70 rps, to different partial loads at 50 rps, 60 rps, as well as at a full load at 90 rps. The testing points at different conditions are presented in the following figure.

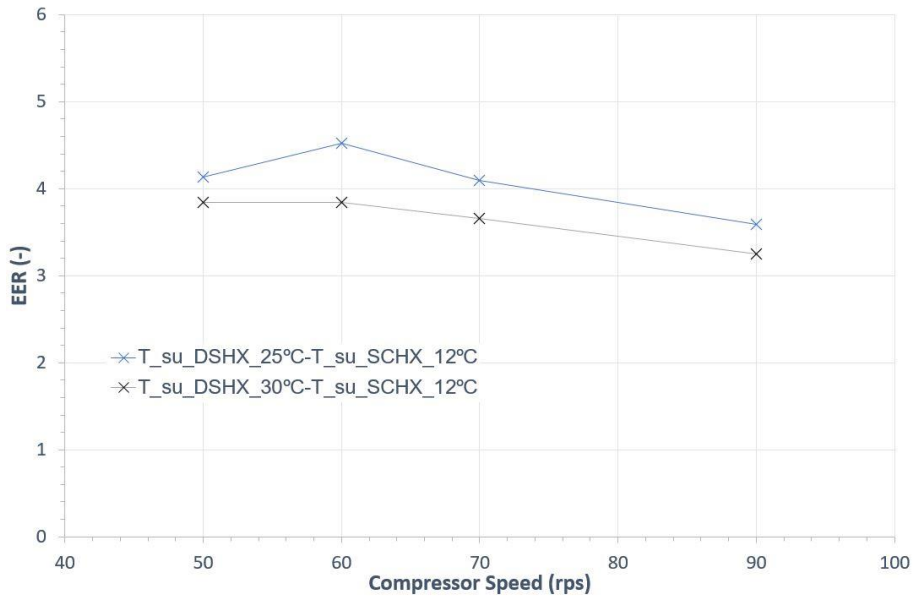


Figure 8. EER against compressor speed, for different DSHX supply temperatures.

It should be mentioned that, as it happened with the pressure drop on the refrigerant side in the air sink DSHX, values around 10 kPa or below are achieved in the water sink DSHX. Pressure drop values achieved in condenser mode in the range of 10 kPa are acceptable values for the refrigerant side, which contrast with the values achieved in evaporator mode. As previously mentioned, in condenser mode, there is not a distributor in the entrance of the DSHX. Therefore, the high pressure drops in evaporator mode are caused by an inappropriate distributor.

The following figure shows the deviation between the dimensioning tool estimated DSHX heat flow and the experimentally obtained value. As it can be seen in Figure 9, the deviation for the same testing conditions is below 15% for all the points tested. The model overpredicts slightly the behavior of the DSHX at ground source condenser mode, but the difference could be considered acceptable.

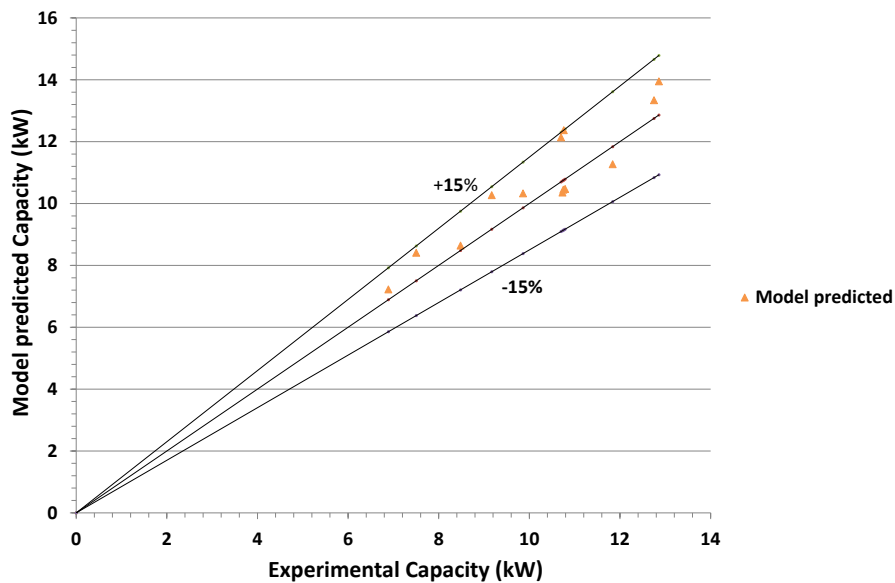


Figure 9. Capacity deviation between predictive model and real behaviour of the DSHX working as ground source condenser.

DSHP in heating mode using water as heat source

The DSHX acts as an evaporator but in this case using water instead of air to evaporate the refrigerant. The water coming from the boreholes flows through the internal tube, delivering heat to the annulus part of the coaxial tube, where the refrigerant evaporates. Furthermore, the SCHX performs as a condenser receiving hot water from Space Heating water loop at 30 °C and 40 °C.

The DSHP has been tested for different water source temperatures, 7 °C, 12 °C and 16 °C to delivery warm water on the SCHX at 35 °C and 45 °C. Several compressor speeds have been investigated from 50 rps to 90 rps. The testing points at different conditions are presented in the following figures. Tendencies can be observed in Fig. 10 and 11 showing the influence of compressor speed on the heat capacity of SCHX and the COP, for different DSHX water/brine supply temperatures.

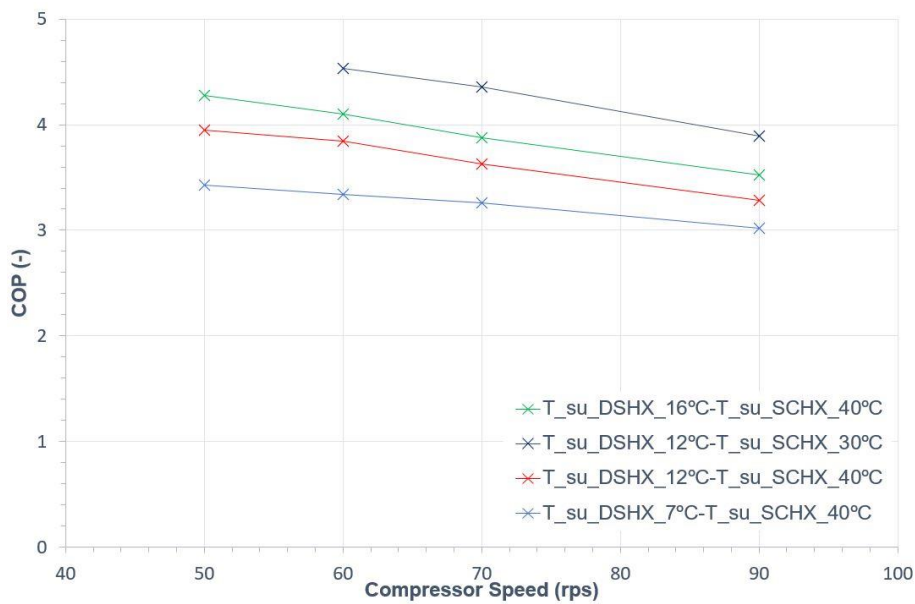


Figure 10. COP against compressor speed, for different DSHX and SCHX supply temperatures.

The COP and the Heating power values are lower than expected, as it happened when using air as the heat source for the evaporator, the pressure drops achieved in the refrigerant side are very high, due to inappropriate distributor. For the highest compressor velocity (5400 rpm), the pressure drop achieves values up to 2 bar, which are too high values. Consequently, the evaporation temperature falls up to 4 K respect to the expected.

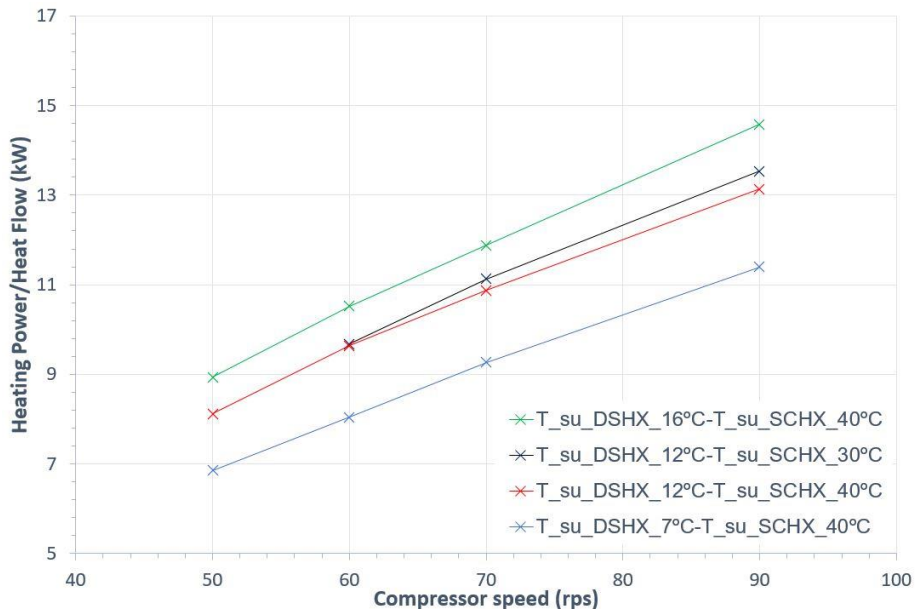


Figure 11. Heating power against compressor speed, for different DSHX and SCHX supply temperatures.

Figure 12 shows the deviation between the experimentally measured heat flow of the DSHX acting as an evaporator and the calculated by the deterministic model/_dimensioning tool. As mentioned previously, the experimentally achieved refrigerant pressure drops in the DSHX were reproduced in the deterministic model in order to obtain the DSHX’s capacity: Therefore, a fair comparison between the experimental and numerical model simulated results was performed. As can be seen the deviation is below 10% for all of the testing points. Therefore, the numerical model predicts the evaporation heat with a good accuracy and could be used as dimensioning tool.

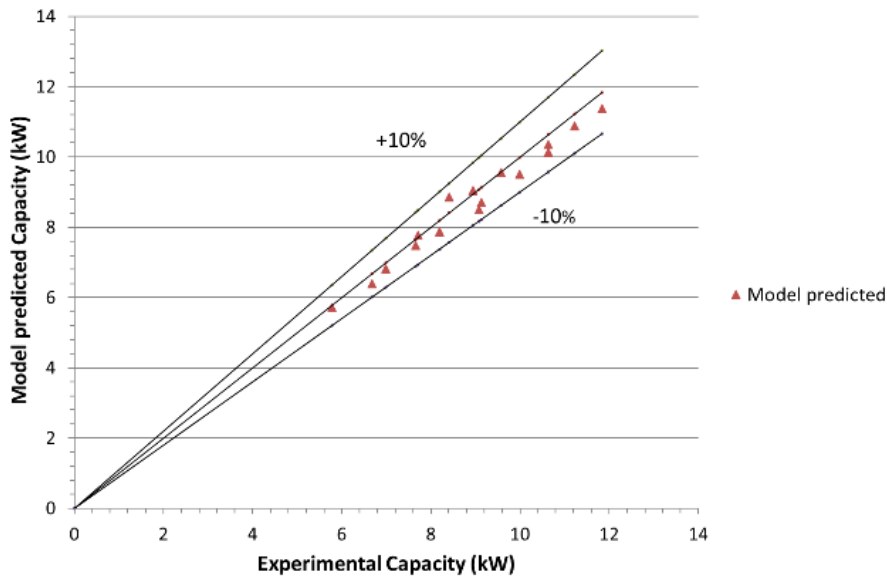


Figure 12. Capacity deviation between predictive model and real behaviour of the DSHX working as ground sink evaporator.

Summary/Conclusions

An experimental testing campaign was conducted to investigate the performance of a Dual source Heat Pump (DSHP) and the innovative Dual source heat exchanger (DSHX) working in a steady state propane reversible Heat Pump. The performance of the DSHX working as evaporator and condenser, both using air or water as heat source/sink was analysed. The DSHP shows promising

performance under the design conditions and the achieved results are in agreement with the expected values in cooling mode and a deviation was found in heating working mode. The experimental results indicate that the dual Source heat exchanger can be a promising technology for developing Dual Heat pumps able to combine both air and/or water as heat source/sink in an efficient way.

In air-water heating mode the DSHP achieved a heating power of 9.1 kW and a COP of 3.2 at design conditions (Air supply:7 °C- Water supply: 40°C) and compressor speed of 70 rps. According to the design a heating capacity of 10.4 kW and a COP of 3.7 were expected. As previously explained, it is suspected that mentioned deviation is due to lower mass flow rate is achieved during the testing campaign for the same compressor velocity (and electricity power consumption). Probably the elevated pressure-drop produced in the distributor is the origin of mentioned deviation.

In air-water cooling mode the DSHP achieved a cooling power of 9.85 kW and a COP of 3.54 at design conditions (Air supply:35 °C-Water supply: 12°C) and compressor speed of 70 rps. According to the design a heating capacity of 9.9 kW and a COP of 3.43 were expected.

In water-water Heating mode a heating capacity of 9.3 kW and a COP of 3.3 at design conditions (Ground supply:7 °C- Water supply: 40°C) and compressor speed of 70 rps were achieved. According to the design a heating capacity of 11.7 kW and a COP of 3.9 were expected. As in case of air-Water heating mode it is suspected that the distributor's elevated pressure drop is on the origin of mentioned capacity reduction.

Finally, in water-water cooling mode cooling capacity of 9.45 kW and a COP of 4.1 at design conditions (Ground supply:30 °C- Water supply: 12°C) and compressor speed of 70 rps were achieved. According to the design a cooling capacity of 10.35 kW and a COP of 4.3 were expected.

The performance of the DSHX working as an evaporator and condenser, both using air or water as heat source/sink, agrees with the design/dimensioning models developed. The validated dimensioning tools will be used for the second prototype design.

Acknowledgements

The authors would like to thank the support of the project TRI-HP project (<https://www.tri-hp.eu/project>). This project has received funding from the European Union's Horizon 2020 research and innovation programme under grant agreement N. 814888.

References: Please use below reference style

- [1] Cai, J., Ji, J., Wang, Y., Zhou, F., Yu, B., *A novel PV/T-air dual source heat pump water heater system: dynamic simulation and performance characterization*, Energy Convers. Manage. 148, 635-645, 2017.
- [2] Grossia, I., Dongellinib, M., Piazzia, A., Morinib, G.L., *Dynamic modelling and energy performance analysis of an innovative dual-source heat pump system*, Hemisphere Applied Thermal Engineering 142, 2018.
- [3] Corberán, J.M., Cazorla-Marín, A., Marchante-Avellaneda, J., Montagud C., *Dual source heat pump, a high efficiency and cost-effective alternative for heating, cooling and DHW production*, International Journal of Low-Carbon Technologies, 13, 161-176, 2018.
- [4] Besagni, G., Croci, L., Nesa, R.; Molinaroli, L., *Field study of a novel solar assisted dual-source multifunctional heat pump*, Renewable Energy 1321185-1215, 2019.
- [5] Simonetti, R.; Molinaroli, L., Manzolini, G., *Experimental and analytical study of an innovative integrated dual-source evaporator for solar-assisted heat pumps*, Solar Energy 194 939-951, 2019.

- [6] Lazzarin, R. M., *Photovoltaic/Thermal (PV/T)/ground dual source heat pump: Optimum energy and economic sizing based on performance analysis*, Energy and Buildings 211, 2020.
- [7] Engineering equation solver. f-chart software. Available: <http://www.fchart.com>
- [8] Chi-chuan, W., Yi-chung, H., Yur-tsai, L., *Convective heat transfer for plain fins. performance of plate finned tube heat exchangers under dehumidifying conditions*, Journal of Heat Transfer, vol. 119/1, pp. 109 – 117, 1997.
- [9] Shah, R., London, A., *Heat transfer in pipe flow. laminar flow forced convection in ducts*, Academic Press, vol. 192, p. 98, 1978.
- [10] V. D. Ingenieure, VDI-Heat Atlas. Springer, 1993.
- [11] Nellis, G., Klein, S., *Heat Transfer*. Cambridge University Press, 2008.
- [12] Incropera, F., DeWitt, P., David, P., *Fundamentals of Heat and Mass Transfer*, 6th ed. New York Wiley, 2007.
- [13] Shah, M., *Comprehensive correlations for heat transfer during condensation in conventional and mini/micro channels in all orientations*, International Journal of Refrigeration, vol. 67, pp. 22–41, 2016.
- [14] Shah, M., *Prediction of heat transfer during condensation in inclined plain tubes*, Applied Thermal Engineering, vol. 94, pp. 82–89, 2016.
- [15] Ould, M., Didi, N., Thome, J., *Prediction of two-phase pressure gradients of refrigerants in horizontal tubes*, International Journal of Refrigeration, vol. 25, pp. 935 – 947, 2002
- [16] Kraus, A., Aziz, A., Welty, J., *Extended Surface Heat Transfer*. John Wiley & Sons, Inc., 2001
- [17] ASHRAE, HVAC Systems and Equipment Handbook: Air-Cooling and dehumidifying coils. American Society of Heating, Refrigerating and Air-Conditioning Engineers, 2008.,
- [18] J. Braun, S. Klein, and P. Mitchell, “Effectiveness models for cooling towers and cooling coils,” ASHRAE Transactions, vol. 92/2, pp. 164 – 174, 1989.
- [19] L. Sun and K. Mishima, *An evaluation of prediction methods for saturated low boiling heat transfer in minichannels*, International Journal of Heat and Mass Transfer, vol. 52, pp. 5323 – 5329, 2009.
- [20] Shah, M. M. *Chart correlation for saturated boiling heat transfer: equations and further study*, ASHRAE Transactions, vol. 88, pp. 185 – 196, 1982
- [21] J. Lebrun, X. Ding, J. Eppe, and M. Wasacz, *Cooling coil model to be used in transient and /or wet regimes.theoretical analysis and experimental validation. proceedings of the third international conference on system simulation in building*, international Conference on System Simulation in Building, pp. 405 – 441, 1990.
- [22] P. Li, J. Seem, and Y. Li, *A new explicit equation for accurate friction factor calculation of smooth pipes*, International Journal of Refrigeration, vol. 34, pp. 1535–1541, 2011

Stability of Nanofluids Towards Their Use in Thermal Management Systems

Roger R. Riehl^{1*} and S M Sohel Murshed²

¹GamaTech Thermal Solutions

Rua Córdoba 34, São José dos Campos, SP 12235-390 Brazil

²Center for Innovation, Technology and Policy Research (IN+)

Department of Mechanical Engineering

Instituto Superior Técnico, Universidade de Lisboa

1049-001 Lisboa, Portugal

*Corresponding author: roger.riehl@gts.com.br

Abstract

The interest in using nanofluids as a key thermal management agent to enhance the heat dissipation capabilities have increased over the last years. Due to their characteristics to enhance the thermal conductivity of the working fluid when compared to the base fluid, new lines of applications have been considered. However, since nanofluids are known to present stabilities issues over time, the use of this special type of working fluid has been limited to a few applications like heat pipes. Nanofluids stability is important to ensure their reliability towards their application in several other thermal management devices, like microchannel heat exchangers. Therefore, this paper presents the latest advances in obtaining reliability related to nanofluids stability, focusing on their use in a more wide range of application.

Keywords: Thermal Management, Nanofluids, Stability, Heat Transfer.

Introduction

Since it appeared as a potential solution to the physical limitation of heat dissipation equipment using regular working fluids, nanofluids have been extensively investigated as a key component in thermal management systems, with a promise of enhancing the overall performance by the addition of solid nanoparticles in a base fluid [1]. Great development of nanofluids applied to passive thermal control devices, such as heat pipes and pulsating heat pipes, have shown the importance and capabilities of this working fluid in enhancing the

overall heat dissipation and transport in those devices [2-6]. However, due to issues related to the stability of nanofluids over time, their application in a more general matter have raised concerns related to their potential use in a wide range of commercial equipment.

Besides the fact that the combination of a base fluid and solid nanoparticles must present a chemical compatibility, the resulting nanofluid must also present stability in its structure in order to be able to perform as expected for a long time, with minimal sedimentation of its solid material that may cause lack in performance [7].

It is now widely considered that one of the main challenges of nanofluids applications particularly in thermal management systems is their long-term stability. Although large numbers of studies have been reported on the influence of stability of nanofluids on their thermal conductivity [8-13], very few studies have been conducted on the issue of stability for the cooling application like in convection heat transfer performance in various systems. Nanofluids stability effects on the thermal performance of heat pipes was critically reviewed by Cacia et al. [14]. The review confirmed that that nanoparticles' deposition on the evaporator surface and wick or groove structures were responsible for the increase or decrease in the thermal performance of heat pipes and stability played a major role for their deposition. Ensuring long-term stability is critical for not only the thermal performance but also for the smooth running and longevity of the systems. Thus it is of outmost important to study and critically analyze the effect of stability of nanofluids toward their application in thermal management systems.

Nanofluids Stability and Issues

Nanofluids stability starts with its preparation. There are two common techniques to prepare nanofluids. The first is one-step methods where nanoparticles are directly synthesis in the host medium and two-step methods where dry nanopowders are mixed or dispersed in a host medium (known as base fluid). Although the former technique yields better stability of nanofluids, the latter one is most widely used due to availability of variety of nanoparticles and also to prepare relatively large quantity of samples for heat transfer application. Despite preparing nanofluids in any of these methods, nanofluids still required other engineering and chemical processing to improve their stability as stability of nanofluids is not only necessary for their optimum thermophysical properties but also critical for their usage as heat transfer fluids in numerous applications. In order to improve the stability researchers commonly and first apply ultrasonication to the prepared or obtained nanofluids. However, ultrasonication parameters such as power, amplitude and importantly optimum time must be obtained for

each sample nanofluids by assessing the level of stability through different type of stability evaluation methods such as spectral absorbency analysis (UV-vis or NIR), electrokinetic potential determination (pH and Zeta potential) as well as microscopic imaging like TEM or SEM. Another widely used method to improve stability is to employ small quantity (within the critical micelle concentration) of suitable surfactant to the nanofluids. Schematic of stability improvement and evaluation of nanofluids is presented in Figure 1. Although it is very challenging to achieve a long-term stability as many factors such as nanoparticle types, size shapes, purity and degree of agglomerations as well as properties of the base fluids are involved in this process, before evaluating thermophysical properties and thermal performance in any systems like convective heat transfer, nanofluids must go through rigorous stability study and be established as stable nanofluids.

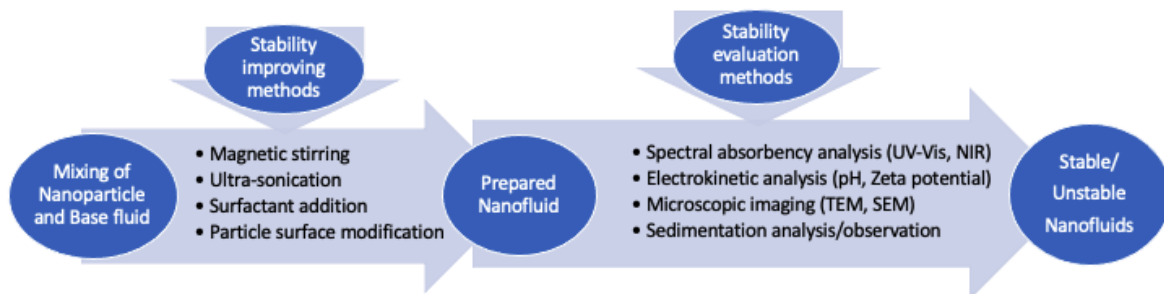


Figure 1. Schematic presentation of stability concept of nanofluids.

Current and Potential Applications of Nanofluids

Considering the enhancement in thermal performance that nanofluids can deliver, they can be potentially applied to any thermal system. However, issues related to stability are the major concern and need to be properly addressed. Initial application of nanofluids have been done in heat pipes with significant enhancements in their performances, resulting in lower heat sources temperatures [15-17]. However, the correct selection of a base fluid and solid nanoparticles plays an important role in this enhancement, as the chemical compatibility check must be properly performed to avoid failure during long term operation. Such issues have been reported in previous studies, but they are usually overlooked by researchers and designers, causing the thermal device to seize its operation compromising the overall thermal management system [18,19].

Another found when applying nanofluids in thermal management systems is related to the correct selection of models that need to be used to predict its behavior. Several authors have reported different models to calculate thermophysical properties like thermal conductivity,

density, viscosity, etc, but even though they used the same base fluid and nanoparticle, there are substantial differences in the results. Such analysis can be made by a direct comparison as presented by Table 1.

Table 1. Thermal enhancement ratio for CuO and water nanofluids.

Author	CuO Nanoparticle Size (nm)	Thermal Enhancement Ratio	Volume Fraction (vol.%)	Temperature (°C)	Sonication Time (h)
Karthikeyan et al [20]	8.0	1.020	0.020	20	0.5
	8.0	1.080	0.090	20	0.5
	8.0	1.130	0.100	20	0.5
	8.0	1.190	0.300	20	0.5
	8.0	1.250	0.800	20	0.5
	8.0	1.316	1.000	20	0.5
Nemade et al [21]	33.0	1.197	0.500	55	1
	42.0	1.134	0.500	55	0.75
	46.0	1.124	0.500	55	0.5
	53.5	1.087	0.500	55	0.25
Khedkar et al [22]	25.0	1.050	0.010	26	1.5
	25.0	1.120	0.020	26	1.5
	25.0	1.130	0.030	26	1.5
	25.0	1.160	0.040	26	1.5
	25.0	1.170	0.050	26	1.5
	25.0	1.320	0.075	26	1.5
Wang et al [23]	42.5	1.080	0.020	25	
	42.5	1.100	0.040	25	
	42.5	1.110	0.100	25	not informed
	42.5	1.125	0.150	25	
	42.5	1.160	0.400	25	
Pryia et al [24]	50.0	1.020	0.004	28	6
	50.0	1.060	0.008	28	6
	50.0	1.100	0.012	28	6
	50.0	1.130	0.016	28	6
	50.0	1.050	0.004	50	6
	50.0	1.160	0.008	50	6
	50.0	1.250	0.012	50	6
	50.0	1.320	0.016	50	6
	50.0	0.950	0.004	55	6
	50.0	1.240	0.008	55	6
50.0	1.330	0.012	55	6	
50.0	1.430	0.016	55	6	

From the several potential applications when using nanofluids, one that has gained attention and has presented substantial development is related to its use in pulsating/oscillating heat pipes (PHPs). Operating by means of liquid slugs/vapor plugs, PHPs are able to transport heat over long distances efficiently with any gravity orientation. Since they are built from meandering tubes bent to form several parallel channels, their low cost construction and high thermal efficiency have attracted the attention for many applications, from military to aerospace. With the continuous need to increase the heat dissipation capabilities of this type of device, nanofluids have found an important application with substantial improvements in the overall PHP's performance [1,15]. Figure 2 shows the schematization of a PHP embedded in the structure to promote the heat dissipation of PCBs.

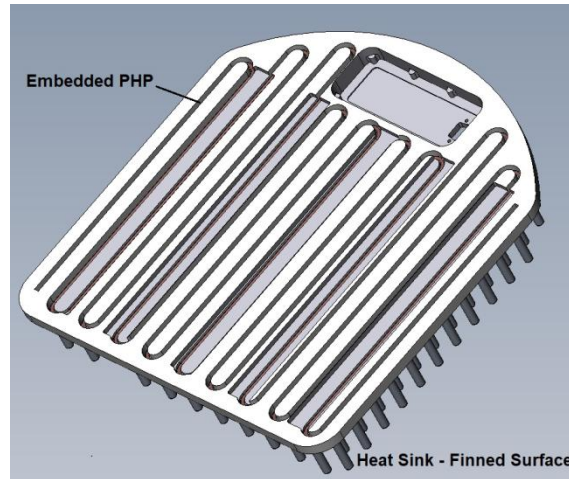


Figure 2. Embedded PHP for heat dissipation of PCBs.

In order to verify the operation of PHPs, Fig. 3 presents the device that has been used for testing with a CuO-methanol nanofluid, using 3.5% w.t. of solid nanoparticles mixed in ultra pure methanol as the base fluid.



Figure 3. PHP utilized during the tests.

Figure 4 presents the schematics of the test rig, where heat was absorbed using a skin heater and dissipated via forced convection promoted by a fan. Thermocouples were placed as shown in the figure, in order to obtain the temperature readings during the PHP's operation. Both evaporator and adiabatic sessions were fully insulated, only keeping the condenser session without insulation.

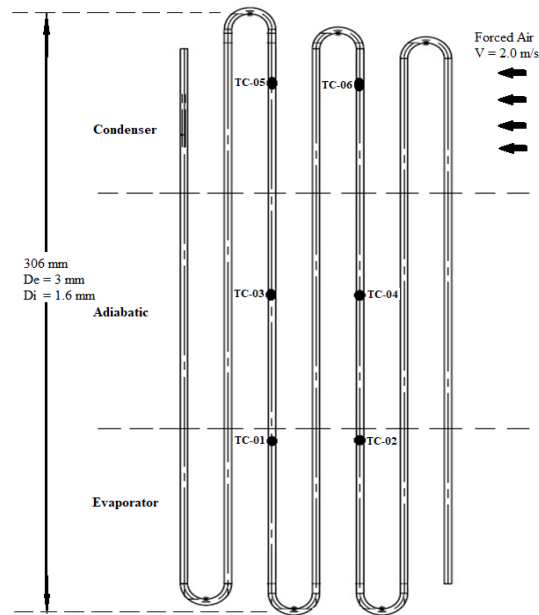


Figure 4. PHP's schematics applied during the tests.

The results presented by Fig. 5 show the intense pulsations obtained during the tests when the PHP was operating with 50W of heat applied to the evaporator. Due to the physical parameters of this device, the critical vapor velocity was generated at a heat load of 45W, which caused the intense pulsations.

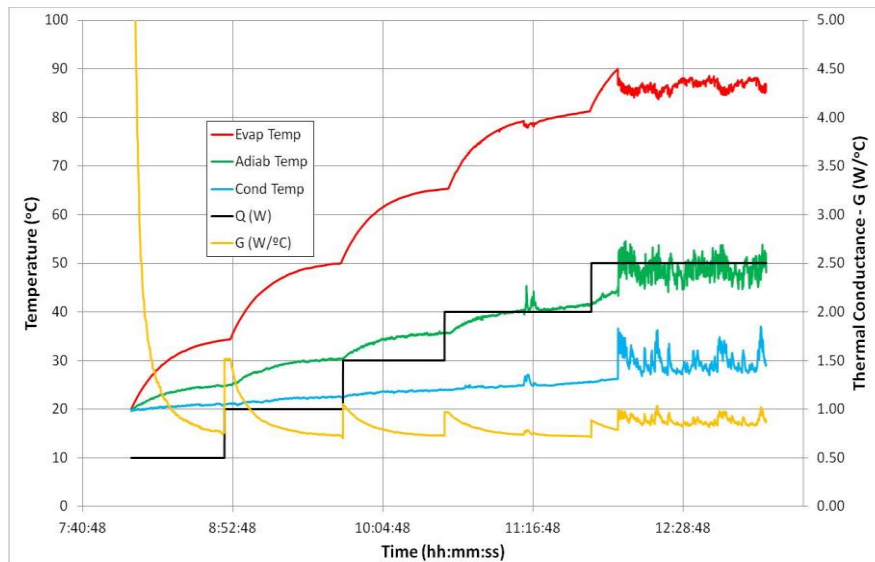


Figure 5. PHP operation with CuO-methanol nanofluid.

Until reaching this power level, the PHP was basically operation under film evaporation conditions that result in lower thermal conductances and high temperature differences

between the evaporator and condenser. When reaching the critical vapor velocity, intense nucleating boiling is observed which is enhanced by the presence of the solid nanoparticles that act like additional nucleation sites, thus resulting in more vapor bubbles formation and displacement.

Figure 6 presents the comparison between the operation of the PHP with the base fluid only (water) and the nanofluid, related to the thermal conductances observed. From the results, the PHP operating with the CuO-water nanofluid presented higher thermal conductances, which represent that the device was performing better with the nanofluid when compared with the operation with the base fluid only.

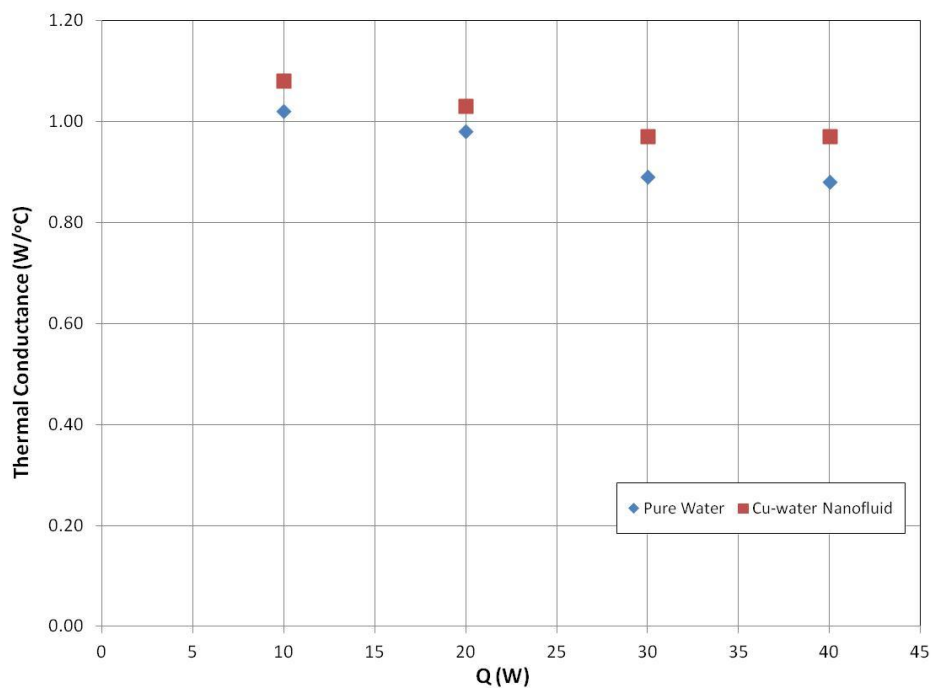


Figure 6. Thermal conductances for the nanofluid operation with the PHP.

The increase in the thermal conductances when using the CuO-methanol nanofluid can be as much as 20% when compared with pure methanol [15]. However, stability of the nanofluid can still be an issue that requires full attention especially when the choice of the base fluid and solid nanoparticle is not in accordance to their chemical compatibility the process utilized to mix them is not entirely appropriate.

Conclusions

The use of nanofluids in thermal management systems has become an important and direct application for this new type of working fluid. Nanofluid stability can play a major role in the

overall thermal management device performance, which will directly impact its operation. Proper chemical compatibility between the base fluid and the solid nanoparticle must be checked to avoid potential instabilities in the mixture, as nanofluids must go through rigorous stability study and be established as stable nanofluids. Considering the application of PHPs with nanofluids, it has shown promising results in several projects when the correct choice of a base fluid and solid nanoparticles is done. Enhancement in the PHP's operation conditions and increase in its thermal conductances can be obtained, which represents that PHPs with nanofluids can be considered remarkable thermal management devices.

Acknowledgments

This work has been partially supported by the FCT, Portugal through project- PTDC/NAN-MAT/29989/2017|NanoCOM.

References

- [1] M. H. Buschmann, A. Huminic, S. Mancin, R. R. Riehl and G. Huminic, "State of the art of heat transfer of heat pipes and thermosyphons employing nanofluids as working fluid", *Journal of Nanofluids*, vol 8, no. 2, pp. 253-266, Feb. 2019. DOI: 10.1166/jon.2019.1597.
- [2] Y. Ji, H. Ma, F. Su and G. Wang, "Particle size effect on heat transfer performance in an oscillating heat pipe", *Experimental Thermal and Fluid Science*, vol. 35, no. 4, pp. 724-727, May 2011. DOI: 10.1016/j.expthermflusci.2011.01.007.
- [3] J. Qu and H. Wu, "Thermal performance comparison of oscillating heat pipes with SiO₂/water and Al₂O₃/water nanofluids", *International Journal of Thermal Sciences*, vol. 50, no. 10, pp. 1954-1962, Oct. 2011. DOI: 10.1016/j.ijthermalsci.2011.04.004.
- [4] J. Qu, H. Wu and P. Cheng, "Thermal performance of an oscillating heat pipe with Al₂O₃-water nanofluids", *International Communications in Heat and Mass Transfer*, vol 37, no. 2, pp. 111-115, Feb. 2010. DOI: 10.1016/j.icheatmasstransfer.2009.10.001.
- [5] T. Parametthanuwat, S. Rittidech, A. Pattiya, Y. Ding and S. Witharana, "Application of silver nanofluid containing oleic acid surfactant in a thermosyphon economizer", *Nanoscale Research Letters*, vol. 6, no. 1, pp. 315, Apr. 2011. DOI: 10.1186/1556-276X-6-315.
- [6] N. K. Gupta, A. K. Tiwari and S. K. Ghosh, "Heat transfer mechanisms in heat pipes using nanofluids – A review", *Experimental Thermal and Fluid Science*, vol. 90, no. 1, pp. 84-100, Jan. 2018. DOI: 10.1016/j.expthermflusci.2017.08.013.

- [7] W. Yu and H. Xie, "A Review on nanofluids: preparation, stability mechanisms, and applications", *Journal of Nanomaterials*, vol. 2012, no. 1, pp. 1687-1704, Sep. 2011. DOI: 10.1155/2012/435873.
- [8] Murshed S.M.S., Nieto de Castro C.A., Lourenço M.J.V., Matos Lopes M. and Santos F.J.V., A review of boiling and convective heat transfer with nanofluids, *Renewable and Sustainable Energy Reviews* 15 (2011) 2342-2354.
- [9] L. Fedele, L. Colla, S. Bobbo, S. Barison, and F. Agresti, "Experimental stability analysis of different water-based nanofluids.," *Nanoscale Res. Lett.*, vol. 6, no. 1, p. 300, Jan. 2011.
- [10] Murshed S.M.S., Nieto de Castro C.A. and Lourenço M.J.V., Effect of surfactant and nanoparticle clustering on thermal conductivity of aqueous nanofluids, *Journal of Nanofluids* 1 (2012) 175-179. (DOI: <http://dx.doi.org/10.1166/jon.2012.1020>)
- [11] Babita, S. K. Sharma, and G. S. Mital, "Preparation and evaluation of stable nanofluids for heat transfer application: A review," *Exp. Therm. Fluid Sci.*, vol. 79, pp. 202–212, 2016.
- [12] Nieto de Castro C.A., Vieira S. I. C., Lourenço M.J.V., and Murshed S.M.S., Understanding stability, measurements, and mechanisms of thermal conductivity of nanofluids, *Journal of Nanofluids* 6 (5) (2017) 804-811. <http://dx.doi.org/10.1166/jon.2017.1388>
- [13] Cacua K., Murshed S.M.S., Pabón E., and Buitrago R, Dispersion and thermal conductivity of TiO₂/water nanofluid- effects of ultrasonication, agitation and temperature, *Journal of Thermal Analysis and Calorimetry*, 140(2020) 109–114 (<https://doi.org/10.1007/s10973-019-08817-1>)
- [14] Cacua K., Buitrago-Sierra R., Herrera B., Pabón E., and Murshed S.M.S., Nanofluids stability effects on the thermal performance of heat pipes: A critical review, *Journal of Thermal Analysis and Calorimetry*, 136(2019) 1597-1614. (<https://doi.org/10.1007/s10973-018-7787-5>).
- [15] R. R. Riehl, "Thermal enhancement using nanofluids on high heat dissipation electronic components", *Journal of Nanofluids*, vol. 8, no. 1, pp. 30-40, Jan. 2019. DOI: 10.1166/jon.2019.1563.
- [16] B.S. Bhullar, D. Gangacharyulu and S.K. Das, "Temporal deterioration in thermal performance of screen mesh wick straight heat pipe using surfactant free aqueous nanofluids", *Heat and Mass Transfer*, vol. 53, no. 1, pp. 241-251, Jan. 2017. DOI: 10.1007/s00231-016-1785-6.

- [17] N. K. Gupta, A. K. Tiwari and S. K. Ghosh, "Heat transfer mechanisms in heat pipes using nanofluids – A review", *Experimental Thermal and Fluid Science*, vol. 90, no. 1, pp. 84-100, Jan. 2018. DOI: 10.1016/j.expthermflusci.2017.08.013.
- [18] J. H. Rosenfeld and N. J. Gernert, "Life test results for water heat pipes operating at 200°C to 300°C", *Proceedings of the STAIF-Space Technology and Applications International Forum*, Albuquerque, NM USA, Feb 10-14, 2008.
- [19] R. R. Riehl, S. M. S. Murshed, "Life Time Expectancy Prediction and Ageing Process of Heat Pipes Using Nanofluids", *Heat Transfer Engineering* <https://doi.org/10.1080/01457632.2020.1818423>.
- [20] N.R. Karthikeyan, J. Philip, B. Raj, Effect of clustering on the thermal conductivity of nanofluids, *Material Chem. Phys.*, 109 (1) 50–55 2008.
- [21] K. Nemade, S. Waghuley, A novel approach for enhancement of thermal conductivity of CuO/H₂O based nanofluids, *Applied Thermal Eng.* 95 271-274 2016.
- [22] R.S. Khedkar, S.S. Sonawane, K.L. Wasewar, Influence of CuO nanoparticles in enhancing the thermal conductivity of water and monoethylene glycol based nanofluids, *Int Comm in Heat and Mass Transfer* 39 665-669 2012.
- [23] X.J. Wang, X.F. Li, Influence of pH on nanofluids' viscosity and thermal conductivity, *Chin Phys Lett* 26 5 056-061 2009.
- [24] K.R. Priya, K.S. Suganthi, K.S. Rajan, Transport properties of ultra-low concentration CuO–water nanofluids containing non-spherical nanoparticles, *Int J of Heat and Mass Transfer* 55 4734-4743 2012.

Influence of nanofluid on a connected thermosyphons

M.Aresti¹, J.Estella¹, A. Azcárate², L.Hurtado², J.Esarte^{1*},

¹NAITEC Centro tecnológico de automoción y mecatrónica. C/Tajonar 20-31006 Pamplona (Spain)

²ALAZ-ARIMA. C/Cañada Real 14, 31195, Berrioplano (Spain)

*Corresponding author: jesarte@naitec.es

Abstract

Current cooling solutions for the renewables sector appear to have bottomed out and have not evolved for a long time in terms of cost, service life, reliability and maintenance. The use of thermosyphons as a cooling element has proven to be highly suitable, in terms of cost and efficiency, in various applications (space, aeronautics, military...) including the renewables sector (ALAZ-ARIMA). On the other hand, the appearance of nanofluids opens a new way of improving the different cooling devices, including thermosyphons. The present work focuses on the experimental analysis of the influence of nanofluids on the thermal transport capacity of a thermosyphon based cooling system designed to cool down a 5 MW PV inverter. The effect that parameters such as type of nanoparticle, size and concentration have on the thermal transport capacity of the thermosyphon are shown. The base fluid is distilled water and the nanofluids studied are based on TiO₂, Al₂O₃ and Cu coated by C (C@Cu). This work aims to show the cooling potential of the thermosyphon + nanofluid technology in the renewable sector.

Keywords: Nanofluids, Thermosyphon, cooling technology.

Introduction

Thermosyphons are passive heat transfer devices characterized by high thermal conductivity. Its operating principle is the phase change of a working fluid [1,2]. Nanofluids emerged as a key component to increase the heat transfer potential of these passive devices. Since their appearance, numerous works [3, 4] have been carried out showing such ability.

There are several challenges that a thermal engineer must face when using nanofluids, one of them is their stability over time [5-7], the other and more important, is their influence on the thermosyphon performance.

Objective and Case Study

Today, the thermosiphon is not a widespread cooling device in the field of renewable energy converters, much less its combination with nanofluids. This work presents a thermosiphon performance when cooling down a 5KW photovoltaic inverter, **figure 1 a)**, and using different nanofluids. In all cases the base fluid is distilled water. Different nanofluids are considered, the commercial ones, **table 1 a)**, and those formulated at home, **table 1 b)**.

The **figure 1 b)** shows a prototype of a thermosyphon pack used for a photovoltaic converter. Tests were done on a single thermosyphon.

Table 1. a) Commercial nanofluids; b) home formulated

a) Commercial Name	NP	Base fluid	NP size (d50)	NP concentration (wt%)	b) Nanofluid
AERODISP® W925	Al2O3	Agua	110	25	
AERODISP® W 630	Al2O3	Agua	140	30	Cu-3KD73+0.5RHEO
AERODISP® W 440	Al2O3	Agua	120	40	Cu-3KD77+0.5RHEO
AERODISP® W 450 ZX	Al2O3	Agua	80	50	Cu-0.5KD73+0.5RHEO
AERODISP® W 640 ZX	Al2O3	Agua	80	40	2-Cu@C-3BYK199+1,5RHEO7420
AERODISP® W 740 X	TiO2	Agua	70	40	4-Cu@C-3BYK199+0,5RHEO7420
CAB-O-SPERSE PG003	Al2O3	Agua		40	
CAB-O-SPERSE PG008	Al2O3	Agua		40	5-Cu@C-3BYK199+1,5RHEO7420

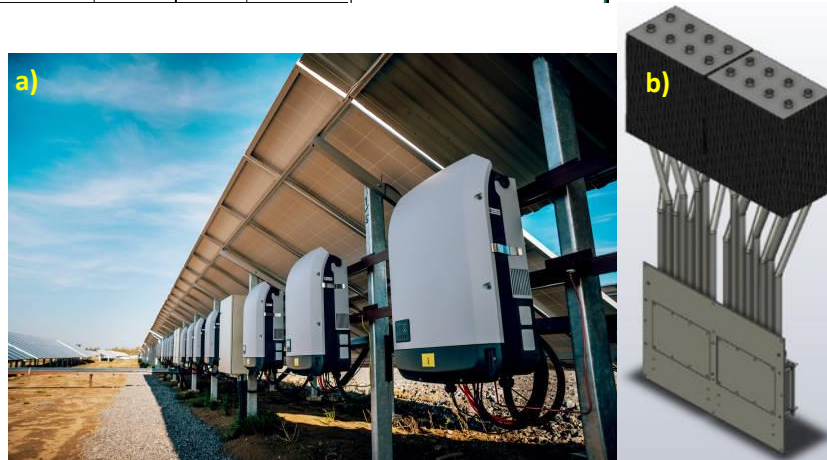


Figure 1. a) 5KW photovoltaic inverter; b) Thermosyphon pack

Discussion and Results

The effect of the type of nanoparticle, concentration and size on the thermosyphon performance, thermal resistance ($^{\circ}\text{C}/\text{W}$), is analysed. The different nanofluid tested are recorded in table 2.

Table 2. Information about the nanofluids tested

Identification	Commercial name	NP type	NP Size (nm)	Concentration (% wt)	
A14	Aerodisp@ W640ZX	Al ₂ O ₃	113	1.5	
A15				3	
A17	CAB-O-SPERSE PG003		131	1.5	
A18				3	
A20	CAB-O-SPERSE PG008		119		
A22	Aerodisp@ W740ZX		TiO ₂	128	0.5
A23		1.5			
A24		3			
A25	CAB-O-SPERSE PG008	Al ₂ O ₃	119	0.05	
A26				0.5	
A27	Aerodisp@ W640ZX		113	0.05	
A28				0.5	
A31	-----		Cu	----	0.05
A32	-----		Cu@C	185	0.05
A34	-----	161.7		0.1	

“Influence of nanofluid on a connected thermosyphons”

A35	-----	Cu	221.5	0.5
A36	-----		181	1
A38	-----		291	0.1
A39	-----		266.7	0.5
A40	-----		271	1

Results are shown in figures below.

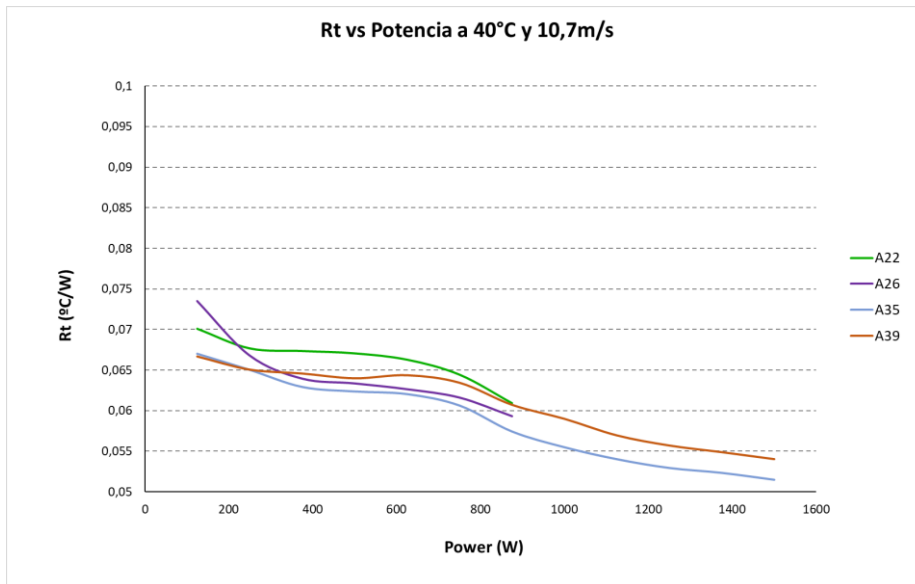


Figure 2. Effect of nanoparticle type on the thermosyphon performance, thermal resistance. NP concentration:0.5% wt

At the same NPs concentration (0.5% wt), the “Cu@C” (A55) nanoparticles allow a lower thermosyphon thermal resistance whatever the heat power is.

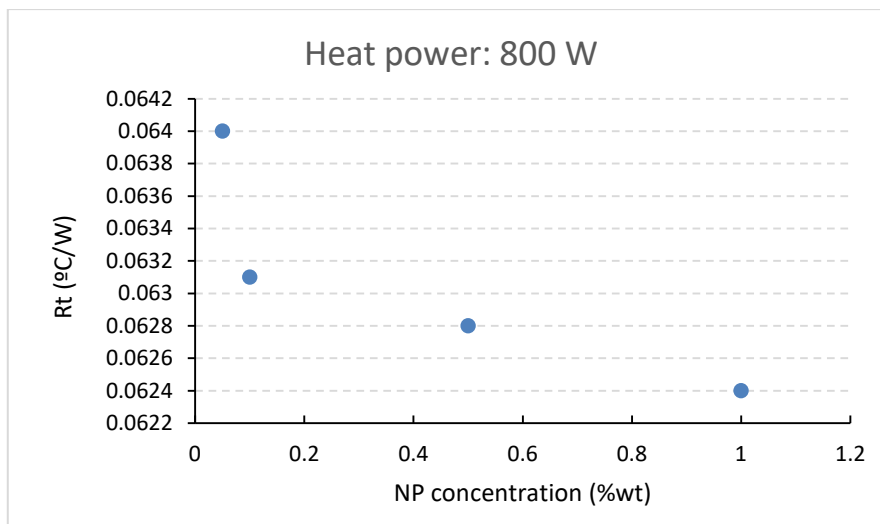


Figure 3. Effect of nanoparticle concentration. NP: Cu

The effect of the NPs concentration is clearly observed in figure 3, the higher the concentration, the lower the thermosyphon thermal resistance, that is, the better its performance. However, the trend is different depending on the heat power to be dissipated, figure 4.

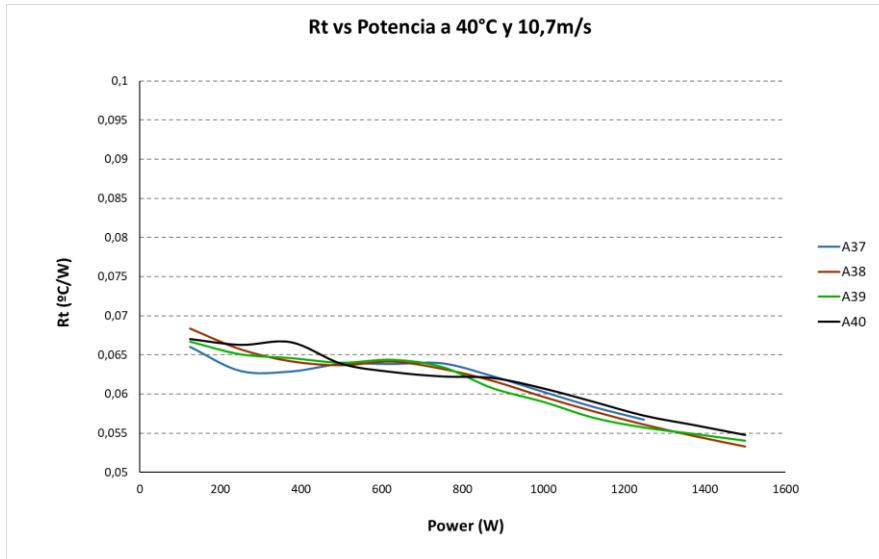


Figure 4. NP concentration vs heat power. Cu as nanoparticle

Other point analysed is the NP size, figure 5.

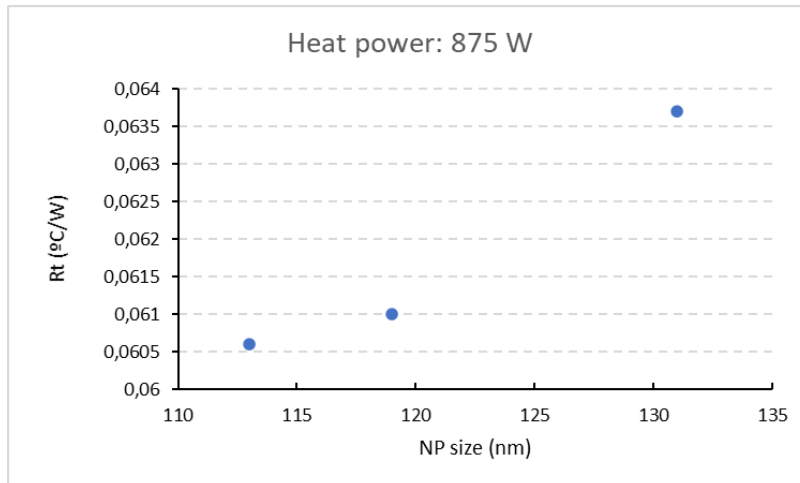


Figure 5. Effect of nanoparticle size. NP: Al_2O_3

The lower the concentration, the lower the thermal resistance.

To quantify the thermosyphon performance improvement when nanofluid is used, two experimental tests are carried out, figure 6. One with distilled water “E05” as working fluid and the other with “A35” nanofluid.

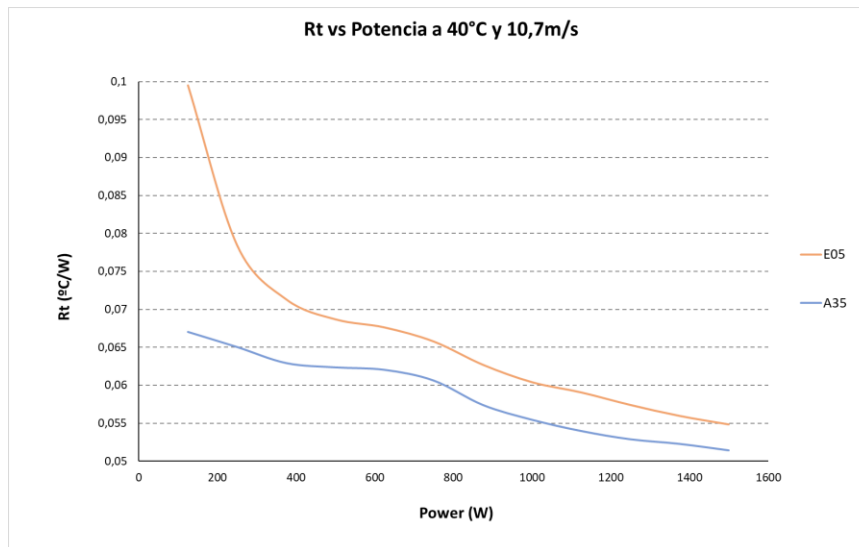


Figure 6. Thermosyphon performance for both A35 nanofluid and base fluid (distilled water)

The improvement of the nanofluid is clearly observed in figure 6. A 8% thermosyphon “Rt” improvement is achieved at any heat power dissipated.

Summary/Conclusions

- Nanofluids present a high improvement capacity for the thermosyphon performance.
- The nanoparticles type, size, concentration, as well as the dispersants used, have a great influence on the thermosyphon performance.
- There is much work to be done, both theoretically and experimentally, to achieve widespread use of nanofluids as elements to improve the cooling capacity of thermosyphons.

References:

- [1] Roger R. Riehl, Tulio C.P.A. Siqueira. Heat transport capability and compensation chamber influence in loop heat pipes performance. *Applied Thermal Engineering* 26 (2006) 1158–1168
- [2] J. Esarte, J.M. Blanco, A. Bernardini, J.T. San-José. Optimizing the design of a two-phase cooling system loop heat pipe: Wick manufacturing with the 3D selective laser melting printing technique and prototype testing. *Applied Thermal Engineering* 111 (2017) 407–419.
- [3] R. R. Riehl and N. dos Santos. Water-copper nanofluid application in an open loop pulsating heat pipe. *Applied Thermal Engineering*, 42:6–10, 2012.
- [4] Y. Naresh, C. Balaji, Experimental investigations of heat transfer from an internally finned two phase closed thermosyphon, *Applied Thermal Engineering* (2016).
- [5] Munish Gupta, Vinay Singha, Rajesh Kumara, Z. Said. A review on thermophysical properties of nanofluids and heat transfer applications. *Renewable and Sustainable Energy Reviews*, 74, 638-670 (2017).
- [5] Duangthongsuk W, Wongwises S. An experimental study on the heat transfer performance and pressure drop of TiO₂ -water nanofluids flowing under a turbulent flow regime. *Int J Heat Mass Transf*; 53(1):334–44 (2010).
- [7] Sarkar J. A critical review on convective heat transfer correlations of nanofluids. *Renewable and Sustainable. Energy Rev*;15(6):3271–7 (2011).

Posters

Numerical model of a latent heat storage unit for industrial application

K. Ingenwepelt¹, M. van der Pal²

¹ Hochschule Düsseldorf, University of Applied Sciences, Münsterstraße 156, 40476 Düsseldorf, Germany

² TNO Energy Transition, Westerduinweg 3, 1755 LE, Petten, The Netherlands

* Corresponding author: kathrin.ingenwepelt@study.hs-duesseldorf.de

Abstract

The heat transfer of a high temperature latent heat storage unit was measured and modelled numerically. The model was fitted to the experimental data. The material stability and (dis)charge times of less than an hour for 10K charging temperature were verified.

Keywords: Latent heat, heat storage, industry.

Introduction/Background

Small-scale PCM heat storage measurement is compared with model calculations. The boundary conditions and assumptions of the numerical, 1-Dimensional Matlab model are shown in *Figure 1*.

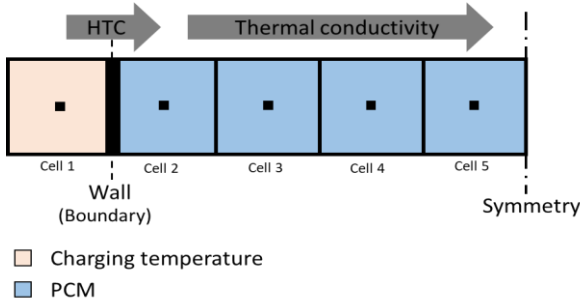


Figure 1: Schematic representation of the model

The thermal conduction of heat propagation in the material is determined by:

$$Q_{i,i+1} = \frac{\lambda \cdot (T_i - T_{i+1}) \cdot A_{i,i+1} \cdot dt}{dx_{i,i+1}} \quad (1)$$

And the transition of heat from charging medium to storage material is calculated by:

$$Q_{1,2} = \frac{(T_1 - T_2) \cdot A_{1,2} \cdot dt}{\frac{1}{\alpha} + \frac{dx_{1,2}}{\lambda}} \quad (2)$$

Discussion and Results

The input data of the model was obtained in small-scale experiments of roughly 120 g storage material in sample tubes. They were placed in a thermal bath, see *Figure 2*. The thermal conductivity is in an order of magnitude of $4.4 \text{ Wm}^{-1}\text{K}^{-1}$ [1].

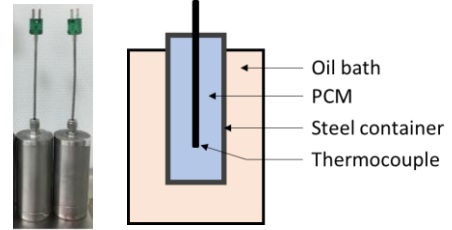


Figure 2: Experimental set-up of cyclic melting & solidification

The oil temperature is used as charging temperature. *Figure 3* shows model and experiment results.

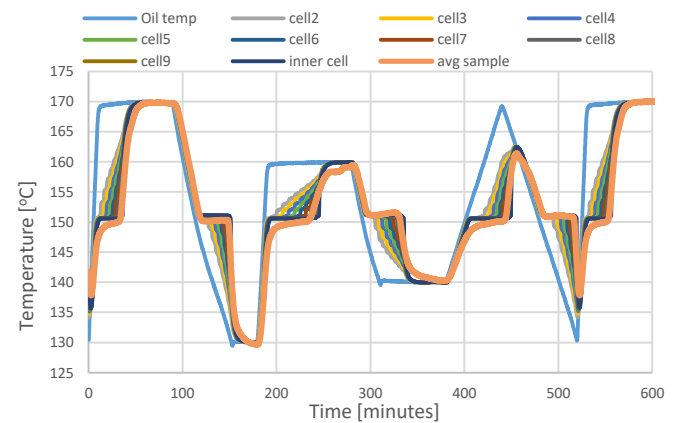


Figure 3: Plot of calculated and measured temperatures

Summary/Conclusions

The optimum heat transfer coefficients were found to be $270 \text{ Wm}^{-2}\text{K}^{-1}$ in liquid and $530 \text{ Wm}^{-2}\text{K}^{-1}$ in solid phase. Higher heat transfer rates are expected when oil is replaced by steam/water[2].

Acknowledgements

This work is part of the Flexsteam project, financially supported by the 'Topsector Energiesubsidie' of the Dutch ministry of economic affairs.

References

- [1] Zhou W., *Preparation and thermal cycling of expanded graphite/adipic acid composite phase change materials*, Akadémiai Kiadó, 2017.
- [2] Stephan P. et al., *VDI heat atlas*, Springer, 2010

Design and characterisation of low NO_x hydrogen diffusion burners for domestic and industrial heating applications

G.López-Ruiz¹, I. Álava¹ and J.M. Blanco²

¹ Ikerlan Technology Research Centre, Basque Research and Technology Alliance (BRTA).

P. J.M. Arizmendiarieta, 2.20500 Arrasate/Mondragón, Spain.

² Energy Engineering Department, School of Engineering, Building I, University of the Basque Country, UPV/EHU, Plaza Ingeniero Torres Quevedo s/n, 48013 Bilbao, Spain

*Corresponding author: gontzal.lopez@ikerlan.es

Abstract

The end use of green hydrogen has been a research topic during the last decades. For instance, different studies have been focused on the use of generated green hydrogen as fuel in domestic or industrial scale burners. The main technological challenge in the design of hydrogen burners is to maintain both a high hydrogen fuel content and acceptable levels of NO_x emissions. This clearly requires new or modified existing combustion devices for hydrogen. In that sense, non-premixed combustion could be a useful approach for the design of hydrogen burners since they eliminate the flashback phenomena. In this context, the present poster shows the main results and conclusions derived from our research line, which is related to the design of low NO_x hydrogen burners.

Keywords: Hydrogen, combustion, NO_x emissions, CFD modelling

Introduction/Background

Within the context of an increasing renewable energy power plants, the energy storage will play an important role in the power grid towards decarbonisation of the energy system [1]. Among others, green hydrogen is becoming a promising energy vector, which could be produced through electrolysis using the energy excess in low demand periods and stored to be afterwards used in different applications [2]. Concerning the use of alternative fuels in domestic and industrial scale boilers, hydrogen can be used as a substitute for natural gas, eliminating the CO₂ and CO emissions derived from its combustion. Nonetheless, due to its physical properties, hydrogen presents several particularities. Among others, it has a wide

flammability limit in air (4-75 vol%), low ignition energy in air (0.019 mJ), low density (0.0899 kg/m³) and high adiabatic flame temperature (2380 K) [3]. In that sense, non-premixed burners, which are commonly used in industrial boilers and gas turbine combustors, are preferable since they ensure safer operating conditions avoiding flashback and explosion risk when fuelled completely by hydrogen. Nonetheless, in non-premixed burners, flames react at near stoichiometric conditions, resulting in near-adiabatic flame temperatures and consequent increase in thermal NO_x formation.

Accordingly, the present poster summarises the most relevant results and conclusions focused on the characterisation of thermal NO_x formation in hydrogen diffusion flames for the design of low NO_x burners in the domestic and industrial sectors.

Discussion and Results

The first research stage accounted for the characterisation of NO_x formation in hydrogen diffusion flames [4]. Single flame configuration was considered through a coaxial jet burner. Experimental and numerical results were used to assess the thermal NO_x formation trends under different operating conditions (thermal power, air excess level and flame regime). Following the approach of [5], the NO_x formation trends were characterised taking as basis microscopic parameters (NO_x formation volumes, NO_x reaction time scales and flow time scales). Finally, NO_x reduction strategies were presented for the design of low NO_x hydrogen diffusion burners.

Based on the initial research stage and a thorough literature review, a novel design approach was considered for the design of low NO_x hydrogen burners for domestic and industrial burners. A new

case study was defined taking as basis existing gas turbine combustor designs. Hence, geometry scaling laws and operating conditions were adapted to study the feasibility of such novel burner for the design of low NO_x hydrogen [6]. Following the same methodology, numerical calculations and experimental measurements were carried out to assess the feasibility of the defined hydrogen burner concept.

Summary/Conclusions

It can be concluded that green hydrogen is a potential alternative towards the decarbonisation of the domestic and industrial sectors. The present poster summarises the most important outcomes derived from the research work related to the characterisation of NO_x formation in hydrogen diffusion flames. The results also showed that low NO_x burners can be designed keeping concentration values below the current European limits.

References

- [1] Miranda P., Science and Engineering of Hydrogen-Based Energy Technologies: Hydrogen Production and Practical Applications in Energy Generation, Elsevier Science, 2018
- [2] Hu G., Chen C., Lu H. T., Wu Y., Liu C., Tao L., Men Y., He G., Li K.G., A review of technical advances, barriers, and solutions

in the power to hydrogen (p2h) roadmap, Engineering 6 (12) (2020) 1364–1380.[doi:https://doi.org/10.1016/j.eng.2020.04.016](https://doi.org/10.1016/j.eng.2020.04.016)

- [3] Warnatz, J., Maas U., Dibble R.W., Combustion: Physical and Chemical Fundamentals, Modelling and Simulation, Experiments, Pollutant Formation., Springer, 2001.
- [4] Lopez-Ruiz G., Alava I., Urresti I., Blanco J.M., Naud B., Experimental and numerical study of NO_x formation in a domestic H₂/air coaxial burner at low Reynolds number, Energy 221 (2021) 119768.[doi:https://doi.org/10.1016/j.energy.2021.119768](https://doi.org/10.1016/j.energy.2021.119768)
- [5] Chen R-H., Driscoll J-F., Nitric oxide levels of jet diffusion flames: Effects of coaxial air and other mixing parameters, Symposium (International) on Combustion 23 (1) (1991) 281–288, [doi:https://doi.org/10.1016/S00820784\(06\)80271-7](https://doi.org/10.1016/S00820784(06)80271-7)
- [6] Lopez-Ruiz G., Alava I., Blanco J.M., Study on the feasibility of the micromix combustion principle in low NO_x H₂ burners for domestic and industrial boilers: A numerical approach, Energy [doi:https://doi.org/10.1016/j.energy.2021.121456](https://doi.org/10.1016/j.energy.2021.121456)

Economic analysis of Absorption Heat Transformers and Compression Heat Pumps for industrial heat upgrade

José Luis Corrales Ciganda ¹ and Asier Martinez-Urrutia ^{1*}

¹Tecnalia, Energy and Environment Division, Area Anardi, 5, Azpeitia E20730, Spain

*Corresponding author: joseluis.corrales@tecnalia.com

Abstract

Absorption Heat Transformers (AHT) and High Temperature Compression Heat Pumps (HTHP) are two mature technologies for the heat recovery and upgrade of industrial waste heat. Temperature Lifts up to 50 K and delivery temperatures up to 150 °C are possible with both technologies, but the initial investment cost and operation costs are different. Based on thermal and electrical performance data from measured devices these costs and the CO₂ emission reduction achieved are compared for a reference case of a device delivering 297 kW of revaluated heat with a temperature 125 °C, using waste heat with temperatures between 75 and 95 °C.

Introduction/Background

The performance of a new AHT in a refinery was thoroughly investigated in [1]. The system with an adiabatic absorption chamber and an innovative non-condensable gases purge system delivered between 200 and 300 kW of revaluated heat with temperatures between 115 and 135 °C.

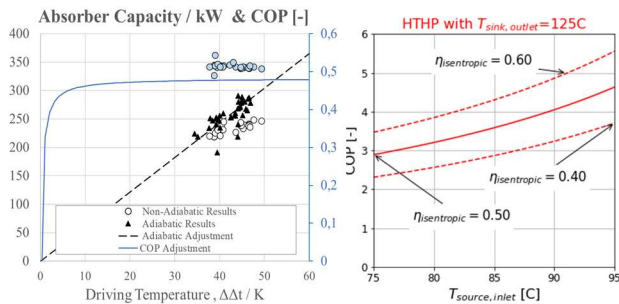


Figure 1: Thermal Performance of AHT and HTHP

Based on the thermal performance of this prototype, the performance of an AHT delivering 297 kW of useful heat at 125°C is compared with that of an HTHP for heat source temperatures between 75 and 95 °C. The investment cost of the AHT increases with decreasing activation temperature that need larger heat exchanger areas. The COP of the HTHP have been calculated assuming constant isentropic efficiencies similar to those of commercial devices.

Discussion and Results

The electric consumption of AHT and HTHP are calculated based on the AHT system from [1]. The electrical consumption of external pumps for HTHP is around 1/3 of those of the AHT, because it has one circuit less and the waste heat flow is smaller.

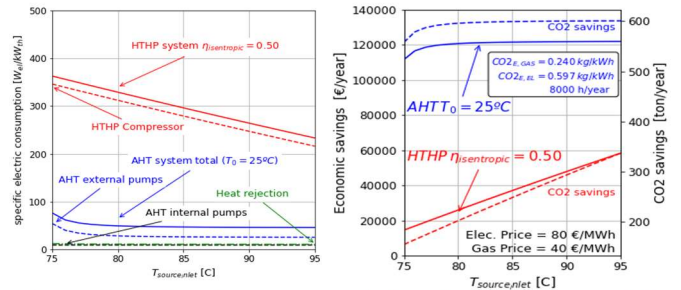


Figure 2: Electrical consumption (left) and yearly savings (right)

The yearly economic and CO₂ savings substituting a gas boiler with both alternatives have been calculated for two scenarios, with different ratios between electricity and gas costs.

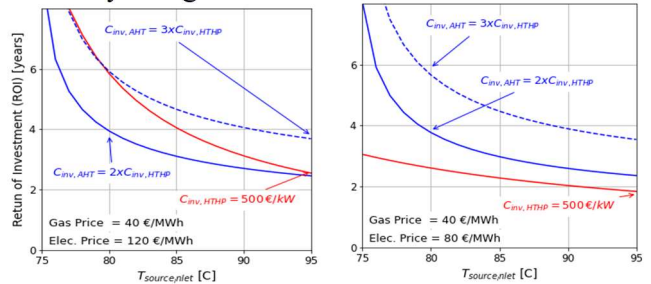


Figure 3: ROI of AHT and HTHP based systems

Summary/Conclusions

The economic and CO₂ savings are between 1.5 and 7.7 times larger for AHT systems, with much lower electricity consumption. Depending on the ratio of electricity and gas costs, the ROI can be better for AHT even with much larger investment costs (C_{inv}).

References

- [1] Martinez-Urrutia, A., et Al. (2020). Experimental results and thermoeconomic analysis of an absorption heat transformer operating in a petrol refinery. ISHPC 2020

LHP model with structured primary wick

J. Esarte^{1*}, J.M^a. Blanco², U. Izquierdo²

¹NAITEC. C/ Tajonar 20. 31006 Pamplona (Spain)

²UPV / E.H.U. Plaza Ingeniero Torres Quevedo. Edif. 1. 48013 Bilbao (Spain)

*Corresponding author: jesarte@naitec.es

Abstract

A mathematical model representing the LHP's performance is developed with special interest in the primary wick (structured wick instead of the traditionally used unstructured wick). The model validation shows a very accurate prediction with respect to the experimental values for a given LHP configuration and operating conditions. The influence of certain design parameters is analysed: diameter of the capillary and length of the tube.

Keywords: capillary pressure, loop heat pipe, wick, two phase cooling.

Introduction/Background

The difficulty in economically and efficiently cooling power electronic devices has led to the development of new architectures and materials [1] as well as to the development of new refrigeration technologies [2]. Among these technologies are the so-called Loop Heat Pipes, "LHP". This work aim is to develop a mathematical model of a LHP composed of a structured primary wick. Likewise, both model validation and design and operation variables influence analysis are carried out.

Discussion and Results

Figure 1 shows the general operation of a LHP. By applying the conservation laws (momentum, mass, and energy) to each of the constituent elements, the LHP's mathematical model is obtained.

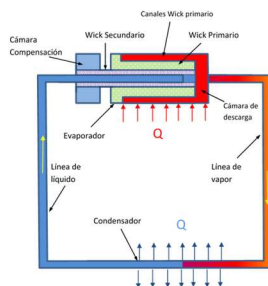


Figure .1: LHP diagram showing the constituent elements

Model accurately predicts the LHP real performance, as depicted in figure 2.

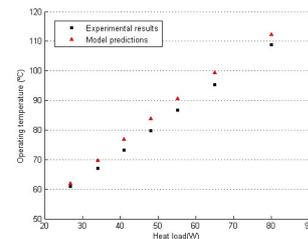


Figure .2: Model validation

The effect of pipe radius is shown in figure 3.

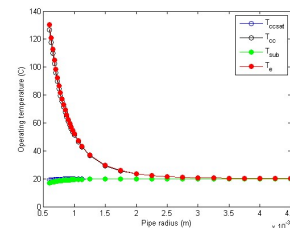


Figure 3: Operating temperature vs tube radius for a tube length "Lv = 0.2m" and condensing temperature Tc = 20 °C

Summary/Conclusions

Model matches the experimental values (less than 4% of drift). The model allows to check the effect of certain parameters on the operating temperature.

Acknowledgements

Authors deeply acknowledge Research group IT1514-22 for the guidance provided to this project.

References

- [1] J. Esarte; J.M Blanco, C.Wolluschek, D.Prieto. "Modules, Systems, and Applications in Thermoelectrics and/or the Materials, Preparation, and Characterization in Thermoelectrics"; Chapter 20-Heat Dissipaters. Volume 1-2 –2012.
- [2] Riehl, R. R., Santos, N., "Water copper nanofluid application in an open loop pulsating heat pipe", Applied Thermal Engineering, 2012.

Structural properties of a transformer oil-based nanofluid under an external electric field - neutron reflectometry study

M. Karpets^{1,2*}, M. Rajnak^{1,2}, V. Petrenko³, I. Gapon^{4,5}, M. Avdeev⁵, Z. Mitroova¹,
L. Bulavin⁴, M. Timko¹ and P. Kopcansky¹

¹Institute of Experimental Physics SAS, Watsonova 47, 040 01 Kosice

²Technical university of Kosice, Letná 9, 04200 Kosice, Slovakia

³BCMaterials, Basque Centre for Materials, Applications and Nanostructures, Pl. 3 Parque Científico UPV/EHU Barrio Sarriena, 48940 Leioa, Spain

⁴Taras Shevchenko National University of Kyiv, 64/13, Volodymyrska Str., Kyiv 01601, Ukraine

⁵Joint Institute for Nuclear Research, Joliot-Curie 6, 141980, Dubna, Russia

*Corresponding author: karpets@saske.sk

Abstract

The aim of the given work is to shed light on bulk structural changes in transformer oil-based ferrofluid (TOFF) with magnetite magnetic nanoparticles (MNPs) as well as the magnetic fluid-solid interfaces under the influence of various electric fields by means of neutron reflectometry (NR). The concentration of the Fe₃O₄ NPs in the magnetic fluids (MFs) was around 0.6 vol %. In the absence of electric field and up to 100 kV/m we observed only wetting MNPs layer at the electrode surface, but with increasing field strength additional MNPs layer was formed. At sufficiently strong electric field (700 kV/m) the second layer became even more saturated than the initial one. The reason of such development is polarization of the particles and their interaction as dipoles. Such layering has a potential effect on more effective heat transfer from electrical conductor (transformer winding) to the cooling liquid.

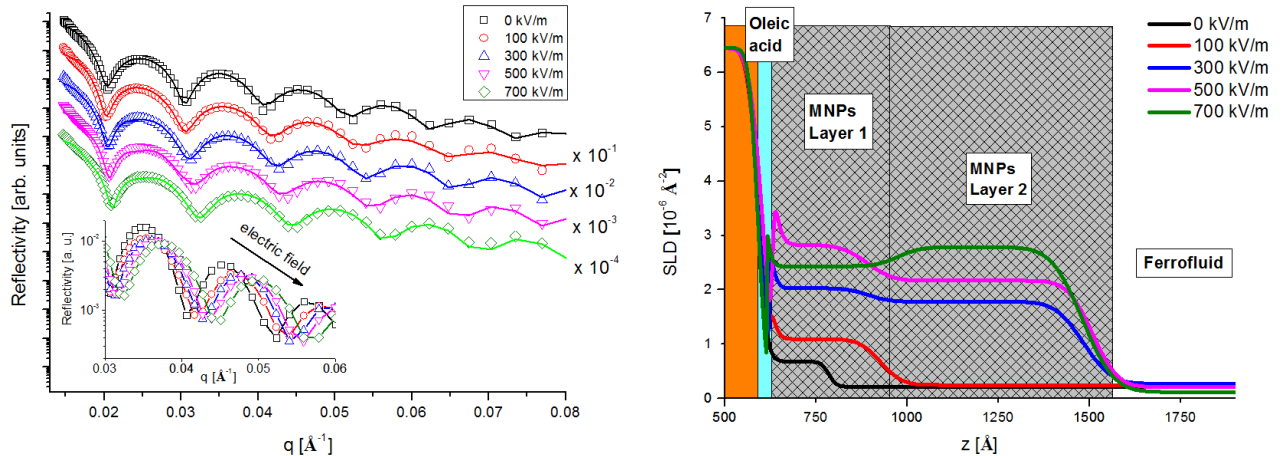
Keywords: transformers, working fluids, transformer oil, ferrofluids.

Introduction/Background

During the transformer operation it is necessary to transfer the heat from the transformer. The insulating liquids are a major part of the insulation system also in other electrical equipment like circuit breakers, switchgears, bushings, cables, capacitors etc. [1]. Due to an increasing demand on the effective cooling, the applied liquid medium has to exhibit high specific heat and thermal conductivity with low viscosity and pour point [2]. It was found that Fe₃O₄ NPs cause an increase in convection heat transfer in the absence of magnetic field [3]. Moreover it was observed that the presence of the NPs in the liquid medium can paradoxically enhance its electro insulating properties too. In the close area around power transformers the essential conditions for the induction of thermomagnetic convection are also well met. Therefore it is crucial to investigate structure of TOFF near surface under working conditions of transformers. NR has been intensively used to study structural changes of ferrofluids under external magnetic fields [4]. In this paper, we present results of NR measurements of TOFF on planar silicon surface under the different homogeneous electric fields.

Discussion and Results

Magnetite MNPs with the mean size 9 nm were synthesized by chemical co-precipitation method from aqueous solution of ferrous and ferric ions, then sterically stabilized by chemisorbing of a single oleic acid layer. Synthesis of MF was performed at IEP SAS. The neutron reflectometer GRAINS with a horizontal sample plane configuration installed at the pulsed IBR-2 reactor at JINR (Russia) was employed for NR measurements. As a preliminary result it was found that application of electric field leads to formation of additional MNPs layer



at the initial wetting layer with further reordering with increasing electric field more than 700 kV/m. Moreover the effect of electric field is visible for 3 hours after switching the field off.

Figure 1. Left: NR data taken when applying electric field from 0 kV/m to 700 kV/m. The solid lines represent fits to the data. Inset: NR data for q -range $[0.03; 0.06] \text{ \AA}^{-1}$. Right: profiles of SLD plotted as a function of distance z from the Si(100) surface determined from the results of the fits.

Summary/Conclusions

The assembling of MNPs of a classical ferrofluid (magnetite coated with oleic acid in transformer oil) in wetting layer on a planar silicon surface with copper electrode film was observed by NR. In the static electric field, the particles are polarized and due to the high dielectric contrast between the transformer oil and magnetite, the induced dipoles are strong enough to activate the attractive interaction. Therefore, iron oxide nanoparticles in magnetic fluids form additional dense layer with thickness about 40 nm between wetting layer and homogenous magnetic fluid. At the critical field, this effect is associated with the decrease in particle concentration in the near electrode region. The observed self-assembled layering could be used as additional barrier at the inner surface of transformer to increase dielectric breakdown voltage of working fluids. Also the secondary flows induction by electric field could disturb the resistive boundary layer and advance heat transfer.

References:

- [1] I. Fofana, 50 Years in the development of insulating liquids, *IEEE Electr. Insul. Mag.* 29, 13, 2013.
- [2] M. Rajnak, Z. Wu, B. Dolnik, K. Paulovicova, J. Tothova, R. Cimbalá, J. Kurimsky, P. Kopcansky, B. Sunden, L. Wadso and M. Timko, Magnetic field effect on thermal, dielectric, and viscous properties of a transformer oil-based magnetic nanofluid, *Energies* 12, 4532, 2019.
- [3] N. Hatami, A. Kazemnejad Banari, A. Malekzadeh, and A. R. Pouranfard, The effect of magnetic field on nanofluids heat transfer through a uniformly heated horizontal tube, *Phys. Lett. A* 381, 510, 2017.

- [4] K. Theis-Bröhl, A. Saini, M. Wolff, J. A. Dura, B. B. Maranville, and J. A. Borchers, Self-assembly of magnetic nanoparticles in ferrofluids on different templates investigated by neutron reflectometry, *Nanomaterials* 10, 1231, 2020.

Optimization of the energy balance at desalination plants

M. Urrestizala^{1*}, J. Azkurreta¹

¹University of the Basque Country (UPV/EHU) Department of Energy Engineering,
Ingeniero Torres Quevedo Plaza, 1, 48013 Bilbao, Biscay

*urrestizala97@gmail.com

Abstract Desalination plants are indispensable systems in some areas for the creation of drinking water, and their biggest obstacle is the large amount of energy required for reverse osmosis, representing more than 50%-60% of production costs, so there has been a huge development in energy recovery systems up to those used today, with almost unbeatable efficiencies.

However, this energy balance could be further improved by using micro-hydraulics at points where a considerable amount of energy is currently wasted, such as in the load-break of the waste water when it is discharged into the sea when it is at a lower level. For this, however, it will be necessary to adapt these technologies with the materials required according to the very specific salinisation characteristics of this water.

Keywords: desalination, energy-recovery, micro-hydro, materials

Introduction/Background

The *Bilbao School Of Engineering* offers a wide variety of training courses and as part of the multidisciplinary nature of industrial engineers, there is an option to study the specialty of *Hydraulic Energy*, in which desalination is analysed from different points of view.

To begin with, within the subject of *Water Resources Management and Hydroelectric Power Plants*, desalination is studied as an alternative to be taken into consideration for the main water resources available to human development, especially in some specific areas.

On the other hand, it is also treated as part of *Fluid Facilities and Technology* subject.

It deals with the operation, calculation and sizing of many of the main elements that make up water plants, and specifically desalination plants, such as the pumps required during the process and the types of turbines that could be employed at different points for energy exploitation, etc.

In addition, within *Exploitation and Maintenance of Hydraulic Systems*, different methods of calculation, statistics and data processing are studied, which are directly applicable to desalination plants and their sizing.

Likewise, desalination is also introduced in the subject of *Fluid Networks*, which is essential for understanding all the civil works involved in a plant of these nature and, above all, for properly sizing all the piping equipment and its corresponding characteristics that the networks must have before, during and after their passing through the plant, depending on their corresponding requirements.

Finally, thanks to *Computational Fluid Mechanics*, it is possible to understand and learn how to use one of the most modern and useful tools on the market, Star CCM+, which can be directly applied, once again, in the most detailed calculations of the different systems that make up these plants.

Bearing all this in mind, the main objective will be to implement what has been learned in order to give a new perspective on desalination plants, specifically on the energy recovery that is required for them to be truly viable, since energy consumption is the biggest cost involved in seawater desalination, representing more than 50%-60% of production costs [1].

Discussion and Results

As is well known, in order to produce the separation of salts and water in the membranes, it is necessary to give the membranes a pressure higher than the osmotic pressure of the salt solution, and it is hence required to bring the seawater to a pressure of approximately 55-80 bar at the membrane inlet [2]. Energy Recovery Systems take advantage of this pressure to return it, to a large extent, to the water entering the membranes and thus reduce the amount of energy to be supplied by the pumps to reach the high pressures mentioned.

HOW IT STARTED

The first idea for energy recovering was to install a traditional reverse pump, which was not very flexible with the variations in the operation of the plant [3].

The introduction of the Pelton turbine solved many of these inefficiencies, as it had a higher recovery efficiency of 88% compared to 77% for the inverted pump, and also allows for variations in inlet pressure. In this case, the power was used to assist the electric motor of the high-pressure pump. This system, however, became obsolete [4].

In an attempt to reduce costs and energy consumption, another, more compact Energy Recovery Unit was developed, in which the pump and turbine were joined in reverse with a single shaft. This was the so-called turbopump. Subsequently, the much smaller turbocharger was developed in a similar way.

HOW IT GOES ON

Currently, the most widely used technology is the Pressure Exchange Chamber. On the one hand, rotational chambers, particularly the ERI (Energy-Recovery Inc.), which makes the two flows, the pressurised brine and the new feed, collide, transferring the energy from the first fluid to the next (see Figure 1), with with efficiencies of 98 % [5].

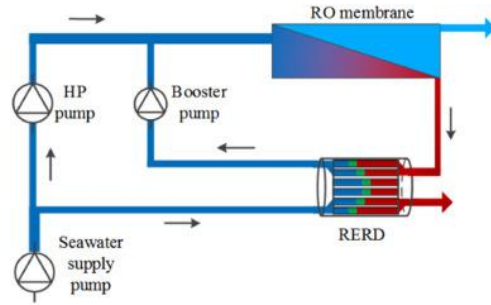


Figura 1. Schematic of Reverse Osmosis system with Rotational Pressure Exchange Chamber [6]

And on the other hand, the displacement ones, with special emphasis on the DWEER (Dual Work Exchanger Energy Recovery), which basically consist of two cylinders with pistons and a set of valves and ultimately perform the same function (see Figure 3), with efficiencies of 96 % [7].

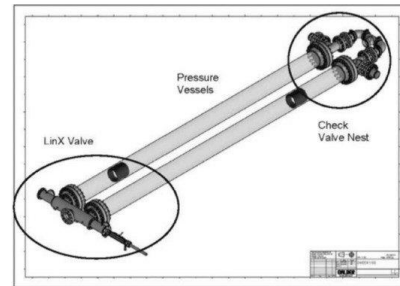


Figura 2. Typical structure schematic view of DWEER [8]

Given the high performance of these new technologies, the margins available for reducing the energy consumption of the desalination process by these means are already quite small, and it would be interesting to combine this with other concepts.

HOW IT CAN BE IMPROVED

One option for improving the energy balance of desalination plants is the hybridisation of the current devices with new renewable technologies, such as micro-hydro, which has been gaining weight in the recent times.

Given that some of the plants, depending on the geography of the area in which they are located, return the brine to the sea at a point several metres below their level, it would be interesting to take advantage of this difference in potential, which is currently

wasted, for the generation of hydroelectric energy.

To achieve this, there is a range of studies for adaptations of traditional Pelton [9, 10, 11], Turgo [10, 12, 13, 14], Banki [15, 16, 17, 18, 19, 20, 21], Francis [22, 23, 24, 25] and Kaplan [26, 27] (see Figure 3) turbines for these lower-than-usual head and flow rates. And there are also new reserarches and technologies designed directly for these new points, which could be suitable for micro-use: variable speed PATs [28, 29, 30], to adapt to the conditions of the plant at each moment while maintaining their performance, gravitational microturbines [31], hydrokinetic turbines [32, 33, 34], or hydro-screw turbines [35, 36](see Figure 4).

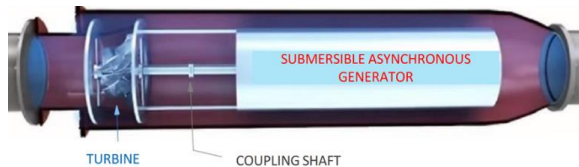


Figura 3. Perga Turbogenerator (Kaplan variation) [27]

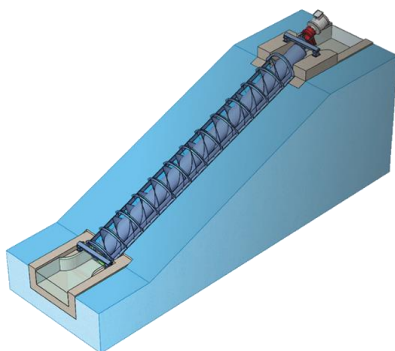


Figura 4. Hidrotor Archimedes Screw Generator (New Technology) [36]

The problem lies in the fact that this water returned to the sea has a very high salinisation, and therefore it would be necessary to adapt the designs of these new technologies by using the appropriate materials to comply with the required characteristics. The special condition to be met by these materials is basically having a *Pitting resistance Equivalent Number* $PREN > 40$ (where $PREN = \% Cr + 3.3 \times \% Mo + 16 \times \% N$), the minimum level of alloying required to resist crevice corrosion in seawater by standards, such as the

Norwegian oil and gas NORSOK standard. Therefore the possible choices would be UNS S31254 [37], UNS S32750, UNS S32760 and UNS 32550.

Conclusions

In summarizing, the technology of energy recovery in desalination plants is at a point of great development, so it is very difficult to further increase its efficiencies. However, it is possible to achieve higher energy balances by hybridisation with micro-hydraulics at lower discharge points.

New lines of research must therefore be able to combine knowledge of microhydraulics and research into the materials that would be required for these physical-chemical characteristics of the brine.

References

- [1] Chaudhry, S. *An Overview of Industrial Desalination*, Proceedings of the ASME Industrial, 2013.
- [2] Gambier, A., Krasnik, Badreddin, E. *Dynamic Modeling of a Simple Reverse Osmosis Desalination Plant for Advanced Control Purposes*, 2007 American Control Conference, 2007.
- [3] Morales F. M., Sánchez, J. M. S. *Mejora de la eficiencia energética en plantas desaladoras: nuevos sistemas de recuperación de energía*, Ingeniería y territorio (Ejemplar dedicado a: Desalación), 2005.
- [4] Gude, V. G. *Energy consumption and recovery in reverse osmosis*, Desalination and Water Treatment, 2011.
- [5] Stover, R. *Retrofits to improve desalination plants*, Desalination and Water Treatment, 2010.
- [6] Jianqiang K. L., Ye, D. F. *Visualization of flow structures in a rotary type energy recovery device by PIV experiments*, Desalination, 2018.
- [7] Wang, Z., Wang, Y., Zhang, Y., Qi, B., Xu, S., Wang S. *Pilot tests of fluid-switcher energy recovery device for seawater reverse osmosis desalination system*, Desalination and Water Treatment, 2012.

- [8] Schneider, B. *Selection, operation and control of a work exchanger energy recovery system based on the Singapore project*, Desalination, 2005.
- [9] Stamatelos, F. G., Anagnostopoulos, J. S., Papantonis, D.E. *Performance measurements on a Pelton turbine model*, Proceedings of the Institution of Mechanical Engineers, Part A: Journal of Power and Energy, 2011.
- [10] Cobb, B.R., Sharp, K.V. *Impulse (Turgo and Pelton) turbine performance characteristics and their impact on pico-hydro installations*, Renew. Energy, 2013.
- [11] Quaranta E., Trivedi, C. *The state-of-art of design and research for Pelton turbine casing, weight estimation, counterpressure operation and scientific challenges*, Heliyon, 2021.
- [12] Benzona, D.S., Aggidisa, G.A., Anagnostopoulos, J.S. *Development of the Turgo Impulse turbine: Past and present*, Applied Energy, 2016.
- [13] Gaiser, K., Erickson, P., Stroeve, P., Delplanqu, J.P. *An experimental investigation of design parameters for pico-hydro Turgo turbines using a response surface methodology*, Renewable Energy, 2016.
- [14] Williamson, S. J., Stark, B. H., Booker, J.D. *Performance of a low-head pico-hydro Turgo turbine*, Appl. Energy, 2013.
- [15] Acharya, N., Kim, C.G., Thapa, B., Lee, Y.-H. *Numerical analysis and performance enhancement of a cross-flow hydro turbine*, Renewable Energy, 2015.
- [16] Desai, V.R., Aziz, N.M. *An Experimental Investigation of Cross-Flow Turbine Efficiency*, ASME. J. Fluids Eng, 1994.
- [17] Girma, M., Dribssa, E. *Flow Simulation and Performance Prediction of Cross Flow Turbine Using CFD Tool*, International Journal of Engineering Research and General Science, 2014.
- [18] Gómez, J.I.G., Higuaita, E.A.P., Gutiérrez, C.A.P. *La turbina Michell-Banki y su presencia en Colombia*, Avances en Recursos Hidráulicos, 2008.
- [19] Motohashi, H., Goto, M., Sato, Y. *Development and field test of open cross flow type micro-waterturbines*, The 14th National Symposium on Power and Energy System, 2010.
- [20] Pereira N., Borges, J. *A study on the efficiency of a cross-flow turbine based on experimental measurements*, Proceedings of the 5th International Conference on Fluid Mechanics and Heat & Mass Transfer, 2014.
- [21] Romero, F., Velásquez, L., Chica, E. *Consideraciones de diseño de una turbina Michell-Banki*, Revista UIS Ingenierías, 2021.
- [22] Lucino, C.V., Rivetti, A., Angulo, M.A., Rodríguez. D., Liscia, S.O. *Funcionamiento de las turbinas Francis fuera de la condición de diseño*, V Jornadas de Investigación, Transferencia y Extensión de la Facultad de Ingeniería, 2019.
- [23] Resiga, R., Muntean, S., Ciocan, G.D. *Jet control of the draft tube vortex rope in Francis turbines at partial discharge*, 23rd IAHR Symposium, 2006.
- [24] Laouari, A., Ghenaiet, A. *Investigation of Steady and Transient Cavitating Flows through a Small Francis Turbine*, Renewable Energy, 2021.
- [25] Magureanu, R., Albu, M., Bostan, V., Dumitrescu, A., Pelizza, M., Andreea, F., Dimu, G., Popa, F., Rotar, M. *Optimal operation of Francis Small Hydro turbines with variable flow*, IEEE International Symposium on Industrial Electronics, 2008.
- [26] Židonis, A., Benzona, D.S., Aggidis, G.A. *Development of hydro impulse turbines and new opportunities*, Renewable and Sustainable Energy Reviews, 2015.
- [27] “Perga - Alisea. Submersible Turbo Generator Ref: TURB 012020 V1.0.”, 2020, <https://alisea.es/wp-content/uploads/2020/06/COMMERCIAL-Presentation-PERGA-ALISEA-turbogenerators.-V.5.0.pdf>.
- [28] “Tecnoturbines- Powering water”, <https://tecnoturbines.com/>
- [29] Nautiyal, H, Varun, Kumar, A. *Reverse running pumps analytical*,

experimental and computational study: A review, Renewable and Sustainable Energy Reviews, 2010

[30] Nautiyal, H., Varun A. K., Yadav, S. *Experimental Investigation of Centrifugal Pump Working as Turbine for Small Hydropower Systems*, Energy Science and Technology, 2011.

[31] Velásquez, L., Chica, E., Posada, J. *Advances in the Development of Gravitational Water Vortex Hydraulic Turbines*, Journal of Engineering Science and Technology Review, 2021

[32] Shimokawa, K., Furukawa, A., Okuma, K., Matsushita, D., Watanabe, S. *Experimental study on simplification of Darrieus-type hydro turbine with inlet nozzle for extra-low head hydropower utilization*, Renew. Energy, 2012.

[33] Gorlov, A.M. *Helical Turbines for the Gulf Stream*, Marine Technology and SNAME news, 1998.

[34] Gorban, A., Gorlov, A.M., Silantyev, V. *Limits of the Turbine Efficiency*, Journal of Energy Resources Technology, 2001.

[35] Raza, A., Saleem, M., Saleem, Y. *Modeling of archimedes turbine for low head hydro power plant in simulink MATLAB*, International Journal of Engineering Research & Technology (IJERT), 2013.

[36] AZ-Renovbles, “Hidrotor. La energía hidráulica sin descansos”, <http://www.hidrotor.com/>.

[37] Kumar, A., Saini, R. *Techno-Economic Analysis of Hydrokinetic Turbines*, 2018

Transformation and installation of CNG refuelling for a Bilbao River's tourist boat.

Alex Segura Coronado^{1,*}, Jesús M^a Blanco Ilzarbe¹ and Roberto González Andrés²

¹UPV/EHU, School of Engineering, Energy Engineering Dept.

Plaza Ingeniero Torres Quevedo 1, 48013 Bilbao

²Nortegas Energía Grupo.

Plaza Euskadi 5, Planta 23, 48009 Bilbao

*Corresponding author: asegura009@ikasle.ehu.eus

Abstract

The purpose of this project is to carry out an economic and technical analysis of the conversion to natural gas of the engine of a tourist boat in the urban environment Bilbao River. The project has to study both the feasibility of a complete change of engine and/or the dualisation of the existing one; the availability of fuel storage in CNG (compressed) mode onboard and the additional necessary safety measures [1].

In addition, the project will provide a solution for refueling from land and at the berth of the boat [2], including the calculation of the equipment necessary to provide CNG supply, refuelling times, electrical energy needs and the surface area that such equipment requires on land [3]. Furthermore flexible connection to the boat, safety and fire protection systems, will be studied.

Keywords: Natural Gas (NG), Compressed Natural Gas (CNG), Carbon Footprint, Air Quality, Net emissions.

Introduction/Background.

Within the strategy for the transition to a decarbonised economy, natural gas is classified as an alternative fuel according to Article 2(1) of Directive 2014/94/EC.

This is presented as a real, available and affordable solution, which allows reducing the carbon footprint of any means of transport, as well as improving air quality in cities by eliminating particulate matter, especially sulfur and nitrogen oxides [4].

Discussion and Results

A short summary of calculations and a succinct discussion of key results through figures and tables will be presented.

Summary/Conclusions

In the future, Natural Gas can even be replaced by 100% renewable Natural Gas biomethane or in the proportion that the market will allow [5], leads to neutral or even negative net emissions (acting as a CO₂ sink)

Acknowledgements

Authors deeply acknowledge Aula Nortegas (Bilbao School of Engineering) for the guidance provided.

References

- [1] Orden ITC/3126/2005, de 5 de octubre, normas de gestión técnica del sistema gasista.
- [2] Khan, M. I., Yasmin, T., & Shakoor, A. (2015). Technical overview of compressed natural gas (CNG) as a transportation fuel. *Renewable and Sustainable Energy Reviews*, 51, 785-797.
- [3] Demirbas, A. (2002). Fuel properties of hydrogen, liquefied petroleum gas (LPG), and compressed natural gas (CNG) for transportation. *Energy Sources*, 24(7), 601-610.
- [4] Semin, R. A. B. (2008). A technical review of compressed natural gas as an alternative fuel for internal combustion engines. *Am. J. Eng. Appl. Sci*, 1(4), 302-311.
- [5] Hesterberg, T. W., Lapin, C. A., & Bunn, W. B. (2008). A comparison of emissions from vehicles fueled with diesel or compressed natural gas. *Environmental science & technology*, 42(17), 6437-6445.

HPC-2021-Poster-P109

Optimizing Carnot battery configuration for waste heat recovery integrated system with ORC

Miroslav Rathan, Jan Spale, Vaclav Novotny

University Centre for Energy Efficient Buildings, Czech Technical University in Prague, Trinecka 1024, Bustehrad, 27343, Czech Republic
Department of Energy Engineering, Faculty of Mechanical Engineering Czech Technical University in Prague, Technicka 4, 166 07 Prague 6, Czech Republic

INTRODUCTION

Industrial waste heat recovery (WHR) and its conversion to power may become more feasible thanks to novel thermally integrated configuration of Carnot Batteries (CB).

WHR in industries:

- Often coupled with high technological cost and lack of incentives
- Many industries which pay high capacity reserve due to oscillations in electricity consumption are also abundant in the excess of waste heat
- Utilizing this waste heat by the means of CB brings an interesting opportunity for the industries

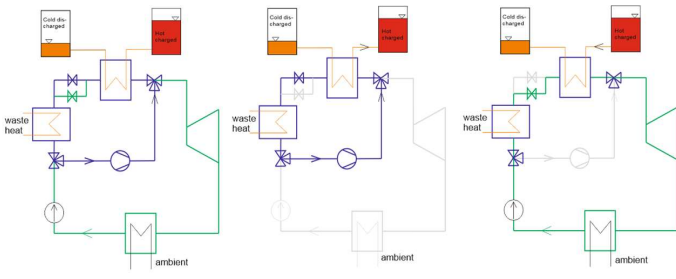
PROPOSED CONFIGURATIONS FOR WHR CB SYSTEMS

Objective – to analyze:

- the possibility of utilization of upgraded heat in the industry
- maximization of the waste heat utilization
- applicability for pilot system

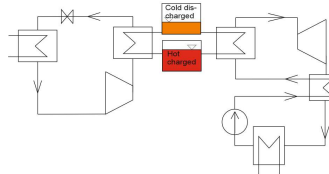
Solution

- **Novel configuration** of a thermally integrated CB improves WH utilization and increases overall performance
- Waste heat is supplied during the discharge process together with the heat from the storage
- The upgraded heat in our analyses needs to be useful for technological purposes
 - 3 discharge options – waste heat + storage; storage only; waste heat only

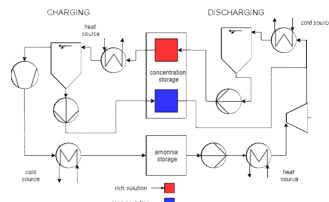


Reference models

- Standard configuration with ORC



- Concentration based storage (similarities with Kalina cycle)

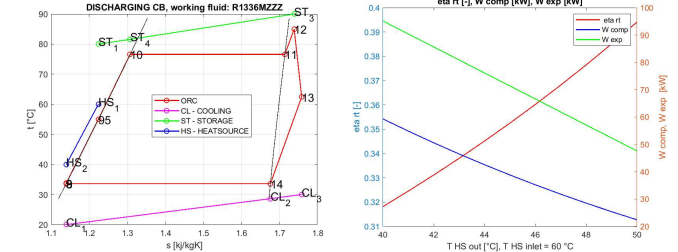


METHODS

- Selected working fluid R1336mzz(z)
- Boundary conditions based on considered pilot plant
- Case study – quenching kiln
 - Heat source: 2 kg/s water, 60 / 50°C
 - Thermal storage: 90 / 80°C
 - Ambient heat rejection 20 / 30°C
- Consequently a comprehensive performance mapping over possible temperatures range

RESULTS

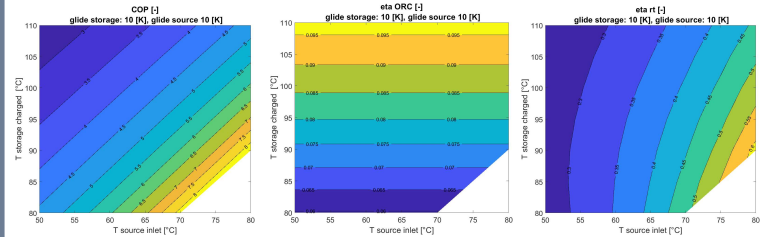
Case study



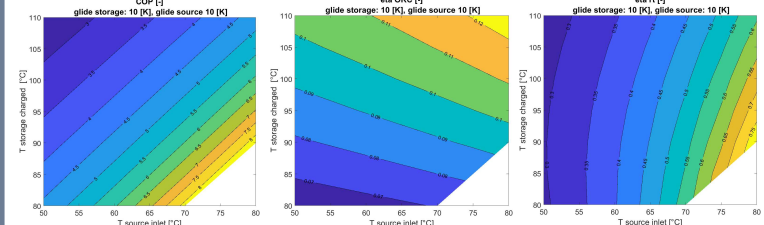
Case	COP	η_{RC}	η_{RT}	W_{char}	$Q_{reutilized}$ (char / disch)	W_{disch}
TI-PTES-standard	4.73	7.39%	35%	22.4 kW	83.7 / 0 kW	15.9 kW
TI-PTES-recup.	4.73	7.93%	37.5%	22.4 kW	83.7 / 0 kW	16.7 kW
Novel WH integr.	4.73	8.33%	39.4%	22.4 kW	83.7 / 41.8 kW	23.3 kW
Concentration concept	n.a.	n.a.	171%	0.5 kW	63 / 63 kW	2.1 kW
WHR only	-	0.02	Infinity	-	0 / 46 kW	0.9 kW

Performance mapping

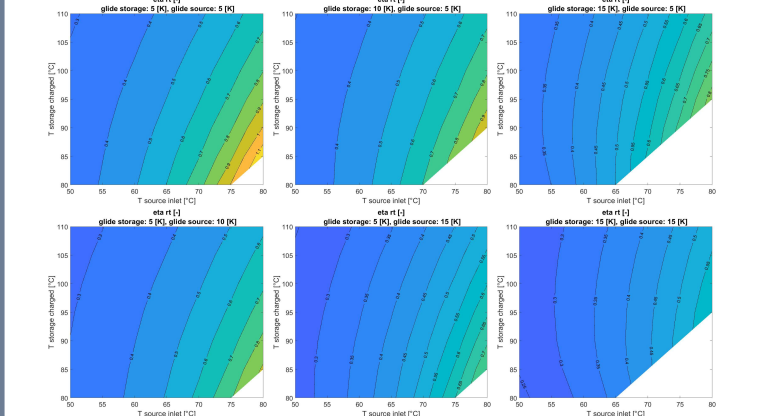
- Reference ORC



- Proposed system



- Sensitivity on source and storage temperature glide



DISCUSSION & CONCLUSIONS

- Potential improvement in WH utilization by a novel reversible ORC CB configuration
 - Round trip efficiency increase along with increase in power
 - May operate at reduced power also when only with WH or only storage
- Experimental validation of the novel configuration is needed to verify whether the increased complexity and cost of the system would be justified, especially part-load

HPC-2021-Poster-P110

Assessment and comparison of a power-to-heat-to-power (P2H2P) storage systems based on resistance heating and Brayton heat pump using liquid salts for energy storage

Václav NOVOTNÝ, František HRDLIČKA

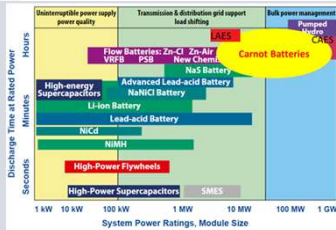
Czech Technical University in Prague, Faculty of Mechanical Engineering, Dpt. of Energy Engineering, Technicka 4, 166 07 Prague 6, Czech Republic

As the penetration of renewables with large intermittency increases, electricity storage demand is rapidly increasing on all levels of duration and capacity, from short-term systems to systems capable of storing energy in order of hours or even days. Considering technically feasible technologies for long term storage, which are however not geographically dependent, the options include Liquid Air Energy Storage (LAES), Power to Fuels (P2F) and Carnot batteries, i.e. Power – to – heat – to – power (P2H2P). Out of these systems, storing electricity into heat has a potential of very low cost in comparison to alternatives.

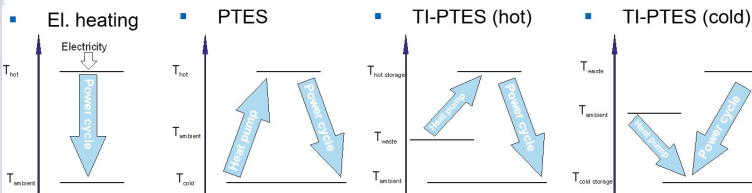
P2H2P SYSTEMS



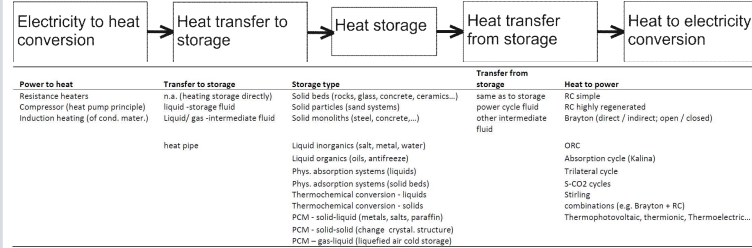
- Power scale from largest electro-chemical batteries to large hydro plants
- Capacity scale from hours to days (in concepts even weeks)
- Interesting for cheap renewable power regardless lower efficiency
- Largely based on existing technologies



Basic working principles:



Range of technological possibilities:



Selected fundamental technologies:

- Hot storage: 2 molten salt tanks (experience from CSP, limiting temperatures for freezing and material decomposition)
- Cold storage: Rocks (< -50°C), Ice slurry (~ 0°C)
- Direct electrical heating + Rankine cycle
- Brayton heat pump + power cycle (working fluids air, Ar, CO₂)

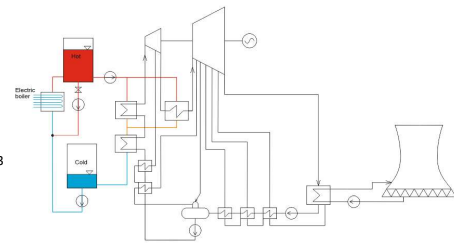
BOUNDARY CONDITIONS

- 30 MWe charging, 10 MWe discharging
- 15 h storage of electrical production
- Salt high temperature considered 380°C (limited corrosion) and 560°C (material limit of nitrate salts)
- Minimum pinch point: 5 - 30 K (based on phase and state)
- Pump, compressor and turbine efficiency: according to real expectations
- Pressure losses: included in Rankine cycle
- Thermal losses: Negligible except for tank over seasonal operation

ANALYSED CONFIGURATIONS & BALANCE MODEL RESULTS

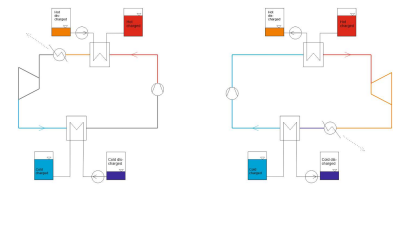
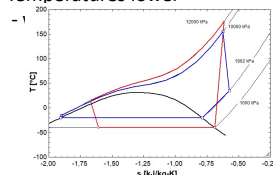
Electrical heating + Rankine cycle

- Highly regenerated
- Classical design of plants
- All technologies proven
- Solar salt 60% NaNO₃ 40% KNO₃ suitable
- (cheaper, discharge T 299°C)



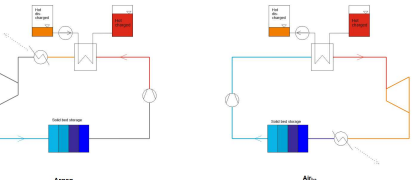
Pumped Thermal Energy Storage

- **With liquid cold storage**
- Considered for CO₂
- Temperatures lower



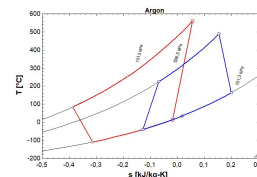
With solid cold storage

- Considered for air and Ar
- Gas at low pressure always at ambient pressure (for tank consideration)
- Compression ratio ~ commercial gas turbines



Pressure ratio:

	1 st cycle	2 nd cycle
CO ₂	12	10
Air	10	5
Ar	23	10

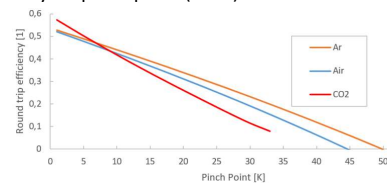


RESULTS & DISCUSSION

Baseline round-trip efficiency

system	RC, 380°C salt	RC, 560°C salt	PTES CO ₂	PTES air	PTES Ar
η [%]	38	43	41.7	36.9	39.0

Sensitivity analysis: pinch point (PTES)



- PTES – potential of additional ~ 3 - 5 p.p. with waste heat recovery
- Amount of salt for storage (15 h, 10 MWe production, RC system): 429 MWh,
- 11.5 M ton, volume 6 140 m³
- i.e. cylinder D 20 x H 20 m
- Thermal loss with 500 mm insulation: 100 kW
- Analysis of seasonal round trip eta with thermal losses: RC system: 30 %

Absorption power cycle with aqueous salt solution for low temperature heat utilization

Vaclav NOVOTNY, Michal KOLOVRATNIK, Hung-Yin TSAI

Faculty of Mechanical Engineering, Czech Technical University in Prague, Technická 4, Prague 6, 16607, Czech Republic
Department of Power Mechanical Engineering, National Tsing Hua University, No. 101, Kuang-Fu Road, Hsinchu, 30013, Taiwan

INTRODUCTION AND STATE OF THE ART

Absorption power cycle (APC)

- Known as Kalina cycle, with water-ammonia fluid, partly commercialized
- Limited application due to technical issues and failures, limited experiments
- Many theoretical works predict benefit from temperature glide, propose complex configurations
- Suggested also combined power and cooling configurations

Water-LiBr working fluid

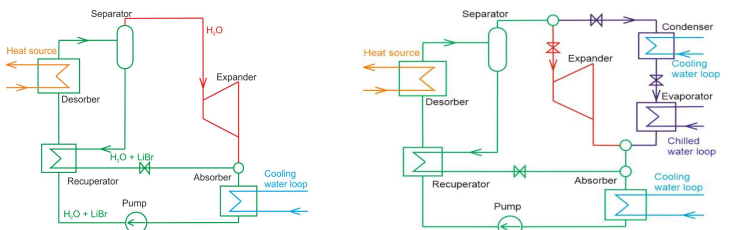
- Fluid common for absorption cooling, only few works suggest for APC
- **Limited literature** on prospect in **waste heat** (generally open loop heat source) utilization by salt APC, **no work on specific combined power & cooling system**
- **No experiments** with salt solution APC reported, limited on actual T glide
- Certain specifics compared to Kalina cycle – LiBr non-volatile, low pressures
 - Turbines appear as suitable expanders, at low T prospect of **3D print**

THESIS OBJECTIVES

- Focusing on salt solution APC
 - Find theoretical benefits and range of prospective applications
 - Upon the theoretical potential, prove technical feasibility of the APC by:
 - Designing and building APC as a proof-of-concept
 - Demonstration of operability of APC and its components, including turboexpander featuring additively manufactured components
 - Provide comparison between theoretical and real operation of key system's components, especially regarding temperature glide and expander feasibility
 - Based on system operation, suggest actual range of applicability and suggested heading of future salt solution APC development

METHODOLOGY & MODELS

- Standard heat and mass balance
- Implementation of fluid properties, HX calculation by elements due to T glide, iterative calculation of equation system in EES
- **Configurations:**
 - Focus on technical feasibility - simple
 - **APC**



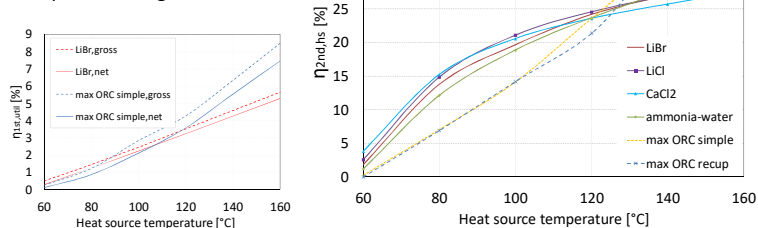
- Considered parasitic load – especially important for low T systems

Key performance indicators

- Cycle efficiency – not suitable for open loop heat source!
- Utilization efficiency – includes cycle efficiency & ability for heat extraction
- Energy & exergy efficiency, gross & net values

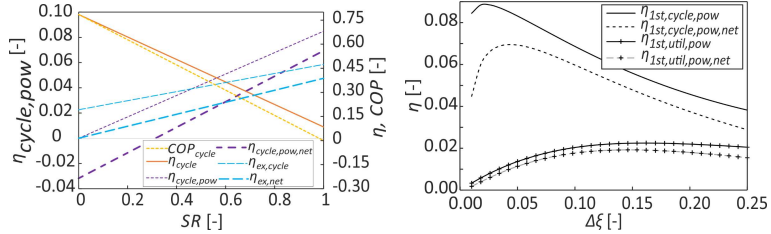
THEORETICAL APC INVESTIGATIONS

- Salt APC superior to ORC below 120°C heat source in WHR applications
- Salt APC slightly better than water-ammonia APC
- All salts similar performance
 - LiBr has most technical exp.
- Importance of gross vs. net W



THEORETICAL APCC INVESTIGATIONS

- Flexible ratio between cooling and power (linear change in parameters)
- Comparable to ORC for W, superior to compression chiller for cold
- Optimal WHR power production at different parameters than cooling

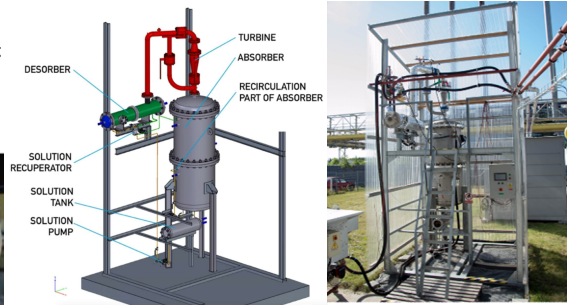


EXPERIMENTAL LiBr APC DEVELOPMENT

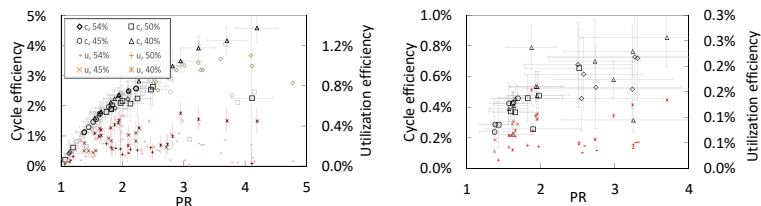
Proof of concept

20 kW_{th}, 300 W_{el} unit

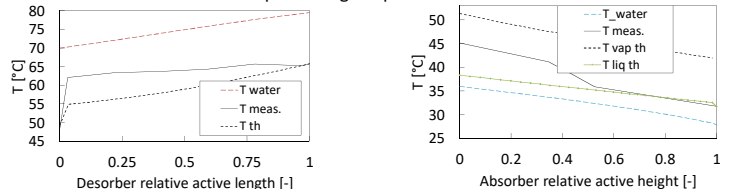
- World 1st reported salt APC
- Expander – nylon 3D printed turbine



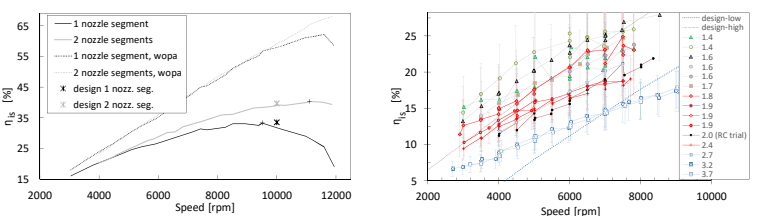
- Potential with state-of-the-art expander (bypass operation) & actual system efficiency



- Theoretical & measured temperature glide profiles for desorber & absorber



- Expander performance – trials with air turbine, comparison with models & APC low pressure vapour (mostly supersonic) turbine measured characteristics



CONCLUSIONS

- Evaluated prospects of salt APC and APCC, suitable for low temperature decentralized applications
- Built world's 1st reported LiBr APC system, investigated its real parameters
 - Temperature glide worse than predicted
 - Heat transfer better in desorber, worse in absorber
- 3D printed polymer turboexpanders, especially for APC, technically feasible, further performance optimization has prospect of higher efficiency

MAIN AUTHOR'S REFERENCES ON THESIS TOPIC

[1] Novotny V, Kolovratnik M. Absorption power cycles for low-temperature heat sources using aqueous salt solutions as working fluids. Int J Energy Res 2017;41:952–75.
[2] Novotny V, Vlodicka V, Masouch J, Kolovratnik M. Possibilities of water-lithium bromide absorption power cycles for low temperature, low power and combined power and cooling systems. Energy Procedia 2011;120:818–25.
[3] Novotny V, Szucs DJ, Špale J, Tsal H-Y, Kolovratnik M. Absorption Power and Cooling Combined Cycle with an Aqueous Salt Solution as a Working Fluid and a Technically Feasible Configuration. Energies 2021, Vol 14, Page 3715 2021;14:3715.
[4] Novotny V, Špale J, Pavlicko J, Szucs DJ, Kolovratnik M. Experimental investigation of a kW scale absorption power cycle with LiBr solution. 6th Int. Semin. ORC pow. Syst., Munich, Germany: 2021.
[5] Novotny V, et al. 3D Printing in Turbomachinery: Overview of Technologies, Applications and Possibilities for Industry 4.0. ASME Turbo Expo 2019 Turbomach. Tech. Conf. Expo., vol. 6, Phoenix: ASME International; 2019, p. V006T24A021.
[6] WeiB AP, Novotny V, et al. Customized ORC micro turbo-expanders - From 1D design to modular construction kit and prospects of additive manufacturing. Energy 2020;209:118407.

Sensitivity analysis of supercritical CO₂ cycles for future high-temperature concentrating solar power plants

D. Novales^{1*}, A. Erkoreka¹, I. Flores¹, U. Oyarzabal¹ and I. Gomez-Arriaran¹

¹ Department of Energy Engineering, Faculty of Engineering of Bilbao, University of the Basque Country (UPV/EHU), Alda. Urquijo s/n, 48013 Bilbao, Spain.

*Corresponding author: email address: davidnovales94@gmail.com

Abstract

In the present study a sensitivity analysis of the S-CO₂ Recompression cycle efficiency was made, considering different compressor and turbine isentropic efficiencies and recuperator effectiveness, as very few real equipment has been developed for these S-CO₂ cycles and uncertainty on the efficiency of these cycles exists. The study was done considering the high temperatures expected to be reached in future concentrating solar power plants. Also, considering these previous conditions, an analysis of the cycle performance for the expected future compressor and turbine efficiencies and recuperator effectiveness was done, achieving a net cycle efficiency of 46.25%. This cycle would be a direct competitor to the current state-of-the art Supercritical Rankine Cycle used in conventional thermal power plants, which can reach cycle net efficiencies up to 45.60%.

Keywords: Supercritical CO₂, Recompression cycle, concentrating solar power

Introduction/Background

New molten salts for concentrating solar power plants are being developed, which would be able to reach temperatures around 700 °C and above [1]. Steam in conventional Rankine cycles could not be superheated above 627 °C due to material limitation [2], but S-CO₂ Brayton cycles would fit such high temperatures, being the Recompression cycle the most efficient S-CO₂ cycle according to the state-of-the art [3].

Discussion and Results

An energy analysis of Recompression cycle was performed for different compressor and turbine isentropic efficiency and recuperator effectiveness. Also, with the expected equipment parameters, a simulation was done to see if Recompression cycle would be competitive against state-of-the art

supercritical Rankine cycle, which can reach efficiencies up to 45.60% in conventional fossil-fuel plants [4]. Results of this simulation are shown in the table below.

Table 1-Comparison between Recompression cycle and supercritical Rankine cycle

	Supercritical Rankine cycle	Recompression cycle (expected equipment parameters)
Cycle net efficiency	> 45.60%	46.25%
Cycle maximum pressure	280 bar	200 bar
Cycle maximum temperature	610 °C	680 °C

Summary/Conclusions

It is concluded that, for the expected parameters of the equipment of the Recompression cycle, it would have a better energy efficiency than the start-of-the art supercritical Rankine cycles.

References

- [1] V.T. Cheang, R.A. Hedderwick, C. McGregor, Benchmarking supercritical carbon dioxide cycles against steam Rankine cycles for Concentrated Solar Power, *Solar Energy* 113 (2015) 199-211.
- [2] M.T. Dunham, B.D. Iverson, High-efficiency thermodynamic power cycles for concentrated solar power systems, *Renewable and Sustainable Energy Reviews* 30 (2014) 758-770.
- [3] D.V.D. Maio, A. Boccitto, G. Caruso, Supercritical Carbon Dioxide Applications for Energy Conversion Systems, *Energy Procedia* 82 (2015) 819-824.
- [4] F. Cziesla, A. Senzel, J. Bewerunge, Lünen – State-of-the Art Ultra Supercritical Steam Power Plant Under Construction, Presented at POWER-GEN Europe, 26-29 May 2009, Cologne, Germany 17 (Jul 1, 2009) 24.

Desalination in the management of the hydraulic resources

I. Arrieta, L. Davila, J. del Olmo, A. García, U. Ozaita, E. Parrón, A.E. Quiñones, I. Sever

Faculty of Engineering Bilbao (EIB/BIE), Specialty of Hydraulic Engineering

Abstract

There are different ways of obtaining hydraulic resources. The most important ones are: in situ resources, like rivers, lakes or wells; water transfer and desalination. This process enables the obtainment of freshwater for human or industrial consumption where the access to drinking water is limited, like deserts or places near the sea.

The desalination process has as its main objective the removal of salt from brackish waters. Once the water is stored, it is submitted to different physical treatment (filtering, decanting, etc.) and chemical processes. After this, it is compressed up to high pressures in order to produce the inverse osmosis. This last step consumes high quantities of energy. Therefore, it is necessary to install systems to recuperate part of the amount of consumed energy.

Keywords: Desalination, brackish water, reverse osmosis, permeable membranes, hydraulic pumps, efficiency

Introduction/Background

We are a group of students pursuing the University Master in Industrial Engineering specialised in Hydraulic Engineering. This project starts with the subject of Hydraulic Resources Management and Hydraulic Power Plants in which the theme of desalination was covered.

The main objective of this investigation is to study the inverse osmosis process, focusing on energy consumption and how it can be recuperated.

Summary/Conclusions

After studying the course of Hydraulic Resources Management and Hydraulic Power Plants, we have increased our knowledge about desalination and the different hydraulic sources and how they can be used in an effective way.

References

Webpage: <https://www.utilities-me.com/news/12448-energy-recovery-bags-49mn-deal-for-for-desalination-projects-in-uae>

Webpage: <http://www.energtrade.com/turbinas-francis/>

CFD Study on the Impact of Combustion and Radiation Models in Aluminium Scrap Furnaces

G. Lopez-Ruiz^{1*}, I. Garcia-Beristain¹, J.M. Blanco Ilzarbe²

¹BCAM – Basque Center for Applied Mathematics, Mazarredo 14, E48009 Bilbao, Basque Country – Spain

²Energy Engineering Department, School of Engineering, Building I, University of the Basque Country, Plaza Ingeniero Torres Quevedo s/n, 48013, Bilbao, Spain

*Corresponding author: glopez@bcamath.org

Abstract

Considering a simplified aluminium scrap furnace, the impact of different combustion and radiation CFD models was studied. The Eddy Dissipation (EDM) and Eddy Dissipation Concept (EDC) models were used to simulate the turbulent combustion process, whereas the radiative heat transfer was solved using the P1 and fvDOM models respectively [1].

Keywords: CFD modelling, Furnaces, Combustion, Radiation

Introduction/Background

Industrial flows can be predicted and reproduced through CFD simulations. Nevertheless, computational costs and modelling difficulties could be prohibitive in problems with strong coupling between different physical phenomena. Since CFD simulations for aluminium scrap furnaces could lead to the mentioned difficulties [1], the present poster summarises a baseline CFD study to evaluate the impact of simple and complex combustion and radiation models in such cases.

Discussion and Results

In comparison with the EDC model, EDM was able to predict the general temperature distribution and recirculation vortices within the chamber, showing more homogeneous temperatures in the post-flame region. The temperature distribution through the aluminium load and the chamber centerline demonstrated that the P1 model was able to predict the temperature distributions with

minor deviations with respect to the fvDOM.

Summary/Conclusions

EDM presents good qualitative results despite the higher peak temperatures and slightly different distributions comparing to the EDC. In terms of accuracy/cost, it can be a good alternative for parametric calculations due to its lower computational cost. Moreover, the P1 and fvDOM models showed similar behaviour, indicating that the P1 model would be sufficient to capture the temperature distribution in the present case.

Acknowledgements

Bizkaiko Foru Aldundiak finantzatu du proiektu hau, 2021eko Teknologia Transferentzia Programaren barruan eta FEDER funtsaren kofinantziazioa ere badauka / Este proyecto ha sido financiado por la Diputación Foral de Bizkaia dentro del Programa Transferencia Tecnológica 2021 y cuenta con cofinanciación del FEDER.



References

- [1] Versteeg, H, Malalasekera, W., An Introduction to CFD, Pearson, 2009.
- [2] Zhou, B., Yongxiang, Y., Reuter, M.A., Boin, U. 4th International Conference on CFD in the Oil and Gas, Metallurgical & Process Industries, 2005.



Desalination Of Brackish Water And Seawater In Spain By The Faculty Of Engineering In Bilbao

M. Díez, D. Herrero, X. Landa, A. Martínez, O. Peña, J. San Juan, P. San Pelayo, I. Serna

Faculty of Engineering in Bilbao - UPV/EHU

Abstract

The water catchment in Spain is of 3188 million of cubic meters per year. This water comes from three different sources: superficial water, underground water or desalination. For any of the sources, the water will undergo a treatment process before human consumption, being the reverse osmosis the main part of desalination plants. From all the water in Spain, 154 million of cubic meters per year are produced by desalination, being the Canary Islands the main producers [1]. In Spain, there are 765 desalination plants, both for seawater and brackish water. The total capacity of these plants is 5 million cubic meters per day [2], which would lead to 1825 million cubic meters per year, quite lower than the real produced amount mentioned before. The main reason for the low production by desalination is the cost derived from the high quantities of energy needed for the reverse osmosis.

Keywords: desalination, reverse osmosis, seawater, brackish water

Introduction

At the Faculty of Engineering Bilbao we have the option to work with a company, but being at the university. They are the so-called "Company rooms". One of the companies working with the University of the Basque Country in this way is the "Consorcio de Aguas Bilbao Bizkaia", and we form de "Water room", in which eight students work in our end of master projects. We have carried out this poster, as part of the program. Even if we come from different academic backgrounds (Industrial Engineering, Chemistry, Renewable energies and so on) the knowledge about desalination is useful for all of us, and doing this research has improved it.

Research

Actually, Spain is one of the countries in the world that produces the most desalination water, as it is the fourth country in terms of installed capacity, behind only Saudi Arabia, the United States and the United Arab Emirates.

There are currently 765 desalination plants installed in Spain with a production of more than 100 m³/day, of which 360 are

seawater desalination plants and 405 are brackish water desalination plants. In terms of production, 99 are high-capacity desalination plants (production between 10.000 and 250.000 m³/day), 450 are half-capacity desalination plants (production between 500 and 10.000 m³/day) and 216 are small-capacity desalination plants (production between 100 and 500 m³/day) [2].

According to the most up-to-date data (AEDyR-Spanish Association of Desalination and Reuse), around 5.000.000 m³/day of desalinated water is currently produced in Spain for water supply, irrigation and industrial applications.



Figure 1. Main desalination plants in Peninsular Spain [3]

The main part of the desalinated water is produced in the Canary Islands, with almost 80% of the total being distributed in these islands. This is due to the lack of other sources and the development of these desalination plants during the years.



Figure 2. Main desalination plants in the Canary Islands [4]

Conclusions

Spain is one of the main countries producing desalination water. That is why the students in areas such as hydraulics should have general knowledge in this topic. With this project, we aim to analyze the situation in Spain and its potential as a source of water.

References

- [1] Instituto Nacional de Estadística (INE), «Survey on water supply and sewerage,» [En línea]. Available: <https://www.ine.es/jaxiPx/Tabla.htm?path=/t26/p067/p01/serie/I0/&file=01001.px&L=1>.
- [2] Asociación Española de Desalación y Reutilización (AEDYR), «Desalation numbers in Spain,» [En línea]. Available: <https://aedyr.com/cifras-desalacion-espana/>.
- [3] Aquae Fundation, «Desalination plants in Spain,» [En línea]. Available: <https://www.fundacionaquae.org/wiki/plantas-desaladoras-en-espana/>.
- [4] Centro Canario del Agua, «Listado de desaladoras de Canarias».

Solar Thermal Façades and Heat Pumps; A case study

P. Elguezabal^{1*}, J.M. Blanco² and J.C. Chica¹

¹TECNALIA, Basque Research and Technology Alliance (BRTA), Astondo Bidea, Edificio 700, Parque Tecnológico de Bizkaia, 48160 Derio, Spain

²Department of Energy Engineering, School of Engineering, UPV/EHU, Plaza Ingeniero Torres Quevedo 1, 48013, Bilbao, Spain

*Corresponding author: peru.elguezabal@tecnalia.com

Abstract (12-pt Times New Roman)

Renewable energy is a necessary factor to consider as part of the process to develop highly efficient buildings. Although intermittently, solar energy is unlimited and with a very high potential to be used to cover energy necessities. Alternatively, Heat Pumps (HP) represent a technology that, if properly and efficiently operated, can also be considered as renewable solution as well.

The interaction of Solar Thermal Façades (STF) [1] and HPs, two technologies that separately have demonstrated its potential are considered in combination for this study. The research considers a case study of Solar Assisted Heat Pump (SAHP) [2] located in Derio, Spain and demonstrates the potential of this combination to significantly improve the energetic efficiency of buildings.

Keywords: Solar Thermal Façade; Unglazed Collector; Solar Assisted Heat Pumps;

Introduction/Background

In the path towards the decarbonization the energetic performance of buildings is one of the key actors. The improvement, renovation and adaptation of all the built heritage implies a mastodontic effort. The solution is not simple neither straightforward. There's no "one fits all" intervention that is always usable, but a set of multiple technologies and systems with different implications and behaviours. There's a necessity to combine and adapt all those different systems, devices and solutions enabling a higher flexibility to cover a wider scope of scenarios.

This study highlights the potential benefits of a SAHP [2], when an unglazed solar façade [3] and a heat pump are used in a synergetic combination. A total surface of 18 m² connected to the source

side of a 6 kW electrically-driven liquid-to-liquid heat pump a result, were installed and tested at Tecnalía's Kubik® experimental building in Derio, Spain.

The combined system was measured during 7 months in 2018 monitoring the performance of both the SAF and of the HP.

Discussion and Results

A short summary of experimentally measured parameters and a succinct discussion of key results through figures and tables will be presented.

Summary/Conclusions

STF and HP individually, both are interesting solutions for improving the efficiency of buildings. But a synergetic combination of both technologies represents a more ambitious opportunity to boost the performance of combined systems.

Acknowledgements

Thanks to Research group IT1415-22.

References

- [1] Zhang, X., Shen, J., Lu, Y., He, W., Xu, P., Zhao, X., Dong, X. Active Solar Thermal Facades (ASTFs): From concept, application to research questions. *Renewable and Sustainable Energy Reviews*, 2015.
- [2] Wang, Z., Guo, P., Zhang, H., Yang, W., Mei, S. "Comprehensive review on the development of SAHP for domestic hot water", *Renewable and Sustainable Energy Reviews*, 2017.
- [3] Munari Probst, M.C., Roecker, C., *Architectural Integration and Design of Solar Thermal Systems*. 1st Edition. EPFL Press. Lausanne, Switzerland, 2011.

Analysis of the heat transfer during the filling and cooling of die cast pieces with large surface through CFD.

Primitivo Carranza Torme^{1,*} and Jesús M^a Blanco Ilzarbe²

¹ UPV/EHU, School of Engineering, Energy Engineering Dept.

Plaza Ingeniero Torres Quevedo 1, 48013 Bilbao, Spain

*Corresponding author: primitivo.carranza@ehu.es

Abstract

In casting steel parts, the old unwritten foundry rules said never to feed or fill the part mold with liquid metal above 0.8 m/s. This rule described very well the existence of defects that appeared when it was not respected. This practical knowledge observes in all the traditional filling methods used in the foundry technique. It's a choice prior to the designer and then transferred to the filling and cooling simulation software.

The definition of the physical problem of what happened at higher speeds has not been addressed until the recent studies of Dr John Campbell. In these studies, the bifilm theory is qualitatively developed, which conceptually describes what they discovered in the aluminum smelter.

Our work continues with this study in steel parts. It works with the defects found in real pieces, recategorizing them and proposing physical simulation alternatives to quantify them. This article also emphasizes in the need to develop a mathematical model of the bifilm theory to be able to implement it in the CFD trading software of the metal and the formation of the faults.

Keywords: Cast, , Bifilm, Steel foundry, Defects, Numerical analysis, Fluid dynamics, Flow 3D.

Introduction.

Since the 1980s, there has been a profound technological change in the field of metals and materials, driven by strong competitive pressures. The boxes of mold and the supply channels need to be carefully optimized in order to control the correct directions of solidification trying to avoid these faults [1]. Finally a fully experimental work was carried out in order to validate the computational model considering different

parameters such as time, temperature, velocity and geometrical design of the mold [2].

Summary/Conclusions

The experiments carried out and their computational verification have allowed us to adapt the costs and design times to propose this verification methodology in large pieces and, therefore, with high costs [3].

And most importantly, we open up a field of research that has not been tackled to date (although it was detected by Professor Campbell's studies) [4] on what happens to metals in a liquid state (temperature greater than 1000°) moving in a very turbulent regime (speeds greater than 1 m/s) involving Reynolds $Re > 4000$.

Acknowledgements

Authors deeply acknowledge the research group IT1514-22 for the guidance provided.

References

- [1] K. Maeda and T.H.C. Childs, Laser sintering of hard metal powders for abrasion resistant coatings. *Journal of Materials Processing Technology*, 149, 1, 609-615 (2004).
- [2] T. Furumoto, T. Ueda, T. Amino and A. Hosokawa, A study of internal face finishing of the cooling channel in injection mold with free abrasive grains, *Journal of Materials Processing Technology*, 211, 1742-1748, (2011).
- [3] Wang, W., Ji, C., Luo, S., Zhu, M., Modeling of Dendritic Evolution of Continuously Cast Steel Billet with Cellular Automaton, *Metallurgical and Materials Transactions B: Process Metallurgy and Materials Processing Science*, 49, 1, 200-212, (2018).
- [4] J. Campbell, *Castings - The New Metallurgy of Cast Metals* 2nd Ed, Butterworth, 2003.

Evaluation of burning alternative fuels in thermal power plants as a previous step towards a full scale implementation

Francisco Peña Fernandez and Jesús M^a Blanco Ilzarbe

UPV/EHU, School of Engineering, Energy Engineering Dept.

Plaza Ingeniero Torres Quevedo 1, 48013 Bilbao, Spain

*Corresponding author: fpfbg@telefonica.net

Abstract

Alternative fuels are being considered in gas turbines given the scarcity and costs of conventional fossil fuels but also due to climate change concerns. This paper is focused on a comparative study of performance and emissions between fossil and alternative fuels.

A fully CFD model was built as a result of the full CHEMKIN® implementation, based on the results provided by a scaled experimental facility, fully monitored and ready for burning both fossil and alternative fuels such as natural gas and a gas derived from biomass respectively. It is demonstrated a good agreement between the experimental data and CFD results, which validates the computational model and justify its use for further characterizations of other fuels prior to a big scale implementation in a thermal power plant.

Keywords: Alternative fuels, bio gas, CFD, efficiency, natural gas.

Introduction.

Natural gas expectations as fuel replacement in some sectors are suffering a substantial increase but the most important fact is that recent increases in crude oil prices have brought alternative fuels into the energy scenario. General Electric, Pratt & Whitney, and other gas turbine manufacturers, have been testing these fuels in their machines for a long time [1]. Today, bio-fuels have an additional attraction as they are considered “renewable sources” which is a strong argument for the success of their implementation [2].

Gas derived from biomass (BG) obtained in fluidized beds has been revealed as a credible option [3]. The gas matrix contains high traces of ashes, which are crucial to be eliminated,

otherwise the gas would not be suitable for burning in gas turbines due to the enormous abrasive action of the exhaust gases caused by the high temperature (around 800°C) combined with a high speed around the blades as described in [4].

Conclusions

The complete methodology for the evaluation of the boiler and global efficiencies associated to the burning of NG and BG (regarding both Gross and Lower Calorific Values) with a innovative improvement on the definition of the “difficult evaluation losses term” has also been carried out here, obtaining for the Bio Gas and Bio Oil values really close to the ones referred to the Natural Gas (such as 92 % and 39 % for boiler and global efficiency respectively).

Acknowledgements

Authors deeply acknowledge the research group IT1514-22 for the guidance provided.

References

- [1] I. Gökalp, E. Lebas, Alternative fuels for industrial gas turbines, *Appl. Therm. Eng.*, 24, 2004, 1655-1663
- [2] J.M. Blanco, F. Peña, Analytical study of the effects of the clogging of a mechanical precipitator unit in air preheaters in a high-performance thermoelectric power plant based on available data. *ASME J. Eng. for Gas Turbines and Power*, 130(2), 2008, 22001-22007.
- [3] M. Moliere, Expanding fuel flexibility of gas turbines, *Journal of Power and Energy*, 219/2, 2005, 109-119.
- [4] J.M. Blanco, F. Mendía, F. Peña, Comparative analysis of CO₂ and SO₂ emissions between combined and conventional cycles with natural gas and fuel oil consumption over the Spanish thermal power plants, *Fuel*, 85, 2006, 1280-1285.

Experimental Study of a Two-Stage Compression R744 refrigeration System with Vapour Injection and Inter-Cooling.

J. Vega¹, S. Gendebien¹ and V. Lemort^{1*}

¹University of Liège, Energy Systems Research Unit, Liège 4000, Belgium.

*Corresponding author: jivega@uliege.be

Abstract

Current trends in CO₂ supermarket refrigeration have somewhat left Two-Stage compression system architectures out of the main spotlight. In this work, a Condensing Unit for CO₂ supermarket refrigeration is tested in a climatic chamber. The system includes a Two-Stage rolling pistons compressor with vapor injection and inter-cooling. The condensing unit is tested in several operating conditions to characterize the system COP, with a special focus on also assessing the compressor performance.

Keywords: CO₂ refrigeration, Two-Stage Compression, Vapour-Injection, Inter-Cooling.

Introduction/Background

The F-gas regulation demand that HVAC&R researchers find cleaner and more efficient technologies. In the refrigeration sector, it has revived the interest in applying carbon dioxide (R744) as a refrigerant fluid. Mainstream attention is leaning primarily towards ejector solutions [1]. However, Vapour-Injection (VI) solutions could offer significant advantages [2]. This work presents an experimental study on a commercial Condensing Unit using a rolling pistons Two-Stage compressor that allows for VI and Inter-Cooling (IC).

Discussion and Results

The COP of the system varies from 3.6 at $T_{gc,out} = 24$ [°C] to 1.6 at $T_{gc,out} = 40.5$ [°C] at Medium Temperature working conditions. The ambient to gas-cooler temperature approach temperature when in subcritical is around 6-8 [K] and 2-4 [K] when in transcritical. Pressure ratios are higher for the first stage of compression. The internal heat exchanger assures that the liquid

flowing to the expansion valve has enough sub-cooling, increasing cooling capacity. For the tested conditions, VI and IC assure that 2nd stage discharge temperature never exceeds 61.7 [°C].

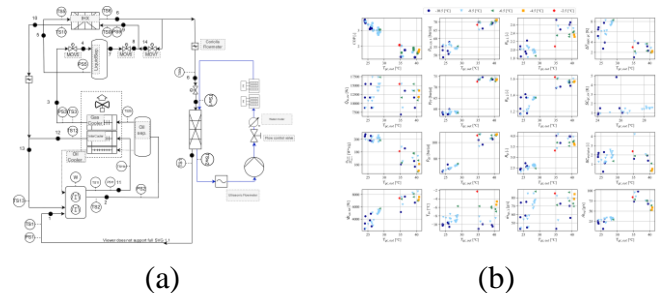


Figure : Schematic of the system architecture (a) and overview of the test results (b).

Summary/Conclusions

A CO₂ commercial Condensing Unit for supermarket refrigeration has been tested. The system includes a Two-Stage rolling pistons compressor that allows for VI and IC. The COP at ambient temperature of 20 [°C] proves to be about 3.0 [-].

Acknowledgements

This work was funded by the National Agency for Research and Development (ANID) / Scholarship Program Doctorado Becas Chile/2017 - 72180512.

References

- [1] Gullo, P., Hafner, A. & Banasiak, K., 2018. Transcritical R744 refrigeration systems for supermarket applications: Current status and future perspectives. *International Journal of Refrigeration*, Volume 93, pp. 269-310.
- [2] Baek, C. et al., 2014. Effects of vapor injection techniques on the heating performance of a CO₂ heat pump at low ambient temperatures. *International Journal of Refrigeration*, Volume 43, pp. 26-35.